SCHOLARLY PUBLICATIONS

A CURRENT AWARENESS BULLETIN
OF RESEARCH OUTPUT

@DTU

(56th Edition)

AUGUST 2017

BY: CENTRAL LIBRARY

DELHI TECHNOLOGICAL UNIVERSITY
(FORMERLY *DELHI COLLEGE OF ENGINEERING)*
GOVT. OF N.C.T. OF DELHI
SHAHBAD DAULATPUR, MAIN BAWANA ROAD
DELHI 110042

PREFACE

This is the **Fifty sixth** Issue of Current Awareness Bulletin started by Delhi Technological University, Central Library. The aim of the bulletin is to compile, preserve and disseminate information published by the faculty, students and alumni for mutual benefits. The bulletin also aims to propagate the intellectual contribution of Delhi Technological University (DTU) as a whole to the academia.

The bulletin contains information resources available in the internet in the form of articles, reports, presentations published in international journals, websites, etc. by the faculty and students of DTU. The publications of faculty and student which are not covered in this bulletin may be because of the reason that the full text either was not accessible or could not be searched by the search engine used by the library for this purpose.

The learned faculty and students are requested to provide their uncovered publications to the library either through email or in CD, etc to make the bulletin more comprehensive.

This issue contains the information published during **August 2017**. The arrangement of the contents is alphabetical. The full text of the article which is either subscribed by the university or available in the web is provided in this bulletin.

Central Library

CONTENTS

1. A New Closed-Form Expressions of Channel Capacity with MRC, EGC and SC Over Lognormal Fading Channel, Diwaker Tiwari, ***3.Sanjay Soni*** and Puspraj Singh Chauhan, Electronics and Communication, DTU

2. A new Heuristic Method RPW Method and Genetic algorithm techniques (hybrid method) For Evaluating Multi Product Assembly Line Balancing – A Case Study, Ashutosh Kumar, Hukam Singh, ***7.Ashutosh Kumar Rai***, and Avnish Kumar Shukla, Mechanical, DTU

3. A Study of Active Brake System of Automobile, ***3.Roop Lal***, ***3.RC Singh***, ***7.Vaibhav Sharma*** and ***6.Vaibhav Jain***, Mechanical, DTU

4. A Unified Approach for Classification of Software Reliability Models, Kuldeep Singh Kaswan, Sunita Choudhary and ***3.Kapil Sharma,*** Computer Science, DTU

5. ACHIEVING ENERGY EFFICIENCY AND STABILITY IN WSN USING A NOVEL MOBILE SINK APPROACH BASED ON BIOGEOGRAPHY BASED OPTIMIZATION, Ajay Kaushik and ***6.Amit Kumar Gautam,*** ECE, DTU

6. An integrative system biology approach to unravel potential drug candidates for multiple age related disorders, ***3.Isha Srivastava***, Pooja Khurana, Mohini Yadav and ***3.Yasha Hasija***, Biotechnology, DTU

7. Analysis of Coverage and Connectivity on Channel Randomness in WSN, Anurag Tanwar, ***6.Sakshi Choudhary*** and Annad Kumar Jha, ECE, DTU

8. Anticancer agent from medicinal plants: a review, ***7.Arpita Roy***, ***6.Tushita Attre*** and ***3.Navneeta Bharadvaja***, Biotechnology, DTU

9. Centella Asiatica: A Pharmaceutically Important Medicinal Plant, ***7.Arpita Roy*** and ***3.Navneeta Bharadvaja***, Biotechnology, DTU

10. Covalent and non-covalent chemical engineering of actin for biotechnological applications, ***6.Saroj Kumar*** and Alf Mansson, Biotechnology, DTU

11. Design and Development of Stand-Alone Renewable Energy based Hybrid Power System for Remote Base Transceiver Station, Priyanka Anand, Sarbjeet Kaur Bath and ***3.Mohammad Rizwan***, Electrical, DTU

12. Design of Polar-Fuzzy-Controller to Impair Current Harmonics in Power System, Harsha Vanjani, Meha Sharma and ***7.1.U. K. Choudhry***, ECE, DTU

13. Detection of circular Rydberg states in lifetime measurements, ***6.Gaurav Sharma*** and ***3.Nitin K. Puri***, Applied Physics, DTU

14. Digitally controlled portable micropump for transport of live micro-organisms, ***7.1.Rishi Kant***, Deepak Singh and Shantanu Bhattacharya, Mechanical, DTU

15. Discussion of "Exact Solution of the Friction Circle Method" by Jozsef Garai, ***3.Anjeshnu Trivedi*** and S.M.ASCE, Civil, DTU

16. Ecological Benefits of Reviving Urban Water Bodies using Rainwater Harvesting, ***6.Paridhi Rustogi*** and ***3.SK Singh***, Environmental, DTU

17. Effect of flyash particles with aluminium melt on the wear of aluminium metal matrix composites, ***6.Vipin K. Sharma***, ***3.R.C. Singh*** and ***3.Rajiv Chaudhary***, Mechanical, DTU

18. Effective Utilization of Fuzzy System and Fuzzy Logic in Manufacturing: A Review of Literature, ***6.S. Singhal***, ***3.Ranganth M.S***, ***6.R. Batra*** and ***6.S. Nanda***, Mechanical, Production &Industrial and Automobile, DTU

19. Energy, exergy, environment and economic analyses and optimization of two-stage absorption–compression combined refrigeration system, Manoj Dixit1, ***3.Akhilesh Arora*** and S. C. Kaushik, Mechanical, DTU

20. Exergy and energy analysis of modified organic rankine cycle for reduction of global warming and ozone depletion, ***3.Radhey Shyam Mishra*** and ***6.Yunis Khan***, Mechanical Production & Industrial and Automobiles, DTU

21. Experimental investigation for enhancing thermal performance of vapour compression refrigeration system using nano fluids, ***3.R.S. Mishra*** and ***6.Devendra Kumar***, Mechanical, Production & Industrial and Automobiles, DTU

22. Experimental Study on Light Transmitting Concrete, ***3.Awadhesh Kumar*** and ***7.Rahul Ahlawat***, Civil, DTU

23. Extractive Summarization using Deep Learning, ***6.Sukriti Verma*** and ***6.Vagisha Nidhi***, DTU

24. Effcient Fingerprint Extraction and Matching Using Smartphone Camera, ***8.Saksham Gupta***, ***8.Sukhad Anand***, and Atul Rai, Computer Science, DTU

25. Finite difference solver for couette flow with applied pressure gradients, ***Mrudang Mathur, 8.Nehal Amit Jajal*** and ***3.Raj Kumar Singh***, Mechanical, DTU

26. Formalism to Study the Effect of Hydrogen on the Plasma-Assisted Growth and Field Emission Properties of the Graphene sheet, ***6.N. Gupta***, ***3.S. C. Sharma*** and ***6.R. Gupta***, Applied Physics, DTU

27. Identification of a Novel Class of BRD4 Inhibitors by Computational Screening and Binding Simulations, Bryce K. Allen, ***3.Saurabh Mehta***, Stuart W. J. Ember, Jin-Yi Zhu, Ernst Schönbrunn, Nagi G. Ayad and Stephan C. Schürer, Applied Chemistry, DTU

28. Integrated Kano Model and QFD in Designing Passenger Car, Mahesh Kumar Shukla, ***3.Ranganath MS*** and BS Chauhan, Mechanical, DTU

29. Investigation of Strength Characteristics of Concrete by Replacing Curing Water with Self Curing Compounds, ***6.Siddharth Jain***, Civil, DTU

30. Isolation, Identification and biomass productivity analysis of microalga Scenedesmus rubescens from DTU Lake, ***Lakhan Kumar, 6.Arpita Roy, 6.Gaurav Saxena, 6.Koyel Kundu*** and ***3.Navneeta Bharadvaja***, Biotechnology, DTU

31. Lead-lag relationship between futures and spot FX market in India, ***6.Varuna Kharbanda*** and ***3.Archana Singh***, DSM, DTU

32. Measurement of low cross section transition using versatile absorption technique, ***6.Gaurav Sharma***, ***6.T. Nandi*** and ***3.Nitin K. Puri***, Applied Physics, DTU

33. Mechanistic insights into the anticancer mode of action of an herbal drug, ***6.Nupur Jauhari***, Nidhi Chadha, ***7.Himani Raina***, ***3.Navneeta Bharadvaja*** and ***7.Garima Soni***, Biotechnology, DTU

34. Modelling graphene sheet growth subjected to plasma containing negatively charged ions, ***N. Gupta***, ***3.S. C. Sharma*** and ***R. Gupta***, Applied Physics, DTU

35. Multiobjective Economic Load Dispatch in 3-D Space by Genetic Algorithm, ***3.N. K. Jain*** and ***3.Uma Nangia*** and Iqbal Singh, Electrical, DTU

36. Optimum yield parameters of MWCNT/MnO2 nanocomposite, Md Zakir Hussain, Sabah Khan, Abhishek Gaur and ***3.Mohd Shuaib***, Mechnical, DTU

37. Organizational Justice Perception: An Unconventional Strategy to Manage Diverse Workforce, ***3.Anu Singh Lather*** and Simran Kaur, DTU

38. Performance Evaluation of Biosignal Ring for Reduction of Pollution Level in Diesel and Petrol Engines, ***3.S. K. Singh***, ***8.Surbhi Jain***, ***8.Tejasvini Ahuja***, ***8.Yukti Sharma*** and ***8.Nidhi Pathak***, Environmental, DTU

39. Photoluminescence and Energy Transfer studies of Dy3+ Ions doped Lithium Lead Alumino Borate Glasses for w-LED and Laser Applications, ***6.Nisha Deopa*** and ***3.A. S. Rao***, Applied Physics, DTU

40. Social Profile Aware AODV Protocol for Ad-Hoc Social Networks, ***7.1.Nagender Aneja*** and Sapna Gambhir, Computer Technology and Applications, DTU

41. Theoretical Investigations to Study the Effect of C2H2/H2 gas ratio on the Multi-walled Carbon Nanotubes Growth, ***6.U. Sharma***, ***3.S. C. Sharma***, ***6.R. Gupta*** and ***6.N. Gupta***, Applied Physics, DTU

42. Thermodynamic analysis of vapour absorption system using waste heat of gas turbine plant with intercooling, ***3.R.S Mishra*** and ***6.Mayank Agarwal***, Mechanical, Production & Industrial and Automobile, DTU

43. Third party logistics (3PL) selection for cold chain management: a fuzzy AHP and fuzzy TOPSIS approach, Rajesh Kr. Singh Angappa Gunasekaran and ***3.Pravin Kumar***, DTU

44. Threshold power of amplitude modulated laser beam in complex plasma, ***6.R. Sharma*** and ***3.S. C. Sharma***, Applied Physics, DTU

45. Usage of electronic resources at University of Delhi: a case study, Narender Kumar and ***3.Lalita***, Central Library, DTU

46. Vapour compression refrigeration systems using nano materials mixed with R718 in secondary circuit of evaporator for enhancing thermodynamic performances, ***3.Radhey Shyam Mishra***, Mechanical, Industrial, Production and Automobiles, DTU

1. *Chancellor*

2. *Pro Vice Chancellor*	***2.1.*** *Ex Pro Vice Chancellor*
3. *Faculty*	***3.1.*** *Ex Faculty*
4. *Teaching-cum-Research Fellow*	***4.1.****Asst. Librarian*
5. *Alumni*	
6. *Research Scholar*	***6.1.*** *Ex Research Scholar*
7. *PG Scholar*	***7.1.*** *Ex PG Scholar*
8. *Undergraduate Student*	***8.1.*** *Ex Undergraduate Student*

Wireless Pers Commun
DOI 10.1007/s11277-017-4719-9

A New Closed-Form Expressions of Channel Capacity with MRC, EGC and SC Over Lognormal Fading Channel

Diwaker Tiwari[1] · **Sanjay Soni**[1] · **Puspraj Singh Chauhan**[1]

© Springer Science+Business Media, LLC 2017

Abstract In this work, we derive the closed-form expressions of channel capacity with maximal ratio combining, equal gain combining and selection combining schemes under different transmission policies such as optimal power and rate adaptation, optimal rate adaptation, channel inversion with fixed rate (CIFR) and truncated CIFR. Various approximations to the intractable integrals have been proposed using methods such as Holtzman and Gauss–Hermite approximations and simpler expressions are suggested. Moreover, as an application, the channel capacity of lognormally distributed fading channel in the interference-limited environment is discussed. The obtained closed-form expressions have been validated with the exact numerical results.

Keywords Channel fading · Wireless communication · Channel capacity · Probability distribution function · Shadowing

1 Introduction

Channel capacity over a fading channel gives an estimation of maximum possible transmission rate with minimal error and thus, is important from both information theoretic as well as practical view point. This parameter has been investigated in [1, 2] over lognormal (LN) shadowing under various power allocation schemes. In [1], Gaofeng et al. have analysed the channel capacity under schemes such as optimal power and rate adaptation (OPRA), optimal rate adaptation (ORA), and channel inversion with fixed rate (CIFR) only for single input- single output (SISO) channel. In [2], Karmeshu et al. have derived closed-form expressions of the channel capacity for ORA, OPRA, CIFR and truncated CIFR using moment generating function (MGF) approach without any diversity schemes and claimed to achieve simpler closed-form expressions compared to [1].

✉ Sanjay Soni
sksoni98fece@gbpec.ac.in

[1] G. B. Pant Engineering College, Pauri, India

Published online: 01 August 2017

The goal of the present work is to derive the closed-form expressions for channel capacity under various definitions such as ORA, OPRA, CIFR and truncated CIFR with various diversity schemes, as maximal ratio combining (MRC), equal gain combining (EGC) and selection combining (SC). The expressions are shown to be mathematically very simple compared to [1, 2] enabling them to explain clearly the behaviour of system over lognormal fading parameters. Moreover, the results are shown to be accurate for entire range of shadowing (2–12 dB) for various wireless applications. In the last, a case of channel capacity in a co-channel interference (CCI) limited environment is discussed and compared for various transmission schemes.

The outline of the paper is as follows. In Sect. 2, closed-form expressions of channel capacity are derived for different diversity schemes. The numerical results and discussions are presented in Sect. 3. In Sect. 4, as an application, a cellular system with CCI environment is considered and the channel capacity is analysed for various transmission schemes. Section 5 concludes the work.

2 Closed Form Expressions for Channel Capacity with Diversity

2.1 MRC and EGC

The instantaneous signal-to-noise ratio (SNR) of maximal ratio combiner and equal gain combiner output are, respectively, given as

$$\gamma_{MRC} = \sum_{k=1}^{L} \gamma_k, \quad \gamma_{EGC} = \frac{1}{L}\left(\sum_{k=1}^{L} \sqrt{\gamma_k}\right)^2$$

where L is the diversity order and γ_k is the instantaneous SNR of kth branch. Sum of lognormal random variable(RV) may be approximated by another lognormal RV, hence mean and standard deviation for MRC and EGC are given by Laourine et al. [3, Section III]

$$\mu_{MRC} = \xi \ln(L\Gamma) - \frac{\sigma_{MRC}^2}{2\xi}, \quad \sigma_{MRC}^2 = \xi^2 \ln\left(\frac{L - 1 + e^{\frac{\sigma^2}{\xi^2}}}{L}\right)$$

$$\mu_{EGC} = \xi \ln\left(\Gamma + \Gamma(L-1)e^{-\frac{\sigma^2}{4\xi^2}}\right) - \frac{\sigma_{EGC}^2}{2\xi}, \quad \sigma_{EGC}^2 = 4\xi^2 \ln\left(\frac{L - 1 + e^{\frac{\sigma^2}{4\xi^2}}}{L}\right)$$

where $\xi = 10/\ln 10$, each branch has average SNR Γ, mean μ and standard deviation σ.

2.2 Selection Combining

For independent and identically distributed (i.i.d.) channel scenario, the cumulative distribution function (CDF) of SC output is given by

$$F_{sc}(\gamma) = (F(\gamma))^L \tag{1}$$

where $F(\gamma)$ is CDF of individual branch output SNR, is given as $Q[(\mu - \ln\gamma)/\sigma]$ and L is the diversity order. This can be further simplified using [4, Eq. (2) and Table II] as

$$F_{sc}(\gamma) \approx \begin{cases} \sum_{r=0}^{L}\sum_{r_1=0}^{r}\left[\binom{L}{r}(-1)^r\binom{r}{r_1}\left(\frac{a_1}{2}\right)^{r-r_1}\left(\frac{a_2}{2}\right)^{r_1}\right. \\ \left.\times exp\left(-\left(\sqrt{b(r+r_1)}\frac{(\ln\gamma-\mu)}{\sqrt{2}\sigma}\right)^2\right)\right] & \text{if} \quad \gamma \geq e^{\mu} \\ \sum_{r=0}^{L}\binom{L}{r}\left(\frac{a_1}{2}\right)^{L-r}\left(\frac{a_2}{2}\right)^{r} exp\left(-\left(\sqrt{b(L+r)}\frac{(\ln\gamma-\mu)}{\sqrt{2}\sigma}\right)^2\right) & \text{if} \quad \gamma < e^{\mu} \end{cases} \tag{2}$$

Probability distribution function (PDF) of SC is obtained by differentiating (2) with respect to γ yields

$$f_{sc}(\gamma) \approx \begin{cases} \frac{L}{\sigma\gamma\sqrt{2\pi}}\sum_{r=0}^{L-1}\sum_{r_1=0}^{r}A_1\exp\left[-\left(\frac{\ln\gamma-\mu}{\sigma\sqrt{2p}}\right)^2\right] & \text{if} \quad \gamma \geq e^{\mu} \\ \frac{L}{\sigma\gamma\sqrt{2\pi}}\sum_{r=0}^{L-1}A_2 exp\left[-\left(\frac{\ln\gamma-\mu}{\sigma\sqrt{2p_1}}\right)^2\right] & \text{if} \quad \gamma < e^{\mu} \end{cases} \tag{3}$$

where $A_1 = \binom{L-1}{r}(-1)^r\binom{r}{r_1}\left(\frac{a_1}{2}\right)^{r-r_1}\left(\frac{a_2}{2}\right)^{r_1}$, $A_2 = \binom{L-1}{r}\left(\frac{a_1}{2}\right)^{L-1-r}\left(\frac{a_2}{2}\right)^{r}$, $p = (b(r+r_1)+1)^{-1}$ and $p_1 = (b(L+r-1)+1)^{-1}$. In Fig. 1, outage probability analysis is presented for different diversity schemes with shadowing 4 dB and diversity order, L = 2, 10.

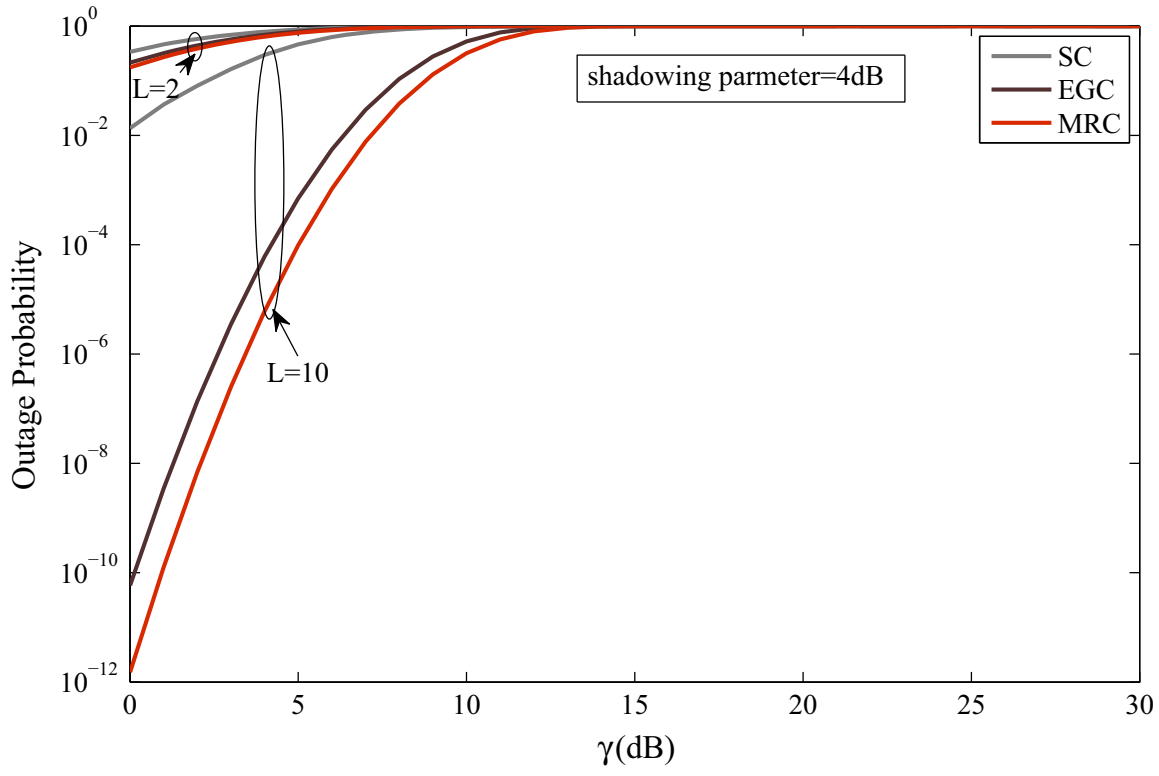


Fig. 1 Comparison of outage probability of signal in lognormal channel using different diversity schemes

2.3 Channel Capacity

In this section, we analyse the channel capacity with various definitions such as OPRA, ORA, CIFR and truncated CIFR and we consider the following possibilities: (1) channel state information (CSI) is known only to the receiver (Rx) (2) it is known to both the transmitter (Tx) and the Rx.

2.3.1 Optimum Power and Rate Adaptation

In this scheme, knowing the CSI, the Tx can adapt its power and transmission rate such that to maximize the capacity. The policy is to allocate the higher power to more deterministic channel and lesser power to the channel having low average SNR, based on water-filling algorithm. The capacity under this category is defined as [5]

$$\frac{C_{OPRA}}{B} = \int_{\gamma_0}^{\infty} \log_2\left(\frac{\gamma}{\gamma_0}\right) f_D(\gamma) d\gamma \tag{4}$$

where B is bandwidth in Hz, $f_D(\gamma)$ is lognormal PDF and subscript D is used to define EGC, MRC and SC diversity techniques. The PDF of EGC and MRC combiner output SNR, is given as

$$f_{EGC,MRC}(\gamma) = \frac{1}{\gamma\sigma_d\sqrt{(2\pi)}} exp\left[-\left(\frac{\ln\gamma - \mu_d}{\sqrt{2}\sigma_d}\right)^2\right] \tag{5}$$

where μ_d and σ_d are parameters of EGC and MRC defined in Sect. 2.1, as μ_{EGC}, μ_{MRC}, σ_{EGC} and σ_{MRC}. The expected value $E[\gamma]$, is $\gamma_{Avg} = exp(\mu_d + \sigma_d^2/2)$ and the variance is $\text{var}(\gamma) = [exp(\sigma_d^2) - 1]exp(2\mu_d + \sigma_d^2)$. We can express the mean in terms of γ_{Avg} and shadowing parameter, as $\mu_d = [\ln\gamma_{Avg} - 0.5\sigma_d^2]$. Optimal cutoff SNR γ_o must satisfy the equation $p(\gamma_o) = 0$, with $p(.)$ is defined as

$$p(x) = \int_{\gamma_o}^{\infty} \left(\frac{1}{x} - \frac{1}{\gamma}\right) f_D(\gamma) d\gamma - 1 \tag{6}$$

The integral in Eq. (4) can be split in two parts and is written as

$$\frac{C_{OPRA}}{B} = 1/\ln 2 \int_{\gamma_o}^{\infty} \ln(\gamma) f_D(\gamma) d\gamma - \ln(\gamma_o)/\ln 2 \int_{\gamma_o}^{\infty} f_D(\gamma) d\gamma \tag{7}$$

In case of maximal ratio and equal gain diversity, the second integral of Eq. (7) is easily computed using outage probability of EGC and MRC combiner output SNR with lognormal distribution as $P_{out}(\gamma_0) = 1 - Q(\frac{\ln\gamma_0 - \mu_d}{\sigma_d})$. Substituting Eq. (5) in the first integral of Eq. (7), making a change of variable $t = \frac{\ln\gamma - \mu_d}{\sigma_d}$, we obtain the closed-form of the capacity, given as

$$\frac{C_{OPRA}}{B} = \frac{1}{\ln 2}\left[\frac{\sigma_d exp(-\phi^2/2)}{\sqrt{2\pi}} + (\mu_d - \ln\gamma_o)Q(\phi)\right] \tag{8}$$

Equation (6) can be simplified using Eq. (5) as $p(x) = \frac{Q(\phi)}{x} - kQ(\sigma + \phi) - 1$, where $k = exp(-\mu_d + (\sigma_d^2/2))$, $\varphi = (\ln x - \mu_d)/\sigma_d$ and $\phi = (\ln \gamma_0 - \mu_d)/\sigma_d$. Equation (8) can further be simplified using an approximation of erfc(x) in [6, Eq. 6] and is given as

$$\frac{C_{OPRA}}{B} = \begin{cases} \sigma_d \exp(-0.5\phi^2)(\alpha + \beta \exp(-1.4\phi)) & \text{if} \quad \phi > 0 \\ 0.5745\sigma_d & \text{if} \quad \phi = 0 \\ \sigma_d[\exp(-0.5\phi^2)(\alpha + \beta \exp(1.4\phi)) - c\phi] & \text{if} \quad \phi < 0 \end{cases} \tag{9}$$

where $\alpha = 0.0685$, $\beta = 0.5071$, and c = 1.44.

In order to evaluate OPRA channel capacity for SC, one can substitute Eq. (3) in Eq. (4) and after some mathematical manipulations, the approximate form is given as

$$\frac{C_{OPRA}}{B} \approx \frac{L}{\ln 2} \begin{cases} \sum_{r=0}^{L-1} \left[\left(\sum_{r_1=0}^{r} \frac{A_1}{2} \sqrt{p} \left(\frac{\sigma\sqrt{2p}}{\sqrt{\pi}} + \mu - \ln \gamma_0 \right) \right) \right. \\ + \frac{A_2}{2} \sqrt{p_1} \left(\frac{\sigma\sqrt{2p_1}}{\sqrt{\pi}} \left(\exp(-t_2^2) - 1 \right) \right. \\ \left. \left. - (\mu - \ln \gamma_0) erf(t_2) \right) \right] & \text{if} \quad \gamma_0 \le e^{\mu} \\ \sum_{r=0}^{L-1} \sum_{r=0}^{r_1} \left[\frac{A_1}{2} \sqrt{p} \left(\left(\frac{\sigma\sqrt{2p}}{\sqrt{pi}} \exp(-t_1^2) \right) \right. \right. \\ \left. \left. + (\mu - \ln \gamma_0) erfc(t_1) \right) \right] & \text{if} \quad \gamma_0 > e^{\mu} \end{cases} \tag{10}$$

where $t_1 = (\ln \gamma_0 - \mu)/(\sigma\sqrt{2p})$ and $t_2 = (\ln \gamma_0 - \mu)/(\sigma\sqrt{2p_1})$. For SC diversity, Eq. (6) becomes

$$p(x) \approx \begin{cases} \sum_{r=0}^{L-1} \left[\left(\sum_{r_1=0}^{r} \frac{A_1}{2} \sqrt{p} \left(\frac{1}{x} - \exp\left(-\mu + \frac{\sigma^2 p}{2} \right) erfc\left(\sigma \sqrt{\frac{p}{2}} \right) \right) \right) \right. \\ \left. + \frac{A_2}{2} \sqrt{p_1} \left(-\frac{1}{x} - \exp\left(-\mu + \frac{\sigma^2 p_1}{2} \right) \left(erfc(z_2) - erfc\left(\sigma \sqrt{\frac{p_1}{2}} \right) \right) \right) \right] & \text{if} \quad x \le e^{\mu} \\ \sum_{r=0}^{L-1} \sum_{r=0}^{r_1} \frac{A_1}{2} \sqrt{p} \left(\left(\frac{erf(s_1)}{x} \right) - \exp\left(-\mu + \frac{\sigma^2 p}{2} \right) erfc(z_1) \right) & \text{if} \quad x > e^{\mu} \end{cases}$$

where $s_1 = (\ln x - \mu)/(\sigma\sqrt{2p})$, $s_2 = (\ln x - \mu)/(\sigma\sqrt{2p_1})$, $z_1 = s_1 + \sigma\sqrt{p/2}$ and $z_2 = s_2 + \sigma\sqrt{p_1/2}$.

2.4 Optimal Rate Adaptation

In this approach the CSI is known only to the Rx. Thus, the Tx does not have any policy to adapt the allocation of its power. The definition of average channel capacity is given by [5]

$$\frac{C_{ORA}}{B} = \int_0^{\infty} \log_2(1 + \gamma) f_D(\gamma) d\gamma \tag{11}$$

Substitution of Eq. (5) in Eq. (11) and resorting to Gauss Hermite (G–H) [7], the closed-form for MRC and EGC schemes can be expressed as

$$\frac{C_{ORA}}{B} \approx \frac{1}{\sqrt{\pi}} \sum_{i=0}^{N} \omega_i \log_2(1+\eta_i) \tag{12}$$

where $\eta_i = exp(\sigma_d v_i \sqrt{2} + \mu_d)$, ω and v are weights and abscissas of G–H integration [7, 8]. It may be noted that N terms series of Eq. (12) can be truncated to just five terms to closely match the exact results with mean square error ($\approx 10^{-4}$) (see Fig. 3). The integral in Eq. (11), can also be solved using an efficient approach given by Holtzman [9], [10, Eq. (18)] that gives the closed-form in terms of just three terms as follows.

2.4.1 Simpler and Accurate Approximations

If z is Gaussian-distributed RV with mean μ and variance σ^2, then, we can have the following approximation [9]

$$\begin{aligned} E[f(z)] &= \int_{-\infty}^{\infty} \frac{f(z)}{\sigma\sqrt{2\pi}} exp\left[-\left(\frac{z-\mu}{\sqrt{2}\sigma} \right)^2 \right], \\ E[f(z)] &\approx \frac{2}{3} f(\mu) + \frac{1}{6} f(\mu + \sigma\sqrt{3}) + \frac{1}{6} f(\mu - \sigma\sqrt{3}) \end{aligned} \tag{13}$$

Substituting Eq. (5) in Eq. (11), making a change of variable $\ln(\gamma) = z$ and using Eq. (13), we can write

$$\frac{C_{ORA}}{B} \approx \frac{2}{3} \log_2(1 + e^{\mu_d}) + \frac{1}{6} \log_2\left(1 + e^{\mu_d + \sigma_d\sqrt{3}}\right) + \frac{1}{6} \log_2\left(1 + e^{\mu_d - \sigma_d\sqrt{3}}\right) \tag{14}$$

Noting that, at higher average SNR of the channel, μ_d is high. As a result, $e^{\mu_d} \gg 1$ and we can write

$$\frac{C_{ORA}}{B} \approx \frac{2}{3}\mu_d + \frac{1}{6}\left(\mu_d + \sigma_d\sqrt{3}\right) + \frac{1}{6}\left(\mu_d - \sigma_d\sqrt{3}\right) = \mu_d = \left[\ln \gamma_{Avg} - 0.5\sigma_d^2\right] \tag{15}$$

This result clearly indicates that the average channel capacity is proportional to the channel SNR on logarithmic basis and the capacity deteriorates with increase in the shadowing which is an obvious impact of shadowing on channel capacity. This is in the tune with the results in [3, Eq.12].

ORA channel capacity with SC diversity is found out by putting Eq. (3) in Eq. (11) and applying Gaussian Quadratures for integral [11], the closed-form yields

$$\frac{C_{ORA}}{B} \approx \frac{1}{\sqrt{\pi}} \sum_{i=0}^{K} \Omega_i \sum_{r=0}^{L-1} \left[\left(\sum_{r_1=0}^{r} A_1 \sqrt{p} \log_2(1+\Delta_i) \right) + A_2 \sqrt{p_1} \log_2(1+\tau_i) \right] \tag{16}$$

where $\Delta_i = \exp(\sigma\delta_i\sqrt{2p} + \mu), \tau_i = \exp(-\sigma\delta_i\sqrt{2p_1} + \mu)$, Ω and δ are weights and abscissas of Gaussian Quadratures for integration for 0 to ∞ [11]. It may be noted that K terms series of Eq. (8) can be truncated to just five terms to match with the exact results with accuracy of ($\approx 10^{-3}$) (see Fig. 7).

2.5 CIFR

Channel inversion with fixed rate is based on the fact that the Tx allocates the power inversely proportional to the channel SNR such that the transmission rate remains constant. The formula for this adaptive scheme is given by [5]

$$\frac{C_{CIFR}}{B} = \log_2\left(1 + \frac{1}{E[1/\gamma]}\right) \tag{17}$$

For MRC and EGC diversity schemes, considering only the term $E[1/\gamma]$ of Eq. (17), using Eq. (5) and applying G–H integration, we get

$$E[1/\gamma] = \int_0^\infty \frac{f_D(\gamma)}{\gamma} d\gamma \approx \frac{e^{-\mu_d}}{\sqrt{\pi}} \sum_{i=1}^{N} \omega_i e^{-\sigma v_i \sqrt{2}} \tag{18}$$

where ω and v are weights and abscissas of G–H integration. After substituting Eq. (18) in Eq. (17), we obtained

$$\frac{C_{CIFR}}{B} \approx \log_2\left(1 + \frac{\sqrt{\pi} e^{\mu_d}}{\sum_{i=1}^{N} \omega_i e^{-\sigma_d v_i \sqrt{2}}}\right) \tag{19}$$

Further using [9] we can approximate $E[\frac{1}{\gamma}]$ as

$$E[1/\gamma] \approx \frac{2}{3} e^{-\mu_d} + \frac{1}{6} e^{-(\mu_d + \sigma_d \sqrt{3})} + \frac{1}{6} e^{-(\mu_d - \sigma_d \sqrt{3})} \tag{20}$$

Further simplifying Eq. (20), we get

$$E[1/\gamma] \approx \frac{1}{6} e^{-(\mu_d + \sigma_d \sqrt{3})} (e^{\sigma_d \sqrt{3}} + 3.732)(e^{\sigma_d \sqrt{3}} + 0.268) \tag{21}$$

Substituting Eq. (21) in Eq. (17), we get,

$$\frac{C_{CIFR}}{B} \approx \log_2\left(1 + \frac{6 e^{(\mu_d + \sigma_d \sqrt{3})}}{(e^{\sigma_d \sqrt{3}} + 3.732)(e^{\sigma_d \sqrt{3}} + 0.268)}\right) \tag{22}$$

For higher values of shadowing σ_d (5–12 dB), $\exp(\sigma_d \sqrt{3}) \gg 0.268$, so the denominator part of Eq. (22) can further be simplified by neglecting 0.268. Finally, we get a simple expression which is valid for shadowing in the range of 5–12 dB having wireless applications and the closed-form is given as

$$\frac{C_{CIFR}}{B} \approx \log_2\left(1 + \frac{6 e^{\mu_d}}{(e^{\sigma_d \sqrt{3}} + 3.732)}\right) \tag{23}$$

Further, we note that for higher values of σ_d (9–12 dB), $e^{\sigma_d \sqrt{3}} \gg 3.732$ (Fig. 1). This further simplifies the expression Eq. (23), as

$$\frac{C_{CIFR}}{B} \approx \log_2(1 + 6 e^{\mu_d - \sigma_d \sqrt{3}}) \tag{24}$$

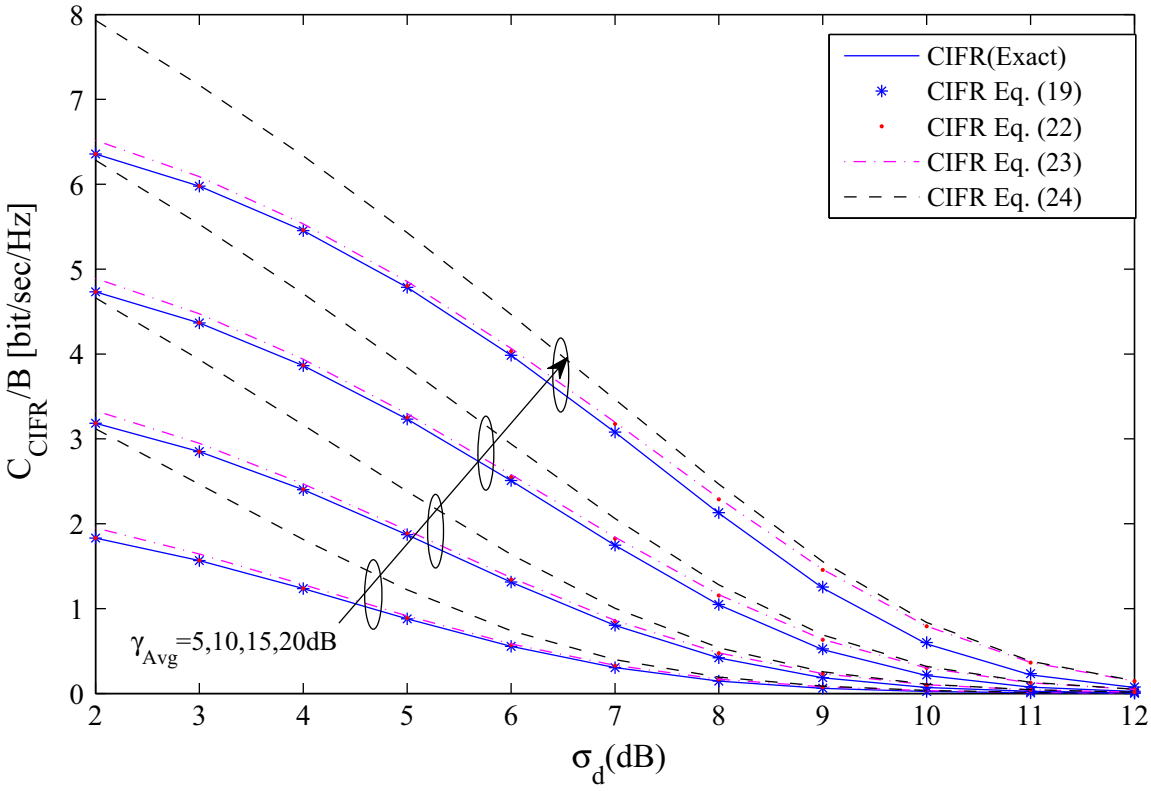


Fig. 2 Channel capacity under CIFR for different values of average SNR with diversity branch, L = 1

The expressions in Eqs. (22)–(24) have the great advantage as they are very simple and are in closed-form. They clearly explain the behaviour of the system with respect to LN parameters.

Figure 2 depicts the plots of channel capacity versus shadowing for several values of average SNR under CIFR policy. It is noted that the approximated expression Eq. (19) has an excellent agreement with exact expression Eq. (17) for all range of average SNR and shadowing parameter. This result also indicates that either on increasing average SNR or decreasing shadowing parameter CIFR channel capacity is increasing. The plot includes the upper bounds developed in Eqs. (23) and (24). Equations (23) and (24) show the tight bound, and loose bound respectively, at lower shadowing range whereas at higher shadowing they behave as a tight upper bound to CIFR capacity.

Moreover, using Eq. (3) we can derive approximate form of $E[1/\gamma]$ of Eq. (18) for SC, as

$$E\left[\frac{1}{\gamma}\right] \approx L\sum_{r=0}^{L-1}\left[\sum_{r_1=0}^{r}\left(A_1\sqrt{p}\exp(T_1)Q(\sigma\sqrt{p})\right) + A_2\sqrt{p_1}\exp(T_2)(Q(-\sigma\sqrt{p_1}))\right] \quad (25)$$

where $T_1 = 0.5\sigma^2 p - \mu$ and $T_2 = 0.5\sigma^2 p_1 - \mu$. Substituting Eq. (25) in Eq. (17) completes the closed-form of CIFR channel capacity.

2.6 TIFR

This policy is adopted to avoid the certain aspect of earlier discussed CIFR strategy where even the poorest channel is also taken into consideration and maximum power is allocated

to maintain a constant transmission rate. Here, this condition is avoided which naturally improves the capacity. Channel capacity under this scheme is defined by [5]

$$\frac{C_{out}}{B} = \log_2\left(1 + \frac{1}{\int_{\gamma_o}^{\infty} \frac{1}{\gamma} f_D(\gamma) d\gamma}\right)[1 - F_D(\gamma_o)] \tag{26}$$

Substituting Eq. (5) in Eq. (26) and considering only the integral part of Eq. (26) and after some manipulations, we obtain

$$\int_{\gamma_o}^{\infty} \frac{1}{\gamma} f_d(\gamma) d\gamma = kQ(\sigma_d + \tau) = \frac{k}{2} erfc\left(\frac{\sigma_d + \tau}{2}\right) \tag{27}$$

where, $k = e^{-\mu_d + \sigma_d^2/2}$, $\tau = (\ln \gamma_o - \mu_d)/\sigma_d$. Substituting Eq. (27) in Eq. (26), we finally get the closed-form of capacity under truncated CIFR for EGC and MRC, as

$$\frac{C_{out}}{B} = \log_2\left(1 + \frac{e^{\mu_d - \sigma_d^2/2}}{Q(\sigma_d + \tau)}\right) Q(\tau) \tag{28}$$

Assuming higher average SNR (i.e. $\gamma_{Avg} \gg 20\,\text{dB}$), $\frac{exp(\mu_d - \sigma_d^2/2)}{Q(\sigma_d + \tau)} \gg 1$ for all range of σ_d, Eq. (28) becomes

$$\frac{C_{out}}{B} \approx 1.44 Q(\tau)\left[\mu_d - \frac{\sigma_d^2}{2} - \ln(Q(\sigma_d + \tau))\right] \tag{29}$$

$$C_{TIFR} = max_{\gamma_0} C_{out}$$

Intergral part of Eq. (26) is obtained by using Eq. (3) for SC diversity scheme, as

$$\int_{\gamma_0}^{\infty} \frac{f(\gamma)}{\gamma} d\gamma \approx \begin{cases} \sum_{r=0}^{L-1}\left[\left(\sum_{r_1=0}^{r} \frac{A_1}{2}\sqrt{p}\left(\exp\left(-\mu + \frac{\sigma^2 p}{2}\right) erfc\left(\sigma\sqrt{\frac{p}{2}}\right)\right)\right)\right. \\ \left. + \frac{A_2}{2}\sqrt{p_1}\left(\exp\left(-\mu + \frac{\sigma^2 p_1}{2}\right)\left(erfc(v_2) - erfc\left(\sigma\sqrt{\frac{p_1}{2}}\right)\right)\right)\right] & \text{if} \quad \gamma_0 \le e^{\mu} \\ \sum_{r=0}^{L-1}\sum_{r=0}^{r_1} \frac{A_1}{2}\sqrt{p}\left(\exp\left(-\mu + \frac{\sigma^2 p}{2}\right) erfc(v_1)\right) & \text{if} \quad \gamma_0 > e^{\mu} \end{cases} \tag{30}$$

where $v_1 = t_1 + \sigma\sqrt{p/2}$, and $v_2 = t_2 + \sigma\sqrt{p_1/2}$. Substituting Eqs. (30) and (2) in Eq. (26) results in closed-form of c_{out} and after maximizing it, we get capacity under truncated CIFR.

Figure 3 depicts the channel capacity under OPRA, ORA and TIFR schemes with respect to shadowing parameter in the range of 2–12 dB. The results include exact plot, closed-forms and approximated closed-form. It is observed that the capacity decreases with the increase in the shadowing indicating deleterious effect of shadowing and the plot is getting shifted upward by increasing the average SNR of the channel which is as expected. The closed-form expression using OPRA scheme Eq. (8) and simplified form Eq. (9) have an excellent agreement with the exact plot for all values of shadowing parameters and average SNR. The closed-form expression using ORA scheme Eq. (12) with N equals to five terms has an

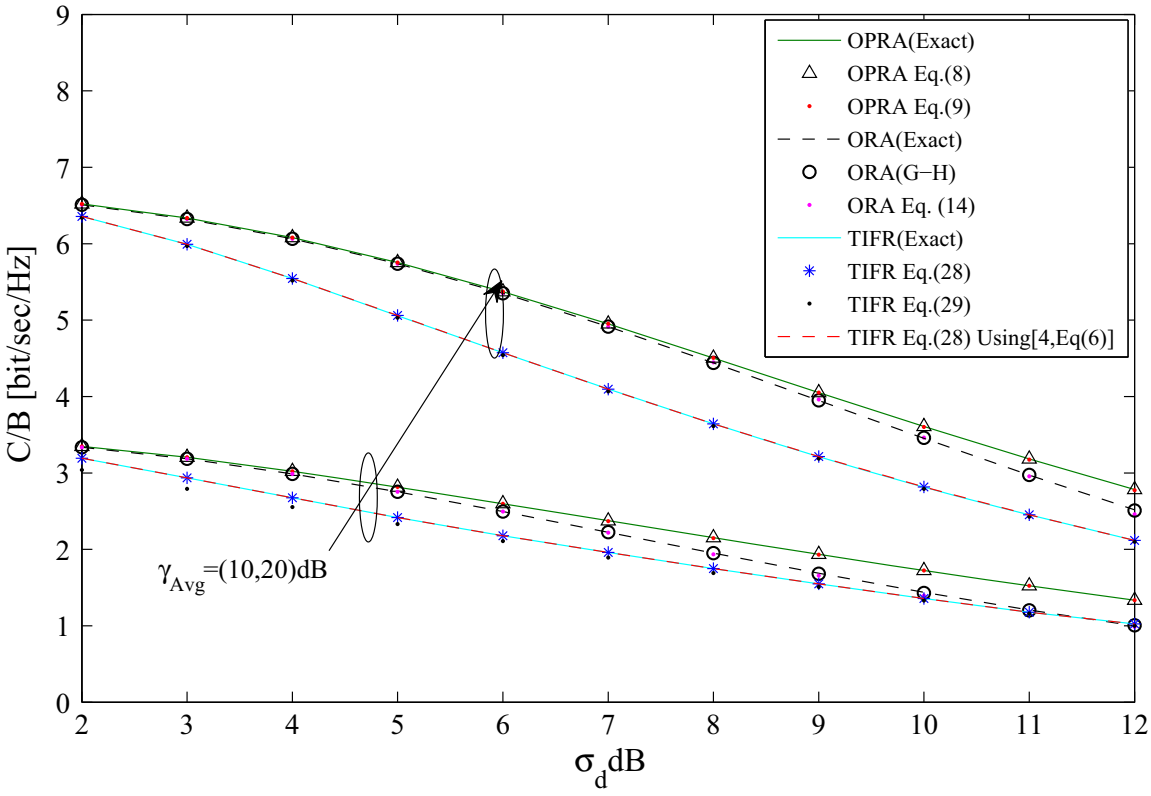


Fig. 3 Channel capacity using OPRA, ORA and TIFR policy with diversity branch, L = 1

excellent agreement with the exact plot. The simplified form Eq. (15) also is noted to have an excellent agreement with exact plot for higher values of average SNR. The closed-form expression using TIFR scheme Eq. (28) and simplified form of Eq. (28) using [6, Eq.6] have an excellent agreement with the exact plot. It is observed that the simplified form Eq. (29) has a slight deviation from the exact result at lower SNR and lower values of shadowing parameter but has an excellent agreement for higher values of average SNR.

3 Numerical Result

This section present the different performance evaluation results explaining the behaviour of slow fading channel under various channel conditions.

Figures 4, 5 and 6 plot, respectively, the capacity under ORA, TIFR, and CIFR adaptive schemes with SC, EGC, MRC diversity techniques. Figure 7 shows comparative analysis of all the four definitions of channel capacity with respect to average SNR for shadowing parameter 6 dB and SC diversity branches L = 1, 10. As expected, on increasing average SNR and diversity order, the capacity increases. It is interesting to observe that the TIFR has higher throughput than CIFR and both seems to be converge at higher average SNR. This convergence happens quiet early rather than large average SNR for higher diversity order. In CIFR policy, large capacity loss is observed with and without diversity. On increasing the diversity branches, all the four capacity plots show improvement whereas quite significant improvement is observed in CIFR as compared to others.

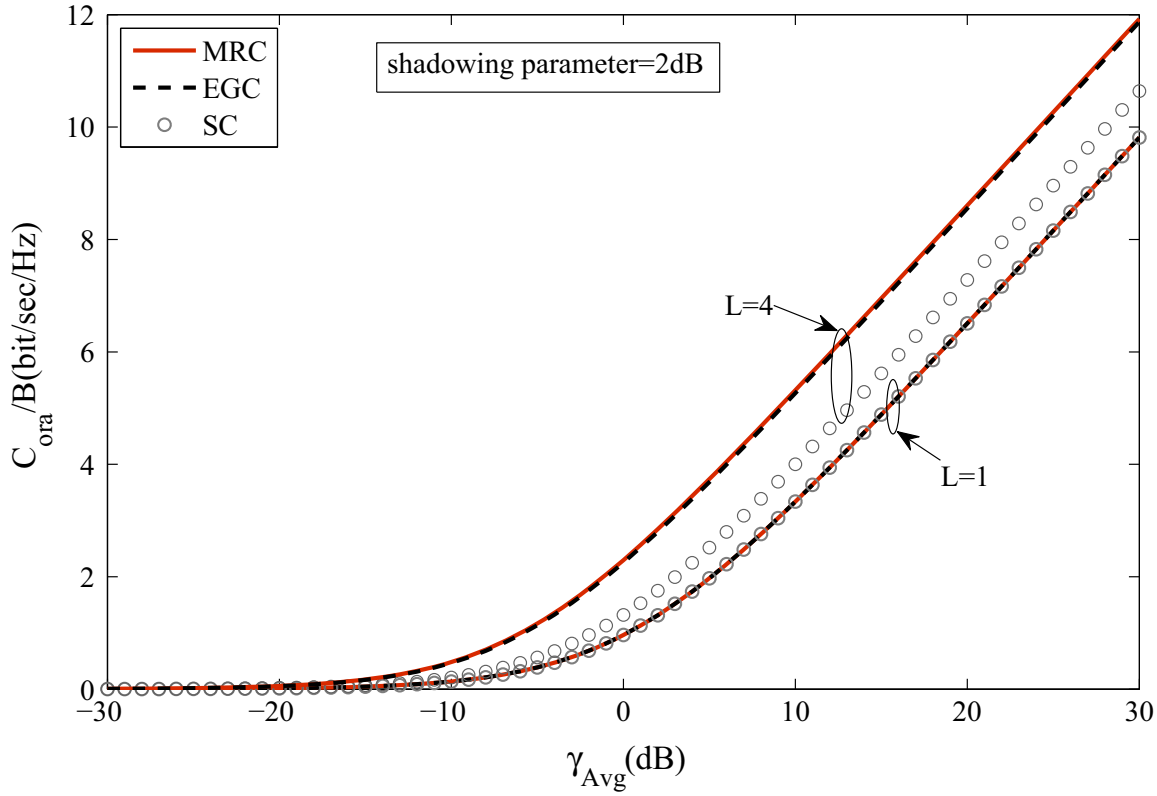


Fig. 4 Comparison of diversity techniques over ORA scheme

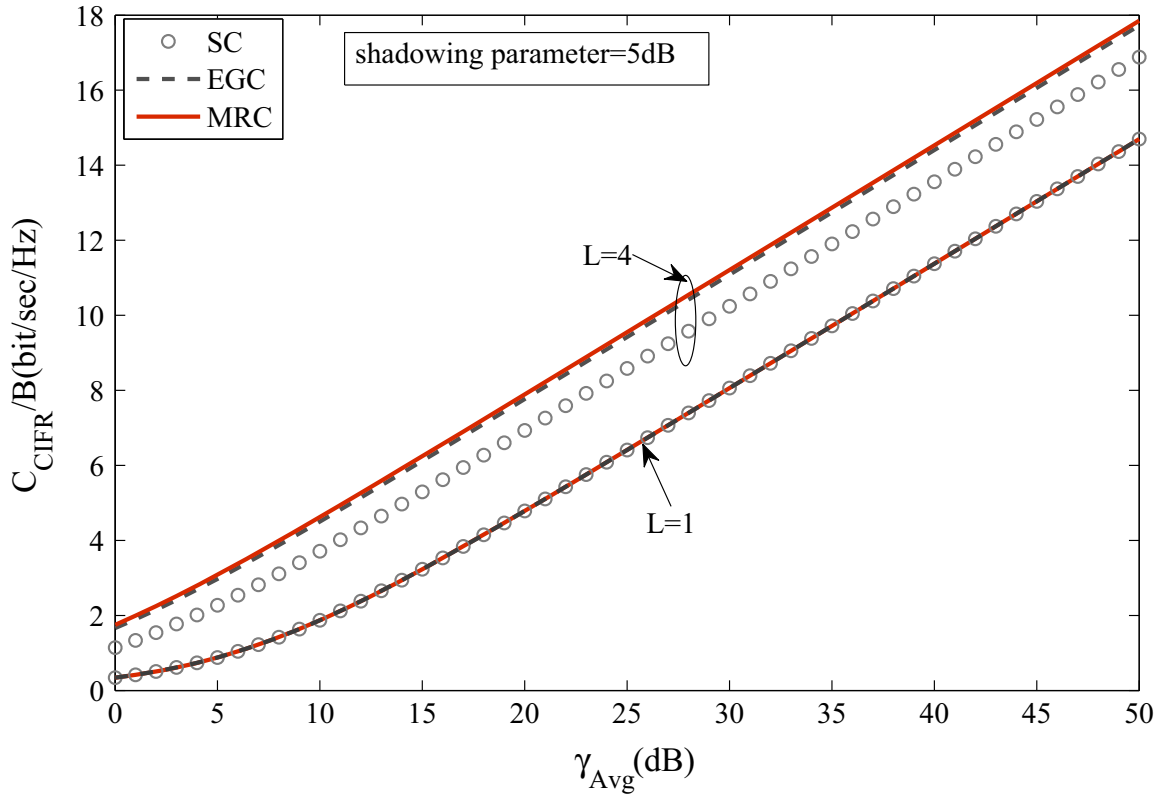


Fig. 5 Comparison of diversity techniques over CIFR scheme

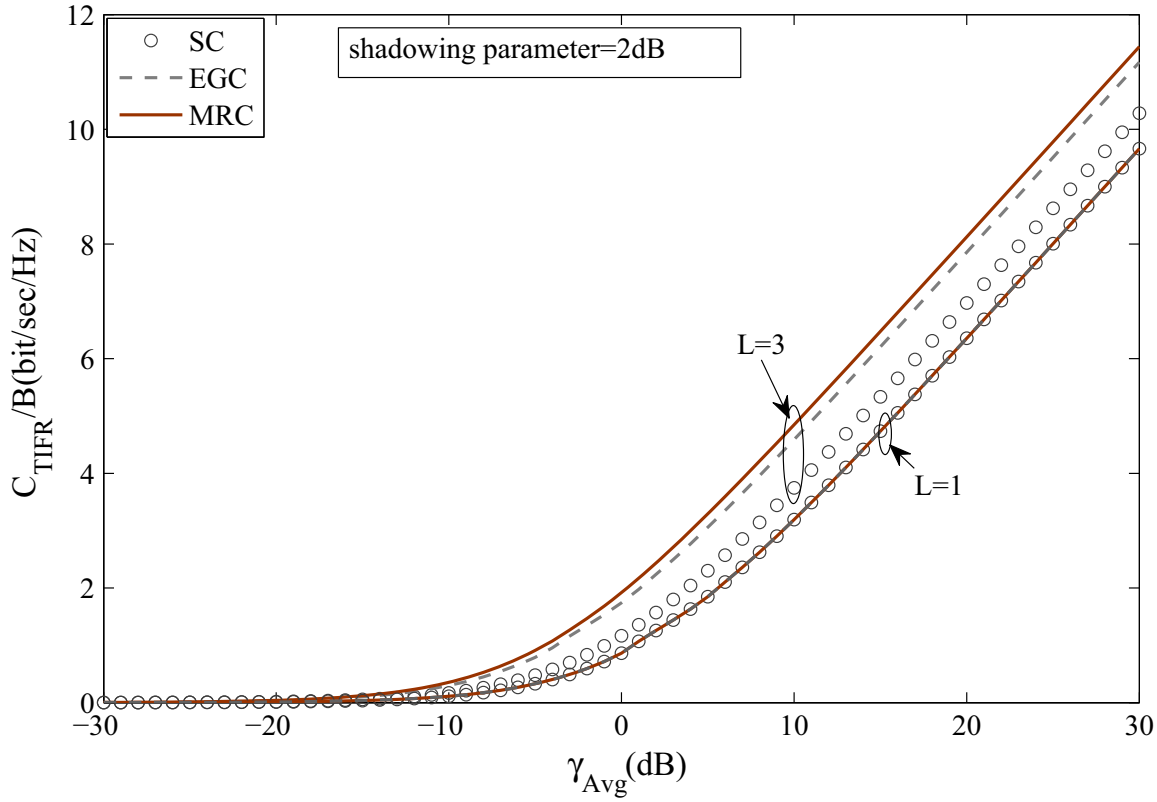


Fig. 6 Comparison of diversity techniques over TIFR scheme

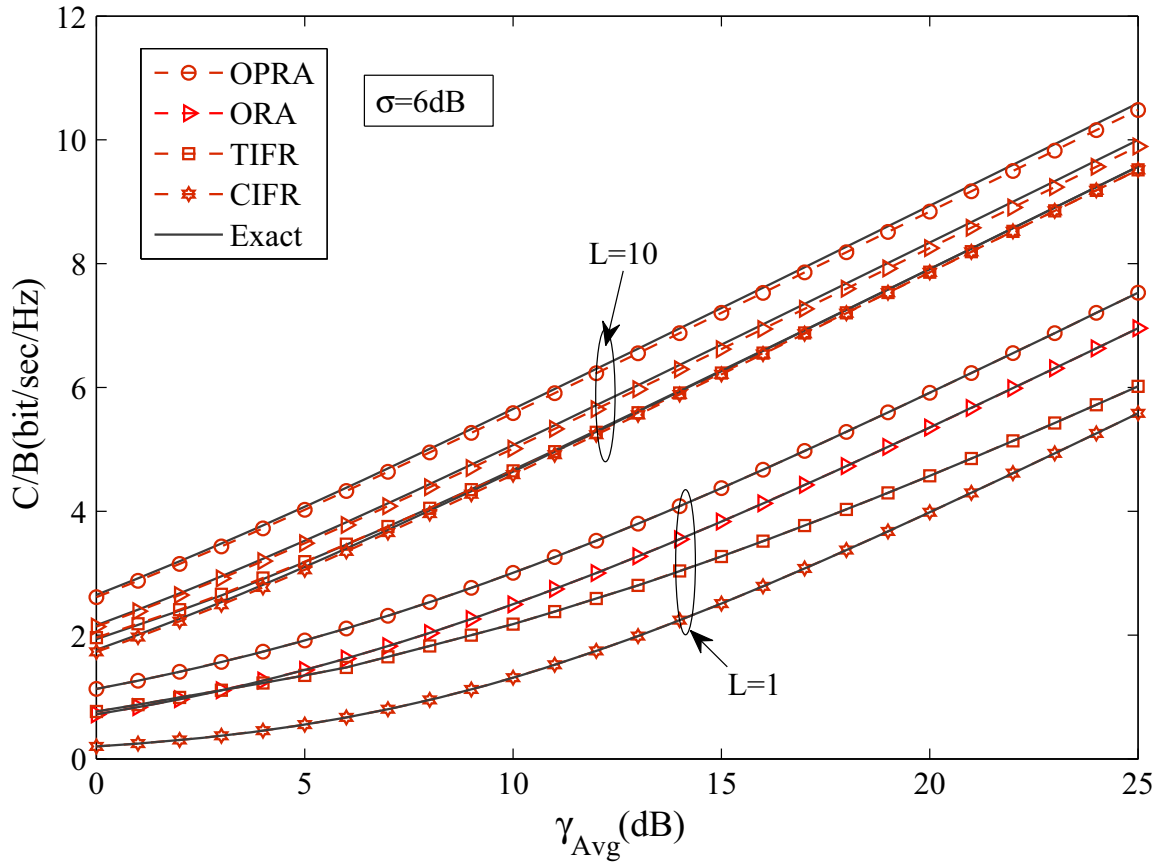


Fig. 7 Comparison of various average channel capacity with selection diversity for (σ = 6 dB, L = 1, 10)

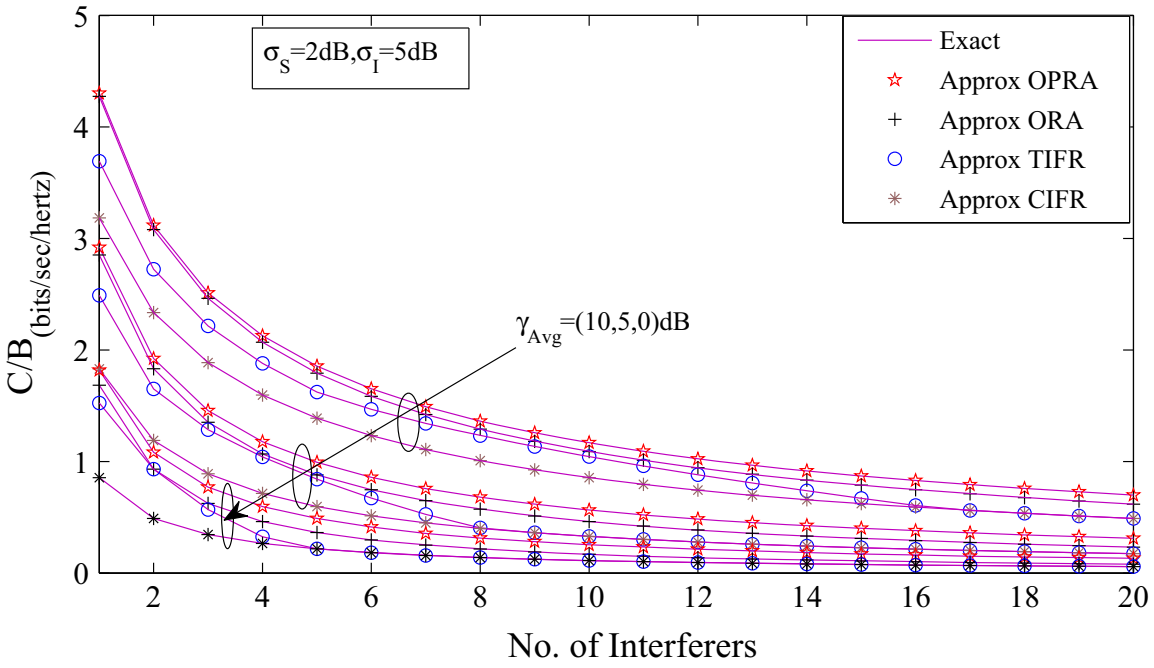


Fig. 8 Comparison of various average channel capacity with number of interferers having shadowing parameter of signal and interferer ($\sigma_S = 2$ dB, and $\sigma_I = 5$ dB) respectively

4 Application

This section deals with the application of evaluating the transmission rate under different adaptive schemes in the presence of lognormal distributed co-channel interference which arise in the cellular system due to frequency reuse scheme. The received Signal to Interference Ratio (SIR) will be as

$$\gamma_{SIR} = \frac{\gamma_r}{\sum_{i=1}^{M_I} \gamma_i} \tag{31}$$

where γ_r is the received power from the desired base station, γ_i is the received power from the ith co-channel interferer and M_I represents the number of interferers. Here all the interferers are considered to be i.i.d. lognormal RVs and according to [3, 12] sum of M_I lognormal distributed RV are approximated by another lognormal RV. Hence γ_{SIR} is a lognormal RV and by applying Eq. (31) on Eqs. (1, 7, 12, 20), we can evaluate transmission rate under different adaptive schemes as shown in Fig. 8. It is evident from the figure that increase in number of interferers have adverse effect on channel capacity.

5 Conclusion

In this work, we have presented accurate closed-form expressions of channel capacity under various adaptive schemes with diversity schemes. The results, thus obtained, are approximated to simple forms under various SNR and shadowing conditions, thus, enabling them to be used directly in several wireless applications. The derived results have the great advantage in terms of easy implementation and have the capability to interpret the system behaviours in lognormal fading conditions.

References

1. Pan, G., Ekici, E., Feng, Q., et al. (2012). Capacity analysis of log-normal channels under various adaptive transmission schemes. *IEEE Communication Letter*, *16*(3), 346–348.
2. Khandelwal, V., & Karmeshu, (2015). Channel capacity analysis over slow fading environment: Unified truncated moment generating function approach. *Wireless Personal Communication*, *82*, 2377–2390.
3. Laourine, A., Stephenne, A., Affes, S., et al. (2007). Estimating the ergodic capacity of log-normal channels. *IEEE Communication Letter*, *11*(7), 568–570.
4. Olabiyi, O., & Annamalai, A. (2012). Inversible exponential-type approximation for the gaussain probability integral Q(x) with application. *IEEE Wireless Communication Letter*, *1*(5), 544–547.
5. Goldsmith, A. (2005). *Wireless communications*. Cambridge: Cambridge University Press.
6. Karagiannidis, G. K., & Lioumpas, A. S. (2007). An improved approximation for the Gaussian Q-function. *IEEE Communication Letter*, *11*(8), 644–646.
7. Shi, Q. (2013). On the performance of energy detection for spectrum sensing in cognitive radio over nakagami-lognormal composite channels. In *Proceedings of IEEE international conference on signal and information processing* (pp. 566–569), China.
8. http://keisan.casio.com/exec/system/1281195844.
9. Holtzman, J. M. (1992). A simple, accurate method to calculate spread multiple access error probabilities. *IEEE Transaction on Communication*, *40*(3), 461–464.
10. Karmeshu, & Khandelwal, V. (2012). On the applicability of average channel capacity in lognormal fading environment. *Wireless Personal Communication*, *68*, 1393–1402.
11. Steen, N. M., Byrne, G. D., Gelbard, E. M. et al. (1969). Gaussian quadratures for the integrals $\int_0^\infty \exp(-x^2)f(x)dx$ & $\int_0^b \exp(-x^2)f(x)dx$. *Mathematics of Computation, 30*, 661–671.
12. Fenton, L. F. (1960). The sum of log-normal probability distributions in scatter transmission system. *IRE Transactions on Communication systems*, *8*(1), 57–67.



Diwaker Tiwari was born in Uttarakhand, India. He received the B.Tech. degree in Electronics and Communication Engineering from Uttarakhand Technical University, Dehradun in 2011. Currently he is pursuing M.Tech. in Digital Signal Processing from Uttarakhand Technical University, Dehradun. His main research interests are in the area of wireless fading channel modeling, cognitive radio.



Sanjay Soni was born in UP, India on March, 1975. He received his Bachelor of Engineering in electronics engineering from Madan Mohan Malviya Engineering College, Gorakhpur in 1997, the M.Tech. degree in communication engineering from IIT Kanpur in 2004, and Ph.D. in wireless Communication Engineering from IIT Kharagpur in 2011. From 1998 to 2007 he was Assistant Professor in the department of Electronics and Communication Engineering, G. B. Pant Engineering college, Pauri. From 2007 he joined IIT kharagpur as a Research Scholar to pursue his Ph.D. In 2010, he joined back to the same institute at the post of Associate Professor. In 2012, he joined Delhi Technological University as an Associate Professor in department of Electronics and Communication. Currently, he is affiliated to G. B. Pant Engineering College, Pauri and is involved in teaching and research in the area of wireless communication. His research interest includes propagation modeling and characterization of wireless channel, time-domain analysis of propagation channel, Diversity and MIMO techniques.



Puspraj Singh Chauhan was born in Kalpi, India. He received his B.Tech. degree in Electronics and Communication Engineering from U.P. Technical University, Lucknow in 2009 and M.Tech. degree in Digital Signal Processing from Uttarakhand Technical University, Dehradun in 2011. He worked as an Assistant Professor in College Of Engineering Roorkee from 2011 to 2015. Presently he is pursuing Ph.D. from G. B. Pant Engineering College, Pauri Uttarakhand. He is reviewer of many international journals and member of IACSIT. His research areas are wireless channel modeling.

Volume 5 Issue 2 (2017) 155-157 ISSN 2347 - 3258
International Journal of Advance Research and Innovation

A new Heuristic Method RPW Method and Genetic algorithm techniques (hybrid method) For Evaluating Multi Product Assembly Line Balancing – A Case Study

Ashutosh Kumar*, [1], Hukam Singh[1], Ashutosh Kumar Rai[2], Avnish Kumar Shukla[1]
[1]Department of Mechanical Engineering, Krishna Engineering College, Ghaziabad (UP), India
[2]Department of Mechanical Engineering Delhi Technological University, Delhi India 110042

Article Info
Article history:
Received 25 January 2017
Received in revised form
20 February 2017
Accepted 28 February 2017
Available online 15 June 2017

Keywords: Assembly Line, Assembly line Balancing Technique, Heuristic Method of Assembly line balancing

Abstract
Assembly line production is one of the widely used production systems. The problem of Assembly Line Balancing deals with the distribution of activities among the workstations which lead to the maximum utilization of Human Resources and facilities without disturbing the work sequence. The problem is motivated by a vehicle-sequencing problem at an Automobile company, Gurugram. A new Heuristic Method i.e. RPW Method and Genetic algorithm techniques(hybrid method) for the Type-I of Multi Product of Assembly Line Balancing Problem(MALBP) have been used. The hybrid method has been developed which is based on the heuristic rules and formulae. The programme is coded in C#(C Sharp). The hybrid method was gave good solutions for straight line balancing problem. The present work of case study provided new knowledge to develop a better tool of assembly line balancing to solve real world problems more efficiently at the shortest possible time and it leads to increase line efficiency and production rate by reducing the number of workstations and also reducing balance delay and smoothness index.

1. Introduction

An assembly line is a sequence of workstations connected together by mechanical material handling equipments in which a dedicated group of tasks are performed in predetermined sequence. The total work content to be performed by the production system is split –up into economical individual work elements which are called task. Among the set of tasks there exist technological precedence relations. The assignment of these tasks to workstation along an assembly line to achieve same or close to same working time at each workstation. The goal of this assignment of task is to create a smooth and continuous flow of product through the assembly line for maximum productivity and minimum idle time at each workstation. A well-balanced assembly line has the advantage of high personnel and facility utilization and equity among the employees work loads.

Assembly lines are flow-oriented production systems which are typical in the industrial production of high quality standardized commodities and even gain importance in low volume production of customized products Among the decision problems which arises in managing such systems, assembly line balancing problems are important tasks in medium –term production planning **[1]**

Assembly line balancing is a classic problem in any business. Assembly is a process by which manufacturing parts are put together to make the finished product. An assembly line is a moving conveyer that passes a series of work stations in a uniform time interval . At each work stations, work is performed on the product by adding parts i.e. completing assembly operations by the operators. If work load is not well balanced, one operator may be busy while the other may remain idle which waste the loss of time, money and man hours. In such situation the efficiency and morale of the organization decreases leading to unhealthy work conditions**[2].**

1.1Multi-Product Line Balancing

Multi-product assembly lines assemble two or more products separately in batches, when more than one product variant has to be assembled in a line. The objective is to assign operations to workstations in order to balance the workload and minimize manpower requirements when more than one product variant has to be assembled in a line. Since assembly process and process times may not be the same for different products, a single line cannot be perfectly balanced for each of the products.

The evolution of the design of a product leads manufacturers to consider families of products. The design of the assembly line has to take this evolution into account as from single product to multi product.

***Corresponding Author,**
E-mail address: ashume2007@gmail.com
All rights reserved: http://www.ijari.org

2. Problem Formulation

The assembly line balancing task is tedious and time consuming. For complex operations in industries like Automotive, computer manufacturing etc it becomes very tedious and time consuming. Also, all the things of assigning the operations on workstations are done manually, and hence skilled labour requires for this task. Though, the assurance cannot be given that the system is running with maximum efficiency. In many industries it has been seen that after assigning the task and implementing, it was found that most of the workstations are running idle, for which again corrective action is taken i.e. also a time consuming process.

A case study for assembly line balancing was proposed to be undertaken at a company of Motorcycle and Scooter in Manesar(Haryana) in consultation with the management of the company. The management agreed to provide all facilities for ALB of engine assembly of different models of bikes. The approach was adopted for ALB of different models of bikes like KTE,KWP,KRP and KVT of above mentioned company.

Despite recent advances in computational techniques and solution procedure efficiency, mathematical Programming and network-based optimization techniques are still computationally prohibitive beyond limited problem dimensions.Therefore, heuristic and Group Genetic Algorithm (GGA) still remain the only computationally efficient and sufficiently flexible methodologies capable of addressing large-scale, real-world ALB situations, particularly for the multi/mixed model.

In this case study, computer based approach has been developed for solving the mixed-model two-sided assembly line balancing problem considering minimizing the number of mated-stations (i.e.,the line length) and minimizing the number of stations (i.e., the number of operators) for a given cycle time.Objective function developed is for minimizing the number of mated-station (i.e.the line length) as the primary objective, and it also minimizes the number of stations (i.e.the number of operators) as a secondary objective. Constraint is the assignment constraint which ensures that each task is assigned to exactly one station. Another constraint is the precedence constraint which ensures that all precedence relations among tasks are satisfied. Also constraint is the cycle time constraint which ensures that each of the finish time of tasks for each model does not exceed the cycle time.

Here the aim was to find out/ reduce number of work stations for the specified industries. The assembly line balancing would assign the tasks according to the precedence relations and some other constraints to each workstation for maximum efficiency possible, and thereby achieving the maximum productivity. The objective was to assign the tasks to the workstations such that the idle time

would be less and the working of each workstation would be closer to cycle time.

3. Methodology

The methodology used for solving the problem of assembly line balancing was Heuristics method and Group Genetic Algorithm(GGA) method. In the present work, the Heuristic Method with genetic algorithm was used to solve the mixed model assembly line balancing problem of type I (MMALBP-I). There were three objectives to be achieved: to minimize the number of workstations, maximize the workload smoothness between workstations, and maximize the workload smoothness within workstations.

3.1 Developed Assembly Line Balancing

For the above problem, a computerized hybrid system has been developed which is based on the heuristic rules and formulae. To solve this problem Heuristic based Rank Positional Weight (RPW) was used with Group Genetic Algorithm. The heuristic based RPW was very suitable and gives more stable results for large number tasks while GGA is used for getting mixed-models assembly line balancing problems. The most important feature of this system is its utility and simplicity for any number of activities to be performed for assembly.

The computerized hybrid system uses the applications of Heuristic and GGA for better results. This system gives the results for mixed model as well as for multi- product assembly line balancing. The system has been developed using the concept 'C++' programming. It is an effective and suitable language for implementation, ease in file handling and better presentation. Hence, the computerized system logic was coded with "C++" programming language. The developed system can be used for any number of tasks which are to be performed on the products. In this system data was entered as number of tasks, task number, task time, precedence, and cycle time. The program runs separately for each variety and results were checked with the present situation.

In this work, a new heuristic namely, RPW Method with GGA for solving Deterministic Assembly Line Balancing problem has been developed. This will be very much useful for the industries to design mass production systems with improved productivity and to compete and survive in the competitive industrial sector in the era of globalization. These results can provide a broad guideline for designing an assembly line in a mass production system with improved productivity. This heuristic is experimented with several problems generated randomly. The performance of the heuristic is compared with that of the existing set of Heuristics methods of Assembly Line Balancing. For this purpose an experiment was designed using a KTE, KWP etc. models of HMSI. Software in C# has been developed for testing the problem.

3.2 Performance Parameters

The performance parameters which were used for analysis of different methods of Assembly Line Balancing are Line Efficiency, Balance Delay and Smoothness Index. The Line Efficiency is used for the calculation of efficiency of the Assembly Line. Line Efficiency represents positive achievement in line utilization of all resources and is the key representation of economic performance. Balance Efficiency and Smoothness Index are representative of the distribution of work with consequent personnel satisfaction combined with increased opportunities for greater output.

3.2.1 Line Efficiency (LE) – It is expressed as ratio of total station time to the cycle time multiplied by the number of workstations.

$$LE = \frac{\sum_{i=1}^{K} ST_i}{c.K}.100\%$$

where: K= total number of workstations,

c = cycle time and ST_i =station time of station i.

3.2.2 Balance Efficiency is Balance Delay which indicates the amount of time lost due to imperfect balancing as a ratio to the total time available i.e.

$$d = \left(\frac{wT_S - T_{wc}}{wT_S} \right)$$

where, d= Balance Delay. A balance delay of zero indicates a perfect balance.

3.2.3 Smoothness Index (SI) – describes relative smoothness for a given assembly line balance. Perfect balance is indicated by smoothness index 0. Smaller value of SI means that more the line is balanced.

$$SI = \sqrt{\sum_{i=1}^{K} (ST_{\max} - ST_i)^2}$$

where: $ST_{\max}$ = maximum station time (in most cases cycle time), ST_i = station time of station *i*

4. Results and Discussion

The heuristic methods like Largest Candidate Rule, Kilbridge And Wester Method, Moodie-Young Method and RPW Method with GGA were applied to the Assembly Line of HMSI. The collected information like description of task, task time, cycle time of line and precedence diagram of Assembly Line were provided to the approach of each Heuristic method and the different parameters like efficiency, balance delay and smoothness index of each station by each method are calculated. The results of all parameters for assembly line are compared. The number of maximum and minimum efficiency and its values were calculated by using all above methods and results are compared among them. The Balance Delay and Smoothness Index were also calculated and compared by applying these methods. The most appropriate method is selected on the basis of comparison for balancing the assembly line and the results of this method were compared to the already existing method of assembly line.

4.1 Hybrid Method

The procedure of this method is similar to the RPW method with basic difference is that allocation of work elements or tasks having same RPW and Rank are then subjected to gentic algorithm procedure.The priority rules are based on task time, the number successors and the number of predessor. The assignment of work elements to the work station is carried out in the following manner

a) The work with the highest positional weight was selected and assigned to the first workstation.
b) The unassigned time was calculated for the work-station by calculating the cumulative time of all works units assigned to the station and this sum was subtracted from the cycle time.
c) The work unit was selected with the next highest positional weight and attempted to assign it to the work-station.
d) If the positional weight and rank of two tasks is same, then the priority rule is followed for assigning of work elements to the workstation according to task time first.
e) If the positional weight, rank and task time of task is same for two or more work elements, then the priority is based on the number of predecessors.
f) If all above parameters are same for two or more different work elements, then priority for assigning of task to workstation is on the basis of number successors.
g) Unassigned work unit is assigned with the highest positional weight to the second work-station, and preceded through the preceding step in the same manner.

The assigning of work units are continued untill the assembly line balancing problem is found.

The approach of hybrid method (RPW method with GGA) is applied in the collected data of all tasks of assembly line of HMSI models and it is found that the rank is not same for any task so the allocation of work elements or tasks to each station is similar to RPW method. It is suitable for solving the balancing problem when the precedence diagram of Assembly Line is complex having some parallel assembly line of product flow. This type of product flow occurs in case of Multi Product Assembly Line Balancing Problem. So this method is suitable and most appropriate technique for balancing Mixed Multi Product Balancing System when the data is vide and complex.

Due to the similarity for assigning of tasks to each workstation, this case study leads to give the performance parameters It is observed that maximum efficiency of 100% was found at 13 work stations

(14, 24, 25, 27, 35, 39, 40, 42, 47, 54, 57, 60 and 62) and minimum efficiency (38.46%) was observed at 1 work station (71) only. Similarly, minimum Balance Delay of 13 work stations(14, 24, 25, 27, 35, 39, 40, 42, 47, 54, 57, 60 and 62) were 0 % and maximum for 1 work station(Station71) is 61.54%. The Smoothness Index of 13 work stations(14, 24, 25, 27, 35, 39, 40, 42, 47, 54, 57, 60 and 62) were minimum i.e.0 and one work station (71) had maximum value of SI i.e.16.

4.2. Analysis Of Case Study

In the course of line balancing, the idle time and the number of workstations on the assembly line was minimized so as to maximize the efficiency of the production line. All the required data is measured and the parameters such as elapsed time at each work station, efficiencies, number of workers, time of each of the workstations etc. is calculated from the existing line. After allocating the work elements on new assembly line, the cost of production and effectiveness of the new line was computed and compared with those of the existing one.

The developed hybrid method was applied in an automotive assembly line for improving the performance. The assembly line has 75 workstations, 229 tasks with cycle time equal to 26 sec. After implementing the hybrid method it was possible to reduce the number of workstations to 71 (a reduction of 4 workstations) considering the same number of tasks with the same cycle time. Further, productivity improved from 81.20% to 85.75%.

Table 4.1 Performance Parameters of Existing practice Vs Developed Method

S.N.	Performanc Parameters	Existing Practice	Developed Method
1	Cycle Time	26	26
2	No.ofWork stations	75	71

Similarly, there has been a reduction of balance delay of about 4.64% showing that the time lost due to imperfect balancing is less in case of hybrid system as compared to the current practice being followed in the organization. Smoothness index also shows a declining trend i.e. 32.16% reduction, indicating a better balanced production line.

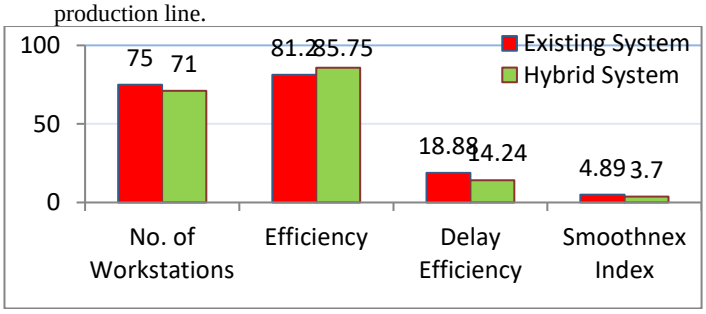


Fig. 1 Existing Practice Vs Developed Method- A Comparison

Fig. 1 shows the comparative variation of performance parameters in case of existing practice being followed at Scooter and motorcycle company in Gurgaon and the developed hybrid assembly line balancing metho d. After implementing the hybrid method it was possible to reduce the number of workstations to 71 (a reduction of 4 workstations) considering the same number of tasks with the same cycle time. Further, productivity improved from 81.20% to 85.75%.

5 Conclusions

This system helped to improve the workstation allocation thereby getting optimum task assignment on each workstation for line balancing problem .The system helped in reducing the number of operators required on the balanced workstations. The computerized system lead to reduce number of stations and gives optimum number of stations based on RPW technique. By reducing the number of work stations, the assembly line result in achieving maximum productivity. The new production line is found to have been increased by a significant amount reducing the overall production cost per unit by increasing line efficiency and reducing delay time.

References

[1] Scholl A, Christian B: State-of-the-art exact and heuristic solution procedures for simple assembly line balancing, European Journal of Operation Res.,168, 2006, 666–693.

[2] Becker C, Scholl A: A survey on problems and methods in generalised assembly line balancing .Eur J Oper Res 168, 2006, 694-715.

[3] Rabbani M, Mahmood Kazemi S: Mixed model U-line balancing type-1 problem: A new approach,Journal of Manufacturing Systems, 31, 2012,131– 138

[4]. Amen M. Heuristic methods for cost-oriented assembly line balancing: A comparison on solution quality and computing time. Int. Journal of Production Economics, 69, 2001, 255-264

[5]. Baybars I. A survey of exact algorithms for the simple assembly line balancing problem. Management Science, 32(8), 1986, 909-932.

[6] Gutjahr A, Nemhauser G. An Algorithm for the Line Balancing Problem in Management Science, 11(2), 1964, 308-315.

[7] Boctor FF. A Multiple-rule Heuristic for Assembly Line Balancing. Journal of the Operational Research Society, 46, 1995, 62-69.

[8] Driscoll J, Abdel-Shafi. Simulation Approach To Evaluating Assembly Line Balancing Solutions, International Journal of Production Research, 23(5), 1985, 975-985.

[9] McMullen, PR, Frazier, GV. A Heuristic For Solving Mixed-Model Line Balancing Problems With Stochastic Task Durations And Parallel Stations, International Journal of Production Economics, 51(3), 1997, 177- 190.

[10] Fleszar K, Hindi KS. An enumerative heuristic and reduction methods for the assembly line balancing problem. European Journal of Operation Res. 145, 2003, 606–620.

[11] Simaria AS, Vilarinho PM. A genetic algorithm based approach to the mixed-model assembly line balancing problem of type II, Computers & Industrial Engineering, 47, 2004, 391–407.

[12] Kim YK, Kim Y, Kim YJ. Two-sided assembly line balancing: a genetic algorithm approach. Prod Plan Control 11 (1), 2010, 44–53.

[13] Bukchin Y, Rabinowitch I. Branch-and-bound based solution approach for the mixed-model assembly line-balancing problem for minimizing stations and task duplication costs. European Journal of Operational Research, 174, 2006, 492–508

[14] Mosadegh HM Zandieh M. Simultaneous solving of balancing and sequencing problems with station-dependent assembly times for mixed-model assembly lines, Applied Soft Computing, 12, 2012, 1359–1370

[15] Tonge, Fred M. Summary of a Heuristic Line Balancing Procedure, Management Science, 7(1), 1960, 21-42.

[16] Jackson JR. A Computing Procedure for a Line Balancing Problem, Management Sci., 2(3), 1956, 261-272.

[17] Özcan U, Toklu B. Balancing of mixed-model two-sided assembly lines, Computers & Industrial Engineering, 57, 2009, 217–227.

[18] Ponnambalam SG, Aravindan P, Naidu GM. A Comparative Evaluation of Assembly Line Balancing Heuristics, Springer-Verlag London Limited, 15, 1999, 577-586

Volume 5 Issue 2 (2017) 251-254 ISSN 2347 - 3258
International Journal of Advance Research and Innovation

A Study of Active Brake System of Automobile

Roop Lal, RC Singh, Vaibhav Sharma, Vaibhav Jain
Mechanical Engineering Department, Delhi Technological University, Delhi 42, India

Article Info
Article history:
Received 25 January 2017
Received in revised form
20 February 2017
Accepted 28 February 2017
Available online 15 June 2017

Keywords: Brake, assist, sensors, anti-lock braking system, electronic braking system, electronic stability control, Traction, Manoeuvre

Abstract
There are many situations where the driver's response is not fast enough to apply brakes to stop and control the vehicle during emergency. So in such cases, there is an urgent need for an active brake system. Brake assist is an active vehicle safety feature designed not only to help drivers come to a stop more quickly during an episode of emergency braking but it automatically applies brakes in case the car in front of car comes too close. There are many sensors along with camera which continuously determines the speed of car in front of our car .If both cars come too close to each other, then brake assist first warns the driver and then apply 20% to 40% of braking capacity automatically and if still driver does not respond it activates emergency brake assist which applies 100% of braking power .During this ABS and EBD (sometimes ESC and TRACTION CONTROL) also comes into play which provides easy manoeuvre control to driver over vehicle.

1. Introduction

Hazardous overtaking maneuvers on 2 lane roads are often cause of severe traffic accidents. Developed driver assistance system aims at warning the driver in overtaking maneuvers, which cannot be performed without a conflict with an oncoming vehicle. The objective is to prompt the driver to abort the maneuver already during overtaking start or in an early stage of passing phase. If there is too little time to react, or driver doesn't react for other reason, system initiates an automatic braking intervention incorporated by Anti lock braking system and brakeforce distribution, which allows driver to drive back behind vehicle that has to be overtaken before oncoming vehicle reaches. This system includes camera, far range radar sensor, accelerator force feedback pedal, and electronic brake system. The distance between our vehicle and the oncoming vehicle is calculated continuously and if value is less than the threshold value then this system comes into action. During emergency braking case, beside different warnings, an automatic braking intervention is released in order to compensate driver's reaction time. [1]

The study predicts that current functionality of brake assist systems can reduce pedestrian fatality rates. The main advantage of the system are: 1)the impact energy is reduced , 2) leading to lower risk of injury and the secondary impact where the pedestrians hits the ground is mitigated. The system involves the working of brakes autonomously in a car prior to impact. Special sensors are used to detect the pedestrians on road. The pre-impact braking systems were assumed to activate the brake few seconds earlier and to provide a braking deceleration up to limit of road surface conditions, but never to exceed 0.6g. The sensor used to detect the pedestrians plays an important role. They have wide field of view so that there is no problem in sensing the pedestrians. For pre-braking system to work precisely the field of view is 40%. [2]

Once a combined vehicle (car-caravan) becomes unstable, it is very difficult for a driver to stabilize it especially under severe driving conditions, such as turning and braking. This is mainly due to the effect of the towed vehicle on the towing vehicle through the hitch jack-knifing. This effect makes handling characteristics of car-caravan combination different from that of a single vehicle. Therefore studies propose a control design concept for an optimum distribution of longitudinal and lateral forces of the four tires of towing vehicle. The mean objective of the control system were to stabilize the motion of an articulated vehicle utilising the tires entire ability in both longitudinal and lateral directions as well as to make handling characteristics of an articulated vehicle similar to those of single one. [3]

Braking process is a highly nonlinear process. The development of an intelligent control strategy of brake actuation pressure during braking and consequently the braking performed is studied. It can be done through dynamic control of brake actuation pressure according to demand by driver and/or ABS/ESC system. This can be studied by modelling the complex dynamic influence of braking regimes (applied pressure, sliding speed and brake interface temperature) versus the change of brake performance. Through the established functional relationship between inputs/outputs provides the possibilities for fill context adjusting of brake actuation pressure to driver demand as well as current and previous value of :1) the vehicle speed, 2) the brake applied pressure, and 3) braking torque. The proposed control system is implemented and experimentally verified using low cost Atmel Atmego 16 microcontroller. [4]

The purpose of this field operational test study is to assess visual attention allocation and brake reaction in response to a brake capacity forward collision warning. The truck driver's reactions immediately after the warning as well as a few second after the warning are analyzed both with and without taking into consideration the predictability of an event and driver distraction. BFCW systems interface should immediately direct visual attention forward threat and allow the driver to make a quick decision about whether or not to brake. The main purpose of study is to improve real world knowledge about the effect of brake capacity forward collision warning on visual attention and brake reaction for the application of effective working of system. In the tests, eye movement and reaction of driver is observed 15 seconds before warning and 15 seconds after the warning. There is a reaction time after the warning which should be minimised by considering all the potential reason for the effectiveness of system. [5]

Systems informing or warning a driver of an imminent collision with a pedestrian or automatically initiating braking have been introduced to the car market. One of the major challenges is to balance system performance against the possibility of undesired system activation. The distinction between desired and undesired system activation can be based on driver discomfort. Through studies driver discomfort can be inferred from brake onset, which refers to start of brake pedal depression, as the most intuitive way for a driver to resolve a conflicting situation. Time to collision (TTC) at brake onset, one of the recorded quantities, might be suitable measure for comfort zone boundaries as it is less affected by driving speed than other measures. Pedestrian speed is found to have a statistically significant influence on brake onset. For pedestrian speed of 1m/s, 90% of drivers braked before 2.6s TTC. For 2m/s this value was 2.2s. These values can be used to differentiate between desired and undesired system activation in the design of an "unjustified system response" test in the assessment of pedestrian safety systems. [6]

Brake reaction time is an important parameter for road safety. Previous research has shown that driver's expectation can impact reaction time when facing hazardous situation, but driving with advances driver assistance systems can help faster more efficient responses, but same time can require a monitoring task and evaluation process that may lead to automation complacency. The paper aimed to test in a real life setting whether automation complacency can be generated by collision warning systems and what components of expectancy can impact the different task involved in an assisted BRT process. More specifically four components of expectancy were investigated: 1) presence/absence of anticipatory info, 2) previous direct experience, 3) reliability of

*Corresponding Author,
E-mail: rooplalrana@gmail.com
All rights reserved: http://www.ijari.org

device, and 4) predictability of the hazarded determined by repeated use of system alerts. [7]

Driver braking behaviour was analysed using time series recording from naturalistic rear end conflicts, including events with or without visual distraction among drivers of vehicles. A simple piecewise liner model could be successfully fitted, per event, to the observed driver decelerations, allowing a detailed elucidation of when drivers initiated braking and how they controlled it. It was found that drivers initiated braking behaviour was strongly dependent on the urgency of the given rear end scenarios kinematics, quantified in terms of visual looming on lead vehicle on the driver's retina. From the previous research, brake reaction time is about 1.5 seconds but it was found that braking could be described as typically starting less that a second after the kinematics as typically starting less than a second after the kinematics urgency reached certain threshold levels, with even faster reaction at higher urgencies. [8]

Active vehicle stability control systems have played a major role in reducing the number of road fatalities over the past few decades. These systems assist the drivers to control the vehicle in harsh driving conditions, inspite of these safety systems road fatalities continue to claim lives. Therefore, further development of such safety enhancement systems is required. Besides, new types of personal vehicle continue to gain popularity in market, such a hybrid and fully electric vehicles. This highlights the importance of development of active safety systems that are tailored for these particular types of vehicles. The data collected after various experimental study and conclusion comes out that prediction model consists of a double track vehicle model augmented with the vehicle dynamics. Integration of vehicle and wheel dynamics makes a separate traction control module unnecessary. Therefore, the optimality of controller cam uses both torque vectoring and differential braking as actuation. The result confirms the effectiveness of the proposed controller in controlling the vehicle directional dynamics and the tire slip ratios. [9]

Two yaw motion control systems that improve a vehicle lateral stability have been studied by Jeonghoon Song and Woo Seong Che. These two yaw motion control systems are braking yaw motion controller (BYMC) and steering yaw motion controller (SYMC). BYMC controls braking pressure of rear inner wheel, while SYMC steers rear wheel to allow the yaw rate to track reference yaw rate. Several types of vehicles yaw moment controller (YMC, also known as ESP, electronic stability control programme or VDC, vehicle dynamic control) has been proposed and developed but among then, BYMC which controls brake pressure is widely studied and most famous because it does not requires any complicated hardware if vehicle is equipped with ABS and YMC. [10]

Electro-mechanical braking force actuators are considered to substitute conventional brake boosters in electric and hybrid-electric vehicles in the forthcoming years. Due to nonlinearities like stick-slip friction effects and parameter uncertainties on one hand and the need for precise tracking of the master-cylinder position on the other hand, the controller design is a non-trivial task. First the system is analyzed in detail, and then the main use-cases are identified. A model is set up and validated against test-rig measurements. A sliding mode control law for the braking-force actuator is derived from a sufficiently detailed model of the vehicles brake system dynamics. It features a simple structure with few controller parameters leading to a remarkably reduced effort in controller parametrization. Since the controller is robust with respect to the model uncertainties, no adaptation of the controller is needed during operation. [11]

Brake assist system was originally introduced to compensate for insuffiecnt braking rates due to unexpected driver reaction. It was found that, despite the ABS, the braking distance in critical situation was not significantly reduced. The reason was that drivers were not pushing the brake pedal strong and quick enough to achieve its full stroke. BAS and ABS proved to be efficient in reducing severity of pedestrian accidents in most case. The findings show that even though most of collisions could not have been completely avoided by implementing these systems, but their consequences would have been reduced in terms of estimated injury severity probability. The effectiveness of BAS+ABS systems for speed reduction increases when driver is unable to brake to full stroke of pedal because in such circumstances, with enough time and space, the system aids in reaching max deceleration available by vehicle. Due to all these advantages in reducing injury severity probability the brake assist system fitting is compulsory in European Union. [12]

The turbo braking assist utilizes the concepts governing turbo machinery and automotive engineering in order to achieve effective braking assistance for modern day disc as well as drum brakes. The principle involved encompasses the targeting of a jet of viscous fluid onto the blade of a rotor wheel. This jet of fluid retards the motion of rotor and in process damps or slows down the rotation of wheels. The major components involved are turbines, or rotor, pump, nozzle, enlarged brake fluid chamber, DOT 5.1 braking fluid. The function of pump is to enable increase of mass flow rate of fluid and also to ensure the continuity of fluid flow in entire circuit. A speed sensor is integrated along with circuit to activate pump only after reaching particular velocity as BA is not necessary at low speed. The turbo brake assist is a potential brake assist in high speed conditions thereby reducing work done by disc or drum brakes. [13]

2.Active Brake System

Now a day's cars have brakes on all wheels which are accomplished by a hydraulic system. Disc and drum brakes are two major types of brakes used in the vehicles. Most of the cars have disc brakes on front wheels and drum brakes on rear wheels. The explanation behind this is the fact that when the vehicle is under braking the momentum (weight) is transferred to the front part and hence the front wheels. Moreover, drum brakes are provided on rear wheels as it is possible that during heavy brakes much weight may come off the rear part, which might result in locking of rear wheels and will cause skidding of wheels. Some sports, and luxury vehicles uses disc brakes over all wheels to improve the performance. Most cars now have load sensitive pressure limiting valve which reduces the brake fluid pressure on rear brakes during heavy brakes and prevent them from locking up.

2.1 Brake hydraulics

The braking system consists of hydraulic circuit. This circuit has a fluid filled master cylinder and slave cylinders which are connected through pipes. The master cylinder is located near the brake pedal. When the brake pedal is pressed, the fluid inside the master cylinder is pushed which increases the pressure of brake fluid in the circuit. This increased pressure is transmitted to all the slave cylinders through the pipes, this further forces the piston out at each slave cylinder. As the result, the brake shoes rubs against the drums and the brakes are applied.

The combined pushing area of the pistons at slave cylinder is much greater than that of the piston at master cylinder. Due to this, the master cylinders' piston has to traverse few inches to move the slave piston by fraction of inch to apply the brake at wheels. Cars are sometimes fitted with two hydraulic circuits to provide the safeguard against failure of one hydraulic circuit. When the brake pedal is released the spring inside the master cylinder pulls the piston back to its original position and this in result reduces the pressure inside the pipes carrying brake fluid and brings it to normal level. The retracting spring pulls the brake shoes to its original position as the pressure at slave cylinder reduces. In this way brakes are released.

2.2 Power-assisted brakes

Modern cars have power assisted brakes to reduce effort needed to apply brake by the driver. For this the main source of such power is the pressure difference between the outside air and the inlet manifold. Servo units serve the purpose of assistance by creating the pressure difference. Direct acting servo is fitted between the brake pedal and the master cylinder.

2.3 Anti-lock braking system

The Anti-lock Brake system is an automotive safety system which permits the wheels of a vehicle to hold tractive motion on the road which is totally dependent to driver inputs while braking. The system prevents the locking state of wheels. Thus maintain the rotation of wheel and avoid uncontrolled skidding. The system uses the principle of limen braking and cadence braking. An ABS system consists of Electronic Control Unit (ECU), speed sensors for each wheel and hydraulic valves. The change in the rotational speed of wheels, due to driver inputs to brakes, is sensed by ECU through sensors. The ECU operates hydraulic valves and maintains the sufficient brake pressure on the brake callipers by reducing or increasing it, as per the situation, such that locking of wheels is prevented and makes them to move safely.

2.4 Electronic brakeforce distribution

The Electronic Brake Force Distribution is an advanced automotive braking technique that automatically regulates the distribution of brake force to each wheel depending upon various factors like weight, speed, etc. The system works parallel with ABS. The EBD system provides maximum break force to the wheel having maximum momentum so that the wheels stop simultaneously in a proper and safe manner. Most of the times, front part of the car majority of weight (weight of engine and other parts) so due to this EBD distributes less braking force to rear brakes, this prevents locking and hence skidding of rear wheels. Sometimes during initial phase of braking EBD distributes more braking force to rear wheels before the effect of weight transfer comes into action and becomes apparent.

2.5 Electronic stability control

The Electronic Stability Control is a computerised technology which improves the vehicle's stability by detecting the loss of steering control. The system measures the amount of steer and speed of vehicle continously.When the conditions of steer and acceleration mismatches for turning of the vehicle and driver losses the control over vehicle stability, the mechanism of system comes into play and maintain the appropriate brake force on wheels to match the rotational speed required for steering the wheels and makes driver to get the control back. ESC is continuously working in the background and monitors the steering angle and direction of vehicle. It continuously analyzes the driver's proposed direction (determined through steering wheel angle subtended) to the vehicle's absolute direction (determined through measured lateral acceleration). The ESC interposes only when it detects a possible loss of steering control. The ESC system works very precisely to make the ride safer.

2.6 Traction control system

Traction control system prevents the controllable spinning of wheels faster than another or than the required speed. It is always coupled with ABS and when the speed sensors detects wheel spinning faster, brakes are applied to that wheel so that proper traction is regained by the wheel. Moreover this braking action over one wheel will cause the transfer of power to the wheel axle with traction due to differential. Sometimes in 4 wheel drive vehicles, the traction control system also reduces engine power transmitted to the wheel which loses traction.

2.7 Active Brake Assist

Reaction time of humans is comparatively less than the modern electronic sensors. The purpose of ACTIVE BRAKE ASSIST is to control and stop the vehicle in safe manner. Various studies and tests have revealed that different drivers react differently to critical situation. Some doesn't press the brakes hard enough, some are hesitant at the beginning, and some are not even able to evaluate the situation properly. A system indented to support the driver in emergency braking situation must be capable of identifying emergency situation as well as should apply the brake precisely and more accurately. For this, sensors are provided along with the camera in the front part of car which monitors the speed of vehicle in front of our vehicle, if any emergency is detected and driver response is not good enough, then vehicle automatically applies the brake (20-40%) and gives audio visual warning to driver and even if driver doesn't response properly it applies the 100% brake pressure, recognising the emergency braking manoeuvre. This system along with ABS, EBD and ESP can not only reduce the braking distance up to great extent but also provide stability to vehicle.

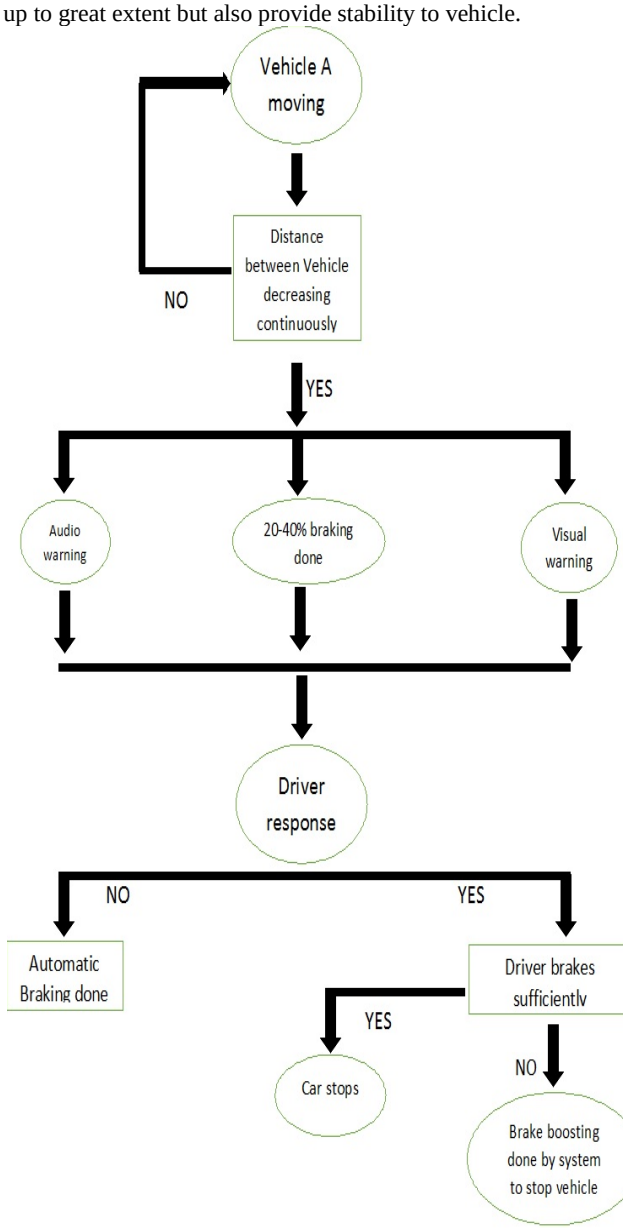


Fig. 1 Brake circuit

3.Methedology

This experiment has been performed using a scale model of car which was being remote controlled and equipped with infra red sensors on front and rear side. Along with sensors, warning lights are provided on the rear side of car to indicate the vehicle behind our vehicle, that our car is under braking.

3.1 Case 1

The car in front of our car retards at a continuous rate and distance between two cars is decreasing to an alarming level.

For such cases, ACTIVE BRAKE ASSIST will first warn the driver if the two vehicles come too close. During this 20-40% brake force will come into action and audio visual warning will be provided to driver and even if driver does not respond and cars come further closer then 100% brake pressure is provided to brakes to stop the car and prevent any type of potential accident.

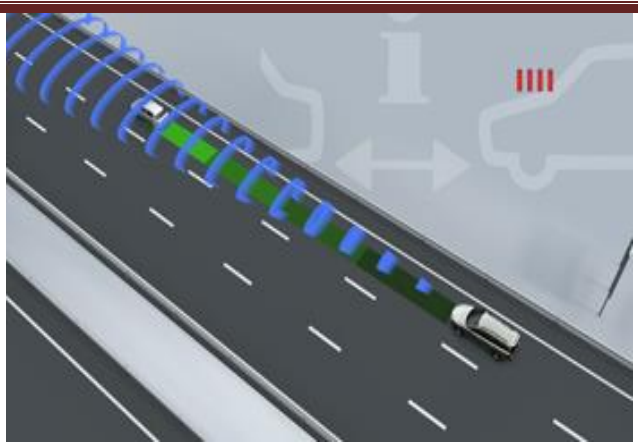


Fig.2 Vehile time on road [14]

3.2 Case 2

If during an emergency situation (that has been detected by Brake assist system) driver doesn't press the brake pedal hard enough to utilise the complete brake force .Then in such cases Brake assist system will automatically apply the brakes using 100% braking force to stop the car within the safe limits and safely.

3.3 Working Principle

Brake assist use radar with help of long range infrared sensors and or cameras to scan ahead of the car for moving and stationary hazards. If a potential collision is detected, audiovisual warnings are provided to the driver and the brakes are primed ready for maximum application. This also allows the car to automatically apply the brakes to slow the car if the driver does not respond to repeated warnings and the system detects an unavoidable collision. Along with this, if in case brakes applied by driver is not hard enough then brake assist provides extra (or remaining) brake power. So we can say brake assist works in two ways or manners .First: provides extra braking power in emergency if brakes applied are not enough, second: it gives warning and automatically applies brakes if driver doesn't respond to emergency situation.

4. Result

When the distance between the vehicle and the object (or vehicle) is decreasing continuously with a rapid rate, the active brake assist system comes into play. Almost 20-40% of braking energy is utilised in automatic braking action with proper amount of brake boosting, during this the audio and video warning catches the driver's attention to respond towards braking. Still if the diver doesn't respond and the distance is in decreasing manner then complete braking energy is utilised automatically to stop the vehicle gradually and safely. This reduces the overall braking distance. It will negotiate many hazardous accidents which harshly harm human life, vehicle and environment resources.

5.Conclusions

The expected benefits of active brake assist are many, particularly given the kinds of situations that active brake assist is designed to address. Nearly 1.3 million people die every year on the world's roads and 20 to 50 million people suffer non-fatal injuries, with many sustaining a disability as a result of their injury. Road traffic injuries are the leading cause of death among young people aged 15-29 years and cost countries 1-3% of the gross domestic product (GDP). The Insurance Institute for Highway Safety (IIHS) in the United States has determined that the kinds of crashes relevant to brake assist are those where the driver saw a hazard, braked, but did not stop in time. Given this, the IIHS estimates that brake assist is relevant to 417,000 crashes per year in the United States only, including 3,080 fatal crashes. With the Active brake assist, all such situations can be easily controlled which endanger not only the human life but also the economical resources involved.

References

[1.] Ken Schmitt, Roman Mannale, Rolf Isermann. Situation analysis, warning and emergency braking for collision avoidance in overtaking situation- PRORETA 2. Munich, Germany, July 12-14, 2010.

[2.] Erik Rosen, Tom Erik Kallhammer, Dick Eriksson, Mathias Nentwich, Rikard Fredriksson, Kip Smith. Pedestrian injury mitigation by autonomous braking. 42, 2010, A49-1957.

[3.] Ossama Mokhiamar. Stabilisation of car-caravan combination using independent steer and drive/or brake forces distribution. Alexandria Engineering Journal 54, 2015, 315-324.

[4.] Dragan Aleksendric, Zivana Jakovljevic, Velimer Cirovic. Intelligent control of braking process. Expert systems with application 39, 2012, 11758-11765.

[5.] Claudia Wege, Sebastian Will, Trent Victor. Eye movement and brake reaction to real world brake capacity forward collision warning – a naturalistic driving study. Accident analysis and prevention 58, 2013, 259-270.

[6.] Nils Lubbe, Johan Davidsson. Drivers comfort boundaries in pedestrian crossing: a study in driver braking characteristics as a function of pedestrian walking seed. Safety science 75, 2015, 100106.

[7.] Daniel Ruscio, Maria Rita Ciceri, Fedrerica Biassoni. How does a collision warning system shape drivers brake response time? The influence and automation complacency on real life emergency braking. Accident analysis and prevention 77, 2015, 72-81.

[8.] Gustav Markkula, Johan Engstrom, Johan Loclin, Jonas Bargaman, Trent Victor. A farewell to brake reaction times? Kinematics dependent brake response in naturalistic rear end emergencies. Accident analysis and prevention 95, 2016, 209-226.

[9.] Milad Jalali, Amir Khajepour, Shik-ken Chen, Bakhtiar Litkouhi. Integrated stability and traction control for electric vehicles using model predictive control. Control Engineering Practice 54, 2016, 256266.

[10.] Jeonghoon Song, Woo Seong Che. Comparison between braking and steering yaw moment controllers considering ABS control aspects. Mechatronics 19, 2009, 1126–1133.

[11.] Daniel Lindvai-Soos, Martin Horn. Modelling, control & implementation of an electro-mechanic braking force actuator for HEV and EV. 7th IFAC Symposium on Advances in Automotive Control .The International Federation of Automatic Control September 4-7, 2013.

[12.] Alexandro Badea-Romero, F. Javier Paez, Arturo Furones, Jose M. Barrios, Juan l. de-Miguel. Assessing the benefits of the brake assist system for pedestrian injury mitigation through real world accident investigations. Safety science 53, 2013, 193-201.

[13.] G. Ramkumar, Amrit Om Nayak, D. Manikandan. Modelling and numerical analysis of high speed turbo braking assists. ICMOC 2012: 10-11 April 2012, India.

[14.] www.howsafeisyourcar.com.au

ISSN: 2321-7782 (Online)
e-ISJN: A4372-3114
Impact Factor: 6.047

Volume 5, Issue 7, July 2017

International Journal of Advance Research in Computer Science and Management Studies

Research Article / Survey Paper / Case Study

Available online at: www.ijarcsms.com

A Unified Approach for Classification of Software Reliability Models

Kuldeep Singh Kaswan[1]
Department of Computer Science
PDM College of Engg., Bahadurgarh
Haryana – India

Sunita Choudhary[2]
Department of Computer Science
Banasthali University, Banasthali
Rajasthan – India

Kapil Sharma[3]
Department of Computer Science & Engineering
Delhi Technological University
Delhi – India

Abstract: ***There are a number of classification schemes for the software reliability models. These classification schemes follow different parameters for classification as SDLC (Software Development Life Cycle) based, failure count based, nature based, software architecture based, randomness based and data requirement based etc. Emphasis of this paper is on the Software Development Life Cycle based classification and then tries to attach these existing classification schemes with the KS Kaswan purposed classification scheme. This study will provide us a new classification approach, which would help to achieve better confidence level in model selection process.***

Keywords: SDLC, software reliability models classification, architecture based, input domain based models.

I. INTRODUCTION

A software reliability model is the form of a random process that describes the behavior of software failure with respect to time [1].

When we develop software, a number of faults are generated and these faults degrade the efficiency of the software. So to remove and estimate such type of errors in the software development, software reliability models help us. In the past few years a lot of work has been carried out in this field of software reliability models, as the consequences, lots of models are in the market today.

In the initial phase of development of software reliability models, these were viewed as a Birth and Death process by Hudson (1967).

But the first influential model was developed by Jelinski and Moranda (JM Model) in 1972. Later on there were many variations of the JM model in market. Goel and Okumoto (1979), Meinhold and Singpurwalla (1983), Karunanithi (1992), Popstojanova et al. (2000), Teng and Pham (2002), Aljahdali (2008), Sharma et al. (2010), Chatterjee et al. (2012), Inoue and Yamada (2013) and Zheng et al. (2013) and Tyagi and Sharma (2014) have their large contribute in this field.

This paper is organized as follows: section II includes existing classifications based on Software development cycle. In section III classification based on other parameters has discussed. Software Development Cycle Phases with Existing Reliability Models Classifications is given in section IV. Summarization of the whole work is given in section V. Finally, the paper concludes with section VI.

© 2017, IJARCSMS All Rights Reserved

II. Classification based on Software Development Life Cycle (SDLC)

In the past few decades a number of software reliability models have been purposed, designed and modified. These models are very useful but some of these have also been suffered from a lot of critiques. To make it easy to select the best one among the existing models, many researchers' categorized these models based on different parameters. In this section, we have reviewed the existing software reliability classification based on SDLC phases.

Ramamoorthy and Bastani [2] classified the existing software reliability models based on the phases of software development life cycle during which the model is applicable. These models are applicable during the testing, debugging, validation or operational phase.

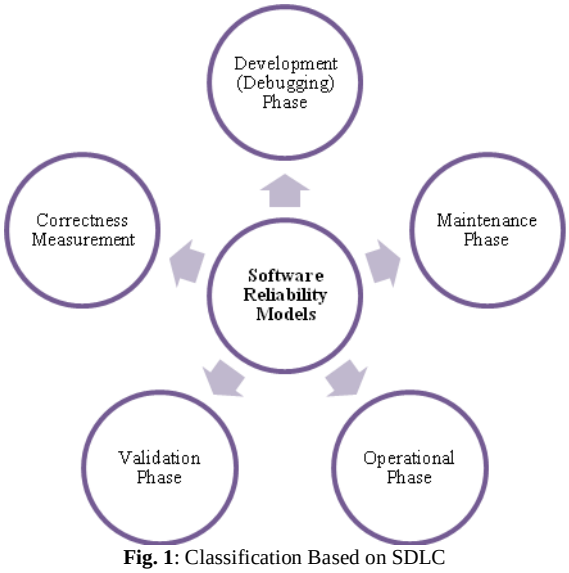


Fig. 1: Classification Based on SDLC

K Sharma [3] discussed about the SDLC based classification of exiting software reliability models. In this classification, the models are categorized as the Requirement phase models, Design phase models, Implementation phase, Testing phase and Validation Phase models.

Zhanwei Hui [4] designed the classification scheme for software reliability models according to the Software Development cycle phases which includes the Requirement phase models, design phase models, Realization models, test and Confirm Phase models.

KS Kaswan [5] classified the models as the same as K Sharma [3] classification but this classification scheme also includes a new family of models as the User Domain models in the maintenance and Operation phase.

III. Classification based on other Parameters

In this section we have reviewed the existing software reliability classification based on different parameters.

a. Based on Nature of Debugging Strategy

Ramamoorthy & Bastani (1986) classified the software reliability models in three categories as [6]

1. Reliability Growth Model

2. Seeding Model

3. Sampling Method Model

Reliability growth models measures and predicts the improvement of reliability through the debugging process. A growth function is used to represent the progress. There are two types of variables, dependent and independent, Reliability, failure rate or cumulative number of errors detected is dependent and time, number of test cases or testing stages are independent variables.

© 2017, IJARCSMS All Rights Reserved

The error seeding models estimates the number of errors in a program by using the capture-recapture sampling technique. These errors can be divided into two categories as existing errors and seeding errors. Existing errors are estimated from the number of seeded errors.

b. Based on Nature of Failure Process

AL Goel (1985) divides models into four classes as given below [7]

1. Time between Failure Models

2. Failure Count Model

3. Fault Seeding Model

4. Input Domain Models

Time between failures models consider the time between failures for the process. Time between two consecutive failures follows a distribution which is depended on the number of remaining faults in the interval.

Failure count model consider the number of faults in specified time intervals rather than in times between failures. Failure rate parameters can be estimated from the observed values of failure counts or from failure counts.

In fault seeding models, a predefined number of artificially generated errors are seeded in the program code. Now by testing we detect the errors and find out the ratio between actual and artificial errors based on the total number of detected errors. This is used to assess software reliability and other relevant measures.

Input domain based models is based on the set of test cases from an input distribution which is assumed to be representative of the operational usage of the program. In this approach we divide the input domain into a set of equivalence classes. From the execution of these set of test cases we obtained the failures and on the behalf of these failures estimate the reliability.

c. Based on Unified SDLC

KS Kaswan (2015) classified the software reliability models according to the unified software development life cycle which includes the four phases as given below [8]

1. Inception

2. Elaboration

3. Construction

4. Transition

In the first phase, inception, of unified software development model, we set the scope of project with its boundary settings, estimate the cost.

In the second phase, Elaboration, continue work on the use-case model, sketch out application architecture and recognize the risk, deal with recognized risk factors to begin validating the system architecture. The final Elaboration phase deliverable is a sketch including expenditure and schedule estimates used for the Construction phase.

Third phase is the construction phase, Unified Modeling Language diagrams are used throughout this phase and encompass Collaboration, State Transition, Activity, Sequence and Interaction Overview diagrams. The implementation is the most significant body of work enhanced during construction.

In the final, transition phase, the system is hand over to the intended users and a complete system testing is being take place.

© 2017, IJARCSMS All Rights Reserved

d. Based on Testing Process

PB Kysetti (2004) emphasized on Black Box and White Box models for software reliability models as given below[9].

1. Single System (White Box)

2. Multi Components System (Black Box)

This model considers the whole software as a single monolithic system and the structure of the model is not considered in the process of reliability estimation of the software system. These models not considered for the structure of the software. Its failure behavior is usually modeled using software reliability growth model.

Multi components based system uses the software architecture of the system. It's a components based software modeling. These models fit in the testing method and the structure of the software being tested.

e. Based on White Box Modeling

White box models are those that model modular software systems considering the architecture of the system. Popstajanova and Trivedi (2001) classified the models as the given below [10]

1. State Based Models

2. Path Based Models

3. Additive Models

State based models uses the program flow graph to represent the architecture of the system taking into the consideration that modules transfer control has a Markov property. The system has the properties of discrete time Markov chain, continuous time Markov chain or semi Markov process.

Path based models has the same common steps as the state based models, consider software architecture with components and interfaces. Initially the different paths in system are obtained so that we can find these reliabilities along the path. The system reliability is the average of all the path reliabilities.

Additive based models do not consider explicitly the architecture of the software. In this class of models the emphasis is on estimating the overall application reliability by components failure data. Additive based models consider software testing phase and each component reliability is modeled by NHPP.

f. Based on Failure Counting Classification

J. D. Musa and K. Okumoto (1984) classified the software reliability models based on the failure counting in software as given below [11]

1. Finite Failure

2. Infinite Failure

All Exponential, Weibull and Pareto are the finite failures categories models.

Software is not completely error free when mean value function of a particular model tends to infinity. Models come under the category of Infinite Failure Time Model.

g. Classification Based on Analytical Modeling

Pham (1999) [12] categories the models as given below:

1. Reliability Growth Models

© 2017, IJARCSMS All Rights Reserved

2. Sampling Method Models

Reliability growth models measures and predicts the improvement of reliability through the debugging process. A growth function is used to represent the progress. There are two types of variables, dependent and independent, Reliability, failure rate or cumulative number of errors detected is dependent and time, number of test cases or testing stages are independent variables.

IV. New Classification Approach for Existing Reliability Model

The integration of the existing classification will create a new structure that will be helpful in understanding the concept of reliability models applicability.

(A) There are two classification scheme, first one is purposed a new classification scheme based on applicability of software reliability models according to the software development life cycle phases including the maintenance phase, which plays a critical role in software development now a days in the competitive world. Second classification scheme based on Unified Software development life cycle, which is applicable on the same class of models.

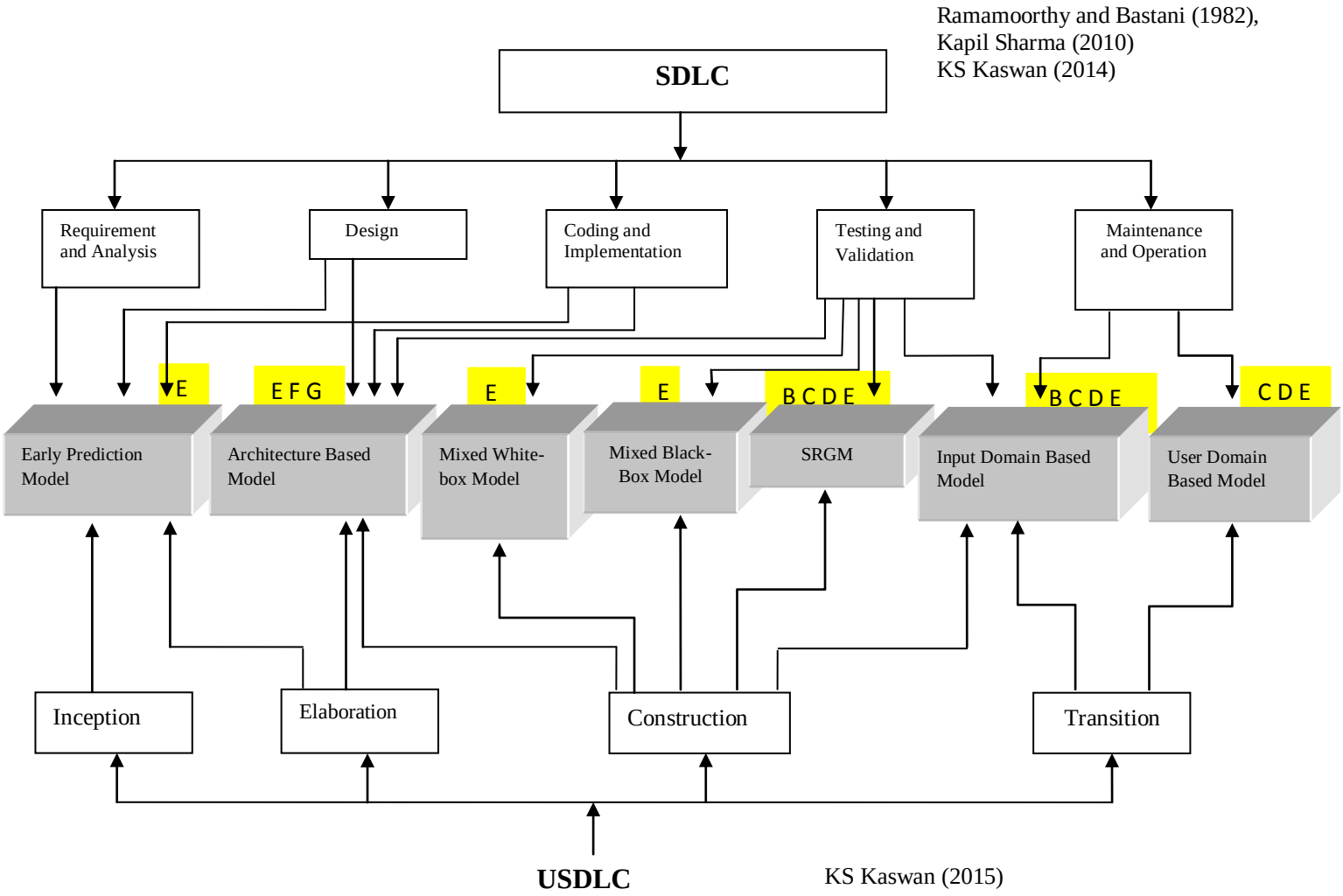


Fig 2: Classification Based on SDLC and USDLC

(B) The number of failures that can be experienced in infinite time is finite or infinite.

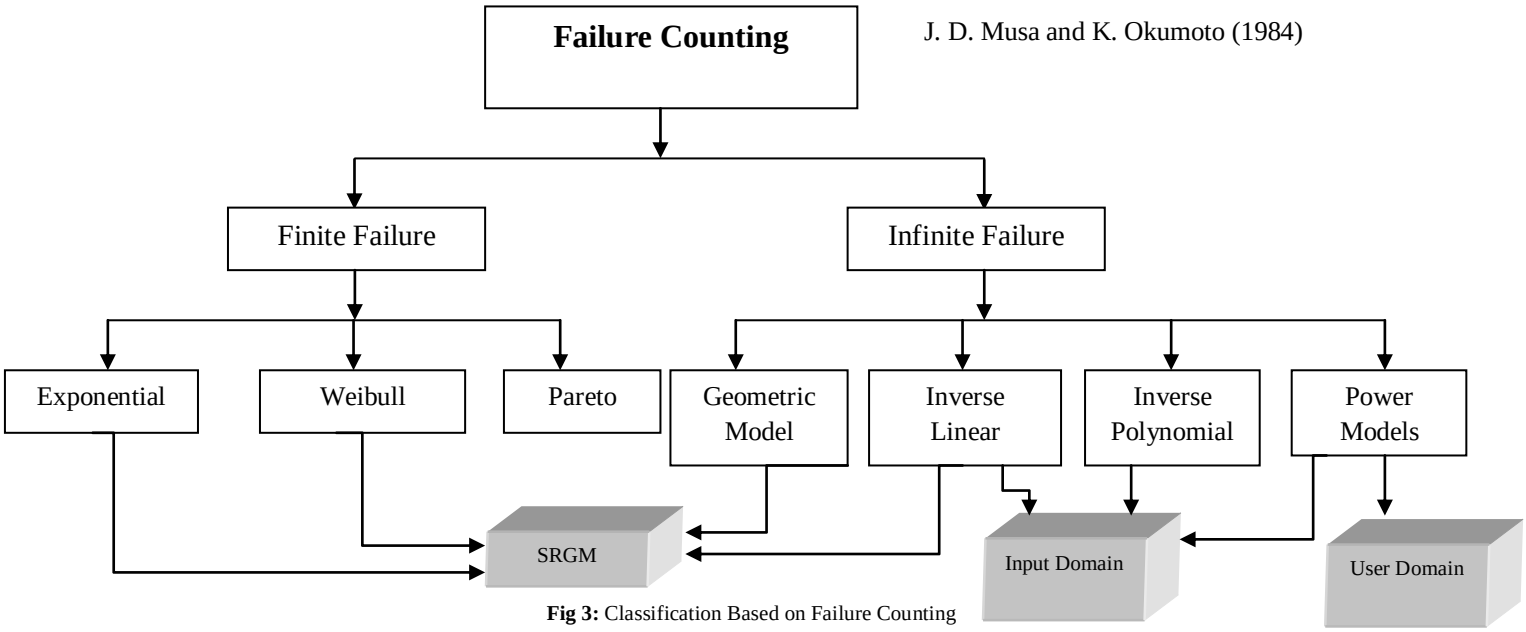


Fig 3: Classification Based on Failure Counting

(C) Software reliability models can be classified based on the nature of the failure process as given below:

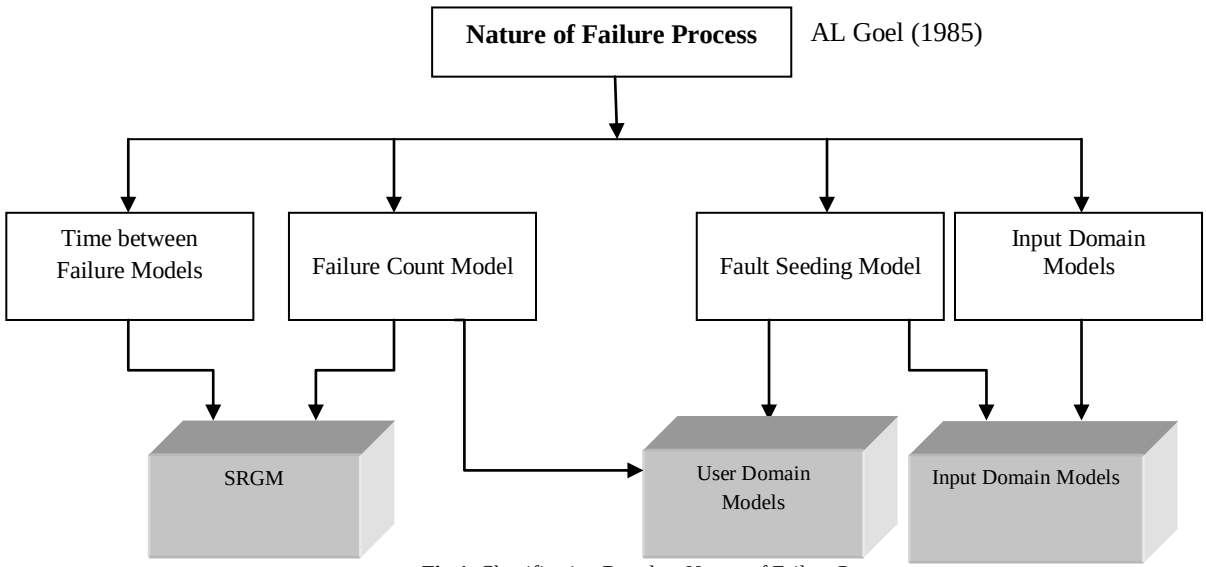


Fig 4: Classification Based on Nature of Failure Process

(D) There are different debugging strategies for the software testing based on these strategies software reliability models can be classified into three different categories as given below:

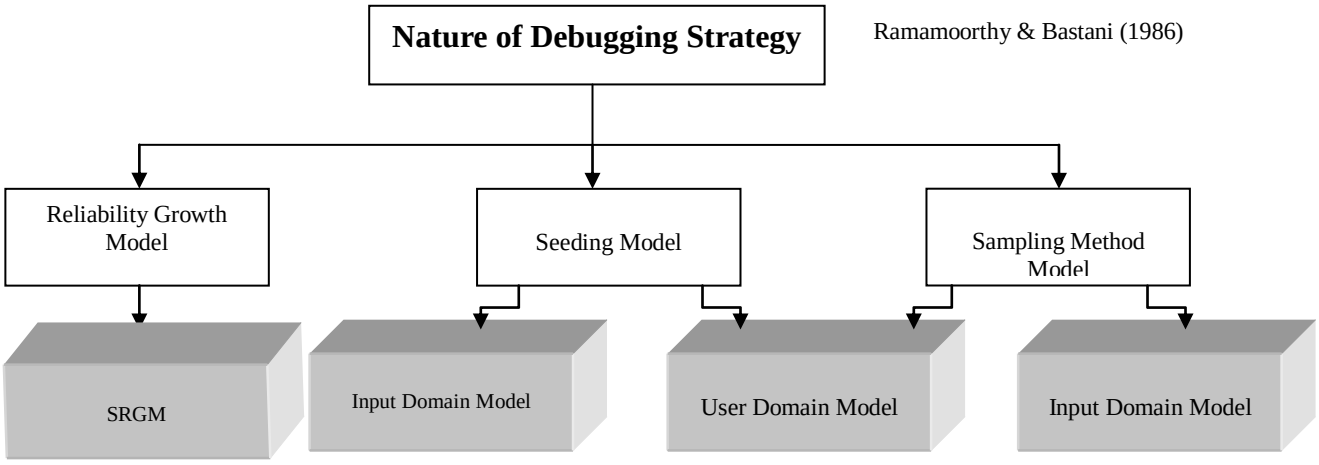


Fig 5: Classification Based on Nature of Debugging Strategy

© 2017, IJARCSMS All Rights Reserved

(E) An analytical model requires some form of data gathered from software failures during software testing and prediction of SWR parameters from the fitted distribution. Analytical models can be further subdivided into Static Models and Dynamic Models based on time dependent behavior of collected data. [12]

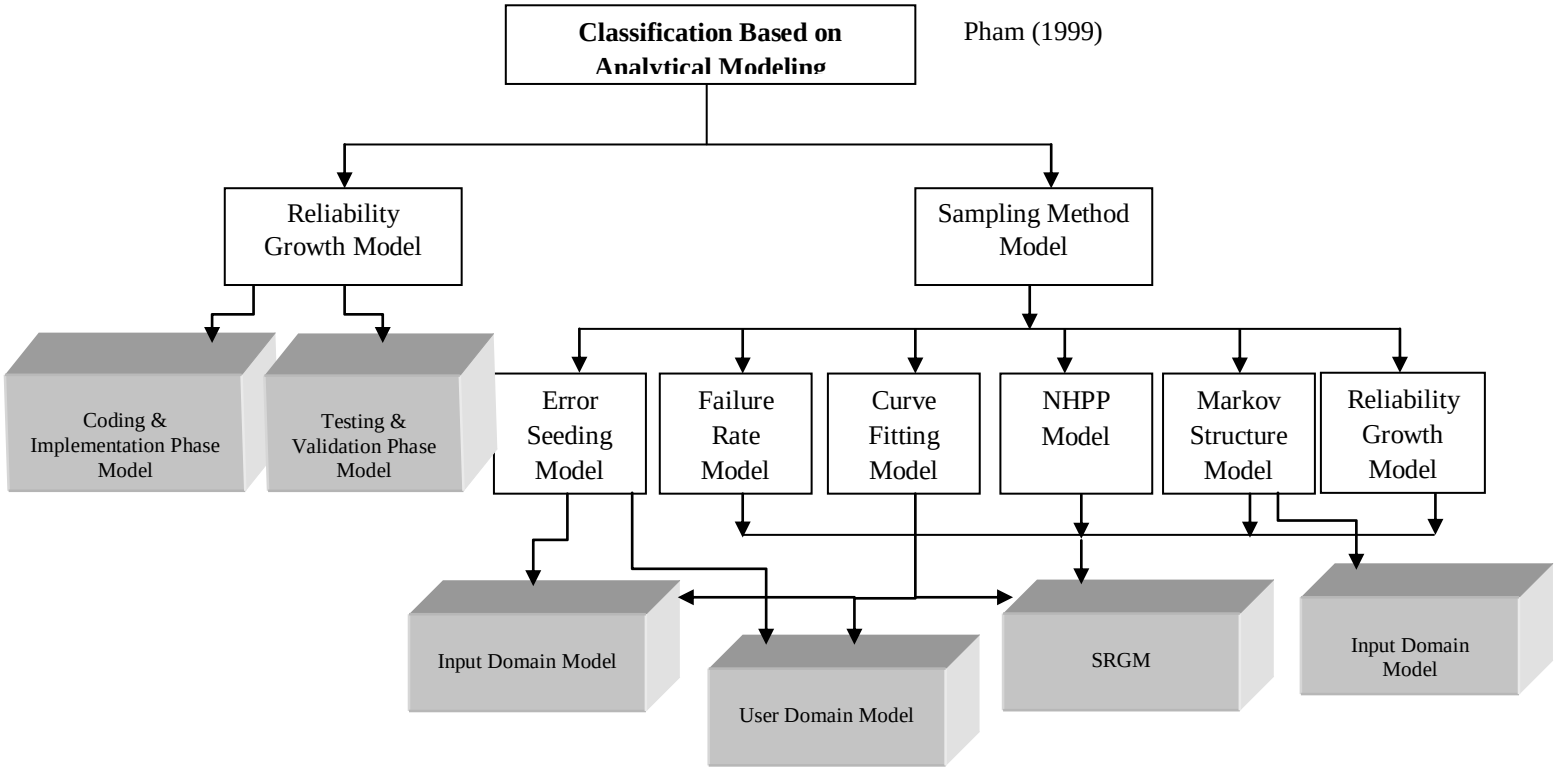


Fig 6: Classification Based on Analytical Modeling

(F) White box modeling approach to software reliability that takes into account the information about the architecture of the software made out of components.

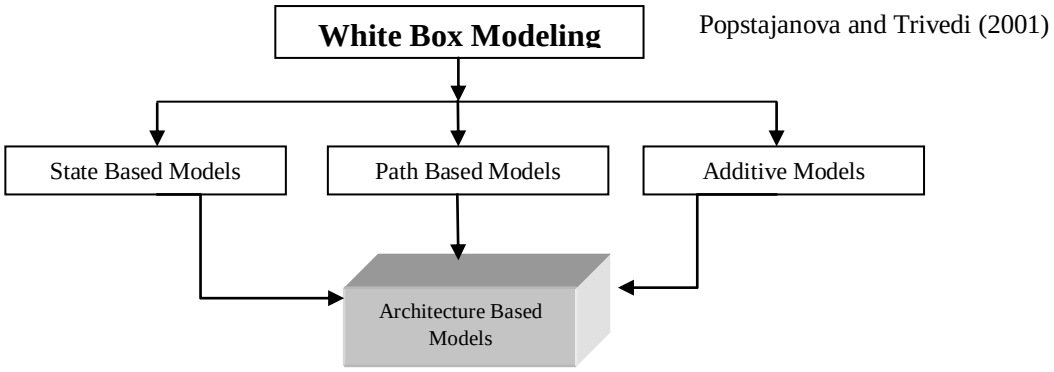


Fig 7: Classification Based on White Box Modeling

(G) In this classification Software Reliability Models are divided into white box and black box models

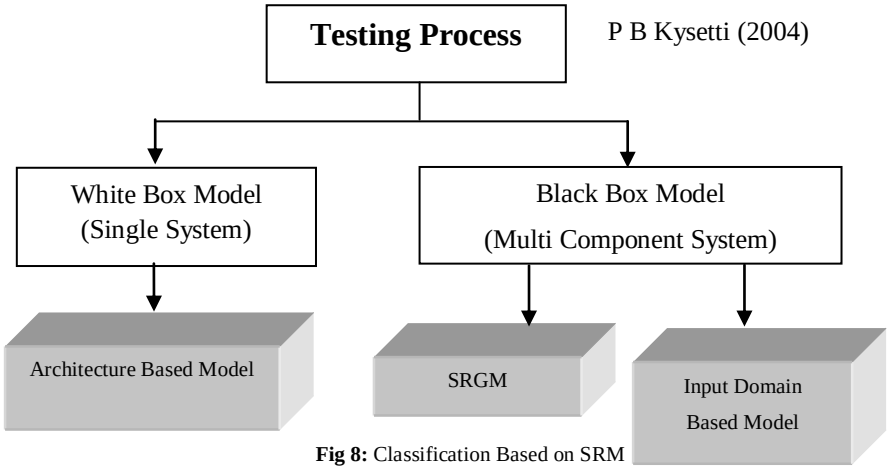


Fig 8: Classification Based on SRM

© 2017, IJARCSMS All Rights Reserved

V. SUMMARIZATION

In this section we summarize the work done by the different authors in the classification of the software reliability models.

Table 1: Summary of Software Reliability Models Classifications

Sr. No.	Author(s)	Year	Criteria for Classification	Proposed Phases by various author(s)	Examples	References
1.	Ramamoorthy & Bastani	1982	SDLC Phases	• Development Phase • Correctness Measurement • Validation Phase • Operational Phase • Maintenance Phase	➢ All existing phases are SDLC phases	[2]
2.	J. D. Musa and K. Okumoto	1984	Failure Counting	• Finite Failure • Infinite Failure	➢ SRGM ➢ Input Domain Based Model ➢ User Domain Based Model	[11]
3.	AL Goel	1985	Nature of Failure Process	• Time between Failure Models • Failure Count Model • Fault Seeding Model • Input Domain Models	➢ SRGM ➢ Input Domain Based Model ➢ User Domain Based Model	[7]
4.	Ramamoorthy & Bastani	1986	Nature of Debugging Strategy	• Reliability Growth Model • Seeding Model • Sampling Method Model	➢ SRGM ➢ Input Domain Model ➢ User Domain Model	[6]
5.	Pham	1999	Analytical Modeling	• Reliability Growth Models • Sampling Method Models	➢ Reliability Growth Model ➢ SRGM ➢ Input Domain Model ➢ User Domain Model	[12]
6.	Popstajanova and Trivedi	2001	White Box Modeling	• State Based Models • Path Based Models • Additive Models	➢ Architecture Based Models	[10]
7.	PB Kysetti	2004	Testing Process	• Single System (White Box) • Multi Components System (Black Box)	➢ Architecture Based Model ➢ SRGM ➢ Input Domain Model Based Model	[9]
8.	K Sharma	2010	SDLC Phases	• Requirement Phase • Design Phase • Implementation Phase • Testing Phase • Validation Phase.	➢ All existing phases are SDLC phases	[3]
9.	Zhanwei Hui	2011	SDLC Phases	• Requirement Phase • Design Phase • Realization • Test • Confirm Phase	➢ All existing phases are SDLC phases	[4]
10.	KS Kaswan	2014	SDLC Phases	• Requirement and Analysis • Design • Coding and • Implementation • Testing and Validation • Maintenance and Operation	➢ All existing phases are SDLC phases	[6]

© 2017, IJARCSMS All Rights Reserved

11.	KS Kaswan	2015	Unified SDLC	• Inception • Elaboration • Construction • Transition	➢ Early Prediction Model ➢ Architecture Based Model ➢ Mixed White-box Model ➢ Mixed Black-Box Model ➢ SRGM ➢ Input Domain Based Model ➢ User Domain Based Model	[8]

This table revealed that the existing software reliability models classifications can be attached with the different phases of the software development life cycle.

VI. CONCLUSION

This paper present an overview on the different existing classifications of software reliability models and showed how these classifications can be attached with the classification purposed by KS Kaswan. This paper will provide user an insight into the classification structure of such models that would be helpful in determining which model to use in a given software development environment. We can easily reject 80% of the models which is not useful for us as per requirement and choose the particular model out of the remaining which is not so difficult task.

References

1. Michael R. Lyu, "Software Reliability Engineering: A Roadmap", IEEE Computer Society, Future of software Engineering, pp: 153-170, 2007.
2. Ramamoorthy&Bastani82 C. V. Ramamoorthy, F. B. Bastani, Software reliability — status and perspectives, IEEE, Trans. Soft. Eng., SE-8, No. 4, July 1982, pp. 354 - 371.
3. Kapil Sharma, Rakesh Garg, C. K. Nagpal, and R. K. Garg, "Selection of Optimal Software Reliability Growth Models Using a Distance Based Approach", IEEE Transactions on Reliability, Vol. 59, no. 2, June 2010
4. Zhanwei Hui, Xiaoming Liu and Song Huang, "Software Reliability Model Metrics: Precision and Robustness", International Journal of Advanced Computer Science, Vol. 1, No. 6, Pp. 250-256, 2011.
5. K. S. Kaswan, Sunita Choudhary and Kapil Sharma, "A New Classification and Applicability of Software Reliability Models", International Journal of Advance Research in Computer Science and Management Studies, Vol. 2, Issue 7, pp. 99-104, 2014
6. F.B. Bastani, C.V. Ramamoorthy, "Input-domain based models for estimating the correctness of process control programs", Reliability Theory (Serra & Barlow, Eds), 1986, pp 321-378; North Holland.
7. Goel85 A. L. Goel, Software Reliability Models: assumptions, limitations, and applicability, IEEE, Trans. Soft. Eng., SE-11, No. 12, Dec. 1985, pp. 1411 - 1423.
8. Kuldeep Singh Kaswan, Sunita Choudhary and Kapil Sharma, "Unified Software Development Process Based Classification of Software Reliability Models", pp. 2078-2083, 2015 IEEE.
9. Praveen Babu Kysetti, "Optimal Test Case Selection for Multi-Component Software System", the Department of Industrial & Manufacturing Systems Engineering, B.S., Bangalore University, India, 2004.
10. Popstojanova, K.G., and Trivedi, K.S., (2001), "Architecture-Based approach to reliability assessment of Software Systems," Preprint submitted to Elsevier 2001, Citseer.
11. J. D. Musa and K. Okumoto, "A Logarithmic Poisson Execution Time Model for Software Reliability Measurement", pp. 230-238, 1984 IEEE.
12. Pham, H. and Zhang, X., "A software cost model with warranty and risk costs", IEEE Transactions on Computers, 48: 71-75, 1999.

© 2017, IJARCSMS All Rights Reserved

Author(s) Profile



Kuldeep Singh Kaswan, was born in Haryana, India in 1982. He received Doctors Degree in Computer Science under the faculty of Computer Science at Banasthali Vidyapith, Rajasthan. He has obtained his Master Degree in Computer Science and Engineering from Choudhary Devi Lal University, Sirsa (Haryana) and Bachelor Degree from Kurukshetra University, Kurukshetra (Haryana). His area of interests includes software engineering and reliability.



Sunita Choudhary, was born in Rajasthan, India in 1978. She received Doctors Degree in Computer Science under the Faculty of Computer Science at the Banasthali University (Rajasthan), India. She has obtained his Bachelor of Science in Computer Science and Master of Computer Application Degrees from Banasthali University in 1999, and 2001 respectively. Presently, she is working as an associate professor in Department of Computer Science at Banasthali University, Rajasthan, India. Her research interests include Algorithms and Distributed Computing.



Kapil Sharma, was born in Haryana, India in 1977. He received Doctors Degree in Computer Science and Engineering under the Faculty of Engineering and Technology at the M. D. University, Rohtak (Haryana), India. He has obtained his Bachelor of Engineering and Master of Technology Degrees in Computer Science & Engineering and Information Technology from M. D. University, Rohtak, and IASE, Rajasthan, India in 2000, and 2005 respectively. Presently, he is working as an associate professor in Department of Computer Science at Delhi Technological University, Delhi, India. His research interests include software engineering, and reliability.

© 2017, IJARCSMS All Rights Reserved

DOI: http://dx.doi.org/10.26483/ijarcs.v8i7.4217

ISSN No. 0976-5697

Volume 8, No. 7, July – August 2017

International Journal of Advanced Research in Computer Science

RESEARCH PAPER

Available Online at www.ijarcs.info

ACHIEVING ENERGY EFFICIENCY AND STABILITY IN WSN USING A NOVEL MOBILE SINK APPROACH BASED ON BIOGEOGRAPHY BASED OPTIMIZATION

Ajay Kaushik
Department of Computer Science and Eng.,
Kurukshetra university, Haryana, India

Amit Kumar Gautam
Department of Electronics and Communication Eng.,
Delhi Technological University Delhi, India

***Abstract*–**Wireless sensor networks are constrained with limited battery lifetime. Cluster head near the base station act as relays to the cluster heads far from the base station resulting in fast depletion of the cluster head close to the base station. To overcome this problem mobile sink have been used in the past. The proposed algorithm finds the optimum path and sojourn location of the mobile sink using biogeography based optimization (BBO). BBO not only converge faster as compared to GA but it also gives more optimized results. The proposed algorithm is compared with previous protocols such as LEACH, GA based clustering, PSO based clustering. The algorithm is implemented using MATLAB simulation tool. The proposed algorithm performs better both in terms of lifetime of the cluster heads as well as lifetime of the entire network.

Keywords – wireless sensor networks, mobile sink, biogeography based optimization, cluster head.

I. INTRODUCTION

Wireless sensor networks (WSNs) are an emerging technology[1] that has potential applications in surveillance, environmentand habitat monitoring, structural monitoring, healthcare, anddisaster management [2]. AWSN monitors an environment by sensingits physical properties. It is a network of tiny, inexpensive autonomousnodes that can acquire, process, and transmit sensory data over wirelessmedium. One or more powerful base stations serve as the destinationof the data. The properties ofWSNs that pose technical challengesinclude dense ad-hoc deployment, dynamic topology, spatial distribution,and constrains in bandwidth, memory, computational resources,and energy.WSN issues such as node deployment, localization, energy-awareclustering, and data aggregation are often formulated as optimizationproblems. Traditional analytical optimization techniques require enormouscomputational efforts, which grow exponentially as the problemsize increases. An optimization method that requires moderate memoryand computational resources and yet produces good results is desirable,especially for implementation on an individual sensor node. Moreover, the sensor nodes near the static sink act as relays for sensors that are far from it and thus will deplete their energy very quickly, resulting energy holes in the sensor field. The energy hole problem leads to a premature disconnection of the network and thus sink gets isolated from the rest of the network due to the death of its neighbours, while most of the sensor nodes are still alive and fully operational. WSN structure is shown in figure 1.
Exploiting the mobility of the sink has been widely accepted as an efficient way to alleviate the energy hole problem in WSNs and further prolong the network lifetime by avoiding excessive transmission overhead at nodes that are close to the sink [3] [4].

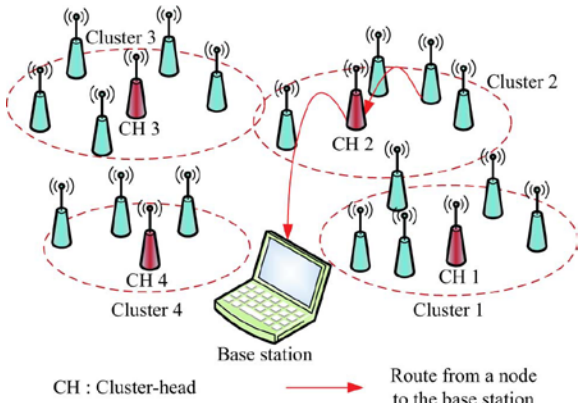


Figure 1 – Structure of a WSN

Clustering algorithms can effectively organize the sensor nodes in the network and using a controlled mobile sink can solve the energy hole problem. However, finding the optimum number of CHs and the optimal moving trajectory for the mobile sink are Non-Deterministic Polynomial -time hard (NP-hard) problems. In this paper, a Mobile Sink based clustering Protocol has been proposed to improve the lifetime of WSNs and to mitigate the energy hole problem. Proposed work uses the Biogeography Based Optimization (BBO) to find the sojourn locations of the mobile sink and the optimum number of CHs and their locations based on minimizing the total dissipated energy in communication process and overhead control packets of all sensor nodes within the network.

II. LITERATURE REVIEW

Traditional-optimization methods include linear, nonlinear, and quadratic programming, Newton-based techniques, and interior-point methods. Their computational complexities

© 2015-19, IJARCS All Rights Reserved

grow exponentially with the problem size. Resource requirements and cost of mathematical programming engines (such as IBM ILOG CPLEX) used for linear, nonlinear, and quadratic programming make them unattractive for resource constrained nodes. This is the motivation for heuristic algorithms such as PSO, genetic algorithm (GA), differential evolution (DE), and bacterial foraging algorithm (BFA). GA facilitates evolution of the population generation by generation using operators such as crossover, mutation, and selection [5]. DE is similar to GA, but it uses a differential operator [6], In LEACH, CH collects and aggregates data from the sensors in its own cluster and passes the data to the sink directly. The problem of LEACH protocol is the randomly selection of CHs. LEACH requires the user to specify the desired probability of CHs that uses in determining whether a node becomes a CH or not. However, Genetic Algorithm based LEACH (LEACH-GA) proposed in [5] uses GA to find the optimal probability of CHs. LEACH-GA improves the CHs threshold function, but still CHs are randomly selected and the residual energy of each node is not considered in CH selection process. A new protocol called Amend LEACH (A-LEACH) was developed in [6] [7], for electing CHs in a distributed fashion and improving the stability period of two-level hierarchical heterogeneous WSNs. WSNs with mobile sinks have attracted a lot of attention recently. In [8] authors developed an Intelligent Agent-based Routing (IAR) protocol to guarantee efficient datadelivery to sink and reduces signal overhead. The idea of IARis choosing some sensors as agents. Then, the sink moves nearan agent and receives data if it is in the range of the agent,and if not, the sink chooses a sensor as a temporary relaynode which receives data from agent and forwards it to sink.Authors in [9] formulated the distance constrained mobile sinkproblem as a mixed integer linear programming and deviseda novel heuristic to find an optimal sojourn tour for the sinkbased on maximizing the sum of sojourn times during the tour.Mobile Sink based Routing Protocol (MSRP) for prolongingthe network lifetime in clustered WSN has been addressedin [10]. In MSRP, the sink moves to CHs having higher energyin the clustered network to collect sensed data from them.A new optimizing LEACH clustering algorithm with mobilesink and rendezvous nodes was introduced in [11]. This algorithmcombines the use of the LEACH algorithm, mobile sinkand rendezvous points to preserve the benefits of the LEACHalgorithm and improve the CH selection process. Moreover,it decreases energy consumption in WSNs further than intraditional LEACH, particularly when the network is large.Mobile sink Improved Energy-Efficient PEGASIS-Basedrouting protocol (MIEEPB) has been presented in [12].MIEEPB introduces the sink mobility in the multi-chainmodel and divides the sensor field into four regions, there fo reachieving smaller chains and decreasing load on the leadernodes. The sink moves along its trajectory and stays for a time at fixed location in each region to guarantee data collection.

III. PROBLEM FORMULATION

The main constraint of a WSN scenario is that sensor nodes are battery operated. When a sensor node aggregates the data, it sends this data to thebase station. If the base station is too far away the sensor node dissipates too much energy and dies. To overcome this problem clustering technique was introduced. In clustering, all the sensor nodes aggregate their data and sends it to a cluster head or gateway. Then this gateway sends the aggregated data to the base station. But this clustering technique suffers with the same bottleneck as the cluster heads are battery operated and they die as soon as their battery gets dissipated [13] [14].

In the proposed algorithm, we device a new mechanism of making the base station or the sink mobile. Rather than sensor nodes or cluster head sending the data to the sink, the sink moves in the vicinity of the cluster heads.

IV. PROPOSED ALGORITHM

The proposed algorithm uses the concept of mobile sink. The algorithm is executed in the following steps:

1. Initially random deployment of sensor nodes is made throughout the deployment area.
2. The entire deployment area is divided into fixed sized hexagonal shaped partitions.
3. Sensor nodes are assigned to corresponding cluster heads and sensor nodes are assigned a unique id.
4. Base station is initially located at the corner of the deployment area.
5. Now for each cell we compute the sojourn location of the mobile sink in such a way in can sense and aggregate data from the cluster head by moving to each cell one by one. Also for each cell we minimize the energy consumption be minimizing the distance between a sensor node and the cluster head, distance between cluster head and the sink and total dissipated energy by the cluster head using BBO
6. Here inside each cell, location of the mobile sink is very important. The location should be chosen in such a way that minimum energy is dissipated in the process of mobile sink sensing and aggregating data from the corresponding cluster heads.
7. For finding the sojourn location of the mobile sink and minimize the energy consumption, we use biogeography based optimization. An illustration of the BBO is given below.

Most energy of the sensor node dissipates in the communication process and overhead control packets. So, the main factor we need to minimize is the dissipation energy. In addition, the numberof CHs can factor into the objective function. Fewer CHs result in greater energy efficiency and higher CHs consumemore energy as CHs drain more power than non-cluster-heads.Therefore, BBO is used to determine the mobile sink locationand the optimal number of clusters and their locations.

A. Overview of BBO

BBO is an evolutionary algorithm based on biogeography based optimization. Biogeography is the way nature distributes species and is analogous to general problem solutions [5]. In past many algorithms like genetic algorithm, particle swarm optimization and ant colony optimization were implemented for obtaining an optimum and fittest solution. BBO is an evolutionary algorithm that is

© 2015-19, IJARCS All Rights Reserved

implemented with the migration of species from one habitat to another habitat to maintain diversity in the population. [6].In BBO an individual is represented by a habitat. A population may contain many habitats like chromosomes in genetic algorithms. For each habitat in the population, habitat suitability index (HSI) value is calculated. HSI is a measure of the goodness of the habitat or solution. A habitat having high HSI value is considered to have higher fitness or more, suitable for population to grow and vice versa for habitat having low HSI value [7]. Based on this HSI value rank of each individual is calculated. Migration operation is performed to maintain diversity in the population in BBO. Migration involves migration of species from habitat having higher HSI value to habitat having lower HSI value [5]. Migration operation is based on immigration rate and emigration rate. A habitat having high HSI value will emigrate its suitability index variable (SIV) to habitat having low HSI value and habitat having low HSI value will immigrate SIV from habitat having high HSI value [8]. This emigration and immigration are done on the basis of emigration rate (mue) and immigration rate (lambda) which are calculated as follows:

Immigration rate (lambda) = $I\ (1 - k_i/n)$ (1)

Emigration rate (mue) = $E(k_i/n)$ (2)

Where

I = maximum immigration rate.

E = maximum emigration rate.

k_i= rank of the habitat.

n = total number of habitats.

B. *Calculation of HSI*

BBO is analogous to the genetic algorithm. In GA we use to calculate the fitness of every chromosome in the population. In BBO we calculate habitat suitability index value of each habitat of the population. The HSI value of a habitat is calculated using the following equation:

HSI = k * Energy (C.H) + (1/(Distance (Sink, C.H) + Distance(Node, C.H))) (3)

where k = constant

Energy (C.H) = residual energy of cluster head.

Distance (Sink, C.H = distance between sink and cluster head.

Distance (Node, C.H) = distance between a node and cluster head.

C. *Biogeography based optimization*

Now wireless clustering and performed using BBO and energy efficient clusters are made using the following technique.

D. *Habitat initialization*

36 sensor nodes are placed at a fixed location. S_N = {s1, s2, s3, s4……. s36}. 6 gateways are chosen as G = {g1, g2, g3…. g6}. Initialize habitats in the ecosystem with each habitat containing 2 vectors, one containing sensor nodes from s1 to s36 and another containing corresponding gateways randomly assigned to sensor nodes. The length of both the vectors is same. Entire population contains many habitats like this. Calculate HSI value of every individual gateway in gateway vector of each habitat with following formula:

HSI = k * Energy (C.H) + (1/(Distance (Sink, C.H) + Distance(Node, C.H))) (4)

For every gateway vector of each habitat, take the sum of HSI of all individual gateways. This will give a total HSI value of entire habitat. Now we have all possible habitats and their HSI values. Sort HSI values in increasing order and assign a rank to each habitat such that worse habitat gets the first rank and best habitat gets the last rank.

E. *Immigration and emigration rates*

Emigration and immigration rates are calculated as follows:

Immigration rate (lambda) = $I\ (1 - k_i/n)$ (5)

Emigration rate (mue) = $E(k_i/n)$ (6)

Where I = maximum immigration rate.

E = maximum emigration rate.

k_i= rank of the habitat.

n = total number of habitats.

Habitats having high HSI value will have a low immigration rate and high emigration rate. SIV will migrate from high HSI value or high emigration rate habitat to the low HSI value of high immigration rate habitat.

F. *Migration operator*

A random number r is generated. For habitat = i, If r < immigration rate (i), choose i as immigrating habitat. Choose habitat with highest HSI value as emigrating habitat. Make a crossover between the two habitats using MPX. This will result in a modified gateway habitat/vector let corresponding to sensor node vector to which gateways have been assigned now using this modified vector. In this the way, we will obtain many modified vector/habitat assigned to sensor nodes. Calculate HSI values of all these resulting habitats again. Retain the habitat with best HSI value. If the HSI value after modification is better than the HSI value before modification, a batter network performance is achieved. The whole scenario is then simulated and optimum output is achieved.

V. RESULTS AND SIMULATION

In this section, several tests are performed using MATLAB 8.1to evaluate the proposed protocol and compare it with otherprotocols [4-6], [11], [12]. In these tests, we assume thatsensors are homogeneous, and each one generates one datapacket per round to be transmitted to the sink. To eliminate theexperimental error caused by randomness, each test was runfor 5 times and the average was taken as the final result. TheAIA parameters are set as p_s=30, p_r=0.9, p_c=0.1, p_h=0.4,w=0.9 and *Maxgen*= 100.

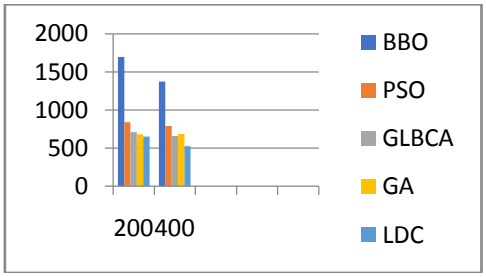


Figure 2 – Proposed work compared with the existing work in terms of network lifetime

© 2015-19, IJARCS All Rights Reserved

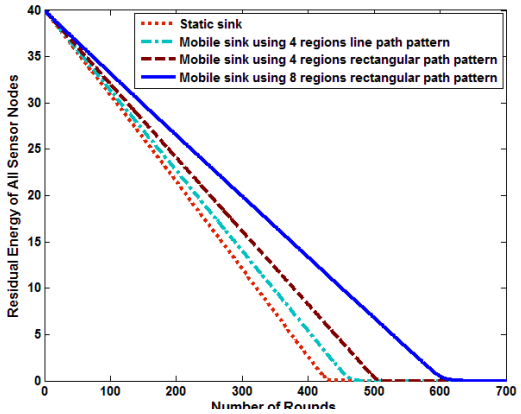


Figure 3 – Proposed work compared with the existing work in terms of relative energy of the sensor nodes.

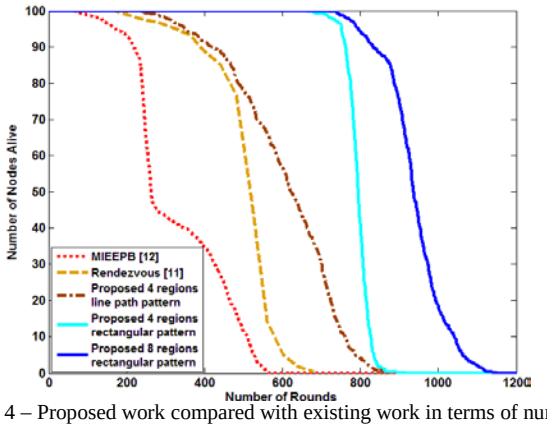


Figure 4 – Proposed work compared with existing work in terms of number of nodes alive.

VI. REFERENCES

[1] J. Yick, B. Mukherjee, and D. Ghosal, "Wireless sensor network survey,"Comput. Netw., vol. 52, no. 12, pp. 2292–2330, 2008.

[2] K. Romer and F.Mattern, "The design space of wireless sensor networks,"IEEE Trans. Wireless Commun., vol. 11, no. 6, pp. 54–61, Dec. 2004.

[3] J. Kennedy and R. Eberhart, "Particle swarm optimization," in Proc.IEEE Int. Conf. Neural Netw., 27 Nov.–1 Dec, 1995, vol. 4, pp. 1942–1948.

[4] Y. del Valle, G. K. Venayagamoorthy, S. Mohagheghi, J. C. Hernandez,and R. Harley, "Particle swarm optimization: Basic concepts, variants andapplications in power systems," IEEE Trans. Evol. Comput., vol. 12, no. 2,pp. 171–195, Apr. 2008.

[5] R. Schaefer, Foundations of Global Genetic Optimization. NewYork:Springer-Verlag, 2007.

[6] K. V. Price, R. M. Storn, and J. A. Lampinen, Differential Evolution: APractical Approach to Global Optimization, (Natural Computing Series).Berlin, Germany: Springer-Verlag, 2005.

[7] K.M. Passino, "Biomimicry of bacterial foraging for distributed optimizationand control," IEEE Control Syst. Mag., vol. 22, no. 3, pp. 52–67, Jun.2002.

[8] R. Hassan, B. Cohanim, and O. de Weck, "A comparison of particleswarm optimization and the genetic algorithm," presented at theAIAA/ASME/ASCE/AHS/ASC 46th Struct., Struct. Dyn. Mater. Conf.,Austin, TX, Apr. 2005.

[9] N. M. A. Latiff, C. C. Tsimenidis, and B. S. Sharif, "Performance comparisonof optimization algorithms for clustering in wireless sensor networks,"in Proc. IEEE Int. Conf. Mobile Ad Hoc Sens. Syst., Oct. 8–11,2007, pp. 1–4.

[10] J. Vesterstrom and R. Thomsen, "A comparative study of differentialevolution, particle swarm optimization, and evolutionary algorithms onnumerical benchmark problems," in Proc. Congr. Evol. Comput., Jun.2004, vol. 2, pp. 1980–1987.

[11] R. V. Kulkarni, G. K. Venayagamoorthy, and M. X. Cheng, "Bio-inspirednode localization in wireless sensor networks," in Proc. IEEE Int. Conf.Syst., Man Cybern., San Antonio, TX, Oct. 2009, pp. 205–210.\

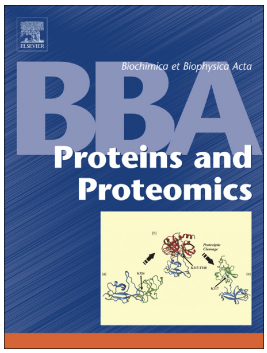
[12] Z. Bojkovic and B. Bakmaz, "A survey on wireless sensor networks deployment,"WSEAS Trans. Commun., vol. 7, no. 12, pp. 1172–1181,2008.

[13] N. A. B. A. Aziz, A.W. Mohemmed, and B. S. D. Sagar, "Particle swarmoptimization and Voronoi diagram for wireless sensor networks coverageoptimization," in Proc. Int. Conf. Intell. Adv. Syst., 2007, pp. 961–965.

[14] J. Hu, J. Song, M. Zhang, and X. Kang, "Topology optimization for urbantraffic sensor network," Tsinghua Sci. Technol., vol. 13, no. 2, pp. 229–236, Apr. 2008.

© 2015-19, IJARCS All Rights Reserved

Accepted Manuscript



An integrative system biology approach to unravel potential drug candidates for multiple age related disorders

Isha Srivastava, Pooja Khurana, Mohini Yadav, Yasha Hasija

PII: S1570-9639(17)30172-3
DOI: doi: 10.1016/j.bbapap.2017.07.016
Reference: BBAPAP 39982

To appear in:

Received date: 11 January 2017
Revised date: 3 July 2017
Accepted date: 21 July 2017

Please cite this article as: Isha Srivastava, Pooja Khurana, Mohini Yadav, Yasha Hasija , An integrative system biology approach to unravel potential drug candidates for multiple age related disorders, (2017), doi: 10.1016/j.bbapap.2017.07.016

This is a PDF file of an unedited manuscript that has been accepted for publication. As a service to our customers we are providing this early version of the manuscript. The manuscript will undergo copyediting, typesetting, and review of the resulting proof before it is published in its final form. Please note that during the production process errors may be discovered which could affect the content, and all legal disclaimers that apply to the journal pertain.

ACCEPTED MANUSCRIPT

An integrative system biology approach to unravel potential drug candidates for multiple age related disorders

Isha Srivastava, Pooja Khurana, Mohini Yadav, Yasha Hasija*

ACCEPTED MANUSCRIPT

*Corresponding author –Yasha Hasija

Email - yashahasija@gmail.com

Address - Department of Biotechnology, Delhi Technological University, Shahbad Daulatpur, Main Bawana Road, Delhi- 110042, INDIA

ACCEPTED MANUSCRIPT

Abstract

Aging, though an inevitable part of life, is becoming a worldwide social and economic problem. Healthy aging is usually marked by low probability of age related disorders. Good therapeutic approaches are still in need to cure age related disorders. Occurrence of more than one ARD in an individual, expresses the need of discovery of such target proteins, which can affect multiple ARDs. Advanced scientific and medical research technologies throughout last three decades have arrived to the point where lots of key molecular determinants affect human disorders can be examined thoroughly. In this study, we designed and executed an approach to prioritize drugs that may target multiple age related disorders. Our methodology, focused on the analysis of biological pathways and protein protein interaction networks that may contribute to the pharmacology of age related disorders, included various steps such as retrieval and analysis of data, protein-protein interaction network analysis, and statistical and comparative analysis of topological coefficients, pathway, and functional enrichment analysis, and identification of drug-target proteins. We assume that the identified molecular determinants may be prioritized for further screening as novel drug targets to cure multiple ARDs. Based on the analysis, an online tool named as 'ARDnet' has been developed to construct and demonstrate ARD interactions at the level of PPI, ARDs and ARDs protein interaction, ARDs pathway interaction and drug-target interaction. The tool is freely made available at http://genomeinformatics.dtu.ac.in/ARDNet/Index.html

Introduction

The tremendous rise in chronic age-related disorders (ARDs), co-morbidities, and geriatric syndromes is already presenting serious challenges for countries all around the world. Meanwhile, a growing number of scientists, led by bio-gerontologists, maintain that the key to minimizing the impact of ARDs lies with the better understanding and potential manipulation of biological mechanisms of aging itself. Well-characterized interventions that slow aging and extend health and vigor may be forerunners of technologies that preserve additional years of healthy productive life in humans. The major risk factors associated with ARDs include advancing age, genetic predisposition, gender, and ethnicity, with aging being the major risk factor.

ACCEPTED MANUSCRIPT

The completion of the sequencing of several genomes has revealed that the complexity of living organisms is not simply correlated with the number of proteins that they have. Rather, it is becoming increasingly clear that the major source of human disorders in the organism at the variation level is single nucleotide polymorphisms, at the pathway level, there are different interactions that proteins undergo. Protein-protein interactions are critical for practically all cellular, signaling, and regulatory pathways. The dysfunction of these pathways is the cause of many age-related disorders. Since, damages and alterations in protein-protein interactions either cause or accelerate human diseases, the control or inhibition of the known interactions represents a prime target for drug discovery.

In our study, complex pathway connotations of ARDs were not only scrutinized by pathway and functional enrichment but also by one more systems biology approach i.e. pathway crosstalk. Several network-based analyses have been reported to study the connection between aging and ARDs. For example, protein-protein interaction (PPI) networks of cancer, longevity, atherosclerosis, T2D, and Alzheimer's disease by Wolfson *et al* defined a common signature of 588 proteins that were shared by these networks [1]. Tacutu *et al*. found that cellular senescence (CS) was closely connected with aging, longevity, and ARDs, and identified proteins, protein-protein interactions and signaling pathways common to these processes [2]. Wang *et al*. also constructed a network connecting aging proteins and disease proteins from a large number of categories and unveiled relations between aging and ARDs [3]. Jialiang Yang *et al* proposed a network model named GeroNet which identifies meaningful proteins that may play key roles in connecting aging and ARDs [4]. However, till date no one has applied systems biology approach to analyze interactions of single nucleotide polymorphism based ARD proteins by applying pathway crosstalk method and drug target interaction exploration.

In the present study, we constructed different aging and ARD networks that unveiled significant interconnections and divulged concealed patterns of aging-ARD association. As resulting ARD Aging protein-protein interaction (PPI) network was too big, MCL algorithm was applied to find biologically relevant clusters [5]. Moreover, we found several trivial modules that specifically represent particular molecular functionality.

Protein-protein interaction network usually consists of few dense nodes ("hubs") that are directly connected to large number of neighbor nodes. According to centrality- lethality rule, if we knock

ACCEPTED MANUSCRIPT

out such hub proteins, it may be lethal for the network [6]. In disease networks, finding out these hub proteins and targeting them could be an effective approach of treating multiple disorders. In our aging-ARD PPI network, prioritization of proteins as hubs was thus performed on the basis of normalized values of betweeness centrality, bottleneckness, and MCC (Maximum Clique Centrality). As a result, we found few relevant hub proteins- NR, STAT3, ESR1, BRCA1, and AKT1 - that can be targeted by a drug molecule to cure multiple ARDs.

The old concept of "one drug one target" has now been transformed into "one drug many targets" [7]. Keeping in view the concept of polypharmacology [8], we thought instead of suppressing the activity of one protein by a ligand we could use that ligand to cease the molecular activity of multiple targets - a) involved in a unique disease pathway or b) belonging to multiple disease pathways. To explore this concept, we applied an approach similar to the one applied by Barabasi for the examination of drug-target interactions [9]. We constructed drug-target bipartite network analysis reveals interesting facts and factors associated with ARD drug and proteins. One of the most important conclusions from drug-target network is that out of 20 hub proteins, only 11 were found to be present there in this network. This implied the role of other nine (PRKCA, EP300, NR, BRCA1, SMAD4, STAT3, YWHAG, NEDD9, NCF2) proteins as potential novel drug targets, since less drug information is currently available for these targets.

The approach we present here not only provides an avenue for network integration, but also promises to shed light on the prevention, diagnosis, and treatment of complex ARDs and Aging.

Materials and Methods:

Retrieval of Aging, Age-related disorders related and essential proteins:

Publicly available data sources were mined for extracting proteins associated with Aging; ARDs and essential proteins. Total 305 aging-associated proteins of human were extracted from GenAge mice, and human. An in-house database, dbAARD was utilized for extracting ARDs associated proteins [12]. Since dbAARD contains information updated till September 2014, the recent information was included into this by OMIM and literature search [13]. A total of 2509 ARDs proteins, belonging to 12 disorder classes, were obtained through dbAARD, OMIM, and literatures. The schema applied for classification of ARDs was taken from dbAARD, which

ACCEPTED MANUSCRIPT

includes pulmonary, psychiatry, ophthalmological, neurodegenerative, bone, cardiovascular, cancer, metabolic, gastrointestinal, pulmonary, muscular and ENT related disorders. Essential proteins were obtained from Online Gene Essentiality database (OGEE). OGEE is an archive of experimentally tested essential and non-essential proteins, associated gene features such as expression profiles, duplication status, and conservation across species, evolutionary origins, and involvement in embryonic development [14].

ARDs-Protein and Protein-protein Interaction Networks

Many resources are available for obtaining protein-protein interaction data, such as STRING [15], MINT [16], Bio grid [17], MIPS [18] and HPRD [19]. Since Human Protein Reference Database (HPRD) is one of the most extensively used database for research purposes and all the enclosed interaction data is experimental, it was selected for fetching human PPI information. We first constructed ARDs and associated proteins bipartite network. Nodes from two sets were connected if a particular node protein was found to be associated with a particular disease. The ARD-protein bipartite network represented total 51 age-related disorders and 2509 unique proteins (Supplementary Figure 1). From this network, we constructed protein and disease projection networks consisting of 1723 nodes and 3492 edges (Supplementary Figure 2). In protein projection network, nodes represented proteins and the two nodes were connected if they share a disorder. Similarly, in disease projection network, nodes represented ARDs and two nodes were connected if they shared common proteins associated with those disorders.

Statistical analysis of topological coefficients of networks

To test the robustness of aging and ARD networks, the topological parameters of these networks were statistically compared by an igraph package of R [21]. The topological features used were clustering coefficient, degree distribution, betweeness centrality, eccentricity, shortest path length, rediality, closeness centrality and topological coefficient. To demonstrate the statistical significance of ARDs, each topological feature was compared with 1,000 randomly generated networks.

Functional Enrichment and Pathway Crosstalk Analysis:

ACCEPTED MANUSCRIPT

In the present work, biological processes and molecular functions of aging proteins associated with ARDs were analyzed. For ensuring the accuracy and quality of results, several statistical tests were carried out such as hypergeometric test, Bonferroni test, BH test, and q – values. The analysis revealed few significant (p-value <0.001) pathways, processes, cellular components and molecular functions enriched in aging and ARD proteins such as signal transduction, DNA repair, glypican pathway and transmembrane receptor protein tyrosine kinase activity. All these are well-studied pathways, molecular functions, and their role in aging and ARDs have already been investigated earlier. Though a lot of research has been performed on glypicans, still a lot needs to be examined such as their role in morphoproteins and participation in signaling pathways. Extensive research on glypicans may help in curing various ARDs and aid in slowing down the aging process. The dominance of signal pathways in ARDs evoked our interest in pathway crosstalk analysis.

Crosstalk analysis was performed among the significantly enriched pathways by quantitatively measuring the shared protein components between each pair of pathways. A pair of pathways was considered to crosstalk if they shared a certain proportion of ARD proteins. To minimize the non-specificity of crosstalk analyses following rules were implemented: -

a) Only pathways with at least 5 ARDs proteins were considered

b) Only pathways with adjusted P values < 0.05 were considered

c) Two pathways in crosstalk were required to share at least 3 ARD proteins.

These rules were applied to ensure that each of the pathways, as well as its crosstalk pair, should be statistically significant and also have a biologically meaningful number of proteins, as some pathways may be too small. The evaluation of crosstalk was carried out with the help of Jaccard and overlap coefficients. For better understanding, a network based on pathway crosstalk was also constructed. To build a comprehensible network, only those pathways were selected whose corrected p-value (Bonferroni Method) was less than 1*10-6 and the average of Jaccard and overlap coefficient was 1 [22].

Network module identification

ACCEPTED MANUSCRIPT

The PPI network of ARDs was very complex with a large number of nodes and edges making it incomprehensible for extracting biologically meaningful interactions. As we know that cellular processes and functions are modular, we decided to identify major clusters/modules enriched in biological function/processes from the complex ARD network. The modular analysis provided better insight into the relationship among various complex ARDs. It has been shown that it is easier to predict the structural and functional behavior of a particular module than that of an individual gene. In the past, module analysis has played a significant role in determining patient survival, understanding metastasis and drug response in different types of cancers [23].

To identify the biologically meaningful modules in the ARD PPI network, different weights were assigned to the protein-protein interactions based on the type of experiment from which that interaction was retrieved. Lowest weight was assigned to interactions that were found in yeast-2-hybrid experiments only and highest weight to those interactions that has been proved in vivo, in vitro and Y2H experiments. These weights were assigned with to represent a ranking of a practitioner's belief in their validity [24] (Supplementary Table 1). Among all the clustering algorithms, we chose Markov clustering algorithm (MCL) method as it is fast and scalable unsupervised clustering algorithm, and is specially designed to fulfill the challenge of finding cluster structure in complex and weighted graphs. Parameters for MCL clustering were obtained from clustering analysis performed on the basis of parameters Granularity parameter = 1.8; and MCL Advanced Settings of: Weak edge weight pruning threshold = 1×10^{-20}, maximum residual value = 1×10^{-6}, and iterations = 16.

Hub Identification

Numerous methods available such as MCC (Maximum Clique Centrality), EPC (Edge Percolated Component), MNC (Maximum Neighborhood Component), DMNC (Density of Maximum Neighborhood Component) are for identification of hubs in a network based on various topological parameters like degree, betweenness centrality, closeness centrality, eccentricity, stress, rediality etc. MCC is the latest method and shown to be comparatively better than all other methods.Among all, MCC captures more essential proteins in the top ranked list in both high degree and low degree proteins [25]. For prioritizing proteins as hubs we also considered other topolical parametes such as betweenness centrality and normalized the data to identify top 20

ACCEPTED MANUSCRIPT

hub proteins to be asssociated with multiple age-related disorders and this clearly explains why these genes are forming hubs in the ARD network (Table 1) (Supplementary Table 2).

Construction of Drug –Target Network

We used all known FDA drugs (approved, experimental and investigational) and their targets to generate a bipartite graph of drug– ARDs protein interactions in which a drug and a ARDs protein are connected to each other if the ARDs protein is a known target of the drug. The network was consist of 2796 nodes and 3385 edges (SupplementaryFigure 3).

Results and discussion:

Analysis of shared proteins in aging and ARDs essential and developmental proteins:

We carried out a gene set enrichment analysis utilizing data of commonality analysis of aging, ARDs, essential and developmental proteins (Supplementary Figure 4) and identified 160 common proteins among aging and age-related disorders overrepresented in transcriptional level activator cell cycle inhibitor p21(Log p-value = 42.2), viral RNP complexes in host cells (Log p-value = 42.2), transcriptional activation of p53 responsive proteins (Log p-value = 42.2), NGF processing (Log p-value = 42.2) COX reactions (Log p-value = 42.2), IRS activation (Log p-value = 35.4), and underrepresented in transmembrane transporter of small molecules (Log p-value = -4), metabolism of proteins (Log p-value = -2.7), protein expression (Log p-value = -2.1), Mitotic MM/G1 phases (Log p-value = -1.8), GPCR downstream signaling (Log p-value = -1.4), mRNA processing (Log p-value = -1.4) (Supplementary Figure 5) Well all of the above significant pathways were well studied earlier [27].

Moreover, we identified a huge number of proteins (565), shared among ARDs and developmental process. Earlier some studies have been performed which indicate the involvement of various developmental proteins in aging and ARDs in *C. elegans*. Researchers have highlighted the role of certain proteins [28]. For example the let418/Mi2 protein exists in fleas, plants and human as well as. So, it may be hypothesized that there can be the high chance of involvement of this protein may play a role in aging, ARDs – susceptibility and developmental processes in humans also. Hence, our study signifies connotation of

ACCEPTED MANUSCRIPT

developmental and ARDs proteins. However, further research on inter-relation of developmental proteins in humans with ARDs is still well needed. We believe that further analysis may throw insights in the development of approaches for curing ARDs and increasing lifespan.

Interaction Networks

Next, we developed an interaction network that may provide novel cues towards connectivity of age-related disorders and in bridging proteins associated with multiple ARDs.

ARDs and Proteins Bipartite Network:

If each ARD inclines to have a dissimilar and distinctive genetic origin, then the bipartite network would be disconnected into many single nodes corresponding to specific disorders or grouped into small clusters of a few closely related disorders. However, the ARDs-protein bipartite network exhibits many connections between both individual disorders and disorder classes. The top most connected disorders were Schizophrenia (n=239), melanoma (n=219), prostate Cancer (n=213), obesity (n=168), hypertension (n=151), lung cancer (n= 140), diabetes mellitus (n=128), rheumatoid arthritis (n=125). This is suggested that the genetic origins of most diseases, in some measure, are shared with one-another. Topological analysis of ARDs-proteins bipartite network showed high neighborhood connectivity of cardiovascular disorders. This suggests broad genetic interconnection of cardiovascular disorder genes.

On the other hand, handful of proteins were found to be connected with many ARDs, for example; MTHFR with nine disorders; FTO, NR and SOD2 with eight disorders; ADIPOQ, AGT and CCL2 with seven disorders. This outcome of network signified that polypharmacological may be prioritized for multiple ARDs.

Aging and ARDs Protein Protein Interaction Network

To test how aging and ARD networks deviated from the whole human PPI network and random networks, we statistically compared the topological parameters of these networks. Comparing ARD proteins network with global PPI network depicted the significant difference in the degree

ACCEPTED MANUSCRIPT

(p-value = 1.202807e-53) and betweenness centrality (p-value = 2.51178e-95) of these networks (Supplementary Figure 6 (A) & (B)). The ARD genes appeared to be more closely connected and were central to the human PPI Network. The comparison of these network with 1,000 random network on the basis of degree (p-value = 1.544349e-50) and eccentricity (p-value = 0.01463993) suggested important clustering of disease/genes in the ARD network compared to random network (Supplementary Figure 6 (C) & (D)). Similar observations were made in a case of aging network. The comparison of aging network with whole PPI network revealed significant differences in the topological parameters i.e.; degree (p-value = 2.346396e - 06) and clustering coefficient (p-value = 2.77471e-43) (Supplementary Figure 6 (E) & (F)). Also, compared to random network, aging network appeared to be more connected as evident from statistically significant values of difference in topological parameters of two networks -degree (p-value = 8.438343e-57) and eccentricity (p-value = 7.334051e-19) (Supplementary Figure 6 (G) & (H)).

Functional enrichment analysis

In the present work, biological processes and molecular functions of aging genes and genes associated with ARDs were analyzed. For ensuring the accuracy and quality of results, several statistical tests were carried out such as hypergeometric test, Bonferroni test, BH test, and q – values. The analysis revealed significant (p-value = <0.001) pathways, processes, cellular components and molecular functions enriched in aging and ARD genes such as signal transduction, DNA repair, glypican pathway, transmembrane receptor protein tyrosine kinase activity (Figure 1). Though some researches have been performed on glypicans, still a lot needs to investigated, such as their role in morphogenesis and participation in signaling pathways. Extensive research on glypicans may help in curing various ARDs and aid us in slowing down the aging process. The dominance of signal pathways in ARDs evoked our interest in pathway crosstalk analysis.

Crosstalk analysis was performed among the significantly enriched pathways by quantitatively measuring the shared protein components between each pair of pathways. A pair of pathways is considered to crosstalk if they share a certain proportion of ARD genes. The evaluation of crosstalk was accomplished with the help of Jaccard and overlap coefficients [22]. Our pathway crosstalk analyses revealed various unique pathway interaction modules that were significantly enriched with ARD genes. These modules were signal transduction, immune systems related; a

ACCEPTED MANUSCRIPT

hemostasis-associated. For better understanding, a network based on pathway crosstalk was also constructed. To build a comprehensible network, only those pathways were selected whose corrected p-value (Bonferroni Method) was less than $1*10^{-6}$ and the average of Jaccard and overlap coefficient was 1 (Supplementary Table 3) [22].

Involvement of the bulk of ARDs genes in signal transduction activity suggested that there may be some signals among various ARDs that interconnect them with each other (Figure 1). This may seem a plausible reason behind the occurrence of multiple ARDs simultaneously. Cluster of signal transduction pathways consisted of signaling pathways such as: signaling events mediated by focal adhesion kinase, Class I PI3K signaling events mediated by Akt, mTOR signaling pathway, Arf6 signaling events, Arf6 downstream pathway, Class I PI3K signaling events, EGF receptor (ErbB1) signaling pathway, PDGFR-beta signaling pathway, Urokinase-type plasminogen activator (uPA), uPAR-mediated signaling and S1P1 pathway.

Search of drug targets by different approches of systems biology network science :-

Drug targets analysed by module analysis

Of all the 243 modules, some non-trivial modules were found to be associated with specific molecular and biological processes (Figure 2). For example, modules 7, 27, 14, 52, and 53 were found to be related to immune response; module 3 overrepresented DNA repair phenomenon; modules 9 and 13 were enriched in proteins involved in mitochondrial pathways; modules 46 and 71 with lipid metabolism; module 28 with GPCR signaling and obesity; module 38 with notch signaling pathway; module 45 with HOX gene family; module 70 with ribosomal activity (Supplementary Table 4). This suggested the modular nature of the biological processes in human PPI network, and mutation in any of the gene of a module may hamper that biological process, thereby leading to particular disorder. Other than pathway specific modules, our result also highlighted disorder specific modules, for example, module 25 represented genes associated with neurodegenerative disorders; module 37 with usher syndrome, module 31 with bone related disorders, module 47 with muscular problems; module 33 and 48 with cardiovascular diseases; modules 22, 43, and 54 were enriched with genes involved in Cancer; cluster number 18 related to chaperon folding activity; and cluster 13 age-related macular degeneration.

ACCEPTED MANUSCRIPT

• Cluster 9 showed a very imperative connection between CRY gene family and tumor-associated genes. Most of the cancer genes in this module were involved in prostate cancer, which may explain the co-occurrence of the cataract in cancer patients. One particular gene BCL2L1, which is central to the module and connects genes involved in cataract and cancer, may act as a potential drug target for curing cataract, prostate cancers and aging (Figure 3 (I)).

• Cluster 15 showed that SETDB1 connects multiple diseases and hence may be used as a therapeutic target for treating multiple ARDs (Figure 3 (II)). Similarly, cluster 32 has the topological location and centrality (center of the clique) of CCL11 such that it can also be used as a therapeutic target for curing multiple ARDs (Figure 3 (III)).

• Further, clusters 1 and 2 showed an important role of cell signaling activity in ARDs and aging, thus indicating the possibility of further examination of these clusters in understanding the mechanism of cell signaling activity and involvement in ARDs/aging (Figure 3 (IV & V)).

Hub identification insights about significant drug targets of ARD network

Insights into significant drug targets of ARD network: Protein-protein interaction network usually consists of few dense nodes ("hubs") that are directly connected to a large number of neighbor nodes. According to centrality- lethality rule, if we knock out such hub proteins, it may be lethal for the network. Finding out hub proteins and targeting them to cure disorders may prone to be effective in treating multiple disorders. Our analysis of ARD network revealed significant hubs nodes with the highest degree. One more relevant topological parameter that has been shown to be effective other than a degree in hub identification in a network is betweenness. Betweenness measures the number of shortest paths transversing through an individual node. Therefore, nodes with highest betweenness control most of the information flow in the network, representing the critical points of the network. Such nodes are called as the ''bottlenecks'' of the network. Bottlenecks in the network can thus be used as potential targets for further analysis [29].

Out of the top 20 identified hub proteins - NR, STAT3, ESR1, BRCA1, and AKT1 have previously been found to be asssociated with multiple age-related disorders and this clearly explains why these genes are forming hubs in the ARD network (Table 1).

ACCEPTED MANUSCRIPT

c) Pharmacological analysis of hub proteins:

The drug industry is growing day by day, but the range of target-based drugs is still very narrow, mainly due to lack of discovery of new targetable drugs. A target may be a protein molecule, carbohydrate, lipid, DNA or RNA, yet most of the drugs target protein molecules. Despite large number of proposed targetable molecules (almost 10,000), FDA has approved only 400 molecular targets. [30].With this premise, we constructed drug target bipartite network. The networks were used for further investigation of hubs/target proteins identified in prior analysis. The analysis of these protein molecules at drug target level revealed some significant results which could provide an impetus in aging and ARD research. One of the most important conclusions from our drug-target network was that out of 20 hub proteins, only 11 were found to be present there in this network. This implied the role of other nine (PRKCA, EP300, NR, BRCA1, SMAD4, STAT3, YWHAG, NEDD9, NCF2) proteins as potential novel drug targets since no drug information is currently available for these targets. To show the interaction of drug, target, and disorders, we have constructed a tripartite network. Since, the constructed network was too complex therefore, exposed subnetworks representing connection of some of the hub target proteins (Figure 4).

Another interesting finding for the purpose of finding drug target was, most of the hub proteins for example PRKCA, TP53, APP, PIK3R1, DCN, and CTNNB1were found to be targeted by single drug, which indicated that there is a pressing need to discover more drugs against these target hub proteins as targeting these hubs may play an important role in targeting multiple ARDs.

Other significant findings from the drug-target network were –

Most of the drugs with high degree in the drug-target network are antipsychiatric drugs and were found to be connected with cardiovascular, metabolic and neurodegenerative disorders. Further investigation on these drugs presented following facts. For example:

- Mirtazapine (DB00370), which is generally used as medicine for psychiatric disorders, also targets ADRB1, SLC6A2, ADRA2A, HRH1, HRH3, HTR2B, and ADRA2A genes which are known to play a role in cardiovascular disorders (Figure 4(I)). This implies that the proteins of

ACCEPTED MANUSCRIPT

these genes may have an active site that could allow binding of this drug, and therefore provides a plausible explanation on why psychiatric disorders patients treated with mirtazapine complain of side-effects such as chest pain and increased heart rate[32]. Elias A. Khamwan has also examined and described the te cause of side effects of antipsychiatric drugs such as mirtazapine on cardiovascular systems[33].

- Similarly, our network represents association of Loxapine (DB00408) with HRH1, ADRB1, SLC62A, HRH2, ADRA2A, DRD1,DRD4, ADRA1A, HTR2C genes (Figure 5 (II)). Loxapine is used for treatment of Schizophrenic patients.These genes are also associated with cardiovascular (HRH1, ADRB1, SLC62A, HRH2, ADRA2A), neurological (DRD1, DRD2), metabolic obesity (ADRA1) and diabetes (HTR2C). This association may be the reason of negative effect of loxapine in case of cardiovascular, neurological, and metabolic symptoms[34].Some researchers have demonstrated that the antipsychotics (e.g. clozapine, olanzapine, risperidone, sertindole, aripiprazole, ziprasidone, quetiapine, loxapine) is associated with cases of arrhythmias, prolonged QTC interval on electrocardiogram (ECG) and orthostatic [35].
- Asenapine (DB06216), an antipshychiatric drug, which is also used for treatment of neurological disorders, also connected with some cardiovascular (HRH1, ADRB1, HTR2B, HRH2, ADRA2A, ADRA1A) and metabolic (HTR2C, ADRA1A, ADRB2) genes (Figure 5(III)). May be these associated genes are the cause behind side effect of asenapine on cardiovascular and metabolic symptoms [36] [33].
- Amitriptyline (DB00321), an antipsychiatric drug was found to be interlinked with OPRD1 gene, which is involved in causation of cancer (Figure 5 (IV)). It might be possible that by targeting OPRD1 with amitriptyline may also cure cancer. Moreover, it has been examined that amitriptyline may have a supportive role in cancer treatment by inhibiting glutathione S-transferase pi (GST-π) and alpha (GST-α) [37].
- Phosphoaminophosphonic Acid Adenylate Ester (DB043395) is an experimental drug. This drugis associated with numerous genes that are involved in different disorders such as ophthalmological, cancer, cardiac, metabolic, psychiatric, neurological and ENT (Figure 5(V)). Additional experiments on association of this drug with these disorders can be beneficial in therapeutics. Certain studies on drug designing of breast cancer have introduced phosphoaminophosphonic acid adenylate as inhibitor of Human p38γ. [38]

ACCEPTED MANUSCRIPT

- **ARDnet**

In this part of work; we have focused on the construction of such tool that can help geneticist, medical practioners and gerontologists to understand association and interrelation of ARDs and associated proteins, pathways, and drugs. In the present work, we introduce ARDnet is an open-source tool with the main goal of constructing networks of age-related disorders associated proteins, drugs, and pathways to assist users to analyze and visualize ARDs related data. ARDnet not only integrates several age-related disorders and their associated proteins information but it also incorporates information about drugs and their ARDs protein target. The tool supports multiple biological data formats such as gene IDs, proteins IDs, DrugIDs etc. This tool is available at http://genomeinformatics.dtu.ac.in/ARDNet/Index.html.

Construction of tool and web implementation: The primary text file format used for each network was JSON file format. JSON (JavaScript Object Notation) is a lightweight data-interchange format [39]. CSS and HTML was used to define styles for web pages, including the design, layout, and variations in display for different devices and screen sizes of ARDnet [40].

ARDnet contents:

1) Age related disorders and protein network construction: ARDnet constructs age related disorders and protein network. This isa bipartite network, in which one node represents proteins and other represents disorders. The ARD-protein bipartite network consists of total 51 age-related disorders and 2509 unique proteins. The user can select name of any or multiple age related disorder and corresponding protein molecule and analyses their interaction. In the constructed network varying size of node represents and number of association of age related disorders with associated protein molecules [Figure 5].

2) Age related protein protein interaction network: The user can construct ARDs protein protein interaction network to show and analyze association of desired proteins. The network information working in backend was consisting of 1723 ARDs proteins and 3492 ARD

ACCEPTED MANUSCRIPT

protein protein interactions. This tool constructs only high interactions, as interactions were rectified on the basis of weights, assigned on the basis of type of experiments used.

3) Age related disorders pathway interaction network :In this part of ARD net, a user can construct network of ARDs related pathways and study their association. This tool constructs only significant ARD pathway interactions as interactions were rectified on the basis of average Jaccard and overlap coefficients.

4) Drug – ARDs target interaction network:ARDnet also constructs the network of ARDs proteins and associated drugs. A user can analyze drug association of ARDs protein of interest. The backend data consists of all known FDA drugs (approved, experimental, and investigational) and their ARDs targets.

Conclusion

A systems biology approach was applied to investigate the interrelation of age related disorders proteins and to search polyphormacological drug targets. Statistical and topological analysis of ARD and Aging network revealed that ARD and aging proteins are centrally located and more strongly connected. It has been examined that there are several proteins common among ARD, Aging, essential and developmental proteins. Further research on shared proteins and pathways can insight new therapeutic approaches to cure ARDs. Dominance of signal transduction pathways was observed in ARDs functional enrichment and pathway crosstalk analysis. Module analysis, hub identification and drug target analysis revealed many molecular determinants such as PRKCA, EP300, NR, AKT1, ESR1, TP53, BRCA1, SMAD3, APP,CALM1, SMAD4,EGFR, PIK3R1,STAT3 ,DCN,NCF2, CTNNB1, YWHAG,CALR,NEDD9, BCL211, CCL11, SETDB1. In this way, network based drug discovery aims to explore and understand the effect of interventions, such as candidate drugs, on the molecular networks that define different states and therefore can significantly complement the existing drug discovery pipelines. Hence, our approach could lead to the introduction of multidrug treatments, side-effect prediction, and the identification of new drug candidates of age related disorders.Moreover, a tool has been constructed which generates age related disorders and proteins, ARD protein protein, ARD pathway interaction, drug target

ACCEPTED MANUSCRIPT

interaction networks. To the best of our knowledge, this is the first tool, which also facilitates ARDs pathway and drug ARDs target network construction and analysis. This tool may be very beneficial for medical practitioners and gerontologists to understand the inter-relation of various aspects of age related disorders.

To conclude, in this work, we have prioritized novel drug targets for multiple ARDs by utilizing *in silico* methods. It should be noted, however, that a drug target might only truly be validated by demonstrating that a given drug is clinically effective and acts through the target. Therefore, we believe that the present study may be used by the experiments to validate these early-stage drug targetsfor multiple ARDs.

CONFLICT OF INTEREST

The authors declare that they have no conflict of interest.

ACKNOWLEDGEMENT

We thank Mr. Lokesh Kumar Gahlot for his valuable inputs in tool construction.

References

1. Wolfson M, Budovsky A, Tacutu R, Fraifeld V. The signaling hubs at the crossroad of longevity and age-related disease networks.The international journal of biochemistry & cell biology. 2009 Mar 31;41(3):516-20.
2. Tacutu R, Budovsky A, Yanai H, Fraifeld VE. Molecular links between cellular senescence, longevity and age-related diseases-a systems biology perspective. Aging (Albany NY). 2011 Dec;3(12):1178-91.
3. Wang, Jiguang, et al. "Disease-aging network reveals significant roles of aging genes in connecting genetic diseases." *PLoSComputBiol* 5.9 (2009): e1000521.
4. Yang J, Huang T, Song WM, Petralia F, Mobbs CV, Zhang B, Zhao Y, Schadt EE, Zhu J, Tu Z. Discover the network mechanisms underlying the connections between aging and age-related diseases. Scientific Reports. 2016;6.

ACCEPTED MANUSCRIPT

5. Enright, Anton J., Stijn Van Dongen, and Christos A. Ouzounis. "An efficient algorithm for large-scale detection of protein families." *Nucleic acids research* 30.7 (2002): 1575-1584.
6. He, Xionglei, and Jianzhi Zhang. "Why do hubs tend to be essential in protein networks?." *PLoS Genet* 2.6 (2006): e88.
7. Scheiber J, Jenkins JL, Sukuru SC, Bender A, Mikhailov D, Milik M, Azzaoui K, Whitebread S, Hamon J, Urban L, Glick M. Mapping adverse drug reactions in chemical space. Journal of medicinal chemistry. 2009 Apr 20;52(9):3103-7.
8. Scheiber J, Jenkins JL, Sukuru SC, Bender A, Mikhailov D, Milik M, Azzaoui K, Whitebread S, Hamon J, Urban L, Glick M. Mapping adverse drug reactions in chemical space. Journal of medicinal chemistry. 2009 Apr 20;52(9):3103-7.
9. Knight ZA, Lin H, Shokat KM. Targeting the cancer kinome through polypharmacology. Nature Reviews Cancer. 2010 Feb 1;10(2):130-7.
10. Knight ZA, Lin H, Shokat KM. Targeting the cancer kinome through polypharmacology. Nature Reviews Cancer. 2010 Feb 1;10(2):130-7.
11. Wang L, Liu H, Chute CG, Zhu Q. Cancer based pharmacogenomics network supported with scientific evidences: from the view of drug repurposing. BioData mining. 2015 Feb 25;8(1):1.
12. Srivastava I, Gahlot LK, Khurana P, Hasija Y. dbAARD& AGP: A computational pipeline for the prediction of genes associated with age related disorders. Journal of biomedical informatics. 2016 Apr 30;60:153-61.
13. Hamosh A, Scott AF, Amberger JS, Bocchini CA, McKusick VA. Online Mendelian Inheritance in Man (OMIM), a knowledgebase of human genes and genetic disorders.Nucleic acids research. 2005 Jan 1;33(suppl 1):D514-7.
14. Chen WH, Minguez P, Lercher MJ, Bork P. OGEE: an online gene essentiality database.Nucleic acids research. 2012 Jan 1;40(D1):D901-6.
15. Franceschini A, Szklarczyk D, Frankild S, Kuhn M, Simonovic M, Roth A, Lin J, Minguez P, Bork P, Von Mering C, Jensen LJ. STRING v9.1: protein-protein interaction networks, with increased coverage and integration. Nucleic acids research. 2013 Jan 1;41(D1):D808-15.
16. Orchard S, Kerrien S, Abbani S, Aranda B, Bhate J, Bidwell S, Bridge A, Briganti L, Brinkman FS, Cesareni G, Chatr-Aryamontri A. Protein interaction data curation: the

ACCEPTED MANUSCRIPT

International Molecular Exchange (IMEx) consortium. Nature methods. 2012 Apr 1;9(4):345-50.

17. Zanzoni A, Montecchi-Palazzi L, Quondam M, Ausiello G, Helmer-Citterich M, Cesareni G. MINT: a Molecular INTeraction database. FEBS letters. 2002 Feb 20;513(1):135-40.
18. Chatr-Aryamontri A, Breitkreutz BJ, Oughtred R, Boucher L, Heinicke S, Chen D, Stark C, Breitkreutz A, Kolas N, O'Donnell L, Reguly T. The BioGRID interaction database: 2015 update. Nucleic acids research. 2015 Jan 28;43(D1):D470-8.
19. Mewes HW, Frishman D, Güldener U, Mannhaupt G, Mayer K, Mokrejs M, Morgenstern B, Münsterkötter M, Rudd S, Weil B. MIPS: a database for genomes and protein sequences.Nucleic acids research. 2002 Jan 1;30(1):31-4.
20. Peri S, Navarro JD, Kristiansen TZ, Amanchy R, Surendranath V, Muthusamy B, Gandhi TK, Chandrika KN, Deshpande N, Suresh S, Rashmi BP. Human protein reference database as a discovery resource for proteomics. Nucleic acids research. 2004 Jan 1;32(suppl 1):D497-501.
21. Tippmann S. Programming tools: Adventures with R. Nature. 2015 Jan 1;517(7532):109-10.
22. Jia P, Kao CF, Kuo PH, Zhao Z. A comprehensive network and pathway analysis of candidate genes in major depressive disorder.BMC systems biology. 2011 Dec 23;5(3):1.
23. Mitra K, Carvunis AR, Ramesh SK, Ideker T. Integrative approaches for finding modular structure in biological networks. Nature Reviews Genetics. 2013 Oct 1;14(10):719-32.
24. Pinkert S, Schultz J, Reichardt J. Protein interaction networks—more than mere modules.PLoSComput Biol. 2010 Jan 29;6(1):e1000659.
25. Chin CH, Chen SH, Wu HH, Ho CW, Ko MT, Lin CY. cytoHubba: identifying hub objects and sub-networks from complex interactome. BMC systems biology. 2014 Dec 8;8(4):1.
26. Vaux V, Pfefferli C, Passannante M, Belhaj K, Essen A, Sprecher SG, Müller F, Wicky C. The Caenorhabditis elegans LET- 418/Mi2 plays a conserved role in lifespan regulation. Aging cell. 2013 Dec 1;12(6):1012-20.
27. Feltes BC, de FariaPoloni J, BonattoD.The developmental aging and origins of health and disease hypotheses explained by different protein networks.Biogerontology. 2011 Aug 1;12(4):293-308.

ACCEPTED MANUSCRIPT

28. Vaux V, Pfefferli C, Passannante M, Belhaj K, Essen A, Sprecher SG, Müller F, Wicky C. The Caenorhabditis elegans LET- 418/Mi2 plays a conserved role in lifespan regulation. Aging cell. 2013 Dec 1;12(6):1012-20.
29. Yu H, Kim PM, Sprecher E, Trifonov V, Gerstein M. The importance of bottlenecks in protein networks: correlation with gene essentiality and expression dynamics.PLoSComput Biol. 2007 Apr 20;3(4):e59.
30. Wishart DS, Knox C, Guo AC, Shrivastava S, Hassanali M, Stothard P, Chang Z, Woolsey J. DrugBank: a comprehensive resource for in silico drug discovery and exploration.Nucleic acids research. 2006 Jan 1;34(suppl 1):D668-72.
31. Yıldırım MA, Goh KI, Cusick ME, Barabási AL, Vidal M. Drug—target network. Nature biotechnology. 2007 Oct 1;25(10):1119-26.
32. Honig A, Kuyper AM, Schene AH, van Melle JP, De Jonge P, Tulner DM, Schins A, Crijns HJ, Kuijpers PM, Vossen H, Lousberg R. Treatment of post-myocardial infarction depressive disorder: a randomized, placebo-controlled trial with mirtazapine. Psychosomatic medicine. 2007 Sep 1;69(7):606-13.
33. PREDICTABLE SE. Side effects of antidepressants: an overview.Cleveland Clinic Journal of Medicine. 2006 Apr;73(4):351.
34. Blackwell B. Adverse effects of antidepressant drugs. Drugs. 1981 Mar 1;21(3):201-19.
35. Pacher, Pal, and Valeria Kecskemeti. "Cardiovascular side effects of new antidepressants and antipsychotics: new drugs, old concerns?." *Current pharmaceutical design* 10.20 (2004): 2463-2475.
36. De Hert M, Detraux J, Van Winkel R, Yu W, Correll CU. Metabolic and cardiovascular adverse effects associated with antipsychotic drugs. Nature Reviews Endocrinology. 2012 Feb 1;8(2):114-26.
37. Kulaksiz-Erkmen G, Dalmizrak O, Dincsoy-Tuna G, Dogan A, Ogus IH, Ozer N. Amitriptyline may have a supportive role in cancer treatment by inhibiting glutathione S-transferase pi (GST-π) and alpha (GST-α). Journal of enzyme inhibition and medicinal chemistry. 2013 Feb 1;28(1):131-6.
38. Pradeep N, Pradhan D, Umamaheswari A. Designing potent inhibitors of human P38γ for effective breast cancer therapy.

ACCEPTED MANUSCRIPT

39. Nandimath J, Banerjee E, Patil A, Kakade P, Vaidya S, Chaturvedi D. Big data analysis using Apache Hadoop. *Information Reuse and Integration (IRI)*, IEEE 14th International Conference on 2013 Aug 14 (pp. 700-703). IEEE.201310.1109/IRI.2013.6642536.

40. Lie HW, Saarela J, Multipurpose Web publishing using HTML, XML, and CSS. *Communications of the ACM*, 1999, 42(10):95-101.10.1145/317665.317681.

ACCEPTED MANUSCRIPT

ACCEPTED MANUSCRIPT

Figures

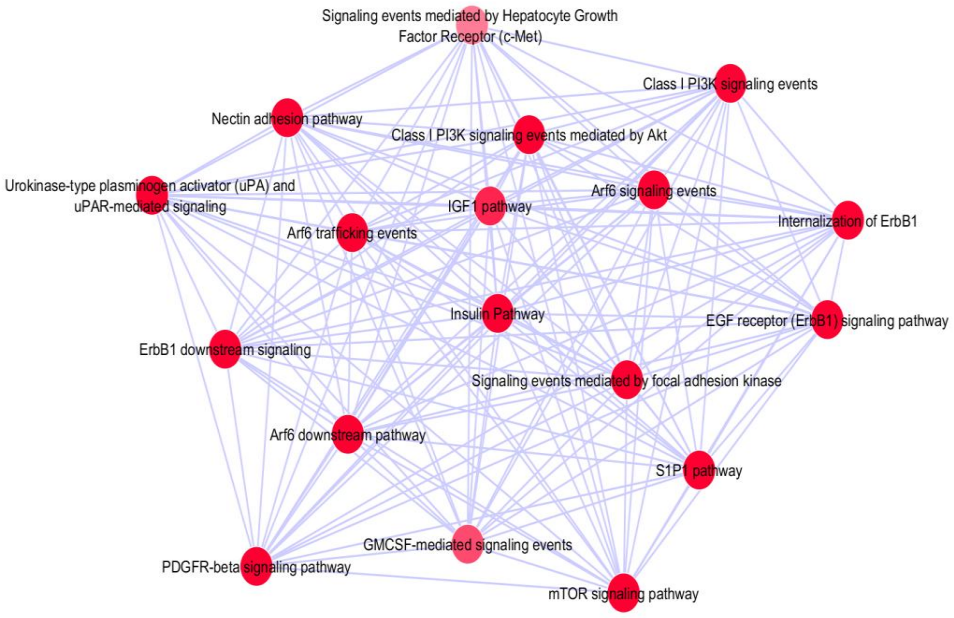


Figure 1 : Signal transduction module obtained by pathway crosstalk analysis

ACCEPTED

ACCEPTED MANUSCRIPT

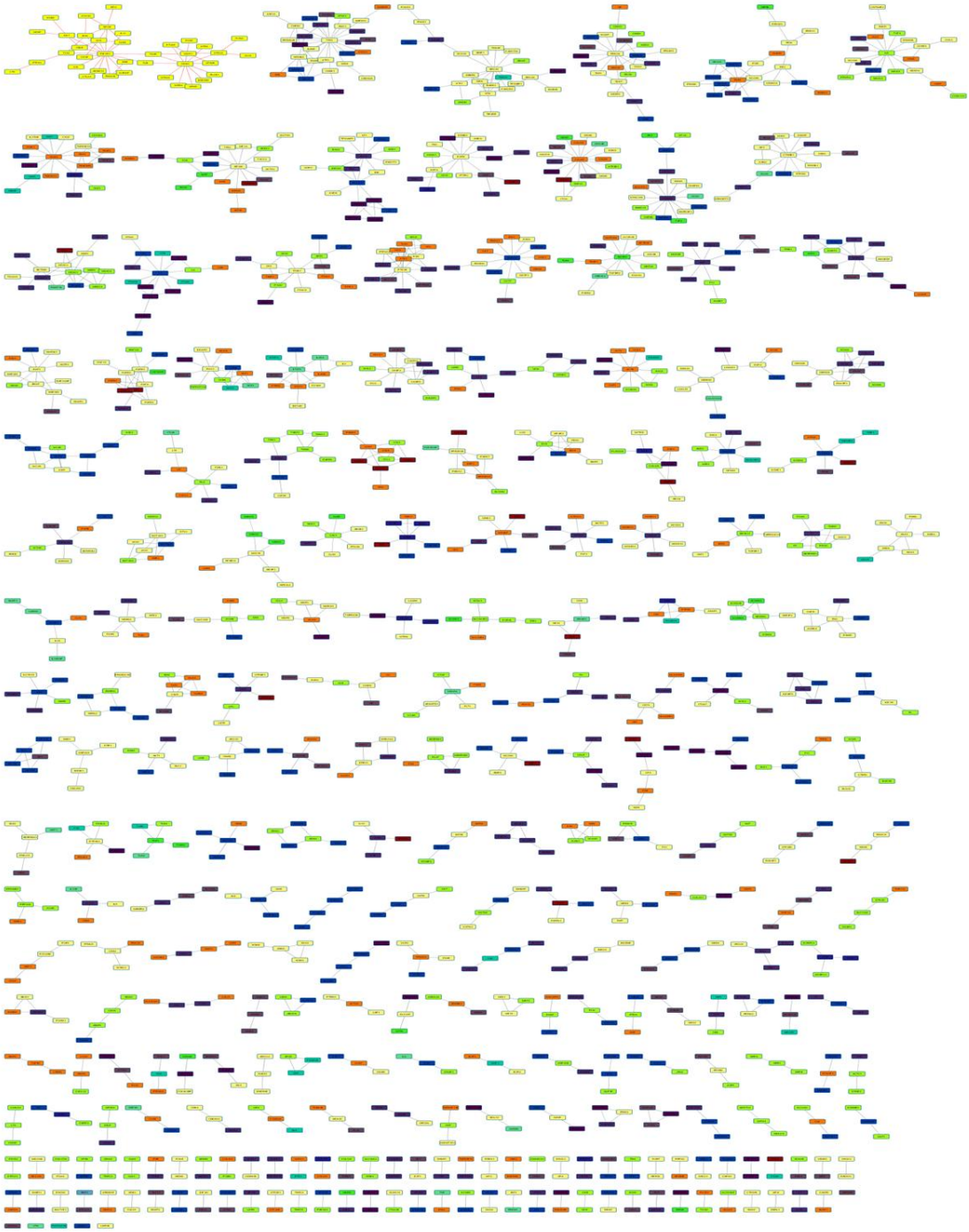
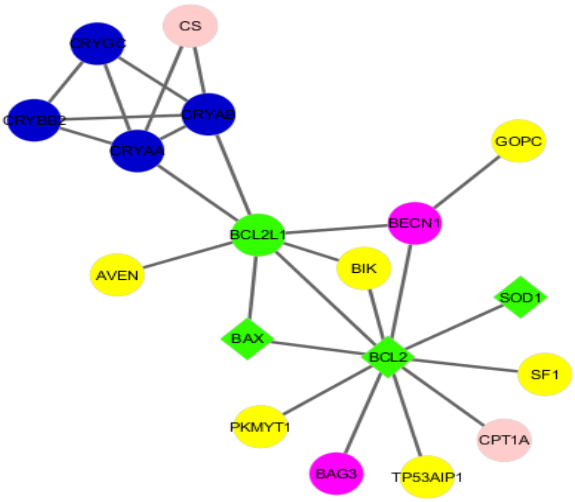
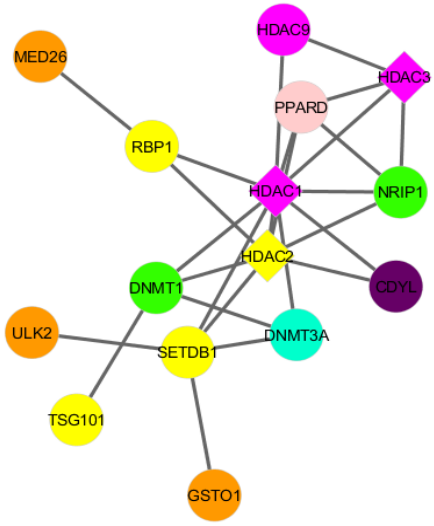


Figure 2: All clusters obtained by MCL algorithm

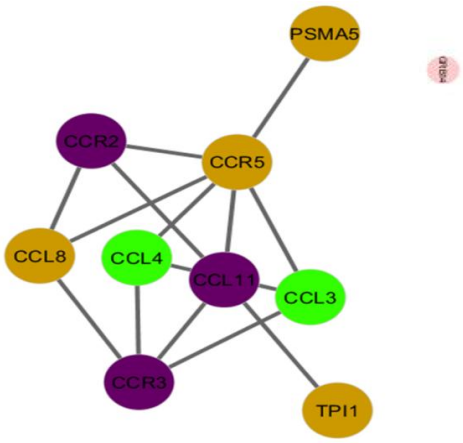
ACCEPTED MANUSCRIPT



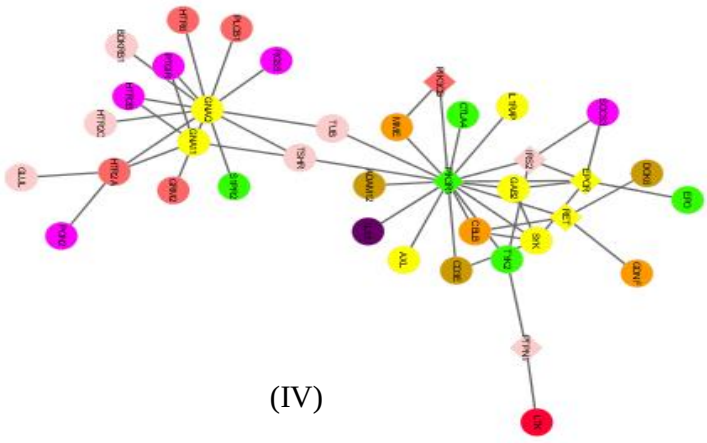
(I)



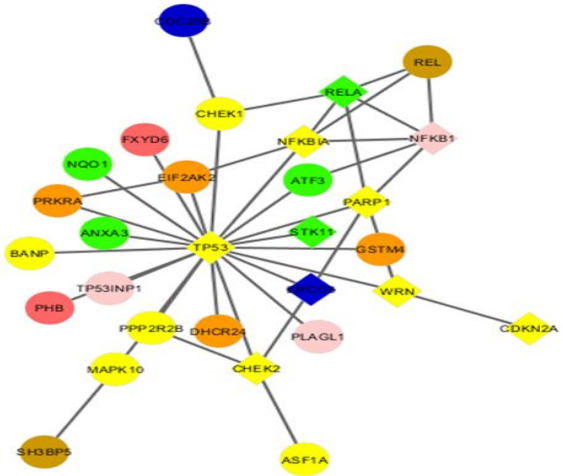
(II)



(III)



(IV)



(V)

Figure 3: Significant clusters:

(I) Cluster 9

(II) Cluster 15

(III) Cluster 32

ACCEPTED MANUSCRIPT

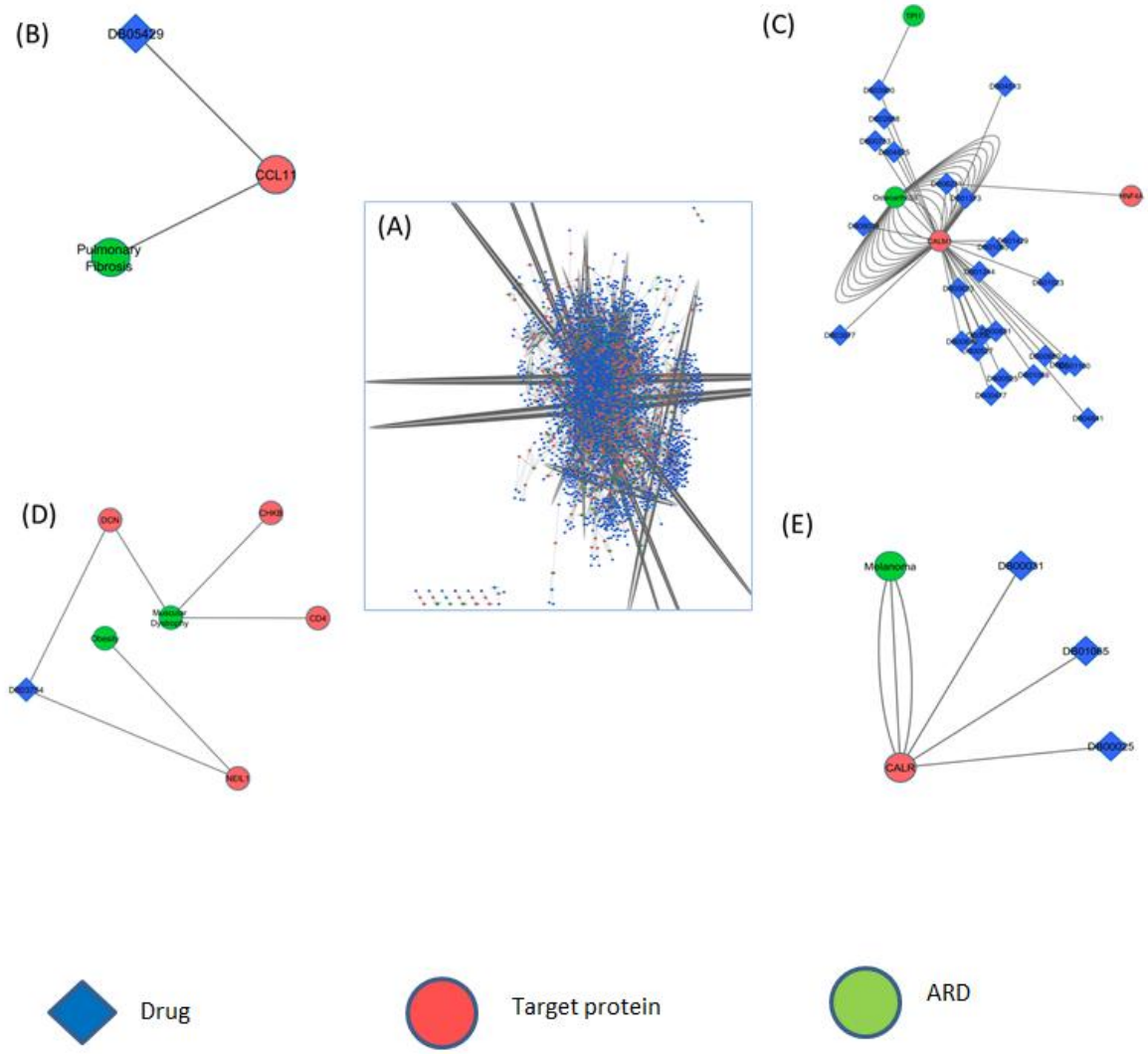
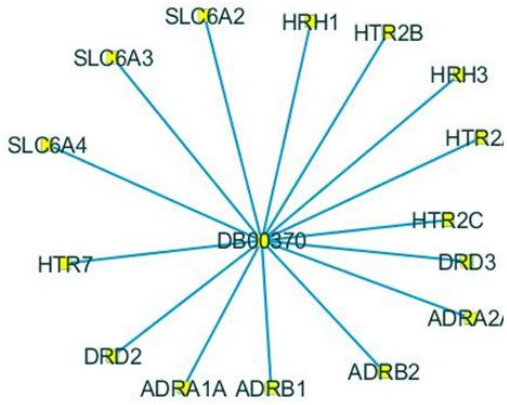
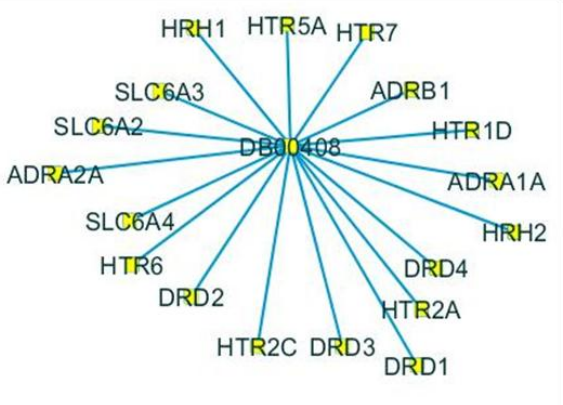


Figure 4: (A) Tripartite network showing association of ARDs-drug- target proteins: subnetworks representing association of hub proteins (B) CCL11 (C) CALM1 (D) DCN (E) CALR

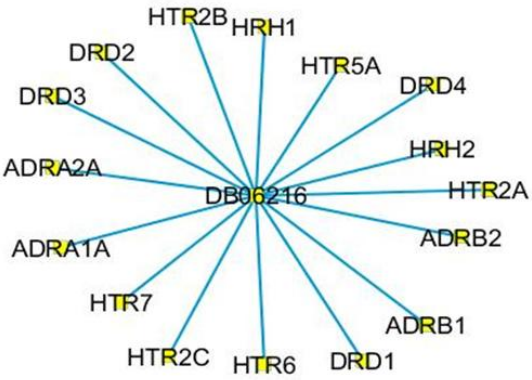
ACCEPTED MANUSCRIPT



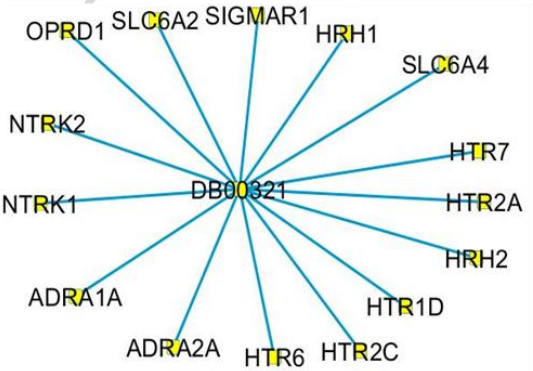
(I)



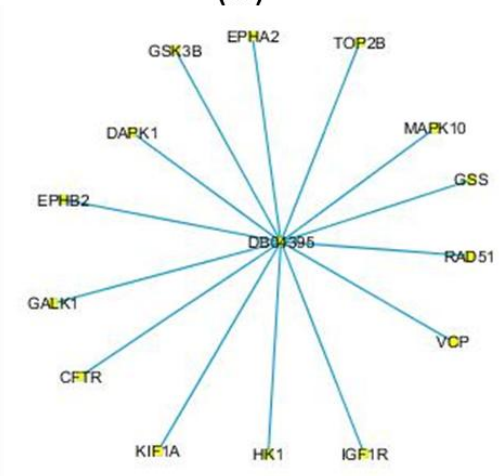
(II)



(III)



(IV)



(V)

Figure 5 : Connection of drugs with target protein molecules :

(I) Mirtazapine
(II) Loxapine
(III) Asenapine
(IV) Amitriptyline
(V) Phosphoaminophosphonic Acid Adenylate

ACCEPTED MANUSCRIPT

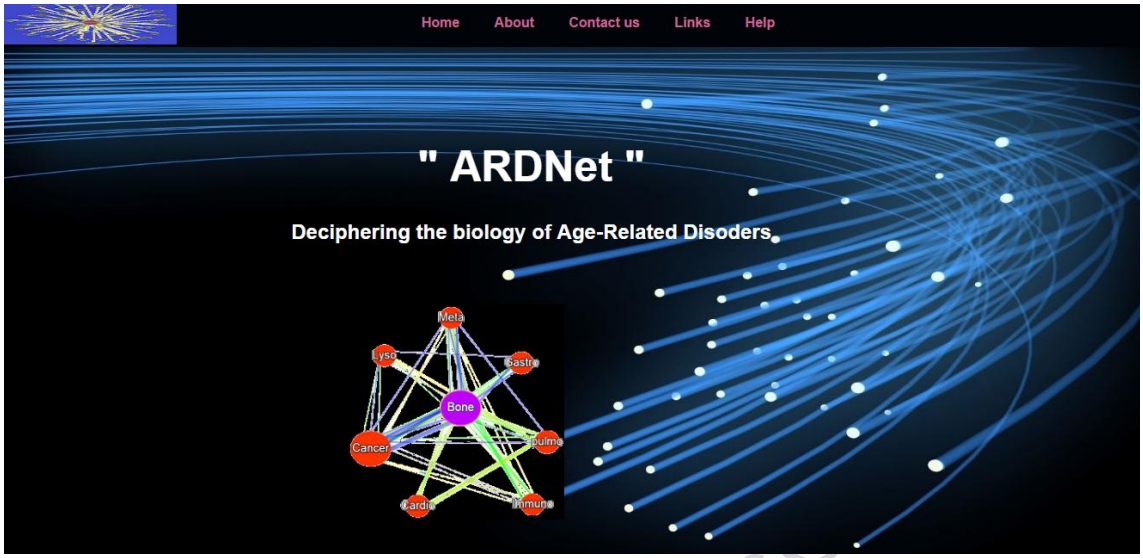


Figure 6: Home page of ARDNet tool

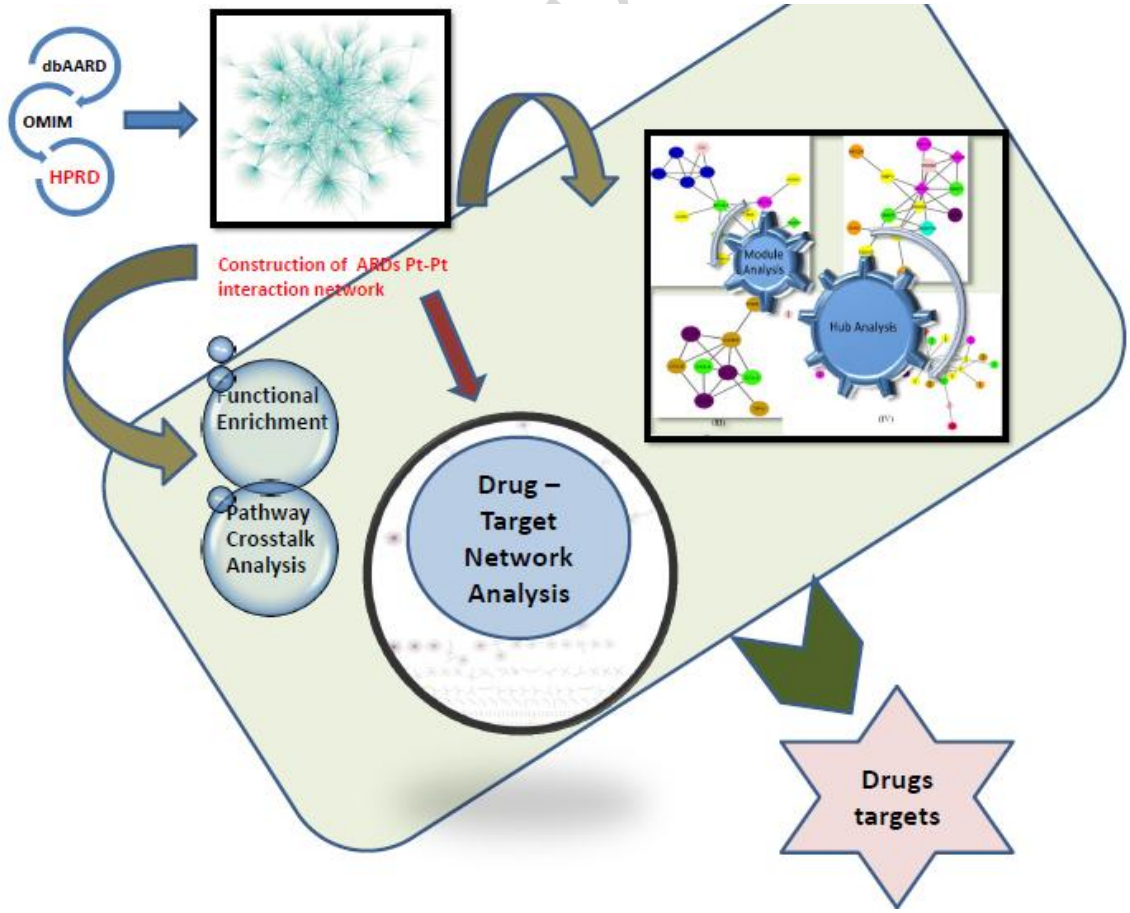
ACCEPTED MANUSCRIPT

Table 1

Protein Name	Disease Name	Disease Class	Aging Associated Hub Proteins
NR	Alzheimer Disease|Crohns Disease|Coronary Artery Disease|Gout|Breast Cancer|Ovarian Cancer|Type 2 Diabetes Mellitus|Age Related Macular Degeneration	Neurological|Gastrointestinal|Cardiovascular|Bone|Cancer|Metabolic|Opthalmological	No
STAT3	Crohns Disease|Multiple Sclerosis|Prostate Cancer	Gastrointestinal|Neurological|Cancer	Yes
ESR1	Osteoporosis|Ovarian Cancer|Systemic Lupus Erythematosus	Bone|Cancer|Immunological	Yes
BRCA1	Prostate Cancer|Breast Cancer|Ovarian Cancer	Cancer	Yes
AKT1	Breast Cancer|Ovarian Cancer|Obesity|Schizophrenia	Cancer|Metabolic|Psychiatric	Yes
SMAD3	Crohns Disease|Osteoarthritis	Gastrointestinal|Bone	No
SMAD4	Deafness|Pancreatic Cancer	ENT|Cancer	No
PIK3R1	Alzheimer Disease|Colon Cancer	Neurological|Cancer	Yes
CALM1	Osteoarthritis	Bone	No
CALR	Melanoma	Cancer	No
DCN	Muscular Dystrophy	Muscular	No
NCF2	Systemic Lupus Erythematosus	Immunological	No

ACCEPTED MANUSCRIPT

NEDD 9	Alzheimer Disease	Neurological	No
YWH AG	Multiple Sclerosis	Neurological	No
TP53	Lung Cancer	Cancer	Yes
PRKC A	Prostate Cancer	Cancer	Yes
EP300	Colon Cancer	Cancer	Yes
EGFR	Lung Cancer	Cancer	Yes
CTNN B1	Colorectal Cancer	Cancer	Yes
APP	Alzheimer Disease	Neurological	Yes



Graphical abstract

ACCEPTED MANUSCRIPT

Research Highlights

- A systems biology approach was applied to investigate the interrelation of age related disorders proteins and to search polyphormacogenic drug targets
- The functional enrichment & pathway crosstalk analysis of ARD genes revealed dominance of signal transduction pathways.
- The analysis of the clusters obtained from MCL clustering revealed interesting observations about the inter-relation of aging genes, ARD genes, and concurrent occurrence of multiple ARDs.
- Interesting and significant findings from the drug-target network regarding drug repurposing.

ACCEPTED MANUSCRIPT

ISSN XXXX XXXX © 2017 IJESC

Research Article Volume 7 Issue No.7

Analysis of Coverage and Connectivity on Channel Randomness in WSN

Anurag Tanwar[1], Sakshi Choudhary[2], Annad Kumar Jha[3]
M.Tech Student[1, 2], Assistant Professor[3]
Department of ECE
Satya College of Engineering, Palwal, Haryana, India [1, 3]
Delhi Technological University, Delhi, India[2]

Abstract:
The wireless Sensor network (WSN) comprises a large number of sensors that are densely deployed in the area of interest to observe a particular phenomenon. There are various applications such as habitat monitoring, military surveillance, weather monitoring etc. where WSN can be used. I critical environment, where human intervention is not possible, battery of sensor node cannot be replaced in case of power drainage. This adversely affects the requirement of good quality of the field as well as extended lifetime of Wireless sensor Network. Therefore, coverage and connectivity which is also a Quality of Service (QOS) is challenging research area in Wireless sensor.

Keywords: WSN, Wireless sensor network, QOS, sensor, Energy efficiency, scalability, fault tolerance, data aggregation,

I. INTRODUCTION

Wireless Sensor Networks (WSNs) have drawn significant attention of the research community in the last few years, because of the rapid advancement in wireless communications, networking and digital electronics devices. The miniaturization of computing and sensing technologies enables the development of tiny, low-power and inexpensive sensors, actuators, and controllers. WSNs generally contain a large number of low-cost, low power and multifunctional sensor nodes that have limited sensing, computing and communication capabilities. A sensor network is designed to sense the event of interest, collect and process the data, and transmit the sensed information towards the sink. Sensor nodes when properly networked and programmed can be useful in sensing the event in the hostile environment where human intervention is not possible [1].

II. SENSOR NOE ARCHITECTURE

Architecture of a sensor node and its major component are illustrated in Fig. 1.1. A sensor node has five basic components: Sensing Unit, Controller, Memory Unit, transceiver unit, power unit and some additional components such as location finding System [3,4].

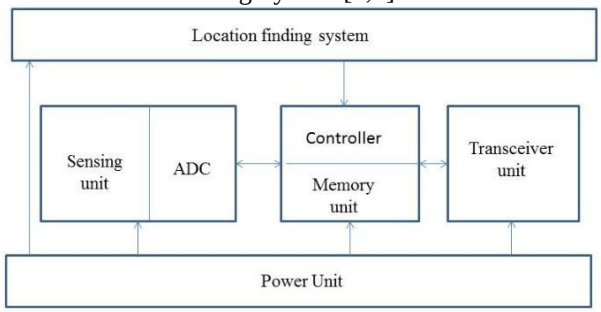


Figure.1. Hardware Architecture of a Sensor Node

The controller is a primary component of a sensor node. Its main task is to collect data from all other sensor nodes, process the data and decide to forward it. The controller also controls the functionality of the other components in the sensor node. The memory component is basically used to store intermediate data or program instructions in random access or read only memory. The communication device is used to interchange data between individual nodes. This device comprises short range radio transceiver. A transceiver is a device that has a aggregated transmitter and receiver in one unit. A sensor is a hardware component that generates a signal when there is a change in the physical condition of the environment such as temperature, humidity, pressure. Because of power constraint the sensor is tiny in size and has low data rate sensing capability. In a sensor node, power supply is one of the most important components. Generally each component in the sensor node is powered by battery. The main consumption of energy is done by communication, sensing and data processing. Therefore, due to limited battery power, each component must operate in an energy efficient manner. In our research work, we have proposed to study coverage and connectivity using deterministic and probabilistic sensing and communication models. Further, to achieve high accuracy and fault tolerance we proposed to develop a model for k-coverage and q-connectivity. To make the model more realistic we planned to use log normal shadowing path loss model and its effect on coverage and connectivity

III. COVERAGE AND CONNECTIVITY IN WSN

Coverage and Connectivity are two most fundamental and important research issues is sensor networks and over the year have been studied intensively by the researchers. The coverage problem determines how well each point around monitoring region is covered by the sensors.

Coverage in WSN: Given a set of sensors S= {s1,s2, …..sn} in a two dimensional area where si(i=1,2,…N) each sensor is located at (xi, yi) and has a sensing radius rs. Any point in the 2-D monitoring region is said to be covered if it is in the sensing radius of at least one sensor node as shown in Fig. 3.1.

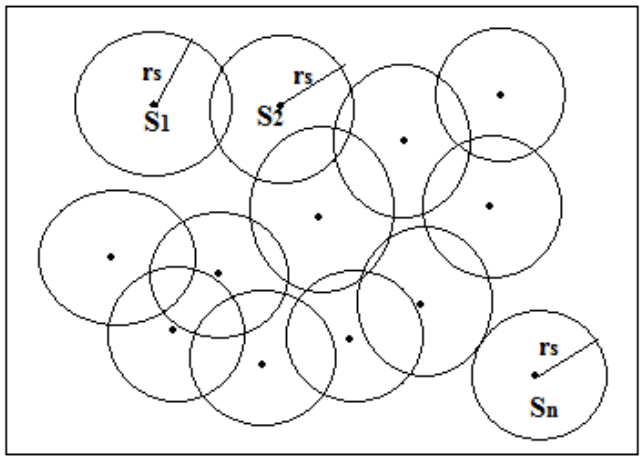


Figure.2. Coverage in Wireless Sensor Networks

Based on application, coverage can be classified into three classes, area coverage, target coverage and barrier coverage.

Area Coverage: In area coverage, a set of sensors is distributed in the monitoring region to monitor the given area. In the area coverage problem the goal is to monitor each point of the region of interest with minimal number of sensor nodes. If each point is covered by at least different working sensor nodes, the area is said to be - covered.

Target Coverage: Target coverage is the term used for monitoring a limited number of predetermined targets in the region of interest. This type of coverage is more suitable for military surveillance. The requirement of target coverage is that each target must be monitored continuously by one or more sensors, provided that every sensor has the capacity to monitor all targets within its sensing range.

***Barrier Coverage*:** Barrier coverage refers to the detection of movement across a barrier by sensor. A strip area with a sensor network deployed over it is considered to be barrier protected, if each and every crossing track through the strip is protected by sensor network. There are several applications of barrier coverage such as deploying sensors on the battlefield to detect illegal intruder, to detect the spread of deadly chemicals, etc.

IV. COVERAGE AND CONNECTIVITY UNDER CHANNEL RANDOMNESS

The Coverage and connectivity had attracted the attention of researchers working in the designing of WSN. Some applications of WSN require coverage and connectivity to make the system more fault tolerance and reliable. In most of the works in this area binary disk model of the channel propagation is used. Therefore, randomness and irregularity present in radio communications because of various environment effects are not considered

System Model

In the system model, it is assumed that sensors are deployed randomly in the 2-D desired sensing area. These sensor nodes are deployed according to a homogeneous Poisson distribution with high density λ. A node with radius can cover up a circular area while neglecting the border effect.

Sensing Model

Sensing coverage is in general modeled by a binary disk model. It is assumed a sensor has circular sensing area so that it senses in all direction uniformly. A sensor node observes an event of interest existing in its sensing range with probability 1 and with probability 0 otherwise.

$$f(d(s, p_t)) = \begin{cases} 1 & \text{if } d(s, p_t) \le r_{\max} \\ 0 & \text{if } d(s, p_t) > r_{\max} \end{cases}$$

Log-Normal Shadowing Path Loss Model

This model is representing the radio propagation in real natural world. Path loss is because of dissipation of the radiated power from the transmitter and the effects of shadowing

$PL(d) = PL(d_0) + 10\eta \log(d / d_0) + X_\sigma$

Where $PL(d_0)$ is the path loss corresponding to a reference distance d_0, η denoted the exponent of path loss that shows the rate of increasing path loss with distance, and X_σ is a Gaussian random variable with mean value as zero and standard deviation σ expressing log-normal shadowing effect

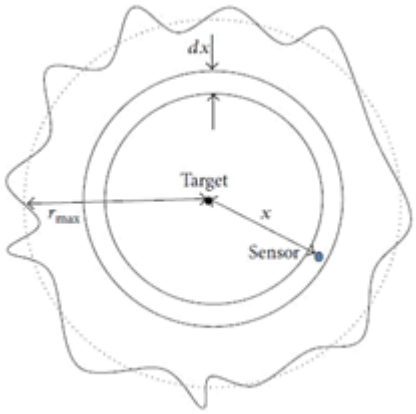


Figure.3. Impact of Shadowing Environment on Sensing

Connectivity in presence of Shadowing

Let us assume a WSN where N sensor nodes are randomly distributed in accordance to a homogeneous Poisson process with intensity (average) λ in the area A. Here
depicts number of nodes per unit area. The probability of a randomly picked sensor node with area A has q neighbours is given by the following equation

$$P(q) = \frac{(\lambda A)^q}{q!} e^{-\lambda A} \qquad \text{Where, } (q = 1, 2, 3.....)$$

V. RESULT ANS PERFORMANCE ANALYSIS

We are doing the performance analysis of a network for k - Coverage and q -Connectivity. Here all nodes are using the lognormal shadowing model for sensing and communication. All the Simulations are performed utilizing MATLAB to find the k -Coverage and q -Connectivity results. Simulation parameters (values) used in the simulation is given in Table 4.1, 4.2, 4.3. To find out the effect of node density and shadowing, we have conducted the following simulations:

- Effect of standard deviation and node density on sensing coverage
- Effect of node density on connectivity
- Effect of communication range on connectivity

Effect of Standard Deviation and Node Density on Sensing Coverage

Table. 1. Simulation parameters for Coverage

S.No	Parameters	values
1.	Number of sensor nodes (N)	100
2.	Area (A)	$1000m^2$ to $3000m^2$
3.	Path loss exponent	3
4.	Transmission power of a sensor node(Ps)	20 W
5.	Threshold of received signal	-58 dB
6.	Effective sensing range(r_{max})	10m

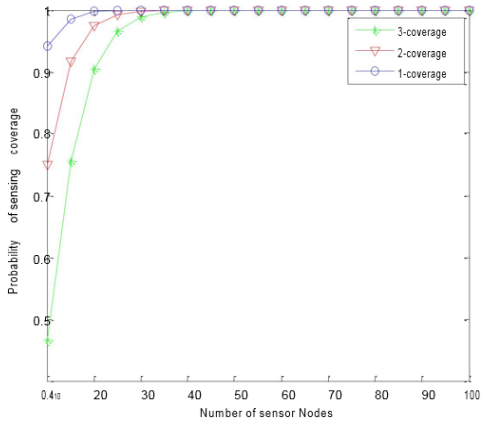


Figure.4. Coverage probability versus sensor nodes at standard deviation = 2 (A=1000 m^2)

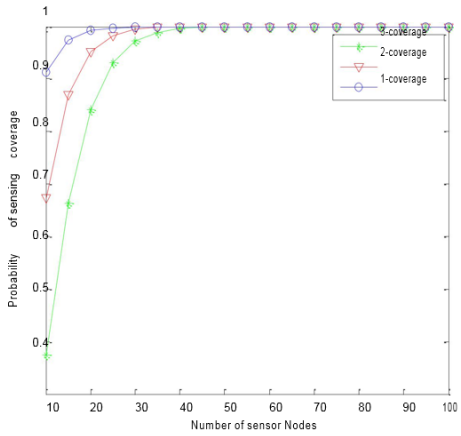


Figure.5. Coverage probability versus sensor nodes at standard deviation = 4 (A=1000 m^2)

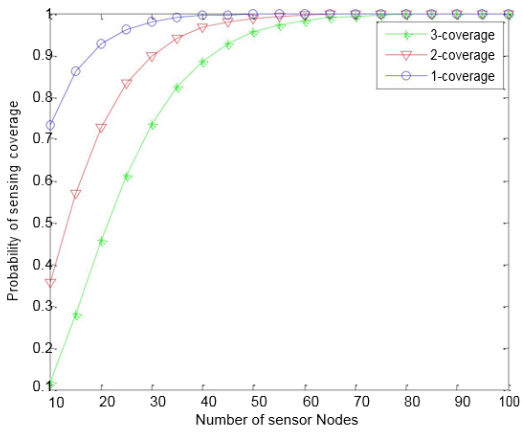


Figure.6. Coverage probability versus sensor nodes at standard deviation = 2 (A=2000 m^2)

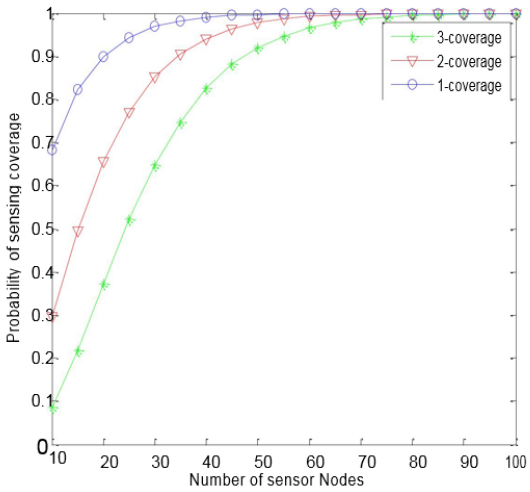


Figure.7. Coverage probability versus sensor nodes at standard deviation = 4 (A=2000 m^2)

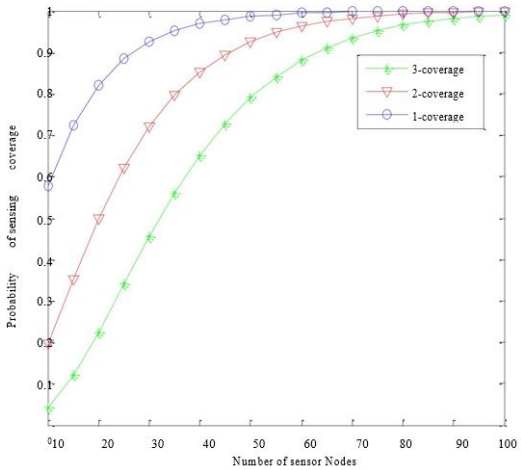


Figure.8. Coverage probability versus sensor nodes at standard deviation = 2 (A=3000 m^2)

We have drawn Figure (5.1), (5.2), (5.3), (5.4), (5.5) for different shadowing parameters (= 2, 4) and Area values (A=1000, 2000, 3000 m^2). When standard deviation is changed from 2 to 4, probability of coverage decreases. So, we require more sensor nodes to achieve the same coverage for = 4 as compared to = 2. Also we can see the effect of increasing Area on probability of coverage for constant number of sensor nodes. When area is increasing Probability of coverage is also decreasing.

Effect of Node Density on Connectivity

Table. 2. Simulation parameters for Connectivity

Parameter	Value
Number of sensor nodes (N)	100
Area (A)	1000 m^2 to 4000 m^2
Effective sensing range (r_{max})	10m

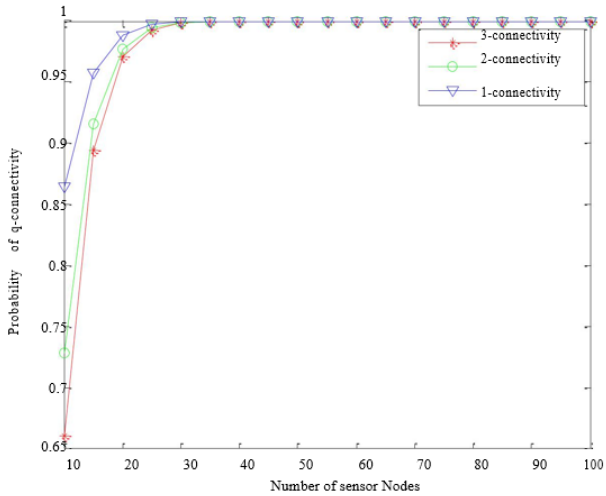


Figure.9. Probabaility of -connectivity versus number of sensor nodes (A=1000 m^2)

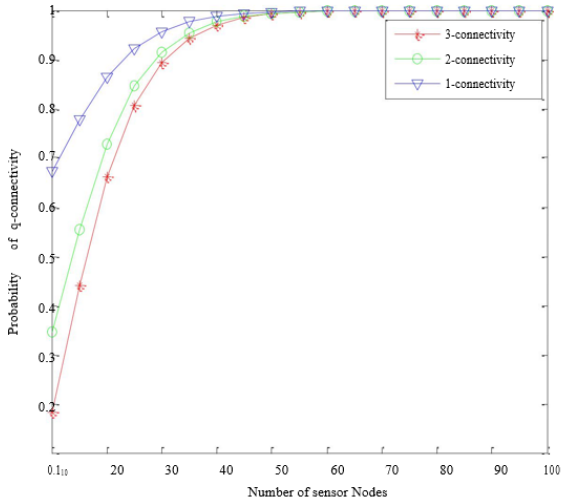


Figure.10. Probabaility of -connectivity versus number of sensor nodes (A=2000 m^2)

Figure (6.1), (6.2) show the variation between probability of *k*-connectivity with number of sensor nodes (*N*). As the number of sensor node increases, the graph shows changeover from low alue of connectivity to high value of connectivity From these graphs we can conclude that for network connectivity greater than or equal to 90%, we require at least 15 sensors (Area A=1000 m$^{2)}$.

Effect of Communication Range on Connectivity

Table.3. Simulation parameters for Communication range

Parameter	Value
Number of sensor nodes (N)	100,150,200
Area (A)	1000 m^2
Effective sensing range (r_{max})	5 m to 25 m

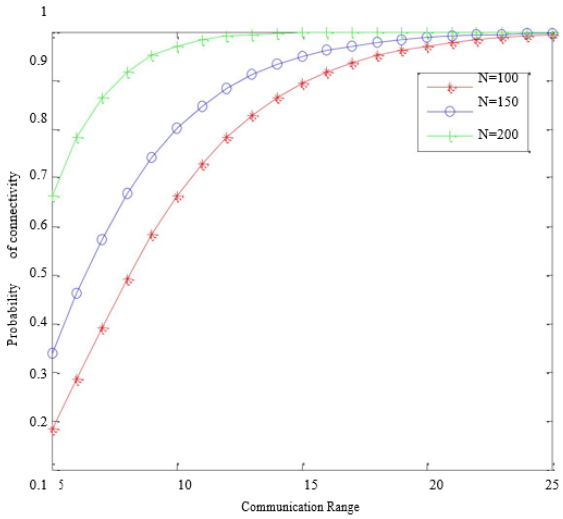


Figure.11. Probability of Connectivity versus communication range (A=1000m^2)

In figure (6.3) we have plotted probability of connectivity vs. communication range. From this we can find that network connectivity is affected by communication range. When the communication range increases, the connectivity of the network also increases.

VI. CONCLUSION & FUTIRE SCOPE

Fault tolerance is one of the most important QoS parameter in the designing of WSN. In this chapter we have evaluated -coverage and -connectivity under lognormal shadowing model. We have shown the effect of node density and shadowing parameter on coverage. We observed that the probability of network connectivity and coverage depends on the standard deviation and node density. For a high value of standard deviation, the probability of network coverage decreases. So we can conclude that there is a significant impact of node density and path loss model (log-normal) on coverage and connectivity.

The contribution to this paper are a set of studies various mathematical models and analysis of these mathematical models through simulation. The main contribution of this paper are summarized below-

- We have developed k-coverage and q-connectivity model to make the network fault tolerable and reliable Effect of node density on connectivity
- Log normal shadowing path loss to capture the radio irregularities has been used to to make the k-coverage and q-connectivity model more realistic

The model developed in this paper has been evaluated analytical as well as through simulations. After examining the simulation results the following observations hav been are made on finding of this work

- More number of sensors is required to maintain the thershold level of coverage when standard deviation of the shadowing environment increses.
- Coverage and connectivity increses when the density of sensor node increases.

When the communication range increses the connectivity of the network also increses

- Every bracketed in-text reference number must have a corresponding end-text reference with full, accurate bibliographic information

- Format bibliographic information as exemplified below. Consult the "How to Present End-Text References" document for examples of other kinds of resources.

VII. FUTURE SCOPE

There are various possibilities of for further investigation of the research work presented in this paper. Some of these possibilities are given below as future direction of research

- This work can also be extended for mobile wireless sensor network so that target tracking can be performed continuously.
- The model developed in this work can be extended for 3-D wireless sensor network such as under water sensor network.
- Substantially more precise propagation models indicating the varition in the radio range with respect to time may be designed.

VIII. REFERENCES

[1]. F. Akyildiz, W. Su, Y Sankarasubramaniam and E Cauiric, "Wireless Sensor Networks: A survery", Computer Netwrorks, Elsevier, vol 38, 2002, pp. 393-433

[2]. W. Dargie, C Poellabauer. "Fundamentals of Wireless Sensor Networks; Theory and Practice", Wiley, 2010

[3]. J. Portilla, A. de Catro, E de. La Torre, T. Riesgo. "A Modular Architecture for Nodes in Wireles Sensor Networks", Journal of Universal Computer Science, vol 12, 2006 pp.328-339

[4]. K Sohrby, D Minoli and T Znati "Wireless Sensor Networks: Technology Protocol and Applications" Wiley-Inderscience, 2007.

[5]. A. Ghosh & S.K Das, "Coverage and connectivity issues in wireless sensor networks: A Survey "Pervasive and Mobile Computing Vol 4, 2008, pp. 115-121

[6]. M.D Penrose, "On k-connectivity for a geometric random graph, "Random structures and algorithms, Vol 15, no 2, 1999, pp. 145-164.

ResearchGate

See discussions, stats, and author profiles for this publication at: https://www.researchgate.net/publication/318721809

Anticancer agent from medicinal plants: a review

Chapter · July 2017

CITATIONS
0

READS
23

3 authors, including:



Arpita Roy
Delhi Technological University
20 PUBLICATIONS **2** CITATIONS
SEE PROFILE



Navneeta Bharadvaja
Delhi Technological University
24 PUBLICATIONS **41** CITATIONS
SEE PROFILE

Some of the authors of this publication are also working on these related projects:



Micropropagation of Plumbago zeylanica View project



Estimation of phytosterols using gas chromatography and green synthesis of silver nano particles in Centell asiatica View project

All content following this page was uploaded by Arpita Roy on 28 July 2017.

The user has requested enhancement of the downloaded file.

Anticancer agent from medicinal plants: a review

3

Arpita Roy, Tushita Attre, Navneeta Bharadvaja*

Plant Biotechnology Laboratory, Department of Biotechnology, Delhi Technological University, New Delhi, 110042, India

*Correspondence: navneetab@dtu.co.in

Copyright: © The Author(s) 2017. Licensee Joanna Bródka. This is an open access chapter licensed under the terms of the Creative Commons Attribution Non-Commercial 4.0 International License (https://creativecommons.org/licenses/by/4.0), which permits unrestricted, non-commercial use, distribution, and reproduction in any medium, provided the original work is properly cited.

ABSTRACT

Cancer is a multistep process and characterized by irregular proliferation of cells. Usually these cells invade and destroy the normal cells, thus creating an imbalance in the body. Cancer is caused due to various factors like tobacco consumption, exposure of body to chemicals, dietary factors and environmental factors. Conventional medication for treatment of cancer has several impacts on healthy cells. There is also a problematic issue of increase in tumor resistance to the current therapeutic agents. Due to this, there is a great need to fight this disease with more effective medication. Natural product plays an important role in fight against cancer and provides a valuable gateway for the use and investigation of new therapeutic agents. Medicinal plants represent a good source of discovery and development of anticancer agents. Medicinal plants contain several biologically active compounds which enable them to cure cancer. They contain various secondary metabolites which include alkaloids, flavanoids, phenolics, carotenoids etc. Benefits of medicine from plant origin over synthetic (chemical) medicine have increased the importance of medicinal plants in the field of healthcare. Numerous medicinal plants are known to possess anticancer activity. Phytocompounds from these plant sources can prevent cancer initiation, promotion and progress by exerting anti-oxidant effects which mediates by the integration of NF-κB, Nrf2 and AP-1 signaling pathways. Overall this chapter provides a comprehensive repository for

Tiezzi A., Karpiński T.M., eds. *New apects in medicinal plants and pharmacognosy.*
DOI: http://dx.doi.org/
JBBooks, Poznań, Poland, 2017

the scientific community working to develop new and improved medicines for cancer which poses serious threat to mankind all across the globe.

Keywords: Medicinal plants; Cancer; Phytocompounds; Anticancer activity.

1. INTRODUCTION

Cancer is an abnormal growth of cells in our bodies that can lead to death. It destroys the normal cells and creates and imbalance in the body. It is one of the most severe health problems in both developing and developed countries. It is very difficult to find the specific cause for cancer. However, tobacco use, alcohol consumption, environmental pollutant, infectious agents, custom habits and lifestyles are some commonly known reasons responsible for this disease.

Environmental factor that contributes to the cancer deaths includes tobacco, obesity, radiation, infection, heredity, stress, environmental pollutants and lack of physical activity (lifestyle, economic and behavioral factors). Smoking causes 90% of lung cancer [1]. It also causes kidney, stomach, pancreas, larynx, and bladder cancer [2]. Tobacco is responsible for about one in five cancer death cases globally [2].

Physical inactivity, obesity and diet are related to 30-35% of cancer deaths [3]. Physical inactivity is believed to contribute to the cancer risk. More than half of the effect from diet is due to the over nutrition. Some specific foods are related to the specific type of cancers like high salt diet causes gastric cancer, aflatoxin B1 causes liver cancer and chewing betel nut causes oral cancer [4].

Exposure to ionizing and non ionizing ultraviolet radiation causes cancer (up to 10%). Source of ionizing radiations includes radon gas and medical imaging; this radiation is not particularly a strong mutagen. When radiation combines with other cancer causing agents then it is more potent like radon with the tobacco smoke [5]. Prolonged ultraviolet ray exposure from sun light leads to skin cancer.

Hereditary also causes cancer in some cases, less that 0.3% population carries genetic mutations that cause cancer. Examples of cancer due to hereditary include inherited mutation in BRCA1 and BRCA2 genes, hereditary non-polyposis colorectal cancer. Some hormones also play an important role in the cancer development by promoting the cell proliferation [6].

Insulin like growth factors and their binding proteins play an important role in proliferation of cancerous cell [7].

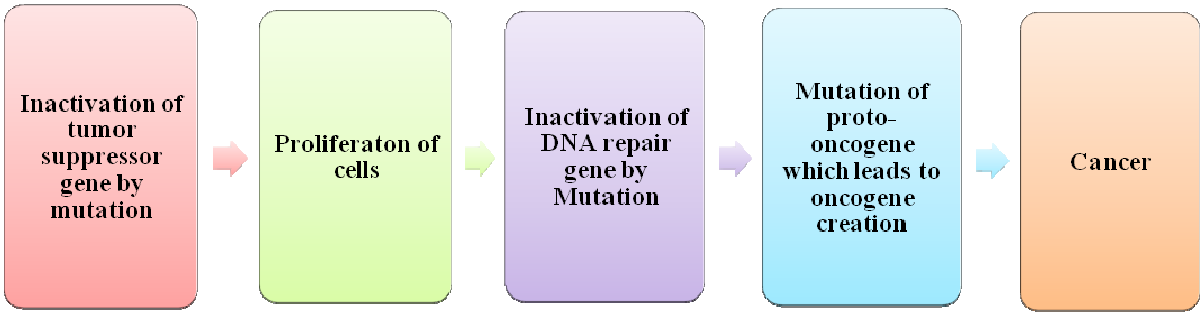


Figure 1. Development of cancer.

'Staging' is a very important parameter in determining the severity of cancer. Depending on the stage of cancer, patients can be recommended drugs accordingly. There are four stages of cancer, each showing different properties and symptoms. These are tabulated as under:

STAGE 1	This is the primary stage of cancer with no visible symptoms. The tumour is not fully grown. A routine medical examination can help detect the presence of first stage cancer. If cancer is detected in this stage it would be easier to cure it.
STAGE 2	The tumour in this case is easily visible through scans. There are a few visible symptoms.
STAGE 3	The benign tumour is fully grown with detectable symptoms.
STAGE 4	This is the terminal stage cancer and no cure is possible in this stage. There is metastasis (spread) of tumour to distant parts of body. There are visible symptoms of cachexia (sudden significant weight loss), patches on skin in case of skin cancer.

There is an alternative approach to categorize cancer based on its severity and expansion as:

T	This is the first stage of cancer, and its severity depends on the spread of tumour from its original location.
N	Cancer is staged 'N', when the tumour spreads from its original location to lymphatic nodes.

M This is the stage where the tumour has metastasized to distant locations in the body and there is no possible cure for it.

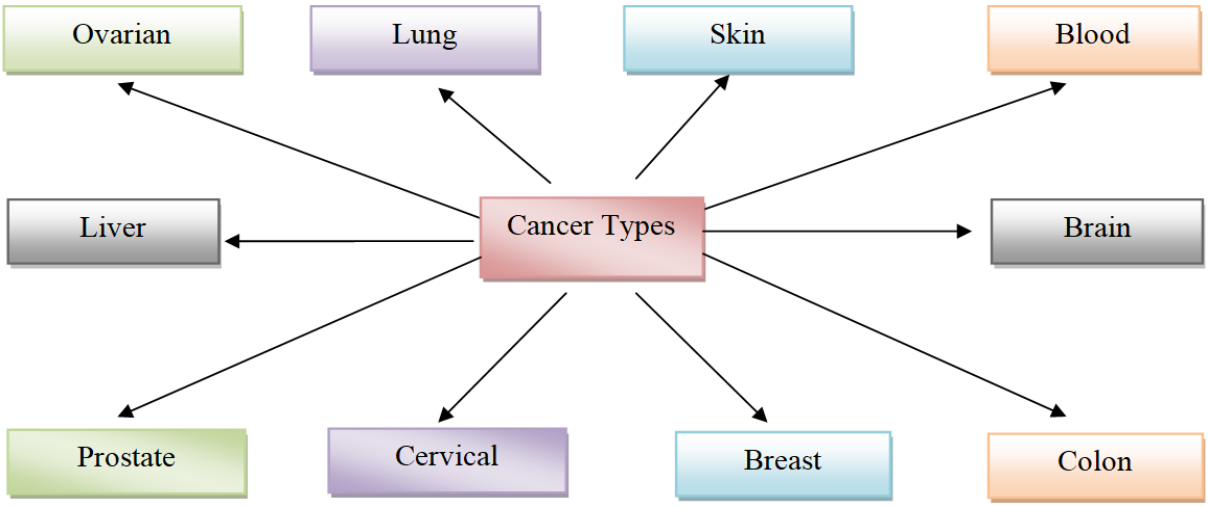


Figure 2. Types of cancer.

The important preventive methods for most of the cancers include dietary changes, stopping the use of tobacco products, treating inflammatory diseases effectively, and taking nutritional supplements that aid immune functions. Current treatment for the cancer includes radiotherapy, chemotherapy and chemically derived drugs. Most commonly used cancer chemotherapy includes anti-metabolites, alkylating agents, platinum analogs and anti-tumor antibiotics. However, chemotherapy and radiotherapy puts patients under lots of strain and further causes health damage. Thus discovery of new anticancer agents from nature, especially plants is currently under investigation. Plants have always been a basis for the traditional medicine systems and they have provided continuous remedies to the mankind for thousands of years. Therapeutic potential of plants is based on the findings of thousands of years of use. First written records on hundreds of medicinal plants including opium and myrrh are listed on the clay tables [8]. Herbal medicines have been used for the centuries to treat various diseases. Herbal medicine uses plant extracts to treat the disease and promote the health of the patient. Aim of the herbal medicine is to restore the ability of body to protect, regulate and heal. Several modern drugs are made from the medicinal plants. Herbal products are taken in form of powder, paste, pills, liquid or raw material (extract). Use of certain herbal products tends to produce side effects and toxicities. In most cases, problem arises due to the

inappropriate use of the herbal products, mislabeling of plant materials, botanical misidentification, etc. This can be toxic when used for inappropriate indications or used in large amount or prepared inappropriately [9]. Therefore investigation on the herbal medicine efficacy is important to prevent from adverse effects. Thus, research has developed ways to find potential use of plant extracts for the treatment of cancer. Many plants have been already used to treat the various forms of cancer. Medicinal plants are considered as a repository of various bioactive compounds and they show wide range of biological activity which includes anti-tumor, anti-viral, anti-inflammatory and anti-malarial activity. Knowledge of the medicinal plants for the preparation of various drugs has been of great significance. Medicinal plants are considered as a rich source of wide variety of ingredients which can be used for the development of drug. Anticancer properties of several medicinal plants are used to find a lead compound that can block the development of cancer. Medicinal plant has various secondary metabolites such as terpenoids, flavanoids, alkaloid and steroids that have different pharmacological properties [10]. Medicinal plants such as *Allium sativum, Annona muricata, Berberies aristata, Catharanthus roseus, Linum usitatissimum, Podophyllum hexeandrum, Rubia cordifolia, Withania somnifera,* etc., show potential role in the inhibition of cancer cell proliferation. Therefore this chapter provides an overview of various medicinal plants and their major bioactive compounds utilized for treatment of cancer.

2. ANTICANCER ACTIVITY OF MEDICINAL PLANTS

2.1. *Allium sativum*

Allium sativum belongs to the Alliaceae family and native to the region between Mediterranean and China. It contains ajoene, allicin, alliin, allixin, γ-glutamyl-S-2-propenyl cysteine, diallyl disulfide, methyl allyl disulfide, S-allyl-cysteine and 1,2-vinyldiithin. Allicin shows antitumor activity in L5178Y lymphoma bearing mice. Methanolic extract of *A. sativum* (MEAS) shows anticancer activity against MCF7, A549 & DU145 and cell carcinoma of the bladder [11, 12].

2.2. *Annona muricata*

Annona muricata belongs to the Annonaceae family and commonly known as

Graviola. It contains acetogenins, β-sitosterol, stigmasterol, phenols, alkaloids, annoionoside, annoionol A, B, C, lycopene, lutein etc. It is distributed in the tropical regions of Central and South America, Western Africa and Southeast Asia. Acetogenins is the main compound and found in the leaves, seeds, bark and fruit of this plant. Acetogenis block the adenosine triphosphate production which inhibits the pump that removes cancer drug from the cell [13]. Acetogenins is identified to be toxic for various cancer cell lines such as pancreatic cancer, breast cancer, colonic adenocarcinoma, liver cancer and lymphoma [14].

2.3. *Astragalus membranaceus*

Astragalus membranaceus belongs to the Fabaceae family and is commonly known as Mongolian milkvetch. It contains astragloside, astraglan, calycosin, soyasapogenoside, quercein, kaempferol, etc. This plant is typically found in parts of China. It is used by the Chinese doctors to treat advanced cases of the liver cancer. A study reported that administration of this plant along with conventional treatment has shown higher survival rate of patients with advanced stage liver cancer as compared to the patients who were given conventional treatment. *Astragalus membranaceus* protects liver from toxic effects of chemotherapy [15]. Swainsonine which is an important compound of this plant is known to prevent metastases [16].

2.4. *Azadirachta indica*

Azadirachta indica belongs to the Meliaceae family and found in India and Indian subcontinent. It contains nimbin, nimbanene, nimbandiol, nimbolide, ascorbic acid, n-hexacosanol and amino acid, nimbiol, etc. It has been used for the treatment of skin cancer, buccal cancer, mammary cancer, prostate cancer and gastric cancer [17]. Ethanolic extract of *Azadirachta indica* causes prostate cancer cell death by apoptosis induction. It acts in a dose dependent manner and increase the fragmentation of DNA [18].

2.5. *Berberis aristata*

Berberis aristata belongs to the Berberidaceae family and commonly found in temperate and sub-tropical regions of Asia, Europe, and America. It is commonly known as Daruhaldi and roots of this plant contain berberine, berbamine, oxyxanthine,

jatrorhizine, epiberberine [19]. Methanolic extract of *B. aristata* showed potential anticancer activity against the human colon cancer cell line and inhibits HT29 cells in a concentration dependent manner [20]. It also significantly inhibits the carcinogenesis induced by 20-methylcholantherene in a dose dependent manner [21].

2.6. *Camellia sinensis*

Camellia sinensis belongs to the Theaceae family and is commonly known as green tea. It contains caffeine, theobromine, gallic acid, catechin, ampelopsin, epicatechin, etc. This plant is native to East Asia, the Indian Subcontinent and Southeast Asia but in today's time it is cultivated also in tropical and subtropical regions in the world. It contains polyphenolics possess anti-cancer and anti-mutagenic activity. Some evidence suggested that this plant has a protective effect against the colon and stomach cancer [22]. A study reported that green tea extract significantly inhibited the liver and leukemia tumor cells from DNA synthesis [16]. It also inhibits the cancer growth by eliminating the free radicals from the body.

2.7. *Cannabis sativa*

Cannabis sativa belongs to the Cannabinaceae family and native to the South Africa. It contains cannabinoids, cannabinol, anandamide, pinene, myrcene, etc. Cannabinoids shows potential inhibition towards cancer based on the experiments performed both in cultured cells and in animal models of cancer [23]. Cannabinoids present an interesting therapeutic potential such as antiemetics, analgesics, appetite stimulants in debilitating diseases, treatment of multiple sclerosis, spinal Tourette's syndrome, cord injuries, glaucoma and epilepsy [24]. Antineoplastic and proapoptotic properties of cannabinoids show emphasis effects of N-acylethanolamines [25]. Cannabinoids induces cancer cell death by apoptosis and inhibits proliferation of cancer cell [26].

2.8. *Catharanthus roseus*

Catharanthus roseus is an important medicinal plant and belongs to the Apocynaceae family. It is commonly known as Madagascar periwinkle. It contains actineoplastidemeric, vinblastin, vincrestine, vindesine, vindeline, tabersonine etc. Catharanthus is native to Madagascar but now-a-days it is being cultivated in Tanzania, Kenya, Kisi and many other

countries. This plant is used for the treatment of cancer, diabetes, fever and hypertension [27]. It contains many bioactive compounds which include vinblastine, vincristine, ajmalicine and serpentine [28]. Vinblastine and vincristin are commonly used for the treatment of leukemia and lymphoma [28].

2.9. *Curcuma longa*

Curcuma longa is commonly known as haldi in Hindi, harida in Sanskrit and turmeric in English. It is belongs to the Zingiberaceae family. This plant is native to Southern Asia and is also used as a coloring agent in Bangladeshi cuisine, Indian cuisine and also for many other purposes. It contains curcumin, curcuminoids, essential oil, turmerone, monoterpenes, diarylpentanoids, diterpenes, sesquiterpenes, triterpenoids, sterols, alkaloid, etc. Curcumin is the active ingredient of this plant, which is a polyphenol derived from plant rhizome and this plant is used for both cancer prevention and treatment. Curcumin shows protective effect by inhibiting the growth of several angiogenesis associates and tumor associated genes [29]. Curcumin possess anti-proliferative property by down regulating the numerous gene expressions which includes activator protein 1, NF-kappa B, cycloxygenase 2, epidermal growth receptor 1, nitric oxidase synthase and tumor necrosis factor [30].

2.10. *Glycine max*

Glycine max belongs to the Fabaceae family and native to East Asia. It is commonly known as Soya bean and rich in selenium, zinc, vitamins, isoflavones, amino acids, phytosterols and saponons. A study reported that soybean agglutinin inhibits the tumor growth in rats [31]. Isoflavones converts cancer cells to the normal by inducing cell differentiation. Genistein induce apoptosis in the cancer cells [16].

2. 11. *Linum usitatissimum*

Linum usitatissimum belongs to the Linaceae family and is rich in lignans. This short-lived perennial plant found in the western and southern Europe and western Asia. These plant lignans are converted to mammalian lignans (enterodiol and enterolactone) by bacterial fermentation in the colon [32] and they can then act as estrogens. Mammalian lignans appear to be anti-carcinogenic, lignan metabolites bear a structural similarity to estrogens and can

bind to estrogen receptors and inhibit the growth of estrogen-stimulated breast cancer [33]. Root extract of *Linum usitatissimum* induce significant amount inhibition of cell vitality and proliferation without performing the strong cytotoxicity in the human breast cell line MCF7 [34].

2.12. *Podophyllum hexeandrum*

Podophyllum hexeandrum belongs to the Podophyllaceae and found in Himalayan region. It is commonly known as Mayapple and contains podophyllotoxin, kaempferol, quercetin, asiragalin, essential oil, podophyllin. Podophyllotoxin has been used for the treatment of testicular and lung cancer as well as in certain leukemias [35]. Podophyllotoxin majorly found in the roots of this plant and used for the treatment of cancers, ulcers, wounds, constipation and tuberculosis [35].

2.13. *Oroxylum indicum*

Oroxylum indicum belongs to the Bignoniaceae family and is native to the Indian subcontinent. It contains baicalein, chrysin, oroxylin, scutellarein, pinostrobin, stigmast-7-en-3-ol. Several studies have shown the anticancer potential of this plant in various models. Ethanol extract (95%) of this plant showed cytotoxic effects against the Hep2 cell lines at 0.05% concentration [36]. Baicalein showed the antitumor effect on the human cancer cell lines and inhibits proliferation of HL-60 cell lines up to 50% at 25-30 µM concentration [37]. Aqueous and methanolic extract of *Oroxylum indicum* showed cytotxicity in selected tested cell lines and both the extracts exhibited moderate level of DNA protection against the oxidative stress [38].

2.14. *Punica granatum*

Punica granatum belongs to the Lythraceae family and fruit bearing deciduous shrub which is commonly known as pomegranate. It is originated in Iran and has been cultivated since ancient times throughout the Mediterranenan region and northern India. It is rich source of phenolic compounds, ellagitannins (ETs) and ellagic acid (EA) that metabolically convert to urolithins by the gut microbiota. Urolithins are found in high concentrations in colorectal cancer patients and urolithins inhibit proliferation of cancer cells and interfere with cell cycle

and induce apoptosis [39]. In a study, potential of pomegranate ellagitannins-derived compounds exhibited anti-proliferative and anti-aromatase activities in breast cancer cells [40].

2.15. *Rubia cordifolia*

Rubia cordifolia belongs to the Rubiaceae family and is commonly known as Indian madder. It contains cordifoliol, cordifodiol, anthraquinone, alizarin, etc. Mollugin showed anticancer activity against the lymphoid leukemia in mice and also inhibited the passive cutaneous anaphylaxis in rats [41]. Quinones and hexapeptides found in this plant showed the potential antitumor activity by 80S ribosome binding and this resulted in the inhibition of peptidyl tRNA and aminoacyl-tRNA binding which is required for the protein synthesis [42].

2.16. *Silybum marianum*

Silybum marianum belongs to the Asteraceae family and native to Southern Europe to Asia. It contains silymarin, silydianin, silychristin, silibinin, tyramine, histamine, essential oil, gamma linoleic acid, mucilage, etc. Silymarinis is the main compound of this plant which showed anticancer property against UV radiation induced skin cancer in mice and reduces the tumor multiplicity up to 78% [43]. Silymarins down regulates the gene product which is associated in the tumor cells proliferation, angiogensis, invasion and metastasis [44]. Silibinin also showed beneficial role in the human breast cancer [45]

2.17. *Taraxacum officinale*

Taraxacum officinale belongs to the Asteraceae family and is commonly known as Dandelions. It is a perennial plant and found in the temperate regions of the world such as Western, Central and Southern Europe, Northwest Africa, Northern Iran and Southwest Asia. It contains glycosides, terpenoids, carotenoids, choline, potassium salts, vitamin A, lecithin, etc. *Taraxacum officinale* decreased cell viability and increased the production of tumor necrosis factor α and interlukine-1α [46]. Leaves, root and flowers extracts of this plant was investigated against progression of tumor, among all the extracts leaf extract showed inhibition of breast cancer cell growth [47].

2.18. *Vernonia amygdalina*

Vernonia amygdalina belongs to the Compositae family and grows in tropical Africa. The bitterness in the plant extract is due factors such as glycoside, saponins, alkaloids and tannins. *Vernonia amygdalina* reverses the tumor in 106 MCF-7 breast cancer cells and also increased the basal apoptotic but decreased the angiogenic activity in mice [48]. *Vernonia amygdalina* shows anticancer activity in the human breast cancer cell lines (MCF-7 and MDA-MB-231) and inhibits the proliferation of cell lines in a dose and time dependent manner [49].

2.19. *Vismia laurentii*

Vismia laurentii belongs to the Guttiferae family and is found in the tropical and sub-tropical regions of world. It contains anthraquinones, xanthones and prenylated anthrones. It is used for the treatment of wounds and skin diseases. Xanthone V1 has shown anticancer potential against numerous cancer cell lines. It induces apoptosis and caspase-3 activity in CCRF-CEM cell line [50]. Fruits and seeds of this plant contain xanthones, naphtoquinones and anthraquinones which are thought to be responsible for the anticancer activity of this plant [51].

2.20. *Withania somnifera*

Withania somnifera is commonly known as ashwagandha in Hindi and Sanskrit, winter cherry in English. It belongs to the Solanaceae family and contains withanolides, withaferins, anferine, isopellertierine and sitoindosise. This plant grows majorly in India (especially Madhya Pradesh), Pakistan, Bangladesh, Sri Lanka and parts of Northern Africa. Due to its medicinal properties, leaves and roots have been used in the Indian traditional system of medicine and marketed globally. Extract of *Withania somnifera* modulates various biological responses [52]. It has been used in various preparations for its anti-stress, anti-peroxidative, anti-ageing, anti-inflammatory, anti-oxidant, anti-tumor, cardiotonic, and immunomodulatory properties [53]. Withanolide A and withaferin A is the main constitute of this plant. Withaferin A which is mostly present in the leaves produces rapid apoptosis in the cancer cells. Cell signaling pathways by this plant formulation largely depends up on the high content of withferin A present in it [53].

3. SOME OTHER MEDICINAL PLANTS WITH ANTI-CANCER ACTIVITY

Plant derived anticancer agents are effective inhibitors of cancer cells lines. Due to which there is a high demand of these plants for the production of therapeutically important compounds. There are several other medicinal plants all over the world, which are being used traditionally for cancer prevention and treatment. Some phytochemicals that are important active constituents of plants, including catechins, ursolic acid, silymarin, hecogenin glycyrrhizin, berberine, campothecin, gallic acid and various types of flavonoids, have shown promise in future cancer management. Some of the other medicinal plants that possess anticancer activity are discussed in the Table 1.

Table 1. List of other medicinal plants with anticancer activity.

Plants	Family	Anti-cancer agents	References
Aegle marmelos	Rutaceae	Lupeol	[54]
Ailanthus altissima	Simaraubaceae	Ailantenol, ailnthanone	[55]
Andrographis paniculata	Acanthaceae	Andrographolide	[56]
Apium graveolens	Umbelliferae	Apigenin	[57]
Aloe ferox	Liliaceae	Aloe-emodin, emodin	[58, 59]
Alpinia galanga	Zingiberaceae	Pinocembrin	[54]
Ananas comosus	Bromeliaceae	Ananas bromelain	[60]
Aphanamixis polystachya	Meliaceae	Amooranin	[54]
Astragalus membranaceus	Papilionaceae	Swainsonine	[61]
Berberis vulgaris	Berberidaceae	Berberine	[54]
Betula utilis	Betulaceae	Betulin	[62]
Bleckeria vitensis	Apocynaceae	Ellipticine	[63]
Brucea antidysenterica	Simaraubaceae	Bruceantin	[63]
Campotheca acuminate	Nyssaceae	Campothecin	[63]
Chlorella pyrenoidosa	Oocystaceae	Lysine	[64]
Cephalotaxus harringtonia	Cephalotaxaceae	Homoharringtonine	[63]
Chelidonium jajus	Papaveraceae	Sanguinarine, chelerythrine, berberine	[65]
Colchicum luteum	Liliaceae	Colchicines, demecolcine	[66]

Plants	Family	Anti-cancer agents	References
Croton lechleri	Euphorbiaceae	Taspine	[67]
Diphylleia grayi	Berberidaceae	Diphyllin	[63]
Dysoxylum binectariferum	Meliaceae	Rohitukine	[63]
Echinops setifer	Asteraceae	Echinopsine	[18]
Erythronium americanum	Liliaceae	α-methylenebutyrolactone	[68]
Euphorbia semiperfoliata	Euphorbiaceae	Jatrophane	[67]
Fagopyrum esculentum	Polygonaceae	Rutin	[66]
Indigofera tinctoria	Leguminosae	Indirubins	[63]
Ginkgo biloba	Ginkoaceae	Ginkgolide	[69]
Glycyrrhiza glabra	Leguminosae	Glycyrrhizin	[70]
Gossypium barbadense	Malvaceae	Gossypol	[71]
Hydrastis canadensis	Ranunculaceae	Berberastine, candaline, hydrastine	[72]
Junchus effuses	Juncaceae	Tridecanone, juncanol, effusol, phenylpropanoid	[18]
Lantana camara	Verbenaceae	Isocamerine, camerine, lantanine, lantadene, micranine	[67]
Larrea tridentate	Zygophyllaceae	Terameprocol	[73]
Lentinus edodes	Agaricaceae	Lentinan	[74]
Lonicera japonica	Caprifoliaceae	Luteolin	[75]
Mappia foetida	Icacinaceae	Camptothecin	[76]
Newbouldia laevis	Bignoniaceae	2-acetylfuro-1,4-naphthoquinone	[51]
Nigella sativa	Ranunculaceae	Thymoquinone, dithymoquinone	[54]
Olea europea	Oleaceae	Oleic acid	[18]
Ocimum sanctum	Lamiaceae	Eugenol, orientin, vicenin	[54]
Oldenlandia diffusa	Rubiaceae	Ursolic acid	[54]
Paris polyphilla	Trilliaceae	Polyphyllin	[77]
Podophyllum hexandrum	Berberidaceae	Podophyllin	[78]
Plumbago zeylanica	Plumbaginaceae	Plumbagin	[79]
Prunella vulgaris	Labiatae	Oleanolic acid, ursolic acid	[54]
Psoralea corylifolia	Fabaceae	Bavachinin, psoralen, psoralidin	[54]

Plants	Family	Anti-cancer agents	References
Pteris multifida	Pteridaceae	Pterokaurane	[67]
Rubia cordifolia	Rubiaceae	Rubidianin, rubiadin, purpurin, xanthopurpurin	[54]
Scrophularia nodosa	Scrophulariaceae	Iridoid	[80]
Taxus brevifolia	Taxaceae	Taxanes, taxol cepholomannine	[81]
Zingiber officinale	Zingiberaceae	Curcumin, gingerenone A, gingeols, zingerone	[82]
Ziziphus nummularia	Rhamnaceae	Betulinic acid, betulin	[83]

4. CONCLUSION

Every year, cancer takes the life of millions of people. Various therapies are available for the cancer treatment but they have several limitations such as kidney damage, gastro-intestinal disorder, etc., due to which an alternative solution to this problem is required. Plant derived compounds possessing anti-cancerous activities have received huge amount of scientific attention. They play vital role in the cancer prevention and treatment. Pharmaceutical research has been done in countries like Germany, USA, Japan, France and China to improve the quality of herbal medicine for the cancer treatment [84]. Plants are the major source of secondary metabolites and an important source of pharmaceutical drugs. Herbal drug treatment is an ideal choice as it is comparatively cheaper and may be highly recommended to the poor and rural people for the effective treatment of cancer. Anticancer agents discovered from medicinal plants have played an important role in cancer treatment. It is documented that medicinal herbs have rich anticancer potential due to their immune-modulatory and antioxidant properties, and on the forefront whenever we talk about anticancer remedies, they are a significant source of synthetic and/or herbal origin. Bioactive compounds significantly influenced the cancer research on various aspects. Secondary metabolites from medicinal plants inhibits the DNA damage, arrest the cell cycle, inhibits the tumor cell angiogenesis and induce apoptosis thus prevents the cancer. Researchers must pay attention to the scientific rigor of studies of herbal drugs in the future to improve the status. Only few medicinal plants have been explored for their biological activity from 1000 species, so further investigations of plants in cancer treatment show a promising activity and it must

be taken into consideration. Therefore in this chapter selected plants have been explored for their biological activity and further more efforts are required to explore potent anticancer plants from nature to save humans life across the world from cancer.

REFERENCES

1. Biesalski HK, Bueno de Mesquita B, Chesson A, Chytil F, Grimble R, Hermus RJ, Köhrle J, Lotan R, Norpoth K, Pastorino U, Thurnham D. European Consensus Statement on Lung Cancer: risk factors and prevention. Lung Cancer Panel. Cancer J Clinic. 1998; 48(3): 167-176; discussion 164-166.
2. Kuper H, Boffetta P, Adami HO. Tobacco use and cancer causation: association by tumour type. J Int Med. 2002; 252(3): 206-224.
3. Kuper H, Adami HO, Boffetta P. Tobacco use, cancer causation and public health impact. J Int Med. 2002; 251(6): 455-466.
4. Kushi LH, Byers T, Doyle C, Bandera EV, McCullough M, McTiernan A, Gansler T, Andrews KS, Thun MJ. American Cancer Society Guidelines on Nutrition and Physical Activity for cancer prevention: reducing the risk of cancer with healthy food choices and physical activity. Cancer J Clinic. 2006; 56(5): 254-281.
5. Park S, Bae J, Nam BH, Yoo KY. Aetiology of cancer in Asia. Asian Pac J Cancer Prev. 2008; 9(3): 371-380.
6. Goubran HA, Kotb RR, Stakiw J, Emara ME, Burnouf T. Regulation of tumor growth and metastasis: the role of tumor microenvironment. Cancer Growth Metastasis. 2014; 7: 9-18.
7. Henderson BE, Bernstein L, Ross RK. Chapter 13: Hormones and the Etiology of Cancer. In: Bast RC, Kufe DW, Pollock RE, et al. Holland-Frei Cancer Medicine (5th ed.). Hamilton, Ontario: B.C. Decker. 2000.
8. Rowlands M-A, Gunnell D, Harris R, Vatten LJ, Holly JMP, Martin RM. Circulating insulin-like growth factor peptides and prostate cancer risk: a systematic review and meta-analysis. Int J Cancer. 2009; 124(10): 2416-2429.
9. Phua DH, Zosel A, Heard K. Dietary supplements and herbal medicine toxicities -when to anticipate them and how to manage them. Int J Emerg Med. 2009; 2(2): 69-76.
10. Sumner J. The natural history of medicinal plants. Timber Press. 2000.
11. Abdullaev FI. Plant derived agents against cancer. In: Gupta SK, editor. Pharmacology and therapeutics in the new millennium. Narosa publishing house: New Delhi, India 2001: 345-354.
12. Karmakar S, Choudhury SR, Banik NL, Swapan RK. Molecular mechanisms of anti-cancer

action of garlic compounds in neuroblastoma. Anticancer Agents Med Chem. 2011; 11(4): 398-407.

13. Thomson M, Ali M. Garlic (*Allium sativum*): a review of its potential use as an anti-cancer agent. Curr Cancer Drug Targets. 2003; 3(1): 67-81.
14. Muriel J. M., Herbs or natural products that decrease cancer growth. Oncol Nursing Forum. 2004; 31(4): E75.
15. Prakash Om, Amit Kumar, Pawan Kumar, Ajeet. Anticancer potential of plants and natural products: a review. Am J Pharmacol Sci. 2013; 1: 104-115.
16. Wang J, Ito H, Shimura K. Enhancing effect of antitumor polysaccharide from Astralagus or Radix hedysarum onC3 cleavage production of macrophages in mice. Department of Pharmacology, Mie University School of Medicine, Japan. Mem Inst Oswaldo Cruz. 1991; 86(2): 159-164.
17. Sakarkar DM, Deshmukh VN. Ethnopharmacological review of traditional medicinal plants for anticancer activity. Int J Pharm Tech Res. 2011; 3: 298-308.
18. Pandey G, Madhuri S. Some medicinal plants as natural anticancer agents. Pharmacognosy Rev. 2009; 3: 259-263.
19. Kumar S, Suresh PK, Vijaybabu MR, Arunkumar A, Arunakaran J. Anticancer effects of ethanolic neem leaf extract on prostate cancer cell line (PC-3). J Ethnopharmacol. 2006; 105(12): 246-250.
20. Saied S, Batool S, Naz S. Phytochemical studies of *Berberis aristata*. J Basic Appl Sci. 2007; 3(1): 1-4.
21. Das S, Basu SP. Cytotoxic activity of methanolic extract of Berberis aristata DC on colon cancer. Global J Pharmacol. 2009; 3(3): 137-140.
22. Sharma K, Bairwa R, Chauhan N, Shrivastava B, Saini NK. Berberis aristata: a review. Int J Res Ayurveda Pharm. 2011; 2(2): 383-388.
23. Dreosti IE. Bioactive ingredients: antioxidants and polyphenols in tea. Nutr Rev. 1996; 54: S51-58.
24. Guzman M. Cannabinoids potential anticancer agents. Nature Rev Cancer. 2003; 3: 745-755.
25. Ben Amar M. Cannabinoids in medicine: a review of their therapeutic potential. J Ethnopharmacol. 2006; 105: 1-25.
26. Pushkarev VM, Kovzun OI, Tronko MD. Antineoplastic and apoptotic effects of cannabinoids. N-acylethanolamines. J Cancer Res Exp Oncol. 2008; 30(1): 6-21.
27. Velasco G, Sánchez C, Guzmán M. Towards the use of cannabinoids as antitumour agents.

Nature Rev Cancer. 2012; 12(6): 436-444.

28. Don G. *Catharanthus roseus*. In: Ross IA, ed. Medicinal plants of the world: chemical constituents, traditional and modern uses. Vol 1. Totowa, New Jersey, USA: Humana Press; 2003: 175-196.
29. Van Der Heijden R, Jacobs DI, Snoeijer W, Hallard D, Verpoorte R. The *Catharanthus* alkaloids: pharmacognosy and biotechnology. Curr Med Chem. 2004; 11(5): 607-628.
30. Pratheeshkumar P, Sreekala C, Zhang Z, et al. Cancer prevention with promising natural products: mechanisms of action and molecular targets. Anti-Cancer Agents Med Chem. 2012; 12(10): 1159-1184.
31. Liener IE. Implications of antinutritional components in soybean foods. Crit Rev Food Sci Nutr. 1994; 34: 31-67.
32. Thompson LU, Robb P, Serraino M, Cheung F. Mammalian lignan production from various foods. Nutr Cancer. 1991; 16: 43-52.
33. Serraino M, Thompson LU. The effect of flaxseed supplementation on the initiation and promotional stages of mammary tumorigenesis. Nutr Cancer. 1992; 17: 153-948.
34. Szewczyk M, Abarzua S, Schlichting A, Nebe B, Piechulla B, Briese V, Richter DU. Effects of extracts from *Linum usitatissimum* on cell vitality, proliferation and cytotoxicity in human breast cancer cell lines. J Med Plants Res. 2014; 8(5): 237-245.
35. Imbert TF. Discovery of podophyllotoxins. Biochimie. 1998; 80: 207-222.
36. Sharma RK, Sharma S, Sharma SS. Seed germination behaviour of some medicinal plants of Lahaul and Spiti cold desert (Himachal Pradesh): implications for conservation and cultivation. Curr Sci. 2006; 90(8): 1113-1118.
37. Narisa K, Jenny MW, Heather MAC. Cytotoxic effect of four Thai edible plants on mammalian cell proliferation. Thai Pharmac Health Sci J. 2006; 1(3): 189.
38. Roy MK, Nakahara K, Na TV, Trakoontivakorn G, Takenaka M, Isobe S, et al. Baicalein, a flavonoid extracted from a methanolic extract of *Oroxylum indicum* inhibits proliferation of a cancer cell line in vitro via induction of apoptosis. J Archiv Pharmazie. 2007; 62(2): 149.
39. Kumar R.A., Rajkumar V., Guha G., Mathe L. Therapeutic potentials of *Oroxylum indicum* bark extracts. Chinese J Nat Med. 2010; 8(2): 121.
40. Adams LS, Zhang Y, Seeram, NP, Heber D, Chen S. Pomegranate ellagitannin-derived compounds exhibit antiproliferative and antiaromatase activity in breast cancer cells in vitro. Cancer Prev Res. 2010; 3: 108-113.
41. Devi PM, Siril EA. Traditional and modern use of Indian madder (*Rubia cordifolia* L.): an overview. Int J Pharmac Sci Rev Res. 2014; 25(1): 154-164.

42. Gupta PP, Srimal RC, Verma N, Tandon JS. Biological activity of *Rubia cordifolia* and isolation of an active principle. Pharmac Biol. 1999; 37(1): 46.

43. Itokawa H, Wang X, Lee KH. Homoharringtonine and related compounds, in anticancer agents from natural products. Cragg GM, Kingston DGI, Newman DJ, eds. Brunner-Routledge Psychology Press, Taylor & Francis Group, Boca Raton, Chapter 4, 2005: 47.

44. Agarwal R, Agarwal C, Ichikawa H, Singh RP, Agarwal BB. Anticancer potential of silymarin: from bench to bed side. Anticancer Res. 2006; 26(6B): 4457.

45. Kim S, Choi JH, Lim HI, Lee SK, Kim WW, Kim JS, et al. Silibinin prevents TPA-induced MMP-9 expression and VEGF secretion by inactivation of the Raf/MEK/ERK pathway in MCF-7 human breast cancer cells, Phytomed. 2009; 16(6-7): 573.

46. Li YL, Gan GP, Zhang HZ, Wu HZ, Li CL, Huang YP, Liu YW, Liu JW. A flavonoid glycoside isolated from *Smilax china* L. rhizome in vitro anticancer effects on human cancer cell lines. J Ethnopharmacol. 2007; 113(1): 115.

47. Hyun NK, Seung HH, Bong KS, Cheorl HK, Young HY, Hyung MK. *Taraxacum officinale* induces cytotoxicity through TNF-α and IL-1α secretion in Hep G2 cells. Life Sci. 2004; 74(9): 1149.

48. Sigstedt SC. Evaluation of aqueous extracts of *Taraxacum officinale* on growth and invasion of breast and prostate cancer cells. Int J Oncol. 2008; 32(5): 1085.

49. Lecia JG, Jetaime R, Ernest B I. *Vernonia amygdalina*: anticancer activity, authentication, and adultration detection. Int J Environ Res Public Health. 2008; 5(5): 342.

50. Wong FC, Woo CC, Hsu A, Tan BKH. The anti-cancer activities of vernonia amygdalina extract in human breast cancer cell lines are mediated through caspase-dependent and p53-independent pathways. PLoS One. 2013; 24: 8.

51. Kuete V, Wabo HK, Eyong KO, Feussi, MT, WienchB, Krusche B, et al. Anticancer activities of six selected natural compounds of some cameroonian medicinal plants. PLoS ONE. 2011; 6: 8.

52. Winters M. Ancient medicine, modern use: *Withania somnifera* and its potential role in integrative oncology. Altern Med Rev. 2006; 11(4): 269-277.

53. Alam S, Katiyar D, Goel R, Vats A, Mittal A. Role of herbals in cancer management. J Phytopharmacol. 2013; 2(6): 46-51.

54. Govind P. Some important anticancer herbs: a review, International Research Journal of Pharmacy, 2011, 2(7), 45-52

55. Chang M. Anticancer medicinal herbs. Human Science and Technology, Publishing House, Changsha, 1992.

56. Kumar RA, Sridevi K, Kumar NV, Nanduri S, Rajagopal S. Anticancer and

immunostimulatory compounds from *Andrographis paniculata*. J Ethnopharmacol. 2004; 92(2-3): 291-295.

57. Sultana S, Ahmed S. Inhibitory effect of celery seeds extract on chemically induced hepatocarcinogenesis: modulation of cell proliferation, metabolism and altered hepatic foci development. Cancer Lett. 2005; 221: 11-20.
58. The effect of aloe-emodin on the proliferation of a new merkel carcinoma cell line. Am J Dermatopathol. 2002; 24(1): 17-22.
59. Pecere T, Gazzola MV, Micignat C. Aloe-emodin is a new type of anticancer agent with selective activity against neuro-ectodermal tumors. Cancer Res. 2000; 60: 2800-2804.
60. The wealth of India ‘a dictionary of Indian raw materials and industrial products. Vol. i (ab), 1985, p. 79.
61. The wealth of India ‘a dictionary of Indian raw materials and industrial products. Vol. i (ab), 1985, p. 109.
62. The wealth of India ‘a dictionary of Indian raw materials and industrial products. Vol. i (ab), 1985, p. 185.
63. Cragg GM, Newman DJ. Plants as a source of anti-cancer agents. J Ethnopharmacol. 2005; 100(1-2): 72-79.
64. Kantrajian HM, Talpaz M, Smith TL, Cortes J, Giles FJ. Homoharringtonine and low-dose cytarabine in the management of late chronic-phase chronic myelogenous leukemia. J Clin Oncol. 2000; 18: 3513-3521.
65. Senchina DS, Shah, Nisarg B, Busch MG. Effects of berberine, chelerythrine, and sanguinarine on proliferation in four human immortalized cell lines. J Iowa Acad Sci. 2012; 119: 1-4, 22-27.
66. Bruneton J. Pharmacognosy, phytochemisty medicinal plants. Lavoisier publisher, France, 1993, pp. 771-777.
67. Chavan SS, Damale MG, Shamkuwar PB, Pawar D. Traditional medicinal plants for anticancer activity. Int J Curr Pharmac Res. 2013; 5: 4.
68. Cavallito CJ, Haskell TH. Alpha-methylene butyrolactone from *Erythronium americanum*. J Am Chem Soc. 1946; 68(11): 2332-2334.
69. Tyler V. Herbs of choice. The therapeutic use of phytomedicinals. New York: Haworth press, 1994, pp. 32-33.
70. Ambasta SP, ed. The useful plants of India. 4th edn, National Institution Sci. Communication, Delhi, 2000, p. 239.
71. Ambasta SP, ed. The useful plants of India. 4th edn, National Institution Sci. Communication, Delhi, 2000, p. 243.
72. Brown PN, Roman MC. Determination of hydrastine and berberine in goldenseal raw materials, extracts, and dietary supplements by high-performance liquid chromatography

with UV: collaborative study. J Aoac Int. 2008; 91(4): 694-701.

73. Prajapati ND, Purohit S, Sharma AK, Kumar T. Handbook of medicinal plants. Agrobios (India), 1st edn, 2003.
74. Ladanyi A, Timar J, Lapis K. Effect of lentinan on macrophage cytotoxicity against metastatic tumor cells. Cancer Immunol Immunother. 1993; 36: 123-126.
75. Mingji P. Cancer treatment with fu zheng pei ben principal. Fujjan Science and Technology publishing house, Fuzhou, 1992.
76. Desai AG, Qazi GN, Ganju RK, El-Tamer M, Singh J, Saxena AK, Bhat HK. Medicinal plants and cancer chemoprevention. Curr Drug Metab. 2008; 9(7): 581-591.
77. Henry SH, Bowers JC. Aflatoxin, hepatitis and worldwide liver cancer risks. Adv Exp Med Biol. 2002; 504: 229-233.
78. Nagar N, Jat RK, Saharan R, Verma S, Sharma D, Bansal K. Podophyllotoxin and their glycosidic derivatives. Pharmacophore. 2011; 2(2): 124-134.
79. Hazra B, Sarkar R, Bhattacharyya S, Ghosh PK, Chel G, Dinda B. Synthesis of plumbagin derivatives and their inhibitory activities against Ehrlich ascites carcinoma in vivo and *Leishmania donovani* promastigotes in vitro. Phytother Res. 2002; 16: 133-137.
80. Ardeshiry LA, Rezaie-Tavirani M, Mortazavi SA, Barzegar M, Moghadamnia SH, Rezaee MB. Study of anti cancer property of *Scrophularia striata* extract on the human astrocytoma cell line (1321). Iran J Pharmac Res. 2010; 9(4): 403-410.
81. Prota AE, Bargsten K, Zurwerra D, Field JJ, Díaz JF, Altmann K-H, et al. Molecular mechanism of action of microtubule-stabilizing anticancer agents. Science. 2013; 339: 587-590.
82. Katiyar SK, Agarwal R, Mukhtar H. Inhibition of tumor promotion in sencar mouse skin by ethanol extract of zingiber officinale rhizome. Cancer Res. 1996; 56(5): 1023-1030.
83. Sarek J, Kvasnica M, Urban MKJ, Hajduch M. Correlation of cytotoxic activity of betulinines and their hydroxy analogues. Bioorg Med Chem Lett. 2005; 15(19): 4196-4200.
84. Gunjan M, Naing TW, Saini RS, Ahmad AB, Naidu JR, Kumar I. Marketing trends & future prospects of herbal medicine in the treatment of various disease. World J Pharmac Res. 2015; 4(9): 132-155.

View publication stats

Current Trends in Biomedical Engineering & Biosciences
ISSN: 2572-1151

Juniper Publishers
key to the Researchers

Mini Review
Volume 5 Issue 3 - June 2017
DOI: 10.19080/CTBEB.2017.05.555661

Curr Trends Biomedical Eng & Biosci
Copyright © All rights are reserved by Navneeta Bharadvaja

Centella Asiatica: A Pharmaceutically Important Medicinal Plant

Arpita Roy and Navneeta Bharadvaja*

Plant Biotechnology Laboratory, Department of Biotechnology, India

Submission: April 04, 2017; **Published:** June 16, 2017

***Corresponding author:** Navneeta Bharadvaja, Plant Biotechnology Laboratory, Department of Biotechnology, Delhi Technological University, New Delhi-110042, India, Email: navneetab@dtu.co.in

Abstract

Centella asiatica (gotu kola) is one of the important rejuvenating herbs for nerve and brain cells and is believed to be capable of increasing intelligence, longevity, and memory. Important bioactive compounds are triterpenoid saponins, including asiaticoside, centelloside, madecassoside, and asiatic acid. It possesses anti-leprotic, anti-viral, anti-bacterial, anti-tumor activities. Due to its medicinal importance, this plant is used for several purposes. Synthesis of nanoparticles from this plant is one of the important applications in the field of nano-biotechnology. This review provides an overall summary of phytoconstitutes, pharmacological activity of Centella asiatica as well as its role in the silver nanoparticles synthesis.

Keywords: Centella asiatica; Asiaticoside; Pharmacological activity; Nanoparticles

Introduction

Medicinal plants are the traditional source of pharmaceutically important compounds which are utilized by the pharmaceutical companies for the preparation of several formulations. In the present time, there has been an increase in the use of herbal products around the world. World Health Organisation (WHO) also stated that more that 80% of the world's population relies on the herbal medicines [1]. The importance of medicinal plants is due to the presence of specific chemical compounds that produce a physiological effect on the human body. These bioactive chemical constituents of plants include saponin, flavanoids, alkaloids, sterols, tannins, phenols [2]. Medicinal plant-based drugs have an advantage over the other drugs because they are simple and offer a broad spectrum of activity. Furthermore, they have very less adverse side effects as compare to the chemotherapeutic drugs. India is rich in medicinal plant diversity and since the ancient times use of drugs of herbal origin is prevalent in the traditional system of medicines such as Ayurveda and Unani. There are about 426 biomes which comprise of different habitat diversity that gives rise to the richest centers for plant genetic resources in the world [3]. Out of 18,665 flowering species, only about 3000 plants has been used for the various formulations in classic system of medicines such as Ayurveda, Siddha and Unani [4].

Centella asiatica is one of the important traditional medicinal plant belonging to family Apiaceae and commonly known as 'Gotu kola', 'Indian Pennywort' or 'Mandookaparni' in India. It is an important perennial medicinal herb found in the tropical and subtropical countries like India, Sri Lanka and Bangladesh. C. asiatica contains several triterpenes, saponins like asiaticoside, asiatic acid, sapogenins, madecassic acid, vellarin, adecassoside, glycosides and centelloside [5]. In India, it grows up to an altitude of 600-1800 meters above the sea level [6,7] on moist, clayey or sandy soils forming a dense green carpet. Centella asiatica has a glabrous stem and long petiolated fleshy leaves rooting at nodes. It is a softly perfumed plant that attains height up to 15cm. Stem is smooth and rooting occurs at the nodes. It grows extensively in damp, marshy, and wet places and flowering occurs during April to June with white to purple or pink flowers [8]. The whole plant is used for medicinal purposes and widely used as a blood purifier as well as for treating high blood pressure, for memory enhancement and promoting longevity [9]. It possesses several important properties like antileprotic, antifeedant, antistress, anti-tuberculosis activities, wound-healing properties, atherosclerosis antibacterial and fungicidal activity [10] Srivastava et al. 1997. It is used in the treatment of leprosy, wound, cancer, fever, allergies, abscesses, asthma, catarrh, convulsions, dysentery, eczema, gonorrhea, hypertension, headache, bronchitis, jaundice, pleuritis, rheumatism, ulcers, spasms, tuberculosis, urethritis, etc. Due to its medicinal importance, this plant is also used for the synthesis of silver nanoparticles. Application of nanoparticles

is growing rapidly due to thier specific characteristics such a size, morphology, and distribution [11]. It gains application in various fields such as health care, biomedical, cosmetics, food and feed, drug environment, health, mechanics, optics, chemical industries, electronics, space industries, energy science, catalysis, etc. Tremendous increase in these technologies had opened applied frontiers and novel fundamentals. This includes the nanoscale materials production and utilization of their mysterious optoelectronic and physicochemical properties [12]. Nanoparticles are generally prepared by various chemical and physical methods which are potentially hazardous the environment. Development of biologically inspired process is an important branch of nanotechnology. Advantage of nanoparticle synthesis from biological source over chemical and physical method is: cost effect, eco-friendly and easily scaled up for large scale synthesis [13]. Use of plant extract for the synthesis of nanoparticles can be an advantageous over other biological processes by eliminating the elaborate process of maintaining cell culture. Reduction and stabilization of silver ions by combination of biomolecules such as proteins, enzymes, amino acids, polysaccharides, phenolics, terpinoids, saponins, alkaloids, tannins and vitamins which are already established in the plant extracts having medicinal values and are environmental benign, yet chemically complex structures Kulkarni & Muddapur 2014. Therefore this review provides an insight into the chemical constituents, pharmacological activity and silver nanoparticles synthesis from Centella asiatica.

Chemical Constituent

Glycosides

Various glycosides have been isolated from this plant which includes Asiaticoside, Madecassoside, Brahmoside, Centelloside, Thakuniside, etc (Srivastava et al., 1997). Among them, asiaticosside, asiatic acid, madecassoside and madecassic acid are the most biologically active compound [14]. Asiaticoside helps in collagen I synthesis in human clinically used as a wound healing agent in combination with madecassic and asiatic ascids [15].

Triterpenic acids

Several pentacyclic triterpenic acids have been isolated and characterized from this plant. They occur either in free state or as aglycones of the naturally occurring saponins.e.g. asiatic acid, madasiatic acid (Srivastava et al., 1997) brahmic acid, isobrahmic acid, thankunic acid, betulic acid , centoic acid, centellic acid, 6b-Hydroxiasiatic acid & terminolic acid [16].

Phytosterols

The plant is reported to possess Stigmasterol, Campesterol, Beta-sitosterol and stigma sterol-b-D-glucopyranoside (Srivastava et al., 1997). Phytosterols have the ability to reduce cholesterol levels and have potential to inhibit stomach, lunch, breast and ovarian cancers [17,18]. Phytosterols also have the potential to reduce the elevated triglyceride levels which is a risk factor for cardio vascular diseases [19]. It was found that the level of triglycerides reduced by 14% by supplementing 1.6g/day of plant sterols in a fermented milk beverage for six weeks [20].

Other constituents

Centella asiatica contains hydrocotylin, glycine, aspartic acid, glutamic acid, alanine and phenylalanine (Srivastava et al., 1997). Leaves contain 3- glucosylquercetin, 3-glucosylkaepferol and 7-glucosylkaempferol (Srivastava et al., 1997). It also contains volatile fatty acid which consists of steric, palmitic, oleic, lignoceric, linolenic and linoleic acids [18]. Amino acids such as glycine, aspartic acid, phenyalanine, glutamine acid and α-analine also found in this plant.

Pharmacological Activities

Wound healing

Titrated extract of Centella asiatica which consist of mixture of three triterpenes (asiaticoside, asiatic acid and madecassic acid) stimulates glycosaminoglycan and collagen synthesis in rats [21]. Asiaticoside and asiatic acid were more active than madacassic acid in wound healing thus it appers to be an effective treatment of wound healing disturbances [22].

Central Nervous System

Mook-Jung et al. [23] reported that asiaticoside derivatives reduce or inhibits H2O2 induced cell death and lower the intracellular free radical concentration and protect against the effects of beta amyloid neurotoxicity. Centella asiatica extract was found to increase brain GABA levels [24].

Memory enhancing

Aqueous extract of Centella asiatica showed significant effect in memory enhancement which is due to the presence of brahminoside, brahmic acid and brahmoside in the plant [25,26]. Rao et al. [27] reported that fresh leaf juice of Centella asiatica improves spatial learning performance and enhanced memory retention in neonatal rats.

Antibacterial

Anonymous [28] reported that asiaticoside was an active agent against Bacillus leprae, Mycobscterium tuberculosis and Entamoeba histolytica. Methanolic extract of Centella asiatica showed inhibition zone against V. alginolyticus, V. vulnificus and Streptococcus sp. [29]. Sankar et al. [30] reported that methanolic extract of Centella asiatica showed antibacterial activity against three Vibrio species that are V. harveyi, V. alginolyticus and V. parahaemolyticus but acetone, chloroform and hexane extract was not shown any antibacterial activity against these species.

Antioxidant

In a study, it was reported that asiaticoside significantly increased the levels of catalase, superoxide dismutase, glutathione peroxidase, ascorbic acid and vitamin E in excision

How to cite this article: Arpita R, Navneeta B. Centella Asiatica: A Pharmaceutically Important Medicinal Plant. Curr Trends Biomedical Eng & Biosci. 2017; 5(3): 555661. DOI: 10.19080/CTBEB.2017.05.555661.

type cutaneous wounds in rats. The level of antioxidant activity was highest during the initial stages of treatment [31]. Jayashree et al. [32] reported that crude extract of C. asiatica showed antioxidant activity in the lymphoma bearing mice.

Cardiovascular

Cesarone et al. [33] reported that in a clinical trial Centella asiatica extracts found to be efficacious in the treatment of reducing ankle, venous insufficiency, foot swelling, edema, improving capillary filtration rate and microcirculatory parameters. Alcoholic extract of whole plant showed cardioprotective activity in ischemia reperfusion induced myocardial infarction in rats [34].

Neuroprotective effects

Ramanathan et al. [35] reported that Centella asiatica extract protects monosodium glutamate-induced neurodegeneration. Water extract of Centella asiatica showed neuroprotective efficacy against 3-nitropropionic acid induced oxidative stress in brain of prepubertal mice enhanced glutathione levels, antioxidant defenses in brain regions [36,37].

Anti-diabetic

Chauhan et al. [38] reported that triterpenic fraction of Centella asiatica is useful in diabetic microangiopathy by improving the microcirculation and decreasing the capillary permeability. Also, a triterpenic fraction of Centella asiatica protects against the deterioration. Methanolic and ethanolic extracts had shown significant protection and lowered blood glucose levels to normal glucose levels in tolerance test. Kabir et al. [39] reported the anti-hyperglycemic activity of this plant in type II diabetic rats.

Application of C. asiatica in silver nanoparticles synthesis

In recent years, there is also a demand for nanoparticles in plant biotechnology. The advantage of using plant materials for the biosynthesis of nanoparticles is an interesting area for the development of new methods of nanomedicine. These particles can be prepared easily by different methods but the biological approach is one of the most effective, less time consuming and eco-friendly. Several nanoparticles have been synthesized by this plant like silver, gold, copper oxide, etc. Among several metal nanoparticles, silver nanoparticles have attained a special focus [40]. Silver nanoparticles are used in various technologies and incorporated into wide array of consumer products that take an advantage of their desirable conductive, optical and anti-bacterial properties. It is used in conductive inks and integrated into composites to enhance the thermal and electrical conductivity. It is used in biosensors and numerous assays where silver nanoparticles materials can be utilized as biological tags for quantitative detection. It incorporated in footwear, paints, wound dressing, cosmetics and plastics for their anti-bacterial properties. Logeswari et al. [41] reported that aqueous extract was utilized for the synthesis of silver nanoparticles and the size of the silver nanoparticles synthesized by Centella asiatica were 33nm and irregular in shape. Rout et al. [42] also reported that aqueous leaf extract was utilized for the synthesis of silver nanoparticles and the size was 30-50nm and spherical and cubic in shape. Palaniselvam et al. [43] reported that leave extract of Centella asiatica used for the silver nanoparticles synthesis and peak obtained at 430nm and the size of synthesized nanoparticles were 50-60nm. Kumar et al. [44] 2017 reported the synthesis of silver nanocollide from an aqueous extract of Centella asiatica and TEM results showed that these nanoparticles are almost spherical in shape with an average diameter of 15nm [45-48].

Conclusion

Centella asiatica has been used for many years for the treatment of various diseases. A significant amount of work has been done on its pharmacological activity and possible applications of chemical compounds from the whole part of the plant. The present review shows that Centella asiatica contains several different phytocompounds like saponins, glycosides, phytosterols, flavonoids, etc. Out of these phytocompounds saponins i.e. asiaticoside is an important one which is responsible for the different pharmacological activity. It was found that asiaticoside is the main phytocompound which helps in the wound healing activity. Centella asiatica also helps in the improvement of neurodegenerative disorder i.e Alzheimer's as it improves the memory. So it can be utilized as drugs for the treatment of neurodegenerative disorders. One of the important applications of this plant is in the synthesis of silver nanoparticles. Silver nanoparticles synthesis from plant source provides a greener approach as it eliminates the use of harsh chemicals.

References

1. Ekor M (2013) The growing use of herbal medicines: issues relating to adverse reactions and challenges in monitoring safety. Frontiers in Pharmacology 4: 177.
2. Vaidya AB (1997) The status and scope of Indian medicinal plants acting on central nervous system. Indian Journal of Pharmacology 29: S340-S343.
3. Ravishankar B, Shukla V (2007) Indian Systems of Medicine: A Brief Profile. African Journal of Traditional, Complementary, and Alternative Medicines 4(3): 319-337.
4. Schippmann UWE, Leaman D, Cunningham AB (2006) A comparison of cultivation and wild collection of medicinal and aromatic plants under sustainability aspects. In: Bogers RJ, Craker LE, Lange (Eds,). Medicinal and Aromatic Plants pp. 75-95.
5. Glasby JS (1991) Dictionary of Plants Containing Secondary Metabolites. Taylor and Francis, London.
6. Tiwari KN, Sharma NC, Tiwari V, Singh BD (2000) Micropropagation of Centella asiatica (L.), a valuable medicinal herb. Plant Cell. Tissue and Organ Culture 63: 179-185.
7. Patra A, Rai B, Rout GR, Das P (1998) Successful regeneration from callus cultures of Centella asiatica (Linn.) Urban. Plant Growth Regulation 24: 13-16.

How to cite this article: Arpita R, Navneeta B. Centella Asiatica: A Pharmaceutically Important Medicinal Plant. Curr Trends Biomedical Eng & Biosci. 2017; 5(3): 555661. DOI: 10.19080/CTBEB.2017.05.555661.

8. Roy A, Kundu K, Saxena G, Kumar L, Bharadvaja N (2016) Effect of Different Media and Growth Hormones on Shoot Multiplication of In Vitro Grown Centella asiatica Accessions. Advanced Techniques in Biology & Medicine 4: 172.

9. Gohil KJ, Patel JA, Gajjar AK (2010) Pharmacological Review on Centella asiatica: A Potential Herbal Cure-all. Indian Journal of Pharmaceutical Sciences 72(5): 546-556.

10. Chakraborty T, Sinha Babu SP, Sukul N0C (1996) Preliminary evidence of antifilarial effect of Centella asiatica on canine dirofilariasis. Fitoterapia 67: 110-112.

11. Ahmed S,Ahmad M, Swami BL, Ikram S (2016) A review on plants extract mediated synthesis of silver nanoparticles for antimicrobial applications: A green expertise. Journal of Advance Research 7(1): 17-28.

12. Korbekandi H, Iravani S (2012) Silver nanoparticles, the delivery of nanoparticles.

13. Dhuper S, Panda D, Nayak PL (2012) Green synthesis and characterization of zero valent iron nanoparticles from the leaf extract of Mangifera indica. Nano TrendsJournal of Nanotechnology, Science and Applications 13(2): 16-22

14. Inamdar PK, Teola RD, Ghogare, AB, Souza NJ (1996) Determination of biologically active constituents in Centella asiatica. Journal of Chromatography A 742: 127-130.

15. Bonte F, Dumas M, Chaudagne C and Maybeck A (1994) Influence of Asiatic acid, madecassic acid and asiaticoside on human collagen I synthesis. Planta Med 60(2): 133-135.

16. Jamil SS, Nizami Q, Salam M (2007) Centella asiatica (Linn.) Urban 6A Review. Natural Product Radiance 6(2): 158-170.

17. Tilvis RS, Miettinen TA (1986) Serum plant sterols and their relation to cholesterol absorption. The American Journal of Clinical Nutrition 43(1): 92-79.

18. Woyengo TA, Ramprasath VR, Jones PJ (2009) Anticancer effects of phytosterols. European Journal of Clinical Nutrition 63 (7): 813-820.

19. Malloy MJ, Kane JP (2001) A risk factor for atherosclerosis: Triglyceride-rich lipoproteins. Advances in Internal Medicine 47: 111-316.

20. Plana N, Nicolle C, Ferre R, Camps J, Cos R, et al. (2008) Plant sterol-enriched fermented milk enhances the attainment of LDL-cholesterol goal in hypercholesterolemic subjects. European Journal of Nutrition 47(1): 32-39.

21. Maquart FX, Chastang F, Simeon A, Birembaut P, Gillery P, et al. (1999) Triterpenes from Centella asiatica stimulate extracellular matrix accumulation in rat experimental wounds. European Journal of Dermatologists 9(4): 289-296.

22. Brinkhaus B, Lindner M, Schuppan D, Hahn EG (2000) Chemical, pharmacological and clinical profile of the east asian medicinal plant Centella asiatica. Phytomedicine 7(5): 427-448.

23. Mook-Jung I, Shin JE, Yun SH, Huh K, Koh JY, Park HK, et al. (1999) Protective effects of asiaticoside derivatives against beta-amyloid neurotoxicity. Journal Neuroscience Res 58(3): 417-425.

24. Chatterjee TK, Chakraborty A, Pathak M, Sengupta GC (1992) Effects of plant extract Centella asiatica (Linn.) on cold restraint stress ulcer in rats. Indian Journal of Experimental Biology 30(10): 89-91.

25. Bradwejn J, Zhou Y, Kosyzycki D (2000) A double-blind, placebo-controlled study on the effects of Gotu kola on acoustic startle response in healthy subjects. Journal of Clinical Psychopharmacology 20: 680-684.

26. Cesarone MR, Incandela L, De Sanctis, MT (2001) Flight microangiopathy in mediumto long-distance flights: prevention of edema and microcirculation alterations with total triterpenic fraction of Centella asiatica. Angiology 52: S33-S37.

27. Rao KGM, Rao SM, Rao SG (2005) Centella asiatica (linn) induced behavioural changes during growth spurt period in neonatal rats. Neuroanatomy 4: 18-23.

28. Anonymous (1988) The Wealth of India: A Dictionary of Indian Raw Materials and Industrial Products. New Delhi, India

29. Wei N, Musa T Sengm W, NAM S (2008) Antimicrobial properties of tropical plants against pathogenic bacteria isolated from aquatic organisms, African Journal of Biotechnology 7(13): 2275-2278.

30. Sankar GK, Ramamoorthy K, Sakkaravarthi K, Elavarsi A (2010) Antibacterial activity of herbal extract on pathogens isolated from the swollen hind gut of P. Monodon (fabricus): Der Pharmacia Sinica 1(3): 17-22.

31. Shukla A, Rasik AM, Jain GK, Shankar R, Kulshrestha DK, et al. (1999a) In vitro and in vivo wound healing activity of asiaticoside isolated from Centella asiatica. Journal of Ethnopharmacology 65(1): 1-11.

32. Jayashree G, Kurup Muraleedhara G, Sudarslal S, Jacob VB (2003) Anti-oxidant activity of Centella asiatica on lymphoma-bearing mice. Fitoterapia 74 (5): 431-434.

33. Cesarone MR, Laurora G, Sanctis MT de, Belcaro (1992) Activity of Centella asiatica in venous insufficiency. Minerva Cardioangiology 40(4): 137-143.

34. Pragada RR, Veeravalli KK, Chowdary KP, Routhu KV (2004) Cardioprotective activity of Hydrocotyle asiatica L. in ischemia-reperfusion induced myocardial infarction in rats. Journal of Ethnopharmacology 93 (1): 105-108.

35. Ramanathan M, Sivakumar S, Anandvijayakumar PR, Saravanababu C, Pandian P (2007) Neuroprotective evaluation of standardized extract of Centella asciatica in monosodium glutamate treated rats. Indian Journal of Experimental Biology 45(5): 425-431.

36. Shinomol KG, Muralidhara (2008) Prophylactic neuroprotective property of Centella asiatica against 3-nitropropionic acid induced oxidative stress and mitochondrial dysfunctions in brain regions of prepubertal mice. Neurotoxicology 29: 948-957.

37. Shinomol KG, Ravikumar H, Muralidhara (2010) Prophylaxis with Centella asiatica confers protection to prepubertal mice against 3-nitropropionic-acidinduced oxidative stress in brain. Phytotheraphy Research 24: 885-892.

38. Chauhan PK, Pandey IP, Dhatwalia VN (2010) Evaluation of the Anti-diabetic Effect of Ethanolic and Methanolic Extracts of Centella asiatica Leaves extract on Alloxan Induced Diabetic Rats. Advances in Biological Research 4(1): 27-30.

39. Kabir AU, Samad MB, D'Costa NM, Akhter F, Ahmed, et al. (2014) Anti-hyperglycemic activity of Centella asiatica is partly mediated by carbohydrase inhibition and glucose-fiber binding. BMC Complementary and Alternative Medicine 14: 31.

40. Singhal GRB, Kasariya K, Sharma AR, Singh RP (2011) Biosynthesis of silver nanoparticles using Ocimum sanctum (Tulsi) leaf extract and screening its antimicrobial activity. Journal of Nanoparticles Research 13: 2981-2988.

41. Logeswari P, Silaqmbarasan S, Abraham J (2013) Ecofriendly synthesis of silver nanoparticles from commercially aviable plant powders and their antibacterial properties. Scientia Iranica 20(3): 1049-1054.

42. Rout A, Jena PK, Pardia UK, Bindhani BK (2013) Green synthesis of silver nanoparticles using leaves extract of Centella asiatica L. for studies against human pathogens. Internation Journal of Pharma and Biosciences 4(4): 661-674.

How to cite this article: Arpita R, Navneeta B. Centella Asiatica: A Pharmaceutically Important Medicinal Plant. Curr Trends Biomedical Eng & Biosci. 2017; 5(3): 555661. DOI: 10.19080/CTBEB.2017.05.555661.

43. Palaniselvam K, Antony, Natanmurugaraj S, Govindanand K (2015) Bioreduction of Centella asiatica L and its bioactive investigation. International Journal of Agriculture and Life sciences 1(1): 14-18.

44. Kumar S, Mitra A, Halde D (2017) Centella asiatica leaf mediated synthesis of silver nanocolloid and its application as filler in gelatin based antimicrobial nanocomposite film. LWT - Food Science and Technology 75: 293-300.

45. Singh S, Gautam A, Sharma A, Batra A (2010) Centella asiatica L. a plant with immense potential but threatened. International Journal of Pharmaceutical Science Review and Research 4: 9-17.

46. Gohil KJ, Patel JA, Gajjar AK (1997) Chemistry and pharmacology of Centella asiatica: a review. Journal of Medicinal & Aromatic Plant Science 19: 1049-1056.

47. Chen YY, Wang CA, Liu HY, Qiu JS, Bao XH (2005) Ag/SiO_2: A novel catalyst with high activity and selectivity for hydrogenation of chloronitrobenzenes. Chemical Communications, 42: 5298-300.

48. Chakraborty T, Sinha Babu SP, Sukul N0C (1996) Preliminary evidence of antifilarial effect of Centella asiatica on canine dirofilariasis. Fitoterapia 67: 110-112.

This work is licensed under Creative Commons Attribution 4.0 License
DOI: 10.19080/CTBEB.2017.05.555661

Your next submission with Juniper Publishers will reach you the below assets

- Quality Editorial service
- Swift Peer Review
- Reprints availability
- E-prints Service
- Manuscript Podcast for convenient understanding
- Global attainment for your research
- Manuscript accessibility in different formats

(Pdf, E-pub, Full Text, Audio)

- Unceasing customer service

Track the below URL for one-step submission
https://juniperpublishers.com/online-submission.php

How to cite this article: Arpita R, Navneeta B. Centella Asiatica: A Pharmaceutically Important Medicinal Plant. Curr Trends Biomedical Eng & Biosci. 2017; 5(3): 555661. DOI: 10.19080/CTBEB.2017.05.555661.

Accepted Manuscript



Covalent and non-covalent chemical engineering of actin for biotechnological applications

Saroj Kumar, Alf Mansson

PII: S0734-9750(17)30101-5
DOI: doi: 10.1016/j.biotechadv.2017.08.002
Reference: JBA 7147

To appear in: *Biotechnology Advances*

Received date: 13 May 2017
Revised date: 9 August 2017
Accepted date: 16 August 2017

Please cite this article as: Saroj Kumar, Alf Mansson , Covalent and non-covalent chemical engineering of actin for biotechnological applications, *Biotechnology Advances* (2017), doi: 10.1016/j.biotechadv.2017.08.002

This is a PDF file of an unedited manuscript that has been accepted for publication. As a service to our customers we are providing this early version of the manuscript. The manuscript will undergo copyediting, typesetting, and review of the resulting proof before it is published in its final form. Please note that during the production process errors may be discovered which could affect the content, and all legal disclaimers that apply to the journal pertain.

ACCEPTED MANUSCRIPT

Covalent and non-covalent chemical engineering of actin for biotechnological applications

Saroj Kumar[a,b,*], Alf Mansson[b,*]

[a] *Department of Biotechnology, Delhi Technological University, Delhi-110042, India*

[b] *Department of Chemistry and Biomedical Sciences, Faculty of Health and Life Sciences, Linnaeus University, SE-391 82 Kalmar, Sweden*

Address for correspondence:

Saroj Kumar[*]
Department of Biotechnology,

Delhi Technological University,
Delhi-110042
E-mail: sarojbiotech@gmail.com; sarojkumar@dtu.ac.in
Phone no: +91-011-27294668
fax no: +91- 011-27871023

Alf Månsson[*]
Department of Chemistry and Biomedical Sciences

Linnaeus University,
SE-391 82 Kalmar,
Sweden
E-mail: alf.mansson@lnu.se
Phone no: +46 – 480 446243
fax no: +46 – 480 446262

ACCEPTED MANUSCRIPT

ACCEPTED MANUSCRIPT

Abstract

The cytoskeletal filaments are self-assembled protein polymers with 8-25 nm diameters and up to several tens of micrometres length. They have a range of pivotal roles in eukaryotic cells, including transportation of intracellular cargoes (primarily microtubules with dynein and kinesin motors) and cell motility (primarily actin and myosin) where muscle contraction is one example. For two decades, the cytoskeletal filaments and their associated motor systems have been explored for nanotechnological applications including miniaturized sensor systems and lab-on-a-chip devices. Several developments have also revolved around possible exploitation of the filaments alone without their motor partners. Efforts to use the cytoskeletal filaments for applications often require chemical or genetic engineering of the filaments such as specific conjugation with fluorophores, antibodies, oligonucleotides or various macromolecular complexes e.g. nanoparticles. Similar conjugation methods are also instrumental for a range of fundamental biophysical studies. Here we review methods for non-covalent and covalent chemical modifications of actin filaments with focus on critical advantages and challenges of different methods as well as critical steps in the conjugation procedures. We also review potential uses of the engineered actin filaments in nanotechnological applications and in some key fundamental studies of actin and myosin function. Finally, we consider possible future lines of investigation that may be addressed by applying chemical conjugation of actin in new ways.

Keywords: Chemical engineering, actin filament, biomolecular motors, nanofabrication, self-assembly, miniaturized sensing device

ACCEPTED MANUSCRIPT

ACCEPTED MANUSCRIPT

Contents

1. Introduction
2. Actin biology - a background to actin engineering
3. Myosin II and the in vitro motility assay for studies of myosin propelled actin filaments
4. Engineering of actin filaments
4.1. Non-covalent approach
4.1.1. Fluorescence labelling of actin filaments by non-covalent approaches
4.1.2. Biotin-strept(avidin) engineering of actin filaments via phalloidin
4.1.3. Natural actin binding proteins in applications of actin filaments
4.1.4. Electrostatics in cargo attachment to actin filaments
4.2. Covalent modification approaches
4.2.1. Covalent modification of primary amines
4.2.2. Covalent modification of sulfhydryl groups
4.2.3. Covalent modification of carboxyl groups
4.2.4. Covalent modification of glutamines
4.3. Different uses of covalent modifications
4.3.1. Covalent conjugation of actin filament with fluorophores
4.3.2. Covalent conjugation of actin filaments with biotin
4.3.3. Covalent cross-linking in actin filaments
4.3.4. Engineering of actin filaments with gold nanoparticles
4.3.5. Engineering of actin filaments with quantum dots without biotin-streptavidin
4.3.6. Engineering of actin filaments with antibodies
4.3.7. Surface-immobilization of actin
5. Use of engineered actin filaments in nanodevices
6. Concluding remarks and perspectives
Acknowledgements
References

ACCEPTED MANUSCRIPT

ACCEPTED MANUSCRIPT

1. Introduction

The protein-based cytoskeleton is central in the eukaryotic cell machinery. Its key filamentous structures are the actin filaments, intermediate filaments and microtubules. Out of these, the actin filaments have central roles in cellular shape changes and motility. The tasks are executed in interaction with molecular motors of the myosin superfamily and by virtue of polymerization, depolymerisation and branching, coordinated by cell signalling via a range of actin binding proteins (Blanchoin et al., 2014; Pollard, T.D., 2016). The actin-myosin interactions underlie aspects of intracellular transport and tension sensing but also cytokinesis and cell locomotion including muscle contraction. Thus, all these components, i.e. the cytoskeletal filaments together with the associated biomolecular motors and other accessory proteins, work effectively together as a biological nanomachine system. This complex system, with unique dynamic characteristics, has inspired hybrid devices or structures for diverse nanotechnological applications such as unique Lab-on-a-chip systems for capture and transportation of analytes to nanoscale sensors. In this regards the actomyosin system has been exploited mainly because of its higher transportation speed compared to the microtubule based systems also used for cargo transportation in nanotechnology (Korten et al., 2010).

In the developments towards actomyosin based nanodevices, several fields have been integrated such as nanotechnology, biotechnology, chemistry, material science, clinical medicine etc. Either myosin II motors together with actin filaments or actin filaments alone have been utilized in efforts towards a variety of applications. This includes the use of actin filaments as templates for the synthesis of nano-scale inorganic structures (Galland et al., 2013; Patolsky et al., 2004; Willner and Willner, 2010; Yao et al., 2009), capture and transportation of cargoes by motor propelled filaments (Iwabuchi et al., 2012; Kaur et al., 2011; Kumar et al., 2016b; Kumar et al., 2013; Kumar et al., 2012; Mansson et al., 2004; Oyama and Hatori, 2016; Persson et al., 2013), integration of filaments and myosin motors into almost complete Lab-on-a-chip systems (Lard et al., 2013) and more recently, novel approaches for parallel biological computation (Nicolau et al., 2016).

For the purpose of these developments, actin filaments have been engineered in different ways, associated with attachment of certain biomolecules (Johnston et al., 2015; Kumar et al., 2016b; Kumar et al., 2013; Kumar et al., 2012; Persson et al., 2013), metallic particles (Kaur et al., 2011; Patolsky et al., 2004; Willner and Willner, 2010), quantum dots (Mansson et al., 2004; Wang et al., 2013; Wu et al., 2003; Yao et al., 2009), organic fluorophores (Balaz and Mansson, 2005; Bombardier et al., 2015; Chazotte, 2010; Kumar et al., 2016b; Kumar et al., 2012; Mansson et al., 2004; Pernier et al., 2016; Persson et al., 2013; Wulf et al., 1979), diamond nanoparticles (Bradac et al., 2016) etc. Moreover, engineering of actin filaments is important not only in nanobiotechnology but also in a range of fundamental cell biological and biophysical studies (e.g. (Barak et al., 1980; dos Remedios et al., 1987; Funatsu et al., 1995; Kaya and Higuchi, 2010; Knight and Offer, 1978; Kozuka et al., 2006; Kuhn and Pollard, 2005; Prochniewicz et al., 1993; Sheetz and Spudich, 1983a; Yanagida et al., 1984).

Both non-covalent and covalent conjugation methods have been used in recent efforts to engineer actin filaments by posttranslational chemical and biochemical methods. Here we will comprehensively review the methods used and the different types of cargoes or probes that have been attached to the actin filaments. Because of the relevance of actin biology and chemistry as well as actin-myosin interactions in this context we will also briefly review these issues. Furthermore, we consider relevant in vitro assays that have been important for developing applications in nanobiotechnology where engineered actin filaments are

ACCEPTED MANUSCRIPT

transported by myosin motors. Finally, we review key applications using engineered actin filaments alone or together with myosin motors.

2. Actin biology - a background to actin engineering

Actin is a globular protein (G-actin) with a molecular mass of about 42 kDa. It is composed of a single polypeptide chain of 375 amino acids (Collins and Elzinga, 1975). Actin is one of the most abundant eukaryotic proteins, it is found in all eukaryotic cells except for the nematode sperm and it is highly conserved between species (Galkin et al., 2010; Kabsch and Vandekerckhove, 1992; Pollard, T., 2016; Pollard, 1990). There are six isoforms of actin in mammals (Perrin and Ervasti, 2010) with only very small differences in amino acid sequence. Based on their isoelectric points,the isoforms are denoted α-actin (three different: skeletal, cardiac and smooth), β-actin and γ-actin (two different: smooth and cytosolic). The α-actins dominate in muscle whereas the β-actin and γ-actins dominate in non-muscular cells (Perrin and Ervasti, 2010). The striated muscle α-actins are the isoforms that, so far, have been utilized in nanotechnological applications (Gazit, 2007; Korten et al., 2010; Kumar et al., 2012; Lard et al., 2013; Mansson, 2012; Mansson et al., 2004; Patolsky et al., 2004; Persson et al., 2013; Yao et al., 2009). This fact is related to the vast previous experience from fundamental studies of α-actin and its expression at high levels in both skeletal muscle and heart muscle. The α-actin is also conveniently isolated and purified from striated muscle using standard protocols such as that in (Pardee and Spudich, 1982). At nearly physiological concentrations of KCl (>50 mM), $MgCl_2$ (~1 mM) and ATP, G-actin monomers (with bound MgATP; MgATP-G-actin) self-assemble into filamentous actin (F-actin) (Fig. 1). Alternatively, $MgCl_2$ may be exchanged for $CaCl_2$ to obtain Ca-actin instead of Mg-actin filaments with different properties in certain regards e.g. related to the mechanism of nucleation of new filaments (Cooper et al., 1983b) and the magnitude of the filament torsional rigidity (Yasuda et al., 1996).

The actin filaments (diameter ~8 nm; e.g.(Blanchoin et al., 2014)) have two protofilaments wound around each other in a right-handed double helix with cross-over every 36 nm (Fig. 1) (Hild et al., 2010; Kabsch et al., 1990; Schoenenberger et al., 2011). The two protofilaments contain 13 G-actin monomers per 36 nm (termed subunits in the following when incorporated into the filaments). The subunits with dimensions of 5.5x5.5x3.5 nm are connected to each other with the nearest neighbours along the filament and with two subunits in the other protofilament, an arrangement that may also be described as 6 left-handed turns per 36 nm. This geometry is relevant to bear in mind because it determines the geometrical arrangement of other molecules or particles conjugated to F-actin.

The crystal structure of the G-actin monomer (Holmes et al., 1990; Kabsch et al., 1990; Otterbein et al., 2001) reveals two domains separated by an inter-domain cleft. Each of these domains, denoted small and large domain, are further subdivided into two smaller subdomains 1 to 4 where subdomains 1 and 2 together comprise the small domain and subdomains 3 and 4 the large domain (Fig. 2A). At high salt concentrations, actin monomers self-assemble into actin filaments (Fig. 2B). Moreover, actin polymerization is appreciably sped up by addition of ATP and divalent cations (Mg^{2+}/Ca^{2+}). The nucleotide binds in the cleft between the large and the small domain. All four subdomains are involved in the interaction with neighbouring subunits in the filament. The subdomains 1 and 3 are located at a part of a terminal subunit in F-actin to which new monomers are added most frequently upon filament elongation. This rapidly growing filament end is referred to as the “plus end” or the “barbed end”. The latter

ACCEPTED MANUSCRIPT

term is due to the filament appearance when it is labelled with myosin motor domains. The other end with lower polymerization rate is known as the minus end or the pointed end (Fig. 2). The critical concentration is the concentration of G-actin monomers at which the equilibrium length at a given end is maintained without net polymerization or depolymerization. The critical concentration is about 10-fold lower (Carlier, 1990) at the barbed end (~0.1 μM (Pollard, 1986b)) than at the pointed end (0.6 μM in (Pollard, 1986b)). This is related to the difference in inter-subunit binding affinity along F-actin between ATP-actin and ADP-Pi actin subunits on the one hand and between ADP-actin-subunits, on the other (Carlier, 1990; Murakami et al., 2010; Pollard, 1986b). Because the ATP is hydrolysed to ADP and Pi (inorganic phosphate) followed by slow Pi-release after G-ATP subunits are added to the plus end, ATP-actin subunits predominate at the plus end whereas ADP-actin subunits dominate at the minus end. The critical concentration also varies with experimental conditions, e.g. [Ca^{2+}], [Mg^{2+}], ionic strength and pH. Clearly, the critical concentrations are important in governing actin filament length and dynamics under different conditions. Particularly, actin monomer concentrations below the critical concentration at the barbed end lead to filament disassembly over time. One unique feature of actin filaments is treadmilling occurring at steady-state G-actin concentrations between the critical concentrations at the plus end and minus end. In this process G-ATP-actin monomers are added at the filament plus end followed by hydrolysis, Pi-release and "transportation" of monomers within the filament towards the minus end where the "transported" monomers are disassembled as G-ADP-actin. (Brieher, 2013; Bugyi and Carlier, 2010; Guo et al., 2010; Kuhn and Pollard, 2005; Pollard, 1986a; Selve and Wegner, 1986; Wang, 1985).

The "critical concentrations" as well as other aspects of actin dynamics and mechanics (cf. (Cooper et al., 1983a; Isambert et al., 1995; Jegou and Romet-Lemonne, 2016; Vavylonis et al., 2005; Weber, 1999) are relevant parameters to consider when engineering actin filaments for various purposes because the parameters may be modified by the engineering. Furthermore, the effect of the modification of a given amino acid residue may differ depending on the added molecule as illustrated (see below for details) by modifications at Cys-374 on actin (previously sometimes referred to as Cys-373). For this and other reasons, e.g. altered mechanical properties of F-actin upon certain modifications (Isambert et al., 1995; McCullough et al., 2008; Vikhorev et al., 2008a), it is important with insights into relevant aspects of actin biology before extensive engineering efforts. In addition to the issues considered briefly above, further key details can be found in previous comprehensive reviews on the subject (Blanchoin et al., 2014; Carlier, 1990; Oosawa, 1975; Pollard, T.D., 2016; Reisler and Egelman, 2007).

3. Myosin II and the in vitro motility assay for studies of myosin propelled actin filaments

Biomolecular motors are bio-nanomachines that transduce chemical free energy from nucleotide triphosphates into generation of force and motion in cells (Bustamante et al., 2004) (Schliwa and Woehlke, 2003). Linear motors move along tracks and perform mechanical work by utilizing chemical free energy derived from the turnover of nucleotide triphosphates such as ATP (Fig. 3) (Cross and Carter, 2000; Eisenberg and Hill, 1978; Huxley, 1969; Kron and Spudich, 1986; Lymn and Taylor, 1971; Rayment et al., 1993a). Myosin II and kinesin I are the two major linear motors that have been explored together with their respective cytoskeletal filaments, actin and microtubules, with the aims to develop bio-nanotechnological applications. This includes lab-on-a-chip devices e.g. for diagnostics or

ACCEPTED MANUSCRIPT

sorting of various cargoes (Agarwal and Hess, 2010; Hanson et al., 2016; Korten et al., 2010; Lard et al., 2013) and, more recently, parallel computation in nanofabricated networks (Nicolau et al., 2016).

The myosins are a large superfamily of actin-associated molecular motors (Foth et al., 2006; Hartman and Spudich, 2012; Korn, 2004; Pollard and Korn, 1973; Sellers, 2000). The Myosin II motors, also known as conventional myosins, have central roles in cellular motility and force generation, not the least, muscle contraction (Berg et al., 2001; Geeves and Holmes, 2005; Huxley, 1969; Rayment et al., 1993a). The myosin motor from fast skeletal muscle has been investigated in considerable detail and has also been exploited for a range of nanobiotechnological applications together with engineered actin filaments. The high speed (~10 μm/s) of actin translocation by fast skeletal muscle myosin II is a distinct advantage in this regard (Bakewell and Nicolau, 2007; Kumar et al., 2012; Lard et al., 2013). A processive myosin motor, myosin V, that takes several steps along an actin filament before detaching, has also been utilized for related purposes (Asokan et al., 2003) but it is appreciably slower.

In contrast to myosin V, myosin II is a non-processive motor. Thus, its lower actin affinity compared to myosin V only allows it to take one step at a time along an actin filament before detaching. In order to allow continuous movement, the myosin II motors must therefore work together in teams, e.g. by being incorporated into a filament or adsorbed in high density to a surface. The issues of processivity and myosin surface density are of relevance for nanotechnological applications where actin filaments are conjugated with other molecules or particles (cargoes). Thus, the transported cargo may cause steric clashes or other intermolecular interactions (e.g. electrostatic) with the surface-adsorbed myosin motors due to high density of the latter, causing blockage of filament transport (Persson et al., 2013). A bulky cargo may also prevent binding of myosin motors to the actin filament which may be particularly critical if non-processive myosin motors are used due to their need to work in large teams for effective filament propulsion (Persson et al., 2013).

The myosin II motor is structurally complex, containing both a fibrous coiled-coil domain and a globular enzymatic domain. The molecular mass and length amount to approximately 520 kDa and 170 nm, respectively (Fig. 4). Two heavy chains are associated to each other via a long (~150 nm) coiled-coil tail (diameter ~2 nm) with two globular head domains extending at their N-terminal ends. Each elongated globular head (10 nm long, 5 nm wide) contains a binding site for actin and a catalytic site for turnover of ATP (Conibear et al., 2003; Cooke, 1997; Holmes et al., 2003; Rayment et al., 1993b; Toyoshima et al., 1987). The tail domain is connected to the motor domains via α-helical neck regions (lever arms) of ~8 nm length. These dimensions are of relevance when myosin motors interact with engineered actin filaments as actin-attached cargoes of similar dimensions may result in steric clashes resulting in inhibited actin-myosin binding.

For nano-biotechnological applications or biochemical studies, myosin II is usually cleaved into different subunits by limited enzymatic digestion using α-chymotrypsin or trypsin (Fig. 4). Controlled enzymatic digestion in the presence of appropriate concentrations of Mg^{2+} and Ca^{2+} (Weeds and Pope, 1977) produces two fragments, heavy meromyosin (HMM) and light meromyosin (LMM). Out of these, HMM contains two fully functional motor domains. The HMM fragment has a mass of approximately 350 kDa and a length of 60-90 nm (Howard, 2001; Sellers, 1999). Each fragment includes the two motor domains and the associated neck domains (with light chains) as well as the N-terminal part of the myosin tail domain. For detailed studies, HMM can be further cleaved into two smaller fragments, subfragment 1 (S1)

ACCEPTED MANUSCRIPT

and subfragment 2 (S2) using papain or α-chymotrypsin under other salt conditions than for production of HMM. Both HMM and S1 have been extensively used for in vitro studies due to their favourable solubility properties (Kron et al., 1991; Lymn and Taylor, 1971; Margossian and Lowey, 1982).
The charge distributions of the HMM tail and motor domain (cf. (Albet-Torres et al., 2010; Mansson et al., 2008) are both influencing the surface adsorption of the motor. In addition, the positively charged actin-binding loops on myosin may interact with negatively charged cargoes attached to the actin filament.

The in vitro motility assay for studies of the relative motion of actin filaments and myosin motors (Fig. 5) was developed by Spudich and co-workers (Kron and Spudich, 1986; Kron et al., 1991; Sheetz and Spudich, 1983b; Spudich et al., 1985). In the version of the assay that is most frequently used today (the gliding in vitro motility assay), fluorescently labelled actin filaments are observed while propelled by surface-immobilized full length myosin molecules or, more often, proteolytically derived or cellularly expressed myosin motor fragments. The gliding motility assay has also been the basis for development of nanobiotechnological applications with transportation of engineered actin filaments as a central element (Kumar et al., 2016b; Kumar et al., 2012; Lard et al., 2013; Nicolau et al., 2016; Patolsky et al., 2004; Vikhorev et al., 2008b). In recent studies of this type, functional HMM was adsorbed to trimethylchlorosilane(TMCS)-derivatized tracks surrounded by topographical barriers and surfaces The latter surfaces were produced from negatively charged polymers without productive HMM-actin interactions (Persson et al., 2010; Sundberg et al., 2006).

4. Engineering of actin filaments

Actin filaments may be engineered to add other molecules or particles to the filament, using either non-covalent or covalent conjugation approaches. Key applications of the engineered filaments are partly considered in this section but also in greater detail in sections 5-6.

4.1. Non-covalent approaches

Actin filaments in cells interact with a range of different actin binding proteins, nucleic acids and divalent metal ions. They may also be affected by various toxins (Carlier, 1989; Dancker et al., 1975; Egelman and Orlova, 2001; Oda and Maeda, 2010; Pollard, 1986a; Pollard et al., 1994; Pollard and Cooper, 1986; Revenu et al., 2004; Strzelecka-Golaszewska et al., 1996; Vandekerckhove, 1990). The functional diversity of the actin binding proteins has been comprehensively reviewed (Blanchoin et al., 2014; Carlier et al., 2015; Dominguez, 2004; dos Remedios et al., 2003; Hild et al., 2010; Pollard, T.D., 2016; Schevzov et al., 2012) as well as the effects of divalent metal ions, nucleotides and some toxins on actin structure and dynamics (Carlier, 1990; Cooper et al., 1983a; Dominguez and Holmes, 2011; Kang et al., 2013; Kinosian et al., 1993; Murakami et al., 2010; Oda et al., 2009; Visegrady et al., 2005). Here we consider the usefulness of some actin binding proteins and, in greater detail, the phallotoxins (e.g. phalloidin) in engineering of actin filaments.

4.1.1. Fluorescence labelling of actin filaments by non-covalent approaches

Phalloidin is a bicyclic heptapeptide which belongs to phallotoxins of the mushroom family *Amanita Phalloides*. The interaction of phalloidin with actin filaments was published in 1974

ACCEPTED MANUSCRIPT

(Lengsfeld et al., 1974; Low and Wieland, 1974). Phalloidin binds specifically, stoichiometrically and firmly to four neighbouring subunits thereby stabilizing the actin filament against depolymerization (Barden et al., 1987; Cooper, 1987; De La Cruz and Pollard, 1996; Faulstich et al., 1993; Oda et al., 2005; Steinmetz et al., 1998; Wehland et al., 1977; Wieland, 1977; Zhukarev et al., 1997). The dissociation rate constant for phalloidin from rabbit skeletal muscle actin filaments is in the range 0.0003-0.0005 s^{-1} with a dissociation equilibrium constants of 10-40 nM (Allen and Janmey, 1994; De La Cruz and Pollard, 1996; Huang et al., 1992).

Fluorescent phalloidin was found to label F-actin in muscle cells (Wulf et al., 1979) allowing observation in the fluorescence microscope. Still to date this is the standard method to fluorescence label actin filaments in cells. More recently, fluorescent phalloidins have also emerged as standard labels for visualizing motility of actin filaments in the in vitro motility assay both for functional studies (Homsher et al., 1992; Kron and Spudich, 1986; VanBuren et al., 1998; Yanagida et al., 1984) and nanotechnological applications (Kumar et al., 2016b; Lard et al., 2013; Nicolau et al., 2016; Nicolau et al., 1999; Sundberg et al., 2006; Suzuki et al., 1997). The use in nanotechnology is uncontroversial. The functional studies, on the other hand, may be complicated to interpret in view of recent evidence that phalloidin binding to the filaments may alter filament properties beyond the stabilization against depolymerisation, e.g. with regard to flexural rigidity and actin-myosin interactions (Diensthuber et al., 2011; Isambert et al., 1995; Tokuraku and Uyeda, 2001; Vikhorev et al., 2008a).

There are different commercially available phalloidin-conjugated fluorophores (Fig. 6) that are all useful for actin filament labelling (Anderl et al., 2012; Balaz and Mansson, 2005; Chazotte, 2010). The most commonly used fluorescent phalloidin is rhodamine-phalloidin (RhPh) (Butkevich et al., 2015; Cano et al., 1992; Chazotte, 2010; Faulstich et al., 1983; Kron et al., 1991; Kumar et al., 2016b; Mahaffy and Pollard, 2008; Olyslaegers and Verbelen, 1998; Waggoner et al., 1989). The latter is a conjugate of phalloidin and the orange-red fluorescent dye, tetramethylrhodamine (TRITC) with excitation and emission centred around 540 nm and 565 nm, respectively. Another frequently used group of photostable fluorescent dyes, with compounds of different excitation and emission spectra are the Alexa fluor compounds. Also these exist in commercially available phalloidin conjugates. For instance, the Alexa Fluor 488 conjugated phalloidin (APh) is a commonly used Alexa fluorophore (Amann and Pollard, 2001a; Bledzka et al., 2016; Carvalho et al., 2013; Kumar et al., 2016b; Mansson et al., 2004; Panchuk-Voloshina et al., 1999; Waterman-Storer et al., 2000) which emits green light with excitation/emission maxima at 495/518 nm.

Phallacidin is another phallotoxin that is also obtained from *Amanita phalloides*. Phallacidin has similar structure and actin-binding properties as phalloidin (Barak et al., 1980; Singhal and Hays, 1988; Yao et al., 2009) and phallacidin-fluorophore conjugates have been synthesized for actin filament labelling (Barak et al., 1980).

A low-affinity alternative to phallotoxins for fluorescence labelling of actin, without evidence for effects on actin dynamics, is the 17-amino-acid peptide, Lifeact, obtained from yeast (Riedl et al., 2008). The dissociation constant of FITC fluorophore Lifeact (F-Lifeact) for binding to actin filaments is about 2 µM whether phalloidin is present or not (Riedl et al., 2008), i.e. the F-actin affinity is about 100-fold lower than for phalloidin. Lifeact has been used for visualization of actin filament dynamics in several cell types (Deibler et al., 2011; Era et al., 2009; Li et al., 2010; Renkawitz et al., 2009; Riedl et al., 2008; Sliogeryte et al., 2016; Vidali et al., 2009) as well as in vivo (Riedl et al., 2010; Schachtner et al., 2012). In

ACCEPTED MANUSCRIPT

another study (Munsie et al., 2009) it was, however, shown that Lifeact cannot visualize some forms of twisted F-actin suggesting that it may not be a universal tool for studies of actin dynamics in live cells. Lifeact can be easily prepared (cf. (Riedl et al., 2008)) and is commercially available.

4.1.2. Biotin-strept(avidin) engineering of actin filaments via phalloidin

Biotin is a water soluble vitamin, also known as vitamin H/vitamin B7, which is found in all living cells in tiny amounts. The binding of biotin to the proteins streptavidin from *streptomyces avidinii* and avidin (from egg white) is among the strongest non-covalent interactions in nature with the very low dissociation constant (K_d) of 4×10^{-14} M (Chivers et al., 2011; Green, 1990; Stayton et al., 1999). This strong binding, together with the high specificity, forms the basis for widespread use in biotechnology (Bayer and Wilchek, 1980; Diamandis and Christopoulos, 1991; Dundas et al., 2013; Wilchek and Bayer, 1984). Further contributing in this regard is the fact that both streptavidin and avidin are tetrameric proteins with four biotin-binding pockets (Gitlin et al., 1990). A genetically engineered tetrameric streptavidin has, however, also been produced with a single binding pocket for biotin. This facilitates certain biotechnological applications where it is essential to avoid the formation of big complexes/aggregates by oligomerization (Howarth et al., 2006; Lim et al., 2013). The binding affinity and stability of this monovalent streptavidin are similar to those of multivalent streptavidin (Howarth et al., 2006). NeutrAvidin is a deglycolated native avidin which is commonly used to reduce non-specific binding due to electrostatic interactions which may be problematic in the biotin-avidin system. The binding affinity of NeutrAvidin with biotin is similar as for streptavidin or avidin (Hiller et al., 1987; van Roy et al., 1993). The, biotin-strept(avidin) bond can be broken in harsh conditions such as high temperatures above 70°C (Holmberg et al., 2005).

Biotin xx phalloidin, binds to actin filaments in a similar way as rhodamine phalloidin. Here, "xx" denotes a spacer arm (atoms spanning the distance from the end of the conjugated amino acid on phalloidin to the end of the biotin molecule). Biotin xx phalloidin has found use in cell biology for staining of actin filaments, e.g. in fixed cells or cells detached from culture dish followed by resuspension in working buffers. Usually, fixed cells or re-suspended cells, are incubated with phalloidin xx biotin followed by incubation with fluorescence labelled streptavidin or Quantum dot/colloidal gold particles that are coated with strept(avidin) to visualize the actin filaments (Baines et al., 1995; Izdebska et al., 2013; Paragas et al., 2002; Timp et al., 2006; Wilson et al., 2000; Wu et al., 2003).

In the in vitro motility assay, negligible difference in the velocity of actin filament propulsion by HMM was observed, whether actin filaments were labelled with rhodamine-phalloidin, Alexa fluor 488 phalloidin or biotin xx phalloidin with 1:1 molar ratio to actin (Balaz and Mansson, 2005). Similar dual labelling of actin filaments with fluorophore-phalloidin and biotin xx phalloidin has also been described in experiments where actin filaments were observed to slide with single quantum dots attached to the filament via streptavidin-biotin bonds (Mansson et al., 2004). The stock solution of Alexa phalloidin and biotin xx phalloidin were prepared at equimolar ratio and incubated with actin filaments overnight at 4°C in the dark. This allows for simultaneous labelling of actin filaments with a fluorophore and biotin e.g. for attachment of streptavidin-coated cargoes on actin (Mansson et al., 2004; Takatsuki et al., 2010; Takatsuki et al., 2011). Rhodamine-phalloidin and biotin phalloidin labelled actin bundles have later been used for transportation of streptavidin coated microbeads (Takatsuki

ACCEPTED MANUSCRIPT

et al., 2010), biotinylated single cells and biotinylated liposomes attached via neutravidin (Takatsuki et al., 2011). Biotin-phalloidin labelled actin filaments have also been used for basic biophysical studies (Hayakawa et al., 2011; Wang et al., 2013).

It is important to consider the fact that several bovine serum albumin (BSA) preparations may be biotinylated to different degrees. This is of relevance because quite high concentration of serum albumins is often employed to reduce undesired non-specific protein-protein interactions both in nanobiotechnological applications and in other in vitro motility assay studies. In such studies it is essential to choose biotin-free BSA to avoid unwanted binding between streptavidin on the actin filament and BSA on the surface or in solution.

4.1.3. Natural actin binding proteins in applications of actin filaments

Actin binding proteins that have been used for engineering of actin filaments for potential applications include gelsolin and CapZ (from striated muscle). These proteins bind to the barbed end of the actin filament and cap it, i.e. prevent further addition of G-actin monomers as well as removal of bound actin subunits. The binding of gelsolin is calcium-regulated and this protein also severs, i.e. cuts actin filaments (Andre et al., 1988; Sun et al., 1999; Weeds et al., 1986; Yin et al., 1981). In contrast, CapZ does not sever F-actin and its binding to pre-existing barbed ends is not regulated by calcium (Hartmann et al., 1989; Isenberg et al., 1980; Kilimann and Isenberg, 1982). Gelsolin and CapZ have been utilised for non-covalent attachment of biotin to actin filaments. In these cases, biotin labelling was first achieved by mixing gelsolin and CapZ with biotinylating reagents followed by purification of the biotinylated proteins for further use. The approach was first used three decades ago in fundamental studies (Spudich et al., 1985) allowing demonstration that only actin and myosin among the muscle proteins is required for production of motion. In these experiments, an array of actin filaments with biotinylated severin (gelsolin-related protein from Dictyostelium discoideum) at the barbed ends was first formed on an avidin-coated surface. Fluid flow was next imposed that oriented the filaments. After immobilization in a parallel manner along the surface the movement of myosin coated beads could be observed upon addition of ATP (Spudich, 2011, 2012; Spudich et al., 1985; Williamson, 1986).

Biotinylated gelsolin, attached to actin filaments, has also been utilized for transportation of drug molecules in gliding in vitro motility assays (Kaur et al., 2009). Unidirectional transportation of myosin coated beads along actin filaments can be achieved by immobilizing the filaments with biotinylated gelsolin in biotin-streptavidin coated microfluidic channels (Lee et al., 2009). Fascin-mediated unipolar arrays of actin filaments (see below) with biotinylated gelsolin (Fig. 7) have also been used for similar purposes (Lee and Famouri, 2013).

The biotin-streptavidin link together with gelsolin has also been used to engineer actin filaments in a range of other ways. Thus, biotin-streptavidin coated surfaces have been used for 1) selective assembly and alignment of biotin-gelsolin labelled actin filaments with specific polarity (Huang et al., 2006), , 2) selective pattering of filaments with controlled length (Wei et al., 2011) and 3) actin polymerization on nanopatterns using a top-down approach (Brough et al., 2007). It has also been shown that actin monomers self-assemble into filaments on streptavidin coated magnetic particles to which biotinylated gelsolin is attached (Brangbour et al., 2011). This method has been used to record force-velocity relationships of growing filaments (Brangbour et al., 2011). Biotinylated-gelsolin engineered actin filaments have also been immobilized in a particular orientation on biotin-streptavidin coated surfaces

ACCEPTED MANUSCRIPT

to facilitate directional sliding of myosin-V and myosin-VI motors (Yuan et al., 2013). Finally, attachment of cargoes to actin via gelsolin, without aid of the biotin-streptavidin link, has also been reported (Suzuki et al., 1996).

Recently (Persson et al., 2013), actin filaments with biotinylated CapZ at their barbed ends were explored for nanoscale cargo transportation driven by HMM. In these experiments, the biotinylated cargoes were attached via streptavidin to CapZ. This study evaluated the effect of cargo size ranging from small molecules (biotin) over individual streptavidin molecules to streptavidin-coated liposomes of >100 nm diameter. In addition, the effect of the mode of cargo attachment was studied, i.e. how motility was affected if the cargo was attached to biotinylated CapZ on the trailing end of the HMM propelled filament or to biotinylated actin subunits along the filament length. The aims were to investigate the potential of using different modes of attachment for differently sized cargoes in development of actomyosin based diagnostic nanodevices and for use in fundamental studies (Persson et al., 2013).

Fascin is an actin-bundling protein that cross-links actin filaments in a parallel arrangement with the filament plus end in the same direction for all filaments. In the cell, fascin is primarily concentrated in cellular extensions with oriented bundles of actin filaments such as filopodia of motile cells, stereocilia in the cochlear sensory cells and invadopodia of importance for matrix invasion by cancer cells (Adams, 1995; Gross, 2013; Jayo and Parsons, 2010; Li et al., 2010; Vignjevic et al., 2003; Yamashiro et al., 1998). Recently, fascin mediated actin-bundles, formed in vitro, have been utilized for nanotechnological application in transportation of rather large cargoes that are not readily transported by myosin induced propulsion of actin filaments (Kumar et al., 2016b; Takatsuki et al., 2010; Takatsuki et al., 2011).

There are a wide range of actin binding proteins in addition to those mentioned above and several of them may find use in nanotechnological applications in the future. For instance, tropomyosin could be useful for stabilizing actin filaments and increase their flexural rigidity, e.g. to reduce error rates in actin-myosin based biocomputation (Nicolau et al., 2016). It may also be of interest to achieve such stabilization while other actin-binding proteins are linked to actin. However, before using several actin binding proteins or toxins together it is important to take into account that effects of one actin-binding protein or phalloidin may alter the binding and/or function of other actin-binding proteins (Gateva et al., 2017; Jegou and Romet-Lemonne, 2016; Johnson et al., 2014; Orlova et al., 1995; Vikhorev et al., 2008a). Such interactions may propagate allosterically and could thus emerge for actin-binding proteins at significant distances from each other along the filament. Furthermore, there may also be appreciable differences in these regards between different isoforms of a given actin-binding protein (cf. (Gateva et al., 2017; Johnson et al., 2014).

4.1.4. Electrostatics in cargo attachment to actin filaments

Globular actin as well as actin filaments are negatively charged at physiological pH. The electrostatic attraction of actin filaments to positively charged molecules, including lipids (Demé et al., 2000; Gicquaud and Wong, 1994; Grimard et al., 1993; Laliberte and Gicquaud, 1988), genetically modified lysozyme (Sanders et al., 2007) and polycations (eg. divalent metal ions and polylysine) (Griffith and Pollard, 1982; Tang and Janmey, 1996) has been studied. Transportation of cargoes attached to actin filaments by electrostatic attraction (Iwabuchi et al., 2012; Oyama and Hatori, 2016) has also been demonstrated. For instance, HMM, from skeletal muscle myosin, has been shown to propel actin filaments loaded with

ACCEPTED MANUSCRIPT

electrostatically bound cationic liposomes (Iwabuchi et al., 2012), as well as, with cationic polystyrene microspheres (Oyama and Hatori, 2016).

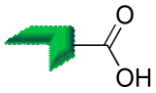
4.2. Covalent modification approaches

A covalent bond is a strong chemical bond (cf. (Grandbois et al., 1999)) that involves the sharing of electron pairs between atoms. Covalent bonds are stable over wide ranges of temperatures and pH. Two or more molecules can be covalently conjugated to actin filaments via specific cross-linker molecules. There are two types of cross-linkers as classified on the basis of their reactive groups at both ends. Homobifunctional cross-linkers have two identical reactive ends, allowing a single-step conjugation reaction. However there are disadvantages with the single-step procedure including polymerization through intramolecular cross-linking by self-conjugation. The use of heterobifunctional cross-linkers avoids this complication due to two different reactive ends and a multi-step conjugation procedure. Whereas both homobifunctional and heterobifunctional cross-linkers may be without a spacer between the reactive groups, the presence of such a spacer minimizes steric constraints during cross-linking. For more details about bioconjugation chemistry, see (Hermanson, 2013; Kumar et al., 2016a; Wong, 1991). The selection of available functional groups on actin is an important step for engineering the filament. This is related to the selection of corresponding reactive groups on suitable cross-linkers. Key functional groups on actin and target reactive groups of cross-linkers that have been used for engineering of actin are listed in Table 1 and some particularly important residues are indicated in Fig. 8. Moreover, amino acids with suitable functional groups, particularly cysteines, can be introduced in appropriate positions in genetically engineered actin (Orlova et al., 2004; Pengelly et al., 2009; Scoville et al., 2009; Teal and Dawson, 2007; Yates et al., 2009) and then covalently modified. For the experiments with genetic engineering, non-muscle actin has generally been expressed in the yeast *Saccharomyces cerevisiae* (cf. (Aspenstrom and Karlsson, 1991)). More recently, however, mammalian actins (e.g. striated muscle α-actin) have also been expressed and engineered in substantial quantities (c.f. (Bai et al., 2014; Bookwalter and Trybus, 2006)) using a baculovirus insect cell expression system. This may open for modification also of these actins to better adapt them to biotechnological application (e.g. with regard to attachment points for other molecules or mechanical properties).

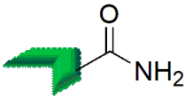
Table 1. Functional groups on actin and corresponding cross-linkers for covalent engineering of actin filaments.

Actin functional groups (key modified residues)	**Cross-linker reactive groups**	**Reference**
Primary amines  (K61, K72, K191, K328, K373)	Isothiocynate/NHS ester/Imidoester	(Bengtsson et al., 2016) (Breitsprecher et al., 2012) (Burtnick, 1984) (Kaya and Higuchi, 2010) (Kumar et al., 2012) (Miki et al., 1987)

ACCEPTED MANUSCRIPT

		(Miller et al., 1988) (Ohara et al., 1982) (Persson et al., 2013) (Skorzewski et al., 2009) (Vikhorev et al., 2008a)
Sulfhydryls  (C374)	Maleimide/Idoacetyl	(Amann and Pollard, 2001b) (Cooper and Pollard, 1982) (Detmers et al., 1981) (Fujiwara et al., 2014) (Knight and Offer, 1978) (Kouyama and Mihashi, 1980) (Kouyama and Mihashi, 1981) (Kozuka et al., 2006) (Kurita et al., 2007) (Miyata et al., 1997) (Prochniewicz et al., 2004) (Yao et al., 2009)
Carboxyls  (E99, E100, E361, E364)	Carbodiimide (EDC)	(Ge et al., 2014) (Gutsche-Perelroizen et al., 1999) (Kaur et al., 2011) (Maciver et al., 1991) (Tsarova et al., 2010) (Wong et al., 2014) (Wu et al., 2014) (Yao et al., 2009)
Carboxamide	Transglutaminase (TGase)	(Eligula et al., 1998) (Kozuka et al., 2006)

ACCEPTED MANUSCRIPT



(Takashi, 1988)

(Q41)

4.2.1. Covalent modification of primary amines

Primary amines are found in the side chain of lysine residues and are also present in the N-terminus of each polypeptide chain. For the engineering of actin, lysines have been modified with reactive groups such as isothiocynate, N-hydroxysuccinimide (NHS) ester and imidoester to allow formation of stable covalent bonds (Fig. 9). Indeed, the primary amine of lysine is the most common functional group which has been targeted for covalent modification or tagging with desired molecules. For such conjugation, precautions should be taken to avoid buffers containing primary amines e.g. Tris or glycine, that will compete with the reaction. Low concentration of sodium azide (<3 mM or 0.02%) in a reaction mixture will, however, not significantly interfere in modification/conjugation reaction with NHS esters (Pierce Thermo Scientific, www.thermoscientific.com/pierce). Interestingly, Tris buffer can be included after a stipulated time to stop further modification. The standard protocol for actin preparation and purification uses 2 mM Tris buffer with pH around 8.5 and with 3 mM sodium azide as an antibacterial agent. Therefore, before proceeding with modification/conjugation, primary amine contaminants must be removed by ultracentrifugation or dialysis. The HEPES and MES buffers (for pH around 8.0 and 6.0, respectively) are suitable to include in the modification/conjugation solutions (Kumar et al., 2013; Kumar et al., 2012). Another precaution that may increase filament conjugation yield would be to use the F-actin form in the modification or conjugation reactions because incorporation of conjugated G-actin into F-actin may be compromised by the covalent modification (Burtnick, 1984; Kumar et al., 2012; Patolsky et al., 2004).
Different lysines on actin may be targeted by the use of different labelling procedures and possibly different fluorescent probes. It was thus shown by (Burtnick, 1984) that Lys-61 was the primary site functionalized with fluorescein isothiocyanate (FITC) after reaction at pH 8.5. In contrast, Alexa-Fluor 488 NHS primarily labelled Lys-328 as suggested by mass spectrometry (Toth et al., 2016) and Lys-373 was the residue primarily labelled with 7-chloro-4- nitrobenzeno-2-oxa-1,3-diazole (NBD-Cl) after pre-labelling of Cys-374 with N-ethylmaleimide (Detmers et al., 1981). In several studies, it has been suggested that covalent modification of lysines with small molecular substances such as biotin, or fluorophores such as rhodamine, has limited effects on actin filament properties, e.g. filament flexural rigidity (Vikhorev et al., 2008a) and myosin propelled actin filament sliding (Kumar et al., 2012; Persson et al., 2013; Vikhorev et al., 2008b). For instance, covalent modification of actin, via lysines, with up to 5 biotins per actin subunit, or with the heterobifunctional cross-linker C6-succinimidyl 6-hydrazinonicotinate acetone hydrazone (C6-SANH) had negligible effects on both the velocity and the fraction of motile filaments in an in vitro motility assay (Kumar et al., 2012; Persson et al., 2013). However, functionalization of Lys-61 with FITC seemed to inhibit polymerization in some (Burtnick, 1984) but not all studies (cf. (Miki et al., 1987)). On the other hand, it was found by (Tait and Frieden, 1982) that labelling of actin with 7-chloro-4-nitro-2,1,3-benzoxadiazole on primarily Lys-372 (after initial labeling of Cys-374 with N-ethylmaleimide) led to increased polymerization rate. Nevertheless, altered polymerization

ACCEPTED MANUSCRIPT

properties as well as altered interactions with actin-binding proteins, need to be considered upon covalent modification of actin via lysines.

4.2.2. Covalent modification of sulfhydryl groups

Sulfhydryl groups are found in the side chain of cysteine and two cysteine molecules may be linked together by their side chains via a disulfide bond (-S-S-). The maleimide and iodoacetamide moieties are reactive groups that have been used for labelling of cysteine residues of actin (Fig. 10). Attachment of a range of fluorophores to actin via Cys-374 has been employed for a wide variety of fundamental studies of actin filament properties and of the actomyosin interaction mechanism (Adachi et al., 1999; Adamek and Geeves, 2014; Amann and Pollard, 2001b; Cooper and Pollard, 1982; Fujiwara et al., 2014; Kouyama and Mihashi, 1981; Kovar and Pollard, 2004; Kozuka et al., 2006; Kuhn and Pollard, 2005; Miyata et al., 1997; Prochniewicz et al., 2004; Tellam and Frieden, 1982). The actin-modification reaction must be carried out in the absence of thiol-containing reducing agents (eg. DTT) because the latter will otherwise compete in the modification reaction. Reducing agent contaminants in F-actin solutions are removed by ultracentrifugation or dialysis prior to the reaction. Modification of cysteine residues by cross-linkers with maleimide and iodoacetamide as reactive groups requires 5 to 10 fold molar excess of cross-linker to be added to the F-actin solution. In order to minimize oxidation of sulfhydryls in the modification reaction, ethylenediaminetetraacetic acid (EDTA) is conveniently included as an antioxidant agent (Hermanson, 2013). The modification reaction may be stopped by addition of free thiols followed by buffer exchange by dialysis/ultracentrifugation to remove excess cross-linker. For more details about the conjugation chemistry (see (Hermanson, 2013; Kim et al., 2008)).

An important issue to consider with regard to attachment of fluorescent probes to actin via Cys-374 is that labelling with certain probes might have functional consequences (see above for similar issues with Lys-labelling). For instance, monomers labelled with rhodamine-maleimide (Amann and Pollard, 2001b) and Oregon green 488 iodoacetamide (Kuhn and Pollard, 2005) have been found to depend on the presence of non-labelled monomers for their incorporation into filaments, i.e. the labelled monomers did not contribute to the elongation rate in these studies. Possible mechanisms for the latter effect have been suggested by ultrastructural data (Otterbein et al., 2001) see also (Murakami et al., 2010). The effects of the rhodamine and Oregon green conjugations are in apparent contrast to labelling of Cys-374 with pyrene that did not seem to affect polymerization rate despite doubling of the critical concentration for filament elongation (Kouyama and Mihashi, 1980; Tellam and Frieden, 1982). Furthermore, interestingly, another chemical modification of Cys-374 with N-ethyl maleimide or (iodoacetamido)tetramethylrhodamine, increased, rather than reduced, the polymerization rate demonstrating the sensitivity of actin properties to small differences in the modification reactions.

4.2.3. Covalent modification of carboxyl groups

Carboxyl groups are found in the side chains of aspartic acid and glutamic acid and are also present in the C-terminus of each polypeptide chain. Carboxyl groups in actin can be covalently attached to an amine group e.g. in 1-Ethyl-3-[3-dimethylaminopropyl] carbodiimide hydrochloride (EDC). The carbodiimide (EDC) is a zero-length cross-linker that

ACCEPTED MANUSCRIPT

enables covalent crosslinking between carboxyl groups in actin and amino groups of other molecules as desired. This can be achieved in one step in MES buffer at pH in the range 4.5 to 6.0. Alternatively, the reaction can be carried out at pH up to 7.5 in other buffers such as PBS, HEPES etc. (Bianco et al., 2007; Combeau et al., 1992; Gutsche-Perelroizen et al., 1999; Maciver et al., 1991; Nyman et al., 2002; Tsarova et al., 2010; Vandekerckhove et al., 1989; Wong et al., 2014). Linking of other molecules to carboxyl groups in actin could also be achieved by two-step EDC/NHS reactions (Ge et al., 2014; Grabarek and Gergely, 1990; Kumar et al., 2013). Here, EDC first reacts with the actin carboxyls to form an active O-acylisourea intermediate. This intermediate next reacts with an amine-containing molecule to form a stable amide bond (Fig. 11). The O-acylisourea intermediate is unstable in water but the stability may be improved by including NHS with EDC in the reaction mixture. NHS reacts with intermediate O-acylisourea to form an amine-reactive NHS ester (Hermanson, 2013). NHS can be replaced with water-soluble sulfo-NHS for improved crosslinking efficiency (Hermanson, 2013). For effective covalent linking between actin and the desired molecules, using EDC/NHS reactions, competing carboxyl and primary amine groups must be removed from the reaction buffer e.g. using dialysis or ultracentrifugation. The carboxyl groups of F-actin can be activated using 2.5 mM EDC and 5 mM NHS. This, activation step is terminated by the addition of 140 mM β-mercaptoethanol to the reaction mixture. Subsequently, activated F-actin is mixed with equal volume of molecules containing primary amines for covalent crosslinking (Yao et al., 2009).

4.2.4. Covalent modification of glutamines

Dansylcadaverine has been attached to glutamines (80-85 % on Gln-41) in a reaction catalysed by transglutaminase (Takashi, 1988) leading to formation of an amide bond between glutamine on actin and a lysine side chain on cadaverine (Lin and Ting, 2006). The Gln-41 conjugation had no inhibiting effect on actin elongation but rather led to increased polymerization rate and lowered critical concentration for filament growth. Furthermore, the modified F-actin, activated myosin ATPase to similar extent as unmodified actin.

4.3. Different uses of covalent modifications

4.3.1. Covalent conjugation of actin filament with fluorophores

Pyrene is a fluorescent molecule that has been extensively used for labelling of actin with the aim to monitor conformational changes associated with binding of myosin, polymerization, depolymerization etc. using in vitro assays. Actin can be covalently conjugated with pyrene via cysteine or lysine residues (Bains et al., 2011; Drummen, 2012). For the purpose of monitoring structural changes, iodoacetamide has been used for attaching pyrene to Cys-374 (Adamek and Geeves, 2014; Cooper et al., 1983a; Cooper and Pollard, 1982; Cooper et al., 1983b; Criddle et al., 1985; Doolittle et al., 2013; Fujiwara et al., 2014; Handel et al., 1990; Kouyama and Mihashi, 1981; Maciver et al., 1991; Pollard, 1984; Pollard and Cooper, 1984; Rosin et al., 2015; Statsuk et al., 2005). Pyrene-conjugated actin monomers (G-actin) polymerize under physiological conditions to form pyrene labelled filamentous actin (F-actin) provided that the monomer concentration is above the critical concentration. It has been found that the latter concentration as well as the polymerization rate of actin labelled with pyrene via the iodoacetamide reactive group is similar to that of native actin (Cooper et al., 1983b; Kouyama and Mihashi, 1981; Tellam and Frieden, 1982). The fluorescence intensity of

ACCEPTED MANUSCRIPT

pyrene when incorporated into an actin filament is higher than that of pyrene in G-actin (Cooper et al., 1983b). Furthermore, the fluorescence signal of pyrene labelled actin is proportional to the polymer weight concentration rather than to the filament length.

For in vitro actin polymerization assays, monitoring of changes in pyrene fluorescence is the most common and simplest method. For instance, the method has both higher sensitivity and is more convenient than methods based on viscosity, spin-down of actin filaments and DNase inhibition upon polymerization (Cooper and Pollard, 1982; Cooper et al., 1983b; Doolittle et al., 2013; Kouyama and Mihashi, 1981). However, there are some disadvantages associated with pyrene as a fluorescent probe. For instance, photo-bleaching occurs significantly with extended exposure times and the excitation wavelength is in the ultraviolet range (Adamek and Geeves, 2014).

As mentioned above, actin filaments have also been covalently labelled with other fluorophores than pyrene, both via lysine and cysteine residues. These other fluorophores include rhodamine or TRITC (Amann and Pollard, 2001b; Bengtsson et al., 2016; Diensthuber et al., 2011; Isambert et al., 1995; Kellogg et al., 1988; Samarin et al., 2003; Shimozawa and Ishiwata, 2009; Vikhorev et al., 2008a), FITC and oregon green (Burtnick, 1984; Handel et al., 1990; Kuhn and Pollard, 2005; Miller et al., 1988; Skorzewski et al., 2009; Smith et al., 2014), Cy3 and Alexa fluor dyes (Adachi et al., 1999; Pernier et al., 2013; Suzuki et al., 2012; Wiesner et al., 2003). The purposes in these studies have generally been to allow use of fluorescence microscopy for investigation of actin filament dynamics and mechanics without the confounding effects of phalloidin binding.

Experiments have also been performed with more than one fluorophore covalently attached to the actin filament, e.g. for fluorescence resonance energy transfer (FRET) studies (dos Remedios et al., 1987; Kozuka et al., 2006; Moens and dos Remedios, 1997). In these studies, doubly fluorophore labelled actin monomers have been copolymerized with unlabelled actin (Kozuka et al., 2006; Miyata et al., 1997; Prochniewicz and Yanagida, 1990). In addition to modifications of lysines and Cys-374 other approaches have also been used for simultaneous conjugation of actin with more than one fluorophore. For instance, (Kozuka et al., 2006) first immobilized tetramethylrhodamine-cadaverine (TMR-cadaverine) on Gln-41, taking advantage of the transglutaminase reaction mentioned above. The TMR-cadavarine-labelled actin was then covalently conjugated with a second fluorophore, indocyanine (IC)-5 maleimide at Cys-374. Finally, the dually labelled monomers were sparsely co-polymerized with biotinylated and non-labelled monomers. After each conjugation step actin was purified by repeated polymerization and depolymerization cycles (Kozuka et al., 2006). Finally, the dually labelled filaments were observed using total internal reflection fluorescence (TIRF) microscopy under different conditions.

4.3.2. Covalent conjugation of actin filaments with biotin

Biotin-engineered actin filaments have several potential applications in nanobiotechnology as well as in fundamental studies of actomyosin function as reported above in relation to biotin-phalloidin. Biotin is chemically composed of an ureido ring fused with a tetrahydrothiophene ring. One carbon atom of the tetrahydrothiopene ring is substituted with a valeric acid. Different reactive groups can be incorporated by derivatizing the valeric acid side chain of biotin for attachment to other molecules e.g. for actin conjugation. For this purpose, there are several ready-to-use biotinylation reagents commercially available for labelling of specific

ACCEPTED MANUSCRIPT

functional groups or residues, including primary amines and sulfhydryls. The most common biotinylation reagents for labelling of lysine residues are sulfosuccinimidyl ester xx biotin, employed in a range of studies (Beausang et al., 2013; Breitsprecher et al., 2012; Holliday et al., 2000; Jansen et al., 2015; Kaya and Higuchi, 2010; Kouchi et al., 1993; Okabe and Hirokawa, 1989; Persson et al., 2013; van der Gucht et al., 2005; Vikhorev et al., 2008b). For labelling of cysteine residues, on the other hand, maleimide xx biotin is the conjugate of choice (Hansen et al., 2013; Ishijima et al., 1998; Jansen et al., 2015; Omote et al., 1999; Smith et al., 2014). The conjugation reaction can be carried out at room temperature or at 4°C followed by purification of the conjugated actin using centrifugation, dialysis or passage through a desalting column. The extent of biotinylation can be determined by 4-hydroxyazobenzene-2-carboxylic acid (HABA) assay (Persson et al., 2013; Vikhorev et al., 2008b). Biotinylated reagents are available with different spacer arms and solubility for optimized interaction of the biotinylated macromolecule with their strept(avidin) binding sites. For instance, the longer spacer arms of biotinylated reagents can enhance the binding affinity of biotinylated actin to target strept(avidin) by reducing the risk of steric hindrance from multiple biotins on the same actin.

Recently, (Persson et al., 2013) studied transportation of TRITC-streptavidin (~5 nm in diameter) by HMM propelled and covalently biotin-engineered actin filaments in the in vitro motility assay. Importantly, covalent biotinylation via lysines was achieved with up to 4 biotins per actin subunit without noticeable effects on motility. The transportation with co-localization of cargo (TRITC-streptavidin) and actin filaments was observed by switching between fluorescence microscopy filter sets for visualization of TRITC-streptavidin and Alexa 488 fluor phalloidin labelled actin filaments. One important finding was that the HMM-propelled and biotin-engineered actin filaments could carry up to one thousand streptavidin molecules with limited effects on motility quality. The high streptavidin/actin-subunit ratio that was possible without deterioration of motility is of interest because it argues against Brownian models of muscle contraction where long uninterrupted runs of single myosin heads along the actin filament are important (Esaki et al., 2007; Kitamura et al., 1999). It also demonstrates a very substantial capacity of actin filaments to transport protein-sized cargoes in nanotechnological applications. For actin transportation by non-processive myosin II one would nevertheless expect that the maximum cargo carrying capacity is limited by insufficient number of actin-myosin interactions rather than by saturation of the cargo binding capacity (He et al., 2012). At cargo densities when the capacity saturates, actin filaments are likely to detach from even the most densely myosin II coated surface.

Streptavidin coated semiconductor quantum dots (~15 to 20 nm diameter) were also transported by biotin-engineered actin filaments (Persson et al., 2013). This is one step towards transporting cargoes larger than streptavidin. Transportation of the streptavidin coated quantum dots via the covalently biotin-engineered filaments was also an improvement compared to previously observed transportation (Mansson et al., 2004) where the streptavidin coated quantum dots were attached to actin filaments via biotin-phalloidin. Important in this regard, e.g. for diagnostics application, is the extended half-life of covalent bonds compared to a half-life for dissociation of the phalloidin-actin interaction of <30 min (De La Cruz and Pollard, 1994). Additionally, for biotin-engineered actin filaments, carrying one or two quantum dots, the sliding velocity was not significantly affected by the cargo loading. Moreover, the travel distance was frequently more than 100 μm which would be sufficient in lab-on-a-chip systems or other nanotechnological applications.

ACCEPTED MANUSCRIPT

Biotin-engineered actin filaments that are propelled by myosin motors were also investigated with respect to their capability to transport streptavidin coated liposome cargoes (> 50 nm diameter) that were fluorescently labelled with calcein (Persson et al., 2013). In this case, an effect of cargo-loading on velocity was observed when more than one liposome was attached to the filament, suggesting that the cargo bulkiness produced an inhibitory effect on sliding. On the other hand the sliding velocity was unaffected for a long time (10 min) if only a single liposome was attached to the filaments. Overall, bulky cargoes seem to affect the fraction of motile filaments and the myosin propelled sliding velocity to appreciably larger degree than small cargoes (of size comparable to quantum dots or less) (Persson et al., 2013).

4.3.3. Covalent cross-linking in actin filaments

The approaches for covalent conjugation described above have also been used to create inter-subunit or intra-subunit cross-links in F-actin. The aims of these studies have been to elucidate steric aspects of inter-subunit interactions on the one hand and the possible importance of dynamic changes in subunit structure or inter-subunit interactions upon binding of myosin and other actin-binding proteins (Elzinga and Phelan, 1984; Knight and Offer, 1978; Prochniewicz et al., 1993). In early cross-linking experiments (Knight and Offer, 1978) it was shown that p-NN'-phenylenebismaleimide could form cross-links between Cys-374 on one actin subunit and a lysine on a neighboring subunit (later found to be Lys-191; (Elzinga and Phelan, 1984). It was also found (Knight and Offer, 1978) that the cross-linking events were random along the filament and that a maximum of 0.5 cross-links per subunit was formed. More recently, covalent cross-links have been introduced between cysteines that had been genetically engineered into predetermined locations on the actin structure (Pengelly et al., 2009; Scoville et al., 2009) for further insight into the geometry and dynamics of inter-subunit and intra-subunit interactions.

For investigation of the role of structural changes within actin subunits in force-producing interactions with myosin, G-actin was internally cross-linked with EDC (Prochniewicz et al., 1993). These cross-linked monomers were then co-polymerized with unmodified monomers into F-actin and different effects on the actin-myosin interaction were studied, considering that the internally cross-linked subunits could not interact productively with myosin. Finally, photo-induced cross-linking, with the formation of actin-subunit dimers, has been observed (Niedermayer et al., 2012) within actin filaments covalently labelled with a variety of fluorophores, either on lysines or cysteine. The cross-linking led to temporary pause in depolymerization, possibly useful as a “molecular switch” for freezing the dynamics of actin filaments by changes in illumination.

4.3.4. Engineering of actin filaments with gold nanoparticles

Gold nanoparticles covalently loaded with drugs (referred to as drug-gold nanocomposites) have been covalently conjugated to actin filaments using EDC/NHS chemistry (Kaur et al., 2011). Three concepts for transportation of drugs into the cell, using such engineered actin filaments and myosin motors were proposed. The first proposed concept is based on electrostatic interaction with the negative charge of the cell membrane. This could possibly be achieved by formation of complexes between negatively charged actin filaments and polycationic polymers or divalent cations. The second concept is based on the interaction of actin filaments with myosin heads located on the cell membrane. The third proposed concept

ACCEPTED MANUSCRIPT

is denoted Biomolecular Adaptor for Retrograde Transport (BART) where myosin in the cell periphery interacts with the actin filaments that carry the drug-gold nanocomposites. These concepts have been postulated to be useful in drug delivery systems and are described in detail elsewhere (Kaur et al., 2011). However, the actin filaments with their cargoes need to be transported to their site of action presumably via the blood stream. A key challenge in this context includes passage of actin filaments over the capillary walls. Furthermore, it is uncertain whether actin function is maintained after exposure to blood and blood plasma (Korten et al., 2013).

In addition to the use in cargo transportation, actin filaments coated with gold nanoparticles have also been explored for design and patterning of actin-based gold nanowires (Gazit, 2007; Patolsky et al., 2004; Willner and Willner, 2010; Wu et al., 2014). In this case, the engineered actin filaments served as a templates for continuous growth of gold nanowires. Gold nanoparticles (1.4 nm), functionalized with a single *N*-hydroxysuccinimidyl active ester first reacted with primary amines on lysine residues to form covalent bonds with actin filaments. The engineered actin filament was then depolymerised by exchange to depolymerizing solution conditions using dialysis. The G-actin monomers that were obtained in this procedure were, on average, conjugated with one gold nanoparticle. The gold nanoparticle-conjugated actin monomers were next allowed to polymerize into gold nanoparticle conjugated actin filaments. This was followed by a catalytic enhancement process to grow a continuous gold nanowire. Additionally, a series of nanowire patterns were also prepared (Patolsky et al., 2004) by forming non-labelled actin filaments and gold labelled actin filaments in a sequential way (Fig. 12). This method has potential applications in nanobiotechnology, including fabrication of metallic nanowires or conductive nanostructures even in three dimensions (Galland et al., 2013; Gazit, 2007; Willner and Willner, 2010; Wu et al., 2014).

4.3.5. Engineering of actin filaments with quantum dots without biotin-streptavidin

In analogy to the use of gold nanoparticles for fabrication of metallic nanowires, quantum dot (QD) engineered actin filaments have been used as templates for fabrication of semiconductor nanowires (Wu et al., 2014; Yao et al., 2009). Such nanowires may be useful in nanotechnological applications e.g. as optical or electrical devices including different sensors. Three different approaches have been described for the covalent interaction of PEG-amine coated quantum dots (amine-QDs) with actin filaments (Fig. 13). Actin filaments were first stabilized by phalloidin or rhodamine phalloidin in solution. Then, one of the following steps (i-iii) followed: (i) The carboxyl groups of the actin filaments were activated using EDC/NHS chemistry to enable spontaneous reaction with amine-QDs. (ii) The sulfhydryl groups (SH) of actin were reacted with amine-QDs using the heterobifunctional cross linker (N-[γ-maleimidobutyryloxy]sulfosuccinimide ester). The sulfoscuccinimide ester moiety of the cross-linker first reacts with the amine-QD followed by removal of excess cross linker by passage through a sephadex spin column. The maleimide moiety of the QD-cross-linker then reacts with sulfhydryl groups of the actin filaments. (iii) Finally, a third approach for creation of QD-templated semiconductor nanowires relied on the attachment of QDs to actin via Phallacidin. The latter compound has similar structure and actin-binding property as phalloidin (Barak et al., 1980; Singhal and Hays, 1988; Yao et al., 2009). Additionally it has readily modifiable carboxyl groups (Yao et al., 2009). In the phallacidin dependent approach, amine-QDs were covalently attached to these carboxyl groups of phallacidin using EDC/NHS chemistry followed by purification using a sephadex spin column.

ACCEPTED MANUSCRIPT

4.3.6. Engineering of actin filaments with antibodies

Antibodies, also known as immunoglobulins (Ig), are glycoproteins that are produced by plasma cells and circulated in the blood plasma and the lymphatic system. Antibodies bind to macromolecular antigens through noncovalent interactions including van der Waals forces and hydrogen bonds. Whereas these interactions are highly specific, the participating bonds are rather weak and may be dissociated by high temperature, low/high pH and/or high ionic strength. Myosin-propelled actin filaments, engineered with antibodies, have been utilized with the aim to develop miniaturized biosensors either to substitute microfluidics driven transportation of antibody captured antigen or to provide a specific detection mechanism (see further sections 5-6). A priori it was expected to be challenging to covalently conjugate polyclonal or monoclonal antibodies to actin filaments without either loosing filament integrity or severely compromising propulsion of the filament by myosin. There are different reasons for these concerns. First, whereas effective antibody-antigen transportation was previously demonstrated with kinesin propelled microtubules (Bachand et al., 2006; Korten et al., 2010; Ramachandran et al., 2006), the actin filaments have fewer surface attachment sites per μm for the myosin motors than microtubules have for kinesin. Furthermore, kinesin 1 is a processive motor that spends a larger fraction of its cycle time attached to microtubules than non-processive myosin II motors spend attached to actin. Therefore, fewer motors need to interact with the microtubules than with the actin filaments for continuous transportation. All this suggests that antibody attachment to actin filaments could have more severe effects on transportation than antibody attachment to microtubules. An additional concern was that the actin polymerization capability might be affected by attachment of bulky cargoes, because even conjugation with small-molecular fluorophores prevented monomers to contribute to the filament elongation rate (see above).

Interestingly, despite the above concerns, recently developed methods (Kumar et al., 2013; Kumar et al., 2012) achieved covalent conjugation of actin filaments with monoclonal and polyclonal antibodies with maintained polymerization capability as well as with maintained myosin propulsion. Furthermore, it was later found (Kumar et al., 2016b) that these filaments with antibodies could also be incorporated into polar fascin-actin bundles with maintained antigen binding as well as myosin propulsion.

In the antibody-actin coupling process (Kumar et al., 2012), actin filaments and antibodies were first separately modified with heterobifunctional cross-linkers followed by the actual cross-linking step (Fig. 14). The described conjugation methods are entirely UV-traceable allowing monitoring of each step (Fig. 15). Moreover, conjugation bands can be seen in SDS-PAGE which is useful for further semi quantitative analysis (Kumar et al., 2012).

Following conjugation, we demonstrated the presence of antibody-conjugated actin monomers as well as antibody conjugated actin filaments (Kumar et al., 2012). We also found that antibody-conjugated actin monomers were copolymerized with non-conjugated monomers to form filamentous actin albeit with a rather limited number of attached antibodies (Kumar et al., 2012).

The capturing of antigen by the antibodies on the actin filaments was evaluated using rhodamine labelled or biotinylated antigen (Kumar et al., 2016b; Kumar et al., 2012). In the case of biotinylated antigen, rhodamine labelled streptavidin was used for staining. Interestingly, we observed negligible effects (Kumar et al., 2012) of antibody-mediated capturing of antigen on the fraction of motile actin filaments and their velocities when the

ACCEPTED MANUSCRIPT

actin filaments were propelled by surface-adsorbed HMM in the presence of 1 mM MgATP. The major challenge identified for future work (Kumar et al., 2012) was the need to improve the antibody labelling procedure for increased density of antibodies along the actin filament.

Nanodiamonds are diamond nanocrystals with interesting mechanical and optical properties and low toxicity (Mochalin et al., 2012). Recently, nanodiamond engineered actin filaments have been prepared (Bradac et al., 2016). Carboxylated nanodiamonds (size ~ 30 nm) were first covalently labelled with monoclonal antibody against α-actin ((5C5) mouse IgM), using well known EDC/Sulfo-NHS protocol. Antibody-conjugated nanodiamonds were then added to a mixture of phalloidin and actin filaments followed by overnight incubation at 4 °C. A new complex of nanodiamond-antibody-actin filaments was thereby formed. Actin filaments engineered with fluorescent nanodiamonds could be visualized for a long time without photobleaching, similar to what has previously been observed with quantum dot labelled actin filaments (Mansson et al., 2004).

4.3.7. Surface-immobilization of actin

Surface immobilization of actin has been explored for a range of different applications. Poly(methyl methacrylate) (PMMA), poly(styrene-maleic acid (PSMA) and poly(t-butyl methacrylate) (PBM) coated flow cell surfaces have been tested for this purpose (Alexeeva et al., 2005). These polymeric surfaces were used for fabrication of microstructures and were activated with EDC/NHS chemistry for 1 h followed by several times wash with pure water. For covalent immobilization or physical adsorption of actin, RhPh or APh labelled globular actin was infused into the flow cell. The PSMA surfaces showed good compatibility with actin. Furthermore, they can be microstructured, are straightforward to activate for covalent immobilization of actin and they lack autofluorescence. Actin filaments have also been immobilized on chitin particles for purification of myosin II (de Souza et al., 2008). In this case, hexamethylenediamine (HEMDA) and glutaraldehyde were first used to activate chitin particles for covalent cross-linking of actin filaments. Affinity chromatography columns were then prepared from chitin-engineered actin filaments to be utilized in the capture of myosin II from extracts (for details see (de Souza et al., 2008)). Finally, MgATP was added in the elution buffer for the removal of myosin II from the actin filaments. This method may be useful for myosin II purification.

5. Use of engineered actin filaments in nanodevices

The possible use of actin filaments and associated motor proteins in nanobiodevices has been reviewed recently (Korten et al., 2010; Mansson, 2012). Whereas these applications are not in immediate focus here, it is of interest to consider examples where the use of engineered actin filaments play a prominent role and pose significant advantages compared to standard methods. For instance, using a suitably nanopatterned in vitro motility assay surface, antibody conjugated actin filaments may capture analytes (antigens) from large (almost millimeter sized) areas and transport them at rates of >10 μm/s to a nanoscale detector (cf. (Katira and Hess, 2010)). This process, using self-propelled antibody-conjugated actin filaments, circumvents several challenges in microfluidics driven transport such as need for bulky accessory equipment and large pressure gradients. In addition to the substitution of microfluidics based transport, actual detection of analytes may also be achieved in unique ways. This includes the detection of inhibited actin filament transport or markedly reduced

ACCEPTED MANUSCRIPT

filament velocity in the presence of analyte (Martinez-Neira et al., 2005) or co-localization and co-transportation of actin filaments and analytes (cf. principles in (Fischer et al., 2009; Kumar et al., 2012; Soto et al., 2008). The latter method uniquely distinguishes specific antibody–antigen binding from non-specific surface binding, with increased sensitivity and specificity compared to methods with surface-immobilized antibodies. Indeed, the fast transportation of the analyte to a nanoscale detector area via myosin based propulsion of actin filaments with model recognition molecules (Lard et al., 2013) represents a more advanced special case of co-transportation. It both achieves appreciable signal enhancement and increased specificity while also overcoming the slow diffusion limited transport to nanoscale detectors (Katira and Hess, 2010).

The use of engineered actin filaments in nanodevices, e.g. to capture an antigen from bulk fluids and transport it to a detector is not entirely straightforward. For instance, the molecular motor driven propulsion of both actin filaments and microtubules, seems to be deleteriously affected by the presence of complex body fluids including blood serum, blood plasma and cell lysates (Korten et al., 2013). More than 100 times dilution was required to eliminate these effects. More recently, we therefore investigated if it was possible to include an initial step with capture of analytes from serum by magnetic particles that were conjugated with antibodies. This allowed exchange of serum for appropriate biological buffer after pelleting the captured analyte using a magnetic force. We presented evidence (Kumar et al., 2013) that antibody engineered actin filaments (same polyclonal antibody as on magnetic particles) could pick up the magnetic particle-polyclonal antibody-analyte complexes with maintained ATP driven transportation by HMM (Fig. 16). Clearly, this approach holds considerable potential. By usage of two different monoclonal antibodies (cf. (Fischer et al., 2009) raised against different epitopes on the analyte target, one type on the magnetic particles and one type on the actin filaments, the method would be much improved. First, the target selectivity would be appreciably increased. Second, the risk would be eliminated for formation of aggregates, via analyte and polyclonal antibodies, between several magnetic particles, on the one hand, and between several actin filaments on the other hand (Kumar et al., 2013).

Further utilization of engineered actin filaments have been recently demonstrated (Kumar et al., 2016b) in the production of a self-propelled high capacity nanocarrier. This was achieved by self-assembling parallel unipolar bundles of actin filaments, conjugated with monoclonal or polyclonal antibodies, using the acin-bundling protein fascin (Fig. 17). With the effort to develop of label-free detection systems using individual antibody engineered actin filaments or actin-bundled nanocarriers we investigated (Kumar et al., 2016b) the capture and transportation of proteins and microvesicles by these types of actin-based polymers. Microvesicles (MVs), are small vesicles pinched off from plasma membrane with diameters ranging from 100 nm to 1000 nm. MVs may have roles in the transportation of molecules and in intercellular communication (Raposo and Stoorvogel, 2013). They have been considered as diagnostic biomarkers for several diseases (cf. references in (Kumar et al., 2016b)) e.g. leukemia. In our recent experiments (Kumar et al., 2016b) we found that polyclonal antibody engineered nanocarriers can be loaded with up to 1 protein antigen per nm length with maintained capability to be transported by HMM in vitro. It was further observed that monoclonal antibody engineered actin filaments were able to capture microvesicles. However, only rarely was the transportation capability maintained. Possible mechanisms for this motility inhibition was discussed previously (Kumar et al., 2016b). Nevertheless, the aggregation of nanocarriers via the microvesicles, a major basis for motility inhibition, is potentially useful for detection (cf. patent (Mansson and Tagerud, 2014)) because the aggregates are readily detected e.g. by fluorescence microscopy (cf. Fig. 18).

ACCEPTED MANUSCRIPT

6. Concluding remarks and perspectives

We have reviewed different approaches for conjugation of actin filaments with nanoparticles and other molecules, such as fluorophores and different macromolecules, demonstrating the existence of a wide spectrum of approaches. These either rely on covalent bonds or specific non-covalently attached linker molecules (actin-binding proteins and toxins) to link conjugates to the actin filament. We have also shown that the different conjugation methods pose different challenges and advantages and their use are associated with different critical steps. Finally we have given examples of a wide range of applications of the different approaches for both nanotechnological applications and fundamental studies. We hope that this review and the huge source of actin as one of the most abundant eukaryotic proteins, will promote a more extensive use of actin conjugation approaches in biotechnology as well as in fundamental studies of actin in health and disease.

Future developments of interest for application of actin filaments in diagnostics and nanoseparation include higher and more consistent antibody-actin conjugation ratios (Kumar et al., 2012) but also covalent tagging with e.g. oligonucleotides. Attachment of oligonucleotides and DNA has been demonstrated for microtubules (Dinu et al., 2006; Hiyama et al., 2009) but, to the best of our knowledge, not yet for actin filaments. In principle, the tagging should be trivially achievable using any of the conjugation methods described above. Oligonucleotide conjugation would be of interest for specific identity tagging (barcoding) of individual filaments but also for applications in nanoseparation and diagnostics where the oligonucleotides on an actin filament may capture complementary oligonucleotides and either cross-link with other filaments to form aggregates (showing presence of the complementary oligonucleotide; Månsson and Tågerud, US patent; (Kumar et al., 2016b; Mansson and Tagerud, 2014)) or be propelled by myosin motors, transporting the complementary nucleotide to a nanoscale detector. A concern in relation to oligonucleotide tagging is that the negatively charged oligonucleotides may interact electrostatically with the positively charged actin binding region of the myosin motor domain. This may compete with the binding of myosin to actin and/or produce electrostatic drag forces that cause a brake on the myosin induced propulsion of the actin filament. These effects are likely to be more severe for the non-processive actomyosin interaction than for the processive microtubule kinesin interaction where the number of available motor-binding sites is also considerably higher than for the myosin-actin interaction. Investigations are needed to clarify whether these challenges can be overcome to produce myosin propelled actin-oligonucleotide conjugates for nanotechnological applications. In addition to the mentioned applications it may also be of interest to attach programmable elements to actin filaments that are switched to another state (e.g. by light; c.f. (Kocer et al., 2005; Nakamura et al., 2014; Velema et al., 2013)) when the filament passes a certain point on a chip. Such elements could possibly also be of value in fundamental studies of actomyosin function by switching on or off functionalities that may change the properties of the filament. Finally, the techniques described above would be equally well applied to other isoforms of actin than α-actins conventionally used for nanotechnological applications. These isoforms may also be readily isolated e.g. using DNAase-1 affinity chromatography (Aspenstrom and Karlsson, 1991; Schafer et al., 1998). A possible reason for using non-α actin isoforms is different properties in certain regards, e.g. different flexural rigidity or incorporation of alternative conjugation sites or modified mechanical properties by genetic engineering (Kang et al., 2014).

ACCEPTED MANUSCRIPT

Acknowledgments

This work was funded by SERB-Department of Science and Technology, Government of India under fast track young scientist scheme (SB/YS/LS-75/2013). S. K. thanks to SERB-DST, Govt. of India for the award of Fast Track Young Scientist (SB/YS/LS-75/2013), The European commission (FP7) under the contract MONAD (NMP4-SL-2009-228971), and the FP7 and Horizon 2020 FET-programmes ABACUS (#613044) and Bio4comp (#732482). Furthermore, funding is acknowledged from The Carl Trygger Foundation, The Swedish Research Council (Project 621-2010-5146 and Project 2015-05290), The Faculty of Natural Sciences and Engineering and the Faculty of Health and Life Sciences at the Linnaeus University.

Conflict of interest: Alf Månsson is a co-founder, co-owner and CEO of the start-up company ActoSense Biotech AB (Kalmar, Sweden) aiming to develop diagnostic devices based on the aggregation of cytoskeletal elements, particularly actin filaments, in solution. Moreover, A Månsson holds two Swedish patents as well as one US and one European patent in this field.

ACCEPTED MANUSCRIPT

ACCEPTED MANUSCRIPT

References

Adachi, K., Kinosita Jr, K., Ando, T., 1999. Single-fluorophore imaging with an unmodified epifluorescence microscope and conventional video camera. Journal of microscopy 195 (Pt 2), 125-132.
Adamek, N., Geeves, M.A., 2014. Use of pyrene-labelled actin to probe actin-myosin interactions: kinetic and equilibrium studies. Exs 105, 87-104.
Adams, J.C., 1995. Formation of stable microspikes containing actin and the 55 kDa actin bundling protein, fascin, is a consequence of cell adhesion to thrombospondin-1: implications for the anti-adhesive activities of thrombospondin-1. Journal of cell science 108 (Pt 5), 1977-1990.
Agarwal, A., Hess, H., 2010. Biomolecular motors at the intersection of nanotechnology and polymer science. Progress in Polymer Science 35(1–2), 252-277.
Albet-Torres, N., Gunnarsson, A., Persson, M., Balaz, M., Hook, F., Mansson, A., 2010. Molecular motors on lipid bilayers and silicon dioxide: different driving forces for adsorption. Soft Matter 6(14), 3211-3219.
Alexeeva, Y.V., Ivanova, E.P., Pham, D.K., Buljan, V., Sbarski, I., Ilkov, M., Brinkies, H.G., Nicolau, D.V., 2005. Controlled self-assembly of actin filaments for dynamic biodevices. NanoBiotechnology 1(4), 379-388.
Allen, P.G., Janmey, P.A., 1994. Gelsolin displaces phalloidin from actin filaments. A new fluorescence method shows that both Ca2+ and Mg2+ affect the rate at which gelsolin severs F-actin. The Journal of biological chemistry 269(52), 32916-32923.
Amann, K.J., Pollard, T.D., 2001a. The Arp2/3 complex nucleates actin filament branches from the sides of pre-existing filaments. Nature cell biology 3(3), 306-310.
Amann, K.J., Pollard, T.D., 2001b. Direct real-time observation of actin filament branching mediated by Arp2/3 complex using total internal reflection fluorescence microscopy. Proceedings of the National Academy of Sciences of the United States of America 98(26), 15009-15013.
Anderl, J., Echner, H., Faulstich, H., 2012. Chemical modification allows phallotoxins and amatoxins to be used as tools in cell biology. Beilstein journal of organic chemistry 8, 2072-2084.
Andre, E., Lottspeich, F., Schleicher, M., Noegel, A., 1988. Severin, gelsolin, and villin share a homologous sequence in regions presumed to contain F-actin severing domains. The Journal of biological chemistry 263(2), 722-727.
Asokan, S.B., Jawerth, L., Carroll, R.L., Cheney, R.E., Washburn, S., Superfine, R., 2003. Two-Dimensional Manipulation and Orientation of Actin−Myosin Systems with Dielectrophoresis. Nano letters 3(4), 431-437.
Aspenstrom, P., Karlsson, R., 1991. Interference with myosin subfragment-1 binding by site-directed mutagenesis of actin. European journal of biochemistry / FEBS 200(1), 35-41.
Bachand, G.D., Rivera, S.B., Carroll-Portillo, A., Hess, H., Bachand, M., 2006. Active capture and transport of virus particles using a biomolecular motor-driven, nanoscale antibody sandwich assay. Small (Weinheim an der Bergstrasse, Germany) 2(3), 381-385.
Bai, F., Caster, H.M., Rubenstein, P.A., Dawson, J.F., Kawai, M., 2014. Using baculovirus/insect cell expressed recombinant actin to study the molecular pathogenesis of HCM caused by actin mutation A331P. Journal of molecular and cellular cardiology 74, 64-75.
Baines, I.C., Corigliano-Murphy, A., Korn, E.D., 1995. Quantification and localization of phosphorylated myosin I isoforms in Acanthamoeba castellanii. The Journal of cell biology 130(3), 591-603.

ACCEPTED MANUSCRIPT

Bains, G., Patel, A.B., Narayanaswami, V., 2011. Pyrene: a probe to study protein conformation and conformational changes. Molecules (Basel, Switzerland) 16(9), 7909-7935.

Bakewell, D.J.G., Nicolau, D.V., 2007. Protein Linear Molecular Motor-Powered Nanodevices. Australian Journal of Chemistry 60(5), 314-332.

Balaz, M., Mansson, A., 2005. Detection of small differences in actomyosin function using actin labeled with different phalloidin conjugates. Analytical biochemistry 338(2), 224-236.

Barak, L.S., Yocum, R.R., Nothnagel, E.A., Webb, W.W., 1980. Fluorescence staining of the actin cytoskeleton in living cells with 7-nitrobenz-2-oxa-1,3-diazole-phallacidin. Proceedings of the National Academy of Sciences of the United States of America 77(2), 980-984.

Barden, J.A., Miki, M., Hambly, B.D., Dos Remedios, C.G., 1987. Localization of the phalloidin and nucleotide-binding sites on actin. European journal of biochemistry / FEBS 162(3), 583-588.

Bayer, E.A., Wilchek, M., 1980. The use of the avidin-biotin complex as a tool in molecular biology. Methods of biochemical analysis 26, 1-45.

Beausang, J.F., Shroder, D.Y., Nelson, P.C., Goldman, Y.E., 2013. Tilting and wobble of myosin V by high-speed single-molecule polarized fluorescence microscopy. Biophysical journal 104(6), 1263-1273.

Bengtsson, E., Persson, M., Rahman, M.A., Kumar, S., Takatsuki, H., Mansson, A., 2016. Myosin-Induced Gliding Patterns at Varied [MgATP] Unveil a Dynamic Actin Filament. Biophysical journal 111(7), 1465-1477.

Berg, J.S., Powell, B.C., Cheney, R.E., 2001. A millennial myosin census. Molecular biology of the cell 12(4), 780-794.

Bianco, P., Nagy, A., Kengyel, A., Szatmari, D., Martonfalvi, Z., Huber, T., Kellermayer, M.S., 2007. Interaction forces between F-actin and titin PEVK domain measured with optical tweezers. Biophysical journal 93(6), 2102-2109.

Blanchoin, L., Boujemaa-Paterski, R., Sykes, C., Plastino, J., 2014. Actin dynamics, architecture, and mechanics in cell motility. Physiological reviews 94(1), 235-263.

Bledzka, K., Bialkowska, K., Sossey-Alaoui, K., Vaynberg, J., Pluskota, E., Qin, J., Plow, E.F., 2016. Kindlin-2 directly binds actin and regulates integrin outside-in signaling. The Journal of cell biology 213(1), 97-108.

Bombardier, J.P., Eskin, J.A., Jaiswal, R., Correa, I.R., Jr., 2015. Single-molecule visualization of a formin-capping protein 'decision complex' at the actin filament barbed end. 6, 8707.

Bookwalter, C.S., Trybus, K.M., 2006. Functional consequences of a mutation in an expressed human alpha-cardiac actin at a site implicated in familial hypertrophic cardiomyopathy. The Journal of biological chemistry 281(24), 16777-16784.

Bradac, C., Say, J.M., Rastogi, I.D., Cordina, N.M., Volz, T., Brown, L.J., 2016. Nano-assembly of nanodiamonds by conjugation to actin filaments. Journal of biophotonics 9(3), 296-304.

Brangbour, C., du Roure, O., Helfer, E., Demoulin, D., Mazurier, A., Fermigier, M., Carlier, M.F., Bibette, J., Baudry, J., 2011. Force-velocity measurements of a few growing actin filaments. PLoS biology 9(4), e1000613.

Breitsprecher, D., Jaiswal, R., Bombardier, J.P., Gould, C.J., Gelles, J., Goode, B.L., 2012. Rocket launcher mechanism of collaborative actin assembly defined by single-molecule imaging. Science (New York, N.Y.) 336(6085), 1164-1168.

Brieher, W., 2013. Mechanisms of actin disassembly. Molecular biology of the cell 24(15), 2299-2302.

ACCEPTED MANUSCRIPT

Brough, B., Christman, K.L., Wong, T.S., Kolodziej, C.M., Forbes, J.G., Wang, K., Maynard, H.D., Ho, C.-M., 2007. Surface initiated actin polymerization from top-down manufactured nanopatterns. Soft Matter 3(5), 541-546.
Bugyi, B., Carlier, M.F., 2010. Control of actin filament treadmilling in cell motility. Annual review of biophysics 39, 449-470.
Burtnick, L.D., 1984. Modification of actin with fluorescein isothiocyanate. Biochimica et biophysica acta 791(1), 57-62.
Bustamante, C., Chemla, Y.R., Forde, N.R., Izhaky, D., 2004. Mechanical processes in biochemistry. Annual review of biochemistry 73, 705-748.
Butkevich, E., Bodensiek, K., Fakhri, N., von Roden, K., Schaap, I.A.T., Majoul, I., Schmidt, C.F., Klopfenstein, D.R., 2015. Drebrin-like protein DBN-1 is a sarcomere component that stabilizes actin filaments during muscle contraction. Nature communications 6.
Cano, M.L., Cassimeris, L., Joyce, M., Zigmond, S.H., 1992. Characterization of tetramethylrhodaminyl-phalloidin binding to cellular F-actin. Cell motility and the cytoskeleton 21(2), 147-158.
Carlier, M.F., 1989. Role of nucleotide hydrolysis in the dynamics of actin filaments and microtubules. International review of cytology 115, 139-170.
Carlier, M.F., 1990. Actin polymerization and ATP hydrolysis. Advances in biophysics 26, 51-73.
Carlier, M.F., Pernier, J., Montaville, P., Shekhar, S., Kuhn, S., 2015. Control of polarized assembly of actin filaments in cell motility. Cellular and molecular life sciences : CMLS 72(16), 3051-3067.
Carvalho, K., Lemiere, J., Faqir, F., Manzi, J., Blanchoin, L., Plastino, J., Betz, T., Sykes, C., 2013. Actin polymerization or myosin contraction: two ways to build up cortical tension for symmetry breaking. Philosophical transactions of the Royal Society of London. Series B, Biological sciences 368(1629), 20130005.
Chazotte, B., 2010. Labeling cytoskeletal F-actin with rhodamine phalloidin or fluorescein phalloidin for imaging. Cold Spring Harbor protocols 2010(5), pdb.prot4947.
Chivers, C.E., Koner, A.L., Lowe, E.D., Howarth, M., 2011. How the biotin-streptavidin interaction was made even stronger: investigation via crystallography and a chimaeric tetramer. The Biochemical journal 435(1), 55-63.
Collins, J.H., Elzinga, M., 1975. The primary structure of actin from rabbit skeletal muscle. Completion and analysis of the amino acid sequence. The Journal of biological chemistry 250(15), 5915-5920.
Combeau, C., Didry, D., Carlier, M.F., 1992. Interaction between G-actin and myosin subfragment-1 probed by covalent cross-linking. The Journal of biological chemistry 267(20), 14038-14046.
Conibear, P.B., Bagshaw, C.R., Fajer, P.G., Kovacs, M., Malnasi-Csizmadia, A., 2003. Myosin cleft movement and its coupling to actomyosin dissociation. Nature structural biology 10(10), 831-835.
Cooke, R., 1997. Actomyosin interaction in striated muscle. Physiological reviews 77(3), 671-697.
Cooper, J.A., 1987. Effects of cytochalasin and phalloidin on actin. The Journal of cell biology 105(4), 1473-1478.
Cooper, J.A., Buhle, E.L., Jr., Walker, S.B., Tsong, T.Y., Pollard, T.D., 1983a. Kinetic evidence for a monomer activation step in actin polymerization. Biochemistry 22(9), 2193-2202.
Cooper, J.A., Pollard, T.D., 1982. Methods to measure actin polymerization. Methods in enzymology 85 Pt B, 182-210.

ACCEPTED MANUSCRIPT

Cooper, J.A., Walker, S.B., Pollard, T.D., 1983b. Pyrene actin: documentation of the validity of a sensitive assay for actin polymerization. Journal of muscle research and cell motility 4(2), 253-262.
Criddle, A.H., Geeves, M.A., Jeffries, T., 1985. The use of actin labelled with N-(1-pyrenyl)iodoacetamide to study the interaction of actin with myosin subfragments and troponin/tropomyosin. The Biochemical journal 232(2), 343-349.
Cross, R.A., Carter, N.J., 2000. Molecular motors. Current Biology 10(5), R177-R179.
Dancker, P., Low, I., Hasselbach, W., Wieland, T., 1975. Interaction of actin with phalloidin: polymerization and stabilization of F-actin. Biochimica et biophysica acta 400(2), 407-414.
De La Cruz, E.M., Pollard, T.D., 1994. Transient kinetic analysis of rhodamine phalloidin binding to actin filaments. Biochemistry 33(48), 14387-14392.
De La Cruz, E.M., Pollard, T.D., 1996. Kinetics and thermodynamics of phalloidin binding to actin filaments from three divergent species. Biochemistry 35(45), 14054-14061.
de Souza, M.G., Grossi, A.L., Pereira, E.L., da Cruz, C.O., Mendes, F.M., Cameron, L.C., Paiva, C.L., 2008. Actin immobilization on chitin for purifying myosin II: A laboratory exercise that integrates concepts of molecular cell biology and protein chemistry. Biochemistry and molecular biology education : a bimonthly publication of the International Union of Biochemistry and Molecular Biology 36(1), 55-60.
Deibler, M., Spatz, J.P., Kemkemer, R., 2011. Actin fusion proteins alter the dynamics of mechanically induced cytoskeleton rearrangement. PloS one 6(8), e22941.
Demé, B., Hess, D., Tristl, M., Lee, L.-T., Sackmann, E., 2000. Binding of actin filaments to charged lipid monolayers: Film balance experiments combined with neutron reflectivity. The European Physical Journal E 2(2), 125-136.
Detmers, P., Weber, A., Elzinga, M., Stephens, R.E., 1981. 7-Chloro-4-nitrobenzeno-2-oxa-1,3-diazole actin as a probe for actin polymerization. The Journal of biological chemistry 256(1), 99-105.
Diamandis, E.P., Christopoulos, T.K., 1991. The biotin-(strept)avidin system: principles and applications in biotechnology. Clinical chemistry 37(5), 625-636.
Diensthuber, R.P., Muller, M., Heissler, S.M., Taft, M.H., Chizhov, I., Manstein, D.J., 2011. Phalloidin perturbs the interaction of human non-muscle myosin isoforms 2A and 2C1 with F-actin. FEBS letters 585(5), 767-771.
Dinu, C.Z., Opitz, J., Pompe, W., Howard, J., Mertig, M., Diez, S., 2006. Parallel manipulation of bifunctional DNA molecules on structured surfaces using kinesin-driven microtubules. Small (Weinheim an der Bergstrasse, Germany) 2(8-9), 1090-1098.
Dominguez, R., 2004. Actin-binding proteins – a unifying hypothesis. Trends in Biochemical Sciences 29(11), 572-578.
Dominguez, R., Holmes, K.C., 2011. Actin structure and function. Annual review of biophysics 40, 169-186.
Doolittle, L.K., Rosen, M.K., Padrick, S.B., 2013. Measurement and analysis of in vitro actin polymerization. Methods in molecular biology (Clifton, N.J.) 1046, 273-293.
dos Remedios, C.G., Chhabra, D., Kekic, M., Dedova, I.V., Tsubakihara, M., Berry, D.A., Nosworthy, N.J., 2003. Actin binding proteins: regulation of cytoskeletal microfilaments. Physiological reviews 83(2), 433-473.
dos Remedios, C.G., Miki, M., Barden, J.A., 1987. Fluorescence resonance energy transfer measurements of distances in actin and myosin. A critical evaluation. Journal of muscle research and cell motility 8(2), 97-117.

ACCEPTED MANUSCRIPT

Drummen, G.P., 2012. Fluorescent probes and fluorescence (microscopy) techniques--illuminating biological and biomedical research. Molecules (Basel, Switzerland) 17(12), 14067-14090.
Dundas, C.M., Demonte, D., Park, S., 2013. Streptavidin-biotin technology: improvements and innovations in chemical and biological applications. Applied microbiology and biotechnology 97(21), 9343-9353.
Egelman, E.H., Orlova, A., 2001. Two conformations of G-actin related to two conformations of F-actin. Results and problems in cell differentiation 32, 95-101.
Eisenberg, E., Hill, T.L., 1978. A cross-bridge model of muscle contraction. Progress in biophysics and molecular biology 33(1), 55-82.
Eligula, L., Chuang, L., Phillips, M.L., Motoki, M., Seguro, K., Muhlrad, A., 1998. Transglutaminase-induced cross-linking between subdomain 2 of G-actin and the 636-642 lysine-rich loop of myosin subfragment 1. Biophysical journal 74(2 Pt 1), 953-963.
Elzinga, M., Phelan, J.J., 1984. F-actin is intermolecularly crosslinked by N,N'-p-phenylenedimaleimide through lysine-191 and cysteine-374. Proceedings of the National Academy of Sciences of the United States of America 81(21), 6599-6602.
Era, A., Tominaga, M., Ebine, K., Awai, C., Saito, C., Ishizaki, K., Yamato, K.T., Kohchi, T., Nakano, A., Ueda, T., 2009. Application of Lifeact reveals F-actin dynamics in Arabidopsis thaliana and the liverwort, Marchantia polymorpha. Plant & cell physiology 50(6), 1041-1048.
Esaki, S., Ishii, Y., Nishikawa, M., Yanagida, T., 2007. Cooperative actions between myosin heads bring effective functions. Bio Systems 88(3), 293-300.
Faulstich, H., Trischmann, H., Mayer, D., 1983. Preparation of tetramethylrhodaminyl-phalloidin and uptake of the toxin into short-term cultured hepatocytes by endocytosis. Experimental cell research 144(1), 73-82.
Faulstich, H., Zobeley, S., Heintz, D., Drewes, G., 1993. Probing the phalloidin binding site of actin. FEBS letters 318(3), 218-222.
Fischer, T., Agarwal, A., Hess, H., 2009. A smart dust biosensor powered by kinesin motors. Nat Nano 4(3), 162-166.
Foth, B.J., Goedecke, M.C., Soldati, D., 2006. New insights into myosin evolution and classification. Proceedings of the National Academy of Sciences of the United States of America 103(10), 3681-3686.
Fujiwara, I., Remmert, K., Piszczek, G., Hammer, J.A., 2014. Capping protein regulatory cycle driven by CARMIL and V-1 may promote actin network assembly at protruding edges. Proceedings of the National Academy of Sciences of the United States of America 111(19), E1970-1979.
Funatsu, T., Harada, Y., Tokunaga, M., Saito, K., Yanagida, T., 1995. Imaging of single fluorescent molecules and individual ATP turnovers by single myosin molecules in aqueous solution. Nature 374(6522), 555-559.
Galkin, V.E., Orlova, A., Schroder, G.F., Egelman, E.H., 2010. Structural polymorphism in F-actin. Nature structural & molecular biology 17(11), 1318-1323.
Galland, R., Leduc, P., Guerin, C., Peyrade, D., Blanchoin, L., Thery, M., 2013. Fabrication of three-dimensional electrical connections by means of directed actin self-organization. Nature materials 12(5), 416-421.
Gateva, G., Kremneva, E., Reindl, T., Kotila, T., Kogan, K., Gressin, L., Gunning, P.W., Manstein, D.J., Michelot, A., Lappalainen, P., 2017. Tropomyosin Isoforms Specify Functionally Distinct Actin Filament Populations In Vitro. Current biology : CB 27(5), 705-713.
Gazit, E., 2007. Use of biomolecular templates for the fabrication of metal nanowires. The FEBS journal 274(2), 317-322.

ACCEPTED MANUSCRIPT

Ge, P., Durer, Z.A., Kudryashov, D., Zhou, Z.H., Reisler, E., 2014. Cryo-EM reveals different coronin binding modes for ADP- and ADP-BeFx actin filaments. Nature structural & molecular biology 21(12), 1075-1081.

Geeves, M.A., Holmes, K.C., 2005. The molecular mechanism of muscle contraction. Advances in protein chemistry 71, 161-193.

Gicquaud, C., Wong, P., 1994. Mechanism of interaction between actin and membrane lipids: a pressure-tuning infrared spectroscopy study. The Biochemical journal 303 (Pt 3), 769-774.

Gitlin, G., Bayer, E.A., Wilchek, M., 1990. Studies on the biotin-binding sites of avidin and streptavidin. Tyrosine residues are involved in the binding site. The Biochemical journal 269(2), 527-530.

Grabarek, Z., Gergely, J., 1990. Zero-length crosslinking procedure with the use of active esters. Analytical biochemistry 185(1), 131-135.

Grandbois, M., Beyer, M., Rief, M., Clausen-Schaumann, H., Gaub, H.E., 1999. How strong is a covalent bond? Science (New York, N.Y.) 283(5408), 1727-1730.

Green, N.M., 1990. Avidin and streptavidin. Methods in enzymology 184, 51-67.

Griffith, L.M., Pollard, T.D., 1982. Cross-linking of actin filament networks by self-association and actin-binding macromolecules. The Journal of biological chemistry 257(15), 9135-9142.

Grimard, R., Tancrede, P., Gicquaud, C., 1993. Interaction of Actin with Positively Charged Phospholipids: A Monolayer Study. Biochemical and biophysical research communications 190(3), 1017-1022.

Gross, S.R., 2013. Actin binding proteins. Cell Adhesion & Migration 7(2), 199-213.

Guo, K., Shillcock, J., Lipowsky, R., 2010. Treadmilling of actin filaments via Brownian dynamics simulations. The Journal of chemical physics 133(15), 155105.

Gutsche-Perelroizen, I., Lepault, J., Ott, A., Carlier, M.F., 1999. Filament assembly from profilin-actin. The Journal of biological chemistry 274(10), 6234-6243.

Handel, S.E., Hendry, K.A., Sheterline, P., 1990. Microinjection of covalently cross-linked actin oligomers causes disruption of existing actin filament architecture in PtK2 cells. Journal of cell science 97 (Pt 2), 325-333.

Hansen, S.D., Zuchero, J.B., Mullins, R.D., 2013. Cytoplasmic actin: purification and single molecule assembly assays. Methods in molecular biology (Clifton, N.J.) 1046, 145-170.

Hanson, K.L., Fulga, F., Dobroiu, S., Solana, G., Kaspar, O., Tokarova, V., Nicolau, D.V., 2016. Polymer surface properties control the function of heavy meromyosin in dynamic nanodevices. Biosensors & bioelectronics.

Hartman, M.A., Spudich, J.A., 2012. The myosin superfamily at a glance. Journal of cell science 125(Pt 7), 1627-1632.

Hartmann, H., Noegel, A.A., Eckerskorn, C., Rapp, S., Schleicher, M., 1989. Ca2+-independent F-actin capping proteins. Cap 32/34, a capping protein from Dictyostelium discoideum, does not share sequence homologies with known actin-binding proteins. The Journal of biological chemistry 264(21), 12639-12647.

Hayakawa, K., Tatsumi, H., Sokabe, M., 2011. Actin filaments function as a tension sensor by tension-dependent binding of cofilin to the filament. The Journal of cell biology 195(5), 721-727.

He, S., Lam, A.T., Jeune-Smith, Y., Hess, H., 2012. Modeling negative cooperativity in streptavidin adsorption onto biotinylated microtubules. Langmuir : the ACS journal of surfaces and colloids 28(29), 10635-10639.

Hermanson, G.T., 2013. Bioconjugate Techniques, 3 ed. Elsevier Science, San Diego.

ACCEPTED MANUSCRIPT

Hild, G., Bugyi, B., Nyitrai, M., 2010. Conformational dynamics of actin: effectors and implications for biological function. Cytoskeleton (Hoboken, N.J.) 67(10), 609-629.
Hiller, Y., Gershoni, J.M., Bayer, E.A., Wilchek, M., 1987. Biotin binding to avidin. Oligosaccharide side chain not required for ligand association. The Biochemical journal 248(1), 167-171.
Hiyama, S., Gojo, R., Shima, T., Takeuchi, S., Sutoh, K., 2009. Biomolecular-motor-based nano- or microscale particle translocations on DNA microarrays. Nano letters 9(6), 2407-2413.
Holliday, L.S., Lu, M., Lee, B.S., Nelson, R.D., Solivan, S., Zhang, L., Gluck, S.L., 2000. The amino-terminal domain of the B subunit of vacuolar H+-ATPase contains a filamentous actin binding site. The Journal of biological chemistry 275(41), 32331-32337.
Holmberg, A., Blomstergren, A., Nord, O., Lukacs, M., Lundeberg, J., Uhlen, M., 2005. The biotin-streptavidin interaction can be reversibly broken using water at elevated temperatures. Electrophoresis 26(3), 501-510.
Holmes, K.C., Angert, I., Kull, F.J., Jahn, W., Schroder, R.R., 2003. Electron cryo-microscopy shows how strong binding of myosin to actin releases nucleotide. Nature 425(6956), 423-427.
Holmes, K.C., Popp, D., Gebhard, W., Kabsch, W., 1990. Atomic model of the actin filament. Nature 347(6288), 44-49.
Homsher, E., Wang, F., Sellers, J.R., 1992. Factors affecting movement of F-actin filaments propelled by skeletal muscle heavy meromyosin. The American journal of physiology 262(3 Pt 1), C714-723.
Howard, J., 2001. Mechanics of Motor Proteins and the Cytoskeleton. Sinauer Associates, Publishers, Sunderland,
MA.
Howarth, M., Chinnapen, D.J., Gerrow, K., Dorrestein, P.C., Grandy, M.R., Kelleher, N.L., El-Husseini, A., Ting, A.Y., 2006. A monovalent streptavidin with a single femtomolar biotin binding site. Nature methods 3(4), 267-273.
Huang, L., Manandhar, P., Byun, K.E., Chase, P.B., Hong, S., 2006. Selective assembly and alignment of actin filaments with desired polarity on solid substrates. Langmuir : the ACS journal of surfaces and colloids 22(21), 8635-8638.
Huang, Z.J., Haugland, R.P., You, W.M., Haugland, R.P., 1992. Phallotoxin and actin binding assay by fluorescence enhancement. Analytical biochemistry 200(1), 199-204.
Huxley, H.E., 1969. The mechanism of muscular contraction. Science (New York, N.Y.) 164(3886), 1356-1365.
Isambert, H., Venier, P., Maggs, A.C., Fattoum, A., Kassab, R., Pantaloni, D., Carlier, M.F., 1995. Flexibility of actin filaments derived from thermal fluctuations. Effect of bound nucleotide, phalloidin, and muscle regulatory proteins. The Journal of biological chemistry 270(19), 11437-11444.
Isenberg, G., Aebi, U., Pollard, T.D., 1980. An actin-binding protein from Acanthamoeba regulates actin filament polymerization and interactions. Nature 288(5790), 455-459.
Ishijima, A., Kojima, H., Funatsu, T., Tokunaga, M., Higuchi, H., Tanaka, H., Yanagida, T., 1998. Simultaneous observation of individual ATPase and mechanical events by a single myosin molecule during interaction with actin. Cell 92(2), 161-171.
Iwabuchi, S., Takahashi, T., Hatori, K., 2012. Transport of actin-decorated liposomes along myosin molecules in vitro. Biochemical and biophysical research communications 422(1), 164-168.

ACCEPTED MANUSCRIPT

Izdebska, M., Gagat, M., Grzanka, D., Grzanka, A., 2013. Ultrastructural localization of F-actin using phalloidin and quantum dots in HL-60 promyelocytic leukemia cell line after cell death induction by arsenic trioxide. Acta histochemica 115(5), 487-495.
Jansen, S., Collins, A., Chin, S.M., Ydenberg, C.A., Gelles, J., 2015. Single-molecule imaging of a three-component ordered actin disassembly mechanism. 6, 7202.
Jayo, A., Parsons, M., 2010. Fascin: A key regulator of cytoskeletal dynamics. The International Journal of Biochemistry & Cell Biology 42(10), 1614-1617.
Jegou, A., Romet-Lemonne, G., 2016. Single Filaments to Reveal the Multiple Flavors of Actin. Biophysical journal 110(10), 2138-2146.
Johnson, M., East, D.A., Mulvihill, D.P., 2014. Formins determine the functional properties of actin filaments in yeast. Current biology : CB 24(13), 1525-1530.
Johnston, A.B., Collins, A., Goode, B.L., 2015. High-speed depolymerization at actin filament ends jointly catalysed by Twinfilin and Srv2/CAP. Nature cell biology 17(11), 1504-1511.
Kabsch, W., Mannherz, H.G., Suck, D., Pai, E.F., Holmes, K.C., 1990. Atomic structure of the actin:DNase I complex. Nature 347(6288), 37-44.
Kabsch, W., Vandekerckhove, J., 1992. Structure and function of actin. Annual review of biophysics and biomolecular structure 21, 49-76.
Kang, H., Bradley, M.J., Cao, W., Zhou, K., Grintsevich, E.E., Michelot, A., Sindelar, C.V., Hochstrasser, M., De La Cruz, E.M., 2014. Site-specific cation release drives actin filament severing by vertebrate cofilin. Proceedings of the National Academy of Sciences of the United States of America 111(50), 17821-17826.
Kang, H., Bradley, Michael J., Elam, W.A., De La Cruz, Enrique M., 2013. Regulation of Actin by Ion-Linked Equilibria. Biophysical journal 105(12), 2621-2628.
Katira, P., Hess, H., 2010. Two-stage capture employing active transport enables sensitive and fast biosensors. Nano letters 10(2), 567-572.
Kaur, H., Chaudhary, A., Kaur, I., Singh, K., Bharadwaj, L.M., 2011. Transportation of drug–gold nanocomposites by actinomyosin motor system. Journal of Nanoparticle Research 13(6), 2295-2303.
Kaur, H., Kumar, S., Kaur, I., Singh, K., Bharadwaj, L.M., 2009. In-Vitro Transportation of Drug Molecule by Actin Myosin Motor System, in: Lim, C.T., Goh, J.C.H. (Eds.), 13th International Conference on Biomedical Engineering: ICBME 2008 3–6 December 2008 Singapore. Springer Berlin Heidelberg, Berlin, Heidelberg, pp. 902-905.
Kaya, M., Higuchi, H., 2010. Nonlinear elasticity and an 8-nm working stroke of single myosin molecules in myofilaments. Science (New York, N.Y.) 329(5992), 686-689.
Kellogg, D.R., Mitchison, T.J., Alberts, B.M., 1988. Behaviour of microtubules and actin filaments in living Drosophila embryos. Development (Cambridge, England) 103(4), 675-686.
Kilimann, M.W., Isenberg, G., 1982. Actin filament capping protein from bovine brain. The EMBO journal 1(7), 889-894.
Kim, Y., Ho, S.O., Gassman, N.R., Korlann, Y., Landorf, E.V., Collart, F.R., Weiss, S., 2008. Efficient site-specific labeling of proteins via cysteines. Bioconjugate chemistry 19(3), 786-791.
Kinosian, H.J., Selden, L.A., Estes, J.E., Gershman, L.C., 1993. Nucleotide binding to actin. Cation dependence of nucleotide dissociation and exchange rates. Journal of Biological Chemistry 268(12), 8683-8691.
Kitamura, K., Tokunaga, M., Iwane, A.H., Yanagida, T., 1999. A single myosin head moves along an actin filament with regular steps of 5.3 nanometres. Nature 397(6715), 129-134.

ACCEPTED MANUSCRIPT

Knight, P., Offer, G., 1978. p-NN'-phenylenebismaleimide, a specific cross-linking agent for F-actin. The Biochemical journal 175(3), 1023-1032.
Kocer, A., Walko, M., Meijberg, W., Feringa, B.L., 2005. A light-actuated nanovalve derived from a channel protein. Science (New York, N.Y.) 309(5735), 755-758.
Korn, E.D., 2004. The discovery of unconventional myosins: serendipity or luck? The Journal of biological chemistry 279(10), 8517-8525.
Korten, S., Albet-Torres, N., Paderi, F., ten Siethoff, L., Diez, S., Korten, T., te Kronnie, G., Mansson, A., 2013. Sample solution constraints on motor-driven diagnostic nanodevices. Lab on a chip 13(5), 866-876.
Korten, T., Mansson, A., Diez, S., 2010. Towards the application of cytoskeletal motor proteins in molecular detection and diagnostic devices. Current opinion in biotechnology 21(4), 477-488.
Kouchi, K., Takahashi, H., Shimada, Y., 1993. Incorporation of microinjected biotin-labelled actin into nascent myofibrils of cardiac myocytes: an immunoelectron microscopic study. Journal of muscle research and cell motility 14(3), 292-301.
Kouyama, T., Mihashi, K., 1980. Pulse-fluorometry study on actin and heavy meromyosin using F-actin labelled with N-(1-pyrene)maleimide. European journal of biochemistry / FEBS 105(2), 279-287.
Kouyama, T., Mihashi, K., 1981. Fluorimetry study of N-(1-pyrenyl)iodoacetamide-labelled F-actin. Local structural change of actin protomer both on polymerization and on binding of heavy meromyosin. European journal of biochemistry / FEBS 114(1), 33-38.
Kovar, D.R., Pollard, T.D., 2004. Progressing actin: Formin as a processive elongation machine. Nature cell biology 6(12), 1158-1159.
Kozuka, J., Yokota, H., Arai, Y., Ishii, Y., Yanagida, T., 2006. Dynamic polymorphism of single actin molecules in the actin filament. Nature chemical biology 2(2), 83-86.
Kron, S.J., Spudich, J.A., 1986. Fluorescent actin filaments move on myosin fixed to a glass surface. Proceedings of the National Academy of Sciences of the United States of America 83(17), 6272-6276.
Kron, S.J., Toyoshima, Y.Y., Uyeda, T.Q., Spudich, J.A., 1991. Assays for actin sliding movement over myosin-coated surfaces. Methods in enzymology 196, 399-416.
Kuhn, J.R., Pollard, T.D., 2005. Real-time measurements of actin filament polymerization by total internal reflection fluorescence microscopy. Biophysical journal 88(2), 1387-1402.
Kumar, S., Kumar, D., Ahirwar, R., Nahar, P., 2016a. Exploring the flexible chemistry of 4-fluoro-3-nitrophenyl azide for biomolecule immobilization and bioconjugation. Analytical and bioanalytical chemistry 408(25), 6945-6956.
Kumar, S., Milani, G., Takatsuki, H., Lana, T., Persson, M., Frasson, C., Te Kronnie, G., Mansson, A., 2016b. Sensing protein antigen and microvesicle analytes using high-capacity biopolymer nano-carriers. The Analyst 141(3), 836-846.
Kumar, S., Ten Siethoff, L., Persson, M., Albet-Torres, N., Mansson, A., 2013. Magnetic capture from blood rescues molecular motor function in diagnostic nanodevices. Journal of nanobiotechnology 11, 14.
Kumar, S., ten Siethoff, L., Persson, M., Lard, M., te Kronnie, G., Linke, H., Mansson, A., 2012. Antibodies covalently immobilized on actin filaments for fast myosin driven analyte transport. PloS one 7(10), e46298.
Kurita, S., Gunji, E., Ohashi, K., Mizuno, K., 2007. Actin filaments-stabilizing and -bundling activities of cofilin-phosphatase Slingshot-1. Genes to cells : devoted to molecular & cellular mechanisms 12(5), 663-676.

ACCEPTED MANUSCRIPT

Laliberte, A., Gicquaud, C., 1988. Polymerization of actin by positively charged liposomes. The Journal of cell biology 106(4), 1221-1227.
Lard, M., Ten Siethoff, L., Kumar, S., Persson, M., Te Kronnie, G., Linke, H., Mansson, A., 2013. Ultrafast molecular motor driven nanoseparation and biosensing. Biosensors & bioelectronics 48, 145-152.
Lee, Y., Carroll, L., Holland, L., Famouri, P., 2009. Unidirectional movement of myosin-driven beads on immobilized F-actin arrays in a microfluidic channel, Nanotechnology Materials and Devices Conference, 2009. NMDC '09. IEEE. pp. 247-250.
Lee, Y., Famouri, P., 2013. Directional transport by nonprocessive motor proteins on fascin-cross-linked actin arrays. Nano letters 13(8), 3775-3782.
Lengsfeld, A.M., Low, I., Wieland, T., Dancker, P., Hasselbach, W., 1974. Interaction of phalloidin with actin. Proceedings of the National Academy of Sciences of the United States of America 71(7), 2803-2807.
Li, A., Dawson, J.C., Forero-Vargas, M., Spence, H.J., Yu, X., König, I., Anderson, K., Machesky, L.M., 2010. The Actin-Bundling Protein Fascin Stabilizes Actin in Invadopodia and Potentiates Protrusive Invasion. Current Biology 20(4), 339-345.
Lim, K.H., Huang, H., Pralle, A., Park, S., 2013. Stable, high-affinity streptavidin monomer for protein labeling and monovalent biotin detection. Biotechnology and bioengineering 110(1), 57-67.
Lin, C.W., Ting, A.Y., 2006. Transglutaminase-catalyzed site-specific conjugation of small-molecule probes to proteins in vitro and on the surface of living cells. Journal of the American Chemical Society 128(14), 4542-4543.
Low, I., Wieland, T., 1974. The interaction of phalloidin. Some of its derivatives, and of other cyclic peptides with muscle actin as studied by viscosimetry. FEBS letters 44(3), 340-343.
Lymn, R.W., Taylor, E.W., 1971. Mechanism of adenosine triphosphate hydrolysis by actomyosin. Biochemistry 10(25), 4617-4624.
Maciver, S.K., Zot, H.G., Pollard, T.D., 1991. Characterization of actin filament severing by actophorin from Acanthamoeba castellanii. The Journal of cell biology 115(6), 1611-1620.
Mahaffy, R.E., Pollard, T.D., 2008. Influence of phalloidin on the formation of actin filament branches by Arp2/3 complex. Biochemistry 47(24), 6460-6467.
Mansson, A., 2012. Translational actomyosin research: fundamental insights and applications hand in hand. Journal of muscle research and cell motility 33(3-4), 219-233.
Mansson, A., Balaz, M., Albet-Torres, N., Rosengren, K.J., 2008. In vitro assays of molecular motors--impact of motor-surface interactions. Frontiers in bioscience : a journal and virtual library 13, 5732-5754.
Mansson, A., Sundberg, M., Balaz, M., Bunk, R., Nicholls, I.A., Omling, P., Tagerud, S., Montelius, L., 2004. In vitro sliding of actin filaments labelled with single quantum dots. Biochemical and biophysical research communications 314(2), 529-534.
Mansson, A., Tagerud, S., 2014. Detection conjugate. US 8,658,38.
Margossian, S.S., Lowey, S., 1982. Preparation of myosin and its subfragments from rabbit skeletal muscle. Methods in enzymology 85 Pt B, 55-71.
Martinez-Neira, R., Kekic, M., Nicolau, D., dos Remedios, C.G., 2005. A novel biosensor for mercuric ions based on motor proteins. Biosensors & bioelectronics 20(7), 1428-1432.
McCullough, B.R., Blanchoin, L., Martiel, J.L., De la Cruz, E.M., 2008. Cofilin increases the bending flexibility of actin filaments: implications for severing and cell mechanics. Journal of molecular biology 381(3), 550-558.
Miki, M., dos Remedios, C.G., Barden, J.A., 1987. Spatial relationship between the nucleotide-binding site, Lys-61 and Cys-374 in actin and a conformational change

ACCEPTED MANUSCRIPT

induced by myosin subfragment-1 binding. European journal of biochemistry / FEBS 168(2), 339-345.
Miller, L., Phillips, M., Reisler, E., 1988. Polymerization of actin modified with fluorescein isothiocyanate. European journal of biochemistry / FEBS 174(1), 23-29.
Miyata, H., Kinosita, K., Jr., Marriott, G., 1997. Cooperative association of actin protomers and crosslinked actin oligomers in filaments at low ionic strength. Journal of biochemistry 121(3), 527-533.
Mochalin, V.N., Shenderova, O., Ho, D., Gogotsi, Y., 2012. The properties and applications of nanodiamonds. Nat Nano 7(1), 11-23.
Moens, P.D., dos Remedios, C.G., 1997. A conformational change in F-actin when myosin binds: fluorescence resonance energy transfer detects an increase in the radial coordinate of Cys-374. Biochemistry 36(24), 7353-7360.
Munsie, L.N., Caron, N., Desmond, C.R., Truant, R., 2009. Lifeact cannot visualize some forms of stress-induced twisted F-actin. Nature methods 6(5), 317.
Murakami, K., Yasunaga, T., Noguchi, T.Q., Gomibuchi, Y., Ngo, K.X., Uyeda, T.Q., Wakabayashi, T., 2010. Structural basis for actin assembly, activation of ATP hydrolysis, and delayed phosphate release. Cell 143(2), 275-287.
Nakamura, M., Chen, L., Howes, S.C., Schindler, T.D., Nogales, E., Bryant, Z., 2014. Remote control of myosin and kinesin motors using light-activated gearshifting. Nature nanotechnology 9(9), 693-697.
Nicolau, D.V., Jr., Lard, M., Korten, T., van Delft, F.C., Persson, M., Bengtsson, E., Mansson, A., Diez, S., Linke, H., Nicolau, D.V., 2016. Parallel computation with molecular-motor-propelled agents in nanofabricated networks. Proceedings of the National Academy of Sciences of the United States of America 113(10), 2591-2596.
Nicolau, D.V., Suzuki, H., Mashiko, S., Taguchi, T., Yoshikawa, S., 1999. Actin motion on microlithographically functionalized myosin surfaces and tracks. Biophysical journal 77(2), 1126-1134.
Niedermayer, T., Jegou, A., Chieze, L., Guichard, B., Helfer, E., Romet-Lemonne, G., Carlier, M.F., Lipowsky, R., 2012. Intermittent depolymerization of actin filaments is caused by photo-induced dimerization of actin protomers. Proceedings of the National Academy of Sciences of the United States of America 109(27), 10769-10774.
Nyman, T., Page, R., Schutt, C.E., Karlsson, R., Lindberg, U., 2002. A cross-linked profilin-actin heterodimer interferes with elongation at the fast-growing end of F-actin. The Journal of biological chemistry 277(18), 15828-15833.
Oda, T., Iwasa, M., Aihara, T., Maeda, Y., Narita, A., 2009. The nature of the globular- to fibrous-actin transition. Nature 457(7228), 441-445.
Oda, T., Maeda, Y., 2010. Multiple Conformations of F-actin. Structure (London, England : 1993) 18(7), 761-767.
Oda, T., Namba, K., Maeda, Y., 2005. Position and orientation of phalloidin in F-actin determined by X-ray fiber diffraction analysis. Biophysical journal 88(4), 2727-2736.
Ohara, O., Takahashi, S., Ooi, T., Fujiyoshi, Y., 1982. Cross-linking study on skeletal muscle actin: properties of suberimidate-treated actin. Journal of biochemistry 91(6), 1999-2012.
Okabe, S., Hirokawa, N., 1989. Incorporation and turnover of biotin-labeled actin microinjected into fibroblastic cells: an immunoelectron microscopic study. The Journal of cell biology 109(4 Pt 1), 1581-1595.
Olyslaegers, G., Verbelen, J.P., 1998. Improved staining of F-actin and co-localization of mitochondria in plant cells. Journal of microscopy 192(1), 73-77.
Omote, H., Sambonmatsu, N., Saito, K., Sambongi, Y., Iwamoto-Kihara, A., Yanagida, T., Wada, Y., Futai, M., 1999. The gamma-subunit rotation and torque generation in F1-

ACCEPTED MANUSCRIPT

ATPase from wild-type or uncoupled mutant Escherichia coli. Proceedings of the National Academy of Sciences of the United States of America 96(14), 7780-7784.
Oosawa, F., 1975. Thermodynamics of the polymerization of protein / Fumio Oosawa and Sho Asakura. Academic Press, London ; New York.
Orlova, A., Prochniewicz, E., Egelman, E.H., 1995. Structural dynamics of F-actin: II. Cooperativity in structural transitions. Journal of molecular biology 245(5), 598-607.
Orlova, A., Shvetsov, A., Galkin, V.E., Kudryashov, D.S., Rubenstein, P.A., Egelman, E.H., Reisler, E., 2004. Actin-destabilizing factors disrupt filaments by means of a time reversal of polymerization. Proceedings of the National Academy of Sciences of the United States of America 101(51), 17664-17668.
Otterbein, L.R., Graceffa, P., Dominguez, R., 2001. The crystal structure of uncomplexed actin in the ADP state. Science (New York, N.Y.) 293(5530), 708-711.
Oyama, T., Hatori, K., 2016. Translocation of cationic polystyrene microspheres associated with actin filaments on a surface coated with myosin motors. 山形大学紀要. 工学 = Bulletin of Yamagata University. Engineering 36, 1-11.
Panchuk-Voloshina, N., Haugland, R.P., Bishop-Stewart, J., Bhalgat, M.K., Millard, P.J., Mao, F., Leung, W.Y., Haugland, R.P., 1999. Alexa dyes, a series of new fluorescent dyes that yield exceptionally bright, photostable conjugates. The journal of histochemistry and cytochemistry : official journal of the Histochemistry Society 47(9), 1179-1188.
Paragas, V.B., Kramer, J.A., Fox, C., Haugland, R.P., Singer, V.L., 2002. The ELF -97 phosphatase substrate provides a sensitive, photostable method for labelling cytological targets. Journal of microscopy 206(Pt 2), 106-119.
Pardee, J.D., Spudich, J.A., 1982. Purification of muscle actin. Methods in cell biology 24, 271-289.
Patolsky, F., Weizmann, Y., Willner, I., 2004. Actin-based metallic nanowires as bio-nanotransporters. Nature materials 3(10), 692-695.
Pengelly, K., Loncar, A., Perieteanu, A.A., Dawson, J.F., 2009. Cysteine engineering of actin self-assembly interfaces. Biochemistry and cell biology = Biochimie et biologie cellulaire 87(4), 663-675.
Pernier, J., Orban, J., Avvaru, B.S., Jegou, A., Romet-Lemonne, G., Guichard, B., Carlier, M.F., 2013. Dimeric WH2 domains in Vibrio VopF promote actin filament barbed-end uncapping and assisted elongation. Nature structural & molecular biology 20(9), 1069-1076.
Pernier, J., Shekhar, S., Jegou, A., Guichard, B., Carlier, M.F., 2016. Profilin Interaction with Actin Filament Barbed End Controls Dynamic Instability, Capping, Branching, and Motility. Developmental cell 36(2), 201-214.
Perrin, B.J., Ervasti, J.M., 2010. The actin gene family: function follows isoform. Cytoskeleton (Hoboken, N.J.) 67(10), 630-634.
Persson, M., Albet-Torres, N., Ionov, L., Sundberg, M., Hook, F., Diez, S., Mansson, A., Balaz, M., 2010. Heavy meromyosin molecules extending more than 50 nm above adsorbing electronegative surfaces. Langmuir : the ACS journal of surfaces and colloids 26(12), 9927-9936.
Persson, M., Gullberg, M., Tolf, C., Lindberg, A.M., Mansson, A., Kocer, A., 2013. Transportation of nanoscale cargoes by myosin propelled actin filaments. PloS one 8(2), e55931.
Pollard, T., 2016. Actin and Actin-Binding Proteins. Cold Spring Harbor perspectives in biology.
Pollard, T.D., 1984. Polymerization of ADP-actin. The Journal of cell biology 99(3), 769-777.

ACCEPTED MANUSCRIPT

Pollard, T.D., 1986a. Assembly and dynamics of the actin filament system in nonmuscle cells. Journal of cellular biochemistry 31(2), 87-95.
Pollard, T.D., 1986b. Rate constants for the reactions of ATP- and ADP-actin with the ends of actin filaments. The Journal of cell biology 103(6 Pt 2), 2747-2754.
Pollard, T.D., 1990. Actin. Curr Opin Cell Biol 2(1), 33-40.
Pollard, T.D., 2016. Actin and Actin-Binding Proteins. Cold Spring Harb Perspect Biol 8(8).
Pollard, T.D., Almo, S., Quirk, S., Vinson, V., Lattman, E.E., 1994. Structure of actin binding proteins: insights about function at atomic resolution. Annual review of cell biology 10, 207-249.
Pollard, T.D., Cooper, J.A., 1984. Quantitative analysis of the effect of Acanthamoeba profilin on actin filament nucleation and elongation. Biochemistry 23(26), 6631-6641.
Pollard, T.D., Cooper, J.A., 1986. Actin and actin-binding proteins. A critical evaluation of mechanisms and functions. Annual review of biochemistry 55, 987-1035.
Pollard, T.D., Korn, E.D., 1973. Acanthamoeba myosin. I. Isolation from Acanthamoeba castellanii of an enzyme similar to muscle myosin. The Journal of biological chemistry 248(13), 4682-4690.
Prochniewicz, E., Katayama, E., Yanagida, T., Thomas, D.D., 1993. Cooperativity in F-actin: chemical modifications of actin monomers affect the functional interactions of myosin with unmodified monomers in the same actin filament. Biophysical journal 65(1), 113-123.
Prochniewicz, E., Walseth, T.F., Thomas, D.D., 2004. Structural dynamics of actin during active interaction with myosin: different effects of weakly and strongly bound myosin heads. Biochemistry 43(33), 10642-10652.
Prochniewicz, E., Yanagida, T., 1990. Inhibition of sliding movement of F-actin by crosslinking emphasizes the role of actin structure in the mechanism of motility. Journal of molecular biology 216(3), 761-772.
Ramachandran, S., Ernst, K.H., Bachand, G.D., Vogel, V., Hess, H., 2006. Selective loading of kinesin-powered molecular shuttles with protein cargo and its application to biosensing. Small (Weinheim an der Bergstrasse, Germany) 2(3), 330-334.
Raposo, G., Stoorvogel, W., 2013. Extracellular vesicles: exosomes, microvesicles, and friends. The Journal of cell biology 200(4), 373-383.
Rayment, I., Holden, H.M., Whittaker, M., Yohn, C.B., Lorenz, M., Holmes, K.C., Milligan, R.A., 1993a. Structure of the actin-myosin complex and its implications for muscle contraction. Science (New York, N.Y.) 261(5117), 58-65.
Rayment, I., Rypniewski, W.R., Schmidt-Base, K., Smith, R., Tomchick, D.R., Benning, M.M., Winkelmann, D.A., Wesenberg, G., Holden, H.M., 1993b. Three-dimensional structure of myosin subfragment-1: a molecular motor. Science (New York, N.Y.) 261(5117), 50-58.
Reisler, E., Egelman, E.H., 2007. Actin structure and function: what we still do not understand. The Journal of biological chemistry 282(50), 36133-36137.
Renkawitz, J., Schumann, K., Weber, M., Lammermann, T., Pflicke, H., Piel, M., Polleux, J., Spatz, J.P., Sixt, M., 2009. Adaptive force transmission in amoeboid cell migration. Nature cell biology 11(12), 1438-1443.
Revenu, C., Athman, R., Robine, S., Louvard, D., 2004. The co-workers of actin filaments: from cell structures to signals. Nat Rev Mol Cell Biol 5(8), 635-646.
Riedl, J., Crevenna, A.H., Kessenbrock, K., Yu, J.H., Neukirchen, D., Bista, M., Bradke, F., Jenne, D., Holak, T.A., Werb, Z., Sixt, M., Wedlich-Soldner, R., 2008. Lifeact: a versatile marker to visualize F-actin. Nature methods 5(7), 605-607.

ACCEPTED MANUSCRIPT

Riedl, J., Flynn, K.C., Raducanu, A., Gartner, F., Beck, G., Bosl, M., Bradke, F., Massberg, S., Aszodi, A., Sixt, M., Wedlich-Soldner, R., 2010. Lifeact mice for studying F-actin dynamics. Nature methods 7(3), 168-169.

Rosin, C., Schummel, P.H., Winter, R., 2015. Cosolvent and crowding effects on the polymerization kinetics of actin. Physical chemistry chemical physics : PCCP 17(13), 8330-8337.

Samarin, S., Romero, S., Kocks, C., Didry, D., Pantaloni, D., Carlier, M.F., 2003. How VASP enhances actin-based motility. The Journal of cell biology 163(1), 131-142.

Sanders, L.K., Xian, W., Guáqueta, C., Strohman, M.J., Vrasich, C.R., Luijten, E., Wong, G.C.L., 2007. Control of electrostatic interactions between F-actin and genetically modified lysozyme in aqueous media. Proceedings of the National Academy of Sciences 104(41), 15994-15999.

Schachtner, H., Li, A., Stevenson, D., Calaminus, S.D.J., Thomas, S., Watson, S.P., Sixt, M., Wedlich-Soldner, R., Strathdee, D., Machesky, L.M., 2012. Tissue inducible Lifeact expression allows visualization of actin dynamics in vivo and ex vivo. European journal of cell biology 91(11-12), 923-929.

Schafer, D.A., Jennings, P.B., Cooper, J.A., 1998. Rapid and efficient purification of actin from nonmuscle sources. Cell motility and the cytoskeleton 39(2), 166-171.

Schevzov, G., Curthoys, N.M., Gunning, P.W., Fath, T., 2012. Functional diversity of actin cytoskeleton in neurons and its regulation by tropomyosin. International review of cell and molecular biology 298, 33-94.

Schliwa, M., Woehlke, G., 2003. Molecular motors. Nature 422(6933), 759-765.

Schoenenberger, C.A., Mannherz, H.G., Jockusch, B.M., 2011. Actin: from structural plasticity to functional diversity. European journal of cell biology 90(10), 797-804.

Scoville, D., Stamm, J.D., Altenbach, C., Shvetsov, A., Kokabi, K., Rubenstein, P.A., Hubbell, W.L., Reisler, E., 2009. Effects of binding factors on structural elements in F-actin. Biochemistry 48(2), 370-378.

Sellers, J.R., 1999. Myosins, 2 ed. Oxford University Press.

Sellers, J.R., 2000. Myosins: a diverse superfamily. Biochimica et biophysica acta 1496(1), 3-22.

Selve, N., Wegner, A., 1986. Rate of treadmilling of actin filaments in vitro. Journal of molecular biology 187(4), 627-631.

Sheetz, M.P., Spudich, J.A., 1983a. Movement of myosin-coated fluorescent beads on actin cables in vitro. Nature 303(5912), 31-35.

Sheetz, M.P., Spudich, J.A., 1983b. Movement of myosin-coated structures on actin cables. Cell motility 3(5-6), 485-489.

Shimozawa, T., Ishiwata, S., 2009. Mechanical distortion of single actin filaments induced by external force: detection by fluorescence imaging. Biophysical journal 96(3), 1036-1044.

Singhal, P.C., Hays, R.M., 1988. Actin filament morphology in living and nonliving cultured mesangial cells: formation and dissolution. Nephron 50(1), 28-33.

Skorzewski, R., Robaszkiewicz, K., Jarzebinska, J., Suder, P., Silberring, J., Moraczewska, J., 2009. Differential binding of tropomyosin isoforms to actin modified with m-maleimidobenzoyl-N-hydroxysuccinimide ester and fluorescein-5-isothiocyanate. Analytical biochemistry 394(1), 48-55.

Sliogeryte, K., Thorpe, S.D., Wang, Z., Thompson, C.L., Gavara, N., Knight, M.M., 2016. Differential effects of LifeAct-GFP and actin-GFP on cell mechanics assessed using micropipette aspiration. Journal of Biomechanics 49(2), 310-317.

Smith, B.A., Gelles, J., Goode, B.L., 2014. Single-molecule studies of actin assembly and disassembly factors. Methods in enzymology 540, 95-117.

ACCEPTED MANUSCRIPT

Soto, C.M., Martin, B.D., Sapsford, K.E., Blum, A.S., Ratna, B.R., 2008. Toward single molecule detection of staphylococcal enterotoxin B: mobile sandwich immunoassay on gliding microtubules. Analytical chemistry 80(14), 5433-5440.
Spudich, J.A., 2011. Molecular motors: forty years of interdisciplinary research. Molecular biology of the cell 22(21), 3936-3939.
Spudich, J.A., 2012. One path to understanding energy transduction in biological systems. Nature medicine 18(10), 1478-1482.
Spudich, J.A., Kron, S.J., Sheetz, M.P., 1985. Movement of myosin-coated beads on oriented filaments reconstituted from purified actin. Nature 315(6020), 584-586.
Statsuk, A.V., Bai, R., Baryza, J.L., Verma, V.A., Hamel, E., Wender, P.A., Kozmin, S.A., 2005. Actin is the primary cellular receptor of bistramide A. Nature chemical biology 1(7), 383-388.
Stayton, P.S., Freitag, S., Klumb, L.A., Chilkoti, A., Chu, V., Penzotti, J.E., To, R., Hyre, D., Le Trong, I., Lybrand, T.P., Stenkamp, R.E., 1999. Streptavidin-biotin binding energetics. Biomolecular engineering 16(1-4), 39-44.
Steinmetz, M.O., Stoffler, D., Muller, S.A., Jahn, W., Wolpensinger, B., Goldie, K.N., Engel, A., Faulstich, H., Aebi, U., 1998. Evaluating atomic models of F-actin with an undecagold-tagged phalloidin derivative. Journal of molecular biology 276(1), 1-6.
Strzelecka-Golaszewska, H., Wozniak, A., Hult, T., Lindberg, U., 1996. Effects of the type of divalent cation, Ca2+ or Mg2+, bound at the high-affinity site and of the ionic composition of the solution on the structure of F-actin. The Biochemical journal 316 (Pt 3), 713-721.
Sun, H.Q., Yamamoto, M., Mejillano, M., Yin, H.L., 1999. Gelsolin, a multifunctional actin regulatory protein. The Journal of biological chemistry 274(47), 33179-33182.
Sundberg, M., Bunk, R., Albet-Torres, N., Kvennefors, A., Persson, F., Montelius, L., Nicholls, I.A., Ghatnekar-Nilsson, S., Omling, P., Tagerud, S., Mansson, A., 2006. Actin filament guidance on a chip: toward high-throughput assays and lab-on-a-chip applications. Langmuir : the ACS journal of surfaces and colloids 22(17), 7286-7295.
Suzuki, H., Yamada, A., Oiwa, K., Nakayama, H., Mashiko, S., 1997. Control of actin moving trajectory by patterned poly(methylmethacrylate) tracks. Biophysical journal 72(5), 1997-2001.
Suzuki, M., Wazawa, T., Mogami, G., Kodama, T., 2012. Role of Water in Actin–Myosin Binding and Actin Polymerization: Rotational and Translational Mobility of Water Molecules. Journal of the Physical Society of Japan 81(Suppl.A), SA003.
Suzuki, N., Miyata, H., Ishiwata, S., Kinosita, K., Jr., 1996. Preparation of bead-tailed actin filaments: estimation of the torque produced by the sliding force in an in vitro motility assay. Biophysical journal 70(1), 401-408.
Tait, J.F., Frieden, C., 1982. Chemical modification of actin. Acceleration of polymerization and reduction of network formation by reaction with N-ethylmaleimide, (iodoacetamido)tetramethylrhodamine, or 7-chloro-4-nitro-2,1,3-benzoxadiazole. Biochemistry 21(24), 6046-6053.
Takashi, R., 1988. A novel actin label: a fluorescent probe at glutamine-41 and its consequences. Biochemistry 27(3), 938-943.
Takatsuki, H., Rice, K.M., Asano, S., Day, B.S., Hino, M., Oiwa, K., Ishikawa, R., Hiratsuka, Y., Uyeda, T.Q., Kohama, K., Blough, E.R., 2010. Utilization of myosin and actin bundles for the transport of molecular cargo. Small (Weinheim an der Bergstrasse, Germany) 6(3), 452-457.
Takatsuki, H., Tanaka, H., Rice, K.M., Kolli, M.B., Nalabotu, S.K., Kohama, K., Famouri, P., Blough, E.R., 2011. Transport of single cells using an actin bundle-myosin bionanomotor transport system. Nanotechnology 22(24), 245101.

ACCEPTED MANUSCRIPT

Tang, J.X., Janmey, P.A., 1996. The polyelectrolyte nature of F-actin and the mechanism of actin bundle formation. The Journal of biological chemistry 271(15), 8556-8563.
Teal, D.J., Dawson, J.F., 2007. Yeast actin with a subdomain 4 mutation (A204C) exhibits increased pointed-end critical concentration. Biochemistry and cell biology = Biochimie et biologie cellulaire 85(3), 319-325.
Tellam, R., Frieden, C., 1982. Cytochalasin D and platelet gelsolin accelerate actin polymer formation. A model for regulation of the extent of actin polymer formation in vivo. Biochemistry 21(13), 3207-3214.
Timp, W., Watson, N., Sabban, A., Zik, O., Matsudaira, P., 2006. Wet electron microscopy with quantum dots. BioTechniques 41(3), 295-298.
Tokuraku, K., Uyeda, T.Q., 2001. Phalloidin affects the myosin-dependent sliding velocities of actin filaments in a bound-divalent cation dependent manner. Journal of muscle research and cell motility 22(4), 371-378.
Toth, M.A., Majoros, A.K., Vig, A.T., Migh, E., Nyitrai, M., Mihaly, J., Bugyi, B., 2016. Biochemical Activities of the Wiskott-Aldrich Syndrome Homology Region 2 Domains of Sarcomere Length Short (SALS) Protein. The Journal of biological chemistry 291(2), 667-680.
Toyoshima, Y.Y., Kron, S.J., McNally, E.M., Niebling, K.R., Toyoshima, C., Spudich, J.A., 1987. Myosin subfragment-1 is sufficient to move actin filaments in vitro. Nature 328(6130), 536-539.
Tsarova, K., Yarmola, E.G., Bubb, M.R., 2010. Identification of a cofilin-like actin-binding site on translationally controlled tumor protein (TCTP). FEBS letters 584(23), 4756-4760.
van der Gucht, J., Paluch, E., Plastino, J., Sykes, C., 2005. Stress release drives symmetry breaking for actin-based movement. Proceedings of the National Academy of Sciences of the United States of America 102(22), 7847-7852.
van Roy, N., Mangelschots, K., Speleman, F., 1993. Improved immunocytochemical detection of biotinylated probes with Neutralite avidin. Trends in genetics : TIG 9(3), 71-72.
VanBuren, P., Begin, K., Warshaw, D.M., 1998. Fluorescent phalloidin enables visualization of actin without effects on myosin's actin filament sliding velocity and hydrolytic properties in vitro. Journal of molecular and cellular cardiology 30(12), 2777-2783.
Vandekerckhove, J., 1990. Actin-binding proteins. Curr Opin Cell Biol 2(1), 41-50.
Vandekerckhove, J.S., Kaiser, D.A., Pollard, T.D., 1989. Acanthamoeba actin and profilin can be cross-linked between glutamic acid 364 of actin and lysine 115 of profilin. The Journal of cell biology 109(2), 619-626.
Vavylonis, D., Yang, Q., O'Shaughnessy, B., 2005. Actin polymerization kinetics, cap structure, and fluctuations. Proceedings of the National Academy of Sciences of the United States of America 102(24), 8543-8548.
Velema, W.A., Stuart, M.C., Szymanski, W., Feringa, B.L., 2013. Light-triggered self-assembly of a dichromonyl compound in water. Chemical communications (Cambridge, England) 49(44), 5001-5003.
Vidali, L., Rounds, C.M., Hepler, P.K., Bezanilla, M., 2009. Lifeact-mEGFP reveals a dynamic apical F-actin network in tip growing plant cells. PloS one 4(5), e5744.
Vignjevic, D., Yarar, D., Welch, M.D., Peloquin, J., Svitkina, T., Borisy, G.G., 2003. Formation of filopodia-like bundles in vitro from a dendritic network. The Journal of cell biology 160(6), 951-962.

ACCEPTED MANUSCRIPT

Vikhorev, P.G., Vikhoreva, N.N., Mansson, A., 2008a. Bending flexibility of actin filaments during motor-induced sliding. Biophysical journal 95(12), 5809-5819.
Vikhorev, P.G., Vikhoreva, N.N., Sundberg, M., Balaz, M., Albet-Torres, N., Bunk, R., Kvennefors, A., Liljesson, K., Nicholls, I.A., Nilsson, L., Omling, P., Tagerud, S., Montelius, L., Mansson, A., 2008b. Diffusion dynamics of motor-driven transport: gradient production and self-organization of surfaces. Langmuir : the ACS journal of surfaces and colloids 24(23), 13509-13517.
Visegrady, B., Lorinczy, D., Hild, G., Somogyi, B., Nyitrai, M., 2005. A simple model for the cooperative stabilisation of actin filaments by phalloidin and jasplakinolide. FEBS letters 579(1), 6-10.
Waggoner, A., DeBiasio, R., Conrad, P., Bright, G.R., Ernst, L., Ryan, K., Nederlof, M., Taylor, D., 1989. Multiple spectral parameter imaging. Methods in cell biology 30, 449-478.
Wang, Y., Ajtai, K., Burghardt, T.P., 2013. The Qdot-labeled actin super-resolution motility assay measures low-duty cycle muscle myosin step size. Biochemistry 52(9), 1611-1621.
Wang, Y.L., 1985. Exchange of actin subunits at the leading edge of living fibroblasts: possible role of treadmilling. The Journal of cell biology 101(2), 597-602.
Waterman-Storer, C., Duey, D.Y., Weber, K.L., Keech, J., Cheney, R.E., Salmon, E.D., Bement, W.M., 2000. Microtubules remodel actomyosin networks in Xenopus egg extracts via two mechanisms of F-actin transport. The Journal of cell biology 150(2), 361-376.
Weber, A., 1999. Actin binding proteins that change extent and rate of actin monomer-polymer distribution by different mechanisms. Molecular and cellular biochemistry 190(1-2), 67-74.
Weeds, A.G., Gooch, J., Pope, B., Harris, H.E., 1986. Preparation and characterization of pig plasma and platelet gelsolins. European journal of biochemistry / FEBS 161(1), 69-76.
Weeds, A.G., Pope, B., 1977. Studies on the chymotryptic digestion of myosin. Effects of divalent cations on proteolytic susceptibility. Journal of molecular biology 111(2), 129-157.
Wehland, J., Osborn, M., Weber, K., 1977. Phalloidin-induced actin polymerization in the cytoplasm of cultured cells interferes with cell locomotion and growth. Proceedings of the National Academy of Sciences of the United States of America 74(12), 5613-5617.
Wei, M.Y., Leon, L.J., Lee, Y., Parks, D., Carroll, L., Famouri, P., 2011. Selective attachment of F-actin with controlled length for developing an intelligent nanodevice. Journal of colloid and interface science 356(1), 182-189.
Wieland, T., 1977. Modification of actins by phallotoxins. Die Naturwissenschaften 64(6), 303-309.
Wiesner, S., Helfer, E., Didry, D., Ducouret, G., Lafuma, F., Carlier, M.F., Pantaloni, D., 2003. A biomimetic motility assay provides insight into the mechanism of actin-based motility. The Journal of cell biology 160(3), 387-398.
Wilchek, M., Bayer, E.A., 1984. The avidin-biotin complex in immunology. Immunology today 5(2), 39-43.
Williamson, R.E., 1986. Organelle Movements along Actin Filaments and Microtubules. Plant physiology 82(3), 631-634.
Willner, I., Willner, B., 2010. Biomolecule-based nanomaterials and nanostructures. Nano letters 10(10), 3805-3815.
Wilson, B.S., Pfeiffer, J.R., Oliver, J.M., 2000. Observing FcepsilonRI signaling from the inside of the mast cell membrane. The Journal of cell biology 149(5), 1131-1142.

ACCEPTED MANUSCRIPT

Wong, S.S., 1991. Chemistry of Protein Conjugation and Cross-Linking. Taylor & Francis, Boca Raton: Florida.

Wong, W., Webb, A.I., Olshina, M.A., Infusini, G., Tan, Y.H., Hanssen, E., Catimel, B., Suarez, C., Condron, M., Angrisano, F., Nebi, T., Kovar, D.R., Baum, J., 2014. A mechanism for actin filament severing by malaria parasite actin depolymerizing factor 1 via a low affinity binding interface. The Journal of biological chemistry 289(7), 4043-4054.

Wu, K.C., Yang, C.Y., Cheng, C.M., 2014. Using cell structures to develop functional nanomaterials and nanostructures--case studies of actin filaments and microtubules. Chemical communications (Cambridge, England) 50(32), 4148-4157.

Wu, X., Liu, H., Liu, J., Haley, K.N., Treadway, J.A., Larson, J.P., Ge, N., Peale, F., Bruchez, M.P., 2003. Immunofluorescent labeling of cancer marker Her2 and other cellular targets with semiconductor quantum dots. Nature biotechnology 21(1), 41-46.

Wulf, E., Deboben, A., Bautz, F.A., Faulstich, H., Wieland, T., 1979. Fluorescent phallotoxin, a tool for the visualization of cellular actin. Proceedings of the National Academy of Sciences of the United States of America 76(9), 4498-4502.

Yamashiro, S., Yamakita, Y., Ono, S., Matsumura, F., 1998. Fascin, an actin-bundling protein, induces membrane protrusions and increases cell motility of epithelial cells. Molecular biology of the cell 9(5), 993-1006.

Yanagida, T., Nakase, M., Nishiyama, K., Oosawa, F., 1984. Direct observation of motion of single F-actin filaments in the presence of myosin. Nature 307(5946), 58-60.

Yao, L., Andreev, G.O., Reshetnyak, Y.K., Andreev, O.A., 2009. Fabrication of semiconductor nanowires by conjugation of quantum dots to actin filaments. Analytical and bioanalytical chemistry 395(5), 1563-1566.

Yasuda, R., Miyata, H., Kinosita, K., Jr., 1996. Direct measurement of the torsional rigidity of single actin filaments. Journal of molecular biology 263(2), 227-236.

Yates, S.P., Loncar, A., Dawson, J.F., 2009. Actin polymerization is controlled by residue size at position 204. Biochemistry and cell biology = Biochimie et biologie cellulaire 87(6), 853-865.

Yin, H.L., Hartwig, J.H., Maruyama, K., Stossel, T.P., 1981. Ca2+ control of actin filament length. Effects of macrophage gelsolin on actin polymerization. The Journal of biological chemistry 256(18), 9693-9697.

Yuan, J., Pillarisetti, A., Goldman, Y.E., Bau, H.H., 2013. Orienting actin filaments for directional motility of processive myosin motors. Nano letters 13(1), 79-84.

Zhukarev, V., Sanger, J.M., Sanger, J.W., Goldman, Y.E., Shuman, H., 1997. Distribution and orientation of rhodamine-phalloidin bound to thin filaments in skeletal and cardiac myofibrils. Cell motility and the cytoskeleton 37(4), 363-377.

ACCEPTED MANUSCRIPT

ACCEPTED MANUSCRIPT

Figure Legends

Fig. 1. Schematic representation of the polymerization of globular (G)-actin into the right-handed double-helical filamentous (F)-actin. Polymerization can be initiated by the addition of polymerization buffer containing potassium chloride and magnesium chloride. Polymerization occurs at both the plus end and the minus end but is faster at the plus end. The plus end and the minus ends are also known as barbed and pointed ends, respectively based on the appearance of the filament in electron micrographs when labelled with myosin S1.

Fig. 2. A model of actin structure. **A.** Uncomplexed crystal structure of globular (G)-actin (PDB file 2ZWH) generated by Oda et al. (Oda et al., 2009). The actin monomer is divided into one large domain and one small domain and further into subdomains (SD 1-4). The large and small domains are divided by an interdomain cleft. **B.** The cryo-electron microscopically generated molecular structure of filamentous actin (PDB file 3G37; (Murakami et al., 2010)) for visualization of α-helical backbones and large side chains in the presence phosphate. Note, that the small and large domains of each subunit are illustrated in different colours. The structures were visualized using Chimera 1.11.2.

Fig. 3. Schematic representation of the movement of a myosin (II) motor towards the rapidly polymerizing plus-end of an actin filament. The arrow indicates the filament movement direction. Figure approximately to scale.

Fig. 4. Schematic representation of the myosin (II) motor and its various fragments that may be obtained by controlled proteolysis. The heavy chains are shown in green whereas the essential light chains (ELC) and the regulatory light chains (RLC) are indicated in pink and blue, respectively. After limited proteolytic cleavage (with trypsin or α-chymotrypsin) at the site approximately indicated by dashed line, heavy meromyosin (HMM) and light meromyosin (LMM) are produced. Further proteolytic digestion with papain or α-chymotrypsin result in S1 and S2 fragments where the S1 fragment contains the myosin motor and neck domain. It is particularly the HMM fragment that has been extensively utilized in nanobiotechnological applications and in the in vitro motility assay for functional studies.

Fig. 5. The in vitro motility assay. **A.** Schematic representation of in vitro motility assay (IVMA) set up using inverted fluorescence microscope. The flow cell is built by fixing a small glass cover slip on top of a large glass slide via double sided adhesive tape. **B**. Principle where HMM molecules (gray) are optimally adsorbed to a suitable surface substrate with their actin binding heads facing away from the surface for effective actin filament (red) propulsion in the presence of ATP. Figure adapted from (Mansson et al., 2008).

Fig. 6. Attachment of wide variety of molecular cargoes via phalloidin as schematically illustrated with rhodamine phalloidin (RhPh;red), Alexa 488 phalloidin (APh; green), biotin phalloidin (yellow) and phalloidin with arbitrary functionality (x; violet).

Fig. 7. Assembling of unipolar actin arrays on biotinylated glass surface via streptavidin. Adapted with permission from (Lee and Famouri, 2013).

ACCEPTED MANUSCRIPT

Fig. 8. The uncomplexed crystal structure of globular (G)-actin (PDB file 2ZWH) showing key amino acids (single-letter amino acid code) that may participate in covalent conjugation processes. Potentially reactive residues illustrated in Blue: glutamines; Green: lysines; Red: cysteines; Turquoise: glutamic acids. The figure was generated and coloured using Chimera 1.11.2 from the Pdb file 2ZWH (Oda et al., 2009).

Fig. 9. Common principles for covalent immobilization of other molecules/particles via primary amines on actin. Green: the actin monomer with primary amine.

Fig. 10. Common principles for covalent immobilization of other molecules and particles to actin via sulfhydryl groups. Green: the actin monomer with sulfhydryl group.

Fig. 11. Common principles for covalent immobilization of other molecules and particles to actin via carboxyl group using EDC/NHS chemistry. Green: the actin monomer with carboxyl group. Molecule with primary amine to be conjugated to actin, shown in violet.

Fig. 12. Fabrication of gold nanowires using actin labelled with gold nanoparticles. Adapted with permission from Patolsky et al. (Patolsky et al., 2004).

Fig. 13. Different strategies adopted by Yao et al., (2009) for fabrication of semiconductor wire using quantum dot labelled actin. Adapted with permission from (Yao et al., 2009).

Fig. 14. Schematic illustration procedure for modifying actin filaments (i, iii) and antibodies (ii, iv) with heterobifunctional cross linkers (C6-succinimidyl 6-hydrazinonicotinate acetone hydrazone (C6-SANH) and C6-succinimidyl 4-formylbenzoate (C6-SFB) followed by conjugation of actin filament with the antibodies (v).

Fig. 15A. Formation of UV traceable bond between C6-SANH-modified actin and 2-sulfobenzaldehyde (2-SB).

Fig. 15B. Formation of UV traceable bond between C6-SFB-modified antibody and 2-hydrazinopyridine.dihydrochloride (2-HP).

Fig. 16. Schematic illustration of magnetic pre-separation of target antigen from serum using antibody bound magnetic particle (i). After exchanging serum for suitable biological buffer (ii) antibody-conjugated actin filaments are added (ii-iii). The actin-antibody-antigen-antibody-MP-complexes are then pelleted by magnetic forces followed by removal of the supernatant (iii). The complexes were then transferred to heavy meromyosin motor surface for in vitro motility assay based evaluation. Figure adapted from (Kumar et al., 2013).

Fig. 17. Schematic illustration of the formation of antibody coated actin bundle, using the actin bundling protein fascin. The bundle contained both antibody-free and antibody-conjugated actin filaments.

Fig. 18. Actin bundles conjugated with Anti-CD45 antibody and labelled with RhPh (red) capturing CFSE labelled CD45+ microvesicle (green) in the in vitro motility assay (A) Unidirectional movement of anti-CD45 antibody-conjugated actin bundles with captured CFSE labelled CD45+ microvesicle (green) (B). Different aggregates of stationary bundles (red) were formed by microvesicles during transportation**.** Actin bundles (red) and microvesicles (green) were visualized in different time intervals in TRITC and FITC filters,

ACCEPTED MANUSCRIPT

respectively. Motile filaments and stationary bundle aggregate indicated by arrows and arrow heads, respectively. Scale bar: 10 μm. Figure adapted from (Kumar et al., 2016b).

ACCEPTED MANUSCRIPT

ACCEPTED MANUSCRIPT

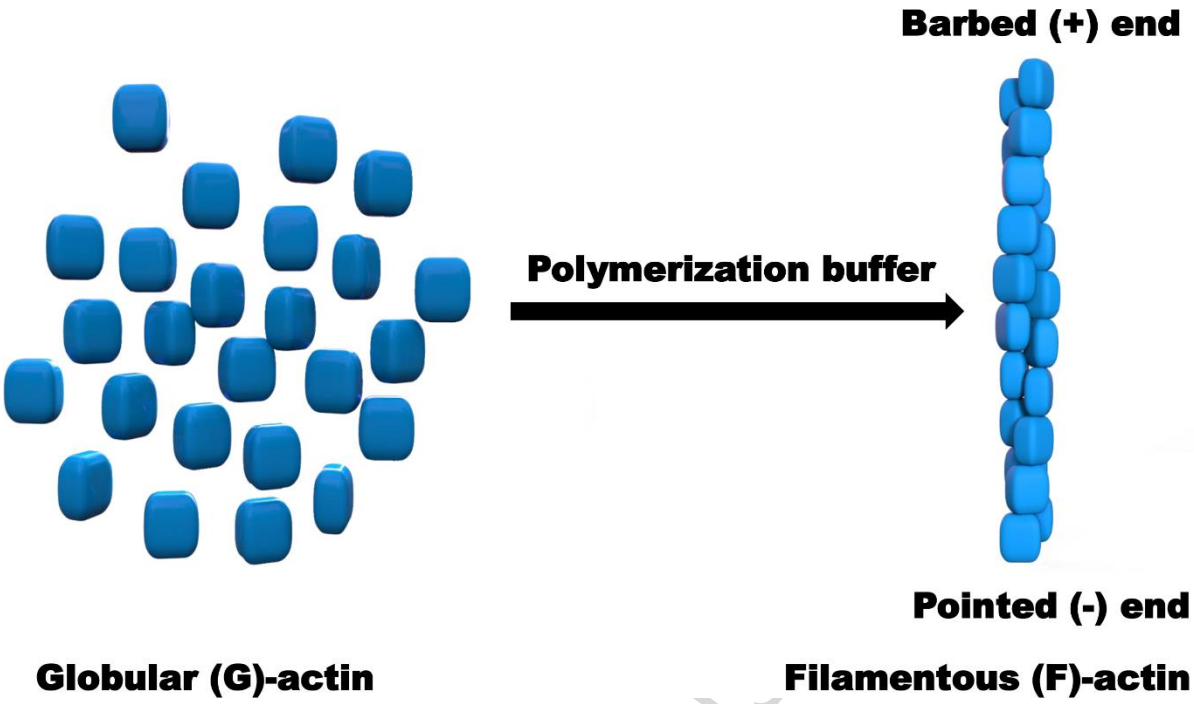


Figure 1

ACCEPTED MANUSCRIPT

ACCEPTED MANUSCRIPT

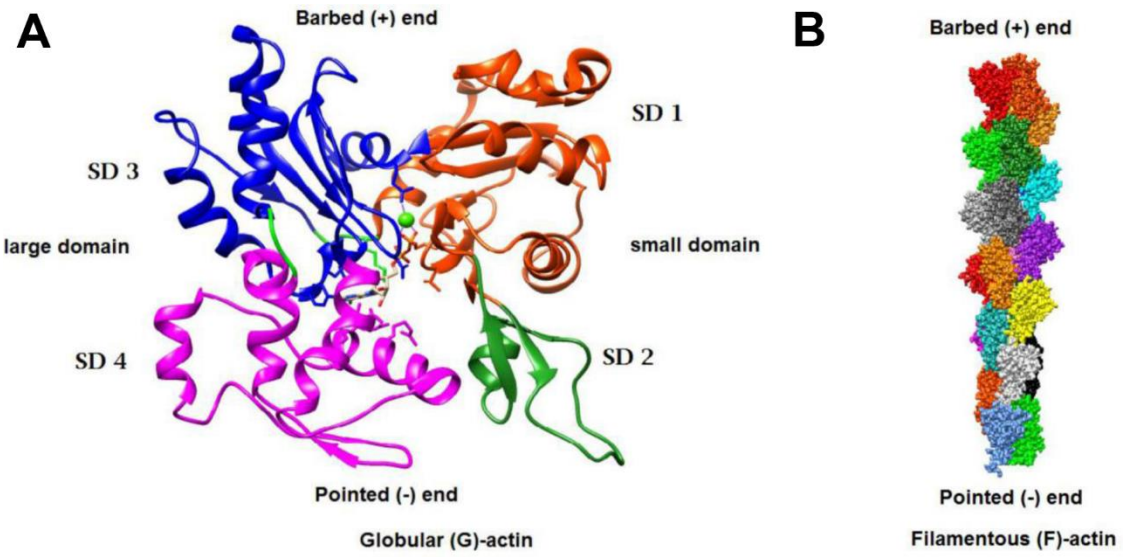


Figure 2

ACCEPTED MANUSCRIPT

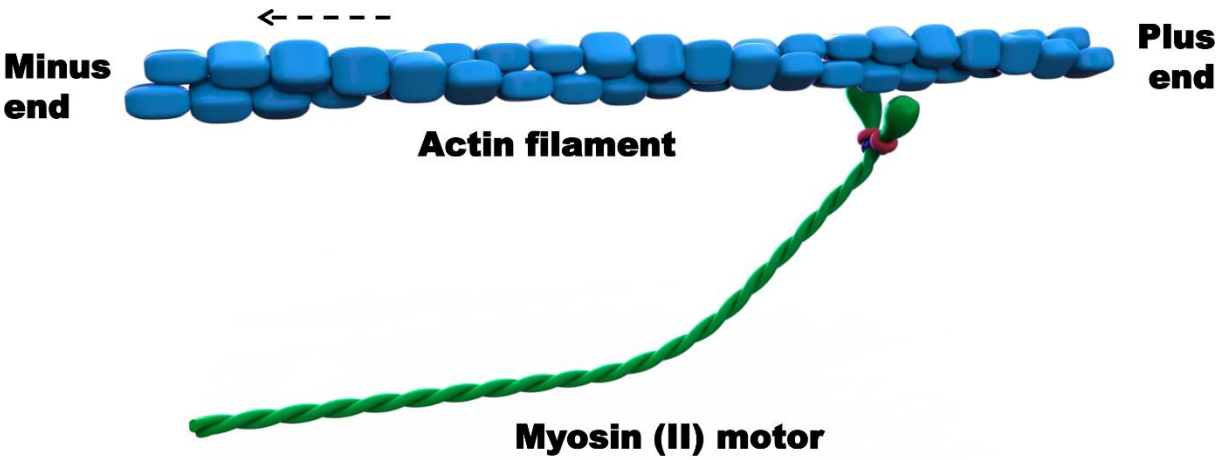


Figure 3

ACCEPTED MANUSCRIPT

ACCEPTED MANUSCRIPT

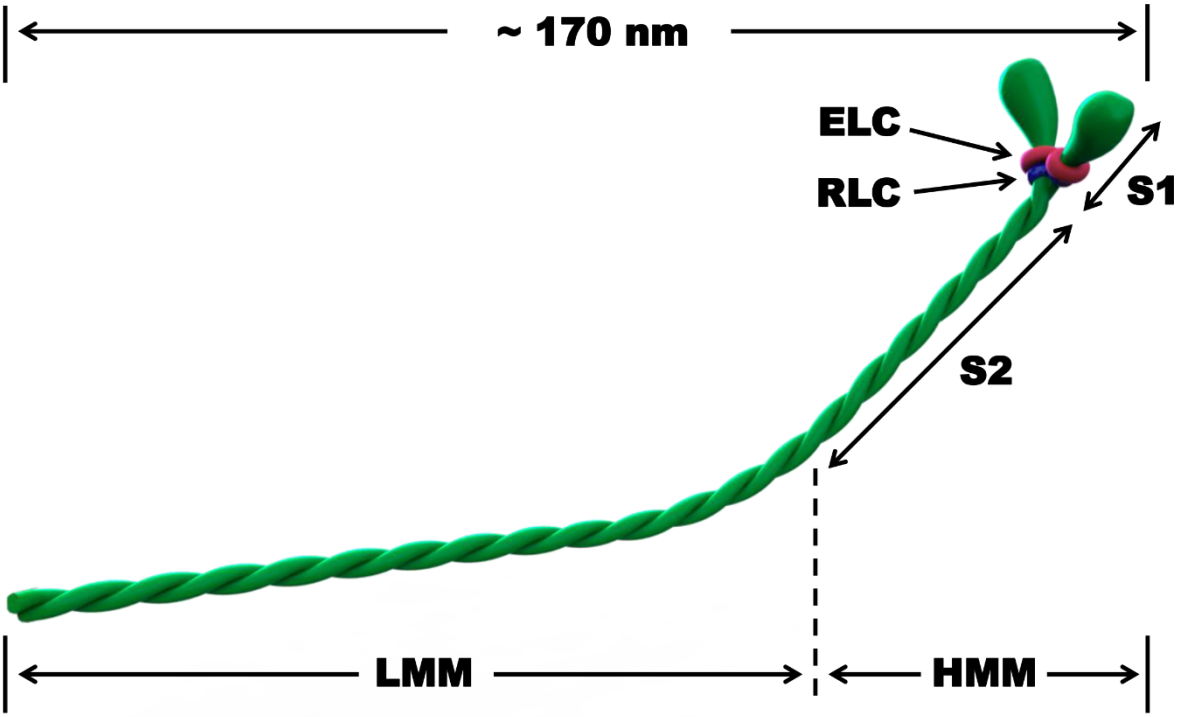


Figure 4

ACCEPTED MANUSCRIPT

ACCEPTED MANUSCRIPT

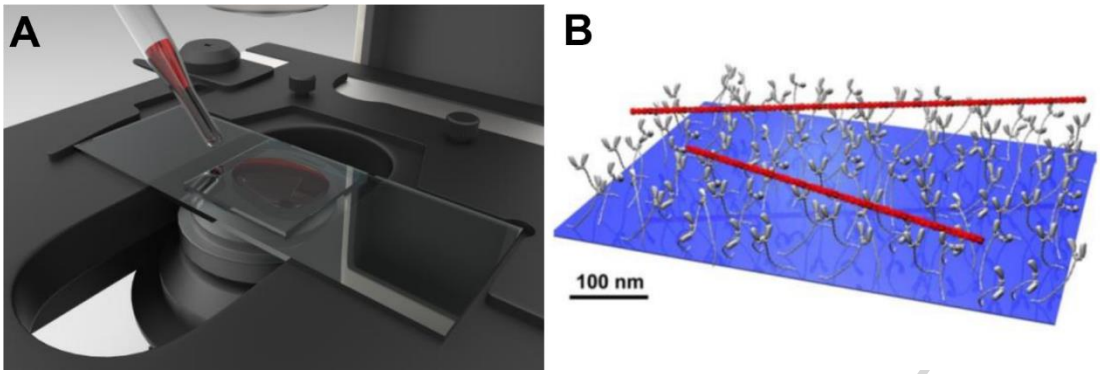


Figure 5

ACCEPTED MANUSCRIPT

ACCEPTED MANUSCRIPT

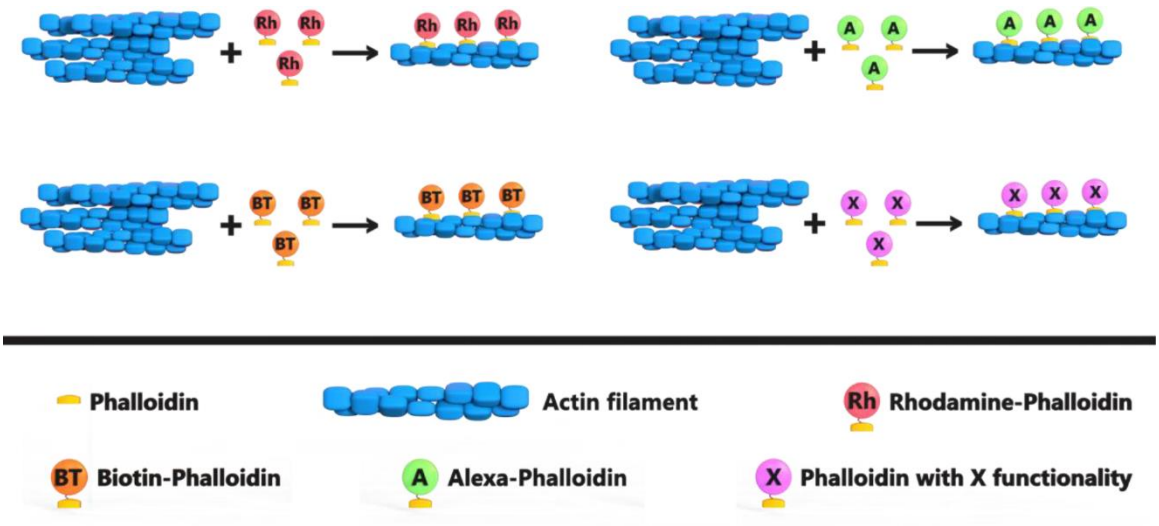


Figure 6

ACCEPTED MANUSCRIPT

ACCEPTED MANUSCRIPT

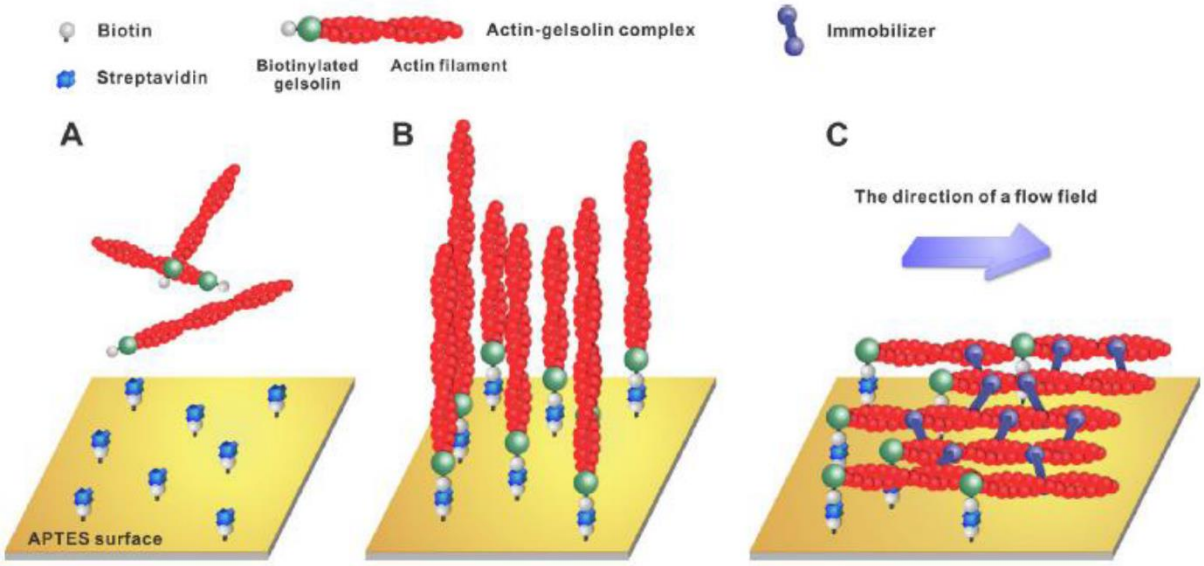


Figure 7

ACCEPTED MANUSCRIPT

ACCEPTED MANUSCRIPT

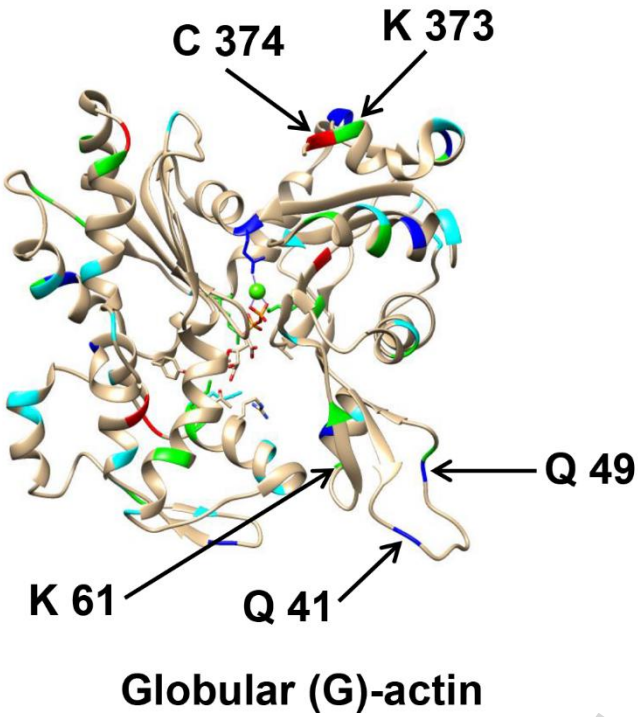


Figure 8

ACCEPTED MANUSCRIPT

ACCEPTED MANUSCRIPT

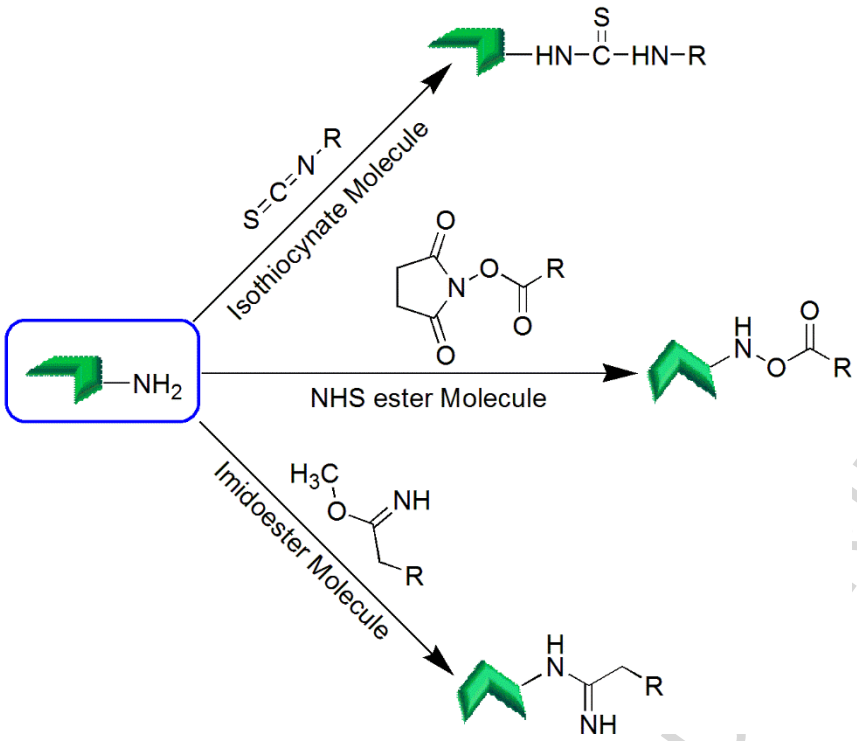


Figure 9

ACCEPTED MANUSCRIPT

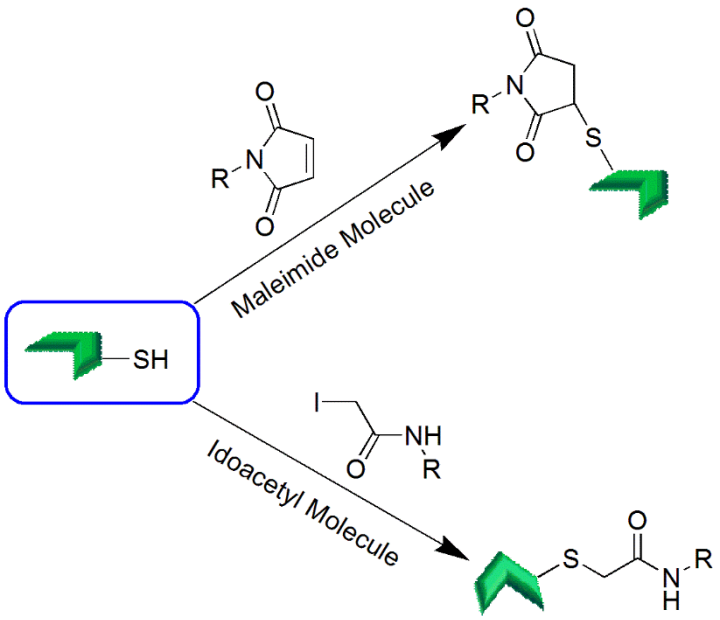


Figure 10

ACCEPTED MANUSCRIPT

ACCEPTED MANUSCRIPT

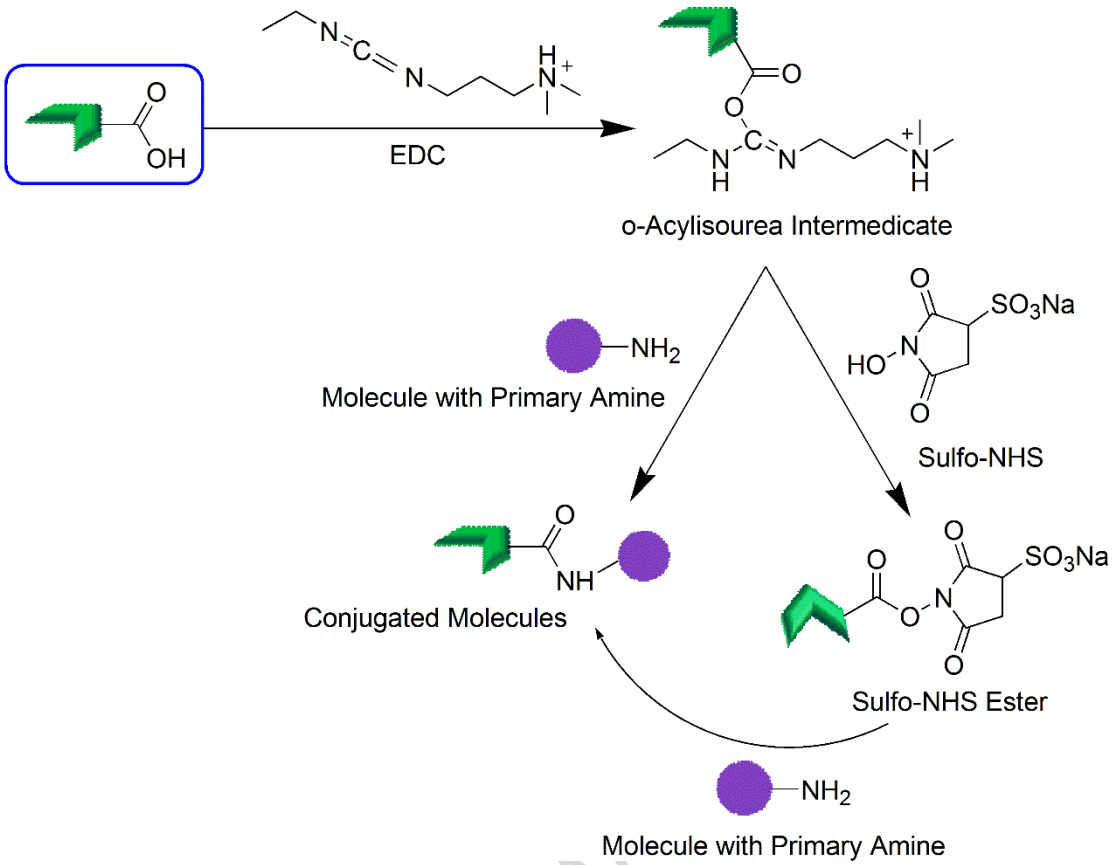


Figure 11

ACCEPTED MANUSCRIPT

ACCEPTED MANUSCRIPT

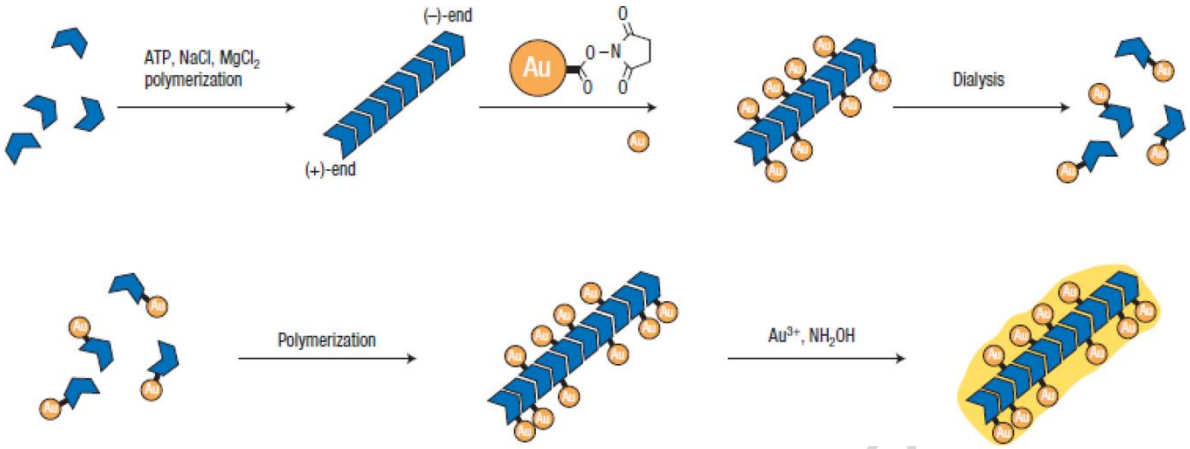


Figure 12

ACCEPTED MANUSCRIPT

ACCEPTED MANUSCRIPT

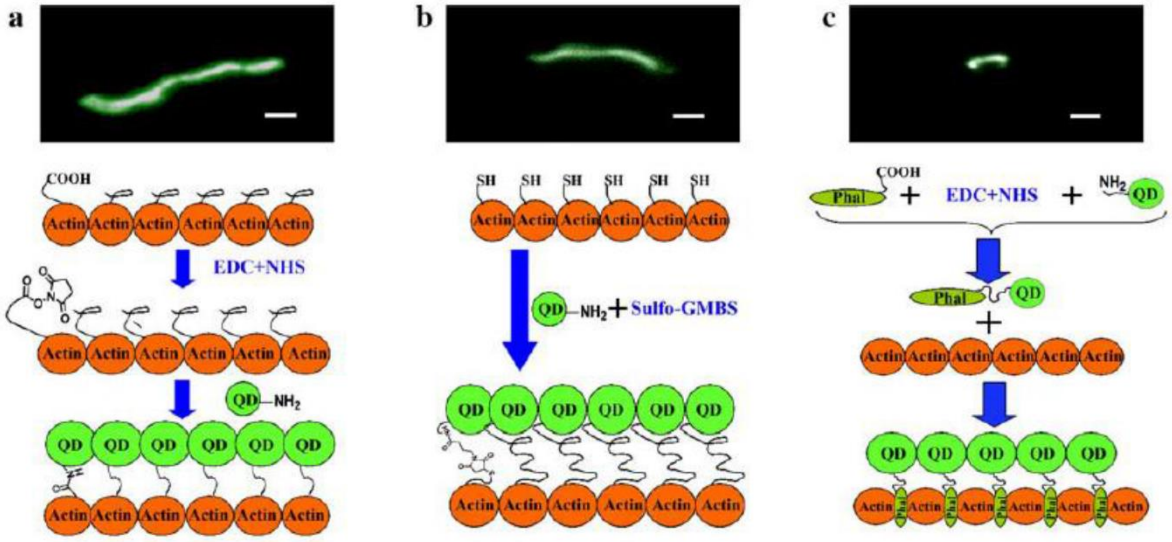


Figure 13

ACCEPTED MANUSCRIPT

ACCEPTED MANUSCRIPT

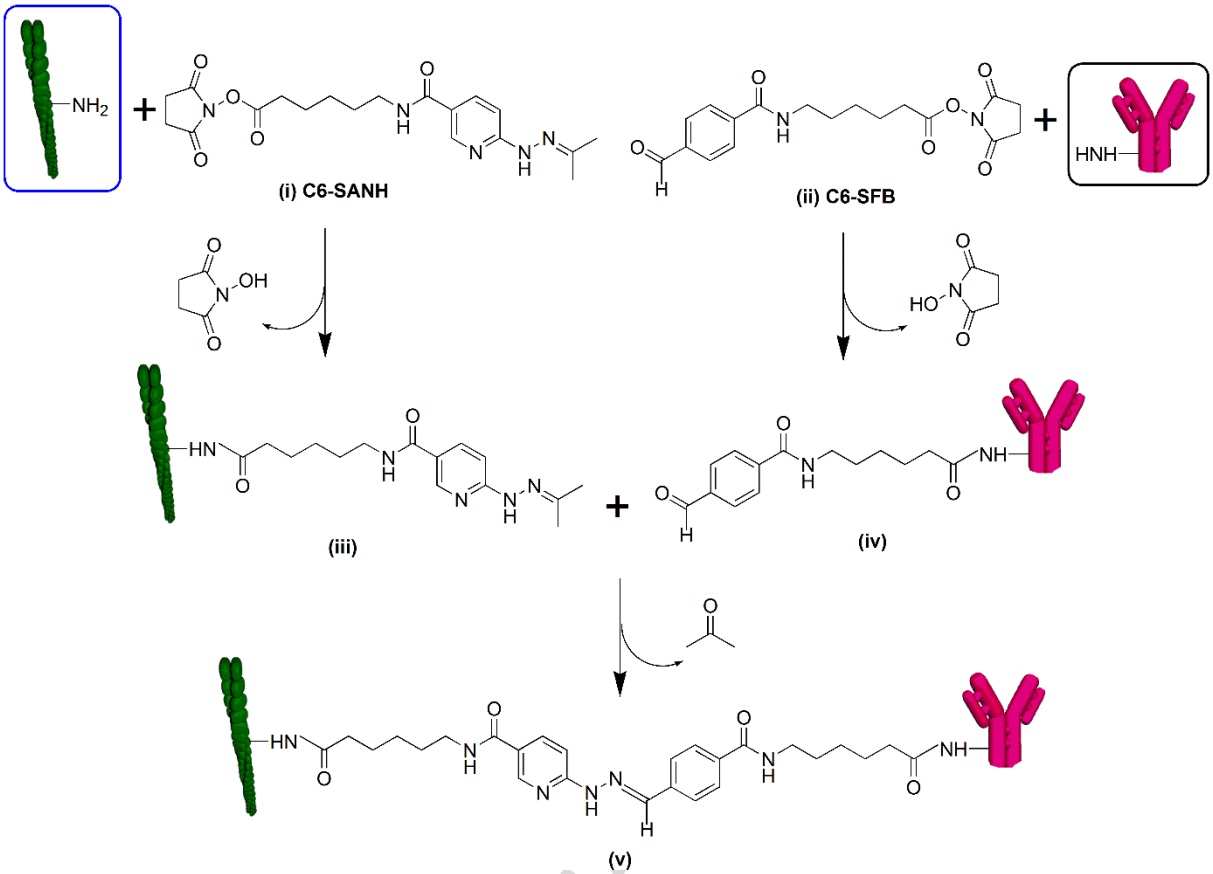


Figure 14

ACCEPTED MANUSCRIPT

ACCEPTED MANUSCRIPT

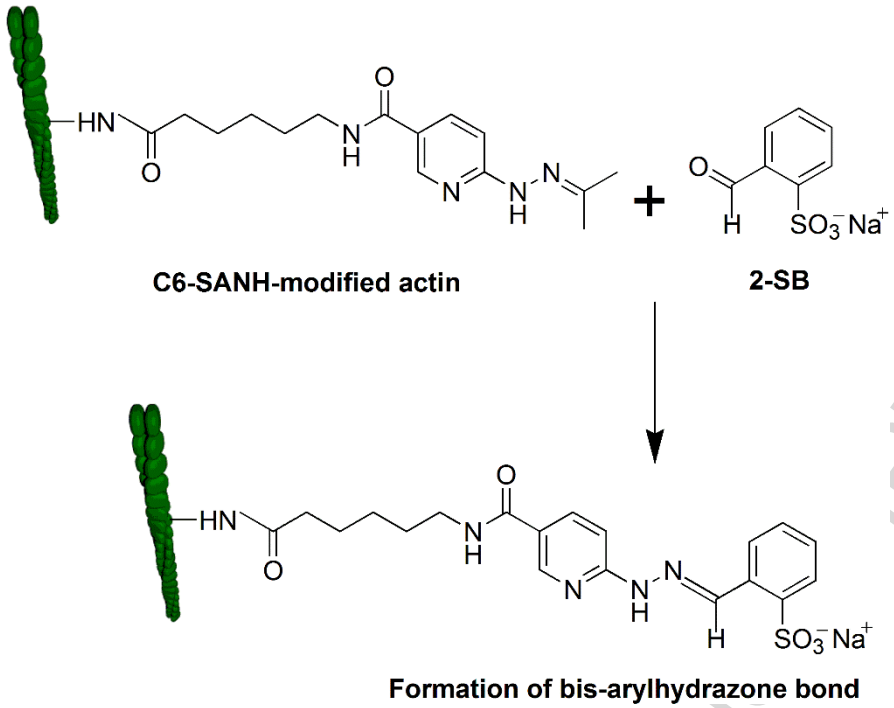


Figure 15A

ACCEPTED MANUSCRIPT

ACCEPTED MANUSCRIPT

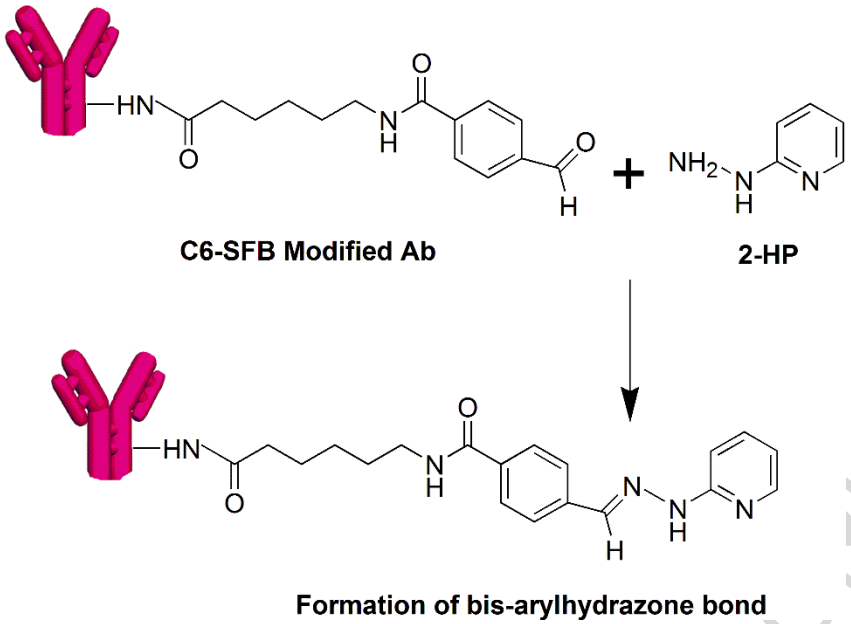


Figure 15B

ACCEPTED MANUSCRIPT

ACCEPTED MANUSCRIPT

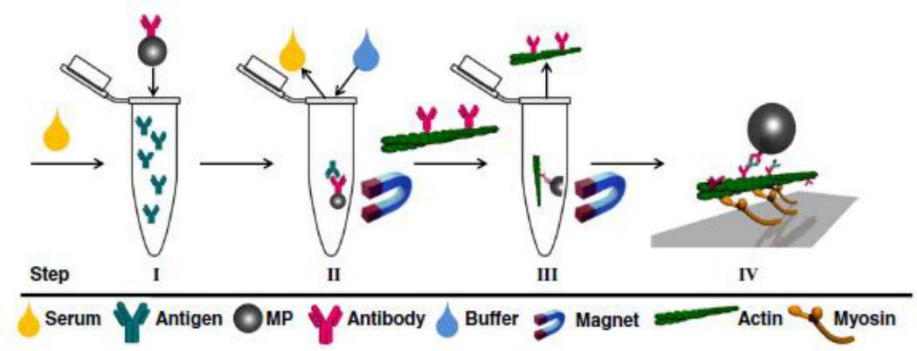


Figure 16

ACCEPTED MANUSCRIPT

ACCEPTED MANUSCRIPT

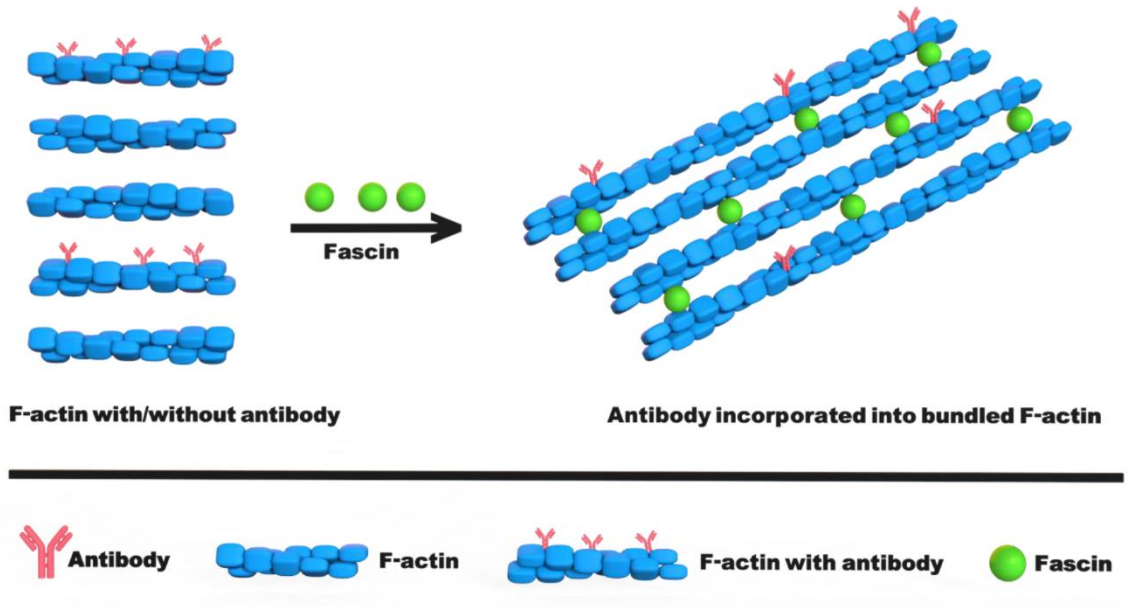


Figure 17

ACCEPTED MANUSCRIPT

ACCEPTED MANUSCRIPT

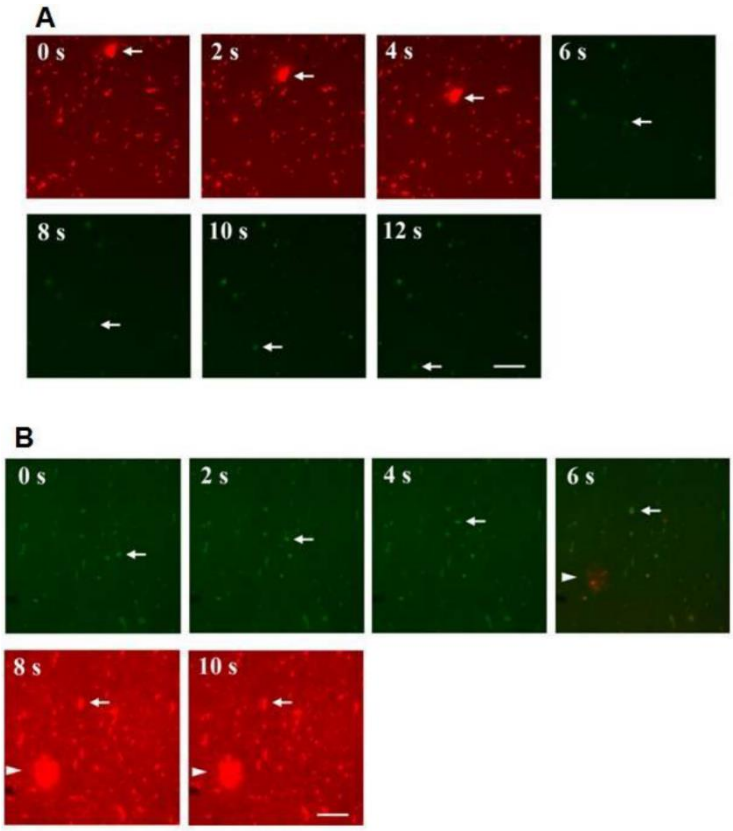


Figure 18

ACCEPTED MANUSCRIPT

Design and Development of Stand-Alone Renewable Energy based Hybrid Power System for Remote Base Transceiver Station

Priyanka Anand
Department of Electrical Engineering
I.K.G. Punjab Technical University
Kapurthala, Punjab, India

Sarbjeet Kaur Bath
Department of Electrical Engineering
G. Z.S. Campus College of Engineering & Technology
Bathinda, India

Mohammad Rizwan
Department of Electrical Engineering
Delhi Technological University
Delhi, India

ABSTRACT
Due to the increasing number of mobile users, there is a huge demand of Base Transceiver Station (BTS) particularly in rural and semi urban areas. These BTS are operated on diesel generator (DG) and also connected with the existing grid supply. However, the grid supply is rarely available in most of the remote locations. Therefore, diesel generators are mainly used for providing the continuous supply to BTS and causes lot of emissions.

In view of the above problems, a renewable energy based hybrid power system is proposed to fulfill the requirement of BTS. In this work, a hybrid model based on solar photovoltaic (SPV)/battery/diesel generator (DG) set is proposed for remote BTS application using HOMER (Hybrid Optimization Model for Electric Renewable) software. Further, techno-economic analysis with environmental benefits has been done and presented in this paper. In addition, sensitivity analysis has been performed for the proposed model. The proposed model gives reduced cost of energy (COE) of $ 0.217 as compared to $ 0.266 of the existing diesel generator system. Also, the reduction in CO_2, CO, UHC, PM, SO_x and NO_x emission is 17.138, 0.419, 0.0473, 0.0318, 0.344, 3.78 tonnes per year respectively.

General Terms
Solar Energy, Diesel Generator, Hybrid System, HOMER.

Keywords
Renewable energy, solar photovoltaic, HOMER, greenhouse gas emissions.

1. INTRODUCTION
The demand of electrical energy is increasing drastically due to rapid industrialization, inventions in new technologies, urbanization and increasing household consumptions etc. However, the power generated from the conventional sources is becoming costly due to the rising prices of fossil fuels and their depletion. Further, a large number of the population of India lives in villages and majority of villages are far from the utility grid. In India, especially small villages in the remote areas have no access of electrical energy or it is limited to a few hours. The electricity from diesel generator (DG) is not a feasible solution due to its fuel cost, transportation and maintenance cost and greenhouse gas (GHG) emissions etc. To provide reliable and cost-effective power supply in remote locations is still challenging [1]. In order to meet these challenges, power generation through renewable energy sources can become a sustainable and environmental friendly alternative in near future. Major types of renewable energy sources such as solar, wind, biogas and small hydro have huge potential to generate power on large extent. In addition, to promote power generation through renewable energy, Government of India has taken many initiatives and fixed a target of adding 175 GW power generation from renewable energy resources by 2022. The capacity addition from different renewable energy sources includes solar energy, wind energy, bio-power and small hydro is 100 GW, 60 GW, 10 GW and 5 GW respectively [2].

However, there are certain drawbacks of renewable energy resources like intermittent nature, dependency on climatic condition that make the system design unreliable and is not sufficient to meet the demand for long periods. For enhancing the reliability of the system the energy storage and/or additional sources are required for backup purpose that causes the increase in the cost of the system which is undesirable. Renewable energy based hybrid system could be a good option for electrification of remote rural areas where grid extension is difficult and not economical [3-6]. It can also deal with limitations in terms of efficiency, fuel flexibility, reliability, economics and emissions. There are several configurations available in the literature like solar photovoltaic (SPV)/hydro/DG hybrid system, SPV/wind/battery/DG hybrid system, SPV/wind/battery hybrid system, SPV/wind hybrid system, SPV/biomass hybrid system, wind/biomass hybrid system etc. which are used for electrification in rural areas [3-29].

Base Transceiver Stations (BTS) are considered as the primary source of energy consumption, which requires a continuous supply of power for its efficient operation. Providing dedicated reliable and cost-effective power supply to BTS in India is a challenging task as most of the remote areas are still not connected to the grid. As a result, most of the mobile towers operate on diesel generators which cause high operational cost, poor service and huge environmental pollution in the form of SO_x, NO_x and other carbon emissions. The government has already taken many initiatives to reduce the pollution caused by various power plants. Combining diesel generator with renewable energy could be a viable solution to mitigate these problems.

Number of papers has been published in the literature related to a hybrid power system. Some of the recent research work [11-22] is described in this paper. These models include SPV/supercapacitors for telecom network in Australia [11], SPV/proton-exchange membrane fuel cell to power remote repeater station in California [12], SPV/battery, SPV/fuel cell, SPV/fuel cell/battery [13], SPV/wind hybrid power systems along with DG for cellular mobile telephone station in India

[14], SPV/Biomass hybrid system for rural area [15], SPV/wind hybrid system to power GSM/CDMA type mobile base station for Bhopal, India [16], wind/SPV/battery [17] for remote telecom station of Nepal, SPV/wind for rural region of Cango [18], SPV/hydro/DG system [19], SPV/DG hybrid system for Nigeria [20], techno-economic and environmental performance of various hybrid systems using HOMER [21], SPV/wind energy based hybrid model for BTS in Nigeria [22] etc.

From above literature, it is observed that a hybrid model for BTS is rarely available in India particularly in Haryana state, India. In view of the above, a case study of remote Base Transceiver Station (BTS) of village Khanpur Kalan, district Sonipat, state Haryana has been selected in this paper. A hybrid model based on SPV, battery, DG has been proposed to fulfill the electricity requirement of remote BTS. The proposed model is developed using HOMER software as discussed in the following sections.

2. DEVELOPMENT of HYBRID MODEL for BTS APPLICATION

Feasibility study and analysis of hybrid model on the basis of the availability and potential of renewable energy in the rural village Khanpur Kalan (29.00 N latitude and 76.99 E longitude) in Sonipat district of Haryana state, India has been done and presented in this paper. In this work, a hybrid model consisting of SPV system along with a DG set and battery has been proposed and shown in Figure 1.

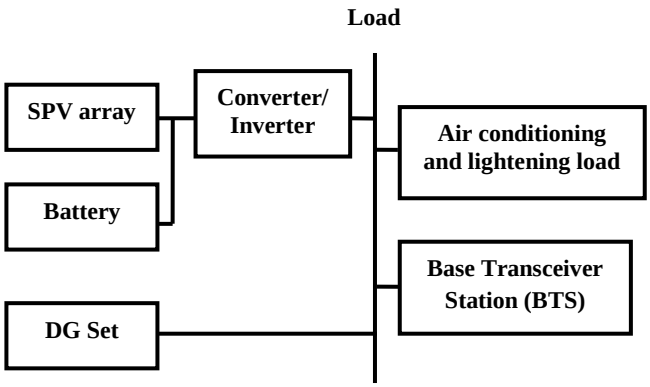


Fig. 1. Block diagram of hybrid model for BTS application

Hybrid Optimization Model for Electrical Renewable (HOMER) software developed at National Renewable Energy Laboratory (NREL) has been used for simulation and optimization purpose [30]. Using HOMER software, simulation of various renewable energy based power system configurations with all the combinations of the components have been done by providing various inputs such as solar irradiance data, hourly load, size and cost of components, etc. It performs several of hourly simulations in order to obtain the best possible match of the supply with the demand. HOMER rejects all infeasible combinations and scales the feasible systems on the basis of net present cost (NPC). A flowchart of the HOMER approach for the development of hybrid model is illustrated in Figure. 2.

The details of various parameters such as renewable energy resource i.e solar energy potential of the area, load profile of the BTS and description of size, cost and other parameters of SPV array, battery, converter, DG etc. in the proposed model have been described in the following sections.

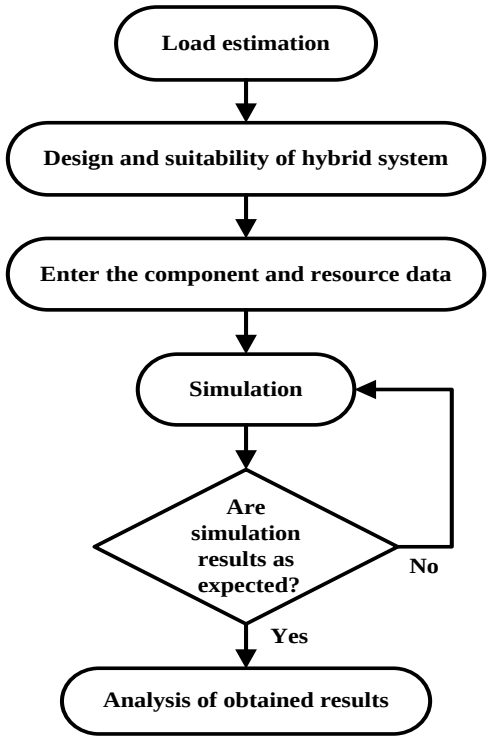


Fig. 2. Flowchart for the design of hybrid power system

2.1 Potential of Solar Energy Resource at Proposed Site

Before designing and development of hybrid model at particular site, it is necessary to identify the availability and potential of solar energy. Therefore, the solar irradiance data for the various months of the year have been obtained by HOMER software for the proposed site based upon its longitude (76.99 E) and latitude (29.00 N) and is shown in Table 1.

Table 1. Solar irradiance data of Khanpur Kalan, Haryana, India

Month	Clearness Index	Solar Irradiance (kWh/m^2/day)
January	0.615	3.742
February	0.624	4.553
March	0.629	5.57
April	0.621	6.375
May	0.607	6.738
June	0.595	6.77
July	0.543	6.091
August	0.539	5.678
September	0.635	5.911
October	0.656	5.077
November	0.643	4.076
December	0.605	3.442
Average	0.605	5.34

From Table 1, it is observed that an annual average global solar irradiance is 5.34 kWh/m^2/day. It is also revealed the maximum solar irradiance is 6.77 kWh/m^2/day in the month

of June and minimum solar irradiance is 3.442 kWh/m^2/day in the month of December.

2.2 Connected Load

Generally, a BTS site load includes BTS components and equipment load with air-conditioning and lighting load. In this work, the estimated annual peak load of the proposed site is 6.3 kW with an average of 151 kWh/day. It is anticipated that the load is identical for every day of the year.

2.3 Cost, Size and Other Parameters of Hybrid System Components

The capital cost, replacement cost and operation and maintenance (O&M) costs play a significant role in determining the optimal size of any hybrid system. The capital cost is the initial investment cost of the component. Replacement cost is the cost of replacing that component with a new one at the end of lifetime of the old one, whereas the operation and maintenance (O&M) cost is the annual cost incurred for the operation and maintenance of the components [30].

Further, in order to get the optimal system, the different sizes of selected components of the proposed hybrid model i.e SPV system, DG, converter and battery has been given as an input in their respective input window in HOMER. The size of components of the proposed hybrid model has been chosen and cost has been estimated and presented in Table 2.

Table 2. Costs and size of components of the proposed hybrid model

Item	Capital Cost ($)	Replacement Cost ($)	O&M Cost	Considered Size
SPV array (1 kW)	1000	0	1 $/year	0, 5, 10, 15, 19, 24 kW
10 KVA diesel generator	610	0	0.1 $/hour	0, 7 kW
Converter (7 kW)	230	230	1 $/year	0, 7, 8, 9 kW
Battery (vision 6FM200D)	150/battery	100/battery	100 $/year	0, 3, 5, 7, 9, 10 (no.)

The various parameters other than cost and size of components of the proposed hybrid model were also taken in to consideration are enumerated below.

The lifetime of the SPV array is considered to be 25 years. The derating factor is assumed to be 80%, which accounts for the reduction of output of SPV array due to the various effects such as dust on the panel, elevated temperature, wire losses etc. [19]. The ground reflectance is the portion of incident solar radiation reflected by the ground, is considered to be 20 % [19]. No tracking system is considered in the SPV system.

The lifespan of the DG is considered as 20000 hours [19]. The minimum load ratio is a minimum amount of allowable load on the diesel generator as a percentage of its rated capacity, is set to be 30% [19]. The cost of diesel fuel also plays an essential role in designing a hybrid power system. In this study, the cost of diesel is taken as $ 0.75 per litre. Intercept coefficient (ratio of no-load fuel consumption of the diesel generator to its rated capacity) is 0.08 L/hr/kW and slope is marginal fuel consumption of the diesel generator, is assumed to be 0.25 L/hr/kW [19]. The heat recovery ratio is not considered in this study.

Converter can work both as an inverter and rectifier on the basis of direction of flow of power. Inverter is used to provide power from the SPV system or battery to the load while the rectifier can be used to store the surplus power from the diesel generator to the battery. The lifetime of an inverter is taken as 20 years with an efficiency of 95%.

The battery is a storage device that has two operating modes i.e charging and discharging. Excess energy from SPV system can be stored and used to deliver for the duration of night time or during load shedding hours. The vision 6FM200D battery has been chosen for the proposed system.

2.4 Economic, Constraint and System Control Inputs

The various economic and constraints inputs such as project lifetime, annual rate of interest, operating reserve etc. were provided as the input information required by the simulation model. The expected project lifetime has been assumed to be 25 years with an annual rate of interest of 9%. The penalty for any capacity shortage has not been considered in the system. There is no capacity shortage for the proposed system and an operating reserve of 10% of hourly load is considered to accounts for the unexpected increase in load. Furthermore, the operating reserve of 25% as a percentage of solar power output has been considered for the proposed system to account for an abrupt decrease in output of SPV array. Operating reserve is basically the safety margin that facilitates to make sure the reliability of the supply in spite of unpredictability in hourly load and solar power output.

In system control input, there are two types of dispatch strategies which are load following and cycle charging. In the load following strategy, whenever DG is needed, then it would generate only that much power which is necessary for accomplishing the load demand. While, in the cycle charging strategy, at whatever time a DG is required for operation, it works at full capacity with excess power used to charge the battery bank [30]. In addition to this strategy, a setpoint state of charge can also be applied, in which the generator does not stop charging the battery until the defined state of charge is achieved. In the present work, cycle charging strategy along with 80% setpoint state of charge is considered [19].

3. SIMULATION RESULT and DISCUSSION

Depending upon the availability, different sources like SPV system, battery, DG set has been selected for the proposed site. Using these sources, the feasibility analysis of various configurations has been done. These configurations include DG set only, DG set with battery, SPV/DG set without battery and SPV/DG set with battery.

Techno-economic analysis of all the above mentioned configurations has been done on the basis of net present cost (NPC), cost of energy (COE) and greenhouse gas (GHG) emissions using HOMER software. The layout of the developed hybrid model is presented in Figure. 3.

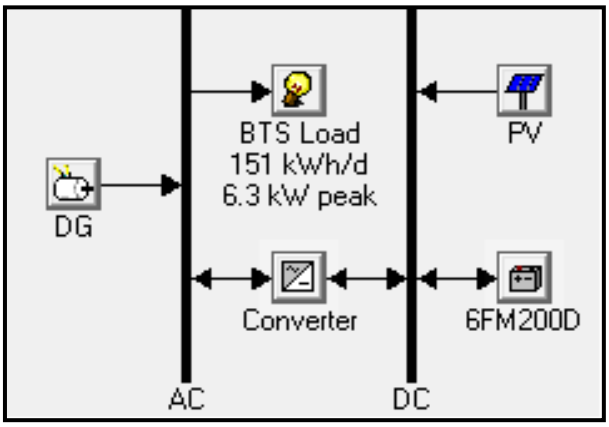


Fig. 3. Layout of the developed hybrid model using HOMER

3.1 Techno-economic and GHG Emissions Analysis

Techno-economic analysis of all the configurations has been done to evaluate the performance of the developed models. Based on the COE and GHG emissions, a suitable model has been selected for the proposed site. By providing the components inputs in HOMER software, simulations of various configurations have been performed on the basis of NPC and an optimized model has been selected. Result of the possible configurations with their rating is presented in Table 3.

Table 3. Various ratings of possible configurations

Configuration	PV (kW)	DG (kW)	Battery (no.)	Converter (kW)
DG set only	--	7	--	--
DG set with battery	--	7	3	1
SPV/DG set without battery	24	7	--	7
SPV/DG set with battery	19	7	3	7

Further, a comparison of all the four possible configurations has been done in terms of initial capital, NPC, annualized cost, COE etc. and is presented in the Table 4.

From Table 4, it is observed that the NPC of SPV/DG set with battery is $ 117599 whereas it is $ 123942 of SPV/DG set without battery, $ 144090 for DG set only and$ 147689 for DG set with battery. In addition, the COE of SPV/DG set with battery is $0.217 whereas it is $ 0.229/kWh, $ 0.266/kWh, $ 0.273/kWh for SPV/DG set without battery, DG set only and DG set with battery respectively. Moreover, the configuration SPV/DG set with battery has least fuel consumption and hours of operation of DG set than SPV/DG set without battery, DG set only and DG set with battery. SPV/DG set with battery hybrid model is still the better option on the basis of economic point of view.

In addition, the contribution of individual components in the NPC in SPV/DG set with battery hybrid model is given in the Table 5.

Table 4. Various cost associated with different configurations

Configuration	Initial Capital Cost ($)	Operating Cost ($/year)	NPC ($)	Annualized Cost ($/year)	COE ($/kWh)	Fuel Consumption (litre)	Hours of Operation of DG Set (hour/year)	Renewable Fraction
DG set only	427	14626	144090	14669	0.266	18683	8760	0.00
DG set with battery	910	14943	147689	15036	0.273	18684	8760	0.00
SPV/DG set without battery	24657	10108	123942	12618	0.229	12796	6914	0.51
SPV/DG set with battery	20107	9925	117599	11972	0.217	12175	6116	0.46

Table 5. Share of individual components in the NPC in hybrid SPV/DG set with battery system

Component	Capital Cost ($)	Replacement Cost ($)	O&M Cost ($)	Fuel Cost ($)	Salvage Value ($)	Total ($)
SPV array	19000	0	187	0	0	19187
DG	427	0	4205	89695	0	94327
Vision 6FM200D	450	437	2947	0	-9	3825
Converter	230	41	10	0	-20	261
System	20107	478	7348	89695	-29	117599

Further, in order to evaluate the economic measures in terms of present value of fuel saved, annual worth, return on investment, payback etc., a comparison has been made in between SPV/DG set with battery hybrid system and DG set only system using HOMER. A DG set only system was selected as base case system and SPV/DG set with battery hybrid system was considered as current system. The result of the economic measures comparison of the SPV/DG set with battery hybrid system and DG set only system are illustrated in Table 6.

Table 6. Economic measures of SPV/DG set with battery hybrid system and DG set only system

Economic Measures	Value
Present worth	$ 26490
Annual worth	$ 2697/year
Return on investment	23.9 %
Internal rate of return (IRR)	23.8 %
Simple payback	4.63 years
Discount payback	5.63 years

It is revealed from Table 6 that the present worth i.e the difference between the NPC of SPV/DG set with battery hybrid system and DG set only system is $ 26490. A positive sign shows that the SPV/DG set with battery hybrid system saves money over the project lifetime compared to DG set only system. Payback is 4.63 years which is a sign of how much time it takes to recover the difference in investment costs between the current system and base case system.

Greenhouse gas emissions analysis is also carried out for all the four possible configurations and presented in Table 7.

From Table 7, it is observed that the configuration of SPV/DG set with battery has least GHG emissions as compared to the SPV/DG set without battery, DG set only and DG set with battery. Therefore, it is concluded in terms of least emission that the hybrid SPV/DG set with battery is found better as compared to SPV/DG set without battery, DG set only and DG set with battery. Moreover, SPV/DG set with battery system has least NPC and COE than the SPV/DG set without battery, DG set only and DG set with battery. Hence, the hybrid SPV/DG set with battery model is proposed because of lesser NPC, lesser COE and smaller amount of GHG emission.

Table 7. Greenhouse gas emissions of different configurations

Pollutant emission	DG Set Only	DG Set With Battery	SPV/DG Set Without Battery	SPV/DG Set With Battery
Carbon dioxide (CO_2) emission (tonnes/year)	49.200	49.200	33.695	32.062
Carbon monoxide (CO) emission (tonnes/year)	1.21	1.21	0.832	0.791
Unburned hydrocarbons (UHC) emission (tonnes/year)	0.135	0.135	0.0921	0.0877
Particular matter (PM) (tonnes/year)	0.0915	0.0916	0.0627	0.0597
Sulphur oxide (SO_x) (tonnes/year)	0.988	0.988	0.677	0.644
Nitrogen oxide (NO_x) (tonnes/year)	10.84	10.84	7.42	S7.06

3.2 Energy Production Analysis

The excess electricity and capacity shortage from various configurations i.e DG set only, DG set with battery, SPV/DG set without battery and SPV/DG set with battery is presented in Table 8.

Table 8. Excess electricity and capacity shortage of various configurations

Configuration	Excess Electricity (kWh/year)	Unmet Electrical load (kWh/year)	Capacity Shortage (%)
DG set only	0	0	0%
DG set with battery	0.0000813 (0.00%)	0	0%
SPV/DG set without battery	16929 (23.2%)	0.0000396	0%
SPV/DG set with battery	8279 (12.8%)	0.0000453	0%

From Table 8, it is observed that the excess energy production of SPV/DG set with battery is 8279 kWh/year (12.8%) without any unmet load whereas it is 16929 (23.2 %) for SPV/DG set without battery, 0 for DG set only and 0.0000813 for DG set with battery respectively.

Further, the contribution of SPV and DG set independently and in combination for each month of the year of hybrid SPV/DG set with battery model is depicted in Figure 4-Figure 6.

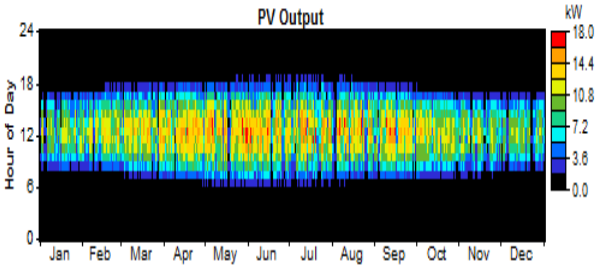


Fig. 4. Electricity production of SPV in SPV/DG with battery hybrid model

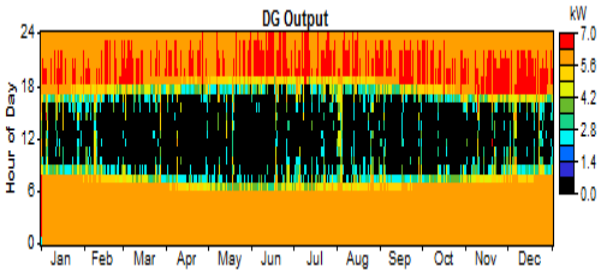


Fig. 5. Electricity production of DG set in SPV/DG with battery hybrid model

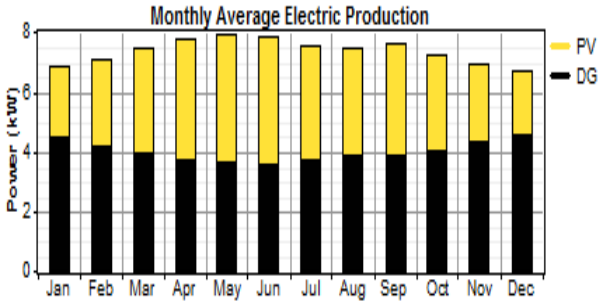


Fig. 6. Electricity production of hybrid SPV/DG with battery model

It is observed from Figure 6 that the energy production is high during May and low during December due to variation in solar irradiance.

3.3 Sensitivity Analysis

In the present study, the sensitivity analysis has been done to evaluate the performance of the proposed model by considering the diesel price and load demand as the sensitivity variables. This analysis has been conducted to study the variation of various parameters and their impacts on the selection of model. In addition, this analysis has been investigated the feasibility of hybrid SPV/DG with battery model at different values of load demand and diesel prices, as mentioned in Table 9.

Table 9. Different values of sensitivity variables

Sensitivity Variable	Different Values of Sensitivity Variable
Diesel price ($)	0.600, 0.650, 0.700, 0.750, 0.800, 0.850
Load demand (kWh/day)	148, 151, 154

The effect of variation in load demand and diesel price on COE, NPC, operating cost and annualized cost are depicted in Figure 7- Figure 10.

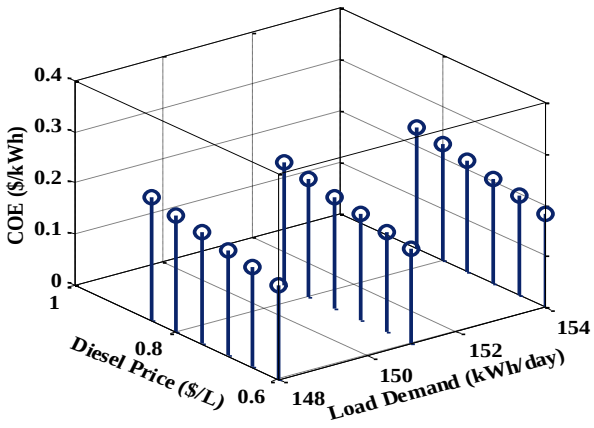


Fig. 7. Effect of variation of load demand and diesel price on COE

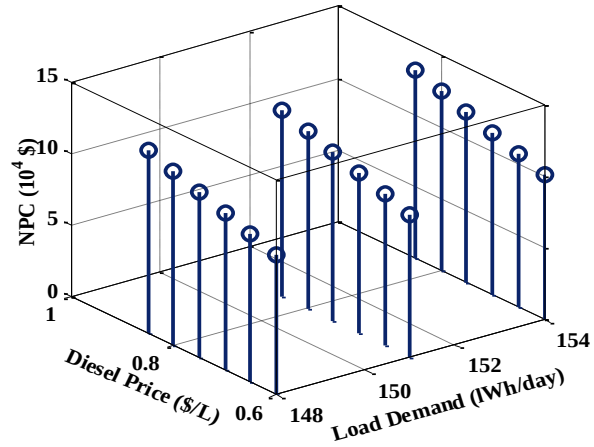


Fig. 8. Effect of variation of load demand and diesel price on NPC

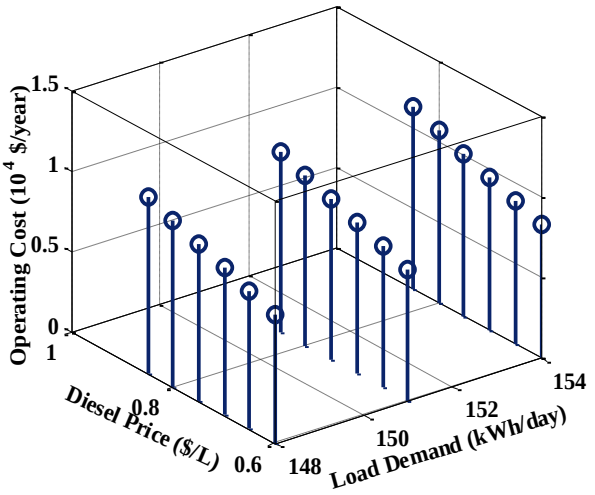


Fig. 9. Effect of variation of load demand and diesel price on operating cost

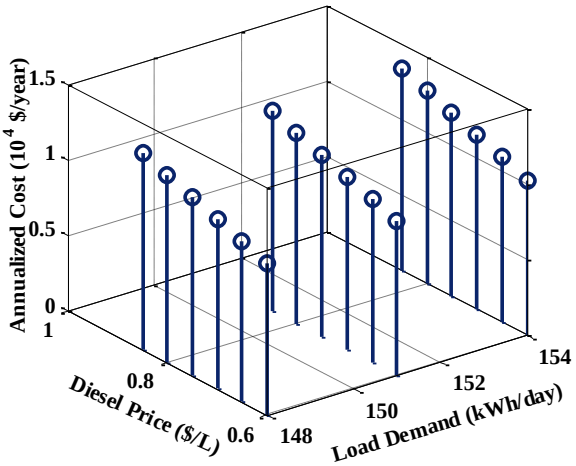


Fig. 10. Effect of variation of load demand and diesel price on annualized cost

From Figure 7- Figure 10, it is revealed that the COE, NPC, operating cost and annualized cost are increasing with increase in diesel price. It is further observed that the operating cost, NPC and annualized cost increases with the increase in load demand while the COE decreases. In addition, the result also shows that SPV/DG with battery hybrid model is still feasible and economical for lower and higher values of diesel prices and load demand.

4. CONCLUSION

In this paper, a sustainable and environment friendly hybrid model based on SPV/DG set with battery is proposed for reliable power supply to BTS. The model is selected on the basis of cost of energy and GHG emissions. The cost of energy from the proposed model is $ 0.217/kWh whereas it is $ 0.266/kWh from the existing diesel generator set. Further, the GHG emissions reduction is about 34% of the proposed model as compared to the existing system which is very significant.

Keeping in view of the above, hybrid model based on SPV/DG set with battery is proposed for the given remote location. The results of the proposed study revealed that the proposed hybrid system can be deployed to provide the cost effective electricity to the BTS load where no other renewable energy resources are available and exploitable. Further, the proposed model would also be helpful in achieving the target of Government of India "Power to all" and "Digital India" etc.

5. ACKNOWLEDGMENT

The first author would like to express gratitude to I.K. Gujral Punjab Technical University, Kapurthala, Jalandhar (Punjab) for providing research facilities for pursuing research work.

6. ABBREVIATIONS AND SYMBOLS

BTS	Base Transceiver Station
CO	Carbon monoxide (Tonnes/year)
COE	Cost of energy ($/kWh)
CO_2	Carbon dioxide (Tonnes/year)
CDMA	Code division multiple axis
DC	Direct current
DG	Diesel generator
FC	Fuel cell
GSM	Global system for mobile communication
GW	Gigawatt
HOMER	Hybrid optimization model for electric renewable
NO_x	Nitrogen oxide (Tonnes/year)
NPC	Net present cost ($)
NREL	National renewable energy laboratory
O&M	Operation and maintenance
PEM	Proton exchange membrane (Tonnes/year)
PM	Particulate matter (Tonnes/year)
SO_x	Sulphur dioxide (Tonnes/year)
SPV	Solar photovoltaic
UHC	Unburned hydrocarbons (Tonnes/year)

Greek Symbols

$	Dollar
%	Percentage

7. REFERENCES

[1] Jain, A., Srinivas, E., Raman, S., Gaddam, R. R., Haritha, V. V. S. S., and Srinath, N. V. 2010. Sustainable energy plan for an Indian village. In Proceedings of IEEE Power System Technology, Hangzhou. 1-8.

[2] Ministry of New & Renewable Energy, Government of India. www.mnre.gov.in.

[3] Kanse-Patil, A. B., Saini, R. P, and Sharma, M. P. 2010. Integrated renewable energy systems for off grid rural electrification of remote area. Renewable Energy. 35(6), 1342-1349.

[4] Setiawan, A. A., Zhao, Y., and Nayar, C. V. 2009. Design, economic analysis and environmental considerations of mini-grid hybrid power system with reverse osmosis desalination plant for remote areas. Renewable Energy. 34(2), 374-383.

[5] Akella, A. K., Sharma. M. P., and Saini, R. P. 2007. Optimum utilization of renewable energy sources in a remote area. Renewable and Sustainable Energy Reviews. 11(5), 894-908.

[6] Rajoriya, A., and Fernandez, E. 2010. Sustainable energy generation using hybrid energy system for remote hilly rural area in India. International Journal of Sustainable Engineering. 3(3), 219-227.

[7] Asrari, A., Ghasemi, A., and Javidi, M. H. 2012. Economic evaluation of hybrid renewable energy systems for rural electrification in Iran- a case study. Renewable and Sustainable Energy Reviews. 16(5), 3123-3130.

[8] Castellanos, J. G., Walker, M., Poggio, D., Pourkashanian, M., and Nimmo, W. 2015. Modelling an off-grid integrated renewable energy system for rural

electrification in India using photovoltaics and anaerobic digestion. Renewable Energy. 74(2), 390-398.

[9] Al-Badi, A. H., and Bourdoucen, H. 2012. Study and design of hybrid diesel–wind standalone system for remote area in Oman. International Journal of Sustainable Energy. 31(2), 85-94.

[10] Rehman, S., and Al-Hadhrami, L. M. 2010. Study of a solar PV-diesel-battery hybrid power system for a remotely located population near Rafha, Saudi Arabia. Energy. 35, 4986-4995.

[11] Robbins, T., and Hawkins, J. M. 1997. Powering telecommunications network interfaces using photovoltaic cells and supercapacitors. In Proceedings of IEEE Telecommunications Energy, Melbourne. 523-528.

[12] Lehman, P. A., Chamberlin, C. E., Zoellick, J. I., and Engel, R. A. 2000. A photovoltaic /fuel cell power system for a remote telecommunications station. In Proceedings of IEEE Photovoltaic Specialists, Anchorage. 1552-1555.

[13] Bajpai, P., Prakshan, N. P., and Kishore, N. K. 2009. Renewable hybrid stand-alone telecom power system modeling and analysis. In Proceedings of IEEE TENCON, Singapore. 1-6.

[14] Nema, P., Nema, R. K., and Rangnekar, S. 2010. Minimization of green house gases emission by using hybrid energy system for telephony base station site application. Renewable and Sustainable Energy Reviews. 14(6), 1635-1639.

[15] Anand, P., Bath, S. K., and Rizwan, M. 2016. Feasibility analysis of Solar-Biomass based standalone hybrid system for remote area. American Journal of Electrical Power and Energy Systems. 5(6), 99-108.

[16] Nema, P., Nema, R. K., and Rangnekar, S. 2010. PV-solar/wind hybrid energy system for GSM/CDMA type mobile telephony base station. International Journal of Energy and Environment. 1(2), 359-366.

[17] Paudel, S., Shrestha, J. N., Neto, F. J., Ferrira, J. A. F., and Adhikari, M. 2011. Optimization of hybrid PV/Wind power system for remote telecom station. In Proceedings of IEEE Power and Energy Systems, Chennai. 1-6.

[18] Kusakana, K., and Vermark, H. J. 2013. Hybrid renewable power systems for mobile telephony base stations in developing countries. Renewable Energy. 51, 419-425.

[19] Anayochukwu, A. V., and Ndubueze, N. A. 2013. Potentials of optimized hybrid system in powering off-grid macro base transmitter station site. International Journal of Renewable Energy Research. 3(4), 861-871.

[20] Anayochukwu, A. V., and Nnene, E. A. 2013. Simulation and optimization of hybrid diesel power generation system for GSM base station site in Nigeria. Electronic Journal of Energy & Environment. 1(1), 37-56.

[21] Amutha, W. M, and Rajini, V. 2015. Techno-economic evaluation of various hybrid power systems for rural telecom. Renewable and Sustainable Energy Reviews. 43, 553-561.

[22] Olatomiwa, L., Mekhilef, S., Huda, A. S. N., and Sanusi, K. 2015. Techno-economic analysis of hybrid PV–diesel–battery and PV–wind–diesel–battery power systems for mobile BTS: the way forward for rural development. Energy Science and Engineering. 3(4), 271–285.

[23] Alsharif, M. H., Nordin, R., and Ismail, M. 2015. Energy optimisation of hybrid off-grid system for remote telecommunication base station deployment in Malaysia. EURASIP Journal on Wireless Communications and Networking. 64, 1-15.

[24] Sawle, Y., and Gupta, S. C. 2015. A noval system optimization of a grid independent hybrid renewable energy system for telecom base station. International Journal of Soft Computing, Mathematics and control. 4(2), 49-56.

[25] Khan, M. J., Yadav, A. K., and Mathew, L. 2017. Techno economic feasibility analysis of different combinations of PV-Wind-Diesel-Battery hybrid system for telecommunication applications in different cities of Punjab, India. Renewable and Sustainable Energy Reviews. 76, 577–607.

[26] Shahzad, M. K., Zahid, A., Rashid, T. U., Rehan, M. A., Ali, and Ahmad, M. 2017. Techno-economic feasibility analysis of a Solar-Biomass off -grid system for the electrification of remote rural areas in Pakistan using HOMER software. Renewable Energy. doi: 10.1016/j.renene.2017.01.033.

[27] Priyanka, Bath, S. K., and Rizwan, M. 2017. Design and optimization of RES based standalone hybrid System for remote applications. In Proceeding of 8th IEEE conference on Innovative Smart Grid Technologies (ISGT 2017) sponsored by IEEE Power and Energy Society (PES), Washington DC, USA. 1-5.

[28] Anand, P., Bath, S. K., and Rizwan, M. 2017. Design of Solar-Biomass-Biogas Based Hybrid System for Rural Electrification with Environmental Benefits. International Journal on Recent and Innovation Trends in Computing and Communication. 5 (6), 450 – 456.

[29] Solanki, C. S. 2012. Renewable Energy Technologies: A Practical Guide for Beginners. New Delhi: PHI learning private limited.

[30] National Renewable Energy Laboratory (NREL) www.nrel.gov/homer.

IOPscience iopscience.iop.org

Home Search Collections Journals About Contact us My IOPscience

Detection of circular Rydberg states in lifetime measurements

This content has been downloaded from IOPscience. Please scroll down to see the full text.

2017 J. Phys.: Conf. Ser. 875 112010

(http://iopscience.iop.org/1742-6596/875/12/112010)

View the table of contents for this issue, or go to the journal homepage for more

Download details:

IP Address: 14.139.251.107
This content was downloaded on 24/08/2017 at 12:08

Please note that terms and conditions apply.

You may also be interested in:

Energy intervals between Rydberg states nD and nF in lithium-7
S A Saakyan, V A Sautenkov and B B Zelener

Harmonic-emission from Rydberg states in the vicinity of metallic nanostructures
I Yavuz, Y Tikman and Z Altun

Rydberg states form molecular probes

H and He atoms in strong magnetic fields
B C Saha and L B Zhao

Investigation of odd-parity Rydberg states of Eu I with autoionization detection
Xiao Ying, Dai Chang-Jian and Qin Wen-Jie

Rydberg States of Atoms and Molecules
D W O Heddle

A new method for detecting the contribution of high Rydberg states to electron-ion recombination
I Orbán, S Böhm, M Fogle et al.

Lifetime measurements and the high-spin structure of 36Cl
S Aydin, M Ionescu-Bujor, F Recchia et al.

Photoionization Spectra of Pd in High Rydberg States
Toshiaki Ishikawa

Detection of circular Rydberg states in lifetime measurements

Gaurav Sharma* [1] **and Nitin K. Puri** * [2]

* Dept. of Applied Physics, Delhi Technological University, New Delhi-110042, India

Synopsis The possible reason for the non detection of the circular Rydberg state during the earlier life time measurements is discussed. It is concluded that for populating and detecting a CRS the energy of the ion, Plasmon frequency of the target, position of measurement and step size between two consecutive steps near the last cascade position plays an important role.

Circular Rydberg states (CRS) have much longer radiative lifetimes than low orbital angular momentum states and are therefore candidates for high-fidelity gate operations [1] and determining the relativistic and the quantum electrodynamic effects, the fundamental constants such as the nuclear mass. The electron in CRS decays through the yrast chain following the electric dipole selection rules. The 2p state, the last candidate of the cascade that leads to emission of Ly-α emission takes place in the H-like heavy ions, is populated very late. Each delayed Ly-α transition originating from certain CRS appears as a hump at a particular delay time. Recently these states has been observed in lifetime measurement [2] in a beam-foil experiment which are supported theoretically [3].

For the formation of particular Rydberg state with principal quantum number n of an ion with core charge Z; it is possible to predict the ionic velocity v>vc [4] such that $vc=wp*(1.43n+ 0.64k)^2/Z$ where wp is the Plasmon frequency of the solid and n and k are the principal and angular quantum numbers. This estimation of the velocity is plotted in fig.1 suggesting that a much higher energy is required to populate low l states compared to CRS. We have examined some earlier lifetime measurement [2,5–8] to understand the non detection of CRS. Table 1 represents some experimental data with the possible CRS populated and the measurements taken during the experiments. It is clear from the table that in most of the experiments the data point was not taken up to the desired cascade position or the step size of the measurements was too large to observe the delayed decay. The crude extract of the analysis realizes that the combination of three parameters play a key role for the detection of CRS through lifetime measurement. First is the velocity of the incident particle and Plasmon frequency for populating a particular (n,l); second is the measurement position should be around the delay interval of last cascade. Another is the precise measurement with small intervals near the last cascade delay interval with step size of the measurement less than or equal to the lifetime of the last candidate of the chain i.e. 2p or 3p, for the detection of CRS.

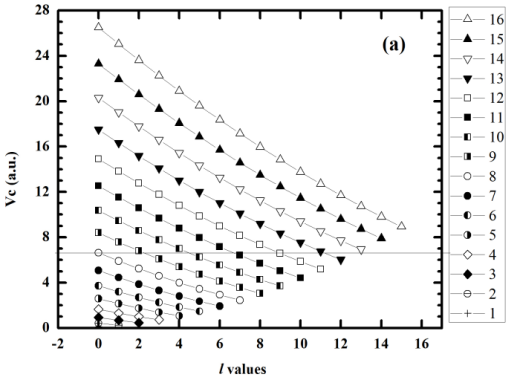


Figure 1. Graphical representation of velocity required to populate a (n,l) level for 125MeV S ions. Horizontal line represents velocity corresponding to 125MeV and the states crossing the line are the possible excitations.

Energy,Species	Nc	d (mm)	M(mm)	Comment
125MeV S [5]	14	3.45	2,20	Δd large
2530 MeV Kr, H-like Kr [6]	35	17 ns	0.2ns	Delay not sufficient
700 MeV Kr He-like Kr [7]	25	108.78	10	
163 MeV Ni He-like Ni [8]	17	18.17	10.5	
164 MeV Fe H-like Fe [2]	17	21.56	36	Observed

Table1. Experimental lifetime data with the measured and possible CRS positions. (Nc is the possible principle quantum number of CRS populated d is corresponding delay, Δd is the step size between two consecutive measurements, and M is experimental measured points)

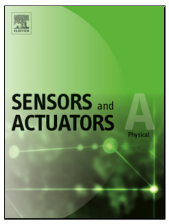
References

[1] M Saffman et *al.* 2010 *Rev.Mod. Phys.* **82** 2313
[2] T. Nandi 2008 *Astrophys. Journal,* **673** L103
[3] N.N. Nedeljković et *al*. 2014 *J. Quant. Spectrosc. Radiat. Transf.* **134** 46
[4] J.Muller and J.Burgdorfer 1991 *Phys.Rev.A* **43** 11
[5] H-D.Betz et.*al*1983 Targets *Phys.Rev.Lett.***50** 34
[6] S.Cheng et *al.* 1993 *Am. Inst. Phys.* **274** 394
[7] S.Cheng et *al*. 1994 *Phys. Rev. A* **50** 2197
[8] T.Nandi et *al*. 2004 *J. Phys. B: At.Mol Opt. Phys.* **37** 703

[1]E-mail: gaurav.kmc891101@gmail.com
[2]E-mail: nitin.phy@dce.edu

Content from this work may be used under the terms of the Creative Commons Attribution 3.0 licence. Any further distribution of this work must maintain attribution to the author(s) and the title of the work, journal citation and DOI.
Published under licence by IOP Publishing Ltd

Accepted Manuscript



Title: Digitally controlled portable micropump for transport of live micro-organisms

Authors: Rishi Kant, Deepak Singh, Shantanu Bhattacharya

PII: S0924-4247(17)30024-9
DOI: http://dx.doi.org/doi:10.1016/j.sna.2017.05.016
Reference: SNA 10125

To appear in: *Sensors and Actuators A*

Received date: 8-1-2017
Revised date: 21-4-2017
Accepted date: 5-5-2017

Please cite this article as: Rishi Kant, Deepak Singh, Shantanu Bhattacharya, Digitally controlled portable micropump for transport of live micro-organisms, Sensors and Actuators: A Physicalhttp://dx.doi.org/10.1016/j.sna.2017.05.016

This is a PDF file of an unedited manuscript that has been accepted for publication. As a service to our customers we are providing this early version of the manuscript. The manuscript will undergo copyediting, typesetting, and review of the resulting proof before it is published in its final form. Please note that during the production process errors may be discovered which could affect the content, and all legal disclaimers that apply to the journal pertain.

ACCEPTED MANUSCRIPT

Digitally controlled portable micropump for transport of live micro-organisms

Rishi Kant[1], Deepak Singh[2], Shantanu Bhattacharya[1,*]

[1]Microsystems Fabrication Laboratory, Department of Mechanical Engineering
[2]Chemistry Department
Indian Institute of Technology, Kanpur

*Corresponding Author Email Address: bhattacs@iitk.ac.in

Abstract

Laser micromachining has been extensively utilized to fabricate polymer based biomedical devices and is well known for producing high throughput fabrication at very low costs. The laser ablated surfaces are very rough and particularly in those micro-devices which are supposed to handle viable cells other micro-electronically inspired fabrication processes are preferred. During the micro-scale fluidic transport as generated by moving members within active micro-devices and also owing to the interfacial shear level close to the surfaces in both active and passive micro-devices there is a general loss of viability of the transported sample. In this work we have developed a hybrid strategy where the laser manufactured PMMA samples are smoothened by a chemical etching step and so obtained smooth surface is used to fabricate multilayer micropump which is actuated by a piezo disc. The micropump is operable at lower voltage 5-7.5 V DC. The flow rates of our device can be programmed through a micro-controller interface and trials are able to yield a viable transportation of solutions containing micro-organisms. The optimized design of the microfluidic chamber used in this work is able to discharge the whole containment from within the fluid chambers while retaining the cell viability.

ACCEPTED MANUSCRIPT

Keywords: Micropump, PMMA, Piezo, fluid transport, viable cell, laser micro machining

ACCEPTED MANUSCRIPT

1. Introduction:

Laser micro-machined components formulate the key features of micro-total analysis system (μTAS) which are used for imparting functionality to the devices like manipulation of miniaturized fluid volumes through micro-scale pumps, valves, mixers [18-22] etc., selective trapping and transport through processes like dielectrophoresis, electrophoresis, electro-osmosis etc. Therefore, their sustained research is quite important for the emerging fields like micro-fluidics, proteomics, genomics etc. which formulate the frontiers of biomedical technology etc [1-4, 16]. However their performance is limited owing to the difficulty faced while handling biologically viable fluids within these structures due to the rough nature of the laser machined surfaces. A lot of research has already towards analysis of the laser machining process with an overall goal of optimizing surface finish and integrity. Y. Huang et. al. [5] provided a preheat treatment of PMMA substrate immersed in water bath at 80 deg. C before carrying out machining operations. They were able to reduce the overall surface roughness (arithmetic mean surface roughness (Ra)) to around 100 nm by bursting all the bubbles formulated within the solidification transition layer. Q. Heng et.al [25] tried to optimized laser machined surface. Cheng et. al.[23] studied the effect of surface roughness on Reynolds number in micro-flows. In some other research modules. M.Bahrami et. al [26] also tried to study the effect of rough surface during micro scale fluid flow. They found out that the flow over a surface having relatively higher surface roughness always led to the formation of eddies and recirculation zones locally which would lead to an overall pressure drop within micro-fluidic channels. This would be a significant factor influencing the viability of the biological species that are transported. There lies a need to develop a strategy that is less complex than underwater laser machining [5] and it could yet produce an equivalent order of magnitude of surface roughness of the laser micro-machined parts so that they can be deployed for viable transport of biofluids. To generate transport within devices a flow actuation is done in an integrated manner within the devices itself. There are various actuation mechanisms by which micro-pumping can be realized such as pneumatic, electrostatic, piezoelectric

ACCEPTED MANUSCRIPT

[43-46] thermo-pneumatic, electromagnetic, magneto-hydrodynamics(MHD), electro-hydrodynamic, shape memory alloy based, ferro-fluid based, phase change based and Ionic conducting polymer film based actuation. Among these the piezo-actuated micro-pumping units have demonstrated good capabilities for fluid transport applications [3, 7-11]. Some of these piezo driven units have catered to different performance ranges as detailed below. Carrozza et.al. [12] used a polymer-brass material to construct a piezoelectric driven micropump. They used a stereo lithography process to fabricate the micro-pump. They were able to achieve maximum flow rates of 2.7 ml/min at 70 Hz frequency and 300 V (applied voltage).The overall size of this micropump unit was around 1270 mm^3. N.T. Nguyen et. al. [13] reported a circular chamber based polymeric micro-pump actuated by piezo discs in which uses SU-8 Photoresist and PMMA for fabrication and delivers flow rate upto an extent of 1 ml/min and max back pressure 200 mm of water at 50 V.

T. Q. Truong et. al. [14] also developed circular chamber based piezoelectric micropump using polymeric lamination technology, they achieved a maximum flow rate 2.9 ml/min with back pressure 1.6 m of water at a high driving voltage ±150 V. They did not mention about portability of the complete system with driving unit etc. In fact looking into literature we have found that there is very less mention of the overall size of the pumping system including the driving unit and the control system etc. We have tried to map the existing status of the micro-pumps in terms of three most important parameters like overall size of the complete system, applied voltage and back pressure [Figure 1].

The work reports a development process of a portable micro-pumping unit fabricated through a combination of a laser micromachining and wet chemical etching processes. The under-water laser machining as reported earlier provides a high throughput solution although it may involve a costlier system. Most of the cost that is involved in under water laser machining happens due to the utilization of higher power, complex optical focusing systems and integration of a work-piece

ACCEPTED MANUSCRIPT

stage in submerged condition. The complexities of the underwater laser machining process can be avoided easily through a two-step methodology as observed in the current work. We have developed and tested a piezo driven micro-pump unit with capabilities like small overall size, low battery power and ability to withstand a back pressure of 500 mm water. The overall size of the pumping device including control instrumentation in this work is designed as Length=90mm, Width=75mm and Depth=60mm. Table 1 presents the list of the various reference numbers represented with detailed specifications of the individual micro pumping systems developed by various researchers. The present micropumping system is contains smaller size, lower voltage requirement and can sustain back pressure upto 500 mm of DI water.

In summary we have developed a functional prototype of a micropump unit using laser micro-machining and wet chemical etching strategies. The surface obtained by this strategy is of low overall roughness and the device realized addresses issues like viable transport of live samples (*micro-organisms)*, use of low overall power per unit flow volume, high portability, low power usage, high pumping efficiency, higher flow-rate and better sustainability to a back pressure range of 500 mm of DI water.

Several modules of predictive modeling have been carried out using the interaction of the discharge volume with the vibrating piezo-disc and the relevant experimental analysis has been carried out on the micro-pumping system. Optimization strategies of mechanical power per unit discharge volume through the containment of the pumping chamber have been thoroughly simulated with complex fluid dynamics models. The pumps developed have further utilized a thin membrane of Poly dimethyl siloxane (PDMS) as a sealing material for the gap between the piezo-disc and the PMMA substrate. This seal dynamically alters the thicknesses during the deflection cycle of the piezo. The complete micro-electronically controlled circuit has been

ACCEPTED MANUSCRIPT

designed & simulated using LT-spice and finally integrated into a PCB block which essentially contains an amplifier and a Pulse Width Modulating (PWM) circuit.

The micro-pumps utilize a total voltage of 7.5 V for providing a volume discharge at 497μl/min and it can withstand a back pressure of 500 mm of DI water. Further we have observed the ability of our miniaturized system to handle micro-organisms without any substantial loss of viability.

2. Design of Micro-pumping system:

The prototype of portable micro-pumping system has been illustrated pictorially in figure 2 which contains a fluid handling system actuated by Piezo, pulse width modulation unit and amplifier unit. The complete description of all these units has been discussed in detail in following lines.

2.1 Heirarchical Design of Fluid Handling System:

The micro-pumping architecture is realized in PMMA using Laser micromachining followed by the pasting of a piezo module over the pumping chamber. The simplicity of our fabrication process is the key feature of this design as it needs very less infrastructure making it an inexpensive design while still maintaining a generally rugged design with good repeatability of pumping action. The micropumping unit is manufactured using four different laminates. The first laminate is a PMMA sheet of 40x20x1.5 mm dimension containing the laser ablated and smoothened micropumping architecture with optimized geometry. The second laminate is made of PDMS material of 40x20x0.01 mm dimension and is pasted using araldite over the first laminate. The thin PDMS layer is realized using spin coating and mould releasing steps and is very crucial for a leakage free micropumping setup. This layer also formulates a confinement for the pump inlet and also the discharge and guides the discharge all the way to the pump outlet.

ACCEPTED MANUSCRIPT

The third layer is actually the piezo actuator disc of diameter 15 mm (PZT 5A, M/S Shenoy industries pvt. Ltd, India.) which is the active part of the micropumping system. There is another fourth laminate which is pasted on the top of the piezo and contains a 14 mm hole centrally for accommodating the piezo displacement over the pumping chamber. There is a 1mm overlap diametrically between the piezo disc and the fourth laminate. The overlapping fourth layer is mainly used to provide a rigid support in combination with the first laminate so that maximum displacement of the piezo (now acting with a clamped boundary) can be realized over the pumping chamber. The displacement of this piezo-disc has been modeled using COMSOL multi-physics. We have also modelled flow rates of the pumping system by using coupled physics model with moving boundary method. The design of the chamber has already been optimized in another earlier work by Kant et. al. [15]. Figure 3 illustrates the schematic of assembly of the different laminates. The PDMS laminate plays a very critical role of rubber like packing by changing its thickness/ form etc. over the relative moving parts of the pumping assembly and prevents any fluid leakage from the pump.

2.2 Numerical modeling of 3D micropump:

A 3 dimensional fluid structure interaction on actuation through a piezo disc module is carried out using Comsol Multiphysics 5.2. The present model of Piezo based micro-pump requires three different physical behaviors to be integrated together viz., (i) Electrostatic behavior (ii) structural behavior and (iii) behavior of fluid flow through the channel structures. The solver is setup in COMSOL with two way coupling scheme as depicted in figure 4 below.

In the first model a coupling between electrostatic physics and structural physics is integrated through its respective governing equations as detailed below. This is done with a purpose of studying the displacement behavior of the Piezo disc due to an applied voltage. In the second

ACCEPTED MANUSCRIPT

model integration is made between the structural physics and the physics of fluid flows by again coupling respective governing equations as detailed below. This coupling is achieved to obtain the fluid velocity that is being pumped out. The solution corresponding to the structural equations from the first model is assumed to be the inputs for the second model. Figure 5 (a) present a CAD drawing used for simulation of micro-pumping domains and figure 5(b) presents meshed geometry of these domains after mesh size optimization.

Physical models used for the three different behaviors are the following:

2.2.1 Electrostatic physics (PZT material):

The governing equations required to solve elctro-sturctural simulation for PZT disc, are following:

$$\boldsymbol{\rho}\frac{\boldsymbol{\partial^2 X}}{\boldsymbol{\partial t}} - (\Delta.\boldsymbol{\sigma}) = \boldsymbol{F} \quad \text{---------- (1)}$$

Neglecting the effect of inertia as PZT is made of thin film, above equation becomes

$$(\boldsymbol{\nabla}.\boldsymbol{\sigma}) + \boldsymbol{F} = \mathbf{0} \quad \text{----------(2)}$$

Generated Stresses ($\boldsymbol{\sigma}$) can be calculated by following equations no. 3 in PZT domain

$$[\boldsymbol{\sigma}]_{6\times1} = [\boldsymbol{C_E}]_{6\times6}[\boldsymbol{\epsilon}]_{6\times1} - [\boldsymbol{e^T}]_{6\times3}[\boldsymbol{E}]_{3\times1} \text{----------(3)}$$

$$\boldsymbol{\epsilon} = \frac{\mathbf{1}}{\mathbf{2}} * [(\boldsymbol{\nabla u})^{\boldsymbol{T}} + (\boldsymbol{\nabla u}) + (\boldsymbol{\nabla u})^{\boldsymbol{T}}(\boldsymbol{\nabla u})] \text{----------(4)}$$

Where ϵ is generated strain due to developed stresses on application of voltage

Using Maxwell equation

$$\boldsymbol{\nabla}.\boldsymbol{D} = \boldsymbol{\rho_v} \text{----------(5)}$$

And electric field is given by equation 6

ACCEPTED MANUSCRIPT

$$\boldsymbol{E} = -\boldsymbol{\nabla V} \text{----------(6)}$$

where

$$\boldsymbol{V} = \boldsymbol{V_0}\, \boldsymbol{Sin}(\boldsymbol{2\pi f t}) \text{----------(7)}$$

So electric displacement can be calculated by equation 8

$$[\boldsymbol{D}]_{3\times 1} = [\boldsymbol{e}]_{3\times 6}[\boldsymbol{\epsilon}]_{6\times 1} - [\boldsymbol{\varepsilon_s}]_{3\times 3}[\boldsymbol{E}]_{3\times 1} \text{----------(8)}$$

$\boldsymbol{\sigma}$is the matrix describing thestate of stress (N/m^2) and has size 6x1 ,$\boldsymbol{C_E}$is the elasticconstant and is defined by a 6X6 matrix (Pa), $\boldsymbol{\epsilon}$ ($\mathbf{unit\ less}$) is the strain matrix [size=6x1], $\boldsymbol{e}$(C/m^2) is coupling matrix (piezoelectricstress-charge form matrix[size 6x3],$\boldsymbol{D}$ (C/m^2) is electrical displacement matrix [size 3x1], $\boldsymbol{\varepsilon_s}$is dielectric permittivity (F/m) matrix [size 3x3], $\boldsymbol{E}$(V/m) is electric field matrix [size 3x1]. $\boldsymbol{u}(\boldsymbol{m})$is displacement vector. F (N)is thebody force,Vis applied voltage,$\boldsymbol{\rho_v}$is electric charge density ($\boldsymbol{\rho_v}$assumed to be $\mathbf{0}$) , $\boldsymbol{f}$ is frequency (Hz). All material properties that are involved in this coupled physics models are listed in table 2.

2.2.2 Structure physics (non PZT materials):

The structural deformation of non PZT material has been modeled using linear elastic material model for quasi-static material model

$$(\boldsymbol{\nabla}.\boldsymbol{\sigma}) + \boldsymbol{F} = \mathbf{0} \text{----------(9)}$$

Where $\boldsymbol{\sigma} = \mathbf{C}(\mathbf{E},\upsilon)\mathbf{*}(\boldsymbol{\epsilon})$

E (MPa) is the young's modulus and $\boldsymbol{\epsilon}$ is the state of strain**, F** is body force**.**

2.2.3 **Fluid physics**:

The working fluid in our model is assumed to be water like and incompressible, so the flow field can be estimated by the commonly used Navier–Stokes equations as follows.

ACCEPTED MANUSCRIPT

$$\boldsymbol{\rho \frac{\partial u_2}{\partial t} + \rho(u_2.\nabla)u_2 = \nabla[-pI + \mu(\nabla u_2 + (\nabla u_2)^{\mathrm{T}})] + F}$$ ----------(10)

$$\boldsymbol{\rho \nabla . u_2 = 0}$$----------(11)

The boundary conditions used for this coupled form are given as initial velocity U = 0 at inlet and p= 0 (gauge pressure) at both inlet as well as outlet. The fluid (water) parameters like density, kinematic viscosity etc. has been accordingly provided for the fluid.

2.2.3 Coupling of fluid-structure model:

The deflection of the piezo disc generated on application of a voltage pulse,is transferred into the structural domainby an elemental mapping between different domains containing dissimilar mesh size. Structural mechanics module of COMSOL solves for the Piezo disc deflection and the Electrostatic module is used to apply the voltage boundary condition for the PZT material. To make a coupling of electro-structural domain, the piezoelectric effect is used to calculate the force and deflection of the piezo disc. The fluid structure coupling is carried out through FSI (Fluid structure interaction)module which takes care of the mesh deformation. It uses ALE (Arbitrary Lagrangian-Eulerian) algorithm to incorporate fluid flow generated by Eulerian formulation in spatial frame with structure mechanics using Lagrangian formulation & material frame.

The essential boundary condition for the two ways coupling of two different domains is made as follows:

$$\boldsymbol{\sigma_s . n = \sigma_f . n}$$----------(12)

Where $\boldsymbol{\sigma_s}$ is stress developed in solid domain, $\boldsymbol{\sigma_f}$ is stress generated in fluid domain and$\boldsymbol{n}$is normal vector.

ACCEPTED MANUSCRIPT

Stress generated in the fluid is estimated by following equation where pressure and convective term of fluid flow is taken into consideration

$$\boldsymbol{\sigma}_{\boldsymbol{f}} = -\boldsymbol{p}_{\boldsymbol{f}} + \boldsymbol{\mu}(\boldsymbol{\nabla u}_{\boldsymbol{f}} + (\boldsymbol{\nabla u}_{\boldsymbol{f}})^{\boldsymbol{T}} \quad (13)$$

The fluid structure boundary (FS boundary)'s velocity should be equalized to the fluid velocity i.e.

$$\boldsymbol{u}_{\boldsymbol{f}} = \boldsymbol{V}_{\textbf{FS boundary}} \quad (14)$$

and derivative of displacement of solid boundary should be equalized to the velocity of the FS boundary i.e.

$$\boldsymbol{V}_{\textbf{FS boundary}} = \frac{\boldsymbol{\partial u_s}}{\boldsymbol{\partial t}} \quad (15)$$

Where $\boldsymbol{u_s}$is displacement vector of the solid domain.

With the help of the above governing equations, the transient behavior of micro-pump has been examined on application of a voltage pulse.

2.2.4 Boundary Conditions:

The model of the brass disc (PZT material) is made with fixed edge constraints all along its periphery. Similarly, the edges of the PDMS layer (formulated a seal between the piezo disc and the pump platformis also kept fixed along its edges. This is to primarily allow for bending at thecentral zone of the piezoon application of the control voltage at the PZT layer. The relative movement between brass layer and PDMS layer is kept zero. In reality as the PDMS is processed in a manner that piezo is placed over the PDMS with an inyermediate quick drying epoxy layer, it leads to a complete adherence between the two and as such the coupling in reality between the

ACCEPTED MANUSCRIPT

piezo and the PDMS layer may be considered as a perfect one. A sinusoidal wave of $V = V_0\, Sin(2\pi ft)$ is applied on the PZT layer. Although asquare pulse (PWM) is used to drive the Piezo disc later but for the simplicity aspect of modeling the phenomena a sinusoidal driving pulse is assumed.

2.2.5 Grid test and convergence studies:

Grid independency test is performed for electro-structural part (Piezo disc and PDMS) for deflection and fluidic part for net flow rate. The deflection caused by Piezo vibration becomes grid independent with mesh size 82771 elements (tetrahedral elements). The flow rate of micropump become grid independent with mesh size 121429(containing tetrahedral, pyramid and prism elements). More details about grid independency are given in supplementary figure 4 for both electro-structural (piezo disc and pdms layer) and fluid domain.

3 Fabrication Methodology:

3.1 Laser Processing of PMMA:

Figure 6 shows complete fabrication methodology. The first step of fabricating the device starts with the LASER micromachining of a sheet of polymethyl methacrylate (PMMA). The processing is further done using a CO_2 laser scanner (M/s Epilog Laser, USA). All machining is done at 25 deg. C room temperature condition and a positive pressure environment. The laser has a high power of 35 Watts and has a total working bed size of 2ft x1ft. The micro-pump geometry was drafted using a CAD package (Coral Draw) which is subsequently used to drive the various stepper motors with the lasing stage and also the working stage. The working stage is capable of movement in the ‘z’ direction and the lasing stage can operate in the raster (engraving) and vector

ACCEPTED MANUSCRIPT

(deep cutting) modes in the x-y plane. Figure 6 shows schematic representation of laser machining set up followed by etching step.

3.2 Use of Hybrid machining strategy for obtaining an overall smooth surface of the pumping architecture:

As discussed earlier in this paper we have used a hybrid machining strategy with a first step of lasing the PMMA surface followed by a wet etching of the Laser scribed PMMA for levelling this further. Extensive optical profilometry has been performed on the Laser etched surface and the post wet etch surface and a comparison is drawn about the efficacy of this newer step. The wet etching is carried out by using a mixture of Toluene (M/s S D Fine-Chem limited, Mumbai, India, CAS no. 108-88-3) and Methanol (M/s LobaChemie Pvt. Ltd.,Mumbai, India, CAS no. 67-56-1) in a Volume ratio of 1:4. Further samples from laser etching step are immersed totally totally within this solution and ultrasonicated at 42 KHz frequency (M/s Citizen Scale (I) Pvt. Ltd., Mumbai, India)inside a laminar fume hood for around 20 minutes at room temperature.

There were no significant change in overall dimensions including depth and width of the channels/ chambers while a significant reduction in the average roughness values to almost an order of magnitude. (Ra changing from 7-22μm (after Laser machining to 458 nm (after wet chemical etching step) [Refer Figure 7 for reconstructed roughness plots and data output from Vecco, optical profilometer and supplementary figure 1].

3.3 Assembly of the piezo-disc on the micro machined PMMA:

The micro-pump three layer assembly as mentioned earlier comprises of PMMA hard substrate with an independently spin casted layer of Poly dimethyl siloxane (acting as a packing layer to prevent leakages) followed by a Piezo Disc (M/s Shenoy Industries Bangalore, India). [refer Figure 3 The PDMS layer is realized using a 10:1 ratio of pre-polymer and curing agent, Sylgard

ACCEPTED MANUSCRIPT

184 (A and B) (M/s Dow Cornig, Midland). The mixture is spin coated on a pre-cleaned (using acetone, methanol, DI water wash) glass slide, coated with a 100 nm Hexa Methyl Di-silazane (HMDS, M/s Sigma Aldrich) acting as a mould release agent, to a thickness (10 micron) defined by the spin speed (200 rpm) in a spin coater (SPIN150 , POLOSTM, THE NETHERLANDS). The layer is heated to 85 deg. C in a hotplate for about 15 minutes till the solvent evaporates and the cross-linker is able to integrate the resin matrix thereby facilitating the easy removal of this layer. It isensured that the thick edges are trimmed to obtain a uniform thickness of 10 microns after the release is executed. This down-sized PDMS membrane is pasted over the PMMA substrate obtained in the earlier step using quick drying epoxy (M/s Araldite® adhesives, Switzerland). In the third step the piezo-disc (M/s Shenoy Industries Banglore, India) has been attached over this PDMS layer using another thin layer of the same quick drying epoxy as in the above step. The PDMS membrane is used to cover the guiding inlet/outlet channels all the way to the inlet/outlet ports stationed in both extremities of the PMMA substrate to prevent and unnecessary loss in the fluid discharge. The piezo disc is further clamped over the surface using another suitably designed protector plate. [Refer Figure 3, 6 and 8 for fabrication details]. Figure 8 shows the whole fabrication protocol through a flow chart.

4. Design of instrumentation for fluid handling:

4.1 Electronic control module (ECM) design:

The micropumps are controlled digitally through a computer and this can also be remotely controlled with a few modifications to the existing wired control system developed in current work. The electronic control module enabling this digital control is composed of three subunits integrated together as shown in the block diagram figure 9. The input power comes from 7.5 V DC battery which is coupled to a signal amplifier with a gain factor of around 13.33. The output

ACCEPTED MANUSCRIPT

of the signal amplifier is fed after a comparison with the input voltage to a pulse width modulating (PWM) circuit which creates a digital pulse signal varying between 0 and 100 V DC. A potentiometer with its knob mechanically coupled to a steeper motor and controlled by ATMEGA 328 micro-controller formulates the interface with the computer. With this coupling strategy, the potentiometer is able to vary voltage from 50 to 100 VDC.

4.2 Design of the driving unit of the micropump:

The micro-pump driving unit consists of Pulsed width modulator and Amplifier both of which were designed using LT-spice IV.

4.2.1 Design of PWM circuit:

Pulsed width modulation circuit is designed to obtain an output frequency range of 38~400 Hz using the circuit design planned in this work. Intuitively a range is important as it signifies the vibrational spectrum of the piezo-disc which obviously has an optimum frequency value for highest output flow rate from the pumping chamber. Figure 9 shows the overall circuit design containing an integrated circuit 556 IC (M/s Texas Instruments, USA), a MOSFET (IRF540, M/s: International Rectifiers) and several other passive circuit components. A potentiometer is used to obtain the output signal as a specific duty cycle. The IC556 is used to generate a Pulsed D.C. output signal of maximum voltage 7.5 V and minimum 0 V which is guided through the potentiometer. The pulsed output is sensed at pin # 5 of Integrated Circuit (IC556).

This output at pin #5 is connected to the gate region of the IRF540, MOSFET. An input voltage of 7.5 V DC is provided to Pin # 14 of the Integrated circuit. The ground terminal of the power source is connected to the IC ground and so is the source pin of the MOSFET. The circuit diagram of PWM is depicted in supplementary figure 2.

The frequency of this circuit design is calculated in such circuits by using following equation.

ACCEPTED MANUSCRIPT

$$f = (1.44)/(((R21 + 2 * R22) * C22)\ )$$ ---------- **(16)**

where resistances R21 and R22 (as indicated in the circuit design) are defined as 33 KΩ and 2K2 KΩ and C22 capacitance is defined as 0.3μF for a maximum design frequency of 400 Hz. The combinations of the resistive / capacitive loads are defined by looking at circuit components with high reliability and easily available. The capacitor C22 can further be varied to 100 nF to 1000 nF to obtain a minimum frequency of 38 Hz.

4.2.2 Design of the Amplifier Circuit:

Supplementary figure 3 shows amplifier circuit which uses LM3478 IC(a switching controller).The Pin no. 1 of this IC is current sense input in which voltage across R4(external sense resistor) is provided. Pin no. 2 of the IC provides compensation for the control loop. Pin no. 3 serves as feedback which adjusts output voltage using a potentiometer (R6) which is mechanically coupled with stepper motor.

Ground pin no. 4 and 5 are analog and power ground pin.M1 mosfet (N-channel, very low gate resistance (26.5 mΩ)) attached to pin no. 6 to achieve high frequency switching and synchronous rectification. R3 (63.4 KΩ) is connected to pin no. 7 to adjust the frequency and shut down of the circuit. V1 (7.5 V DC) is provided to pin no. 8 and output is achieved on V2 terminal.

5. Experimentation and Measurements:

5.1 Measurement of deflection of the piezo disc:

The deflection of the piezo disc is studied using a single point laser source through which it can scan the top surface of the piezo by recording the displacement at the geometric centre of the disc through the laser sensor (MICRO-EPSILON, Germany Model OptoNCDT 1700) and analyzing the recorded data as a displacement time data through a software ILD 1700 Tool

ACCEPTED MANUSCRIPT

V2.31. A detail of the deflection measurement as recorded with applied voltage is represented in figure 10.

5.2 Measurement of discharge rate of the micro-pumps:

A test rig was prepared using a sheet of acrylic machined tracks containing and guiding transparent silicone tubing (ID:1/1600, M/s Upchurch Scientific) in a straight manner. The tubings were further connected to the outlet port of the micro-pump assembly and carried the pump discharge parallel to an embedded linear scale (least count 200 μm). The scale was chosen in a manner so that graduations over it would be distinctly visible with respect to the moving fluid meniscus inside the silicone tubing. The velocity of flow was estimated by capturing a digital video at a high frame rate (30 FPS) of this whole process and using the length readout from the scale and time read out from the frame rate of capture of the videos to calculate the discharge velocity. Same procedure is applied to measure flow rate against pressure head also.

5.3 Sample preparation for viability studies of micro-organisms transported through Micropumping unit:

Investigations were carried out in regards to the viability of flown in sample of micro-organisms inside the fluid handling device and another round of studies are performed on the output. E. coli DH5α cells were grown in LB (Luria-Bertani, M/S Banglore Genei) culture medium at 37 °C overnight in a shaking incubator (Mahendra Scientifics, India). Growth was detected by measuring the optical density (OD600) of the growth medium and an OD600 of about 2.5 was estimated to be reflective of late exponential growth phase. The final cell numbers were detected by serial dilution and plating on brain heart infusion (BHI) agar. The culture was diluted, plated, and counted using a trans-illuminator (M/s Bangalore Genie) and Image-J software. The master

ACCEPTED MANUSCRIPT

solution containing the cells was diluted to seven orders of magnitude and this diluted solution was plated. This solution was further passed through the micropumping unit multiple times and each time the viability was studied by plating the discharge.

6. Results and Discussion:

6.1 Theoretical Estimation of the flow discharge:

The Piezo Disc attached to the micro-pumping chamber is modeled using COMSOL multiphysics (version 5.2) and the methodology for the same is detailed earlier. The maximum displacement which is obtained at the geometric center of the disc is represented by figure 11. The maximum deflection obtained by the disc is 6.0 microns in the –ve Z direction corresponding to an input voltage level of 100 V pulse DC signal. This signal level is the maximum generated by the 7.5 V DC battery coupled to the amplified circuit and chopped through the PWM circuit.

The simulation platform is now utilized to predict the outlet discharge from the pumping unit. The piezo displacement in case of the piezo disc sitting on the top of the pumping chamber adds velocity head to the fluid within the chamber. The stream line plot output of this coupled simulation is represented in next section by figure 12 and 13. Figure 13 shows more flow towards the left of the non-circular chamber shape which can be observed by looking at the streamline formation trend at various zones of the chamber viz., right flank, left flank and central zone. In case of the circular chamber (Figure 12) such a demarcation is not visible and the flow is mainly attributed to the nozzle/ diffuser orientation of the connecting fluid channels to the chamber. Figure 14 depicts the net average flow rate of micro-pump with respect to time which is very similar to flow rate’s experimental values as simulated.

ACCEPTED MANUSCRIPT

6.2 Studies related to Piezo deflection and flow rate:

Figure 12 shows a line plot for the voltage versus displacement of the piezo disc (geometric centre) using single point laser scanner. The maximum deflection as predicted by the COMSOL module earlier of the piezo disc is obtained as 6 micro-meters. This is the basis of all the control circuit design as detailed in above sections. Experimental observations related to the discharge rate of the micro-pump corresponding to an output voltage of 50-100 Volt is plotted with respect to variable operational frequencies (frequency varied between 38-400 HZ). We observe an optimum frequency of 128Hz which is corresponding to resonance conditions of the piezo disc in all applied voltages [Figure 15(a) and (b)]. The maximum discharge rate at the piezo frequency is observed to be 497 microliters/min corresponding to an operational voltage of 100 Volts and frequency of 128 Hz. The pumps are also observed to be offering an overall back pressure level of 200 mm of water column under an applied voltage of 65 V which increases all the way to 500 mm water column pressure when a voltage of 100 V is applied at the resonating frequency corresponding to the piezo disc. Figure 12 (a)~d shows generation of eddies and vortices during suction and pumping stroke with respect to disc position, which poses restriction on use of piezoelectric micropump for transportation of biological samples as it increases chance of cell deformation and lysing[47]. While the modified design (Figure 13 (a)~(d)) shows absence of these eddies and vortices which makes this pump useful for cell suspended biological entities. The comparison of numerical and experimental values of flow rate is presented here for resonating frequency 128 Hz and 100 V in figure 15(a).

6.3 Viability studies of microorganisms

The microorganism's viability is studied on both smooth and rough surface of micropumping chamber. The details of studies are incorporated in following section.

ACCEPTED MANUSCRIPT

6.3.1 Cell viability after transportation through the pumping unit containing smooth surface:

The initial sample diluted to a concentration of 10^3 cfu/ml was plated using brain heart infusion (BHI) agar. The culture was diluted, plated, and counted using transilluminator (M/s Bangalore genie) and Image-J software. Figure 16 shows the counting of cells at pre and post transport stages using Image-J. The initial sample recorded a count of 402 colonies and then recorded the viable colonies to be within 386-398 for three trials where the output solution was passed through the fluid handling device for 1,2 and 3 times respectively and plated each time. Subsequent passes through the micropumping architecture using the piezo actuator to transport the sample solution. This indicates incomplete squeezing of the solution volume contained within the micro-pumping chamber even at peak performance levels. So, definitely this module is integrable with the bioassay by providing a soft transport of micro-organism cells while retaining a high level of cell viability.

6.3.2 Cell viability after transportation through the pumping unit containing rough surface:

Supplementary table 1 shows the counting of cells at pre and post transport stages using Image-J. The original sample recorded a count of 205 colonies and then this sample is passed through micropumping unit containing rough surface 1,2 and 3 times and found 152,98 and 70 colony forming units respectively. This shows that cell viability is reduced much more on rough surface in comparison to smooth surface.

ACCEPTED MANUSCRIPT

7. Conclusions:

In this work we have described CO_2 laser micro-manufacturing and chemical etching hybrid process to achieve an overall minimum surface roughness of 458 nm for micro-fluidic application. We have further realized a piezo-actuated fluid handling module for manipulation of miniaturized fluid. We have simulated through the fluid structure interaction route and predicted the flow behavior in time of the micropumping unit. The integrated fluid handling module has been thoroughly tested for viable transport of micro-organisms (E. Coli DH5α cells) through micropumping chamber containing rough and smooth surface. It is found that smooth surface increases the cell viability during transportation of fluid containing microorganisms in comparison to rough surface.

Whole micropumping system has an overall size of dimension (Length=90mm, Width=75mm and Depth=60mm), input voltage of 7.5 V DC and maximum flow rate of 497 microliter/min at atmospheric pressure and 45 microliter/minute at a back pressure of 500 mm of DI water. The technology so realized is quite useful for portable applications related to micro-scale fluid transport of viable biological samples.

8. Acknowledgement

The authors would like to acknowledge the financial support of the National Program on Micro and Smart Structures through the funded project. The author also would like to thank Prof. R. Gurunath (Department of Chemistry, IIT Kanpur) for providing valuable laboratory support for culture of microorganisms. They would also like to thank the support obtained from DST unit of Nanosciences and also the 4i Laboratory of IIT Kanpur.

ACCEPTED MANUSCRIPT

9. References:

[1] J. Khandurina, T. E. McKnight, S. C. Jacobson, L. C. Waters, R. S. Foote , J. M. Ramsey, Integrated system for rapid PCR-based DNA analysis in microfluidic devices, Anal. Chem., 72 (2000) 2995-3000.

[2] M. T. Taylor, P. Nguyen, J. Ching , K. E. Petersen , Simulation of microfluidic pumping in a genomic DNA blood-processing cassette, J. Micromech. Microeng.13(2003) 2.

[3] S. Böhm, B. Timmer, W. Olthuis, P. Bergveld, A closed-loop controlled electrochemically actuated micro-dosing system, J. Micromech. Microeng.10 (2000) 498.

[4] T. Bourouina, A. Bossebuf, J.P. Grandchamp, Design and simulation of an electrostatic micropump for drug-delivery applications, J. Micromech. Microeng. 7 (1997) 186.

[5] Y. Huang, S. Liu, W. Yang and C. Yu, Surface roughness analysis and improvement of PMMA-based microfluidic chip chambers by CO_2 laser cutting, Appl. Surf. Sci. 256 (2010) 1675-1678.

[6] J. Yen Cheng, C. W.Wei, K. H. Hsu and T. H. Young, Direct-write laser micromachining and universal surface modification of PMMA for device development, Sens. Actuator B-Chem. 99 (2004) 186-196.

[7] B. D. Iverson, S. V. Garimella, Recent advances in microscale pumping technologies: a review and evaluation, Microfluid Nanofluidics 5 (2008) 145-174.

[8] S. Böhm, W. Olthuis, P. Bergveld, A plastic micropump constructed with conventional techniques and materials, Sens Actuators A Phys 77 (1999) 223-228.

ACCEPTED MANUSCRIPT

[9] L. Sheng Jang, Y. Jie Li, S. Ju Lin, Y. Chu Hsu, W. Sung Yao, M. Ching Tsai, C. Cheng Hou, A stand-alone peristaltic micropump based on piezoelectric actuation, Biomedical microdevices, 9 (2007) 185-194.

[10] O. Chan Jeong, S. S. Yang, Fabrication and test of a thermo pneumatic micropump with a corrugated p+ diaphragm, Sens Actuators A Phys 83 (2000) 249-255.

[11] E. Meng, X. Q.Wang, H. Mak and Y.C. Tai, A check-valved silicone diaphragm pump, In Micro Electro Mechanical Systems, 2000, The Thirteenth Annual International Conference, 62-67.

[12] M. C. Carrozza, N. Croce, B. Magnani and P. Dario, A piezoelectric-driven stereolithography-fabricated micropump, J. Micromech.Microeng.5 (1995) 177.

[13] N.Trung Nguyen, T.Q. Truong, A fully polymeric micropump with piezoelectric actuator, Sens. Actuator B-Chem. 97 (2004) 137-143.

[14] T. Quang Truong, N.T. Nguyen, A polymeric piezoelectric micropump based on lamination technology, J. Micromech. Microeng.14 (2004) 632.

[15] R. Kant, H. Singh, M. Nayak , S. Bhattacharya, Optimization of design and characterization of a novel micro-pumping system with peristaltic motion, Microsyst Technol 19(2013), 563-575.

[16] X. Chen, C. C. Liu, H. Li, Microfluidic chip for blood cell separation and collection based on cross flow filtration, Sens. Actuator B-Chem.130 (2008), 216-221.

[17] J. Lawrence, L. Li, Modification of the wettability characteristics of polymethyl methacrylate (PMMA) by means of CO_2, Nd: YAG, excimer and high power diode laser radiation, Materials Science and Engineering, A303(2001) 142-149.

[18] D. J. Laser, J. G. Santiago, A review of micropumps, J. Micromech. Microeng.14 (2004), R35.

ACCEPTED MANUSCRIPT

[19] J. Goulpeau, D. Trouchet, A. Ajdari, P. Tabeling, Experimental study and modeling of polydimethylsiloxane peristaltic micropumps, J. Appl. Phys., 98 (2005), 044914.

[20] E. Stemme, G. Stemme, A valveless diffuser/nozzle-based fluid pump, Sens. Actuator A-Phys., 39(1993) 159-167.

[21] R. Zengerle, J. Ulrich, S. Kluge, M. Richter, A. Richter, A bidirectional silicon micropump, Sens. Actuator A-Phys., 50(1995), 81-86.

[22] B. Husband, B. Minqiang, A. G. Evans , T. Melvin, Investigation for the operation of an integrated peristaltic micropump, J. Micromech. Microeng.14 (2004), S64.

[23] Y. Chen, C. Zhang, M. Shi , G. P. Peterson, Role of surface roughness characterized by fractal geometry on laminar flow in microchannels, Phys. Rev. E 80 (2009) 026301.

[24] N. C. Nayak, Y. C. Lam, C. Y. Yue ,A. T. Sinha, CO_2-laser micromachining of PMMA: the effect of polymer molecular weight, J. Micromech. Microeng. 18 (2008) 095020.

[25] Q. Heng, C. Tao, Z. Tie-chuan, Surface roughness analysis and improvement of microfluidic channel with excimer laser, Microfluid Nanofluid 2 (2006) 357-360.

[26]J. Paulo Davim, N. Barricas, M. Conceicao ,C. Oliveira, Some experimental studies on CO_2 laser cutting quality of polymeric materials, J Mater Process Tech, 198 (2008) 99-104.

[27] M. Bahrami, M. M. Yovanovich , J. R. Culham, Pressure drop of fully developed, laminar flow in rough microtubes, J Fluid Eng-T ASME 128 (2006) 632-637.

[28] D. Snakenborg, H. Klank, J. P. Kutter, Microstructure fabrication with a CO_2 laser System, J. Micromech.Microeng.14 (2004) 182.

[29] D. Sik Lee, J. S. Ko, Y. T. Kim, Bidirectional pumping properties of a peristaltic piezoelectric micropump with simple design and chemical resistance., Thin Solid Films 468 (2004) 285-290.

ACCEPTED MANUSCRIPT

[30] J. G Smits, Piezoelectric micropump with three valves working peristaltically, Sens. Actuator A-Phys. 21(1990) 203-206.

[31] H. T. G. V. Lintel, F. C. M. V. d. Pol , S. Bouwstra, A piezoelectric micropump based on micromachining of silicon, Sensors and actuators 15(1988) 153-167.

[32] Si Shoji, S. Nakagawa, M. Esashi, Micropump and sample-injector for integrated chemical analyzing systems, Sens. Actuator A-Phys. 21 (1990) 189-192.

[33] A. Olsson, G. Stemme, E. Stemme, A valve-less planar fluid pump with two pump chambers, Sens. Actuator A-Phys. 47 (1995) 549-556.

[34] R. Zengerle, J. Ulrich, S. Kluge, M. Richter and Richter.A., A bidirectional silicon micropump, Sens. Actuator A-Phys. 50 (1995) 81-86.

[35] IMM thinXXS XXS, 2000.[Online]. Available: www.thinxxs.com.

[36] MIP Implantable product information, [Online]. Available: www.debiotech.sa.

[37] M. Esashi, S. Shoji and A. Nakano, Normally close microvalve and micropump fabricated on a silicon wafer, In Micro Electro Mechanical Systems, 1989, Proceedings, An Investigation of Micro Structures, Sensors, Actuators, Machines and Robots, 29-34.

[38] H. Q. Li, D. C. Roberts, J. L. Steyn, K. T. Turner, J. A. Carretero, O. Yaglioglu , Y. H. Su, A high frequency high flow rate piezoelectrically driven MEMS micropump, In Proceedings IEEE Solid State Sensors and Actuators Workshop, Hilton Head (2000).

[39] A. Olsson, P. Enoksson, G. stemme , E. Stemme, Micromachined flat-walled valveless diffuser pumps, J. Microelectromech. Syst. 6 (1997) 161-166.

[40] T. Gerlach, H. Wurmus, Working principle and performance of the dynamic micropump, Sens. Actuator A-Phys. 50 (1995) 135-140.

[41] V. Gass, B. H. V. D. Schoot, S. Jeanneret and N. F. De Rooij, Integrated flow-regulated

ACCEPTED MANUSCRIPT

silicon micropump., Sens. Actuator A-Phys. 43 (1994) 335-338.

[42] A. Olsson, P. Enoksson, G. Stemme , E. Stemme, A valve-less planar pump isotropically etched in silicon, J. Micromech. Microeng.6 (1996) 87.

[43] F. K. Forster, R. L. Bardell, M. A. Afromowitz, N. R. Sharma and A. Blanchard, "Design, fabrication and testing of fixed-valve micro-pumps, ASME-PUBLICATIONS-FED, 234(1995) 39-44.

[44] M. Koch, N. Harris, A. G. Evans, N. M. White and A. Brunnschweiler, A novel micromachined pump based on thick-film piezoelectric actuation, In Solid State Sensors and Actuators1997. TRANSDUCERS'97 Chicago., 1997 International Conference, 1(1997) 353-356.

[45] P. Griss, G. Stemme, Side-opened out-of-plane microneedles for microfluidic transdermal liquid transfer, J. Microelectromech. Syst. 12 (2003) 296-301.

[46] S. S. Wang, X. Y. Huang ,C. Yang, Valveless micropump with acoustically featured pumping chamber, Microfluid Nanofluid 8 (2010) 549-555.

[47] I. Biswas, R. Ghosh, M. Sadrzadeh, A. Kumar, Nonlinear deformation and localized failure of bacterial streamers in creeping flows, Sci. Rep. 6 (2016) 32204.

[48] A. Cerf, J. C. Cau, C. Vieu, E. Dague, Nanomechanical properties of dead or alive single-patterned bacteria, Langmuir 25(2009) 5731–5736.

ACCEPTED MANUSCRIPT



Rishi Kant received the B.Tech. degree in Mechanical Engineering from the University Institute of Engineering and Technology, Chhatrapati Shahu Ji Maharaj University, Kanpur, India, in 2004 and the M.E. degree in Mechanical Engineering from Delhi College of Engineering, University of Delhi, New Delhi, India, in 2007. He was a Research Assistant with the Design Manufacturing Integration (DFM) Laboratory, Indian Institute of Technology, New Delhi, from 2007 to 2008. He received his Ph.D. degree in mechanical engineering from IIT Kanpur, India. He is currently working as Project Scientist at the Indian Institute of Technology Kanpur. His research interests include Bio-MEMS, Microfluidics and Micro/Nanofabrication for fluidic, Diagnostics and other applications.



Dr. Deepak Singh received his B.Sc. degree in Botany and Chemistry from Udai Pratap College Varanasi and M.Sc. in Industrial Biotechnology from Chaudhary Charan Singh University Campus, Meerut, U.P., India. He is a Ph.D. with biochemistry specialization from Indian institute of Technology, Kanpur, India. Presently he is working as Project Scientist at I.I.T. Kanpur, India. His research interests include Microbial Biotechnology/ Protein Biochemistry/ Molecular Diagnostics.

ACCEPTED MANUSCRIPT



Shantanu Bhattacharya received the B.S. degree in industrial and production engineering from the University of Delhi, New Delhi, India, in 1996, the M.S. degree in mechanical engineering from Texas Tech University, Lubbock, TX, USA, in 2003, and the Ph.D. degree in biological engineering from the University of Missouri, Columbia, MO, USA, in 2006.He was a Senior Engineer with Suzuki Motors Corporation from 1996 to 2002. He also completed postdoctoral training at the Birck Nanotechnology Center, Purdue University, West Lafayette, IN, USA, for one year. Currently, he serves as a Professor at the Department of Mechanical Engineering at the Indian Institute of Technology at Kanpur. His research interests include design and development of microfluidics and MEMS platforms for varied engineering applications.

ACCEPTED MANUSCRIPT

Caption for figures and tables

Figure 1: 3-D plot of (1) Applied Voltage vs (2) Micro pump size vs (3) Back pressure has been generated out of the current state of art

Figure: 2 (a) CAD drawing of prototype (b) Rapid prototyped portable micropump

Figure 3: Various layers of piezo based micropump assembly

Figure 4: Steps involved for two way coupled FSI (Fluid structure Interaction)

Figure 5: (a) Representing piezoelectric, brass (structure), microfluidic domain (b) Represents meshed domains

Figure 6: Schematic diagram of CO_2 laser micromachining process and subsequent etch step

Figure 7: (a) Reconstructed image of PMMA surface after wet etching at 50 °C (b) Reconstructed 3D surface image of a post wet etched PMMA (c) Output measurement indicated Ra value of 458 nm.

Figure 8: Flowchart of fabrication methodology

Figure 9: Block Diagram for electronic control module of the Micropumping setup

Figure 10: Observations related to the piezo deflection with applied voltages.

Figure 11: Displacements of the piezo disc on application of DC voltage signal the center of the disc is the most deflected

Figure 12 : Simulation for circular micropumping chamber (a) piezo disc deflection at upward position (suction stroke) (b) streamlines generated into circular chamber during suction stroke (c) piezo disc deflection at downward position (pumping stroke) (d) streamlines generated into circular chamber during pumping stroke

Figure 13 : Simulation for modified micropumping chamber (a) piezo disc deflection at upward position (suction stroke) (b) streamlines generated into chamber during suction stroke (c) piezo disc deflection at downward position (pumping stroke) (d) streamlines generated into chamber during pumping stroke

Figure 14: Net Flow rate during pumping at 128 Hz and 100 pulsed VDC.

Figure 15: (a) Experimental flow rates with various actuation frequencies at different input volatage (b) ability to deliver against the pressure heads of water at DC voltages 65 and 100 V respectively

ACCEPTED MANUSCRIPT

Figure 16: Bacterial cell viability before and after passing through micropump

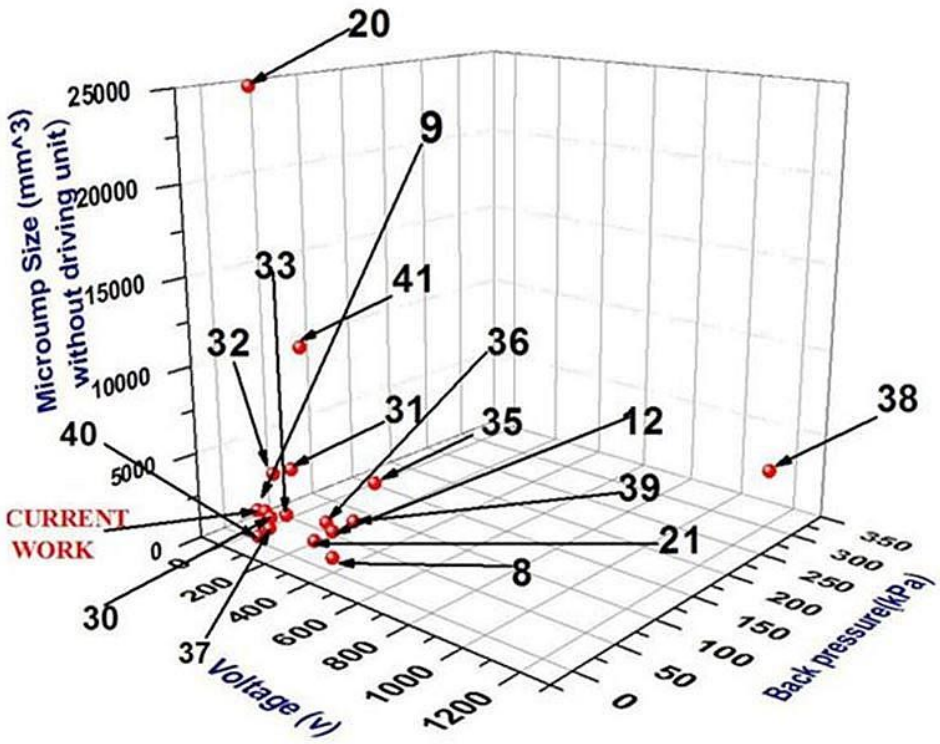


Figure 1: 3-D plot of (1) Applied Voltage vs (2) Micro pump size vs (3) Back pressure has been generated out of the current state of art

ACCEPTED MANUSCRIPT

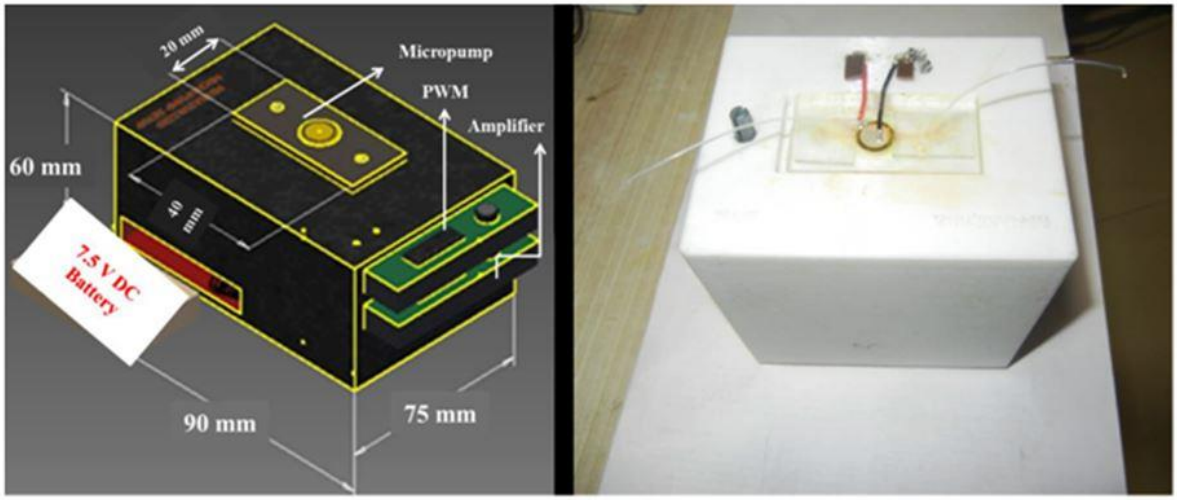


Figure: 2 (a) CAD drawing of prototype (b) Rapid prototyped portable micropump

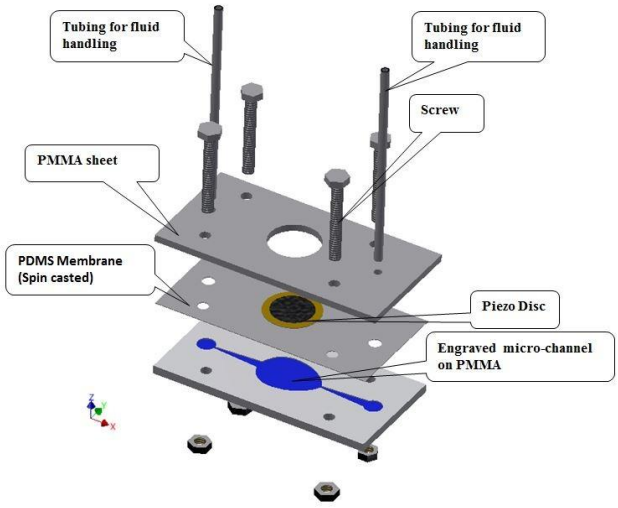


Figure 3: Various layers of piezo based micropump assembly

ACCEPTED MANUSCRIPT

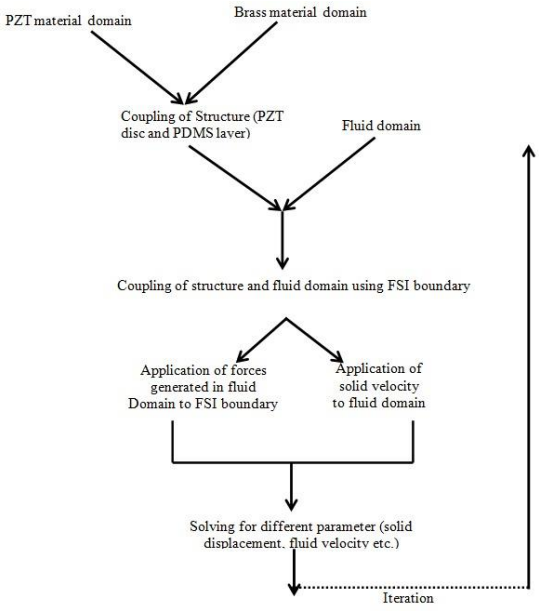


Figure 4 : Steps involved for two way coupled FSI (Fluid structure Interaction)

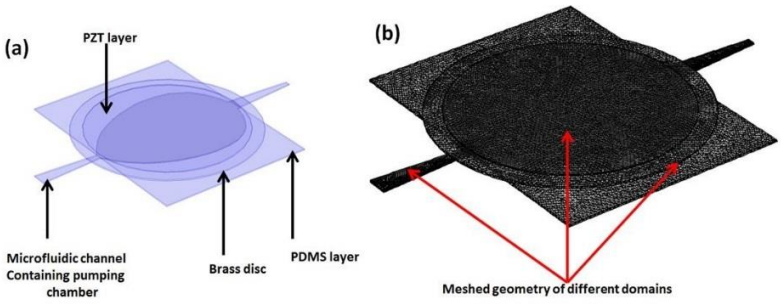


Figure 5: (a) Representing piezoelectric, brass (structure), microfluidic domain (b) Represents meshed domains

ACCEPTED MANUSCRIPT

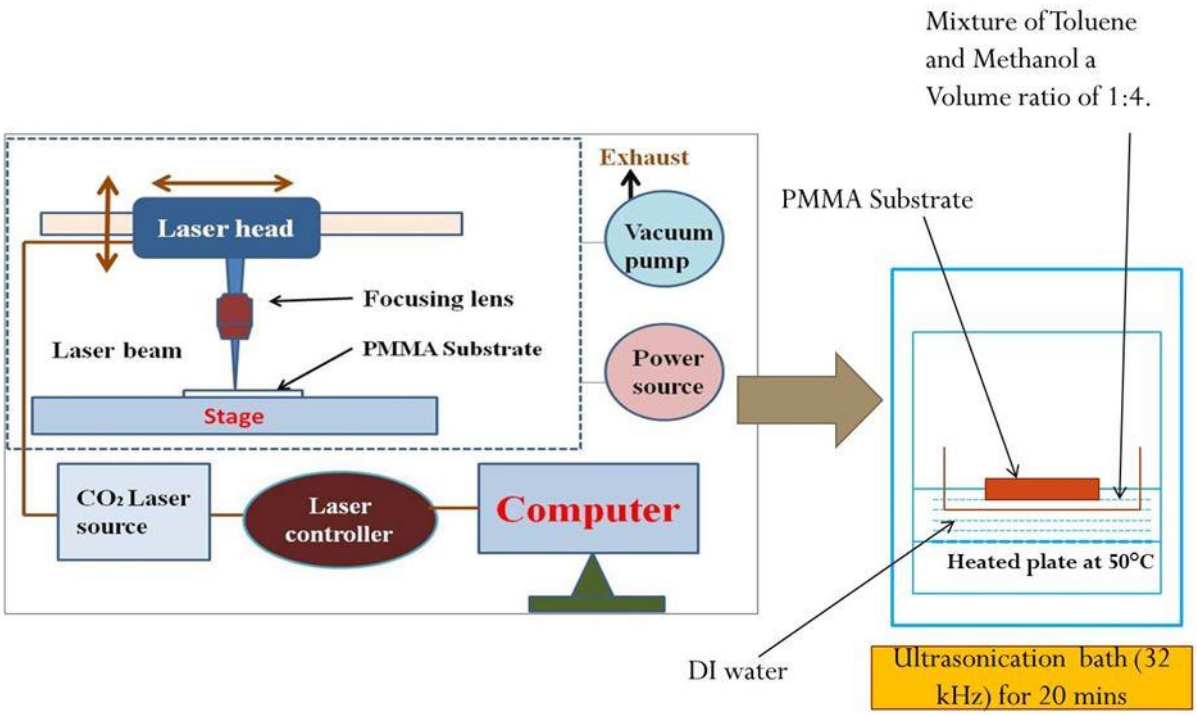


Figure 6: Schematic diagram of CO_2 laser micromachining process and subsequent etch step

ACCEPTED MANUSCRIPT

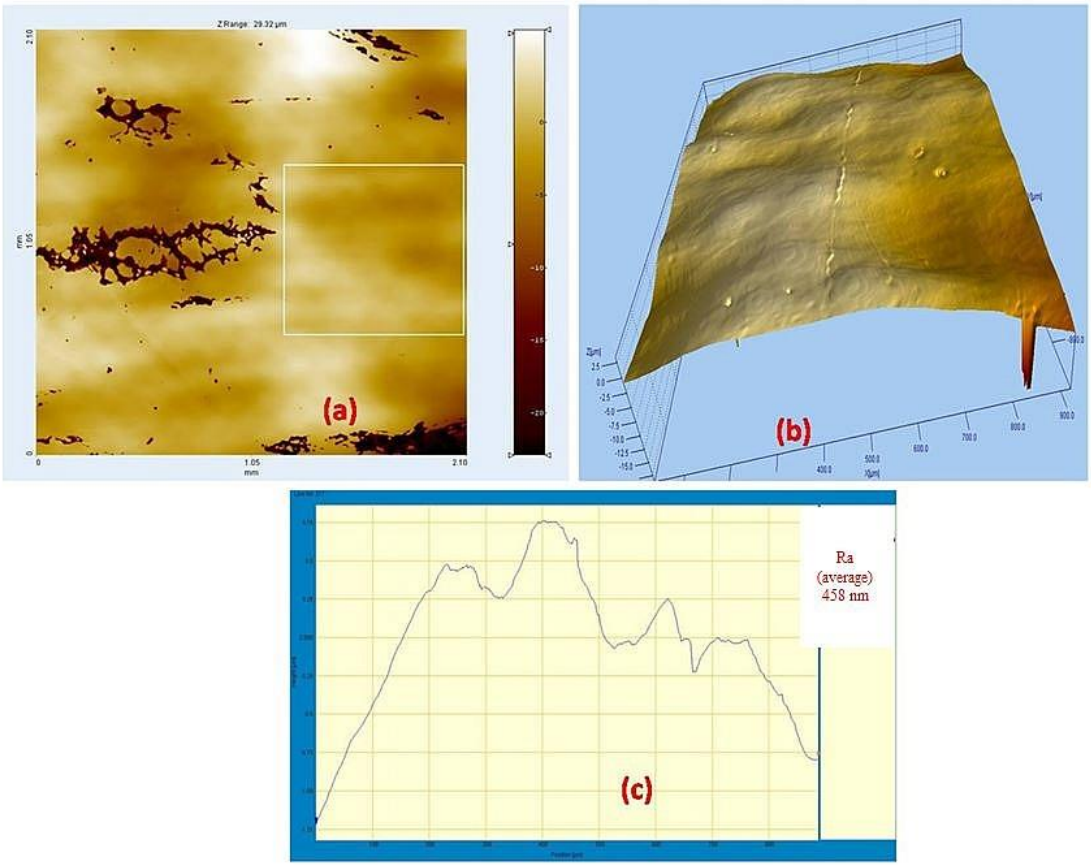


Figure 7: (a) Reconstructed image of PMMA surface after wet etching at 50 °C (b)Reconstructed 3D surface image of a post wet etched PMMA (c) Output measurement indicated Ra value of 458 nm.

ACCEPTED MANUSCRIPT

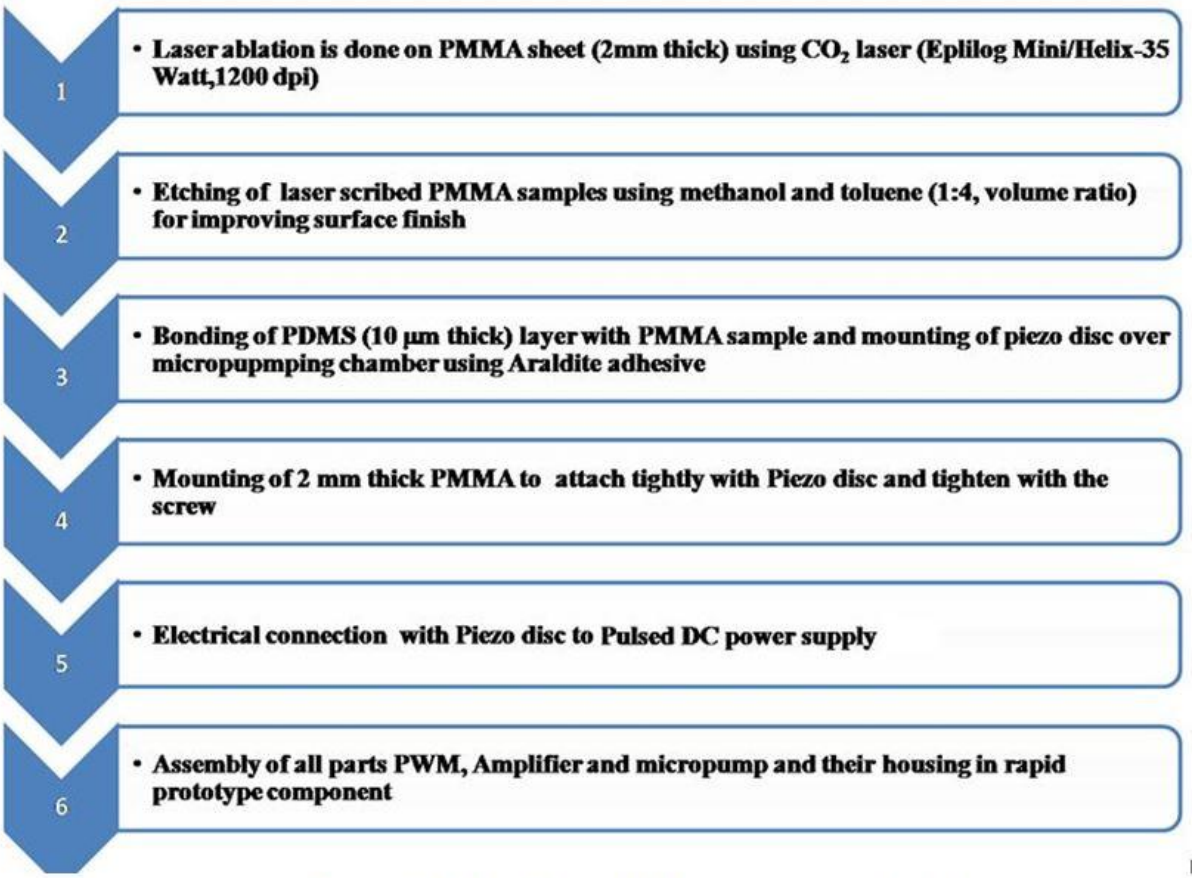


Figure 8: Flowchart of fabrication methodology

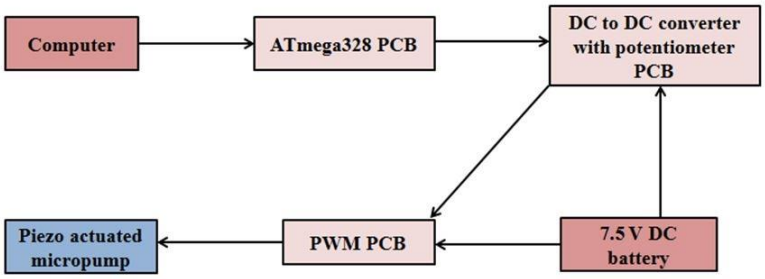


Figure 9: Block Diagram for electronic control module of the Micropumping setup

ACCEPTED MANUSCRIPT

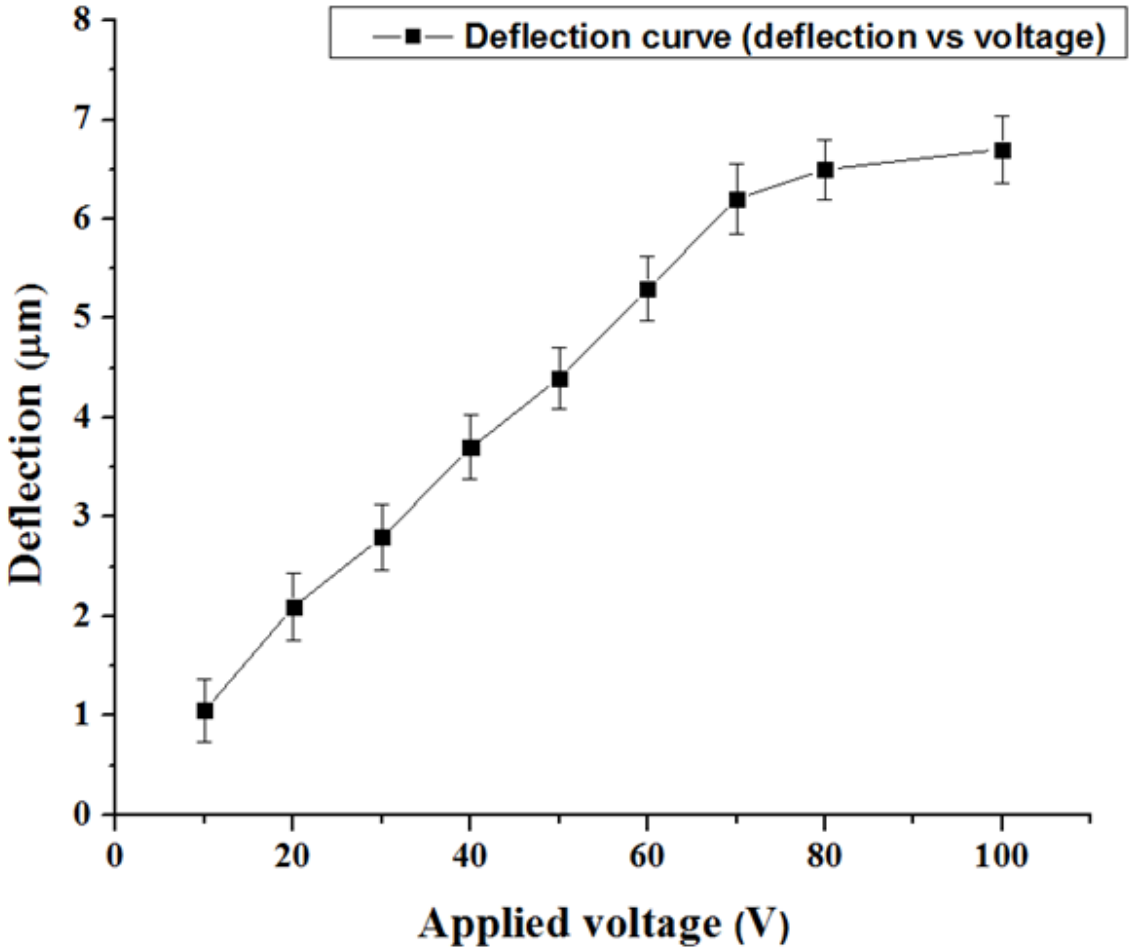


Figure 10

ACCEPTED MANUSCRIPT

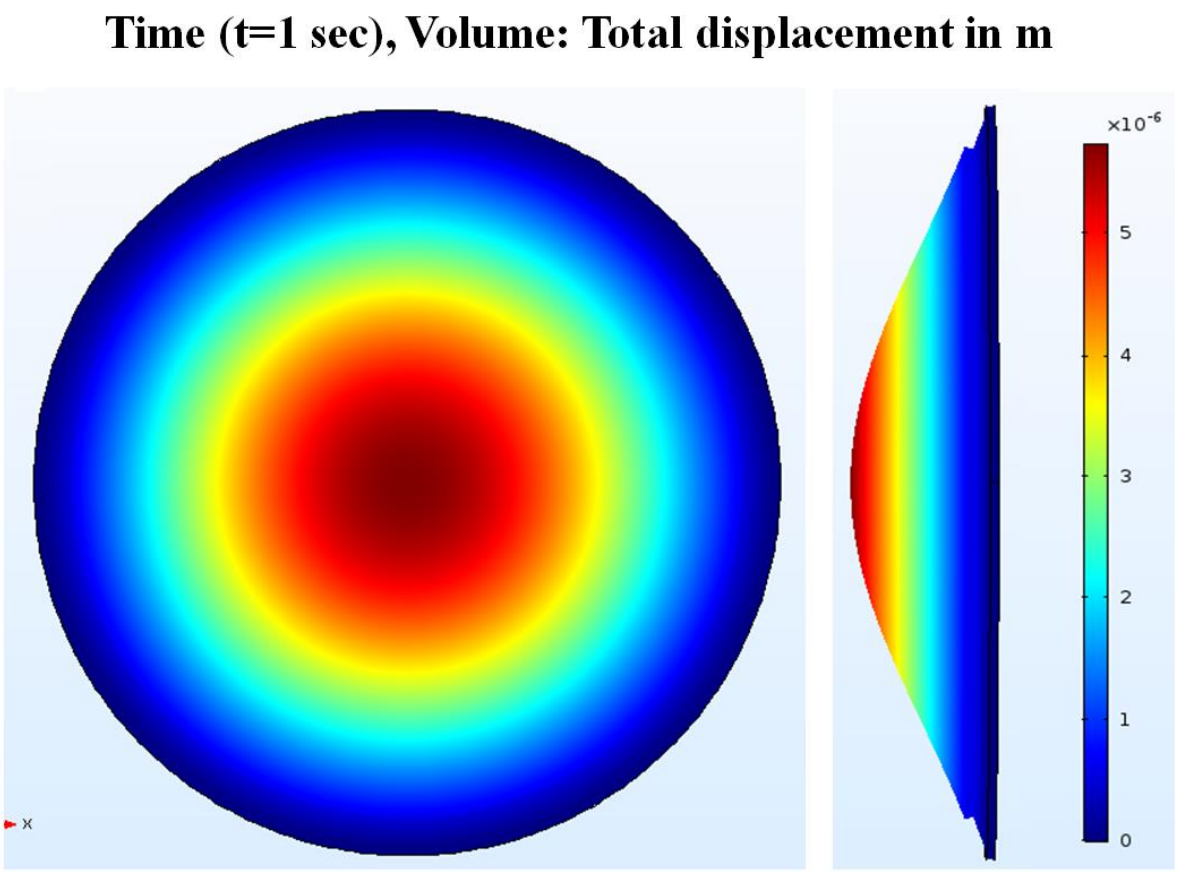


Figure 11

ACCEPTED MANUSCRIPT

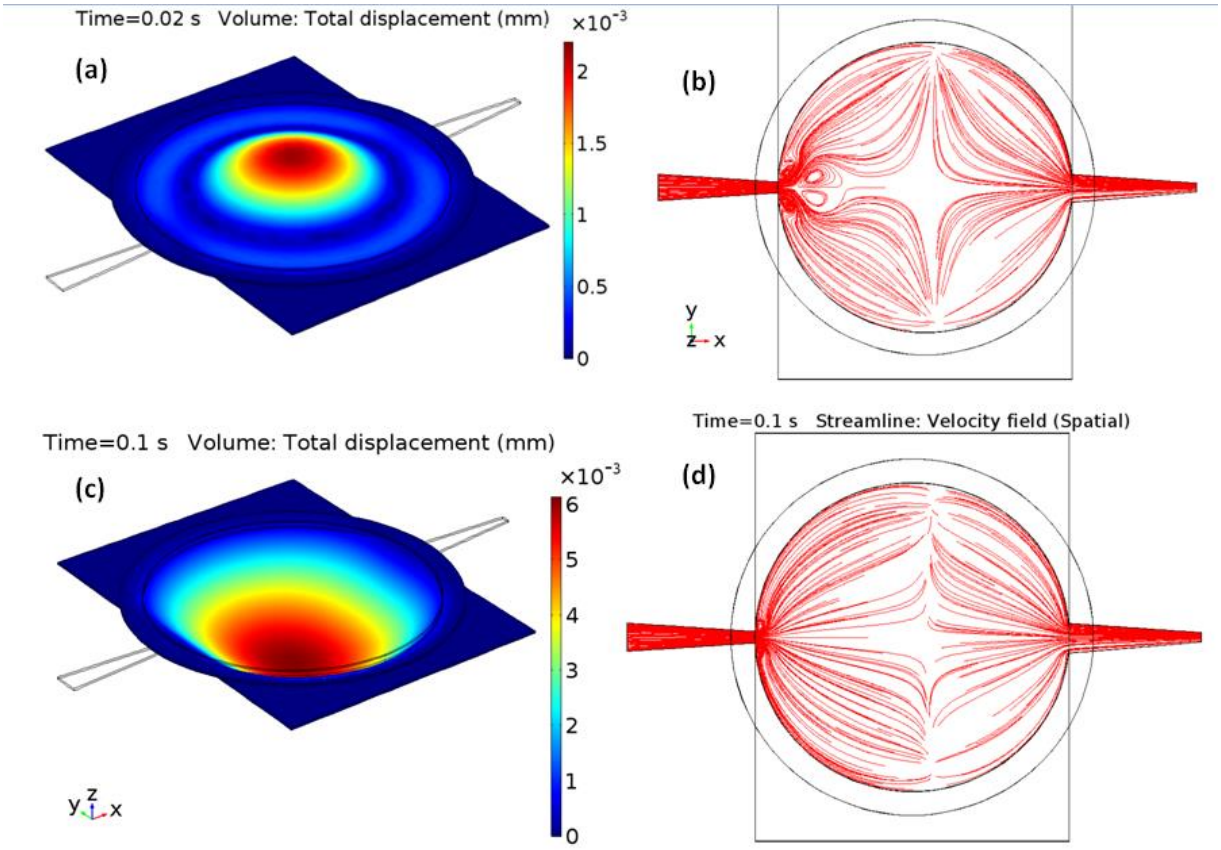


Figure 12

ACCEPTED MANUSCRIPT

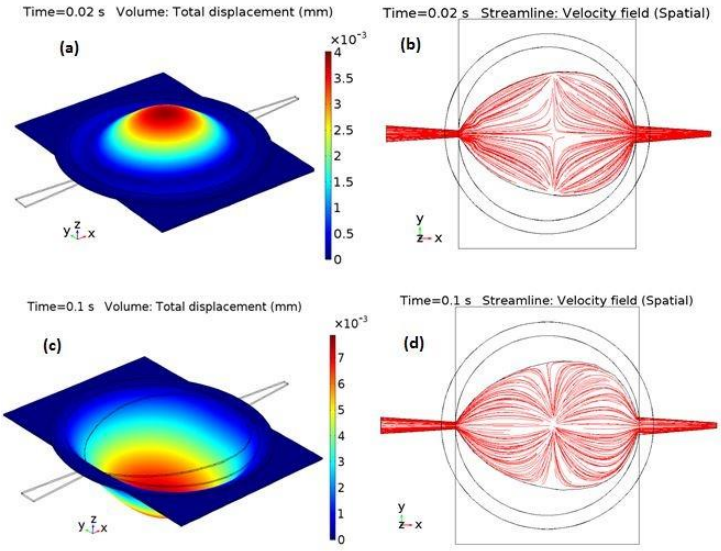


Figure 13 : Simulation for modified micropumping chamber (a) piezo disc deflection at upward position (suction stroke) (b) streamlines generated into chamber during suction stroke (c) piezo disc deflection at downward position (pumping stroke) (d) streamlines generated into chamber during pumping stroke

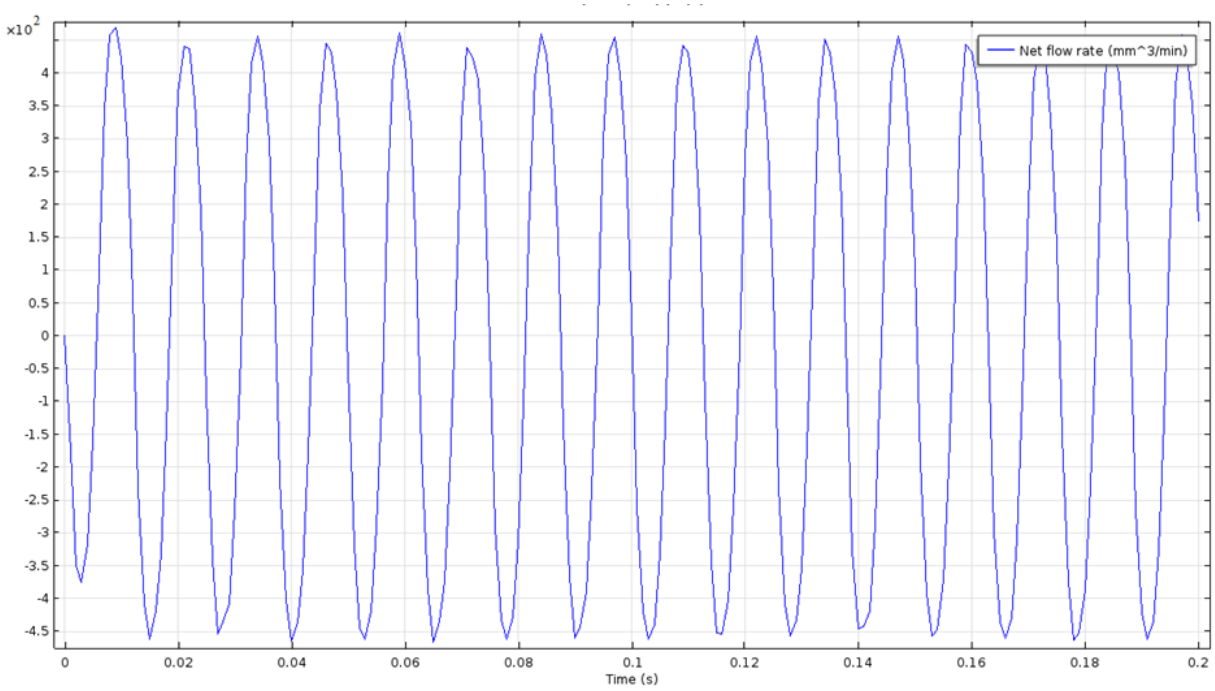


Figure 14

ACCEPTED MANUSCRIPT

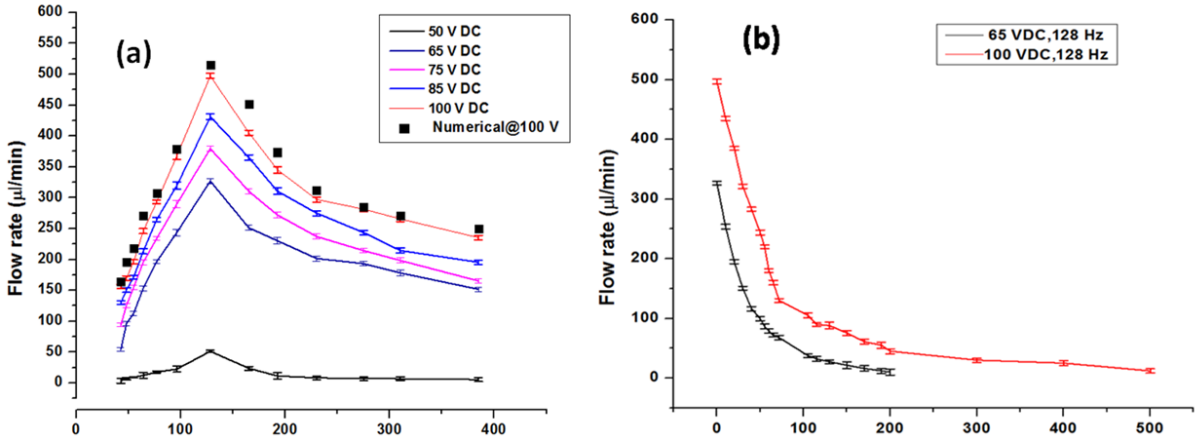


Figure 15

ACCEPTED MANUSCRIPT

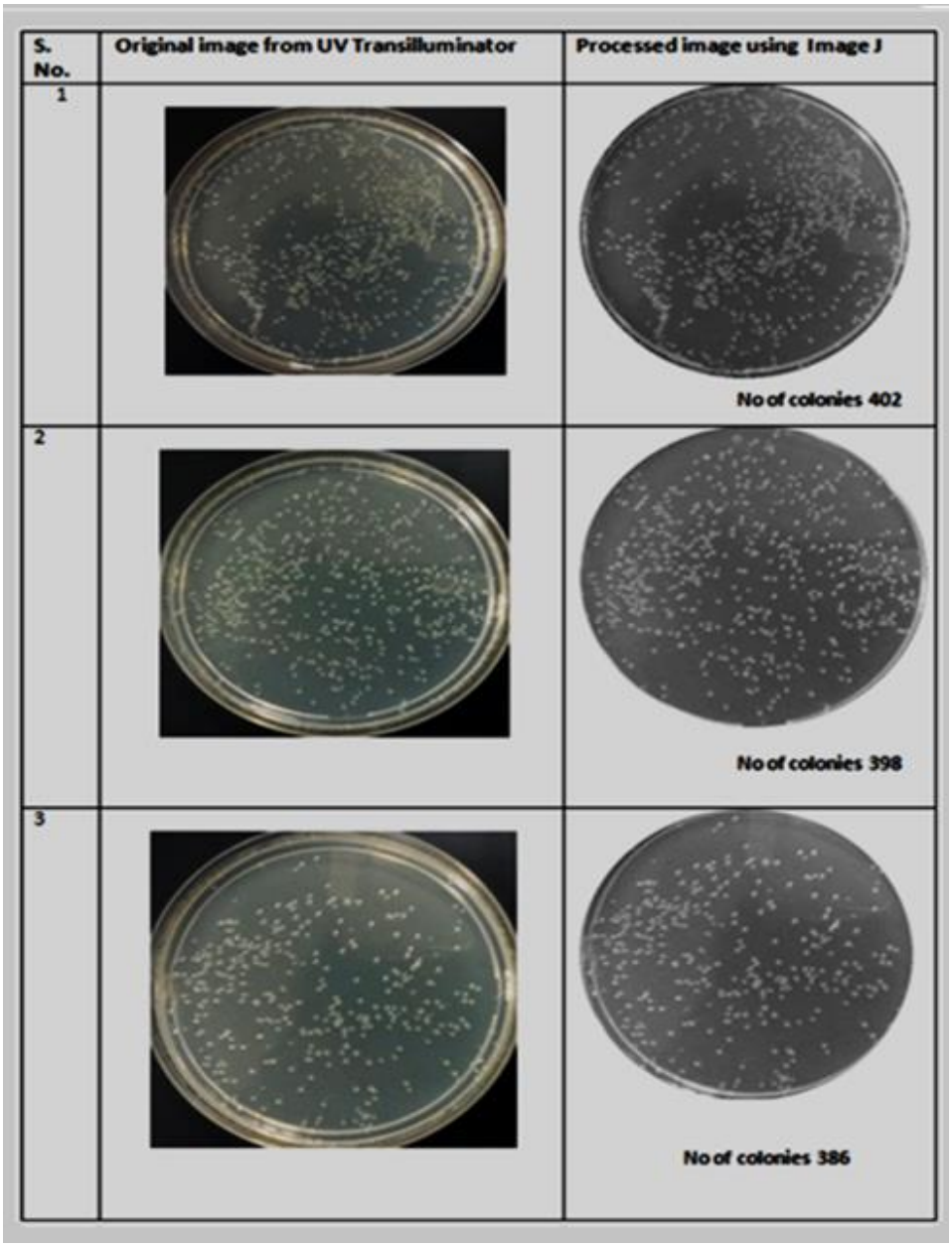


Figure 15

ACCEPTED MANUSCRIPT

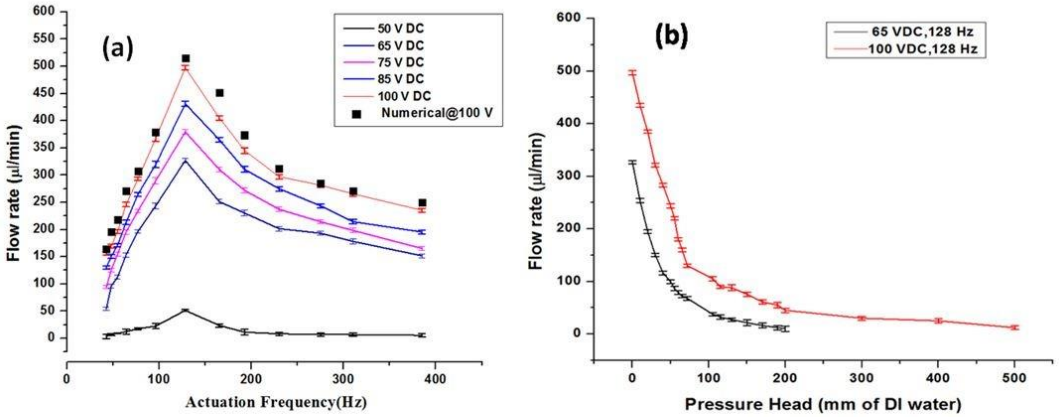


Figure 17: (a) Experimental flow rates with various actuation frequencies at different input volatage (b) ability to deliver against the pressure heads of water at DC voltages 65 and 100 V respectively

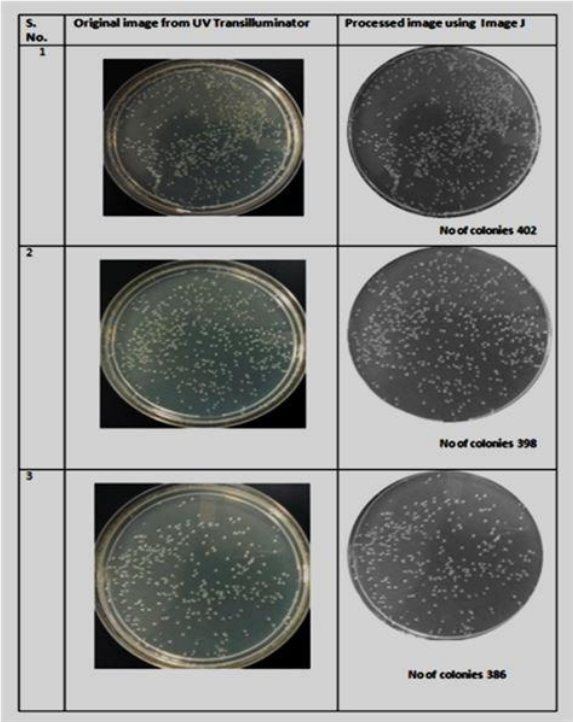


Figure 18: Bacterial cell viability before and after passing through micropump

ACCEPTED MANUSCRIPT

Table 1: List of various references presented in Figure 1 with detailed specification of individual systems.

Reference	Actuator	Micropump's body matrial	Diaphragm material	Working fluid	Applied voltage(V_{PP})	Frequency(Hz)	Back pressure (kPa)	Flow rate (ml/min)	Package Size(mm^3)	Portability size of complete system(mm^3)
Stemme 1993	Piezoelectric(PZT)	Brass	Brass	Water	20	110	21	4.4	25000	N/R
Foster 1995	PZT	Si-glass	Glass	Water	150	114	N/R	0.038	N/R	N/R
Carrozza 1995	PZT	Polymer-brass	Brass	Water	300	70	25	2.7	1270	N/R
Bohm 1999	PZT	Plastic	Brass	Water	350	50	12	1.9	290	N/R
Thin XXS2000 2003	PZT	Microinjection molded plastic	Plastic	Water	450	20	35	2.5	4600	N/R
Zengerle 1995	Electrostatic flap	Silicon	Silicon	Water	200	300	29	0.16	98	N/R
MIP Implantable 2003	PZT	Glass-Silicon	Silicon	Water	150	0.2	55	0.0017	357	N/R
Shozi 1990	PZT	Glass-Silicon	Silicon	Water	100	50	N/R	0.022	4000	N/R
Li 2000	PZT	Si-glass	Silicon	Silicon oil	1200	3500	304	3	3300	N/R
Van de Pol 1990	Thermo Pneumatic air	Glass-Silicon	Silicon	Water	6	1	5.1	0.034	3000	N/R
Jeong 2000	Thermo Pneumatic air	Glass-Silicon	Silicon	Water	8	4	0	0.014	N/R	N/R
Meng 2000	Pneumatic	Silicon-thermo plastic silicon	Silicon rubber	Water	N/A	5	5.9	3.9	N/R	N/R

ACCEPTED MANUSCRIPT

		rubber								
Bohm 1999	Electromagnetic flap	Plastic	Silicon rubber	Water	5	50	10	2.1	1000	N/R
S.S. Wang 2010	PZT	PMMA	Adhesive layer	Water	150	55	1.4	0.6	N/R	N/R
Ling Sheng Jang 2007	PZT	Silicon-glass	Pyrex	Water, Blood	150	100 kHz	3.2	0.122	1980	25x10^5

ACCEPTED MANUSCRIPT

Table 2: Material and properties and layer sizes

Material	properties	Magnitude	Size of different layer
PZT-5A	C_E **Elasticity constant (Pa)**	$\begin{bmatrix} 12.03 & 7.52 & 7.51 & 0 & 0 & 0 \\ 7.51 & 12.1 & 7.51 & 0 & 0 & 0 \\ 7.51 & 7.51 & 11.1 & 0 & 0 & 0 \\ 0 & 0 & 0 & 2.11 & 0 & 0 \\ 0 & 0 & 0 & 0 & 2.11 & 0 \\ 0 & 0 & 0 & 0 & 0 & 2.26 \end{bmatrix} \times 10^{10}$	**PZT layer thickness=60μm** **PZT layer diameter =12 mm** **Brass layer thickness=100μm** **Brass disc diameter =15 mm**
	e **Coupling matrix(C/m^2)**	$\begin{bmatrix} 0 & 0 & -5.35 \\ 0 & 0 & -5.35 \\ 0 & 0 & 15.78 \\ 0 & 12.29 & 0 \\ 12.29 & 0 & 0 \\ 0 & 0 & 0 \end{bmatrix}$	
	ϵ_s **Dielectric permittivity (F/m)**	$\begin{bmatrix} 8.11 & 0 & 0 \\ 0 & 8.11 & 0 \\ 0 & 0 & 7.35 \end{bmatrix} \times 10^{-9}$	
PDMS	**Density**	**965 kg/m^3**	
	Poisson ratio	**0.49**	

ACCEPTED MANUSCRIPT

	Young's modulus	**0.8 MPa**	
	Fluid (water) Density	**997 kg/m^3**	
	Kinematic viscosity	**0.0014 kg/m s**	
	Nozzle/Diffuser angle and length is taken 7°, 6 mm respectively.		
	Microorganism (E. coli DH5α cells (live cells))		
	Young's modulus [48]	**2-3 MPa**	

Discussion of "Exact Solution of the Friction Circle Method" by Jozsef Garai

DOI: 10.1061/(ASCE)GM.1943-5622.0000618

Anjeshnu Trivedi, S.M.ASCE[1]

[1]Graduate Student, Dept. of Civil Engineering, Indian Institute of Technology (BHU), Varanasi 221005, India.

Downloaded from ascelibrary.org by Delhi Technological University - Delhi College of Engg on 08/12/17. Copyright ASCE. For personal use only; all rights reserved.

The friction circle method has invoked a keen interest among field engineers ever since it was originally proposed by Gilboy (1934) and modified by Taylor (1937). The example of several slope failures indicates that the failure surface is often cylindrical, which is circular in section in a homogeneous and isotropic soil mass (Petterson 1955; Steward et al. 2011). The author has presented an interesting account on the exact solution of friction circle method using a radii incremental factor k for the friction circle. Accordingly, the stability can be evaluated on the condition of the equilibrium of forces and limit equilibrium of actuating and resisting forces concurrently acting on a point that is assumed for the equilibrium of moments at the supposed stability limit. Such a supposition contradicts the kinematic admissibility of the problem because the values of soil resistance originating in cohesion and friction at limit equilibrium are indeterminate. This discussion aims to focus on an interesting result obtained by the author; several other investigators, namely, Taylor (1937, 1948), Petterson (1955), Fröhlich (1955), Arredi (1966), and Spencer (1973); and the discusser with innate similarities but using different approaches. The author has proposed the exact solution assuming a symmetric pressure distribution function. The discusser, having assumed a variance in the pressure distribution, proposes a solution that returns the author's solution as a particular case. This discussion shows the evaluation of controlling factor k, graphically, by trials of incrementally changing the radii of the friction circle upon widening the central angle of the sliding slope and, second, selecting a distribution of normal pressure on slip circle by conceptualizing the distribution as a function of infinitesimal changes in the central angle of the sliding slope (α).

The exact solution should be based on the equilibrium of force attributable to cohesion (C), intergranular force (P), and weight (W) in the case of symmetric and asymmetric pressure distribution about the bisector of the angle subtended at the slip circle. Second, prior to failure, the moment of weight (W) about the center of the slip circle (O) must be less than the analogous moment of P and C.

Thus, at the limit equilibrium of forces,

$$\vec{W} = \vec{C} + \vec{P} \tag{1}$$

$$\vec{P} = \vec{N} + \vec{T} \tag{2}$$

$$T = N \tan\phi \tag{3}$$

where P = intergranular force that acts at a distance of R_{fc} from O, as shown in Fig. 1; R = radius of slip slope; N = normal force; T = friction force; and ϕ = friction angle. The position and line of action of intergranular force P is dependent on the normal force N and the friction force T. The position and value of N and T depend on the pressure distribution pattern and the central angle of the sliding slope.

The moments of forces is presented as

$$Wx = PR_{fc} + CR_c \tag{4}$$

where x, R_{fc}, and R_c = perpendicular distances from O to the line of action of forces, W, P, and C, respectively. The value of x can be estimated graphically. The value of R_c can be calculated as proposed by the author. The value of R_{fc} can be calculated as

$$R_{fc} = kR \sin\phi \tag{5}$$

where R = radius of the slip slope.

Thus, from Eqs. (1)– (5), it is implied that the value of the radius of the friction circle R_{fc} is a function of the central angle of the slope circle and the pressure distribution.

The value of k depends on the pressure distribution function, as shown in Figs. 1–3. The slope circles are shown using AB as a chord and $\overline{\text{AB}}$ as the arc of the slip circle, respectively. The radius of the friction circle R_{fc} is constructed incrementally as $kR \sin\phi$, where k is a function of the central angle of the sliding slope (α) and the distribution of pressure about the bisector of the slip circle. Symmetric distribution of pressure along the slope circle is shown in Fig. 1.

The value of k is presented in simplified form as

$$k = k_\alpha k_{\alpha\sigma} \tag{6}$$

where k_α captures the influence of the central angle of sliding slope, and $k_{\alpha\sigma}$ carries the effect of the distribution of normal pressure. For $k_{\alpha\sigma} = 1$(symmetric distribution of pressure), Eq. (6) returns $k = k_\alpha$. The value of k_α is presented as

$$k_\alpha = \frac{\alpha/2}{\sin(\alpha/2)} \tag{7}$$

where α = central angle of the sliding slope in radians.

A plot for the friction circle with asymmetric pressure distribution on the slope circle with a central angle of sliding slope is shown in Figs. 2 and 3, respectively. Fig. 4 shows an increase in the radius of the friction circle with an increase in the central angle of the sliding slope for symmetric and asymmetric pressure distribution about the bisector of the angle subtended at the slip circle. Fig. 5 illustrates the variation of k for symmetric and asymmetric pressure distributions ($k_{\alpha\sigma} = 1$, $k_{\alpha\sigma} > 1$, and $k_{\alpha\sigma} < 1$) with a central angle of the sliding slope.

The value of $k_{\alpha\sigma}$ can be estimated independently as

$$k_{\alpha\sigma} = f(z_\sigma) \tag{8}$$

where z_σ = distribution function of pressure on the slip surface that depends on the central angle of the slip surface and the graphical pressure distribution along the slip surface, as shown in Figs. 1–3.

Downloaded from ascelibrary.org by Delhi Technological University - Delhi College of Engg on 08/12/17. Copyright ASCE. For personal use only; all rights reserved.

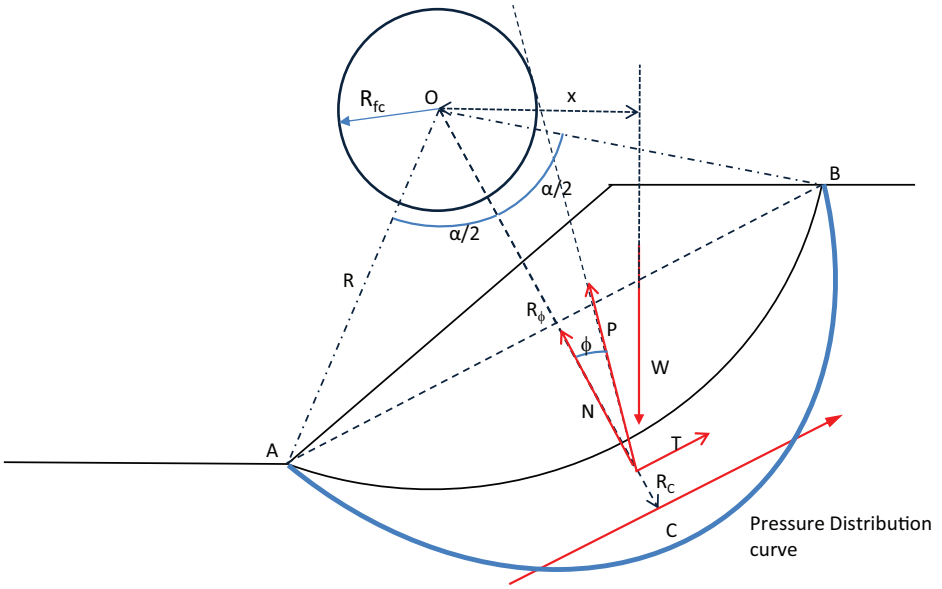


Fig. 1. Equilibrium of forces on a slip circle for symmetric pressure distribution about bisector of slip circle $k_{\alpha\sigma} = 1$

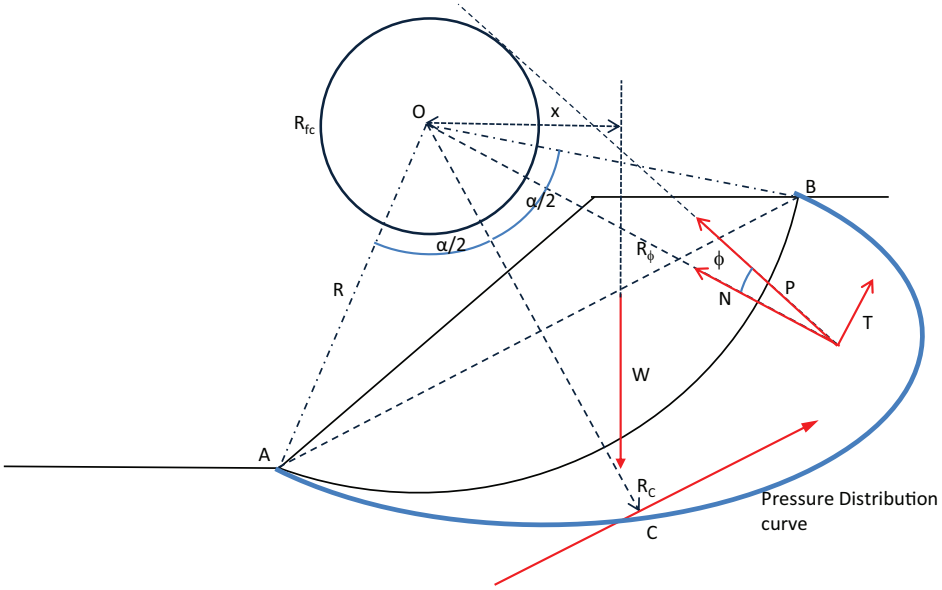


Fig. 2. Equilibrium of forces on a slip circle for asymmetric pressure distribution about bisector of slip circle $k_{\alpha\sigma} > 1$

$$k_\alpha * k_{\alpha\sigma} = \left[\frac{\alpha/2}{\sin(\alpha/2)}\right] \tag{9}$$

η is a parameter of indeterminacy depending on the moment of the pressure distribution function.

It is important to emphasize the fact that the exact solution, as already proposed by Taylor (1948), for the specific stress distribution may result in similar outcomes as Eq. (9).

Eq. (7) is a special case of Eq. (9) at $k_{\alpha\sigma} = 1$, which implies that $\eta = 1$.

For the values of $\eta \neq 1$, Eq. (9) can be represented as

$$\ln k_\alpha + \ln k_{\alpha\sigma} = \eta \ln \frac{\alpha/2}{\sin(\alpha/2)} \tag{10}$$

$$k_{\alpha\sigma} = e^{(\eta-1)\ln k\alpha} \tag{11}$$

Eq. (8) is alternatively presented as Eq. (11), where $k_{\alpha\sigma}$ is shown to depend on a parameter of indeterminacy, η, which itself depends on a ratio of asymmetry of pressure distribution denoted by η_σ. Explicitly, η_σ is a ratio of the radius of a friction circle of asymmetric pressure distribution to the radius of a friction circle of symmetric pressure distribution.

For $\eta > 1$,

$$\eta_\alpha = R_{fc} \text{ of asymmetric pressure distribution (Fig. 2)} / R_{fc} \text{ of symmetric pressure distribution (Fig. 1)} \tag{12}$$

Downloaded from ascelibrary.org by Delhi Technological University - Delhi College of Engg on 08/12/17. Copyright ASCE. For personal use only; all rights reserved.

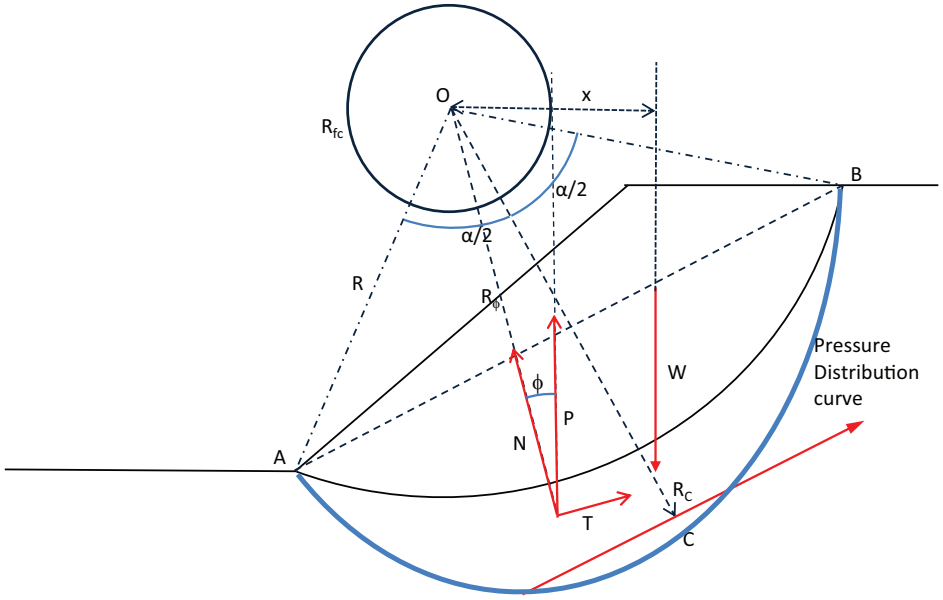


Fig. 3. Equilibrium of forces on a slip circle for asymmetric pressure distribution about bisector of slip circle $k_{\alpha\sigma} < 1$

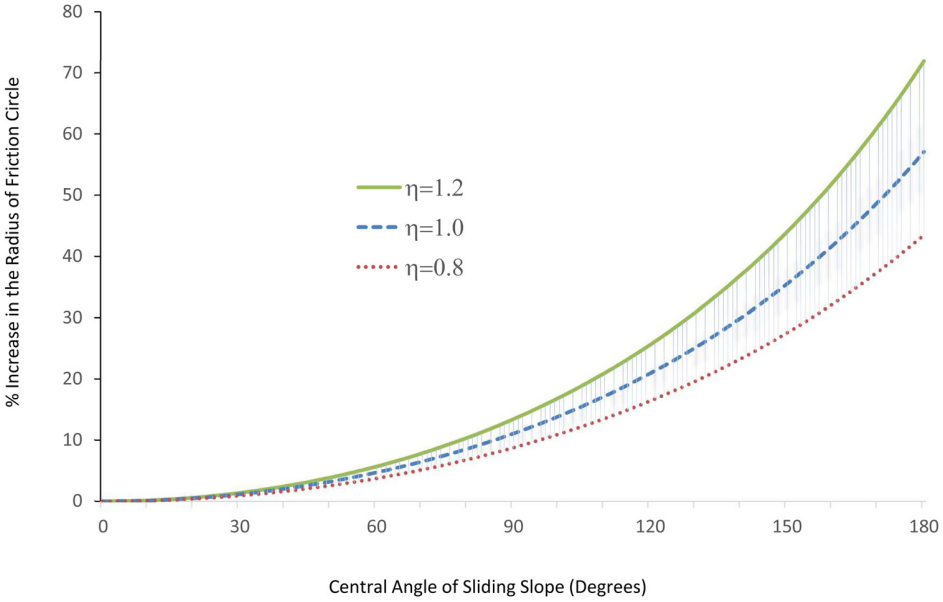


Fig. 4. Increase in the radius of friction circle with central angle of sliding slope on equilibrium of forces on a slip circle for symmetric and asymmetric pressure distribution about bisector of slip circle at $\eta = 0.8$, 1, and 1.2

$$\eta_\sigma = k_{\alpha\sigma}(\text{Fig. } 2)/k_{\alpha\sigma}\ (\text{Fig. } 1) \tag{13}$$

Similarly, for $\eta < 1$,

$$\eta_\sigma = R_{fc} \text{ of asymmetric pressure distribution (Fig. 3)}/R_{fc} \text{ of symmetric pressure distribution (Fig. 1)} \tag{14}$$

$$\eta_\sigma = k_{\alpha\sigma}(\text{Fig. } 3)/k_{\alpha\sigma}\ (\text{Fig. } 1) \tag{15}$$

because $k_{\alpha\sigma}$ (Fig. 1) = 1.

Therefore, on the basis of Eqs. (12)–(15):

$$\eta_\sigma = \left\{\frac{\alpha/2}{\sin(\alpha/2)}\right\}^{(\eta-1)} \tag{16}$$

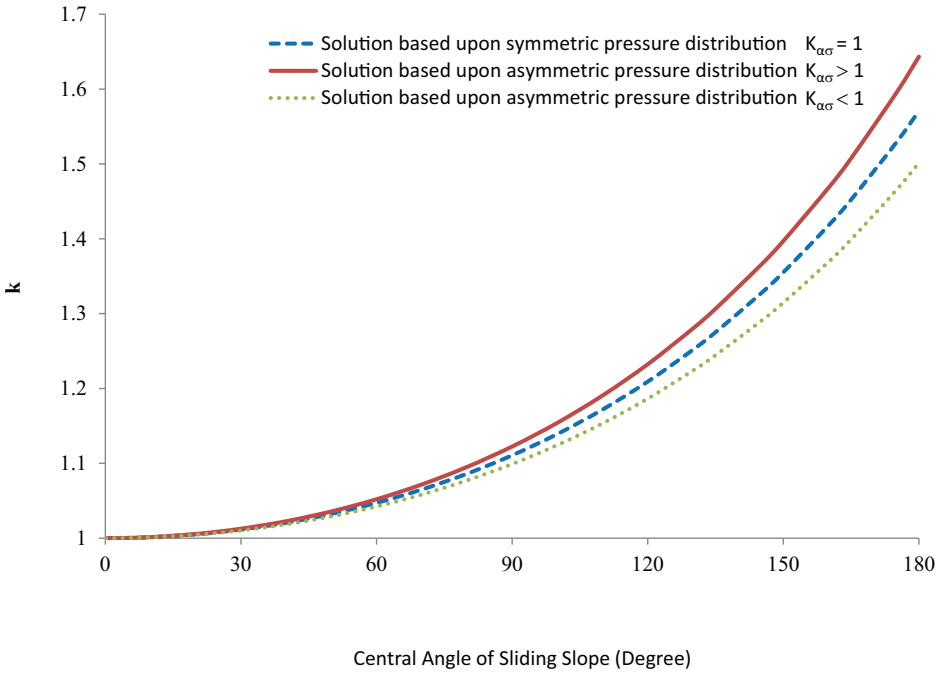


Fig. 5. Values of k with central angle of sliding slope on equilibrium of forces on a slip circle for symmetric and asymmetric pressure distribution about bisector of slip circle

$$\eta = 1 + (\ln \eta_\sigma)/\ln\left[\frac{\alpha/2}{\sin(\alpha/2)}\right] \tag{17}$$

Fig. 4 shows an increase in the radius of the friction circle with an increase in the central angle of the sliding slope for the values of $\eta = 0.8$, 1, and 1.2. Figs. 2 and 3 are shown as illustrative examples of a parameter of indeterminacy, $\eta > 1$ and $\eta < 1$, respectively.

Thus, the solution for k, as proposed by the discusser, complements the exact solution of the friction circle method proposed by the author.

Acknowledgments

The discusser is thankful to the reviewers, the editors of this manuscript, and Prof. A. Trivedi of the Dept. of Civil Engineering, Delhi Technological University, Delhi, India, for making useful suggestions to improve the presentation of this discussion.

References

Arredi, F. (1966). "A re-examination of the friction circle method for the stability analysis of slopes." *Meccanica*, 1(3–4), 48–68.
Fröhlich, O. K. (1955). "General theory of stability of slopes." *Géotechnique*, 5(1), 37–44.
Gilboy, G. (1934). "Mechanics of hydraulically filled dams." *J. Boston Soc. Civ. Eng.*, 20(7), 185–203.
Petterson, K. E. (1955). "The early history of circular sliding surfaces." *Géotechnique*, 5(4), 275–296.
Spencer, E. (1973). "Thrust line criterion in embankment stability analysis." *Géotechnique*, 23(1), 85–100.
Steward, T., Sivakugan, N., Shukla, S. K., and Das, B. M. (2011). "Taylor's slope stability charts." *Int. J. Geomech.*, 10.1061/(ASCE)GM.1943-5622.0000093, 348–352.
Taylor, D. W. (1937). "Stability of earth slopes." *J. Boston Soc. Civil Eng.*, 24(3), 197–246.
Taylor, D. W. (1948). *Fundamentals of soil mechanics*, Wiley, New York.

Downloaded from ascelibrary.org by Delhi Technological University - Delhi College of Engg on 08/12/17. Copyright ASCE. For personal use only; all rights reserved.

Volume 5 Issue 2 (2017) 283-285 ISSN 2347 - 3258
International Journal of Advance Research and Innovation

Ecological Benefits of Reviving Urban Water Bodies using Rainwater Harvesting

Paridhi Rustogi*, SK Singh
Department of Environmental Engineering, Delhi Technological University, New Delhi 110042, India

Article Info
Article history:
Received 25 January 2017
Received in revised form
20 February 2017
Accepted 28 February 2016
Available online 15 June 2017

Keywords: Rainwater harvesting, Ecosystem services, Groundwater recharging, Integrated water resource management (IWRM)

Abstract
Water bodies across India are facing a myriad of ecological challenges due to rapid industrialization and urbanization. As India continues to develop, focus is shifting from preservation and conservation of natural resources to greater economic growth. Issues likeloss of watershed, increasing pollution levels, deteriorating water balance, encroachment and illegal constructions have led to a reduction in the number of urban water bodies and a dire lack of groundwater recharge has impacted the health of existing water bodies over time. Such issues coincide with an influx of population in India's cities leading to an increase in demand of water resources for personal consumption and for industry. To cater to this rising demand for water across India, augmenting the number of water bodies and improving their health is crucial from a public health and ecological perspective. Water bodies like ponds and lakes provide various ecosystem services that are required to manage microclimate, biodiversity and nutrient cycling. In the Indian context, millions rely on these ecological services provided by water bodies and historically rainwater harvesting has been used as an easy, low-cost and locally adoptable technique to maintain water storage. Its application to revive water bodies can help revitalise water bodies and provide ecological benefits in the process. Implementation of community water management schemes with maximum people's participation is crucial to ensure the success of such schemes. Similar studies across India and the world lay precedent for such practices and can ameliorate the water shortages faced at a micro level in today's day and age.

1. Introduction

Urban Indian cities are facing a water crisis due to loss of watershed, increasing levels of pollution, deteriorating water balance, lowering of water table and a dire lack of groundwater recharge [1]. Such issues have become a great concern in the Indian context which motivated the Indian Government's Twelfth Five Year Plan to launch a completely revamped programme on Repair, Renovation and Restoration (RRR) of water bodies [2]. Increasingly, the government and civil society are rediscovering the ecological benefits provided by healthy water bodies and there is a growing movement to revive urban water bodies.

Water determines the full potential of any country [3]. Optimum development and efficient utilization of water resources becomes paramount in a country like India which has an ever-rising populace and a seemingly insatiable water demand. However, today the biodiversity of lake and pond ecosystems is increasingly threatened by anthropogenic activities – may it be due to industrialization by-products, pollution or urbanization[4].

Even before tackling the sustainability conundrum, there is a lot of debate about how to best define a water body such as ponds and lakes. Any depression in the ground which collects and retains adequate precipitation can be considered as a lake or pond based on the size of the water body. Both ponds and lakes catch and conserve rainwater, which can percolate into the soil and help in recharging the groundwater level. The water from ponds and lakes can be used for a variety of purposes for both human and animal consumption, for irrigation, recreational purposes etc. Water bodies can be formed due to geological and ecological events of different varieties. They can also be artificially created to induce the positive effects of water bodies, such as sustaining life at many levels and helping to maintain the biodiversity of a region.

In rural areas, ponds and lakes perform significant environmental, social and economic functions, ranging from being a source of drinking water, recharging groundwater, acting as sponges to control flooding, supporting biodiversity and providing livelihoods. These water bodies, whether manmade or natural, fresh water or brackish play a vital role inmaintaining environmental sustainability[5]. Although the role of water bodies in urban spaces is less clearly defined, there is scientific consensus that they provide invaluable ecosystem services and any urban space must have a balance between urbanisation and green and blue spaces to be deemed healthy.

***Corresponding Author,**
E-mail: paridhirustogi@gmail.com
All rights reserved: http://www.ijari.org

2 Status of Water Bodies in India

India is known for its diversity and houses a wide range of water bodies across its length and breadth in a vast variety of climates. The water impoundments include natural lakes, wetlands and coastal lagoons, as well as constructed reservoirs and tanks. The enormity of conducting a thorough survey of the lakes and ponds across India isn't lost on city planners and there isn't conclusive data on the same on a national level. However, it is possible to discuss the general conditions in which water management is carried out in India in the recent past and its current status.

Water bodies all over the country are exhibiting varying degrees of environmental degradation caused by encroachments, eutrophication and siltation. High population density places direct pressure on the catchments of water bodies. While there are efforts to address these issues, the ground reality points toward a decline in the number of water bodies. Local people lack the knowledge to restore water bodies and delays in restoration cause irreparable damage to the health of water bodies.A lack of coordination among different governmental agencies, ineffectiveness of legislation and the over compassing lack of an integrated approach to water management are the challenges that are faced in reviving water bodies in urban areas.

Encroachment is a major reason for loss of water bodies. In the process, water bodies are drained and the area is reclaimed for constructional purposes. Such activities contribute to a loss of heritage and a loss of biodiversity including disappearance of plant, avian and fish species. In the case of lack of maintenance of existing water bodies there is a dire impact on public health. Incidences of waterborne diseases like jaundice, typhoid and gastroenteritis rise and vector transmitted diseases like malaria also increase among the population living near the area. Additionally, in many Indian lakes that are considered famous, uncontrolled pressure and pollution from tourists has resulted in disturbance to the biodiversity of flora and fauna, which thrive on the lake [6].

2.1 Importance of Water Bodies in the Indian Context

Historically in India, tanks (tankas), ponds (johads, taalab) and lakes (taal) have always played an important role in irrigation, supplying drinking water, ecology, tourism/culture and domestic use. Over the centuries, people India have used basic engineering skills to develop a wide variety of techniques to meet their water needs. Over time, there has been a shift away from traditional knowledge and traditional water management practices in both rural and urban areas.Perhaps, in part decades of British rule is to blame for negatively impacting water based knowledge leading to a severe disruption of water management structures.

In countries where poverty and inequality are rampant such as

developing and least developing countries, people are more directly dependent on ecosystem services as their lives are more intimately related to nature and natural resources. Such a scenario makes them highly vulnerable when natural ecosystems are degraded [7]. Increased water stress has a profound impact on food production and India is already struggling to be food secure. In such a scenario there is a pressing need to revive traditional water management systems to reduce social vulnerabilities and safeguard agricultural and environmental cycles. To achieve this, restoration of streams in urban areas and study and management of such designed ecosystems as unique ecosystems are advocated, with the aim of optimizing services to urban populations [8].

3 Rainwater Harvesting in India

The practice of rainwater harvesting and reusing stored water for domestic purposes has been prevalent in India since ancient times[3, 9]. Historically, settlements grew around temples, and over time temples and tanks became nearly inseparable. Evidence of tank irrigation in Tamil Nadu dates back to the Sangam period of 150 BC to 200 AD, and by the early medieval period (750−1300), tank irrigation was thriving throughout the region[10].

Efficient management of water in traditional farming systems like Kattas and Surangams in North Kerala and Karnataka, Zabo system of Nagaland and Bamboo drip irrigation of Meghalaya and Apatani valley in Arunachal Pradesh can be found all through India [11], where rainwater harvesting and water resource management has been an integral part of communities since centuries.

Usage of rainwater harvesting in recent times in areas like North East India [12] and Kerala [3] have shown immense potential for its applications in other parts of the country and proven its importance in ecosystem revival [13]. In fact, rainwater harvesting in South Asia differs from the rest of the world as it has a history of continuous practice for at least the last 8000 years [14]. Further, an integrated perspective of traditional knowledge on adaptation strategies, such as the rainwater harvesting system is particularly useful to comprehend vulnerability and adaptation to environmental stresses at the local scale.

Rainwater harvesting and storage are important mechanisms for adapting to climate change and are in use in parts of Africa that are currently experiencing high variability of rainfall [15]. Climate change stands to affect India adversely in the coming years due to our sizable population and rising demand for resources and hence revival and rejuvenation of water bodies in Indian cities is crucial. As climate extremes increase, rainwater harvesting can be used as mechanism to build the resilience of societies towards uncertainties. Utilizing sound knowledge of historical adaptive processes can help in learning and developing future tools to combat climate vulnerabilities [14].

In the light of such evidence, organisations are increasingly engaged in promoting 'traditional' water harvesting systems for enhancing sustainability, reducing vulnerabilities or even drought-proofing semiarid regions of the countryside [16]. This approach needs to be introduced to India's urban spaces to replicate the positive impacts on communities and ecology.

3.1 Use of Rainwater Harvesting to Revive Water Bodies

Recent initiatives, both at community and government level, have made use of long neglected water harvesting traditions. The results show that reviving water harvesting systems stimulate rural development and restores local ecosystems[17]. The positive effects of such schemes have found to surpass economic benefits as they impact the public health positively. Further, helping people become self-reliant by improving their local natural resource base is a viable and effective strategy for poverty alleviation.

In urban areas, rainwater will have to be harvested using rooftops and open spaces. Harvesting rainwater not only reduces the possibility of flooding, but also decreases the community's dependence on groundwater for domestic uses. Apart from bridging the demand–supply gap, recharging improves the quality of groundwater, raises the water table in wells/bore-wells and prevents choking of drains. Energy to pump groundwater is also saved as the water table rises [18].

Use of rainwater harvesting in Sukhomajri village in Chandigarh wherevillagers built small tanks to capture rainwater, erstwhile drought-struck Ralegan Siddhi village in Maharashtra where locals constructed storage ponds, reservoirs and gully plugs to combat drought and River Arvari in drought-prone Rajasthan which was brought back to life by rainwater harvesting are instances of water bodies being revitalised by the power of rainwater harvesting [17].

Achieving such success in urban spaces is a different ballgame but has been attempted by different methodologies. The restoration of HauzKhas lake in New Delhi lays precedent that water bodies in urban areas can be restored and developed into functional ecosystems [19]. The success of HauzKhas lake has shown that restoration of ecosystem services garners public support and necessitates public participation. Such restoration efforts could be extended to other water bodies in Delhi and to urban water bodies across the country.

4.1 Ecosystems and their Services

Ecosystem services are the benefits people obtain from ecosystems. These include provisioning services such as food and water; regulating services such as flood and disease control; cultural services such as spiritual, recreational, and cultural benefits; and supporting services, such as nutrient cycling, that maintain the conditions for life on Earth[20]. These services are more than just goods, and include critical life-supporting services or processes, which are commonly neglected or taken for granted by society as an economic valuation isn't granted to them [21].

Economic valuation of ecosystem services and biodiversity can make explicit to society in general and policy making in particular, that biodiversity and ecosystem services are scarce and that their depreciation or degradation has associated costs to society. If these costs are not imputed, then policy would be misguided and society would be worse off due to misallocation of resources [22]. In fact, restoration costs more in the long-run than using resources judiciously.

Ecosystem services are valuated in a manner of ways and it has been found that hybridising methods leads to removing an individual method's drawbacks. While social, economic and cultural parameters are considered for finding appropriate valuations, involving the viewpoints of stakeholders in the process leads to more meaningful results. An assessment of the condition of ecosystems, the provision of services, and their relation to human well-being requires an integrated approach. This enables a decision process to determine which service or set of services is valued most highly and how to develop approaches to maintain services by managing the system sustainably [20].

In a nutshell, economies of the worldare reliant on ecological life-support systems and in that manner the value of ecological services can be considered asinfinite. As natural resources and ecosystem services become more stressed and scarce, their value is bound to increase. If and when (judging by the current trend of consumption) tolerable thresholds for irreplaceable ecosystem services are breached, their value will tend to infinity. Owing to such dependence on current and future trends and practices, huge uncertainties are involved in the precise estimation of the value of ecosystem services[23].

4. Ecosystem Services Provided by Water Bodies

Ecosystem services are categorised primarily as provisioning and regulating services. Provisioning services are products directly or indirectly obtained from an ecosystem. Water bodies provide fresh water which can be used for a variety of purposes. Regulating services on the other hand, are benefits obtained from regulation of ecological processes. Fresh water can be considered an example of linkages between provisioning and regulating services [23], as fresh water is both a product and a regulating factor.

Water bodies participate in core ecosystem processes likewater cycling and carry outecosystem functionssuch as water provisioning, purification and regulation[22]. They also provide

regulating services like climate regulation, water regulation, erosion control, etc. One of the crucial services is water purification and waste treatment. Ecosystems can be a source of impurities in fresh water but also can help to filter out and decompose organic wastes introduced into inland waters and coastal and marine ecosystems. They can also help in the regulation of human diseases. Changes in ecosystems can directly change the abundance of human pathogens, such as cholera, and can alter the abundance of disease vectors, such as mosquitoes.

In addition to these services, water bodies also provide a range of invaluable cultural services These are the nonmaterial benefits people obtain from ecosystems through spiritual enrichment, cognitive development, reflection, recreation, and aesthetic experiences. To encompass the above, supporting services are those that are necessary for the production of all other ecosystem services. They differ from provisioning, regulating, and cultural services in that their impacts on people are either indirect or occur over a very long time, whereas changes in the other categories have relatively direct and short-term impacts on people.

5. Conclusions

As new environmental threats are predicted to become threats to all freshwater systems, it is necessary to augment the water quantity available in urban cities through natural methods like rainwater harvesting. For a model like this to work, it is crucial for local people to collaborate with other stakeholders to successfully utilise resources and ensure the protection and conservation of green and blue spaces in cities. Further, implementation of integrated water resource management strategies are essential to maintain, augment and manage India's water resources.

Ecosystem restoration has proven critical in returning ecosystem goods and services, when there is positive recovery (Bosire, 2010), and hence there is hope that carrying out pond and lake revival still has innumerable merits for biotic and abiotic components of an ecosystem. The ecological benefits of such an undertaking and substantial and civil society and governmental agencies should join forces to ensure such activities are promoted.

References

[1.] R Singh. Conserving Waterscapes in Context of Urban Delhi. Natural Heritage Division, Intach, 2012.

[2.] M Shah. Water: Towards a Paradigm Shift in the Twelfth Plan'. Economic & Political Weekly, XLVIII (3), 2013.

[3.] MP Samuel, A Mathew. Rejuvenation of Water Bodies by Adopting Rainwater Harvesting and Groundwater Recharging Practices in Catchment Area- A Case Study. The 12th World Lake Conference, 1997, 766–776.

[4.] L Christer, B Hansson. Environmental Threats to Lake and Pond Ecosystems, 2002.

[5.] R Reddy, VB Rao, C Sarala. Proceedings of 4th International Conference on Hydrology and Watershed Management (ICHWAM-2014): With a focal theme on ecosystem resilience-rural and urban water requirements, 29th October - 1st November, 2014.

[6.] MS Reddy, NVV Char. Management of Lakes in India'. Ministry of Water Resources, 2004.

[7.] World Resources Insitute. The Wealth of the Poor: Managing Ecosystems to Fight Poverty. United Nations Development Programme United Nations Environment Programme World Bank World Resources Institute, 2005.

[8.] NB Grimm, SH Faeth, NE Golubiewski, CL Redman, J Wu, X Bai, JM Briggs. Global change and the ecology of cities. Science New York, 319 (5864), 2008, 756–760.

[9.] Ministry of Water Resources, GOI. Guidelines for the Continuation of Scheme on Repair, Renovation and Restoration (RRR) of Water Bodies in XIIth Plan, 2013.

[10.] KJ Van Meter, NB Basu, E Tate, J Wyckoff. Monsoon harvests, The living legacies of rainwater harvesting systems in South India. Environmental Science and Technology, 48(8), 2014, 4217–4225.

[11.] S Narain, A Agarwal. Dying wisdom : rise, fall and potential of India's traditional water harvesting systems. Center for Science and Environ, 1997.

[12.] SV Ngaachan. Rainwater Harvesting and its Diversified Uses for Sustainable Livelihood Support in NEH Region of India, ICAR Research Complex for NEH Region 2005.

[13.] M Armar-Klemesu. Urban Agriculture and Food Security, Nutrition and Health. Urban Agriculture and Food Security, Nutrition and Health, 2000, 99–117.

[14.] DN Pandey, AK Gupta, DM Anderson. Rainwater harvesting as an adaptation to climate change. Current Science, 85(1), 2003, 46–59.

[15.] E Boelee, M Yohannes, M Mccartney, P Cecchi, S Kibret, F Hagos, H Laamrani. Options for water storage and rainwater harvesting to improve health and resilience against climate change in Africa 2020, 2013, 509–519.

[16.] S Gupta. Demystifying 'Tradition': The Politics of Rainwater Harvesting in Rural Rajasthan, India. Water Alternatives, 4(3), 2011, 347–364.

[17.] Agarwal, A., & Narain, S. (2000). Water harvesting : community-led natural resource management. International Institute for Environment and Development.

[18.] R Kumar,RD, Singh, KD Sharma. Water Resources of India. Current Science, 89(5), 2005, 794–811.

[19.] R Singh, M Bhatnagar. Urban Lakes and Wetlands: Opportunities and Challenges in Indian Cities-Case Study of Delhi. In 12th edition of the World Wide Workshop for Young Environmental Scientists-Urban Waters: Resource or Risks? 2012

[20.] J Alcamo, EM Bennett. Ecosystems and their Services'. Ecosystems and Human Well-Being: A Framework for Assessment, 2003, 49–70.

[21.] J Bosire. Scientific Understanding of Ecosystem Services. Western Indian Ocean, 3(1), 2010, 21–23.

[22.] U Pascual, R Muradian, L Brander,E Gómez-baggethun, B Martín-lópez, M Verma, RK Turner. The Economics of Valuing Ecosystem Services and Biodiversity. The Economics of Ecosystems and Biodiversity: Ecological and Economic Foundations, (March), 2010, 183–255.

[23.] R Costanza, R Arge, R De Groot, S Farberk, M Grasso, B Hannon, P Suttonkk. The Value of the World's Ecosystem Services and Natural Capital'. Nature, 387, 1997, 253–260.

Engineering Science and Technology, an International Journal xxx (2017) xxx–xxx

HOSTED BY

Contents lists available at ScienceDirect

Engineering Science and Technology, an International Journal

journal homepage: www.elsevier.com/locate/jestch

Full Length Article

Effect of flyash particles with aluminium melt on the wear of aluminium metal matrix composites

Vipin K. Sharma [a,b,*], R.C. Singh [b], Rajiv Chaudhary [b]

[a] Maharaja Agrasen Institute of Technology, Rohini sec-22, Delhi 110086, India
[b] Delhi Technological University, Bawana Road, Delhi 110042, India

ARTICLE INFO

Article history:
Received 13 March 2017
Revised 6 July 2017
Accepted 10 August 2017
Available online xxxx

Keywords:
Stir casting
Pin on disc
Composite
Aluminium
Flyash

ABSTRACT

The present work deals with the fabrication and tribological testing of an aluminium flyash composite. The metal matrix selected was aluminium and flyash contents in different percentages were reinforced in it to fabricate the required metal matrix composite (MMC). Stir casting method was used to fabricate the MMC with 2–4–6% weight of flyash contents in aluminium. Tribological analysis of the tribo pairs formed between the smooth surfaces of cast iron disc and smooth MMC pin has been considered and friction force and wear of the MMC were investigated by using a Pin-on-disc setup. It was observed that the MMC with 6% weight of flyash content in aluminium matrix results in less wear (0.32 g) and 4% weight of flyash content gives the low coefficient of friction (0.12) between the tribopairs of cast iron surface and MMC surface.

© 2017 Karabuk University. Publishing services by Elsevier B.V. This is an open access article under the CC BY-NC-ND license (http://creativecommons.org/licenses/by-nc-nd/4.0/).

1. Introduction

The metal alloys and composite materials have a vast application in the automobile, aircraft and allied industries. Reinforcement used in the metal matrix affects the strength and durability of the material in comparison to their constituent parent materials. Present scenario directly links the mechanical field and its research with the automobile and aircraft industries. It is the need of the society to decrease the rate of consumption of the fossil fuel (exhaustible) Mazaheri and Shabani [7], Shabani et al. [12]. In order to achieve it, the efficiency of the automobile needs to be improved. This can be done by reducing the total weight of the automobile whose major components are the engine and the frame. Aluminium in its alloy form is currently being used for the manufacturing of various engine parts. The limitation of aluminium is that it is prone to scratches and indentations very easily. So, a need arises to fabricate an aluminium-based composite which will be wear resistant in nature by the addition of suitable reinforcements in defined proportion. Aluminium matrix composites have excellent ability to bear tensile as well as compressive forces Shabani and Mazahery [13]. Research has been going on by attempting different reinforcement materials into the aluminium matrix to improve and enhance the properties of the composite. For the fabrication of the composites, casting, powder metallurgy, friction stir processing, ball milling and hot rolling and vacuum hot pressing are some of the techniques which are used by researchers. However casting process is largely used because of its low cost and high production rate Faraji et al. [4], Baghani et al. [3], Shabani et al. [14], but formation of clusters and agglomeration of reinforced particles in the base metal is one of the main problems of casting process Mazahery and Shabani [7]. Recently Shamsipour et al. [17] proposed a semi-solid-metal (SSM) processing for the fabrication of the composites. Widespread research has been done to study the wear behavior of the aluminium MMCs as it provides better wear resistance as compared to the alloy.

Boron carbide Mazahery and Shabani [8], Al_2O_3, TiC, SiC, are the most used reinforcement material for MMCs. Recently non-metallic components like rock dust particles, rice husk ash (RHA), few-layer graphene (FLG) are used as reinforcement and these all resulted in improvement in mechanical properties of the composites.

TiC nanoparticles were reinforced into the matrix of Al-Si alloy by Shamsipour et al. [17], Shamsipour et al. [16]. The addition of TiC particles enhances the hardness of the aluminium alloy and hence decreases the wear rate. Mazahery and Shabani [9] and Shabani et al. [14] used the TiB_2 coated B_4C particulates in Al-Si matrix and tested it against a hardened steel disc on a pin on disc machine. It was reported by authors that as the volume fraction of the coated B_4C increases wear rate decreases. Some iron parti-

* Corresponding author at: Maharaja Agrasen Institute of Technology, Rohini sec-22, Delhi 110086, India.
E-mail address: vipin.dtu@gmail.com (V.K. Sharma).
Peer review under responsibility of Karabuk University.

http://dx.doi.org/10.1016/j.jestch.2017.08.004
2215-0986/© 2017 Karabuk University. Publishing services by Elsevier B.V.
This is an open access article under the CC BY-NC-ND license (http://creativecommons.org/licenses/by-nc-nd/4.0/).

Please cite this article in press as: V.K. Sharma et al., Effect of flyash particles with aluminium melt on the wear of aluminium metal matrix composites, Eng. Sci. Tech., Int. J. (2017), http://dx.doi.org/10.1016/j.jestch.2017.08.004

cles from the hardened steel disc were also got transfer to the composite. In another research by Shamsipour et al. [17] optimum combination of the different inputs of the compocasting was found out and used for the fabrication of the Aluminium metal composites using TiC particles as reinforcement. Rahimipour et al. [11] used the technique of artificial neural network algorithm to predict that Al-20% B_4C provides better wear resistance as compared to other percentages of the B_4C reinforcement.

The size of the reinforcement particles also affects the tribological properties of the composites. Tofigh and Shabani [21] investigated the effect of the different size of B_4C particles on the aluminium composite. It was reported that large B_4C particles showed better wear resistance during the abrasive wear. Also, the surface roughness of Al-B_4C composite material decreases with increase in particle size of B_4C in an aluminium matrix. Similarly, Al_2O_3 in different volume percentages were reinforcement in the aluminium matrix by Shabani and Mazahery [13], Shabani et al. [15]. The Al_2O_3 helps in reducing the wear rate, however the friction coefficient increases with the addition of Al_2O_3 in the matrix of the aluminium. Steel machining chips of the order of 105 μm were reinforced in different wt.% in the copper matrix by Alaneme and Odoni [1]. In was reported that the hardness, strength along with wear resistance of the copper improved with the addition of steel chips. Kumar et al. [5] developed an Al5052/ZrB_2 composite with different percentage of (0, 3, 6, 9 and 10 vol%) ZrB_2 particles by reaction of molten AA5052 with using two inorganic salts K_2ZrF_6 and KBF_4. It was reported that with the increase in the percentages of the reinforcement the hardness and density of the composite also get increased. The strength of the formed composite also got improved with increasing the amount of ZrB_2 till 9% of ZrB_2 and then it started decreasing.

Sharma et al. [18] focuses on the production of aluminium (Al6082-T6) matrix composites reinforced with various weight percentages of silicon nitride particles by conventional stir casting route. The percentage of reinforcement is varied from 0 wt% to 12 wt% in a stage of 3 wt%. The ductility of the aluminium composite decreases with the increase in silicon nitride, however, hardness and ultimate strength increases.

In the recent time, the focus of the researchers has been on the use of non-metallic particulates. Prakash et al. [10] used the technique of powder metallurgy for the fabrication of composite of Aluminium 6061 T6 with rock dust particles. The excess of rock dust particles decreases the hardness of the aluminium composite but the low amount of in the range of 10% helps in improving the wear resistance of the composite. A combination of ball milling and the hot rolling process was adopted by Shin and Bae [20] to produce a composite of aluminium alloy 2024 Al2024) with few-layer graphene FLG). Microstructure and mechanical properties were tested by the authors for the developed composite. At 7% vol of FLG the aluminium showed improved tensile strength properties. Sharma et al. [19] focus on the effect of graphite particles on the microstructure of Al6082 metal matrix composites. Authors used conventional casting Stir) process for the production of the composite material. The addition of graphite as reinforcement in the aluminium matrix is not desired as it decreases the hardness of the composite. Almost same findings were reported by Alaneme and Sanusi [2] for the hardness of the aluminium-graphite-rice husk ash (RHA) composite. However, strength and toughness of the 0.5% graphite and up to 50% RHA got increased. Authors also reported that with graphite component the composites resulted in greater susceptibility to wear however as it is increased from 0.5 to 1.5% the wear resistance decreases. Based on the previous research articles it could be concluded that metallic as well non-metallic reinforcement is being used to fabricate the aluminium matrix composites. The amount of reinforcement is generally very low for non-metallic reinforcement. So as a non-metallic reinforcement in the form of flyash was selected as the reinforcement into the aluminium matrix. Flyash is produced as a by-product from the burning of pulverized coal in power generation plants. It is harmful to humans if inhaled through the air. So by looking at harmful effects and to reduce the flyash contents from the atmosphere, it was decided to use flyash in a positive way to enhance the mechanical properties of the aluminium composites. In this paper, the influence of flyash contents on the aluminium matrix was studied and a potential composite material is proposed for various mechanical applications like engines and bearings.

2. Experimentation

MMC was manufactured with the help of a stir casting process. Stir-casting is the process of melting the material with continuous stirring and immediately pouring the melt into a preformed cavity, then cooling it and allowing it to solidify. In stir-casting, the particles often tend to form agglomerates, which can be only dissolved by vigorous stirring at high temperature. The stir casting set up (Fig. 1) consists of a furnace, crucible and a rotor attached to the motor. The aluminium metal was melted in the crucible which was heated to a temperature of about 900 °C, while the reinforcement material (flyash) was added externally in a fixed proportion of 2–4–6% weight. Aluminium and flyash were mixed with the help of a specially designed stirrer, at a rotational speed of 100 rpm with the aid of the rotor for uniform mixing. The stirrer used had a length of 95 cm and exactly plus sign blade having zigzag angle 90° of each side. The length of every side of stirrer blade was 9 cm each.

The molten mixture of aluminium with flyash was poured in the predefined cavity of required dimensions. After subsequent cooling and secondary machining processes, different specimens were made for testing of wear and coefficient of friction. The percentages of different elements of the composite were analyzed and represented in Table 1.

A pin on disc setup (Fig. 2) was used to measure the wear and frictional force. For the pin-on-disc wear test, two specimens are required. One, a cylindrical pin which is positioned perpendicular to the flat circular counter disc. In this work, the disc rotates at some rotational speed and pin specimen was pressed against the disc at a specified load by means of a lever with attached weights. The amount of wear is determined by weighing pin specimens before and after the test.

A cast iron specimen of 165 mm diameter and 8 mm thickness was used as a counter disc. Surface grinding and lapping processes were used on the disc to make it smooth. The surface roughness value achieved on disc specimen was 0.2 μm Ra.

Aluminium flyash composite material was used as pin specimen of 30 mm length and 10 mm diameter. The bottom surface of the

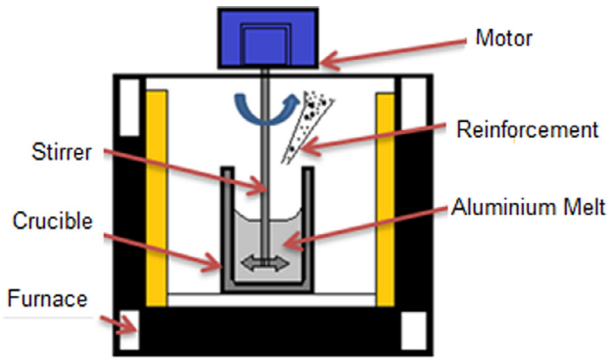


Fig. 1. Stir Casting setup representation.

Please cite this article in press as: V.K. Sharma et al., Effect of flyash particles with aluminium melt on the wear of aluminium metal matrix composites, Eng. Sci. Tech., Int. J. (2017), http://dx.doi.org/10.1016/j.jestch.2017.08.004

Table 1
Elemental percentage in various specimens.

Element	Sample 1 (low flyash 2% wt)	Sample 2 (Medium flyash 4% wt)	Sample 3 (High flyash 6% wt)
Si	9.901	10.296	10.35
Fe	1.202	1.313	1.2266
Cu	0.6284	0.6703	0.694
Mg	0.0723	0.097	0.876
Zn	0.5841	0.6021	0.636
Ni	0.106	0.1155	0.1157
Pb	0.400	0.3177	0.2937
Al	86.886	86.355	86.30

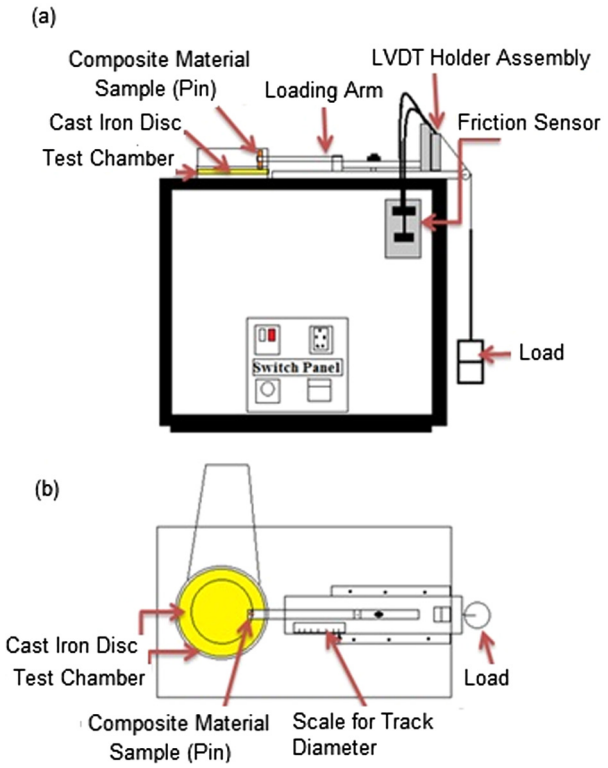


Fig. 2. Pin on disc setup (a) Front view (b) Top view.

pin was also made smooth. The surface roughness of the pin specimen was 0.2 μm Ra.

The test was done under dry conditions without using any lubricating oil. For performing the wear tests ASTM G99 standards were used. The test conditions for the experimentation are given in Table 3. The amount of wear of the samples was recorded using the weight difference method, for that a weighing balance with least count of 0.00001 g has been used. The pin on disc machine is equipped with friction sensors which are used to obtain the frictional force. The frictional force was used to calculate the coefficient of friction (See Table 2).

Table 2
Pin-on-Disc machine specification.

Parameter	Value	
Disc speed	Range (rpm)	200–2000
	Sensor	Drive output
	Least count (rpm)	1
Load Parameters	Range (N)	0–200
	Specification	20 kg Beam type load cell
	Least count (N)	0.1
Machine Parameters	Range (mm)	2
	Sensors specs	LVDT, make: Syscon
	Least count (μm)	0.1
Wear Track Diameter (mm)		150–50

Table 3
Test conditions for experimentation.

S. No.	Test Condition	Values
1.	rpm	600, 780, 1110
2.	Load (N)	19.6
3.	Track Diameter (mm)	70, 100, 130
4.	Pin diameter, Height (mm)	10, 30
5.	Disc diameter, height (mm)	165, 8
6.	Sliding distance (m)	2000
7.	Temperature (°C)	28
8.	Humidity (%)	50–60

The whole experimental work has been done in three steps, one each for each sample of the composite and repeated three times for accuracy. Before starting the experiment test both, disc and pin surfaces were cleaned with acetone. In order to maintain same input parameters for experimental work, duration of the experimental run, the load applied and relative speed of the disc were kept constant.

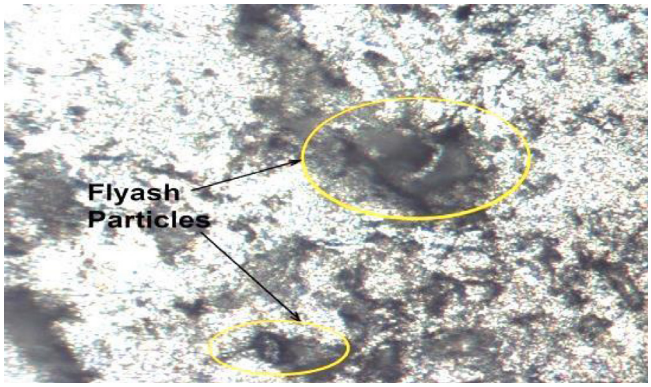
In the first step, the sample 1 having low flyash content was inserted into a properly designed pin holder on the machine. The disc was made to rotate at 780 rpm and track diameter was selected as 100 mm. The load applied by using dead weights was 19.6 N.

In the second step, the sample 2 having medium flyash content was mounted on the machine and track diameter was selected as 130 mm at 600 rpm at 19.6 N of the load. Similarly for third step sample 3 having high flyash content was mounted at a track distance of 70 mm with 1115 rpm of the disc at 19.6 N of the load. The total sliding distance in each was kept at 2000 m.

3. Result and discussion

3.1. Surface analysis

The performance of the aluminium matrix composite depends on the uniformity of the reinforced particles in its matrix. Agglomeration and sedimentation of the reinforced particle results in the fabrication of non-homogeneous composite. To determine the distribution of flyash particles and presence of the porosity in the composite an optical microscope was used. For optical micrographs, the three samples surfaces were cleaned properly. The



(a). Micrograph for low flyash sample

Fig. 3(a). Micrograph for low flyash sample.

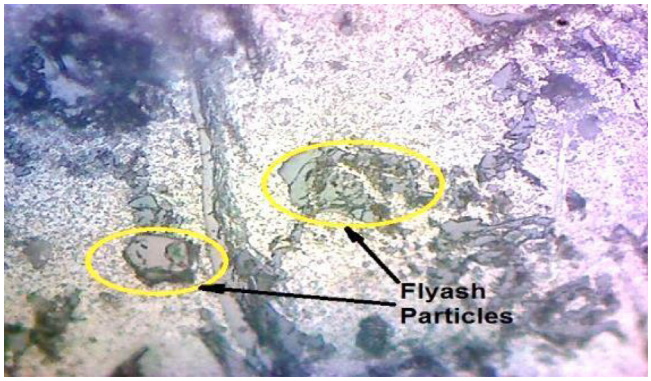
Please cite this article in press as: V.K. Sharma et al., Effect of flyash particles with aluminium melt on the wear of aluminium metal matrix composites, Eng. Sci. Tech., Int. J. (2017), http://dx.doi.org/10.1016/j.jestch.2017.08.004

cleaned samples were then inspected under a microscope and images have been obtained (Figs. 3(a), 3(b), 3(c)). It is seen that for all samples the flyash particles are evenly distributed in the aluminium matrix. Figs. 3(b) and (c) also represents the accumulative nature of the flyash particles as their amount increases. Later SEM analysis of the wear area on the composite was also done to understand the different mechanisms of wear during the frictional and wear testing of the composite.

The SEM analysis was done using a scanning electron microscope (HITACHI E 3700N) at 1000 magnification. The obtained SEM images of the different samples are presented in Figs. 4(a)4 (b)4(c).

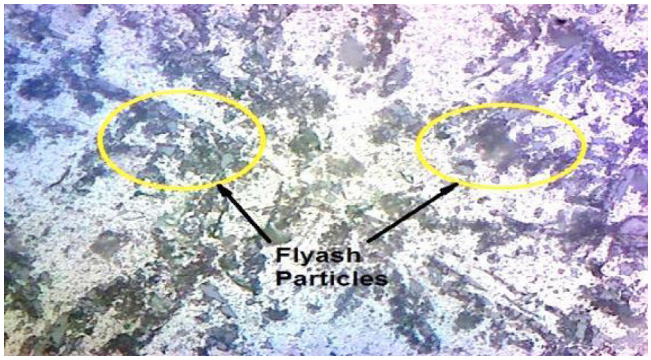
Figs. 5(a)5(b)5(c) represents the SEM images of the wear area on the three samples. It is seen from Fig. 5(a) that the wear surface of the low flyash content sample have many grooves, wedge sections and ploughing on it, which clearly indicates the abrasive wear of the surface. These grooves, wedge sections and ploughing are also visible in a very limited amount in the medium flyash content sample. The sample with high flyash contents indicates the very low amount of wedge sections, grooves, and ploughing as visible from the Fig. 5(c). The wear surface clearly indicates that the flyash contents help in keeping the surface particles together and increases the wear resistance.

Tribological behavior of the aluminium matrix composites is generally a function of applied load, reinforcement particle size, nature and volume fractions. The processing route for the fabrication of the composite also influences the properties.



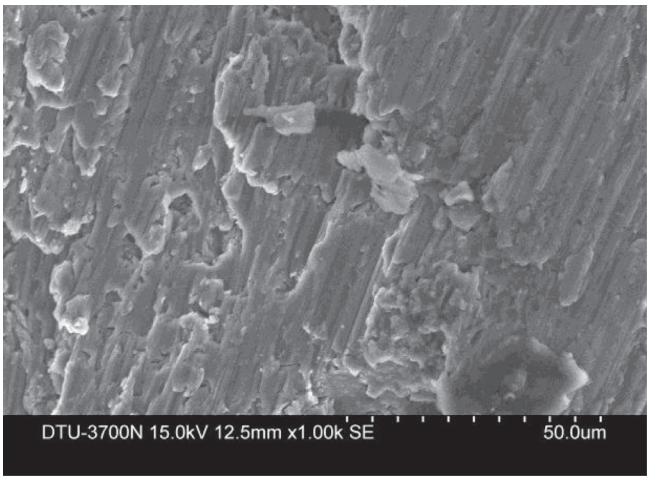
(b). Micrograph for medium flyash sample

Fig. 3(b). Micrograph for medium flyash sample.



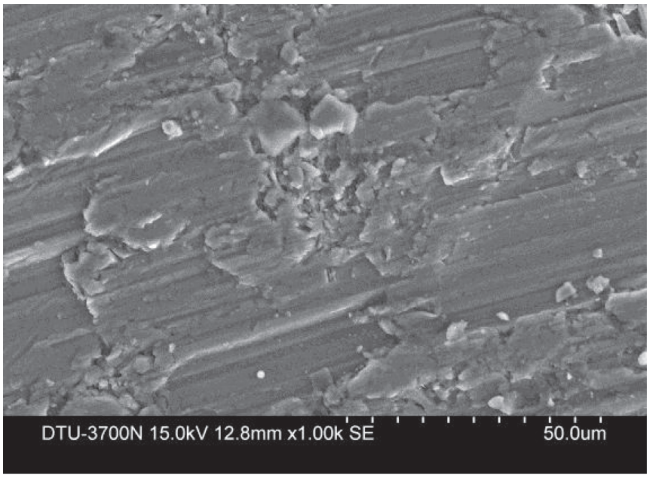
(c). Micrograph for high flyash sample

Fig. 3(c). Micrograph for high flyash sample.



(a). SEM images of sample 1 (Low flyash content)

Fig. 4(a). SEM images of sample 1 (Low flyash content).



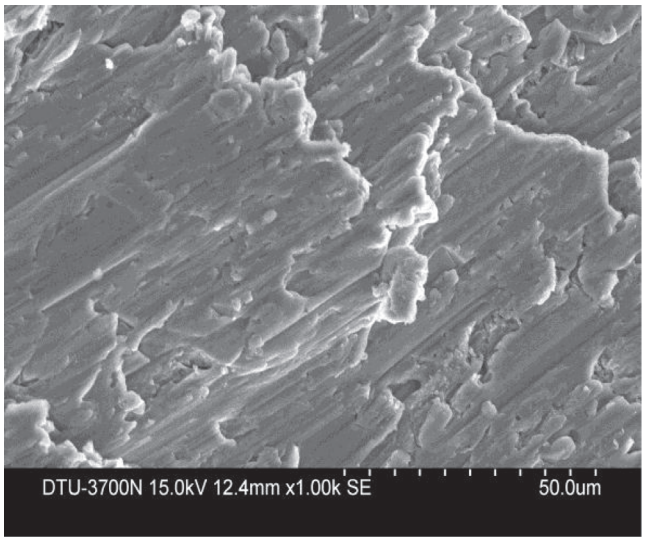
(b). SEM images of sample 1 (Low flyash content) after wear test.

Fig. 4(b). SEM images of sample 1 (Low flyash content) after wear test.

The weight loss of the aluminium composite reinforced with different flyash contents is represented in Fig. 6., it is quite clear that weight loss of the composites decreases as the flyash contents in the composite increases. The flyash contents present in aluminium matrix resist the destructive action of the wear tests and hence increases the wear resistance of the composites. For sample 1 (2% Flyash), sample 2 (4% flyash) and sample 3 (6% flyash), the amount of wear obtained are 0.44 g, 0.43 g, and 0.38 g respectively. The nature of wear is mostly abrasive.

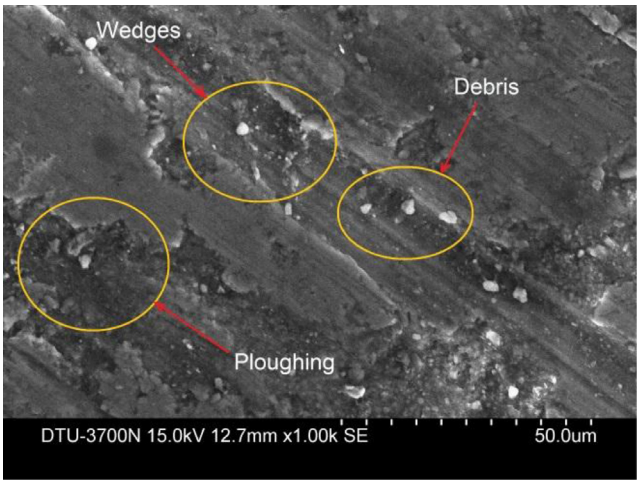
The coefficient of friction is plotted with respect to sliding time. Data was accumulated for the coefficient of friction with the help of frictional sensor (Fig. 2.) which is linked to the pin on disc machine through computer software. It can be seen from Fig. 7 that the coefficient of friction is maximum for a sample having a high content of flyash for the initial stages and lowest for a sample having medium flyash content. It is observed that the coefficient of friction in the medium flyash content sample is less as compared to the other two samples. In composites, the reinforcement in the composite supports the applied load which in result decreases

Please cite this article in press as: V.K. Sharma et al., Effect of flyash particles with aluminium melt on the wear of aluminium metal matrix composites, Eng. Sci. Tech., Int. J. (2017), http://dx.doi.org/10.1016/j.jestch.2017.08.004



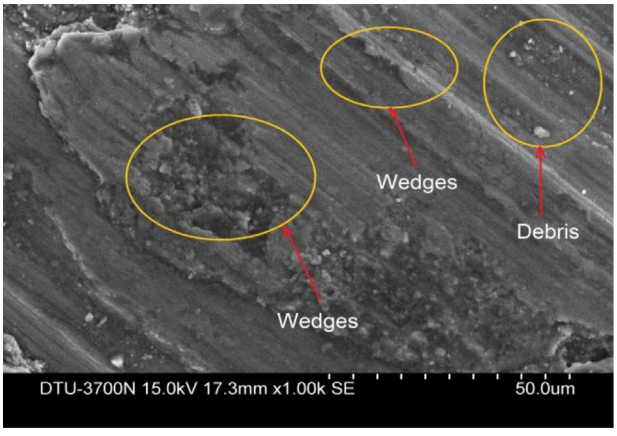
(c). SEM images of sample 3 (High flyash content)

Fig. 4(c). SEM images of sample 3 (High flyash content).



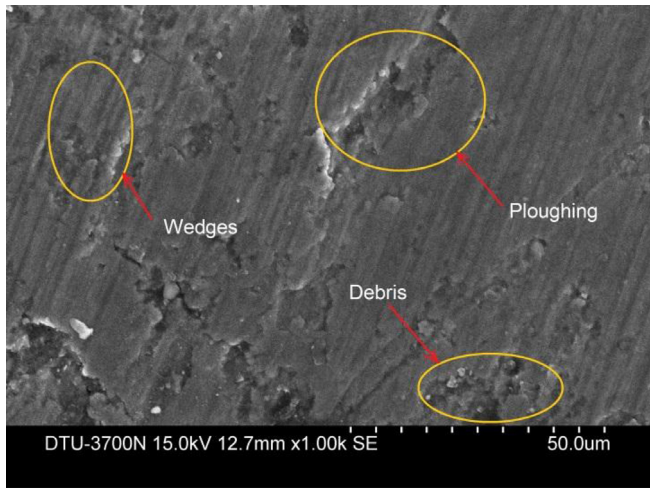
(a). SEM images of sample 2 (low flyash content) after weartest.

Fig. 5(a). SEM images of sample 2 (low flyash content) after wear test.



(b). SEM images of sample 2 (medium flyash content) afterwear test

Fig. 5(b). SEM images of sample 2 (medium flyash content) after wear test.



(c). SEM images of sample 3 (High flyash content) after wear test.

Fig. 5(c). SEM images of sample 3 (High flyash content) after wear test.

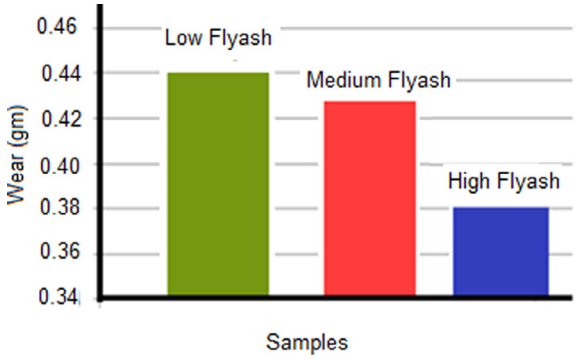


Fig. 6. Variation of Wear for low, medium and high content flyash specimens.

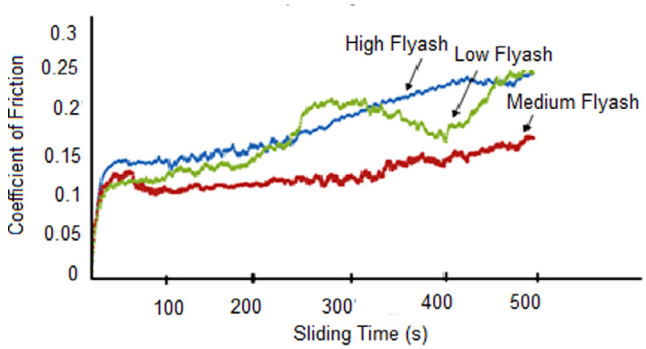


Fig. 7. Coefficient of frictional with sliding time.

the contact area between the pin and disc surface. Hence sample 2 resulted in less coefficient of friction as compared to sample 1 Lim et al. [6]. It can also be seen from Fig. 7 that as the flyash content further increases from 4% to 6%, the coefficient of friction increases with sliding time. A large number of flyash particles comes in contact with the counter disc and these particles start destructing itself, and thus increases the coefficient of friction.

Please cite this article in press as: V.K. Sharma et al., Effect of flyash particles with aluminium melt on the wear of aluminium metal matrix composites, Eng. Sci. Tech., Int. J. (2017), http://dx.doi.org/10.1016/j.jestch.2017.08.004

4. Conclusion

Aluminium flyash composites were prepared by using stir casting process with different weight % (2, 4 and 6%) of reinforcement particles. From the current research work following conclusions are drawn.

1. Flyash contents are successfully used to fabricate the aluminium matrix composite.
2. The optical microstructure of the composites indicates the distribution of the flyash components throughout the aluminium matrix.
3. The wear resistance of the fabricated composites increases with the increase in the flyash contents. The composites with high flyash contents resulted in 13.6% less wear as compared to low flyash content composites.
4. The sample with medium flyash content (4%) resulted in the lowest average coefficient of friction (0.12) and sample with high flyash contents (6%) shows the maximum average coefficient of friction (0.161). So the amount of flyash contents in the aluminium matrix is limited to 4%. More addition of flyash contents tends to increase the coefficient of friction between the tribopairs.

Acknowledgements

Authors would like to thank Mr. Rajesh Bohra technical staff of KOM/DOM lab of Delhi Technological University, Delhi, India.

References

[1] K.K. Alaneme, B.U. Odoni, Mechanical properties, wear and corrosion behavior of copper matrix composites reinforced with steel machining chips, Eng. Sci. Technol. An Int. J. 19 (2016) 15931599.
[2] K. Alaneme, K. Sanusi, Microstructural characteristics, mechanical and wear behaviour of aluminium matrix hybrid composites reinforced with alumina, rice husk ash and graphite, Eng. Sci. Technol. An Int. J. 18 (2015) 416422.
[3] A. Baghani, A. Bahmani, P. Davami, N. Varahram, M.O. Shabani, Numerical investigation of the effect of sprue base design on the flow pattern of aluminum gravity casting, Defect Diffus. Forum. 344 (2013) 4353.
[4] A. Faraji, A. Bahmani, M. Goodarzi, S. Seyedein, M. Shabani, Numerical and experimental investigations of weld pool geometry in GTA welding of pure aluminum, J. Cent. South Univ. 21 (2014) 2026.
[5] N. Kumar, R.K. Gautam, S. Mohan, In-situ development of ZrB2 particles and their effect on microstructure and mechanical properties of AA5052 metal-matrix composites, Mater. Des. 80 (2015) 129136.
[6] S.C. Lim, M. Gupta, L. Ren, J.K.M. Kwok, The tribological properties of Al–Cu/SiCp metal-matrix composites fabricated using the rheocasting technique, J. Mater. Process. Technol. 89 (90) (1999) 591596.
[7] A. Mazahery, M.O. Shabani, Experimental investigation on the aging response, hardness and total impact energy absorption of sr-modified heat-treatable cast automotive aluminum alloys, Trans. Indian Inst. Metals. 67 (2014) 753759.
[8] A. Mazahery, M.O. Shabani, Ascending order of enhancement in sliding wear behavior and tensile strength of the compocast aluminum matrix composites, Trans. Indian Inst. Metals. 66 (2013) 171176.
[9] A. Mazahery, M.O. Shabani, Tribological behaviour of semisolid – semisolid compocast Al – Si matrix composites reinforced with TiB 2 coated B 4 C particulates, Ceram. Int. 38 (2012) 18871895.
[10] K.S. Prakash, R.S. Moorthy, P.M. Gopal, V. Kavimani, Effect of reinforcement, compact pressure and hard ceramic coating on aluminium rock dust composite performance, Int. J. Refract Metal Hard Mater. 54 (2016) 223229.
[11] M.R. Rahimipour, A.A. Tofigh, A. Mazahery, M.O. Shabani, Strategic developments to improve the optimization performance with efficient optimum solution and produce high wear resistance aluminum–copper alloy matrix composites, Neural Comput. Applic. 24 (2013) 15311538.
[12] M.O. Shabani, A. Mazahery, A. Bahmani, P. Davami, N. Varahram, Solidification of A356 Al alloy: experimental study and modeling, Kovove Mater. 49 (2011) 253258.
[13] M.O. Shabani, A. Mazahery, Suppression of segregation, settling and agglomeration in mechanically processed composites fabricated by a semisolid agitation processes, Trans. Indian Inst. Metals. 66 (2013) 6570.
[14] M. Shabani, A. Mazahery, P. Davami, M. Razavi, Silicon morphology modelling during solidification process of A356 Al alloy, Int. J. Cast. Metals Res. 25 (2012) 5358.
[15] M.O. Shabani, A.A. Tofigh, F. Heydari, A. Mazahery, Superior tribological properties of particulate aluminum matrix nano composites, nanoscale and nanostructured materials and coatings, Protect. Metals Phys. Chem. Surf. 52 (2016) 244248.
[16] M. Shamsipour, Z. Pahlevani, M.O. Shabani, A. Mazahery, Squeeze casting of electromagnetically stirred aluminum matrix nanocomposites in semi-solid condition using hybrid algorithm optimized parameters, Kovove Mater. 55 (2017) 3343.
[17] M. Shamsipour, Z. Pahlevani, M.O. Shabani, A. Mazahery, Optimization of the EMS process parameters in compocasting of high-wear-resistant Al-nano-TiC composites, Appl. Phys. A 122 (2016) 114.
[18] P. Sharma, S. Sharma, D. Khanduja, Production and some properties of Si_3N_4 reinforced aluminium alloy composites, J. Asian Ceram. Soc. 3 (2015) 352359.
[19] P. Sharma, S. Sharma, D. Khanduja, A study on microstructure of aluminium matrix composites, J. Asian Ceram. Soc. 3 (2015) 240244.
[20] S. Shin, D. Bae, Deformation behavior of aluminum alloy matrix composites reinforced with few-layer grapheme, Compos. A Appl. Sci. Manuf. 78 (2015) 4247.
[21] A.A. Tofigh, M.O. Shabani, Efficient optimum solution for high strength Al alloys matrix composites, Ceram. Int. 39 (2013) 74837490.

Please cite this article in press as: V.K. Sharma et al., Effect of flyash particles with aluminium melt on the wear of aluminium metal matrix composites, Eng. Sci. Tech., Int. J. (2017), http://dx.doi.org/10.1016/j.jestch.2017.08.004

ResearchGate

See discussions, stats, and author profiles for this publication at: https://www.researchgate.net/publication/297909292

Application of Fuzzy Logic and Fuzzy Systems in Machining: A Literature Review

Conference Paper · March 2016

CITATIONS
0

READS
68

4 authors, including:



Dr Ranganath Muttanna Singari
Delhi Technological University, Formerly Delhi college of Engineering, Delhi, India
83 PUBLICATIONS **167** CITATIONS

SEE PROFILE

Some of the authors of this publication are also working on these related projects:



Dates Extended for Full manuscript Submission at ICAPIE 2016, Delhi, India View project



Working in the area of Tribology (Engine tribology, bearing design, tribology by nano particles and tubes.
View project

All content following this page was uploaded by Dr Ranganath Muttanna Singari on 30 July 2016.

The user has requested enhancement of the downloaded file.

Proceedings of the 2016 International Conference on Industrial Engineering and Operations Management
Kuala Lumpur, Malaysia, March 8-10, 2016

Effective Utilization of Fuzzy System and Fuzzy Logic in Manufacturing: A Review of Literature*

S. Singhal*, Ranganth M.S., R. Batra, S. Nanda
Department of Mechanical, Production &Industrial and Automobile Engineering Department
Delhi Technological University
New Delhi, India
suhm_snhl@hotmail.com

***Abstract*— Fuzzy Logic has found widespread use in medicinal sciences, behavioral sciences, engineering, businesses etc. due to ever increasing complexities in these systems at the core of which lies vagueness, uncertainty and imprecision in information. The proposition of fuzzy set theory especially Fuzzy Inference System (FIS) led to an explosion of its application in diverse fields including manufacturing owing to their ability to handle numeric and linguistic information in the same framework. This study focuses on use of FIS in widely varying manufacturing scenarios including injection molding, machining, decision making, cost optimization, etc. The emphasis is first laid down on a review of various fuzzy tools and their evolution and application in past two decades. It is then shifted to area specific application of FIS and its combination with neural networks.**

Keywords— fuzzy logic; fuzzy system; set membership; ANN; Taguchi method

I. INTRODUCTION

The history and foundations of Artificial Intelligence can be traced back to a conference in 1956 held in Dartmouth College where the term was originally coined. Since then it has emerged from being a mere theory to a concept with rampant application in intelligent computing systems nowadays. Zadeh's article on proving convexity of disjoint fuzzy sets in 1965 paved the way for their popularity and acceptability in the academia but still found very limited use in the industry. Fuzzy systems are applied to artificial intelligence for representing the knowledge of experts or acquired through learning process. Additionally, fuzzy systems provide a rich and robust method of building systems that include multiple conflicting, cooperating, and collaborating knowledge. It is a method specifically developed to incorporate uncertainty by processing information termed as grey (white for perfect information and black for complete absence of information) into a decision making model.

Essentially, fuzzy logic allows for considering reasoning that is approximate rather than precise by use of linguistic variables as both inputs and responses. Fuzzy based inference systems or FIS provide a much simplified platform where the development and analysis of models require reduced development time than other approaches. This has resulted in its widespread within the industry as well for a wide variety of applications. It considers variables to be included in a set based on their degrees of membership, rather than absolute membership. Instead of precision and accuracy, fuzzy logic carries along a level of tolerance for imprecision. Fuzzy logic attempts to mimic the human mind to effectively employ modes of reasoning that are approximate rather than exact. By allowing for the inclusion of imprecision in memberships, fuzzy logic allows for the detection of imprecise dependencies among concepts. The approach differs from the use of crisp sets in which an element is either a member of the set or not. Fuzzy sets, on the other hand, allow elements to be partially in a set. Each element is given a degree of membership in a set. This membership value can range from 0 (not an element of the set) to 1 (a member of the set). It is clear that if one only allowed the extreme membership values of 0 and 1, that this would actually be equivalent to crisp sets. A membership function is the relationship between the values of an element and its degree of membership in a set.

A fuzzy inference system (FIS) is a system that uses fuzzy set theory to map inputs to outputs (or responses). The most popular and widely used FIS are Mamdani and Sugeno types. They comprise of a fuzzification interface, a rule database, a decision making unit and defuzzification interface. The first two parts of the fuzzy inference process, fuzzifying the inputs and applying the fuzzy operator, are the same in both the types. The main difference lies in the fact that output membership functions in Sugeno type are either linear or constant. Although the Mamdani type system has gained widespread acceptance owing to it being intuitive and well suited to human input, Sugeno type systems are still considered a notch higher due to computational efficiency, suitability to mathematical analysis and guaranteed continuity of output surfaces.

This research focuses on application of these intelligent systems to manufacturing and attempts to find the reason behind its widespread acceptance beginning with small history of evolution of artificial intelligence and fuzzy logic. It then gives a clear picture regarding the background of the techniques prominently used and fuzzy logic as a whole. The study then clearly demarcates the application of FIS and fuzzy techniques in a variety of industries and research purposes.

II. Literature Review

A. History

Long back before the fuzzy logic had emerged, ancient Greek philosophy conceived the traditional notions of set membership and logic and later, fuzzy logic is proved to be a great alternative to these traditional notions. The efforts of Aristotle and the philosophers who preceded him are largely responsible for the success of mathematics. The postulation of the so-called "Laws of Thought" was the result of their efforts to develop a concise theory of logic, and later mathematics [1]. One of these laws is the "Law of the Excluded Middle" which states that every proposition must either be true or false. But when the first interpretation of this law was proposed by Parminedes (around 400 B.C.), strong objections emerged; one of these was a proposal by Heraclitus that things can be simultaneously True and not True. It was Plato who laid the foundation for what has become fuzzy logic, indicating that there could be a third region (beyond True and False) where these opposites "toppled about". Hegel, Marx, and Engels were among the modern philosophers of those times who echoed thoughts of Plato. The first attempts for formulation of a multi-valued logic were made around the end of the nineteenth century. But it was Pole Jan Lukasiewicz who first introduced a well-known system of multi-valued logic of Aristotle in the 1920s. In his system of logic, Lukasiewicz defined a third truth value other than true and false [2]. But in 1930s, some renowned mathematicians such as Brouwer, and von Neumann proposed the possibility of an infinite number of truth values.

B. Background

Lotfi A. Zadeh , a professor for computer science at the University of California in Berkeley, pioneered Fuzzy Logic in 1965 [3, 4, 5] to address the issues of application complexities arising due to nonlinearities, poorly defined dynamics, absence of apriori information, imprecision, uncertainties and vague description of the system [6]. He laid the foundation of fuzzy sets which he defined as 'a class of objects with a continuum of grades of membership' [3]. He made the use of some of the notions of set membership such as union, intersection, complement, relation, etc. in the same sense as they are used in set membership. At that time, his concept had to face a lot of criticisms, some of which were from his colleagues. Some mathematicians thought that the notions of fuzzy would encourage some sort of imprecise thinking while some believed 'fuzzification' is a kind of scientific permissiveness. Due to the above reasons, fuzzy logic developed slowly and its applications came into light after a long time. First industrial applications of fuzzy logic were seem in Europe in 1970s. Later, it became popular because of ease of its applications in decision making and data analysis.

In decision making problems, a robust performance evaluation method is a requisite process. In real world problems, these evaluation techniques can handle cases of subjectivity, fuzziness and imprecise information and the implementation of fuzzy sets theory can provide a more precise and optimized value in evaluation systems [7]. Several researchers have emulated the above approach through analytical hierarchy process (AHP), for example in personnel selection [8, 9] and shipping performance evaluation [10], where all the fuzzy sets were aggregated for evaluation.

C. Applications:Optimization of machining process

Researchers have attempted to apply methodology of fuzzy system in various areas of application. One of these is the optimization of machining with the application of fuzzy system. The implementation of fuzzy system proved to be highly helpful in case of very complex or highly nonlinear processes, in the absence of any simple mathematical model or the need of processing of expert knowledge. Tarng, Tseng and Chung (1997) used fuzzy set theory to develop a new pulse discriminator in EDM process. In EDM process, cutting performance indexes such as material removal rate (MRR) and surface roughness have strong relationship with the EDM discharge pulses. Hence it is very important to develop a pulse discriminator in order to classify various discharge pulses in EDM for optimizing of machining productivity. The fuzzy pulse discriminator (FPD) consisted of a fuzzifier, a knowledge base and an inference engine. In FPD, the EDM discharge pulses were classified based on the linguistic rules attained from the knowledge of experts and expressed mathematically through the fuzzy sets theory. Since the membership functions of FPD have a great influence on its classification performance, the relevant membership functions have been synthesized automatically with the application of a machine learning method. This method was based on a simulated annealing algorithm which is a heuristic search technique. This approach could classify EDM discharge pulses correctly and instantly under varying cutting conditions [11]. The aim of the work done by Tzeng and Chen (2006) was to develop a robust, versatile and high speed EDM technique. This aim was achieved by optimizing the machining precision and accuracy with the application fuzzy logic analysis incorporation with the Taguchi dynamic method. They employed a fuzzy logic system to study the association of machining precision with machining accuracy. The fuzzy system is composed of a fuzzifier, an inference system, a data base, a rule base and defuzzifier. They used ANOVA to determine the process parameters that significantly affect the MPCs and a confirmatory test of the calculated optimal process showed that targeted MPCs have improved [12]. Lin, Wang, Yang and Tarng applied the Taguchi method with fuzzy logic to improve the electrical discharge machining (EDM) process with multiple performance characteristics (MPCs) by transforming the optimization of these complicated MPCs into the optimization of a single multi-response performance index (MRPI). With considerations of the MPCs (electrode wear ratio (EWR) and material removal rate (MRR), the machining parameters (the workpiece polarity, pulse-on time, duty factor, open discharge voltage, discharge current and dielectric fluid) are optimized. The Taguchi method can optimize performance characteristics by adjusting the process parameters and increase the insensitivity of the performance of the system to sources of

variation. As a result, the Taguchi method has become a powerful tool in the design of experiment (DOE) methods. It uses a special orthogonal array design to study the entire parameter space preventing the conduction of a large number of experiments. A fuzzy reasoning of the MPCs has been carried out by the fuzzy logic unit. The fuzzy logic unit comprises a fuzzifer, membership functions, a fuzzy rule base, an inference engine, and a defuzzifer [13].

Ramanujan, Venkatesan, Saxena, Pandey, Harsha et al. attempted to combine the multi-responses of the dry turning operation into a single multi-performance index using principal component function based on fuzzy system as well as design of experiment based on Taguchi method. The aim of their work was to optimize the machining parameters during dry turning operation of Inconel 625 to minimize surface roughness and power consumption and maximize material removal rate. The entire machining parameter space is investigated using L9 orthogonal array. The fuzzy reasoning grades are evaluated and are optimized using the Taguchi method. A hybrid principal component analysis based on fuzzy syatem was employed because it takes into account all the principal components to obtain the multi-performance index and reduces error [14]. Hsu and Shu developed a realistic approach to work on imprecise output data observed during the measurements of the products quality. They introduced a general method which combined the vector of fuzzy numbers to produce the membership function of fuzzy eliminator of the Taguchi index for further process capability testing. The Taguchi index, also called the loss-based process capability index Cpm, was proposed by Hsiang and Taguchi (1985) to measure process capability, wherein the output process data is precise. Process capability index provides statistical measures to check whether a process binds to the specified manufacturing capability prerequisite. In this approach, Hsu and Shu proposed two fuzzy inference criteria, the critical value and the fuzzy P-value, to assess the manufacturing process capability based on Cpm. They applied the proposed methodology to the luminous intensity of LED sources data to check for its applicability [15].

Lin, Chung and Huang(2001) tried to improve the wire-EDM machining accuracy at corner parts without compromising with its cutting feed rate. He presented a new control strategy based on fuzzy logic to improve the cutting precision. With the application of fuzzy logic control, software implementation and incorporation of expert knowledge without any need for an explicit mathematical model can be done easily. The fuzzy rules are developed based on the physical characteristics and experimental data of the wire-EDM process and on the past experience of the operator. Using this approach, machining errors of corner parts are found to be reduced to less than 50% of those in normal machining, while the machining process time is increased not more than 10% of the normal value [16]. In finish turning operation, the interrelated machining parameters are present which make it is difficult to evaluate the total machining performance (TMP) including surface finish, tool-wear rate, dimensional accuracy, cutting power and chip breakability. Fang and Jawahir provided a new technique to evaluate each facet of the TMP in finish turning of steels. They established a machining reference database providing a fundamental and quantitative standard and a knowledge pool giving all the major factors influencing the TMP. The effects of these factors have been quantified with the application of fuzzy-set method. They proposed a series of fuzzy-set models to evaluate quantitative values of the TMP for any specific input conditions, encompassing work material properties, tool geometries, chipbreaker types and cutting conditions [17].

Çaydaş, Hasçalık and Ekici (2009) adopted an adaptive neuro-fuzzy inference system (ANFIS) model for predicting the average surface roughness and white layer thickness (WLT) in the wire-EDM process. ANFIS model is made by the fusion of fuzzy inference system (FIS) and artificial neural network (ANN) approaches as it uses the modeling function of FIS and the learning ability of ANN. It follows a hybrid learning algorithm which merges the gradient method with the least squares method to optimize the process parameters. The machining parameters which were input to the model are pulse duration, open circuit voltage, dielectric flushing pressure and wire feed rate. Fuzzy if-then rules of Sugeno type make the rule base of ANFIS. To predict the desired performance parameters, the authors performed normalization of measured performances using standard min-max normalization methodology, feature reduction using principal component analysis (PCA) and ANFIS tests using computer simulation. It was concluded that the proposed approach can be of great use for optimization of surface roughness and WLT in the wire-EDM process [Ref: An adaptive neuro-fuzzy inference system (ANFIS) model for wire-EDM]. Fuzzy logic coupled with artificial neural networks (ANN) has been widely utilized in many domains [18]. Kuo and Cohen (1998) proposed a self-organizing and self-adjusting fuzzy model (SOSAFM) which was based on the integration of these two technologies. They presented an online eatimation system which can be applied in the manufacturing control area. In this approach, Kohonen's feature mapping is employed to divide the inputs and outputs to the system and error back propagation (EBP)-type learning algorithm is used to improve training parameters of ANNs. Evaluation of the proposed methods was done by conducting some physical experiments for manufacturing process control. SOSAFM is found to be better than the multiple regression and artificial neural network both with respect to speed and accuracy for the purpose of multi-sensor integration [19]. For predicting the surface roughness of the workpiece after the completion of end milling process, Lo (2003) employed an adaptive-network based fuzzy inference system (ANFIS). Considering that spindle speed, feed rate and depth of cut are the three parameters of milling process that have a major influence on the surface roughness, these performance parameters were analyzed. A comparison between the triangular and trapezoidal membership functions was made during the training process of ANFIS to examine the accuracy in predicting the surface roughness by these two membership functions. Results showed very satisfactory predicting accuracy when either of the membership functions is used while the prediction accuracy of ANFIS has reached as high as 96% when a triangular membership function is employed [20].

Many researchers adopted grey relational analysis based on the grey system theory to solve the complicated interrelationships among the multiple responses. In their paper, Lin and Lin also attempted the application of grey-fuzzy logic based on orthogonal array for the optimization of electrical discharge machining (EDM) process with MPCs. The effects of machining parameters (pulse on time, duty factor and discharge current) to the MPCs (EWR, MRR and surface roughness) were studied and analyzed. The experimental plan was designed based on L9 orthogonal array. Grey relational coefficient (GRC) for each process response is calculated to analyze the degree of relation of the multiple responses. Fuzzy reasoning of the MPCs is done using fuzzy logic and the experimental data was analyzed using the technique of analysis of variance (ANOVA). It was concluded that these approaches could greatly improve the process responses such in the EDM process [21]. Lin, Lin and Ko (2002) applied the grey relational analysis based on an orthogonal array and fuzzy-based Taguchi method for improving MPCs in the electrical discharge machining (EDM) process. The influence of the machining parameters (pulse on time, duty factor, and discharge current) on the MPCs (electrode wear ratio, material removal rate, and surface roughness) is investigated. The entire machining parameter space is investigated using L9 orthogonal array. The grey relational analysis method comprises of grey relational generation, calculation of grey relational coefficient and computation of grey relational grade to convert the optimization of complicated MPCs into optimization of a single grey relational grade. In fuzzy-based Taguchi method, S/N ratio corresponding to each MPC is evaluated and fuzzified and fuzzy reasoning grade is obtained by using the max–min fuzzy inference and centroid defuzzification methods to convert the optimization of complicated MPCs into optimization of a single fuzzy reasoning grade. Both approaches can produce very similar experimental results but the calculation using the grey relational analysis is much simpler than that the fuzzy logic analysis [22].

D. Applications:Selection of performance parameters

Machining data play a vital role in the efficient utilization of machine tools and thus significantly influences the overall manufacturing costs. Machining Data Handbook [23], published by Metcut Research Associates, is a vast information source that compiles machining data for different combinations of tool-work. Baradie (1980) suggested the need and importance of computerization of the Machining data Handbook which would provide an easy access to an immense collection of machining data and lead to the integrated automation of the manufacturing process. He demonstrated the implementation of a fuzzy logic model for metal cutting operation to develop a computerized machining database system that could be a great aid to the process planner for establishment of the strategy for selecting machining data for a specific machining process [24]. In Machinability data hand book [23], one may find different tool materials possible for each work material and hardness. So it proves to be an ample way for selecting cutting parameters in machining processes. But in some cases, uncertainty may occur if more than one choice is applicable for a particular cutting condition. To overcome this problem, Hashmi, Baradie and Ryan (1998) applied fuzzy logic principles for selection process. The material hardness and the cutting speed are considered the fuzzy input and output variables respectively. The fuzzy if-else rules are synthesized based on the information extracted from the used machine tool. The triangular shaped membership functions are employed for both input and output. He compared the cutting speed values predicted using the fuzzy logic model with the speed values recommended by the Machinability Data Handbook and the results showed a good correlation between two speed values [25].

Balazinski, Bellerose and Czogala (1993) developed a fuzzy decision support system (FDSS) based on the compositional rule of inference (CRI). CRI preserves a maximum amount of information contained in the rules and the observations. It is based on the inference method of approximate reasoning applied for handling imprecise information. They attempted the application of FDSS to the choice and modification of cutting parameters considering metal cutting processes to be stochastic, nonlinear and ill-defined. The reasonable results showed that the proposed method would be appropriate for such kinds of decision problems [26]. The parameter selection of the EDM is an obscure problem which is difficult to model as it depends on heuristics and is based on experts' experiences. Fuzzy set theory can play a major role in such problems and fuzzy logic can be employed to emulate the performance of the expert and provide decision making abilities in the presence of certain degree of vagueness. Following this approach, Yilmaz, Eyercioglu and Gindy (2006) developed a user-friendly intelligent system based on fuzzy logic to make the selection of EDM parameters easy and accurate. A compact selection method is used based on expert rules which are evaluated by the fuzzy set theory. A fuzzy model has been developed which uses fuzzy expert rules, triangular membership functions for fuzzification and centroid area method for defuzzification processes. A system has been implemented based on the proposed model which helps an unskilled user to select important parameters according to the specific operation [27].

CONCLUSION

This paper is based on the state of the art review of the application of fuzzy logic and fuzzy system in various sectors of manufacturing, specifically in machining processes. First, a brief definition of fuzzy logic and fuzzy inference system is provided. It is followed by a description on origin of the notion of fuzzy logic and stating the efforts of many brilliant minds of their times who were responsible for the success of fuzzy logic. This paper includes the work done in the field of manufacturing based on fuzzy system. From the literature, it was concluded that fuzzy logic has a wide areas of application where fuzzy, imprecise and vague information is available.

REFERENCES

[1] S. Korner, "Laws of thought," Encyclopedia of Philosophy, Vol. 4, MacMillan, NY: 1967, pp. 414-417

[2] C. Lejewski, "Jan Lukasiewicz," Encyclopedia of Philosophy, Vol. 5, MacMillan, NY: 1967, pp. 104-107

[3] L.A. Zadeh, "Fuzzy Sets," Information and Control, 1965

[4] L.A. Zadeh, "Outline of A New Approach to the Analysis of Complex Systems and Decision Processes," 1973.

[5] L.A. Zadeh, "Fuzzy algorithms," Info. & Ctl., Vol. 12, pp. 94-102, 1968,.

[6] M. F. Azeem, "Fuzzy inference system– theory and applications", InTech, Croatia, April, 2012, ISBN 978-953-51-0525-1.

[7] D. Zhou, J. Ma, E. Turban, N. Bolloju, "A fuzzy set approach to the evaluation of journal grades", Fuzzy Sets and Systems, Volume 131, Issue 1, Pages 63-74, 1 October 2002.

[8] Saaty, T. (1995). The Analytic Hierarchy Process: RWS publications Pittsburgh, PA.;

[9] F.A. Taylor III, A.F. Ketcham, D. Hoffman, "Personnel evaluation with AHP", Management Decision, Vol. 36 Iss: 10, pp.679 – 685, 1998

[10] T. Chou, & G. Liang, "Application of a fuzzy multi-criteria decision-making model for shipping company performance evaluation", Maritime Policy & Management, 28(4), pp. 375-392, 2001.

[11] Y. S. Tarng, C. M. Tseng and L. K. Chung, "A Fuzzy Pulse Discriminating System For Electrical Discharge Machining", International Journal of Machine Tools and Manufacture, Vol. 37, No. 4, pp. 511-522, 1997.

[12] Y. F. Tzeng and F. C. Chen, "Multi-objective optimization of high speed electrical discharge machining process using a Taguchi fuzzy-based approach", Materials and Design, Vol. 28, pp. 1159 – 1168, 2007.

[13] J. L. Lin, K. S.Wang, B. H. Yan, and Y. S. Tarng, ''Op- timization of the electrical discharge machining process based on the Taguchi method with fuzzy logics'' Journal of Materials Processing Technology,Vol.102, pp.48-55, 2000.

[14] R. Ramanujam, K. Venkatesan, Vimal Saxena, Rachit Pandey, T. Harsha, Gurusharan Kumar, "Optimization of Machining Parameters Using Fuzzy Based Principal Component Analysis during dry turning operation of Inconel 625 – A hybrid approach", Procedia Engineering, Volume 97, pp. 668-676, 2014.

[15] Bi-Min Hsu, Ming-Hung Shu, "Fuzzy inference to assess manufacturing process capability with imprecise data", European Journal of Operational Research, Volume 186, Issue 2, pp. 652-670, 16 April 2008.

[16] C. T. Lin, I. F. Chung, and S. Y. Huang, "Improvement of machining accuracy by fuzzy logic at corner parts for wire-EDM", Fuzzy Sets and Systems, Vol. 122, pp. 499 – 511, 2001.

[17] X. D. Fang and I. S. Jawahir, "Predicting total machining performance in finish turning using integrated fuzzy-set models of the machinability parameters", International Journal of Production Research, Vol. 32, Issue 4, pp. 833 – 849, 1994.

[18] U. Çaydaş, A. Hasçalık, S. Ekici, "An adaptive neuro-fuzzy inference system (ANFIS) model for wire-EDM", Expert Systems with Applications, Volume 36, Issue 3, Part 2, pp. 6135-6139, April 2009.

[19] R.J. Kuo, P.H. Cohen, "Manufacturing process control through integration of neural networks and fuzzy model", Fuzzy Sets and Systems, Volume 98, Issue 1, pp. 15-31, 16 August 1998.

[20] Ship-Peng Lo, "An adaptive-network based fuzzy inference system for prediction of workpiece surface roughness in end milling", Journal of Materials Processing Technology, Volume 142, Issue 3, pp. 665-675, 10 December 2003.

[21] J. L. Lin and C.L. Lin, "The use of grey-fuzzy logic for the optimization of the manufacturing process", Journal of Materials Processing Technology, pp. 9 – 14, November 2005.

[22] C. L. Lin, J. L. Lin, and T. C. Ko, "Optimisation of the EDM Process Based on the Orthogonal Array with Fuzzy Logic and Grey Relational Analysis Method", The International Journal of Advanced Manufacturing Technology, Volume 19, Issue 4, pp. 271 - 277, February 2002.

[23] Metcut Research Associates Inc., Machining Data Handbook, 3rd edn, Vols I and 2. Cincinnati, 1980.

[24] M. A. El-Baradie, "A fuzzy logic model for machining data selection", International Journal of Machine Tools and Manufacture, Vol. 37, No. 9, pp. 1353 – 1372, 1997.

[25] K. Hashmi, M.A El-Baradie, and M. Ryan, "Fuzzy-logic based intelligent selection of machining parameters", Journal of Materials Processing Technology, Vol. 94, Issues 2–3, pp 94–111, September 1999.

[26] M. Balazinski, M. Bellerose, E. Czogala, "Application of fuzzy logic techniques to the selection of cutting parameters in machining processes", Fuzzy Sets and Systems, Volume 63, Issue 3, pp. 307-317, 10 May 1994

[27] O. Yilmaz, O. Eyercioglu , and N. N. Z. Gindy, "A user-friendly fuzzy-based system for the selection of electro discharge machining process parameters", Journal of Materials Processing Technology, Vol. 173, No. 3, pp. 363 - 371, March 2006.

View publication stats

Clean Techn Environ Policy
DOI 10.1007/s10098-017-1404-3

ORIGINAL PAPER

Energy, exergy, environment and economic analyses and optimization of two-stage absorption–compression combined refrigeration system

Manoj Dixit[1,3] · Akhilesh Arora[2] · S. C. Kaushik[1]

Received: 26 October 2016 / Accepted: 28 July 2017
© Springer-Verlag GmbH Germany 2017

Abstract In the present paper, integration of a two-stage absorption refrigeration system with a compression refrigeration system is proposed for utilizing low-temperature heat and reducing electric energy consumption. The proposed system is analyzed and compared with vapor compression system from the viewpoint of energy, exergy, environment and economics. The proposed system reduces the electricity consumption by 89.3% and CO_2 emission from 112.6 to 12.1 ton/year. The size and cost of the system are determined by designing the heat exchangers. The optimization is also performed with the objective of minimizing the annual cost of plant operation which includes fuel exergy cost, initial investment and maintenance cost and environmental damage cost due to CO_2 emission. The annual cost of its operation is 21.6% less than equivalent vapor compression refrigeration system which is further reduced by 18.2% through system optimization.

Keywords Absorption · Cost · Environment · Exergy · Optimization · Refrigeration

List of symbols

A	Area (m^2)
c_{CO_2}	Cost of unit carbon dioxide emission ($/ton)
c_{el}	Cost of unit electricity ($/kWh)
$\dot{C}_{env}$	Annual environment damage cost ($/year)
$\dot{C}_{op}$	Annual operational cost ($/year)
$\dot{C}_{plant}$	Annual cost of plant operation ($/year)
COP	Coefficient of performance
CRF	Capital recovery factor
$\dot{E}$	Exergy flow rate (kW)
$\dot{E}D$	Rate of exergy destruction (kW)
h	Specific enthalpy (kJ/kg)
HP	High pressure
HPA	High-pressure absorber
HPG	High-pressure generator
HPSTV	High-pressure solution throttle valve
i_r	Rate of interest (%)
LMTD	Log mean temperature difference
LP	Low pressure
LPA	Low-pressure absorber
LPG	Low-pressure generator
LPSTV	Low-pressure solution throttle valve
LiBr	Lithium bromide
$\dot{m}$	Mass flow rate (kg/s)
m_{CO_2}	Annual emission of carbon dioxide (ton)
n	Life span of the refrigeration plant
p	Pressure (kPa)
PR	Pressure ratio
$\dot{Q}$	Heat transfer rate (kW)
ref	Refrigerant
RTV	Refrigerant throttle valve
s	Specific entropy (kJ/kg/K)
SCR	Solution circulation ratio
STV	Solution throttle valve
SHE	Solution heat exchanger
T	Temperature (°C or K)
$T_{cond,VAR}$	Absorption section condenser temperature (°C)

✉ Manoj Dixit
mandixdtu@gmail.com

[1] Centre for Energy Studies, Indian Institute of Technology, New Delhi 110016, India

[2] Mechanical Engineering Department, Delhi Technological University, Delhi 110042, India

[3] Mechanical Engineering Department, Faculty of Engineering, Dayalbagh Educational Institute, Agra 282005, India

Published online: 03 August 2017

$T_{\text{cond,VCR}}$	Compression section condenser temperature (°C)
TSACCR	Two-stage absorption–compression combined refrigeration
t_{op}	Annual hours of plant operation (h)
VAR	Vapor absorption refrigeration
VCR	Vapor compression refrigeration
$\dot{W}$	Work transfer rate (kW)
x	Concentration of lithium bromide in solution
$\dot{Z}_{\text{CI}}$	Annual levelized capital investment cost ($/year)
$\dot{Z}_{\text{CI \& OM}}$	Annual levelized capital investment plus operation maintenance cost ($/year)
$\dot{Z}_{\text{OM}}$	Annual levelized operation maintenance cost ($/year)

Greek letters

ϵ	Effectiveness
η	Efficiency
η_{ex}	Exergetic efficiency
λ	Carbon dioxide emission factor (kg/kWh)
ϕ	Maintenance cost factor

Subscripts

0	Represents dead state
1, 2, 3…	State points
cond	Condenser
cc	Cascade condenser
comp	Compressor
el	Electricity
evap	Evaporator
gen	Generator
HPG	High-pressure generator
HPP	High-pressure pump
HX	Heat exchanger
in	Inlet
LPG	Low-pressure generator
LPP	Low-pressure pump
out	Outlet
p	Pump
ref	Refrigerant
SHE	Solution heat exchanger

Introduction

The energy and environmental issues associated with conventional vapor compression refrigeration (VCR) systems have paved the way for vapor absorption refrigeration (VAR) systems primarily because of latter's ability to harness renewable energy and recover waste heat without damaging the environment. However, on the performance front VAR systems lag far behind compression systems and therefore integration of these two cooling technologies is looked upon as a potential alternative. This allows the retention of merits and at the same time rejection of shortcomings of both VAR and VCR technologies. The schematic diagrams and working of single-stage VCR system are described by Reddy et al. (2012) and VAR system by Kaushik and Arora (2009).

There are number of research studies on absorption–compression combined refrigeration systems. Garimella et al. (2011) proposed a novel absorption–compression cascade cycle for providing cooling at 5 °C (for space conditioning and low heat flux applications) and −40 °C (for high heat flux applications) for ship applications. Cimsit and Ozturk (2012) reported that absorption–compression cascade system consumes 48–51% less electricity than consumed by equivalent VCR system. Wang et al. (2012) found that solar-assisted absorption–compression cascade system requires 50% less electric power as compared to VCR system. Seyfouri and Ameri (2012) analyzed various configurations of absorption–compression integrated system powered by microturbine. The compression section was operated directly by microturbine, whereas the absorption section was powered by its waste heat.

The exergy-based analysis of VAR systems integrated with traditional VCR systems is reported by many researchers. Colorado and Velazquez (2013) carried out the exergy analysis of absorption–compression cascade refrigeration system in which single-effect VAR system is cascaded with single-stage VCR system. Jain et al. (2013) carried out the first and second law-based thermodynamic analysis of absorption–compression cascade refrigeration system and compared the same with the conventional VCR system. They found that their system consumed 61% less electricity as compared to traditional VCR system; however, its exergetic efficiency was found to decrease to half of that for an equivalent VCR system. Patel et al. (2017) conceptualized and analyzed a new absorption–compression cascade system of 1850 kW cooling capacity for industrial cooling. In the new system, two-stage VCR cycle with flash intercooler was cascaded with single-stage absorption cycle. LiBr–H_2O was the working pair for absorption cycle, while ammonia was the refrigerant for the two-stage compression cycle. The overall COP and exergetic efficiency of the system was found to be 0.45 and 53.59% for evaporator temperature of −45 °C, sink temperature of 40 °C and generator temperature of 90 °C. It is found in the literature that exergy-based studies of absorption–compression combined refrigeration systems are scant and are limited to single-effect configurations only.

In most of the studies, single-effect configuration of VAR is integrated with VCR systems and it is to be noted that the commercially available single- and double-effect

VAR systems require heat source of temperature greater than 100 °C (Medrano et al. 2001). Therefore, a lot of thermal energy which is available below 100 °C from sources like solar, geothermal, industrial waste heat remains unutilized and gets wasted. A two-stage VAR system promises the utilization of low-temperature heat sources between 60 and 80 °C (Herold et al. 1996). Also, from the viewpoint of utilization of solar energy using low-cost flat-plate collectors, Kim and Machielsen (2002) recommended the use of double-stage absorption chiller. The efficiency of solar collectors increases when it operates at low temperature; therefore, higher global efficiency of the solar absorption cooling system can be obtained by double-stage cycle in comparison with single-stage cycles (Izquierdo 2004).

Arivazhagan et al. (2005) carried out theoretical study on half-effect (two-stage) R134a–DMAC absorption refrigeration system with low-temperature heat sources for cold storages. For the baseline system, the COP varied from 0.35 to 0.46, whereas the second law efficiency was found to vary between 28 and 44%. Arivazhagan et al. (2006) experimentally investigated a half-effect VAR cycle using R134a–DMAC pair. The performance of the half-effect VAR cycle was assessed in terms of COP, exergetic efficiency and degassing range.

Domínguez-Inzunza et al. (2014) studied the performance of single-effect, half-effect and double-effect in series, double-effect inverse and triple-effect absorption cooling systems operating with ammonia–lithium nitrate. The COP obtained was 0.3 for half-effect systems at the lowest evaporator and generator temperatures. Crepinsek et al. (2009) examined the performance of single-effect and half-effect absorption cycles for refrigeration temperatures below 0 °C on the basis of coefficient of performance and circulation ratio.

Izquierdo et al. (2005) carried out exergetic analysis of a double-stage LiBr–H_2O absorption cycle driven by solar energy from flat-plate solar collectors. The system attained COP of 0.37 for the condensation temperature of 50 °C, and the required generation temperature was about 80 °C. Gebreslassie et al. (2010) performed exergy analysis of half-effect, single-effect, double-effect and triple-effect LiBr–H_2O absorption cycles taking into account only unavoidable exergy destruction. Gomri (2010) performed thermodynamic analysis of a solar-driven 10 kW two-stage absorption cooling system based on the principles of energy and exergy. Arora et al. (2016) computed the optimum parameters of half-effect LiBr–H_2O absorption refrigeration system for various operating conditions on the basis of energy and exergy analyses.

The concepts of thermoeconomics have been applied by many researchers for the evaluation and optimization of various energy conversion systems in general and refrigeration systems in particular. Misra et al. (2003, 2005) carried out thermoeconomic optimization of single-effect and series flow double-effect LiBr–H_2O absorption refrigeration systems. Garousi Farshi et al. (2013) analyzed series, parallel and reversed flow double-effect absorption refrigeration systems from the viewpoint of exergoeconomics. So far only energy and exergy analyses of two-stage VAR systems have been carried out but thermoeconomic analysis which is quite essential for their practical application is missing.

Therefore, integration of two-stage VAR system with VCR system for the utilization of low-temperature heat is proposed in the present study. The comprehensive energy and exergy analysis of two-stage absorption–compression combined refrigeration (TSACCR) system is carried out. Thermoeconomic analysis is also performed. The design of heat exchangers is done to estimate the size and cost of the system. The penalty cost of carbon dioxide emission is also determined through environmental analysis for the cost estimation purpose. In addition to this, the paper compares the two-stage absorption–compression combined refrigeration system with equivalent VCR system from the viewpoint of energy, exergy, economics and environment. Finally, system optimization is carried out to further improve the performance and cost of the system.

System description

The two-stage absorption–compression combined refrigeration system is shown in Fig. 1. It consists of absorption section (two-stage vapor absorption refrigeration system) and compression section (vapor compression refrigeration system) which are thermally coupled through cascade condenser. The cascade condenser is a heat exchanger which allows heat transfer from compression section to absorption section.

The absorption section comprises of evaporator (EVAPORATOR-VAR), low-pressure absorber (LPA), high-pressure absorber (HPA), low-pressure generator (LPG), high-pressure generator (HPG), condenser, low-pressure solution heat exchanger (LPSHE), high-pressure solution heat exchanger (HPSHE), low and high-pressure pumps (LPP and HPP), high-pressure and low-pressure solution throttle valve (HPSTV and LPSTV) and refrigerant throttle valve (RTV-2). The condenser and HPG operate at same pressure which is the highest system pressure. The LPG and HPA operate at an intermediate pressure, and the LPA and evaporator operate at same pressure which is the lowest pressure in the absorption section. The refrigerant, water, is circulated through the evaporator, cascade condenser, LPA, LPG, HPA, HPG and condenser. After water vapor has condensed in the condenser, it returns to the

evaporator through refrigerant throttle valve (RTV-2). However, the absorbent lithium bromide aqueous solution is circulated within two separate stages, i.e., a low-pressure (LP) stage between the LPA and the LPG, and a high-pressure (HP) stage between the HPA and the HPG. The compression section is nothing but a typical vapor compression refrigeration cycle which rejects its condenser heat to the absorption section through cascade condenser. The external water to be cooled first enters evaporator of absorption section and then into compression section evaporator.

The major purpose of combining the absorption refrigeration system and compression refrigeration system is to bring down the electrical energy consumption of compressor of VCR system. There are various ways of combining absorption refrigeration and compression refrigeration systems like series combination (cascading) and parallel combination. In series combination, compression section rejects thermal load to the absorption section through cascade condenser. The power consumption is reduced in the compressor of the compression section due to lower temperature at compressor exit as compared to equivalent VCR system.

In parallel combination, the water is successively cooled in the evaporators of absorption section and compression section. The power consumption is reduced in the compressor of the compression section as half of the cooling duty is shared by the absorption section. The present system offers the advantages of both series and parallel configurations by combining absorption refrigeration system and compression refrigeration system in series and parallel simultaneously.

Mathematical modeling

The mathematical modeling of TSACCR system incorporates the thermodynamic model as well as economic model of the system. Engineering Equation Solver (EES) (Klein and Alvarado 2005) is used to do mathematical modeling. It is based on certain assumptions which are given below.

Assumptions

For the analysis of the two-stage absorption–compression combined refrigeration system, following assumptions are made:

- All the components of the system operate under steady-state conditions.
- Pressure losses in different components and connecting pipelines are neglected.
- The potential, kinetic and chemical exergies are neglected.
- The solutions are at equilibrium at the exit of the generators and the absorbers.
- Refrigerant is saturated at the exit of evaporators and condensers.
- The system operates far away from crystallization limit.
- Water is used for heating, cooling and chilling operations.

Energetic and exergetic analysis

For the energy and exergy analysis of the two-stage absorption–compression combined refrigeration system, the principles of mass and material conservation, energy balance and exergy balance are applied to each component of the system. Each component is treated as a control volume with inlet and outlet streams, heat transfer and work interactions. The application of above-mentioned principles is presented in the following equations.

$$\sum \dot{m}_{\mathrm{i}} - \sum \dot{m}_{\mathrm{o}} = 0 \tag{1}$$

$$\sum \dot{m}_{\mathrm{i}} x_{\mathrm{i}} - \sum \dot{m}_{\mathrm{o}} x_{\mathrm{o}} = 0 \tag{2}$$

$$\sum \dot{Q} - \sum \dot{W} = \sum \dot{m}_{\mathrm{o}} h_{\mathrm{o}} - \sum \dot{m}_{\mathrm{i}} h_{\mathrm{i}} \tag{3}$$

where $\dot{Q}$ and $\dot{W}$ are heat transfer rates and work transfer rates crossing the system boundary, respectively.

The first law-based performance of the two-stage absorption–compression combined refrigeration system is expressed in terms of coefficient of performance (COP):

$$\mathrm{COP} = \frac{\dot{Q}_{\mathrm{evap}}}{\dot{Q}_{\mathrm{HPG}} + \dot{Q}_{\mathrm{LPG}} + \dot{W}_{\mathrm{HPP}} + \dot{W}_{\mathrm{LPP}} + \dot{W}_{\mathrm{comp}}} \tag{4}$$

where $\dot{Q}_{\mathrm{evap}}$ is the cooling output of both the evaporators, $\dot{Q}_{\mathrm{HPG}}$ and $\dot{Q}_{\mathrm{LPG}}$ are heat input to HPG and LPG, respectively, and $\dot{W}_{\mathrm{HPP}}$, $\dot{W}_{\mathrm{LPP}}$ and $\dot{W}_{\mathrm{comp}}$ are the electrical power consumed by high-pressure side pump, low-pressure side pump and compressor, respectively.

The exergy is defined as the maximum possible reversible work that can be obtained by bringing the state of the system to equilibrium with that of environment. The exergy flow rate of stream at each operating point, considering only physical component, is calculated using Eq. (5)

$$\dot{E} = \dot{m}[(h - h_0) - T_0(s - s_0)]. \tag{5}$$

The rate of exergy destruction in a component for steady-state process is expressed as:

$$\dot{\mathrm{ED}} = \sum \dot{E}_{\mathrm{in}} - \sum \dot{E}_{\mathrm{out}} + \sum \dot{Q}\left(1 - {}^{T_0}/_{T}\right) - \sum \dot{W}. \tag{6}$$

Here, $\dot{E}_{in}$ is the exergy of stream entering the component and $\dot{E}_{out}$ is the exergy of stream exiting the component.

The exergetic efficiency for the system is given by Eq. (7)

$$\eta_{ex} = 1 - \frac{\sum \dot{E}D}{\dot{E}_{19} - \dot{E}_{20} + \dot{E}_{25} - \dot{E}_{26} + \dot{W}_{HPP} + \dot{W}_{LPP} + \dot{W}_{comp}}. \quad (7)$$

Economic analysis

The economic analysis involves the estimation of initial investment cost and operational cost which includes the cost of fuel (electricity and heat). Heat exchangers, compressors and pumps are the main components of the refrigeration system. In order to calculate the initial cost of heat exchangers, their area is required to be calculated.

Design of heat exchangers

The generators, absorbers, condenser, evaporator and cascade condenser are designed as shell and tube heat exchangers (Bakhtiar et al. 2011), whereas HPSHE and LPSHE are considered as single pass annular heat exchangers (Florides et al. 2003). The material for all heat exchangers is copper (Florides et al. 2003).

The required heat exchanger surface area (A) for given thermal load ($\dot{Q}$) is calculated using Eq. (8)

$$\dot{Q} = U \cdot A \cdot \text{LMTD}. \quad (8)$$

The overall heat transfer coefficient (U) is determined by Eq. (9)

$$U = \left[\left(\frac{D_o}{D_i}\right)\left(\frac{1}{h_i}\right) + \left(\frac{D_o}{D_i}\right)F_i + \left(\frac{D_o}{2k}\right)\ln\left(\frac{D_o}{D_i}\right) + F_o + \left(\frac{1}{h_o}\right)\right]^{-1}. \quad (9)$$

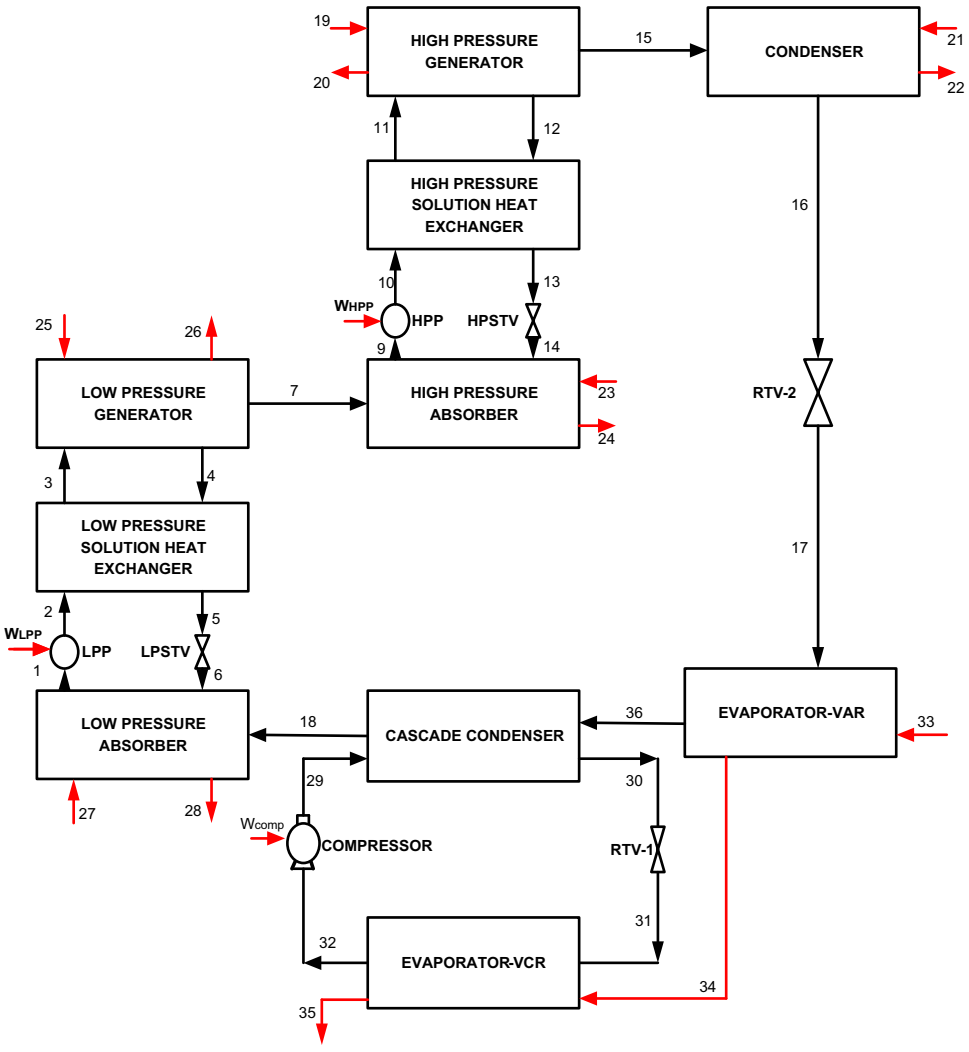


Fig. 1 Schematic diagram of two-stage absorption–compression combined refrigeration system

LMTD is the logarithmic mean temperature difference of a heat exchanger. The fouling factors for both inside (F_i) and outside surfaces (F_o) of tube are taken as 0.09 m^2/K/kW (Bakhtiar et al. 2011). The inside diameter (D_i) and outside diameter (D_o) of tube for generators, absorbers, condenser, cascade condenser and evaporator are 13.56 and 14.96 mm, respectively. The length of tube for these components is considered as 0.3 m. In case of solution heat exchangers, the inside and outside diameters of external pipe are 13.56 and 14.96 mm while that of internal pipe are 8.80 and 9.50 mm, respectively.

Capital investment and operation maintenance cost

For heat exchanger, the initial capital investment cost is the function of its area (A) and is given as (Kizilkan et al. 2007)

$$Z_{HX} = 516.621A + 268.45. \tag{10}$$

The cost function for pump and compressor is (Sayyaadi and Nejatolahi 2011)

$$Z_p = 308.9\dot{W}^{0.25} \tag{11}$$

$$Z_{comp} = \left(\frac{573\dot{m}_{ref}}{0.8996 - \eta_{comp}}\right) PR_{comp} \ln(PR_{comp}). \tag{12}$$

Here, PR_{comp} is the pressure ratio across compressor and $\dot{m}_{ref}$ is the mass flow rate of refrigerant through it. The isentropic efficiency of compressor (η_{comp}) is (Sayyaadi and Nejatolahi 2011):

$$\eta_{comp} = 0.85 - 0.046667\, PR_{comp}. \tag{13}$$

The initial cost of other items including solution throttle valves, refrigerant throttle valves, connecting pipes, refrigerant etc., is quite less as compared to cost of other items (Gebreslassie et al. 2012). So, it is considered as 1% of the total capital investment cost of the system in the present case.

The annual capital investment and operation maintenance cost for a component is given by the following equation

$$\dot{Z}_{CI\,\&\,OM} = \dot{Z}_{CI} + \dot{Z}_{OM}. \tag{14}$$

Here, $\dot{Z}_{CI}$ is the annual levelized capital investment and $\dot{Z}_{OM}$ is the annual levelized operation maintenance cost, given as (Bejan et al. 1996)

$$\dot{Z}_{CI} = CRF \cdot Z_k \tag{15}$$

$$\dot{Z}_{OM} = \emptyset \cdot \dot{Z}_{CI}. \tag{16}$$

Here, Z_k is the initial capital investment of an equipment ($), $\emptyset$ is a factor which takes into account the cost of maintenance and its value is taken as 0.06 (Singh and Kaushik 2013) and the CRF, the capital recovery factor for interest rate of i_r and life span of n years is given by Eq. (17)

$$CRF = \frac{i_r(1+i_r)^n}{(1+i_r)^n - 1}. \tag{17}$$

Operational cost

The operational cost of the system is the cost of exergy associated with heat input ($\dot{E}_{heat}$) and electrical energy supply ($\dot{W}_{el}$). It is expressed as:

$$\dot{C}_{op} = \left(c_{el}\dot{W}_{el} + c_{heat}\dot{E}_{heat}\right)t_{op}. \tag{18}$$

Here, c_{el} is the cost of unit electrical exergy input and its value is taken as 0.075 $/kWh (Sayyaadi and Nejatolahi 2011) and c_{heat} is the unit cost of heat exergy input and it is assumed that heat is available free of cost and t_{op} is the annual hours of operation of the refrigeration plant.

Environmental analysis

The emission of carbon dioxide during the generation of electricity from fossil fuels causes serious damage to environment. The environmental damage cost is given as (Aminyavari et al. 2014):

$$\dot{C}_{env} = (m_{CO_2}/1000)c_{CO_2}. \tag{19}$$

Here, c_{CO_2} is the unit penalty cost of CO_2 emission which is different in different countries. Aminyavari et al. (2014) and Carlsson et al. (2016) reported that its value varies from 22 to 117 $/ton. In the present work, it is taken as 50 $/ton (Carlsson et al. 2016). The amount of carbon dioxide emitted m_{CO_2} is given by Eq. (20)

$$m_{CO_2} = \lambda \dot{W}_{el} t_{op}. \tag{20}$$

Here λ is the carbon dioxide emission factor, and its value is considered as 0.968 kg/kWh (Zare et al. 2012).

Thermoeconomic optimization

The laws of thermodynamics are combined with the principles of economics to perform thermoeconomic analyses. The thermoeconomic model of TSACCR system consists of three elements, (a) objective function, (b) equality constraints and (c) inequality constraints for optimization. The objective function is an economic parameter, and it is to be either maximized or minimized. The equality constraints are provided by the mathematical model together with thermodynamic properties. The inequality constraints allow the operation of TSACCR system within safe limits and are specified by the limits of the decision variables.

In the present study, the objective function is the minimization of annual cost of plant operation. Annual cost of plant operation is expressed as:

$$\dot{C}_{\text{plant}} = \dot{Z}_{\text{CI \& OM}} + \dot{C}_{\text{op}} + \dot{C}_{\text{env}}. \quad (21)$$

The decision variables are the design parameters which maximize or minimize the objective function. The temperatures of generators, absorbers, condenser, evaporator, cascade condenser and effectiveness of solution heat exchangers are chosen as decision variables. The thermoeconomic optimization of TSACCR system is carried out using direct search method. It offers the advantage of handling discontinuous and non-differentiable function (Deb 2012). The same method is also used by Cimsit et al. (2015) and Jain et al. (2015) for thermoeconomic optimization of absorption–compression cascade refrigeration systems.

Input parameters

The thermodynamic and thermoeconomic analyses of two-stage absorption–compression combined refrigeration system are carried out using a computer program developed in EES software. The parameters considered for the base case are given in Table 1. The streams of hot water enter HPG and LPG at 75 °C and exit at 70 °C. The inlet and outlet temperatures for cooling water used in condenser, HPA and LPA are 27 and 32 °C, respectively. The external water to be cooled enters evaporator of absorption section at 16 °C and evaporator of compression section at 11 °C and exits from it at 6 °C. The degree of overlap in cascade condenser is considered to be 5 °C; therefore, compression section condenser temperature is considered 11 °C for the base case.

Table 1 Input data for the base case of TSACCR system

Parameters	Value
Cooling capacity, $\dot{Q}_{\text{evap}}$ (kW)	100
Environment pressure, P_0 (kPa)	101.3
Environment temperature, T_0 (°C)	25
HPG temperature, T_{HPG} (°C)	65
LPG temperature, T_{LPG} (°C)	65
Compression section evaporator temperature, $T_{\text{evap,VCR}}$ (°C)	1
Absorption section evaporator temperature, $T_{\text{evap,VAR}}$ (°C)	6
Condenser temperature, T_{cond} (°C)	37
HPA temperature, T_{HPA} (°C)	37
LPA temperature, T_{LPA} (°C)	37
Effectiveness of HPSHE, ϵ_{HPSHE}	0.6
Effectiveness of LPSHE, ϵ_{LPSHE}	0.6
Pump efficiency, η_{p}	0.9
Interest rate, i_{r} (%)	15
Life span of system, n (years)	15
annual operation of hours, t_{op} (h)	5000

Model validation

Since no work either experimental or theoretical is available on the proposed two-stage absorption–compression combined refrigeration system, mathematical model of two-stage vapor absorption refrigeration system and vapor compression refrigeration system is validated separately. The results of two-stage absorption refrigeration system obtained from present model are compared with the results of Izquierdo et al. (2005). The input conditions considered for model validation are: $T_{\text{evap}} = 5$ °C, water to be chilled enters the evaporator at 15 °C and leaves it at 8 °C, inlet temperature of hot water to generators $= T_{\text{gen}} + 10$ °C, temperature drop of hot water in generators $= 7$ °C. The temperatures of condenser, HPA and LPA are considered same, and the external cooling water streams undergo temperature rise of 7 °C with inlet temperature $= T_{\text{cond}} - 10$ °C. The maximum difference in the prediction of COP is 2.38% (Table 2). The results of validation indicate a good agreement between the present results and those reported in the literature. Thus, the present model is reliable.

The compression section model is validated by comparing its results with those of Colorado and Rivera (2015). For comparison, the input parameters of Colorado and Rivera (2015) are considered in the present model. For the cooling capacity of 50 kW, condenser and evaporator temperatures of 35 and −10 °C, comparison is presented in Table 3, which shows that model is valid.

Table 2 Comparison of COP of present model with Izquierdo et al. (2005) for double-stage vapor absorption refrigeration system

T_{cond}	T_{gen}	Izquierdo et al. (2005)	Present model	Difference (%)
25	42	0.46	0.46	0
30	52	0.44	0.44	0
35	60	0.43	0.43	0
40	69	0.42	0.41	2.38

Table 3 Model validation of VCR system

Parameters	Colorado and Rivera (2015)	Present model	Difference (%)
COP	3.01	3.02	0.33
$\dot{W}_{\text{comp}}$	16.60	16.55	0.30
$\dot{Q}_{\text{cond}}$	66.60	66.55	0.07

Results and discussion

Once the model is developed and verified successfully, it is used for analyzing and optimizing the TSACCR system. The performance of TSACCR system is evaluated and compared with that of equivalent conventional VCR system.

Comparative performance of TSACCR and VCR systems

The TSACCR system is compared with equivalent VCR system from the viewpoint of energy, exergy, environment and economics for the same operating conditions and cooling capacity. For VCR system, evaporator temperature and condenser temperature are 1 and 37 °C, respectively. The condenser cooling water inlet and outlet temperatures are 27 and 32 °C, whereas evaporator chilled water inlet and outlet temperatures are 16 and 6 °C, respectively.

Energy analysis

Table 4 presents the results of energy analysis for both TSACCR and equivalent VCR systems. The main objective of combining absorption refrigeration system with compression refrigeration system is to bring down the electricity consumption in the latter. It is clear from Table 4 that integration reduces electricity requirement by 89.3% by equally sharing the cooling load and by decreasing the condensation temperature (for VCR it is 37 °C, whereas for compression section of TSACCR system it is 11 °C only). With the lowering of the heat rejection temperature, the mass flow rate of refrigerant R410A is found to decrease by 21.6%. This not only reduces compressor work but also decreases condenser heat load. The combined system, however, has to pay a penalty for this, in terms of reduced COP. The COP of TSACCR system is merely 0.38, whereas for VCR system it is 4.30. It is so because combined system requires a significant amount of heat. However, this low-temperature heat can be easily supplied by solar, geothermal or waste heat sources. On the other hand, if coefficient of performance is calculated considering only the electrical input, then its performance is far better than conventional VCR system. The electrical COP (COP_{el}) of TSACCR system is 40.13.

Table 4 Results of energy analysis

Parameters	VCR	TSACCR	
		Compression section	Absorption section
COP_{total}	4.30	0.38	
COP	4.30	20.05	0.40
$\dot{W}$ (kW)	23.28	2.49	0.002
$\dot{Q}_{HPG}$ (kW)	–	–	127.09
$\dot{Q}_{LPG}$ (kW)	–	–	130.68
$\dot{Q}_{HPA}$ (kW)	–	–	127.13
$\dot{Q}_{LPA}$ (kW)	–	–	125.88
$\dot{Q}_{cc}$ (kW)	–	52.49	–
$\dot{Q}_{cond}$ (kW)	123.28	52.49	107.26
$\dot{Q}_{evap}$ (kW)	100	100	

Table 5 Results of exergy analysis

Parameters	VCR	TSACCR
η_{ex} (%)	21.21	12.98
$\dot{E}D_{total}$ (kW)	16.50	27.69
$\dot{E}D_{HPG}$ (kW)	–	3.73
$\dot{E}D_{LPG}$ (kW)	–	4.98
$\dot{E}D_{HPA}$ (kW)	–	4.32
$\dot{E}D_{LPA}$ (kW)	–	6.06
$\dot{E}D_{cc}$ (kW)	–	1.01
$\dot{E}D_{cond}$ (kW)	3.60	2.65
$\dot{E}D_{evap,VCR}$ (kW)	3.88	1.48
$\dot{E}D_{evap,VAR}$ (kW)	–	1.40
$\dot{E}D_{HPSHE}$ (kW)	–	0.72
$\dot{E}D_{LPSHE}$ (kW)	–	0.39
$\dot{E}D_{comp}$ (kW)	5.85	0.55
$\dot{E}D_{RTV}$ (kW)	3.17	0.31

Exergy results

Table 5 shows the results of exergy analysis for both TSACCR and equivalent VCR systems. The rate of exergy destruction in two-stage absorption–compression combined refrigeration system is 67.82% higher than that in VCR system due to the presence of large number of components. The exergetic efficiency, which represents the degree of thermodynamic perfection, for combined and VCR systems are 12.98 and 21.21%, respectively. For VCR system, compressor is the major source of exergy destruction because of its non-isentropic compression process, whereas for combined system LPA and LPG are the main sites of thermodynamic imperfection because of temperature difference between working fluid and external water.

Environment and economic analyses

Table 6 presents the results of environment and economic analysis of both TSACCR system and equivalent VCR system for same operating conditions. The carbon dioxide emission in the atmosphere is the main parameter that quantifies the impact of a system on environment. For same cooling capacity CO_2 emission for TSACCR system is only

Table 6 Results of environment and economic analyses

Parameters	VCR	TSACCR
$\dot{C}_{plant}$ (\$/year)	15,648	12,272
$\dot{C}_{op}$ (\$/year)	8729	936
$\dot{C}_{env}$ (\$/year)	5633	604
$\dot{m}_{CO_2}$ (ton/year)	112.6	12.1
A_{HPG} (m^2)	–	10.37
A_{LPG} (m^2)	–	17.30
A_{HPA} (m^2)	–	6.64
A_{LPA} (m^2)	–	7.01
A_{cc} (m^2)	–	26.53
A_{cond} (m^2)	4.54	3.97
$A_{evap,VCR}$ (m^2)	8.01	10.36
$A_{evap,VAR}$ (m^2)	–	4.24
A_{HPSHE} (m^2)	–	13.60
A_{LPSHE} (m^2)	–	7.02
A_{total} (m^2)	12.55	107.04
Z_{total} (\$)	7090	59,200

12.1 ton/year, whereas for VCR system it is 112.6 ton/year. The less consumption of electricity in compression process is responsible for such a significant reduction in CO_2 emission in case of TSACCR system. As a result, environment damage cost for combined system is 89.28% less than that for VCR system. The operational cost for TSACCR system is also significantly less as compared to VCR system due to reduction in compressor work.

The initial capital investment cost of TSACCR system is much higher than that of the VCR system due to the requirement of large heat exchange area. The total heat exchange area for combined system is 107.04 m^2, and the corresponding initial investment cost is \$59,200 whereas for VCR system area and initial investment costs are 12.55 m^2 and \$7090, respectively. The annual cost of plant operation, which includes operational cost, environmental damage cost and initial investment cost, of TSACCR system is \$2376 less than equivalent VCR system.

Parametric analysis

The proper selection of operating parameters is essential for keeping control of cost and size of two-stage absorption–compression combined refrigeration system which are the major challenges for its practical implementation. Thus, the effect of important parameters like temperatures of generator, condenser, evaporator, absorber, effectiveness of solution heat exchangers on thermodynamic performance and cost of TSACCR system are explored in this section. During the parametric analysis, only one variable is varied while others are kept constant at their base case values as given in Table 1.

Effect of compression section evaporator temperature

Figure 2 shows the variation of COP and exergy destruction with evaporator temperature of compression section. Keeping the inlet and outlet temperatures of external chilled and other design parameters constant, increase in evaporator temperature of compression section from −2 to 4 °C causes the compression work to decrease by 48.8% because of decrease in specific volume of refrigerant at compressor suction. The COP of the system is improved from 0.380 to 0.388 with 6 °C rise in evaporator temperature. Also, decrease in compression work causes reduction in cascade condenser heat load, which further reduces the heat load of all the heat exchangers of the absorption section. Consequently, mass flow rate of external water drops substantially, which is quite desirable.

The rise in evaporator temperature of compression section causes reduction in the thermal gradient between the chilled water and the evaporator, resulting in decline of its exergy destruction rate from 2.08 to 0.90 kW. The exergy destruction in all other components is also found to decrease; as a result, exergy destruction of complete system decreases by 7.33% with the rise in evaporator temperature as shown in Fig. 2. Correspondingly, the exergetic efficiency increases from 12.61 to 13.36%. Thus, high value of evaporator temperature is desired from the viewpoint of energy and exergy.

Figure 3 shows the variation of annual cost of plant operation ($\dot{C}_{plant}$), annual capital investment and operation maintenance cost ($\dot{Z}_{CI\&OM}$), annual operational cost ($\dot{C}_{op}$) and annual environment damage cost ($\dot{C}_{env}$) with evaporator temperature of compression section. The 6 °C rise in evaporator temperature increases evaporator's area from 7.3 to 18.6 m^2 due to reduction in overall heat transfer coefficient and LMTD across it. The total area of the system increases from 97.7 to 125.3 m^2, resulting in 25.75% increase in $\dot{Z}_{CI\&OM}$. Contrary to this, the operational cost and the environmental damage cost decline by 48.84% each because of reduction in compression work. Since the contribution of operational cost and environmental damage cost to total cost of the plant is less as compared to initial capital investment, the aggregate effect is increase in the annual cost of plant operation by 12.90%. Thus, from cost point of view low evaporator temperature is preferable. Hence, the system with high value of evaporator temperature is not essentially optimum due to better energy, exergy and environmental performance. Lower exergy destruction value does not lead to optimum design of heat exchangers as the cost of the refrigeration system is higher.

Effect of absorption section evaporator temperature

Figure 4 shows the effect of absorption section evaporator temperature on COP as well as exergy destruction rate. With the increase in evaporator temperature from 5 to 9 °C and keeping compression section condenser temperature and other parameters constant, the LPA pressure (=pressure of EVAP-VAR) increases. This causes reduction in LiBr mass fraction in weak solution (x_1) which further causes reduction in solution circulation ratio of low-pressure side of absorption section from 9.64 to 7.06. Consequently, $\dot{Q}_{\mathrm{LPG}}$ decreases from 131.87 to 127.59 kW resulting in enhancement of COP by almost 2%. Also, the decrease in $\dot{Q}_{\mathrm{LPG}}$ results in reduction in exergy destruction rate in LPG. The irreversibility in cascade condenser and absorption section evaporator is found to decrease by 65.86 and 47.73%, respectively, as LMTD across them decreases with increase in absorption section evaporator temperature. As a consequent, the total exergy destruction of the combined system decreases as shown in Fig. 4. The exergetic efficiency increases from 12.92 to 13.14%. Hence, temperature of evaporator of absorption section should be high from the standpoint of energy and exergy analysis.

The effect of absorption section evaporator temperature on various costs of TSACCR system is shown in Fig. 5. The increase in its temperature from 5 to 9 °C causes total heat exchange area to increase by 58.61% resulting in hike in initial capital investment cost from $56,044 to $86,935. Thus, $\dot{Z}_{\mathrm{CI\,\&\,OM}}$ registers an increase of 55.12% while operational cost and environmental damage cost remain unchanged with the rise in absorption section evaporator temperature. The annual cost of plant operation is therefore increased from 11,700 to 17,300 $/year. Hence, from economic view point low temperature of absorption section evaporator is recommended.

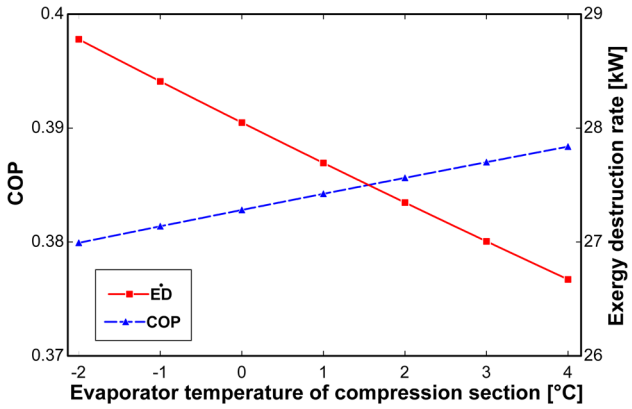


Fig. 2 Variation of COP and exergy destruction with evaporator temperature of compression section

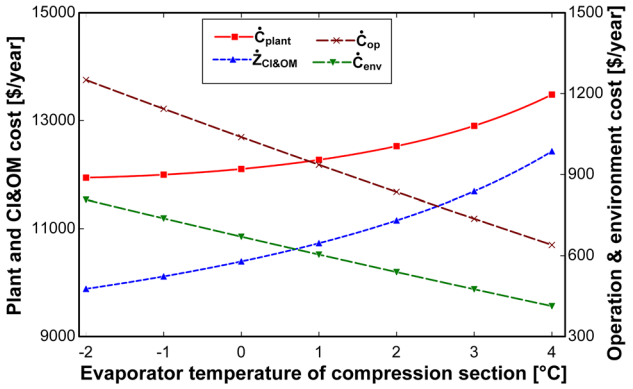


Fig. 3 Variation of cost with evaporator temperature of compression section

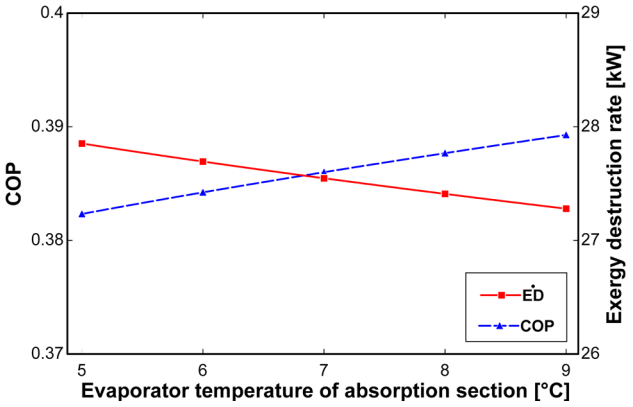


Fig. 4 Variation of COP and exergy destruction with evaporator temperature of absorption section

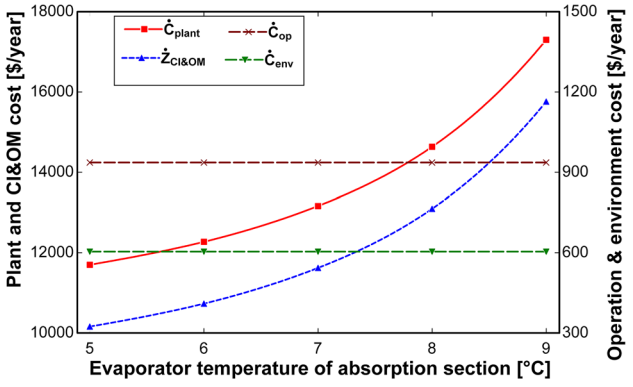


Fig. 5 Variation of cost with evaporator temperature of absorption section

Effect of compression section condenser temperature

Figure 6 shows the effect of compression section condenser temperature ($T_{\mathrm{cond,VCR}}$) on COP and exergy destruction rate. With the increase in $T_{\mathrm{cond,VCR}}$ keeping other conditions constant, the compression work increases

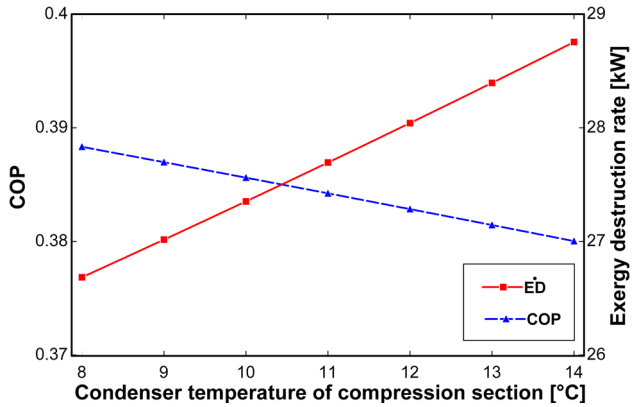


Fig. 6 Variation of COP and exergy destruction with condenser temperature of compression section

by 93.40% due to increase in compressor discharge pressure. This causes reduction in COP by 2.13% and enhancement in exergy destruction rate by 7.76%. The exergetic efficiency of the system is therefore decreased from 13.35 to 12.62%. The increase in compression work due to rise in $T_{\text{cond,VCR}}$ causes additional emission of 7.8 tons of CO_2 in the atmosphere. Thus, energy, exergy and environmental analysis recommend low condensing temperature of compression section.

Figure 7 shows the effect of compression section condenser temperature on various costs of TSACCR system. The increase in $T_{\text{cond,VCR}}$ causes an increase in LMTD of cascade condenser from 2 to 8 °C, resulting in decrease in cascade condenser area. The total area of the system is decreased by 62.18%. So, $\dot{Z}_{\text{CI\&OM}}$ reduces by almost 60.39%. However, the operational cost shows increasing trend with the increase in $T_{\text{cond,VCR}}$ due to increase in compression work. Also, the increase in compression section condenser temperature leads to additional payment of environmental damage cost of 387.3 $/year. The annual cost of plant operation is reduced by 53.78% due to 6 °C rise in $T_{\text{cond,VCR}}$. Therefore, high value of condenser

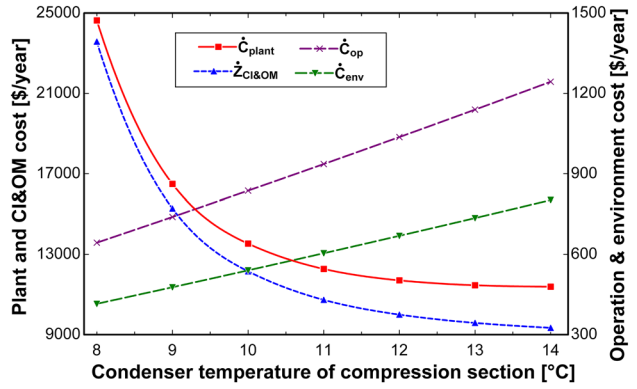


Fig. 7 Variation of cost with condenser temperature of compression section

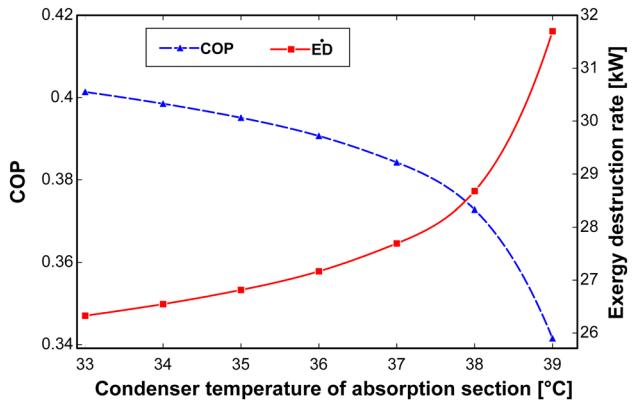


Fig. 8 Variation of COP and exergy destruction with condenser temperature of absorption section

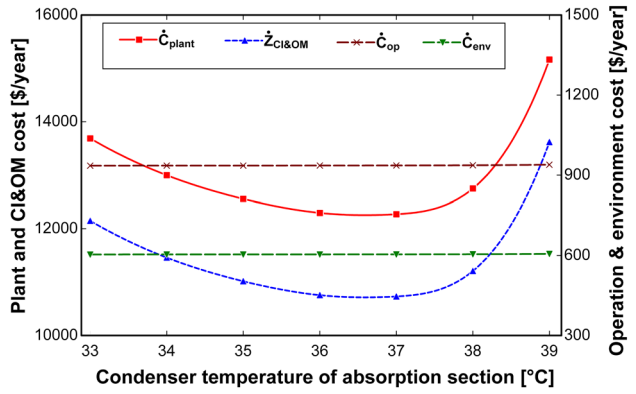


Fig. 9 Variation of cost with condenser temperature of absorption section

temperature of compressor section is justified by the economic analysis of the system.

Effect of absorption section condenser temperature

Figure 8 shows the effect of absorption section condenser temperature ($T_{\text{cond,VCR}}$) on COP and exergy destruction rate. It is to be noted that temperatures of HPA, LPA and absorption section condenser are equal. As $T_{\text{cond,VCR}}$ increases, both energetic and exergetic performance deteriorates gradually up to 38 °C and then they undergo swift deterioration. The COP is reduced from 0.40 to 0.34, while exergy destruction rate is increased by 20.39%. The exergetic efficiency of the system is decreased from 13.53 to 11.61%. With the increase in condenser temperature, solution circulation ratio increases which results in increase in heat input to generators and thus COP and exergetic efficiency reduce with $T_{\text{cond,VCR}}$. The compression section remains unaffected with the variation in absorber section condenser temperature; therefore, environmental performance remains unaltered. Thus, energy and exergy analysis

recommends low value of absorption section condenser temperature.

Figure 9 shows the effect of absorption section condenser temperature on various costs of the system. The operational cost and environmental cost remain almost constant with variation in $T_{\text{cond,VCR}}$ due to constant compression work and negligibly small pump work. With the increase in $T_{\text{cond,VCR}}$ from 33 to 39 °C, the area of condenser of absorption section is found to decrease from 10.32 to 3.08 m^2 due to reduction in overall heat transfer coefficient and LMTD across it. The total area of the system achieves its minimum value (107 m^2) at 37 °C. Consequently, $\dot{Z}_{\text{CI\&OM}}$ and $\dot{C}_{\text{plant}}$ attain minimum values (10,732 and 12,272 $/year) at 37 °C of absorption section condenser temperature, other conditions being same as the base case.

Effect of generator temperature

Figure 10 shows the variation of COP and exergy destruction with generator temperature ($T_{\text{gen}} = T_{\text{HPG}} = T_{\text{LPG}}$), keeping input conditions across generators and other components of system as constant (same as base case). With the increase in T_{gen} from 62 to 68 °C, the heat requirement in generators is observed to decrease by 2.8%. The heat load of absorbers is also found to decrease with increase in T_{gen}. The compressor work remains unaffected with the variation in generator temperature due to the fixed evaporator and condenser temperatures of compression section. With 6 °C rise in T_{gen}, the COP of the system increases from 0.372 to 0.387 whereas exergy destruction rate decreases by 4.4% due to reduction in temperature gradient between external hot water and generators. Therefore, high generator temperature is desirable from energy and exergy point of view.

Figure 11 shows the effect of generator temperature on various costs of the system. It is found that areas of

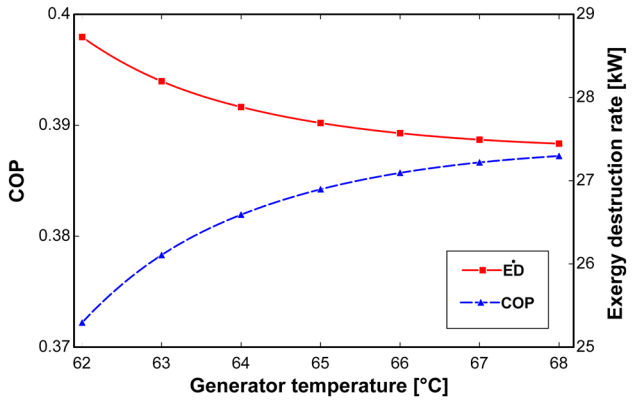


Fig. 10 Variation of COP and exergy destruction with generator temperature

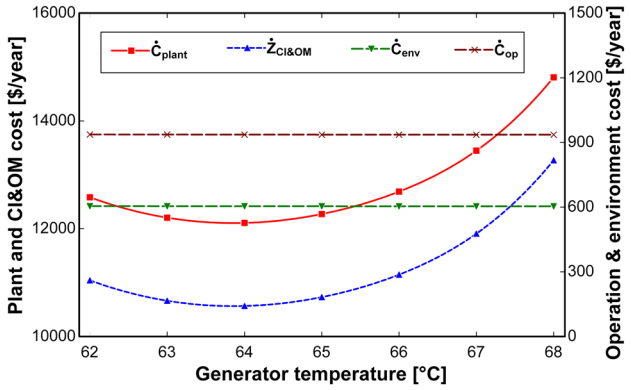


Fig. 11 Variation of COP and exergy destruction with generator temperature

generators increase, even though their thermal loads decrease, because of reduction in their LMTD and overall heat transfer coefficients. The areas of solution heat exchangers and absorbers exhibit declining trends with the rise in T_{gen}. The net effect is that the total area of the system attains minimum value of 105.3 m^2 at 64 °C. Consequently, $\dot{Z}_{\text{CI\&OM}}$ (10,567 $/year) and annual cost of plant operation (12,591 $/year) are also found to be minimum at 64 °C of generator temperature. The environmental damage cost and operation cost remains almost unchanged with generator temperature. Hence, economics of the system does not justify its operation at high generator temperature.

Effect of effectiveness of solution heat exchanger

Figure 12 shows the variation of COP and exergy destruction with effectiveness of solution heat exchangers ($\epsilon_{\text{SHE}} = \epsilon_{\text{HPSHE}} = \epsilon_{\text{LPSHE}}$). The increase in ϵ_{SHE} from 0.5 to 0.7 with other design conditions remaining fixed causes thermal load across them to increase by 40%, whereas thermal load across generators and absorbers are found to decrease by 3.9 and 4%, respectively. Thus, the COP is improved from 0.377 to 0.392 and exergy destruction rate is diminished by 4.5%. Hence, high value of solution heat exchanger effectiveness is encouraging from both energy and exergy standpoint.

Figure 13 shows the effect of effectiveness of solution heat exchanger on various costs of TSACCR system. The environmental damage cost and the operational cost remain constant with the change in solution heat exchanger effectiveness. The increased heat load of solution heat exchangers causes its area to increase with ϵ_{SHE}. Accordingly, total area of the system increases from 100.2 to 117.6 m^2. Consequently, $\dot{Z}_{\text{CI\&OM}}$ and $\dot{C}_{\text{plant}}$ increases by, respectively, 16.27 and 14.11% with the increase in effectiveness of solution heat exchangers. Hence,

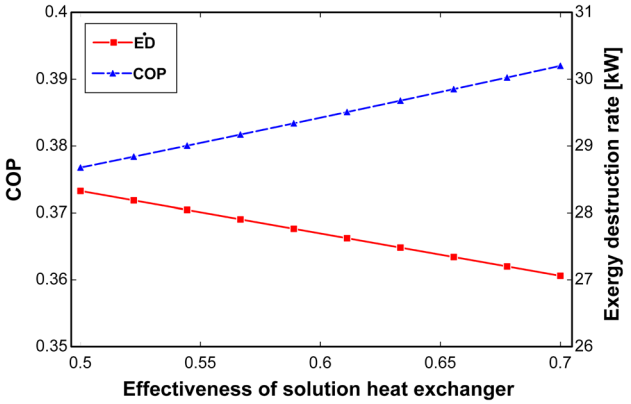


Fig. 12 Variation of COP and exergy destruction with effectiveness of solution heat exchanger

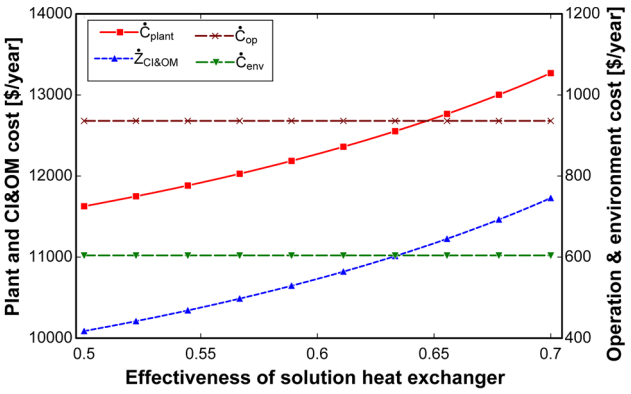


Fig. 13 Variation of cost with effectiveness of solution heat exchanger

economics does not permit the system to operate at high values of effectiveness of solution heat exchangers.

Thermoeconomic optimization

The annual cost of plant operation for two-stage absorption–compression combined refrigeration system for base case conditions (Table 1) is 12,755 $/year which can be further lowered through optimization. A trade-off among cost of input exergy, environmental damage cost and initial capital investment cost is attained by system optimization. The decision variables are simultaneously varied within a range, while other input parameters are kept constant. Temperatures of generators, compression section evaporator, compression section condenser and absorption section condenser are varied ±3 °C from their base case values. The absorption section evaporator temperature is varied from 5 to 9 °C as water is the refrigerant in the absorption section. The effectiveness of solution heat exchangers is changed ±10% from its base case value.

Table 7 shows the optimum values of performance indicators and other outputs together with decision

Table 7 Results of optimization

Parameters	Optimized values
$\dot{C}_{plant}$ ($/year)	10,038
$\dot{C}_{op}$ ($/year)	1151
$\dot{C}_{env}$ ($/year)	743
$\dot{Z}_{CI\&OM}$ ($/year)	8144
Z_{total} ($)	44,926
COP_{total}	0.38
$\dot{W}$ (kW)	2.94
$\dot{E}D_{total}$ (kW)	28.43
η_{ex} (%)	12.72
A_{total} (m^2)	80.8
$\dot{m}_{CO_2}$ (ton/year)	14.8
$T_{evap,VCR}$	1.1
$T_{cond,VCR}$	13.2
T_{gen}	62.2
$T_{evap,VAR}$	5.1
$T_{cond,VAR}$	36.1
ϵ_{SHE}	0.51

variables. The initial cost of two-stage absorption–compression combined system is so high that it is dominating the annual cost of plant operation. Therefore, the objective of minimization of annual cost of plant operation is achieved by reducing the initial capital investment. The optimization cuts the initial investment cost further by 24.1% by reducing the required heat exchange area from 107.04 to 80.80 m^2. The decrease in initial investment cost is achieved at the expense of exergetic and environmental performance. The exergy destruction rate is observed to increase by 2.6% while COP remains constant, with system optimization. The operational cost and environmental damage costs are therefore increased by 22.9% as compared to their base case values. Thus, the optimization of two-stage absorption–compression combined refrigeration system results in the reduction of the annual cost of plant operation by 18.2% in comparison with its base case value.

Conclusions

In the present study, a two-stage absorption–compression combined refrigeration system is analyzed and compared with equivalent VCR system based on energy, exergy, environment and economic aspects. Firstly, the designing of heat exchangers is performed for water chilling application in order to estimate the size and cost of the system. The parametric study reveals that low exergy destruction may not lead to optimum design of heat exchanger as cost becomes high. The high value of evaporator temperatures and low value of absorber and condenser temperatures are

desirable from thermodynamic viewpoint but again it is uneconomical as it leads to increase in system size and thus cost.

Following are the conclusions which can be made based on the energy, exergy, environment and economic analysis of two-stage absorption–compression refrigeration system and its comparison with equivalent vapor compression refrigeration system:

- The integration of absorption system with compression system results in reduction in electrical energy consumption by 89.3%.
- Annual CO_2 emissions are reduced from 112.6 to 12.1 ton by integration.
- The environmental damage cost is reduced by 89.3% by integrating absorption system with compression system.
- The annual cost of two-stage absorption–compression combined refrigeration system is 21.6% less than equivalent VCR system which can be further reduced by 18.2% through optimization.

References

Aminyavari M, Najafi B, Shirazi A, Rinaldi F (2014) Exergetic, economic and environmental (3E) analyses, and multiobjective optimization of a CO_2/NH_3 cascade refrigeration system. Appl Therm Eng 65:42–50

Arivazhagan S, Murugesan SN, Saravanan R, Renganarayanan S (2005) Simulation studies on R134a–DMAC based half effect absorption cold storage systems. Energy Convers Manag 46:1703–1713

Arivazhagan S, Saravanan R, Renganarayanan S (2006) Experimental studies on HFC based two-stage half effect vapour absorption cooling system. Appl Therm Eng 26:1455–1462

Arora A, Dixit M, Kaushik SC (2016) Computation of optimum parameters of a half effect water–lithium. J Therm Eng 2(2):683–692

Bakhtiar B, Fradette L, Legros R, Paris J (2011) A model for analysis and design of H_2O–LiBr absorption heat pumps. Energy Convers Manag 52:1439–1448

Bejan A, Tsatsaronis G, Moran M (1996) Thermal design and optimization. Wiley, New York

Carlsson B, Meir M, Rekstad J, Preib D, Ramschak T (2016) Replacing traditional materials with polymeric materials in solar thermosiphon systems—case study on pros and cons based on a total cost accounting approach. Sol Energy 125:294–306

Cimsit C, Ozturk IT (2012) Analysis of compression–absorption cascade refrigeration cycles. Appl Therm Eng 40:311–317

Cimsit C, Ozturk IT, Kincay O (2015) Thermoeconomic optimization of LiBr–H_2O—R134a compression–absorption cascade refrigeration cycle. Appl Therm Eng 76:105–115

Colorado D, Rivera W (2015) Performance comparison between a conventional vapor compression and compression–absorption single-stage and double-stage systems used for refrigeration. Appl Therm Eng 87:273–285

Colorado D, Velazquez VM (2013) Exergy analysis of a compression–absorption cascade system for refrigeration. Int J Energy Res 37:1851–1865

Crepinsek Z, Goricanec D, Krope J (2009) Comparison of the performances of absorption refrigeration cycles. WSEAS Trans Heat Mass Transf 3(4):65–76

Deb K (2012) Optimization for engineering design, 2nd edn. PHI Learning Private Limited, New Delhi

Domínguez-Inzunza LA, Hernández-Magallanes JA, Sandoval-Reyes M, Rivera W (2014) Comparison of the performance of single-effect, half-effect, double effect in series and inverse and triple-effect absorption cooling systems operating with the NH_3–$LiNo_3$ mixture. Appl Therm Eng 66:612–620

Florides GA, Kalogirou SA, Tassou SA, Wrobel LC (2003) Design and construction of a LiBr–water absorption machine. Energy Convers Manag 44:2483–2508

Garimella S, Brown AM, Nagavarapu AK (2011) Waste heat driven absorption/vapor-compression cascade refrigeration system for megawatt scale, high-flux, low-temperature cooling. Int J Refrig 34:1776–1785

Garousi Farshi L, Mahmoudi SMS, Rosen MA, Yari M, Amidpour M (2013) Exergoeconomic analysis of double effect absorption refrigeration systems. Energy Convers Manag 65:13–25. doi:10.1016/j.enconman.2012.07.019

Gebreslassie BH, Medrano M, Boer D (2010) Exergy analysis of multi-effect water–LiBr absorption systems: from half to triple effect. Renew Energy 35:1773–1782

Gebreslassie BH, Groll EA, Garimella SV (2012) Multiobjective optimization of sustainable single-effect water/lithium bromide absorption cycle. Renew Energy 46:100–110

Gomri R (2010) Solar energy to drive half-effect absorption cooling system. Int J Therm Environ Eng 1(1):1–8

Herold KE, Radermacher R, Klein SA (1996) Absorption chillers and heat pumps. CRC Press, Boca Raton

Izquierdo M (2004) Crystallization as a limit to develop solar air-cooled LiBr–H_2O absorption systems using low-grade heat. Sol Energy Mater Sol Cells 81:205–216. doi:10.1016/j.solmat.2003.11.002

Izquierdo M, Venegas M, García N, Palacios E (2005) Exergetic analysis of a double stage LiBr–H_2O thermal compressor cooled by air/water and driven by low grade heat. Energy Convers Manag 46:1029–1042. doi:10.1016/j.enconman.2004.06.016

Jain V, Kachhwaha SS, Sachdeva G (2013) Thermodynamic performance analysis of a vapour compression–absorption cascaded refrigeration system. Energy Convers Manag 75:685–700

Jain V, Sachdeva G, Kachhwaha SS (2015) NLP model based thermoeconomic optimization of vapor compression–absorption cascaded refrigeration system. Energy Convers Manag 93:49–62

Kaushik SC, Arora A (2009) Energy and exergy analysis of single effect and series flow double effect water–lithium bromide absorption refrigeration systems. Int J Refrig 32(6):1247–1258

Kim D, Machielsen C (2002) Evaluation of air-cooled solar absorption cooling systems. In: Proceeding of the 7th international sorption heat pump conference, pp 117–122

Kizilkan O, Sencan A, Kalogirou SA (2007) Thermoeconomic optimization of a LiBr absorption refrigeration system. Chem Eng Process 46:1376–1384

Klein SA, Alvarado F (2005) Engineering equation solver, version 7.441. F Chart Software, Middleton

Medrano M, Bourouis M, Coronas A (2001) Double-lift absorption refrigeration cycles driven by low-temperature heat sources using organic fluid mixtures as working pairs. Appl Energy 68:173–185. doi:10.1016/S0306-2619(00)00048-9

Misra RD, Sahoo PK, Sahoo S, Gupta A (2003) Thermoeconomic optimization of a single effect water/LiBr vapour absorption refrigeration system. Int J Refrig 26:158–169. doi:10.1016/S0140-7007(02)00086-5

Misra RD, Sahoo PK, Sahoo S, Gupta A (2005) Thermoeconomic evaluation and optimization of a double effect H_2O/LiBr vapour absorption refrigeration system. Int J Refrig 28(3):331–343

Patel B, Kachhwaha SS, Modi B (2017) Thermodynamic modelling and parametric study of a two stage compression-absorption refrigeration system for ice cream hardening plant. Energy Procedia 109:190–202

Reddy VS, Panwar NL, Kaushik SC (2012) Exergetic analysis of vapour compression refrigeration system with R134a, R143a, R152a, R404A, R407C, R410A, R502 and R507A. Clean Technol Environ Policy 14:47–53

Sayyaadi H, Nejatolahi M (2011) Multi objective optimization of a cooling tower assisted vapour compression refrigeration system. Int J Refrig 34:243–256

Seyfouri Z, Ameri M (2012) Analysis of integrated compression–absorption refrigeration systems powered by a microturbine. Int J Refrig 35:1639–1646

Singh OK, Kaushik SC (2013) Thermoeconomic evaluation and optimization of a Brayton–Rankine–Kalina combined triple power cycle. Energy Convers Manag 71:32–42. doi:10.1016/j.enconman.2013.03.017

Wang L, Ma A, Tan Y, Cui X, Cui H (2012) Study on solar assisted cascade refrigeration system. Energy Proc 16:1503–1509

Zare V, Mahmoudi SMS, Yari M, Amidpour M (2012) Thermoeconomic analysis and optimization of an ammonia–water power/cooling cogeneration cycle. Energy 47:271–283

International Journal of Research in Engineering and Innovation (IJREI)
journal home page: http://www.ijrei.com
ISSN (Online): 2456-6934



Exergy and energy analysis of modified organic rankine cycle for reduction of global warming and ozone depletion

Radhey Shyam Mishra, Yunis Khan

Department of Mechanical Production & Industrial and Automobiles Engineering
Delhi Technological University Delhi-110042

Abstract

There is great importance of using the Organic Rankine cycle plant in world. Low and medium grade energy from the low grade energy source is converted into the useful high grade energy. These low and medium grade energy sources are geothermal, solar energy, exhaust from the engine and other industrial waste energy. In this study the solar energy source is used. The main purpose of the solar integrated power plant is to mitigate the emission and risk associated with the already running plants and the other important purpose of integration of solar energy into already running power cycles is to minimize the cost keeping running already existing equipments. In this work exergy and energy analysis of Organic Rankine cycle with the solar heating source for organic fluid is done and bleeding regeneration is used for obtaining good performance. The performance of system is compared with different organic fluids like R134a, R407C, R404A, and R410A at different organic Rankine cycle maximum temperature and maximum pressure. R410A shows maximum in efficiency by regeneration around 64%. R410A shows maximum organic Rankine cycle efficiency of 16.51%. Exergetic efficiency of cycle with regeneration 61.78%, 64.75%, 60.14%and 48.51% for R407C, R410A, R404A and R134a respectively. Due to highest Exergy and energy efficiency and also it has low global warming potential and zero ozone depletion potential. R410A is useful for organic Rankine cycle for practical applications and there is no problem such as flammability and explosion risks.
© 2017 ijrei.com. All rights reserved

*Keywords***:** Modified organic Rankine Cycle, Energy Exergy Analysis, Thermodynamic analysis, Thermal Power Plant

1. Introduction

A regenerator is installed that heat the organic fluid (liquid) by the high temperature vapour that is coming from the organic turbine. In many organic fluid when expanded in orc turbine, at the exit give superheated vapor this vapor enthalpy is used in heating organic fluid that results heat addition required in the boiler is reduced. and condenser temperature is again set 35˚C.some steam at intermediate pressure the organic fluid vapor is extracted .this bled of vapor is goes to heater for heating the organic liquid coming out from the pump-1.after gating heat from heater liquid is heated and then go to the pump -2 .from pump -2 it is pumped to the evaporator pressure. Main purpose of the bleeding regeneration is that it is reduced the heat addition in evaporator. Several solar integrated combined cycles (ISCCs) are being used in all the world (USA Africa, North America ,Italy,) and there are many projects are processing (China, Mexico, USA). ISCCs have several advantages as compared to solar thermal power plants, because these give higher conversion solar efficiency and it have very low investment cost. Many entrepreneurs and owners are ready to invest the many due to it low risk associated with the smaller plants as compared to the solar thermal power plants. The procedure for changing over the vitality in a fuel into electric power incorporates the formation of mechanical work, which is then changed over into electric power by a generator. Contingent upon fuel sort and thermodynamic process, the in general productivity of this change can be as low as 31 %. This implies 66% of the inert vitality of the fuel goes up squandered. For instance, steam electric power plants which utilizes boilers to combust a petroleum derivative normal 33% efficiency. Basic cycle gas turbine (GTs) plants normal just shy of 30 percent productivity on gaseous petrol, and

Radhey Shyam Mishra
Email Id: rsmishradtu@gmail.com

around 25 % on fuel oil. Quite a bit of this squandered vitality misfortunes as warm vitality in the hot fumes gasses from the ignition procedure.
To build the general proficiency of electric power plants, various procedures can be consolidated to recoup and use the leftover warmth vitality in hot fumes gasses. In joined cycle mode, control plants can accomplish electrical efficiencies up to 60 %. The expression alludes to the consolidating of numerous thermodynamic cycles to create control. Joined cycle operation utilizes a heat recovery boiler (HRB) that assimilates warm from high temperature deplete gasses to deliver natural vapor, which is then provided to a natural turbine to produce additional electric power. The procedure for making vapor to create work utilizing a natural turbine depends on the Rankine cycle.

2. Organic Rankine Cycle

Organic Rankine Cycles have gotten more consideration amid the most recent decade. This cycle takes after the crucial principles of regular Rankine cycles working with steam in like manner plants however has a few points of interest over steam Rankine cycle which made it prevalent. Firstly this cycle can work on low pressures and temperatures in comparison to the conventional Rankine cycle and reveals a better result than steam Rankine cycle especially from low grade heat sources because it has working fluids include such as variety of HCs and other refrigerants what's more, as per scope of open heat source pressure and temperatures, different outputs can be obtained by using useful working fluids, secondly, it can also work without multi-stage turbines and feed-water heaters and that thing makes it simple using.

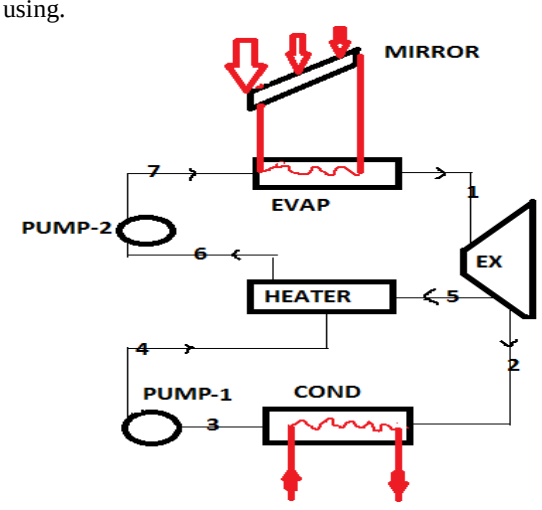


Figure: 1 Organic Rankine cycle without regeneration

Although this, solar parabolic collectors are a tremendous source of heat energy but these have low grade thermal energy. Because of this ,these solar collectors give only some KWs to some megawatts of power generation mainly near factories and rural areas to generate own electricity consumption without the necessity for connection to grid that may be costly. Disadvantages of solar ORCs are comparatively high costs and low thermal efficiency (10 to 25 % according to working fluids and working conditions) mainly because of low HTF (Heat transfer fluids) temperature in solar collector. As described before, the organic fluid works in ORC cycles are classified into HCs and refrigerants, some of those are dry liquids which mean they have a +ve slope T-S graph in the immersion vapor area. This makes it reasonable for some organic liquids to works legitimately without superheating to an extraordinary possibility and make no harm turbine. It has been appeared in this review, an examination of various dry organic liquids with or without superheating and recuperations has been done to reveal the difference in cycle effectiveness and execution of the system that encourages us to settle on a choice to pick the system condition as indicated by our requirements.

2.1 Principle of solar heating

The organic Rankine cycle works on the principle of a turbo generator which works as a simple steam turbine to convert thermal power into mechanical power and then into electrical power by an electrical generator. Besides of using steam of water, orc system evaporates organic fluid, classified by a molecular weight higher than the water that leads to slow rotation of the organic expander that also leads to the less erosion of metallic parts and the blades. Organic Rankine cycle is normally a Rankine cycle in which besides of using water other organic fluid is used like R134a, R407C, R404A, R410A etc. Evaporator is nothing but is the simple heat exchanger, or it can be used as a series of heat exchangers. It is also can be called a boiler, because it produces organic vapour for the ORC turbine by taking energy from the solar heat source. This heat source is nothing simple solar heat flate plate collector. From solar plate heat collector the heat is taken by the evaporator and the in evaporator working fluid is heated and converted in to the hot vapor this vapor goes to the expander and this heat energy converted in to the rotation of expander. Instead of the flat, plate heat collector there concentrated parabolic heat collector can be used.
The economizer works as a heat exchanger which preheats the organic fluid (liquid) to get the temperature to the saturation temperature (boiling point), that liquid to be supplied to a thick-walled boiler drum. That drum is installed where finned evaporator tubes is located that circulate heated organic fluid. The solar radiation incident on to the evaporator tubes, and the heat is being absorbed and then the vapor is being created of in the tubes. This vapor-liquid mixture goes to the boiler drum where the vapour is separated from the hot liquid by using moisture cyclones and separators. And that separated liquid is again recirculated to the evaporator tube. The

function of the some boiler drums is also to storage and water treatment functions. There are several other design of steam boiler in which another design is a once-through, where thin-walled components are used in place of boiler drum which are better for handling changes in exhaust gas temperature and vapour pressures during frequently stops and starts. In other designs, duct burners can be used for adding heat to the exhaust gas current and boost vapour manufacturing; it's have been used to generate vapour even if no not sufficient exhaust gas flow is there.
Saturated vapour from boiler drums or any once-through boiler system has been sent to super heater to produce dry vapour that is requirement for the organic turbine. And the organic fluids goes to the preheaters, that are placed where very low amount of heat is available and then this fluid takes energy from the and heated by the heat exchanger liquids such as the mixture of glycol water and from there very economic and useful amount of heat is extracted.
The superheated organic vapour produced from the evaporator is supply to organic turbine where it is expanded by the turbine blades, and gives rotation to turbine shaft. The mechanical energy delivered to the generator driving shaft is transformed into high grade energy (electricity). After exiting the organic turbine, the organic vapor goes to the condenser which paths the condensed organic liquid back to evaporator.
In this research the main purpose is the selection the working fluid which is given the maximum exergetic and the first law efficiency and low global warming potential and the zero ozone depletion potential.
And give lower exergy destruction in the each component. Some important properties of working fluids. Are given in Table-1.

Table: 1 properties of the working fluids

Working fluids	Constituents	Toxicity	Flammability	ODP	GWP
R407C	R32(23%),R 125(25%), R134(52%)	None toxic	None flammability	0	1526
R410A	R125(50%), R32(50%)	None toxic	None flammability	0	1725
R134a	Tetra floro ethane	None toxic	None flammability	0	1300
R404A	R125(44%), R143a(52%) R134a(4%)	None toxic	None flammability	0	3260

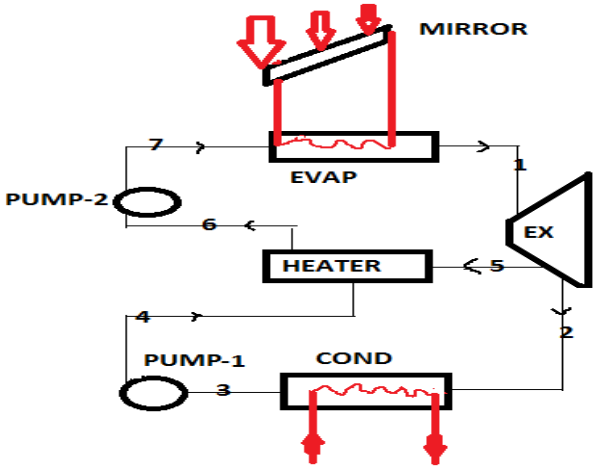


Figure: 2 Organic Rankine cycle with regeneration

This is the organic Rankine cycle without regeneration, working fluid flows from 1 point to 2-3-4-1.in evaporator working fluids gets heated from the solar radiation .and then is heated from saturated liquid to super heated vapor .after that this vapor goes to the turbine and there it is expanded, and heat energy is converted in the mechanical energy and after the expansion the mechanical energy further it is transformed in to the electrical energy in generator. After the expansion the remaining vapor which has some heat energy goes to the condenser where heat from the vapor rejected from the condenser .in condenser cooling water is enter for cooling purpose after then it is pumped to the boiler pressure by liquid pump. Then again the heating process is done and the cycle is repeated
A regenerator is installed that heat the organic fluid (liquid) by the high temperature vapour that is coming from the organic turbine. In many organic fluid when expanded in orc turbine, at the exit give superheated vapor this vapor enthalpy is used in heating organic fluid that results heat addition required in the boiler is reduced. and condenser temperature is again set 35˚C.some steam at intermediate pressure the organic fluid vapor is extracted .this bled of vapor is goes to heater for heating the organic liquid coming out from the pump-1.after gating heat from heater liquid is heated and then go to the pump -2 .from pump -2 it is pumped to the evaporator pressure. Main purpose of the bleeding regeneration is that it is reduced the heat addition in evaporator.
Kelly et al [1] demonstrated that the most efficient way for converting solar thermal energy into electricity is to withdraw feed water from the heat recovery steam generator (HRSG) downstream of the last economizer, to produce high pressure saturated steam and to return the steam to the HRSG for superheating and reheating. The integrated solar plant concept offers an effective means for the continued development of parabolic trough technology. In a careful plant design, solar thermal to electric conversion efficiencies will exceed, often by a significant amount, those of a solar-only parabolic trough project. An integrated plant bears only the incremental

capital cost of a larger Rankine cycle, which provides further reductions in the levelized cost of solar energy.

He Ya Ling et al [2] proposed a model for a typical parabolic trough solar thermal power generation system with Organic Rankine Cycle (PT-SEGS–ORC) was built within the transient energy simulation package TRNSYS. They found that the heat loss of the solar collector (qloss) increases sharply with the increase in pinter at beginning and then reaches to an approximately constant value. The variation of heat collecting efficiency (η_{hc}) with v is quite similar to the variation of gloss with pinter. However, Idn and θ exhibit opposite effect on η_{hc}. In addition, it is found that the optimal volume of the thermal storage system is sensitively dependent on the solar radiation intensity. The optimal volumes are 100, 150, 50, and 0 m^3 for spring equinox, summer solstice, autumnal equinox and winter solstice, respectively.

Gang et al. [3] proposed the innovative configuration of low temperature solar thermal electricity generation with regenerative Organic Rankine Cycle (ORC), mainly consisting of small concentration ratio compound parabolic concentrators (CPC) and the regenerative ORC. The effects of regenerative cycle on the collector, ORC, and overall electricity efficiency are then analyzed. The results indicate that the regenerative cycle has positive effects on the ORC efficiency but negative ones on the collector efficiency due to increment of the average working temperature of the first-stage collectors. And found that the regenerative cycle optimization of the solar thermal electric generation differs from that of a solo ORC. The system electricity efficiency with regenerative ORC is about 8.6% for irradiance 750 W/m2 and is relatively higher than that without the regenerative cycle by 4.9%.

Manolakos D et al [4] proposed co-generation system producing electricity and freshwater by a solar field driven supercritical organic Rankine cycle (SORC) coupled with desalination. The proposed system can use parabolic trough solar collectors (among other options) to produce 700 kW thermal energy with temperatures up to 400°C at peak conditions. Thermal energy is delivered to the SORC which uses hexamethyldisiloxane (MM) as the working organic fluid and could achieve cycle efficiency close to 21%. The SORC condensation process is undertaken by the feed seawater to reduce thermal pollution. Due to the elevated temperature of the preheated seawater, the RO unit specific energy consumption decreases.

Nafey and Sharaf [5] carried out design and performance analysis using MatLab/SimuLink computational environment. The cycle consists of thermal solar collectors (Flat Plate Solar Collector (FPC), or Parabolic Trough Collector (PTC), or Compound Parabolic Concentrator (CPC)) for heat input, expansion turbine for work output, condenser unit for heat rejection, pump unit, and Reverse Osmosis (RO) unit. Reverse osmosis unit specifications used in this work is based on Sharm El-Shiekh RO desalination plant. Different working fluids such as: butane, iso butane, propane, R134a, R152a, R245ca, and R245fa are examined for FPC. R113, R123, hexane, and pentane are investigated for CPC. Dodecane, nonane, octane, and toluene are allocated for PTC. Exergy and cost analysis are performed for saturation and superheated operating conditions. Toluene and Water achieved minimum results for total solar collector area, specific total cost and the rate of exergy destruction.

Sharaf et al [6] carried out thermo-economic analysis of PTSC integrated with an ORC and a multi-effect distillation. Two scenarios of generation were considered in their study: the first one was with only water production and the second one was with both power and water production. The comparison is implemented according to the operation of Parabolic Trough Collector (PTC) with toluene organic oil and water working fluids. Therminol-VP1 Heat Transfer Oil (HTO) is considered for indirect vapor generation operation across the solar field and evaporator heat exchanger. The comparisons are manipulated according to 100 m^3/day of distillate product as a case study. As a result, only desalination technique is considered more attractive than desalination and power technique due to higher gain ratio and lower solar field area needed.

Delgado-Torres and Garcia Rodriguez et al [7] & [8] conducted thermodynamic analysis of a thermal system which consists of an ORC, a PTSC, and an RO (Reverse Osmosis). Initially they analyzed the system assuming only water production through RO then they extended their study to include both electrical and water production the main objective of their study was to examine the effect of different organic fluids on the aperture area of the PTSC.

Al-Sulaiman et al. [9] & [10] proposed the energetic performance analysis of PTSC integrated with an ORC in which the waste heat from the ORC is used for cogeneration was conducted. It was found that there was an energy efficiency improvement, when tri generation was used, from 15% to 94% (utilization efficiency). On the other hand using exergy analysis, found that there was an exergetic efficiency improvement from 8% to 20% when tri generation is used as compared to only power generation.

Al-Sulaiman [11] carried out solar field sizing and overall performance analysis of different vapor cycles. The systems considered are parabolic trough solar collectors integrated with either a binary vapor cycle or a steam Rankine cycle (SRC). The binary vapor cycle consists of an SRC as a topping cycle and an organic Rankine cycle as a bottoming cycle. Seven refrigerants are examined for the bottoming cycle: R600, R600a, R134a, R152a, R290, R407c, and ammonia. Founds that significant reduction in the solar field size is gained due to the performance improvement when the binary vapor cycle is considered as compared to a steam Rankine cycle with atmospheric condensing pressure; however, SRC with vacuum pressure has the best performance and smallest solar field size. It further reveals that the R134a binary vapor cycle

has the best performance among the binary vapor cycles considered and, thus, requires the smallest solar field size while the R600a binary vapor cycle has the lowest performance.

Fahad A. Al-Sulaiman [12] carried out detailed exergy analysis of thermal power system driven by parabolic trough solar collectors (PTSCs). The power is produced using either a steam Rankine cycle (SRC) or a combined cycle, in which the SRC is the topping cycle and an organic Rankine cycle (ORC) is the bottoming cycle. Seven refrigerants for the ORC were examined: R134a, R152a, R290, R407c, R600, R600a, and ammonia. The R134a combined cycle demonstrates the best exergetic performance with a maximum exergetic efficiency of 26% followed by the R152a combined cycle with an exergetic efficiency of 25%. Alternatively, the R600a combined cycle has the lowest exergetic efficiency, 20–21%.

Milad Ashouri et al [13] carried out analysis of a photovoltaic through collector (PTC) integrated with an organic Rankine cycle (ORC) for small scale electricity generation near Tehran. The system includes a solar field, a storage tank, and a small scale ORC engine. Performance evaluation has been done by means of commercial software Thermoflex19. A comparison of different working fluids is presented and results shows that Benzene has the best performance among fluids butane, n-pentane, isopentane, R123 and R245fa for the system conditions described.

Dimityr Popov [14] proposed a concept for innovative hybridization of gas turbine combined cycle plant and solar power system. This conceptual plant is named as Solar Assisted Combined Cycle, as the solar energy is indirectly involved in power generation. The proposed solar hybridization can be accomplished in two ways. The first solar assisted option introduces mechanical chillers for a complete cooling of gas turbine inlet air. The next solar assisted option does the same but with an absorption chiller. They find that the configuration with absorption chillers has lower specific incremental plant capital costs and requires smaller land area than the others.

Wang et al [15] analyzed a 1.6 kWe solar ORC using a rolling piston expander. An overall efficiency of 4.2% was obtained with evacuated tube collectors and 3.2% with flat-plate collectors. The difference in terms of efficiency was explained by lower collector efficiency (71% for the evacuated tube vs. 55% for the plate technology) and lower collection temperature.

S. Quoilin et al [16] carried out thermodynamic modeling of a proposed small scale PTSC integrated with an ORC for power production, considering different design options to be located in a rural location in South Africa and presented an optimization and sizing procedure of heat exchangers in a small scale solar driven ORC by pinch and pressure drop and optimized it by turbine input pressure and evaporator temperature. Then they further focused on the evaluation of the thermodynamic performance of the system. With conservative hypotheses, and real expander efficiency curves, it was found that an overall electrical efficiency between 7% and 8% reached. This efficiency is steady-state efficiency at a nominal working point. The comparison between working fluids showed that the most efficient fluid is Solkatherm. R245fa also shows a good efficiency and has the advantage of requiring much smaller equipment.

Maria E Madejar et al.[17] presents the quasi-steady state simulation of a regenerative organic Rankine cycle (ORC) integrated in a passenger vessel, over a standard round triple used experimental data like exhaust gas temperature, engine speed, electricity demand on board for simulation purpose and to estimate the average net power production of the ship over a round trip.

Finally he conclude that the maximum net power production of the ORC during the round trip was estimated to supply approximately 22% of the total power demand on board. The results showed potential for ORC as a solution for the maritime transport sector to accomplish the new and more restrictive regulations on emissions, and to reduce the total fuel consumption.

Harrison Warren et al.[18] proposes enhancement of power generation unit-organic Rankine cycle (ORC) system through the electric energy storage and proposes the use of an electric energy storage (EES) device in conjunction with a PGU-ORC. The idea is to use the energy stored by EES at different times of the day so that continuous operation of the PGU is not required. The potential of the proposed PGU-ORC-EES system is assessed by evaluating the performance in terms of operational cost, primary energy consumption (PEC)

He concluded that the potential of a PGU-ORC-EES system to reduce the operational cost, CDE, and PEC compared with a conventional system. Performance of simulations of a restaurant facility at 12 different geographical locations reflecting a variety of climate conditions. Results indicated that the addition of EES is beneficial to the PGU-ORC system for most locations in terms of the three evaluated parameters.

Ayad M. Al Jubori et al [19] proposed Modelling and parametric analysis of small-scale axial and radial outflow turbines for Organic Rankine Cycle applications using a range of organic working fluids (R141b, R245fa, R365mfc, iso butane and n–pentane).

And he conclude that the efficiency of axial small scale turbine is better than radial out flow turbine .axial turbine have efficiency 82.5% and power output 15.15kw.and on other hand the efficiency of radial outflow efficiency is 79.05% and power output is 13.625kw with n-pentane as the working fluid in both cases. The maximum cycle thermal efficiency was 11.74% and 10.25% for axial and radial-outflow turbine respectively with n-pentane as the working fluid and a heat source temperature of 87 _c

Jui-Ching Hsieh et la [20] Design and preliminary results of a 20-kW trans critical organic Rankine cycle with a screw expander for low-grade waste heat recovery and they examine a trans critical Rankine cycle with screw expander with R218 as the working fluid in both sub

critical and super critical state of working fluid they used the low grade heat at 90 -100_C.and they used two centrifugal pumps in series .for control controlling the pressure used variable frequency drive (VFD).

Finally they concluded the efficiency of the expander and the working fluid pump is peak at peak pressure. the output power was not significantly effected by heat source temperature but thermal efficiency slightly decreased by increasing heat source temperature The present TRC system successfully converted the low-grade heat into approximately 20 kW of power. The thermal efficiency of the TRC system was 5.7%, 5.38%, and 5.28% for the heat source temperatures 90, 95, and 100 _C, respectively, with the VFD at 50 Hz.

Dong junqi et al [21] proposed Experimental investigation on heat transfer characteristics of plat heat exchanger applied in organic Rankine cycle (ORC) .and experimentally study the single phase and boiling heat transfer characteristics of three types of working fluids on plate types of heat exchangers surface. These three working fluid are water and 50%coolant and R 245fa.and heat transfer dimensionless empirical equation for three types of working fluids are provided.

Finally he obtained evaporation heat transfer empirical equation for the organic fluid R245fa is given with the mean absolute error9.97%which prevents 90% data with error less than ±20%.

Ayad Al Jubori et la [22] proposed Three dimensional optimization of small-scale axial turbine for low temperature heat source driven organic Rankine cycle Advances in optimization techniques can be used to enhance the performance of turbines in various applications. However, limited work has been reported on using such optimization techniques to develop small-scale turbines for organic Rankine cycles. This paper investigates the use of multi-objective genetic algorithm to optimize the stage geometry of a small-axial subsonic turbine.

And he concluded that using working fluid R123 for a turbine with mean diameter of 70 mm, the maximum isentropic efficiency was about 88% and power output of 6.3 kW leading to cycle thermal efficiency of 10.5% showing an enhancement of 14.08% compared to the baseline design. Such results highlight the potential of the 3D optimization technique to improve the organic Rankine cycle performance.

Constantine N. Michos et al.[23] proposed the backpressure effect of an Organic Rankine Cycle (ORC) evaporator on the exhaust line of a turbocharged, V12 heavy duty diesel engine, for typical marine and power generation applications has been investigated using the commercial software Ricardo WAVE. Three different state-of-the art turbocharging strategies are assessed in order to counterbalance the increased pumping losses of the engine due to the boiler installation: fixed turbine, Waste-Gate (WG) and Variable Geometry Turbine (VGT). At the same time, the And he concluded that engine side point of view, a VGT turbocharger is the most favorable solution to withstand increased backpressure, while, regarding the ORC side, between the considered fluids and layouts, acetone and a recuperated cycle show the most promising performance.

3. Outcomes from Literature review and Research gap identified

By incorporation of solar energy in organic Rankine cycle plant the output of plant can be increased. From literature survey of solar integrated ORC plant, it is found that detailed energy and exergy analysis of Organic Rankine cycle plant and combined cycle power plant are done earlier. From literature survey it is found that energy and exergy analysis of solar operated organic Rankine cycle with regeneration and selection of working fluid are not done yet. Solar energy is used for reheating source for the heating of working fluid in the evaporator.

In the present study thermodynamic analysis of Organic Rankine cycle plant with solar reheating source is investigated and comparison of various organic fluids is carried out to find best organic fluid which will give maximum efficiency. The effect of regeneration on organic Rankine cycle plant. It is proposed to examine the effect of following parameters on the efficiency of organic Rankine cycle and Organic Rankine cycle plant of solar heated cycle plant and evaluation of better organic fluid for global warming and ozone depletion.

- Effect of using regeneration in system on efficiency and exergy destruction.
- Effect of Organic turbine inlet temperature.
- Effect of Organic turbine inlet pressure.
- Effect of various organic fluids.
- And find maximum exergy destruction component.
- Effect of varying solar plate area.

4. Thermodynamic Analysis

For thermodynamics (energy and exergy) analysis of organic Rankine cycle with the regeneration and solar heating source is considered .which is given in figure .In this figure there are four component which are given as

- An organic expander
- A condenser
- Two pumps
- An evaporator

All stages are defined by the numbers at stage 1 the organic fluid which in vapor forms goes to the organic expander where it is expanded and gives the work W_{ex}

After expansion the organic fluids goes to condenser for rejection of the heat from the remaining organic vapor at stage 2 and heat Q_r heat is rejected. After rejection of heat it goes to pump 1 giving work of Wc_1 where it is brought to the heater pressure or intermediate pressure where some part of vapor is extracted for heating purpose for the organic liquid. The organic vapor is extracted from the turbine at the stage 5.and it is mixes at the heater .after

mixing and getting heat the it goes to the pump 2 at the stage of 6 and pump-2 increases the pressure to the evaporator pressure at the stage of 7 and Wc2 work is done the stage of 7 saturated fluid goes to the evaporate where heat is taken by the liquid working fluid is heated by solar heating constant temperature heat source .Qs heat is supplied to the working fluid and then cycle is repeated.

4.1 Thermodynamic Model

In this present work, a parametric study with various temperature and pressure at organic turbine inlet has been considered to determine efficiency and performance of organic fluid in system. The following assumptions are there to simplify the analysis, also taking energy analysis

1. Assumed all the components are steady-state process and steady flow.
2. The changes in the kinetic energy and the potential energy are assumed to be negligible.
3. There are negligible heat and pressure loss in pipes that are connecting all the components to each other.
4. Expander and pumps work adiabatically.
5. Pressure drops in feed heater and condenser are neglected.
6. It is assumed the vapor after expansion is saturated.
7. Liquid after pump 1 is saturated.
8. No pressure loss in evaporator.
9. Constant heat source and 100 % is solar collector efficiency.

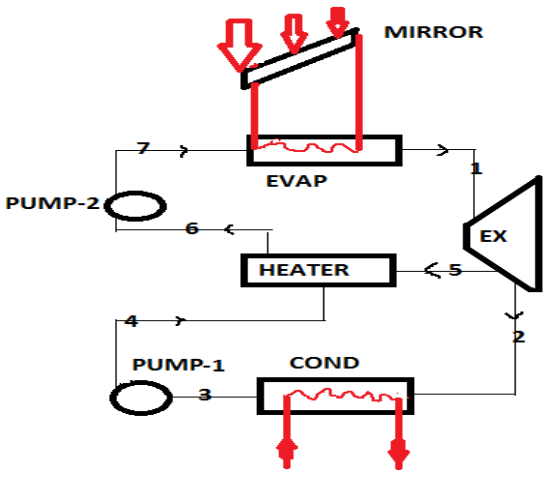


Figure: 3 Model for organic Rankine cycle with regeneration

4.2 Energy Analysis

Based on assumptions, the equations for mass balance and energy are written for each component. Each component in a solar heated source organic Rankine cycle plant is shown in Fig.3 considered as control volume.

Mass Balance

$\sum m_{in} = \sum m_{out}$

Energy balance

$Q - W + \sum m_{in} - \sum m_{out} = 0$

4.3 Energy changes in the each component of organic Rankine cycle with regeneration cycle plant

4.3.1 Organic Rankine expander

Organic expander is a work obtaining device in which organic fluid is expanded from evaporator pressure to condenser pressure adiabatically. The isentropic work output of expander.

$W_{EX} = m_f * (h_1 - h_{2s})$

Organic expander efficiency given as,

$\eta_{EX} = (h_1 - h_2)/(h_1 - h_{2s})$

Actual organic turbine work is

$W_{EX} = (h_1 - h_2)$

4.3.2 Condenser

Condenser is a heat exchanger in which heat is rejected to environment is given by

$Q_{cond} = (m_f - m_x) * (h_2 - h_3)$

4.3.3 Organic pump 1

Organic pump is used for increasing pressure of organic fluid from condenser pressure to boiler pressure. Ideal work of organic pump

$W_{OPi} = (m_f - m_x) * v_3 * (P_5 - P_2)$

Organic pump efficiency as,

$\eta_{OP} = W_{OPi} / W_{OP}$

Actual organic pump work is given by

$W_{OP1} = m_f * v_3 * (P_5 - P_2) / \eta_{OP}$

4.3.4 Organic pump 2

Organic pump is used for increasing pressure of organic fluid from condenser pressure to boiler pressure. Ideal work of organic pump.

$W_{OPi} = m_f * v_6 * (P_1 - P_5)$

Organic pump efficiency as,

$\eta_{OP} = W_{OPi} / W_{OP}$

Actual organic pump work is given by

$W_{OP2} = m_f * v_6 * (P_1 - P_5) / \eta_{OP}$

4.3.5 Feed heater

Feed water heater is the device in which the vapor is extracted from the turbine and mixes with liquid and heat is transferred from vapor to the liquid. And feed liquid is heated.

Energy balance in feed heater is given as

$m_f * h_6 = (m_f - m_x) * h_4 + m_x * h_5$

4.3.6 Evaporator

Evaporator is a device in the organic fluid is heated by solar collectors heater and working fluid is converted in to the vapor this vapor goes to the expander.
Heat is given by evaporator per unit mass as

$q_s = h_7 - h_1$

Total heat supplied to the working fluid from solar energy collector

$Q_s = I_s * A_s$

Mass flow rate is calculated as

$m_f = Q_s / q_s$

4.3.7 Efficiency of Organic Rankine cycle

It is the ratio of the net work output of ORC and total heat supplied in ORC

$\eta_{ORC} = (W_{OT} - W_{OP1} - W_{OP2}) / Q_S$

4.4 Exergy Analysis

Exergy loss or destruction is given by

$$\dot{E}D_i = \sum(\dot{m}e)_{in} - \sum(\dot{m}e)_{out} + \left[\sum\left(\dot{Q}\left(1 - \frac{T_o}{T}\right)\right)_{in} + \sum\left(\dot{Q}\left(1 - \frac{T_o}{T}\right)\right)_{out}\right] \pm \sum \dot{W}$$

4.5 Exergy analysis of the each component of the organic Rankine cycle plant with regeneration

Exergy destruction in organic expander given as

$ED_{EX} = m_f*[(h_2 - h_1) - T_0*(s_2 - s_1)] + m_{x*}[(h_5 - h_2) - T_0*(s_5 - s_2)] - W_{EX}$

Exergy destruction in condenser given as

$ED_{cond} = (m_f - m_x)*[T_0*(s3-s2) + q_r*T_0/T_c]$

Exergy destruction in pump given as

$EDpump1 = (m_f - m_x)*T_0*(s_4-s_3)$

Exergy destruction in pump 2 given as

$EDpump\ 2 = m_f*T_0*(s_7-s_6)$

Exergy destruction in the feed heater given as

$ED_{HE} = m_x*Ex_5 + (m_f - m_x)*Ex_4 - m_f*Ex_6$

Exergy destruction in the evaporator given as

$ED_{EVAP} = m_f*[T_0*(s1-s7) - qs*T_0/T_H]$

Exergy transfer from evaporator given as

$ET_{EVAP} = Qs*(1 - T0/T_H)$

Second law efficiency of orc plant given as

$\dot{\eta}_{second} = (W_{EX} - W_{pump1} - W_{pump2}) / ET_{EVAP}$

Exergy destruction ratio given as

$EDR = (ED_{EX} + ED_{cond} + ED_{pump1} + ED_{pump2} + ED_{HE} + ED_{EVAP}) / ET_{EVAP}$

5. Results and Discussion

A computational model is developed by using Engineering equation Solver (Klein and Alvarado, 2005) for evaluating Exergy and the energy analysis of organic Rankine cycle plant with Solar reheating source and Regeneration from vapor bled of. The input data for evaluation are mentioned in chapter 4 except the parameter, whose effect is discussed in particular plot, has been varied. The following input parameters have been taken for computation of first law and second law efficiency and results are given below.

Organic expander inlet pressure
$P_1 = 4000$ kPa
Organic expander inlet temperature
$T_1 = 100\ ^{\circ}C$
Isentropic efficiency of Organic expander
$\eta_{EX} = 0.80$
Condenser fixed temperature
$Tc = 35^0$ C
Isentropic efficiency of both pumps
$\eta_{pump} = 0.60$
Intermediate or bled off pressure
$P_5 = 1000$ kPa
Organic expander inlet pressure
$P_1 = 2500$ to 4500 kPa
Organic expander outlet pressure
$P_2 = 500$ kPa
Solar irradiation on CSP collector
$I_S = 700\ W/m^2$
Condenser Temperature
$Tc = 35\ ^{\circ}C$
Constant heat source temperature
$T_H = 127^0C$
Dead State Temperature
$To = 25^0C$
Organic fluid used
R404A, R410A, R407C and R134a

5.1 Comparisons of different working fluids with Regeneration and Solar reheating source

Figure 4 to 6 shows comparison of the efficiency against the organic turbine inlet pressure and temperature. It is obvious that the efficiency of organic Rankine cycle increases with regeneration. By using the regeneration heat supplied to the organic cycle plant decreases hence the rate of evaporation increase which results output increases and hence the organic Rankine cycle efficiency increases.

5.2 Comparison of the various organic fluids

Figure 4 to 6 shows variation of efficiencies of the system at organic turbine inlet pressure, temperature, mass of vapor extracted, and the comparison fluids also done to the maximum work done by the turbine, Among all organic fluid the shows maximum efficiency of the

organic Rankine cycle which is about 16.51% and R134a, R407C, R410A and R404A have maximum organic Rankine cycle efficiency of 12.37%, 15.75%, 16.51.% and 15.34% respectively at 4000kPa maximum pressure and 200˚C maximum temperature of ORC fluid.
And mass of fluid extracted at intermediate pressure also plotted in figure with respect to the inlet temperature of organic expander.

5.3 Exergy efficiency

Variation of the Exergy efficiency of various organic fluids with maximum pressure and maximum temperature, of organic cycle is shown in figure 7 to 9. It is seen that the Exergy efficiency of the organic Rankine cycle increases with maximum pressure and maximum temperature.

5.4 Exergy destruction ratio

Exergy destruction ratio is plotted with respect to the inlet temperature and pressure of expander and what was the effect on cycle founded.it is shown in fig10 and 11.

5.5 Expander output

Expander output with respect to the temperature and pressure inlet of the expander is plotted in figures 12 and 13.

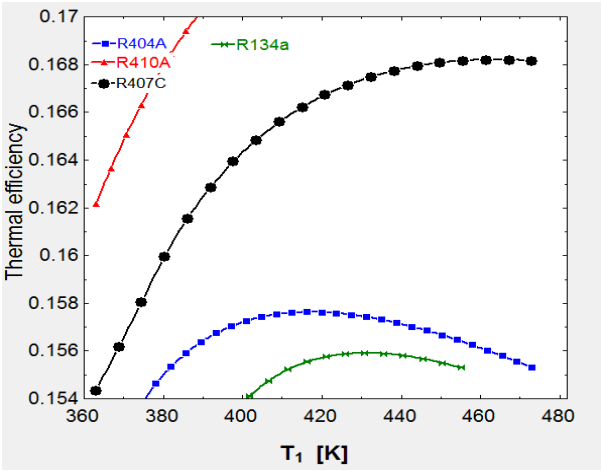


Figure 4: Variation of thermal efficiency of organic rankine cycle with expander inlet tempreture.

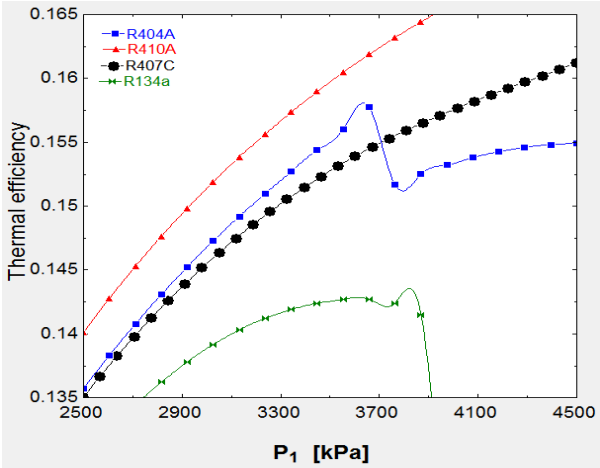


Figure 5: Variation thermal efficiency of organic rankine cycle with turbine inlet pressure

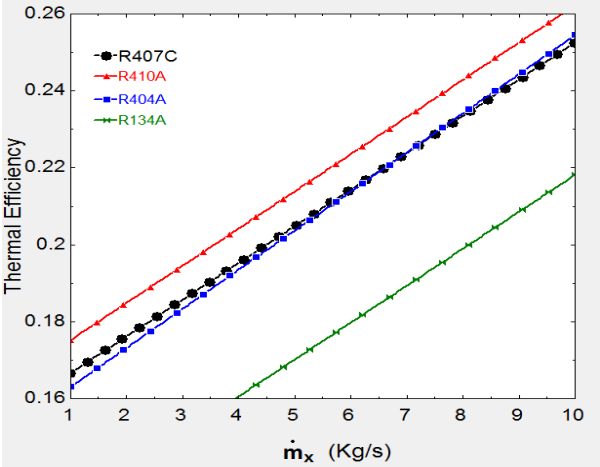


Figure 6: Variation of thermal efficiency with extraction mass from expander

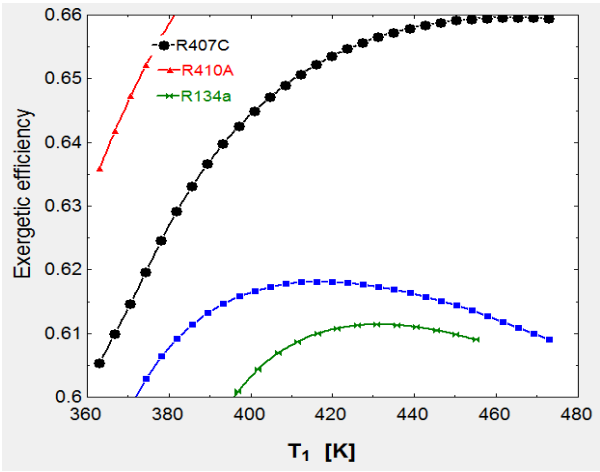


Figure 7: Variation of exergetic efficiency with inlet temperature of expander

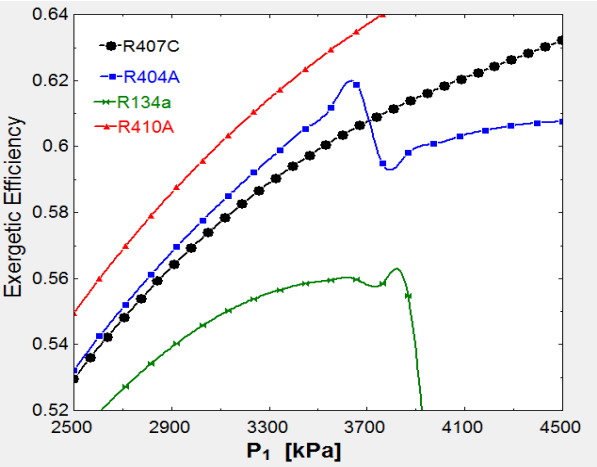


Figure 8: Variation of exergetic efficiency with the inlet pressure of expander

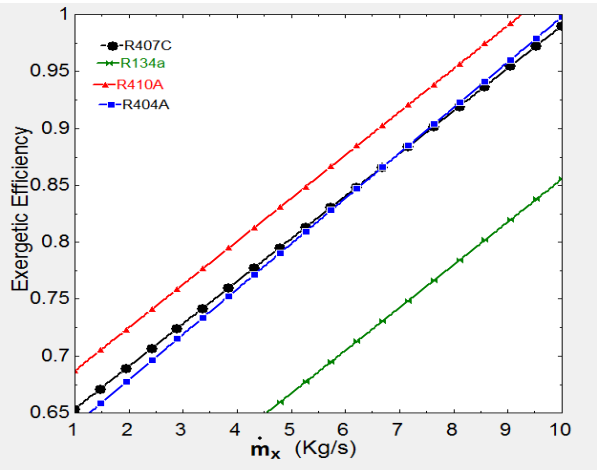


Figure 9: Variation of exergetic efficiency with mass extracted from expander

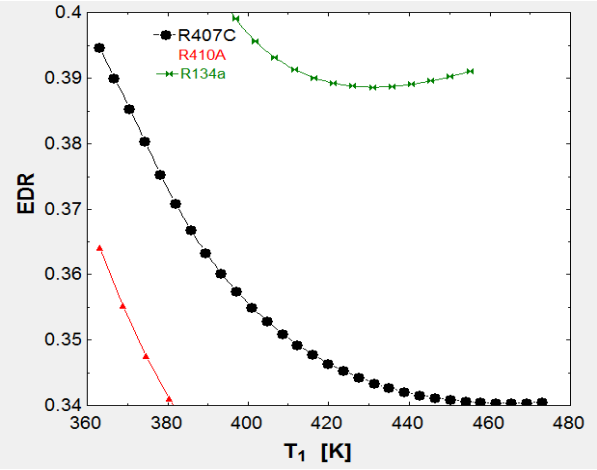


Figure 10: Variation of EDR with the inlet temperature of expander

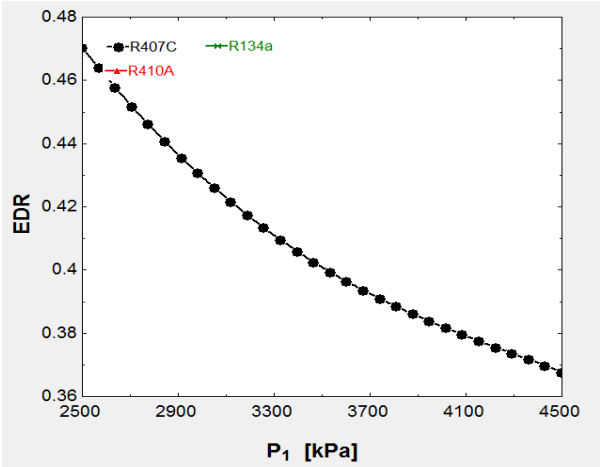


Figure 11: Variation of EDR with the inlet pressure of expander

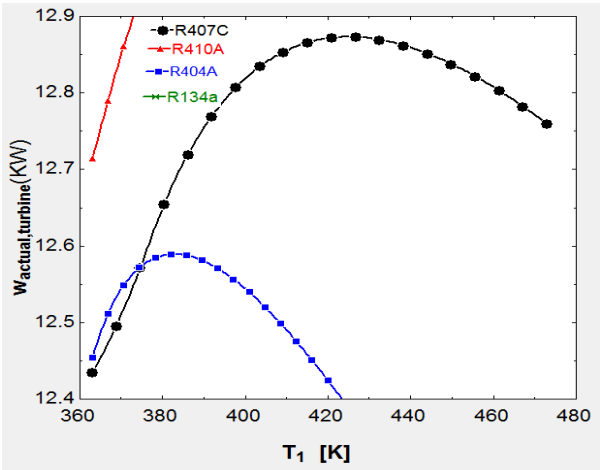


Figure 12: Variation of turbine work output with the inlet temperature of the expander

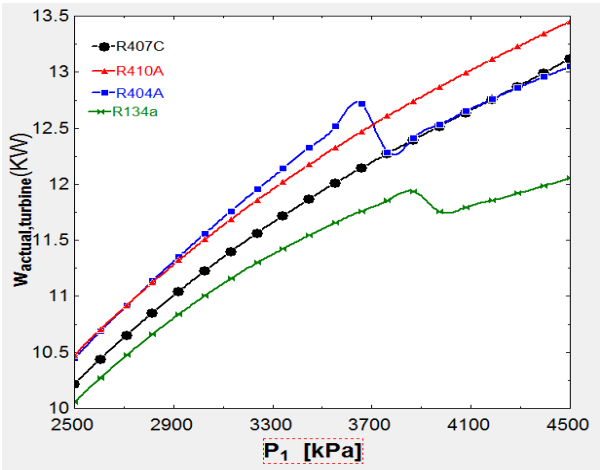


Figure 13: Variation work output of expander with the inlet pressure of expander

6. Conclusion

An extensive first law (energy) and second law (Energy) analysis of R134a, R407C, R410A, and R404A Organic fluids in cycle with regeneration and reheating is presented. Conclusions of this analysis are summarized as follows:

1. Exegetic efficiency (second law efficiency) and Energy efficiency (first law efficiency) of Organic Rankine cycle using R134a, R407C, R410A, and R404A organic fluids with regeneration is higher than without regeneration.
2. R410A have higher first law efficiency and Exergetic efficiency (second law efficiency) in Organic Rankine cycle but R407C have higher first law efficiency and Exergetic efficiency (second law efficiency) improvement from basic system.
3. From solar reheating source there is no effect of area of solar collectors on the first law and second law efficiency.
4. Exergetic efficiency of plant increases rapidly with respect to the inlet expander temperature. And maximum for R410A among all selected working fluids.
5. Exergetic efficiency for the R410A is maximum among the other selected working fluids and increases gradually with inlet pressure of expander.
6. Thermal efficiency for the plant is increases with respect to inlet temperature of expander.
7. Thermal efficiency for the R410A is maximum among the selected working fluids and increases gradually with respect to the inlet expander temperature.
8. Exergy Destruction Ratio is lowest for R410A and decreases with the inlet temperature of the expander.
9. Work output for R410A is maximum among the other selected working fluids .And increases with increase in inlet temperature.
10. Since work output is maximum for the R404A than R410A but decrease rapidly at 3700kPa pressure.
11. Thermal efficiency is increases with the extraction mass for regeneration from the expander
12. Exergetic efficiency is also increases with the increase in mass extraction. That's why R410A is selected for organic Rankine cycle power generation and this also suitable for low global warming and ozone depletion.

References

[1] Kelly B, Herrmann U, Hale MJ. "Optimization studies for integrated solar combined cycle systems" In: Proceedings of solar forum 2001, solar energy: the power to choose; 2001 April 21–25, Washington DC, USA.

[2] He Ya-Ling, Mei Dan-Hua, Tao Wen-Quan, Yang Wei-Wei, Liu Huai-Liang. "Simulation of Parabolic trough solar energy generation system with organic Rankine cycle" Applied Energy 2012;97 :630–641.

[3] Gang Pei, Li Jing, Jie Ji. "Analysis of low temperature solar thermal electric generation using regenerative organic Rankine cycle" Appl Thermal Eng 2010; 30:998–1004.

[4] Li C, Kosmadakis G, Manolakos D, Stefanakos E, Papadakis G, Goswami DY."Performance investigation of concentrating solar collectors coupled with a transcritical organic Rankine cycle for power and seawater desalination cogeneration Desalination" 2013;318:107–17.

[5] Nafey AS, Sharaf MA. "Combined solar organic Rankine cycle with reverse osmosis desalination process: energy, exergy, and cost evaluations" Renew Energy 2010; 35:2571–2580.

[6] Sharaf MA, Nafey AS, García-Rodríguez Lourdes. "Exergy and thermo-economic analyses of a combined solar organic cycle with multi-effect distillation (MED) desalination process Desalination" 2011,272:135–147.

[7] Delgado-Torres AM, García-Rodríguez Lourdes. "Preliminary design of seawater and brackish water reverse osmosis desalination systems driven by low temperature solar organic Rankine cycles (ORC)" Energy Conveyers Manage 2010; 51:2913–2920.

[8] Delgado-Torres AM, García-Rodríguez Lourdes. "Analysis and optimization of the low temperature solar organic Rankine cycle (ORC)" Energy Convers Manage 2010; 51:2846–56.

[9] Al-Sulaiman Fahad A, Hamdullahpur Feridun, Dincer Ibrahim" Performance assessment of a novel system using parabolic trough solar collectors for combined cooling, heating, and power production" Renew Energy 2012;48:161–72.

[10] Al-Sulaiman Fahad A, Dincer Ibrahim, Hamdullahpur Feridun. "Exergy modeling of a new solar driven trigeneration system" Sol Energy 2011; 85:2228–2234.

[11] Al-Sulaiman Fahad A. "Energy and sizing analyses of parabolic trough solar collector integrated with steam and binary vapour cycles" Energy 10.1016/ j. energy.2013.05.020. [inpress].

[12] Fahad Al-Sulaiman Fahad" Exergy analysis of parabolic trough solar collectors integrated with combined steam and organic Rankine cycles" 2013 Elsevier Ltd.

[13] Milad Ashouri, Mohammad Hossein Ahmadi , Michel Feidt "Performance Analysis of Organic Rankine Cycle Integrated with a Parabolic Through Solar Collector" licensee MDPI, Basel, Switzerland.

[14] Dimityr Popov "Innovative solar augmentation of gas turbine combined cycle plants" 2013 Elsevier Ltd.

[15] Wang, X.D., Zhao, L., Wang, J.L., Zhang, W.Z., Zhao, X.Z., Wu, W., 2010b"Performance evaluation of a low-temperature solar Rankine cycle system utilizing R245fa" Solar Energy 84, 353–364.

[16] S. Quoilin, M. Orosz, H. Hemond, V. Lemort "Performance and design optimization of a low-cost solar organic Rankine cycle for remote power generation" Solar Energy 85 (2011) 955-966.

[17] Maria E. Mondejar , Fredrik Ahlgren , Marcus Thern , Magnus Genrup "Quasi-steady state simulation of an organic Rankine cycle for waste heat recovery in a passenger vessel" Applied Energy 185 (2017) 1324–1335.

[18] Harrison Warren, Pedro J. Mago, Alta Knizley, Rogelio Luck "Performance enhancement of a power generation unit–organic Rankine cycle system through the addition of electric energy storage" Journal of Energy Storage 10 (2017) 28–38.

[19] Ayad M. Al Jubori , Raya K. Al-Dadah , Saad Mahmoud , Ahmed Daabo "Modelling and parametric analysis of small-scale axial and radialoutflow turbines for Organic Rankine Cycle applications" Applied Energy 190 (2017) 981–996.

[20] Jui-Ching Hsieh a,⇑, Ben-Ran Fu b, Ta-Wei Wanga, Yi Cheng a, Yuh-Ren Lee a, Jen-Chieh Chang "Design and preliminary results of a 20-kW transcritical organic Rankine cycle with a screw expander for low-grade waste heat recovery" Applied Thermal Engineering 110 (2017) 1120–1127.

[21] Dong Junqi , Zhang Xianhui , Wang Jianzhang "Experimental investigation on heat transfer characteristics of plat heat exchanger applied in organic Rankine cycle (ORC)" Applied Thermal Engineering 112 (2017) 1137–1152.

[22] Ayad Al Jubori , Raya K. Al-Dadah , Saad Mahmouda, A.S. Bahr Ennil , Kiyarash Rahbar Three dimensional optimization of small-scale axial turbine for low temperature heat source driven organic Rankine cycle" Energy Conversion and Management 133 (2017) 411–426.

[23] Constantine N. Michos , Simone Lion , Ioannis Vlaskos , Rodolfo Taccani "Analysis of the backpressure effect of an Organic Rankine Cycle (ORC) evaporator on the exhaust line of a turbocharged heavy duty diesel power generator for marine applications" Energy Conversion and Management 132 (2017) 347–360.

International Journal of Research in Engineering and Innovation (IJREI)
journal home page: http://www.ijrei.com
ISSN (Online): 2456-6934

Experimental investigation for enhancing thermal performance of vapour compression refrigeration system using nano fluids

R.S. Mishra, Devendra Kumar

Department of Mechanical, Production & Industrial and Automobiles Engineering
Delhi Technological University, Delhi-110042 (India)

Abstract

For increasing first law efficiency in terms of COP and Second law efficiency (Exergetic Efficiency) of VCR systems.the experiment is performed on VCR system to study the effect of silver oxide Nano particle(50nm) in base fluid of ethyl glycol (50:50 ratio with water) with concentration factor 0.02 to 0.06g by volume % on hot side of system (condenser side). For high efficiency out-put, the plate type heat exchanger has been taken in the VCR system. Test results show that the performance parameters such as exergetic efficiency of the system improved in the range of 1.9-5.96% and heating capacity was improved by 26-82% respectively by using 0.06 Vol% silver Nano fluid compared to water as cold based fluid for considerable range of cold base fluid flow rate. It was observed that the exergy destruction is decreasing in the range of 29-31.28%, 65.77-70.01%, 14.31-16.03%, 17-23% in compressor, condenser, evaporator and expansion valve respectively. High volume ratio (0.015 Vol%) of silver Nano fluid shows a very less effect on thermal performance parameters of system for different base fluid mass flow rates.
© 2017 ijrei.com. All rights reserved

.*Keywords:* VCR, Nano Materials, Performance Evaluation , Experimentation

1. Introduction

The increasing demand of energy leads to global warming and environmental imbalance in the society. In order to satisfy the needs, utilization of energy available at the systems should be in best way. The primary function of system based on vapour compression refrigeration technology is to reject heat at higher temperature and absorb at lower temperature. Heat rejected by condenser generally not utilized for constructive applications instead of this heat is wasted either to the surrounding or to the water circulating from cooling tower. Like milk plant, vapour compression refrigeration system is used for cooling of milk for the purpose of preserving the same for long time and heat rejected by condenser is wasted to water circulating from cooling tower. In same plant large amount heat is also required for heating of milk to kill bacteria. This much amount of heat is taken either from burning of diesel or other non-renewable resources. It is very important to increase coefficient of performance, exergy efficiency, and sustainability index on the other hand reduction of exergy destruction in the components of vapour compression refrigeration system. Along with above mentioned parameters, it is also important to utilization of energy available at vapour compression refrigeration system. In view of above factors experimental test rig was fabricated which is used for both cooling and heating of water. Cooling is done by evaporator and utilizes the waste heat from condenser is for heating of water. Silver nanofluid with 0.01% and 0.05% volume concentration ratio used as cooling base fluid for enhancing of heating. The purpose of using of nanofluid to improve the performance parameters like effectiveness, exergy efficiency, sustainability index and decrease the irreversibility in components of VCR. The leakage test of developed test rig was done by filling of nitrogen gas. After successful completion of leakage test, test rig has been evacuated by using of vacuum pump. The vacuum was held for 30 hr and after that the correct amount of R22 was charged in refrigerant circuit. After completion of leakage testing and charging of refrigerant, cooling base fluid pump, cooling secondary fluid pump, chilled water pump and chilled secondary fluid pump was switched on. Chilled water mass flow rate (300 kg/hr) remain constant for considered number of experiments. Thermostat attached with heating coil used to maintain constant inlet

Corresponding author: R.S. Mishra
Email Id: rsmishra@dce.ac.in

temperature (T_7 =26^{0}C) of chilled secondary fluid and thermostat of same configuration attached with cooling coil for constant inlet condition (T_{11} =22^{0}C) of cooling secondary fluid. Then compressor of refrigerant circuit was switched on. Before collection of experimental data, system was allowed to run until the steady state condition was reached. Experimental data were recorded six times during one hour. Experiments were done with water followed by 0.01 and 0.05 vol% silver nanofluid as cooling base fluid with same above described procedure. It should be noted that any fluid to be heated or cooled can be used as cooling or chilled secondary fluid. In the present study water is used in both cooling and secondary fluid circuit.

2. Literature Review

S.No	Author	Journal	Year	Findings	Conclusions
1	Elcock et al.	Argonne National Laboratory	2007	They found that TiO_2 nanoparticles can be used as additives to enhance the solubility of the mineral oil with the hydro fluorocarbon (HFC) refrigerant. Author also reported that refrigeration systems using a mixture of HFC134a and mineral oil with TiO_2 nanoparticles appear to give better performance by returning more lubricant oil to the compressor	TiO_2 nanoparticles can be potentially used in refrigeration system.
2	Hindawi	Hindawi	2009	It has been carried out by experimental study on boiling heat transfer characteristics of R22 refrigerant with Al_2O_3 nanoparticles and found that the nanoparticles enhanced the refrigerant heat transfer characteristics by reducing bubble sizes	Nanoparticles can be used to enhance heat transfer capabilities
3	Eastman et al.	Mater Res Soc Symp Proc	1996	They investigated the pool boiling heat transfer characteristics of R11 refrigerant with TiO_2 nanoparticles and showed that the heat transfer enhancement reached by 20% at a particle loading of 0.01 g/L.	TiO_2 nano particles can be used to enhance the heat transfer capability of R11 refrigerants.
4	Liu et al.	Chemical Engineering and Technology	2006	They investigated the effects of carbon nanotubes (CNTs) on the nucleate boiling heat transfer of R123 and HFC134a refrigerants. Authors reported that CNTs increase the nucleate boiling heat transfer coefficients for these refrigerants.	CNT have a potential to increase the nucleate boiling heat transfer coefficient of the refrigerants.
5	Jiang et al.	International Journal of Thermal Sciences	2009	The experimental results showed that the thermal conductivity of carbon nanotubes (CNT) Nano refrigerants are much higher than those of CNT–water Nano fluids or spherical nanoparticle–R113 Nano refrigerants. Authors reported that the smaller the diameter of CNT larger the thermal conductivity enhancement of CNT Nano refrigerant.	CNT with smaller diameter can be used to enhance the thermal conductivity of the refrigerants
6	Hwang et al.	Current applied Physics	2006	They suggested that thermal conductivity enhancement of Nano fluids is greatly influenced by thermal conductivity of nanoparticles and base fluid. For instance, thermal conductivity of water based Nano fluid with multiwall carbon nanotubes has noticeably higher thermal conductivity compared to SiO_2 nanoparticles in the same base fluid.	Multiwall carbon nanotubes has the higher thermal conductivity among the other Nano particles.
7	Yoo et al.	Thermochimica Acta	2007	They argued that surface to volume ratio of nanoparticles is a dominant factor. Surface to volume ratio is increased with smaller sizes of nanoparticles. 150% thermal conductivity enhancement was observed in poly (a-olefin) oil by addition of multiwall carbon nanotubes (MWCNT)	Surface to volume ratio is an dominant factor to enhance the thermal properties of Nano fluid.

8	Yang.Y	University of Kentucky	2006	He reported, a 200% thermal conductivity enhancement for poly (a-olefin) oil containing 0.35% (v/v) MWCNT. It is important to note that this thermal conductivity enhancement was accompanied by a three order of magnitude increase in viscosity.	MWCNT nanoparticles can increase the thermal conductivity as well as viscosity
9	Eastman	Applied Physics Letters	2001	He observed 40% thermal conductivity enhancement for ethylene glycol with 0.3% (v/v) copper nanoparticles (10 nm diameter), although the authors also added that about 1% (v/v) thioglycolic acid helpful for dispersion of nanoparticles in base fluid. The addition of this dispersant yielded a greater thermal conductivity than the same concentration of nanoparticles in the ethylene glycol without the dispersant.	Dispersant can be used to enhance the conductivity.
10	Kang et al.	Experimental Heat Transfer	2006	They reported a 75% thermal conductivity enhancement for ethylene glycol with 1.2% (v/v) diamond nanoparticles between 30 and 50 nm diameter. Despite of these remarkable results, some researchers also measured the thermal conductivity of Nano fluids and found no anomalous results.	Diamond nanoparticles can be used to enhance the thermal conductivity of ethylene glycol.
11	Lee et al.	International Journal of Heat and Mass Transfer	2008	They revealed that optimum combination of pH level and surfactant leads to 10.7% thermal conductivity enhancement of 0.1% Cu/H2O Nano fluid. They also concluded that during Nano fluid preparation stage thermal conductivity of Nano fluid is affected by pH level and addition of surfactant.	PH level and surfactant potentially used to enhance the thermos-physical properties.
12	Jiang et al.	International Journal of Thermal Sciences	2009	They added that thermal conductivity of Nano fluids also depend on the nanoparticles size and temperature	Size and temperature can be affected to the thermal properties of Nano-particles.
13	Wu et al.	Journal of Engineering Thermophysics	2008	They observed that the pool boiling heat transfer was enhanced at low TiO_2 nanoparticles concentration in R11 but deteriorated under high nanoparticles concentration.	Low concentration of TiO_2 in R11 can affectively enhanced the pool boiling heat transfer.
14	Trisaksri et al	International Journal of Heat and Mass Transfer	2009	They investigated TiO_2 in HCFC 141b in a cylindrical copper tube and found that the nucleate pool boiling heat transfer deteriorated with increasing nanoparticle concentrations especially at higher heat fluxes.	Increasing concentration and heat flux can badly affect to the thermal properties of Nano particles.
15	Hao et al.	International Journal of Refrigeration	2009	They investigated flow boiling inside a smooth tube at different nanoparticles concentration, mass fluxes, heat fluxes, and inlet vapor qualities in order to analyze the influence of nanoparticles on the heat transfer characteristics of refrigerant-based nanofluid. Authors observed that the heat transfer coefficient of refrigerant-based nanofluid in flow boiling is larger than that of pure refrigerant and the maximum enhancement is about 29.7% when observed with a mass fraction of 0–0.5 wt%.	Nanoparticle can enhance the heat exchange capability of refrigerants.

16	Hao et al.	International Journal of refrigeration	2010	They studied experimentally the nucleate pool boiling heat transfer characteristics of refrigerant/oil mixture with diamond nanoparticles. The results indicate that the nucleate pool boiling heat transfer coefficient of R113/VG68 oil mixture with diamond nanoparticles is larger than that of R113/oil mixture by 63.4%. Enhancement in same factor increases with the increase of nanoparticles concentration in the nanoparticles/oil suspension and decreases with the increase of lubricating oil concentration.	Refrigerant/oil mixture with diamond nanoparticles can be used to enhance the thermal conductivity.
17	Wang et al.	Proceedings of the 4th symposium on refrigeration and air condition	2006	They carried out an experimental study of boiling heat transfer characteristics of R22 with Al_2O_3 nanoparticles and found that nanoparticles enhanced the refrigerant heat transfer characteristics by reduction of bubble sizes that moved quickly near the heat transfer surface.	R22 with Al_2O_3 nanoparticles showed the better thermal properties
18	Li et al.	Proceedings of the 12th symposium on engineering thermo physics	2006	They investigated the pool boiling heat transfer characteristics of R-11 with TiO_2 nanoparticles and showed that the heat transfer enhancement reached by 20% at a particle loading of 0.01 g/L.	R-11 with TiO_2 nanoparticles and showed the pool boiling heat transfer characteristics.
19	Peng et al.	International Journal of Refrigeration	2009	They investigated the influence of CuO nanoparticles on the heat transfer characteristics of R-113 refrigerant-based nanofluids and presented a correlation for prediction of heat transfer performance of refrigerant based nanofluids. Authors reported that the heat transfer coefficient of refrigerant-based nanofluids is higher than that of pure refrigerant.	CuO in 113 refrigerant-based nanofluids can enhanced the heat transfer characteristics
20	Kumar and Elansezhian	J Front Mech Engg	2014	They experimentally investigated the effect of varying concentration of ZnO nanoparticles on various performance parameters like COP, suction temperature, input power and pressure ratio with 152a as working fluid in vapour compression refrigeration system. They found that 0.5% v ZnO nanoparticles with R152a gives maximum COP of 3.56 and 21% reduction in power input. Pressure ratio decreases with increase in ZnO concentration.	
21	Mahbubul et al.	International Journal of Heat and Mass Transfer	2013	They measured thermo physical properties, pressure drop and heat transfer performance of Al_2O_3 nanoparticles and R-134a mixture. Thermal conductivity of Al_2O_3/R-134a nano refrigerant increased with temperature and augmentation of particle concentration. It was also observed that pumping power, viscosity, pressure drop, and heat transfer coefficients of the nanorefrigerants show significant increment with the increase of volume fractions. The frictional pressure drop also shows rapid increment with 3 vol. % particle fraction.	The pumping power, viscosity, pressure drop, and heat transfer coefficients of the nano refrigerants shows significant increment with the increase of volume fractions.

3. Description of experimental test rig and instrumentation

As shown in Fig.1 experimental test rig comprising of refrigerant, chilled water, chilled secondary fluid, cooling base fluid and cooling secondary fluid circuits. Refrigerant circuit used R22 as working fluid consists of single cylinder hermetically sealed reciprocating compressor, plate type condenser, thermal expansion valve, plate type evaporator and accessories like filter, drier, power meter used for measurement of electricity consumed by compressor and sight glass.

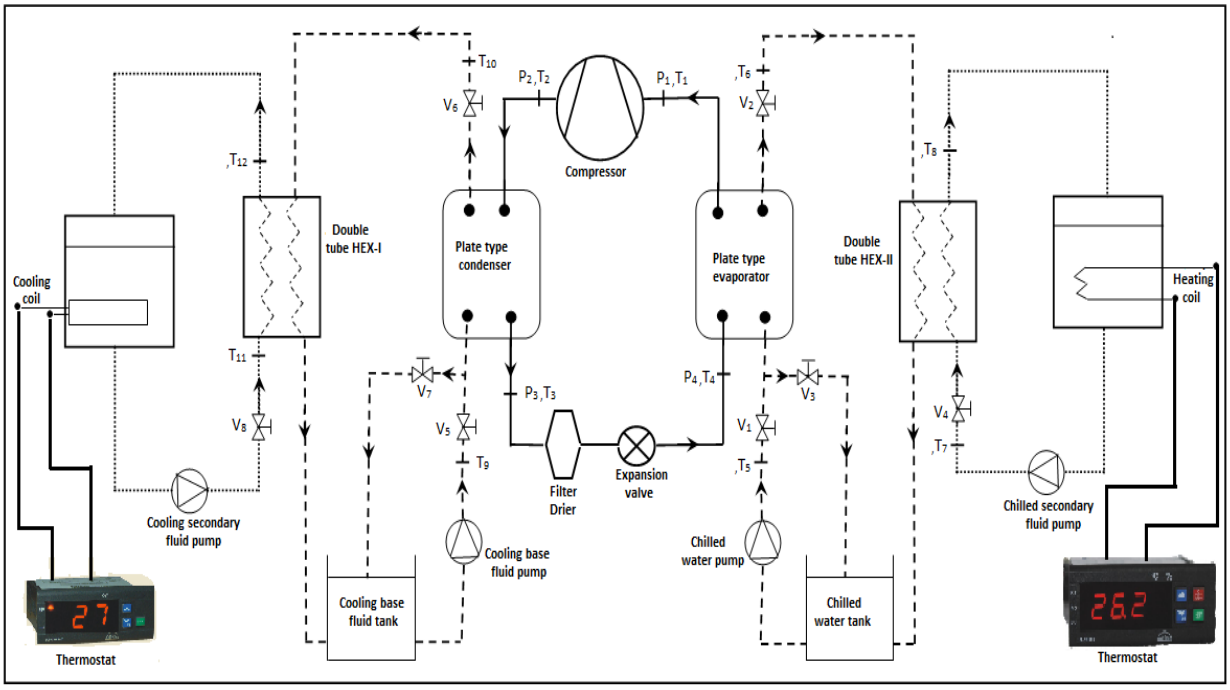


Figure: 1 Experiment test rig of vapour compression refrigeration system

Due to high heat transfer coefficient and compact design, plate type heat exchangers were used as evaporator and condenser. For convenient and easy installation valves were mounted at various desired locations. The whole system is placed in well insulated chamber within 0.03°C control to the surrounding conditions.

Cooling base fluid may be supplied with either water or nanofluid .Chilled water circuit consist of plate type evaporator, double tube heat exchanger for heat transfer between chilled water & chilled secondary fluid and chilled water pump for circulation of chilled base fluid throughout the circuit. Cooling base fluid circuit consist of plate type condenser, tube in tube heat exchanger for exchange of heat between cooling base fluid & cooling secondary fluid and cooling base fluid pump for circulation of cooling base fluid. Water is supplied to both chilled and cooling secondary circuit. Chilled secondary circuit comprised of chilled secondary fluid pump, double tube HEX-I and thermostat for maintaining the temperature of chilled secondary fluid. Cooling secondary circuit consists of double tube HEX-II, cooling secondary fluid pump and thermostat for maintaining the temperature of cooling secondary fluid. Piping network of discussed circuits is well insulated with respect to environmental conditions.

In order to gauge the various operating parameters such as refrigerant pressure, temperatures at desired points of discussed circuits, flow rate and electricity consumption, a requisite instrumentation system is installed in the experimental test rig. RTD type thermocouples were positioned for measurement of temperatures at desired locations of experimental test rig. Pressures at compressor suction, condenser inlet, inlet of expansion valve and evaporator's inlet were measured using calibrated bourdon tube type pressure manifold.

Electricity consumed by compressor is measured by digital watt meter. Water flow rates through secondary circuits were measured by using a digital balance capable of reading 0.001 g and a stopwatch capable of reading 0.01 s.

4. Energy and Exergy Analysis

The idea of energy efficiency was given first law of thermodynamic. Energy efficiency or cooling effectiveness is the ratio of output in the form cooling effect to input in the form of energy consumed by compressor. First law analysis limited to evaluate only cooling effectiveness of the system as mentioned below.

4.1 Cooling effectiveness in terms of COP

$$\varepsilon_{cooling} = \frac{\dot{Q}^{+}_{evap}}{\dot{W}^{+}_{comp}}$$

Second law of thermodynamics gives the idea of exergy generation in work producing as well as work consuming systems. Exergy generation also gives the concept of amount of constructive or destructive energy for the systems and impact on surrounding Exergy destruction in each component of considered system is calculated as per following equations

Exergy Balance in Compressor

$$\dot{E}_{1-2} = T_a \left[\frac{\dot{m}_f(k_{f2} - k_{f1}) + \dot{W}^{+}_{comp} - \dot{m}_f(j_{f2} - j_{f1})}{T_a} \right]$$

Exergy Balance in Evaporator

$$\dot{E}_{4-1} = \left(T_a \begin{pmatrix} \dot{m}_f(j_{f1} - j_{f4}) - \\ \dot{m}_f(k_{f1} - k_{f4}) \end{pmatrix} + \sum \dot{Q}^{+}_{evap} \left(1 - \frac{T_a}{T_L}\right) \right)$$

Exergy Balance in Condenser

$$\dot{E}_{2-3} = \left(T_a \begin{pmatrix} \dot{m}_f(j_{f3} - j_{f2}) - \\ \dot{m}_f(k_{f3} - k_{f2}) \end{pmatrix} - \sum \dot{Q}^{-}_{cond} \left(1 - \frac{T_a}{T_H}\right) \right)$$

Exergy Balance in Expansion valve

$$\dot{E}_{3-4} = \dot{m}_f \begin{pmatrix} (j_{f4} - j_{f3}) - \\ T_a(k_{f4} - k_{f3}) \end{pmatrix}$$

Exeretic efficiency

$$\xi = \frac{\dot{EP}}{\dot{W}^{+}_{comp}} = \frac{\left|\dot{Q}^{+}_{evap}\left(1 - \frac{T_a}{T_L}\right)\right|}{\dot{W}^{+}_{comp}}$$

Exergy destruction ratio based on exergy output

$$EDR = \frac{\sum \dot{E}_{\alpha}}{\dot{EP}} = \frac{1}{\xi} - 1$$

4.2 Sustainability index

$$£ = \frac{1}{1 - \xi}$$

Cooling base fluid mass flow rate and its temperature rise will leads to evaluation of heating capacity ($\dot{Q}^{-}_{cond}$) of condenser as follow:

$$\dot{Q}^{-}_{cond} = \dot{m}_{cbf} c_{P,cbf} \left(T_{cbf,o} - T_{cbf,i}\right)$$

Similarly chilled water mass flow rate and its temperature fall will leads to evaluation of cooling capacity ($\dot{Q}^{+}_{evap}$) of evaporator as given below:

$$\dot{Q}^{+}_{evap} = m_{chw} c_{P,chw} \left(T_{chw,i} - T_{chw,o}\right)$$

4.3 Specific heat of nano fluid

In order to evaluate the heating capacity of Nano fluid, effective specific heat should be determined. Mass fraction mixture rule is used for calculation of effective specific heat, which is as follow:

$$C_{P,nf} = \frac{(1 - \phi_v)\rho_{bf} C_{P,bf} + \phi_v \rho_P C_{P,p}}{\rho_{nf}}$$

5. Preparation of Nano fluid

In literature one-step and two-step methods are commonly used for preparation of nanofluid. Eastman et al. developed one-step procedure for preparation of nanofluid. In this method problem of agglomeration was reduced by great extent and preparation and dispersion of solid nanoparticles in base fluid concurrently occurred. This method leads to uniform and stable distribution of nanoparticles in the base fluid. In order to produce nanofluids in large scale one step procedure is not economical. Zhu et al. developed another method for preparation of nanofluids called two-step method. In this process nanoparticles directly dispersed in base fluid. Dispersion is done by either bath type or probe type ultrasonicator.

In this manuscript two-step method is adopted for preparation of silver nanoparticles and water mixture. Silver nanoparticles of spherical morphology with average particle size 50 nm size and bulk density 0.312 g/cm^3. The TEM image, UV spectrophotometer analysis and raman analysis of silver nanoparticles presented in Fig. 2-4 respectively. As per 0.01 and 0.05% volume concentration ratio silver nanoparticles were measured by digital balance and mixed with water. Probe type ultrasonicator as shown in Fig.6 was used for stable and uniform distribution of nanoparticles in base fluid for 30 min. As shown in Fig 7-13 shows no settlement of nanoparticles and water mixture were observed after 2, 4, 6, 8, 10, 12 and 14 h respectively. As a result 0.01 and 0.05% volume solution has selected for solubility test. Fig 14-16 shows test plate type heat exchanger used in test rig and setup of VCR respectively.

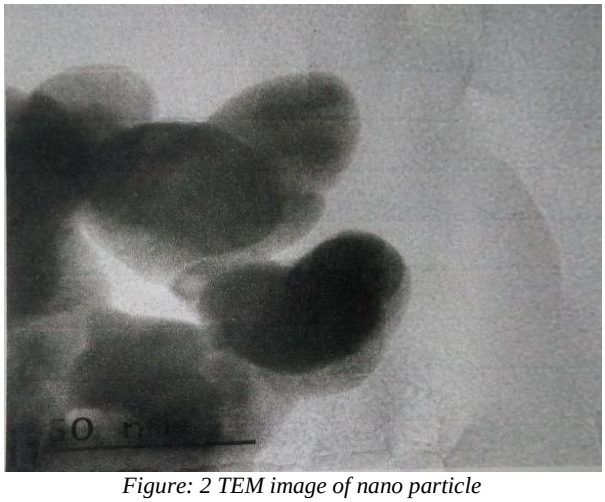


Figure: 2 TEM image of nano particle

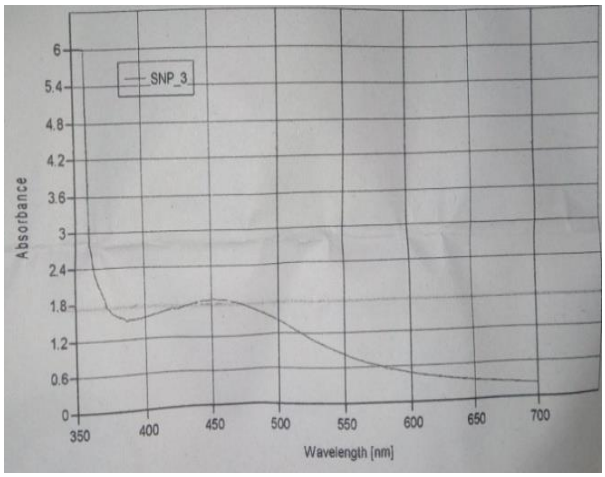


Figure: 3 UV spectrophotometer of silver

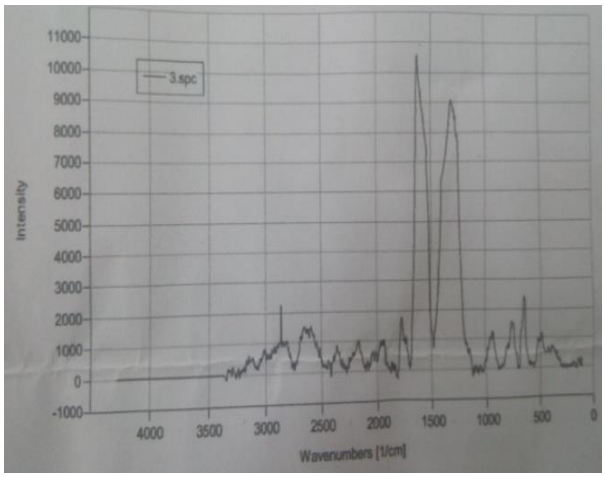


Figure: 4 Raman analysis of silver nanoparticles



Figure: 5 volume concentration ratio silver nanoparticles were measured by digital balance



Figure: 6 Probe type ultrasonicator

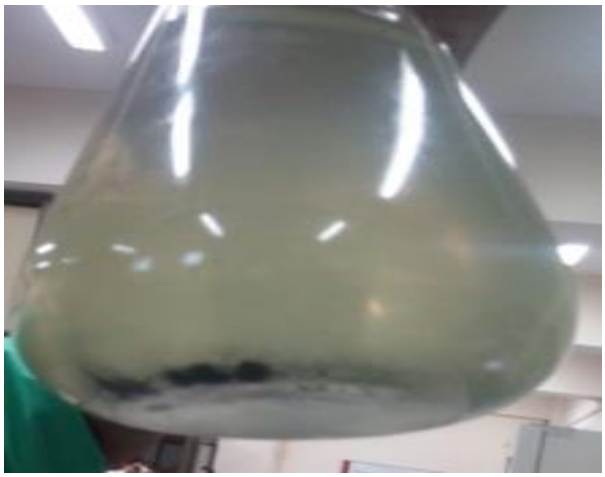


Figure: 7 Nano particle settlement after (2 hours)



Figure: 8 Nano particle settlement after 4 hours



Figure: 11 Nano particle settlement after 10 hours



Figure: 9 Nano particle settlement after 6 hours



Figure: 12 Nano particle settlement after12 hours



Figure: 10 (Nano particle settlement after 8 hours



Figure: 13 Nano particle settlement after 14 hours



Figure: 14 Plate type Heat Exchanger



Figure: 15 Plate type Heat Exchanger



Figure: 16 Plate type heat exchanger with cooling tower in VCR assembly

6. Results and Discussions

Fig.17-18 represents the effect of variation of mass flow rate of cooling base fluid on working pressures of refrigerant circuit. The variation of condensing pressure and evaporating pressure with mass flow rate of cooling base fluid as shown in fig 17-18 respectively. It was observed that with increase of mass flow rate of cooling base fluid, operating pressures decreases due to enhancement of heat exchange between refrigerant and cooling base fluid. Both of these figures also revealed that variation of mass flow rate give a more prominent effect on condensing pressure rather than evaporating pressure. Deviation of evaporation and condensation pressures with various working parameters were studied with water, 0.01 and 0.05 vol. % silver nanofluid as cooling base fluid. Pertaining to evaporation pressure, reveals that water gives highest while 0.05 vol. % silver nanofluids gives lowest evaporating pressure. The average values of condensation pressure for water, 0.01 and 0.05 vol. % silver nanofluid as cooling base fluids are 1417.06, 1393.57 and 1230.73 kpa while their evaporation pressures are 196.13, 192.26 and 169.16 kpa respectively over wide range of cooling base fluid mass flow rate (Fig.17-18). Mean condensation pressure of water and 0.01 vol. % silver nanofluid are greater than 0.005 vol% silver nanofluid by 15.13% and 13.23% respectively. On the other hand average evaporation pressure of water and 0.001 vol. % silver nanofluids are higher than 0.001 vol. % silver nanofluid by 15.94% and 13.65% respectively.
Variation of cooling effectiveness verses mass flow rate of cooling base fluid is shown in Fig.19. It is evident that higher mass flow rate of cooling base fluid responsible for lower compressor work due to decreasing of compressor to evaporator ratio and increases cooling & heating effectiveness. Increases cooling & heating capacity and decrement in compressor work increases the cooling and heating effectiveness of the system. Average cooling effectiveness of system using 0.05 vol. % silver nanofluid as cooling base fluid is higher than that of water by 14.98% as cooling base fluid over considered range of mass flow rate of cooling base fluid. Fig. 20-21 show the impact of mass flow rate of cooling base fluid on exergy efficiency and exergy destruction ratio respectively. Since exergy efficiency is the ratio of useful output in term of cooling capacity $\left[\dot{Q}_f^+ \left(1 - \frac{T_a}{T_L}\right)\right]$ to the input energy given to the system. As discussed input energy given in term of compressor work gets lower down with increase of mass flow rate of cooling base fluid. Like compressor work numerator of exergy efficiency also follow the same trend. Combined effect of both discussed terms increase the exergy efficiency .It is clear that behavior of curve of Fig.20 is almost opposite to the Fig.21.The behavior of trends is due to fact that exergy destruction ratio and exergy efficiency are inversely proportional to each other. Behavior of Sustainability index with change of mass flow rate of cooling base fluid was also analyzed through Fig.22. The sustainability index is the function of exergy efficiency. Trend of sustainability index with mass flow rate of cooling base fluid is almost same as of exergy efficiency with same variable. It is concluded that increase of cooling base fluid mass flow rate put less adverse effect on the environmental conditions. The sustainability index is the function of exergy efficiency. Sustainability index determines the impact on environmental or surrounding conditions. Lower sustainability index of the system put adverse effect on the environmental conditions. Average

value of sustainability index of the system using water, 0.01 vol% and 0.05 vol% nanofluid as cooling base fluid are 1.147, 1.148., and 1.152 respectively.

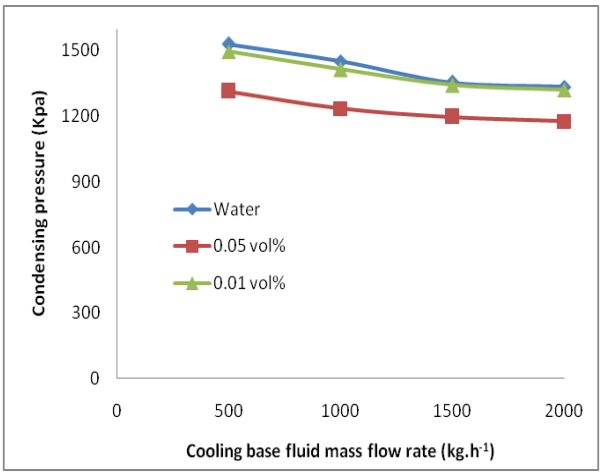


Figure: 17 Condensing pressure versus cooling based fluid mass flow rate

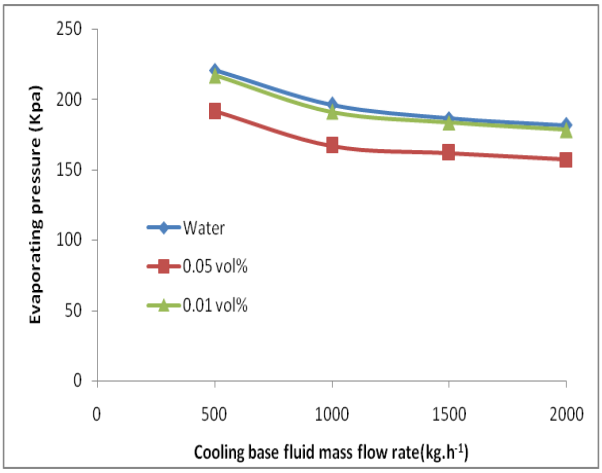


Figure: 18 Evaporating pressure versus cooling based fluid mass flow rate

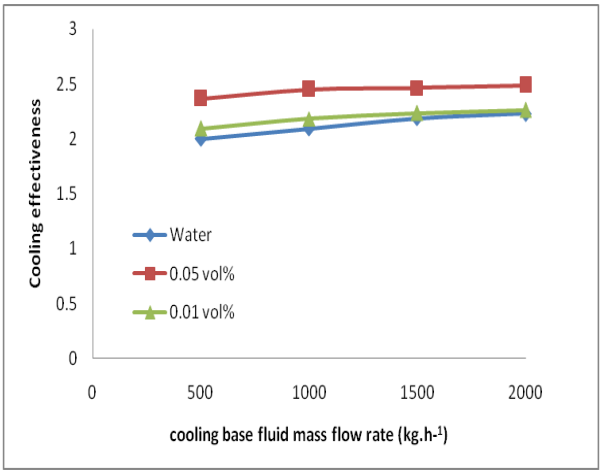


Figure: 19 Cooling effectiveness vs cooling mass flow rate

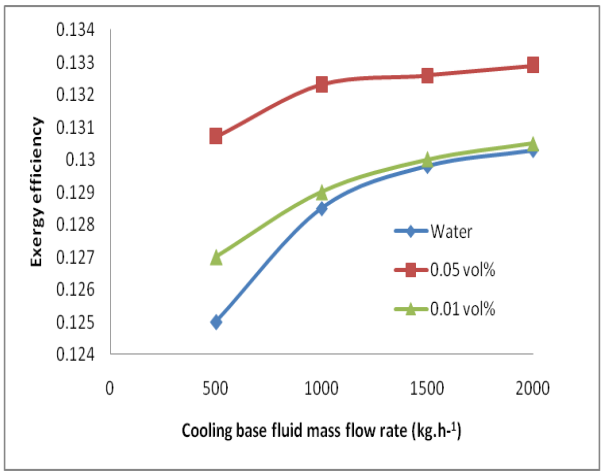


Figure: 20 Exergy efficiency versus versus cooling based fluid mass flow rate

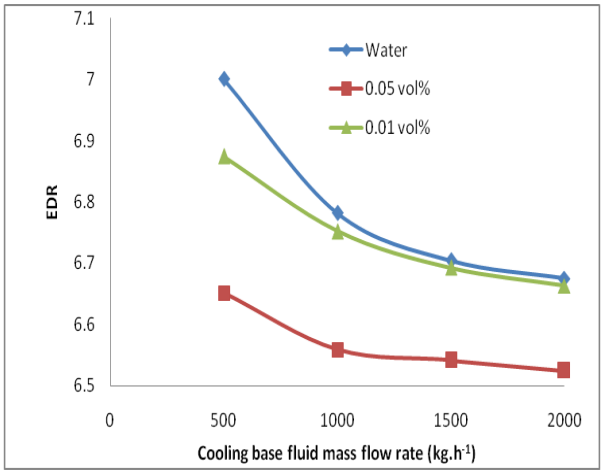


Figure: 21 Exergy destruction ratio versus cooling based fluid mass flow rate

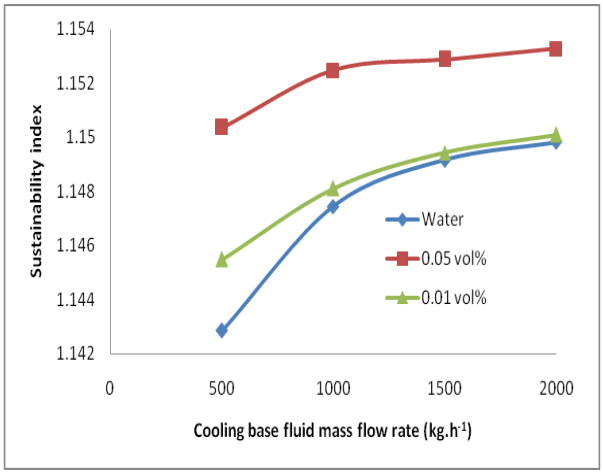


Figure: 22 Sustainability index versus cooling based fluid mass flow rate

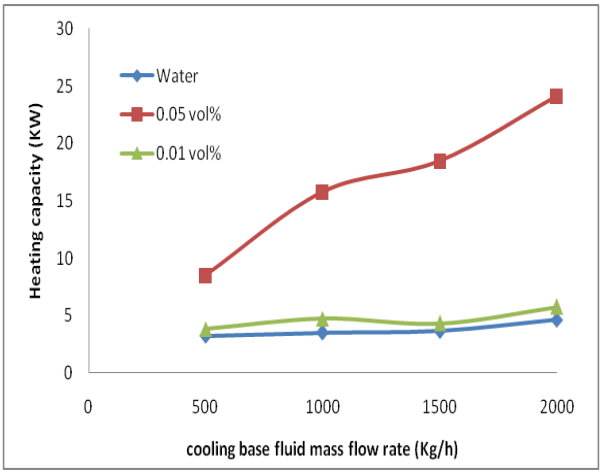


Figure: 23 Heat capacity versus cooling based fluid mass flow rate

Heating capacity is the product of mass flow rate, specific heat and temperature rise of cooling base fluid. By keeping constant mass flow rate of water and discussed percentage of nanofluid remaining two factors i.e specific heat and temperature difference of cooling base fluid responsible for increase of heat transfer between refrigerant through condenser and cooling base fluid. Average specific heat of 0.05 and 0.01 vol% nanofluid is higher than water; also temperature rise of 0.05 vol% of nanofluid is much higher than water and 0.01 vol% nanofluid over entire range of cooling base fluid mass flow rate. This increase in heat transfer termed as heating capacity of condenser, maximum 80% heat capacity higher when 0.05 vol% nanofluids is used instead of water at 2000 Kg/h cooling base fluid mass flow rate. Table-1 illustrates the variation of exergy destruction in compressor, condenser, expansion valve & evaporator with variation in mass flow rate of cooling base fluid. Exergy destruction in component is due to depletion of input energy in particular component. It also gives idea about best and worst component of the system. It was observed that expansion valve and compressor are the best and worst component of the system respectively for entire range of mass flow rate of cooling base fluid. It is clear that average exergy destruction. Experiment is done to give valuable suggestion for increasing efficiency of cryogenics systems.Experiment is performed on VCR system to study the effect of Silver oxide Nano particle (50nm) in base fluid of ethyl glycol (50:50 ratio with water) with concentration factor 0.02g to 0.06g by volume % on hot side of system (Condenser side).For high efficiency out-put Plate Type heat exchanger are taken in the system. Test results show that The parameters such as exergy efficiency, heating capacity of the considered system improved in the range of 1.9-5.96% and 26-82% respectively by using 0.06 Vol% silver Nano fluid compared to water as cold based fluid for considerable range of cold base fluid flow rate. Exergy destruction decreases in the range of 29-31.28%, 65.77-70.01%, 14.31-16.03%, 17-23% in compressor, condenser, evaporator and expansion valve respectively. whereas 0.015 Vol% silver Nano fluid shows very less effect on performance parameters of system for different base fluid mass flow rates.

Over wide range of mass flow rate of cooling base fluid in compressor, condenser, expansion valve and evaporator is lowest by 29.92, 67.16, 20.11 and 14.8% respectively when 0.05 vol. % silver nanofluid compared to water used as cooling base fluid. Mean exergy destruction in compressor, condenser, capillary tube & evaporator ***is*** 873.18, 180.65, 22.50 and 97.36 W respectively which ishighest in case of water used as secondary fluid through evaporator. 7.13, 18.88,3.68 and 1.57 % reduction of exergy destruction in compressor, condenser, expansion valve & evaporator respectively by using of 0.01 vol. % silver nanofluid used as cooling base fluid compared to water

Table .1. Variation of exergy destruction in compressor, condenser, expansion valve & evaporator with variation in mass flow rate of cooling base fluid

Cooling base fluid mass flow rate (Kg/h)	**Water**				**0.01 vol%**				**0.05 vol%**			
	$\dot{E}_{1-2}$ **(W)**	$\dot{E}_{2-3}$ **(W)**	$\dot{E}_{3-4}$ **(W)**	$\dot{E}_{4-1}$ **(W)**	$\dot{E}_{1-2}$ **(W)**	$\dot{E}_{2-3}$ **(W)**	$\dot{E}_{3-4}$ **(W)**	$\dot{E}_{4-1}$ **(W)**	$\dot{E}_{1-2}$ **(W)**	$\dot{E}_{2-3}$ **(W)**	$\dot{E}_{3-4}$ **(W)**	$\dot{E}_{4-1}$ **(W)**
500	918.2	206.2	23.83	99.13	856.3	173.4	22.81	97.82	708.9	123.4	19.5	86.72
1000	869.6	185.9	22.47	98.44	814.4	155.5	21.62	96.73	677.8	109.6	18.61	85.35
1500	867.5	169.1	22.28	96	807.4	142.6	21.52	94.62	666.6	101.9	18.61	83.77
2000	837.4	161.4	21.41	95.85	781.84	136.19	20.85	94.22	648.1	97.36	18.2	83.16

7. Conclusion

(1) Test results show that the parameters such as exergy efficiency, heating capacity of the considered system improved in the range of 1.9-5.96% and 26-82% respectively by using 0.06 Vol% silver Nano fluid compared to water as cold based fluid for considerable range of cold base fluid flow rate.
(2) Exergy destruction decreases in the range of 29-31.28%, 65.77-70.01%, 14.31-16.03%, 17-23% in compressor, condenser, evaporator and expansion valve respectively. whereas 0.015 Vol% silver Nano fluid shows very less effect on performance parameters of system for different base fluid mass flow rates.
(3) Experiments performed on compressor to improve the performance of system using different mineral oil. Because different Nano particle are helpful for achieving high output of system and performance of system enhanced up to 6%.

References

[1] Elcock D. Potential, Impacts of nanotechnology on energy transmission applications and needs, Environmental Science Division, Argonne National Laboratory (2007).
[2] Hindawi, Special issue on heat transfer in nanofluids (2009).
[3] Eastman JA, Choi US, Thompson LJ and Lee S, Enhanced thermal conductivity through the development of nanofluids, Mater Res Soc Symp Proc, 457 (1996) 3–11.
[4] Liu MS, Lin MCC, Huang IT and Wang CC, Enhancement of thermal conductivity with CuO for Nanofluids, Chemical Engineering and Technology 29(1) (2006) 72–77.
[5] Jiang W, Ding G and Peng H, Measurement and model on thermal conductivities of carbon nanotube nanorefrigerants, International Journal of Thermal Sciences 48 (2009) 1108–1115.
[6] Hwang YJ, Ahn YC, Shin HS, Lee CG, Kim GT and Park HS, Investigation on characteristics of thermal conductivity enhancement of nanofluids, Current Applied Physics 6(6) (2006) 1068–1071.
[7] Yoo DH, Hong KS and Yang HS, Study of thermal conductivity of nanofluids for the application of heat transfer fluids, Thermochimica Acta 2007;455(1–2):66–69.
[8] Yang Y. Carbon nanofluids for lubricant application. University of Kentucky (2006).
[9] Eastman JA, Choi SUS, Li S, Yu W, and Thompson LJ, Anomalously increased effective thermal conductivities of ethylene glycol-based nanofluids containing copper nanoparticles. Applied Physics Letters 78(6) (2001) 718–720.
[10] Kang H.U, Kim S.H and Oh J.M., Estimation of thermal conductivity of nanofluid using experimental effective particle, Experimental Heat Transfer 19(3) (2006) 181–191.
[11] Lee J.H, Hwang K.S, Jang S.P, Lee B.H, Kim J.H and Choi SUS, Effective viscosities and thermal conductivities of aqueous nanofluids containing low volume concentrations of Al2O3 nanoparticles. International Journal of Heat and Mass Transfer 51 (2008) 2651–2656.
[12] Jiang W, Ding G and Peng H., Measurement and model on thermal conductivities of carbon nanotube nanorefrigerants. International Journal of Thermal Sciences 48 (2009) 1108–1115.
[13] Wu X.M, Li P, Li H and Wang W.C, Investigation of pool boiling heat transfer of R11 with TiO_2 nano-particles. Journal of Engineering Thermophysics 29(1) (2008) 124–126.
[14] Trisaksri V and Wongwises S, Nucleate pool boiling heat transfer of TiO_2–R141b nanofluids, International Journal of Heat and Mass Transfer 52 (2009) 1582–1588.
[15] Hao P, Guoliang D, Weiting J, Haitao H and Yifeng G, Heat transfer characteristics of refrigerant-based nanofluid flow boiling inside a horizontal smooth tube. International Journal of Refrigeration 32 (2009) 1259–1270.
[16] Hao P, Guoliang D, Haitao H, Weiting J, Dawei Z and Kaijiang W. Nucleate pool boiling heat transfer characteristics of refrigerant/oil mixture with diamond nanoparticles. International Journal of refrigeration 33 (2010) 347–358.
[17] Wang K.J, Ding G.L and Jiang WT, Nano-scale thermal transporting and its use in engineering, Proceedings of the 4th symposium on refrigeration and air condition (2006) 66–75.
[18] Li P, Wu XM and Li H, Pool boiling heat transfer experiments of refrigerants with nanoparticles TiO_2, Proceedings of the 12th symposium on engineering thermo physics, (2006) 325–333.
[19] Peng H, Ding G, Jiang W, Hu H and Gao Y, Heat transfer characteristics of refrigerant-based nanofluid flow boiling inside a horizontal smooth tube. International Journal of Refrigeration 32 (2009):1259–1270.
[20] D.Sendil Kumar and R. Elansezhian, ZnO nanorefrigerant in R152a refrigeration system for energy conservation and green environment, J Front Mech Engg (2014) 1-6.
[21] I.M. Mahbubul,S.A. Fadhilah, R. Saidur, K.Y. Leong and M.A. Amalina, Thermophysical properties and heat transfer performance of Al_2O_3/R-134a nanorefrigerants, International Journa l of Heat and Mass Transfer 57 (2013) 100–108.

arXiv:1708.04439v1 [cs.CL] 15 Aug 2017

Extractive Summarization using Deep Learning

Sukriti Verma and Vagisha Nidhi

Delhi Technological University
Shahbad Daulatpur, Main Bawana Road,
Delhi-110042, India
{dce.sukriti,vagisha.nda}@gmail.com
http://dtu.ac.in/

Abstract. *This paper proposes a text summarization approach for factual reports using a deep learning model. This approach consists of three phases: feature extraction, feature enhancement, and summary generation, which work together to assimilate core information and generate a coherent, understandable summary. We are exploring various features to improve the set of sentences selected for the summary, and are using a Restricted Boltzmann Machine to enhance and abstract those features to improve resultant accuracy without losing any important information. The sentences are scored based on those enhanced features and an extractive summary is constructed. Experimentation carried out on several articles demonstrates the effectiveness of the proposed approach.*

Keywords: Unsupervised, Single Document, Deep Learning, Extractive

1 Introduction

A summary can be defined as a text produced from one or more texts, containing a significant portion of the information from the original text(s), and that is no longer than half of the original text(s) [1]. According to [2], text summarization is the process of distilling the most important information from a source (or sources) to produce an abridged version for a particular user and task(s). When this is done by means of a computer, i.e. automatically, we call it Automatic Text Summarization. This process can be seen as a form of compression and it necessarily suffers from information loss but it is essential to tackle the information overload due to abundance of textual material available on the Internet.

Text Summarization can be classified into extractive summarization and abstractive summarization based on the summary generated. Extractive summarization is creating a summary based on strictly what you get in the original text. Abstractive summarization mimics the process of paraphrasing a text. Text(s) summarized using this technique looks more human-like and produces condensed summaries. These techniques are much harder to implement than the extractive summarization techniques.

In this paper, we follow the extractive methodology to develop techniques for summarization of factual reports or descriptions. We have developed an approach

for single-document summarization using deep learning. So this paper intends to propose an approach by referencing the architecture of the human brain. It is broken down into three phases: feature extraction [3], feature enhancement, and summary generation based on values of those features. Since it can be very difficult to construct high-level, abstract features from raw data, we use deep learning in the second phase to build complex features out of simpler features extracted in the first phase. These extracted features depend highly on how factual the given document is. In the end, we have run the proposed algorithm on several factual reports to evaluate and demonstrate the effectiveness of the proposed approach based on the measures such as Recall, Precision, and F-measure.

2 Related Works

Most early work on text summarization was focused on technical documents and early studies on summarization aimed at summarizing from pre-given documents without any other requirements, which is usually known as generic summarization [4]. Luhn [5] proposed that the frequency of a particular word in an article provides a useful measure of its significance. A number of key ideas, such as stemming and stop word filtering, were put forward in this paper that have now been understood as universal preprocessing steps to text analysis. Baxendale [6] examined 200 paragraphs and found that in 85% of the paragraphs, the topic sentence came as the first one and in 7% of the time, it was the last sentence. This positional feature has been used in many complex machine learning based systems since. Edmundson [7] focused his work around the importance of word frequency and positional importance as features. Two other features were also used: cue words, and the skeleton structure of the document. Weights were associated with these features manually and finally sentences were scored. During evaluation, it was found that around 44% of the system generated summaries matched the target summaries written manually by humans.

Upcoming researchers in text summarization have approached it problem from many aspects such as natural language processing [8], statistical modelling [9] and machine learning. While initially most machine learning systems assumed feature independence and relied on naive-Bayes methods, other recent ones have shifted focus to selection of appropriate features and learning algorithms that make no independence assumptions. Other significant approaches involved Hidden Markov Models and log-linear models to improve extractive summarization. More recent papers, in contrast, used neural networks towards this goal.

Text Summarization can be done for one document, known as single-document summarization [10], or for multiple documents, known as multi-document summarization [11]. On basis of the writing style of the final summary generated, text summarization techniques can be divided into extractive methodology and abstractive methodology [12]. The objective of generating summaries via the extractive approach is choosing certain appropriate sentences as per the requirement of a user. Due to the idiosyncrasies of human-invented languages and gram-

mar, extractive approaches, which select a subset of sentences from the input documents to form a summary instead of paraphrasing like a human [13], are the mainstream in the area.

Almost all extractive summarization methods have three main obstacles. The first obstacle is the ranking problem i.e. how you rank words, phrases and/or sentences. The second obstacle is the selection problem i.e. how to select a subset of those ranked units [14]. The third obstacle is the coherence problem i.e. how to ensure that the selected units form an understandable summary rather than being a set of disconnected words, phrases and/or sentences. Algorithms that determine the relevance of a textual unit, that is words, phrases and/or sentences, with respect to the requirement of the user are used to solve the ranking problem. The selection and coherence problems are solved by methods that improve diversity, minimize redundancy and pick up phrases and/or sentences that are somewhat similar so that more relevant information can be covered by the summary in lesser words and the summary is coherent. Our approach solves the ranking problem by learning a certain set of features for each sentence. On the basis of these features, a score is calculated for each sentence and sentences are arranged in decreasing order of their scores [15]. Even with a list of ranked sentences, it is not a trivial problem to select a subset of sentences for a coherent summary which includes diverse information, minimizes redundancy and is within a word limit. Our approach solves this problem as follows. The most relevant sentence is the first sentence in this sorted list and is chosen as part of the subset of sentences which will form the summary. Then the next sentence selected is a sentence having highest Jaccard similarity with the first sentence and is picked from the top half of the list. This process is recursively and incrementally repeated to select more sentences until limit is reached.

3 Proposed Approach

3.1 Preprocessing

Preprocessing is crucial when it comes to processing text. Ambiguities can be caused by various verb forms of a single word, different accepted spellings of a certain word, plural and singular terms of the same things. Moreover, words like a, an, the, is, of etc. are known as stop words. These are certain high frequency words that do not carry any information and dont serve any purpose towards our goal of summarization. In this phase we do:

1. **Document Segmentation:** The text is divided into paragraphs so as to keep a track of which paragraph each sentence belongs to and what is the position of a sentence in its respective paragraph.
2. **Paragraph Segmentation:** The paragraphs are further divided into sentences.
3. **Word Normalization:** Each sentence is broken down into words and the words are normalized. Normalization involves lemmatization and results in all words being in one common verb form, crudely stemmed down to their

roots with all ambiguities removed. For this purpose, we use Porters algorithm.
4. **Stop Word Filtering:** Each token is analyzed to remove high frequency stop words.
5. **PoS Tagging:** Remaining tokens are Part-of-Speech tagged into verb, noun, adjective etc. using the PoS Tagging module supplied by NLTK [16].

3.2 Feature Extraction

Once the complexity has been reduced and ambiguities have been removed, the document is structured into a sentence-feature matrix. A feature vector is extracted for each sentence. These feature vectors make up the matrix. We have experimented with various features. The combination of the following 9 sentence features has turned out most suitable to summarize factual reports. These computations are done on the text obtained after the preprocessing phase:

1. **Number of thematic words:** The 10 most frequently occurring words of the text are found. These are thematic words. For each sentence, the ratio of no. of thematic words to total words is calculated.

$$Sentence_Thematic = \frac{No.\ of\ thematic\ words}{Total\ words} \tag{1}$$

2. **Sentence position:** This feature is calculated as follows.

$$Sentence_Position = \begin{cases} 1, \text{if its the first or last sentence of the text} \\ cos((SenPos - min)((1/max) - min)), \text{otherwise} \end{cases} \tag{2}$$

where, SenPos = position of sentence in the text
min = th x N
max = th x 2 x N

N is total number of sentences in document
th is threshold calculated as 0.2 x N
By this, we get a high feature value towards the beginning and ending of the document, and a progressively decremented value towards the middle.
3. **Sentence length:** This feature is used to exclude sentences that are too short as those sentences will not be able to convey much information.

$$Sentence_Length = \begin{cases} 0, \text{if number of words is less than 3} \\ No.\ of\ words\ in\ the\ sentence, \text{otherwise} \end{cases} \tag{3}$$

4. **Sentence position relative to paragraph:** This comes directly from the observation that at the start of each paragraph, a new discussion is begun and at the end of each paragraph, we have a conclusive closing.

$$Position_In_Para = \begin{cases} 1, \text{if it is the first or last sentence of a paragraph} \\ 0, \text{otherwise} \end{cases} \tag{4}$$

5. **Number of proper nouns:** This feature is used to give importance to sentences having a substantial number of proper nouns. Here, we count the total number of words that have been PoS tagged as proper nouns for each sentence.
6. **Number of numerals:** Since figures are always crucial to presenting facts, this feature gives importance to sentences having certain figures. For each sentence we calculate the ratio of numerals to total number of words in the sentence.

$$Sentence_Numerals = \frac{No.\ of\ numerals}{Total\ words} \tag{5}$$

7. **Number of named entities:** Here, we count the total number of named entities in each sentence. Sentences having references to named entities like a company, a group of people etc. are often quite important to make any sense of a factual report.
8. **Term Frequency-Inverse Sentence Frequency (TF ISF):** Since we are working with a single document, we have taken TF-ISF feature into account rather than TF-IDF. Frequency of each word in a particular sentence is multiplied by the total number of occurrences of that word in all the other sentences. We calculate this product and add it over all words.

$$TF - ISF = \frac{log(\sum_{all\ words} TF * ISF)}{Total\ words} \tag{6}$$

9. **Sentence to Centroid similarity:** Sentence having the highest TF-ISF score is considered as the centroid sentence. Then, we calculate cosine similarity of each sentence with that centroid sentence.

$$Sentence_Similarity = cosine_sim(sentence, centroid) \tag{7}$$

At the end of this phase, we have a sentence-feature matrix.

3.3 Feature Enhancement

The sentence-feature matrix has been generated with each sentence having 9 feature vector values. After this, recalculation is done on this matrix to enhance and abstract the feature vectors, so as to build complex features out of simple ones. This step improves the quality of the summary.

To enhance and abstract, the sentence-feature matrix is given as input to a Restricted Boltzmann Machine (RBM) which has one hidden layer and one visible layer. A single hidden layers will suffice for the learning process based on

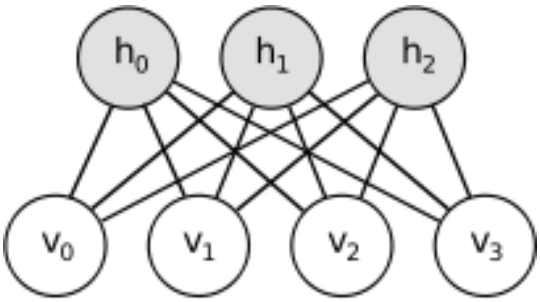


Fig. 1. A Restricted Boltzmann Machine [17]

the size of our training data. The RBM that we are using has 9 perceptrons in each layer with a learning rate of 0.1. We use Persistent Contrastive Divergence method to sample during the learning process [17]. We have trained the RBM for 5 epochs with a batch size of 4 and 4 parallel Gibbs Chains, used for sampling using Persistent CD method. Each sentence feature vector is passed through the hidden layer in which feature vector values for each sentence are multiplied by learned weights and a bias value is added to all the feature vector values which is also learned by the RBM. At the end, we have a refined and enhanced matrix. Note that the RBM will have to be trained for each new document that has to be summarized. The idea is that no document can be summarized without going over it. Since each document is unique in the features extracted in section 3.2, the RBM will have to be freshly trained for each new document.

3.4 Summary Generation

The enhanced feature vector values are summed to generate a score against each sentence. The sentences are then sorted according to decreasing score value. The most relevant sentence is the first sentence in this sorted list and is chosen as part of the subset of sentences which will form the summary. Then the next sentence we select is the sentence having highest Jaccard similarity with the first sentence, selected strictly from the top half of the sorted list. This process is recursively and incrementally repeated to select more sentences until a user-specified summary limit is reached. The sentences are then re-arranged in the order of appearance in the original text. This produces a coherent summary rather than a set of haywire sentences.

4 Results and Performance Evaluation

Several factual reports from various domains of health, technology, news, sports etc. with varying number of sentences were used for experimentation and evaluation. The proposed algorithm was run on each of those and system-generated summaries were compared to the summaries produced by humans.

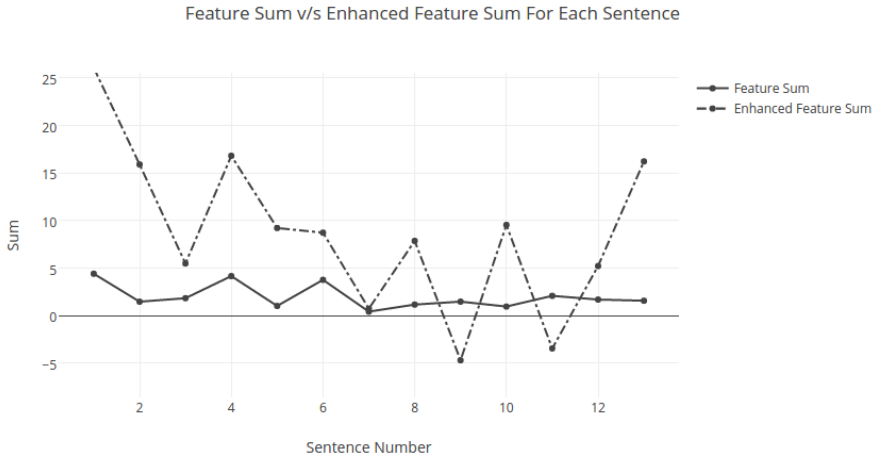


Fig. 2. Comparison between feature vector sum and enhanced feature vector sum

Feature Extraction and Enhancement is carried out as proposed in sections 3.2 and 3.3 for all documents. The values of feature vector sum and enhanced feature vector sum for each sentence of one such document have been plotted in Fig 2. The Restricted Boltzmann Machine has extracted a hierarchical representation out of data that initially did not have much variation, hence discovering the latent factors. The sentences have then been ranked on the basis of final feature vector sum and summaries are generated as proposed in section 3.4.

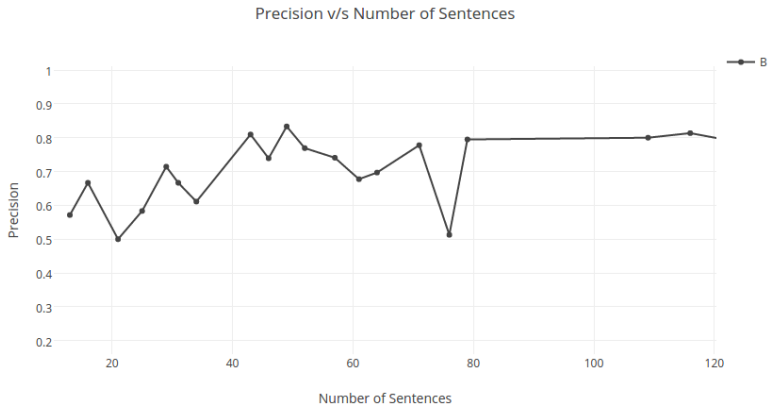


Fig. 3. Precision values corresponding to summaries of various documents

Evaluation of the system-generated summaries is done based on three basic measures: Precision, Recall and F-Measure [18].

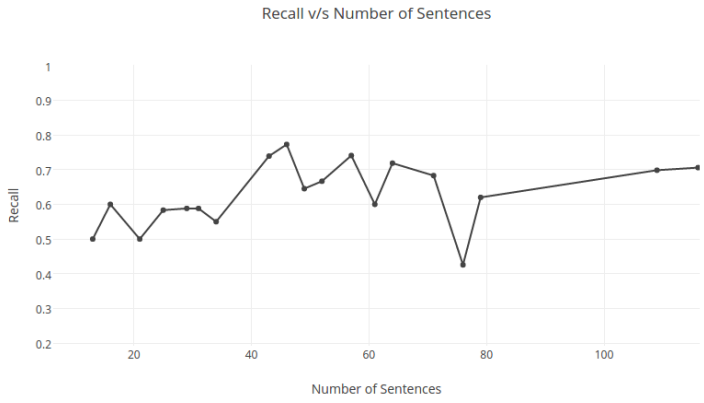


Fig. 4. Recall values corresponding to summaries of various documents

It can be seen that as the number of sentences in the original document cross a certain threshold, the Restricted Boltzmann Machine has ample data to be trained successfully and summaries with high precision and recall values are generated. See Fig 3 and 4.

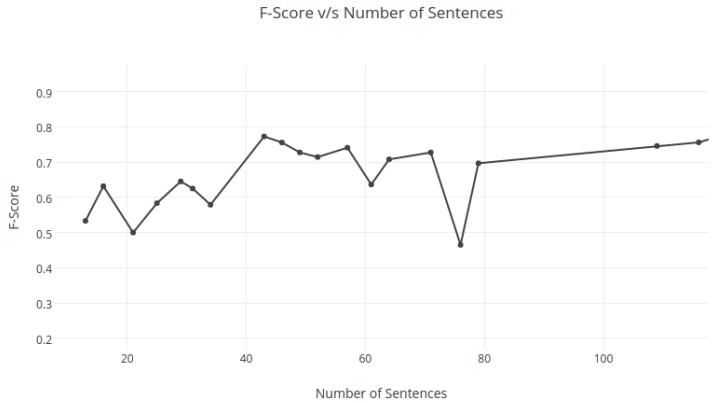


Fig. 5. F-Measure values corresponding to summaries of various documents

F-Measure is defined as follows [19]:

$$F - Measure = \frac{2 * Recall * Precision}{Recall + Precision} \tag{8}$$

5 Comparative Analysis

The existing approach was executed for the same set of articles with just one layer of RBM, rather than two as it specifies and average values of Precision, Recall and F-Measure were plotted for drawing a comparison between the existing approach and the proposed approach, while keeping the amount of computation constant.

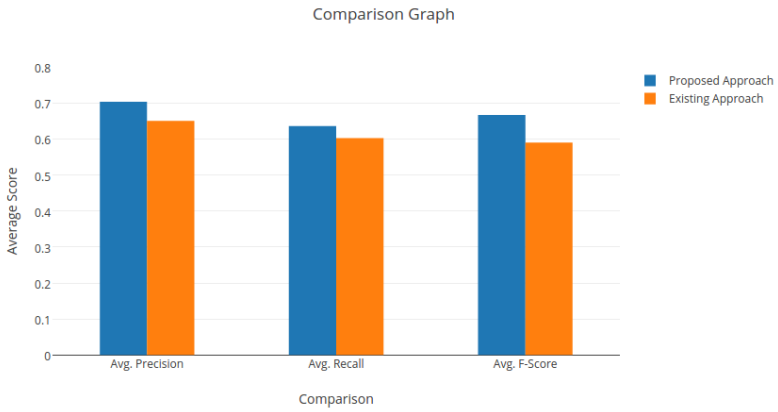


Fig. 6. Precison, Recall and F-Measure values for the proposed approach (*left bars*) and the existing approach (*right bars*)

The proposed approach has an average precision value of 0.7 and average recall value of 0.63 which are both higher than those of the existing approach. Hence, the proposed approach responds better for summarization of factual reports.

6 Conclusion

We have developed an algorithm to summarize single-document factual reports. The algorithm runs separately for each input document, instead of learning rules from a corpus, as each document is unique in itself. This is an advantage that our approach provides. We extract 9 features from the given document and enhance them to score each sentence. Recent approaches have been using 2 RBMs stacked on top of each other for feature enhancement. Our approach uses only

one RBM and, works effectively and efficiently for factual reports. This has been demonstrated by hand-picking factual descriptions from several domains and comparing the system-generated summaries to those written by humans. This approach can further be developed by adapting the extracted features as per the user's requirements and further adjusting the hyperparameters of the RBM to minimize processing and error in encoded values.

Acknowledgments. We would like to extend our gratitude to Dr. Daya Gupta, Professor, Department of Computer Science and Engineering, Delhi Technological University for providing insight and expertise that greatly assisted this research.

References

1. Hovy, E. H.: Automated Text Summarization, In Ruslan Mitkov (ed): The Oxford Handbook of Computational Linguistics 583598 (2005)
2. Mani, I., House, D., Klein, G., Hirschman, L., Firmin, T., Sundheim, B.: The TIPSTER SUMMAC Text Summarization Evaluation. In: Proceedings of the ninth conference on European chapter of the Association for Computational Linguistics, pp. 7785. Association for Computational Linguistics Stroudsburg, PA, USA (1999). doi: 10.3115/977035.977047
3. Chuang, W.T., Yang, J.: Extracting Sentence Segments for Text Summarization: A Machine Learning approach. In: Proceedings of the 23rd Annual International ACM SIGIR Conference on Research and Development in Information Retrieval, pp. 152-159. ACM New York, NY, USA (2000). doi: 10.1145/345508.345566
4. Berger, A., Mittal ,V.: Query relevant summarization using FAQs. In: Proceedings of the 38th Annual Meeting on Association for Computational Linguistics, pp. 294301. Association for Computational Linguistics Stroudsburg, PA, USA (2000). doi: 10.3115/1075218.1075256
5. Luhn, H. P.: The Automatic Creation of Literature Abstracts. IBM Journal of Research and Development, vol. 2, issue 2, 159165 (1958). doi: 10.1147/rd.22.0159
6. Baxendale, P.: Machine-Made Index for Technical Literature - An Experiment. IBM Journal of Research and Development, vol. 2, issue 4, 354–361 (1958). doi: 10.1147/rd.24.0354
7. Edmundson, H. P.: New methods in Automatic Extracting. Journal of the ACM, vol. 16, issue 2, 264285 (1969). doi: 10.1145/321510.321519
8. Zhang, Y., Wang, D., Li, T.: iDVS - An Interactive Multi-Document Visual Summarization System: Machine Learning and Knowledge Discovery in Databases, LNCS, vol. 6913, pp. 569-584. Springer, Heidelberg (2006). doi: 10.1007/978-3-642-23808-6_37
9. Darling, W.M., Song, F.: Probabilistic Document Modeling for Syntax Removal in Text Summarization. In: Proceedings of the 49th Annual Meeting of the Association for Computational Linguistics: Human Language Technologies, pp. 642-647. ACM Press, Stroudsburg, PA, USA (2011).
10. Wan, X., Xiao, J.: Single Document Keyphrase Extraction using Neighborhood Knowledge. In: Proceedings of the Twenty-Third AAAI Conference on Artificial Intelligence (2008).

11. Shen, D., Sun, J.T., Li, H., Yang, Q., Chen, Z.: Document Summarization using Conditional Random Fields. In: Proceedings of the 20th international joint conference on Artifical Intelligence, pp. 2862-2867. Morgan Kaufmann Publishers Inc. San Francisco, CA, USA (2007).
12. Wong, K.F., Wu, M.J., Li, W.J.: Extractive Summarization Using Supervised and Semi-supervised Learning. In: Proceedings of the 22nd International Conference on Computational Linguistics Volume 1, pp. 985-992. Association for Computational Linguistics Stroudsburg, PA, USA (2008).
13. Chen, E.K., Yang, X.K., Zha, H.Y., Zhang, R., and Zhang, W.J. (2008). Learning Object Classes from Image Thumbnails through Deep Neural Networks. In IEEE International Conference on Acoustics, Speech and Signal Processing. IEEE (2008). doi: 10.1109/ICASSP.2008.4517738
14. Jin, F., Huang, M.L., and Zhu, X.Y.: A Comparative Study on Ranking and Selection Strategies for Multi Document Summarization. In: Proceedings of the 23rd International Conference on Computational Linguistics: Posters, pp. 525-533. Association for Computational Linguistics Stroudsburg, PA, USA (2010).
15. Singh, S.P., Kumar, A., Mangal, A., Singhal, S.: Bilingual Automatic Text Summarization Using Unsupervised Deep Learning. In: 2016 International Conference on Electrical, Electronics, and Optimization Techniques. IEEE (2016). doi: 10.1109/ICEEOT.2016.7754874
16. Natural Language Toolkit for Python, `http://www.nltk.org/`
17. Deep Learning Tutorials, `http://deeplearning.net/tutorial/`
18. Performance Evaluation of Information Retrieval Systems, `web.stanford.edu/class/cs276/handouts/lecture8-evaluation.ppt`
19. PadmaPriya, G., Duraiswamy, K.: An Approach for Text Summarization using Deep Learning Algorithm. Journal of Computer Science, vol. 10, issue 1, 19 (2014). doi: 10.3844/jcssp.2014.1.9

arXiv:1708.00884v1 [cs.CV] 2 Aug 2017

Efficient Fingerprint Extraction and Matching Using Smartphone Camera

Saksham Gupta, Sukhad Anand[1], and Atul Rai[2]

[1] Department of Computer Science, Delhi Technological University, Rohini,Delhi 110042
sakshamgupta_2k14@dtu.ac.in , sukhad.anand@gmail.com
[2] Staqu Technologies,Gurgoan, Haryana 11004515
atual.rai@staqu.com

Abstract. In the previous decade, there has been a considerable rise in the usage of smartphones.Due to exorbitant advancement in technology, computational speed and quality of image capturing has increased considerably. With an increase in the need for remote fingerprint verification, smartphones can be used as a powerful alternative for fingerprint authentication instead of conventional optical sensors. In this research, we propose a technique to capture finger-images from the smartphones and pre-process them in such a way that it can be easily matched with the optical sensor images.Effective finger-image capturing, image enhancement, fingerprint pattern extraction, core point detection and image alignment techniques have been discussed. The proposed approach has been validated on FVC 2004 DB1 & DB2 dataset and the results show the efficacy of the methodology proposed. The method can be deployed for real-time commercial usage.

Keywords: Finger-image, Gabor Filter, Core point, Histogram, Remote Verification, FVC

1 Introduction

Over the past decade, fingerprint verification has been used irresistibly in various domains including criminal identification, legal matters and user authentication.With advancement in automated fingerprint identification systems, accompanied by an increasing need for reliable authentication has resulted in widespread deployment of fingerprint authentication in broad applications such as background checks of employees, access to secure facilities, user access authentication in smartphones and remote verification.

Remote verification includes verifying the authenticity of a user's located at access regions. Identity proofing can be used for diverse applications including secure fund transfer,medical-identity proofing and ATM security.The need for remote verification has been immensely growing especially in developing countries like India which need to verify users located at remote regions for government-related services. One prime example is remote e-KYC(Know your customer Service) started by Indian Government. Generally, these services require fingerprint

authentication which is generally done with optical sensors, difficult to be made accessible in rural areas. With the dawn of the age of smartphones, the overhead of providing optical sensors at outlying regions can be considerably reduced with the help of smartphones.

We propose an approach to use smartphone camera to extract fingerprints of a user which can be further used for authentication by matching with images available in any database consisting of optical sensor images.

2 Related Work

Substantial research has been done in the field of finger-photo recognition.Some of the considerable work include Derawi et al. [1] who proposed finger-image recognition with two different smartphones.Neurotechnology, Verifinger 6.0 Extended SDK commercial minutia extractor has been used for the feature extraction.The verification results of the Neurotechnology algorithm on the processed images are used for comparison.Stein et al.[2] proposed a technique for authentication of users on smartphones using finger-image authentication. The proposed method provides algorithms for the capture process to ensure reliable finger-image recognition. Various preprocessing techniques have been described to enhance the recognition rates. In 2015 Anush et. al.[3] proposed Scatnet based feature representation[4] and matching algorithm for finger-image images.

The above approaches fail to produce reliable results which could be used for remote verification. None of the above-discussed approaches have dealt matching between finger-image captured using a smartphone camera and optical sensor images.

[5] gives a detailed description of various techniques used for Fingerprint Recognition.The paper discusses major techniques used in past for feature extraction. These techniques include Minutiae Based Technique, Pattern Matching or Ridge Feature Based Techniques, Correlation Based Technique and image-based technique.The paper also describes various enhancement techniques used in the past.

3 Approach

As shown in Fig.1 the proposed fingerprint verification algorithm involves effective image capturing to get a clear and enhanced image.After a clear image has been captured the image has to be preprocessed which involves histogram equalization and removing superfluous noise in the image.After the finger-image has been preprocessed, the fingerprint pattern consisting of frictional ridges has been extracted so that the finger-image can be further matched with optical sensor images. After the fingerprint pattern has been extracted, the core point of the finger has to be located so that the finger-image can be properly cropped and aligned with the optical sensor images available.Finally, the image is matched with the database of optical sensor images available.

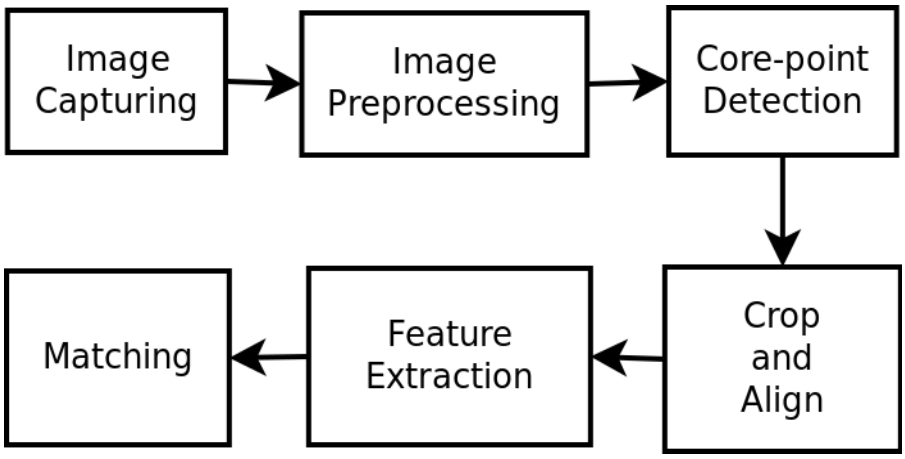


Fig. 1. Overview of the proposed methodology

3.1 Image Capturing

A custom UI application was developed over Open camera application[6] for effective image capturing.The UI developed is shown in the Fig.2. The application ensures quality image capturing. Features of the UI include a custom ROI to constrain the location of the fingerprint in the image which eliminates the need for background-separation and finger-image alignment with optical sensor images.

Multiple Images are captured in quick succesion by varying exposure during each capture.Finally, an HDR image is extracted which is processed further.

Region of Intereset(ROI) It is a rectangular bounding box which constrains the user to capture finger-image in a particular orientation resulting in desired image alignment.

High Dynamic Range(HDR) A well-known problem in images is due to varied lighting and to ensure that every detail, be it well lit or be it in shadow is captured by the camera we use HDR technique. HDR ensure finger-image quality and capture every minuscule detail. We use a five-bracket system in which we vary the exposure of the camera and capture the image at each of these exposures. These five photos are then combined to form a single high detail image.

3.2 Finger-image Pre-processing

For precise and unerring authentication using fingerprint matching, the minutiae have to be extracted with an extraordinary amount of precision.For voracious

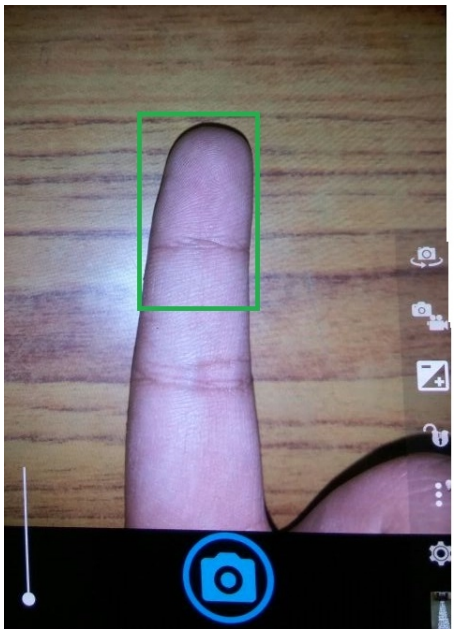


Fig. 2. Custom UI built upon Open Camera Application

minutiae extraction, the noise from the image has to be completely eliminated i.e the image has to be enhanced. CLAHE(Contrast limited adaptive histogram equalization) is superior in terms of accuracy as compared to adaptive histogram equalization because it overcomes its problem of superfluous noise amplification which would have produced infelicitous results. ClAHE captures and improves the local edge information which is essential to the process of fingerprint extraction.

The image is converted from RGB format to a grayscale image and is partitioned into small non-overlapping regions of equal size called tiles. Histogram equalization is applied to each tile separately. Histogram equalization improves the contrast of the image by stretching out the intensity range at points where pixels have been clustered.

The contrast enhancement can be restricted by restricting the slope of cumulative distribution graph which depends on the slope of the transformation function.This eventually reduces the value of histogram at that pixel value. CLAHE achieves this by clipping the histogram at predefined value which limits the slope of cumulative distribution

Superfluous noise in the resultant image is minimized by setting up a clip limit.A clip limit reduces the maximum height of a histogram equalization graph of pixel vs intensity which in turn reduces the amplified noise.After histogram equalization the adjacent tiles are joined together using bilinear interpolation to

completely purge the artificially induced boundaries. The results obtained after applying CLAHE to the image have been shown in Fig.3.

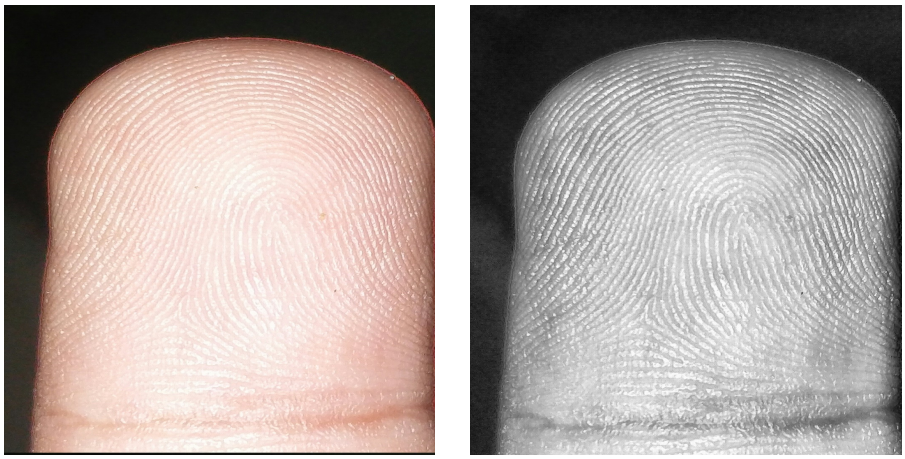


Fig. 3. (a)Original Image captured by Custom UI (b)Image after application of pre-processing

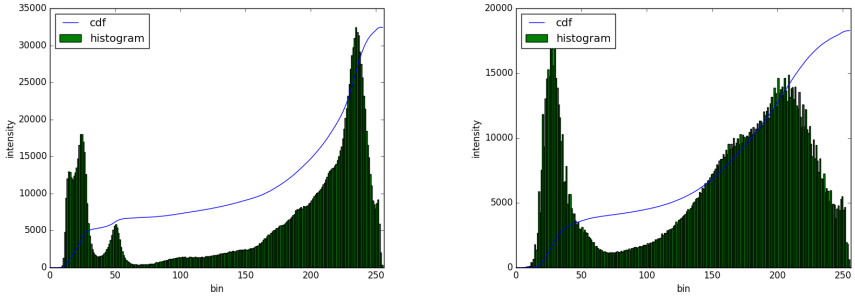


Fig. 4. (a)Histogram of Captured image (b) Histogram of Captured Image after application of CLAHE.

3.3 Finger-image Pattern Extraction

To facilitate feature extraction and matching we need to transform our finger-image. Feature Extraction only works well when the image has clear demarcation

of ridge-valley structure. To highlight this ridge-valley structure in the finger-image multiple convolutions of 2D Gabor filters varied over range of theta values are used. A detailed explanation of each process is described below:-

Gabor Filter A 2D Gabor filter is defined by sinusoidal plane wave multiplied by a Gaussian function. Discrete domain Gabor filter is given in Eq.1,2.

$$G_c[i,j] = Be^{-\frac{(i^2+j^2)}{2\varphi}} \cos(2\pi f(i\cos\Omega + j\sin\Omega)) \tag{1}$$

$$G_s[i,j] = Ce^{-\frac{(i^2+j^2)}{2\varphi}} \sin(2\pi f(i\cos\Omega + j\sin\Omega)) \tag{2}$$

where B and C are normalising factors, f is frequency in the texture and Ω gives texture oriented in particular direction, φ is the size of the image.Above equations can be derived from 1D Gabor Kernels given by

Real

$$g(a,b;\phi,\Omega,\psi,\varphi,\gamma) = exp(-\frac{a'^2+\gamma^2 b'^2}{2\varphi^2})\cos(2\pi\frac{a'}{\phi}+\psi) \tag{3}$$

Imaginary

$$g(a,b;\phi,\Omega,\psi,\varphi,\gamma) = exp(-\frac{a'^2+\gamma^2 b'^2}{2\varphi^2})\sin(2\pi\frac{a'}{\phi}+\psi) \tag{4}$$

where

$$a' = a\cos\Omega + b\sin\Omega \tag{5}$$

and

$$b' = -a\sin\Omega + b\cos\Omega \tag{6}$$

where ϕ is the wavelength of the sinusoidal factor, ψ is the phase offset,$\varphi$is the standard deviation of the Gaussian envelope and γ represents the spatial aspect ratio and specifies the ellipticity of the support of the Gabor function.

Variation in Kernel's Multiple kernels are formed by altering the value of theta in Eq.1,2 above over a range(generally from 0 to pie in steps of pi/16).

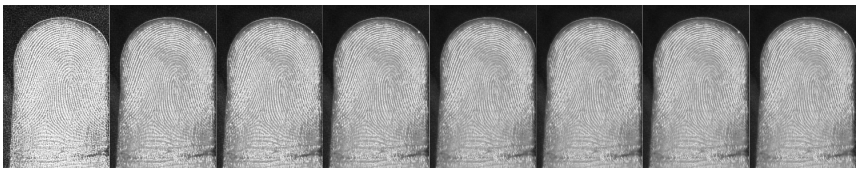


Fig. 5. Gabor Convolutions for different Kernel size,left to right:k=15,18,19,20,24,28,30,35

Convolutions Convolution is performed using the kernels generated.Eq.7 describe the convolution model used

$$H(x,y) = \sum_{i=0}^{M_i-1} \sum_{j=0}^{M_j-1} I(x+i-a_i, y+j-a_j)K(i,j) \tag{7}$$

Here I is input image K is kernel, a_i and a_j is the value of anchor point in the kernel and M_i and M_j gives kernel size.

3.4 Core-point Detection

A crucial determinant in fast fingerprint authentication or verification is the relative alignment of the two fingerprints being matched. A precise alignment reduces computation by preventing the comparison of each minutiae features set.Additionally the cropping of finger-image is centered around the core-point.

In the proposed work, the latest technique for core point detection proposed by G. A. Bhagat et al. [7] has been used. As the fingerprint consists of frictional ridges.The proposed approach uses ridge orientation map for localizing the core point.

The accuracy has been amplified by using an adaptive smoothing technique as described in [8]. The smoothed orientation map is obtained by

$$\theta_s(a,b) = \frac{1}{2}\arctan\left(\frac{\sum_{(m,n)\epsilon\Omega(s)} \sin(2\theta_o(m,n))}{\sum_{(m,n)\epsilon\Omega(s)} \cos(2\theta_o(m,n))}\right) \tag{8}$$

where $\theta_s(a,b)$ is the smoothed orientation of the block (i,j),$\Omega(s)$ is the surrounding neighborhood of the block and s is the consistency level and $\theta_o(k,l)$ provides the initial orientation i.e the angle made by ridges passing through neighbourhood centred at (m,n). The computation time has been minimized by dividing the image into smaller blocks of size $r*r$ where r is slightly larger than the width of the frictional ridges.

A binary set aligned in square shape is presented which scans the segmented smoothed orientation map. The core point is finally detected using the method proposed by[7].

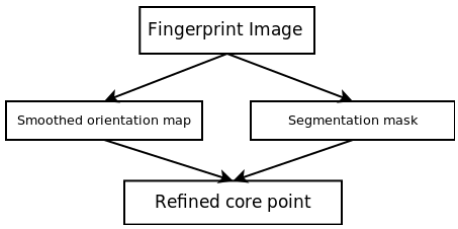


Fig. 6. Oveview of Core-point Detection Algorithm

3.5 Finger-image Alignment

After the core point of the fingerprint has been determined, the image has to be properly aligned with the images of the optical sensor images for accurate matching.

The image also has to be cropped about the core point. Cropping is necessary because if complete image is given for matching it would result in comparison of large number of non-useful minutiae sets which would ultimately result in increased overhead time and will also result in improper matching.

The images obtained from the optical sensor and the finger-image have a phase difference of 180^0.Hence the images captured using smartphones have to be flipped so that the images can be precisely matched.

3.6 Feature Extraction and Matching

For the purpose of feature extraction and matching, We used open source application SouceAFIS[9]. The software is based on MINDTCT template extractor[10] and Bozorth3 [11] matching technique. SourceAFIS allow modification in FAR(False Accept Rate) and FRR(False Rejection Rate) so that ERR(Equal Error Rate) can be computed.

4 Results

As our approach is based on heterogeneous matching of fingerprints i.e. matching between images prints acquired from the optical sensor and smartphone camera we used the standard optical sensor database FVC 2004(DB1,DB2)[12] . Finger-images were captured using a smartphone having a 16 MP camera and resolutio of 1920x1080.

A custom android application was developed for accurate image acquisition. The application was built upon Open-Camera[6].Fig2 depicts the application.The bounding box represents the ROI required to enforce alignment.To ensure image quality 5 frames are captured with different exposures in the burst mode and finally an HDR image is generated.

Experiments were performed by transfiguring various parameters, which have been described below:

Gabor kernel size As described above in section_ multiple Gabor filter convolutions are applied to highlight the ridge-valley structure of the print. Gabor filter is applied to the images in the form of a 2-D convolution kernel. Experiments were made upon different Gabor kernel sizes to ensure maximum matching accuracy. The curve shown in Fig 7 depicts the relationship between various Kernel sizes and the matching scores obtained using SourceAFIS matcher.

From the curve, we conclude that the matching score achieve its maxima for a kernel size of 21 with a score of 74.23. Thus a Gabor filter of square kernel size of 21 supplies best results for our experiments. Further results are computed using this kernel size only.

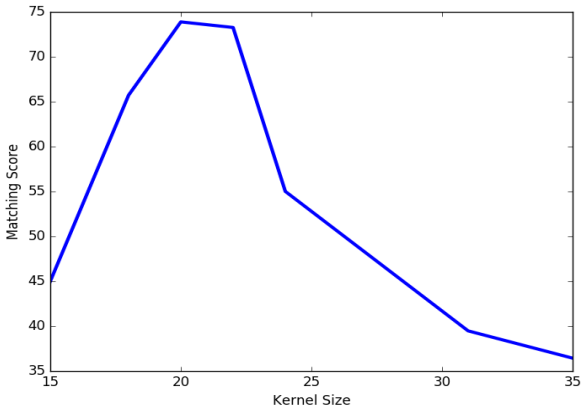


Fig. 7. Matching Score for different kernel sizes of 2D Gabour filters

Effective area of interest around the core point After core point detection, different dimensions for cropping area around the core point were considered to find its dependence on matching score.Fig 8(a) represents the desired dependency relationship.

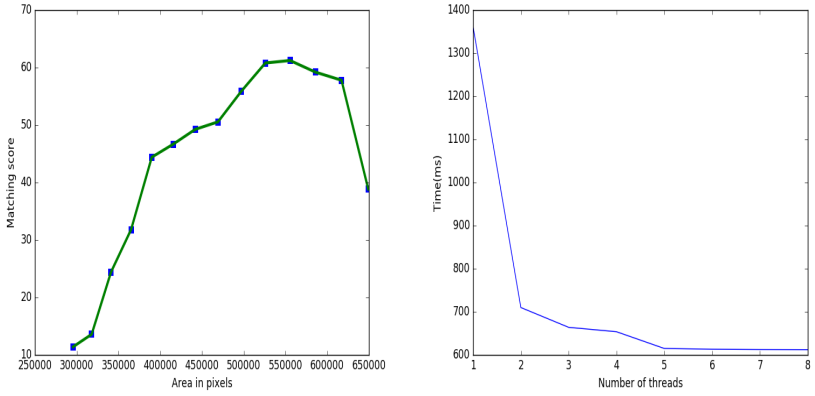


Fig. 8. (a)Matching Score(SourceAFIS) varied over area of cropping(b)Processing Time required to find Gabor convolutions over multiple threads.

From the curve, we can ascertain that the optimal dimensions of the effective region of interest to achieve maximum accuracy are 800x700 pixels around the core point detected.

Threading Our approach consists of convolutions of multiple Gabor filters which is a computationally expensive activity. For a multi-processor system, applying threading can significantly speed up the convolution process. Fig 8(b) depicts the time of execution for different number of threads. From the graph it is evident that computation time decreases drastically as the number of threads are increased and saturates around a thread count of 5.

Accuracy The ROC curve of the experiments performed with different thresholds of the matcher is shown in Fig.9.As the value of the threshold is increased, both true positive rate and the false positive rate decrease and vice versa. ERR for the proposed technique on the FVC 2004 database lies between the range of 6% - 15%, thus making the approach feasible for commercial usage in real-time.

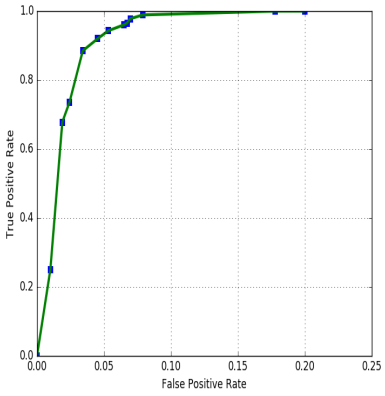


Fig. 9. ROC curve obtained by varying threshold values of the matcher

5 Conclusion and Future Work

By this study, we conclude that fingerprint authentication can be performed using Smartphone cameras. We were able to match the finger-images obtained using the camera with the fingerprints obtained using the optical sensor. The EER was 6% - 15% which is well within the acceptable limits. Thus this technique can be efficiently used by people not having easy access to fingerprint sensors. The technique can be greatly improved by adjusting the Gabor filter parameters optimal to the setting of finger-image capturing. Further better minutiae extractor and matcher can be used to accurately match the prints. As the technology evolves more powerful smartphone cameras shall be able to capture higher resolution images which will ultimately lead to better extraction of the ridge-valley structure.

References

1. Derawi, Mohammad Omar; Yang, Bian; Busch, Christoph, "Fingerprint Recognition with Embedded Cameras on Mobile Phones", "Security and Privacy in Mobile Information and Communication Systems: Third International ICST Conference, MobiSec 2011, Aalborg, Denmark, May 17-19, 2011, Revised Selected Papers",2012,pp. 136-147,doi:10.1007/978-3-642-30244-2_12
2. Fingerphoto Recognition with Smartphone Cameras Chris Stein, Claudia Nickel, Christoph Busch Hochschule Darmstadt - CASED Mornewegstrae 32 D-64295 Darmstadt
3. On Smartphone Camera based Fingerphoto Authentication Anush Sankaran, Aakarsh Malhotra, Apoorva Mittal, Mayank Vatsa, Richa Singh IIIT Delhi, India
4. L. Sifre and S. Mallat. Rotation, scaling and deformation invariant scattering for texture discrimination. In CVPR, pages 12331240, 2013. 2,
5. J. Rajharia, PC. Gupta, A. Sharma, "Fingerprint Based Identification System: A Survey", International Journal of Computer Technology and Electronics Engineering(IJCTEE) Vol 1 Issue 3, 2012
6. Mark Harman, Open Camera, Retrieved from https://opencamera.sourceforge.net/
7. G A Bhagat, A. H. Khalil and N. S. Abdel Kader, Fast and accurate algorithm for core point detection in fingerprint images, Journal of Egyptian Informatic, vol. 14, no.1, pp. 15-25, 2013.
8. M. Liu, X. Jiang, A.C. Kot,"Fingerprint reference point detection",EURASIP J Appl Signal Process,4 (2002), pp. 498 - 509
9. Robert Vazan,"Fingerprint Recognition Toolkit", 2015, url:http://sourceafis.org/
10. C. I. Watson, M. D. Garris, E. Tabassi, C. L. Wilson, "User's Guide to NIST Biometric Image Software", National Institute of Standards and Technology, url: http://ws680.nist.gov/publication/get_pdf.cfm?pub_id=51097
11. C. I. Watson, M. D. Garris, E. Tabassi, C. L. Wilson, "User's Guide to NIST Biometric Image Software", National Institute of Standards and Technology, url: http://ws680.nist.gov/publication/get_pdf.cfm?pub_id=51096
12. Fingerprint Verification Competition, http://bias.csr.unibo.it/fvc2004/, 2004

Volume 5 Issue 2 (2017) 247-250 ISSN 2347 - 3258
International Journal of Advance Research and Innovation

Finite difference solver for couette flow with applied pressure gradients

MrudangMathur, Nehal Amit Jajal, Raj Kumar Singh
Mechanical Engineering Department, Delhi Technological University, Delhi 42, India

Article Info
Article history:
Received 25 January 2017
Received in revised form
20 February 2017
Accepted 28 February 2017`
Available online 15 June 2017

Keywords: Coutte flow, pressure gradient, fluid mechnics

Abstract
A finite difference scheme was used to obtain solutions to a two dimensional CouetteFlow problem with applied pressure gradients. The solution to the non dimensionalizedCouette Flow problem was then obtained via Implicit methods and the results were subsequently validated with the analytical solution of the same problem.
Finite difference scheme used returned satisfactory results under varying input conditions and was successfully validated on the Couette Flow problem through comparison with the analytical solution.

1. Introduction

The foundation of modern fluid mechanics are the Navier-Stokes equation. It is an unsteady, nonlinear and second order partial differential equation. Thus making it an equation to which no analytical solution has been formulated to date. This has led to an alternate approach to solving the equation, this involves using numerical methods to obtain approximate solutions to the equation. The finite difference method is one such scheme developed which replaces all the partial derivatives and other terms in a partial differential equation by approximations. A numerical method for solving incompressible viscous flow problems was first introduced in 1947 by Alexandre Joel Chorin from Courant Institute. This method uses the velocities and the pressure as variables, and is equally applicable to problems in two and three space dimensions.Numerical methods and finite difference methods have been used in various applications such as modelling Navier-Stokes equations for vortex generation, pipe flow, couette flow, static structural analysis, wave analysis etc. It is seen that numerical methods have been adapted to solve a wide array of problems and prove to be a cheaper alternative to an experimental result. However it can't be ignored that numerical methods make use of approximations and thus the mathematical models have to be tested for various boundary conditions and governing equations for obtaining a reliable solution for the problem. A lot of research is being conducted on the stability of such numerical models as well as the reliability of the solution obtained by these methods.

2.Theory

Couette flow is the flow between two parallel plates. Here, one plate is at rest and the other is moving with a velocity U. Let us assume the plates are infinitely large in z direction, so the z dependence is not there. Figure 2.1 illustrates the flow between two plates.The governing equation is:

$$\frac{dp}{dx} = \mu \frac{\partial^2 y}{\partial x^2} \qquad [1]$$

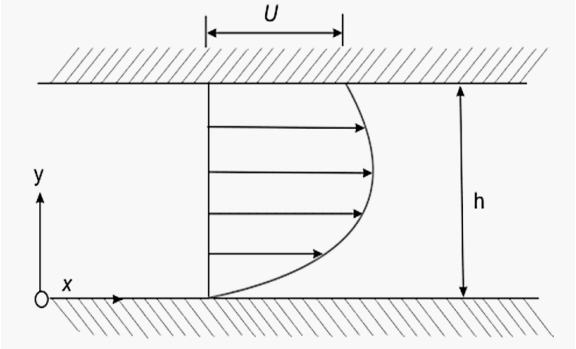


Fig 1 Couette Flow between two pipes

Upon integrating the given differential equation, we get

$$u = \frac{1}{2\mu}\frac{dp}{dx}y^2 + C_1 y + C_2 \qquad [2]$$

Invoking the condition (at y = 0, u = 0), C_2 becomes equal to zero.

$$u = \frac{1}{2\mu}\frac{dp}{dx}y^2 + C_1 \qquad [3]$$

Invoking the other condition (at y = h, u = U),

$$C_1 = \frac{U}{h} - \frac{1}{2\mu}\frac{dp}{dx}h \qquad [4]$$

Inserting the constants into the original solution we obtain the expression for u, which is

$$u = \frac{y*U}{h} - \frac{h^2}{2\mu}\frac{dp}{dx}\frac{y}{h}(1 - \frac{y}{h}) \qquad [5]$$

The above result can be non-dimensionalized to give

$$\frac{u}{U} = \frac{y}{h} + P\frac{y}{h}(1 - \frac{y}{h}) \qquad [6]$$

$$P = -\frac{h^2}{2\mu U}\frac{dp}{dx} \qquad [7]$$

When P > 0, i.e. for a negative or favorable pressure gradient in the direction of motion, the velocity is positive over the whole gap between the channel walls. For negative value of P (P < 0), velocity there is a positive or adverse pressure gradient in the direction of motion and the over a portion of channel width can become negative and back flow may occur near the wall which is at rest. Figure 2 shows the effect of dragging action of the upper plate exerted on the fluid particles in the channel for different values of pressure gradient.

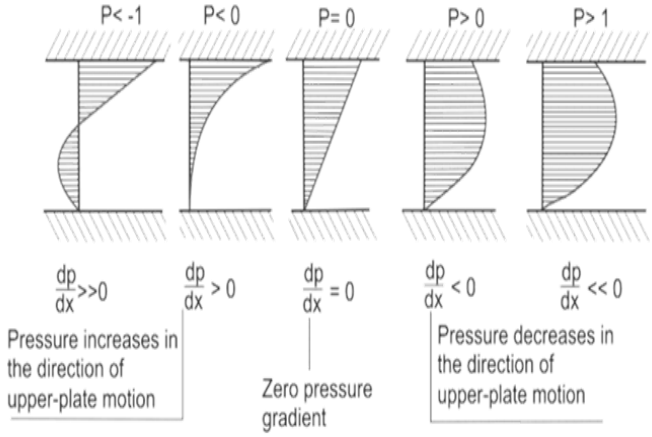


Fig 2 Variation of flow with Pressure Factor

3.Methodology

3.1 Mathematical Formulation

To formulate a Finite Difference Model a time marching scheme was used which approached a steady state solution in a certain

*Corresponding Author,
E-mail: rajkumarsingh@dce.ac.in
All rights reserved: http://www.ijari.org

number of time steps. The Couette Flow equation for an unsteady flow can be given by [7]. The velocity, distance and time was then non-dimensionalized as [8-10] respectively and then substituted into the the unsteady flow equation [11].The equation for Couette Flow with an applied pressure gradient was similarly non-dimensionalized [12] with *P*[13] being the non-dimensional pressure gradient. In all the equations $Re_D$is the Reynolds Number and $\mu$is the viscosity of the liquid.

$$\rho\frac{\partial u}{\partial t} = \mu\frac{\partial^2 u}{\partial y^2} \quad [1]$$

$$u' = \frac{u}{u_e} \quad [8]$$

$$y' = \frac{y}{D} \quad [9]$$

$$t' = \frac{t}{D/u_e} \quad [10]$$

$$\frac{\partial u'}{\partial t'} = \frac{\partial^2 u'}{Re_D \partial y'^2} \quad [11]$$

$$\frac{\partial u'}{\partial t'} = \frac{\partial^2 u'}{Re_D \partial y'^2} + \frac{2P}{Re_D} \quad [12]$$

$$P = \frac{-D^2}{2\mu u_e}\frac{\partial p}{\partial x} \quad [13]$$

The governing equations were then converted into Finite Difference form using the Crank-Nicolson method which is implicit and second order in time [14]. In order to simplify the solution procedure [14] can be written as [15] with the constants [16-18].

$$\frac{u_j^{n+1}-u_j^n}{\Delta t} = \frac{1}{Re_D}\frac{(u_{j+1}^{n+1}+u_{j+1}^n)+(-2u_j^{n+1}-2u_j^n)+(u_{j-1}^{n+1}+u_{j-1}^n)}{2\Delta y^2} + \frac{2P}{Re_D} \quad [14]$$

$$Au_{j-1}^{n+1} + Bu_j^{n+1} + Au_{j+1}^{n+1} = K_j \quad [15]$$

$$A = -\frac{\Delta t}{Re_D 2(\Delta y)^2} \quad [16]$$

$$B = 1 + \frac{\Delta t}{Re_D(\Delta y)^2} \quad [17]$$

$$K_j = \left[1 - \frac{\Delta t}{Re_D(\Delta y)^2}\right]u_j^n + \frac{\Delta t}{Re_D 2(\Delta y)^2}\left(u_{j+1}^n + u_{j-1}^n\right) + \frac{2P}{Re_D} \quad [18]$$

A tri-diagonal matrix can now be constructed and a matrix equation can be developed for N nodes just as seen in the case without an external pressure factor. The equations have to be solved using Thomas's algorithm for tri-diagonal matrix.The results generated from the implicit finite difference solver are validated by comparing them to analytical results for the same Couette flow problem. The solver accurately predicts the velocity gradient even when an external pressure is applied to the Couette flow problem.

3.2 Code Development

Both the methods, explicit as well as implicit, solvers are developed using the MATLAB programming language. Separate functions were made for each case and the results were then evaluated. MATLAB is a programming language with powerful functions and operators for matrix calculations and hence developing a code involving matrix calculations becomes relatively easier. MATLAB also has various features of obtaining graphical results from the numerical results generated. This makes it simple to compare and validate results with analytical results. The solver algorithm has been depicted in figure 3.

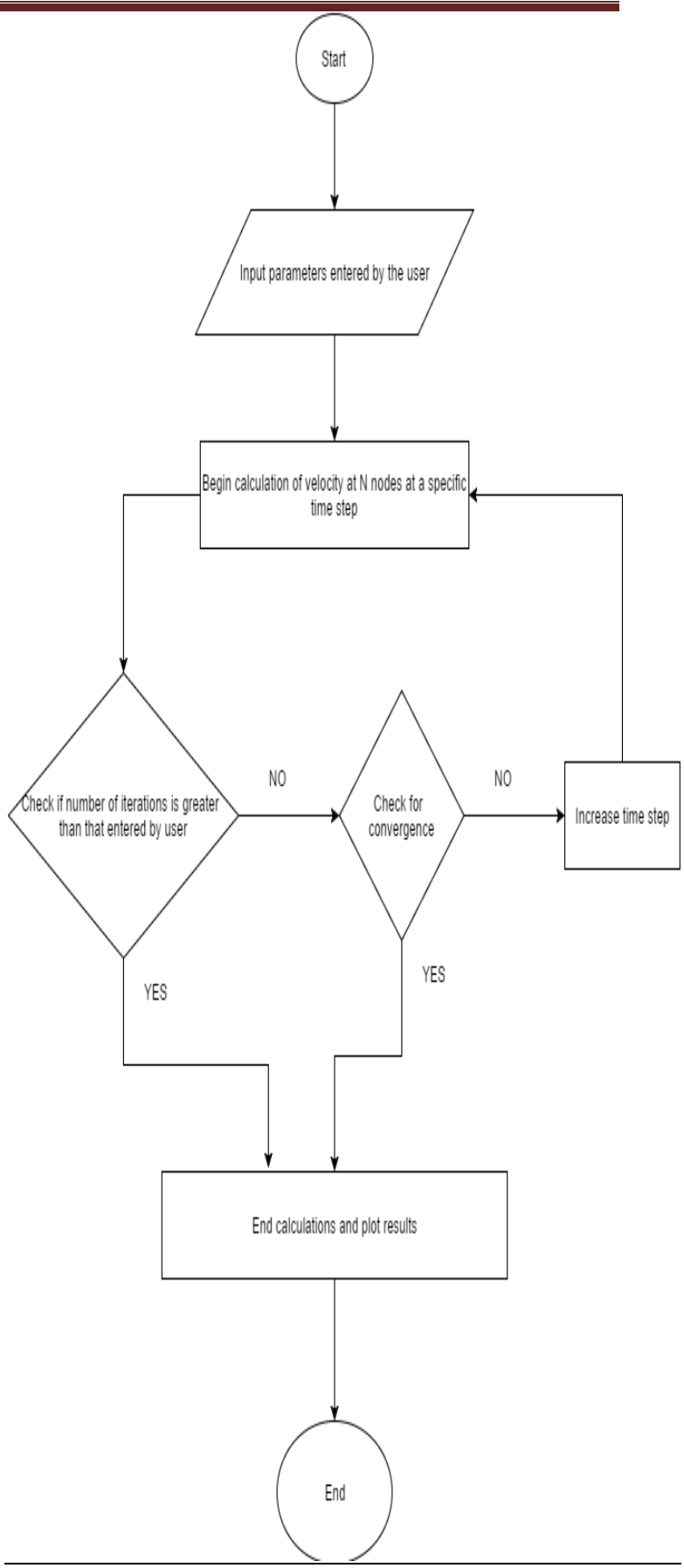


Fig 3 Algorithm used by the solver

4.Results

All numerical solutions employ the following fixed parameter values:

$$Re = 2000 \qquad \partial t = 0.1$$
$$N = 1000$$

Solutions have been obtained against a varied value of *P*; the non-dimensional pressure:

$$P \in \{-3, -2, -1, 0, 1\}$$

4.1 Change in error with respect to time

As shown in figure 4.1 the error between the analytical solution and numerical solution reduce over time. This is consistent with our assumption that the Truncation Error decreases with an increase in time. The change in error for three distinct values of *P* have been depicted in the aforementioned figure 4.

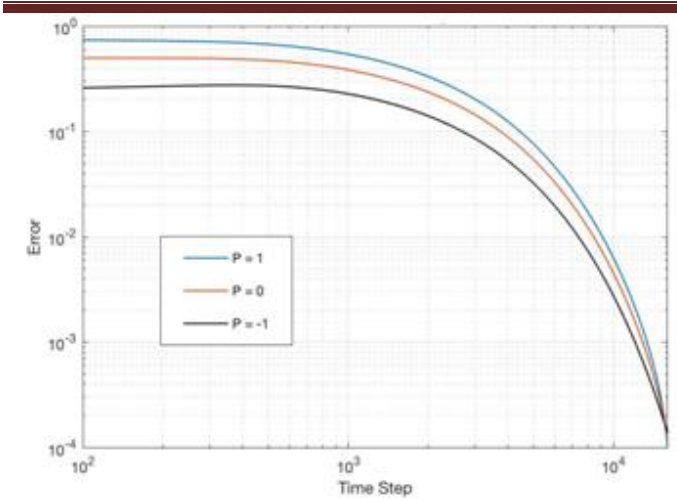


Fig 4 Error Vs Time

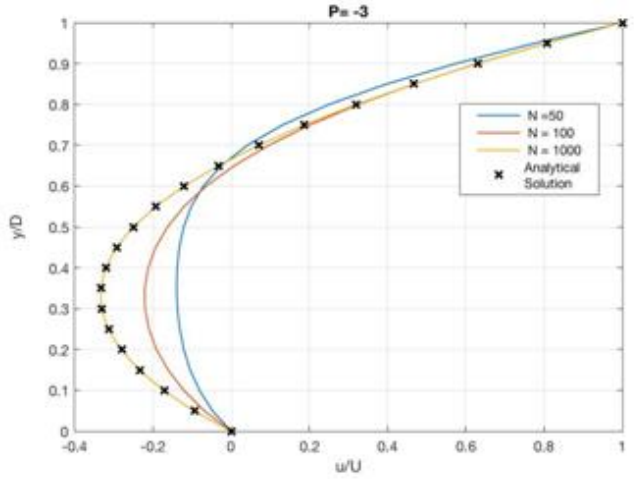


Fig 5(a): Normalized Velocity profile

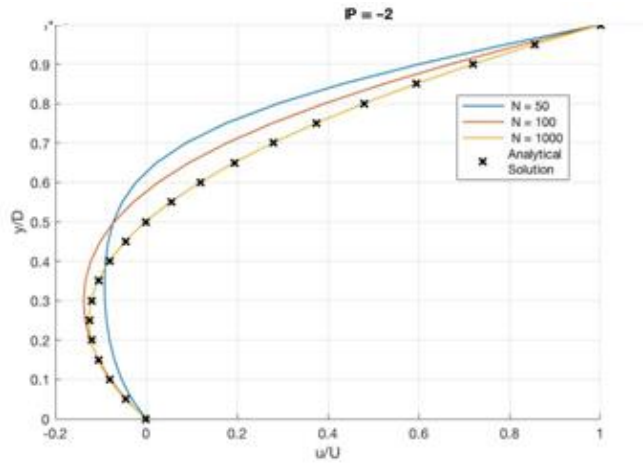


Fig 5(b): Normalized Velocity profile

4.1 Convergence of Velocity Profiles

It can be observed from figures 4 to figure 8 that as the number of time steps increases i.e. the solution moves forward in the time domain; the transient velocity profile approaches the Steady-State velocity profile obtained from the analytical solution of the Couette Flow problem. The solution will continue to converge to the exact solution with the Truncation Error reducing with each advancement in time. This process will continue till infinity. To break out of the infinite loop created we have fixed the number of time steps the code must simulate. This has allowed us to obtain an acceptable value of truncation error and gives us the freedom to choose the quality of results we require.

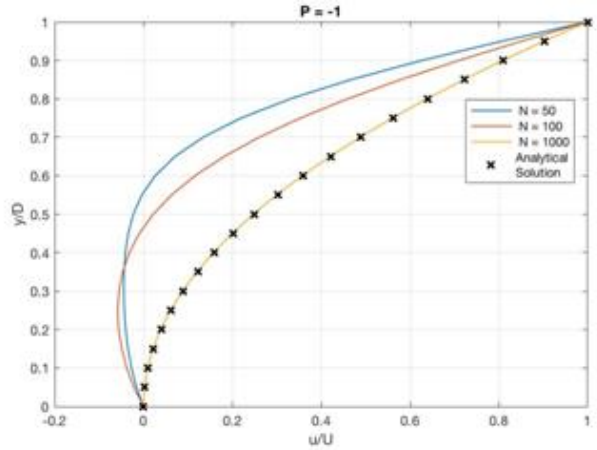


Fig 5(c): Normalized Velocity profile

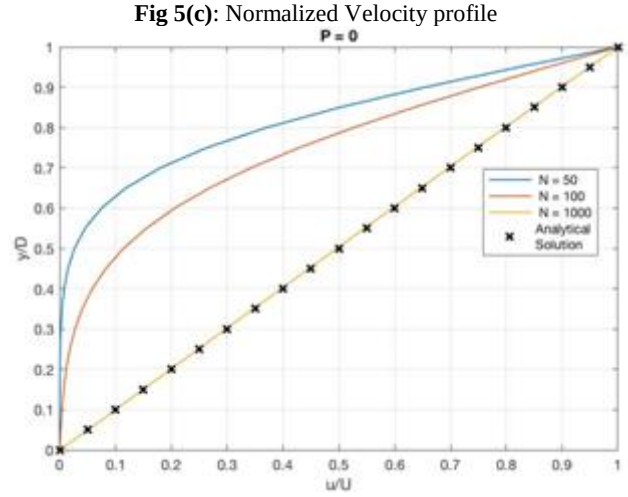


Fig 5(d): Normalized Velocity profile

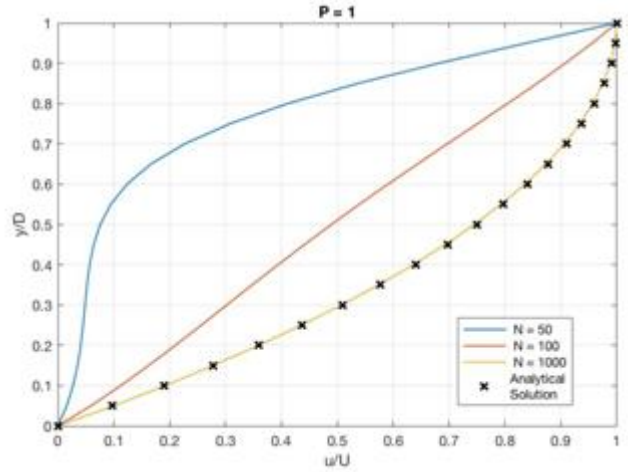


Fig 5(e): Normalized Velocity profile

5.Conclusions

The Finite Difference Scheme used returned satisfactory results under varying input conditions and was successfully validated on the Couette Flow problem through comparison with the analytical solution. There is a large scope of work that can be done to further this solution strategy i.e. the scheme and formulation can be adapted to 2 and 3 dimensional flows taking into account the effects of turbulence as well as heat transfer in possible applications.

References

[1] Yunus A Çengel, John M Cimbala. Fluid Mechanics: Fundamentals and Applications, TMH-2013

[2] Alexandre Joel Chorin. A Numerical Method for Solving Incompressible Viscous Flow Problems. Journal of Computational physics, 135 (2), 1997, 118-125
[3] John D Anderson, JR.Computational Fluid Dynamics: The Basics with Applications.
[4] MA Maa Touga, M Ayadi. Numerical simulation of the second-order Stokes theory using finite difference method, Alexanderia Engineering Journal, 55(3), 2016, 3005-3013
[5] Hoffman JD, Frankel S. Marcel Dekker, Inc., Numerical methods for engineers and scientists, McGraw- Hill 1992.
[6] C Wayne Mastin. Implicit finite difference methods on composite grids, Journal of Computational and Applied Mathemitics, 20, 1987, 317-323

Formalism to Study the Effect of Hydrogen on the Plasma-Assisted Growth and Field Emission Properties of the Graphene sheet

N. Gupta[1], S. C. Sharma[1], and R. Gupta[1]

[1]*Department of Applied Physics, Delhi Technological University (DTU),ShahbadDaulatpur, Bawana Road, Delhi-110042, India.*

Abstract

The catalytic growth of graphene grown via plasma enhanced chemical vapor deposition depends significantly on hydrogen in the feed gas. The effect of hydrogen on the dimensions of graphene has been investigated through a theoretical model that incorporates the charging rate of the graphene sheet; number density of all the plasma species, i.e., electrons, positively charged ions, and neutral atoms; and the growth rate of the graphene sheet. The numerical calculations have been carried out for typically glow discharge parameters and it is found that the thickness and height of the graphene sheet decreases with increase of the hydrogen gas density. Using the results obtained, the effect of hydrogen on the field emission properties of the graphene sheet has been proposed. It is found that the field enhancement factor β increases with the increase of hydrogen gas density. Some of the results of the present investigation are in accordance with the existing experimental observations. The results of the present model can serve as a major tool in analyzing the field emission characteristics of the graphene sheet.

I .Introduction

Hydrogen plays a dual role in the PECVD growth of graphene sheet (GS).It acts as an activator for the dissociation of hydrocarbon species into more active species and also as an etching reagent of graphene [1]. Thus, hydrogen gas number density profile plays a significant role on the growth of carbon nanostructures. The growth rate of carbon nanostructures decreases with the increase of hydrogen gas number density [2]. The number of layers of GS also get affected by the hydrogen gas number density [3] and thus the field enhancement factor which depends on the geometry of emitter [4] also get affected by the hydrogen gas density [5].

II. Model

The present model considers the growth of GS in the plasma consisting of electrons, positively charged ions and neutrals of CH_4 (denoted as A) and H_2 (denoted as B). The GS is formed due to following processes: (a) fragmentation of catalyst film into catalyst nanoparticles, (b) nucleation of carbon clusters, (c) diffusion and collision of these carbon clusters to form

graphene islands (of radius a_{gh} = 50 nm), (d) formation of vertical GS on account of stress developed due to coalescence of graphene islands.

A. Growth rate equation for the graphene sheet

$$l\frac{d(\lambda\times\tau)}{dt}=\left(\left(\frac{\eta_A}{\nu}\times\Lambda_1 e^{\left(-\left\{\frac{\varepsilon_d+\varepsilon_{in}}{k_B T_s}\right\}\right)}\right)\frac{\pi a_{gh}^2}{2\pi a_{gh}}\times\left(j_{iAghn}\right)+\left(\beta_{CH_4} j_{CH_4 ghn}\right)\right)\times\frac{\mu_{ghn}}{\rho_{ghn}}, \quad (1)$$

$$\left[\lambda(t)\times l\right]\frac{d(\tau)}{dt}=\left\{\phi_{iA} e^{\left(\frac{-\delta E_{tdh}}{k_B\theta_{su}}\right)}+\phi_{iB}(1-\alpha_t)+\phi_{iB}+\alpha_{CH}\left(\phi_{iB}p_d+\gamma_0\nu e^{\left(\frac{-\delta E_i}{k_B\theta_{su}}\right)}\right)\right\}\frac{\lambda(t)}{\eta_{iB}}+\beta_{CH_4}\pi a_{gh}^2 j_{CH_4 ghn}, \quad (2)$$

where l, λ and τ denote the length, height and thickness of the GS, respectively, η_A and η_{iB} are the number density of neutral A and ion B, respectively, μ_{ghn} is the mass of the growing GS and ρ_{ghn} is the density of the GS [6].

Eq.(1) describes the increase in area of the GS on account of diffusion and attachment of carbon atoms at the graphene island boundaries and ion (j_{iAghn}) & neutral (j_{CH4ghn}) collection current at the growing GS [6]. Eq. (2) depicts the decrease in thickness of the GS due to the etching effect of hydrogen [6].

B. Kinetic equation of positively charged ion density and neutral atoms

$$\frac{d\eta_{ik}}{dt}=\kappa_k\eta_k-\delta_A\eta_e\eta_{ik}-\eta_{ghn}j_{ikghn}-\psi_{adik}+\psi_{dpik} \quad (3)$$

$$\frac{d\eta_k}{dt}=\delta_k\eta_e\eta_{ik}-\kappa_k\eta_k+\eta_{ghn}\left(1-\beta_{ik}\right)j_{ikghn}-\eta_{ghn}\beta_k j_{kghn}, \quad (4)$$

where η_{ik} and η_k are the number density of ion and atom, respectively (*k* refers to A or B type of species), and η_e is the electron number density.

The Eq. (3) describes the kinetics of positively charged ions in the plasma due to ionization of neutral atoms (κ_k is the coefficient of ionization), recombination of electrons and ions (δ_k is the coefficient of recombination of electrons and ions), ion collection current at the GS surface, adsorption (ψ_{adik} is the adsorption flux) and desorption of ions (ψ_{dpik} is the desorption flux), and loss to the discharge wall. The term ψ_{thdh} represents the flux of type 2 ion on

account of thermal dehydrogenation [6]. This term would not be accounted for the kinetics of positively charged ion density of type A.

The Eq. (5) describes the kinetics of neutral atomsin the plasma due to recombination of electrons and ions, ionization of neutral atoms, ion and neutral collection current at the GS surface.

RESULTS AND DISCUSSION

We have carried out calculations to study the effect of hydrogen number density on the growth and field emission properties of the GS for typically glow discharge parameters such as at t = 0; $\eta_{e0} = 10^9 cm^{-3}$, $\eta_{e0} = 0.6\eta_{iA0}$, $\eta_{A0} = 10^{10} cm^{-3}$, and $\beta_{ik} = \beta_k = 1$. In the present investigation, we have varied the number densities of hydrogen gas and have studied its repercussion on the dimensions (i.e., thickness and height) and field enhancement factor β of GS.

Fig.1 and 2 illustrate the variation of thickness and height of GS with time for different number density of hydrogen species in the plasma, respectively. From Fig.1 it can be seen that the thickness of the GS decreases with increase of the hydrogen number density. This is due to the augmentation of the etching of carbon atoms with increase of the hydrogen gas number density. It can be seen from Fig.2 that the height of the GS decreases with increase of the hydrogen gas number density. This is ascribed to the fact that on increasing the hydrogen gas density, the number density of carbon species decreases, and therefore the carbon species available for growth of height of GS get reduced. The similar observation has also been reported earlier for other carbon-based nanostructures [2].

Using the above results, the field enhancement factor $\beta = \lambda/\tau$ is calculated using the saturated value of λ and τ corresponding to different number densities of H_2 gas from Fig.1 and 2. It is found that the β increases with the augmentation of the hydrogen number density (cf. Fig.3). This result is due to the fact that height has little influence on β,[7] therefore, $\beta \propto 1/\tau$. Moreover, the thickness of GS decreases with the hydrogen gas number density (cf. Fig.1). Hence, β increases with increasing hydrogen number density. The results of Fig.1 and 3 are in compliance with the experimental observations of Chan *et al.* [4] and Malesevic *et al.*[7],respectively.

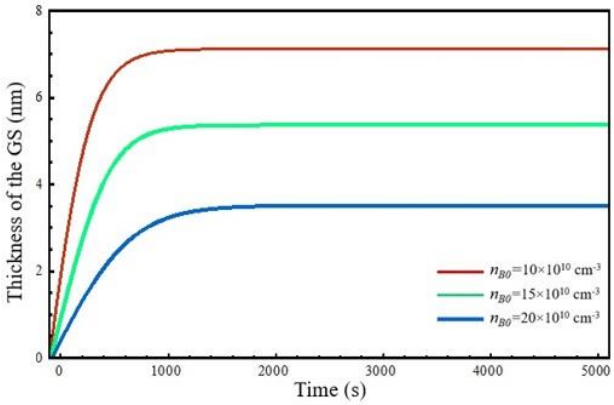


Fig.1. Time evolution of thickness of the graphene sheet for different number density of the hydrogen species in the plasma.

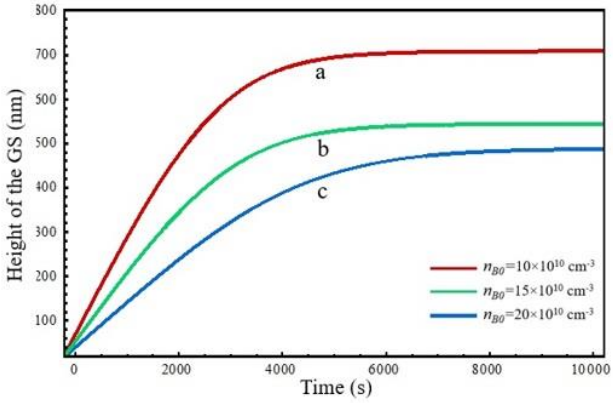


Fig.2. Time evolution of height of the graphene sheet for different number density of the hydrogen species in the plasma.

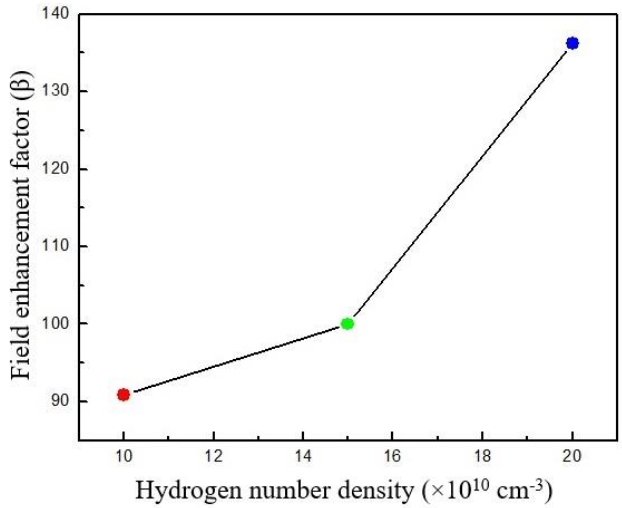


Fig.3. Variation of field enhancement factor of the GS with hydrogen species number density in the plasma.

References

[1]Kim Y S, Lee J H, Kim Y D, Jerng S-K, Joo K, Kim E, Jung J, Yoon E,Park Y D,Seo S, and Chun S-H 2013Nanoscale **5** 1221

[2] Vanpaemel J,van der Veen M H,Cott D J, Sugiura M,Asselberghs I,Gendt S De, and Vereecken P M 2015 J. Phys. Chem. C **119** 18293

[3]Denysenko I, and Ostrikov K 2007 Appl. Phys. Lett. **90** 251501

[4] Chan S H, Chen S H, Lin W T, Li M C, Lin Y C, and Kuo C-C 2013Nanoscale Res. Lett. **8** 28

[5]Kim Y, Song W, Lee S Y, Jeon C, Jung W, Kim M, and Park C-Y 2011 Appl. Phys. Lett. **98** 263106.

[6] Sharma S C and Gupta N 2015, Phys. Plasmas **22** 123517

[7] Malesevic A, Kemps R, Vanhulsel A, Chowdhury M P, Volodin A, andHaesendonck C V 2008 J. Appl. Phys. **104** 084301

This is an open access article published under an ACS AuthorChoice License, which permits copying and redistribution of the article or any adaptations for non-commercial purposes.

ACS OMEGA

Article

http://pubs.acs.org/journal/acsodf

Identification of a Novel Class of BRD4 Inhibitors by Computational Screening and Binding Simulations

Bryce K. Allen,[†,‡] Saurabh Mehta,[†,‡,§] Stuart W. J. Ember,[∥] Jin-Yi Zhu,[∥] Ernst Schönbrunn,[∥] Nagi G. Ayad,[⊥,#,¶] and Stephan C. Schürer*[,†,‡,¶]

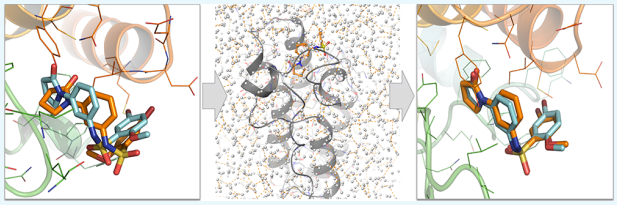
[†]Department of Molecular and Cellular Pharmacology, Miller School of Medicine, [‡]Center for Computational Science, [⊥]Center for Therapeutic Innovation Miller School of Medicine, [#]Miami Project to Cure Paralysis, Department of Psychiatry and Behavioral Sciences, Miller School of Medicine, and [¶]Sylvester Comprehensive Cancer Center, Miller School of Medicine, University of Miami, Miami, Florida 33136, United States

[§]Department of Applied Chemistry, Delhi Technological University, Delhi 110042, India

[∥]Drug Discovery Department, H. Lee Moffitt Cancer Center and Research Institute, Tampa, Florida 33612-9416, United States

Supporting Information

ABSTRACT: Computational screening is a method to prioritize small-molecule compounds based on the structural and biochemical attributes built from ligand and target information. Previously, we have developed a scalable virtual screening workflow to identify novel multitarget kinase/bromodomain inhibitors. In the current study, we identified several novel *N*-[3-(2-oxo-pyrrolidinyl)phenyl]-benzenesulfonamide derivatives that scored highly in our ensemble docking protocol. We quantified the binding affinity of these compounds for BRD4(BD1) biochemically and generated cocrystal structures, which were deposited in the Protein Data Bank. As the docking poses obtained in the virtual screening pipeline did not align with the experimental cocrystal structures, we evaluated the predictions of their precise binding modes by performing molecular dynamics (MD) simulations. The MD simulations closely reproduced the experimentally observed protein−ligand cocrystal binding conformations and interactions for all compounds. These results suggest a computational workflow to generate experimental-quality protein−ligand binding models, overcoming limitations of docking results due to receptor flexibility and incomplete sampling, as a useful starting point for the structure-based lead optimization of novel BRD4(BD1) inhibitors.



INTRODUCTION

Epigenetics refers to changes in gene expression that are not due to DNA sequence modifications.[1] Epigenetic modifications occur due to the coordinated activities of three classes of epigenetic proteins, namely, writers, readers, and erasers.[2] Epigenetic readers recognize specific modifications, such as histone acetylation and nucleotide methylation, which promote nucleosome remodeling. Importantly, regulatory posttranslational modifications of proteins such as lysine acetylation have emerged as essential marks for regulating transcription, metabolism, and cell signaling.[3] Bromodomain proteins are a family of epigenetic reader domain proteins that bind acetylated lysine residues, particularly in the N-terminal tails of histones, facilitating decondensation of chromatin and regulation of gene expression. Of the 61 bromodomain modules found in 42 diverse proteins of the human proteome, bromodomain and extra-terminal (BET) proteins include family members BRD2, BRD3, BRD4, and BRDT.[4] These proteins contain two bromodomains termed bromodomain 1 (BD1) and bromodomain 2 (BD2) and exhibit a high level of sequence conservation in the amino terminal; however, more divergence has been characterized in the carboxy terminal of this protein family.[5] Bromodomain-containing protein 4 (BRD4) has been linked to the expression of oncogenes such as MYC and is a promising target for cancer therapy.[6] Specifically, researchers observe BRD4 overexpression in various cancers, including glioblastoma and squamous cell carcinoma, among others.[7] Recently, the discovery and development of BET protein inhibitors allow for the treatment of cancer cells in vitro and in vivo, with many studies demonstrating promising results.

Additionally, the structural topology of BRD4 consists of four α helices (α_z, α_A, α_B, and α_C) linked by ZA and BC loops that have been shown to be responsible for substrate specificity.[8] Previous structure determination of BRD4 with acetylated histone peptides demonstrates acetyl-lysine binding in the central hydrophobic cavity, where a hydrogen bond forms with N140. This conserved binding motif was also observed in previously characterized BRD4 inhibitors.[8]

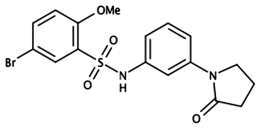
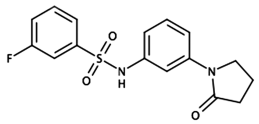
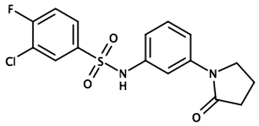
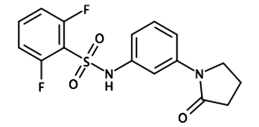
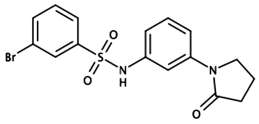
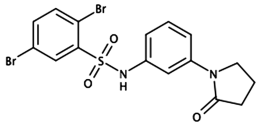
Recent advances in computational methods and power facilitate high-throughput approximation of binding free energies and dynamics with increasing accuracy.[9] The classical "lock-and-key" theory of protein−ligand binding, in which a

Received: May 4, 2017
Accepted: July 27, 2017
Published: August 21, 2017

 © 2017 American Chemical Society

DOI: 10.1021/acsomega.7b00553
ACS Omega 2017, 2, 4760−4771

Table 1. Biochemical Activity and Docking Scores of *N*-[3-(2-Oxo-pyrrolidinyl)phenyl]-benzenesulfonamide Derivatives

Enamine ID	Structure	BRD4 IC_{50} (μM)*	Initial Docking Score	Optimized Docking Score
Z115668302		11 ± 0.181	-8.02	-10.21
Z115668110		24 ± 0.322	-8.72	-10.18
Z115668200		26 ± 0.202	-8.78	-10.06
Z115668236		21 ± 0.254	-7.81	-9.97
Z115668228		41 ± 0.811	-8.59	-9.90
Z115668152		44 ± 1.363	-7.59	-9.04

[a]Values expressed as mean ± standard error of the mean of three experiments in triplicate.

rigid receptor is thought to accommodate a small molecule, has given way to dynamic molecular models that aim to incorporate induced changes of small-molecule ligand and receptor conformation upon binding. Accordingly, such models can lead to better results and more accurate predictions.[10,11] Structure-based virtual screening methods, such as docking, typically search for energetically favorable conformations and atomic interactions of a small-molecule binding to a protein pocket and often use empirical scoring functions to estimate binding free energy to various degrees of accuracy but minimally to enrich actives out of a pool of mostly inactive compounds. In contrast to ligand-based models, which do not use a protein structure and rely on correlations between chemical topology and binding affinity, structure-based models can predict the atomic interactions through which a new small molecule binds to a protein of interest and can estimate how energetically favorable that interaction is. If correct, these models are useful for the development and optimization of lead compounds. Although structure-based methods can be highly predictive, for flexible proteins it can be challenging to find the best "induced-fit" binding pose and accurately predict (or rank order) their binding affinity. Molecular dynamics (MD) simulation can help solve that problem, and advances in computer hardware and user-friendly software have enabled much higher throughput simulation of multicomponent dynamic molecular systems, including those with protein and ligand components.[12−14] Several examples have demonstrated that MD can improve structure-based virtual screening by predicting stable low-energy ligand−receptor binding conformations.[15−19] Although computationally intensive, this approach has the potential to produce an accurate binding model even if no cocrystal structure is available, which is often a limiting factor with many druggable targets.[20] Furthermore, alchemical free energy calculations have recently been shown to provide robust and accurate protein−ligand binding energies. However, these are among the most computationally intensive methods and require extensive sampling to converge accurately.[21−24] In this study, we were primarily interested in accurate pose prediction and activity ranking and therefore did not computationally investigate more expensive free-energy methods.

DOI: 10.1021/acsomega.7b00553
ACS Omega 2017, 2, 4760−4771

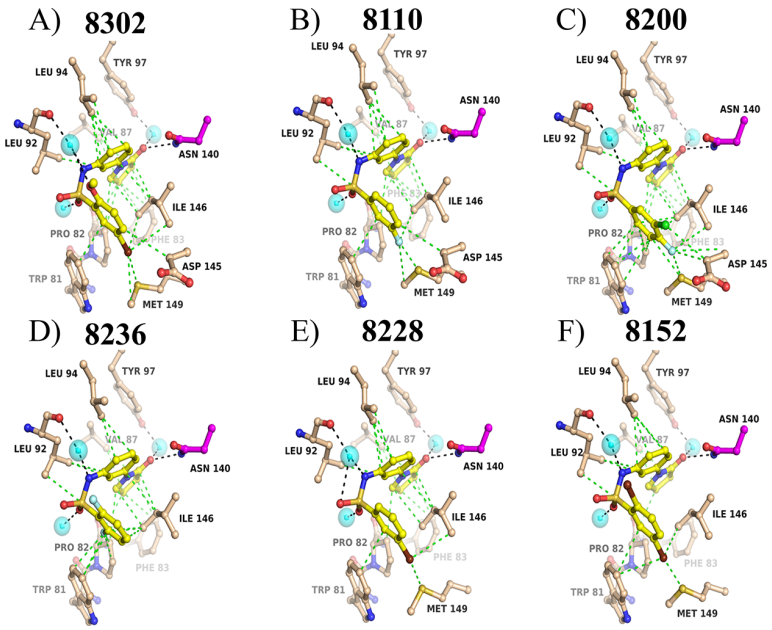


Figure 1. Cocrystal structures of *N*-[3-(2-oxo-pyrrolidinyl)phenyl]-benzenesulfonamide BRD4 binders. Conserved interactions are observed between all compounds and the BRD4 N140 acetyl-lysine binding motif. Interactions with P82, V87, P82, D145, I146, and M149 are also observed across binding interactions with this scaffold.

Here, we report the identification of six novel *N*-[3-(2-oxo-pyrrolidinyl)phenyl]-benzenesulfonamide derivatives that scored high in an ensemble docking virtual screening workflow. We determined their BRD4(BD1) binding affinity biochemically and resolved the cocrystal structures for these compounds, which were deposited in the Protein Data Bank (PDB).[25] Because the docking poses obtained in the virtual screening pipeline did not align with the later determined experimental cocrystal structures, we ran MD simulations on the original docking poses and were able to closely reproduce the experimental cocrystal structure binding poses for all compounds. These results suggest that binding conformation and atomic protein−ligand interactions of a novel class of BRD4 inhibitors can be accurately predicted using published cocrystal structures and MD simulations. Docking studies based on the MD-optimized binding models suggest improved performance in terms of enriching known actives and to rank order activity of a novel chemotype, which we extensively characterized. Our results provide a useful starting point for the structure-based lead optimization of BRD4(BD1) inhibitors.

RESULTS

We had previously reported a scalable virtual screening workflow using kinase machine learning classifiers and parallel ensemble docking to identify a novel dual kinase BET inhibitor.[26] Briefly, we first prioritized 908 compounds using kinase machine learning models and then docked these compounds into several structures of BRD4(BD1) obtained from the PDB that were selected and processed to represent diverse cocrystal ligands as well as to include and exclude conserved cocrystal water. Here, we report the biochemical AlphaScreen, an AlphaScreen counter assay, and differential scanning fluorimetry (DSF) to confirm the activity of six BRD4 inhibitors identified via the virtual screening pipeline (see Experimental Section). Several of these compounds had IC_{50} values in the range of 11−44 μM as determined via a BRD4(BD1)-acetylated histone interaction assay (Table 1, Supplementary Table 1). All six compounds are *N*-[3-(2-oxo-pyrrolidinyl)phenyl]-benzenesulfonamides, a previously unreported druglike scaffold for BRD4. As they were novel compounds, we produced cocrystals and resolved their structures (Figure 1). Analysis of the cocrystal structures displayed some interactions that were predicted by our ensemble docking model (Supplementary Figures 1 and 2). The cocrystal structures are also very useful to interpret the structure−activity relationships (SARs) observed for that series (see Discussion and Conclusions). However, when comparing the best docking poses with the experimentally determined structures, we observed differences in ligand binding conformation with ligand root-mean-square deviation (RMSD) ranging from 1.57 to 2.35 Å (Supplementary Table 2). We were interested in improving the computational pose predictions, and specifically, whether MD simulations would converge to the experimental cocrystal binding pose. Our motivation was to reliably predict the correct binding pose of a new chemotype of BRD4(BD1) in the absence of a cocrystal structure, which is much more time-consuming and expensive to obtain than running MD simulations.

A 50 ns all-atom explicit water MD simulation was performed for all active *N*-[3-(2-oxo-pyrrolidinyl)phenyl]-benzenesulfonamide derivatives starting from the docking results. Each MD system was created from the docked protein−ligand complex that corresponded to the best docking score (i.e., the BRD4(BD1) PDB structure that resulted in the highest absolute docking score with its corresponding docked ligand). Simulation trajectory analysis showed ligand binding pose stabilization after 20 to 30 ns as quantified by ligand RMSD from starting coordinates. Over that time frame, ligand RMSD relative to the starting (docked) conformation changed by approximately 2 Å and was then stable (Supplementary Table 2). Interactions throughout the trajectories showed conserved interactions with N140, which is a well-described

DOI: 10.1021/acsomega.7b00553
ACS Omega 2017, 2, 4760−4771

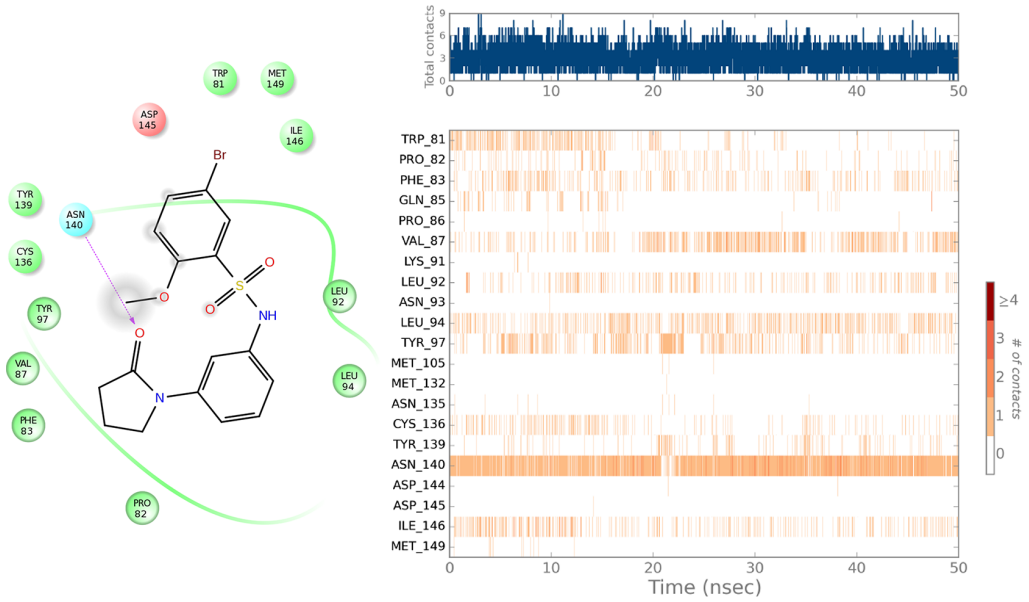


Figure 2. Binding interactions of compound 8302 with BRD4 throughout the molecular simulation. Primary receptor ligand interactions (hydrogen bonds, hydrophobic, ionic, water bridges) of 8302 for the duration of the MD simulation with BRD4(1). The top panel shows the total number of specific contacts the protein makes with the ligand over the course of the trajectory. The bottom panel shows which residues interact with the ligand over the simulation time. Some residues make more than one specific contact with the ligand, which is represented by a darker shade of orange, according to the scale to the right of the plot. The visualizations were generated using the Desmond simulation interactions diagram component.

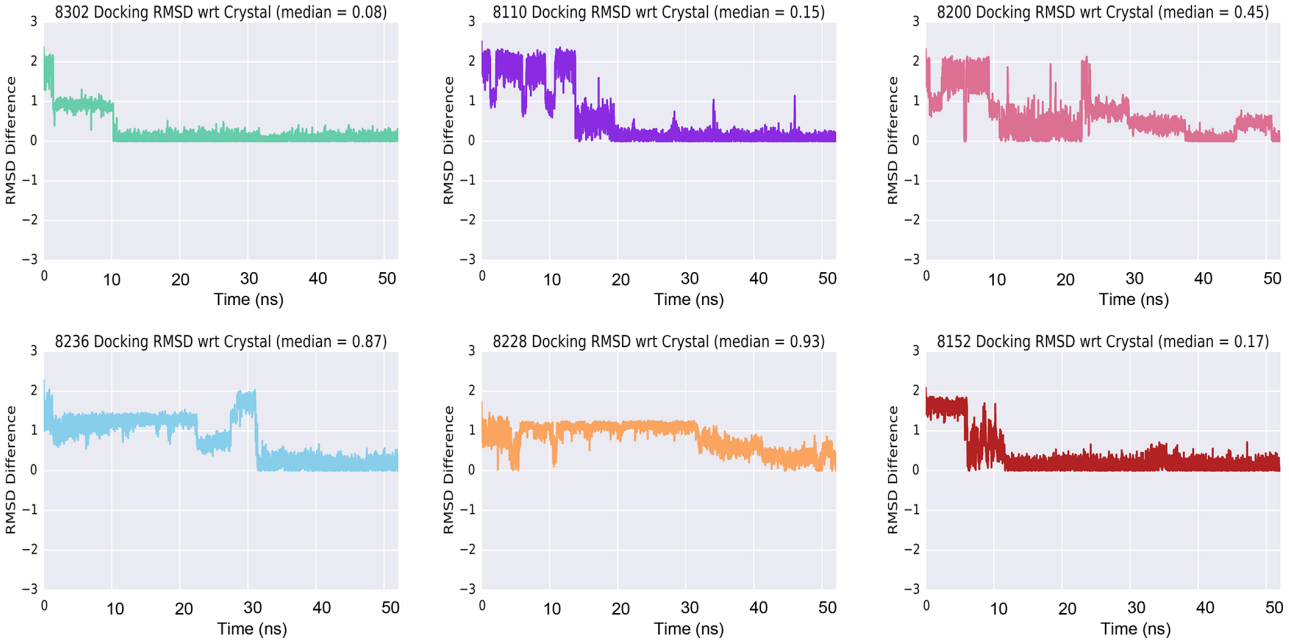


Figure 3. *N*-[3-(2-Oxo-pyrrolidinyl)phenyl]-benzenesulfonamide ligand RMSD relative to the cocrystal pose over the duration of the MD simulation. Each panel illustrates how the ligand pose RMSD (Å) converged during the MD simulation from the original docking pose (obtained using a published cocrystal structure of a different chemotype) toward the experimentally determined cocrystal structure.

residue necessary for BRD4 inhibitor binding (Figure 2).[8] To assess whether the ligand conformation approaches the experimental binding pose, we transformed the default trajectory ligand RMSD relative to frame zero (the starting docked pose) into a representation relative to the cocrystal ligand pose using E1. The definition of RMSD is found in E2. The transformed trajectories are depicted in Figure 3 and illustrate how the docking poses, which are quite different from the experimental cocrystal structure, converge to RMSD within 0.08−0.46 Å, corresponding to the experimentally determined reference pose.

For further illustration, we extracted the final frame from each simulation and overlaid it onto the experimental cocrystal structure. Figure 4 shows that these poses are essentially identical. For the most active compound (8302), we calculated the heavy-atom RMSD of the protein binding site (5 Å around

DOI: 10.1021/acsomega.7b00553
ACS Omega 2017, 2, 4760−4771

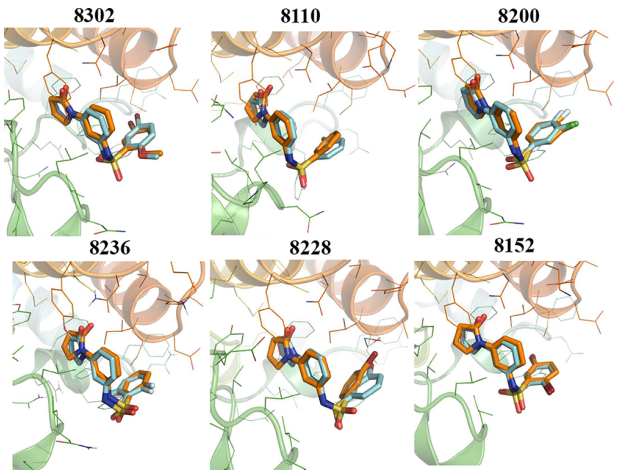


Figure 4. Overlay of ligand poses obtained by docking after MD optimization and experimental cocrystal structure. Bound ligand after MD shown in orange, and cocrystal ligand shown in teal. Ligand RMSD < 0.5 Å in all cases. Ligand poses after MD corresponded much more closely to the experimentally determined conformations compared to the initial docking poses.

the ligand) before and after the simulations and observed a 1.84 Å change in the binding site geometry during the simulation.

To demonstrate that the protein structure and the protein−ligand pose remain stable after the 50 ns MD simulation and that the simulation time of 50 ns is appropriate, we ran a 500 ns simulation of the best compound (8302) in BRD4(BD1) starting with the same docking pose as the initial simulations. Supplementary Figure 10 shows the protein and ligand heavy-atom RMSD of the 8302−BRD4(BD1) complex over the duration of 500 ns and clearly illustrates that both the protein and the ligand RMSD remain stable. The protein RMSD levels out at between 3 and 3.5 Å, which suggests that the binding site adjustment throughout the simulation (RMSD 1.8 Å) is significant.

Our results demonstrate that via MD simulations (starting from the best docking poses) we can reliably reproduce the experimentally observed cocrystal protein−ligand complexes much more accurately than docking alone (Supplementary Table 2). Although not unexpected, this is an important and encouraging result from the perspective of virtual screening, rational drug design, and lead optimization.

We next determined whether the protein−ligand complexes optimized by MD (but not using our experimental cocrystal structures) would improve the ability to identify and rank order active compounds compared to the original models based on the previously published PDB cocrystal structures. We asked whether optimizing ligand docking poses using MD could improve computational predictions without the need to obtain cocrystal structures. Although all-atom explicit solvent MD simulations can be computationally expensive, methods such as minimization with implicit solvent neglect important water contributions to BRD4(BD1) binding and do not sample the protein−ligand interface sufficiently to escape static local minima and reliably predict the correct pose. To test this, we extracted three frames from the MD trajectory (after stabilization of the ligand RMSD) of the three most active ligands (8302, 8110, and 8200) and prepared docking models. Known active and decoy compounds were redocked using the three models, and docking scores were aggregated as before (see Methods). Using the MD-optimized model, docking predictions for the experimentally determined active compounds better reflected their BRD4 activity; the most active compounds received better docking scores. The receiver operating characteristic area under the curve (ROC) score using previously known BRD4 actives was slightly improved, suggesting that the MD-optimized docking models do not result in decreased predictive performance for other BRD4 scaffolds but tend to globally improve predictive performance (Supplementary Figure 4).

Using the optimized models, we then redocked the 908 compounds from which our lead compounds had originally been identified. All *N*-[3-(2-oxo-pyrrolidinyl)phenyl]-benzenesulfonamide derivatives scored consistently better compared to the original models, and they better correlated quantitatively to their experimentally determined BRD4 activity (Figure 5, Supplementary Figure 5). In addition to correlating experimental pIC_{50} values with docking scores (Supplementary Figure 5a), we also computed molecular mechanics-generalized Born surface area (MM-GBSA) binding free energies and observed the same trend in which the computed estimated binding free energy tracked the experimental activity much better postoptimization, compared to preoptimization (Supplementary Figure 5b).

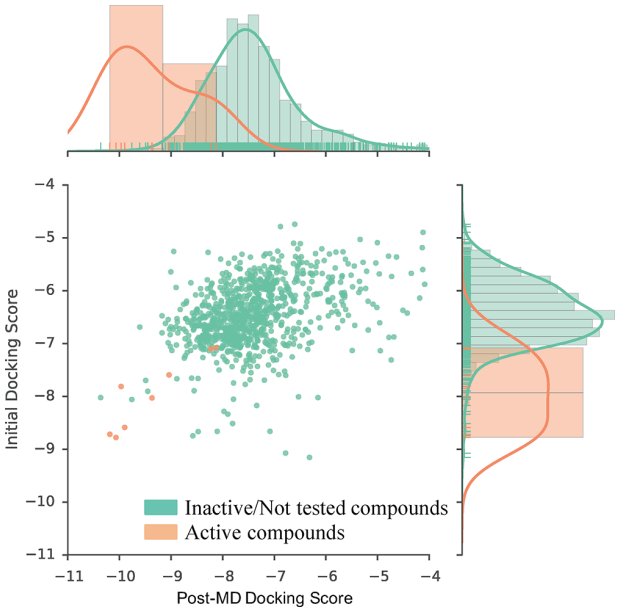


Figure 5. Ensemble docking score distribution of the initial and the MD-optimized docking models. The plot shows the distribution of active compounds (peach) and inactive compounds (teal). The vertical (y) axis and histogram on the right correspond to the distribution of the original docking scores (before MD optimization). The horizontal (x) axis and histogram on the top of the plot correspond to the docking scores after MD optimization. The MD-optimized docking scores show much better separation between active and inactive compounds.

To demonstrate that the MD-optimized docking model improves the enrichment of commercially available compounds determined to be active against BRD4, a log−enrichment curve was calculated. The MD-optimized docking model better ranked active compounds compared to the initial docking model before MD (Supplementary Figure 6). Enrichment

DOI: 10.1021/acsomega.7b00553
ACS Omega 2017, 2, 4760−4771

factors (EFs) for the top 1% best scoring compounds were 51 and 38 for the MD-optimized and initial docking models, respectively (Supplementary Table 3). The 908 compounds from which the *N*-[3-(2-oxo-pyrrolidinyl)phenyl]-benzenesulfonamide derivatives were identified included four additional sulfonamide compounds that were not prioritized in our original docking study and therefore not ordered or tested. Although the optimized docking scores of these compounds also improved (scores initially ranging from −6.56 to −6.83 and improving to the range −7.09 to −7.54), their optimized score would not have placed them among the top compounds for experimental testing, suggesting that our method does not indiscriminately result in better docking scores for the chemotype it was optimized with but better separates actives from inactives. In addition to better separating the active sulfonamide compounds from the remaining compounds and thus more confidently predicting their activity, the optimized model generally better separated active compounds from their presumed inactive decoys. Compounds that were purchased, but found to be inactive, scored more poorly (Figure 5). Together, these results suggest that the predictive performance of a docking model can be improved upon structural optimization using MD simulations. As expected, this improvement is particularly effective for compounds of the same scaffold as the optimized bound ligand, but an overall improvement of enrichment and predictive performance for known active BRD4 compounds is also evident. Most importantly however, we were able to reproduce the experimental binding pose via MD starting from a docking pose of a receptor of a different cocrystal ligand. This approach therefore appears useful for structure-guided lead optimization without the need for a cocrystal structure.

To investigate the novelty of the sulfonamide compound series, Tanimoto similarities against all known BRD4 compounds using ECFP4 chemical fingerprints were computed (Supplementary Figure 7a). Nine of the most similar (0.3−0.4) reported BRD4 inhibitors are shown in Supplementary Figure 7b. Although this cutoff would not be significant enough to consider them likely active based on the similarity alone, we further investigated the compounds, which included PFI-1 (compound **4** in Supporting Figure 7) and derivatives as well as phenyl isoxazole sulfonamide compounds (compounds **1**−**3** in Supporting Figure 7) from GSK.[27,28] These compounds are structurally distinct from our *N*-[3-(2-oxo-pyrrolidinyl)phenyl]-benzenesulfonamides, particularly the 2-oxo-pyrrolidinyl moiety that forms the characteristic hydrogen bonding interaction with BRD4 N140. We also computed the 3D shape similarity of our novel sulfonamide BRD4 binders to all known inhibitors using the ROCS package from OpenEye[29] (see Methods). There was no single shape or color ROCS similarity score greater than 0.5 and the Tanimoto Combo score, which includes both shape and color scoring, varied between 0.2 and 0.7 for all of the known BRD4 compounds (Supplementary Figure 8a). Tanimoto Combo is a combination of both shape Tanimoto and color Tanimoto scoring functions (the score ranges from 0 to 2), and many perceive it as the best global 3D similarity scoring metric in the ROCS package.[29] Supplementary Figure 8b shows the top six most shape-similar compounds, including phenyl isoxazole sulfonamide compounds also enriched in the ECFP4 similarity study, and isoxazole azepine compounds, which share similar binding interactions in their amino-isoxazole moiety.[28,30]

To investigate perceived pharmacophoric similarity of the well-characterized PFI-1 to our compounds, we aligned the cocrystal structure of the most active compound in our series, 8302, with PFI-1. Supplementary Figure 9 illustrates similarity in binding orientation; we determined RMSD to be 1.1 Å. The sulfonamide and the aromatic substituents are well-aligned, and both compounds exhibit the key hydrogen bond interaction with N140 via their 2-oxo-pyrrolidinyl (8302) and tetrahydroquinazoline-2-one moieties. However, this interaction is to be expected and is the characteristic binding motif of most BRD4(BD1) inhibitors. Additionally, 8302 maintains hydrophobic interactions with Y81, W83, and I146, which is distinct from PFI-1 (see Discussion). This characterization suggested that our compounds are pharmacophorically somewhat similar to PFI-1 but topologically and electrostatically distinct.

DISCUSSION AND CONCLUSIONS

We discovered a new class of BRD4 inhibitors, characterized the compounds biochemically, produced cocrystal structures, and studied the binding dynamics of these novel compounds as a starting point for future optimization.

Our virtual screening protocol used a high-throughput ensemble docking protocol employing various BRD4 protein structures that were prepared to incorporate or exclude conserved cocrystal water. The rationale of our approach was to sample a number of representative and feasible receptor conformations and binding modes (e.g., with or without water bridges). However, despite using an ensemble method, significant deviations of predicted versus experimental cocrystal ligand binding conformations were observed on the order of ∼2 Å heavy-atom RMSD per ligand. Receptor flexibility and specifically induced receptor conformational changes upon small-molecule binding as well as water molecules participating in binding are highly complex processes and challenging to predict accurately, in particular via high-throughput virtual screening such as docking, including ensemble docking with data fusion. Novel chemotypes with no ligand-similar experimental cocrystal structures are therefore especially difficult to model. We identified several novel active compounds, and we extensively characterized these inhibitors biochemically and determined the cocrystal structure of all six compounds. With that information, we explored the binding dynamics of these ligands in the BRD4(BD1) structure with the goal to predict the correct, experimentally determined, cocrystal binding pose starting from previously published cocrystal structures, such that it would not be required to obtain a cocrystal structure for the new chemotype. Secondarily, we were interested to improve the relative binding affinity predictions and enrichment of active compounds. The consideration of binding dynamics is particularly relevant for flexible protein domains and for targets where water frequently participates in binding such as with BET proteins.

Addressing these issues, we demonstrated that we can generate accurate binding models of *N*-[3-(2-oxo-pyrrolidinyl)-phenyl]-benzenesulfonamide derivatives in BRD4 using molecular docking followed by 50 ns all-atom explicit water MD simulations. The obtained binding poses were essentially equivalent to experimental cocrystal structures. With the availability of advanced force fields and algorithms implemented in user-friendly software and increased computational power, relatively short (50 ns) MD simulations can now be employed routinely. The time frame of 50 ns appears sufficient to generate a stable ligand receptor conformation almost exactly

DOI: 10.1021/acsomega.7b00553
ACS Omega 2017, 2, 4760−4771

reproducing the experimentally determined binding pose, if the starting docking conformation can assist in separating active from inactive compounds. This was further supported by a simulation with a 10-fold increased simulation time (500 ns) of the most active compound in which the protein and ligand RMSD remain stable (Supplementary Figure 10). We showed that these optimized models can better prioritize compounds and result in improved enrichment of known actives and in particular the sulfonamide compounds. This improvement is likely due to the increased sampling of ligand and protein states and convergence toward more energetically favorable conformations, which are likely different from the initial crystal structure conformation bound to a different chemotype. RMSD of just the BRD4(BD1) binding site heavy atoms during the simulation illustrated the adjustment of the binding site geometry compared to other chemotypes. Our results are significant in that *N*-[3-(2-oxo-pyrrolidinyl)phenyl]-benzenesulfonamide represents a novel scaffold of BRD4 binders, quantified by 2D structure and 3D shape-based similarity comparisons to previously reported actives.

The first potent inhibitors of BET proteins, (+)-JQ1[31] and I-BET762,[32,33] were developed based on compounds found to increase the apolipoprotein A-1 (ApoA1) activity in anti-inflammatory phenotypic screens. Both compounds are triazolodiazepines and share a common binding mode in the acetyl-lysine binding site of BET proteins. The structure of the BRD4-1 and (+)-JQ1 complex (PDB ID: 3MXF) shows that the triazole ring functions as an acetyl-lysine mimic by occupying the same position as the acetyl group in histone tail peptides. The two adjacent nitrogen atoms of the triazole ring replicate the carbonyl group of acetyl-lysine with one hydrogen bond interaction with the amide side chain of the conserved asparagine residue (N140 in BRD4-1) and another to the hydroxyl side chain of Y97, courtesy of a bridging hydrogen bond through a water molecule of the structurally conserved ZA channel. (+)-JQ1 binding is further stabilized through extensive hydrophobic interactions: the pendant 4-chlorophenyl substituent of the diazepine ring occupies the hydrophobic WPF (tryptophan, proline, and phenylalanine) shelf (W81-P82-F83) present in all BET family members and the dimethyl-substituted thieno ring packs between the same WP motif and L92 of the ZA loop. Notably, the natural bend of the thienodiazepine core arcs (+)-JQ1 is effectively over the WPF shelf and is critical to attaining the near-perfect shape complementarity of this chemotype. Like (+)-JQ1, the pyrrolidinone moiety of our *N*-[3-(2-oxo-pyrrolidinyl)-phenyl]-benzenesulfonamide chemotype functions as an acetyl-lysine mimic with the oxygen atom, establishing both a direct hydrogen bond to N140 and a ZA channel-mediated bridging hydrogen bond to Y97. In contrast to (+)-JQ1, these compounds form an additional bridging water-mediated hydrogen bond through the sulfonamide nitrogen atom to the main chain carbonyl of L92. Although our compounds also contain substituted phenyl rings which occupy a similar position to the 4-chlorophenyl substituent of (+)-JQ1, they lack many of the stabilizing hydrophobic interactions afforded to (+)-JQ1 by the larger thienodiazepine-based core, such as $\pi-\pi$ stacking and van der Waals interactions between the dimethyl-substituted thieno ring and P82 and L92, respectively. Given the importance of extensive hydrophobic interactions to the positioning of small-molecule inhibitors in the BRD4 acetyl-lysine binding site, the reduced availability of these in our chemotype likely explains their reduced affinity compared to (+)-JQ1 ($IC_{50:BRD4(BD1)}$ = 77 nM).

Following the discovery that triazolodiazepines are potent inhibitors of BET proteins, further research aimed to identify new chemotypes which mimicked the acetyl-lysine moiety using fragment-based screening approaches. Lead optimization of one such hit led to the development of the dihydroquinazolinone PFI-1 ($IC_{50:BRD4(BD1)}$ = 220 nM).[34] An analysis of the BRD4(BD1) and PFI-1 complex (PMID: 4E96) reveals that the carbonyl and NH of the cyclic urea function as a hydrogen bond donor/acceptor pair with the side chain of N140. Like the acetyl-lysine carbonyl, the quinaolinone carbonyl of PFI-1 also establishes a ZA channel-mediated bridging hydrogen bond to Y97. Furthermore, PFI-1 forms an additional bridging water-mediated hydrogen bond through the sulfonamide nitrogen atom to the backbone carbonyl of L92 in the ZA loop. Similarly to (+)-JQ1, the 2-methoxyphenyl substituent is directed into the hydrophobic WPF shelf. Superimposition of our cocrystal structures with that of the BRD4-PFI-1 complex reveals a remarkably conserved binding mechanism. The pyrrolidinone and urea carbonyls of our *N*-[3-(2-oxo-pyrrolidinyl)phenyl]-benzenesulfonamides and PFI-1, respectively, overlap with one another and serve as the principal acetyl-lysine mimicking moieties, establishing direct hydrogen bonds to N140 and water-mediated hydrogen bonds to Y97. The central phenyl ring of our compounds occupies the same space as the dihydroquinazolinone phenyl of PFI-1. Noticeably, both chemotypes contain a sulfonamide linker that introduces a sharp ∼120° turn in their planar core structures, thereby directing the sulfonamide phenyl rings toward the hydrophobic WPF shelf. Likewise, the sulfonamide nitrogen in both chemotypes establishes an additional bridging water-mediated hydrogen bond to the main chain carbonyl of L92.

Another widely explored chemotype is the dimethylisoxazoles, as represented by the prototypical member I-BET151/GSK1210151A ($IC_{50:BRD4(BD1)}$ = 790 nM).[35] The BRD4-1 and I-BET-151 cocrystal structures (PDB ID: 3ZYU) demonstrate that the isoxazole moiety serves as an acetyl-lysine mimic binding deep within the pocket, forming a direct hydrogen bond to the side chain of N140 and a water-mediated hydrogen bond to the side chain of Y97 through the isoxazole oxygen and nitrogen atoms, respectively. Additionally, the quinolone nitrogen atom forms a water-mediated bridging hydrogen bond to the main chain carbonyls of P82 and Q85 and to the amide side chain of Q85. Like the thienodiazepine core of (+)-JQ1, the quinolone core of I-BET151 packs between the WP motif and Leu92, and the pyridyl group interacts with the hydrophobic WPF shelf (albeit in a different orientation due to the stereochemistry of the preceding carbon). Comparison of the I-BET151 and *N*-[3-(2-oxo-pyrrolidinyl)phenyl]-benzenesulfonamide binding modes shows that the carbonyl oxygens of the respective isoxazole and pyrrolidinone moieties overlap in agreement with their acetyl-lysine mimicking properties. However, other aspects of their binding are different in line with their highly divergent scaffolds. Apart from both chemotypes directing a phenyl substituent to the WPF shelf, like the preceding discussion of the (+)-JQ1 binding mechanism, our compounds lack many of the hydrophobic and stacking interactions formed by I-BET151, reducing their respective affinities toward BRD4-1.

Finally, an inspection of other common BRD4 inhibitor chemotypes, including the quinazolones (e.g., RVX-208),[36] diazobenzenes (e.g., MS436),[37] and triazolopyridazines (e.g.,

DOI: 10.1021/acsomega.7b00553
ACS Omega 2017, 2, 4760−4771

bromosporine),[38] shows that the prevailing commonality is the presence of an acetyl-lysine mimicking moiety which overlays with the pyrrolidinone of our *N*-[3-(2-oxo-pyrrolidinyl)-phenyl]-benzenesulfonamides. Interestingly, many members of these other chemotypes do not contain a pendant phenyl substituent directed toward the hydrophobic WPF shelf in a manner analogous to that of the 4-chlorophenyl and 2-methoxyphenyl moieties of (+)-JQ1 and PFI-1, respectively, despite retaining modest activity against BRD4-1, indicating that occupying the WPF shelf at this position with an aromatic substituent is not essential for potency. However, it is noteworthy that these compounds do have alternative aromatic and hydrophobic substituents, which can engage in other elaborate $\pi-\pi$ stacking and van der Waals interactions with residues at the entrance of the acetyl-lysine binding pocket of BRD4-1, features which are absent from our compounds.

Taken together, the *N*-[3-(2-oxo-pyrrolidinyl)phenyl]-benzenesulfonamide chemotype reported in this work contains a pyrrolidinone moiety as an acetyl-lysine mimic, which establishes a direct hydrogen bond to the conserved N140 in BRD4-1. In this regard, our chemotype provides a novel chemical starting point to the development of structurally diverse BET inhibitors and illustrates the large chemical diversity accommodated by this protein pocket. However, unlike many of the most potent BET inhibitors such as (+)-JQ1 and I-BET151, our compounds lack many of the $\pi-\pi$ stacking and hydrophobic interactions necessary for further stabilization inside of the acetyl-lysine binding site, likely explaining the reduced potency of this chemotype.

From the interaction diagrams (Figure 1 and Supplementary Figure 2) of our six cocrystal structures of *N*-[3-(2-oxo-pyrrolidinyl)phenyl]-benzenesulfonamide ligands, it is evident that all six compounds bind with the acetyl-lysine binding motif of bromodomain in a similar manner, presumably explaining the relatively narrow range of the observed IC_{50} values (11−44 μM) (Table 1). However, in the case of 8302, the presence of an additional H bond acceptor (−OMe group at the ortho position of the terminal phenyl ring, with respect to the sulfonamide functionality) appears to provide improved binding because of better stabilization of the water network. Adding relatively small halogen atoms, for example, F (in cases of 8110, 8200, and 8236) and Cl (8200), to the terminal phenyl ring does not change the binding significantly. However, adding bulky atoms such as Br, especially at the ortho position (8152) of the phenyl ring, seems to weaken the binding because of steric hindrance. Future SAR and optimization to include substituents enabling interactions observed with the most potent inhibitors (as described above) would be predicted to significantly improve potency.

EXPERIMENTAL SECTION

BRD4 Biochemical Activity Data. The activity data of known BRD4 inhibitors were extracted from the ChEMBL18 database (May 7, 2014) and also curated from the recent literature.[27,30,31,39−43] We utilize only compounds with reported concentration response activity data ($IC_{50}/K_d/K_i$). Chemical structures were standardized including protonation states (neutral form, protonate acids, and deprotonate bases), tautomer standardization, removal of salts/addends, and assigning the correct stereochemical and geometric configuration using Pipeline Pilot 8.0 (Accelrys) (ambiguous stereochemistry or geometric configuration is handled by LigPrep, see below); unique IDs were assigned corresponding to unique structure representations. Activity data were *p*-transformed ($-\log_{10}$) and aggregated by unique compound ID using the median activity *p*-value. We provide aggregate and standardized activity data of compounds tested in the Library of Integrated Network-based Cellular Signatures (LINCS) program (http://www.lincsproject.org/), which is available via the LINCS data portal (http://lincsportal.ccs.miami.edu/).

To estimate enrichment and determine thresholds for docking score significance, the 246 unique BRD4 inhibitors from ChEMBL were submitted to generate decoy sets from the directory of useful decoys, enhanced (DUD-E).[44] DUD-E generated 50−100 decoy molecules per submitted ligand SMILES. The protocol for preprocessing the 246 original ligands and the corresponding 15 250 decoy compounds (15 496 compounds total) for docking is below.

Ensemble Docking Protocol and Data Fusion. *BRD4 Docking Models.* We used the Schrödinger 2014.2 software suite for structure-based manipulations and simulations unless otherwise indicated.[26] Seven BRD4 cocrystal structures were selected from the PDB from 65 available structures (January 2014). Three crystal structures for the extensively characterized BRD4 inhibitors, namely, JQ1 (3MXF), I-BET151 (3ZYU), and I-BET762 (3P5O), were chosen. Other PDB crystal structures included 4HXS, 4C67, 4LR6, and 4LYW. Overall, the selection criteria included the atomic resolution of the X-ray crystal structure, diversity in the cocrystal ligand scaffold, and ligand interactions in the binding site. From the seven crystal structures chosen, we identified conserved waters found in/around the ligand binding sites to incorporate likely ligand−protein water bridges into our models. To do this, we aligned all BRD4 crystal structures and determined which waters fell within 5 Å of the active site. We then kept these waters specifically in the preparation process of two out of the seven crystal structures, in addition to those that we had already prepared. This amounted to nine prepared crystal structures with which to produce docking models as described previously.

BRD4 protein structures were preprocessed using the protein preparation workflow in Maestro 9.5 to assign bond orders and refine the structure including hydrogen bond optimization and constrained minimization. Where needed, missing side chains were added using Schrödinger Prime. For each structure, one protein chain with the cocrystal ligand was kept, and water molecules were deleted beyond 5 Å from heteroatom groups. In addition, the internal hydrogen bond network was optimized, followed by constrained energy minimization.

For the resulting nine structure representations, docking grids were generated around the cocrystal binding sites using Schrödinger Glide in the default settings. Redocking each cocrystal ligand into its corresponding structure validated models; in each case, the cocrystal pose was reproduced with RMSD values <1 Å.

Ligand Preparation. Ionization states, tautomeric forms, and 3D conformations for 15 496 SMILES (246 known BRD4 ligands and 15 250 decoy compounds) were generated using LigPrep (Schrödinger 2014.2). The default conditions were maintained, except for the ionization states which were generated at the target pH of 7 ± 2 using Epik including the original state. The resulting 3D ligand representations were exported as structure data files, and unique IDs were assigned based on unique canonical structures to facilitate postdocking hierarchical data fusion as previously described.

Docking Protocol. Ligand representations obtained via LigPrep for all (BRD4 known active and decoy) compounds

DOI: 10.1021/acsomega.7b00553
ACS Omega 2017, 2, 4760−4771

were docked against all nine prepared BRD4(1) models using Glide (Schrödinger 2014.2) in standard precision (SP) with the default settings, except writing out at most 5 poses per ligand representation and including 25 poses per ligand for postdocking minimization. All docking results were exported from Maestro 9.5 as delimited text files. The docking scores were aggregated hierarchically at three levels, at each level generating average and top docking scores as follows: (i) for each unique ligand representation structure, the scores of all corresponding docking poses were aggregated; (ii) pose-aggregate scores of unique ligand representations (generated in LigPrep) were aggregated by unique (original) compound structure (across ionization states and tautomers); and (iii) aggregate compound scores were combined across all protein structures. At the ligand representation level, we considered top and average top 3 and average top 5 pose scores; at the compound level, the top and average of all corresponding ligand representations; and at the protein level, the top and average top 3 and top 5 scores, giving a total of 18 aggregation methods. On the basis of the model evaluation results for all aggregation methods, for the final results we used the top scores obtained across all levels; for each ligand structure, this corresponds to the best pose for the best ligand representation in the best protein-docking model.

Optimized Docking Models. We generated optimized docking models from three MD simulation frames of the three most active sulfonamide compounds (8302, 8110, and 8200) at 40, 45, and 50 ns in the simulation, respectively. Docking was performed using Glide (Schrödinger 2014.2) in SP with the default settings (keeping cocrystal waters within 5 Å of the ligand), except writing out at most 5 poses per ligand representation and including 25 poses per ligand for postdocking minimization. Maestro 9.5 allows export of all docking results as delimited text files. The docking scores were aggregated first by pose for each ligand representation, then across all representations for each ligand (e.g., tautomers and protonation states), and then across the protein structure (docking) models for 8302, 8110, and 8200, at each level generating average and top docking scores as described previously.[26]

MM-GBSA Energy Calculations. Prime MM-GBSA calculations were carried out using the initial and MD-optimized receptor−ligand complexes. All default parameters were used, including the VSGB 2.0 solvation model. Calculations were performed using the Schrödinger 2016.3 software suite.

Evaluation and Characterization of Computational Predictions. The docking method optimization was evaluated by the ROC score using the known BRD4 inhibitors and the large decoy dataset (described above). The ROC score show sensitivity over 1—specificity, that is, true positive rate over the false positive rate. On the basis of the model evaluation results for all permutations of top and average scores across poses, ligand representations, and protein structure models, we ended up using the top scores obtained across all levels; for each ligand structure, this corresponds to the best pose for the best ligand representation in the best protein-docking model termed. ROC curves for the initial and MD-optimized (best) docking scores are shown in Supplementary Figure 4. Additionally, EF at 1% top scoring compounds and correlation of aggregate docking scores and activity data were calculated for the 908 commercially available compounds for which activity information had been determined (Supplementary Figure 5, Supplementary Table 3). EF at 1% is [true positives (top 1%)/number of samples (top 1%)]/[positives (total)/number of samples (total)], that is, the ratio of true positives detected in the subset divided by the fraction of overall (total) positives. Also, a log−enrichment curve was calculated for the initial and MD-optimized docking models for predicted commercially available compounds (Supplementary Figure 6).

MD Simulations. All-atom (OPLS2005 force field) explicit water MD simulations were performed using the Desmond 2014.2 software suite (D. E. Shaw Research) via Maestro 9.8.[12,14,45] MD systems were built using the highest scoring docking pose for each sulfonamide compound. Specifically, PDB structures 4HXS for 8236 and 8228, 3MXF for 8110, and 4LR6 for 8302, 8152, and 8200. The system boundary distances were specified as 10.0 Å in each dimension in an orthorhombic box. For all simulations, the Desmond default OPLS_2005 force field with simple point charge water model and NPT (temperature (T), pressure (P), and the number of particles-(N)) ensemble was used. Desmond automatically places Na^+ ions to neutralize the system and a salt concentration of 0.15 M and performs multiple rounds of energy minimization and model relaxation before the production simulation. Each 50 ns simulation was run on the Pegasus cluster from the Center for Computational Science at the University of Miami (http://ccs.miami.edu/hpc/) using 48 processors and completed in approximately 50 h. Simulation analysis was performed using the Desmond trajectory analysis software.

The 500 ns MD simulation of ligand 8302 in BRD4 (BD1) (starting from the best pose docked into 4LR6 as above) was performed using the same parameters as described above, but it was run on an Exxact Quantum TXR410-0128R equipped with Nvidia Tesla M40 GPUs using the GPU-accelerated Desmond software (v2016.3) and one GPU.

Analysis of MD Simulations. MD result analysis consisted of computing both the simulation event analysis and simulation interaction diagrams and exporting the results to a spreadsheet and diagram for analysis. Calculation of the trajectory ligand RMSD differences relative to the target experimental cocrystal pose (in contrast to the default starting docking pose) RMSD was as follows

$$\mathrm{RMSD}_{(\mathrm{Pi,Po})} - \mathrm{RMSD}_{(\mathrm{Pn,Po})} + \mathrm{RMSD}_{(\mathrm{Pn,Pr})} = \mathrm{RMSD}_{(\mathrm{Pi,Pr})} \quad \text{(E1)}$$

where Pi refers to the ligand pose as the time index i, Pn is the final ligand pose at the end of the simulation, Po is the starting ligand pose, that is, the docking pose, and Pr is the experimentally determined reference ligand pose.

The definition of RMSD in the course of an MD simulation is

$$\mathrm{RMSD}_x = \sqrt{\frac{1}{N}\sum_{j=1}^{N} (p_j'(t_i) - p_j(t_{\mathrm{ref}}))^2} \quad \text{(E2)}$$

where $p_j'(t_i)$ corresponds to the position atom j of the ligand with N atoms at time t_i, in our case Pi, and $p_j(t_{\mathrm{ref}})$ corresponds to the position of the ligand atom at a reference time point (usually time 0). E1 transforms RMSD of Pi relative time point 0 (Po) into RMSD relative to the absolute (simulation independent) reference pose Pr, the experimental ligand conformation. These calculations were implemented in Python after exporting RMSD data from Maestro for all six MD trajectories.

Ligand Shape Similarity. The ROCS 3.2.0 shape similarity screening software (Open Eye Scientific)[29,46] was utilized to

DOI: 10.1021/acsomega.7b00553
ACS Omega 2017, 2, 4760−4771

evaluate ligand 3D shape and electrostatic similarity between the experimentally determined active *N*-[3-(2-oxo-pyrrolidinyl)phenyl]-benzenesulfonamide compounds to all known BRD4 active compounds. The ROCS query was created from six aligned sulfonamide compounds exported from their best BRD4 docking pose (see above). The option to merge color atoms was selected, best hits defined as 100, shape only set to false, rank by set to Tanimoto Combo, and random starts set to 50. The Tanimoto Combo score was the main metric evaluated by our study.

Experimental Determination of Binding Activity. *BRD4(1) AlphaScreen and DSF Assays.* To perform the BRD4(1) AlphaScreen and DSF assays, we followed the same protocol described previously.[26] Compounds were obtained from *Enamine, LLC*, and the supplier provided purity confirmed ≥95% for each compound based on high-performance liquid chromatography; the traces can be found in the Supporting Information. To confirm assay results, we perform a PerkinElmer TruHits counter screen with the same assay system to determine if any compounds were interacting with the assay components, allowing for the determination of possible false positives.

X-Ray Crystallography and Structure Determination. Crystals of BRD4-1 were grown in the presence of 1 mM ligand and 10% (v/v) DMSO from vapor-diffusion hanging drops using reservoir as described previously,[47] harvested in cryoprotectant (reservoir containing 25% (v/v) ethylene glycol and 0.5 mM ligand) and flash frozen in a stream of nitrogen gas. X-ray diffraction data were recorded at −180 °C in the Moffitt Cancer Center Structural Biology Core using Cu Kα X-rays generated by a Rigaku MicroMax 007-HF X-ray generator, focused by mirror optics, and equipped with a Rigaku CCD Saturn 944 system and a Rigaku R-AXIS HTC imager. Data were reduced and scaled with XDS;[48] PHENIX[49] was employed for phasing and refinement, and model building was performed using Coot.[50] The structure was solved by molecular replacement using Phaser[51] and the monomer of PDB entry 4O7A[47] as the search model. Initial models for the small-molecule ligands were generated using MarvinSketch (ChemAxon, Cambridge, MA) with ligand restraints from eLBOW of the PHOENIX suite. All structures were validated by MolProbity[52] and phenix.model_vs_data.[53] Figures were prepared using PyMOL (Schrödinger, LLC).

■ ACCESSION CODES

Atomic coordinates and structure factors for complexes of BRD4(BD1) with compounds 8110, 8152, 8200, 8228, 8236, and 8302 have been deposited in the PDB under accession codes 5TI2, 5TI3, 5TI4, 5TI5, 5TI6, and 5TI7, respectively.

■ ASSOCIATED CONTENT

Supporting Information

The Supporting Information is available free of charge on the ACS Publications website at DOI: 10.1021/acsomega.7b00553.

Input coordinates of MD simulations and various other structures and result files are available in the Github repository: https://github.com/schurerlab/molecular-modeling (PDF)

■ AUTHOR INFORMATION

Corresponding Author

*E-mail: sschurer@miami.edu, sschurer@med.miami.edu (S.C.S.).

ORCID

Saurabh Mehta: 0000-0002-9174-128X

Stephan C. Schürer: 0000-0001-7180-0978

Author Contributions

B.K.A. and S.M. performed computational modeling, molecular dynamics, data curation, and data integration; B.K.A. developed code and performed biological experiments. S.W.J.E., J.-Y.Z., and E.S. conducted X-ray diffraction and DSF experiments. B.K.A. and S.C.S. performed data analysis. S.C.S. designed the study, and S.C.S. and N.G.A. advised the project. B.K.A., S.W.J.E., S.M., and S.C.S. wrote the manuscript. All authors contributed to and reviewed the manuscript.

Funding

This work was in part supported by grants U54CA189205 (Illuminating the Druggable Genome Knowledge Management Center, IDG-KMC) and U54HL127624 (BD2K LINCS Data Coordination and Integration Center, DCIC). The IDG-KMC is a component of the Illuminating the Druggable Genome (IDG) project (https://commonfund.nih.gov/idg) awarded by the NCI. The BD2K LINC DCIC is awarded by the National Heart, Lung, and Blood Institute through funds provided by the trans-NIH Library of Integrated Network-based Cellular Signatures (LINCS) Program (http://www.lincsproject.org/) and the trans-NIH Big Data to Knowledge (BD2K) initiative (http://www.bd2k.nih.gov). Both IDG and LINCS are NIH Common Fund projects. This work was in part supported by NS067289 to NGA.

Notes

The authors declare no competing financial interest.

■ ACKNOWLEDGMENTS

The authors would like to thank ChemAxon for providing the academic research license for their Cheminformatics software tools including JChem for Excel and the Marvin tools. The authors thank D. E. Shaw Research and Schrödinger for the Molecular Dynamics (MD) simulation package and Open Eye Scientific Software for their academic research licenses. S.M. gratefully acknowledges the receipt of CREST fellowship award (BT/IN/DBT-CREST Awards/29/SM/2012-13) from the Department of Biotechnology (DBT), Ministry of Science and Technology, Government of India. S.C.S. acknowledges computational resources of the Drug Discovery program of the Center for Computational Science at the University of Miami. The authors thank the Moffitt Structural Biology Core for use of the X-ray crystallography facility.

■ REFERENCES

(1) Allen, B. K.; Stathias, V.; Maloof, M. E.; Vidovic, D.; Winterbottom, E. F.; Capobianco, A. J.; Clarke, J.; Schurer, S.; Robbins, D. J.; Ayad, N. G. Epigenetic pathways and glioblastoma treatment: insights from signaling cascades. *J. Cell. Biochem.* **2015**, *116*, 351−363.

(2) Zoghbi, H. Y.; Beaudet, A. L. Epigenetics and Human Disease. *Cold Spring Harbor Perspect. Biol.* **2016**, *8*, a019497.

(3) Gil, J.; Ramírez-Torres, A.; Encarnación-Guevara, S. Lysine acetylation and cancer: A proteomics perspective. *J. Proteomics* **2017**, *150*, 297−309.

DOI: 10.1021/acsomega.7b00553
ACS Omega 2017, 2, 4760−4771

(4) Gallenkamp, D.; Gelato, K. A.; Haendler, B.; Weinmann, H. Bromodomains and their pharmacological inhibitors. *ChemMedChem* **2014**, *9*, 438−464.
(5) Muvva, C.; Singam, E. R. A.; Raman, S. S.; Subramanian, V. Structure-based virtual screening of novel, high-affinity BRD4 inhibitors. *Mol. BioSyst.* **2014**, *10*, 2384−2397.
(6) Bandopadhayay, P.; Bergthold, G.; Nguyen, B.; Schubert, S.; Gholamin, S.; Tang, Y.; Bolin, S.; Schumacher, S. E.; Zeid, R.; Masoud, S.; Yu, F.; Vue, N.; Gibson, W. J.; Paolella, B. R.; Mitra, S. S.; Cheshier, S. H.; Qi, J.; Liu, K.-W.; Wechsler-Reya, R.; Weiss, W. A.; Swartling, F. J.; Kieran, M. W.; Bradner, J. E.; Beroukhim, R.; Cho, Y.-J. BET bromodomain inhibition of MYC-amplified medulloblastoma. *Clin. Cancer Res.* **2014**, *20*, 912−925.
(7) Pastori, C.; Daniel, M.; Penas, C.; Volmar, C.-H.; Johnstone, A. L.; Brothers, S. P.; Graham, R. M.; Allen, B.; Sarkaria, J. N.; Komotar, R. J.; Wahlestedt, C.; Ayad, N. G. BET bromodomain proteins are required for glioblastoma cell proliferation. *Epigenetics* **2014**, *9*, 611−620.
(8) Liu, Z.; Wang, P.; Chen, H.; Wold, E. A.; Tian, B.; Brasier, A. R.; Zhou, J. Drug Discovery Targeting Bromodomain-Containing Protein 4. *J. Med. Chem.* **2017**, *60*, 4533−4558.
(9) Sliwoski, G.; Kothiwale, S.; Meiler, J.; Lowe, E. W., Jr. Computational methods in drug discovery. *Pharmacol. Rev.* **2014**, *66*, 334−395.
(10) Teague, S. J. Implications of protein flexibility for drug discovery. *Nat. Rev. Drug Discovery* **2003**, *2*, 527−541.
(11) Ma, B.; Kumar, S.; Tsai, C.-J.; Nussinov, R. Folding funnels and binding mechanisms. *Protein Eng.* **1999**, *12*, 713−720.
(12) Bowers, K. J.; Dror, R. O.; Shaw, D. E. The midpoint method for parallelization of particle simulations. *J. Chem. Phys.* **2006**, *124*, 184109.
(13) Ge, H.; Wang, Y.; Li, C.; Chen, N.; Xie, Y.; Xu, M.; He, Y.; Gu, X.; Wu, R.; Gu, Q.; Zeng, L.; Xu, J. Molecular dynamics-based virtual screening: accelerating the drug discovery process by high-performance computing. *J. Chem. Inf. Model.* **2013**, *53*, 2757−2764.
(14) Bowers, K. J.; et al. Scalable Algorithms for Molecular Dynamics Simulations on Commodity Clusters. *Proceedings of the ACM/IEEE Conference on Supercomputing (SC06)*, 2006.
(15) Chen, H.; Li, S.; Hu, Y.; Chen, G.; Jiang, Q.; Tong, R.; Zang, Z.; Cai, L. An Integrated In Silico Method to Discover Novel Rock1 Inhibitors: Multi- Complex-Based Pharmacophore, Molecular Dynamics Simulation and Hybrid Protocol Virtual Screening. *Comb. Chem. High Throughput Screening* **2016**, *19*, 36−50.
(16) Abbasi, M.; Sadeghi-Aliabadi, H.; Hassanzadeh, F.; Amanlou, M. Prediction of dual agents as an activator of mutant p53 and inhibitor of Hsp90 by docking, molecular dynamic simulation and virtual screening. *J. Mol. Graphics Modell.* **2015**, *61*, 186−195.
(17) Afzal, O.; Kumar, S.; Kumar, R.; Firoz, A.; Jaggi, M.; Bawa, S. Docking based virtual screening and molecular dynamics study to identify potential monoacylglycerol lipase inhibitors. *Bioorg. Med. Chem. Lett.* **2014**, *24*, 3986−3996.
(18) Ali, M. R.; Latif, R.; Davies, T. F.; Mezei, M. Monte Carlo loop refinement and virtual screening of the thyroid-stimulating hormone receptor transmembrane domain. *J. Biomol. Struct. Dyn.* **2015**, *33*, 1140−1152.
(19) Arrigoni, A.; Bertini, L.; De Gioia, L.; Papaleo, E. Inhibitors of the Cdc34 acidic loop: A computational investigation integrating molecular dynamics, virtual screening and docking approaches. *FEBS Open Bio* **2014**, *4*, 473−484.
(20) Cavasotto, C. N.; Orry, A. J. W.; Murgolo, N. J.; Czarniecki, M. F.; Kocsi, S. A.; Hawes, B. E.; O'Neill, K. A.; Hine, H.; Burton, M. S.; Voigt, J. H.; Abagyan, R. A.; Bayne, M. L.; Monsma, F. J., Jr. Discovery of novel chemotypes to a G-protein-coupled receptor through ligand-steered homology modeling and structure-based virtual screening. *J. Med. Chem.* **2008**, *51*, 581−588.
(21) Aldeghi, M.; Heifetz, A.; Bodkin, M. J.; Knapp, S.; Biggin, P. C. Accurate calculation of the absolute free energy of binding for drug molecules. *Chem. Sci.* **2016**, *7*, 207−218.
(22) Cappel, D.; Hall, M. L.; Lenselink, E. B.; Beuming, T.; Qi, J.; Bradner, J.; Sherman, W. Relative Binding Free Energy Calculations Applied to Protein Homology Models. *J. Chem. Inf. Model.* **2016**, *56*, 2388−2400.
(23) Dickson, B. M.; de Waal, P. W.; Ramjan, Z. H.; Xu, H. E.; Rothbart, S. B. A fast, open source implementation of adaptive biasing potentials uncovers a ligand design strategy for the chromatin regulator BRD4. *J. Chem. Phys.* **2016**, *145*, 154113.
(24) Ran, T.; Zhang, Z.; Liu, K.; Lu, Y.; Li, H.; Xu, J.; Xiong, X.; Zhang, Y.; Xu, A.; Lu, S.; Liu, H.; Lu, T.; Chen, Y. Insight into the key interactions of bromodomain inhibitors based on molecular docking, interaction fingerprinting, molecular dynamics and binding free energy calculation. *Mol. BioSyst.* **2015**, *11*, 1295−1304.
(25) Bernstein, F. C.; Koetzle, T. F.; Williams, G. J. B.; Meyer, E. F., Jr.; Brice, M. D.; Rodgers, J. R.; Kennard, O.; Shimanouchi, T.; Tasumi, M. The Protein Data Bank: a computer-based archival file for macromolecular structures. *J. Mol. Biol.* **1977**, *112*, 535−542.
(26) Allen, B. K.; Mehta, S.; Ember, S. W. J.; Schonbrunn, E.; Ayad, N.; Schürer, S. C. Large-Scale Computational Screening Identifies First in Class Multitarget Inhibitor of EGFR Kinase and BRD4. *Sci. Rep.* **2015**, *5*, 16924.
(27) Fish, P. V.; Filippakopoulos, P.; Bish, G.; Brennan, P. E.; Bunnage, M. E.; Cook, A. S.; Federov, O.; Gerstenberger, B. S.; Jones, H.; Knapp, S.; Marsden, B.; Nocka, K.; Owen, D. R.; Philpott, M.; Picaud, S.; Primiano, M. J.; Ralph, M. J.; Sciammetta, N.; Trzupek, J. D. Identification of a chemical probe for bromo and extra C-terminal bromodomain inhibition through optimization of a fragment-derived hit. *J. Med. Chem.* **2012**, *55*, 9831−9837.
(28) Bamborough, P.; Diallo, H.; Goodacre, J. D.; Gordon, L.; Lewis, A.; Seal, J. T.; Wilson, D. M.; Woodrow, M. D.; Chung, C.-w. Fragment-based discovery of bromodomain inhibitors part 2: optimization of phenylisoxazole sulfonamides. *J. Med. Chem.* **2012**, *55*, 587−596.
(29) Hawkins, P. C. D.; Skillman, A. G.; Nicholls, A. Comparison of shape-matching and docking as virtual screening tools. *J. Med. Chem.* **2007**, *50*, 74−82.
(30) Gehling, V. S.; Hewitt, M. C.; Vaswani, R. G.; Leblanc, Y.; Côté, A.; Nasveschuk, C. G.; Taylor, A. M.; Harmange, J.-C.; Audia, J. E.; Pardo, E.; Joshi, S.; Sandy, P.; Mertz, J. A.; Sims, R. J., 3rd; Bergeron, L.; Bryant, B. M.; Bellon, S.; Poy, F.; Jayaram, H.; Sankaranarayanan, R.; Yellapantula, S.; Srinivasamurthy, N. B.; Birudukota, S.; Albrecht, B. K. Discovery, Design, and Optimization of Isoxazole Azepine BET Inhibitors. *ACS Med. Chem. Lett.* **2013**, *4*, 835−840.
(31) Filippakopoulos, P.; Qi, J.; Picaud, S.; Shen, Y.; Smith, W. B.; Fedorov, O.; Morse, E. M.; Keates, T.; Hickman, T. T.; Felletar, I.; Philpott, M.; Munro, S.; McKeown, M. R.; Wang, Y.; Christie, A. L.; West, N.; Cameron, M. J.; Schwartz, B.; Heightman, T. D.; La Thangue, N.; French, C. A.; Wiest, O.; Kung, A. L.; Knapp, S.; Bradner, J. E. Selective inhibition of BET bromodomains. *Nature* **2010**, *468*, 1067−1073.
(32) Mirguet, O.; Gosmini, R.; Toum, J.; Clément, C. A.; Barnathan, M.; Brusq, J.-M.; Mordaunt, J. E.; Grimes, R. M.; Crowe, M.; Pineau, O.; Ajakane, M.; Daugan, A.; Jeffrey, P.; Cutler, L.; Haynes, A. C.; Smithers, N. N.; Chung, C.-w.; Bamborough, P.; Uings, I. J.; Lewis, A.; Witherington, J.; Parr, N.; Prinjha, R. K.; Nicodème, E. Discovery of epigenetic regulator I-BET762: lead optimization to afford a clinical candidate inhibitor of the BET bromodomains. *J. Med. Chem.* **2013**, *56*, 7501−7515.
(33) Nicodeme, E.; Jeffrey, K. L.; Schaefer, U.; Beinke, S.; Dewell, S.; Chung, C.-w.; Chandwani, R.; Marazzi, I.; Wilson, P.; Coste, H.; White, J.; Kirilovsky, J.; Rice, C. M.; Lora, J. M.; Prinjha, R. K.; Lee, K.; Tarakhovsky, A. Suppression of inflammation by a synthetic histone mimic. *Nature* **2010**, *468*, 1119−1123.
(34) Picaud, S.; Da Costa, D.; Thanasopoulou, A.; Filippakopoulos, P.; Fish, P. V.; Philpott, M.; Fedorov, O.; Brennan, P.; Bunnage, M. E.; Owen, D. R.; Bradner, J. E.; Taniere, P.; O'Sullivan, B.; Muller, S.; Schwaller, J.; Stankovic, T.; Knapp, S. PFI-1, a highly selective protein interaction inhibitor, targeting BET Bromodomains. *Cancer Res.* **2013**, *73*, 3336−3346.

DOI: 10.1021/acsomega.7b00553
ACS Omega 2017, 2, 4760−4771

(35) Dawson, M. A.; Prinjha, R. K.; Dittmann, A.; Giotopoulos, G.; Bantscheff, M.; Chan, W.-I.; Robson, S. C.; Chung, C.-w.; Hopf, C.; Savitski, M. M.; Huthmacher, C.; Gudgin, E.; Lugo, D.; Beinke, S.; Chapman, T. D.; Roberts, E. J.; Soden, P. E.; Auger, K. R.; Mirguet, O.; Doehner, K.; Delwel, R.; Burnett, A. K.; Jeffrey, P.; Drewes, G.; Lee, K.; Huntly, B. J. P.; Kouzarides, T. Inhibition of BET recruitment to chromatin as an effective treatment for MLL-fusion leukaemia. *Nature* **2011**, *478*, 529−533.
(36) Picaud, S.; Wells, C.; Felletar, I.; Brotherton, D.; Martin, S.; Savitsky, P.; Diez-Dacal, B.; Philpott, M.; Bountra, C.; Lingard, H.; Fedorov, O.; Muller, S.; Brennan, P. E.; Knapp, S.; Filippakopoulos, P. RVX-208, an inhibitor of BET transcriptional regulators with selectivity for the second bromodomain. *Proc. Natl. Acad. Sci. U.S.A.* **2013**, *110*, 19754−19759.
(37) Zhang, G.; Plotnikov, A. N.; Rusinova, E.; Shen, T.; Morohashi, K.; Joshua, J.; Zeng, L.; Mujtaba, S.; Ohlmeyer, M.; Zhou, M.-M. Structure-guided design of potent diazobenzene inhibitors for the BET bromodomains. *J. Med. Chem.* **2013**, *56*, 9251−9264.
(38) Picaud, S.; Leonards, K.; Lambert, J.-P.; Dovey, O.; Wells, C.; Fedorov, O.; Monteiro, O.; Fujisawa, T.; Wang, C.-Y.; Lingard, H.; Tallant, C.; Nikbin, N.; Guetzoyan, L.; Ingham, R.; Ley, S. V.; Brennan, P.; Muller, S.; Samsonova, A.; Gingras, A.-C.; Schwaller, J.; Vassiliou, G.; Knapp, S.; Filippakopoulos, P. Promiscuous targeting of bromodomains by bromosporine identifies BET proteins as master regulators of primary transcription response in leukemia. *Sci. Adv.* **2016**, *2*, No. e1600760.
(39) Filippakopoulos, P.; Picaud, S.; Fedorov, O.; Keller, M.; Wrobel, M.; Morgenstern, O.; Bracher, F.; Knapp, S. Benzodiazepines and benzotriazepines as protein interaction inhibitors targeting bromodomains of the BET family. *Bioorg. Med. Chem.* **2012**, *20*, 1878−1886.
(40) Vidler, L. R.; Filippakopoulos, P.; Fedorov, O.; Picaud, S.; Martin, S.; Tomsett, M.; Woodward, H.; Brown, N.; Knapp, S.; Hoelder, S. Discovery of novel small-molecule inhibitors of BRD4 using structure-based virtual screening. *J. Med. Chem.* **2013**, *56*, 8073−8088.
(41) Chung, C.-w.; Coste, H.; White, J. H.; Mirguet, O.; Wilde, J.; Gosmini, R. L.; Delves, C.; Magny, S. M.; Woodward, R.; Hughes, S. A.; Boursier, E. V.; Flynn, H.; Bouillot, A. M.; Bamborough, P.; Brusq, J.-M.; Gellibert, F. J.; Jones, E. J.; Riou, A. M.; Homes, P.; Martin, S. L.; Uings, I. J.; Toum, J.; Clément, C. A.; Boullay, A.-B.; Grimley, R. L.; Blandel, F. M.; Prinjha, R. K.; Lee, K.; Kirilovsky, J.; Nicodeme, E. Discovery and characterization of small molecule inhibitors of the BET family bromodomains. *J. Med. Chem.* **2011**, *54*, 3827−3838.
(42) Zhao, L.; Cao, D.; Chen, T.; Wang, Y.; Miao, Z.; Xu, Y.; Chen, W.; Wang, X.; Li, Y.; Du, Z.; Xiong, B.; Li, J.; Xu, C.; Zhang, N.; He, J.; Shen, J. Fragment-based drug discovery of 2-thiazolidinones as inhibitors of the histone reader BRD4 bromodomain. *J. Med. Chem.* **2013**, *56*, 3833−3851.
(43) Fedorov, O.; Lingard, H.; Wells, C.; Monteiro, O. P.; Picaud, S.; Keates, T.; Yapp, C.; Philpott, M.; Martin, S. J.; Felletar, I.; Marsden, B. D.; Filippakopoulos, P.; Müller, S.; Knapp, S.; Brennan, P. E. [1,2,4]triazolo[4,3-a]phthalazines: inhibitors of diverse bromodomains. *J. Med. Chem.* **2014**, *57*, 462−476.
(44) Mysinger, M. M.; Carchia, M.; Irwin, J. J.; Shoichet, B. K. Directory of useful decoys, enhanced (DUD-E): better ligands and decoys for better benchmarking. *J. Med. Chem.* **2012**, *55*, 6582−6594.
(45) Shivakumar, D.; Williams, J.; Wu, Y.; Damm, W.; Shelley, J.; Sherman, W. Prediction of Absolute Solvation Free Energies using Molecular Dynamics Free Energy Perturbation and the OPLS Force Field. *J. Chem. Theory Comput.* **2010**, *6*, 1509−1519.
(46) Grant, J. A.; Gallardo, M. A.; Pickup, B. T. A fast method of molecular shape comparison: A simple application of a Gaussian description of molecular shape. *J. Comput. Chem.* **1996**, *17*, 1653−1666.
(47) Ember, S. W. J.; Zhu, J.-Y.; Olesen, S. H.; Martin, M. P.; Becker, A.; Berndt, N.; Georg, G. I.; Schönbrunn, E. Acetyl-lysine binding site of bromodomain-containing protein 4 (BRD4) interacts with diverse kinase inhibitors. *ACS Chem. Biol.* **2014**, *9*, 1160−1171.
(48) Kabsch, W. XDS. *Acta Crystallogr., Sect. D: Biol. Crystallogr.* **2010**, *66*, 125−132.
(49) Adams, P. D.; Afonine, P. V.; Bunkóczi, G.; Chen, V. B.; Davis, I. W.; Echols, N.; Headd, J. J.; Hung, L.-W.; Kapral, G. J.; Grosse-Kunstleve, R. W.; McCoy, A. J.; Moriarty, N. W.; Oeffner, R.; Read, R. J.; Richardson, D. C.; Richardson, J. S.; Terwilliger, T. C.; Zwart, P. H. PHENIX: a comprehensive Python-based system for macromolecular structure solution. *Acta Crystallogr., Sect. D: Biol. Crystallogr.* **2010**, *66*, 213−221.
(50) Emsley, P.; Lohkamp, B.; Scott, W. G.; Cowtan, K. Features and development of Coot. *Acta Crystallogr., Sect. D: Biol. Crystallogr.* **2010**, *66*, 486−501.
(51) McCoy, A. J.; Grosse-Kunstleve, R. W.; Adams, P. D.; Winn, M. D.; Storoni, L. C.; Read, R. J. Phaser crystallographic software. *J. Appl. Crystallogr.* **2007**, *40*, 658−674.
(52) Chen, V. B.; Arendall, W. B.; Headd, J. J.; Keedy, D. A.; Immormino, R. M.; Kapral, G. J.; Murray, L. W.; Richardson, J. S.; Richardson, D. C. MolProbity: all-atom structure validation for macromolecular crystallography. *Acta Crystallogr., Sect. D: Biol. Crystallogr.* **2010**, *66*, 12−21.
(53) Afonine, P. V.; Grosse-Kunstleve, R. W.; Chen, V. B.; Headd, J. J.; Moriarty, N. W.; Richardson, J. S.; Richardson, D. C.; Urzhumtsev, A.; Zwart, P. H.; Adams, P. D. phenix.model_vs_data: a high-level tool for the calculation of crystallographic model and data statistics. *J. Appl. Crystallogr.* **2010**, *43*, 669−676.

DOI: 10.1021/acsomega.7b00553
ACS Omega 2017, 2, 4760−4771

Volume 5 Issue 2 (2017) 241-242 ISSN 2347 - 3258
International Journal of Advance Research and Innovation

Integrated Kano Model and QFD in Designing Passenger Car

Mahesh Kumar Shukla[1], Ranganath MS[2], BS Chauhan[3]
[1]Department of Mechnical Engineering, Gyan Ganga College of Technology, Jabalpur (MP), India
[2] Department of Mechanical Engineering Delhi Technological University, Delhi-42, India
[2]Department of Mechanical Engineering Delhi Technical Campus, Greater Noida, India

Article Info
Article history:
Received 25 January 2017
Received in revised form
20 February 2017
Accepted 28 February 2017
Available online 15 June 2017

Keywords:
Kano Model, QFD, Passenger car

Abstract
Now a days cars are necessity of everybody's life and are not luxury. The growing economy of the country has increased tremendous demand of vehicles particularly passenger car. The competition in car market has been rockted up resulting customer satisfaction become a key factor for business success.
QFD starts with customer need in order to achieve their optimum satisfaction. QFD is co-relating data about customer's attribute and technical attribute. The integration of Kano Model supports QFD towards innovation and improvement of the product. It helps to adopt changes in view to achieve satisfaction and delight the customer. The Kano Model also helps to understand the types of the customer expectations and satisfaction.

1. Introduction

During last few years, sales of passenger car in India has recorded a strong domestic sales growth. In the fiscal year 2015-16 as per SSAI, 23,960,940 vehicles including passenger car are rolled out. Out of that, the overall passenger car sales was 13% market sale. The competition for passenger car markets as well as numbers of customer rocketed, therfore, the customer satisfaction also become a key factor for business success. The impact on customer requirements to satisfy them. Changes due to fact that competitors introducing new features in the existing product frequently.

2. Review of QFD Methodology

Qualify Function Deployment is one of the best approach to convert the customer needs into quality characteristics in order to develope a design qality of the product. This methodology applies data about importance and customer satisfaction by identifying customer attributes. This is an impotant tool to transfer the voice of the customer in to the product specification. The concept of QFD was first introduced by Dr. Yogi Akao in 1966 and developed during 1970's. At USA, it was introduced and adopted in 1983.

Q.F.D. is customer oriented approach which helps product designer in developing new product by proviiding data of customer needs. Most of the conventional technique that aimed to time out relative importance between requirements, including assuming that customer have previous knowledge about the product and its attributes (Deszle et al. 1999). Once the customers requirement are identified, a set of design attributes are correlated in a metrix known as "House of Quality". The output of that is useful to establish. The competitive target with respect to customer voice with certain priorities that helps to increase the customer satisfaction.

The first step of the methodology is to capture the basic needs of the customer i.e. "what".

On identifying the requirements, a quantative market research is essential to know the competitive position of the product in terms of customer's satisfaction. Also to evaluate the importance of their requirement as expressed by the rider. A set of design attributes that could fulfil their needs is worked out.

Next is to traslate the voice of the customer to technical attribute. Therefore it is essential to refine the vogue ambigous needs of the customer prior to trasform into measurable technical requirements. Thereafter appropriate and feasible relationship between customer attributes and technical atrributes is established with the help of "House of Quality" metrics. The result thus obtained is applied while designing the product (2.2) KANO MODEL.

The customer seldom speaks with basic quality issues of the existing product. The conventional Q.F.D. process assumes that the relationship between importance and satisfaction are linear and independent several studies have shown that relationship between importance and satisfaction is not always linear (Anderson and Mittal 2000; Ting and Shah, 2002; Tortini & Silveira 2005). Kano Model (Kano et al.; 1984) suggested analysis of improvement opportunities in product considering that relationship is non linear.

***Corresponding Author,**
E-mail: mkshukla21045@gmail.com
All rights reserved: http://www.ijari.org

3.QFD: SWOC Analysis

The quality of product is too much dependent on how well the rproduct fulfil the customer need. Q.F.D. is one structured approach to translate the voice of customer which become driver for the design and development of the product to satisfy the requirement of a customer. This method is in relatively easy to apply and highly flexebile & customerable (Dey 1993) summarizes some of the key issues of the QFD concept as :-

- QFD is a planning process as opposed to a tool for problem solving.
- The customer wants & needs - their requirements are the inputs to the metrix. The process can not begin without those inputs. QFD essentially forces an organization to get in touch with the people who use the product.
- It uses a metrix to display information vital to the project in brief outline format.
- This collection of information in the metrix format facilities examinating cross checking and anlysis. It helps in organization set competitive targets and determine the priority action issues.
- The out put resulting from analysis of QFD metrix in two fold. First the competitive forgets are established for key action item related to the customer's voice. Second, certain priority issues are selected for special emphasis. An effective response to the targets and to selected priority issues will result in increased customer satisfaction. In view to aseess the success QFD methodology, it is essential to understand how the success can be obtained. There are many success stories pertaining to the application of QFD in design & development of product. The researchers must aware about strength, weekness, opportunity & constraints regarding use of QFD technique before adopting it Revelletal (1998) present an analysis to understand the ground realities of the process.

The Kano Model classific customer requirments under three categories -

- **Basic requirement**- which fulfills the basic function of product. In absence of that, the performance is not sufficient to satisfy the customer. Moreover, if sufficient performance is there, the customer may not be satisfied.
- **Performance Requirement -** In this case the customer satisfaction is proportional to the performance level. The customer satisfaction will increase or decrease as per performance level.
- **Excitment Requirement -** These are meant for delighting the customer. The features present in the product beyond the expectation of the customer will delight. On the other hand, in absence of that customer do not mentioned dis-satisfaction.

4. Role of QFD and Kano Model in Design Passenger Car

Product Life cycle of passenger car in the country is dependent on Life style of the people, growing economy and availability of production infrastructure. Now the days customer have become more selective and understand various technical attributes of the product with competitive cost. Therefore identification of excitment, basic and performance requirements have become major issues to attract customer.

Tan and Pawitra (2001) propose integrating Kano Model in the QFD (2001) determine Kano Category for each requirement. These categories can be organised as per customer requirement to cape with Basic performance, excitment and neutral.

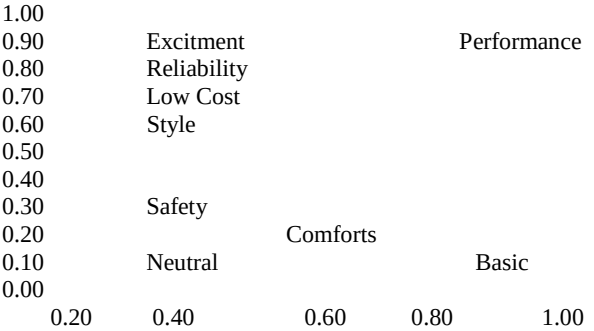
Table 1: Classification of requirements as Primary, Secondary and Territory.

S.No.	Primary	Secondary	Teritory
1.	Reliability	Vehicle Performance	Upgraded Power Transmission Pick up Millage acceleration Maximum speed Torque Engine Capacity
2.	Safety	Passenger Feel Safe Safe in accident Meet Regulatory Requirement	ABS Bags Indicators
3.	Comforts	Extra for passenger Enough Legs Room Comfort for Long Riding AC and Heater System	Night Vision Lamp fog lamp Rear view camera Rigid Design Erogonomically Designed Seats
4.	Cost	Purchase/Replacement Cost Service Cost Operating Cost	Low Low Low

Berger et al. (1953) proposed Customer Satisfaction Coefficient (CSC) which shows the percentage of the customer get satisfied as well as dissatisfied with positive and negative question respectively. That is shown in the scotter diagram in different quadrents as specified in figure 3.

The CS coefficient shows how strongly a product requirement influences customer satisfaction or vice-versa. QFD process is applied towards importance rating and performance, compasred to the competitors to as certain the most optimum level of customer satisfaction.

Table 2 - Coefficient of passenger Car for customer satisfactio (CSC) [8]



5. Conclusions

Automobile market today has become most lubracetive market in the country. With growing economy and raising quality life of people are the main driver of competable market. The success of business now depend on satisfaction of rider.

The Kano Model can help business to fulfill basic, performance and excitment related requirements to achieve optimum satisfaction of the customer. This paper shows various organised customer requirement. The integration of Kano Model in QFD helps to open perspective innovated product with now features.

References

[1.] Jouko Koski. Quality Function Deployment in requirement Engg. A Review and Case Studes, Master Thesis 2003.

[2.] Midhun Eliyas, V Hima Kiran Vithal. Concept Design of Special vehicle for Indian Military, SAS sTech. Journal Vl. 13(1), 2014.

[3.] Dr. Sturat Burge. A function Approach to Quality Function Deployment, BHW and System Engg. Co, 2007.

[4.] Akao. Quality Function Deployment : Integrating customer requirements in to product design. Translated by Glenn Mazur, Productivity Press, Combridge 1999.

[5.] RG Day. Quality Function Deployment: From perspective of competitive advantage, http: //akao.leve,hasa.gov/dfc/qf, 1993

[6.] R Hamidullah, S Akbar Noor, W Shah, Inayeillah. QFD as a Tool for improvement of Car Dash Board. Journal of Quality Technology Management, 6(1) 2010.

[7.] Gerson Tontini. Integrating the Kano Model & QFD for Designing New Product. Total quality management 18(6), 2007.

[8.] Tentini 2003

International Journal of Engineering Technology, Management and Applied Sciences

IJETMAS

www.ijetmas.com July 2017, Volume 5, Issue 7, ISSN 2349-4476

Investigation of Strength Characteristics of Concrete by Replacing Curing Water with Self Curing Compounds

Siddharth Jain

Research Scholar, Delhi Technological University, New Delhi & Assistant Professor, Civil Engineering Department, Krishna Institute of Engineering and Technology,

ABSTRACT

In today's world, concrete is most popular and widely used material in construction sector due to its good compressive strength and durability. Depending upon its usability the mix proportion (cement, fine aggregate, coarse aggregate and water) are prepared to produce plain concrete. Plain concrete needs ambient atmosphere for curing for a minimum period of 28 days in order to attain desired strength. Any laxity in curing will badly affect the strength and durability of concrete. Self-curing concrete is one of the special concretes in mitigating insufficient curing due to human negligence, paucity of water in arid areas, inaccessibility of structures in difficult terrains and in areas where the presence of fluorides in water will badly affect the characteristics of concrete. The present study involves the use of shrinkage reducing admixtures like POLYETHYLENE GLYCOL (PEG 400) as internal curing compound and CUREFREE-C as external curing compound[1]. These curing compounds are used in concrete which helps in self curing and helps in better hydration and hence good compressive strength. They trap the moisture within the structure and prevent it from evaporation (by creating a thin film or by block the pores containing water) which normally occurs due to the hydration process .In the present study, the affect of curing compounds on compressive strength and flexural strength is studied. From the study of M. Manoj Kumar et al[2], we vary the percentage of PEG by weight of cement from 0% to 2% as the dosage of internal curing compound and 0.25% of CUREFREE-C by weight of cement was fixed as the dosage of external curing compound The test results were studied both for M25 and M30 mixes .The results shows that PEG 400 and CUREFREE-C could help in self curing by giving strength on par with that of the conventional curing method.

KEYWORDS: Curing, Polyethyelene Glycol, Curefree-C, Strength Characteristics

INTRODUCTION

Curing can be performed in a number of ways to ensure that an adequate amount of water is available for cement hydration to occur. However, good curing is not always practical in many cases. Negligence given to proper curing at construction sites has been a topic of discussion since a very long time. Several investigators asked the question whether there will be self-curing concrete. Therefore, the need to develop self-curing agents attracted several researchers. The concept of self-curing agents is to reduce the water evaporation from concrete, and hence increase the water retention capacity of the concrete compared to conventional concrete. These compounds will rise to the finished concrete surface and effectively seal the surface against evaporation. It was found that water soluble polymers can be used as self-curing agents in concrete.

The use of self-curing admixtures is very important from the point of view that water resources are getting valuable every day (i.e., each 1 m^3 of concrete requires about 3 m^3 of water for construction most of which is for curing).The benefit of self-curing admixtures is more significant in desert areas where water is not adequately available.

OBJECTIVE

The main objective is to evaluate the use of self-curing agent in place of conventional curing method (Ponding Method). In this study strength of concrete containing self-curing agents (Using internal as well as external curing agents) is investigated and compared to that of conventional concrete Akeem et al [3].

www.ijetmas.com July 2017, Volume 5, Issue 7, ISSN 2349-4476

Table 1. Combination of various mixes

S. No.	Type of Concrete Mix for one grade
1	Conventional concrete mix
2	Concrete mix with PEG-400 as internal curing compound with different proportions.
3	Concrete mix with CUREFREE-C as external curing compound

CHEMICAL SUBSTANCES USED IN THE STUDY

POLY ETHYLENE GLYCOL-400(PEG-400) (USED AS AN INTERNAL CURING COMPOUND)

Polyethylene glycol is a condensation polymer of ethylene oxide and water with the general formula $H(OCH_2CH_2)_nOH$, where n is the average number of repeating oxyethylene groups typically from 4 to about 180. The abbreviation (PEG) is termed in combination with a numeric suffix which indicates the average molecular weights. One common feature of PEG appears to be the water-soluble nature. Polyethylene glycol is non-toxic, odourless, neutral, lubricating, non-volatile and non-irritating and is used in a variety of pharmaceuticals. Thus, it is a shrinkage reducing admixture.

CUREFREE-C (USED AS AN EXTERNAL CURING COMPOUND)

It is a Liquid membrane-forming curing compound and is used on the principle that concrete gets enough water from pre-matured concrete for uninterrupted hydration after placement. For application on freshly cast concrete or newly exposed concrete surface after removal of formwork to form a temporary membrane which will provide sufficient moisture for effective curing to take place. The membrane eventually breaks down and disintegrate after which the surface can be painted. It is useful for large areas of concrete such as pavements, runways, bridge decks and industrial floors. It is also used for vertical or sloping surface as of chimneys, towers, silos, canal lining, columns and beams where water curing is difficult or unreliable.

Table 2. Specimens casted for testing purpose

S. No.	NATURE OF CURING	M25		M30	
		CUBE	BEAM	CUBE	BEAM
1.	CONVENTIONAL(PONDING)	6	6	6	6
2.	EXTERNAL CURING (CUREFREE-C)	6	6	6	6
3.	INTERNAL CURING (PEG-400 having quantity 0.5%)	6	6	6	6
4	INTERNAL CURING (PEG-400 having quantity 1%)	6	6	6	6
5	INTERNAL CURING (PEG-400 having quantity 1.5%)	6	6	6	6
6	INTERNAL CURING (PEG-400 having quantity 2%)	6	6	6	6

EXPERIMENTAL WORK CONDUCTED

Various test were done on the ingredients of concrete to collect data require for mix design as well as to study their physical properties. The proportions of ingredients for M25 and M30 for all the three types of mixes were determined by mix design and same proportions were used for casting the concrete specimens (cubes and beams).Some of the salient points are:

www.ijetmas.com July 2017, Volume 5, Issue 7, ISSN 2349-4476

a. Mix designs were done as per IS: 10262-2009 [4].
b. Materials were weighed by weigh batching.
c. Each set consists of 2 specimens (cubes and beams) and the test strength of the sample has been taken as the average strength of the specimens.
d. 72 numbers of cubes 150mm x 150mm x 150mm were casted to determine the compressive strength of various mixes of concrete at the end of 7 and 28 days.
e. 72 numbers of beams 100mm x 100mm x 500mm were casted to determine the flexural strength of various mixes of concrete at the end of 7 and 28 days.
f. The details of all the mix design are shown in the table 3:-

Table3. Mix design proportions of various mixes for M25 grade of concrete

MIX	W/C RATIO	CEMENT	WATER	FA	CA
		Kg	Kg	Kg	Kg
Conventional	0.50	395	195.24	642.62	1164.14
PEG-400	0.50	395	195.24	642.62	1164.14
CUREFREE-C	0.50	395	195.24	642.62	1164.14

Table4. Mix design proportions of various mixes for M30 grade of concrete

MIX	W/C RATIO	CEMENT	WATER	FA	CA
		Kg	Kg	Kg	Kg
Conventional	0.45	438	195.57	611.25	1159.2
PEG-400	0.45	438	195.57	611.25	1159.2
CUREFREE-C	0.45	438	195.57	611.25	1159.2

Table 5.Quantity of various proportions of PEG 400 and Curefree- C in both mixes

Material Used	Quantity in Kg for M25	Quantity in Kg for M30
Conventional concrete mix	0	0
PEG 400 (0.5% of cement content)	1.96	2.19
PEG 400 (1% of cement content)	3.95	4.38
PEG 400 (1.5% of cement content)	5.93	6.57
PEG 400 (2% of cement content)	7.9	8.76
CUREFREE-C (0.25% of cement content)	0.988	1.1

www.ijetmas.com July 2017, Volume 5, Issue 7, ISSN 2349-4476

TEST RESULTS FOR VARIOUS MIXES:

Average Compressive and Flexural strength for 7 and 28 days obtained by taking average of 3 specimens for each day are compiled in Table 6.

Table6. Comparative Strength test results of various mixes for M25 Grade of Concrete (Target strength is 31.6 N/mm^2)

MIX	AVERAGE COMPRESSIVE STRENGTH(N/mm^2)		AVERAGE FLEXURAL STRENGTH(N/mm^2)	
	7 DAYS	28 DAYS	7 DAYS	28 DAYS
CONVENTIONAL CURING	23.26	32.29	3.92	5.18
PEG PROPRTION 0.5%	19.6	28	2.32	3.3
1%	21.49	38.7	2.58	3.6
1.5%	22.3	31.8	2.53	3.7
2%	21	30	2.18	3.1
CUREFREE-C (.25%)	22.19	31.7	2.75	3.9

ANALYSIS AND COMPARATIVE STUDY OF COMPRESSIVE STRENGTH FOR VARIOUS PROPORTION OF PEG 400 FOR M25 GRADE OF CONCRETE

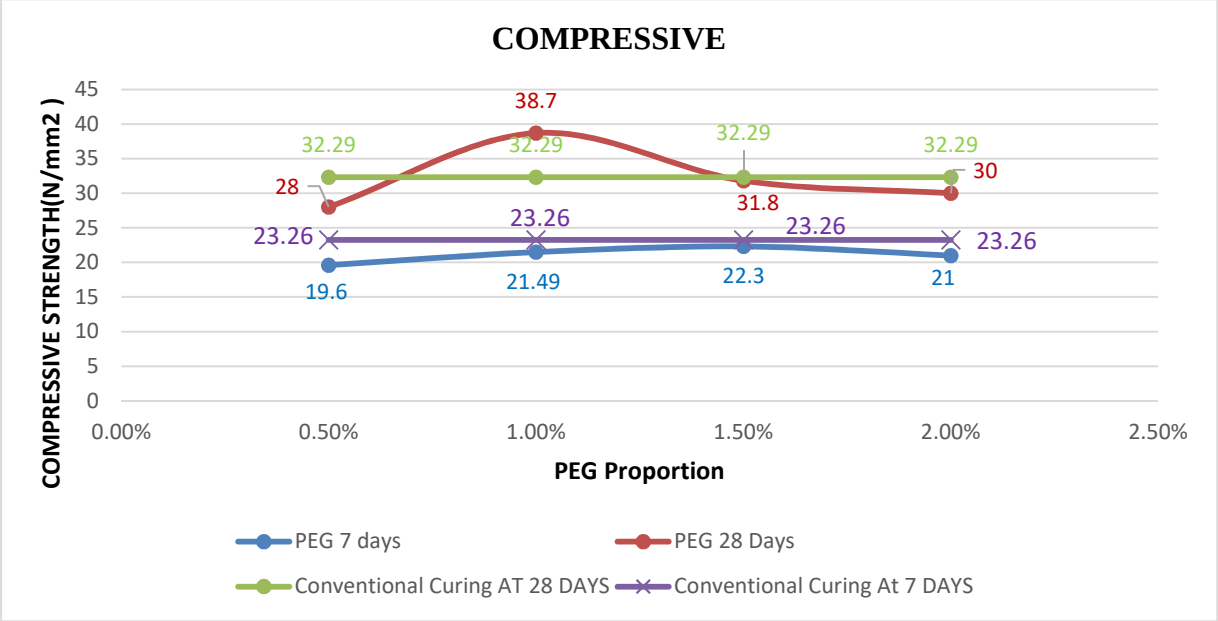


Fig. 1. Compressive Strength of M25 grade concrete for various proportion of PEG 400

The compressive test done on concrete cubes for all the three mixes for 7 and 28 days are depicted in the figure 1. The pattern clearly depicts that the concrete made from internal and external curing agents shows at par strength as compared to concrete made from normal (conventional) curing. Concrete made from curing compounds doesn't fall short of the minimum strength requirement i.e. 25MPa as per IS 456(2000)[5].The strength achieved from curing compounds is more than 25 MPa.

www.ijetmas.com July 2017, Volume 5, Issue 7, ISSN 2349-4476

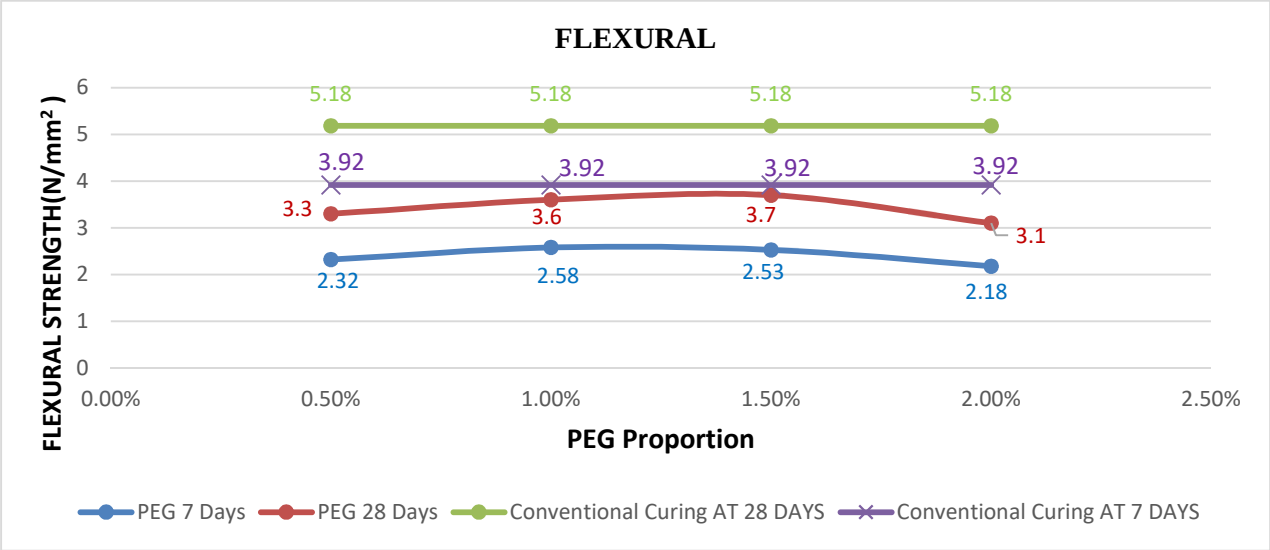


Fig. 2. Flexural Strength of M25 grade concrete for various proportion of PEG 400

The Flexural test done on concrete beams for all the mixes for 7 and 28 days are depicted in the figure 2. The pattern clearly depicts that the concrete beam made from PEG-400 and CUREFREE-C shows at par flexural strength as compared to concrete made from conventional curing. Concrete made from curing compounds doesn't fall short of the minimum strength requirement as per IS 456(2000)[5] provisions for M25 grade of concrete i.e. $0.7(fck)^{1/2}$. The strength achieved from curing compounds is much above the required value.

Table7. Comparative Strength test results of various mixes for M30 grade of concrete (Target strength is 38.25 N/mm²)

MIX	AVERAGE COMPRESSIVE STRENGTH (N/mm²)		AVERAGE FLEXURAL STRENGTH (N/mm²)	
	7 days	28 days	7 days	28 days
CONVENTIONAL	28.29	39.48	3.93	5.04
PEG 0.5%	24.77	35.40	2.65	3.82
1 %	27.3	37.7	2.98	4.11
1.5%	28.8	38.9	2.99	4.32
2.0%	26.11	37.4	3.1	4.09
CUREFREE-C (0.25%)	27.19	38.8	3.13	4.37

www.ijetmas.com July 2017, Volume 5, Issue 7, ISSN 2349-4476

5.2 ANALYSIS AND COMPARATIVE STUDY OF COMPRESSIVE STRENGTH FOR VARIOUS PROPORTION OF PEG 400 FOR M30 GRADE OF CONCRETE

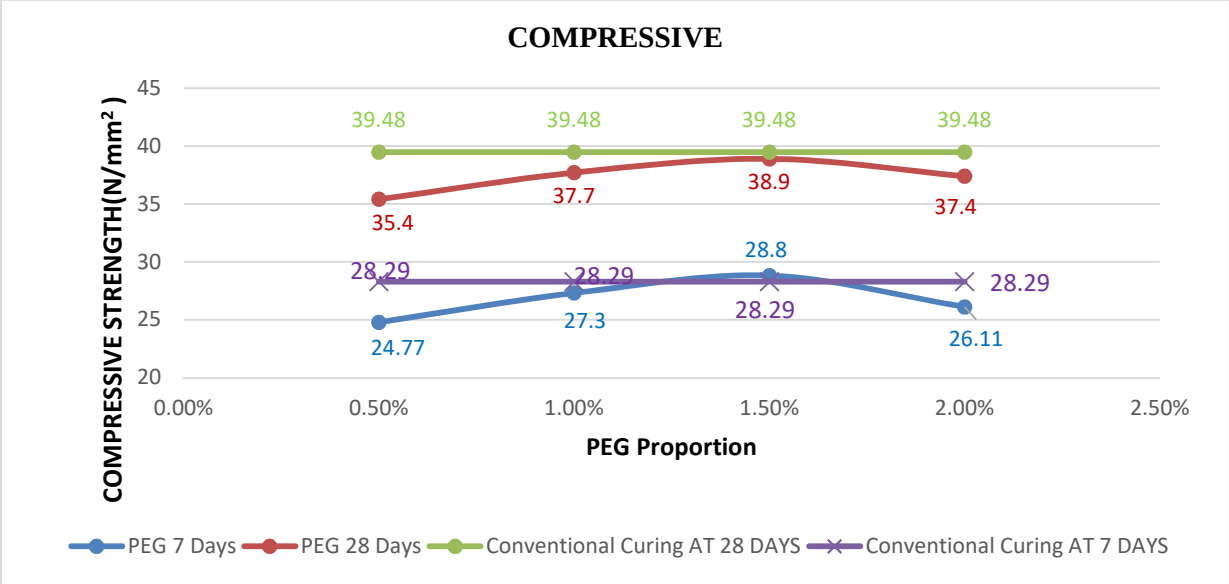


Fig. 3. Compressive Strength of M30 grade concrete for various proportion of PEG 400

The compressive test done on concrete cubes for all the three mixes for 7 and 28 days are depicted in the figure 3. The pattern above clearly depicts that the concrete made from internal and external curing agents shows at par strength as compared to concrete made from normal (conventional) curing. Concrete made from curing compounds doesn't fall short of the minimum strength requirement i.e. 30 MPa as per IS 456(2000)[5]. The strength achieved from curing compounds is much above 30 MPa.

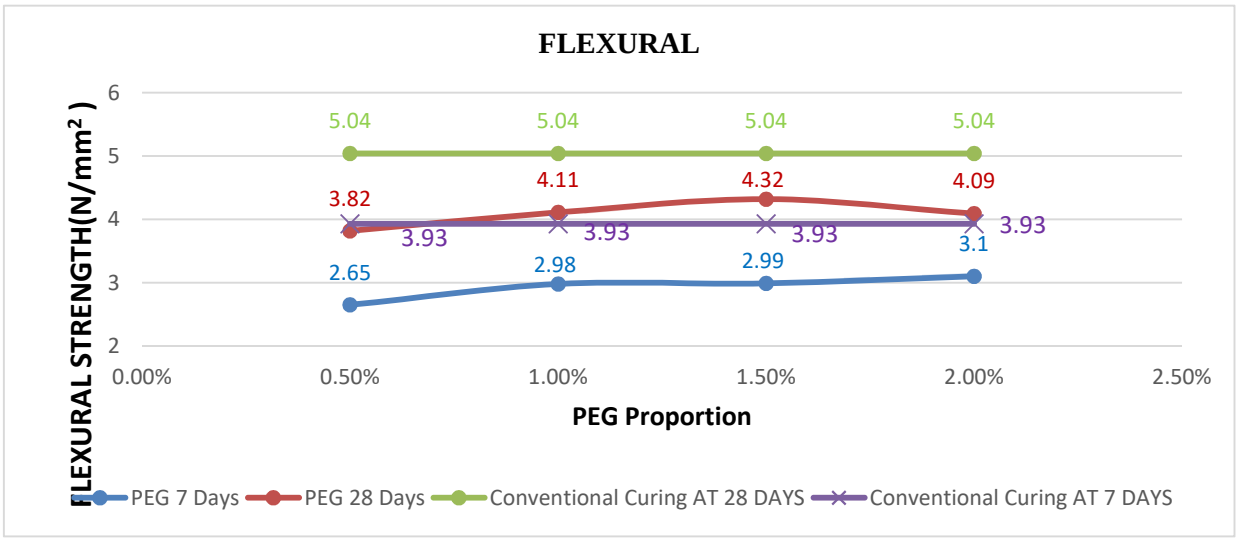


Fig. 4. Flexural Strength of M30 grade concrete for various proportion of PEG 400

www.ijetmas.com July 2017, Volume 5, Issue 7, ISSN 2349-4476

The Flexural test done on concrete beams for all the mixes for 7 and 28 days are depicted in the figure 4. The pattern above clearly depicts that the concrete beam made from PEG-400 and CUREFREE-C shows at par flexural strength as compared to concrete made from conventional curing. Concrete made from curing compounds doesn't fall short of the minimum strength requirement as per is 456(2000)[5] provisions for M30 grade of concrete i.e. $0.7(f_{ck})^{1/2}$. The strength achieved from curing compounds is much above the required value.

DISCUSSION

The test results are obtained by keeping the mix proportions constant without any inclusion of plasticizers and super-plasticizers. Only curing compounds are additionally added in the mix as a substitute of curing water.

- The Strength of concrete achieved by conventional curing is at par as compared to internal and external curing methods. The results obtained from conventional curing method (ponding) are under ideal conditions when the specimens are kept completely submerged in water for 7 days and 28 days. Such long and ideal curing conditions may not be possible under actual site conditions. Thus these results do not give a true picture of conditions existing at construction sites.
- Concrete mixes prepared using curing compounds are at par with specified target strength values calculated during design mix for both M25 and M30 grade of concrete. Also it can be seen that more than the minimum strength as per the codal provisions has been achieved by the specimens cured through curing compounds. The strength achieved by the PEG-400 and CUREFREE-C is comparable for both types of mix i.e. M25 and M30. The results obtained after the use of curing compounds show a better picture of the actual site conditions in comparison to those obtained from conventional curing techniques. Only the environmental conditions existing at site and laboratory may vary. Rest all parameters are more or less the same.
- The Compressive Strength achieved by cubes and beams cured through curing compound (both PEG-400 and CUREFREE-C) is 20% more than that achieved through conventional curing method for M25 and is nearly 99% of that achieved through conventional curing method for M30 grade of concrete.
- The Flexural Strength achieved by cubes and beams cured through curing compound (both PEG-400 and CUREFREE-C) is nearly 71% of that achieved through conventional curing method for M25 and is 86% of that achieved through conventional curing method for M30 grade of concrete.
- The extra cost of procuring water from deep underground or far off sources specially in developing areas can be saved by the use of curing compounds. Also conditions supervision by labour to ensure good moisture and temperature conditions for maintaining satisfactory curing conditions is avoided. Thus any fault or delay in curing would not affect the structural strength in the long run.

CONCLUSIONS

The aim of the project was to compare the test results based on curing conditions only. No changes have been done in the mix design for the mix. The results achieved from the tests conducted on specimen casted using curing compounds are very satisfactory. Results show that there is continuous increase in the strength of specimens for a period of 28 days. Higher strength results can be easily achieved by the use of plasticizers and super–plasticizers, reduction of water cement ratio and the addition of external cementitious compounds. Curing compound has the advantage of being used and left with no further maintenance. The strength results of conventionally cured specimens have been obtained after 28 days of proper curing which may not be possible at site as continuous vigilance is required to see that the surface moisture is not lost. In this regard, the strength results obtained by the use of self curing compounds are at par with that of site conditions.

The results show that curing compounds have the potential of replacing water as the curing agent. Further study is required to check the durability of self cured concrete structures.

www.ijetmas.com July 2017, Volume 5, Issue 7, ISSN 2349-4476

REFRENCES

[1] Sathanandham.T, Gobinath.R, Naveen Prabhu. M, Gnanasundar.S, Vajravel.K, Sabariraja.G, Manojkumar.R and Jagathishprabhu .R, "Preliminary Studies of Self Curing Concrete with Addition of Polyethylene Glycol", IJERT, Vol: 2, Issue: 11, November 2013.

[2] M. Manoj Kumar and D. Maruthachalam, "Experimental Investigation of Self Curing Concrete", IJASTR, Vol: 2, Issue: 3, March-April 2013.

[3] Akeem Ayinde Raheem,Aliu Adebayo Soyingbe and Amaka John Emenike, "Effect of Different Curing Methods on Density and Compressive Strength of Concrete", IJAST, Vol: 3, No: 4, April- 2013.

[4] IS 10262 (2009), "Indian Standard Concrete Mix Proportioning Guidelines (First revision)".

[5] IS 456 (2000), "Indian Standard Code of Practice for Plain and Reinforced Concrete (Fourth revision)".

Journal of Algal Biomass Utilization
J. Algal Biomass Utln. - Copyright © PHYCOSPECTRUM
ISSN: 2229 – 6905

Isolation, Identification and biomass productivity analysis of microalga *Scenedesmus rubescens* from DTU Lake

Lakhan Kumar, Arpita Roy, Gaurav Saxena, Koyel Kundu, Navneeta Bharadvaja*
Plant Biotechnology Laboratory, Department of Biotechnology, Delhi Technological University, Delhi, India
*Correspondence: navneetab@dtu.co.in

Abstract
Due to the increasing demand of energy by leaps and bounds, it is requisite to identify the local solution for the generation of energy to mitigate the future demand. Microalgae are the most abundant and rapidly growing photosynthetic microorganisms capable of sequestering CO_2 from the environment and water to produce biomass in comparison to other energy crops. Herewith, we have focussed on the isolation and characterization of a potential microalgae strain from the local water bodies under natural environmental conditions which provides an edge to commercialization of microalgae biofuel production. Microalgae sample obtained from Delhi Technological University's lake was used. Light microscope, Scanning electron microscope, Fourier transform infrared spectroscopy and 28S rDNA analysis were performed for identification of microalgae. With the help of these potential identification tools, microalga Scenedesmus rubescens was identified. After the identification, effect of various abiotic factors such as light (intensity, color and period), pH of medium, shaking period and temperature on algal growth rate and biomass productivity was studied. Scenedesmus rubescens provided maximum biomass productivity in white light of 36W intensity under illumination of 16 hours. pH 8, 24 hours shaking period and 26±2ºC temperature were also found to be best for this microalga.

Keywords: Microalgae, *Scenedesmus rubescens*, FTIR, SEM, 28S rDNA, Biomass productivity.

Introduction

Microalgae utilises sunlight and fix CO_2 during photosynthesis and produces biomass more efficiently and rapidly than terrestrial plants. They have been considered for biomass to energy production, based on their fast growth rate, biomass productivity and compatibility for the various kinds of biofuels. They accumulate large amounts of storage lipids primarily in the form of triacylglycerols (TAG). The fatty acid profile is important in selecting microalgae as a feedstock for biodiesel production. An algae-based bio-refinery could potentially integrate several different conversion technologies to produce biofuels including biodiesel, aviation fuel (commercial and military), ethanol, and methane, as well as valuable co-products including oils, protein, and carbohydrates, etc[1,2]. Wastewater from industrial and domestic sources is also a potential source for microalgal biomass production which can be utilized in the production of biofuels. Due to fast industrial growth, water and air pollution level has increased tremendously and it is causing environmental degradation. So, it is required to treat wastewater and various emissions before discharging them into the environment [3.] Microalgae are known to its nutrient removal efficiency from the industrial effluents and wastewater.[4, 5.] As fossil fuels are depleting at very fast rate, we need to explore newer eco-friendly and economically sustainable sources of energy to meet the global demand.
The isolation of microalgae from local water bodies like lakes or ponds is a useful strategy for obtaining potential species tolerant to the conditions prevalent in the area, such an organism tending to have the ability to grow without applying any extra effort with having good biomass productivity. High lipid or carbohydrate producing microalgae are the desired ones for the production of biodiesel and bioethanol respectively. Analysis of the bulk biochemical composition of the microalgae is essential for the understanding of biological processes happening in the cell and abiotic factors affecting the accumulation of various metabolites within the cell. As per required biofuel production, it is desired to know the biomolecules composition of the cell for determination of the optimum use of biomass for biofuel production. The lipid-rich microalgae are suitable feedstock for biodiesel production while carbohydrate-rich microalgae are best sources for bioethanol production. Several factors either biotic or abiotic influences microalgal growth. Abiotic factors include the intensity and amount of light, the temperature, salinity and pH of the medium and nutrient concentrations etc [6-9].
Bacteria, cyanobacteria, fungi, competition by other microalgae and predation by other aquatic organisms come under biotic factors which limit the algal growth. Other operational factors like dilution and shear rate, the process and frequency of harvesting, depth of the tank etc. also influence the microalgal growth rate and thus the biomass productivity. The microalgal biomass and the biochemical composition's amount may be influenced and improved by manipulating the surrounding environment [10, 11].

To optimise the biomass productivity, the influence of various abiotic factors such as light intensity, light colour, light period, pH of medium, shaking period and temperature on algal growth rate has been studied in the present study. In these experiments, only one factor at a time was variable while all other conditions were kept constant.

The culture conditions which were controlled for the algal growth were light, temperature, pH and constant mixing or aeration. Isolated *Scenedesmus rubescens* will be investigated for biofuel production, wastewater treatment, heavy metal removal from waste water and green synthesis of Nanoparticle in the next study.

Materials and Methods

Sample collection and isolation of microalgae

For microalgae isolation, the freshwater sample, collected from Delhi Technological University's lake (DTU Lake) was first filtered for the removal of solid and undesired particles and, then inoculated in BG-11 Medium. For growth, this preparation was incubated at 27ºC in an artificial light chamber under illumination with a white fluorescent light at 300µmol/m^2 s^{-1} on a photoperiod of 16L: 8D for one week. After proper growth of microalgae was observed in the culture flask, the culture was spread onto BG11 Agar plate, and kept at the same growth conditions. Colonies were sub-cultured repeatedly into the same medium under same growth conditions until a culture dominated by the pure strain was developed. The sub-cultured individual colonies were picked and transferred into the BG-11 medium and scaled up successfully. Thus isolated and established pure culture was obtained.

The isolated microalga was cultivated in the BG11 medium at similar conditions for 24days in a working volume of 200 ml in Erlenmeyer flasks. Flasks were agitated twice or thrice a day manually to prevent any deposition at the base of the flask and to ensure proper mixing. Cultivation lasted for up to 24 days with samples being taken on a period of 24 hours and analysed on spectroscopy as well as by calculating dry cell mass of the sample. The dry cell weight of the microalgal culture was estimated by taking 50ml of culture and centrifuging it at 3000 rpm for 10 minutes and hence separated biomass was dried in an oven for the time till the complete dry condition is achieved. After a substantial period of growth, 100ml of the sample was taken and biomass was harvested and preserved for the identification purpose.

Growth Medium:

For growth of the microalgal isolate, BG11 (ATCC medium 616) media was used. The composition of media consists (gram/litre):Sodium nitrate ($NaNO_3$),1.5; ($K_2HPO_4.3H_2O$) 0.04;Magnesium Sulphate ($MgSO_4.7H_2O$),0.075; Calcium Chloride ($CaCl_2.2H_2O$),0.036; Citric Acid,0.006; Ferric Ammonium Citrate,0.006; EDTA (disodium magnesium salt),0.001;Na_2CO3,0.01; and one millilitre of **A5** Solution which contains (gram/litre):H_3BO_3,2.86; $MnCl_2.4H_2O$,1.81; $ZnSO_4.7H_2O$,0.222; $Na_2MoO_4.2H_2O$,0.39; $CuSO_4.5H_2O$,0.079; $Co(NO_3)_2.6H_2O$,0.0494. The pH of medium was kept 8.

Identification of isolated microalgae

Morphological Identification

Isolated microalgae species was examined under light microscope and scanning electron microscope (SEM) for cell morphology. SEM was performed for the absolute morphological determination of the microalgae isolate. Scanning Electron Microscope provides the absolute morphological details of the material and this property is utilised for the characterization of the microalgae. FTIR spectroscopy was also performed for the biochemical composition characterization[12].The biomolecules composition *i.e.* lipid, carbohydrate, protein, chlorophylls etc. of algal biomass is usually investigated and analysed by the conventional chemical extraction method followed by gravimetric determination and spectroscopy[13]. For rapid determination of the isolated microalgal sample for its biochemical composition, use of FTIR is a highly advanced technique and powerful analytical tool[13, 14]. FTIR is a non-destructive and rapid method, which helps in identification of the vibrational structure of materials[15]. The IR spectrum of the microalgal sample was recorded on FTIR at room temperature under region 4000-400 cm^{-1}. Analysis of composition, shape and intensity of absorption at specific wave numbers reveals information about functional groups and molecular structure that can then be used for identification [13, 16].

Molecular Identification

28S rDNA molecular examination was performed for identification of the isolated microalgae (Eurofins Genomics India Pvt. Ltd. Bangalore, India). DNA was isolated from the culture by using Nucleospin DNA extraction kit. Its quality was evaluated on 2.0% Agarose gel, a single band of high-molecular weight DNA has been observed. Fragment of 28S rDNA gene was isolated and amplified by Merk PCR amplification kit. A single discrete PCR amplicon band of 800 bp was observed when resolved on Agarose. The PCR amplicon was purified to remove contaminants. Forward and reverse DNA sequencing reaction of PCR amplicon was carried out with 28SF (5ACCCGCTGAATTTAAGCATA3) and 28SR (5CCTTGGTCCGTGTTTCAAGA3) primers using BDT v3.1 Cycle

sequencing kit on ABI 3730xl Genetic Analyzer (3730xl ABI-96 Capillary machine). Consensus sequence of 28S rDNA gene was generated from forward and reverse sequence data using aligner software.

Biomass productivity Analysis in different culture conditions

Light intensity

The isolated microalga was cultivated under six different light intensity regime in BG11 medium having pH 8 and light period of 16L: 8D for 24 days and growth was monitored by spectrophotometer. Reading was noted at a period of two and three days and plotted to derive a growth curve on the basis of absorbance and time.

Light colour

Isolated microalga was inoculated in BG11 medium having pH 8 and growth was monitored for 24 days. Three different colours Red, Blue and White colour light was given to the flask by wrapping flask with red and blue coloured transparent polyethylene sheet onto the flask. One flask was left unwrapped and kept directly under the white light.

Light period

Three different light periods i.e. 24L: 0D, 16L: 8D and 12L: 12D were given to the microalgal culture separately and growth was monitored. BG11 medium with pH 8 was used as a growth medium. The experiment was done for 24 days and growth pattern was plotted.

pH

Microalgal biomass productivity was calculated under different pH regimes. pH ranges from 6 to 11 were used under white light with a light period of 16L: 8D at room temperature for the growth of microalgae. BG11 medium was prepared and pH was set and autoclaved before the inoculation.

Temperature

Three different temperature regimes 18°C (±2), 26°C (±2) and 30°C (±2) were provided to the microalgae culture and allowed to grow under white light with a light period of 16L: 8D at room temperature for the growth of microalgae.

Shaking period

Three different shaking periods were provided to the microalgae culture under white light with a light period of 24h at room temperature for the growth of microalgae. Microalgae culture flasks were kept on a shaker for agitation purpose. One flask was kept on continuous shaking for the entire growth period. Second flask was given an 18 hours shaking on daily basis. Third flask was manually shaked for twice or thrice a day.

Results and Discussion

Freshwater microalga was isolated and its morphology was determined by Light microscope, SEM and FTIR. Characteristics and morphological features of the isolate have demonstrated its close similarity with microalgae *Scenedesmus sp*. The microalgae isolate was finally identified as *Scenedesmus rubescens* based on 28s rDNA molecular identification.

Isolation and identification of microalgae

Light Microscope Studies

Inverted light microscope (Magnus) determined that cells are spherical in shape. The colour of colony is green and it can be easily perceived by the Figure-1.

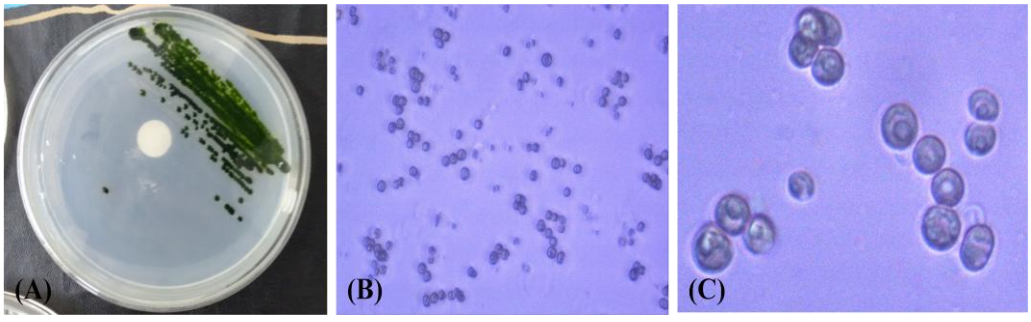
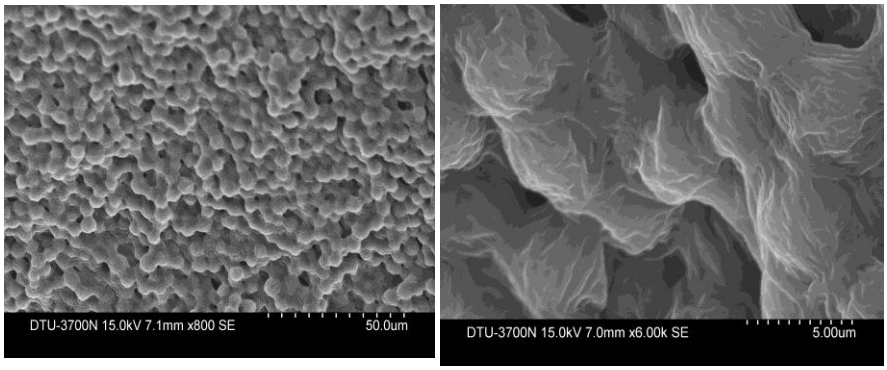


Figure-1: Isolated colonies of microalga *Scenedesmus rubescens* in agar plate (a) and under inverted light microscope (20X) (b) and 40X (C) enriched with BG-11 media. The isolated colonies were further used to establish pure culture, morphological, molecular and biomass productivity analysis.

Scanning Electron Microscope Studies:

In examining the physical structures of microalgae, SEM provides good visual images of possible microalgal structure and morphology. It scans solid samples with a beam of electrons, which interacts with the atoms that make up the sample to produce signals. These signals contain topographic information about the samples[2]. The average cell size was in the range of 5.6-5.8µm (Figure 2).



(a) **(b)**

Figure-2: Morphological determination of microalga *Scenedesmus rubescens* by scanning electron microscope (S-3700) (a) depict the resolution of microalga at 800 SE and (b) at 6000 SE. With the help of these resolutions average size of 5.8 microns has been confirmed. DTU: Delhi Technological University; 3700N

Fourier Transform Infrared Spectroscopy Studies

FTIR provides the metabolic fingerprinting of the material by discriminating and identifying the various functional groups present in it. The composition and structure of molecules and functional groups can be determined by analysing the position/width and infrared light absorption of the sample. Biomolecules such as lipid, carbohydrate and protein etc. has their own characteristics IR spectra, which is rich in molecular composition and functional aspects and which allow identification and quantification based upon absorbance For microalgae sample, the sample is analyzed in 4000-400 cm^{-1} wave number range with a resolution of 4 cm^{-1}[13, 15-17]. Following FTIR chromatogram (Figure-3) and table (Table-1) shows the presence of various functional groups attributed the protein; lipid and carbohydrate present in the *Scenedesmus rubescens* (Figure 3)**.**

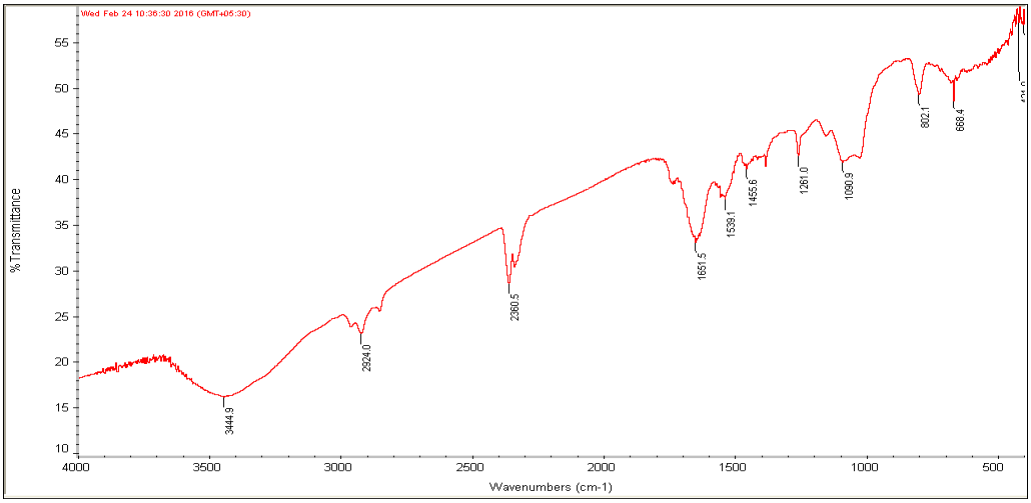


Figure-3: FTIR Spectra (4000-400 cm^{-1}) of *Scenedesmus rubescens.* Characteristic functional groups contributing to the formation of % transmittance bands at specific wave numbers.

Table-1: Tentative assignment of bands found in FTIR spectra of *Scenedesmus rubescens.* [12, 14, 18]

S. No.	Typical band assigned to lipid and carbohydrate	Wave number range cm $^{-1}$	Main peak cm^{-1} *(Scenedesmus rubescens)*
1	Water V(O-H) stretching Protein V(N-H) stretching	3029-3639	3444.9
2	Lipid –carbohydrate mainly Vas (CH2) and Vs(CH2) stretching	2809-3012	2924
3	Protein amide I band mainly V(C=O) stretching	1583-1709	1651.5
4	Protein amide II band mainly σ(NH)bending V(C-N) stretching	1481-1585	1539.1
5	Protein σas (CH2) and σ s(CH3) bending of methyl lipid as (CH2) bending of methyl	1425-1477	1455.6
6	Nucleic acid (other phosphate containing compounds) Vas> P=0 stretching of phosphodiesters	1191-1356	1261.0
7	Carbohydrate V (-O-C) of polysaccharides. Nucleic acid (other phosphate containing compounds) Vas> P=0 stretching of phosphodiesters	1072-1099	1090.9
8	Carbohydrate V(C-O-C) of polysaccharides	980-1072	1026

Molecular Identification studies:

The 28S rDNA gene sequence was used to carry out basic Local Alignment Search Tool (BLAST) with the nrdatabase of NCBI genebank database. Based on maximum identity score first ten sequences were selected and aligned using multiple alignment software program Clustal W. Distance matrix was generated using RDP database and the phylogenetic tree was constructed using MEGA 4 (Table 2).

Table-2: Sequences producing significant alignments. Nearest relatives (Accession Number, % Identicity) observed in GenBank when BLAST was performed with microalgae consensus sequence. Microalgae displayed the maximum identity with *Scenedesmus rubescens*, JX289896.1

Description	Max score	Total score	Query cover	E value	Ident	Accession
Scenedesmus rubescens isolate EP1H8 28S ribosomal RNA gene, partial sequence	778	778	99%	0	94%	JX289896.1
Acutodesmus obliquus partial 28S rRNA gene, strain KGE18	773	773	99%	0	93%	HE965014.1
Asterarcys sp. MS3 18S ribosomal RNA gene, partial sequence; internal transcribed spacer 1, 5.8S ribosomal RNA gene, and internal transcribed spacer 2, complete sequence; and 28S ribosomal RNA gene, partial sequence	761	761	99%	0	93%	KM893430.1
Scenedesmus obliquus partial 28S rRNA gene, isolate YSL009	761	761	99%	0	93%	FR751197.1
Scenedesmus obliquus partial 28S rRNA gene, isolate YSL012	761	761	99%	0	93%	FR751168.1
Scenedesmus obliquus partial 28S rRNA gene, isolate YSR007	761	761	99%	0	93%	FR751165.1
Scenedesmus obliquus isolate YSW14 large subunit ribosomal RNA gene, partial sequence	761	761	99%	0	93%	HM103381.1
Scenedesmus obliquus partial 28S rRNA gene, isolate YSR016	758	758	99%	0	93%	FR751169.1
Scenedesmus obliquus isolate YSL02 28S ribosomal RNA gene, partial sequence	758	758	99%	0	93%	GU732415.1
Acutodesmus obliquus partial 28S rRNA gene, strain KGE31	756	756	99%	0	93%	HF536545.1

Biomass Productivity Analysis

Microalgal growth depends upon the various environmental factors mainly light, pH, temperature, and availability of nutrients as they not only influence the photosynthetic activity of the microalgae but also affects the biochemical composition, cellular metabolism and morphology. Other factors such as shaking and species richness are also important factors influencing microalgal growth and metabolism. As a whole, these environmental factors significantly affect the CO2 fixation and photosynthesis, thus resulting into alteration of carbon fixation and biochemical composition [19-25]. The isolated microalgal sample was inoculated in BG11 medium and incubated at room temperature under a photoperiod of 16L: 8D for growth. Microalgal growth was monitored on a regular basis on spectrophotometer by observing absorbance at 670nm. A growth curve was plotted for a period of 24 days between absorbance and number of days. Figure-5 shows the absorbance noted on various days of culture. This isolated sample was then used as inoculums in the various experiments.

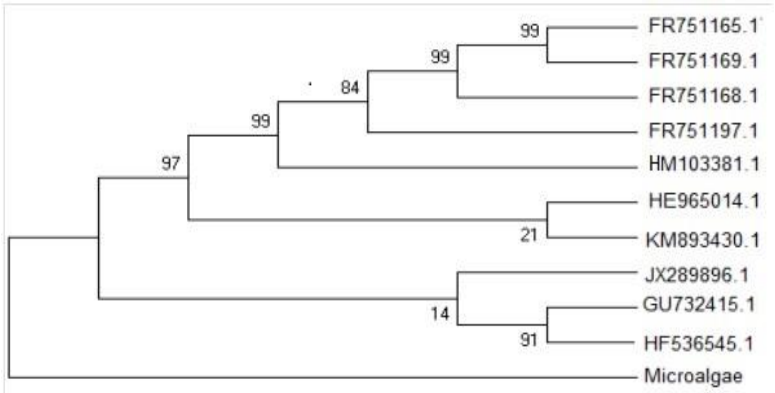


Figure-4: The evolutionary history was inferred using the Neighbour-Joining method. The phylogenetic tree was constructed using MEGA 4

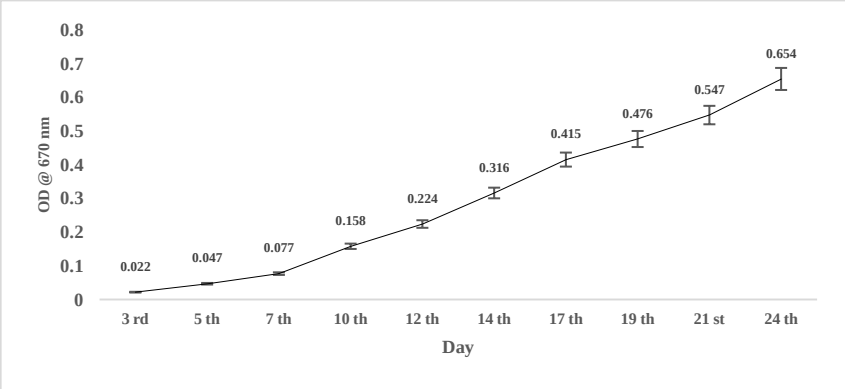


Figure 5: Growth curve of isolated microalga *Scenedesmus rubescens* for a period of 24 days. OD: optical density; 670 nm.

Proper light intensity is a requisite condition for the photosynthesis reaction [33] as it affects the algal growth through its impact on photosynthesis reaction. Growth rate is maximum at optimum intensity and the rate decreases as the intensity increases or decreases in comparison to optimum condition [34]. At light intensity more than the optimum, photo-inhibition reaction occurs and thus reduction in light utilization efficiency [24, 36-38]. This efficiency can be enhanced by allowing the culture to remain in longer dark period while using high light intensities. During this prolonged dark period photosynthesis system works efficiently by optimally utilising captured photons and converting this light energy into chemical energy by avoiding photo-inhibition effects [37]. This happens because high light intensity disrupts the chloroplast lamellae [38] and inactivation of enzymes involved in carbon dioxide fixation [39]. However, algal growth rate under increasing light intensities depends upon the types of algal species as well as other culture conditions like temperature and pH etc. [34].

The growth was allowed in six different light intensities 10, 15, 25, 36, 60 and 100 Watt in BG11 medium having pH 8 and light period of 16L: 8D for 24 days and growth was monitored by spectrophotometer at 670nm. All the intensities were provided by yellow light bulb except one, 15watt. For 15watt light intensity, a white fluorescent light was used. Initially a high growth rate was noticed in the flask maintained at 100 W intensity conditions. Later on, the growth rate was found high in the flask maintained at 36 W. Colour of light has a very significant effect on the biomass productivity. The fact established well by higher growth observed in flask with the 15 W flasks in this experiment. Reading was noted at a period of two or three days and plotted to derive a growth curve on the basis of absorbance and time (Figure-6). Biomass productivity was recorded on spectrophotometer at 670 nm when allowed to grow under three different light colours white, blue and red light. During first two weeks, high growth rate was observed in white light condition, after that a significant change was observed in algal growth. Blue and red light both conditions showed the comparable growth rate to the white in third week onwards of microalgae culture. In an experiment done on light intensity, it was found that 15 W white fluorescent lights gives high biomass productivity in comparison to yellow light with having intensity 100 watt. The maximum biomass productivity was achieved in white light condition (1.56 mg/ml) followed by red (1.37mg/ml) and blue light (0.83mg/ml) (Figure-7).

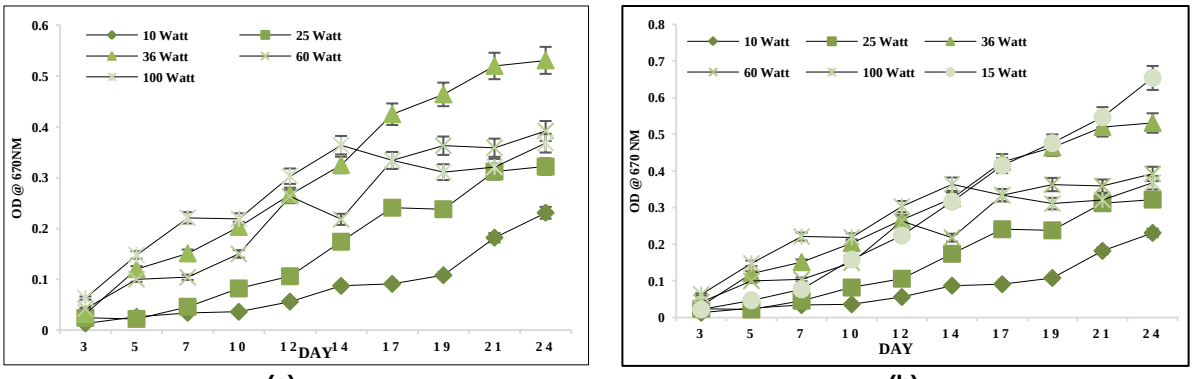


Figure 6: Effect of light intensities on biomass growth and productivity of microalga. (a) Compares the biomass productivity of all intensities of yellow colour light where 36 W provided maximum productivity while (b) compares the productivity with 15 W fluorescent lights. The biomass productivity of 15 W fluorescent lights is better than 36 W yellow lights. OD: optical density; 670 nm.

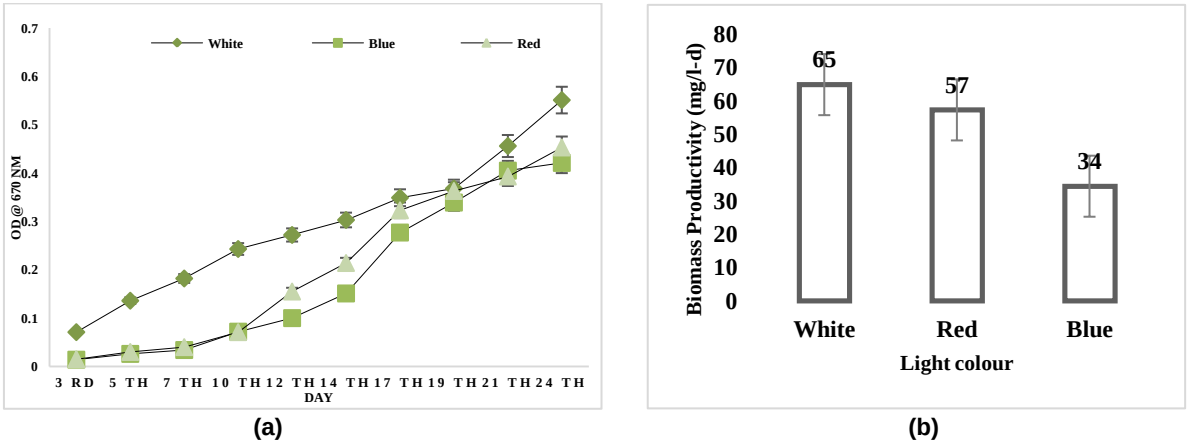


Figure 7: Effect of light colour on biomass growth and biomass productivity of microalga. (a) Compares the growth of microalga in three different light colour and white colour provides maximum growth. (b) Also supports the fact that white colour light is suitable for microalga as it provides maximum biomass productivity. OD: optical density; 670 nm.

Light period is important mainly because of dark reactions as well as CO_2 fixation. Studies showed that dark phase is beneficial for microalgae growth because certain enzymes of pentose cycle which is used in photosynthesis and carbon dioxide fixation are active during dark phase and inactive during light phase[40]. Colours of light for providing illumination to microalgae culture has substantial effect on growth rate due to the wavelength spectral energy of various light colours. Wu and Merchuk [36] studied the effect of light and dark periods on the microalgal growth and found that with increasing photon flux density, specific growth increases up to a certain value and then it decreases with increased photon flux density. When cultured under three different photoperiods, microalgal growth rate was observed highest in a photoperiod of 16 L: 8D hour's dark with biomass productivity of 1.39mg/ml at the end of 24 days of cultivation. When grown under 24 hours' light supply the microalgal culture shown the biomass productivity of 1.33mg/ml while under 12 hours' photoperiod the biomass productivity was 1.07 mg/ml (Figure-8).

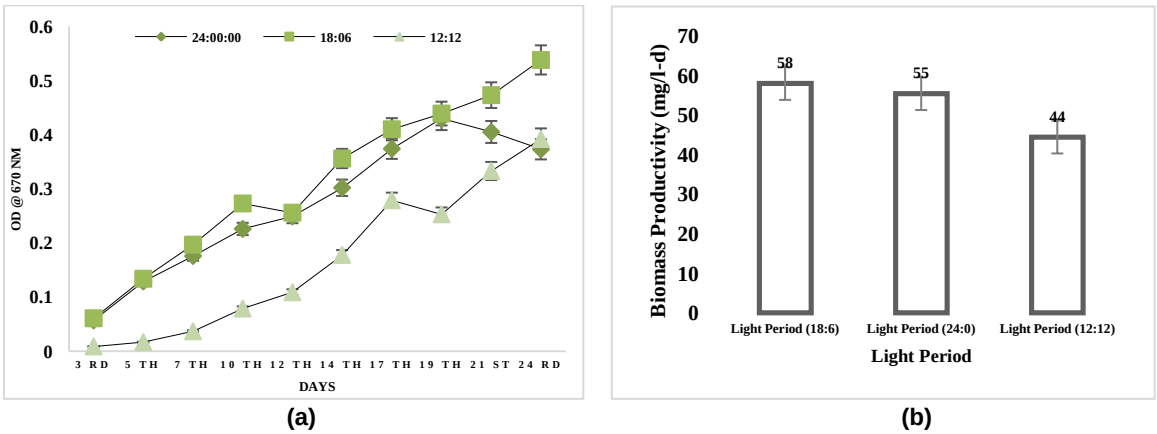
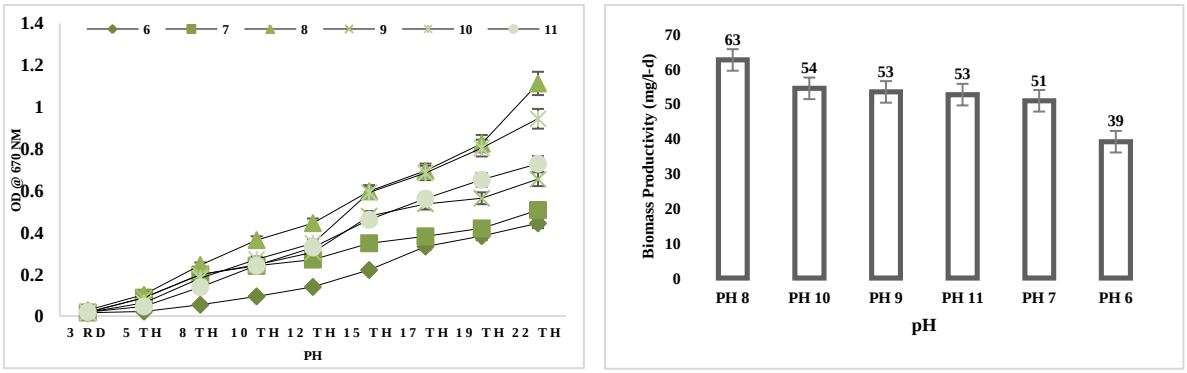


Figure 8: Effect of light period (light: dark) on biomass growth and biomass productivity of microalga. (a) represents a comparison of growth in three different light periods and 18L:06D shows maximum growth. (b) 18L:06D also provided maximum biomass productivity. OD: optical density; 670 nm.

pH is one of the important factors for algal growth as it can affect the activity of different enzymes. Studies on the effect of pH on microalgae demonstrate that different algal species have a different level of tolerance to pH. The pH of the media has also the significant effect on the morphology of the algal cells. It influences the carbon availability, metabolism and thus the biochemical composition [26]. The pH determines the solubility and accessibility of CO_2 and essential nutrients, and because it can have a significant impact on algal metabolism [6, 27]. The pH of the culture media rises significantly during cultivation due to the uptake of inorganic carbon. Highest microalgal biomass productivity was observed at a pH 8 with biomass productivity of 1.50mg/ml among six

different media pH, 6 (0.94 mg/ml), 7(1.22 mg/ml), 8(1.50 mg/ml), 9(1.28 mg/ml), 10 (1.31 mg/ml) and 11(1.26 mg/ml) when tested in BG-11 for highest growth rate and biomass productivity (Figure-9).

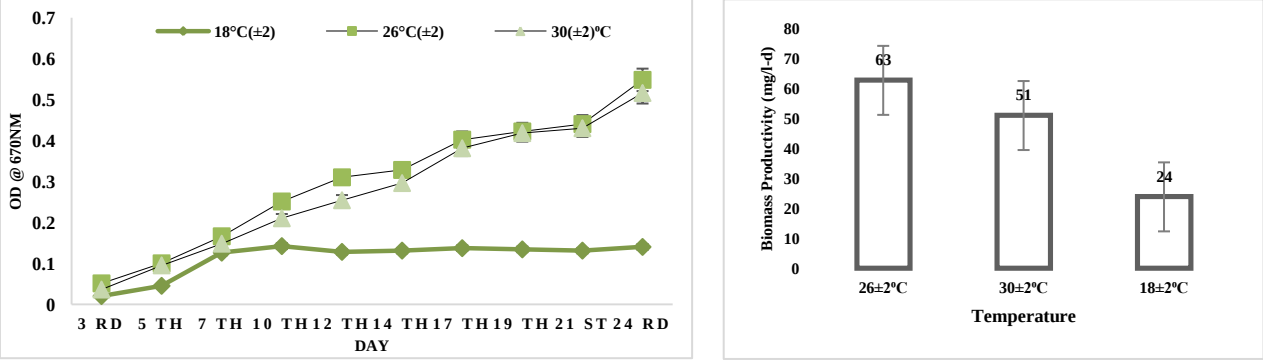


(a) **(b)**

Figure 9: Effect of pH on biomass growth and biomass productivity of microalga. (a) & (b) both represent maximum growth and biomass productivity at pH 8. Alga favours alkaline pH for its growth and biomass productivity. OD: optical density; 670 nm.

Photo-inhibition also depends upon the temperature of the culture medium. Low temperature enhances the light inhibition and thus affects the nutrients uptake rate as well as decrease the fluidity in the cell membrane. Temperature beyond the optimum affects the protein synthesis and thus results into reduction of growth rate [29]. It influences the CO_2 assimilation and O_2 evolving activity of the PS II system of photo-synthesis. It has been reported that it influences microalgal growth rate, cell morphology, various biomolecules composition and nutrient compositions. Various studies based on temperature dependent photo-inhibition suggest that at low temperature, electron transport decreases at a particular photon flux due to decreased rate of CO_2 assimilation. Low temperature causes inhibition of reactive oxygen species and therefore resulting in reduced photo-inhibition by protecting photo system II of photosynthesis system[30]. Morris et al [19] reported that protein synthesis rate increases at lower temperature with marine microalgae *Phaeodactylum tricornutum* [31]. Very similar to this, Rhee and Gotham[32] also reported a significant increment in protein concentration in Scenedesmus sp. at lower temperature.

Out of three different temperature regimes 18°C(±2), 26°C(±2), and 30°C(±2), the maximum biomass yield (1.51 mg/ml) was observed in the flask maintained at 26°C(±2). Microalgal culture has shown very less growth at a temperature or below 18°C (±2) with biomass productivity (0.57 mg/ml), while there was very less difference in growth was observed at 30°C(±2) (1.22 mg/ml), when to compare to high biomass yielding temperature regime (figure-10).

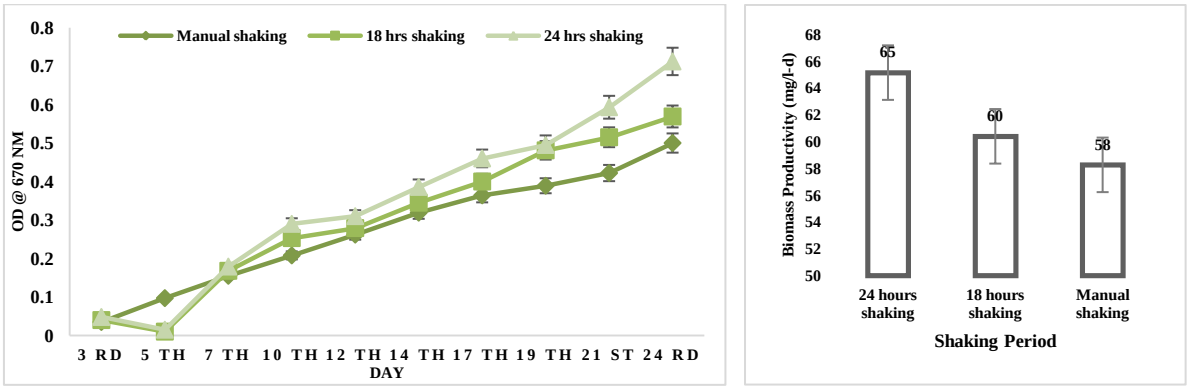


(a) **(b)**

Figure 10: Effect of temperature on biomass growth and productivity of microalgae. (a) And (b) both represent that maximum growth and productivity was found at temperature 26°C (±2). Growth was almost same at 30°C (±2) which represents that this microalgae can be grown within a range of temperature from 26-30°C (±2). OD: optical density; 670 nm.

In high dense culture, self-shading occur which results in decrease in light absorption capacity of photosynthetic antenna. Thus shaking is essential for mixing of nutrients and to prevent the settling of biomass. Agitation or shaking provides proper mixing which plays an important role in the increasing of microalgal biomass productivity [27].

In this experiment, out of three shaking conditions 24hours on shaking, 18 hours a day on shaking and manual shaking, 24 hours on shaking gave the highest biomass productivity 1.56 mg/ml while 18 hours shaking and manual shaking resulted in to 1.45 mg/ml and 1.40mg/ml biomass productivity respectively (figure-11).



(a) **(b)**

Figure 11: Effect of shaking period on biomass growth and productivity of microalga. (a) Represents comparative growth of microalga in different shaking period while (b) provides information of biomass productivity. Shaking of 24 hours is found best for both growth as well as biomass productivity of microalga. OD: optical density; 670 nm.

Conclusion

Based on morphology and molecular examination, microalgae isolated were identified as *Scenedesmus rubescens.* Effects of various culture conditions on green microalgae isolate *Scenedesmus rubescens* has been studied and thus concluded that the maximum growth rate and biomass productivity can be achieved by providing light having intensity, color and photoperiods of 36W, White and 16 hours respectively. Alkaline pH especially pH 8 supports the maximum growth rate and thus maximum biomass productivity. The optimum growth rate was observed in the 24h shaking period and 26 (±2) ºC temperatures. In future, effect of these culture conditions on biochemical composition of microalga will be studied to finalise the best culture condition for obtaining compatible feedstock for biofuels. Additionally, the microalga will be tested for its nutrient and heavy metal removal capacity from wastewater, biofuel production and nanoparticles synthesis.

Acknowledgement

Authors are grateful to the Department of Biotechnology, Delhi Technological University, Delhi, India for providing the necessary research facilities. We are also thankful to Eurofins Genomics India Pvt. Ltd. Bangalore, India for 28s molecular identification. We sincerely thank Department of Chemistry and Department of Physics, DTU for SEM, FTIR analysis.

References

1. Singh A, Olsen, SI (2011) A critical review of biochemical conversion, sustainability and life cycle assessment of algal biofuels. Applied energy 88: 3548-3555.
2. Z. Bi, B. B. He (2013) Characterization of microalgae for the purpose of biofuel production. American Society of Agricultural and Biological Engineers ISSN 2151-0032, Vol. 56(4): 1529-1539.
3. Singh, L., Pavan kumar, A.R., Lakshmanan, R., (2012) Effective removal of Cu2+ ions from aqueous medium using alginate as biosorbent. Ecol. Eng. 38, 119–124.
4. Giuliano Dragone, Bruno Fernandes, António A. Vicente, and José A. Teixeira, (2010) Third generation biofuel from microalgae. Current Research, Technology and Education Topics in Applied Microbiology and Microbial Biotechnology 1355-66.
5. Chisti, Y. (2007) Biodiesel from microalgae. Biotechnol. Adv., 25:294–306.
6. Teresa M. Mata, Ricardo Almeida , Nídia S. Caetano (2013) Effect of the Culture Nutrients on the Biomass and Lipid Productivities of Microalgae *Dunaliella tertiolecta. CHEMICAL ENGINEERING TRANSACTIONS. VOL. 32,* ISBN 978-88-95608-23-5; ISSN 1974-9791
7. Sharma R, Singh GP, Sharma VK (2012) Effects of Culture Conditions on Growth and Biochemical Profile of Chlorella Vulgaris. J Plant Pathol Microb 3:131.doi: 10.4172/2157-7471.1000131
8. Izabela Krzeminska, Barbara Pawlik-Skowronska, Magdalena Trzcinska, Jerzy Tys (2014) Influence of photoperiods on the growth rate and biomass productivity of green microalgae. Bioprocess Biosyst Eng , 37:735–741
9. Grobbelaar JU (2009). Upper limits of photosynthetic productivity and problems of scaling. J Appl Phycol, 21:519–522

10. Becker E.W. (1988) Micro-algae for human and animal consumption, in Micro-algal biotechnology, M.A. Borowitzka and L.J. Borowitzka, Editors. Cambridge University press: Cambridge. p. 222–256.
11. Karin Larsdotter (2006) Wastewater treatment with microalgae –a literature review. VATTEN 62:31–38. Lund.
12. Indhumathi Ponnuswamy, Soundararajan Madhavan, Syed Shabudeen (2013) Isolation and Characterization of Green Microalgae for Carbon Sequestration, Waste Water Treatment and Bio-fuel Production. International Journal of Bio-Science and Bio-Technology Vol. 5, No. 2
13. Joshua J. Mayers, Kevin J. Flynn , Robin J. Shields (2013) Rapid determination of bulk microalgal biochemical composition by Fourier-Transform Infrared spectroscopy. Bioresource Technology 148 215–220.
14. *Roberta Miglio, Stefano Palmery, Mario Salvalaggio, Lino Carnelli, Federico Capuano, Raffaella Borrelli* (2013) Microalgae triacylglycerols content by FT-IR spectroscopy. J Appl Phycol 25:1621–1631
15. *Vitaly Erukhimovitch, Marina Talyshinsky, Yelena Souprun, Mahmoud Huleihel* (2003) *Spectroscopic* evaluation of carbohydrate levels in cell line treated with red microalgal polysaccharides. Spectroscopy 17 447–451
16. Ng Ching Yin, Zahira Yaakob, Ehsan Ali, Aung Min Min and Ng Sheng Wa (2011) Characterization of Various Microalgae for Biodiesel Fuel Production. Journal of Materials Science and Engineering A 1 80-86
17. Lisette D'Souza, Prabha Devi, Divya Shridhar M.P., Chandrakant G. Naik (2008) Use of Fourier Transform Infrared (FTIR) Spectroscopy to Study Cadmium-Induced Changes in *Padina Tetrastromatica* (Hauck). Analytical Chemistry Insights :3 135–143
18. *DY Duygu, AU Udoh, TB Ozer, A Akbulut, IA Erkaya, K Yildiz, D Guler* (2012) Fourier transform infrared (FTIR) spectroscopy for identification of Chlorella vulgaris Beijerinck 1890 and Scenedesmus obliquus (Turpin) Kützing 1833. African Journal of Biotechnology. Vol.11(16), pp. 3817-3824 , DOI: 10.5897/AJB11.1863. ISSN:1684-5315
19. Morris I., Glover H., Yentsch C. (1974) Products of photosynthesis by marine phytoplankton: The effect of environmental factors on the relative rates of protein synthesis. *Mar. Biol.*, *27*, 1–9.
20. Sukenik A., Carmeli Y., Berner T. (1989) Regulation of fatty acid composition by irradiance level in the eustigmatophyte *Nannochloropsis* sp. *J. Phycol. 25*: 686–692.
21. Thompson P.A., Guo M., Harrison P.J. (1992) Effects of variation in temperature. I. On the biochemical composition of eight species of marine phytoplankton. *J. Phycol. 28*: 481–488.
22. Chen C.Y., Durbin E.G. (1994) Effects of pH on the growth and carbon uptake of marine phytoplankton. *Mar. Ecol.-Prog. Ser. 109*: 83–94.
23. Kilham S., Kreeger D., Goulden C. Lynn S. (1997) Effects of nutrient limitation on biochemical constituents of *Ankistrodesmus falcatus*. *Freshw. Biol. 38*: 591–596.
24. Gordillo F.J.L., Goutx M., Figueroa F.L., Niell F.X. (1998) Effects of light intensity, CO2 and nitrogen supply on lipid class composition of *Dunaliella viridis*. *J. Appl. Phycol. 10*:135–144.
25. Visviki I., Santikul D. (2000) The pH tolerance of *Chlamydomonas applanata* (*Volvocales*, *Chlorophyta*). *Arch. Environ. Contam. Toxicol. 38*: 147–151.
26. J.W. Hargreaves & B.A. Whitton (1976) Effect of pH on growth of acid stream algae, British Phycological Journal, 11:3, 215-223, DOI: 10.1080/00071617600650491
27. Goldman, J.C. (1973) Letter: Carbon dioxide and pH: Effect on species succession of algae. *Science 182*, 306–307.
28. Hu Qiang , Yair Zarmi & Amos Richmond (1998) Combined effects of light intensity, light-path and culture density on output rate of Spirulina platensis (Cyanobacteria), European Journal of Phycology, 33:2, 165-171, DOI: 10.1080/09670269810001736663
29. Konopka A., Brock T.D. (1978) Effect of temperature on blue-green algae (cyanobacteria) in Lake Mendota. *Appl. Environ. Microbiol. 36*, 572–576.
30. Vonshak A., Torzillo G. (2004) Environmental Stress Physiology. In *Handbook of Microalgal Culture*; Richmond, A., Ed.; Blackwell: Oxford, UK
31. Cuhel R.L., Ortner P.B., Lean D.R.S. (1984) Night synthesis of protein by algae. *Limnol. Oceanogr. 29*, 731–744.
32. Rhee G.Y., Gotham I.J. (1981) The effect of environmental factors on phytoplankton growth:Temperature and the interactions of temperature with nutrient limitation. *Limnol. Oceanogr. 26*, 635–648.
33. Stockenreiter M., Haupt F., Graber A.K., Seppälä J., Spilling K., Tamminen T., Stibor H. (2013) Functional group richness: Implications of biodiversity for light use and lipid yield in microalgae. *J. Phycol.*

34. Sorokin C., Krauss R.W. (1958) The Effects of light intensity on the growth rates of *green algae*. *Plant Physiol. 33*: 109–113.
35. You T., Barnett S.M. (2004) Effect of light quality on production of extracellular polysaccharides and growth rate of *Porphyridium cruentum*. *Biochem. Eng. J. 19*: 251–258.
36. Wu X., Merchuk J.C. (2001) A model integrating fluid dynamics in photosynthesis and photoinhibition processes. *Chem. Eng. Sci. 56*: 3527–3538.
37. Long S., Humphries S., Falkowski P.G. (1994) Photoinhibition of photosynthesis in nature. *Annu. Rev. Plant Biol. 45*: 633–662.
38. Brody M., Vatter A.E. (1959) Observations on cellular structures of *Porphyridium cruentum*. *J. Biophys. Biochem. Cytol. 5*: 289–294
39. Iqbal M., Zafar S. (1993) Effects of photon flux density, CO2, aeration rate, and inoculum density on growth and extracellular polysaccharide production by *Porphyridium cruentum*. *Folia Microbiol. 38*: 509–514.
40. Weibao Kong , Hao Song , Yuntao Cao , Hong Yang , Shaofeng Hua and Chungu Xia (2011) The characteristic of biomass production, lipid accumulation and chlorophyll biosynthesis of Chlorella vulgaris under mixotrophic cultivation. Afr. J. Biotechnol., vol. 10, pp., 11620-11630.

emeraldinsight

International Journal of Managerial Finance

Lead-lag relationship between futures and spot FX market in India
Varuna Kharbanda, Archana Singh,

Article information:

To cite this document:
Varuna Kharbanda, Archana Singh, (2017) "Lead-lag relationship between futures and spot FX market in India", International Journal of Managerial Finance, https://doi.org/10.1108/IJMF-01-2017-0001
Permanent link to this document:
https://doi.org/10.1108/IJMF-01-2017-0001

Downloaded on: 31 August 2017, At: 01:39 (PT)
References: this document contains references to 56 other documents.
To copy this document: permissions@emeraldinsight.com
The fulltext of this document has been downloaded 15 times since 2017*
Access to this document was granted through an Emerald subscription provided by emerald-srm:544911 []

For Authors

If you would like to write for this, or any other Emerald publication, then please use our Emerald for Authors service information about how to choose which publication to write for and submission guidelines are available for all. Please visit www.emeraldinsight.com/authors for more information.

About Emerald www.emeraldinsight.com

Emerald is a global publisher linking research and practice to the benefit of society. The company manages a portfolio of more than 290 journals and over 2,350 books and book series volumes, as well as providing an extensive range of online products and additional customer resources and services.

Emerald is both COUNTER 4 and TRANSFER compliant. The organization is a partner of the Committee on Publication Ethics (COPE) and also works with Portico and the LOCKSS initiative for digital archive preservation.

*Related content and download information correct at time of download.

Downloaded by Delhi Technological University At 01:39 31 August 2017 (PT)

The current issue and full text archive of this journal is available on Emerald Insight at:
www.emeraldinsight.com/1743-9132.htm

Lead-lag relationship between futures and spot FX market in India

Varuna Kharbanda and Archana Singh
Delhi School of Management, Delhi Technological University, Delhi, India

Received 2 January 2017
Revised 25 June 2017
Accepted 25 June 2017

Abstract

Purpose – The purpose of this paper is to study the lead-lag relationship between the futures and spot foreign exchange (FX) market in India to understand the price discovery mechanism and the relationship between these two markets.

Design/methodology/approach – The estimation of lead-lag relationship is realized in three steps. First unit root and stationarity tests (Augmented Dickey-Fuller, Phillips-Perron, and Kwiatkowski-Phillips-Schmidt-Shin) are applied to check the stationarity of the data. Second, cointegration tests (Engle and Granger's residual based approach and Johansen's cointegration test) are applied to determine long run relationship between the markets. Third, error correction estimation is carried out by applying Vector Error Correction Model (VECM) to determine the leading market.

Findings – The study finds that there is a long run relationship between the futures and spot market where the futures market has emerged as the leading market for the four currencies studied in the paper.

Originality/value – Majorly, the studies on Indian FX market limit themselves to identifying the efficiency of the market and the studies which talk about the lead-lag relationship focus on the Indian stock market. This paper enhances the existing literature on Indian FX market by exploring the less explored subject of the lead-lag relationship between futures and spot FX market in India.

Keywords Cointegration, Error correction, Foreign exchange (FX), Lead-lag relationship

Paper type Research paper

1. Introduction

A lead-lag relationship in a spot and futures market observes the linkage between the two markets and reflects how well the new information is reflected in the prices and thus reveals how the price is discovered in the market. In simple terms, it identifies the leading and the lagging market. The issues of price discovery and lead-lag relationship between the market components are topics of interest to participants like traders, economists, analyst, etc. (Debasish and Mishra, 2008). If the prices adjust to the new information promptly in both the markets, then arbitrage opportunities do not exist for the traders, and the market becomes fully efficient. However, if one market is discovered as a lead market, then this means that the discovery of price in that market would provide valuable information about the price in the other market. Thus, arbitragers, traders, and analyst can take benefit of such information and earn profits, develop price forecasting models, etc.

The matter of lead-lag relationship and price discovery has achieved more importance since the integration of the world market which has led to the growth of industry and business. One of the prime markets which play a pivotal role in integrating businesses all over the world is currency market or foreign exchange (FX) market also called FX or forex market. This market provides a platform for participants to buy and sell foreign currencies at predetermined or existing prices and consists of central banks, public and private banks, multi-nationals, hedge funds, investment banks, exchange brokers, and investors.

1.1 Indian FX market

The Indian FX market was highly regulated initially. An important year in the history of Indian FX market was 1978 when Reserve Bank of India (RBI) allowed banks to participate in intra-day FX trading. Because of which the volume of trade in the FX market increased.

International Journal of Managerial Finance
1743-9132
DOI 10.1108/IJMF-01-2017-0001
© Emerald Publishing Limited

Downloaded by Delhi Technological University At 01:39 31 August 2017 (PT)

But still the markets were highly regulated by RBI and the value of rupee was determined by the weighted pool of currencies of India's major trading partners. More reforms were introduced in the 1990s and radical changes were brought with the policies of liberalization, privatization and globalization along with the shifts in the currency regime in India (RBI, 2007). The RBI followed a gradualist approach for the development of the FX market.

Many reforms were brought in the forex market to make it more competitive. For this, an expert group was formed in 1994 to study the market in detail (RBI, 2007). Foreign Exchange Management Act introduced in the year 2000 replaced the old and stringent Foreign Exchange Regulation Act. This new act liberalized export-import policy, FDI, and FII investments and expanded the list of activities to undertake FX transactions. To deepen the markets further banks were given freedom to invest in foreign stocks, fix trade limits and use derivatives. Corporates were also allowed to use these financial instruments to manage risk. These reforms brought a new age of FX market in India.

Subsequently the Indian FX market witnessed increase inflows and outflows of various currencies. The corporates were also actively using forwards to manage currency risk at the Over-the-Counter (OTC) market. But the OTC market was not exchange regulated. A need was therefore felt to have an organized and structured market which would provide an orderly risk management system. One of the biggest developments in the forex market was the introduction of currency futures. RBI in its report in April 2008 listed many benefits of the currency futures like a further development of domestic FX market, efficient method of credit risk transfer through the exchange, hedging instrument against fluctuations, etc. Therefore, currency futures were introduced for the market participants on August 28, 2008. Initially, these were available only for US dollar (USD) but in the year 2010 the currency futures expanded to include Euro, Pound, and Yen also.

There is no denying the fact that the OTC market remained attractive to most participants with FX exposure as this market provided flexibility to customize the contracts for specific requirements. But the corresponding development of a better structured and controlled market was important to bring efficiency, stability, and transparency in the FX market. Currency futures comes with various advantages like offering price transparency, controlling counter party default risk, higher accessibility etc. Additionally, it is comparatively easy for the participants to transact in the futures market because of lower transaction cost in comparison to the spot market. Futures market also helps in bringing out private information into the market by offering transparency and anonymity to its participants. Thus, an important advantage offered by futures is better price discovery.

Price discovery implies determining the price of an asset or an instrument in a market. This price is determined by the interaction of the forces of demand and supply i.e. through the interaction of buyers and sellers. The typical participant in the derivatives market like hedger has private information and whenever new information arrives on the market, these participants by their actions, feed their private information into the system which causes the price of the derivative to change and reach a new equilibrium. Since the popularity of the futures market is increasing, more activity in this market implies more information is reaching the market. An efficient market is one where there is no pull and push of these forces; the information is freely available to all the market participants. But this is seldom seen. It then becomes imperative to understand these pull and push forces, better called as the lead and lag relationship between major market components.

Over the years upsurge in market participants like mutual funds, insurance companies, and multinational corporations, etc., increasing number of hedgers, speculators and arbitragers and thriving derivative products have added to the development and complexity of Indian FX market which produces the annual turnover of over $400 billion. The Indian forex market has come a long way regarding a variety of instruments, participants and

Downloaded by Delhi Technological University At 01:39 31 August 2017 (PT)

overall market turnover (RBI, 2014). India's approach to exchange rate management has been to contain the volatility of capital flows.

The RBI has taken various measures to ensure that the Indian FX market meet the global challenges. India has been pursuing a calibrated approach which requires deep and liquid FX market with wide range of instruments especially hedging instruments, to reduce volatility resulting from large capital flows (RBI, 2015). Steps have been taken to bring the offshore Non-Deliverable Forward market onshore by liberalizing currency futures market. Going further the focus is to bring better alignment between OTC and exchange traded currency futures. The importance of currency risk management by corporates has increased many folds, and RBI has sensitized the corporate and the banking system about the need for hedging from time to time (RBI, 2015).

India today is an attractive destination for investors and has seen a rise in inflows and outflows of different foreign currencies. Indian forex market has become more complex and deep with various participants using many different derivative instruments for trading and hedging risk. This changing structure of the market and rising participants stressed on the need to bring efficiency, stability and transparency in the market and therefore currency futures were introduced. Thus, two motivations for the study are identified. First, Indian regulatory body RBI has been regularly making many policy changes to make forex market more efficient. It, therefore, becomes essential to study the significant components of the market like futures to comprehend the working of the market better. Understanding price discovery and the lead-lag relationship in the futures and the spot market is one step toward that. Second, more development of derivatives market and specifically futures market has focused a great deal of research toward empirically testing causality relationships. But most of this research has focused on the developed markets. Further, Indian researchers have studied price discovery and lead-lag in the stock market and currency markets have been left unexplored.

The present study is an attempt to examine the less explored area of price discovery in the Indian FX market by investigating the lead-lag relationship between the futures and the spot currency prices. It is essential to study the lead-lag relationship in the Indian FX market because first, it is important to determine the location of price discovery, to find out which market is more efficient. Second, this would help regulators to frame improved policies for regulation. Third, corporates use futures for hedging currency risk and can use this information to formulate better hedging strategies. Fourth, the behavior of the financial market and the lead-lag relationship of its components is of importance to arbitragers who are required to complete two transactions in a short span of time. Finally, speculators take a position in the market by anticipating future price movement and the lead-lag relationship would provide them with vital clues to take an informed position.

The present study thus, analyses the futures and the spot data for four currencies, USD, Great Britain Pound (GBP), EURO and Japanese Yen (JPY). The rest of this paper is divided into six sections. Literature review is discussed in Section 2, objectives of the study are stated in Section 3, Section 4 discusses research methodology, Section 5 presents' empirical results and analysis and Section 6 offers a conclusion to the study.

2. Literature review

This section discusses the existing research work on the lead-lag relationship in the developed as well as the emerging markets. A related concept with the lead-lag relationship is the efficiency of the market which is also discussed briefly.

Efficiency in a market could be operational, informational or price related, etc. Efficiency in a financial market implies the informational efficiency. Informational efficiency means how correctly the price of an asset reflects the new information. In a perfectly efficient market the price would reflect all the new information and there would be no disequilibrium.

Downloaded by Delhi Technological University At 01:39 31 August 2017 (PT)

Many different studies have explored the issue of efficiency in a FX market like Aron and Ayogu (1997), Wickremasinghe (2004), Ibrahim *et al.* (2011), Kühl (2007), Phengpis (2006), Kurihara (2011) and Lee and Sodoikhuu (2012).

Most of these studies found the forex market to be inefficient which further meant that price in the market did not reflect all the available information and there could be a lead-lag relationship between the market variables. The lead-lag relationship in the variables is observed due to market frictions like less restrictive regulation, lower transaction cost and greater liquidity, etc. in one market which enables speedy informational flow in that market. These advantages are observed in the futures market and theoretically, futures lead the spot market and play an important role in price discovery. Currency futures comes with various advantages like offering price transparency, controlling counter party default risk, higher accessibility etc. An important advantage offered by futures is better price discovery. A popular approach to understanding the price discovery function is to examine the lead-lag relationship between the market variables.

Downloaded by Delhi Technological University At 01:39 31 August 2017 (PT)

2.1 Lead-lag relationship in developed markets

Crain and Lee (1995) used regression and correlation analysis to explore the adjustment of spot and futures exchange and interest rates to new announcements in the USA. They focused on how long the volatility continued for higher than normal levels and tested for the lead-lag relationship between the futures and the spot on the day of the announcement. The overall result showed that the speed of the price adjustment was slower in the spot market compared to the futures market. The price discovery role of futures market was confirmed. Chatrath and Song (1998) investigated the impact of US macroeconomic announcements in the JPY futures and spot markets. The results suggested that the futures market reacted more efficiently to new information. Thus, futures price lead the spot price and played a more significant role in price discovery.

Asche and Guttormsen (2002) examined the relationship between the commodity futures and spot market prices traded at IPE by applying Engle and Granger and Johansen cointegration methods and found that the futures prices lead the spot prices. Rosenberg and Traub (2008) compared price discovery in the spot and futures FX markets for the currencies traded at CME using the methods of Hasbrouck (1995) and Gonzalo and Granger (1995) and found that spot market played a dominant role in price discovery. Frino *et al.* (2006) estimated the time-varying relationship between changes in cash market quotes and changes in currency futures quotes to identify the source of price discovery in the Australian dollar currency market. They found the currency spot market to be the main contributor for price discovery and lead the futures market.

Tse *et al.* (2006) examined the contribution of floor-traded futures and electronic futures and spot trading to the price discovery in JPY and euro futures markets. They found that electronic futures contracts contributed more to price discovery for the euro, and the electronic spot trading market contributed more to price discovery for the JPY. The electronic trading systems lead more to price discovery than the floor trading system in both the markets. Andersen *et al.* (2007) considered the real-time interactions among USA, British and German – stock, bond, and FX markets during news announcements and found that the bond market reacted most strongly to announcements. They further found direct spillover effects of these announcements among the equity markets across nations. Cabrera *et al.* (2008) investigated price discovery based on electronic trading systems for of euro and JPY exchange rates and found spot market to play a dominant role in price discovery process for both these currencies.

Chen and Gau (2010) used the information shares approach and the common factor component weight approach to examine price discovery in spot and futures for the EUR-USD and the JPY-USD markets during macroeconomic announcements. They concluded that spot

price lead the futures price and was dominant in discovering price. However, they also noted that since FX futures market attracted more informed traders when the announcements were released it contributed more to price discovery during the macroeconomic announcements. Tornell and Yuan (2012) examined the relation between the activities of market participants like speculators and hedgers in the futures market and the movement in spot exchange rates. They displayed that peaks and troughs of net positions were useful in predicting spot exchange rates. However, there was low correlation of other trade position with the market movements.

The above studies confirmed futures as the leading market for some economies and spot as the leading market for some economies. The reasons for this could be varied. The market which attracts participants and comparatively disseminates information more quickly emerges as the leading market. The policies of an economy, the global attractiveness of an economy, the operational and transaction costs etc. together determine the leading market.

2.2 Lead-lag relationship in emerging markets

Nieto *et al.* (1998) studied the spot and futures prices in the Spanish stock index market and found that the futures lead the spot prices toward long run equilibrium and played a dominant role in price discovery. Min and Najand (1999) investigated the lead-lag relation between spot and futures markets in Korea and found that futures lead the spot market by thirty minutes. Kenourgios (2004) used cointegration tests and an error correction model in Athens Stock Exchange to examine the informational linkage between price movements of futures index and the underlying cash market. They found two-way causality between the spot index and the futures index markets. Thus, each market contained useful information about the consequent price movements in the other market.

Ünlü and Ersoy (2012) used cointegration and developed an error correction model to examine the interaction between spot and futures contracts of Turkish Lira-USD exchange rate. They concluded that there was a two-way causality between futures and spot. de Boyrie *et al.* (2012) investigated the price discovery in the spot and futures markets for Brazilian real, South African rand and Russian ruble by employing multiple structural analysis, VECM model and reduced form computation model. The findings indicated that the futures market lead the spot market for the Brazilian real, thus played a dominant role in price discovery. Spot market lead the futures market for Russian ruble and played a prominent role in price discovery. The results were mixed for South African rand. Sriram and Senthil (2013) analyzed the relationship between futures and spot market of currency (dollar) by employing Johansen cointegration test, GARCH (1,1) for volatility and Impulse response function. They found a long term relationship between the two markets where spot caused futures.

Ilter and Alguner (2013) investigated the price discovery and lead-lag in the stock index futures and spot market using VECM model and concluded that futures market was an important price discovery tool. Garcia *et al.* (2014) studied price discovery in the FX markets in Brazil using high-frequency data of the FX market. They found that the futures market dominated the price discovery process. Bashir *et al.* (2014) investigated the relationship between forward and spot exchange rate in Pakistan using regression and concluded the market to be inefficient since the forward exchange rate did not fully reflect all available information. Judge and Reancharoen (2014) explored lead-lag between the spot and the futures market in Thailand and concluded that spot market lead the futures market. They then constructed a trading strategy by error correction model and the lead-lag relationship and found that it outperformed the benchmark buy and hold return strategy. Srivastava and Singh (2015) investigated the available literature on the pricing of currency futures to understand the empirical analysis employed by various researchers. They also employed VECM method and found the markets to be inefficient in developing countries like India.

Downloaded by Delhi Technological University At 01:39 31 August 2017 (PT)

Sehgal *et al.* (2015) investigated the price discovery and volatility spill overs between futures and spot prices of four major international currencies traded on two trading platforms in India. Their results confirmed stronger volatility spill overs from futures to spot in short-run while the inverse was found in the long run.

Here too the studies showed futures as the leading market for some economies and spot as the leading market for some economies. This implies that the lead-lag relationship in the market is determined by the features of that market i.e. the policies of the regulatory authority, the number of participants in the market, the speed of information travel, the transactional cost involved and the transparency of operations.

The emerging markets are comparatively more volatile than the developed markets (Upper and Valli, 2016). This hints toward a more developed hedging market in the emerging economies. But it does not appear to be like this. The ratio of FX derivatives turnover to foreign trade in emerging market is lower in comparison to advanced economies (BIS, 2016). Additionally, the financial markets in the emerging economies have less complex products and narrower set of instruments. The OTC market is more active in the emerging economies than the exchange traded market. The BIS in its report in 2016 reasoned that it is still difficult and costly for the investors in emerging markets to hedge their exposures compared to their peers in advanced economies.

Despite all these reasons, FX market in emerging economies is attracting investors toward themselves. As per the 2016 Triennial Surveys report of BIS, several emerging market currencies showed a remarkable rise in global importance. Mexican peso became the world's eleventh most actively traded currency. Asian market currencies like the Korean won, Indian rupee and Thai baht advanced in the ranking by two or three places (see Table I). The main reason for this growth is the rise in global competitiveness of these countries, rising foreign currency debt in the corporates balance sheet and increase in foreign investors in emerging markets. Thus, these emerging markets have become extremely exposed to global financial flows (Domanski *et al.*, 2016).

2.3 Futures market in India

Futures contract were first introduced in the stock market in India in the year 2000. Since then there is a growing body of literature which analysis the pricing and the lead-lag relationship between the market components in the Indian stock market. Mukherjee and

Currency distribution of OTC foreign exchange turnover
Percentage shares of average daily turnover in April 2016

	2013		2016	
Currency	Share	Rank	Share	Rank
USD	87.0	1	87.6	1
EUR	33.4	2	31.4	2
JPY	23.0	3	21.6	3
GBP	11.8	4	12.8	4
AUD	8.6	5	6.9	5
CAD	4.6	7	5.1	6
CNY	2.2	9	4.0	8
MXN	2.5	8	1.9	11
KRW	1.2	17	1.7	15
RUB	1.6	12	1.1	17
INR	1.0	20	1.1	18
BRL	1.1	19	1.1	19
TBH	0.3	27	0.4	24

Source: BIS Triennial Central Bank Survey 2016

Table I. World currency ranking

Downloaded by Delhi Technological University At 01:39 31 August 2017 (PT)

Mishra (2004) investigated the lead-lag relationship between the Indian NIFTY futures and spot index and found that the spot lead the futures market. Debasish and Mishra (2008) employed Bivariate GARCH model to examine price discovery and the lead-lag relationship between futures and spot markets for stock index futures contracts of NSE and BSE. They concluded that futures market played a more dominant role in price discovery. Debasish (2009) used GARCH to study volatility in the Indian spot market after the introduction of Nifty index futures and found no structural change in the market. Spot returns volatility was not significant in explaining the returns. Mallikarjunappa and Afsal (2010) determined the lead-lag relationship between spot and futures stock market in India by applying the cointegration test, building VECM and EGARCH model. They found a two-way lead-lag relationship between the two markets where price discovery took place simultaneously. Choudhary and Bajaj (2012) applied the Johansen's cointegration, Engle and Granger's model, Granger causality test and Vector Error Correction Model (VECM) to investigate the role of spot and futures markets in the absorption of new information. They also explored price discovery and found two-way information flow between the two markets.

With the introduction of futures contracts in FX market, in late 2008, many studies were conducted to gain a better understanding of the functioning of the FX market. Most of these studies focused on studying the entire currency derivatives market or the features and growth of the futures market, movements and volatility of different currencies exchange rate and on corporates hedging FX risk. Anand and Kaushik (2008) examined the motivation behind the use of currency derivatives for corporate forex risk management and identified seven motivating factors for the use of derivatives. Guru (2009) discussed the global trends in the forex market and the developments in Indian market focusing on the emergence of currency futures. Goyal and Arora (2010) studied the impact of central bank intervention and communication on the volatility of exchange rate in India through GARCH analysis. Behera (2011) used multivariate GARCH model to examine the linkage between the offshore and onshore market for the Indian rupee. Sivarajadhanavel and Chandrakumaramangalam (2012) discussed the exchange rate risk management and its impact on company's profitability the Indian IT industry. Goyal (2016) described the features of forex markets and emphasized on the process of liberalization, drawing the implication for central bank intervention. She focused on the global integration and deepening of Indian forex markets. Very few studies explored the price discovery and lead-lag relationship in FX market like Sriram and Senthil (2013) and Srivastava and Singh (2015) (already discussed above). This study enhances the existing literature by studying this less explored area. Therefore, the objective of this study is to analyze the lead-lag relationship between the currency futures and spot market and understand the relationship between the two.

3. Objectives of the study

To understand the lead-lag relationship between the futures and spot currency market in India, the following objectives are formulated for the study:

(1) to analyze the relationship of the currency futures and spot market for the four currencies – USD, GBP, EURO, and JPY; and

(2) to determine the lead-lag relationship between the futures and spot market for the four currencies – USD, GBP, EURO, and JPY.

4. Research methodology

4.1 Data

The currency futures started trading on NSE in August 2008. Initially, futures were traded only in USD. Later on, in 2010 three other currencies (GBP, EURO, and JPY) were also

Downloaded by Delhi Technological University At 01:39 31 August 2017 (PT)

permitted for trade. For the present study, data are collected for all these four currencies from February 2010 till June 2016. The spot data are also collected for the same period. The futures data are available on NSE website, and the spot data are available on RBI website. All the data are converted into its log form for analysis.

4.2 Methodology

In practice, most economic time series is non-stationary (Gujarati *et al.*, 2011). Therefore, it is necessary to check the series for stationarity. The present study applies Augmented Dickey-Fuller (ADF) test, Phillips-Perron (PP) test and Kwiatkowski-Phillips-Schmidt-Shin (KPSS) test to check for stationarity. Then to explore the relationship between futures and spot, cointegration tests are applied. The present study applies the Engle and Granger's residual based approach and Johansen's cointegration to determine the long run equilibrium between the two markets. VECM is further applied to determine the leading market.

Engle and Granger's residual based approach was developed in 1987. This technique checks for the presence of cointegration between two variables. It is the basic and most used technique to establish if two variables are related in the long run. If the futures and spot market appear to be cointegrated then this would mean that futures and spot influence each other prices and one market leads another to achieve long run equilibrium. Johansen cointegration method is more complex than Engle and Granger's method. This method uses two maximum likelihood ratios – the trace test and maximum eigenvalue test to find out the cointegration. This method is useful to know if there is more than one cointegrating relationship between the variables. Additionally, if the cointegration between the variables is established then the VECM method is used to identify the leading market. These techniques are used by various researchers like Asche and Guttormsen (2002), Kenourgios (2004), Frino *et al.* (2006), Ünlü and Ersoy (2012), de Boyrie *et al.* (2012), Sriram and Senthil (2013), Ilter and Alguner (2013).

4.2.1 Unit root and stationary tests. The ADF and PP tests are unit root test. Both these test check for the presence of unit root in the time series data and have the presence of unit root under the null hypothesis. The stationary test has stationary under the null hypothesis (Brooks, 2014). KPSS test is such stationary test. The results of both unit root test and the stationary test can be compared to see if the same conclusion is obtained. Applying these tests together make the results more robust. Such joint use of both the test is known as confirmatory data analysis. This study thus applies both the unit root test and stationary test.

4.2.2 Cointegration test. The variables would be cointegrated if the linear combination of I(1) variables will be I(0) (Brooks, 2014). To put simply, if the two-individual series are integrated of order one i.e. I(1) and their linear combination is integrated of order zero i.e. I(0) then both the series are said to be cointegrated. Cointegration establishes a long run relationship between the variables since these variables may deviate in the short run, but their association will be established in the long run (Brooks, 2014). The present study employs Engle and Granger's two step model (residual based approach) and Johansen's cointegration method.

Under Engle and Granger's two step model, the OLS regression equation for the variables is formulated to estimate the coefficient of relationship between the variables and then unit root test is applied on the residuals of the equation. Johansen's Cointegration Method uses two maximum likelihood ratios instead of OLS method to test for cointegration. The trace test examines the number of linear combinations and brings to the conclusion of at least one cointegrating relationship and maximum eigenvalue test examines the possibility of 'm' possible cointegrating relationships. This test can also be used for more than two variables.

Downloaded by Delhi Technological University At 01:39 31 August 2017 (PT)

Once the cointegrating relationship between two variables in identified, it implies that there is a long run equilibrium relationship between the variables. Therefore, an error correction model must be constructed to determine the pull and push which drive the variables toward equilibrium (Choudhary and Bajaj, 2012).

4.2.3 VECM. VECM is an error correction mechanism applied to know the lead-lad relationship of the two cointegrating series. VECM is estimated by using following OLS equations:

$$\Delta S_t = \propto_{s,\,0} + \sum_{i=1}^{p-1} \propto_{s,\,i} \Delta S_{t-i} + \sum_{i=1}^{p-1} \beta_{s,\,i} \Delta F_{t-i} + \alpha_s Z_{t-1} + \varepsilon_{s,\,t} \quad (1)$$

$$\Delta F_t = \propto_{F,0} + \sum_{i=1}^{p-1} \propto_{F,\,i} \Delta S_{t-i} + \sum_{i=1}^{p-1} \beta_{F,\,i} \Delta F_{t-i} + \alpha_F Z_{t-1} + \varepsilon_{F,\,t} \quad (2)$$

F_t is futures price series and S_t is spot price series, $\propto_{s,\,0}$ and $\propto_{F,\,0}$ are intercept terms, $\propto_{s,\,i}$, $\propto_{F,\,i}$, $\beta_{s,\,i}$ and $\beta_{F,\,i}$ are the short-run coefficients. Z_{t-1} is the error correction term. The number of lags is identified by using the Akaike Information Criterion (AIC) for the model. Decision is made by looking at α_S and α_F values. If these are significant, it means there is bi-directional relation between the two markets, lead or lag market is also identified by looking at these values. *T*-test and *F*-test are used to know the significance of the coefficient of error correction and coefficient of lagged values, respectively (Choudhary and Bajaj, 2012).

4.2.4 Lag selection. Selection of lag is an important step for carrying out VECM. This paper uses AIC for optimal lag selection. Lower the AIC value, the better the model, and thus, the lag which provides the lowest AIC value is chosen for the currency. This is shown in Table II. The number of lags chosen for USD is 4, GBP is 6, EURO is 4, and JPY is 1.

5. Empirical results and analysis

The descriptive statistics of the data are presented in Table III. Standard deviation is highest for USD for both futures and spot market whereas it is lowest for JPY for both futures and spot market. This means that INR witnesses most variation in its price against USD and least variation in its price against JPY. The 2016 BIS survey on FX declared USD to be the dominant currency since it was on one side of 88 percent of all trades. Indian corporates and market are also more exposed to USD movements. INR is witnessing more variation against USD over the past few years because of various reasons. Initially, Euro Zone crisis strengthen the USD against various emerging market economies including India, then tightening of interest rates by the US Fed in 2015 led to the reallocation of FII's

Lags	EURO	GBP	JPY	USD
1	−15.76501	−15.83127	*−14.89622*	−16.57657
2	−15.76718	−15.83163	−14.89518	−16.58434
3	−15.76331	−15.8300	−14.88958	−16.58627
4	*−15.77100*	−15.8400	−14.89327	*−16.59733*
5	−15.7678	−15.83681	−14.89036	−16.59454
6	−15.7666	*−15.84132*	−14.88528	−16.59081
7	−15.7639	−15.83693	−14.88044	−16.58785
8	−15.7618	−15.83539	−14.8850	−16.5970

Notes: The Italics values are the lowest AIC values for each currency and corresponds to the number of lags taken for that currency. The number of lags chosen for USD is 4, GBP is 6, EURO is 4 and JPY is 1

Table II. Lag selection criteria – AIC value

Downloaded by Delhi Technological University At 01:39 31 August 2017 (PT)

Downloaded by Delhi Technological University At 01:39 31 August 2017 (PT)

Table III.
Descriptive statistics

Particulars	L_USDS	L_USDF	L_GBPS	L_GBPF	L_EURS	L_EURF	L_JPYS	L_JPYF
Mean	4.015308	4.017732	4.463956	4.466167	4.25834	4.260521	4.062646	4.06506
Median	4.021122	4.022334	4.479619	4.482296	4.257231	4.258463	4.054217	4.056989
Maximum	4.228887	4.229167	4.663704	4.67063	4.515991	4.514972	4.278331	4.275554
Minimum	3.783018	3.782256	4.184293	4.187152	4.026601	4.029539	3.848657	3.853334
SD	0.141599	0.141706	0.137882	0.137999	0.107463	0.107466	0.095314	0.095128
Skewness	−0.284981	−0.28596	−0.371469	−0.372186	0.023479	0.023983	0.333585	0.32581
Kurtosis	1.643511	1.644282	1.667026	1.670078	2.212284	2.219587	2.327971	2.316779
Jarque-Bera	125.2046	125.2128	134.6809	134.3342	36.01292	35.3561	51.86145	51.55255
Probability	0.0000	0.0000	0.0000	0.0000	0.0000	0.0000	0.0000	0.0000
Sum	5573.248	5576.611	6195.971	6199.039	5910.576	5913.603	5638.953	5642.304
Sum Sq. Dev.	27.80976	27.85182	26.36906	26.41359	16.01752	16.01831	12.60056	12.5515
Observations	1,388	1,388	1,388	1,388	1,388	1,388	1,388	1,388

Notes: L_USDS – Log of USD spot, L_USDF – Log of USD future; L_GBPS – Log of GBP spot, L_GBPF – Log of GBP future; L_EURS – Log of EURO spot, L_EURF – Log of EURO future; L_JPYS – Log of JPY spot, L_JPYF – Log of JPY future

portfolio away from emerging markets like India. This brought a lot of volatility in the Indian market with INR fluctuating against USD. Japan, on the other hand, has been struggling with stagnation and low inflation. Additionally, it is not a dominant currency in the list of India's trading partners. Therefore, INR witnessed the least variation in its price against JPY. In the case of skewness, the futures and spot market is negatively skewed for USD and GBP, and it is positively skewed for Euro and JPY. Since the value of kurtosis is less than three for all the four currencies in both futures and spot market, this means that the tails of the curve for all the currencies in both the markets are shorter and thinner. The skewness and kurtosis of the log series of the currencies in the futures and spot market violate the assumption of normal distribution.

5.1 Unit root test results

The result of ADF unit root test and PP unit root test show that the series contain unit root at level, but the series does not contain any unit root at first difference (results available by request). Thus, the hypothesis that the series contains unit root is rejected at first difference. This further shows that both the futures and spot series are integrated of order one, i.e. I(1). Under KPSS stationary test, the null hypothesis states that the series is stationary against the alternative that the series is non-stationary. The result (available by request) verified that the series becomes stationary at first difference. Thus, the hypothesis that the series is stationary is not rejected at first difference.

The results of both unit root test and stationary test, i.e. confirmatory data analysis show that the futures and spot series for all the four currencies, i.e. USD, GBP, EURO and JPY become stationary at first difference. Thus, all these series are integrated of order one, i.e. I(1).

5.2 Engle-Granger two step model

In this two steps procedure first OLS equation for futures and spot is estimated, then ADF test is applied on the residuals of this equation to check if the residuals are stationary. This study has run the following regression equation involving two variables – futures and spot, which are integrated of order one (as shown by the unit root test above). Linear combination of the futures and the spot is indicated by the following equation:

$$S_t = \alpha_o + \alpha_1 F_t + \varepsilon_t \tag{3}$$

ε_t is the residuals or the error term.

The result for the four currencies displayed in Table IV, indicates that the residuals of the OLS equation formed are stationary. This means that these two variables i.e. futures and spot for all the four currencies are cointegrated.

Currencies	OLS equation	ADF test on residuals (level) *t*-value	*p*-value
USD	$L_USDS = 0.001689 + 0.998976 \times L_USDF$	−33.14149	0.0000
GBP	$L_GBPS = 0.003245 + 0.998779 \times L_GBPF$	−33.18814	0.0000
EURO	$L_EURS = 0.000485 + 0.999374 \times L_EURF$	−31.98499	0.0000
JPY	$L_JPYS = -0.006091 + 1.000905 \times L_EURF$	−36.44622	0.0000

Notes: L_USDS – Log of USD spot, L_USDF – Log of USD future; L_GBPS – Log of GBP spot, L_GBPF – Log of GBP future; L_EURS – Log of EURO spot, L_EURF – Log of EURO future; L_JPYS – Log of JPY spot, L_JPYF – Log of JPY future

Table IV. Engle-Granger cointegration result

Downloaded by Delhi Technological University At 01:39 31 August 2017 (PT)

5.3 Johansen cointegration test

The result for this test is displayed in Table V. The two ratios which confirm the results are trace test and maximum eigenvalue test. The null hypothesis of this test at the vector "0" is that there is no cointegration between the series. For trace and maximum eigenvalue test and their corresponding *p*-value for all the currencies, we have rejected the null hypothesis as this value is less than 0.05 for all the currencies. This means that there is cointegration between the two series, i.e. futures and spot for all the currencies. The null hypothesis at "at most 1" is that there is at most one cointegrating relationship. Again, for trace and maximum eigenvalue test and their corresponding *p*-value, we cannot reject the null hypothesis of at most one cointegrating relationship as this value is greater than 0.05.

Both the ratios i.e. trace and maximum eigenvalue statistics show that there is an association between these two variables in the long run and there exists one cointegrating equation between the variables. Thus, both variables move together in the long run.

The above results confirm the long run equilibrium relationship between the futures and spot market for all these four currencies. This result is consistent with the Asche and Guttormsen (2002), Kühl (2007), Ünlü and Ersoy (2012), Sriram and Senthil (2013), Srivastava and Singh (2015) and Sehgal *et al.* (2015).

5.4 VECM

Once the cointegration between two variables is identified an error correction model is constructed to identify the pull and push force and determine the leading market. VECM is the adjustment procedure between futures and spot to attain the long run equilibrium. The lead-lag relationship is understood and the market making less adjustment to reach the long run equilibrium is identified as the leading market. The results of VECM are displayed in Tables VI-IX.

Notice the error correction coefficient ($E_{t\text{-}1}$) for all the markets. This coefficient is smaller for futures market in comparison to the spot market for USD, GBP, EURO, and JPY. This means that the futures make less adjustment to reach the equilibrium in comparison to spot. As a leader never compromise, this implies that the futures market leads the spot market for four the currencies under study. Further, the coefficients for the lagged values of the independent variable are significant in both futures and spot for these currencies, this indicates a feedback relationship between the futures and spot in FX market. Thus, the new information flows both ways from futures to spot and from spot to futures in the FX market in India but spot makes more adjustments for reaching the long run equilibrium.

The futures market leads the spot market because it is easy to transact in the futures market because of lower transaction cost. Additionally, it is easy to execute a futures contract and with low cash because it is a levered instrument compared to the actual spot market which requires more investment and longer implementation time. Participants also prefer futures because it offers transparency and anonymity to them. As a result, the futures

Table V. Johansen cointegration result

Currencies	Vector	Test statistics		Critical value 5%		Probability value	
		λ_{Trace}	λ_{Max}	λ_{Trace}	λ_{Max}	λ_{Trace}	λ_{Max}
USD	0	277.5991	277.2900	15.49471	14.26460	0.0001	0.0001
	1	0.309172	0.309172	3.841466	3.841466	0.5782	0.5782
GBP	0	300.5955	298.7870	15.49471	14.26460	0.0001	0.0001
	1	1.808438	1.808438	3.841466	3.841466	0.1787	0.1787
EURO	0	287.8238	285.8372	15.49471	14.26460	0.0001	0.0001
	1	1.986505	1.986505	3.841466	3.841466	0.1587	0.1587
JPY	0	260.3162	257.5447	15.49471	14.26460	0.0001	0.0001
	1	2.771470	2.771470	3.841466	3.841466	0.0960	0.0960

Downloaded by Delhi Technological University At 01:39 31 August 2017 (PT)

Currency	USD	
Variables	ΔS_t	ΔF_t
C	0.000212** [1.73923]	0.000236** [1.66792]
E_{t-1}	−0.651901* [−8.37863]	0.251995* [2.79463]
Δ $USDS_{t-1}$	−0.307814* [−4.28772]	−0.382295* [−4.59491]
Δ $USDS_{t-2}$	−0.057634 [−0.88423]	−0.220859* [−2.92375]
Δ $USDS_{t-3}$	0.145473* [2.59502]	0.013748 [0.21161]
Δ $USDS_{t-4}$	0.118599* [3.13602]	0.020693 [0.47214]
Δ $USDF_{t-1}$	0.370318* [5.10361]	0.361810* [4.30252]
Δ $USDF_{t-2}$	0.135377** [2.02998]	0.275351* [3.56267]
Δ $USDF_{t-3}$	−0.049722 [−0.83352]	0.081311 [1.17613]
Δ $USDF_{t-4}$	−0.134594* [−2.88564]	−0.02487 [−0.46009]
F-statistics	84.10196	4.466498

Notes: Standard errors in ( ) and t-statistics in [ ]. *Testifies that values are significant at 1 percent level (critical value: 2.58); **testifies that values are significant at 5 percent level (critical value: 1.96)

Table VI.
VECM result for USD

Currency	GBP	
Variables	ΔS_t	ΔF_t
C	0.000131 [0.86323]	0.000148 [0.84541]
E_{t-1}	−0.950348* [−9.12887]	-0.025394 [−0.21193]
Δ $GBPS_{t-1}$	0.084971 [0.89107]	0.028998 [0.26420]
Δ $GBPS_{t-2}$	0.212992** [2.47707]	0.085696 [0.86589]
Δ $GBPS_{t-3}$	0.367484* [4.67977]	0.245224** [2.71319]
Δ $GBPS_{t-4}$	0.286972* [4.04111]	0.210968** [2.58113]
Δ $GBPS_{t-5}$	0.207517* [3.43935]	0.236826* [3.41022]
Δ $GBPS_{t-6}$	0.136977* [3.33940]	0.133759]* [2.83319
Δ $GBPF_{t-1}$	0.026421 [0.27058]	0.050407 [0.44851]
Δ $GBPF_{t-2}$	−0.163228*** [−1.85242]	−0.068749 [−0.67786]
Δ $GBPF_{t-3}$	−0.305883* [−3.81303]	−0.179742*** [−1.94669]
Δ $GBPF_{t-4}$	−0.321126* [−4.40755]	−0.220281** [−2.62682]
Δ $GBPF_{t-5}$	−0.223966* [−3.47612]	−0.266376* [−3.59202]
Δ $GBPF_{t-6}$	−0.154218* [−3.08189]	−0.179484** [−3.11629]
F-statistics	46.60062	2.944147

Notes: Standard errors in ( ) and t-statistics in [ ]. *Testifies that values are significant at 1 percent level (critical value: 2.58); **testifies that values are significant at 5 percent level (critical value: 1.96); ***testifies that values are significant at 10 percent level (critical value: 1.65)

Table VII.
VECM result for GBP

market is more liquid and offers speedy price discovery. These reasons also explain why many studies observed a lead-lag relation from futures to spot like Crain and Lee (1995), Chatrath and Song (1998), Asche and Guttormsen (2002), Nieto *et al.* (1998), Min and Najand (1999), de Boyrie *et al.* (2012), Ilter and Alguner (2013) and Garcia *et al.* (2014).

6. Conclusion

Over the years, India has gained importance globally with increasing inflows and outflows of various currencies. Also upsurge in market participants like mutual funds, insurance companies, and multinational corporations, etc., increasing number of hedgers, speculators and arbitragers and thriving derivative products have added to the development and complexity of Indian FX market. With complexity comes a need to understand the market. Understanding the lead-lag relationship and eventual price discovery in the market is one of the ways to understand the nuances of the market. The relationship of the currency futures and spot

Downloaded by Delhi Technological University At 01:39 31 August 2017 (PT)

Currency	EUR	
Variables	ΔS_t	ΔF_t
C	0.0000919** [0.56689]	0.000102** [0.56858]
E_{t-1}	−0.814866* [−9.06470]	0.066296 [0.66503]*
Δ $EURS_{t-1}$	−0.138365* [−1.69178]	−0.222256* [−2.45049]
Δ $EURS_{t-2}$	0.055667 [0.75961]	−0.070449* [−0.86686]
Δ $EURS_{t-3}$	0.128848* [2.05128]	0.015154 [0.21755]
Δ $EURS_{t-4}$	0.155764* [3.52166]	0.071892 [1.46569]
Δ $EURF_{t-1}$	0.255691* [3.05315]	0.257937* [2.77734]
Δ $EURF_{t-2}$	0.032639* [0.43016]	0.151289* [1.79796]
Δ $EURF_{t-3}$	−0.119538 [−1.78210]	−0.015011 [−0.20180]
Δ $EURF_{t-4}$	−0.146789]* [−2.78195	−0.072946 [−1.24664]
F-statistics	64.65989	3.287942

Table VIII.
VECM result for EURO

Notes: Standard errors in ( ) and t-statistics in [ ]. *Testifies that values are significant at 1 percent level (critical value: 2.58); **testifies that values are significant at 5 percent level (critical value: 1.96)

Currency	JPY	
Variables	ΔS_t	ΔF_t
C	0.000184 [0.87247]	0.00019 [0.81347]
E_{t-1}	−0.682496* [−9.62283]	0.228556* [2.90070]
Δ $JPYS_{t-1}$	−0.197447* [−4.08397]	−0.168* [−3.12787]
Δ $JPYF_{t-1}$	0.251529* [4.62478]	0.176458* [2.92046]
F-statistics	128.8086	3.68986

Table IX.
VECM result for JPY

Notes: Standard errors in ( ) and t-statistics in [ ]. *Testifies that values are significant at 1 percent level (critical value: 2.58)

market for the four currencies – USD, GBP, EURO and JPY is analyzed through Engel-Granger and Johansen Cointegration test. These results confirm the long run equilibrium relationship between the futures and spot market for these currencies. This long run relationship reveals working of an error correction mechanism which helps the market in reaching the equilibrium in the long run. The results of the present study reveal that the spot market follows the futures market to attain this equilibrium. The price, therefore, is first reflected in the futures and then participants like arbitragers and speculators by their actions to take advantage of this mis-match, move the spot market price toward equilibrium too. Thus, the futures market leads the spot market to attain the long run equilibrium and this further means that the futures market is playing a major role in price discovery and is more efficient in disseminating new information. This further implies that the Indian forex market is informationally inefficient.

Regulators like SEBI and RBI can use this information to formulate improved policies for the further growth of the markets. The results show that futures market leads price discovery which further implies that participants are more attracted toward futures market. Since the investors are only attracted toward a fair, efficient, and manipulation free market and higher number of market participants mean a rational and democratic price discovery, it becomes imperative for the regulators to ensure better surveillance and scrutiny of the markets. This is required to ensure better market integrity and maintaining efficient markets. These results would also help the traders, treasures and analysts to formulate improved trading and hedging strategies by developing improved price forecasting models. Arbitragers can take advantage of the short-term disequilibrium in the market and by identifying the leading market they can take the benefit of the price difference between two markets. Speculators too can take a better position in the market by understanding price discovery process.

Downloaded by Delhi Technological University At 01:39 31 August 2017 (PT)

A possible extension of this study could be to investigate further if the leading role of futures in India could be associated with the volatility in the market. Additionally, corporate hedging of FX risk has gained importance in recent years and RBI has been sensitizing the corporate and the banking system about the need for hedging. Futures being an efficient price discovery tool, it may be the best option for the hedgers to hedge the forex risk. A further scope of the research would be to investigate hedging efficiency of futures.

References

Anand, M. and Kaushik, K.P. (2008), "Management motivations for use of foreign currency derivatives in India", *IIMB Management Review*, Vol. 20 No. 3, pp. 324-339.

Andersen, T.G., Bollerslev, T., Diebold, F.X. and Vega, C. (2007), "Real-time price discovery in global stock, bond and foreign exchange markets", *Journal of International Economics*, Vol. 73 No. 2, pp. 251-277.

Aron, J. and Ayogu, M. (1997), "Foreign exchange market efficiency tests in Sub-Saharan Africa", *Journal of African Economies*, Vol. 6 No. 3, pp. 150-192.

Asche, F. and Guttormsen, A.G. (2002), "Lead lag relationships between futures and spot prices", Working Paper No. 2/02, The Research Council of Norway, Bergen, January.

Bashir, R., Shakir, R., Ashfaq, B. and Hassan, A. (2014), "The efficiency of foreign exchange markets in Pakistan: an empirical analysis", *The Lahore Journal of Economics*, Vol. 19 No. 1, pp. 133-149.

Behera, H.K. (2011), "Onshore and offshore market for Indian rupee: recent evidence on volatility and shock spillover", *Macroeconomics and Finance in Emerging Market Economies*, Vol. 4 No. 1, pp. 43-55.

BIS (2016), "Triennial central bank survey foreign exchange turnover in April 2016", available at: www.bis.org/publ/rpfx16fx.pdf (accessed May 5, 2017).

Brooks, C. (2014), *Introductory Econometrics for Finance*, 3rd ed., Cambridge University Press, Cambridge, MA.

Cabrera, J., Wang, T. and Yang, J. (2008), "Do futures lead price discovery in electronic foreign exchange markets?", *Journal of Futures Markets*, Vol. 29 No. 2, pp. 137-156.

Chatrath, A. and Song, F. (1998), "Information and volatility in futures and spot markets: The case of the Japanese yen", *Journal of Futures Markets*, Vol. 18 No. 2, pp. 201-223.

Chen, Y.L. and Gau, Y.F. (2010), "News announcements and price discovery in foreign exchange spot and futures markets", *Journal of Banking & Finance*, Vol. 34 No. 7, pp. 1628-1636.

Choudhary, K. and Bajaj, S. (2012), "Intraday lead/lag relationships between the futures and spot market", *Eurasian Journal of Business and Economics*, Vol. 5 No. 9, pp. 165-186.

Crain, S.J. and Lee, J.H. (1995), "Intraday volatility in interest rate and foreign exchange spot and futures markets", *Journal of Futures Markets*, Vol. 15 No. 4, pp. 395-421.

Debasish, S.S. (2009), "Effect of futures trading on spot-price volatility: evidence for NSE Nifty using GARCH", *The Journal of Risk Finance*, Vol. 10 No. 1, pp. 67-77.

de Boyrie, M.E., Pavlova, I. and Parhizgari, A.M. (2012), "Price discovery in currency markets: evidence from three emerging markets", *International Journal of Economics and Finance*, Vol. 4 No. 12, pp. 12-61.

Debasish, S.S. and Mishra, B. (2008), "An econometric study of lead-lag relationship between futures and spot markets in India", *Paradigm*, Vol. 12 No. 2, pp. 87-92.

Domanski, D., Kohlscheen, E. and Moreno, R. (2016), "Foreign exchange market intervention in EMEs: what has changed?", BIS quarterly review, September, available at: www.bis.org/publ/qtrpdf/r_qt1609f.pdf (accessed May 5, 2017).

Frino, A., Jarnecic, E., Tan, A.S. and Stevenson, M. (2006), "Sources of price discovery in the Australian dollar currency market", available at: http://ro.uow.edu.au/cgi/viewcontent.cgi?article=1926&context=commpapers (accessed April 29, 2017).

Garcia, M., Medeiros, M. and Santos, F. (2014), "Price discovery in Brazilian FX markets", Working Paper No. 622, PUC-Rio, available at: www.economia.puc-rio.br/mgarcia/140603%20Price%20discovery%20FX%20market%20v07.pdf (accessed April 29, 2017).

Downloaded by Delhi Technological University At 01:39 31 August 2017 (PT)

Gonzalo, J. and Granger, C. (1995), "Estimation of common long-memory components in cointegrated systems", *Journal of Business and Economic Statistics*, Vol. 13 No. 1, pp. 27-35.

Goyal, A. (2016), "Foreign exchange markets, intervention, and exchange rate regimes", in Roy, M. and Roy, S.S. (Eds), *International Trade and International Finance*, Springer, New Delhi, pp. 469-492.

Goyal, A. and Arora, S. (2010), "The Indian exchange rate and Central Bank action: a GARCH analysis", Working Paper No. 2010-009, Indira Gandhi Institute of Development Research, Mumbai, available at: www.igidr.ac.in/pdf/publication/WP-2010-009.pdf (accessed May 4, 2017).

Gujarati, D., Porter, D. and Gunasekar, S. (2011), *Basic Econometrics*, 5th ed., McGraw Hill Education, New Delhi.

Guru, A. (2009), "Forex derivative markets in India: developments thus far and road ahead", available at: https://papers.ssrn.com/sol3/papers.cfm?abstract_id=1420615 (accessed June 2, 2016).

Hasbrouck, J. (1995), "One security, many markets: determining the contributions to price discovery", *Journal of Finance*, Vol. 50 No. 4, pp. 1175-1199.

Ibrahim, J., Salleh, S.I.M. and Abdullah, N. (2011), "A trace and maximal eigen value analysis of spot-forward forex rates in OECD countries", *International Journal of Business and Social Science*, Vol. 2 No. 2, pp. 200-204.

Ilter, H.K. and Alguner, A. (2013), "Lead lag relationship and price discovery in Turkish stock exchange and futures markets", *African Journal of Business Management*, Vol. 7 No. 41, pp. 4254-4262.

Judge, A. and Reancharoen, T. (2014), "An empirical examination of the lead-lag relationship between spot and futures markets: Evidence from Thailand", *Pacific-Basin Finance Journal*, Vol. 29, pp. 335-358.

Kenourgios, D. (2004), "Price discovery in the Athens derivatives exchange: evidence for the FTSE/ASE-20 futures market", available at: www.researchgate.net/publication/23744105_Price_discovery_in_the_Athens_derivatives_exchange_Evidence_for_the_FTSEASE-20_futures_market (accessed April 29, 2017).

Kurihara, Y. (2011), "Is the Tokyo foreign exchange market efficient from two perspectives of forward bias and anomaly?", *Modern Economy*, Vol. 2 No. 4, pp. 597-601.

Kühl, M. (2007), "Cointegration in the foreign exchange market and market efficiency since the introduction of the Euro: Evidence based on bivariate cointegration analyses", available at: http://wwwuser.gwdg.de/~cege/Diskussionspapiere/68.pdf (accessed July 1, 2016).

Lee, Y.H. and Sodoikhuu, K. (2012), "Efficiency tests in foreign exchange market", *International Journal of Economics and Financial Issues*, Vol. 2 No. 2, pp. 216-224.

Mallikarjunappa, T. and Afsal, E.M. (2010), "Price discovery process and volatility spillover in spot and futures markets: evidences of individual stocks", *Vikalpa*, Vol. 35 No. 2, pp. 49-62.

Min, J.H. and Najand, M. (1999), "A further investigation of the lead-lag relationship between the spot market and stock index futures: early evidence from Korea", *Journal of Futures Markets*, Vol. 19 No. 2, pp. 217-232.

Mukherjee, K. and Mishra, R.K. (2004), "Lead-lag relationship between equities and stock index futures market and it's variation around information release: empirical evidence from India", available at: www.nseindia.com/content/research/comppaper155.pdf (accessed May 8, 2016).

Nieto, M.L., Fernández, Á. and Muñoz, M.J. (1998), "Market efficiency in the Spanish derivatives markets: an empirical analysis", *International Advances in Economic Research*, Vol. 4 No. 4, pp. 349-355.

Phengpis, C. (2006), "Market efficiency and cointegration of spot exchange rates during periods of economic turmoil: another look at European and Asian currency crises", *Journal of Economics and Business*, Vol. 58 No. 4, pp. 323-342.

RBI (2007), "Report on currency and finance", available at: https://rbidocs.rbi.org.in/rdocs/publicationreport/pdfs/77577.pdf (accessed June 15, 2015).

RBI (2014), "Inaugural address by Shri Harun R. Khan, Deputy Governor, Reserve Bank of India at the 25th Annual Forex Assembly", available at: https://rbidocs.rbi.org.in/rdocs/Speeches/PDFs/IFEM061014FL.pdf (accessed August 22, 2016).

Downloaded by Delhi Technological University At 01:39 31 August 2017 (PT)

RBI (2015), "Keynote address by Shri G. Mahalingam, Executive Director, Reserve Bank of India at the India Treasury Summit", available at: https://rbidocs.rbi.org.in/rdocs/Speeches/PDFs/ITSP27022015F.pdf (accessed April 7, 2017).

Rosenberg, J.V. and Traub, L.G. (2008), "Price discovery in the foreign currency futures and spot market", FRB of New York Staff Report No. 262, available at: www.newyorkfed.org/medialibrary/media/research/staff_reports/sr262.pdf (accessed on September 5, 2016).

Sehgal, S., Ahmad, W. and Deisting, F. (2015), "An investigation of price discovery and volatility spill overs in India's foreign exchange market", *Journal of Economic Studies*, Vol. 42 No. 2, pp. 261-284.

Sivarajadhanavel, P. and Chandrakumaramangalam, S. (2012), "Exchange rate risk in the foreign exchange market: a challenge on corporate profitability", *Bonfring International Journal of Industrial Engineering and Management Science*, Vol. 2 No. 3, pp. 8-11.

Sriram, M. and Senthil, M. (2013), "Market efficiency and volatility spill over in spot & futures currency market (wrt $ and Rupee)", *International Journal of Management Excellence*, Vol. 1 No. 3, pp. 45-53.

Srivastava, A. and Singh, M. (2015), "A study on pricing of currency futures in Indian currency market", *International Journal of Research in Finance and Marketing*, Vol. 5 No. 6, pp. 1-11.

Tornell, A. and Yuan, C. (2012), "Speculation and hedging in the currency futures markets: are they informative to the spot exchange rates", *Journal of Futures Markets*, Vol. 32 No. 2, pp. 122-151.

Tse, Y., Xiang, J. and Fung, J.K. (2006), "Price discovery in the foreign exchange futures market", *Journal of Futures Markets*, Vol. 26 No. 11, pp. 1131-1143.

Ünlü, U. and Ersoy, E. (2012), "The causal relationship between foreign currency futures and spot markets: evidence from Turkey", *Investment Management and Financial Innovations*, Vol. 9 No. 2, pp. 208-212.

Upper, C. and Valli, M. (2016), "Emerging derivatives markets?", BIS Quarterly Review, available at: www.bis.org/publ/qtrpdf/r_qt1612g.pdf (accessed April 29, 2017).

Wickremasinghe, G. (2004), "Efficiency of foreign exchange markets: a developing country perspective", available at: www.buseco.monash.edu.au/units/dru/papers/working-papers-04/0304-foreign-exchange-markets.pdf (accessed June 24, 2015).

Further reading

Adelegan, O.J. (2009), "The derivatives market in South Africa: lessons for Sub-Saharan African Countries", Working Paper No. 09-196, International Monetary Fund, available at: www.imf.org/external/pubs/ft/wp/2009/wp09196.pdf (accessed April 26, 2017).

Andersen, T.G., Bollerslev, T., Diebold, F.X. and Vega, C. (2003), "Micro effects of macro announcements: real-time price discovery in foreign exchange", *The American Economic Review*, Vol. 93 No. 1, pp. 38-62.

Hull, J.C. and Basu, S. (2014), *Options, Futures, and Other Derivatives*, 8th ed., Pearson Education, Delhi.

Österholm, P. and Hjalmarsson, E. (2007), "Testing for cointegration using the Johansen methodology when variables are near-integrated", Working Paper No. 07-141, International Monetary Fund, available at: www.imf.org/external/pubs/ft/wp/2007/wp07141.pdf (accessed June 10, 2016).

RBI (2008), "Report of the internal working group on currency futures", available at: https://rbidocs.rbi.org.in/rdocs/PublicationReport/Pdfs/84213.pdf (accessed April 7, 2017).

Sehgal, S., Rajput, N. and Deisting, F. (2013), "Price discovery and volatility spill over: evidence from Indian commodity markets", *The International Journal of Business and Finance Research*, Vol. 7 No. 3, pp. 57-75.

Corresponding author
Varuna Kharbanda can be contacted at: varunakharbanda@gmail.com

For instructions on how to order reprints of this article, please visit our website:
www.emeraldgrouppublishing.com/licensing/reprints.htm
Or contact us for further details: **permissions@emeraldinsight.com**

Downloaded by Delhi Technological University At 01:39 31 August 2017 (PT)

IOPscience iopscience.iop.org

Home Search Collections Journals About Contact us My IOPscience

Measurement of low cross section transition using versatile absorption technique

This content has been downloaded from IOPscience. Please scroll down to see the full text.

2017 J. Phys.: Conf. Ser. 875 042009

(http://iopscience.iop.org/1742-6596/875/5/042009)

View the table of contents for this issue, or go to the journal homepage for more

Download details:

IP Address: 14.139.251.107
This content was downloaded on 24/08/2017 at 12:07

Please note that terms and conditions apply.

You may also be interested in:

Analysis of metastable state population in fast ion beams
M Vujovic, M Matic and B Covic

MORE ABSORPTION TOWARD CYG X-3.
T. C. Weekes, H. P. Murphy, R. Schild et al.

Temperature measurement of cold atoms using transient absorption of a resonant probe through an optical nanofibre
Ravi Kumar, Vandna Gokhroo, Vibhuti Bhushan Tiwari et al.

Absorption measurements of quadrupole transition probabilities 6S-nD in caesium vapour
B Sayer, R Wang, J C Jeannet et al.

Heterodyne Doppler-free two-photon absorption and dispersion in rubidium vapour
D Bloch, M Ducloy and E Giacobino

Fabrication of ordered Bi2S3 nanowire arrays
X S Peng, G W Meng, J Zhang et al.

Calibration and quality assurance procedures at the far UV linear and circular dichroism experimental station DISCO
F Wien, M Paternostre, F Gobeaux et al.

Applications of photoluminescence excitation spectroscopy to the study of indium gallium phosphide alloys
A M White, E W Williams, P Porteous et al.

Measurement of low cross section transition using versatile absorption technique

Gaurav Sharma* [1], **T. Nandi**[†] **and Nitin K. Puri**[† 2]

*Dept. of Applied Physics, Delhi Technological University, New Delhi-110042, India

[†]Inter University Accelerator centre, New Delhi 110067,India

Synopsis The various possibilities of the X-ray absorption spectroscopy is explored in a beam foil experiment. The technique is used for the successful detection of a low cross section process and enhancing the detector resolution which gets degraded due to high intensity ratio. The lifetime measured with the technique matches with the value when absorber is not used.

The versatility of x-ray absorption technique is experimentally explored for enhancing the detector resolution and rejuvenating the very low probable transitions, lost in the pile up region during a beam-foil experiment. The dependence of Beer Lambert's law on the energy plays the key role in measuring the veiled peaks in the spectrum. In a pileup affected x-ray spectrum of collision between 130MeV Ti with 80μg/cm^2 thick carbon target; 4 peaks are successfully rejuvenated. Dependence of absorption coefficient on E^{-3}[1], where E is the energy of incident photons can provide a good tool to handle the intensities of the different energies differently. A transition 10^4 times weaker than one-electron-one-photon (OEOP), possibly originating by filling two-core-vacancies (two-electron-one-photon (TEOP[2]) $1s^{-2} \rightarrow 2s^{-1}2p^{-1}$) in He-like Ti, is detected.

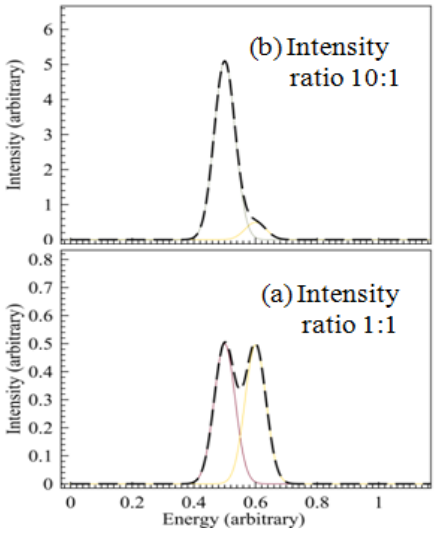


Figure 1. Resolution degradation: Effect of Intensity of the neighbourhood peaks on the resolution of the detector.

Multiple Aluminum absorber layers (10μm each) is used to suppress the pile up and high count rate photons with low energy to rejuvenate the TEOP transition and resolve the K_β and K_α which is obscured due to high intensity ratio and pile-up contamination respectively. We have experimentally confirmed that the lifetime value measured by using this technique (67.11ps) and without absorber (67.34ps) is same within the error limits. The measured branching ratio of this weak transition with OEOP is 1.38E-04. The energy of the spectral lines and the branching ratios of the TEOP/OEOP transitions find potential implications in understanding the multi-electron transitions in ion-solid collisions.

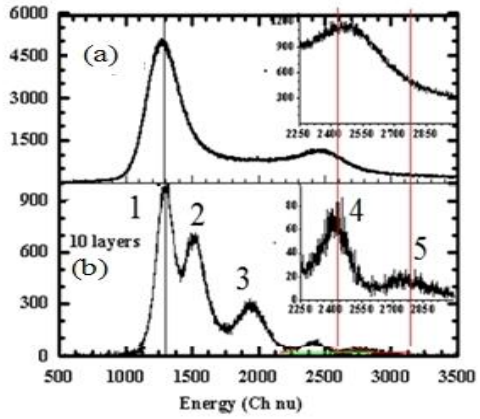


Figure 2. Experimental results: (a) and (b) are experimental x-ray spectrum without and with x-ray absorbers. Part (d) showing new peaks evolved from the spectrum after employing the technique.

References

[1] Newville M 2004 Fundamentals of XAFS *Fundamentals of XAFS* p 1–2 chapter 1

[2] Hoszowska J et.al 2011 *Phys. Rev. Lett.* **107** 053001

[1]E-mail: gaurav.kmc891101@gmail.com
[2]E-mail: nitin.phy@dce.edu

he terms of the Creative Commons Attribution 3.0 licence. Any further distribution
author(s) and the title of the work, journal citation and DOI.
Published under licence by IOP Publishing Ltd

Jauhari N, Raina H, Soni G, Chadha N and Bharadvaja N (2017) Mechanistic insights into the anticancer mode of action of an herbal drug. *Bioinspired, Biomimetic and Nanobiomaterials*, http://dx.doi.org/10.1680/jbibn.17.00003

Bioinspired, Biomimetic and Nanobiomaterials

Research Article
Received 18/01/2017 Accepted 31/05/2017
Keywords: computational studies/natural materials/protein

ice | science

ICE Publishing: All rights reserved

ice Institution of Civil Engineers publishing

Mechanistic insights into the anticancer mode of action of an herbal drug

Nupur Jauhari MSc
Research Scholar, Delhi Technological University, Delhi, India
Himani Raina MTech
Student, Delhi Technological University, Delhi, India
Garima Soni MTech
Student, Delhi Technological University, Delhi, India
Nidhi Chadha MSc
Research Scholar, Institute of Nuclear Medicine and Allied Sciences, Delhi, India
Navneeta Bharadvaja PhD*
Assistant Professor, Department of Biotechnology, Delhi Technological University, Delhi, India

Medicinal plants are a vast repository of natural compounds with therapeutic effects against various ailments. Bioactive compounds of these plants have shown to possess anticancer activities. Cancer is one of the fatal diseases causing premature deaths across the world. Two important metabolites, serpentine, a major secondary metabolite of *Rauwolfia serpentina*, and amarogentin, isolated from *Swertia chirata*, are found to possess anticancer properties. A comparable in silico analysis of the two anticancer agents serpentine and amarogentin has been done to evaluate their ability to inhibit two potential molecular targets for cancer, nuclear factor-κB (NF-κB) and cyclo-oxygenase-2 (COX-2). The least binding energies of amarogentin with NF-κB and COX-2 are –7·173 and –7·649, respectively, which are better than that of serpentine. The molecular simulation of amarogentin and serpentine suggests that amarogentin has better binding affinities with both cancer targets. Amarogentin is thermodynamically more stable with COX-2 than with NF-κB. Amarogentin is a potent anticancer agent as evidenced by the inhibition of COX-2. This finding would be beneficial to people with cancer.

1. Introduction

The pharmacological journey of treating many life-threatening diseases such as cancer is successful only when it is diagnosed at early phases. Most of the world today is widely affected by cancer, as it has become the leading cause of death today. People's ever-changing lifestyle has enormously contributed to the rising number of cancer cases in society.[1] Conventional treatments for cancer are associated with many side-effects, and in addition, they present inadequate anticancer activity.[2] This necessitates the discovery of more persuasive, less toxic and highly specific anticancer agents as a more feasible treatment option for cancer.[3] This is how the role of medicinal plants comes into play, as a healthy substitute for synthetic drugs. The exploitation of medicinal plants as a potential therapeutic alternative for cancer is already well known.[4,5] More than 3000 plants have been known to possess anticancer properties.[6] Further, the relevance of plant-based drugs for the treatment of cancer is rising at a rate of 10–40% globally.[5,7,8] Out of the available medications for cancer, approximately 60% are significantly attributed to plant sources.[9]

Two important metabolites, serpentine from *Rauwolfia serpentina*[10] and amarogentin from *Swertia chirata*,[11] are found to have potential anticancer properties.[12,13] The use of plant metabolites with anticancer properties to inhibit molecular targets for cancer that include proteins (transcription factors, inflammatory mediators, enzymes) or signaling pathways that regulate the mechanism of cell proliferation and related events is the preferred choice of cancer therapy.[14]

An important and age-old medicinal plant *S. chirata*, commonly known as 'Chirata', belongs to the family Gentianaceae and is utilized for the treatment of multifarious disorders.[15] This medicinally important family contains many plants famous for their bitter taste and renowned as conventional medicines for appetite improvement and fever. It has great importance in the Indian system of medicine (Ayurveda) as antipyretic, antihelminthic, antiperiodic and as laxative, and is being used for the cure of asthma and leucorrhoea. Pharmacological properties of this herb are still at experimental stage but are well known to possess a number of useful metabolites with anti-inflammatory and hepatoprotective action.[16,17] Crude extracts of *S. chirata* showed the presence of three main phytochemicals, namely, mangiferin, swertiamarin and amarogentin, and their derivatives, the presence of which was confirmed through high-performance liquid chromatography.[18] Amarogentin, the most acerbic substance, is a secoiridoid glycoside with a bitter taste even at a dilution of 1:58 000 000[19] and is proven to inhibit cell proliferation as well as induce apoptosis in epithelium during carcinogenesis. It has been explained that the extract of *S. chirayita* controls programmed cell death and, at the same time, suppresses cell proliferation at the target site.[12] 7,12-Dimethylbenz [*a*]anthracene (DMBA)-induced carcinogenesis model of mice was taken for cytotoxic study, and cytotoxicity test revealed IC50 value of amarogentin is 0·5 mg. The extract of *S. chirayita*, rich in amarogentin, downregulates cyclo-oxygenase-2 (COX-2) protein expression in DMBA-induced skin lesion, while amarogentin-induced caspase-3 maturation was noticed, which is responsible for the initiation of apoptosis.[12] A group of researchers delivered novel research on the chemopreventive role of amarogentin in liver

***Corresponding author e-mail address:** navneetab@dtu.co.in

Downloaded by [The Institution of Civil Engineers] on [30/08/17]. Copyright © ICE Publishing, all rights reserved.

carcinogenesis by way of modulation of cell cycle and apoptosis on carbon tetrachloride (CCl_4)/*N*-nitrosodiethylamine-induced liver carcinogenesis mouse model system.[20] Amarogentin inhibits platelet activation by the suppression of phospholipase C (PLC) γ2, protein kinase C (PKC) and mitogen-activated protein kinase (MAPK) pathway.[21] Thus, amarogentin possesses the capability to prevent or treat thromboembolic disorders as well as carcinogenic activities. Indian snakeroot (*Rauvolfia serpentine*), an important medicinal plant, belongs to the family Apocynaceae. The root extract of this plant contains alkaloid and is used to produce antihypertensive drugs worldwide.[22] The antitumor activity of *R. serpentine* in different mouse sarcomas in vivo was noticed.[23,24] A stable cell line F-Habp07 has been designed by overexpressing human hyaluronan binding protein 1 (Habp1) in murine fibroblasts, and its accumulation in the mitochondria is responsible for excess reactive oxygen species (ROS) generation without any external stimuli.[13] A reduction in ROS generation, inhibition of p65 subunit of nuclear factor-κB (NF-κB) nuclear translocation and enhancement in glutathione were noticed when experimented with serpentine. They revealed a novel non-cytotoxic antioxidant serpentine efficacy, which is found to be comparable with other well-known antioxidants.

The present scenario demands more efficient targeted therapies for cancer that are particularly aimed at cancerous cells or the processes involved in their metastasis to other parts of the body and survival. A number of molecular targets for cancer have been recently identified. One of the potent targets to inhibit various diseases is NF-κB, a ubiquitous transcription factor. NF-κB was first identified in 1986.[25] It is well known for its function in regulating cell-signaling responses. As the name indicates, it is a nuclear factor bound to an enhancer component of the immunoglobulin kappa light chain gene in B cells. NF-κB controls over 500 different gene products and is a known mediator of inflammation. It comprises a Rel homology domain (deoxyribonucleic acid (DNA)-binding domain/dimerization domain) on a nuclear localization sequence; these sequences are maintained from *Drosophila* to humans. It is also involved in the regulation of cell signaling responses. The abnormal activation and expression of NF-κB are responsible for various ailments, including cancers, diabetes mellitus, cardiovascular diseases, autoimmune diseases, viral replication, septic shock, neurodegenerative disorders, ataxia telangiectasia, arthritis, asthma, inflammatory bowel disease and several other inflammatory conditions. The regulation of cellular proliferation and differentiation, immune system response and the process of programmed cell death or apoptosis are widely attributed to this transcription factor. Therefore, targeted therapies aimed at inhibiting NF-κB-associated signaling holds a great potential to combat numerous ailments.[26] A total of five genes, NF-κB1 (p50/p105), NF-κB2 (p52/p100), RelA (p65), c-Rel and RelB, constitute the assembly of NF-κB. The NF-κB proteins are classified into two categories.[27] The ones that are synthesized in their mature form and the others in their precursor form. In the normal state, the NF-κB dimer remains inactively present in the cytoplasm due to their interaction with NF-κB inhibitors. In response to a variety of cytokines, growth factors (epidermal growth factor receptor and insulin growth factor receptor) and tyrosine kinases, NF-κB is activated. In addition, signaling pathways, such as Ras/MAPK and PI3K/Akt, are responsible for the activation of NF-κB. The induced NF-κB activation is a highly regulated process. However, the molecular alterations of cancer cells may cause impaired NF-κB activation. The unregulated NF-κB activation may lead to the upregulation or downregulation of genes involved in the regulation of apoptosis, cell cycle control, adhesion, or migration. These altered processes play a major task in the development and progression of cancer and clearly suggest the role of NF-κB in cancer.[28] Various experimental studies proved NF-κB as a potential target against many ailments. Inhibition in tumor formation and growth of natural killer/T-cell lymphoma cell lines induced by the Epstein–Barr virus through the NF-κB and PI3K/Akt pathways was explored.[29] Paris saponin II (PSII), an active component of the Chinese herbal medicine *Rhizoma paridis*, reduces angiogenesis and the development of human ovarian cancer mouse model by suppressing NF-κB signaling.[30] Thus, the inhibition of NF-κB signaling pathway can reduce the menace of many chronic ailments.

Another potent molecular target for cancer therapy is COX-2, which is also formally called prostaglandin H2 synthase-2. This enzyme, with two known isoforms COX-2 and COX-1, has a well-established role in the formation of prostanoids from arachidonic acid. The two isoforms are distinct in the manner that COX-1 is native to most types of cells and is a housekeeping enzyme with almost constant amounts under either physiological or pathological condition. On the other hand, COX-2 is rapidly present in diseased situations and often absent in normal state. The induction of COX-2 has been first done by a viral oncogene[31] or by a tumor promoter.[32] Experimental studies have also justified its role in a variety of growth factors and mitogens for the induction of COX-2.[33,34] Thus, COX-2 has a strong relevance to cellular proliferation and cancer.[35] The development of COX-2 inhibitors can be the potential therapeutic approach for cancer. The prevention of colon cancer with the use of COX-2 has already been reported in several animal models.[36] As the mechanism of action of anti-inflammatory agents is well studied in clinical research, there is a strong background to develop potent COX-2 inhibitors for human trials.[37] A team of researchers have examined four genes, RassF1A, APC, Rar-beta and prostaglandin-endoperoxide synthase 2 (PTGS2), in placental samples and compared them with maternal white blood cells. PTGS2 was found to be hypomethylated in the placentas compared to the maternal cells, which has an important clinical implication to, for example, placental abnormalities.[38] Normal mammary gland lymphangiogenesis, mammary tumor-associated lymphangiogenesis, tumor cell invasion into lymphatics and metastasis were found to be reduced in rodent models of postpartum breast cancer through COX-2 inhibition during the involution window.[39] The involvement of genotypic

Downloaded by [The Institution of Civil Engineers] on [30/08/17]. Copyright © ICE Publishing, all rights reserved.

polymorphisms in COX-2 to increase breast cancer risk in Taiwanese females was also examined.[40] Their findings implied that the C allele of G-765C, polymorphic variants of COX-2, was linked with a reduced risk of breast cancer and could be considered as an early detection and prognostic marker for breast cancer. Liver cancer is one of the most common malignancies and the leading cause of death worldwide. Hepatocellular carcinoma, liver cirrhosis, hepatitis and several liver diseases can be the result of the invasion and migration of hepatitis C virus (HCV). The invasion of HCV is enhanced by HCV non-structural protein 3, while the matrix metalloproteinase-9 and COX-2 are responsible for the migration of HCV.[41] Therefore, COX-2 is an experimentally proven target for many diseases, including cancer.

In the present study, a comparable analysis of two anticancer agents, serpentine, a major secondary metabolite of *R. serpentine*, and amarogentin, isolated from *S. chirata*, has been explored for their ability to inhibit potential molecular targets for cancer, NF-κB, and COX-2. In silico approach comprising molecular modeling, docking and simulation strategy is hereby analyzed to find the significant outcome in support of the proposed idea of NF-κB activation suppression and COX-2 inhibition by plant secondary metabolites that possess anticancer properties.

2. Results and discussion

2.1 Homology modeling

The protein sequence of COX-2 (604 AA, UniProtKB accession number: P35354) was retrieved from Uniprot. After using the Basic Local Alignment Search Tool (Blast), the structure of COX-2 from *Mus musculus* (PDB ID: 1PXX) was selected as best template based on their sequence percentage identity.

The automated homology modeling software Prime, version 3.1 (Schrödinger, LLC, New York, 2012 (license: Institute of Nuclear Medicine and Allied Sciences, INMAS)) on Linux operating environment was used to check the three-dimensional (3D) model of the enzyme.

2.2 Molecular docking

The results in Table 1 indicate the docking score, which clearly suggests that amarogentin could be a potential inhibitor of both COX-2 and NF-κB compared to serpentine. The two-dimensional representation of this best-fit receptor–ligand interaction is shown in Figure 1, which clearly illustrates the participation of interacting amino acid residues.

The residues shown in Figure 1 are present in the binding cavity of COX-2 and directly participate in several bond formations with amarogentin. These are present in the ligand binding site responsible for the function of protein.

In the process of molecular docking, the docking score is used to predict the strength of the binding affinity of the two docked

Table 1. Docking results ranked based on XP Glide score

Ligand/protein	COX-2	NF-κB
Amarogentin	–7·649	–7·173
Serpentine	–4·064	–4·687

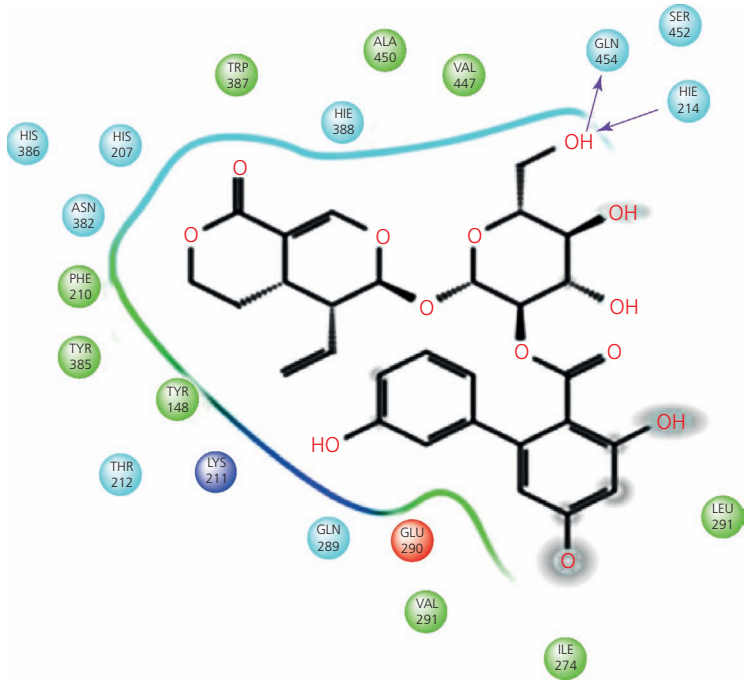


Figure 1. Two-dimensional representation of the docked complex

Downloaded by [The Institution of Civil Engineers] on [30/08/17]. Copyright © ICE Publishing, all rights reserved.

molecules, which is necessary for further study of the establishment of the probable anticancer drug. The binding score represents better protein–ligand binding interaction. In the present study, serpentine and amarogentin are the small organic compounds (probable drug) which are docked to target protein NF-κB and COX-2. Abnormal activation and expression of NF-κB are responsible for various ailments, including cancers. The regulation of cellular proliferation and differentiation, immune system response and process of programmed cell death or apoptosis are widely attributed to this transcription factor. Therefore, targeted therapies aimed at inhibiting NF-κB-associated signaling hold a great potential to combat numerous ailments like cancer. On the other hand, COX-2 is rapidly present in diseased situations and often absent in normal state. Experimental studies have also justified its role in a variety of growth factors and mitogens for the induction of COX-2. Thus, COX-2 has a strong relevance to cellular proliferation and cancer. The development of NF-κB and COX-2 inhibitors can be the potential therapeutic approach for cancer. The two anticancer agents serpentine and amarogentin are docked to target protein – that is, NF-κB and COX-2 with a good binding score represent them as the probable anticancer drug.

2.3 Molecular dynamic simulation

The molecular dynamic (MD) simulation result file was analyzed using the analysis options in the Desmond Molecular Dynamics System, version 3.1 (D. E. Shaw Research, New York, 2012; Schrödinger (license: Inmas)) program. The pressure value widely fluctuated over the course of the 1000 ps simulation run, but this behavior is not unexpected. The running average of these data shows that the average value of the pressure is 1·05 bar and the case is the same with the volume (Figure 2).

In order to analyze MD simulation, the calculation of root-mean-square deviation (RMSD) for the trajectories of COX-2 docked with amarogentin was correspondingly done using the initial complex structure (zero frames of the trajectory) as a reference. Figure 3 clearly illustrates that the complex has attained stability as the RMSD is less than 2·5 Å for the entire simulation span. The duration of simulation taken in the study permits rearrangement of side-chains of the drug–protein complex to find their most stable binding modes. To conclude the result of this simulation, the study proposes amarogentin as a probable and a valuable natural ligand for cancer target COX-2.

The role of NF-κB is prominent in the activation of proinflammatory genes, including cytokines, chemokines and adhesion molecules and could be a potent therapeutic target for anti-inflammatory drugs. Various experimental studies proved NF-κB and COX-2 as the potential targets of many disorders. The inhibition of NF-κB and COX-2 by *Operculina turpathum* extract to suppress oral squamous cell carcinoma cell lines was explored.[42] NF-κB acts as the inducer for large B-cell lymphomas, which can be blocked by inhibiting NF-κB.[43] Another study revealed that NF-κB regulates a set of genes that increases murine fibroblasts.[44] An

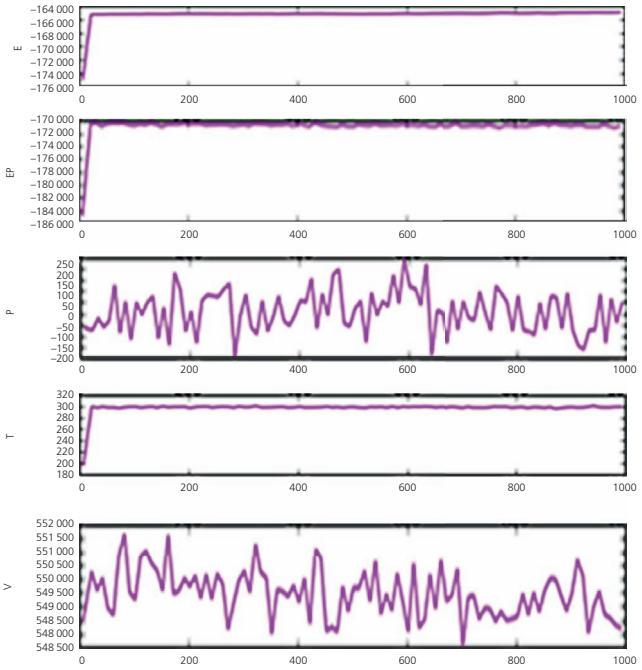


Figure 2. Simulation quality analysis

enormous amount of data exhibits the involvement of transcription factor NF-κB in the progression of cancer, which advocates NF-κB as a potent therapeutic target. Current studies revealed that COX-2 has been found to be involved in apoptosis resistance, angiogenesis and tumor progression, and inhibitors exclusively used for COX-2 can prevent the progression of cancer.[45] The anticancer potential of amarogentin was revealed by in vivo inhibition of cancer cell proliferation in mice xenograft model, and amarogentin was shown to cause apoptosis of cancer cells.[46] Amarogentin-rich purified fraction was observed to suppress cell proliferation and cause apoptosis at the target site.[47] Another experimental study proved that amarogentin-rich methanolic extract of *S. chirata* suppressed COX-2 protein expression in vivo, which leads to the pathway through which amarogentin controls the carcinogen-induced abnormally high rate of proliferation of cells.[12] The similar study proved a reduction in skin carcinogenesis in a mouse model by the downregulation of COX-2 expression through amarogentin. Further, in the same study, amarogentin–COX-2 complex was found to be more stable compared to the amarogentin–COX-1 complex in molecular dynamics simulation.[48] COX-2 is responsible for the conversion of arachidonic acid (AA) to prostaglandins by way of two-step catalytic mechanism. The process begins with the oxidization of AA to intermediate prostaglandin, hydroperoxy endoperoxide (PGG2), known as the cyclo-oxygenation step, and later, PGG2 is reduced into hydroxyl endoperoxide (PGH2), which has a vital role as the precursor for several prostanoids, identified as peroxidation step.[49] The catalytic domain is one of the three functional domains of COX-2, which possesses the active site for ligand binding.[50] Amarogentin specifically binds at the catalytic site inside the hydrophobic channel. The analysis of two ligand–protein

Downloaded by [The Institution of Civil Engineers] on [30/08/17]. Copyright © ICE Publishing, all rights reserved.

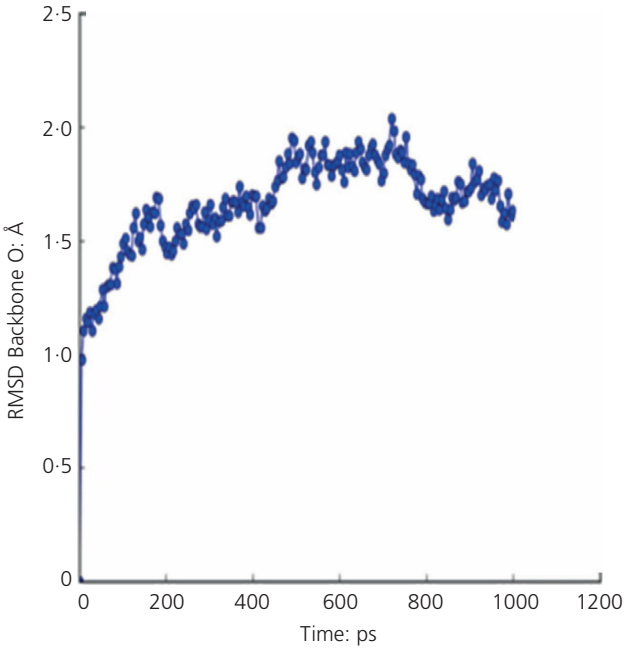


Figure 3. Plot showing RMSD of the backbone of COX-2/ Amarogentin (complex)

complexes revealed that both interactions are reasonably stable, with amarogentin proving more well fixed inside the binding cavity of COX-2. Therefore, the complex was subjected to MD simulation analysis to evaluate the stability of the complex in bodily conditions. The enzyme COX-2 significantly encourages tissue growth by inhibiting apoptosis, prominently at the tissue damage repair site,[51] and increases DNA synthesis mechanism by enhancing cell proliferation and cell mobility.[52] It can also be induced in the different tissues of the body in the inflammatory condition and tumorigenic signals. Amarogentin is well studied for its anticancer properties, suppression of cell proliferation and induction of apoptosis at the target site. In the present study, molecular docking complex showed the participation of interacting amino acid, which is a response to good docking score. Hydrophobic and hydrogen-bond interactions strengthen the amarogentin–COX-2 complex. To explore the behavior of amarogentin–COX-2 in close vicinity, MD simulation was performed. The analysis of MD, like RMSD, remained stable throughout the MD run, confirming the stable binding of the complex. The docked complex of the ligand target and the protein provides a detailed picture of the key binding site, and thus, it gives prospects to explore further the interplay of the binding site residues at the molecular level and will help in the in vitro exploration of the mechanism involved in natural anticancer agents. The overall stability of the simulated complex of COX-2 and amarogentin can help explore the observed results to further levels of study and investigation. Cancer is a well-known life-threatening disease, prevalent in society nowadays. Natural agents from medicinal plants have been proven to have great potential in cancer therapeutics. Computational analysis of these agents can provide a rational approach to discover naturally occurring potent antitumor agents. In the present study, molecular modeling, docking and dynamic simulation studies were used as the basic approach in evaluating the comparative inhibition capability of two potential anticancer agents against cancer targets. Docking studies have been done to compare the binding of serpentine and amarogentin with both the potent targets NF-κB and COX-2. The least binding energies of COX-2 with amarogentin and serpentine are −7·649 and −4·064, respectively, while the values are −7·173 and −4·687, respectively, in the case of NF-κB with both ligands. These energy values show that amarogentin and COX-2 have a better binding affinity than other docked complexes. Amino acid residues Gln, Van, Ala, Trp, His, Asp, Phe, Tyr, Thr, Lys and Glu are present in the binding cavity of the COX-2, and docking studies explored their bond formation with amarogentin. These results support the hypothesis that amarogentin has the potential to disrupt the activity of COX-2, being accounted by hydrophobic and hydrogen (H)-bond interactions. This method of computational analysis has thus provided a rational approach to propose that *S. chirata*-derived amarogentin can serve as a potent anticancer agent through its ability to mediate the inhibition of cancer targets like COX-2 and NF-κB. RMSD of COX-2 and amarogentin complex has attained a stationary phase during the later stage of the simulation and that is always 2·5 Å for the entire simulation length, suggesting the stability of the complex. The simulation length applied in the complete study was long enough to permit the rearrangement of side-chains of the indigenous as well as the drug-complexed protein to get their best stable binding mode. In conclusion, the present MD simulations made the dynamic structural stability of COX-2 with the drug amarogentin clear, together with the inhibitory mechanism. Thus, the result of the study proposes that amarogentin is a better potential natural anticancer agent compared to serpentine and can be explored further as a potent inhibitor of other molecular targets of cancer as well.

3. Experimental

3.1 Target structure prediction

Three-dimensional structure of the p65 subunit of NF-κB (PDB ID: 1NFI) was available in protein data bank (PDB). The 3D structure of COX-2 was generated by the homology modeling method using Prime, version 3.1 (Schrödinger, LLC, New York, 2012 (license: Inmas)). A Blastp search was made against the PDB database to identify the maximum matching template for modeling. The best model was validated the Structural Analysis and Verification Server and Verify_3D.[53]

3.2 Ligand preparation

Three-dimensional coordinates of amarogentin (CID: 115149) and serpentine (CID: 73391) were retrieved in .sdf format from the PubChem database of the National Center for Biotechnology Information. These .sdf files were converted to .pdb format by the Open Babel tool. Ligand coordinates were prepared and processed using Ligprep, version 2.5 (Schrödinger, LLC, New York, 2012 (license: Inmas)) module.

Downloaded by [The Institution of Civil Engineers] on [30/08/17]. Copyright © ICE Publishing, all rights reserved.

3.3 Active site prediction

Estimated binding pockets of both receptors were defined using Sitemap, version 2.6 (Schrödinger, LLC, New York, 2012 (license Inmas)) application of Maestro 9.3.5 (license: Inmas).

3.4 Molecular docking

The receptor structures were prepared and minimized within the protein preparation wizard of Maestro 9.3.5 (license: Inmas). Grids for each site were generated. The docking study of modeled COX-2 and 1NFI was done using Glide, version 5.8 (Schrödinger, LLC, New York, 2012 (license: Inmas)).[54] Docking calculations were performed using the XP (Extra Precision Mode) scoring function and with the OPLS 2005 force field.

3.5 Molecular dynamic simulation

The MD simulation study of the best-docked complex was done with the help of Desmond Molecular Dynamics System, version 3.1 (D. E. Shaw Research, New York, 2012; Schrödinger (license: Inmas)) as implemented in the Schrödinger package. TIP3 model was used to describe the water molecule. The final system was composed of approximately 50 000 atoms. For 1 ns of the production runs, a time step of 5 ps with NPT (Constant Number, Pressure, Temperature) ensemble at 310 K was used to simulate the docked complex.

4. Conclusions

COX-2 is one of the most striking topics in modern biological, biochemical and pharmacological research, and in the recent years, numerous studies shedding light on its inhibition/regulation have increased manifold. Natural ligands are the center of interest in this context due to negligible harmful effects. A comparative computational analysis on amarogentin and serpentine has been done with the two potent anticancer targets COX-2 and NF-κB. The result of the study proposes that amarogentin is a better potential natural anticancer agent compared to serpentine. In silico analysis offered a rationalization of the power of naturally occurring amarogentin to inhibit COX-2. The prominent value of the binding energy involved in the binding of amarogentin to COX-2 consolidates the thermodynamic stability of the binding. Conclusively, the results strongly suggest that amarogentin is a potent anticancer agent as evidenced by the inhibition of COX-2.

Acknowledgements

The authors would like to thank the vice chancellor of Delhi Technological University and the head of the Department of Biotechnology and Institute of Nuclear Medicine and Allied Sciences, Delhi, for providing the facility and support to conduct the research work.

REFERENCES

1. Ahmedin J, Freddie B, Melissa MC *et al.* (2011) Global cancer statistics. *CA Cancer Journal for Clinicians* **61(2)**: 69–90.
2. Mans DR, Rocha AB and Schwartsmann G (2000) Anti-cancer drug discovery and development in Brazil: targeted plant collection as a rational strategy to acquire candidate anti-cancer compounds. *Oncologist* **5(3)**: 185–198.
3. Alonso-Castro AJ, Villarreal ML, Salazar-Olivod LA *et al.* (2011) Mexican medicinal plants used for cancer treatment: pharmacological, phytochemical and ethnobotanical studies. *Mexico Journal of Ethnopharmacology* **133(3)**: 945–972.
4. Gerson-Cwilich R, Serrano-Olvera A and Villalobos-Prieto A (2006) Complementary and alternative medicine (CAM) in Mexican patients with cancer. *Clinical and Translational Oncology* **8(3)**: 200–207.
5. Tascilar M, De Jong FA, Verweij J and Mathijssen RH (2006) Complementary and alternative medicine during cancer treatment: beyond innocence. *Oncologist* **11(7)**: 732–741.
6. Graham JG, Quinn ML, Fabricant DS and Farnsworth NR (2000) Plants used against the cancer – an extension of the work of Jonathan Hartwell. *Journal of Ethnopharmacology* **73(3)**: 347–377.
7. Cassileth BR and Deng G (2004) Complementary and alternative therapies for cancer. *Oncologist* **9(1)**: 80–89.
8. Molassiotis A, Panteli V, Patiraki E *et al.* (2006) Complementary and alternative medicine use in lung cancer patients in eight European countries. *Complement Therapeutic Clinical Practice* **12(1)**: 34–39.
9. Gordaliza M (2007) Natural products as leads to anticancer drugs. Spain. *Clinical and Translational Oncology* **9(12)**: 767–776.
10. Oliver W and Rudolf M (2002) Anhydronium bases from *Rauvolfia serpentine*. *Phytochemistry* **61(6)**: 705–709.
11. Joshi P and Dhawan V (2005) *Swertia chirayita* – an overview. *Current Science* **89(4)**: 635–640.
12. Saha P, Mandal S, Das A and Das S (2006) Amarogentin can reduce hyperproliferation by downregulation of COX-2 and upregulation of apoptosis in mouse skin carcinogenesis model. *Cancer Letters* **244(2)**: 252–259.
13. Dutta S, Chowdhury AR, Srivastava SK, Ghosh I and Datta K (2011) Evidence for serpentine as a novel antioxidant by a redox-sensitive HABP1 overexpressing cell line by inhibiting its nuclear translocation of NF-Kb. *Free Radical Research* **45(11–12)**: 1279–1288.
14. Grover A, Singh R, Shandilya A *et al.* (2012) Ashwagandha derived withanone targets TPX2-Aurora a complex: computational and experimental evidence to its anticancer activity. *PLoS One* **7(1)**: e30890.
15. Gaur RD (1999) *Flora at the District Garhwal North West Himalaya: with Ethnobotanical Notes*. Transmedia, Srinagar, India.
16. Mandal S, Das PC, Joshi PC *et al.* (1992) Anti-inflammatory action of *Swertia chirata*. *Fitotherapia* **63**: 122–128.
17. Karan M, Vasisht K and Handa SS (1999) Antihepatotoxic activity of *Swertia chirata* on carbon tetrachloride induced hepatotoxicity in rats. *Phytotherapy Research* **13(1)**: 24–30.
18. Phoboo S, Pinto MS, Barbosa AC *et al.* (2013) Phenolic-linked biochemical rationale for the anti-diabetic properties of *Swertia chirata* (Roxb. ex Flem.). *Karst Phytotherapy Research* **27(2)**: 227–235.
19. Singh A (2008) Phytochemicals of the Gentianaceae: a review of pharmacological properties. *International Journal of Pharmaceutical Sciences and Nanotechnology* **1(1)**: 33–36.
20. Pal D, Sur S, Mandal S *et al.* (2012) Prevention of liver carcinogenesis by amarogentin through modulation of G1/S cell cycle checkpoint and induction of apoptosis. *Carcinogenesis* **33(12)**: 2424–2431.
21. Yen TL, Lu WJ, Lien LM *et al.* (2014) Amarogentin, a secoiridoid glycoside, abrogates platelet activation through PLC (phospholipase C) γ 2-PKC (protein kinase C) and MAPK (mitogen-activated protein kinases pathway) pathways. *Biomed Research International* **2014(2014)**: 1–9.
22. Woodson RE, Youngken HW, Schlittler E and Schneider JA (1957) *Pharmacognosy, Chemistry, and Pharmacology*, 1st edn. Little, Brown and Company Toronto, ON, Canada.
23. Belken M and Hardy W (1957) Effects of reserpine. *Science* **125(3241)**: 233–234.
24. Nelson M, Nelson DS and Hopper KE (1981) Tumor growth in mice with the depressed capacity to mount inflammatory responses: possible role of macrophages. *American Journal of Pathology* **104(2)**: 114–124.

Downloaded by [The Institution of Civil Engineers] on [30/08/17]. Copyright © ICE Publishing, all rights reserved.

25. Sen R and Baltimore D (1986) Inducibility of k immunoglobulin enhancer-binding protein Nf-κB by a posttranslational mechanism. *Cell* **47(6)**: 921–928.
26. Grover A, Shandilya A, Punetha A, Bisaria VS and Sundar D (2010) Inhibition of the NEMO/IKKB association complex formation, a novel mechanism associated with the NF-κB activation suppression by *Withania somnifera*'s key metabolite Withaferin A. *BMC Genomics* **11(4)**: S25.
27. Karin M and Ben-Neriah Y (2000) Phosphorylation meets ubiquitination: the control of NF-[kappa] B activity. *Annual Review of Immunology* **18(1)**: 621–663.
28. Dolcet X, Llobet D, Pallares J and Matias-Guiu X (2005) NF-κB in development and progression of human cancer. *Virchows Archive* **446(5)**: 475–482.
29. Sun L, Zhao Y, Shi H, Ma C and Wei L (2015) LMP-1 induces survivin expression to inhibit cell apoptosis through the NF-κB and PI3K/Akt signaling pathways in nasal NK/T-cell lymphoma. *Oncology Reports* **33(5)**: 2253–2260.
30. Yang M, Zou J, Zhu H *et al.* (2015) Paris saponin II inhibits human ovarian cancer cell-induced angiogenesis by modulating NF-κB signaling. *Oncology Reports* **33(5)**: 2190–2198.
31. Xie W, Chipman JG, Robertson DL, Erikson RL and Simmons DL (1991) Expression of a mitogen-responsive gene encoding prostaglandin synthase is regulated by mRNA splicing. *Proceedings of the National Academy of Sciences of the United States of America* **88(7)**: 2692–2696.
32. Kujubu DA, Fletcher BS, Varnum BC, Lim RW and Herschman HR (1991) Tis10, a phorbol ester tumor promoter-inducible mRNA from Swiss 3t3 cells, encodes a novel prostaglandin synthase/cyclooxygenase homolog. *Journal of Biological Chemistry* **266(10)**: 12866–12872.
33. Bakhle YS and Botting RM (1996) Cyclooxygenase-2 and its regulation in inflammation. *Mediators of Inflammation* **5(5)**: 305–323.
34. Smith WL, DeWitt D and Garavito RM (2000) Cyclo-oxygenases: structural, cellular and molecular biology. *Annual Review of Biochemistry* **69(1)**: 145–182.
35. Bakhle YS (2001) Cox-2 and cancer: a new approach to an old problem. *London Britain Journal of Pharmacology* **134(6)**: 1137–1150.
36. Marnett LJ and Dubois RN (2002) Cox-2: a target for colon cancer prevention. *Annual Review of Pharmacology and Toxicology* **42(1)**: 55–80.
37. Vane JR, Flower RJ and Botting RM (1990) History of aspirin and its mechanism of action. *Stroke* **21(4)**: 12–23.
38. Mohammad N, Yaqinuddin A, Kakal F *et al.* (2013) Frequent hypomethylation of PTGS2 gene promoter in human term placenta. *Italian Journal of Anatomy and Embryology* **118(2)**: 211–216.
39. Lyons TR, Borges VF, Betts CB *et al.* (2015) Cyclooxygenase-2-dependent lymphangiogenesis promotes nodal metastasis of postpartum breast cancer. *Journal of Clinical Investigation* **124(9)**: 3901–3912.
40. Su CH, Hsiao CL, Chang WS *et al.* (2014) Evaluation of the contribution of cyclooxygenase 2 genotypes to breast cancer in Taiwan. *Anticancer Research* **34(11)**: 6711–6716.
41. Lu L, Zhang Q, Wu K *et al.* (2015) Hepatitis C virus NS3 protein enhances cancer cell invasion by activating matrix metalloproteinase-9 and cyclooxygenase-2 through ERK/p38/NF-κB signal cascade. *Cancer Letters* **356(2)**: 470–478.
42. Arora R, Bharti V, Gaur P *et al.* (2017) *Operculina turpethum* extract inhibits growth and proliferation by inhibiting NF-κB, COX-2 and cyclin D1 and induces apoptosis by up regulating P53 in oral cancer cells. *Archives of Oral Biology* **80(1)**: 1–9.
43. Lam LT, Davis RE, Pierce J *et al.* (2005) Small molecule inhibitors of IkappaB kinase are selectively toxic for subgroups of diffuse large B-cell lymphoma defined by gene expression profiling. *Clinical Cancer Research* **11(1)**: 28–40.
44. Hanson JL, Hawke NL, Kashatus D and Baldwin A (2004) The nuclear factor kappaB subunits RelA/p65 and c-Rel potentiate but are not required for Ras-induced cellular transformation. *Cancer Research* **64(20)**: 7248–7255.
45. Khan MN and Lee YS (2009) Cyclooxygenase inhibitors: scope of their use and development in cancer chemotherapy. *Medicinal Research Reviews* **31(2)**: 161–201.
46. Zhao JG, Zhang L, Xiang XJ *et al.* (2016) Amarogentin secoiridoid inhibits *in vivo* cancer cell growth in xenograft mice model and induces apoptosis in human gastric cancer cells (SNU-16) through G2/M cell cycle arrest and PI3K/Akt signalling pathway. *Journal of Balkan Union of Oncology* **21(3)**: 609–617.
47. Saha P, Mandal S, Das A and Das S (2004) Evaluation of the anticarcinogenic activity of *Swertia chirata* Buch.Ham, an Indian medicinal plant, on DMBA induced mouse skin carcinogenesis model. *Phytotherapy Research* **18(5)**: 373–378.
48. Shukla S, Bafna K, Sundar D and Thorat SS (2014) The bitter barricading of prostaglandin biosynthesis pathway: understanding the molecular mechanism of selective cyclooxygenase-2 inhibition by amarogentin, a secoiridoid glycoside from *Swertia chirayita*. *PLoS One* **9(3)**: e90637.
49. Vane JR, Bakhle YS and Botting RM (1998) Cyclooxygenases 1 and 2. *Annual Review of Pharmacology and Toxicology* **38(1)**: 97–120.
50. Claria J (2003) Cyclooxygenase-2 biology. *Current Pharmaceutical Design* **9(27)**: 2177–2190.
51. Cao Y and Prescott SM (2002) Many actions of cyclooxygenase-2 in cellular dynamics and in cancer. *Journal of Cellular Physiology* **190(3)**: 279–286.
52. Kimura A, Tsuji S, Tsujii M *et al.* (2000) Expression of cyclooxygenase-2 and nitrotyrosine in human gastric mucosa before and after *Helicobacter pylori* eradication. *Prostaglandins, Leukotrienes and Essential Fatty Acids* **63(5)**: 315–322.
53. Colovos C and Yeates TO (1993) Verification of protein structures: patterns of nonbonded atomic interactions. *Protein Science* **2(9)**: 511–519.
54. Friesner RA, Banks JL, Murphy RB *et al.* (2004) Glide: a new approach for rapid, accurate docking and scoring: method and assessment of docking accuracy. *Journal of Medicinal Chemistry* **47(7)**: 1739–1749.

How can you contribute?

To discuss this paper, please submit up to 500 words to the journal office at journal@ice.org.uk. Your contribution will be forwarded to the author(s) for a reply and, if considered appropriate by the editor-in-chief, it will be published as a discussion in a future issue of the journal.

ICE Science journals rely entirely on contributions from the field of materials science and engineering. Information about how to submit your paper online is available at www.icevirtuallibrary.com/page/authors, where you will also find detailed author guidelines.

Downloaded by [The Institution of Civil Engineers] on [30/08/17]. Copyright © ICE Publishing, all rights reserved.

Modelling graphene sheet growth subjected to plasma containing negatively charged ions

N. Gupta[1], S. C. Sharma[1], and R. Gupta[1]

[1]*Department of Applied Physics, Delhi Technological University (DTU), Shahbad Daulatpur, Bawana Road, Delhi-110042*

Abstract

The paper presents a theoretical model to investigate the effects of negatively charged ions in the reactive plasma on the graphene sheet growth. The present model considers the graphene sheet growth subjected to reactive plasma containing electrons, positively as well as negatively charged ions, and neutrals. The key equations accounted in the present model are charging rate of the graphene sheet, kinetics of all plasma species, the growth rate equation of the graphene sheet. Numerical calculations have been carried out for typical glow discharge plasma parameters and it is found that graphene sheet area decreases with increase in the relative number densities of negatively charged ions in the plasma.

I. Introduction

The plasma species, particularly negatively charged ions in the plasma play a significant role on the growth of the nanostructures in the plasma enhanced chemical vapour deposition. Choi and Kushner [1] have illustrated that negatively charged ions are trapped in the electropositive plasmas and therefore have a long residence time resulting in the growth of critically large clusters. Ostrikov *et al.* [2] have shown that the negative ions in plasma affect the charging and trapping of particulates through the modification of sheath/presheath structure despite of negligible negative ion currents collected by the particles. Levko *et al.* [3] have studied the influence of electronegative gas SF_6 on the plasma stability.

II. Model

In order to investigate the role of negative ions in plasma on the growth of graphene sheet, we consider the embryonic growth of graphene sheet in a plasma consisting of electrons, positively charged ions of carbon source gas i.e., methane (denoted as type A) and neon (denoted

as type B), negatively charged ions $\left(SF_6^-\right)$ and neutrals of type A and B. In addition, we assume the positively charged ions to be singly ionised.

A. Charging of the graphene sheet

$$\frac{dq}{d\tau} = j_{iAg} + j_{iBg} - \gamma_e j_{eg}, \tag{1}$$

where q is the charge on the graphene sheet, j_{ikg} is the ion collection current (where *k* refers to A or B type of ion), and j_{eg} is the electron collection current. Equation (1) represents the charged developed on the graphene sheet on account of accretion of ions and electrons on the graphene sheet surface (γ_e is the sticking coefficient of electrons).

B. Kinetic equations of the plasma species

$$\frac{dn_{ik}}{dt} = \lambda_k n_k - \alpha_k n_e n_{ik} - n_g j_{ikg,} \tag{2}$$

$$\frac{dn_k}{dt} = \alpha_k n_e n_{ik} - \lambda_k n_k - n_g \left(1-\gamma_{ik}\right) j_{ikg} - n_g \gamma_k j_{kg,} \tag{3}$$

$$\frac{dn_{i-}}{d\tau} = \beta_r \frac{dn_s}{d\tau} = \sum_k^{A,B} \lambda_k n_k - \sum_k^{A,B} \alpha_k n_e n_{ik} - \gamma_e n_g j_{eg}, \tag{4}$$

$$\frac{dn_e}{d\tau} = (1-\beta_r)\frac{dn_s}{d\tau} = \sum_k^{A,B} \lambda_k n_k - \sum_k^{A,B} \alpha_k n_e n_{ik} - \gamma_e n_g j_{eg}, \tag{5}$$

where n_{ik}, n_k, n_{i-}, and n_e are the number densities of ions (of type *k*), neutrals (of type *k*), negatively charged ions and electrons, respectively. $\beta_r = \frac{n_{SF_6^-}}{n_{C^+}}$, is the relative density of negatively charged ions.

Equation (2) represents the growth rate of ions (here, k refers to A or B type of ion) in plasma due to ionisation of neutrals (λ_k is the coefficient of ionization), recombination of electrons and ions (α_k is the coefficient of recombination), and ion collection current at the graphene sheet surface. Equation (3) represents the growth rate of neutrals of type k in plasma on account of recombination of electrons and ions, neutralisation of atoms collected at the graphene sheet surface, account of electron-ion recombination, and neutral collection current (j_{kg}) [4].

Equations (4) and (5) represents the growth rate of negatively charged ions and electrons in plasma, respectively on account of ionization of neutral atoms, electron –ion recombination and electron collection current at the surface of graphene sheet.

C. Growth rate equation of the mass of the graphene sheet

$$\frac{dm_g}{d\tau} = m_A \gamma_A j_{Ag} + m_{iA} \gamma_{iA} j_{iAg}, \qquad (6)$$

where $m_g (= \rho_g (l_g \times A_g))$, ρ_g, and A_g are the mass, density and area of the graphene sheet, respectively. Equation (6) represents the increase in mass of the graphene sheet due to accretion of neutrals and ions of type A.

III. Results and Discussion

We have solved Equations (1)-(6) simultaneously for the typical glow discharge parameters with appropriate boundary conditions i.e., $n_{e0} = (1-\beta_r) n_{s0}$, $n_{s0} = 10^{10} cm^{-3}$, $n_{iA0} = n_{iB0} = n_{s0}$, $n_{i-0} = \beta_r n_{s0}$, $n_{A0} = n_{B0} = n_{s0}$, $T_{e0} = T_{-0} = 0.8eV$, $T_{i0} = 2200K$, $T_{n0} = 2000K$, and $\gamma_e = \gamma_{ik} = \gamma_k = 1$. The other parameters of the text are $m_{iA} \approx m_A$ =12 amu (Carbon), $m_{iB} \approx m_B$ =20 amu (Neon), m_{i-}= 146 amu (sulphur hexafluoride), $\alpha_{A0} \approx \alpha_{B0}$=$10^{-7}$ cm^3/sec.

Figure 1 shows the time variation of the area (A_g) of the graphene sheet for different relative number densities of negatively charged ions (β_r =0.1, 0.2, 0.3, 0.4). It can be seen from Figure 1 that the area of the graphene sheet decreases with increase of the relative number densities of negatively charged ions in the plasma. This is because the neutral atoms available for accretion on the graphene sheet surface decreases as the relative number densities of negatively charged ions increases (cf. Figure 2). Figure 2 shows the time variation of the number density of neutral atoms of type A for different relative number densities of negatively charged ions (β_r =0.1, 0.2, 0.3, 0.4). It can be seen from Figure 2 that on increasing the relative negatively charged ion density, the neutral atom density of type A atoms decays faster. This is because, on increasing the negatively charged ion density in plasma, for a fixed value of positive ion density, more and more neutral atoms ionises to produce ions and electrons. Thus, the neutral atoms

available for accretion decreases and as a result the area of the graphene sheet decreases.

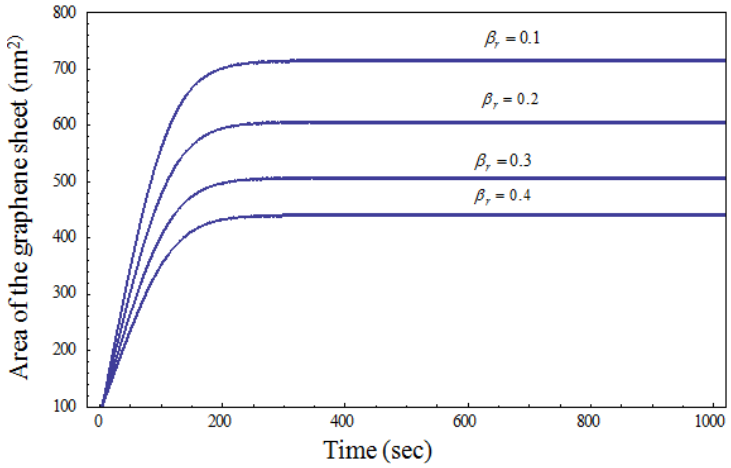


Figure1. Time variation of the area of the graphene sheet for different relative number densities of negatively charged ions (β_r =0.1, 0.2, 0.3, 0.4).

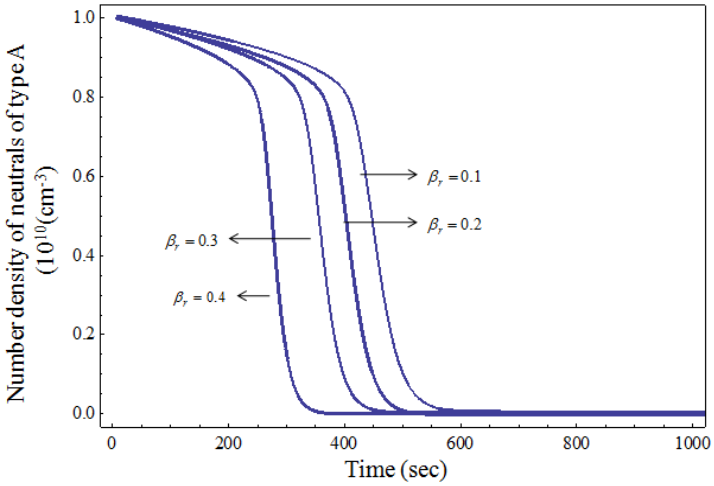


Figure2. Time variation of the number density of neutrals of type A for different relative number densities of negatively charged ions (β_r =0.1, 0.2, 0.3, 0.4).

References

[1] S. J. Choi and M. J. Kushner, J. Appl. Phys. **74**, 853 (1993).

[2] K. Ostrikov, S. Kumar, and H. Sugai, Phys. Plasmas **8**, 3490 (2001).

[3]D. Levko and L. L. Raja, Plasma Sources Sci. Technol. **25** (2016) 064003.

[4] M. S. Sodha, S. Misra, S. K. Mishra, and S. Srivastava, J. Appl. Phys. **107**, 103307 (2010).

J. Inst. Eng. India Ser. B
DOI 10.1007/s40031-017-0280-x

ORIGINAL CONTRIBUTION

Multiobjective Economic Load Dispatch in 3-D Space by Genetic Algorithm

N. K. Jain[1] · **Uma Nangia**[1] · **Iqbal Singh**[2]

Received: 12 August 2015 / Accepted: 13 April 2017
© The Institution of Engineers (India) 2017

Abstract This paper presents the application of genetic algorithm to Multiobjective Economic Load Dispatch (MELD) problem considering fuel cost, transmission losses and environmental pollution as objective functions. The MELD problem has been formulated using constraint method. The non-inferior set for IEEE 5, 14 and 30-bus system has been generated by using genetic algorithm and the target point has been obtained by using maximization of minimum relative attainments.

Keywords MELD · Non-inferior set · Maximization of minimum relative attainments · Target point

List of Symbols

$a_i, b_i, c_i,$	Fuel cost coefficients of the ith generator
$d_i, e_i, f_i,$	Pollution coefficients of ith generator
P_D	Total load demand
P_i, P_j	Real power injections at the ith, jth generator
P_{gi}	Real power generation of ith generator
$P_{gi\,\min}$	Minimum real power generation of ith generator
$P_{gi\,\max}$	Maximum real power generation of ith generator
F_C	Total cost of generation in $/h
F_E	Environmental pollution in kg/h
E_i	Amount of pollution in terms of oxides of nitrogen emissions for the ith generator
F_L	System transmission losses
B_{ij}	Loss coefficients
Z	Multiobjective function
τ_i	Minimum relative attainment of ith objective
$Z_{iatZ(i+k)}$	Worst feasible value of ith objective
NG	Total number of generators
$g_i(X)$	Inequality constraint

Introduction

Economic load dispatch [1, 2] allocates loads to plants at minimum cost while meeting the constraints. It is an optimization problem which minimizes the total fuel cost of all committed plants while meeting the demand and losses. The optimal power system operation is achieved when various objectives of power systems simultaneously attain their minimum values. In this paper, three objectives of power systems—cost of generation (F_c), system transmission losses (F_L), environmental pollution (F_E) have been considered. These are conflicting in nature and cannot be handled by single objective optimization techniques. Single objective optimization techniques give optimal solution in respect of a single aspect but the values of other objectives may be intolerably bad. Therefore, the way out lies in multiobjective approach [3–6] to problem solving. Recently, Genetic Algorithm (GA) has been implemented to solve various power systems problems-economic load dispatch, multiobjective economic load dispatch, optimal power flow etc. genetic algorithm is an intelligent optimization technique and is capable of locating the global optima. Some authors [7] made the review on the current development techniques in Genetic Algorithm. In this paper, the authors have explained the theoretical aspects of

✉ N. K. Jain
uma.nangia62@gmail.com

[1] Department of Electrical Engineering, Delhi Technological University, Delhi 110042, India

[2] Brickworks Limited., New South Wales, Australia

Published online: 05 August 2017

genetic algorithms and their applications. Song et al. [8] used Fuzzy Logic Controlled Genetic Algorithm (FCGA) to solve environment economic dispatch problem. The authors tested it on six generator test system and compared with conventional GA and Newton–Raphson method and observed that the proposed method provided improved performance. Nanda and Narayanan [9] used GA to solve ELD problem considering line flow constraints. Hong and Li [10] studied the effectiveness of GA for a system consisting of multiple cogenerators and multiple buyers in a deregulated market. They implemented successfully on IEEE 30 and IEEE 118-bus system. Abido [11] proposed a novel approach based on GA for solving ELD problem considering environmental objectives. His method provided a representative and manageable non-inferior set. Hong and Li [12] used GA for short-term scheduling of an autonomous system containing diesel generators, wind power, solar photovoltaics and batteries. They compared their result with Simulated Annealing (SA) and found that GA required fewer iterations. Sunny and David [13] proposed Constrained Elitist Genetic Algorithm (CEGA) for scheduling of a Nigerian power plant. The proposed approach was found to perform better than conventional genetic algorithm. Jain et al. [14] formulated Multiobjective Economic Load Dispatch (MELD) problem by constraint method and generated the non-inferior set in 2D space using GA. The Target Point (TP) was obtained by maximization of minimum relative attainments method. Kaur et al. [15] implemented GA to minimize the fuel cost of generators on two different sets of problems with two different load demands. Significant reduction in fuel cost was achieved.

The ideal situation where one would like to operate the power systems is one where all the three objectives—F_C, F_L and F_E attain their minimum values simultaneously. Such a point is called the Ideal Point (IP) and is represented by ($F_{C\ min}$, $F_{L\ min}$, $F_{E\ min}$) in 3D space. Such a point is infeasible. The solution of multiobjective optimization gives a number of solutions called non-inferior solutions. Power system analyst chooses one of these solutios as the Target Point (TP) as per his satisfaction and requirement.

In this paper, MELD problem considering—F_C, F_L, F_E has been formulated using constraint method. Non-inferior solutions have been generated using Genetic Algorithm and the TP has been obtained by Maximization of Minimum Relative Attainments (MMR) method.

Genetic Algorithm

Genetic Algorithms are a way of solving problems by mimicking the same processes Mother Nature uses. They use the same combination of selection, recombination and mutation to evolve a solution to a problem. Genetic algorithms tend to thrive in an environment in which there is a very large set of candidate solutions and in which the search space is uneven and has many hills and valleys. A population of points (usually double the size of design variables) is used for starting the procedure instead of a single design point. Therefore, GA is less likely to get trapped at a local optimum. GAs uses only the value of objective function and not the derivatives in search procedure.

In GAs the design variable are represented as strings of binary variables that correspond to the chromosomes in natural genetics. The objective function value corresponding to a design vector plays the role of fitness in natural genetics. In every new generation, a new set of strings is produced by using randomized parents selection and crossover from the old generation. Although randomized, GAs are not simple random search techniques. They efficiently explore the new combinations with the available knowledge to find a new generation with better fitness or objective function value.

MELD in 3-D Space

The objective function for cost of generation F_c is:

$$F_c = \sum_{i=1}^{NG} a_i P_i^2 + b_i P_i + c_i \quad \text{i} = 1, 2. \ldots . .\text{NG} \tag{1}$$

The transmission loss is expressed as:

$$F_L = \sum_{i}^{NG} \sum_{j=1}^{NG} P_i B_{ij} P_j \tag{2}$$

The objective function to minimize environmental pollution is given as.

$$F_E = \sum_{i=1}^{NG} d_i P_i^2 + e_i P_i + f_i \qquad \text{i} = 1, 2. \ldots . .\text{NG} \tag{3}$$

Problem Formulation of MELD in 3-D Space

In 3-D space, the problem has been formulated using constraint method as:

Minimize

$$F_c(P_{gi}) \tag{4a}$$

s.t.

$$P_{gi\,\min} < P_{gi} < P_{gi\,\max} \tag{4b}$$

$$P_D + P_L - \sum_{i=1}^{NG} P_{gi} = 0 \tag{4c}$$

$$F_L \leq L_1 \tag{4d}$$

$$F_E \leq E_1 \tag{4e}$$

where, E_1 lies between $F_{E\,\min}$ and $F_{E\,\max} L_1$ lies between $F_{L\,\min}$ and $F_{L\,\max}$.

The non-inferior set in 3-D space has been obtained by minimizing cost keeping loss and pollution fixed at values

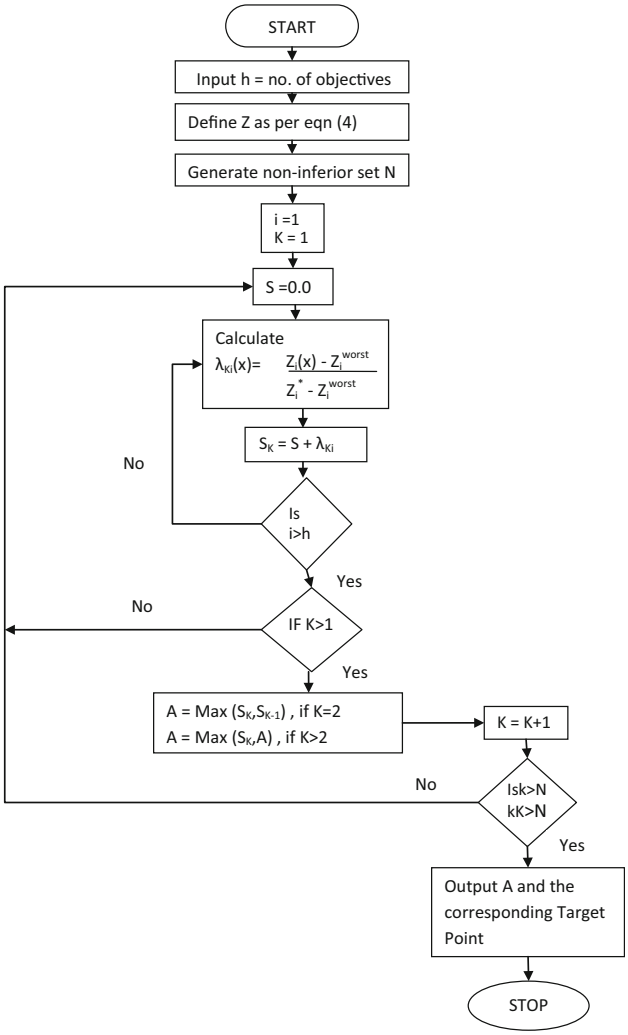


Fig. 1 Flow chart for maximization of minimum relative attainments

between their ranges. The domain in which system transmission losses and environmental pollution are supportive has also been explored.

The range of emission F_E which lies between $F_{E\,min}$ and $F_{E\,max}$ has been obtained by solving the following problem: Minimize

$$F_E(P_{gi}) \tag{5a}$$

s.t.

$$P_{gi\,min} < P_{gi} < P_{gi\,max} \tag{5b}$$

$$P_D + P_L - \sum_{i=1}^{NG} P_{gi} = 0 \tag{5c}$$

$$F_L \leq L_1 \tag{5d}$$

where, L_1 lies between $F_{L\,min}$ & $F_{L\,max}$.

Maximization of Minimum Relative Attainments

This method [6, 13] assumes that all the objectives are being minimized and seeks the solution which maximizes the minimum relative attainment, $\tau_i(x)$ by any objective $Z_i(x)$ of its ideal reference value $Z_{i\ min}$ relative to its worst feasible value $Z_{iatZ(i+k)}$.

$$\tau_i(x) = \frac{Z_{i(x)} - Z_{iatZ(i+k)}}{Z_{i\min} - Z_{iatZ(i+k)}} \qquad i = 1, 2, -, k,\ k+1 \ldots\ldots h \tag{6}$$

where, h is the number of objectives. This method is explained in the flow chart as shown in Fig. 1.

Computational Results in 3-D Space

The non-inferior set and minimum relative attainments for IEEE 5, 14 and 30 bus systems in 3-D space are shown in Tables 1, 2 and 3 respectively. Columns 2, 4 and 6 of these tables show non-inferior set whereas columns 3, 5 and 7 show the relative attainments of F_c, F_L and F_E respectively. Row 1 of Table 1 reveals that F_E has minimum value of

Table 1 Non-inferior set and minimum relative attainments in 3-D space (IEEE 5-bus system)

S.no. (1)	F_C ($/h) (2)	τ_C (3)	F_L (MW) (4)	τ_L (5)	F_E (kg/h) (6)	τ_E (7)	Σ_τ (8)
1	762.668	0	5.060	1	120.7	1	2
2	762.273	0.2320	5.065	0.9642	121.4	0.9278	2.1240
3	762.007	0.3890	5.070	0.9285	122	0.8650	2.1820
4	761.824	0.4976	5.075	0.8928	122.5	0.8144	2.2040
5	*761.668*	*0.5896*	*5.080*	*0.8571*	*123*	*0.7628*	*2.2090*
6	761.536	0.6674	5.085	0.8214	123.5	0.7110	2.1998
7	761.466	0.7087	5.090	0.7850	123.8	0.6800	2.1737
8	761.423	0.7340	5.095	0.7500	124	0.6590	2.1430
9	761.326	0.7912	5.10	0.7140	124.5	0.6080	2,1130
10	760.999	0.9840	5.15	0.3570	127.6	0.2886	1.6296
11	760.972	1	5.20	0	130.4	0	1

Table 2 Non-inferior set and minimum relative attainments in 3-D space (IEEE 14-bus system)

S.no. (1)	F_C ($/h) (2)	τ_C (3)	F_L (MW) (4)	τ_L (5)	F_E (kg/h) (6)	τ_E (7)	Σ_τ (8)
1	1172.500	0	7.218	1	499	1	2
2	1169.35	0.1330	7.239	0.9610	504	0.8480	1.9420
3	*1163.28*	*0.3920*	*7.286*	*0.8740*	*508*	*0.7270*	*1.9930*
4	1161.80	0.4540	7.377	0.7060	512	0.6060	1.7660
5	1157.42	0.6411	7.432	0.6051	516	0.4848	1.7310
6	1153.62	0.8020	7.483	0.5110	520	0.3630	1.6760
7	1152.90	0.8330	7.532	0.4206	524	0.2424	1.4963
8	1151.03	0.9128	7.653	0.1970	528	0.1212	1.2310
9	1148.98	1	7.760	0	532	0	1

Table 3 Non-inferior set and minimum relative attainments in 3-D space (IEEE 30-bus system)

S.no. (1)	F_C ($/h) (2)	τ_C (3)	F_L (MW) (4)	τ_L (5)	F_E (kg/h) (6)	τ_E (7)	Σ_τ (8)
1	1281.30	0	8.830	1	523	1	2
2	1280.47	0.0838	9.020	0.8330	528	0.8790	1.7958
3	1276.60	0.4747	9.290	0.6660	533	0.7080	1.8407
4	*1273.65*	*0.7720*	*9.440*	*0.5000*	*538*	*0.6130*	*1.8850*
5	1272.16	0.9232	10.002	0.3300	543	0.2509	1.5041
6	1271.60	0.9797	10.004	0.1660	548	0.2560	1.4017
7	1271.40	1	10.408	0	553	0	1

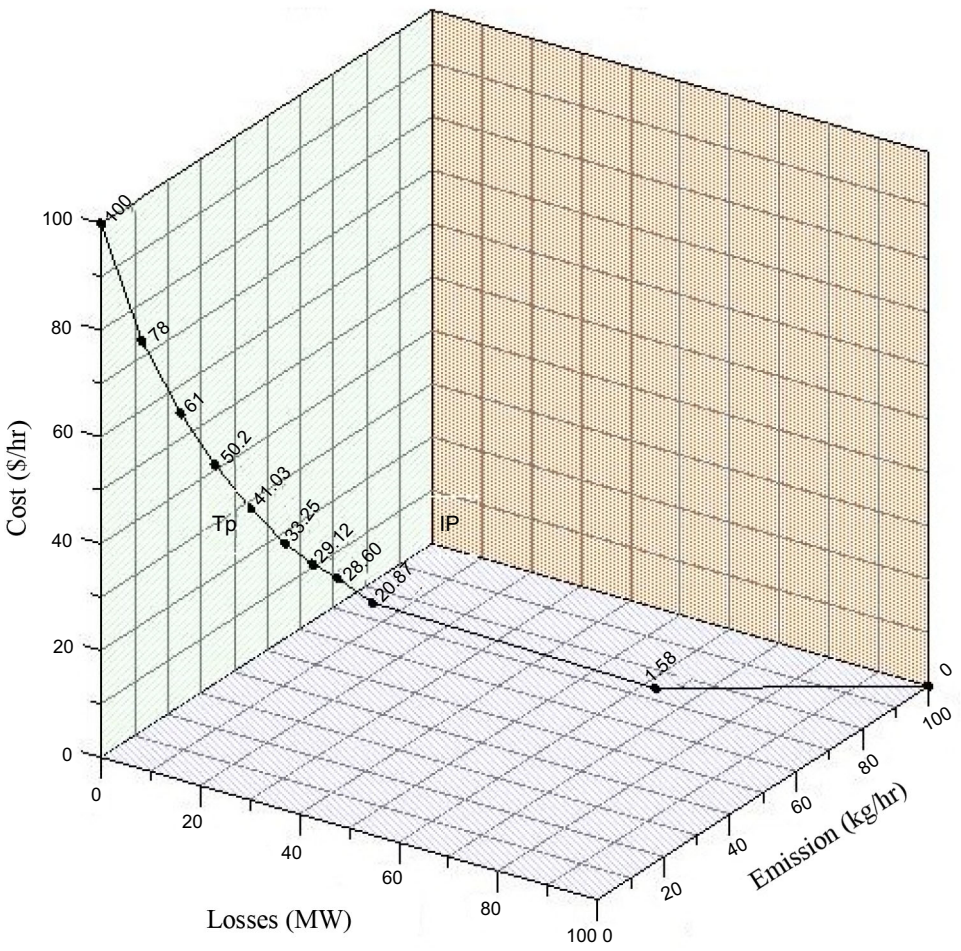


Fig. 2 Non-inferior set of IEEE 5 bus system in 3-D space

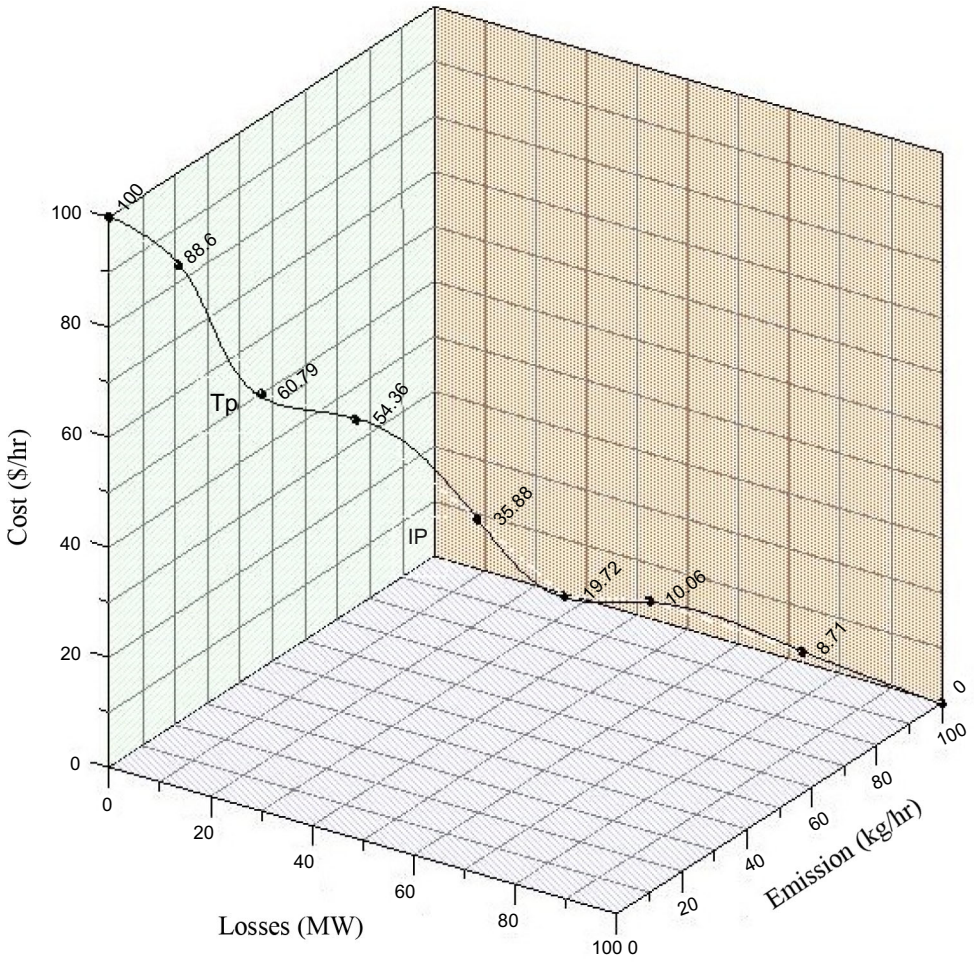


Fig. 3 Non-inferior set of IEEE 14 bus system in 3-D space

120.7 kg/h. F_L has minimum value of 5.06 MW at the same point. However, F_C for this point is 762.668 $/h which is not minimum. So, this cannot be the TP. Minimum value of F_C is 760.972 $/h (Row 11) at which F_E and F_L are not minimum. So, this also cannot be the TP. This means neither the solutions corresponding to row 1 nor row 11 can serve the purpose of TP. In order to search for TP, calculation of minimum relative attainments have been carried out.

The relative attainments of the objectives are added and the result is shown in the last column of Table 1. TP is one for which the sum is maximum as highlighted (italics) above in row 5. It represents the alternative corresponding to maximum of minimum relative attainments. TP achieved for 5-Bus system in 3-D space is $F_C = 761.668$ $/h, $F_L = 5.080$ MW and $F_E = 123$ kg/h.

Row 1 of Table 2 reveals that F_E has minimum value of 499 kg/h. F_L has minimum value of 7.218 MW at the same point. However, F_C for this point is 1172.50 $/h which is not minimum. So, this cannot be the target point. Minimum value of F_C is 1148.98 $/h (Row 9) at which F_E and F_L are not minimum. So, this also cannot be the TP. This means neither the solutions corresponding to row 1 nor row 9 can serve the purpose of TP. Therefore Minimum relative attainment of each objective has been calculated to locate TP. The relative attainments of the objectives are added and the result is shown in the last column of Table 2. Target Point is one for which the sum is maximum as highlighted (italics) above in row 3. It represents the alternative corresponding to maximum of minimum relative attainments. TP achieved for 14-Bus system in 3-D space is $F_C = 1163.28$ $/h, $F_L = 7.286$ MW and $F_E = 508$ kg/h.

Row 1 of Table 3 reveals that F_E has minimum value of 523 kg/h. F_L has minimum value of 8.83 MW at the same point. However, F_C for this point is 1281.30$/h which is not minimum. So, this cannot be TP. Minimum value of F_C is 1271.40$/h (Row 7) at which F_E and F_L are not minimum. So, this also cannot be the TP. This means neither the solutions corresponding to row 1 nor row 7 can serve the purpose of TP. Therefore, minimum relative attainment of each objective has been calculated to locate TP. The relative attainments of the objectives are added and the result is shown in the last column of Table 3. The Target Point is one for which the sum is maximum as highlighted

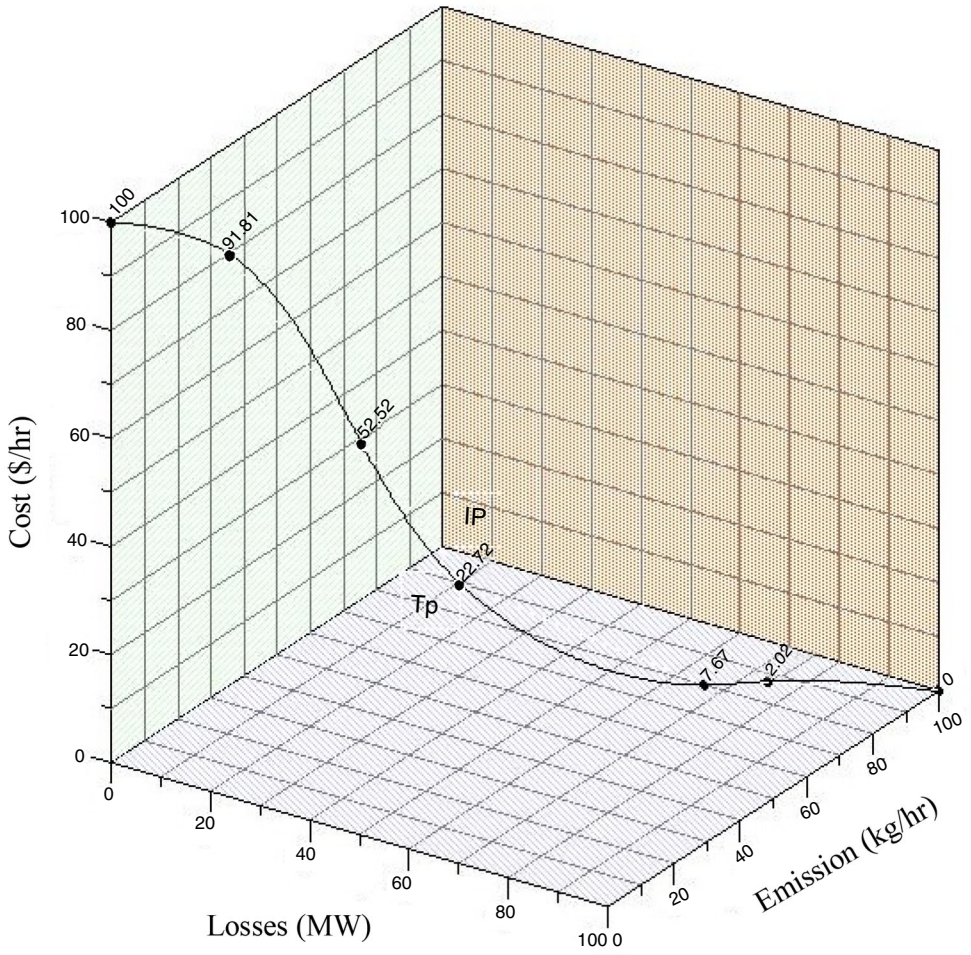


Fig. 4 Non-inferior set of IEEE 30 bus system in 3-D space

(italics) above in row 4. It represents the alternative corresponding to maximum of minimum relative attainments. TP for 30-Bus system in 3-D space is $F_C = 1273.65$ \$/h, $F_L = 9.44$ MW and $F_E = 538$ kg/h.

Discussion

The IP for 5, 14 and 30 bus systems in 3-D space are (760.972 \$/h, 5.060 MW, 120.7 kg/h), (1148.98 \$/h, 7.218 MW, 499 kg/h) and (1271.40 \$/h, 8.83 MW, 523 kg/h) respectively. However, it can be realized that the ideal point as defined and located above cannot be achieved in practice. So, an attempt is made to obtain the TP which gives equal satisfaction levels for all the objectives. Such a point is obtained by the use of MMR. The TPs obtained in this paper compare well with the results reported in [9].

The TP Point in 3-D space have been displayed by 3-D graph drawn with MATLAB. In these graphs, the origin represents the ideal points i.e. ($F_{C\ min}$, $F_{L\ min}$, $F_{E\ min}$). X-axis represents the % distance of the system transmission losses F_L from the origin, i.e.

$$\%\ \text{distance from origin along X-axis} = \frac{F_L - F_{L\min}}{F_{L\max} - F_{L\min}} \times 100 \quad (7)$$

Similarly, Y-axis represents the % distance of F_C from the origin, i.e.

$$\%\ \text{distance from origin along Y-axis} = \frac{F_C - F_{C\min}}{F_{C\max} - F_{C\min}} \times 100 \quad (8)$$

and, Z-axis represents the % distance of pollution F_E from the origin, i.e.

$$\%\ \text{distance from origin along Z-axis} = \frac{F_E - F_{E\min}}{F_{E\max} - F_{E\min}} \times 100 \quad (9)$$

The non-inferior sets of IEEE 5, 14 and 30 bus systems are scaled and plotted in Figs. 2, 3 and 4 respectively. 3-D curve is also drawn connecting these points. In these graphs, the target point is marked as TP.

Conclusions

Constraint method has been used to generate non-inferior set in 3-D space for IEEE 5, 14 and 30 bus systems. This technique is computationally fast and has no limitation in handling more than three objectives. MMR has been used to obtain the TP. It has been observed that if cost of generation (F_C) increases then system transmission losses (F_L) and environmental pollution decrease and vice versa. However, the objectives may not always follow the conflicting and supportive behaviors in all the domains. It was observed that computational effort can be minimized by choosing smaller population size and lesser value of stall generations.

References

1. C.L. Wadhwa, *Electrical Power System* (New Age International Publisher Ltd, New Delhi, 2009)
2. W.D. Steveson, *Elements of Power System Analysis* (McGraw Hill Book Co., New York, 1962)
3. J.L. Cohon, *Multi-objective Programming and Planning* (Academic Press, New York, 1978)
4. S. Marglin, *Public Investment Criteria* (MIT Press, Cambridge, 1967)
5. J.L. Cohon, D. Marks, Multiobjective screening models and water resources investment. Water Resour. Res. **9**, 826 (1973)
6. U. Nangia, N.K. Jain, C.L. Wadhwa, Multiobjective load flow studies through maximization of minimum relative attainments. J. IE(I) **77**, 154–159 (1996)
7. N. Chaiyaratana, A.M.S. Zalzala Recent developments in evolutionary and genetic algorithms: theory and applications. In: Second International Conference on Genetic Algorithms in Engineering Systems: Innovations and Applications, 1997, GALESIA 97 (Conf. Publ. No. 446) 2–4 Sept. 1997, pp. 270–277
8. Y.H. Song, G.S. Wang, P.Y. Wang, A.T. Johns, Environmental/economic dispatch using fuzzy logic controlled genetic algorithms. IEE Proc. Gener. Transm. Distrib. **144**(4), 377–382 (1997)
9. J. Nanda, R.B. Narayanan, Application of genetic algorithm to economic load dispatch with line flow constraints. Int. Electr. Power Energy Syst. **24**, 723–729 (2002)
10. Y.Y. Hong, C.L. Li, Genetic algorithms based economic dispatch for cogeneration units considering multiplant multibuyer wheeling. IEEE Trans. Power Syst. **17**(1), 134–140 (2002)
11. M.A. Abido, A novel multiobjective evolutionary algorithm for environmental economic power dispatch. Electr. Power Syst. Res. **65**(1), 71–81 (2003)
12. Y.Y. Hong, C.L. Li, Short term real power scheduling considering fuzzy factor in an autonomous system using GA. IEEE Trans. Gener. Transm. Distrib. **152**(6), 684–691 (2006)
13. O. Sunny, C. David, Constrained elitist genetic algorithm for economic load dispatch: case study on nigerian power system. Int. J. Comput. Appl. **76**(5), 27–33 (2013)
14. N.K. Jain, U. Nangia, J. Jain GA based multiobjective economic load dispatch by maximization of minimum relative attainments. In: Fifth India International Conference on Power Electronics (IICPE-2012), DTU, Dec. 6–8, 2012, pp. 25–28
15. A. Kaur, H.P. Singh, A. Bhardwaj Analysis of economic load dispatch using genetic algorithm. Int. J. Appl. Innov. Eng. Manag. **3**(3), March 2014. ISSN2319-4847

Volume 5 Issue 2 (2017) 279-282 ISSN 2347 - 3258
International Journal of Advance Research and Innovation

Optimum yield parameters of MWCNT/MnO_2 nanocomposite

Md Zakir Hussain[1], Sabah Khan[1], Abhishek Gaur[2], Mohd Shuaib[3,*]
[1]Department of Mechnical Engineering, Jamia Millia Islamia, New Delhi-25, India
[2]Department of Mechnical Engineering, Ambedkar Institute of Technology, Sakharpur, New Delhi, India
[3] Department of Mechnical Engineering, Delhi Technological University, Delhi, India

Article Info
Article history:
Received 25 January 2017
Received in revised form
20 February 2017
Accepted 28 February 2017
Available online 15 June 2017

Keywords: Multiwalled carbon nanotubes; yield; solution method; taguchi method;

Abstract
The objective of this study is to illustrate the optimum parameters adopted to evaluate maximum yield of MWCNT/MnO_2 nanocomposite. In this paper, the effect of stirring time, Concentration of H_2SO_4 (aq) solution, solution temperature and drying time on yield of MWCNT/MnO_2 nanocomposite was investigated. The orthogonal array, signal-to-noise ratio, and percentage contribution of all parameters are employed to study the yield of MWCNT/MnO_2 nanocomposite. After conducting the experiments the yield was measured and Signal to noise ratio was calculated. With the help of graphs, optimum parameter values were obtained at parameter level $A_2B_2C_2D_1$.
The percentage contributions of parameters and regression analysis confirmed the concentration of H_2SO_4 has significant effect on yield of MWCNT/MnO_2 powder.

1. Introduction

Taguchi method optimizes the variation occurs in a process with the help of design of experiments. The objective of Taguchi method is to produce high quality product at low cost and the product or process is most robust with respect to noise factors. Taguchi's approach to parameter design provides the design engineer with an efficient method for determining near optimum design parameters for performance and cost [1, 2]. The Taguchi method use orthogonal arrays from design of experiments theory to study many variables with a small number of experiments. Using orthogonal arrays significantly reduces the number of experimental configurations to be studied. Gh. Tahmasebi et al.[3] presented optimization of Nano calcium carbonate production parameters to achieve the optimum production rate by using Taguchi method. It was found that the optimum level of process parameters were solution flow rate of 9 lit/min, gas flow rate of 20 lit/min, and solution concentration of 70 gr/lit and the production rate was enhanced by 168% in comparison to the mean value of the experimental results. I. Lozić et al. used Taguchi method of experimental design to evaluation the spray drier process parameters influence on particle size diameter of alumina powder [4]. The analysis of the results showed that in order to achieve the smallest particle size the best combination of parameters for is lower concentration and pump performance as well as higher value of inlet temperature and spray flow rate. Sheng-Meng Wang et al. [5]applied Taguchi's quality engineering to the in-situ supercritical fluid extraction and chemical derivatization of amphetamines from water to afford the optimal experimental conditions and hence achieved the highest recoveries of the analytes and the best robustness of the quantitation out of the least number of experimental runs. Achyut K. Pandaa used Taguchi method to identify the factors and their interactions that may affect the thermo-catalytic degradation of waste polypropylene to liquid fuel in a batch reactor [6]. The yield of liquid fuel in this process was greatly influenced by factors such as temperature, catalyst concentration and acidity of catalyst. From regression model, It was found that yield of liquid fuel in this process were highly dependent on temperature followed by acidity of catalyst and catalyst concentration.
S Kamaruddin et al. attempted to improve the quality characteristic of an injection molding product by optimizing the injection molding parameters using the Taguchi method [7]. The analysis of the results shows that the optimal combination for low shrinkage are low melting temperature, high injection pressure, low holding pressure, long holding time and long cooling time. Arshad Noor Siddiquee et al. focused on optimizing deep drilling parameters based on Taguchi method for minimizing surface roughness and experiments were conducted on CNC lathe machine using solid carbide cutting tool on material AISI 321 austenitic stainless steel [8]. Four cutting parameters such as cutting fluid, speed, feed and hole depth, each at three levels except the cutting fluid at two levels were considered. The cutting parameters such as speed, feed, and cutting fluid mainly influenced the surface roughness. Zahid A. Khan et al. investigated the effect of the wire electrical discharge machining process parameters on the surface roughness average and the kerf width of the stainless steel (SS 304) [9]. The pulse ON time is found to be the most influential factor for both the surface roughness and the kerf width. The analysis of variance showed that the pulse ON time was the most significant controlled factor for affecting the multiple responses in the electrical discharge machining. P. Jayaraman et al. presented a novel approach for the optimization of machining parameters on turning of AA 6063 T6 aluminium alloy with multiple responses based on orthogonal array with grey relational analysis [10]. They found that the feed rate, depth of cut were prominent factors which affect the turning of aluminium alloy. Md. Israr Equbal et al. studied hot closed die forging of spring saddle and DEFORM TM 3D FEM based simulation software was used to examine the effect of design and process parameters on forging load and billet temperature loss [11]. Grey relational analysis, along with Taguchi method were employed to optimize the forging load and billet temperature loss simultaneously.
In the present research, optimized yield parameters of MWCNT/MnO_2 nanocomposite has been investigated without consideration of interaction effect based on the Taguchi's method which is a powerful tool used in design of experiments.

2. Process optimization by using Taguchi method

2.1 Selection of yield parameters with their levels

Total nine experiments were conducted between 2 hr.-4hr. stirring time, 1.9M-2.1 M concentration of H_2SO_4(aq), 75 ^{0}C- 95 ^{0}C solution temperature, and 12 hr.-48 hr. drying time. The yield parameter and their levels is shown in table 1. Taguchi's L9 orthogonal array was used to design the experiments with four factors such as stirring time, Concentration of H_2SO_4 (aq) solution, solution temperature and drying time at three levels. Taguchi's L9 Orthogonal Array is shown in table2.

Table1: Yield parameters and their levels

Parameter	Level-1	Level-2	Level-3
Stirring time (A)	2	3	4
Concentration of H_2SO_4(aq) (B)	1.9	2.0	2.10
Solution temperature (C)	75	85	95
Drying Time (D)	12	24	48

Table 2: L9 Orthogonal Array

Parameter/Level			
1	1	1	1
1	2	2	2
1	3	3	3
2	1	2	3
2	2	3	1
2	3	1	2
3	1	3	2
3	2	1	3
3	3	2	1

***Corresponding Author,**
E-mail: shuaib89141@gmail.com
All rights reserved: http://www.ijari.org

2.1.1 Materials

Multiwall Carbon nanotubes (purity > 95%) used as filler material and purchased from Redex Nano Laboratory, Uttar Pradesh, India.



Fig. 1: MWCNT



Fig.2: $KmnO_4$

2.1.2 Synthesis of powder of MWCNT/MnO_2 nanocomposite

A novel technique [12, 13] has been used to synthesize MWCNT/MnO_2 nanocomposite. In short, the experimental synthesis process of the nanocomposite is described below.

A 500-ml beaker is charged with 0.1 gram multiwall carbon nanotube immersed in 250 ml at 1.9 M- 2.1M concentration level of boiling sulphuric acid (H_2SO_4) aqueous solution at stirring time 2 hr.- 4 hr. After dispersion, 4 gram $KMnO_4$ powder were added at different temperature parameter level ie. 75^0C-95^0C along with stirring. The yield was observed and the solution color changed from purple to brown. The system was then cooled down to room temperature. The obtained yield was washed with de-ionized water and acetone to remove the remaining ions, and then dried at 65 ^{0}C in a laboratory oven for 12hr.-48 hr. The experimental setup is shown in figure 3.



Fig.3: Experimental setup

3.Chemical characterization of MWCNT/ MnO_2 nanocomposite powder

3.1 XRD pattern of MWCNT/ MnO_2 nanocomposite

X-ray diffraction is non-destructive technique which gives the information about the crystallographic structure. The crystallographic structure of the nanocomposite was investigated MiniFlex, with Cu Kα radiation operated at 30kV and15mA, Start-10^0 Stop-70^0 and Step increment 0.02^0.

Figure 4(a) shows the xrd pattern of MWCNT. The XRD pattern of the MWCNT shows diffraction peaks at 26.6^0 indexed at (002) reflection of graphite [12-14].

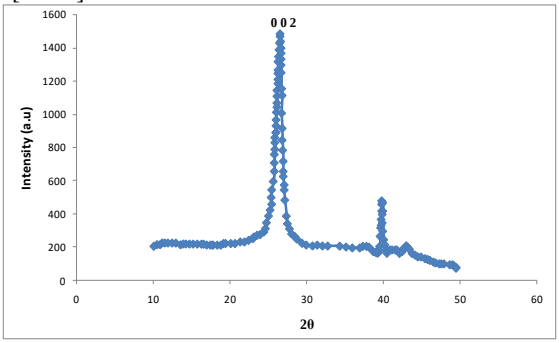


Fig. 4(a): XRD Pattern of MWCNT

The XRD data of MWCNT/MnO2 nanocomposite is shown in figure: 4(b). In addition to (002) reflection, the other diffraction peak can be indexed to the tetragonal α-MnO2 single-crystal structure, space group: I4/m (87) with lattice constants of a = 0.982 nm and c = 0.2863 nm and it also confirmed the formation of MWCNT/MnO2 nanocomposite [12, 13].

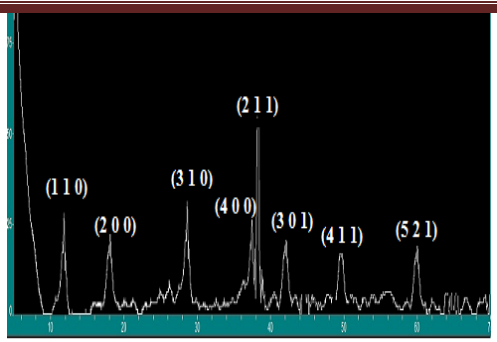


Fig.4 XRD pattern of 5 wt% MWCNT/MnO_2 nanocomposite

4. Experimental results analysis and discussion

4.1 Signal to noise ratio

The signal to noise ratio (S/N ratio) was used to measure the sensitivity of the quality characteristic being investigated in a controlled manner. The S/N ratio can be defined as S/N ratio [14].

$$\eta = -10\log(MSD) \quad (1)$$

Where, *MSD: mean*-square deviation for the response.

To obtain optimum yield, the-higher-the-better response has been used. Table 3 shows the experimental response yield data and the corresponding S/N ratio.

Table3: Experimental yield and S/N ratio results for L9 orthogonal array

	Parameter/Level					
Experiment No.	Stirring time (A)	Concentration (B)	Solution temperature (C)	Drying Time (D)	Yield (gm)	S/N ratio
1	1(2)	1(1.9)	1(75)	1(12)	1.80	5.249022
2	1(2)	2(2.0)	2(85)	2(24)	1.94	5.756035
3	1(2)	3(2.1)	3(95)	3(48)	1.88	5.483157
4	2(3)	1(1.9)	2(85)	3(48)	1.85	5.343435
5	2(3)	2(2.0)	3(95)	1(12)	1.96	5.845121
6	2(3)	3(2.10)	1(75)	2(24)	1.89	5.529236
7	3(4)	1(1.9)	3(95)	2(24)	1.81	5.153571
8	3(4)	2(2.0)	1(75)	3(48)	1.89	5.529236
9	3(4)	3(2.10)	2(85)	1(12)	1.87	5.436832

Figure 5 shows the S/N response graph for total yield. The initial optimum combination of parameter level is $A_2B_2C_2D_1$ as shown in table 4. Fig.6 to Fig.9 shows the variation of yield with different parameters at different levels.

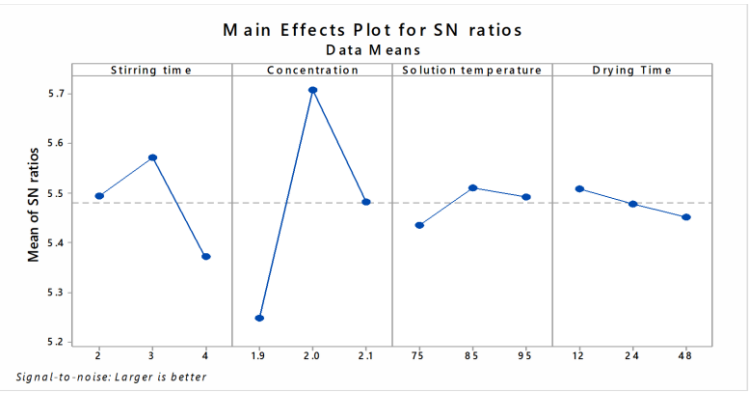


Fig. 5: S/N response graph

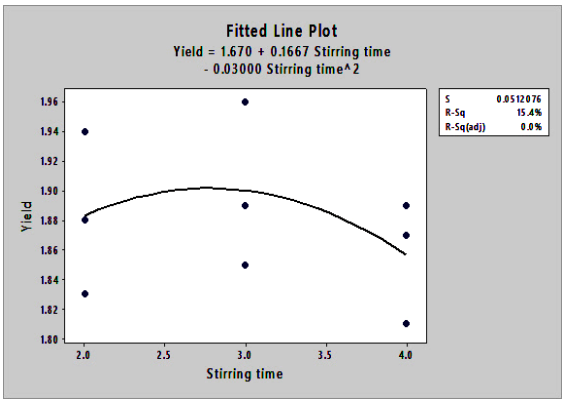


Fig.6: Fitted line plot yield with stirring time

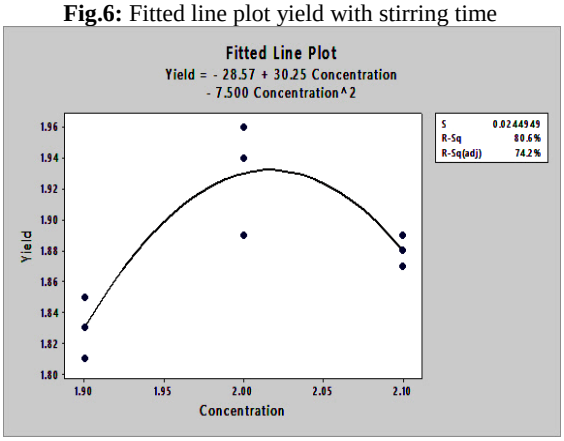


Fig.7: Fitted line plot yield with concentration

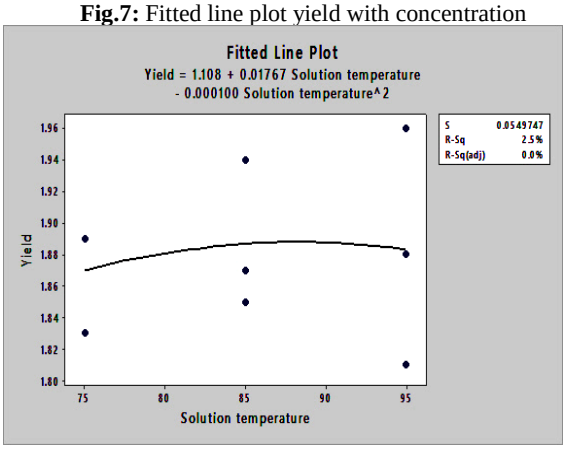


Fig.8: Fitted line plot yield with solution temperature

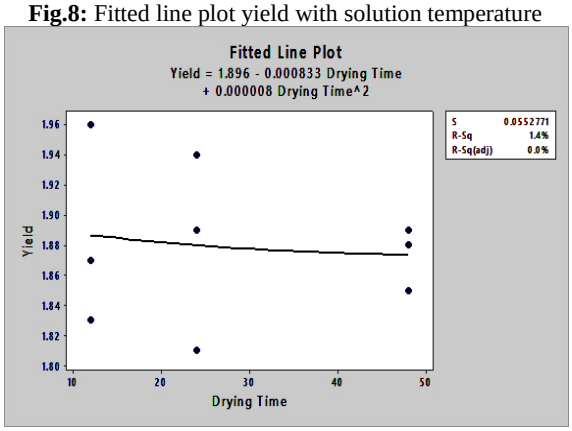


Fig.9: Fitted line plot yield with drying time

Table 4: Initial optimum level of parameters

Sl. No	Parameter	Level
1	Stirring time	3 hr.
2	Concentration of H_2SO_4(aq)	2.0M
3	Solution temperature	85^0C
4	Drying Time	24 hr.

4.2 Analysis of Variance (ANOVA)

The analysis of variance is used to find the relative importance of parameters on yield of MWCNT/ MnO_2 nanocomposite. The contributions of parameter concentration of H_2SO_4 (aq) was 80.9146%. Similarly, the contribution of other parameters is shown in table 5. The concentration of H_2SO_4 has significantly effect on yield and the yield was maximum at 2.0 M.

Table 5: Percentage contributions of parameters

Source	DF	Seq SS	% contribution
Stirring time	2	0.060704	1.53765
Concentration	2	0.319438	80.9146
Solution temperature	2	0.009524	2.4125
Drying Time	2	0.005117	1.2962
Residual Error	0	-	-
	8	0.394784	-

4.3. Regression Analysis

The regression analysis gives the relationship between yields with different parameters. The relationship is given below.

Yield=1.373-

0.0133 Stirring time+ 0.250 Concentration+ 0.00067 Solution temperatu re - 0.00036 Drying Time

The Regression Analysis confirmed the effect of concentration of H_2SO_4 yield was significant in comparison to another factors consideration.

5.Conclusions

The yield of MWCNT/MnO_2 was measured under different experimental conditions. The S/N response graph shows initial optimum combination of parameter level $A_2B_2C_2D_1$. The percentage contributions of parameters confirmed the parameter concentration of H_2SO_4 has significant effect on response and optimum concentration level of H2SO4 is 2M solution. Regression analysis also confirmed process parameter concentration of H_2SO_4 has significant effect on response.

Reference

[1] R Kackar. Off-Line Quality Control, Parameter Design, and the Taguchi Method, Journal of Quality Technology, 17(4), 176-188.

[2] DM Bryne, S Taguchi. The Taguchi Approach to Parameter Design, ASQC Quality Congress Transactions, Anaheim, CA, 168.

[3] Gh. Tahmasebi Pour and S. M. Mirzaee Moghadam .Optimization of Nano Calcium Carbonate Production Process Using Taguchi Method. International Journal of Materials, Mechanics and Manufacturing, 2(1), 2014

[4] I Lozić, T Penović, S Kurajica. Appliance of Taguchi Method of Experiment Design on Alumina Powder Preparation Process Using Spray-Drier. International conference on materials, tribology, recycling Vela Luka, 2011.

[5] SM Wang, YS Giang, YC Ling. Taguchi's method in optimizing the experimental conditions of simultaneous supercritical fluid extraction and chemical derivatization for the gas chromatographic-mass spectrometric determination of amphetamine and methamphetamine in aqueous matrix. forensic science journal, 1, 2002,47-53

[6] AK Pandaa, RK Singh. Optimization of Process Parameters by Taguchi Method: Catalytic degradation of polypropylene to liquid fuel. International journal of multidisciplinary and current research, 2013

[7] S Kamaruddin, ZA Khan, SH Foong. Application of Taguchi Method in the Optimization of Injection Moulding Parameters for Manufacturing Products from Plastic Blend. IACSIT International Journal of Engineering and Technology, 2(6), 2010.

[8] AN Siddiquee, ZA Khana, P Goel, M Kumar, GAgarwal, NZKhan. Optimization of Deep Drilling Process Parameters of AISI 321 Steel using Taguchi Method. 3rd International Conference on Materials Processing and Characterisation (ICMPC 2014). Procedia Materials Science 6, 2014, 1217 – 1225.

[9] ZA Khan, AN Siddiquee, NZ Khana, U Khan, GA Quadir. Multi response optimization of Wire electrical discharge machining process parameters using Taguchi based Grey Relational Analysis. 3rd International Conference on Materials Processing and Characterisation (ICMPC 2014), Procedia Materials Science 6, 2014, 1683 – 1695

[10] P Jayaraman, LMahesh Kumar. Multi-response Optimization of Machining Parameters of Turning AA6063 T6 Aluminium Alloy using

Grey Relational Analysis in Taguchi Method. Procedia Engineering 97, 2014, 197 – 204
[11] MI Equbal, R Kumar, MShamim, RK Ohdar. A grey-based Taguchi method to optimize hot forging process, 3rd International Conference on Materials Processing and Characterisation (ICMPC 2014), Procedia Materials Science 6, 2014, 1495 – 1504
[12] Y Chen, CG Liu, CLiu, GQ Lu, HM Cheng. Growth of single-crystal α-MnO_2 nanorods on multi-walled carbon nanotubes. Materials Research Bulletin, 42(11), 2007, 1935– 1941.
[13] MZ Hussain, S Khan, R Nagarajan, U Khan, V Vats. Fabrication and Microhardness Analysis of MWCNT/MnO_2 Nanocomposite. Journal of Materials, Article ID 6070468, 2016
[14] RK Roy. A Primer on the Taguchi method. Competitive Manufacturing Series. Van Nostrand Reinhold, New York. 1990

Proceedings of International Conference on Strategies in Volatile and Uncertain Environment for Emerging Markets
July 14-15, 2017
Indian Institute of Technology Delhi, New Delhi
pp.228-241

Organizational Justice Perception: An Unconventional Strategy to Manage Diverse Workforce

Anu Singh Lather[1] and Simran Kaur[2]

Abstract

It has been proposed that a perception of organizational justice plays an important role in explaining the relationship between subordinates and their supervisors, and in turn, the resulting influence on firm's sustainability. The study reports responses from 107 employees from Delhi NCR. Prior to the main study, pilot study was conducted on 20 employees, explicitly to evaluate the scale properties. This study disclosed that the Behavioral outcomes (Task performance behavior, Employee Silence and Organisational Counterproductive Behavior) stanching from distributive, procedural and interactional justice is significantly mediated by Emotional Intelligence, Social Desirability and age of employees. The limitations of common method bias and cross sectional data are discussed in light of implications for future research. This study answers the vital question that what should be done to increment the perception about organizational fairness of diverse workforce.

Keywords: Counterproductive Behavior, Emotional Intelligence, Employee Silence, Organizational Justice, Social Desirability, Task Performance.

1. Introduction

One of the world's largest democracies, India, is also the world's most diverse society. Due to increase in the complication of business operations, it has become imperative to have employees from different backgrounds and cultures. Workplace diversity denotes the assortment of differences among individuals in an organization. Diversity covers education, religion, region, race, gender, age, personality, emotional intelligence, social intelligence, sociability and other individual differences as well. Diversity not only comprises of perception about themselves, but also perception towards others. These perceptions influence their interaction with others. Nowadays people from various backgrounds come together to work for undertaking various responsibilities. Based on the Fairness Heuristic Theory of Organizational Justice, this paper aims to propose that Organizational Justice perception of diverse workforce can be managed in order to get various behavioral outcomes.

2. Organizational Justice

Organizational Justice can be defined as perception of equity and response to that perception in the organization (Greenberg, 1987). Organizational Justice can be classified under three broad categories namely - Distributive Justice, Procedural justice, and Interactional Justice. Distributive Justice refers to appropriateness of outcomes. It is inherent nature of employees to feel that

1. Pro Vice Chancellor, Delhi Technological University, Shahbad Daulatpur, Delhi
2. Research Scholar, Guru Gobind Singh Indraprastha University, Dwarka, India

they are not treated in equality with others in terms of various outcomes like salary, benefits, and status prerequisites as compared to their individual attributes like qualification, skills, seniority, age and social status (Adams, 1965). Procedural Justice can be defined as the fair means by which outcomes are allocated. It also stresses upon the role of participants in decision making process. Interactional Justice refers to how one treats another. If one person shares all information, interactions are often treated as fair.

3. Literature Review

In an attempt to address the issue of establishing standards of justice in organization to reduce unfair incidents in diverse organizations, we integrate Organizational Justice Dimensions and theories into workforce diversity literature. The behavioral outcomes resulting from Organizational Justice Perception are divided into three categories: Good: Task Performance Behavior, Bad: Withdrawal Behavior and, Ugly: Work Deviance Behavior.

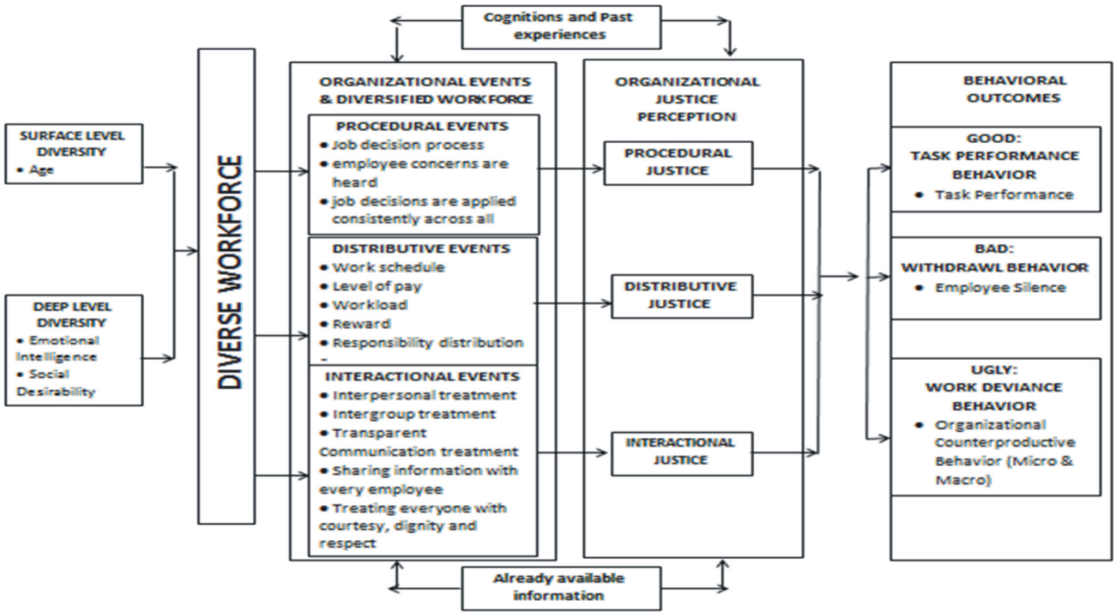
- Good: Task Performance Behavior- Earley (1984) incorporated procedural justice and goal-setting theory and established that workers will perform better if given a chance to participate in goal setting. Kanfer *et al*. (1987) found a negative relationship between procedural justice and performance. In case of Interactional Justice, it has been found out that it influences task performance. Masterson *et al*. (2000) examined the influence of both procedural and interactional justice on the performance of university clerical and staff employees. Their results revealed a non-significant relationship between procedural justice and performance However, performance was positively correlated with the interactional justice measure. There have not been many studies to analyze the relationship between Distributive Justice and task Performance. But to mention a few, Robbins, Summers, Miller, and Hendrix (2000) measured the unique effects of distributive justice, procedural justice and interpersonal justice on employee performance at a textile products company. It was found out that the measure relating to interpersonal justice was the only justice variable to explain unique variance in employee performance. Weaver and Conlon (2003) measured distributive, procedural, and interactional justice and found that distributive justice was the only justice measure significantly correlated with performance.
- Bad: Withdrawal Behavior- The researches in the field of Job withdrawal are imperative due to various factors. One of such factor is the complications attached withdrawal behavior such as absenteeism, intention to leave or employee silence. In this study, we will discuss only one form of withdrawal: Employee Silence. Pinder and Harlos (2001) found out that employee silence can be caused due to any kind of injustice: Distributive, Procedural or Interactional. It means that if there is any kind of unfairness related to distribution of resources, procedures of the organization or interpersonal interaction, can result into withdrawal behavior in the form of employee silence.
- Ugly: Work Deviance Behavior- Work Deviance behavior include theft, white-collar crime, drug and alcohol abuse, disciplinary problems, sexual harassment, and verbal and physical abuse (Ones, 2002). Unfortunately, very few of these behaviors have been studied in relation to organizational justice. Aquino *et al*. (1999) defined deviance as voluntary behavior that violates organizational norms, or threatens the well-being of the organization or its members. He further differentiated between organizational deviance (acts that are aimed at the organization, such as arriving late, ignoring a supervisor's instructions, or using company property in an unauthorized manner) and interpersonal deviance (acts directed at some individual within the organization, such as teasing a coworker, gossiping about a supervisor, making obscene comments or gestures at a coworker, or making ethnic, racial, or religious).

4. Objectives

1. To study the relationship between Organizational Justice (Distributive Justice, Procedural Justice, Interactional Justice) and Behavioral outcomes (Task Performance, Employee Silence, Organizational Counterproductive behavior)
2. To determine the impact of Age on relationship between Organizational Justice and Behavioral outcomes.
3. To determine the impact of Emotional Intelligence on relationship between Organizational Justice and Behavioral outcomes.
4. To determine the impact of Social Desirability on relationship between Organizational Justice and Behavioral outcomes.

5. Proposed Model

The proposed model consists of three dimensions: Diverse Workforce (Surface level and Deep level Diversity), Organizational Events and Diverse Workforce (Heuristic Experiences) and Organizational Justice Perception of Diverse workforce and Behavioral Outcomes. Diverse Workforce (Surface level and Deep level Diversity): There are two levels of workforce diversity: Surface level diversity and deep level diversity (Harrison *et al.*, 1998). According to them, surface level diversity is, "differences among group members in overt, biological characteristics that are typically reflected in physical features" (p. 97). These kinds of diversities are visible and easily identified by others. This may include diversity in terms of age, gender, caste, religion, region, education level, and so on. On the other hand, Deep level Diversity is more subjective in nature. It basically includes an individual's personal characteristics like personality traits, beliefs, values. This type of diversity is usually less evident as compared to surface level diversity. Organizational Events & Diverse Workforce (Heuristic Experiences): Fairness heuristic theory (Lind, 2001; Van den Bos and Lind, 2002)-with the related uncertainty management model of justice (Van den Bos, 2001; Van den Bos and Lind, 2002)-is focused on discovering the cognitive processing of fairness information. This theory is basically based on the assumption that group members have natural tendency of uncertainty which they need to manage. These uncertainties can be related to fear of exploitation by group authorities or fear of rejection. In order to overcome these uncertainties, group members start looking for signals in the external environment which confirm the credibility of the group and to feel secure that they are also part of that group. In organizational setup, this theory is equally applicable. In organization an employee is constantly exposed to the fear of exploitation or rejection. Thus in order to feel secure in the organization, they start looking for the signals in the organization. One such imperative signal is perception towards fairness in the organization. Organizational justice perception will determine the credibility of the organizational authorities.



We classified various organizational events into three categories: Procedural events, Distributive events, and Interactional events. These events have been referred to as Heuristic experiences. On the basis of Procedural Justice, we suggested Procedural Events. These events are related to the understanding of diverse workforce about how their work outcomes such as pay, performance appraisal, equal opportunity for all, rewards and incentives, have been influenced by fair process and fair diversity related policies and procedures. Based on Distributive Justice, we proposed Distributive Events which refers to comparison of work outcomes in terms of pay, opportunities for promotion, and so on. There can be comparison between various social groups such as Male- Female, Minority- Majority race, Hindu- Muslim employees, etc. Such comparisons can also be made on the basis of individual differences such as emotional intelligence, social intelligence, and desire to socialize. On the basis of Interactional Justice, we suggested Interactional events which describes the intergroup and interpersonal interactions between diverse background individuals in the organization.

6. Hypotheses

H1	There is a significant relationship between Organizational Justice (Distributive Justice, Procedural Justice, Interactional Justice) and Behavioral outcomes (Task Performance, Employee Silence, Organizational Counterproductive behavior)
1.1.	There is a significant relationship between Distributive Justice and Task Performance.
1.2.	There is a significant relationship between Procedural Justice and Task Performance.
1.3.	There is a significant relationship between Interactional Justice and Task Performance.
1.4.	There is a significant relationship between Distributive Justice and Employee Silence.
1.5.	There is a significant relationship between Procedural Justice and Employee Silence.
1.6.	There is a significant relationship between Interactional Justice and Employee Silence.
1.7.	There is a significant relationship between Distributive Justice and Organizational Counterproductive behavior.

1.8.	There is a significant relationship between Procedural Justice and Organizational Counterproductive behavior.
1.9.	There is a significant relationship between Interactional Justice and Organizational Counterproductive behavior.
H2	There is a significant relationship between Organizational Justice (Distributive Justice, Procedural Justice, Interactional Justice) and Behavioral outcomes (Task Performance, Employee Silence, Organizational Counterproductive behavior)
2.1.	There is a significant relationship between Distributive Justice and Task Performance.
2.2.	There is a significant relationship between Procedural Justice and Task Performance.
2.3.	There is a significant relationship between Interactional Justice and Task Performance.
2.4.	There is a significant relationship between Distributive Justice and Employee Silence.
2.5.	There is a significant relationship between Procedural Justice and Employee Silence.
2.6.	There is a significant relationship between Interactional Justice and Employee Silence.
2.7.	There is a significant relationship between Distributive Justice and Organizational Counterproductive behavior.
2.8.	There is a significant relationship between Procedural Justice and Organizational Counterproductive behavior.
2.9.	There is a significant relationship between Interactional Justice and Organizational Counterproductive behavior.
H3	Emotional Intelligence will mediate the relationship between Organizational Justice Distributive Justice, Procedural Justice, Interactional Justice) and Behavioral outcomes (Task Performance, Employee Silence, Organizational Counterproductive behavior)
1.1.	Emotional Intelligence will mediate the relationship between Distributive Justice and Task Performance.
1.2.	Emotional Intelligence will mediate the relationship between Procedural Justice and Task Performance.
1.3.	Emotional Intelligence will mediate the relationship between Interactional Justice and Task Performance.
1.4.	Emotional Intelligence will mediate the relationship between Distributive Justice and Employee Silence.
1.5.	Emotional Intelligence will mediate the relationship between Procedural Justice and Employee Silence.
1.6.	Emotional Intelligence will mediate the relationship between Interactional Justice and Employee Silence.
1.7.	Emotional Intelligence will mediate the relationship between Distributive Justice and Organizational Counterproductive behavior.
1.8.	Emotional Intelligence will mediate the relationship between Procedural Justice and Organizational Counterproductive behavior.
1.9.	Emotional Intelligence will mediate the relationship between Interactional Justice and Organizational Counterproductive behavior.
H4	Social Desirability will mediate the relationship between Organizational Justice (Distributive Justice, Procedural Justice, Interactional Justice) and Behavioral outcomes (Task Performance, Employee Silence, Organizational Counterproductive behavior)
1.1.	Social Desirability will mediate the relationship between Distributive Justice and Task Performance.

1.2. Social Desirability will mediate the relationship between Procedural Justice and Task Performance.

1.3. Social Desirability will mediate the relationship between Interactional Justice and Task Performance.

1.4. Social Desirability will mediate the relationship between Distributive Justice and Employee Silence.

1.5. Social Desirability will mediate the relationship between Procedural Justice and Employee Silence.

1.6. Social Desirability will mediate the relationship between Interactional Justice and Employee Silence.

1.7. Social Desirability will mediate the relationship between Distributive Justice and Organizational Counterproductive behavior.

1.8. Social Desirability will mediate the relationship between Procedural Justice and Organizational Counterproductive behavior.

1.9. Social Desirability will mediate the relationship between Interactional Justice and Organizational Counterproductive behavior.

7. Research Design

The suggested mediated relationship was tested on a sample of 107 employees from Delhi NCR area. Prior to the main study, pilot study was conducted on 30 employees, explicitly to evaluate the scale properties. The scales used were (i) the seventeen item, three-factor organizational justice scale (distributive, procedural, interactional justice) developed by Moorman (1993); (ii) Task Performance Behavior Indicator developed by Williams and Anderson (1991); (iii) Counterproductive Work Behavior Checklist developed by Paul E. Spector and Suzy Fox (2001); (iv) Employee Silence Scale was self-developed by the researchers; (v) Emotional Intelligence scale developed by Wong's Emotional Intelligence Scale (2004). After pilot study, all the scales were found to be reliable and hence further main study was conducted.

Hypothesis	Independent Variable	Dependent Variable	Mediating Variable	Statistical Techniques
H1	Organizational Justice (Distributive Justice, Procedural Justice, Interactional Justice)	Behavioral outcomes (Task Performance, Employee Silence, Organizational Counterproductive behavior)	-	Regression Analysis
H2	Organizational Justice (Distributive Justice, Procedural Justice, Interactional Justice)	Behavioral outcomes (Task Performance, Employee Silence, Organizational Cou nterproductive behavior)	Age	Regression Analysis and PROCESS macro is SPSS by Hayes
H3	Organizational Justice (Distributive Justice, Procedural Justice, Interactional Justice)	Behavioral outcomes (Task Performance, Employee Silence, Organizational Counter productive behavior)	Emotional Intelligence	Regression Analysis and PROCESS macro is SPSS by Hayes
H4	Organizational Justice (Distributive Justice, Procedural Justice, Interactional Justice)	Behavioral outcomes (Task Performance, Employee Silence, Organizational Counterproductive behavior)	Social Desirability	Regression Analysis and PROCESS macro is SPSS by Hayes

8. Data Analysis

Linear Regression in SPSS using the PROCESS macro by Hayes (2013) was the main technique used in this study. Simple linear regression is used to analyze the relationship between variables and PROCESS macro which does the centering and an interaction term automatically, is used to study the mediation effect.

H1: There is a significant relationship between Organizational Justice (Distributive Justice, Procedural Justice, and Interactional Justice) and Behavioral outcomes (Task Performance, Employee Silence, Organizational Counterproductive behavior).

To test the hypothesis H1.1 to H1.9, we conducted regression analysis (Table2). It was found out that all dimensions of Organisational Justice significantly predicted the variance in Task Performance, Employee Silence and Organisational Counterproductive Behavior.

Predictor	Dependent Variable	R	R Square	F	Sig.
Distributive Justice	Task Performance	.114	.013	1.375	.000
Procedural Justice	Task Performance	.098	.00	1.015	.000
Interactional Justice	Task Performance	.129	.017	1.782	.000
Distributive Justice	Employee Silence	.439	.193	25.129	.000
Procedural Justice	Employee Silence	.401	.616	20.141	.000
Interactional Justice	Employee Silence	.411	.169	21.313	.000
Distributive Justice	Organizational Counterproductive behavior	.070	.005	.510	.004
Procedural Justice	Organizational Counterproductive behavior	.036	.001	.136	.007
Interactional Justice	Organizational Counterproductive behavior	.059	.003	.368	.000

H2: Age will mediate the relationship between Organizational Justice (Distributive Justice, Procedural Justice, and Interactional Justice) and Behavioral outcomes (Task Performance, Employee Silence, Organizational Counterproductive behavior)

Table 3 shows the mediating effects of Age on relationship between Organisational Justice's Dimension and Behavioral outcomes. It was found that there is significant mediation of Age in relationship between Procedural Justice, Interactional Justice and Task Performance Behavior; Distributive Justice, Interactional Justice and Employee Silence; Procedural Justice, Interactional Justice and Organisational Counterproductive Behavior.

MODEL	Dependent Variable	Predictors	R	R^2	F change	Sig F Change
Model 1	TP	DJAge	.393	.155	9.525	0.000
	TP	DJ X Age	.394	.157	0.56	0.837
Model 2	TP	PJAge	.395	.156	9.603	.000
	TP	PJ X Age	.398	.158	.005	.047
Model 3	TP	IJAge	.406	.165	10.290	.000
	TP	IJ X Age	.049	.169	.169	.026
Model 4	ES	DJAge	.414	.171	10.736	.000
	ES	DJ X Age	.419	.180	.576	.045
Model 5	ES	PJAge	.404	.163	10.158	.000
	ES	PJ X Age	.405	.164	.005	..967
Model 6	ES	IJAge	.414	.171	10.736	.000
	ES	IJ X Age	.419	.179	.576	.045
Model 7	CPB	DJAge	.060	.004	.186	.830
	CPB	DJ X Age	.075	.006	.219	.640
Model 8	CPB	PJAge	.037	.001	.070	.933
	CPB	PJ X Age	.052	.003	.146	.704
Model 9	CPB	IJAge	.060	.004	.186	.830
	CPB	IJ X Age	.075	.006	.219	.640

H3: Emotional Intelligence will mediate the relationship between Organizational Justice (Distributive Justice, Procedural Justice, and Interactional Justice) and Behavioral outcomes (Task Performance, Employee Silence, Organizational Counterproductive behavior)

Table 4 shows the mediating effects of Emotional Intelligence on relationship between Organisational Justice's Dimensions and Behavioral outcomes. It was found that there is significant mediation of Emotional Intelligence in relationship between Distributive Justice, Procedural Justice, Interactional Justice and Task Performance Behavior; Distributive Justice, Procedural Justice, Interactional Justice and Employee Silence; Procedural Justice, Interactional Justice and Organisational Counterproductive Behavior.

MODEL	Dependent Variable	Predictors	R	R^2	F change	Sig F Change
Model 1	TP	DJEI	.429	.184	11.757	.000
	TP	DJ X EI	.443	.196	1.471	.002
Model 2	TP	PJEI	.433	.187	11.992	.000
	TP	PJ X EI	.439	.193	.657	.004
Model 3	TP	IJEI	.436	.190	12.234	.000
	TP	IJ X EI	.447	.200	1.225	.002
Model 4	ES	DJEI	.504	.254	17.743	.000
	ES	DJ X EI	.584	.342	13.632	.000
Model 5	ES	PJEI	.457	.209	13.699	.000
	ES	PJ X EI	.581	.337	19.994	.000
Model 6	ES	IJEI	.474	.224	15.039	.000
	ES	IJ X EI	.541	.293	.10.007	.002
Model 7	CPB	DJEI	.629	.396	34.127	.000
	CPB	DJ X EI	.633	.400	.670	.415
Model 8	CPB	PJEI	.630	.397	34.305	.000
	CPB	PJ X EI	.632	.399	.317	.050
Model 9	CPB	IJEI	.630	.397	34.221	.000
	CPB	IJ X EI	.631	.398	.196	.006

H4: Social Desirability will mediate the relationship between Organizational Justice (Distributive Justice, Procedural Justice, and Interactional Justice) and Behavioral outcomes (Task Performance, Employee Silence, Organizational Counterproductive behavior)

Table 5 shows the mediating effects of Social Desirability on relationship between Organisational Justice's Dimension (Distributive, Procedural and Interactional Justice) and Behavioral outcomes (Task Performance, Employee Silence, Organizational Counterproductive behavior). It was found that there is significant mediation of Emotional Intelligence in relationship between Distributive Justice, Procedural Justice, Interactional Justice and Task Performance Behavior; Distributive Justice, Procedural Justice, Interactional Justice and Employee Silence; Procedural Justice, Interactional Justice and Organisational Counterproductive Behavior.

MODEL	Dependent Variable	Predictors	R	R^2	F change	Sig F Change
Model 1	TP	DJSD	.223	.050	2.728	.070
	TP	DJ X SD	.238	.057	.762	.385
Model 2	TP	PJSD	.212	.045	2.456	.091
	TP	PJ X SD	.233	.054	1.015	.316
Model 3	TP	IJSD	.236	.056	3.074	.050
	TP	IJ X SD	.250	.063	.735	.039
Model 4	ES	DJSD	.488	.239	16.290	.000
	ES	DJ X SD	.489	.239	.123	.727
Model 5	ES	PJSD	.459	.211	13.898	.000
	ES	PJ X SD	.461	.212	.161	.689
Model 6	ES	IJSD	.460	.211	13.934	.000
	ES	IJ X SD	.461	.212	.990	.075
Model 7	CPB	DJSD	.603	.363	29.678	.000
	CPB	DJ X SD	.617	.381	2.839	.009
Model 8	CPB	PJSD	.595	.354	28.435	.000
	CPB	PJ X SD	.608	.370	2.628	.010
Model 9	CPB	IJSD	.604	.365	29.856	.000
	CPB	IJ X SD	.620	.384	3.272	.007

9. Discussion

It was found that all dimensions of Organisational Justice significantly predicted the variance in Task Performance (Greenberg and Colquitt, 2005; Devonish and Greenidge, 2010; Culbertson and Mills, 2011; Suliman and Kathairi, 2012), Employee Silence (Pinder and Harlos, 2001) and Organisational Counterproductive Behavior (Aquino *et al*., 1999). It means positive perception about fairness in the organization can improve the task performance of employees. Employee Silence and Organisational Counterproductive Behavior can be controlled by improving Organisational justice perception. This study also disclosed that there is significant mediation of Age in relationship between Procedural Justice, Interactional Justice and Task Performance Behavior, Distributive Justice, Interactional Justice and Employee Silence; Procedural Justice, Interactional Justice and Organisational Counterproductive Behavior. This relationship was also established by Wagner and Rush (2000). According to their study, a person's inspiration should take part clinched alongside unselfish conduct change with age whereas context-relevant attitudes might become more remarkable to more young representatives and ethical judgement to more seasoned specialists. It was further revealed that there is significant mediation of Emotional Intelligence in relationship between Distributive Justice, Procedural Justice, Interactional Justice and Task Performance Behavior; Distributive Justice, Procedural Justice, Interactional Justice and Employee Silence; Procedural Justice, Interactional Justice and Organisational Counterproductive Behavior. It was also found out that there is significant mediation of Emotional

Intelligence in relationship between Distributive Justice, Procedural Justice, Interactional Justice and Task Performance Behavior; Distributive Justice, Procedural Justice, Interactional Justice and Employee Silence; Procedural Justice, Interactional Justice and Organisational Counterproductive Behavior. By improving Organizational Justice perception of diverse workforce, organization will be able to engage in continuous improvement in terms of efforts to create Fair Diversified Workplace. The proposed model bridges the gap between literature of Organizational justice and Diversity Management. It provides the theoretical and practical implications for creating fair environment for diverse workforce in order to get favorable behavioral outcomes.

10. Theoretical and Practical Implications

The literature of diversity management lacks the research on fairness perception of diverse workforce and very few studies tried to establish a link between Organizational Justice Perception of diverse workforce on the behavioral outcomes. Moreover most of the researchers emphasized on the power difference between the "minorities" and "authorities" (Fairclough, 1992), but by incorporating Fairness principles in the Diversity Management theories, this problem is also resolved. We propose that positive Organizational Justice perception of diverse workforce, in relation with various Heuristic experiences, will result in favorable behavioral outcomes. The senior management personnel must have liberal thinking and should be able to sensitize towards diverse workforce. Further to this, organizations must design specific responsibility centers for managing diversity in the organizations, in order to successfully implement diversity policies (Kalev and Dobbim, 2006). Senior management support is imperative for Fair Diversity Management because they are the one who are involved in various Organizational events, which may act as heuristic experience event for the diverse workforce. They have the authority to ensure fairness in terms of distribution of resources, policies and procedures and interpersonal interaction with diverse workforce. This perception will further lead to favorable or unfavorable behavior outcomes. In case of positive organizational justice perception, a person may exhibit "Good Behavior" such as Effective Task performance. On the other hand in case of negative Organizational Justice Perception, a person may reveal "Bad Behavior" or "Ugly behavior", depending upon the level of dissatisfaction. Top level management can thus try to change Organizational Justice perception by manipulating various organizational events, in order to get favorable behavioral outcomes. For instance, management can have monthly discussions regarding distribution, Procedural and Interactional events special in regard to diverse workforce. The diverse workforce may be encouraged to freely share their opinions, experiences and ideas and this input can be used to improve the diversity management policy of the organization.

References

- Adams, J.S. (1965) Inequity in Social Exchange, in Berkowitz, L. (Ed.), *Advanced in Experimental Social Psychology*, Academic Press: New York, NY, pp. 267-99. (The) Age (2004), "Ageism a looming issue'', The Age, 18 August, available at: www.theage.com.au/ articles/2004/08/17/ 1092508474168.html.
- Ambrose, M., Hess, R.L., and Ganesan, S. (2007) The Relationship between Justice and Attitudes: An Examination of Justice Effects on Event and System-Related Attitudes, *Organizational Behavior and Human Decision Processes*, 103(7), 21-36.
- Aquino, K., Galperin, B., and Bennett, R. (2004) Social Status and Aggressiveness as Moderators of the Relationship between Interactional Justice and Workplace Deviance, *Journal of Applied Social Psychology*, 34(5), 1001-9.
- Arredondo, P. (1996) Successful Diversity Management Initiatives: A Blueprint for Planning and Implementation, Sage: Newbury Park, CA.
- Atkinson, R. (1999) Discourses of Partnership and Empowerment in Contemporary British Urban Regeneration, *Urban Studies*, 36(7), 59-72.

- Bies, R.J., and Moag, J.F. (1986) Interactional Justice: Communication Criteria of Fairness, in Lewick, R.J., Sheppard, B.H. and Bazerman, M.H. (Eds), Research on Negotiations in Organizations, JAI Press: Greenwich, CT, 43-55.
- Bies, R.J., and Tripp, T.M. (1995) Beyond Distrust: 'Getting even' and the Need for Revenge, in Karmer, R.M. and Tyler, T.T. (Eds), Trust in Organizations, Sage: Newbury Park, CA, 246-60.
- Brass, D.J., Galaskiewicz, J., Greve, H.R., and Tsai, W. (2004) Taking Stock of Networks and Organizations: A Multilevel Perspective, *Academy of Management Journal*, 47(6), 795-819.
- Brief, A.P. (1998) Attitudes in and Around Organizations, Sage: Thousand Oaks, CA.
- Brockner, J. (1990) Scope of Justice in the Workplace: How Survivors React to Co-Worker Layoffs, *Journal of Social Issues*, 46(1), 95-106.
- Brockner, J., Ackerman, G., and Fairchild, G. (2001) When do Elements of Procedural Fairness Make a Difference? A Classification of Moderating Differences", in Greenberg, J. and Cropanzano, R. (Eds), *Advances in Organizational Justice*, Stanford University Press: Stanford, CA, 179-212.
- Byrne, D. (1971) *The Attraction Paradigm*, Academic Press: New York, NY.
- Byrne, Z.S., and Cropanzano, R. (2001) The History of Organizational Justice: The Founders Speak", in Cropanzano, R. (Ed.), *Justice in the Workplace: From Theory to Practice*, Lawrence Erlbaum Associates: Mahwah, NJ, 3-26.
- Castilla, E.J. (2005) Social Networks and Employee Performance in a Call Center, *American Journal of Sociology*, 110(5), 1243-84.
- Colquitt, J.A. (2001) On the Dimensionality of Organizational Justice: A Construct Validation of Measure*, Journal of Applied Psychology*, 86(3), 386-400.
- Cox, T.H. (2001) *Creating the Multicultural Organization, A Strategy for Capturing the Power of Diversity*, John Wiley and Sons: San Francisco, CA.
- Cox, T.H. (2002) Taking Diversity to the Next Level, *Executive Excellence*, 19(4), 19.
- Coperheart, L., and Dragan, M. (2007) *Social Justice: Theories, Issues, and Movements*, Rutgers University Press: New Brunswick, NJ.
- Cropanzano, R., and Byrne, Z.S. (2001) When it's Time to Stop Writing Policies: A Procedural Justice Perspective, *Human Resource Management Review*, 11(1-2), 31-54.
- Cropanzano, R., and Prehar, C.A. (1999) Using Social Exchange Theory to Distinguish Procedural from Interactional Justice, Paper Presented at the Society for Industrial and Organizational Psychology, Atlanta.
- Cropanzano, R., and Rupp, D.E. (2003) An Overview of Organizational Justice: Implication for Work Motivation, in Porter, L.W., Bigley, G.A. and Steers, R.M. (Eds), *Motivation and Work Behavior*, McGraw-Hill Irwin: Burr Ridge, IL, 82-95.
- Cropanzano, R., and Wright, T.A. (2003) Procedural Justice and Organizational Staffing: A Tale of Two Paradigms, *Human Resource Management Review*, 13(1), 7-39.
- Cropanzano, R., Byrne, Z.S., Bobocel, D.R., and Rupp, D.E. (2001) Moral Virtues, Fairness Heuristics, Social Entities and other Denizens of Organizational Justice, *Journal of Vocational Behavior,* 58(2).
- Folger, R., and Cropanzano, R. (2001) Fairness Theory: Justice as Accountability, in Greenberg, J. and Cropanzano, R. (Eds), *Advances in Organizational Justice*, Stanford University Press: Stanford, CA, pp. 1-55.
- Folger, R., and Konovsky, M.A. (1989) Effects of Procedural Justice, Distributive Justice and Reactions to Pay Raise Decisions, *Academy of Management Journal*, 32(1), 115-30.
- Fortin, M., and Fellenz, M.R. (2008) Hypocrisies Off: Towards a more Reflexive Ethical Base in Organizational Justice Research and Practice, *Journal of Business Ethics*, 78(3), 415-33.
- Freeman, R.E. (1984) *Strategic Management: Stakeholder Approach*, Pitman/Ballinger: Boston, MA.
- Friedman, R.A., and Krackhardt, D. (1997) Special Capital and Career Mobility: A Structural Theory of Lower Returns to Education for Asian Employees*, Journal of Applied Behavioral Science,* 33(3), 316-34.

- Garstka, T., Hummert, M., and Branscombe, N. (2005) Perceiving Age Discrimination in Response to Intergenerational Inequity', *Journal of Social Issues*, 61(2), 321-42.
- Gilbert, J.A., and Ivancevich, J.M. (2000) Valuing Diversity: A Tale of Two Organizations, *Academy of Management Executives*, 24(1), 93-105.
- Gilbert, J.A., Stead, B.A., and Ivancevich, J.M. (1999) Diversity Management: A New Organizational Paradigm, *Journal of Business Ethics*, 21(1), 61-76.
- Gopinath, C., and Becker, T.E. (2000) Communication, Procedural Justice and Employee Attitudes: Relationship under Conditions of Diverstiture, *Journal of Management*, 26(2), 63-83.
- Greenhaus, J.H., Prasuraman, S., and Wormley, W.M. (1990) Effects of Race on Organizational Experiences, Job Performance Evaluations and Career Outcomes, *Academy of Management Journal*, 33(1), 62-86.
- Guillory, W.A. (2002) The Unifying Force of Diversity, *Executive Excellent*, 19(6), 7.
- Harrison, D.A., Price, K.H., and Bell, M.P. (1998) Beyond Relational Demography: Time and the Effects of Surface- And Deep-Level Diversity on Work Group Cohesion, *Academy of Management Journal*, 41, 96-107.
- Heneman, R.L., Waldeck, N.E., and Cushnie, M. (1996) Diversity Considerations in Staffing Decision-Making", in Kossek, E.E. and Lobel, S.A. (Eds), *Managing Diversity: Human Resource Strategies for Transferring the Workplace*, Blackwell: Hoboken, NJ, 74-100.
- Herring, C. (2009) Does Diversity Pay?: Race, Gender, and the Business Case for Diversity, *American Sociological Review*, 74(2), 208-224.
- Krehbiel, P.J., and Cropanzano, R. (2000) Procedural Justice, Outcome Favourability and Emotion, *Social Justice Research*, 13(4), 337-58.
- Leventhal, G.S., Karuza, J., and Fry, W.R. (1980) Beyond Fairness: A Theory of Allocation Preferences, in Mikula, G. (Ed.), *Justice and Social Interaction*, Plenum: New York, NY, 167-218.
- Liff, S. (1999) Diversity and Equal Opportunities: Room for a Constructive Compromise?, *Human Resource Management Journal*, 9(1), 65-76.
- Lind, E.A., and Tyler, T.R. (1988) *The Social Psychology of Procedural Justice*, Plenum: New York, NY.
- Lind, E.A., Kanfer, R., and Earley, P.C. (1990) Voices, Control and Procedural Justice: International Upper-Level Female and Male Managers, *Journal of Applied Psychology*, 91(4), 777-85.
- Maltesta, R.M., and Bryne, Z.S. (1997) The Impact of Formal and Interactional Procedures on Organizational Outcomes, Paper Presented at the Society for Industrial and Organizational Psychology, St Louis, MO.
- Masterson, S.S., Lewis, K., Goldman, B.M., and Taylor, M.S. (2000) Integrating Justice and Social Exchange: The Differing Effects of Fair Procedures and Treatment on Work Relationships, *Academy of Management Journal*, 48(4), 738-48.
- Mill, J.S. (1961b) *Essential Works of John Stuart Mill Max Learner*, Bantam Books: New York, NY.
- Milliken, F.J., and Martins, L.L. (1996) Searching for Common Threads: Understanding the Multiple Effects of Diversity in Organizational Groups, *Academy of Management Journal,* 21(2), 402-33.
- Thomas, R.R. (2001) *From Affirmative Action to Affirming Diversity, Harvard Business Review of Diversity*, Harvard Business School Publishing Corporation: Boston, MA, 1-32.
- Tsui, A.S., Egan, T.D., and O'Reilly, C.A. (1992) Being Different: Relational Demography and Organizational Attachment, *Administrative Science Quarterly*, 37(4), 549-79.
- Turner, J.C. (1987) *Rediscovering the Social Group: A Self-categorization Theory*, Basil-Blackwell: London.
- Tyler, T.R. (1999) Why People Cooperate with Organizations: An Identity-Based Perspective, *Research in Organizational Behavior,* 21, 201-46.
- Tyler, T.R., and Cain, A. (1981) The Role of Distributional and Procedural Fairness in the Endorsement of Formal Leaders, *Journal of Personality and Social Psychology*, 41, 642-55.

- Tyler, T.R., and Lind, E.A. (1992) A Relational Model of Authority in Groups, *Advances in Experimental Social Psychology*, 25, 115-91.
- Tyler, T.R., and Smith, H.J. (1998) Social Justice and Social Movements, in Gilbert, D.T. and Fiske, S.T. (Eds), *Handbook of Social Psychology*, Vol. 2, McGraw-Hill: New York, NY, 595-629.
- Van den Bos, K., Lind, E.A., and Wilke, H.A.M. (2001) The Psychology of Procedural and Distributive Justice Viewed from the Perspective of Fairness Heuristic Theory, in Cropanzano, R. (Ed.*), Justice in the Workplace: From Theory to Practice*, Lawrence Erlbaum Associates: Mahwah, NJ, 49-66.
- Van Knippenberg, D., and Schippers, M.C. (2007) Work Group Diversity, *Annual Review of Psychology*, 58, 515-41.
- Watson, G.W. (2003) Ideology and the Symbolic Construction of Fairness in Organizational Change, *Journal of Organizational Change Management*, 16(2), 154-68.
- Weiss, H.M., Suckow, K., and Cropanzano, R. (1999) Effects of Justice Conditions on Discrete Emotions, *Journal of Applied Psychology*, 84(5), 786-94.
- Werhane, P.H., and Freeman, R.E. (1999) Business Ethics: The State of the Arts, *International Journal of Management Review*, 1(1), 1-16.

ResearchGate

See discussions, stats, and author profiles for this publication at: https://www.researchgate.net/publication/318659638

Performance Evaluation of Biosignal Ring for Reduction of Pollution Level in Diesel and Petrol Engines

Article · July 2017

DOI: 10.15680/IJIRSET.2017.0607152

CITATIONS
0

READS
3

5 authors, including:



S. K. Singh
Delhi Technological University
117 PUBLICATIONS **375** CITATIONS

SEE PROFILE

Some of the authors of this publication are also working on these related projects:



Groundwater pollution modeling View project

All content following this page was uploaded by S. K. Singh on 24 July 2017.

The user has requested enhancement of the downloaded file.

ISSN(Online): 2319-8753
ISSN (Print): 2347-6710

International Journal of Innovative Research in Science, Engineering and Technology

(An ISO 3297: 2007 Certified Organization)

Website: www.ijirset.com

Vol. 6, Issue 7, July 2017

Performance Evaluation of Biosignal Ring for Reduction of Pollution Level in Diesel and Petrol Engines

S. K. Singh[1], Surbhi Jain[2], Tejasvini Ahuja[2] Yukti Sharma[2], Nidhi Pathak[2]

Professor, Department of Environmental Engineering, Delhi Technological University, Bawana Road, Delhi, India[1]

UG Student, Department of Environmental Engineering, Delhi Technological University, Bawana Road, Delhi, India[2]

ABSTRACT*:* Air pollution has become a growing problem in megacities and large urban areas throughout the globe, and transportation is recognized as the major source of air pollution in many cities, especially in developing countries. Contribution of automobiles is reported in the range of 40 to 80% of the total air pollution. The challenge facing megacities is how to reduce the adverse environmental impacts and other negative effects of transportation without giving up the benefits of mobility. This research paper includes the testing of biosignal ring developed by Wellan International Limited for reduction of pollution levelsin petrol and diesel vehicles. The ring when attached to the inlet of the engine acts on the fuel through biosignals. The biosignals help in atomization of the fuel and reduces the pollutants by further enhancing the combustion process, and thus reducing the unburnt pollutant particles from the engine exhaust. The ring was tested on diesel and petrol engines. For diesel engine reduction in smoke was measured, while in the petrol engine parameters such as CO, CO2, SOx and NOx were measured before and after attaching the ring. The percentage reduction of the pollutants obtained from the ring for the diesel engine is about 16.4%, and in petrol engine, significant reduction in the pollutants is observed. If this device is incorporated in the vehicles, it can substantially reduce the pollution emitted from the vehicles and can even increases the efficiency of the engine.

KEYWORDS*:* Biosignal, Vehicular pollution, Efficiency of engine, Atomization, Diesel engine, Petrol engine

I. INTRODUCTION

A biosignal is any signal in living beings that can be continually measured and monitored. The term biosignal is often used to refer to bioelectrical signals, but it may refer to both electrical and non-electrical signals. The usual understanding is to refer only to time-varying signals, although spatial parameter variations (e.g. the nucleotide sequence determining the genetic code) are sometimes subsumed as well. There are various types of biosignals. Some of them are stated. Electrical biosignals, or bioelectrical time signals, usually refers to the change in electric current produced by the sum of an electrical potential difference across a specialized tissue, organ or cell system like the nervous system. Thus, among the best-known bioelectrical signals are: Electroencephalogram (EEG) is an electrophysiological monitoring method to record electrical activity of the brain. EEG measures voltage fluctuations resulting from ionic current within the neurons of the brain. Electrocardiography (ECG) is the process of recording the electrical activity of the heart over a period of time using electrodes placed on the skin [6]. Electromyography (EMG) is an electro diagnostic medicine technique for evaluating and recording the electrical activity produced by skeletal muscles. Mechanomyogram (MMG) is the mechanical signal observable from the surface of a muscle when the muscle is contracted. At the onset of muscle contraction, gross changes in the muscle shape cause a large peak in the MMG. Electrooculography (EOG/E.O.G.) is a technique for measuring the cornea-retinal standing potential that exists between the front and the back of the human eye. The resulting signal is called the electrooculogram .Electro dermal activity (EDA) is the property of the human body that causes continuous

ISSN(Online): 2319-8753
ISSN (Print): 2347-6710

International Journal of Innovative Research in Science, Engineering and Technology

(An ISO 3297: 2007 Certified Organization)

Website: www.ijirset.com

Vol. 6, Issue 7, July 2017

variation in the electrical characteristics of the skin. Magnetoencephalography (MEG) is a functional neuroimaging technique for mapping brain activity by recording magnetic fields produced by electrical currents occurring naturally in the brain, using very sensitive magnetometers. Biosignals may also refer to any non-electrical signal that is capable of being monitored from biological beings, such as Mechanical signals (e.g. the mechanomyogram or MMG), Acoustic signals (e.g. phonetic and non-phonetic utterances, breathing), Chemical signals (e.g. pH, oxygenation) and Optical signals (e.g. movements).

Biosignals have various applications like water purification, non-invasive diagnosis, potential for direct interfaces and health monitoring, biosignal monitoring system for mobile telemedicine, ways of interaction using biosignlas etc. For water purification, biosignals can be used by storing in rings called power rings. POWER RINGS work through biosignals, which have been stored in the rings' interior. These signals penetrate all pipes and tubes to influence the water which is passing through. As a result, the vibrations or oscillations created in the water are changed in such a way that lime, rust, scale or bio-fouling matter no longer accumulate within a piped system and are washed out in minute particles. They can also be used for non-invasive diagnosis. In recent years, a particular challenge has arisen in non-invasive medical diagnostic procedures. Because biosignals recorded on the body surface reflect the internal behaviour and status of the organism or its parts, they are ideally suited to provide essential information of these organs to the clinician without any invasive measures. Potential for direct interfaces and health monitoring: Biosignals are harnessed to enable enhanced computer interfaces. In particular, biosignals can serve for passive health monitoring for the elderly who want to remain at home but need some level of support as they age. Such devices can directly manipulate computer interfaces to give people with limited peripheral mobility some control over their environment. Biosignal monitoring system for mobile telemedicine is yet another application. In this, a prototype integrated mobile telemedicine system has been designed that is compatible with existing public mobile telecommunication network. The mobile telemedicine system consists of two parts. One is a physiological signal measuring part, and the other is a PC system for the signal processing and telecommunication. The system uses NetMeeting to transmit video, audio and patient biosignals from a moving ambulance to a hospital and delivers to the personal computer of the doctor. This PC based mobile telemedicine system is flexible enough to accommodate newer components in wireless communication and portable sensing technologies. There can be ways of interactions using biosignals. A prototype earphone was developed with three kinds of biosignals - pulse wave, electromyogram (EMG) and acceleration sensors. Using this system three new applications were invented, namely, automatic music selection, tactile and visual communication and automatic metadata annotation. Innumerous methods to control pollution have been employed since the awareness of pollution rise has been spread. For example, a muffler is installed in the engine to control the noise and vibrations due to knocking. Earlier, a positive Crankcase Ventilation (PCV) system was used in the automobiles. In this system, the exhaust gasses were sent back into the crankcase so that complete combustion of the un-burnt particles could be carried out. But, this did not prove to be an effective method since the efficiency was not as desired. Also, the exhaust gasses caused harm to the crankcase. These days, a new technology has been developed. IC engines employ catalytic convertor at their exhaust valves to reduce the smoke emissions. Inside the catalytic convertor, the smoke emissions are adsorbed on the catalyst which makes them unstable, thereby atomizing them. The atomized exhaust gets converted into non-toxic molecules which enter the atmosphere. It proves to be very efficient in reducing the smoke emissions from the engine exhaust valves. In this paper study for reduction of pollution levels in emissions from petrol and diesel vehicles has been done.

II. LITERATURE SURVEY

POLLUTION CONTROL BY BIOSIGNALS

Each elemental molecule has its own specific natural atomic/molecular oscillation. In simple terms, oscillations are best described as vibrations or waves that are given off by that element. Molecules are formed when atoms of different elements fuse together because of natural affinity. This attraction is caused by the oscillations emitted by the atoms. In other words, elements recognize each other by their unique oscillations. If the oscillations of various atoms are neutralized their attraction ceases. This is the basis of pollution control by biosignals. The molecules of the fuel are targeted in order to reduce pollution cause by combustion of these particles. When the fuel particles are

ISSN(Online): 2319-8753
ISSN (Print): 2347-6710

International Journal of Innovative Research in Science, Engineering and Technology

(An ISO 3297: 2007 Certified Organization)

Website: www.ijirset.com

Vol. 6, Issue 7, July 2017

acted upon by the biosignals, it leads to the atomization of the fuel. So, when the fuel is burned in engine, it leads to the better and uniform combustion. High frequency biosignals are modulated and stored into an appropriate device which is basically high-quality information storage materials (base material crystals) which are capable of storing such vibrations for indefinite periods of time and releasing them again. These biosignals penetrate any kind of material and they are absorbed by the fuel as interference or resonance vibrations. Whenever extra atoms are forcibly fused to form a molecule by the use of a catalyst, the resultant molecule is unstable and will break apart. Biosignal emissions cause such a situation, resulting in a breakdown within molecules. The dispersed atoms are then targeted by the ring to keep from restructuring. The high frequency oscillations that are generated by the energy field interact with the molecular structure of the fuel, removing harmful elements from your fuel and oil. This causes the fuel to become cleaner and finer, leading to better combustion and lesser number of unburnt particles or pollutants and hence reducing pollution.

FUNCTIONING OF THE POWER RING

Power ring consists of high-quality information storage materials (base material crystals) which are capable of storing such vibrations for indefinite periods of time and releasing them again. These vibrations penetrate any kind of material and they are absorbed by the water as interference or resonance vibrations (hydrogen bridges or water molecules). Within fractions of a second, this information passes through the pipe into the water and is effective even with high flow rates. Power rings can be deployed for water of any quality. No chemical substances, magnetic fields or electromagnetic radiations are released into the environment. The basis of this technology is the realization of the latest knowledge of modern quantum theory.

Frequency patterns from the ultra-fine range (quantum vibrations) are modulated onto POWER RINGS by means of a laser technology. Elements recognize each other by their unique oscillations. Thus, a water molecule is formed when oxygen is attracted to combine with 2 atoms of hydrogen. If the oscillations of various atoms are neutralized their attraction ceases. That is the function of Power ring emissions. Whenever extra atoms are forcibly fused to form a molecule by the use of a catalyst, the resultant molecule is unstable and will break apart. Power ring emissions cause such a situation, resulting in a breakdown within molecules. The dispersed atoms are then targeted by the ring to keep from restructuring.

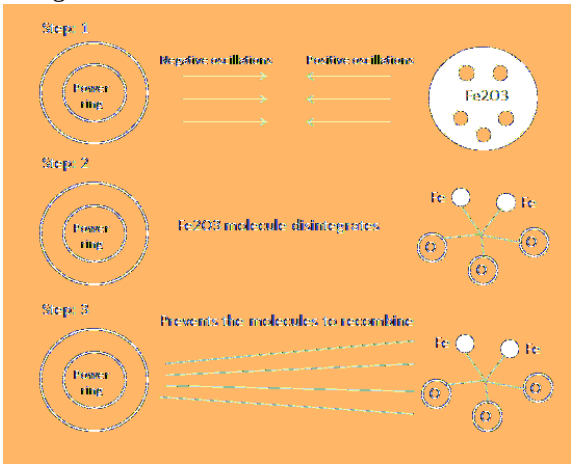


Figure 1 Functioning of a biosignal ring

HARNESSING OF SIGNALS

The molecular fundamental oscillations of various substances has been isolated, mapped and stored in the Ring. This technology works using specifically modulated molecular oscillations not dependent upon magnetic forces or electrical pulses. Based on these oscillations of elements and molecules, a power ring has been developed. The aim is to influence the original oscillation of the element that has been targeted through new active oscillations in such a way that the physical properties of the element or of the molecules are modified. These manufactured oscillations are then programmed into the Power Ring and super imposed by a proprietary Laser Technology. This alloy can

ISSN(Online): 2319-8753
ISSN (Print): 2347-6710

International Journal of Innovative Research in Science, Engineering and Technology

(An ISO 3297: 2007 Certified Organization)

Website: www.ijirset.com

Vol. 6, Issue 7, July 2017

store an almost unlimited number of active oscillations and emit these to a liquid in a constant and stable format, independent of the ambient temperature. The active oscillations create a field within the ring, which penetrates all piping material and thus passes into the water or fluid.

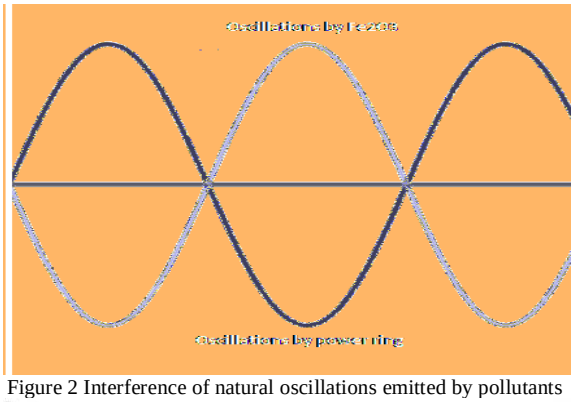


Figure 2 Interference of natural oscillations emitted by pollutants

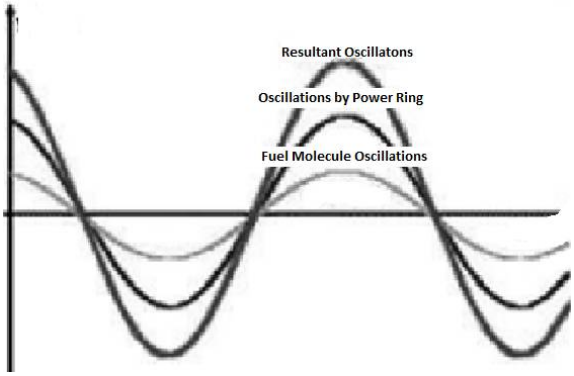


Figure 3 Overlaying of natural oscillations emitted by pollutants

This Principle results in an 'Interference' or 'Overlaying' of natural oscillations emitted by pollutants in the liquid. Interference and Overlaying can best be described as cancelling sound using equal and opposite waves or playing two adjacent musical notes together to create another note.

VEHICULAR POLLUTION

The large majority of today's cars and trucks travel by using internal combustion engines that burn gasoline or other fossil fuels. The process of burning gasoline to power cars and trucks contributes to air pollution by releasing a variety of emissions into the atmosphere. Emissions that are released directly into the atmosphere from the tailpipes of cars and trucks are the primary source of vehicular pollution. But motor vehicles also pollute the air during the processes of manufacturing, refueling, and from the emissions associated with oil refining and distribution of the fuel they burn.

The principal air-quality pollutant emissions from petrol, diesel, and alternative-fuel engines are carbon monoxide, oxides of nitrogen, un-burnt hydrocarbons and particulate matter. It is emissions of these pollutants that are regulated by the Euro emissions standards. Modern cars, if kept in good condition, produce only quite small quantities of the air quality pollutants, but the emissions from large numbers of cars add to a significant air quality problem. Carbon monoxide, oxides of nitrogen, and un-burnt hydrocarbons are gases, and are generally invisible. Particulate matter is usually invisible although under certain operating conditions diesel engines will produce visible particles, appearing as smoke. Petrol engines will also produce visible particles if they are burning engine oil or running "rich".

ISSN(Online): 2319-8753
ISSN (Print): 2347-6710

International Journal of Innovative Research in Science, Engineering and Technology

(An ISO 3297: 2007 Certified Organization)

Website: www.ijirset.com

Vol. 6, Issue 7, July 2017

PARAMETERS OF VEHICULAR POLLUTION

Cars and trucks produce air pollution throughout their life, including pollution emitted during vehicle operation, refueling, manufacturing, and disposal. Additional emissions are associated with the refining and distribution of vehicle fuel. Air pollution from cars and trucks is split into primary and secondary pollution. Primary pollution is emitted directly into the atmosphere; secondary pollution results from chemical reactions between pollutants in the atmosphere. Some of the major pollutants from motor vehicles are particulate matter, hydrocarbons, nitrogen oxides, carbon mono oxide and sulphur dioxide. Particulate matter(PM) are particles of soot and metals which give smog its murky colour. Fine particles — less than one-tenth the diameter of a human hair — pose the most serious threat to human health, as they can penetrate deep into lungs. PM is a direct (primary) pollution and a secondary pollution from hydrocarbons, nitrogen oxides, and sulphur dioxides. Diesel exhaust is a major contributor to PM pollution. Hydrocarbons (HC) pollutants react with nitrogen oxides in the presence of sunlight to form ground level ozone, a primary ingredient in smog. Hydrocarbons contribute to ground-level ozone formation leading to risk of damage to the human respiratory system. Some kinds of hydrocarbons, in addition, are both carcinogenic and indirect greenhouse gases. Nitrogen oxides (NOx) pollutants cause lung irritation and weaken the body's defenses against respiratory infections such as pneumonia and influenza. Oxides of nitrogen include nitrogen dioxide (NO2) High levels of exposure have been linked with increased hospital admissions due to respiratory problems, while long-term exposure may affect lung function and increase the response to allergens in sensitive people Carbon monoxide (CO) when inhaled, blocks oxygen from the brain, heart, and other vital organs. Fetuses, new-born children, and people with chronic illnesses are especially susceptible to the effects of CO. Carbon monoxide reduces the blood's oxygen-carrying capacity which can reduce the availability of oxygen to key organs. Sulphur dioxide (SO2) Power plants and motor vehicles create this pollutant by burning sulphur-containing fuels, especially diesel. Sulphur dioxide can react in the atmosphere to form fine particles and poses the largest health risk to young children and asthmatics.

STANDARDS OF VEHICULAR POLLUTION

The standards are set by Central Pollution Control Board under the ministry of Environment and Forests and climate change. These are called Bharat Stage Emission Standards that regulate the output of the air pollutants from internal combustion engine equipment. These standards based on European regulations were first introduced in 2000.The standard active now is Bharat Stage-IV norms which has been implemented since 2012.These norms help in bringing down pollution levels. Exposure to air pollution can lead to a number of cardiovascular and respiratory diseases.

Table 1 Emission norms for passenger cars

Norms	CO(g/km)	HC+ NOx(g/km)
1991Norms	14.3-27.1	2.0(Only HC)
1996 Norms	8.68-12.40	3.00-4.36
1998Norms	4.34-6.20	1.50-2.18
India stage 2000 norms	2.72	0.97
Bharat stage-II	2.2	0.5
Bharat Stage-III	2.3	0.35(combined)
Bharat Stage-IV	1.0	0.18(combined)

ISSN(Online): 2319-8753
ISSN (Print): 2347-6710

International Journal of Innovative Research in Science, Engineering and Technology

(An ISO 3297: 2007 Certified Organization)

Website: www.ijirset.com

Vol. 6, Issue 7, July 2017

Table 2 Emission norms for two or three wheelers

Norms	CO(g/km)	HC+ NOx(g/km)
1991Norms	12-30	8-12 (only HC)
1996 Norms	4.5	3.6
India stage 2000 norms	2.0	2.0
Bharat stage-II	1.6	1.5
Bharat Stage-III	1.0	1.0

Table 3 Emission norms for heavy diesel vehicles

Norms	CO(g/kmhr)	HC (g/kmhr)	NOx (g/kmhr)	PM(g/kwhr)
1991Norms	14	3.5	18	-
1996 Norms	11.2	2.4	14.4	-
India stage 2000 norms	4.5	1.1	8.0	0.36
Bharat stage-II	4.0	1.1	7.0	0.15
Bharat Stage-III	2.1	1.6	5.0	0.10
Bharat Stage-IV	1.5	0.96	3.5	0.02

MEASUREMENT OF VEHICULAR POLLUTION

There are three approaches available to measure vehicle emissions. The first approach involves bringing vehicles into a laboratory, placing the vehicles on a dynamometer, and measuring their emissions as they are operated. The second approach is to place emission measurement and exhaust flow measurement equipment onto the vehicles and measure emissions from the vehicles as they are operated in the field. The third option is to use remote sensing to detect emissions from vehicles as they drive by. The traditional way to measure emissions from vehicles is to bring them into the laboratory and measure emissions as they are operated on a dynamometer. In the better laboratories, the dynamometers can vary the load that they place on a vehicle on a second by second basis. Some older dynamometers are only capable of maintaining a steady load that can be changed, but only while the vehicle is not being tested. In either case, a load is placed on the vehicle that is equivalent to a load that the vehicle might experience while it is operating on a roadway and the emissions are measured from the vehicle. The actual emission measurements are typically made using a Constant Volume Sampling (CVS) system. This system works by pulling a constant volume of air that is larger than the amount of gases emitted by the vehicle being tested through a sampling duct. The exhaust gases from the vehicle being tested are mixed with this makeup air. The makeup air must, of course, be free of gases and particulate matter in order to not distort the testing process. On-road vehicle emissions measurement equipment has only become realistically available since about 2003. The equipment is often referred to as portable emissions measurement equipment or PEMs.

III. MATERIALS AND METHODS

Opacity of smoke and smoke density factor has been measured to study the vehicular pollution from diesel engine with the help of smoke meter. Testing has been done as per IS: 8118:2008. Smoke meter, Model no: 437C

ISSN(Online): 2319-8753
ISSN (Print): 2347-6710

International Journal of Innovative Research in Science, Engineering and Technology

(An ISO 3297: 2007 Certified Organization)

Website: www.ijirset.com

Vol. 6, Issue 7, July 2017

manufactured by AVL India Private Ltd was used and the analysis was done in the CASRAE lab, Delhi Technological University, Delhi. CO, NO_X, C_xH_y, SO_2 and Fuel efficiency has been measured from a Wagon R petrol Engine with the help of digas analyser Model no: 444 manufactured by AVL India Private Ltd. To test the increase in efficiency of the fuel by power ring, first the emissions of the engine without installing the power ring was tested. The engine was allowed to warm up for 30 minutes and then the emissions were tested by the respective instrument. The test was repeated by installing the power ring at the inlet of the fuel pipe.

IV. RESULTS AND DISCUSSION

The exhaust from the WagonR petrol engine, model: ED2 2009/10 having engine dynamometer was tested. The test was performed using Low Gas Analyzer in Biodiesel Laboratory. The various parameters recorded are listed in Table 4 and 5.

Table 4: Parameters of petrol emission tested without ring

CO	NO	C_xH_y	SO_2	NO_x	Fuel Efficiency (%)	T_c
277.1	42.3	1306	1.5	160.1	90.40	144s

Table 5: Parameters of petrol emission tested with ring

CO	NO	C_xH_y	SO_2	NO_x	Fuel Efficiency (%)	T_c
265.1	87.5	975.4	0	114.9	95.30	158s

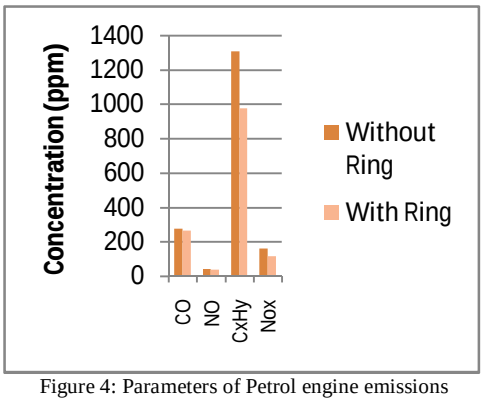


Figure 4: Parameters of Petrol engine emissions

The exhaust from Honda City Car having 4 stroke engine was also tested at Pollution Checking centre in Chandigarh, Haryana (PUC center code P087) with and without the ring. These results would help in realizing the benefits of the ring for practical purposes in the consumer vehicles. The results obtained from the test are as follows:

ISSN(Online): 2319-8753
ISSN (Print): 2347-6710

International Journal of Innovative Research in Science, Engineering and Technology

(An ISO 3297: 2007 Certified Organization)

Website: www.ijirset.com

Vol. 6, Issue 7, July 2017

Table 5: Parameters of Petrol Emission in vehicle without ring

RPM	CO	CO_2	O_2	λ
2647	0.185	13.60	0.38	1.1548

Table 6: Parameters of Petrol Emission in vehicle with ring

RPM	CO	CO_2	O_2	λ
2526	0.0003	17.31	0.07	1.002

The exhaust from the Indica diesel engine, model: AG80ED2 2010/11 having engine dynamometer was tested. The test was performed using Smoke Meter in the Biodiesel Laboratory. Opacity of the smoke measured with and without ring is listed in Table 7 and 8.

Table 7: Parameters of diesel engine emission tested without ring

N(%) Opacity	K(m^{-1}) Smoke density factor	T(^oC) Heating Chamber Temperature	n(min^{-1}) rpm	t(^oC Oil Temperature
17.3	0.42	52	972	25
16.9	0.41	55	972	26

Table 8: Parameters of diesel engine emissions tested with ring

N(%) Opacity	K(m^{-1}) Smoke density factor	T(^oC) Heating Chamber Temperature	n(min^{-1}) rpm	t(^oC) Oil Temperature
14.4	0.36	55	970	24
14.6	0.37	56	970	24

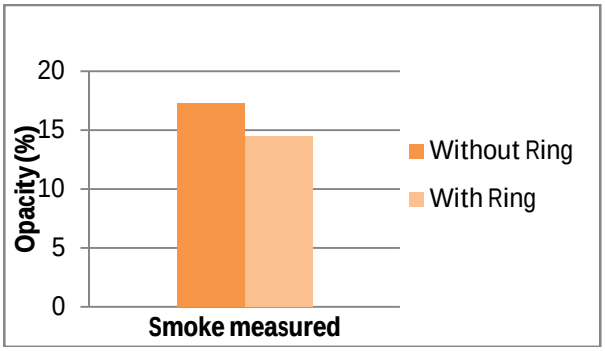


Figure 5: Comparison of diesel engine emissions

There is a reduction in smoke emissions after installation of the Power Ring. The reductions in Petrol and Diesel engine thus calculated have been summed up in Table 9 and 10.

ISSN(Online): 2319-8753
ISSN (Print): 2347-6710

International Journal of Innovative Research in Science, Engineering and Technology

(An ISO 3297: 2007 Certified Organization)

Website: www.ijirset.com

Vol. 6, Issue 7, July 2017

Table 9: Percentage reduction in emissions in petrol engine

Parameters	Without Ring	With ring	Reduction (%)
CO	277.1	265.1	4.3
NO	42.3	87.5	11.3
C_xH_y	1306	975.4	25.3
SO_2	1.5	0	100
No_x	160.1	114.9	28.3

Table 10: Percentage reduction in emissions in diesel engine

Parameter	Without Ring	With ring	Reduction (%)
Opacity	17.3	14.4	16.76
	16.9	14.6	13.6

This purpose of the study was to find the performance evaluation of biosignal ring to reduce the level of pollution in diesel and petrol engines. According to the tests performed on the diesel and petrol engine, it can be observed that a significant decrease in the pollutants released by the engine can be achieved with the help of the ring. The overall reduction in diesel engines with the aid of the ring was found to be about 16.18%, which shows that if these rings are fitted in diesel engine it can give a remarkable outcome in alleviating pollution levels. In case of petrol engine, considerable reduction in the value of various parameters was observed. The reduction percentage in hydrocarbons is about 25.3% and that in nitrogen oxides is 28.3%. It is also noteworthy to see that besides reducing pollution levels, the fuel efficiency of the petrol engine has also increased from 90.40% to 95.30% as recorded from the instrument. It was also observed that time taken by the engine to consume 100 mL of fuel without the ring was 144 seconds, and on the application of the ring the time was reduced to 158 seconds. This goes on to show that the application of the ring is of importance not only in reducing pollutants from engine but also in increasing the efficiency of the engine.

V. CONCLUSION

From the results obtained, we see that the Power Ring is very efficient in reducing the pollutants from the atmosphere. Various parameters constituting the smoke in have significantly decreased in the engine exhaust after installation of the ring. The ring works effectively on diesel as well as petrol engines. In petrol engines, maximum reduction is in the oxides of nitrogen. Besides reducing the pollution, it proves to be economical to install the ring into to engine inlets of the motor vehicles. It is so because an increase in burning capacity of the fuel is observed. This indicates increase in fuel efficiency which makes the fuel last longer.

If the ring is incorporated in vehicles, it can prove to be beneficial for consumers on a daily basis. According to our observations due to the insertion of ring the same engine requires 7 minutes more to consume 1 litre of petrol which means that one can save a litre of petrol on an average if he or she travels 10 km daily. As obtained from results the fuel efficiency in petrol engine has increased from 90.4% to 95.3%. Also, a remarkable reduction of 16.18% is obtained in Diesel engine exhaust.

Hence, it can be concluded that the Power Ring is the much needed means to get the rising levels of pollution in control and further also proves to be economical. We recommend the incorporation of Power ring in private and govt. vehicles to be made compulsory.

The idea of the Power Ring is to atomize the fuel at the very inlet of the engine. This gives two positive results, firstly, burning the fuel much more efficiently and secondly, minimizing the emission of the un-burnt carbon particles. This not only helps in reducing the pollution at the exhaust valve, but also increases the efficiency of the fuel by about 5-30%, making it last longer. The Power Ring can be installed in petrol engines, diesel engines and generators. The installation process being simple, it can be attached on the fuel pipe by any individual. Since, automobiles contribute to 80-90% of the air pollution; there is tremendous scope of this Power Ring in the present as well as in the future as it is high time for mankind to act on the rising levels of air pollution especially in megacities.

ISSN(Online): 2319-8753
ISSN (Print): 2347-6710

International Journal of Innovative Research in Science, Engineering and Technology

(An ISO 3297: 2007 Certified Organization)

Website: www.ijirset.com

Vol. 6, Issue 7, July 2017

REFERENCES

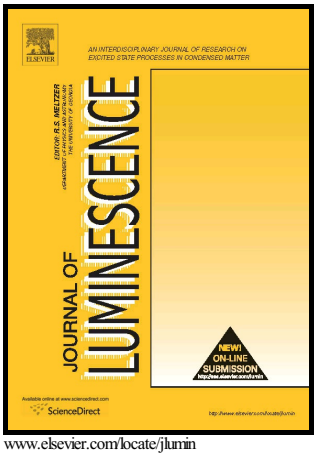
1. *"Remote heartbeat monitor will outperform current technology". University of Sussex Bulletin. 8 February 2002. Retrieved 14 June 2015.*
2. *"New non-invasive sensor can detect brainwaves remotely". University of Sussex. 24 October 2002. Retrieved 14 June 2015.*
3. *T. J. Sullivan; S.R. Deiss; G. Cauwenberghs A Low-Noise, Non-Contact EEG/ECG Sensor. Biomedical Circuits and Systems Conference, 2007 (BIOCAS 2007, IEEE). pp. 154–157 (November 2007).*
4. *C J Harland; T D Clark; R J Prance. "Electric potential probes - new directions in the remote sensing of the human body". Measurement Science and Technology. (February 2002).*
5. Brouse, Andrew. "A Young Person's Guide to Brainwave Music: Forty years of audio from the human EEG." — Biotechnological Performance Practice / Pratiques de performance biotechnologique (July 2012).
6. Ortiz, Miguel. "A Brief History of Biosignal-Driven Art: From biofeedback to biophysical performance."— Biotechnological Performance Practice / Pratiques de performance biotechnologique (July 2012).
7. Lopes, Pedro and jefchippewa. "Performing Biological Bodies: An open conversation with Marco Donnarumma, Claudia Robles and Peter Kirn at Body Controlled" — Bio Interfacing. Biotechnological Performance Practice / Pratiques de performance biotechnologique (July 2012).
8. Biotechnological Performance Practice / Pratiques de performance biotechnologique (July 2012).
9. ForEG, GümşelEB, OzgonO, Prediction of ABC Removal by Different Materials from Landfill Leachate: Modeling of Experimental Results XYZ Technique, The Scientific World Journal, vol. 52, no. 2, (2013).
10. Rosen (Ed.), Erwin M. The Peterson automotive troubleshooting & repairmanual. Grosset& Dunlap, Inc. ISBN 978-0-448-11946-5. (1975).
11. "Infrared Remote Sensing Of On-Road Motor Vehicle Emissions In Washington State"
12. HE Kebin,ZHANGQiang, HOU Hong, Point source of pollution: Local effects and its control,Types and amount of vehicular pollution, vol.1 (2010).
13. Jones, M. "Advanced opacitymeters: their potential role in future emission testing legislation for Diesel vehicles", Proc. of the 6th ETH Conference on Nanoparticle Measurement, Zurich, August 2002, http://nanoparticles.ch/archive/2002_Jones_PR.pdfJames Lents, Micheal Walsh, Kebin He, Nicolus Davis, SebestianTolvett, Haunliu, Handbook of air quality management (2002).
14. Central pollution control board 2008 vehicular emissions. Available: cpcb.nic.in/vehicular/exhaust.php.
15. Akane Sano, Takashi Tomita, Haruo Oba , Application using earphone with biosignal sensors, (2009)
16. M.A.Hasan, , "Detection and processing techniques of FECG Signal for fatal monitoring", biological procedures Online, 33 pages.
17. Yang J, 2009, "A New Filtering algorithm for removing salt and pepper Noise,", international conference on environmental science and information application technology,1,355-358 (2009).
18. Anders S, Lotze M. Grodd W., Birbaumer N. Brain activity underlying emotional valence and arousal:A response-related Fmri study. Human brain mapping, Vol. 23, p. 200-209 (2004).
19. SK Singh, DN Rao Evaluation of plants for their tolerance to air pollution - Proceedings of symposium on air pollution control, 1983
20. M Agrawal, SK Singh, J Singh, DN Rao Biomonitoring of air pollution around urban and industrial sites.- Journal of Environmental Biology, (1991).
21. Allaa M Aenab, SK Singh, Ali Jabir Lafta, "Air Quality Assessment: A Statistical Approach to Stationary Air Monitoring Stations", International Journal of Advanced Research, 3(3): 68-80, (2015).
22. Gour, A.A., Singh, S.K., Tyagi, S.K. and Mandal, A. (2015) Variation in Parameters of Ambient Air Quality in National Capital Territory (NCT) of Delhi (India), Atmospheric and Climate Sciences; 5:13-22. http://dx.doi.org/10.4236/acs.2015.51002
23. JR Goldsmith, LT Friberg - Effects of air pollution on human health Air pollution - Academic Press New York (1977).
24. St. Fleur, Nicholas (10 November 2015). "Atmospheric Greenhouse Gas Levels Hit Record, Report Says". New York Times. Retrieved, (11 November 2015).
25. Saber, E.M.; Heydari, G. "Flow patterns and deposition fraction of particles in the range of 0.1–10 μm at trachea and the first third generations under different breathing conditions". Computers in Biology and Medicine. 42 (5): 631–638. doi:10.1016/j.compbiomed.2012.03.002. PMID 224450+97. (May 2012).
26. A Katiyar, SK Singh, AK HaritashEFFECT OF ODD EVEN SCHEME TO COMBAT AIR POLLUTION IN NCT OF DELHI. International journal of Advanced Research 5 (2), 1215-1222, (2017).
27. Shishir Bansal, S.K. Singh "SUSTAINABILITY STUDIES OF TRANSPORTATION CORRIDORS: A REVIEW", International Journal of Advanced Research (2016), Volume 4, Issue 3, 1906-1917(2016).
28. Allaa M Aenab, SK Singh, Ali Jabir Lafta, "Air Quality Assessment: A Statistical Approach to Stationary Air Monitoring Stations", International Journal of Advanced Research, 3(3): 68-80. (2015).
29. AM Aenab, SK Singh, AJ Lafta, Critical Assessment of Air Pollution by ANOVA Test and Human Health Effects, Atmospheric Environment, Volume 71, pp 84-91, (2013)
30. Anunay A. Gour, S.K. Singh, S.K. Tyagi, Anubha Mandal, (2013), "Weekday/Weekend Differences in Air Quality Parameters in Delhi, INDIA", International Journal of Research in Engineering & Technology (IJRET), ISSN 2321-8843, Vol. 1, Issue 5, 69-76, (October, 2013).
31. A.A. Gour, S. K. Singh, A. Mandal (2016). "A glance at the world: Composition, trends and impacts of municipal solid waste in India", Waste Management – **Elsevier**. 55 (2016).
32. Diksha Gupta, **S.K Singh**. Energy Use And Greenhouse Gas Emissions From Waste water Treatment Plants. International Journal of Environmental Engineering- inderscience , 7(1): 1-10, **DOI**: 10.1504/IJEE.2015.069251, (2015).
33. Kumar Amrit, Mishra, RK, SK Singh. GIS application in urban traffic air pollution exposure study : A research review. SS Science and technology journal, Vol.2 No.1. pp 25-37, (2015).
34. Shashank Shekhar Singh, **Singh S K** and Shuchita Garg. Environmental Concerns in National Capital Territory of Delhi, India. J Climatology & Weather Forecasting 2015, 3:3 http://dx.doi.org/10.4172/2332-2594.1000147, (2015).

View publication stats

Author's Accepted Manuscript

Photoluminescence and Energy Transfer studies of Dy^{3+} Ions doped Lithium Lead Alumino Borate Glasses for w-LED and Laser Applications

Nisha Deopa, A.S. Rao



www.elsevier.com/locate/jlumin

PII: S0022-2313(17)30033-9
DOI: http://dx.doi.org/10.1016/j.jlumin.2017.07.052
Reference: LUMIN14928

To appear in: *Journal of Luminescence*

Received date: 9 January 2017
Revised date: 11 July 2017
Accepted date: 27 July 2017

Cite this article as: Nisha Deopa and A.S. Rao, Photoluminescence and Energy Transfer studies of Dy^{3+} Ions doped Lithium Lead Alumino Borate Glasses for w-LED and Laser Applications, *Journal of Luminescence* http://dx.doi.org/10.1016/j.jlumin.2017.07.052

This is a PDF file of an unedited manuscript that has been accepted for publication. As a service to our customers we are providing this early version of the manuscript. The manuscript will undergo copyediting, typesetting, and review of the resulting galley proof before it is published in its final citable form. Please note that during the production process errors may be discovered which could affect the content, and all legal disclaimers that apply to the journal pertain.

ACCEPTED MANUSCRIPT

Photoluminescence and Energy Transfer studies of Dy^{3+} Ions doped Lithium Lead Alumino Borate Glasses for w-LED and Laser Applications

Nisha Deopa, A. S. Rao*

Department of Applied Physics, Delhi Technological University, Bawana Road, New Delhi-110 042, India.

*Corresponding author. Tel.: +91 85860 39007; fax: +91 01127871023. E-mail: drsrallam@gmail.com

Abstract

Lithium Lead Alumino Borate (LiPbAlB) glasses doped with Dy^{3+} ions with varying concentration were synthesized by using the melt quenching technique to understand their feasibility in solid state lighting and laser devices. From the absorption spectra, bonding parameters (δ) were evaluated to understand the nature of bonding between Dy^{3+} ions and its surrounding ligands. Judd-Ofelt intensity parameters estimated from the experimental oscillator strengths were used to evaluate various radiative parameters for the fluorescent levels of Dy^{3+} ions. From the decay curves, the experimental lifetimes were measured and coupled with the radiative lifetimes to evaluate the quantum efficiency. The decay profile changes from exponential to non-exponential with increase in Dy^{3+} ion concentration resulting decrease in experimental lifetimes. Inokuti-Hirayama model applied to the decay spectral profiles confirm dipole-dipole interaction responsible for their conversion from exponential to non-exponential. By exciting the glasses with different n-UV radiations, the CIE chromaticity coordinates and correlated color temperatures (CCT) were calculated to understand the utility of as-prepared glasses in cool white light generation. From the evaluated radiative parameters, CIE co-ordinates, CCT temperatures, emission cross-sections, quantum efficiency and confocal images, it was observed that LiPbAlB glass with 0.5 mol% Dy^{3+} ions are more suitable for the development of w-LEDs and Lasers.

Accepted manuscript

ACCEPTED MANUSCRIPT

1. Introduction

Quite recently, Solid State Lighting (SSL) based devices are playing an important role in science and technology and attracting researchers along with lighting industries. SSL devices are capable of saving tremendous amount of energy and showing environmental friendliness by reducing almost 28 million metric tons carbon emission per annum worldwide [1]. Further, SSL based devices are having applications in diversified fields like cellular phone screens, white Light Emitting Diodes (w-LEDs), traffic signals, liquid crystal displays, magneto-optical devices etc. [2–4]. SSL based devices have paved a path for the tremendous development of w-LEDs, which are far better than the conventional light sources like incandescent lamps, electric bulbs and tube lights, because of their longer life span, compact size, high efficiency, less energy consumption [5,6]. Conventionally, w-LEDs are fabricated by using two different approaches. The first one is by exciting yellow phosphor (YAG:Ce^{3+}) with blue LED chip (InGaN) and the second one is by using mixed phosphors (RGB) excited with the help of UV LED [7–10]. However both the methods have some drawbacks; the first method suffers from low color rendering index (CRI) and high color correlated temperature (CCT=7750K) while the second one suffers with low luminescent efficiency [11,12]. The phosphor in the form of powder will be encapsulated in the epoxy region made up of polymer material and the emission of w-LED strongly depends upon the thickness of such polymer material as well as on the concentration of phosphor. However, the epoxy region deteriorates at high temperature, high energy and high excitation sources. Therefore, glasses doped with Rare Earth (RE) ions are the best alternatives for phosphors as there is no epoxy region involved. Over and above, the simpler manufacture procedure, low production cost, homogeneous light emission, higher transparency and less damage due to heat also makes glasses superior over phosphors [13] .

Accepted manuscript

ACCEPTED MANUSCRIPT

Among the various glass formers available in periodic table, boric acid (B_2O_3) is said to be one of the best glass formers as it is capable of forming the glass alone with good transparency, thermal stability, lower melting point and good RE ion solubility [4,13,14]. In general, B_2O_3 is having less scientific interest because of its high phonon energies around 1300 cm^{-1}, which allows emission predominantly through non-radiative process [15]. Nevertheless, such high phonon energies possessed by borate glasses can be reduced considerably by adding heavy metal oxides (HMO) such as lead oxide (PbO) and bismuth oxide (BiO) [16]. Among the HMOs mentioned above, PbO in B_2O_3 can suppress non-radiative decay and enhances the luminescent efficiency. Further, PbO-B_2O_3 binary glass systems are having relatively higher chemical durability than the other glasses and possessing applications in enamels, seals, solders and photonic devices [4, 5, 16]. Addition of Al_2O_3 to a borate glass not only makes it to act as a good network modifier, but also improves the chemical stability, mechanical strength and emission properties of the host glass [17]. Presence of lithium oxide (Li_2O) in a borate glass can enhance the chemical stability and modifies physical as well as chemical properties [18]. Considering the scientific patronages offered by the aforementioned chemical constituents, for the present work, we prepared a host namely Lithium Lead Aluminoborate (LiPbAlB) glass doped with Dy^{3+} ions at different concentrations, with an aim to understand the suitability of such glasses for their utility in w-LEDs and other optoelectronic devices.

Inorganic compound possess unique optical properties when doped with RE ions and led the way for advancement of luminescent materials in various applications. Recently RE doped glasses fascinated many researchers as well as scientist due to their 4f electronic configuration which causes emission from ultraviolet to infrared region having various application in optical amplifiers, solid state lasers, fluorescent lamps etc. [19–21]. Furthermore, RE doped glasses are

Accepted manuscript

ACCEPTED MANUSCRIPT

better than the phosphors because of their lower production cost, simple manufacture procedure, good thermal stability and high doping capacity [6,22]. Among all the RE ions, trivalent dysprosium (Dy^{3+}) with $4f^9$ electronic configuration is a potential candidate for visible lasers as it gives visible emission between its f-f transitions. The photoluminescence (PL) spectra of Dy^{3+} ions consist of two intense peaks in blue (470-500 nm) and yellow (570-600 nm) regions corresponding to the transitions $^4F_{9/2} \rightarrow {}^6H_{15/2}$ and $^4F_{9/2} \rightarrow {}^6H_{13/2}$ respectively. In spite of this, Dy^{3+} ions are very useful as they are capable to act as single phase white light emitting sources, electron trapping materials and mercury free luminescence lamps etc. [23]. It is the foremost challenge for researchers to optimize the local field environment of Dy^{3+} ions doped glasses for generating white light emission having suitable yellow to blue (Y/B) intensity ratio. The suitable Y/B ratio can be achieved for near white light emission by varying the Dy^{3+} ions concentration in the host matrix. Further, the emission of Dy^{3+} ions from the transition $^4F_{11/2} \rightarrow {}^6H_{9/2}$ is suitable for 1.32 μm optical transmission in fiber amplification [24–26]. Dy^{3+} ion doped amorphous and crystalline materials also possess fluorescence in yellow to orange (570-590 nm) and NIR (1.35 and 3.0 μm) regions and are useful in lasers and telecommunications [27,28].

Structural and mechanical properties of lead borate glasses have been extensively studied by many researchers [29, 34]. Few researchers have studied the optical properties of RE ions doped borate, Li-borate and Al-borate and lead borate glasses [35-38]. The intresting optical results reported in the above mentioned papers prompted us to study the optical and luminescence properties of Dy^{3+} doped lead borate glasses added with lithium and aluminium.

Accepted manuscript

ACCEPTED MANUSCRIPT

2. Experimental

Lithium Lead Alumino Borate glasses having the chemical composition $10Li_2O$-10PbO-(10-x) Al_2O_3 -$70B_2O_3$-xDy_2O_3 (where, x = 0.1, 0.5, 1.0, 1.5, 2.0 and 2.5 mol % designated as Glass A, B,C,D,E and F respectively) were prepared by conventional melt quenching technique using the analar grade chemicals Li_2O, PbO, Al_2O_3, B_2O_3 and Dy_2O_3 as starting materials. These chemicals in the above proportion were weighed, mixed and then crushed in an agate mortar using acetone as wetting medium until the homogeneous mixture is formed. The homogeneous mixture was kept into a silica crucible and heated at 1100^0 C in an electrical furnace for 5 hours and desired melt samples were prepared. The melt sample is poured in brass plate having temperature 350^0C and quenched with another brass plate to obtain transparent glass sample of uniform thickness. The glass samples then annealed for 4 hours in another electrical furnace (350^0C) to remove thermal strains. Finally, Dy^{3+} doped LiPbAlB glass samples were obtained to study their luminescence properties. Densities of the as-prepared glasses were evaluated by using Archimedes method taking water as an immersion liquid with an accuracy of ±0.01 gm/cm^3. Brewster's angle method was used to calculate refractive indices of the as-prepared glasses by using He-Ne laser (650 nm line) with ± 0.01 accuracy. The room temperature (300K) optical absorption spectra were recorded in the wavelength range 350-1800 nm using Shimadzu 3600 UV-vis-NIR spectrophotometer with a spectral resolution of 0.1 nm. The PL and PL Excitation (PLE) spectra were recorded by using Shimadzu RF-5301-PC spectrofluorophotometer fitted with Xenon flash lamp. The decay curves were recorded by using Edinburgh FLSP900 equipment with a spectral resolution of 0.1 nm, having xenon lamp as an excitation source. Confocal images were recorded under 405 nm Continuous Wave (CW) diode laser excitation source using Olympus BX51confocal microscope instrument equipped with XY piezo stage.

Accepted manuscript

ACCEPTED MANUSCRIPT

3. Results and discussion

3.1 Absorption Spectral Analysis and Bonding Parameters

The optical absorption spectrum of 0.5 mol% Dy^{3+} ions doped LiPbAlB glass (glass B) recorded in UV-vis and NIR regions along with the assignment of bands originated from $^6H_{15/2}$ ground state has been depicted in Fig. 1. The spectrum consist several absorption bands corresponding to the transitions $^6H_{15/2} \rightarrow {}^6H_{11/2}$, $^6F_{11/2}$ + $^6H_{9/2}$, $^6F_{9/2}$ + $^6H_{7/2}$, $^6F_{7/2}$, $^6F_{5/2}$, $^6F_{3/2}$, $^4F_{9/2}$, $^4I_{15/2}$, $^4F_{7/2}$ + $^4I_{13/2}$, $^6P_{7/2}$, $^4M_{17/2}$ + $^6P_{3/2}$. The identification of energy levels with proper assignments has been done as per the report published by Carnall et.al [39]. The band positions of activator ions at 390 nm ($^6H_{15/2} \rightarrow {}^6P_{7/2}$) and 425 nm ($^6H_{15/2} \rightarrow {}^4F_{7/2}$+$^4I_{13/2}$) are very weak because of the strong absorption possessed by the host glass in that region. The transition corresponding to $^6H_{15/2} \rightarrow {}^6H_{9/2}$+$^6F_{11/2}$ is having high intensity as compared to other transitions and is hypersensitive obeying the selection rule $|\Delta S| = 0, |\Delta L| \leq 2, |\Delta J| \leq 2$ [40]. The bonding parameters (δ) values were evaluated from the nephelauxetic ratio ($\overline{\beta}$) using the following formula [41,42]

$$\delta = \frac{1-\overline{\beta}}{\overline{\beta}} X\ 100 \qquad (1)$$

The value of 'δ' strongly depends upon the ligand field environment around the RE ions and may be negative or positive showing ionic or covalent nature respectively. The 'δ' values for the titled glasses from glass A-F are -1.93, -0.87, -0.74, -0.63, -0.58 and -0.54 respectively. It is observed that the titled glasses possess ionic nature which decreases gradually with increase in Dy^{3+} ions concentration.

3.2 Band gap and Urbach's Analysis

Accepted manuscript

ACCEPTED MANUSCRIPT

From the absorption spectra, the optical band gap for the as-prepared glasses were estimated by using Davis and Mott's expression [43]

$$\alpha h\vartheta = B(h\vartheta - E_{opt})^n \quad (2)$$

here, α is absorption coefficient, h is Plank's constant, ϑ is frequency, B is bonding trailing parameter and E_{opt} is optical band gap energy. The value of n can be 1/2, 2, 1/3 and 3 corresponding to direct allowed, indirect allowed, direct forbidden and indirect forbidden transitions respectively. The value of absorption coefficient can be evaluated by following expression [44]

$$\alpha(\vartheta) = \frac{1}{d}\ln\left(\frac{I_0}{I_t}\right) \quad (3)$$

here, $\alpha(\vartheta)$ is absorption coefficient, d is thickness of the glass sample, I_0 is intensity of incident radiation and I_t is intensity of transmitted radiation. The optical band gap energies (E_{opt}) were evaluated using Tauc's plot by extrapolating the liner region of the plot drawn for $(\alpha h\upsilon)^{1/2}$ versus $h\upsilon$ as shown in Fig. 2. The band tailing parameter along with optical bandgap for direct and indirect allowed transition are placed in Table 1. From Table 1, it is observed that the optical band gap energy decreases while band tailing parameter increases with Dy^{3+} ions concentration. That is because RE oxides changes the oxygen bonding in glassy network resulting in the formation of non-bridging oxygen (NBO). The NBO so formed are associated with the valence band maximum (VBM) and increasing NBO shifts towards the conduction band which in turn lead to have a fall in the band gap values.

Further, it is investigated that in a glassy matrix, the fundamental absorption edge represents the extent of exponential tail and arises due to association of inter-band transition tails and follows the Urbach rule. The following expression explains Urbach rule [45]

Accepted manuscript

ACCEPTED MANUSCRIPT

$$\alpha(\vartheta) = C \exp\left(\frac{h\vartheta}{\Delta E}\right) \quad (4)$$

Here, C is constant, and ΔE is Urbach energy, represents the optical transition between the localized band tails of valence band and the conduction band that extended into the band gap. The ΔE values evaluated from the inverse of the slope of the linear region are given in Table 1. From Table 1, it can be observed that, the values of ΔE are increasing with concentration. The Inset in Fig. 2 shows the variation of direct, indirect band gap and Urbach's energy values against Dy^{3+} ion content in the titled glasses.

In the present work, glasses with higher Dy^{3+} ion concentration are possessing higher Urbach energies than the other glasses indicating the presence of long range order originating from the minimum number of defects. Further, the Urbach energy values are increasing while optical band gap values are decreasing. Furthermore, ΔE is not only responsible for disorderliness in the amorphous material but also the formation of the defects. From Table 1, the relatively lower values of ΔE are found which indicates minimum defect as well as less disorderliness that in turn enhances the optical properties.

3.3 Oscillator Strengths and J-O intensity parameters

From the absorption spectral features, observed transition intensities for Dy^{3+} doped LiPbAlB glasses were estimated with the help of area under the curve, using the following expression [46]

$$f_{exp} = 4.318 \times 10^{-9} \int \varepsilon(\vartheta) d\vartheta \quad (5)$$

here, $\varepsilon(\vartheta)$ is the molar extinction coefficient at a wavenumber ϑ cm^{-1}. The J-O theory has been successfully applied to the measured oscillator strengths for evaluating J-O intensity parameters (Ω_2, $\Omega_4$and Ω_4) by using least square fit analysis [46,47]. The essential expressions for

Accepted manuscript

ACCEPTED MANUSCRIPT

evaluating calculated oscillator strengths (f_{cal}) and root mean square deviations (δ_{rms}) were collected from the literature [48]. Table 2 gives the experimental oscillator strengths (f_{exp}), f_{cal} along with δ_{rms} for Dy^{3+} ions in LiPbAlB glasses. Smaller δ_{rms} values obtained between the f_{exp} and f_{cal} indicates the validity of J-O theory in evaluating J-O parameters for their subsequent usage in calculating various radiative parameters. The reliable J-O intensity parameters evaluated from least square fit analysis along with spectroscopic quality factor ($\chi = \frac{\Omega_4}{\Omega_6}$) are tabulated in Table 3 along with the values reported in literature for comparison [14,19,20,49-52]. "χ" predicts the channel by which RE ions can relax through luminescence from the metastable states [53]. J-O intensity parameters are important to learn the effect of host glass matrix on the radiative properties of doped RE ions because it is connected with interaction of central field ions, inter configurational radial integrals and crystal field parameters with the surrounding environment [54]. As shown in Table 3, the J-O intensity parameters are following the same trend ($\Omega_2 > \Omega_6 > \Omega_4$) for all the as-prepared Dy^{3+} doped LiPbAlB glasses. Generally, magnitude of Ω_2 is used to study covalency between doped RE ions and oxygen atom and magnitude of Ω_4, Ω_6 are related to bulk properties such as viscosity and rigidity.

In this report magnitude of J-O intensity parameters (Ω_2, Ω_4 and Ω_6) increases with the increase in the intensity of hypersensitive transitions and vice versa. The intensity of hypersensitive transition is maximum for glass B (0.5 mol% Dy^{3+}) and minimum for glass F (2.5 mol% Dy^{3+}) showing higher symmetry of crystal field at the Dy^{3+} ions site for glass B and lower symmetry of crystal field at the Dy^{3+} ions site for glass F. Among the as-prepared glasses, the value of χ is highest for glass B (0.5 mol% Dy^{3+}). Therefore glass B is potential candidate for lasing action because of larger χ which is characteristics of higher stimulated emission cross-section.

Accepted manuscript

ACCEPTED MANUSCRIPT

3.4 Analysis of PL Spectra and Evaluation of Radiative Properties

In order to record the PL spectra, it is essential to know the excitation wavelength. The excitation spectra recorded for the as-prepared glasses by monitoring emission at 483 nm is shown in Fig. 3. The spectra consist of four excitation bands at wavelength 322, 348, 362 and 384 nm corresponding to the transitions $^6H_{15/2}\rightarrow{}^4M_{17/2}$, $^6P_{7/2}$, $^6P_{5/2}$, and $^4I_{13/2}$ respectively. Many sharp excitation bands spreading from nUV to blue region indicates that the as-prepared glasses can be act as potential candidates for w-LED applications under the excitation of nUV/blue wavelength. Among the four excitation peaks, a band at 348 nm corresponding to $^6H_{15/2}\rightarrow{}^6P_{7/2}$ transition is more intense and is used as an excitation wavelength to record the PL for all the glasses. The PL spectra of Dy^{3+} ions doped LiPbAlB glasses recorded under 348 nm excitation exhibit two intense peaks centered at 483 nm (blue region) and 572 nm (yellow region) corresponding to the electronic transitions $^4F_{9/2}\rightarrow{}^6H_{15/2}$ and $^4F_{9/2}\rightarrow{}^6H_{13/2}$ respectively , as shown in Fig. 4. Further, Fig. 5 shows the variation of integrated emission intensities of yellow and blue bands with Dy^{3+} ions content showing high intensity for 0.5 mol% (glass B). However, we have also recorded the emission spectra for Dy^{3+} doped LiPbAlB glasses at different excitations (322, 362, and 384 nm) to know the variation in emission intensity and is shown in Fig. 6. Transition related to $^4F_{9/2}\rightarrow{}^6H_{15/2}$ is magnetic dipole in nature whereas transition related to $^4F_{9/2}\rightarrow{}^6H_{13/2}$ is electric dipole following the selection rules (S=0, L=2 and J=2). Among the two transitions, intensity of $^4F_{9/2}\rightarrow{}^6H_{15/2}$ is higher than $^4F_{9/2}\rightarrow{}^6H_{13/2}$ transition as shown in Fig. 4 and 5. This is because the transition corresponds to $^4F_{9/2}\rightarrow{}^6H_{15/2}$ observed in blue region is hypersensitive in nature and strongly influenced by the environment around Dy^{3+} ions [55].

The partial energy level diagram explaining excitation, emission, energy transfer along with the possible cross-relaxation channels observed for glass D depicted in Fig. 7. From Fig. 7 it is

Accepted manuscript

ACCEPTED MANUSCRIPT

observed that radiative transition takes place from $^4F_{9/2}$ excited state and emits intense blue and yellow color. The intensity of the as-prepared glasses increases for $^4F_{9/2}\rightarrow{}^6H_{13/2}$ and $^4F_{9/2}\rightarrow{}^6H_{15/2}$ transitions with increase in the Dy^{3+} ions concentration up to 0.5 mol % and beyond it decreases. Such reduction in intensity observed due to concentration quenching through resonant energy transfer (RET) between Dy^{3+}– Dy^{3+} ions explaining self-quenching mechanism [56,57].The feasible non-radiative cross-relaxation channels along with resonant energy transfer are given bellow [58]

CR1: $^4F_{9/2} + {}^6H_{15/2} \rightarrow {}^6H_{5/2} + ({}^6H_{7/2}, {}^6F_{9/2})$

CR2: $^4F_{9/2} + {}^6H_{15/2} \rightarrow {}^6F_{3/2} + ({}^6H_{9/2}, {}^6F_{11/2})$

RET: $^4F_{9/2} \rightarrow {}^6H_{15/2}$

On the other hand, to study PL performance of the as-prepared Dy^{3+} doped LiPbAlB glasses, radiative parameters such as radiative transition probability (A_R), luminescence branching ratio (β_R), total transition probability (A_T) and radiative lifetime (τ_R) were evaluated with the help of suitable expression given in the literature [59] for both the fluorescent levels ($^4F_{9/2}\rightarrow{}^6H_{13/2,}$ $^4F_{9/2}\rightarrow{}^6H_{15/2}$) by using J-O parameters. The enhanced value of stimulated emission cross-section (σ_{se}) is very essential for achieving high gain along with low threshold for continuous wave laser action applications and also useful in identifying potential laser transition of Dy^{3+} ions in LiPbAlB host matrix. The stimulated emission cross-section can be evaluated by the following equation [51,60].

$$\sigma_{se}(a_j, b_{j'}) = \left[\frac{{\lambda_p}^4}{8\pi c n^2 \Delta\lambda_p}\right] A_R(a_j, b_{j'}) \qquad (6)$$

Accepted manuscript

ACCEPTED MANUSCRIPT

here, λ_P is emission peak wavelength, $\Delta\lambda_p$ is the line width (FWHM) of the transition. The values of radiative parameters A_R, β_R and A_T for Dy^{3+} doped LiPbAlB glasses were evaluated and presented in Table 4. The values of σ_{se} along with emission peak wavelength (λ_P), effective band widths ($\Delta\lambda_P$), branching ratios (β_R & β_{exp}), gain band width (σ_{se} x $\Delta\lambda_p$) and optical gain parameter (σ_{se} x τ_R) for the titled glasses were tabulated in Table 5. The variation in $\Delta\lambda_P$ ensues due to splitting of transitional levels and site to site variation of ligand field around Dy^{3+} ions in the glass matrix. From Table 5, it is observed that value of $\Delta\lambda_P$ increases up to glass B and decreases thereafter. Among all the glasses, glass B exhibits highest σ_{se} value for both transitions $^4F_{9/2}\rightarrow$ $^6H_{13/2}$ and $^4F_{9/2}\rightarrow$ $^6H_{15/2}$. The higher value of σ_{se} observed for glass B for both the transitions are in good agreement with reported values [61,62] and placed in Table 5. The relatively higher value of β_R & β_{exp} makes them as promising candidates for lasing emission through $^4F_{9/2}\rightarrow$ $^6H_{15/2}$ (483 nm) emission channel. RE doped amorphous material possess the properties of a good optical fiber only if σ_{se} x $\Delta\lambda_p$ and optical gain parameter σ_{se} x τ_R are having higher values. It can be seen from Table 5 that the values of σ_{se}, λ_P, $\Delta\lambda_P$, β_R, β_{exp}, σ_{se} x $\Delta\lambda_p$ and σ_{se} x τ_R are highest for glass B than the other as-prepared glasses. The reasonably larger values observed for all the above mentioned parameters of glass B for the transitions $^4F_{9/2}\rightarrow$ $^6H_{13/2}$ and $^4F_{9/2}\rightarrow$ $^6H_{15/2}$ (nm) makes them potential candidate for solid state laser applications. A comparison between the aforementioned parameters in different Dy^{3+} glassy hosts have been done and tabulated in Table 6. It is observed from the Table 6 that Glass B is having highest values of laser parameter than the other reported glasses.

3.5 Colorimetry Calculations

Accepted manuscript

ACCEPTED MANUSCRIPT

The colorimetric parameters for the as-prepared Dy^{3+} doped LiPbAlB glasses under different excitation (322, 348, 362, 384 nm) wavelengths were calculated and presented in Table 7. Among all the glasses, glass B possess excellent white light chromaticity coordinates (x=0.304, y=0.360) under 348 nm excitation and lies very close to CIE standard D65 illuminant (x=0.310, y=0.340) also standard equal energy white point (x=0.333, y=0.333) [5]. From Table 7, calculated values of CIE chromaticity coordinates can be seen which are in good agreement with some reported glasses like GP10 (0.309, 0.341) [5], NbFS (0.330, 0.370) [63], LBO (0.342, 0.372) [64] PKAlCaFDy05 (0.32, 0.36) [65], silicate (0.39, 0.44) [6], BBS05 (0.31, 0.34) [66]. Further, correlated color temperature (CCT) is another important parameter for characterizing key features of the illuminant and can be defined as temperature of Planckian black body whose color coordinates are closer to the standard white light source. CCT can be evaluated using the following expression proposed by McCamy [67]

$$CCT = -449n^3 + 3525n^2 - 6823.2n + 5520.3 \quad (7)$$

here, $n = \frac{x-x_e}{y-y_e}$, $x_e = 0.332, y_e = 0.186$. The value of CCT for all the as-prepared Dy^{3+} doped LiPbAlB glasses under different excitation (322, 350, 362, 384 nm) were represented in Table 7 and are found to be in cool white light region (6000-7000 K). It is observed that for optimized glass sample i.e., for glass B under 448 nm excitation, CCT is 6654 K which is also close to D65 illuminant. Higher the CCT better the visual acuity along with higher brightness perception.

Another important parameter in colorimetric calculations is color purity or color saturation and it can be defined as the distance of separation between the color coordinate points of material under investigation to the color coordinates of equal energy point divided by distance between

Accepted manuscript

ACCEPTED MANUSCRIPT

equal energy point and dominant wavelength point. The value of color purity can be evaluated from the expression [68]

$$Color\ purity = \frac{\sqrt{(x-x_{ee})^2+(y-y_{ee})^2}}{\sqrt{(x_d-x_{ee})^2+(y_d-y_{ee})^2}} \quad (8)$$

here, (x, y), (x_{ee}, y_{ee}) and (x_d, y_d) denotes the chromaticity coordinates of test sample, equal energy point and dominant wavelength respectively. It is reported that color purity parameter must have low values for white light generation [63]. The values of dominant wavelength points can be seen from Fig. 8 and color purity calculated for optimized glass (glass B) under different excitations 322, 348, 362, 384 nm are $15.36x10^{-2}$, $7.61x10^{-2}$, $8.09x10^{-2}$, $12.02x10^{-2}$ respectively. Fig. 8 shows the CIE color coordinates of glass B under different excitations (322, 348, 362 and 384 nm). From the above colorimetric results, it is observed that glass B at 348 nm excitation is very efficient for white light generation and fabrication of w-LED with commercial nUV/Blue LED chip as an excitation source.

The yellow to blue intensity ratio (Y/B) is another important parameter for white light generation and has been evaluated for all the four excitation peaks (325, 350, 362 and 384 nm) for the titled glasses, tabulated in Table 7. The variation in Y/B intensity ratio encountered which may be due to the addition of Dy^{3+} in amorphous matrix which causes impact on the local environment host matrix in turn changes the intensity of hypersensitive transition.

3.6 Time Resolved Photoluminescence Analysis

The luminescence decay profiles recorded for the emission transitions $^4F_{9/2} \rightarrow {}^6H_{15/2}$ (483 nm) and $^4F_{9/2} \rightarrow {}^6H_{13/2}$ (572 nm) under 348 nm excitation are shown in Fig. 9(a) and 9(b) respectively. The decay profiles are showing single exponential nature up to 0.5 mol% of Dy^{3+} ions and non-exponential beyond it. The non-exponential behavior arises due to energy transfer between donor

Accepted manuscript

ACCEPTED MANUSCRIPT

(excited Dy^{3+} ion) and acceptor (unexcited Dy^{3+} ion) ions in the amorphous matrices. It is worth to note that the experimental lifetime values are comparatively smaller that the radiative lifetimes calculated by J-O theory. This discrepancy arises due to non-radiative relaxation of the donors and also due to interaction of Dy^{3+} ions with the OH- stretching modes present in the sample under investigation [16]. The non-radiative relaxation can be evaluated by using the following expression

$$\frac{1}{\tau_{exp}} = \frac{1}{\tau_R} + W_{NR} \qquad (9)$$

Such non-radiative relaxation rates evaluated are given in Table 8. From the data present in Table 8, it is conspicuous that, Glass B possesses less non-radiative relaxation rates when compared with the other LiPbAlB glasses under investigation. Obviously such glasses with less non-radiative relaxation rates are prone to give higher stimulated emission cross-sections and quantum efficiencies. Quantum efficiency (η) is defined as ratio of number of photons emitted to the photons absorbed and for the RE doped glasses, it can be evaluated by taking the ratio of experimental to radiative lifetimes. The values of η measured for all the LiPbAlB glasses are presented in Table 8. From Table 8, it is observed that glass B possesses relatively higher quantum efficiency value than the remaining LiPbAlB glasses. The decrease in experimental lifetime can be attributed to the concentration quenching observed because of cross-relaxation processes among the energy levels of same energy and resonant energy transfer from the donor in the excited state ($^4F_{9/2}$) to the acceptor ($^6F_{15/2}$ and $^6F_{13/2}$) in the ground state as shown in Fig. 5.

3.7 Inokuti-Hiryama (I-H) model Analysis

The nature of interaction between donor-acceptor ($Dy^3 - Dy^{3+}$) and energy transfer behavior for higher Dy^{3+} concentrations in LiPbAlB glasses have been analyzed through decay profiles using

Accepted manuscript

ACCEPTED MANUSCRIPT

I-H model [69]. According to I-H model, energy transfer between donor-acceptor should be faster than the energy migration and the luminescence intensity decay in such a case is given by

$$I_t = I_0 \exp\{-\frac{t}{\tau_0} - Q(\frac{t}{\tau_0})^{\frac{3}{S}}\} \quad (10)$$

where, I_0 is intensity at $\tau = 0$, τ_0 is intrinsic decay time of donors in the absence of acceptors and Q is energy transfer parameter which can be expressed as follows

$$Q = \frac{4\pi}{3} \Gamma(1 - \frac{3}{S}) N_0 R_0^3 \quad (11)$$

here, the value of S explains energy transfer mechanism and the interaction can be dipole-dipole for S=6, (Γ(X)=1.77) dipole-quadrupole for S=8, (Γ(X)=1.43) and quadrupole-quadrupole for S=8, (Γ(X)=1.3) respectively. N_0 is concentration of acceptor ions, R_0 is critical energy transfer distance. The energy transfer probability and donor acceptor interaction parameter can be evaluated by using the following expression

$$C_{DA} = R_0^{(S)} \tau_0^{-1} \text{ and } W_{ET} = C_{DA} R_0^{(S)} \quad (12)$$

The I-H fitting applied for the decay profiles of higher Dy^{3+} ion concentration in LiPbAlB glasses (Glass C to Glass F) are shown in Fig.10. As shown in Fig.10, the decay profiles for higher concentrations are well fitted to I-H model taking S=6, which confirms that the interaction is dipole-dipole in nature between Dy^{3+} ions. The values of R_0, C_{DA} and Q evaluated from the aforementioned equations are presented in Table 8 along with some reported values [16,39,70-73]. It is observed that R_0 value is decreasing while Q and C_{DA} values are increasing with increase in Dy^{3+} ions in the glasses under investigation. This may be due to efficient energy migration between $Dy^{3+} - Dy^{3+}$ ions via cross-relaxation channels as shown in Fig. 7.

4. Conclusions

Accepted manuscript

ACCEPTED MANUSCRIPT

Lithium Lead Aluminoborate (LiPbAlB) glasses doped with varying concentration of dysprosium were prepared by using quenching technique and thoroughly studied for their utility in w-LEDs and Lasers. The optical band gap, band tailing parameters, Urbach energies and bonding parameters were evaluated from the optical absorption spectra. The nature of bonding between Dy^{3+} ions and its surrounding ligands found to be ionic in nature, which decreases linearly with increase in RE ion concentration. Under n-UV excitation, the titled glasses emit intense white light with the combination of blue and yellow emission bands and intensity of blue emission band is found to be higher than yellow band. The CIE chromaticity coordinates (0.306, 0.342) fall in the pure white region and are in close proximity to the commercial pc-LED and (National Television System Committee) NTSC white light. This result is also in consistent with confocal images recorded for the titled glasses. The value of CCT confirms that the emission takes place in cool white light region, and are in good agreement with daylight and commercial w-LEDs. The decay profile of Dy^{3+} doped LiPbAlB glasses are found to be perfectly single exponential for lower concentration and non-exponential for higher concentration and experimental lifetime decreases with increasing Dy^{3+} ions concentration. Inokuti-Hirayama model applied to the decay spectral profiles confirm dipole-dipole interaction responsible for their conversion them from exponential to non-exponential. From the above mentioned results it is concluded that among the titled glasses, glass B is potential candidate for the fabrication of laser active materials as well as cool w-LEDs and contributing to environment saving through its SSL applications.

Accepted manuscript

Acknowledgement

The authors are very much thankful to Dr. G. Vijaya Prakash, IIT-Delhi and Dr. D. Haranath, CSIR-NPL, Delhi for their experimental help in the present work.

ACCEPTED MANUSCRIPT

References

[1] Bergh A, Craford G, Duggal A, Haitz R. The promise and challenge of solid-state lighting. Phys Today 2001;54:42–7.

[2] Savage JA. Materials for infrared fibre optics. Mater Sci Reports 1987;2:99–138.

[3] Deopa N, Rao AS, Mahamuda Sk, Gupta M, Jayasimhadri M, Haranath D, Prakash GV. Spectroscopic studies of Pr^{3+} doped lithium lead alumino borate glasses for visible raddish organge luminescent device applications. J Alloys Compd 2017;708: 911–921.

[4] Pisarski WA, Goryczka T, Płonska M, Pisarska J. Structure and properties of rare earth-doped lead borate glasses. Mater Sci Eng B 2005;122:94–9.

[5] Jha K, Jayasimhadri M. Spectroscopic investigation on thermally stable Dy^{3+}doped zinc phosphate glasses for white light emitting diodes. J Alloys Compd 2016;688:833–40.

[6] Sun XY, Huang SM, Gong XS, Gao QC, Ye ZP, Cao CY. Spectroscopic properties and simulation of white-light in Dy^{3+}doped silicate glass. J Non Cryst Solids 2010;356:98–101.

[7] Kitai A. Luminescent Materials and Applications, John Wiley. 2008.

[8] Nakamura S, Fasol G. The Blue Laser Diode, Springer, Berlin. 1996.

[9] Kuo CH, Sheu JK, Chang SJ, Su YK, Wu LW, Tsai JM, et al. n-UV+Blue/Green/Red White Light Emitting Diode Lamps. Japan Soc Appl Phys 2003;42:2284–7.

[10] Jha K, Vishwakarma AK, Jayasimhadri M, Haranath D. Multicolor and white light

Accepted manuscript

ACCEPTED MANUSCRIPT

emitting Tb^{3+}/Sm^{3+} co-doped zinc phosphate barium titanate glasses via energy transfer for optoelectronic device applications. J Alloys Compd 2017;719:116–24.

[11] Chiu CH, Liu CH, Huang SB, Chen TM. White-Light-Emitting Diodes Using Red-Emitting $LiEu(WO_4)_{2-x}(MoO_4)_x$ Phosphors. J Electrochem Soc 2007;154:181–4.

[12] Ci Z, Sun Q, Qin S, Sun M, Jiang X, Zhang X, et al.Warm white light generation from a single phase Dy^{3+} doped $Mg_2Al_4Si_5O_{18}$ phosphor for white UV-LEDs. Phys Chem Chem Phys 2014;16:11597–604.

[13] Masai H, Yamada Y, Suzuki Y, Teramura K, Konemitsu Y, Yoko T. Narrow Energy Gap between Triplet and Singlet Excited States of Sn^{2+} in Borate Glass. Sci Rep 2013;3:3541–8.

[14] Mahamuda Sk, Swapna K, Packiyaraj P, Rao AS, Prakash GV. Lasing potentialities and white light generation capabilities of Dy^{3+} doped oxy-fluoroborate glasses. J Lumin 2014;153:382–92.

[15] Swapna K, Mahamuda Sk, Rao AS, Jayasimhadri M, Sasikala T, Moorthy LR. Optical absorption and luminescence characteristics of Dy^{3+} doped Zinc Alumino Bismuth Borate glasses for lasing materials and white LEDs. J Lumin 2013;139:119–24.

[16] Arunkumar S, Venkataiah G, Marimuthu K. Spectroscopic and energy transfer behavior of Dy^{3+} ions in B_2O_3-TeO_2-PbO-PbF_2-Bi_2O_3-CdO glasses for laser and WLED applications. Spectrochim Acta - Part A Mol Biomol Spectrosc 2015;136:1684–97.

[17] Deopa N, Rao AS. Spectroscopic studies of Sm^{3+} ions activated lithium lead alumino borate glasses for visible luminescent device applications. Opt Mater 2017;72:31-9.

Accepted manuscript

ACCEPTED MANUSCRIPT

[18] Padmaja G, Kistaiah P. Infrared and Raman Spectroscopic Studies on Alkali Borate Glasses : Evidence of Mixed Alkali Effect. J Phys Chem A 2009;113:2397–404.

[19] Swapna K, Mahamuda S, Rao AS, Jayasimhadri M, Moorthy LR. Visible fluorescence characteristics of Dy^{3+} doped zinc alumino bismuth borate glasses for optoelectronic devices. Ceram Int 2013;39:8459–65.

[20] Saleem SA, Jamalaiah BC, Jayasimhadri M, Rao AS, Jang K, Moorthy LR. Luminescent studies of Dy^{3+} ion in alkali lead tellurofluoroborate glasses. J Quant Spect Radi Transf 2012;112:78–84.

[21] Babu AM, Jamalaiah BC, Kumar JS, Sasikala T, Moorthy LR. Spectroscopic and photoluminescence properties of Dy^{3+}-doped lead tungsten tellurite glasses for laser materials J Alloys Compd 2011;509:457–62.

[22] Kiran N, Kumar AS. White light emission from Dy^{3+} doped sodium lead borophosphate glasses under UV light excitation. J Mol Struct 2013;1054–1055:6–11.

[23] Yang Z, Dong H, Liang X, Hou C, Liu L, Lu F. Preparation and fluorescence properties of color tunable phosphors Ca3Y2(Si3O9)2:Dy^{3+}. Dalt Trans 2014;2:3–7.

[24] Praveena R, Vijaya R, Jayasankar CK. Photoluminescence and energy transfer studies of Dy^{3+}doped fluorophosphate glasses. Spectrochim Acta - Part A 2008;70:577–86.

[25] Reddy CM, Dillip GR, Raju BDP. Spectroscopic and photoluminescence characteristics of Dy^{3+} ions in lead containing sodium fluoroborate glasses for laser materials. J Phys Chem Solids 2011;72:1436–41.

[26] Machewirth DP, Wei K, Krasteva V, Datta R, Snitzer E, Jr GHS. Optical characterization

Accepted manuscript

ACCEPTED MANUSCRIPT

of Pr^{3+} and Dy^{3+} doped chalcogenide glasses. J Non Cryst Solids 1997;213:295–303.

[27] Rai VK, Rai SB, Rai DK. Optical studies of Dy^{3+}doped tellurite glass : Observation of yellow-green upconversion. Opt Commun 2006;257:112–9.

[28] Kaminski AA. Crystalline Lasers: Physical Processes and Operating Schemes, Chemical Rubber Company, Boca Raton, FL, 1996. n.d.

[29] Hannora AE. Synthesis of lead-borate glasses using high energy ball milling (attritor). J Non Cryst Solids 2015;429:1-4.

[30] Kumar RR, Bhatnagar AK, Rao JL. EPR of vanadyl ions in alkali lead borate glasses. Mater Lett 2002;57:178-82.

[31] Sasikumar MV, Rajesh D, Balakrishna A, Ratnakaram YC. Optical absorption and photoluminescence properties of Dy^{3+} doped heavy metal borate glasses–effect of modifier oxides. J Mol Struct 2013;1041:100-5.

[32] Martin V, Wood B, Zwanziger UW, Zwanziger JW. Structural aspects of the photoelastic response in lead borate glasses. J Non Cryst Solids 2011;357:2120-5.

[33] Pisarski WA, Pisarska J, Maczka M, Lisiecki R, Grobelny L, Goryczka T, Dominiak-Dzik G, Ryba-Romanowski W. Rare earth-doped lead borate glasses and transparent glass–ceramics: Structure–property relationship. Spectrochim Acta - Part A 2011;79:696-700.

[34] Rada M, Rada S, Pascuta P, Culea E. Structural properties of molybdenum-lead-borate glasses. Spectrochim Acta - Part A 2010;77:832-7.

[35] Janek J, Soltys M, Zur L, Pietrasik E, Pisasrska **J,** Pisarski WA. Luminescence investigations of rare earth doped lead-free borate glasses modified by MO (M = Ca, Sr,

Accepted manuscript

ACCEPTED MANUSCRIPT

Ba). Mater Chem Phys 2016;180:237-43.

[36] Mallur SB, Czarnecki T, Adhikari A, Babu PK. Compositional dependence of optical band gap and refractive index in lead and bismuth borate glasses. Mater Res Bull 2015;68:27-34.

[37] Mallur SB, Ooi HG, Ferrell SK, Babu PK. Effect of metal and semiconducting nanoparticles on the optical properties of Dy^{3+} ions in lead borate glasses. Mater Res Bull 2017;92:52-64.

[38] Pawar PP, Munishwar SR, Gedam RS. Intense white light luminescent Dy^{3+} doped lithium borate glasses for W-LED: A correlation between physical, thermal, structural and optical properties. Solid State Sci 2017;64:41-50.

[39] Carnall WT, Fields PR, Rajnak K. Electronic Energy Levels in the Trivalent Lanthanide Aquo Ions. I. Pr^{3+}, Nd^{3+}, Pm^{3+}, Sm^{3+}, Dy^{3+}, Ho^{3+}, Er^{3+}, and Tm^{3+}. J Chem Phys 1968;49:4424–42.

[40] Thulasiramudu A, Buddhudu S. Optical characterization of Sm^{3+} and Dy^{3+} : ZnO – PbO – B_2O_3 glasses. Spectrochim Acta - Part A 2007;67:802–7.

[41] Jorgensen CK. The Nephelauxetic Series. Prog Inorg Chem 1962;4:73.

[42] Carnall WT, Gschneidner KA, Eyring (Eds.) L. Hand book of Physics and Chemistry of Rare-Earths. vol. 3, 1987, p. 171–208.

[43] Davis EA, Mott NF. Conduction in non-crystalline systems V. Conductivity, optical absorption and photoconductivity in amorphous semiconductors. Philos Mag 1970;22:903–22.

Accepted manuscript

ACCEPTED MANUSCRIPT

[44] Agarwal A, Seth VP, Sanghi S, Gahlot P, Goyal DR. Optical band gap studies and estimation of two photon absorption coefficient in alkali bismuth borate glasses. Radiat Eff Defects Solids 2013;158:793–801.

[45] Altaf M, Chaudhry MA, Zahid M. Study of Optical Band Gap Of Zinc-Borate Glasses. J Res Sci 2003;14:253–9.

[46] Judd BR. Intensities of Rare-Earth Ions. Phys Rev 1962;127:750–61.

[47] Ofelt GS. Intensities of Crystal Spectra of RareEarth Ions. J Chem Phys 1962;37:511–20.

[48] Babu P, Jayasankar CK. Spectroscopic properties of Dy^{3+} ions in lithium borate and lithium fluoroborate glasses. Opt Mater 2000;15:65–79.

[49] Ratnakaram YC, Naidu DT, Vijayakumar A, Rao JL. Studies on optical absorption and luminescence properties of Dy^{3+} doped mixed alkali borate glasses. Opt Mater 2004;27:409–17.

[50] Shin YB, Heo J. Mid-infrared emissions and multiphonon relaxation in Dy^{3+} doped chalcohalide glasses. J Non Cryst Solids 1999;253:23–9.

[51] Krupke WF. Induced-Emission Cross Sections in Neodymium Laser Glasses. IEE J Quantum Electron 1974;10:450–7.

[52] Jamalaiah BC, Moorthy LR, Seo HJ. Effect of lead oxide on optical properties of Dy^{3+} ions in $PbO – H_3BO_3 – TiO_2 – AlF_3$ glasses. J Non Cryst Solids 2012;358:204–9.

[53] Murthy DVR, Jamalaiah BC, Sasikala T, Moorthy LR, Jayasimhadri M, Jang K, et al. Optical absorption and emission characteristics of Pr^{3+} doped RTP glasses. Phys B 2010;405:1095–100.

Accepted manuscript

ACCEPTED MANUSCRIPT

[54] Sardar DK, Chandrasekharan S, Nash KL, Gruber JB. Optical intensity analyses of Er^{3+}:$YAlO_3$. J Appl Phys 2008;104:23102–8.

[55] Raju GSR, Jung HC, Park JY, Kanamadi CM, Moon BK, Jeong JH, et al. Synthesis and luminescent properties of Dy^{3+} : GAG nanophosphors. J Alloys Compd 2009;481:730–4.

[56] Dexter DL. A Theory of Sensitized Luminescence in Solids. J Chem Phys 1953;21:836–50.

[57] Dexter DL, Schulman JH. Theory of Concentration Quenching in Inorganic Phosphors. J Chem Phys 1954;22:1063–70.

[58] Linganna K, Rao CS, Jayasankar CK. Optical properties and generation of white light in Dy^{3+}doped lead phosphate glasses. J Quant Spectrosc Radiat Transf 2013;118:40–8.

[59] Cases R, Chamarro MA, Alcala R, Rodriguez VD. Optical properties of Nd^{3+} and Dy^{3+}ions in ZnF_2-CdF_2 based glasses. J Lumin 1991;48:509–14.

[60] Peacock RD. The intensities of lanthanide f ↔ f transitions. Struct Bond 1975;22:83–122.

[61] Venkateswarlu C, Seshadri M, Ratnakaram YC. Influence of mixed alkalis on spectroscopic parameters of Sm^{3+}, Dy^{3+} doped chloroborate glasses. Opt Mater 2011;33:799–806.

[62] Babu P, Jang KH, Kim ES, Shi L, Vijaya R, Lavín V, et al. Optical properties and energy transfer of Dy^{3+}doped transparent oxyfluoride glasses and glass–ceramics. J Non Cryst Solids 2010;356:236–43.

[63] Krishnaiah K V, Kumar KU, Jayasankar CK. Spectroscopic properties of Dy^{3+}doped oxyfluoride glasses for white light emitting diodes. Mater Express 2013;3:61–70.

Accepted manuscript

ACCEPTED MANUSCRIPT

[64] Sun XY, Wu S, Liu X, Gao P, Huang SM. Intensive white light emission from Dy^{3+}doped $Li_2B_4O_7$ glasses. J Non Cryst Solids 2013;368:51–4.

[65] Nayab S, Moorthy LR, Jayasankar CK. Optical and luminescence properties of Dy^{3+}ions in phosphate based glasses. Solid State Sci 2013;22:82–90.

[66] Mishra L, Sharma A, Vishwakarma AK, Jha K, Jayasimhadri M, Ratnam B V, et al. White light emission and color tunability of dysprosium doped barium silicate glasses. J Lumin 2016;169:121–7.

[67] McCamy CS. Correlated color temperature as an explicit function of chromaticity coordinates. Color Res Appl 1992;17:142–4.

[68] Kuo TW, Liu WR, Chen TM. High color rendering white light-emitting-diode illuminator using the red-emitting Eu^{2+}activated CaZnOS phosphors excited by blue LED. Opt Express 2010;18:8187–92.

[69] Inokuti M, Hirayama F. Influence of Energy Transfer by the Exchange Mechanism on Donor Luminescence. J Chem Phys 1965;43:1978.

[70] Basavapoornima C, Jayasankar CK, Chandrachoodan PP. Luminescence and laser transition studies of Dy^{3+} : K – Mg – Al fluorophosphate glasses. Phys B 2009;404:235–42.

[71] Babu SS, Babu P, Jayasankar CK, Tröster T, Sievers W, Wortmann G. Optical properties of Dy^{3+}doped phosphate and fluorophosphate glasses. Opt Mater 2009;31:624–31.

[72] Suthanthirakumar P, Marimuthu K. Investigations on spectroscopic properties of Dy^{3+} doped zinc telluro- fluoroborate glasses for laser and white LED applications. J Mol Struct

Accepted manuscript

ACCEPTED MANUSCRIPT

2016;1125:443–52.

[73] Kesavulu CR, Jayasankar CK. White light emission in Dy^{3+}doped lead fluorophosphate glasses. Mater Chem Phys 2011;130:1078–85.

Accepted manuscript

Figure captions

Fig. 1. Absorption Spectrum of 0.5 mol% of Dy^{3+} ions in LiPbAlB glass.

Fig. 2. Indirect bandgap plot of 0.5 mol% of Dy^{3+} ions in LiPbAlB glass (glass B) [Inset shows the variation of Urbach energy, direct and indirect bandgaps with Dy^{3+} ion concentration in LiPbAlB glasses].

Fig. 3. Excitation spectra of Dy^{3+} ions in LiPbAlB glasses under 483 nm emission.

Fig. 4. PL spectra of Dy^{3+} ions in LiPbAlB glasses under 348 nm excitation.

Fig. 5. PL spectral intensity variations of $^4F_{9/2} \rightarrow {}^6H_{15/2}$ (blue) and $^4F_{9/2} \rightarrow {}^6H_{13/2}$ (yellow) transitions of Dy^{3+} ions in LiPbAlB glasses.

Fig. 6. PL spectra of 0.5 mol% Dy^{3+} ions in LiPbAlB glass under different excitation wavelengths (384, 362, 348 and 322 nm).

ACCEPTED MANUSCRIPT

Fig. 7. Energy level diagram of 0.5 mol% Dy^{3+} ions in LiPbAlB glass with excitation, emission and cross-relaxation channels.

Fig. 8. CIE chromaticity coordinates and confocal images of Dy^{3+} ions in LiPbAlB glasses.

Fig. 9 (a). The decay spectral profiles of $^4F_{9/2} \rightarrow {}^6H_{15/2}$ (483 nm) emission transition of Dy^{3+} ions in LiPbAlB glasses under 348 nm excitation.

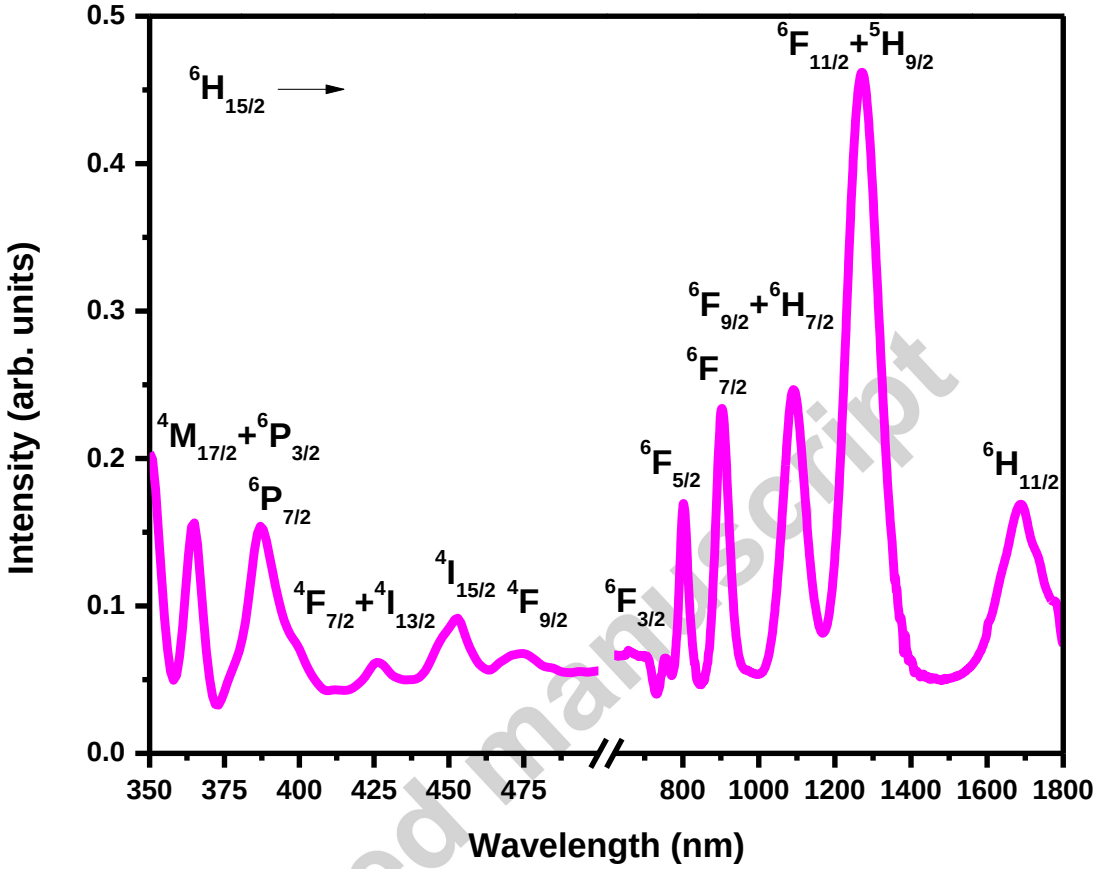
Fig. 9 (b). The decay spectral profiles of $^4F_{9/2} \rightarrow {}^6H_{13/2}$ (572 nm) emission transition of Dy^{3+} ions in LiPbAlB glasses under 348 nm excitation.

Fig. 10. I-H Fitted decay curves for $^4F_{9/2} \rightarrow {}^6H_{15/2}$ (483 nm) emission transition of Dy^{3+} ions in LiPbAlB glasses under 348 nm excitation.

Fig. 1.

Accepted manuscript

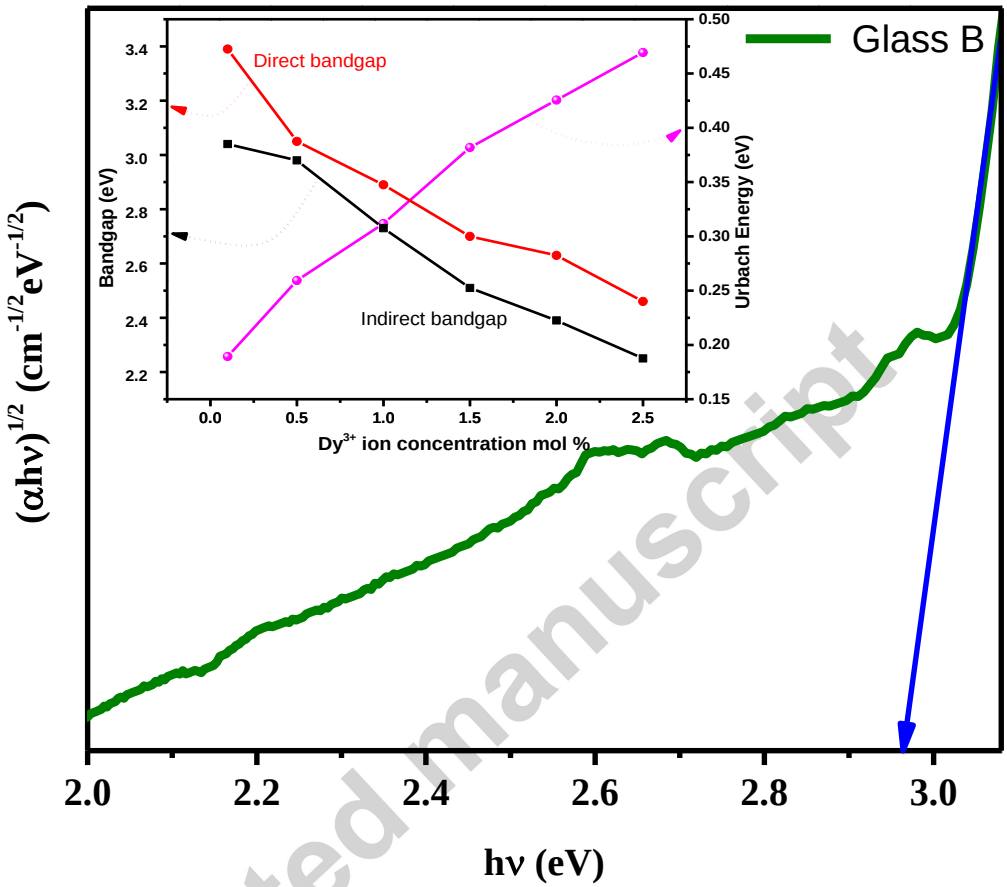
ACCEPTED MANUSCRIPT



Accepted manuscript

Fig. 2.

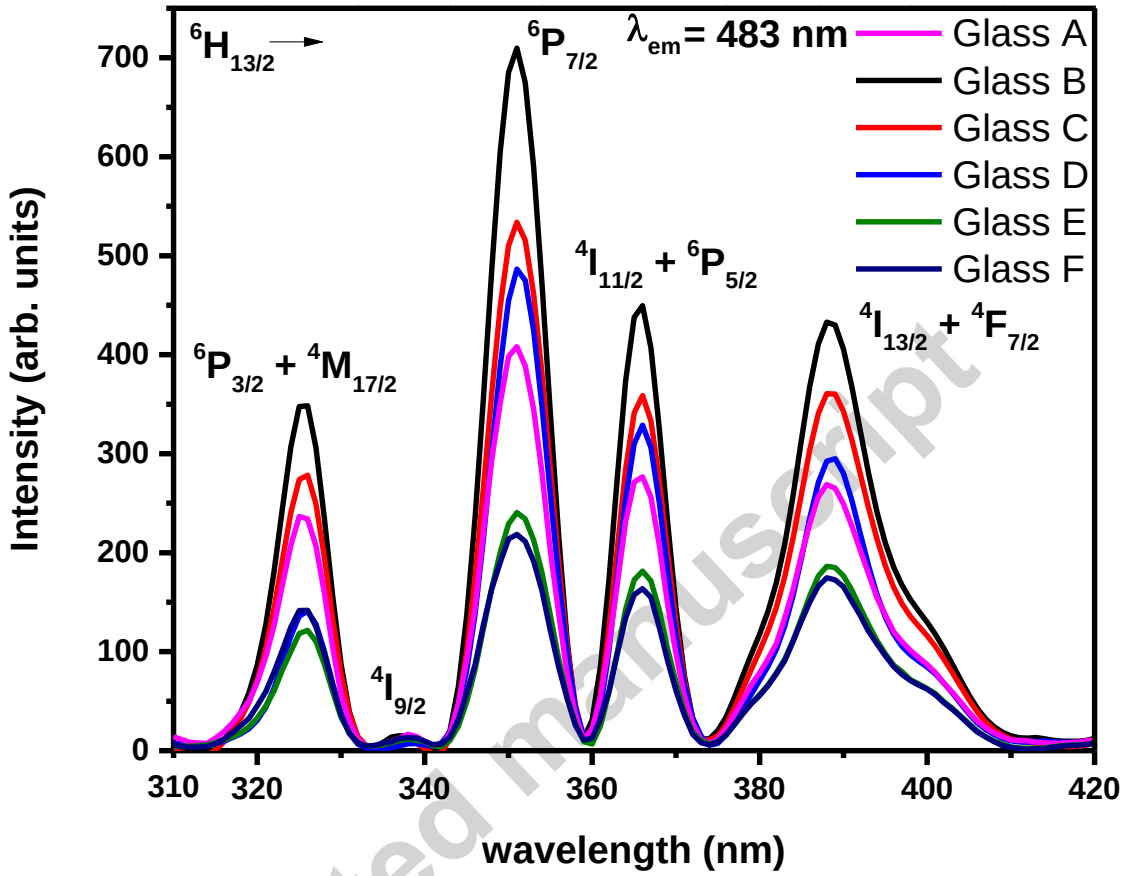
ACCEPTED MANUSCRIPT



Accepted manuscript

Fig. 3.

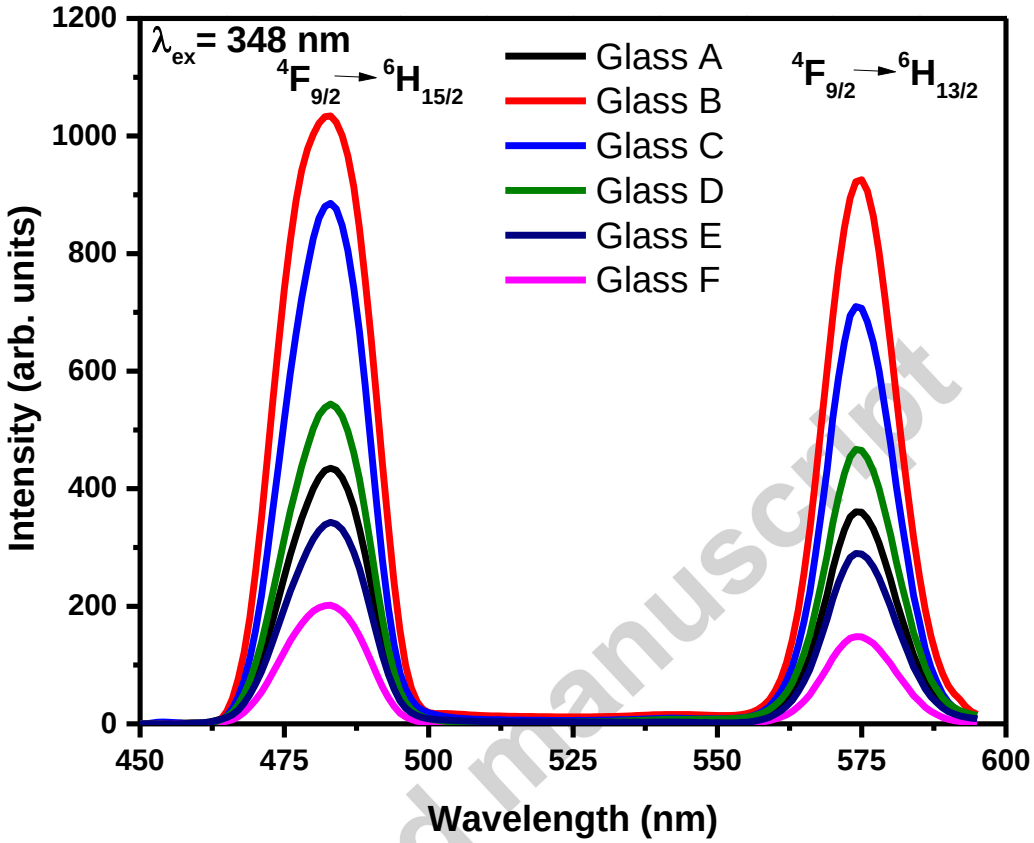
ACCEPTED MANUSCRIPT



Accepted manuscript

Fig. 4.

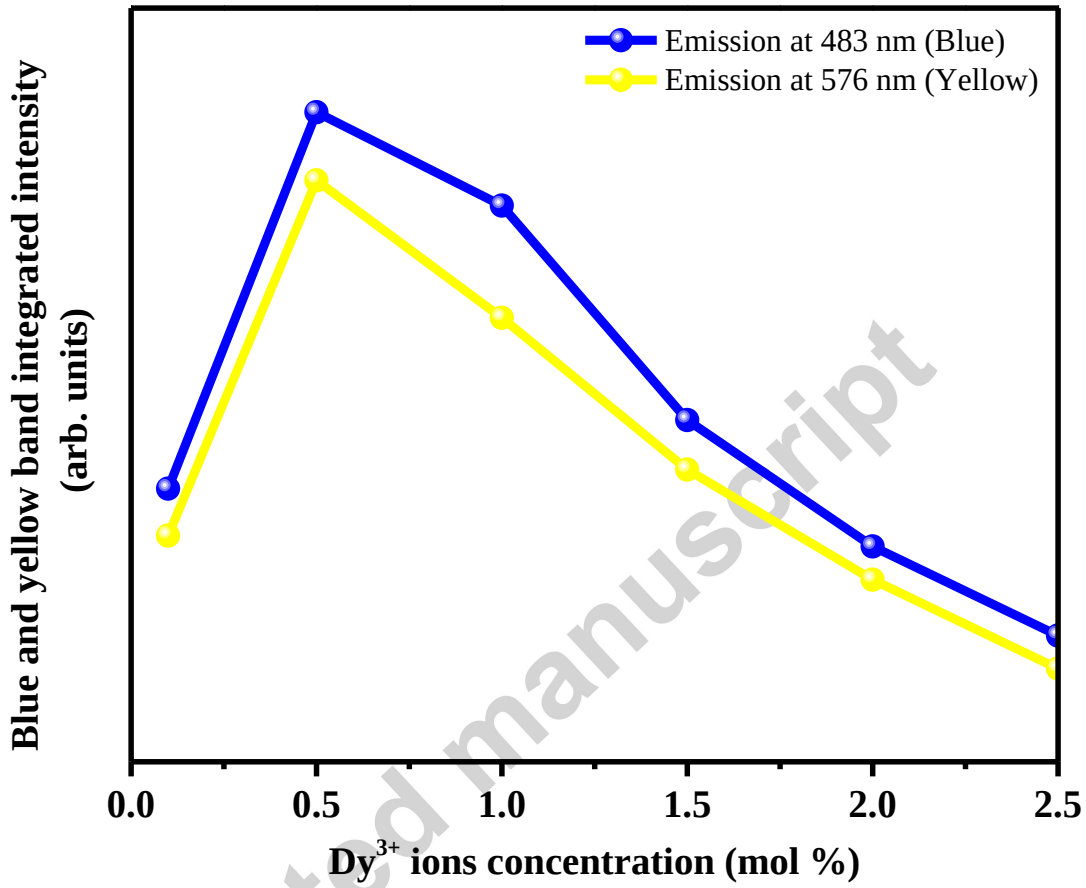
ACCEPTED MANUSCRIPT



Accepted manuscript

Fig. 5.

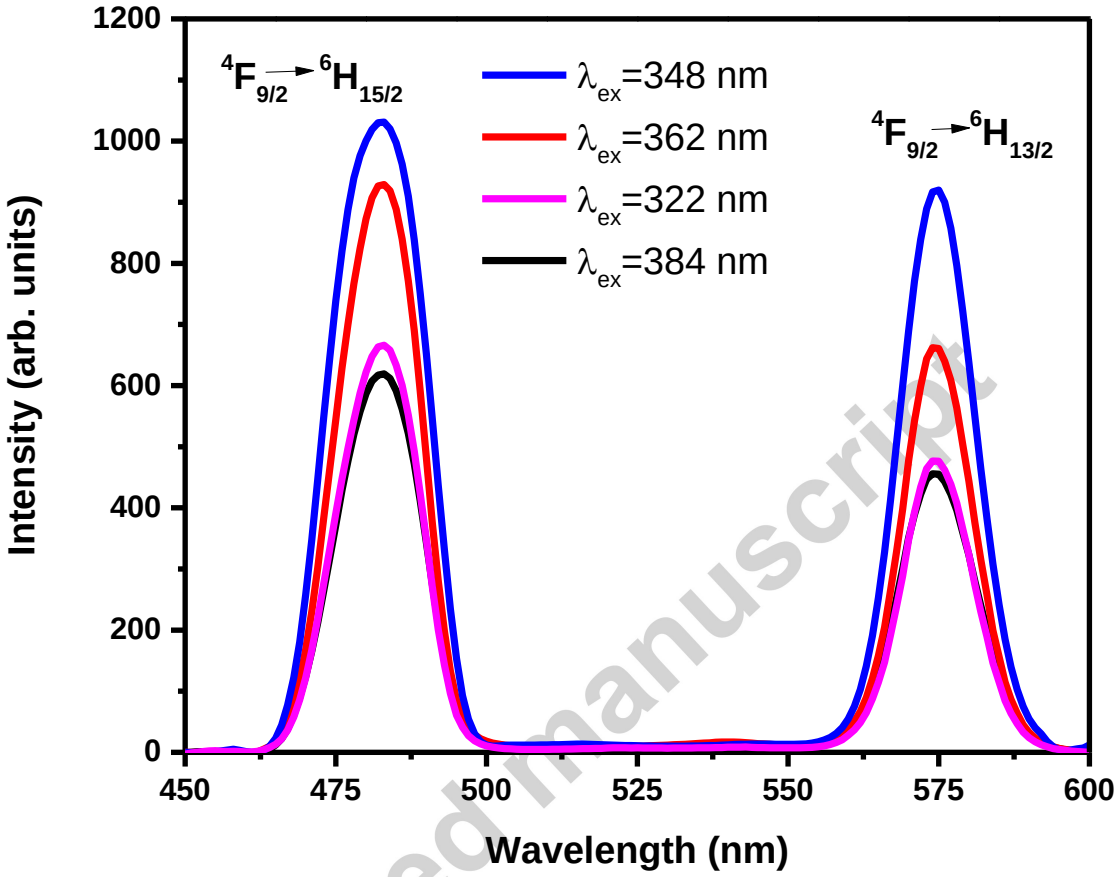
ACCEPTED MANUSCRIPT



Accepted manuscript

Fig. 6.

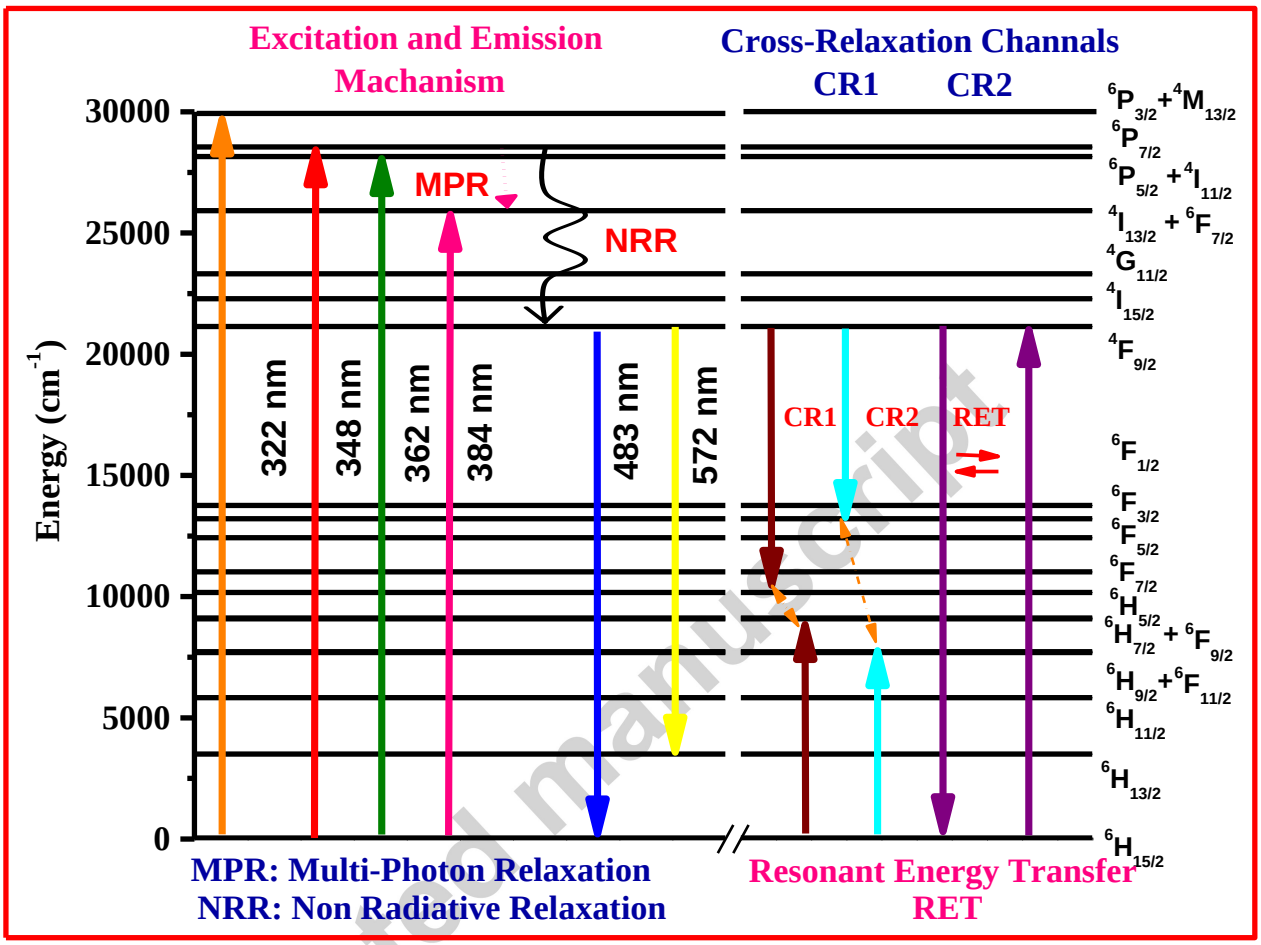
ACCEPTED MANUSCRIPT



Accepted manuscript

Fig. 7.

ACCEPTED MANUSCRIPT



Accepted manuscript

ACCEPTED MANUSCRIPT

Fig. 8.

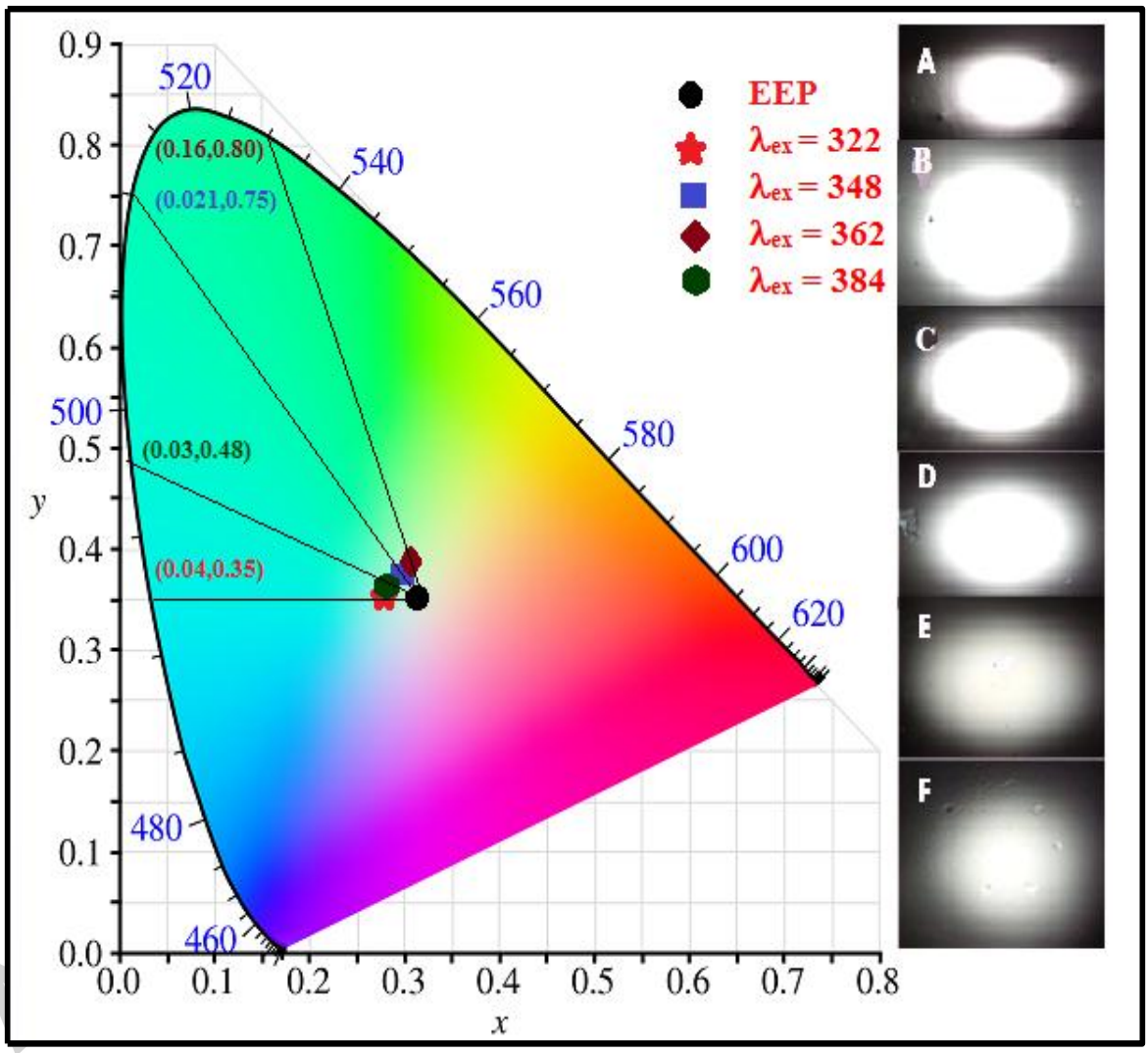
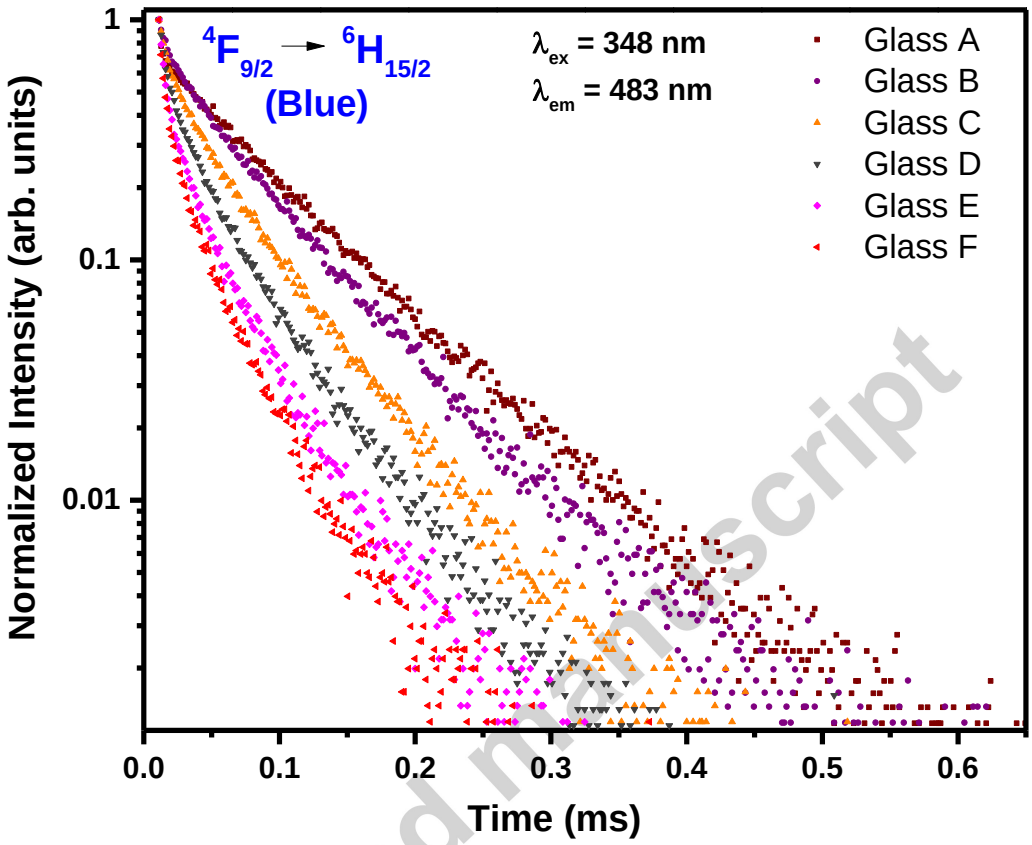


Fig. 9 (a).

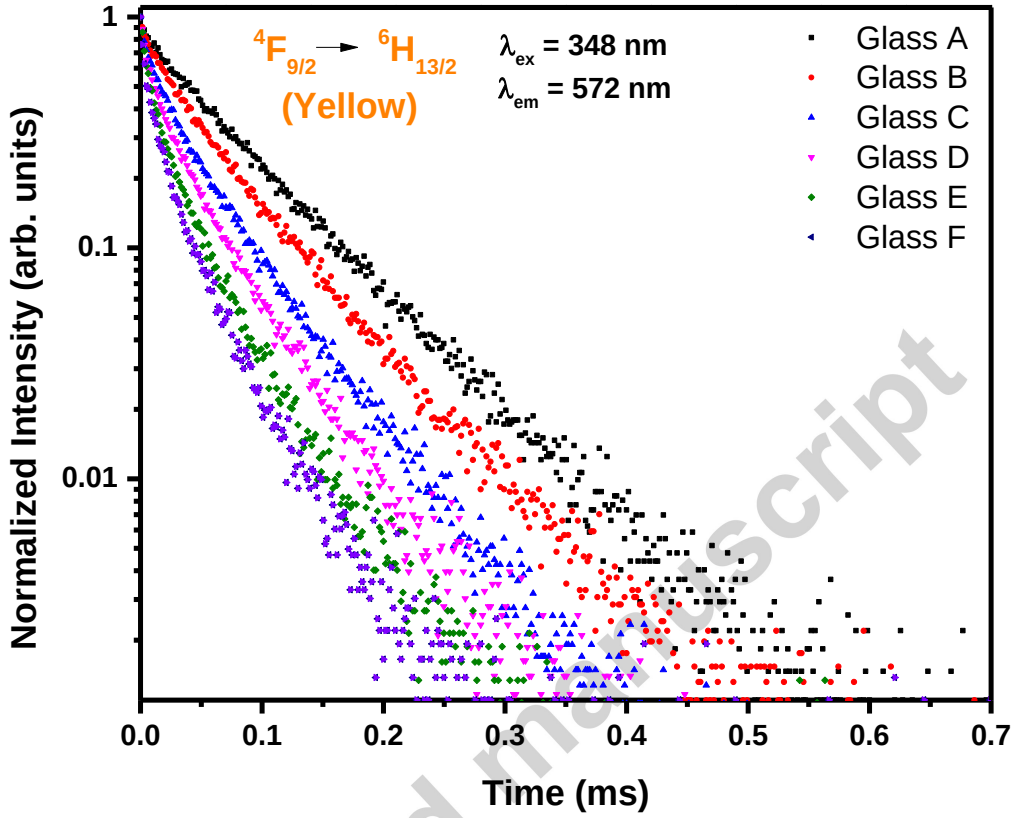
ACCEPTED MANUSCRIPT



Accepted manuscript

Fig. 9 (b).

ACCEPTED MANUSCRIPT



Accepted manuscript

Fig. 10.

ACCEPTED MANUSCRIPT

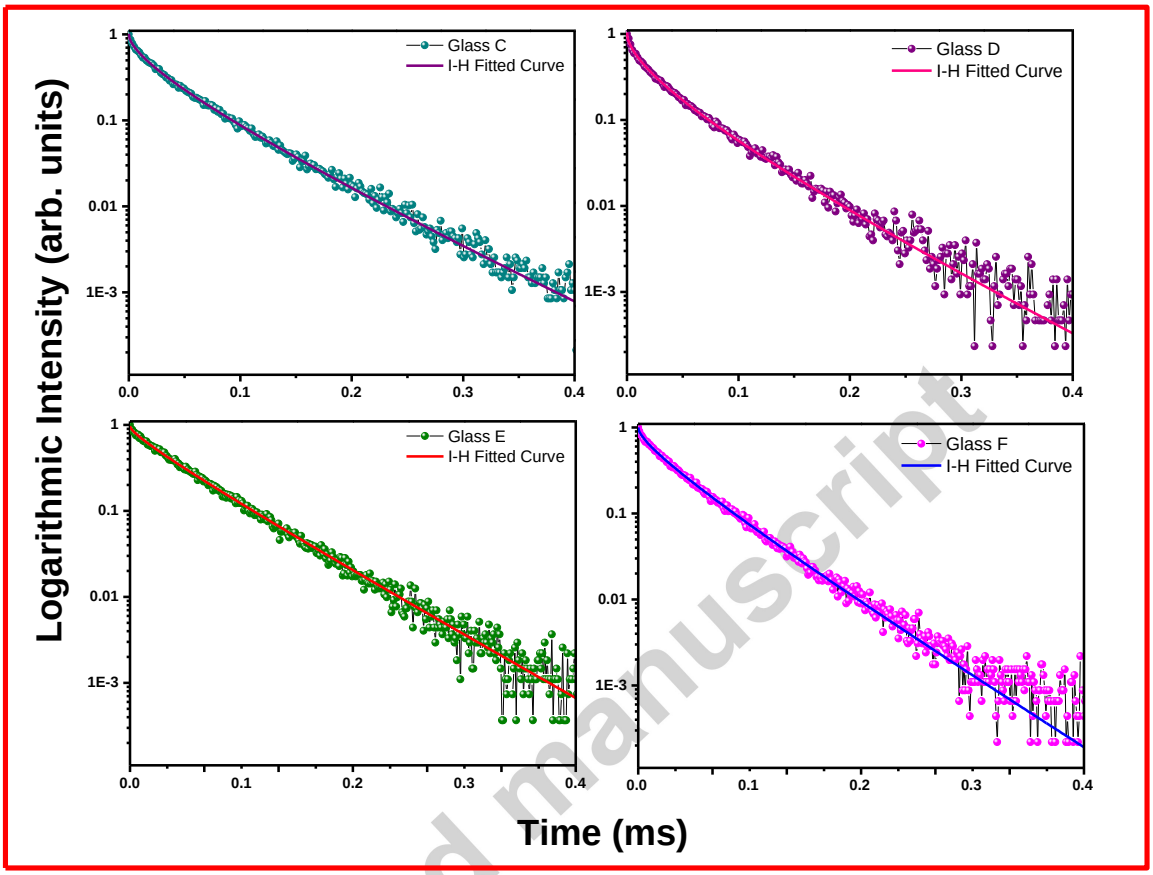


Table 1 Optical band gap (E_{opt}), band tailing parameter (B) for indirect and direct allowed transitions along with Urbach energy (ΔE) of Dy^{3+} ions in LiPbAlB glasses.

Glass Samples	n = 1/2 (Indirect allowed)		n = 2 (Direct allowed)		Urbach energy (ΔE) (eV)
	E_{opt} (eV)	B ($cm^{-1/2}$ eV)	E_{opt} (eV)	B ($cm^{-1/2}$ eV)	
Glass A	3.15	2.00	3.45	70.55	0.28
Glass B	3.14	2.01	3.37	93.58	0.36

Accepted manuscript

ACCEPTED MANUSCRIPT

Glass C	3.05	2.17	3.19	102.34	0.38
Glass D	3.00	2.38	2.92	115.46	0.43
Glass E	2.90	2.53	2.75	120.32	0.47

Table 2 Experimental (f_{exp} x 10^{-6}), calculated (f_{cal} x 10^{-6}) oscillator strengths, refractive index (n) and r.m.s deviation (δ_{rms} x10^{6}) of Dy^{3+} ions in LiPbAlB glasses.

Transitions	**Glass A**		**Glass B**		**Glass C**		**Glass D**		**Glass E**		**Glass F**	
from $^6H_{15/2}$→	**f_{exp}**	**f_{cal}**	**f_{exp}**	**f_{cal}**	**f_{exp}**	**f_{cal}**	**f_{exp}**	**f_{cal}**	**f_{exp}**	**f_{cal}**	**f_{exp}**	**f_{cal}**
$^6H_{11/2}$	3.98	4.01	4.65	4.64	3.50	3.52	3.25	2.57	2.55	2.07	2.02	1.72
$^6F_{11/2} + {}^6H_{9/2}$	8.35	8.47	9.98	10.1 1	8.31	8.39	7.28	7.37	6.23	6.29	5.96	6.00
$^6F_{9/2} + {}^6H_{7/2}$	4.29	4.50	5.11	5.37	4.89	4.88	4.09	4.35	3.79	3.74	3.40	3.12
$^6F_{7/2}$	4.28	4.49	5.28	5.55	4.20	4.75	3.70	4.65	2.85	3.80	2.09	3.07
$^6F_{5/2}$	3.23	2.29	4.02	3.52	3.59	2.79	2.66	2.43	2.12	1.96	1.86	1.55
$^6F_{3/2}$	1.54	0.55	1.73	1.82	1.10	0.52	0.80	0.45	0.66	0.37	0.36	0.29
$^4F_{9/2}$	0.92	0.43	1.60	0.52	0.83	0.42	0.56	0.37	0.42	0.29	0.24	0.24
$^4I_{15/2}$	1.95	1.15	2.08	1.62	1.84	1.23	1.58	1.12	1.21	0.88	0.73	0.63
$^4F_{7/2} + {}^4I_{13/2}$	1.18	0.79	1.82	0.86	0.92	0.64	0.50	0.59	0.38	0.36	0.29	0.30
$^6P_{7/2}$	3.94	3.06	4.24	3.96	4.06	3.69	3.89	3.48	2.98	3.30	2.09	2.27
$^4M_{17/2} + {}^6P_{3/2}$	3.78	3.12	3.98	3.14	2.33 8	2.11	1.72 7	0.98	1.18 3	0.89	0.77 6	007
n	2.02		2.22		2.34		2.39		2.48		2.59	
δ_{rms} (x10^{-6})	±0.98		±0.99		±0.80		±0.86		±0.42		±0.40	

Accepted manuscript

ACCEPTED MANUSCRIPT

Table 3 Judd-Ofelt Parameters ($\Omega_\lambda \times 10^{-20}$cm^2) and Spectroscopic quality factor ($\chi = \frac{\Omega_4}{\Omega_6}$) of Dy^{3+} ions in LiPbAlB glasses along with the other reported values.

Glass System	Ω_2	Ω_4	Ω_6	χ	**Trend**	**References**
Glass A	7.02	3.01	4.93	0.61	$\Omega_2 > \Omega_6 > \Omega_4$	present work
Glass B	7.16	4.82	5.04	0.95	$\Omega_2 > \Omega_6 > \Omega_4$	present work
Glass C	4.89	2.73	3.62	0.73	$\Omega_2 > \Omega_6 > \Omega_4$	present work
Glass D	4.18	1.65	3.03	0.54	$\Omega_2 > \Omega_6 > \Omega_4$	present work
Glass E	3.17	0.71	2.26	0.32	$\Omega_2 > \Omega_6 > \Omega_4$	present work
Glass F	2.86	0.66	1.67	0.40	$\Omega_2 > \Omega_6 > \Omega_4$	present work
ZnAlBiBDy	12.03	2.33	2.74	0.85	$\Omega_2 > \Omega_6 > \Omega_4$	[14]
OFBDy1.0	27.9	10.9	11.2	0.97	$\Omega_2 > \Omega_6 > \Omega_4$	[19]
ZnAlBiB1.0	4.66	1.61	2.71	0.59	$\Omega_2 > \Omega_6 > \Omega_4$	[20]
PYBDy10	7.75	2.31	2.70	0.85	$\Omega_2 > \Omega_6 > \Omega_4$	[49]
D0LBE	5.319	0.54	1.54	0.35	$\Omega_2 > \Omega_6 > \Omega_4$	[50]
D1LBE	6.45	2.02	3.87	0.52	$\Omega_2 > \Omega_6 > \Omega_4$	[50]
LSG	19.08	1.88	6.04	0.31	$\Omega_2 > \Omega_6 > \Omega_4$	[51]

Accepted manuscript

ACCEPTED MANUSCRIPT

$Ge_{25}Ga_{10}S_{65}$	13.1	12.5	11.6	1.07	$\Omega_2 > \Omega_6 > \Omega_4$	[52]

Table 4 Transition probability (A_R) (s^{-1}), luminescence branching ratio (β_R) and total transition probability (A_T) (s^{-1}) for the observed emission transitions of Dy^{3+} ions in LiPbAlB glasses.

Transition	A_R	β_R	A_T	τ_R
Glass A				
$^4F_{9/2} \rightarrow {}^6H_{13/2}$	2296.85	0.5924	3877.47	257
$^4F_{9/2} \rightarrow {}^6H_{15/2}$	944.05	0.2435		
Glass B				
$^4F_{9/2} \rightarrow {}^6H_{13/2}$	3487.31	0.5889	5921.57	168
$^4F_{9/2} \rightarrow {}^6H_{15/2}$	1447.19	0.2444		
Glass C				
$^4F_{9/2} \rightarrow {}^6H_{13/2}$	2925.71	0.5801	5043.72	198
$^4F_{9/2} \rightarrow {}^6H_{15/2}$	1239.48	0.2457		
Glass D				
$^4F_{9/2} \rightarrow {}^6H_{13/2}$	2621.30	0.5798	4521.20	221
$^4F_{9/2} \rightarrow {}^6H_{15/2}$	1093.71	0.2419		
Glass E				
$^4F_{9/2} \rightarrow {}^6H_{13/2}$	2220.36	0.5741	3867.86	258
$^4F_{9/2} \rightarrow {}^6H_{15/2}$	913.31	0.2361		
Glass F				
$^4F_{9/2} \rightarrow {}^6H_{13/2}$	2138.63	0.5793	3691.89	270
$^4F_{9/2} \rightarrow {}^6H_{15/2}$	789.82	0.2139		

Accepted manuscript

Table 5 Emission peak wavelength (λ_P) (nm), effective band widths ($\Delta\lambda_P$) (nm), measured and experimental branching ratios (β_R & β_{exp}), stimulated emission cross-sections (σ_{se}) (cm^2), gain band width ($\sigma_{se} \times \Delta\lambda_P$) ($cm^3$) and optical gain parameter ($\sigma_{se} \times \tau_R$) ($cm^2$ s) for the emission transitions of Dy^{3+} ions in LiPbAlB glasses.

Spectral parameters	Glass A	Glass B	Glass C	Glass D	Glass E	Glass F
$\boldsymbol{\lambda_P = 483\ nm}$			$^4F_{9/2} \rightarrow {}^6H_{15/2}$ **(Blue)**			
$\Delta\lambda_P$	16.34	18.65	16.54	16.49	16.40	16.31
β_R	0.199	0.203	0.232	0.209	0.190	0.160
β_{exp}	0.569	0.574	0.566	0.546	0.538	0.507

ACCEPTED MANUSCRIPT

σ_{se} (x 10^{-22})	24.9	28.7	23.5	20.5	15.9	9.61
$\sigma_{se} \times \Delta\lambda_P$ (x 10^{-28})	40.7	51.1	38.6	33.1	26.1	23.0
$\sigma_{se} \times \tau_R$ (x 10^{-25})	4.61	6.41	4.63	4.46	4.10	3.81
$\boldsymbol{\lambda_P = 572\ nm}$			**$^4F_{9/2} \rightarrow {}^6H_{13/2}$ (Yellow)**			
$\Delta\lambda_P$	14.01	14.84	13.98	13.71	13.5	13.01
β_R	0.433	0.629	0.619	0.615	0.610	0.605
β_{exp}	0.430	0.433	0.425	0.413	0.411	0.403
σ_{se} (x 10^{-22})	23.8	27.6	23.3	20.3	15.8	13.0
$\sigma_{se} \times \Delta\lambda_P$ (x 10^{-28})	33.3	42.3	32.6	27.6	21.4	17.0
$\sigma_{se} \times \tau_R$ (x 10^{-25})	4.80	6.11	4.64	4.48	4.09	3.52

Table 6 Comparison of laser parameters of Dy^{3+} doped LiPbAlB glass with other reported hosts

Glass system	$\Delta\lambda_P$	β_R	β_{exp}	σ_{se} (x 10^{-22})	$\sigma_{se} \times \Delta\lambda_P$ (x 10^{-28})	$\sigma_{se} \times \tau_R$ (x 10^{-25})	reference
Glass B	18.65	0.203	0.574	28.7	51.1	6.41	This work
OFBDy1.0	10.9	0.232	0.586	26.5	28.7	6.16	[14]
ZnAlBiBDy	17.39	0.183	0.527	4.61	….	….	[15]
Dy:KLTB	21	….	0.530	26.34	….	….	[20]
LTTDy10	17.50	0.130	0.51	2.87	….	1.06	[21]
PKBAFD10	14	0.132	0.40	0.41	….	….	[24]
LCZSFBDy	18.92	0.21	0.60	5.83	….	….	[25]
Tellurite	15.1	0.33	….	0.57	….	….	[27]

Table 7 Colorimetric parameters of Dy^{3+} ions in LiPbAlB glasses under different excitation wavelengths.

Accepted manuscript

ACCEPTED MANUSCRIPT

Excitation Wavelength	Parameters	Glass Samples					
		Glass A	**Glass B**	**Glass C**	**Glass D**	**Glass E**	**Glass F**
322 nm	(x, y)	(0.299, 0.349)	(0.293, 0.355)	(0.306, 0.364)	(0.314, 0.368)	0.309, 0.365)	(0.313, 0.369)
	Y/B ratio	0.81	0.71	0.78	0.79	0.82	0.73
	CCT (K)	7008	7252	6601	6247	6445	6289
348 nm	(x, y)	(0.298, 0.352)	(0.304, 0.360)	(0.307, 0.369)	(0.315,0.373)	(0.309,0.368)	(0.311, 0.369)
	Y/B ratio	0.74	0.89	0.80	0.85	0.84	0.73
	CCT (K)	7060	6654	6501	6165	6434	6338
362 nm	(x, y)	(0.299, 0.361)	(0.304, 0.365)	(0.306, 0.366)	(0.309, 0.368)	(0.309, 0.368)	(0.309, 0.371)
	Y/B ratio	0.79	0.73	0.77	0.79	0.80	0.73
	CCT (K)	6950	6667	6572	6440	6448	6450
384 nm	(x, y)	(0.298, 0.350)	(0.294, 0.348)	(0.302, 0.355)	(0.307, 0.361)	(0.385, 0.436)	(0.389, 0.434)
	Y/B ratio	0.79	0.71	0.76	0.79	0.73	0.76
	CCT (K)	7089	7351	6868	6572	4219	4120

Table 8 Experimental lifetime (τ_{exp}) (μs), energy transfer parameter (Q), critical transfer distance (R_0) (Å), donor acceptor interaction parameter (C_{DA}, 10^{-41} cm^6 s^{-1}), quantum efficiency (η) and non-radiative decay rates (W_{NR}) for $^4F_{9/2} \rightarrow {}^6H_{15/2}$ transition of Dy^{3+} ions in LiPbAlB glasses along with the other reported values.

Name of sample	τ_{exp}	η (%)	Q	R_0	C_{DA}	W_{NR}
Glass A	172.9	67.28	----	----	----	1893
Glass B	155.58	92.60	----	----	----	475
Glass C	139.39	70.39	1.23	2.20	1.06	2124

Accepted manuscript

ACCEPTED MANUSCRIPT

Glass D	130.32	58.96	1.65	2.12	1.30	3149
Glass E	124.67	48.32	1.83	2.01	7.29	4145
Glass F	110.91	41.07	2.35	1.98	8.02	5312
0.1DPTFB	503	75	0.255	1.018	1.53	504 [16]
3DPTFB	138	25	3.72	9.04	7.50	5470 [16]
PKAZFDy10	610	90	0.63	6.7	1.10	164 [39]
PKMAFDy	760	70	0.4	5.99	4.612	410 [70]
PKBAFD1Dy	660	88	0.61	6.9	1.14	175 [71]
0.05DZTFB	797	73	0.023	5.105	3.89	337 [72]
PbFPDy10	572	59	0.589	9.72	6.50	717 [73]

Accepted manuscript

Wireless Pers Commun
DOI 10.1007/s11277-017-4718-x

Social Profile Aware AODV Protocol for Ad-Hoc Social Networks

Nagender Aneja[1] · **Sapna Gambhir**[1]

© Springer Science+Business Media, LLC 2017

Abstract Ad-hoc social networks are required to strengthen local communication between people. Mobile ad-hoc social networks have emerged as self-configuring and self-organizing social networks to facilitate interactions among different mobile users without Internet. Contextual routing based on social patterns has been proposed and advantageous for ad-hoc social networks. Social profile aware routing protocol proposed in this paper allows users to use social networking applications using social routing protocol. The protocol has been implemented on network simulator ns-2 and is also available as a patch file for other researchers. Results indicate protocol has low overhead with 64 nodes. Results have been presented for packet delivery ratio, and average end-to-end delay. The need of multi-hop social network was also studied and observed that probability of nodes being connected at mult-hop increases with increment of number of nodes and geographical area.

Keywords Ad-hoc social network · Peer-to-peer network · Network simulator · Social network · Ad-hoc network · Routing protocol

1 Introduction

Inexpensive smart phones and revolution in communication technology have fostered attention in online social networking services. The online social networking services [8, 13, 17, 25] have become very popular to connect with people having similar interests and share text and images with the connected users. Despite popularity of online social networking services there are certain limitations that can only be overcome by new design of ad-hoc social network. People now demand ad-hoc social network in scenarios such as

✉ Nagender Aneja
naneja@gmail.com

Sapna Gambhir
sapnagambhir@gmail.com

[1] Department of Computer Engineering, YMCA University of Science and Technology, Faridabad, India

Published online: 01 August 2017

conferences, fairs and exhibitions where location based social networking services to find new similar users and sharing text and images are in need. Although, participants can do personal meetings but sharing text, images, files or group discussion are not possible in such scenarios. Current online social network doesn't support location based ad-hoc social networking. Additionally, these online social networking services need Internet infrastructure and this may not be true always due to security concerns at public gathering, or short time presence by people from different countries or regions, or due to natural disaster.

Android 4.0 and later devices with appropriate hardware have made possible to connect users with each other at a distance larger than bluetooth using Wi-Fi Peer-to-Peer networking [12] without any Internet access point and this has opened new research challenges. Number of researchers have worked at research issues in ad-hoc social network [1, 4, 6, 9, 18, 23], developing ad-hoc social network on mobile devices [11, 15, 16, 20, 22, 24, 29], to know user experiences [10, 26], profile matching [2, 3, 21], and social routing [7, 15, 27]. Many researchers have presented papers in the area of contextual routing due to the fact that mobile devices have patterns in their movements as these are carried by human beings. This paper proposes a routing protocol that determines path from source to destination with intermediate nodes as nodes that have similar interests with similarity value defined by source node.

The paper is organized as follows. Section 2 presents literature survey of work that is related to designing routing protocols based on contextual or social characteristics of the users. Section 3 defines problem and technical issues handled in this paper. Section 4 provides definitions and examples used in the proposed routing protocol. Section 5 presents the proposed protocol named Social Profile Aware Ad hoc On-Demand Distance Vector Routing Protocol in Ad hoc Social Network (SPA-AODV) and its implementation. Section 6 presents experimental results on ns-2 implementation of SPA-AODV.

2 Related Work

Li et al. [16] proposed MobiSN, a semantics-based framework for self-configured mobile ad-hoc social network implemented in Java. MobiSN provides functions and services such as friend matchmaking, automatic forming of groups, and generation of ontology-based profiles etc. However, MobiSN considers common ancestor and root concept in calculating the similarity of two concepts. Further, it is difficult for developers to create applications and services for ad-hoc social network to fulfill heterogeneous requirements of different ASN users.

Palani et al. [19] proposed using interest and contact occurrence for efficient file distribution. The authors proposed using interest mining that is identification of nodes interests, area structure, constructs a familiar-interest nodes with common contacts into communities. Xia et al. [28] presented a survey on socially aware networking to exploit social properties of nodes. The basis of networking that is socially aware is that the mobile devices are usually carried by people. Mobility of devices or nodes is actually due to mobility of users and by exploring social relationships, catching the mobility regularities of mobile devices as well as predicting the contact opportunities can be used to design routing protocols. Designing routing protocols based on social patterns is advantageous but is not advantageous if nodes deviate from social pattern. Therefore, there is a need for routing protocol that finds the best path based on user defined parameters.

Kayastha et al. [14] did a survey of data delivery services involving the social relationship among mobile users and presented network architecture and protocol design

issues. One of open research issues and future directions that authors raised is utilizing context-aware data distribution in Mobile peer-to-peer network.

Therefore, literature survey indicates that research has been done in the area of ad-hoc social network. However, no work has been proposed in the designing a multi-hop routing protocol that establishes social aware path based on user defined parameters. As discussed above, the routing protocol proposed in this paper uses local contact information and similarity values to determine path that is shortest and intermediate nodes have higher similarity. The path with intermediate nodes having intermediate similarity is important as it will be more stable path due to frequent contact pattern.

3 Problem Statement

A mobile ad-hoc network is infrastructure-less network of mobile devices connected with each other for a particular purpose without any centralized base station. Each mobile device in mobile ad-hoc network is free to move, changes links to other devices, and acts as a router to forward communication packets of other nodes.

The problem of routing and communication in ad-hoc social network is defined as broadcasting user profile with dynamic interests to find similar users and creating ad-hoc social network. There are research issues in creating ASN e.g. as we know that each user has its preferences for similarity, some users may be more strict in selecting their friends and so they are interested to connect with others only if similarity is significantly high while some other users are liberal in selecting and knowing other friends. Sapna et al. [10] surveyed that user preferences for average profile similarity is 75%. One of other issues is to create multi-hop social network using ad-hoc network. Multi-hop social network allows intermediate nodes to forward profiles of other nodes.

Another research issue in ASN is creating location-based user-timeline of some or all users having similarity value higher than required by a user. This will help a user to see all similar users in a time line and for selecting personal communication. The application of this solution will be beneficial to transfer text, images, files etc among users connected by ad-hoc network without Internet. Some of scenarios may be like short duration international conferences and workshop when users attending the conferences and workshop come from other countries and want to share images and files but may not have mobile Internet or centralized wifi network due to security concerns.

This paper proposes a routing and communication algorithm to create ad-hoc social network so that a user is able to find other similar users with customized threshold similarity value in a multi-hop network. Customized similarity in multi-hop network will help two users e.g. A and B to find other similar users where A is interested to find other users with at least 50% threshold while B with 70% similarity threshold. The proposed algorithm has been implemented in ns-2 since ns-2 provides functionalities of multi-hop ad-hoc network and is very popular among computer networks researchers.

Figure 1 shows a network topology comprising of five nodes N_0, N_1, N_2, N_3, N_4. Nodes N_0, N_3, N_4 are in range of each other and node N_3 is in range of N_1 but not in range of N_2. Edges are represented by values of similarity metric for profiles of connecting nodes. Profile Similarity between N_0 and N_3 is 0.43 and is represented by the edge between N_0 and N_3. Neighbors of a node are represented by Nb. Therefore, neighbors of node $Nb(N_3) = \{N_0, N_1, \text{and } N_4\}$

In order to facilitate communication between nodes, node N_0 and N_2, there may be two options. The first option is that the routing algorithm finds path that is shortest between N_0 and N_2. The other option may be to find a path that may be longer but all nodes on the path

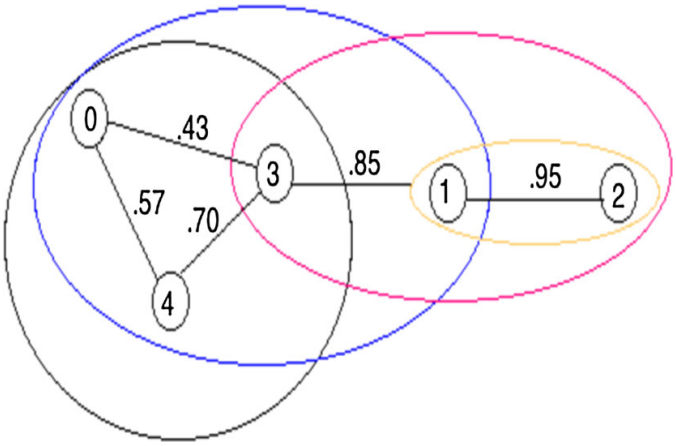


Fig. 1 Ad-hoc network of five nodes with edges represented by similarity measures

have similarity greater than required by the source node N_0. The motivation to create such a path is due to the reason that ASN is based on mutual cooperation and nodes having similar interests will be motivated to maintain the ad-hoc network. Additionally, there is pattern among nodes as mobile nodes are carried by human beings.

The routing protocol proposed in this paper covers both situations. The protocol allows setting Profile Similarity value by source node at the time of simulation. If there is some value, the routing algorithm selects a path so that the nodes on the path are similar to the source node, which is the second situation. However, if we set profile similarity to null, the the routing algorithm automatically selects the shortest path.

4 Preliminaries

The protocol Social Profile Aware Ad-hoc On-Demand Distance Vector Routing Protocol in Ad-hoc Social Network (SPA-AODV) has two phases namely Preprocessing Phase and Route Establishment Phase. The routing protocol proposed in this paper can be explained with below definitions and example.

The definitions used in the paper include Profile Unit, Profile Store, Local Profile, Global Profile, and Similarity Measure. Profile unit includes social profile of a user while Profile Store stores profiles of all others users. Two types of social profiles, location-based Local Profile and location-independent Global Profile are defined to find similar nodes. Similarity is calculated using Cosine Similarity as proposed in [3].

Definition 1 (*Profile Unit*) Profile Unit is used by each node to exchange its own profile in the multi-hop network periodically (Table 1).

Type identifies that packet is a Profile Unit. *Profile Vector* is a vector that includes interests of the user. *Source* is the source address. *Hop Count* computes distance from source in terms of hop count that is subsequently incremented at every intermediate node. *Source Sequence Number* is the sequence number that each node maintains and is increased continuously. Sequence number helps node to have freshness of Profile Unit received from one particular source node. $Life - Time$ is the life time of the packet after which the packet is discarded.

Definition 2 (*Profile Store*) Profile Store keeps all received profiles from other nodes that may be used to create social network (Table 2).

Type identifies the packet. *Neighboring node* is the address of the neighboring node that is at one-hop network and is similar to the node. *Profile Vector* is the profile of the

Table 1 Format of Profile Unit (PU) to exchange interests

Type	Profile Vector	Source	Hop Count	Source Sequence Number	Life-Time

Table 2 Format of Profile Store (PS) to store received profiles

Type	Neighboring Node	Profile Vector	Similarity Metric	Hop Count	Sequence Number	Life Time (seconds)

neighboring node. *Similarity Metric* is the value that quantifies similarity of a user profile with profiles of neighboring nodes. Higher Similarity value indicates that node is highly similar. *Hop Count* is the distance of source node from node which received Profile Unit.

Definition 3 (*Local Profile*) At each geographical location e.g, office and home, a user may have different Interests. *Local profile* is defined as a vector of weights of different keywords used by a mobile user to set interests at particular geographical location or a zone.

Definition 4 (*Global Profile*) *Global Profile* is a vector that is union of all local profiles.

Example 1 (*User Profile*) Assuming that $Zone_1$ comprises of sports category so that $Zone_1 = \{Football, Cricket\}$ and $Zone_2$ comprises of music related Keywords so that $Zone_2 = \{Sitar\ and\ Guitar\}$. Example weighted local profiles of a $User_A$ for $Zone_1$ and $Zone_2$ may be $Local\ Profile_{\{A,Z1\}} = \{1, 2\}$ and $Local\ Profile_{\{A,Z2\}} = \{3, 2\}$. The values in the vector indicates that the $User_A$ has interest weights for keywords Football and Cricket in $Zone_1$ as 1 and 2 while in $Zone_2$ for Sitar and Guitar as 3 and 2 respectively. Therefore, the Global Profile of the user A will be $Global\ Profile_A = \{1, 2, 3, 2\}$.

Definition 5 (*Similarity Measure (Cosine Similarity)*) between two vectors (or two profiles) is a measure that calculates similarity in terms of cosine of the angle between two profiles and provides a measure to know similarity as following:

$$\begin{aligned} Similarity(user_A, user_B) &= \frac{user_A \cdot user_B}{|user_A|.|user_B|} \\ Similarity(user_A, user_B) &= \frac{\Sigma a_i \cdot b_i}{\sqrt{\Sigma {a_i}^2} \cdot \sqrt{\Sigma {b_i}^2}} \end{aligned} \tag{1}$$

Definition 6 (*Route_REQ*). Route_REQ is used by an originating node to find users that have similar interests greater than threshold provided by the originating node while the destination may be at distance more than one-hop away (Table 3).

Type identifies that it is Route_REQ packet. Profile Vector is the vector of dynamic interests of the originating node. REQ-ID is the message id that originating node maintains for sending any updated interests or requests. Threshold is the minimum value of similarity metric that originating node is looking for so as to find new user. SRC is address of the originating node and SRC-Seq is the sequence number of source node.

Definition 7 (*Route_REP*) Route_REP is sent by the destination node that has interests similar to the originating node greater than threshold value (Table 4).

Type identifies that it is Route_REP packet. Profile Vector is the vector of dynamic interests of the destination node. DST is address of the destination node and DST-Seq is the sequence number of destination node. SRC is the address of the originating node that originated ROUTE_REQ request and for which reply is being sent by destination node.

Table 3 Format of Route_REQ to find similar users

Type	Profile Vector	REQ-ID	Threshold	SRC	SRC-Seq

Table 4 Format of Route_REP to find similar users

Type	Profile_vector	DST	DST-Seq	SRC	Life-Time

5 Social Profile Aware Ad Hoc On-Demand Distance Vector Routing Protocol in Ad hoc Social Network (SPA-AODV)

This section will explain two phases of SPA-AODV, Phase 1 that is preprocessing phase and Phase 2 that is Route Establishment Phase.

5.1 Phase 1: Preprocessing Phase

Phase 1 of the proposed routing protocol is preprocessing phase to create and maintain social profiles in a multi-hop ad-hoc network. The preprocessing phase uses *Profile Unit* to exchange profiles with neighbors. The received profiles are stored in respective *Profile Store*.

Algorithm 1 Profile Table Routine: Preprocessing Phase

Trigger: Periodically in all nodes $Node_i$
Send and receive Hello Packets with Profile Vectors
Notations:
$Node_i$ receiving Profile Unit from $Node_j$
PT_i = Profile Table of $Node_i$
$PT_{i.j}$ = Profile Entry of $Node_j$ in table of $Node_i$
$LProfile_i$ = Local Profile vector of $Node_i$
$GProfile_i$ = Global Profile vector of $Node_i$
$LProfile_{i.j}$ = Local Profile match computed by $Node_i$ with local profile of $Node_j$
$GProfile_{i.j}$ = Global Profile match computed by $Node_i$ with global profile of $Node_j$
for (for all nodes $Node_i$ receiving hello packets from $Node_j$) **do**
    compute $LProfile_{i.j}$ and $GProfile_{i.j}$
    if $PT_{i.j} \notin PT_i$ and $LProfile_{i.j} \geq threshold$ **then**
        write $LProfile_j$ and $GProfile_j$ in PT_i
        Increment Hop Count
        Update Sequence if fresh
        Broadcast in Neighborhood
    end if
    if $PT_{i.j} \in PT_i$ and $LProfile_{i.j} \geq threshold$ **then**
        update $LProfile_j$ and $GProfile_j$ in PT_i
        Increment Hop Count
        Update Sequence If fresher
        Broadcast in Neighborhood
    end if
end for
End Function

All nodes periodically exchange profiles with other nodes to setup and maintain ad-hoc social network. Nodes also compute similarity value of its profile with other received profiles in order to create ad-hoc social network. Nodes keep profiles and network information in their individual Profile Store when value of profile similarity metric is greater than the threshold

Table 5 Profile Store for Node N_3

Profile Store (PS) for N_3						
Type	Neighboring node	Profile vector	Similarity metric	Hop count	Sequence number	Life time (s)
1	N_0	PV_{N_0}	0.43	1	xxx2	40
1	N_4	PV_{N_4}	0.70	1	xxx2	42
1	N_1	PV_{N_1}	0.85	1	xxx2	41
1	N_2	PV_{N_2}	0.91	2	xxx2	30

value that can be customized by the user. For example, as in Fig. 1, node N_3 exchanges profile with neighboring nodes $\text{Nb}(N_3) = \{N_0, N_1, N_4\}$ periodically using Profile Units. Life-Time and Source Sequence number are also updated as profile units are exchanged periodically. All Nodes $\{N_3, N_0, N_1, N_4\}$ compute similarity measures with the received profiles. Profile Store is updated periodically as profile units are received and computed. Table 5 presents routing and communication table of N_3 after preprocessing phase.

When a node wants to communicate in ad-hoc social network, it finds destination ids from Profile Table and establishes the path with all the nodes in profile table as explained in following section.

5.2 Phase 2: Route Establishment Phase—Social Aware Routing

This phase explains routing and communication protocol in order to create multi-hop ad-hoc social network. This phase uses Route_REQ and Route_REP packets.

Algorithm 2 Route Request Algorithm

Trigger: $Node_i$ receives route request of $Node_A$ from $Node_j$ for destination $Node_D$
Notations:
$Node_A$ is Source Node and $Node_D$ is Destination Node
$Node_i$ = Intermediate Receiving Node
$Node_j$ = Intermediate Sending Node
$RREQ_A$ = Route Request Packet generated by $Node_A$
$SeqNO_j$ = Sequence number of $Node_j$
RT_i = Routing table of $Node_i$
$RT_{i.j}$ = Routing table entry in RT_i for route of $Node_j$
$LProfile_{A.D}$ = Local Profile match computed by $Node_A$ for $Node_D$
$GProfile_{A.D}$ = Global Profile match computed by $Node_A$ for $Node_D$
TH_A = Threshold requested by $Node_A$ in Route Request $RREQ_A$
For All $Node_i$
if $Node_i \neq D$ **then**
  if First $RREQ_j$ from $Node_j$ **then**
    Create entry for $Node_j$ in RT_i with $Node_j$ as nexthop
    Broadcast $RREQ_A$ in its neighborhood
  else
    if $SeqNO_j$ is newer OR TH_A less and equal ($LProfile_{A.D}$, $GprofileA.D$ **then**
      update RT_i with entry $RT_{i.j}$ with its nexthop $node_j$
      Broadcast $RREQ_A$ in its neighborhood
    end if
  end if
end if
End Function

Algorithm 3 Route Reply Algorithm

Trigger: $Node_i$ Receives Route Reply of $Node_D$ from $Node_j$ for source node $Node_A$
Notations:
$Node_A$ is Source node and $Node_D$ is destination node
$Node_i$ = Intermediate Receiving Node
$Node_j$ = Intermediate Forwarding Node
$RREP_D$ = Route Reply Packet of $Node_D$
$SeqNO_D$ = Sequence number of $Node_D$
RT_i = Routing table of node $Node_i$
$RT_{i.j}$ = Route Entry of $node_j$ in RT_i
$LProfile_{A.D}$ = Local Profile match computed by $node_A$ for $Node_D$
$GProfile_{A.D}$ = Global Profile match computed by $node_A$ for $Node_D$
TH_A =Threshold requested by $Node_A$ in Route Request $RREQ_A$
For All $Node_i$s
if $Node_i \neq A$ **then**
  if First $RREQ_j$ from $Node_j$ **then**
    Create entry for $Node_j$ in RT_i with $Node_j$ as nexthop
  else
    if $SeqNO_j$ is newer OR TH_A less and equal ($LProfile_{A.D}$, $GprofileA.D$ **then**
      update RT_i with entry $RT_{i.j}$ with its nexthop $node_j$
    end if
  end if
end if
End Function

Suppose, N_0 wants to setup a path with highly similar user with similarity at least 5% (0.50) that may be at number of hops greater than one. N_0, as shown in example 1 is one-hop connected with nodes N_3 and N_4 with profile similarity metric 0.43 and 0.57 respectively. Node N_0 will create Route_REQ packet as shown in Table 6 and broadcast this packet in the network.

Route_REQ is received by all nodes i.e. N_1, N_2, N_3, N_4. All nodes compute similarity value with the profile vector received from N_0 and reply by sending Route_REP if similarity is greater than or equal to 0.50. In the example shown in Fig. 1, assume that nodes N_4, N_1, N_2 will send Route_REP using reverse path (Table 7).

Table 6 Route_REQ packet that is broadcasted by N_0 to find similar users with similarity greater than 0.5 i.e. 50%

Route_REQ of N_0					
Type	Profile vector	REQ-ID	Threshold	SRC	SRC-Seq
Type	(1,0,0)	1	0.50	N_0	xxx2

Table 7 Route_REPs received by N_0

ROUTE_REP of N_0					
Type	Profile_vector	DEST	DEST-Seq	SRC	Life-Time
Type	(1,0,1)	N_0	xxx2	N_4	41
Type	(0,0,1)	N_0	xxx2	N_1	41
Type	(0,1,0)	N_0	xxx2	N_2	41

Node N_0 also compute similarity with profile vector received in Route_REPs send an acknowledgment to the node with which is maximum similar to originating node. In this case, an ad-hoc social network will be created between N_0 and N_2.

5.3 Implementation of SPA-AODV Routing Protocol in Ad-Hoc Social Networkc

This section discusses implementation of ad-hoc social network routing protocol SPA-AODV in ns-2. The proposed protocol is modification of AODV routing protocol and helps nodes having similar interests to create a social network. Implementation of the protocol in ns-2 is discussed in following sub sections. The ns-2 uses OTcl scripting on frontend and C++ on back end. OTcl is used to make simulation scenario while real processing happens at the backend. The following sections will discuss as about changes those have been made at backend so that ad-hoc social network can be created in script file in frontend and changes be made to see the efficiency of the ad-hoc social network. The new framework is called ns-2 ad-hoc social network (NS-ASN) and is a patch file for ns-2 to update libraries. ns-2c was chosen to implement ad-hoc social network since it is very popular among researchers to implement multi-hop ad-hoc network. Additionally, ns-2 is an open source and so there is full freedom to modify the code. Ad hoc On Demand Distance Vector (AODV) [5] was selected as a base routing protocol to modify and implement ad-hoc social network. The implementation is explained with help of below sections.

5.4 Brief Description of AODV Routing Protocol

AODV algorithm enables dynamic multi-hop routing between mobile nodes without requiring nodes to maintain routes to destinations that are not active. The destination sequence number created by destination is maintained for each routing table entry to ensure freshness of information and loop freedom. The protocol defines three types of messages Route Requests (RREQs), Route Replies (RREPs) and Route Errors (RERRs) and are received via UDP with normal IP header. RREQ is broadcasted when a node needs a route to a destination. Nodes receiving RREQs caches route to originator for unicasting RREP. RREP is initiated by destination or intermediate node having fresh path to destination. Freshness is indicated if sequence number of destination in the table is at least great as contained in RREQ. RERR is transmitted in case of any broken link. Each node maintains precursor list that includes next hops for each destination. The precursor list is maintained based on RREP. Each entry of routing table has following fields:

- Destination IP Address
- Destination Sequence Number
- Valid Destination Sequence Number flag
- Other state and routing flags (e.g., valid, invalid, repairable, being repaired)
- Network Interface
- Hop Count (number of hops needed to reach destination)
- Next Hop
- List of Precursors
- Lifetime (expiration or deletion time of the route)

5.4.1 Message Formats in AODV

This section explains formats of various messages RREQ, RREP, RRER, and RREP-ACK used in AODV Routing Protocol (Tables 8, 9, 10, 11, 12).

5.5 Entries in different AODV Files for Ad-Hoc Social Network Routing Protocol

The ad-hoc social network routing protocol was registered as *ASN* so as to provide options to user in frontend tcl script to change routing protocol to other options like DSDV, AODV, or ASN for comparison and other experiments. Header of new ad-hoc social network routing to be used at application layer and routing layer was registered as *ASN* in files $ns - packet.tcl$ and $ns - mobilenode.tcl$. Node is also linked to routing agent in $ns - mobilenode.tcl$ by passing value *ASN* from main script file. The passed value of routing protocol helps node to take routing decision by using nodes profiles. $ns - lib.tcl$ was modified to register *ASN* as routing agent so that $ns - mobilenode.tcl$ can recognize when value of *ASN* is passed from main script file. In order to simulate ad-hoc social

Table 8 RREQ format

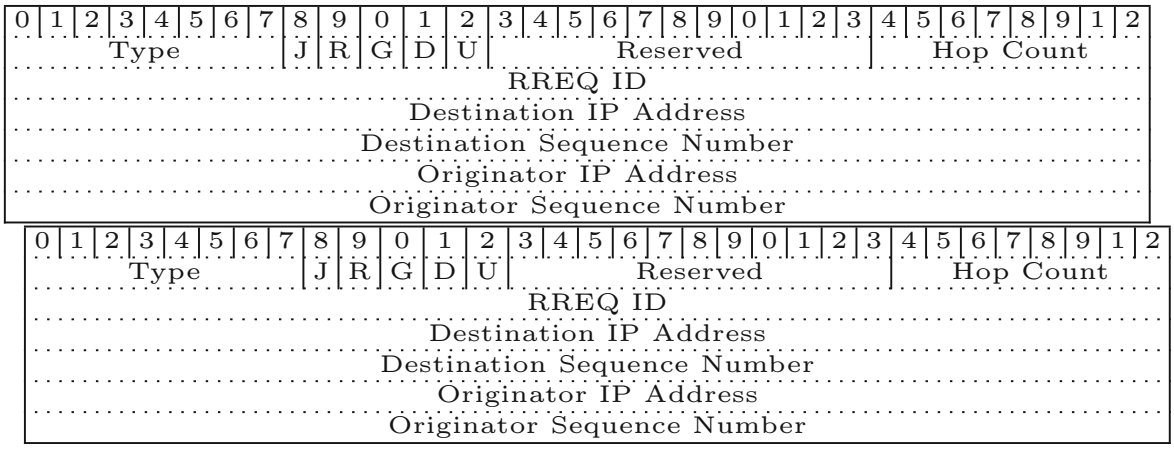


Table 9 RREP format

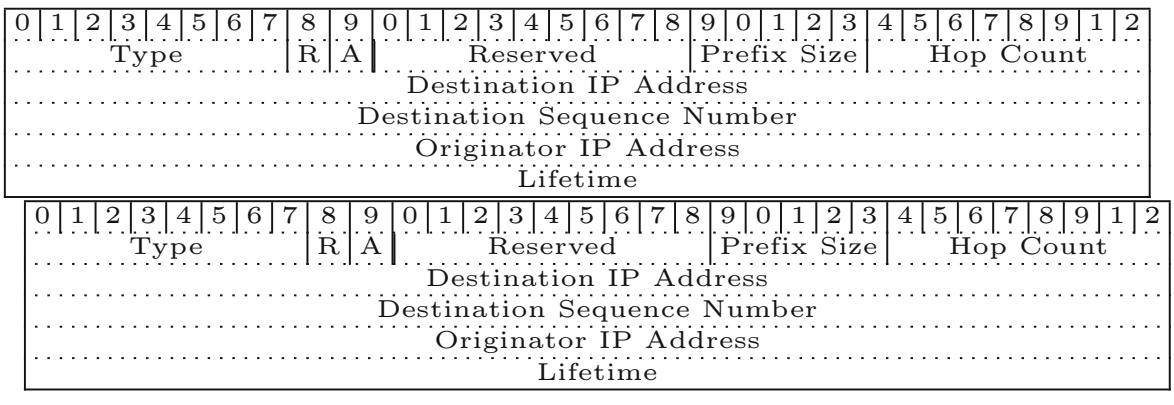


Table 10 RRER format

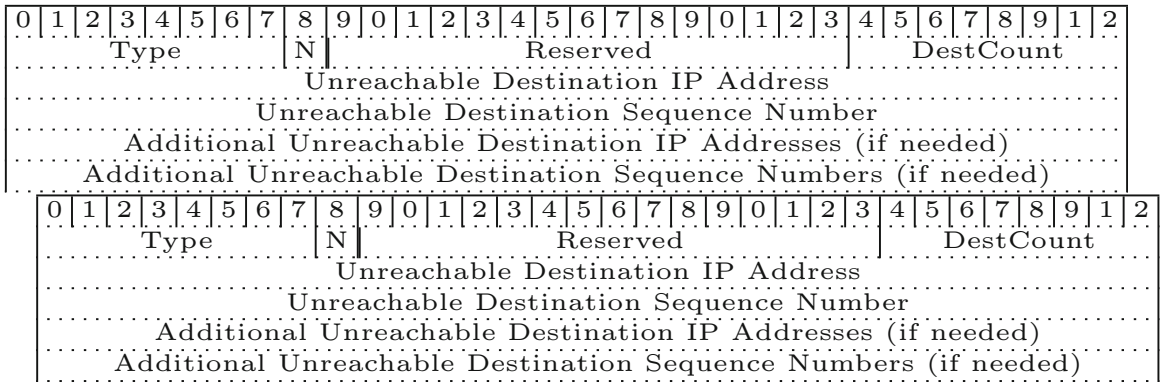


Table 11 Route reply acknowledgment (RREP-ACK) message format

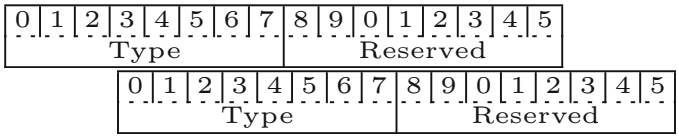
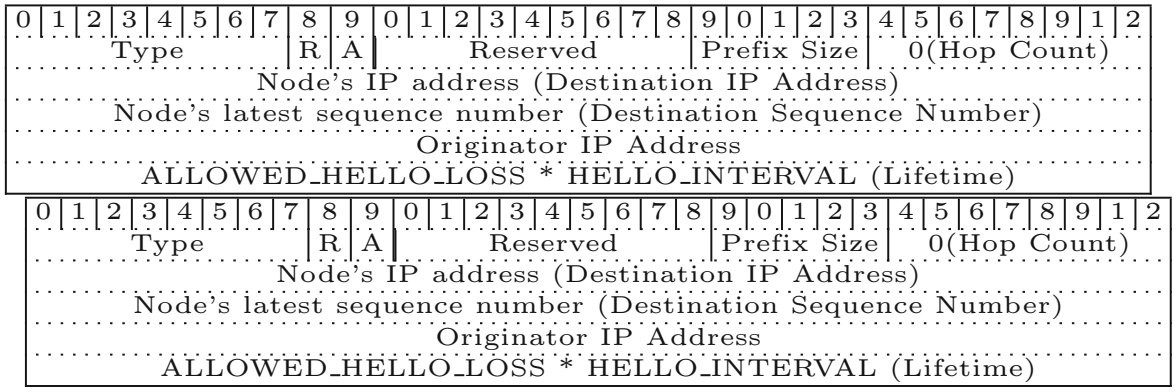


Table 12 Hello message (RREP with TTL = 1)



network with different parameters variables related to dynamic number of users, their profiles, and number of zones were registered in appropriate ns-2 files. Since number of nodes were already implemented in ns-2 at frontend in current version of ns-2 , therefore, this paper specifically implemented profiles of users and number of zones in $ns - mobilenode.tcl$. The simulation area was divided into number of zones to get results on location based social networing. Profiles were simulated dynamically with help of pre-defined zonal-dictionary in the tcl script. The dictionary, for the purpose of simulations, included ten keywords for each zone e.g. dictionary of 40 words was assumed for 4 zones. For purpose of one profile i.e. global profile, the profile of the user was updated by

randomly selecting keyword from dictionary of size 40, whereas to implement local profiles, the random keyword was selected from zonal-dictionary. Local profile was updated by randomly selecting keyword index from zonal-dictionary based on the zone determined from current location of the node. Keyword corresponding to the keyword index was passed to local profile as new interest for the user at the current location. All local profiles based on locations visited by a mobile node are stored, however, it is best to store limited amount of previous profiles in real implementation. The number of limited profiles may be based on historical data, density of profile and frequency of visits by a user at particular locations.

Initially, the simulated scenario was implemented to generate new interests every 10 s to update the profile. However, experiments results indicated that as interests were changing so frequently after every 10 s, most of the nodes were not able to establish connections. This interpretation is also in alignment of real-time scenario where interests of users change dynamically but not so frequently. Therefore, the assumption of building interests was optimized by diving the simulating scenario into two phases.

A preprocessing phase as first phase was introduced. The processing phase was restricted to be 10% of the total simulation time. Therefore, nodes can generate and update their interests to build local profile within preprocessing time. After preprocessing time, nodes were restricted to update their local profiles but these can freely connect with other nodes based on the final local profile after completion of preprocessing phase.

The local profile of a user is a two dimensional profile in which first dimension represents zone id and second dimension is index of a keyword from dictionary and value of the array element indicates weight for that key word. e.g. lprofile[2][3] = 4 means interest level of a node for third keyword of dictionary in second zone is 4.

Similarly, global profile of a user is one-dimensional array, where the dimension indicates the index of keyword. e.g. gprofile[3] = 8 indicates that interest level of a user for 3rd keyword. In terms of local profile, it may possible that random number 3 was generated two times in four respective zones. If this is the case, then lprofile[0][3] = lprofile[1][3] = lprofile[2][3] = lprofile[3][3] = 2 will give us gprofile[3] = 8.

Dimension of the zones were also computed and set according to provided number of zones and simulation area defined. e.g. if area defined is 2000 × 2000 and number of zones is 4, then this function divides area of 2000 × 2000 into four zones such that each each zone[0 to 3] is of 500 × 500.

mobilenode.h was modified to include method declarations for setting profiles, getting set profiles, and getting current zone of the node based on mobility pattern. The profile is set within preprocessing phases based on random number and current dictionary. *mobilenode.cc* was modified to bind local profiles and number of zones so that these variables are available in C++ files from TCL files. The function to set profile of a node was also defined here. The profile of a node is set simultaneously for local profile and global profile.

asn.cc was created to provide multi-hop routing in ad-hoc social network. Some of the functions included in this file include *sendhello*, *recevhello*, *sendFriendRequest*, *sendFriendReply*, and *sendFriendRequest*.

sendhello is used to create social network in preprocessing phase. The packet includes a local and global profile vector and is broadcasted among neighbors during preprocessing phase which is 10% of the simulation time. Once preprocessing time is over, *sendhello* is not broadcasted due to the requirement to restriction on updations in profiles. However, if required *sendhello* may easily be set to broadcast as per pre-defined time interval.

recevhello is used to receive hello messages from other neighboring nodes and further broadcasts the received packets to its neighboring nodes. This is how, *ASN* protocol establishes multi-hop social network in ad-hoc network. In order to avoid network congestion by unnecessary packets, the broadcasting nodes is configured to verify updates in the profile vector. Profile of other nodes is broadcasted only if there is some change in the profile than the one received previously. All nodes keep profiles of other nodes in their profile table and they also compute similarity value of own profile with received profiles. Similarity value is also stored in the profile table.

sendFriendRequest includes profile of sending node, threshold of similarity score, and destination address. The destination address is the address][of the node with which sending node has computed that similarity score is greater than threshold and it wants to communicate. This packet is broadcasted to neighboring nodes in order to establish path. Neighboring node(s) may reply to sending or forwarding node in case they have path for this destination or else will further forward the request packet to their neighbors so that the packet eventually reach destination node or its neighbors.

The protocol is optional as far as sending reply from intermediate nodes is concerned. If the option is on, then sending node may receive multiple replies else it will receive only one reply generated by destination node. In case of multiple replies, sending node only considers the first reply and discard all other replies if sequence number is not fresh. Path is updated when sending node receives fresh path with higher sequence number or updated profile with similarity score higher than threshold.

sendFriendReply includes profile of sending node, which is actually a destination of *sendFriendRequest*. The threshold is not required because receiving of request packet indicates that similarity score for source and destination is within desired limit. *sendFriendReply* packet includes profile so that all intermediate nodes can refresh their profile table and routing table with updated information.

routeResolve is the first module that is called by sending node before sending*sendFriendRequest*. The objective of *routeResolve* is to determine path for destination. If path to destination doesn't exist, the node sends *sendFriendRequest* and wait for *sendFriendReply* before sending data packets. This will be the case for first data packet for which most likely path to destination will not exist with sending node. However, for subsequent data packets since path exist, these will just be forwarded until an error is received on this path.

cmu − trace.cc was modified to register *ASN* packets so that their data is available in the trace file for further analysis. Hello packets for establishment of social network, route request and route reply from friend node in network were included in the trace file. Log movement function of the *mobilenode.cc* was modified to log node profile values for local profile and movement locations in the trace file. The paper logged local profiles only, but global profiles can also be logged similarly. Global profiles can also be created on-the-fly by adding local profiles as global profiles essentially is summation of local profiles.

5.6 Data Flow for SPA-AODV in ns-2 to Implement Ad-Hoc Social Network

This section explains data flow and operations with help of Fig. 2 in ns-2 when simulation is running. Figure 2 explains the protocol stack that is implemented by modifying protocol stack of ns-2 to create ad-hoc social network.

Packets are generated from a *source agent* and directed to *entry*. The packet is then passed to *address de − multiplexer*, which is an instance of class DestHashClassifier derived from class Classifier. If the destination of the packet is the node, the packet is sent

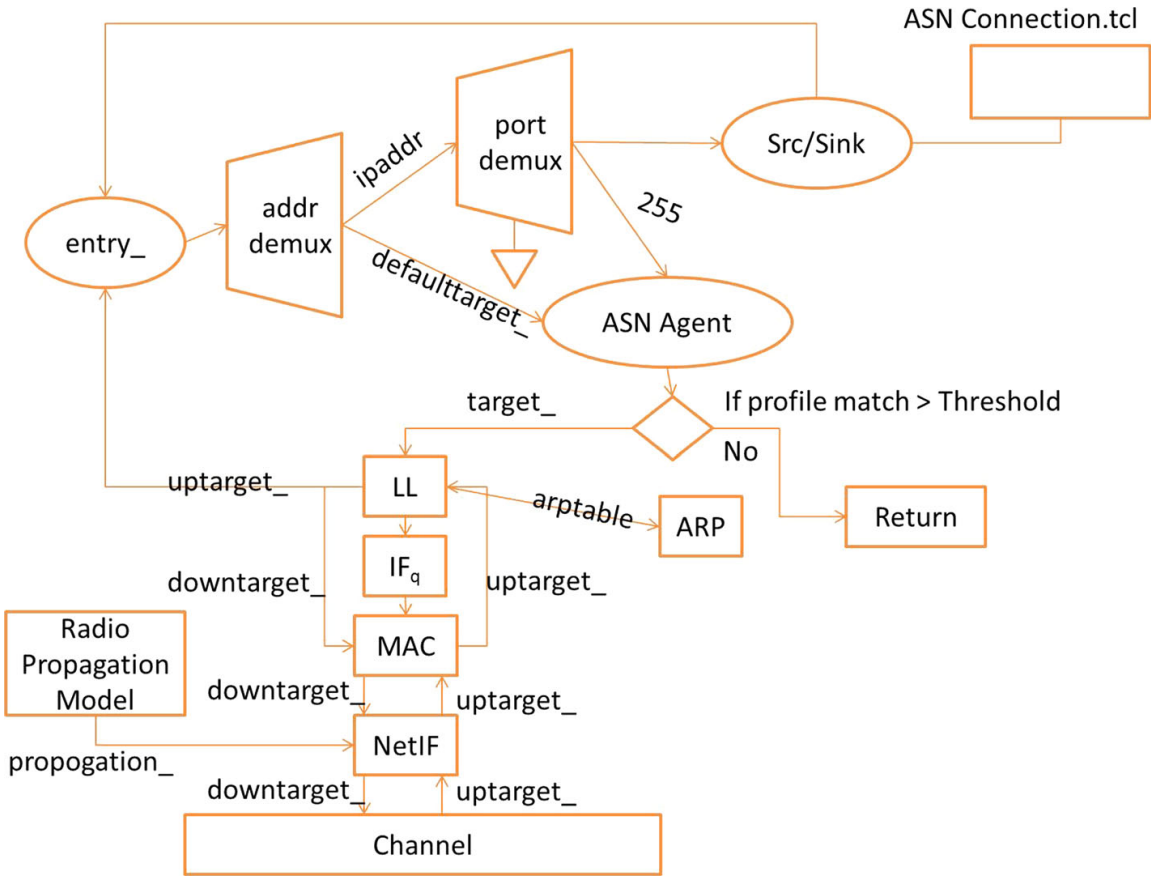


Fig. 2 Modified data flow in ns2 for ad-hoc social network

to *port de − multiplexer*. At *port de − multiplexer*, different packets are handed to corresponding *sink* agent. Note that, port number 255 is reserved for *routingagent*, which is a special agent named *ASN Agent* receives routing packets and forwards if similarity of its own profile with the received profile is greater than threshold. The threshold value may be set to NULL as discussed above if all nodes are to be considered in the route.

5.7 Mobility Model

Each node in the simulation was configured to have local and global interests where the local interests are further configured based on the current zone. The simulations were conducted in different geographical areas e.g. 1000×1000, 1500×1500, and 2000×2000. Each of the geographical region was divided into number of zones and nodes were distributed in different zones based on their index. Network of 32 nodes and 8 zones were distributed in zones so that node with index i was initially assigned to zone(i%zmax). A node at a current time is configured to have two profiles local and global profiles and wherein the local profile depends on the current zone. Nodes were allowed to move from one zone to another zone after a pause time of 1000 s with a speed varying between 1 and 3 m/s. As nodes move from one zone to another zone, local profile of the node is also updated. This study was a limited study to see performance of matching global profiles, however, future study will include performance of matching local profiles. The protocol had already implemented such that profile store include local as well as global profile.

The protocol has been configured to send packets including local and global profiles but current results proposed in this research include matching global profiles. Therefore, source and destination nodes matched each others' global profile to establish path.

5.8 Connection Scenario

To study performance of ad-hoc social network a node was chosen randomly and allowed to established simultaneous connection with nodes in its profile store and with those nodes for which profile match was greater than predetermined threshold. For example, in a network of 32 nodes, a node with id say 5 was chosen to find nodes in its profile store so that the profile match is greater than the threshold limit. Node 5 established connection with all the nodes one by one after 100 s interval to send 1000 packets with 512 bytes payload. Delivery ratio and end-to-end delay were studied to know performance of the proposed routing algorithm in the study.

6 Experiment Results

This section presents performance of the social network in ns-2 ad-hoc network based on delivery ratio and end-to-end delay.

Figures 3 and 4 represents ns-2 screenshots during simulations. Figure 3 represents initial position of 64 nodes evenly distributed into four zones. Figure 4 represents nodes displaying their dynamic interests and their motion e.g. nodes N_0 and N_2 are displayed as moving from their respective zones to $Zone_3$.

6.1 Overhead Results

This section presents network overhead results in terms of control packets. Overhead is defined in terms of number of control packets sent for one data packet. Control packets are used to establish social network on the top of ad-hoc network and data packets are sent for actual communication after the social network has been established. Once a social network is established, then nodes look for on-demand routing for exchanging data packets. As control packets are overhead for network communication, this section presents results on number of control packets used for establishing social network. As an example to explain number of control packets, let us take $Node_0$ is interested to establish social network with other similar nodes having profile similarity greater than predetermined threshold. In order to create social network, a node may has to broadcast its profile at regular intervals. We may assume that each node sends 10, 000 data packets with $512MB$ payload. However, actual number of data packets depend on other factor such data simulation time, frequency interval, and establishment of path. Figures 5 and 6 present results for number of control packets sent and overhead for different number of nodes such as 4, 8, 32, 64, and 128 in a network of four zones. Figures 5 and 6 demonstrate that number of control packets increase as nodes are increased.

Results indicate that network of 64 nodes works fine as routing overhead is 30%. However, having number of nodes about 128 gives worst performance as overhead is equal to one that means one control packet for each data packet.

We found number of control packets increased with increasing number of nodes as in Fig. 5. Till 64 nodes, Routing overhead is around 30% as in Fig. 6 however, with 128 nodes overhead is more (in Fig. 6). So, large ad-hoc social network s are not much

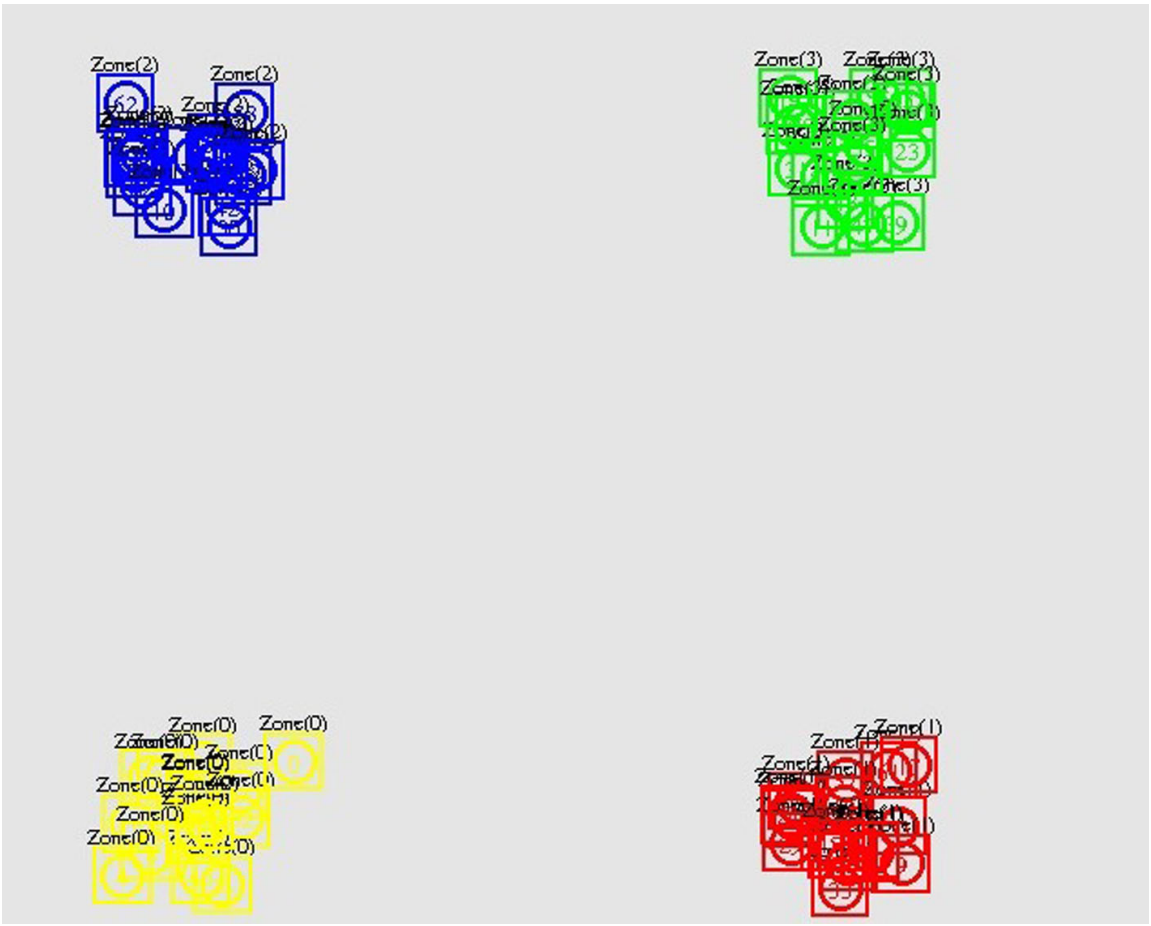


Fig. 3 Initial Position of 64 nodes in four zones

favorable to establish. There is need to improve the number of control packets used even though Packet Deliver Ratio (PDR) and Average End to End Delay (AEED) is low as shown in next subsection.

6.2 Packet Delivery Ratio

The protocol proposed in this paper requires nodes to first complete their profile tables. Nodes send data packets to other nodes with which profile similarity is greater than threshold. This section presents results as ratio of how many data packets delivered. In order to compute packet delivery ratio, nodes were moved with speed varying from 1 to 3 m/s. The speed of 1–3 m/s is reasonable due to fact that in ad-hoc network humans may walk but still may be within range of ad-hoc social network.

Figure 7 represents that packet delivery ratio is reduced as speed of nodes is increased. Reduction of packet delivery ratio is due to the reason that nodes may become unreachable as they move from one location to another or packets were dropped till new path was established. Packet delivery ratio is also reduced as number of nodes are increased.

6.3 Average End-to-End Delay

End-to-End Delay is sum of all delays incurred by all data packets at intermediate nodes, source node and destination node while packet moves from source to destination like packet acquisition time, packet forwarding time etc.

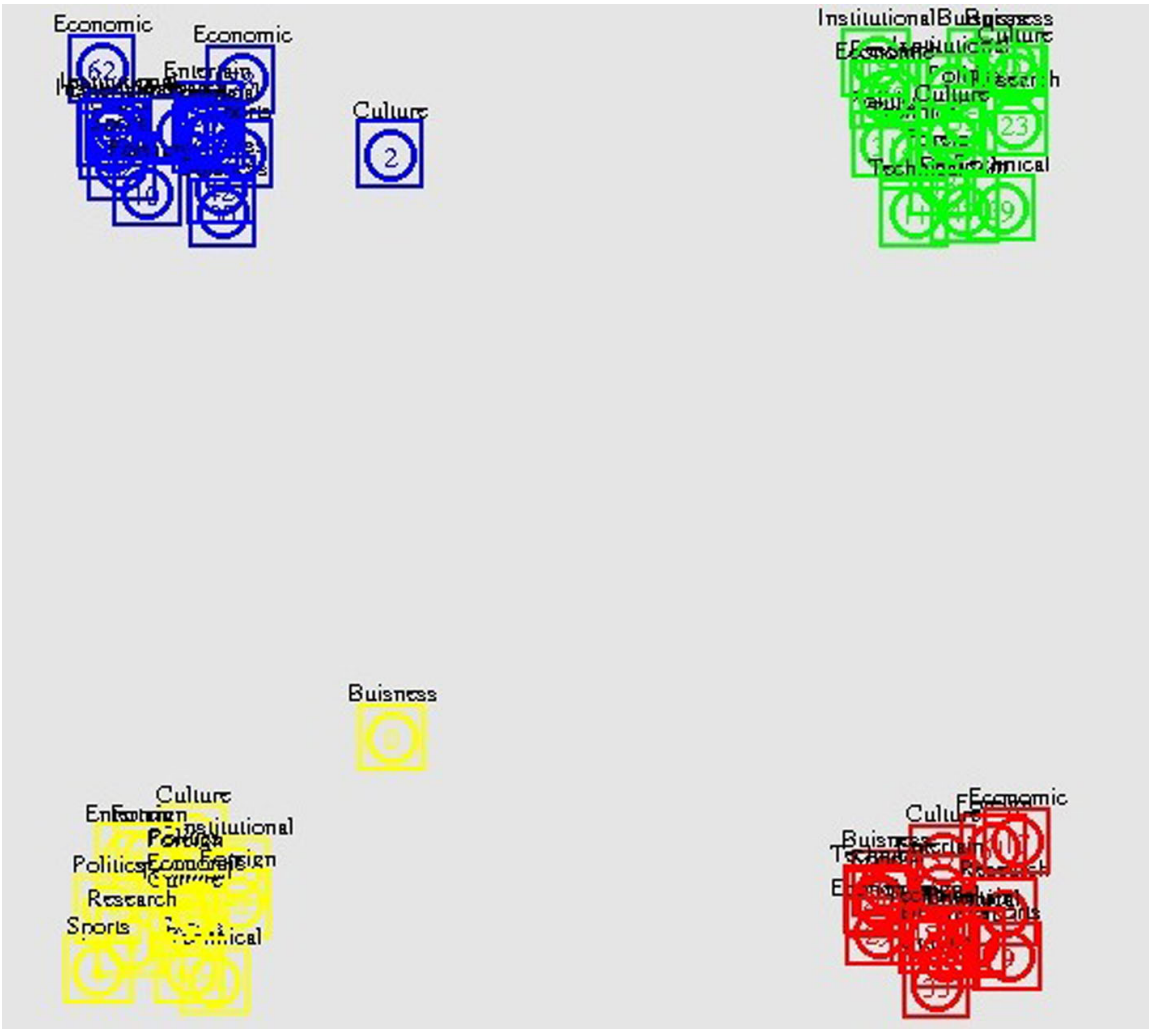


Fig. 4 Nodes N_0 and N_2 moving to $Zone_3$

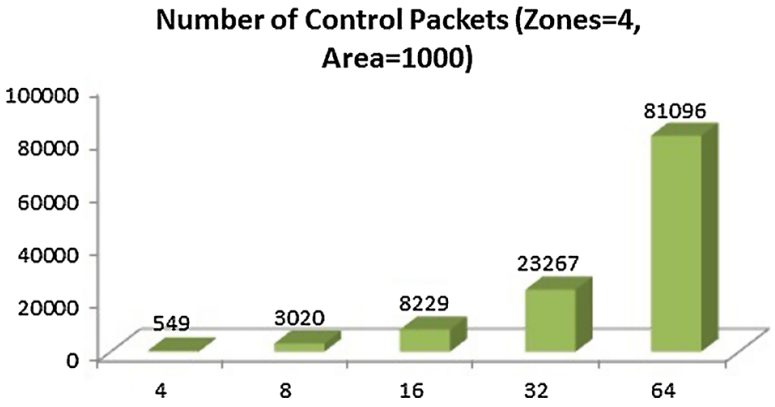


Fig. 5 Number of control packets for four zones and 1000 × 1000 area

Figure 8 indicates average end-to-end delay increases as number of nodes are increased. This may also be due to increase in time spent in finding node in profile table as size increases and time to compute similarity of profile matching. Figure 8 also indicates that average end-to-end delay increases as number of zones increases. This may be due to the assumption that profile is based on dictionary or zone based dynamic interests. Dimension

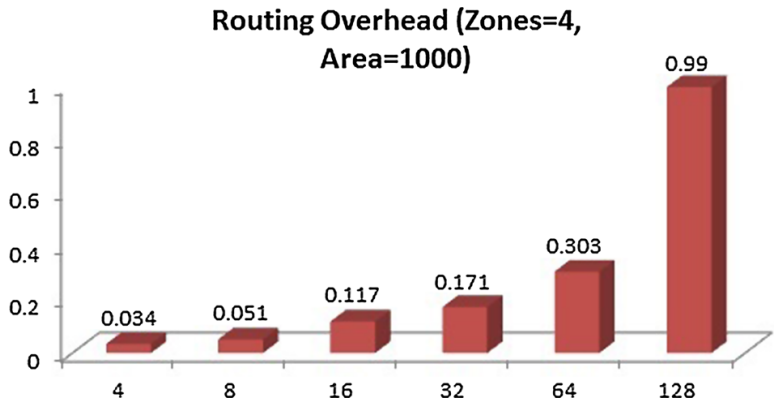
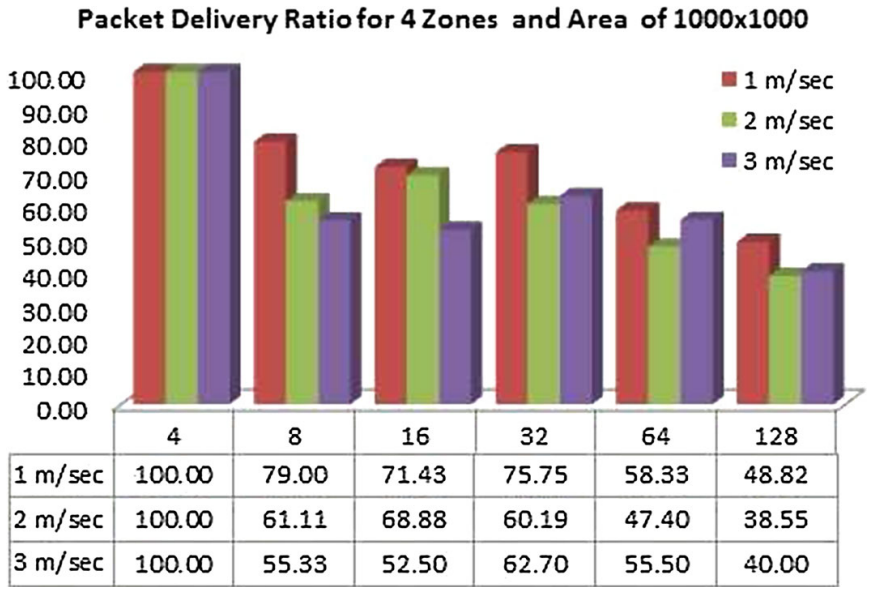


Fig. 6 Overhead for four zones and 1000 × 1000 area



	4	8	16	32	64	128
1 m/sec	100.00	79.00	71.43	75.75	58.33	48.82
2 m/sec	100.00	61.11	68.88	60.19	47.40	38.55
3 m/sec	100.00	55.33	52.50	62.70	55.50	40.00

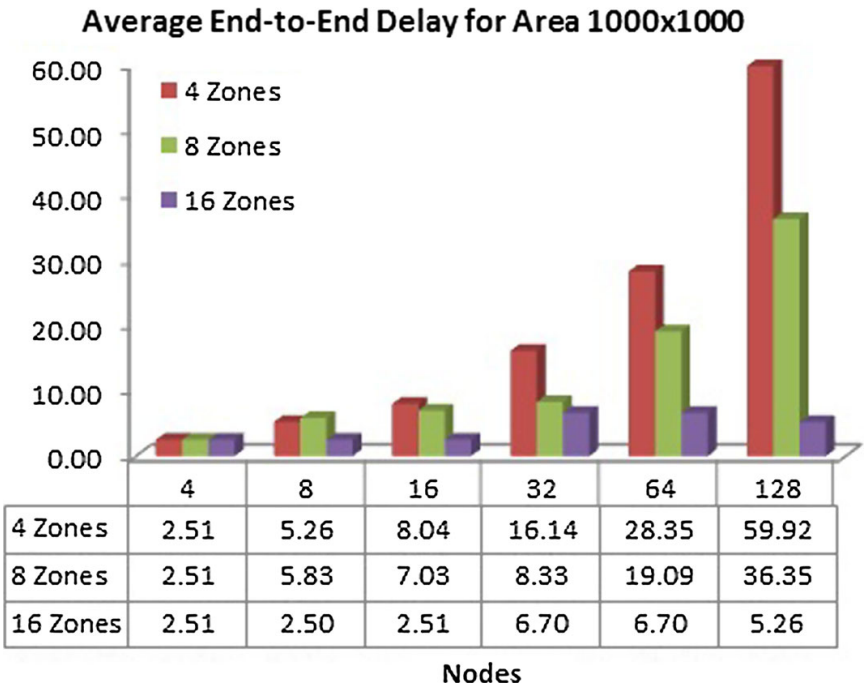
Fig. 7 Packet delivery ratio for 4 zones and 1000 × 1000 area

of profile vector increases as number of zones increase. Further, increased dimension of profile vector reduces the chances of having more similar nodes. Since, number of similar nodes are reduced, therefore, average end-to-end delay was also reduced due to less number of nodes forming social network.

Average end-to-end delay was also studied with varying size of regions over which node spread during experiment. Regions were varied from 1000 × 1000, 1500 × 1500 and 2000 × 2000. Average end-to-end delay was reduced with increase in size of region.

6.4 Need of Multihop Ad-hoc Social Network

This section presents results on need of multi-hop ad-hoc network. The objective of the result is to know if the multi-hop social network should be implemented in ad-hoc network as implementing multi-hop ad-hoc network will create additional packets. The experiments were conducted to see as in how many cases multi-hop ad-hoc network was established based on similarly of global profiles which are matched above than a predetermined threshold. Results indicated that it terms of low density of nodes social network was created with hop count of one whereas in high density of nodes the social network was



	4	8	16	32	64	128
4 Zones	2.51	5.26	8.04	16.14	28.35	59.92
8 Zones	2.51	5.83	7.03	8.33	19.09	36.35
16 Zones	2.51	2.50	2.51	6.70	6.70	5.26

Fig. 8 Average end-to-end delay for 1000 × 1000 area

Table 13 Need of multi-hop ad-hoc social network

No of nodes	No of nodes with a match mutihop	Max nodes at multihop per node	Area of network
8	0	0	1000 by 1000
16	2	2	1000 by 1000
32	10	3	1000 by 1000

created with hop count of two or three. One of the reason for single hop count network in low density network may be due to the reason that nodes are at greater distance from each other and packets may not be delivered. However, when nodes are dense, the profile packet will be distributed to more number of nodes and it increases the probability of getting creating social network with hop count greater than one (Table 13).

Results indicate that in an area of size 1000 × 1000, none of pair of nodes created multi-hop social network and all nodes got connected with similar nodes directly at single hop. However, multi-hop social network was created by two nodes in network of 16 nodes and by ten nodes in network of 32 nodes. Therefore, as number of nodes increase, chances of nodes getting connected at multi hop also increases. As a result, multi-hop may not be a requirement if the total number of nodes are low but is useful if number of nodes are more.

7 Conclusion

The contextual routing protocol for ad-hoc social network proposed in this paper is based on social connections and is dynamic to be configured by users' preferences. Simulation indicates that the routing protocol has low overhead of 64 nodes and therefore, the ad-hoc

routing protocol works best to provide location-based multi-hop social connections for 64 users. There is a need to further improve the protocol for 128 and higher number of nodes. The impact of mobility nature of nodes was studied and found that packet delivery ratio decreases as speed of nodes is increased. Number of nodes up to 32 with speed of up to 3 m/s works fine, however, as we increase the number of nodes speed of 1 m/s is fine but performance degrades as speed is increased more than 1 m/s. Number of zones or number of local profiles were studied and observed that having low number of zones and more nodes increases the delay. This result on the delay was surprising as it shows protocol works best with increasing number of zones and low number of nodes. However, the reason of this can be explained as the overall geographical area of the simulation was fixed and the area was distributed into number of zones. Increment in number of zones implies more zones but with reduced size and also implies low number of nodes per zone. This scenario helps to reduce the average end-end-to end delay. Therefore, this paper concludes that contextual routing that is based on social profiles of the users works best for 64 nodes. Further, research work is needed so that this can be used for 18 or higher nodes.

References

1. Aneja, N., & Gambhir, S. (2012). Various issues in ad-hoc social networks. In: Proceedings of national conference on recent trends in computer science and information technology (RTCSIT) (pp. 6–9). India: Echelon Institute of Technology Faridabad Haryana. http://echeloninstitute.org/images/download/proceedingRTCSIT.pdf.
2. Aneja, N., & Gambhir, S. (2014). Geo-social profile matching algorithm for dynamic interests in ad-hoc social network. *Social Networking*, *3*(5), 240–247. doi:10.4236/sn.2014.35029. http://www.scirp.org/journal/PaperDownload.aspx?paperID=51108.
3. Aneja, N., & Gambhir, S. (2015). Geo-social semantic profile matching algorithm for dynamic interests in ad-hoc social network. In *2015 IEEE international conference on computational intelligence communication technology (CICT)* (pp. 354–358). doi:10.1109/CICT.2015.50. http://ieeexplore.ieee.org/xpl/articleDetails.jsp?arnumber=7078725.
4. Bennett, J. D., Rajakarunanayake, Y. N., Diab, W. W., Karaoguz, J., & Kellerman, M. C. (2013). Ad hoc social networking. http://www.google.com/patents/US20130091209.
5. Charles, P. (2003) Ad hoc on-demand distance vector (AODV) routing. https://www.ietf.org/rfc/rfc3561.txt.
6. Chatterjee, S. (2013). Ad hoc networking based on content and location. http://www.google.com/patents/US8386620.
7. Chung, E., Joy, J., & Gerla, M. (2015). Discoverfriends: Secure social network communication in mobile ad hoc networks. CoRR abs/1505.07487. http://arxiv.org/abs/1505.07487.
8. Facebook Inc. Facebook. https://www.facebook.com/.
9. Gambhir, S., & Aneja, N. (2013). Ad-hoc social network: A comprehensive survey. *International Journal of Scientific and Engineering Research*, *4*(8), 156–160. http://www.ijser.org/researchpaper%5CAd-hoc-Social-Network-A-Comprehensive-Survey.pdf.
10. Gambhir, S., Aneja, N., & Mangla, S. (2015). Need of ad-hoc social network based on users dynamic interests. In *IEEE 2015 international conference on soft computing techniques and implementation (ICSCTI)*.
11. Gambhir, S., Mangla, S., & Aneja, N. (2016). Software Design for social profile matching algorithm to create ad-hoc social network on top of android. In *IEEE international conference on computing for sustainable global development*.
12. Google Inc. Creating P2P connections with Wi-Fi. URL http://developer.android.com/training/connect-devices-wirelessly/wifi-direct.html.
13. Google Inc. Google+. URL https://plus.google.com/.
14. Kayastha, N., Niyato, D., Wang, P., & Hossain, E. (2011). Applications, architectures, and protocol design issues for mobile social networks: A survey. *Proceedings of the IEEE*, *99*(12), 2130–2158. doi:10.1109/JPROC.2011.2169033.

15. Li, H., Bok, K., & Yoo, J. (2015). A mobile social network for efficient contents sharing and searches. *Computers and Electrical Engineering*, *41*, 288–300. doi:10.1016/j.compeleceng.2014.05.016. http://www.sciencedirect.com/science/article/pii/S0045790614001670.
16. Li, J., & Khan, S. U. (2009). MobiSN: Semantics-based mobile ad hoc social network framework. In *Proceedings of the 28th IEEE conference on global telecommunications, GLOBECOM'09* (pp. 883–888). Piscataway, NJ: IEEE Press. http://dl.acm.org/citation.cfm?id=1811380.1811526.
17. LinkedIn Inc. LinkedIn. URL https://www.linkedin.com/.
18. Mangla, S., & Gambhir, S. (2015). Research challenges in ad-hoc social network (ASN). *International Journal of Advance Research in Science and Engineering*, *4*(1), 124–128. http://www.ijarse.com/images/fullpdf/159a.pdf.
19. Palani, S., Kumar, S., & Madhuri, P. (2015). Influencing social networks for P2P substance-based file distribution in disjointed MANETs. *International Journal of Computer Applications*, *122*(2), 1–3.
20. Pietilainen, A. K., Oliver, E., LeBrun, J., Varghese, G., & Diot, C. (2009). Mobiclique: Middleware for mobile social networking. In *Proceedings of the 2nd acm workshop on online social networks, WOSN '09* (pp. 49–54). New York, NY: ACM. doi:10.1145/1592665.1592678.
21. Raad, E., Chbeir, R., & Dipanda, A. (2010). User profile matching in social networks. In *Proceedings of the 2010 13th international conference on network-based information systems, NBIS '10* (pp. 297–304). Washington, DC: IEEE Computer Society. doi:10.1109/NBiS.2010.35.
22. Sarigol, E., Riva, O., Stuedi, P., & Alonso, G. (2009). Enabling social networking in ad hoc networks of mobile phones. *Proceedings of the VLDB Endowment*, *2*(2), 1634–1637. doi:10.14778/1687553.1687611.
23. Seada, K., & Perkins, C. (2006) Social networks: The killer app for wireless ad hoc networks? http://research.nokia.com/sites/default/files/tr/NRC-TR-2006-010.pdf.
24. Trieu, Q. L., & Pham, T. V. (2012). STARS: Ad-hoc peer-to-peer online social network. In *Computational collective intelligence. technologies and applications—4th international conference, ICCCI 2012*, Ho Chi Minh City, Vietnam, November 28–30, 2012, proceedings, part I, pp. 385–394. doi:10.1007/978-3-642-34630-9_40.
25. Twitter Inc. Twitter. URL https://twitter.com/.
26. Vaananen-Vainio-Mattila, K., Saarinen, P., Waljas, M., Hannikainen, M., Orsila, H., & Kiukkonen, N. (2010). User experience of social ad hoc networking: Findings from a large-scale field trial of twin. In *Proceedings of the 9th international conference on mobile and ubiquitous multimedia*, MUM '10 (pp. 10:1–10:10). New York, NY: ACM. doi:10.1145/1899475.1899485.
27. Xia, F., Liu, L., Li, J., Ma, J., & Vasilakos, A. (2015). Socially aware networking: A survey. *IEEE Systems Journal*, *9*(3), 904–921. doi:10.1109/JSYST.2013.2281262.
28. Xia, F., Liu, L., Li, J., Ma, J., & Vasilakos, A. V. (2015). Socially aware networking: A survey. *IEEE Systems Journal*, *9*(3), 904–921. doi:10.1109/JSYST.2013.2281262.
29. Zhang, D., Zhang, D., Xiong, H., Hsu, C. H., & Vasilakos, A. (2014). BASA: Building mobile ad-hoc social networks on top of android. *IEEE Network*, *28*(1), 4–9. doi:10.1109/MNET.2014.6724100.



Nagender Aneja has completed Master in Engineering in Computer Technology and Applications from Delhi College of Engineering and is pursuing Ph.D. at Department of Computer Science and Engineering, YMCA University of Science and Technology, Faridabad, India. He is working as IP Manager at Innovation and Enterprise Office, Universiti Brunei Darussalam. His research interests include Computer Networks, Mobile Ad-hoc Networks, Peer-to-peer Networking, Sensor Networks, Social Networking, and Network Security.



Sapna Gambhir has completed her doctorate in Computer Engineering in 2010 from Jamia Milia Islamia, Delhi, India. She has teaching experience of 14 years during which published many papers in various national/ international conferences and journals. Currently, she is guiding 3 Ph.D. scholars. She is working in Department of Computer Engineering at YMCA University of Science and Technology, Faridabad (Haryana), India. Her current areas of interest are Network Security, Mobile Ad-hoc Networks and Wireless Sensor Networks., Online Social Networks.

Theoretical Investigations to Study the Effect of C_2H_2/H_2 gas ratio on the Multi-walled Carbon Nanotubes Growth

U. Sharma[1], S. C. Sharma[1], R. Gupta[1], N. Gupta[1]

[1]*Department of Applied Physics, Delhi Technological University (DTU), Shahbad Daulatpur, Bawana Road, Delhi-110042, India*

ABSTRACT

Carbon Nanotubes are large macromolecules that are unique for their size, shape, and extraordinary physical properties. Their enthralling structures have sparked much interest in recent years and a large expanse of research has been devoted to their understanding. The theoretical model to investigate the effect of acetylene/hydrogen **(**C_2H_2/H_2) gas ratio on the plasma assisted growth of multi-walled carbon nanotubes (MWCNTs) is developed. The present model accounts the charging rate equation of the MWCNTs, kinetics and energy balance equations of all the plasma species, energy balance of MWCNTs, and growth rate of MWCNTs in the reactive plasma composed of Acetylene + Hydrogen + Argon. In our investigations, it is established that the MWCNTs growth rate increases with increase in the acetylene/hydrogen gas ratio. Moreover, it is also found that the diameter of the CNT decreases with decrease in gas ratio.

I. INTRODUCTION

Plasma enhanced chemical vapor deposition (PECVD) has garnered attention than other methods due to the advantages of a highly efficient and vertical growth of nanotubes at low-temperature [1-5]. In PECVD, the main parameters are the growth temperature, growth time, type of substrate, catalyst, the composition of gases used in PECVD, types of feed or reducing or carrier gases and respective flow rates, etc. The effect of various carrier gases such as argon (Ar), hydrogen (H_2), nitrogen (N_2) and ammonia (NH_3) and their flow rates on the growth of CNTs have been experimentally observed [6-9].

Yap *et al.* [6] have studied that the impact of the addition of different gases to the carbon source gas and found that addition of argon dilutes C_2H_2 and hence reduces the number of molecules reacting. Also, the addition of H_2, as well as N_2, reduces the growth density of MWCNTs. Kayastha *et al.* [7] modified the growth of MWCNTs by the addition of specific carrier gases. On adding argon to acetylene, the growth density was increased and adding H_2 and N_2 decreases the growth density of MWCNTs. Toussi *et al.* [8] investigated different flow rates of Ar carrier gas and found that on increasing the flow rate the yield of CNTs was increased.

In the present study, we try to reason as to why different carrier gases have the observed effects on growth of CNTs. In Sec. II, we have developed a theoretical model consisting of the charging rate equation of CNT, kinetics of all the plasma species, and growth rate of CNT in reactive plasma to study the effect of C_2H_2/H_2 gas ratio on the multi-walled CNTs growth. The outcomes of the study have been discussed in Sec. III and finally, the study is concluded in Sec. IV.

II. MODEL

Following Sodha *et al.* [9], we have considered a reactive plasma composed of acetylene (C_2H_2), hydrogen (H_2) and argon (Ar). The reactive plasma consists of electrons, neutrals and ions of acetylene (type A) and hydrogen (type B) in the present study. For simplicity of the problem, the average radius of multi-walled nanotubes has been considered.

A. Balance equation for electron density in plasma

$$\frac{dn_e}{d\tau} = \left(\beta_A n_A + \beta_B n_B\right) - \left(\alpha_A n_e n_{iA} + \alpha_B n_e n_{iB}\right) - \gamma_e n_{ct} n_{ect}, \quad (1)$$

where β_j and α_j represents the neutral atom ionization coefficient and the ions-electrons recombination coefficient, respectively. The Eq. (1) incorporates the rise in rate of density of electrons due to neutral atom ionization (first term) and the decline due to recombination of electron and ions (second term), and collection current of electrons at the CNT surface (third term).

B. Balance equation for ion density in plasma

$$\frac{dn_{iA}}{d\tau} = \beta_A n_A - \alpha_A n_e n_{iA} - n_{ct} n_{iAct}, \quad (2)$$

$$\frac{dn_{iB}}{d\tau} = \beta_B n_B - \alpha_B n_e n_{iB} - n_{ct} n_{iBct}, \quad (3)$$

The Eqs. (2) and (3) incorporates the rise in rate of density of ions due to neutral atom ionization (first term) and the decline due to recombination of electrons and ions (second term), and collection current of ions (i.e., n_{ijct}) at the CNT surface (third term).

C. Balance equation for neutral atom density in plasma

$$\frac{dn_A}{d\tau} = \alpha_A n_e n_{iA} - \beta_A n_A + n_{ct}\left(1-\gamma_{iA}\right) n_{iAct} - n_{ct}\gamma_A n_{Act}, \quad (4)$$

$$\frac{dn_B}{d\tau} = \alpha_B n_e n_{iB} - \beta_B n_B + n_{ct} n_{iBct}, \quad (5)$$

The Eqs. (4) and (5) incorporates the rise in rate of density neutrals due to recombination of electrons and ions (first term), decline due to ionization (second term), and rise due to the neutrals collected because of neutralization at the CNT surface (third term). The extra term in the Eqs. (4) is due to the deposition of type A neutrals (i.e., n_{jct}) at the CNT surface.

D. Mass Balance equation of CNT

$$\frac{dm_{ct}}{d\tau} = \left(m_A \gamma_A n_{Act} + m_{iA} \gamma_{iA} n_{iAct}\right), \qquad (6)$$

where $m_{ct} = \frac{4}{3}\pi a^3 \rho_{ct}$ represents the CNT mass and ρ_{ct} represents the CNT density. The Eq. (6) represents the rise in the CNT mass density due accretion of neutrals and ions of A type species.

III. RESULTS AND DISCUSSION

We have solved the above stated equations along with others simultaneously cited in the work of Sodha *et al.* [9] for the kinetics and energy balance of all the plasma species and charging of CNT. Keeping hydrocarbon density constant, we are changing the C_2H_2/H_2 gas ratio by varying the hydrogen neutral atom density.

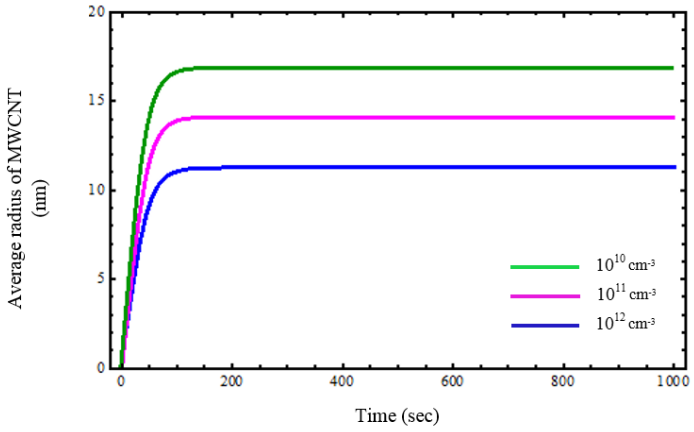


Figure 1. Temporal behaviour of average radius of MWCNTs for different C_2H_2/H_2 gas ratios.

Figure 1 illustrates the temporal behaviour of the average radius of MWCNTs for varying C_2H_2/H_2 gas ratios. It is observed that with time, the average radius of the CNT initially increases and then acquires saturation. The figure also indicates the decline in the average radius with the increasing hydrogen neutral atom density, i.e., the decreasing gas ratio.

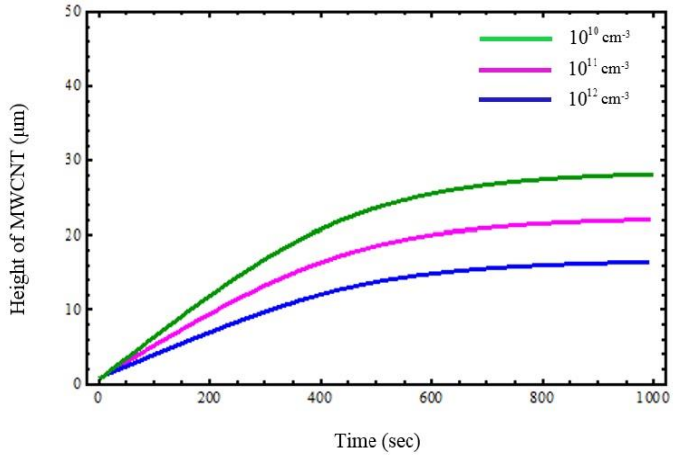


Figure 2. Temporal behaviour of height of MWCNTs for different C_2H_2/H_2 gas ratios.

Figure 2 illustrates temporal behaviour of the height of MWCNTs for varying C_2H_2/H_2 gas ratios. It can be seen that with the increase in hydrogen neutral atom density with time, the height of the CNT and thereby the growth rate increases with the decrease in hydrogen neutral atom density, i.e., the increasing gas ratio.

With the decreasing gas ratio, the nanotubes of lesser radius and height were produced because H_2 dilutes C_2H_2 thereby reducing its concentration, which reduces the hydrocarbon density.

IV. CONCLUSION

It is evaluated from our study that on decreasing the acetylene/hydrogen (C_2H_2/H_2) gas ratio, the growth rate of the MWCNT decreases. The MWCNTs dimensions also declines with the decrease in gas ratio. The field emission characteristics of MWCNT based emitters can be analyzed better from the obtained results of the study.

REFERENCES

[1] C. Bower, W. Zhu, S. Jin, and O. Zhou, *Appl. Phys. Lett.* **77**, 830 (2000).

[2] V. I. Merkulov, D. H. Lowndes, Y. Y. Wei, G. Eres, and E. Voelkl, *Appl. Phys. Lett.* **76**, 3555 (2000).

[3] K. B. K. Teo, M. Chhowalla, G. A. J. Amaratunga, W. I. Milne, D. G. Hasko, G. Pirio, P. Legagneux, F. Wyczisk, and D. Pribat, *Appl. Phys. Lett.* **79**, 1534 (2001).

[4] L. Delzeit, I. McAninch, B. A. Cruden, D. Hash, B. Chen, J. Han, and M. Meyyappan, *J. Appl. Phys.* **91**, 6027 (2002).

[5] H. Sato, H. Takegawa, and Y. Saito, *J. Vac. Sci. Technol., B* **21**, 2564 (2003).

[6] Y. K. Yap, V. Kayastha, S. Hackney, S. Dimovski, and Y. Gogotsi, *Mater. Res. Soc. Symp. Proc.* **818**, M11.31.1 (2004).

[7] V. Kayastha, Y. K. Yap, S. Dimovski, and Y. Gogotsi, *Appl. Phys. Lett.* **85**, 3265 (2004).

[8] S. M. Toussi, A. Fakhru'l-razi, A. L. Chuah, and A. R. Suraya, *Sains Malays.* **40**, 197 (2011).

[9] M. S. Sodha, S. Misra, S. K. Mishra, and S. Srivastava, *J. Appl. Phys.* **107**, 103307 (2010).

International Journal of Research in Engineering and Innovation (IJREI)
journal home page: http://www.ijrei.com
ISSN (Online): 2456-6934

Thermodynamic analysis of vapour absorption system using waste heat of gas turbine plant with intercooling

R.S Mishra, Mayank Agarwal

Department of Mechanical, Production & Industrial and Automobile Engineering
Delhi Technological University, delhi-110042

Abstract

It is rightly been said that necessity is mother of invention same scenario is here in power sector which is in demand for some changes to fulfil the hunger of increasing demand of increasing population , to cater the requirement there are two method either to opt for advance technology or go for optimum use of present resources which could be made possible by reducing the losses , it can be curbed at small level like switching off appliances when not in use , at large scale it can be done my making modification in the present cycle used for power production. This paper mainly deals with the reduce the work input of gas turbine plant in auxiliary equipment, mostly in air compressor by reducing the work input through intercooling and utilizing same heat energy for useful purpose using vapour absorption system.

© 2017 ijrei.com. All rights reserved

Keywords: Vermiculite, Mechanical, Isotherms, Thermodynamics

1. Introduction

In this work attention is drawn towards use of better technology and methods to use the energy resources, we have both conventional and non-conventional sources in nature which fulfil our day to day needs. We are being a human being always search for better resources and technology. Which could make our life simple and comfortable, for this we are totally dependent on machine, consuming power and its consumption is increasing day by day. It is also stated and verified by our scientist and scholars that no machine can run without consuming power. Otherwise it would be perpetual machine, second thing no machine can convert energy input into usable form 100%. Presently gas turbine plants solar powered plants are gaining importance because they are using the clean source of raw material as well raw material Availability is al-so there as both work on renewable resources, natural gas and Sunlight. Here gas power cycle thermodynamic study is done with modification in intercooling technique used until.

1.1 Gas Power Plant

In gas power plant "Brayton cycle" is used for power production is shown in shown in fig. 1.
All these process are can be accompanied in two ways. Either in closed cycle or in open cycle. In closed cycle same fluid is circulated again heat addition and heat rejection process is carried out with the help of heat exchanger.

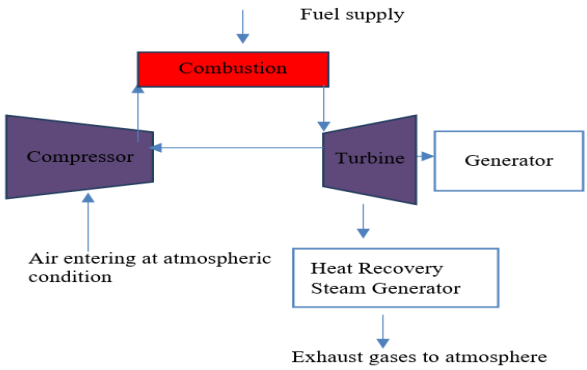


Figure 1: Layout of Gas turbine Power Plant working under Brayton cycle [20]

Radhey Shyam Mishra
Email Id: rsmishradtu@gmail.com

1.2 Vapour absorption system of refrigeration

Refrigeration and air-conditioning is a application of thermodynamics in which comfort is provided to human being as well it aims at protecting the perishable goods at varying environmental temperatures.

Refrigeration is practiced from very early period when we use to store water in earthen pots, in which water at the boundary of pots is evaporated by the surrounding air, the water which evaporates takes the heat of water present in the pot and thus cooling effect is seen.

Today we are facilitated with mechanical refrigeration system which use mechanical energy to carry out refrigeration effect as it includes evaporator, condenser, compressor/pump, and expansion device. In vapour absorption system which found lesser application to those of vapour compression system we use low grade energy resources to that of other refrigeration device in this we use generator, pump, and absorber working with heat which is low grade energy heat against the compressor which uses high grade mechanical energy.

Refrigeration effect producing capability of a machine is defined with the help of term called coefficient of performance, in heat engine it is termed as efficiency. It is given as ratio of desired effect to work input/ heat input. Difference in vapour compression system and vapour absorption system is shown in table 1.

Table 1 Difference between VCRS & VARS [22]

Vapour Compression System (VCRS)	Vapour Absorption System (VARS)
Coefficient of Performance = Desired Effect/Work Input to Compressor	Coefficient of Performance = Desired Effect/ Heat Supplied to Generator
It uses compressor for creating pressure difference	It uses heat energy and variation of concentration as driving force between evaporator and absorber

2. Literature Review

Cheung et al [1] carried out Performance assessment for multistage absorption cycles of 11 multistage multi-effect absorption cycles which include water lithium bromide, ammonia water and their cascade configurations, increment in no of stages is done by them to increases the no of absorption cycle and by increasing the effect they made maximum use of available energy from a stage, in this work evaluation is made for air conditioning applications with the help of energy balance and mass balance across each component taking temperature of evaporator to be 4°C and temperature of condenser 35°C. A no of cycle 8 in no were selected for a detailed simulation. The result shows that highest COP was obtained for approach temperature of 0°C in which three stage water lithium bromide cycle was cascaded with two single stage ammonia water cycle.

M.Gordon et al [2] conducted a design and analysis of a general thermodynamic model for absorption chiller, in this they derive the relation to show the effect on coefficient of performance due to varying cooling rates. Model analysis results are compared with performance data of already published works and found model analysis was useful when chiller performance and coefficient of performance of chiller varies with time.

Chen et al [3] carried out evaluation of a refrigeration cycle working on solar energy as well as electricity further to improve efficiency of combined cycle principle of a heat transformer is applied because solar energy can only be fruitful if it is continuously available so for this thermal reservoir is required but here a source of electricity is used in place of it when solar energy is not available. A thermodynamic model was formed and with help of computer program its performance is evaluated. Present work COP, and parameters were compared with those of traditional vapour absorption system. Which shows that present work overcome shortcoming of currently running vapour absorption system. Horuz [4] did theoretical study on performance comparison between water ammonia and lithium bromide water based vapour absorption system the study include the comparison of system using two different refrigerants that is lithium bromide water and ammonia water solution and parameters COP, the cooling capacity and other parameters are studied and concluded that ammonia water solution is less efficient than lithium bromide water solution but it is free from effect of crystallization. Talbi et al [5] conducted theoretical study of energy recovery from exhaust gases of diesel engine for air conditioning and its effect on performance. Earlier the exhaust from such resources have been utilized for combined heat and power applications here in this work performance of four different configuration of a turbocharger diesel engine and absorption refrigeration unit is studied. They examines the interfacing of Vapour Absorption Refrigeration system with diesel engine and estimate the performance enhancement. It is found that pre-intercooled turbocharger engine configuration cycle offers considerable benefits. Kalinowskia et al [6] did study for application of vapour absorption which is used for waste heat recovery from low temperature in the LNG recovery process. They found Liquefied natural gas recovery process require low temperature cooling which commonly uses vapour compression system but due to high power consumption it is substituted by vapour absorption system which is powered by waste heat of electric power generating gas turbine reducing overall energy consumption. In their study a potential replacement of propane chillers with absorption refrigeration was analyzed and found that single effect ammonia water vapour absorption system could replace propane chillers. Engler et al [7] carried out a simulation and comparative investigation of ammonia water absorption cycle for heat pump applications. They found that in residential and small commercial ammonia water cycle can be used for winter heating and summer cooling throughout the year

with better COP then other alternatives. Several cycle were analyzed from a single effect generator absorber heat exchange with variations. Their objective was a comprehensive study of various ammonia water cycles, with varying operating conditions and varying design parameters for comparing their performance by starting from single effect system to varying its components and analyzing effect of each component which showed COP has increased from 0.5 to 1.08. Da-wen sun [8] carried outperformance comparison of the ammonia water and ammonia sodium thiocyanate and NH3 –LiNO3 absorption refrigeration system. he compared the three on the basis of air conditioning application where he found that ammonia water solution can be replaced with the above two mentioned substitutes with the help of a computer program and found that performance of sodium thiocyanate was better than other two. Aleixo Manzela et al [9] did experimental study for vapour absorption system using engine exhaust gas as energy source. In their work they represented experimental study of the exhaust gas energy availability and the effect of absorption system on the engine performance, the exhaust emissions and the power economy of the vehicle. For this they tested a productive automotive engine in bench test dynamometer and absorption system connected at the exhaust pipe. They tested engine at varying opening of a throttle valve that is 25%, 50% and 75% respectively. The refrigerator reached a steady state after operating for 3 hours, but it depends upon engine throttle valve opening. Results showed that Addition of vapour system reduced the carbon monoxide emission but it increases the emission of hydrocarbons. Shenyi Wu et al [10] carried out experimental study that can be seen in vapour absorption cycle. In their work they opt for multistage multi effect vapour absorption system compared to those of single effect and double effect, in this multi stage they use generator at high pressure after double effect to run the double effect system with the moto to utilize input heat three times to improves the efficiency. Fathi et al [11] carried out study of an irreversible model of solar operated absorption refrigerator. General solar refrigerator uses the solar collector and refrigeration system and operates between two limits that is maximum COP and providing maximum cooling capacity. They work for a new system in which not only irreversible effect due to heat conduction would be considered but also friction, eddy and other effects would be analyzed, as these affect the working of absorption system when it operates continuously. They derived the analytical relations of the optimal refrigeration COP and maximum cooling capacity of the system. Also comparison was made with the earlier results of single stage absorption system. They obtained results which describe the optimal performance of varying temperature values to 4 different level thus absorption refrigeration affected by irreversibility. Jose´ Fernandez-Searaet al [12] carried out mathematical analysis of crucial matter of water effect in ammonia water absorption system of refrigeration effect with flooded evaporators. They analyzed the effect of the ammonia purification and liquid entrainment and blowdown from evaporator, for this they developed mathematical model based on single stage vapour absorption system with complete condensation. For the purification of ammonia analysis is done through murphee efficiencies of the stripping and rectifying sections of distillation column.

M. Mostafavi [13] carried out thermodynamic analysis of diesel cycle combined with absorption refrigeration unit for naturally aspirated diesel engine. The analysis was made on the basis of laws of thermodynamics which help to formulate mathematical relations amongst network, the exhaust gas temperature of the diesel engine as a function of pressure ratio and temperature ratio of the cycle. These relations helped in calculations of magnitude of thermal energy available and the amount of thermal energy required for running of vapour absorption system. The variations in work output of diesel engine and its efficiency at different configurations as a function of cycle pressure are given and a diagram has also been plotted for cooling capacity required for air conditioning purpose. Alberto V et al [14] did design and modelling for heat recovery from trawler chiller fishing vessels to run an on board ammonia water absorption system. In this synthetic oil was used as a heat transfer medium and worked in closed cycle as it is re-circulated. It used two heat exchangers fluid to solution heat exchanger and gas to fluid heat exchanger. Modelling is done and verified using computer programs, these help in study of influence of geometric design parameters and thermal operating condition on the heat exchanger and thermal performance of system. Ahmed et al [15] carried out the study based on thermodynamic parameters for integrated ammonia water absorption refrigeration system and marine diesel engine. In their study they found marine diesel engine utilizes only 48% of the energy supplied rest was released to atmosphere as a waste to water which is used as a coolant now they integrate the diesel engine with vapour absorption refrigeration system to utilize this waste energy also reducing load on coolant.

Mathapati1 et al [16] carried out study on vapour absorption system using LiBr-water solution for air conditioning of the automobile using the waste heat of same automobile which was earlier going into waste in the atmosphere. They did mathematical modelling for the utilization of the exhaust coming out of the internal combustion engine. Cooling load of the vehicle is estimated and feasible study is carried out for calculating energy available in exhaust gas of the automobile.

Balaji et al [17] carried out study on utilizing waste heat of sugar industry in their study through use of vapour absorption system. They work with the aim to reduce the dependence of industries on fossil fuels as fuel price is increasing day by day by exploiting maximum to its waste exhaust, as in sugar industry turbine exhaust carry a large amount of waste heat. This amount of energy which was earlier going in waste now employed to run the vapour

absorption system using LiBr-water solution in single effect and describe various parts of vapour absorption system. Bajpai [18] carried out design and analysis of solar operated vapour absorption system. In his work he aim to produce the cooling effect in which he opt for both vapour compression system and vapour absorption system but found that vapour absorption system to be better alternative because of low power consumption as well as lesser moving parts. Then he calculated the parameters required for solar panel to fulfil the heat requirement of the generator. Bhore et al [19] did designing for experimental analysis of heat recovery using Vapour Absorption system of waste heat of internal combustion engine. They have opted for ammonia water solution for waste heat recovery and utilizing this system for the air conditioning process.

After going through rich literature it is found that the vapour absorption system has been a topic of research from very early period because of increasing dependence on fossil fuels and reduction in fossil reserves day by day, also cycle and process presently used such as vapour compression system for refrigeration, rankine cycle in power plants, Brayton cycle in gas power plants, internal combust-ion engine of automobile all of these uses high grade of energy and due to irreversibility in the process they reject large amount of heat which is discharged in the atmosphere as a part of low grade energy. The second law statement given by kelvin-planck and clausius also emphasis that no heat engine or machine can produce power by consuming 100% of the available energy. Also to maximum energy can be obtained from the energy source when it reaches its dead state according to the availability postulates. For day to day process surrounding environment is supposed to be the dead state but the energy carrying fluid which leave the device is not at dead state and possess some amount of thermal energy, kinetic energy and pressure energy, many device had been invented by our great scholar till date like organic Rankine cycle which work on the principle of Rankine cycle but uses organic fluid like R134a for waste heat recovery from the cycle, it is mostly used as bottom cycle coupled with Rankine cycle which is used as top cycle in combined cycle plant. In present work waste heat recovery is done for the purpose of air conditioning and refrigeration which is in present demand because the device presently in use are vapour absorption system single stage, cascaded vapour absorption system which make use of compressor, consuming large amount of power. So to reduce the power consumption in our day to day life and increasing efficient use of present resources and reducing wastage, air conditioning and refrigeration process is carried out with the help of vapour absorption system.

In terms of gap identified, all the cycle studied and analysed till date worked mostly with LiBr-H_2O solution, also till now no one worked for gas turbine power plant waste heat recovery using vapour absorption system though models have been formulated with the organic Rankine cycle using as a bottoming cycle in waste heat recovery accompanied with heat recovery steam generator. The main objective of this paper is to utilize waste heat of gas turbine plant for the purpose of providing human comfort using vapour absorption system, and to reduce the thermal load on the atmosphere which was due to use of water as a coolant in thermal and gas plant which releases waste heat to ponds and atmosphere.

3. Thermodynamic Analysis of Gas Power Cycle

Gas power plant have got rich history in electricity generation from gas turbine was carried out using natural gas in early 1930/1940 in Switzerland with the output of 4 megawatts then reheat gas turbine was developed in 1945 with a world record of 10 MW with increasing its capacity to 40 MW in Switzerland. Then development in gas power production increases just like fire in forest. In1961 the first combined cycle plant began operation in Austria. Its generative capacity was 75MW after that gas power plant working on combined cycle increased exponentially. One reason seen was that of its greater efficiency and lower emission than any other plant.

Gas power plant is a compact in working to that of thermal plant because it accommodate compressor, combustion chamber and turbine in a single part. Combustion and expansion process is assumed to be isentropic and work on fundamental law of expansion and compression here air is reference because gas power cycle woks on atmospheric air as a working which is supplied energy through burning of fuel, natural gas is used as fuel in gas power plant. In this paper, the above relation is not taken into consideration for compression and expansion process. Because it work on an assumption that specific heat is constant for air with varying temperature, but in actual practice specific heat of air vary with temperature, also compression process is always accompanied with change in temperature of air between two states.

For isentropic process in which specific heat varies with the temperature then for that case

P_1/P_2 = Prelative1/Prelative2

P relative 1= exponential (s_1/R)

After compression fluid that is air in compressed form pass to air pre heater it is also a type of heat exchanger in which heat of exhaust gases leaving the turbine is utilized to preheat the air this preheated air is passed through combustion chamber where by burning of fuel which is mostly gaseous fuel (natural gas), chemical energy is changed to heat energy in the presence of the dense air. So this high pressure and kinetic energy carrying gas impinges the turbine fixed and moving blades arranged alternatively. Thus passing over the blade of the turbine the pressure energy of gas is transformed to kinetic energy imparted to the rotor also kinetic energy of the gas is delivered to the rotor of the turbine.

3.1 T-S diagram of gas power cycle

T-S diagram for gas power plant working cycle is shown in figure 2 showing the process occurring in the gas power cycle. In this diagram process 1-2 represent the isentropic compression process followed by isobaric heat addition process 2-3 at this point gas is taken out from turbine and send for reheating process 4-5 after reheating of gas it is again impinged on the blades of turbines, reheating is mainly done to remove moisture attack on the blades of turbine which is due to condensation of gas (gas contains water vapour after process of combustion as a by-product). After leaving reheater it is expanded isentropically during process 5-6. In T-S diagram it is clearly shown that work of expansion is more to that of work of compression and at last exhaust gas is released in atmosphere for open cycle and in case of closed cycle it reach at its original state.

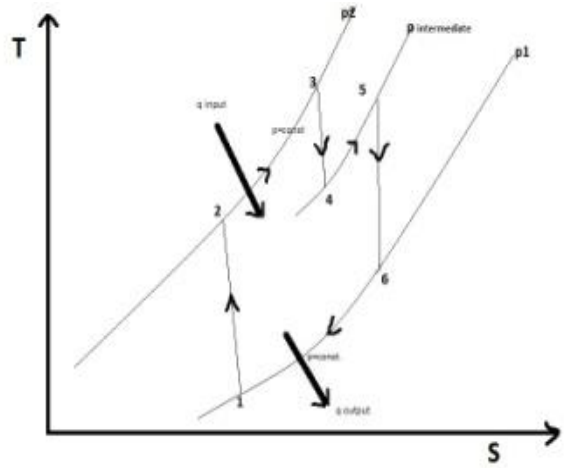


Figure 2: T-S diagram for gas power plant [21]

3.2 Intercooling

Intercooling is a process of heat transfer from hot fluid coming out of first stage of compression to the fluid which circulates the heat absorbed and released in atmosphere. Intercooling is required for compression process for reduction in compressor work and increase the overall work output of the cycle because a large portion of turbine work goes in compression process. Heat rejection in intermediate stages of compression is beneficial with use of intercooler but use of aftercooler is not required to fulfil any purpose. The intercooling is done to reduce the specific volume of the fluid, as with increase in pressure temperature of fluid also increases due to which its specific volume increases significantly and compressor has to handle a large volume of fluid thus increasing the overall work input. For pressure regulated devices such as pressure hammer, pressure regulated valve, compression is carried out in single stage and there is no need for intercooling, whereas for axial compressor used in gas turbine compression is done for a large amount of fluid which is circulated per second so in this case intercooling is done. The cooling Process is isobaric process that is it takes place at constant pressure, and the gas is cooled to the initial temperature at each stage of intercooling. Multistage compression with intercooling is especially attractive when a gas is to be compressed to very high pressures. In the P-V diagram and T-s diagram drawn below shows the effect of intercooling on work done on the compressor, in this air is taken at inlet condition of pressure p_1 and temperature t1 and undergoes to compression process thereby attaining pressure p_x and temperature t^2. So to minimize the work done expression for work done equated to zero and this results in intermediate pressure.

$P_x = (P_1 * P_2)^{0.5}$

The temperature of the fluid is reduced to initial condition as that of the inlet to calculate the minimum work done.

3.3 T-S diagram and P-V diagram for intercooling

In figure 3. T-S diagram is shown in which process 1-2 which was earlier following straight line follows zig-zag path showing that at intermediate pressure fluid temperature is reduced to its initial value

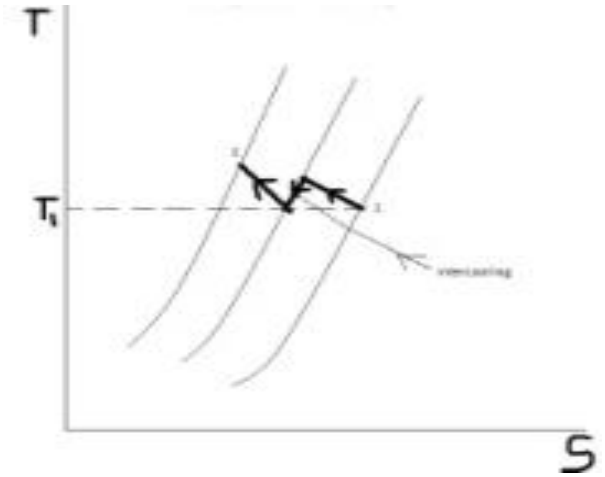


Figure 3: T-S diagram for Intercooling [21]

The P-V diagram showing compression process following polytropic process with and without intercooling is depicted in figure 4 it shows this shows that area under the curve is reduced when the process is followed by intercooling as in P-V diagram area under the curve gives the amount of work done on compressor and it is our aim in this work to reduce the work done.

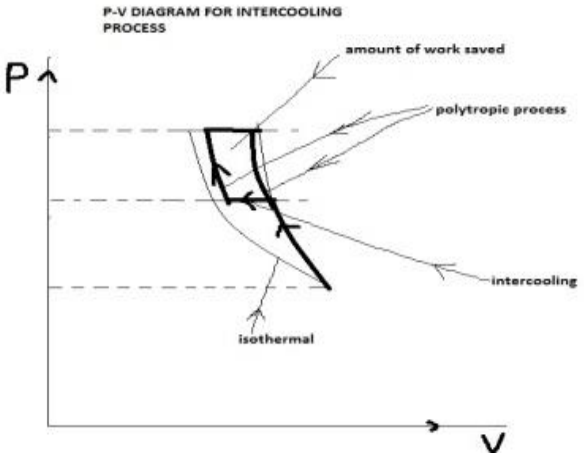


Figure 4: P-V diagram for intercooling process [21]

3.4 Entropy Calculation

Entropy measure the degree of randomness, for a process entropy is always associated and entropy change of isolated system is always positive. Entropy concept was originated from the clausius inequality in which equality sign is for reversible process and inequality for irreversible process. Entropy change is always equal to net transfer for a process across the boundary to the temperature of boundary. A process is said to be carried out when there is change in state of system from one state to another. Entropy change can be calculated for both reversible and irreversible process for irreversible process entropy change is equated to that of entropy change for reversible process if both the process are carried out at same end states hence entropy is property which depend on the states not on the path followed.

Properties of air utilized in this work are taken from thermodynamic table 2 with initial condition of air at temperature of 300K and 1bar pressure

Table-2 Air properties

Temperature in degree Celsius	Enthalpy in KJ/Kg	Relative pressure P_r	Entropy s^0
300	300.19	1.3860	1.70203
400	400.98	3.806	1.99194
410	411.12	4.153	2.01699

3.5 Thermodynamic Analysis of Vapour Absorption Cycle

Vapour absorption system was developed by a French scientist to overcome shortcoming of vapour compression system in which compressor is used to extract the vapour from the evaporator and compress the large volume of the vapour, so the vapour absorption system was invented which uses heat energy instead of work for producing high COP. Vapour absorption system work on a principle of chemistry " like dissolve like" in which some liquids which have great affinity of absorbing large quantity of vapours and converting their state from vapour to liquid, reducing their volume significantly. A vapour absorption system is a heat operated device in which the refrigerant is continuously absorbed and liberated from the absorbent. In absorption system refrigerant is absorbed by the weak solution of refrigerant in water which is coming out of generator. This weak solution absorb the vapours of ammonia and hence lowers the pressure in the absorber to absorb more and more refrigerant, absorption of ammonia refrigerant by weak solution is exothermic process so some cooling is also provided to increase cooling capacity.

This strong solution formed in the absorber is pumped to the generator with the help of a pump, which is then heated by some external means to remove the refrigerant vapours, these vapours passed to the condenser where it is converted to a high pressure liquid ammonia then this ammonia pass through throttle valve to the evaporator where it absorb heat of substance to be cooled in form of latent heat of vaporization and produce the required cooling effect. But in addition to above process there is need for some auxiliaries to increase the efficiency of the system and make it economical it includes analyzer, a rectifier and two heat exchangers. Such that vapour generated in the generator contains some amount of water vapour in addition to ammonia refrigerant which would choke the flow passage in the condenser, in order to remove these vapours rectifier is used. Before reaching the rectifier it is passed through analyser where removal of water takes place in analyser vapours of ammonia are brought in contact to the aqua richest in ammonia and by cooling the vapour with water as a coolant. As in this work aqua ammonia absorption system is being used for waste heat recovery. So for design and analyses it is necessary to represent the process on the concentration enthalpy chart, for design parameter to be selected is the temperature and pressure of condenser and evaporator. In present work water is taken as a coolant in condenser at a temperature of 25^0C so for this saturation temperature pressure to be calculated as 10 bar.

In evaporator considering condition of positive pressure and protecting from condition of vacuum pressure is assumed to be 1 bar and for this saturation pressure temperature for "R717" found to be -33^0 C. secondly for heat load estimation from gas plant it is found that refrigeration effect of 14 TR is required in evaporator so for these values calculation is done. In this work analysis is done with the help of tables generated from the (Ziegler and Trepp,1984; Patek, 1995; Xu and Goswami, 1999 and Alamdari, (2007)correlations solution made available by "Shankar Ganesh, N" in his phd work.

3.6 Flow chart of vapour absorption system

The figure 5 shows the flow chart of single effect vapour absorption system following the path of ammonia

refrigerant passing through different components like evaporator, condenser, generator, pump, and analysis is started with condition of condenser and evaporator load.

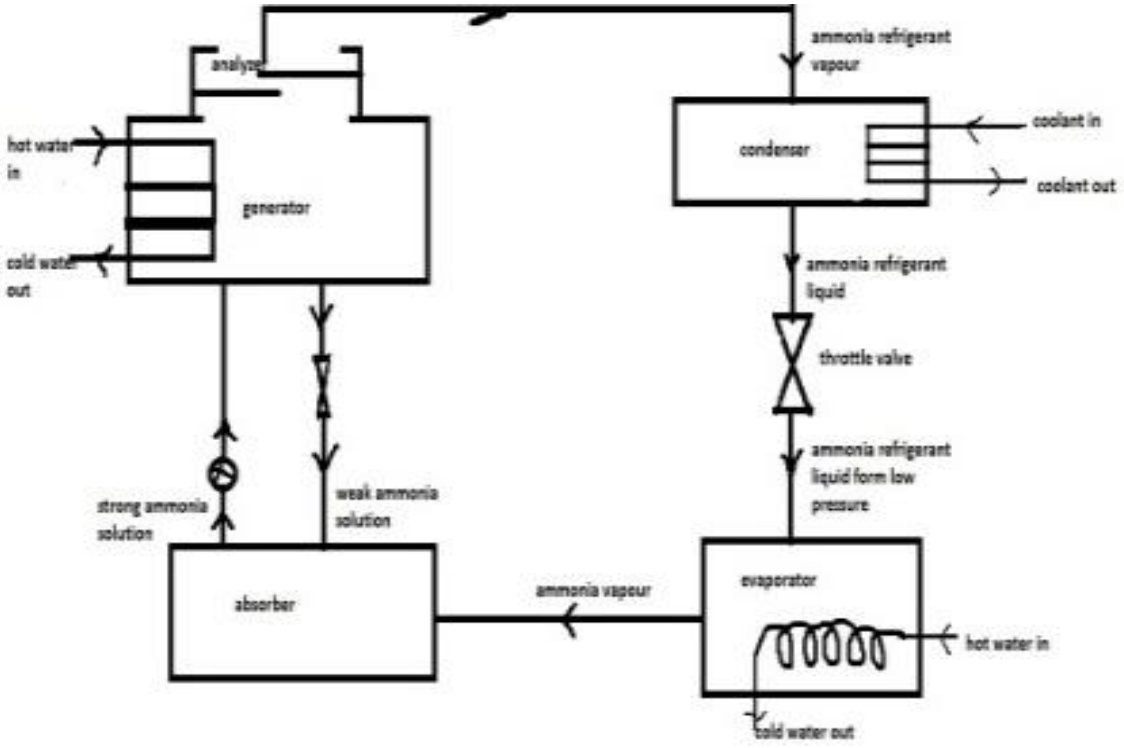


Figure 5: Vapour Absorption System flow chart [22]

3.7 Computation of Relative pressure

Entropy as defined in above discussion shows that it is function of internal energy and enthalpy, internal energy is a function of specific heat at constant volume and temperature similarly enthalpy is a function of specific heat at constant pressure and temperature. It is the property of specific heat that it vary with temperature so with variation in temperature specific heat would also vary and thus entropy which is dependent factor of both internal energy and enthalpy would vary with temperature so entropy is analyzed in two ways.

Entropy change for constant specific heat

$s_2-s_1 = c_{v,avg} \ln (t_2/t_1) + R \ln (v_2/v_1)$

$s_2-s_1 = c_{p,avg} \ln(t_2/t_1) – R \ln(p_2/p_1)$

Entropy change for variable specific heat

$s_2-s_1= s^0_2 - s^0_1 – R \ln (p_2/p_1)$

where s^0_1= entropy with respect to zero degree reference temperature

for isentropic process $s_2-s_1= 0$;

and thus

$p_2/p_1 = \exp(s^0_2 - s^0_1 / R)$

$p_2/p_1 = \exp(s^0_2 / R) / \exp(s^0_1 / R)$

$\exp(s^0_2 / R) = p_{rel,1}$

$\exp(s^0_1 / R) = p_{rel,2}$

$p_{rel,1}$= relative pressure at 1st state

$p_{rel,2}$= relative pressure at 2nd stage

Assumptions made in the vapour absorption System are

1. Steady state condition.
2. Friction in pipes is neglected.
3. Compression process is carried out at entropy change zero.
4. Pure refrigerant is flowing through condenser and evaporator in vapour absorption system.
5. Effectiveness of heat exchangers used is 100%.
6. Mass flow rate is unity in gas turbine operation.

With the help of figure 6 analysis is done. It is seen that gas power plant is operating without intercooling process with following conditions

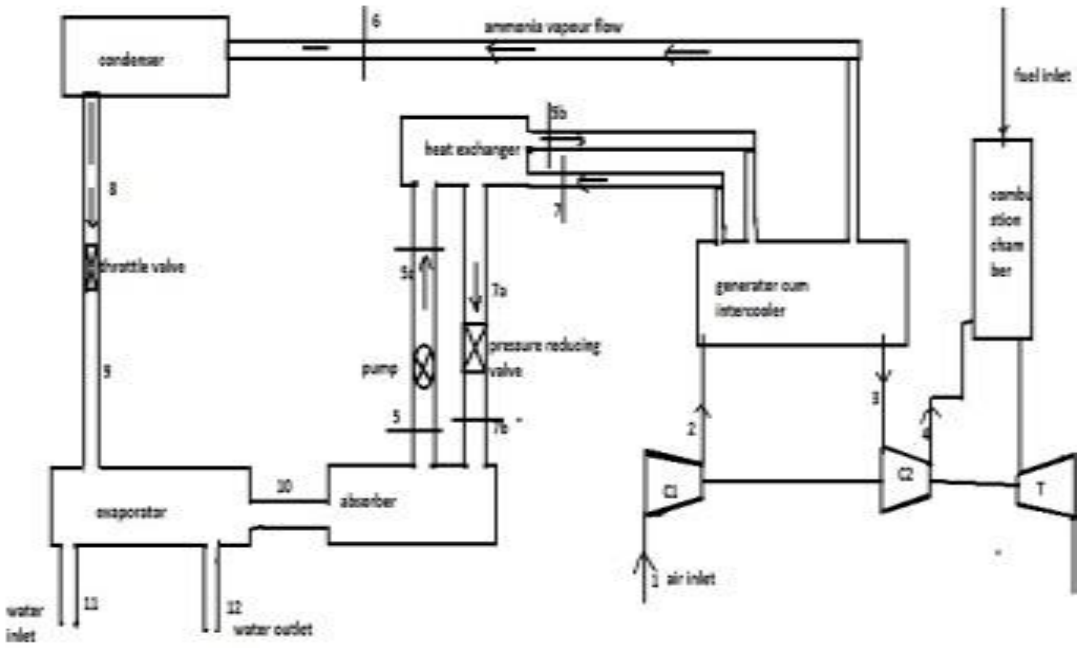


Figure 6: ammonia VAR system [22]

Assuming air is taken from atmosphere which is available at temperature of 298k and at this value enthalpy of the air is calculated with the help of table which is 298.18kj/kg.

In this work assuming compression is taken to be isentropic as mentioned above also taking condition of variation of specific heat with the temperature so for this condition, using concept of relative pressure in which condition at another state is calculated as follows, definition of relative pressure is already made in chapter 3 of this work.

$P_{relative1}$= r*P $_{relative\ 2}$

Where r = pressure ratio for compression process it is taken from 6-20 for optimum values of operation .in this work compression ratio taken is 8.

$P_{relative1}$ = 1.3543

So $P_{relative2}$= 8 * 1.3543

For this value of $P_{relative2}$= 10.834

Temperature and enthalpy is found with the help of interpolation

Temperature = 536k

Enthalpy= 540.51 kj/kg

Therefore work done for this process = enthalpy after compression – enthalpy at inlet of compression process

Work done = 540.51-298.18 = 242.33 kJ/kg

Case 2nd as this done in this work with modification of present cycle and shown in figure 7 in case intercooling process is carried out for compression process so calculation of work input in this case is given as,

Intermediate pressure for compression process is given as ,$P_{intermediate}$= (P_{inlet}*P_{outlet})*0.5

Work supplied to compressor = 2*work supplied in single stage

But P_{outlet} / P_{inlet}= 8;

Therefore $P_{intermediate}$ / P $_{inlet}$= 8^0.5

P $_{relative\ intermediate}$= (8^0.5)*1.3543 = 3.8305

For this value of intermediate pressure $T_{intermediate}$ and $h_{intermediate}$ is calculated

T $_{intermediate}$ = 400.69k

$h_{intermediate}$= 401.60kJ/kg

Work done = 2*($h_{intermediate}$- h $_{inlet}$) = 2*103.4 =206.8 kJ/kg

Amount of heat rejected = mass flow rate of air* Cp*change in temperature = 1*1.005*(400.69-298)

= 103.20 kJ/kg

Calculations for vapour absorption system For absorption system calculation is started from condenser liquid and temperature of the coolant in this work water has been taken as a condenser coolant which is available at a temperature of 25^0C so for this temperature pressure is taken to be 10 bar from figure 7 above at point 6 with condition of pure ammonia refrigerant vapour with quality 100% enthalpy is given by

H_6= 1480 kJ/ kg ("from EES software after defining parameters")

Point 8 in figure 7 shows the condition of pure ammonia refrigerant in liquid which loses its latent heat in the condenser to the water flowing through it. So enthalpy at condenser outlet is;

H_8= 316.8 kJ/kg

Point 9 is the state of the refrigerant after passing through throttle valve.so enthalpy at this point is

H_9= 316.8

After that it passes through the evaporator and absorb the heat of substance to be cooled and change itself from liquid to vapour state by absorbing heat in form of latent heat.

H_{10}= 1418 kJ/kg

For the calculation of mass flow rate of ammonia refrigerant in the evaporator assuming refrigerant load of 14TR.with the given heat input at generator

So for producing refrigeration effect of 14TR amount of refrigerant circulated is

$M_{ammonia}$* (h10-h_9) = 14TR

$M_{ammonia}$= 0.0447 kg/s = 0.45kg/s

Temperature of air at inlet of generator which is supplying heat to the generator is 127.54^{0}C

The concentration of weak solution leaving generator is calculated with the use of tables and chart given in the references. Using method of interpolation at 10 bar pressure, with taking values of temperature at different concentration using enthalpy concentration chart So from method of interpolation it is found that value of concentration; that is X=0.186

Now calculation of concentration of strong ammonia solution leaving the absorber is found as follows

Concentration of strong solution = concentration of weak solution + gasifying factor

Gasifying factor in this work = 0.044

Therefore the concentration of strong solution is 0.186+0.044 = 0.23

The enthalpy =355.637 kJ/kg = h_5 =h_{5a}

From figure-6, it is found at point 5 solution is strong solution whose enthalpy is calculated using chart and tables at pressure of 1 bar which is evaporator pressure at which it is maintained as mentioned earlier in the previous discussion. From point 5 strong solution pass through the pump at a higher pressure with condition of 5a, but enthalpy at this point is same to that of point 5.Similarly enthalpy of weak solution leaving the generator h_7= 423.36 Heat given by the generator is;

Overall mass balance for absorber

$M_{ammonia}$+ M $_{7b}$= M_5;

Ammonia mass balance for the absorber

$M_{ammonia}$+ (0.186) M_{7b}= 0.23* M_5

Heat supplied to the generator, M_{5b}* h_{5b} + Qg = M_{7b}*h_7 + M_6*h_6

3.8 Analysis of system using lithium bromide absorption system

In above method coefficient of performance of vapour absorption system was found low using single effect vapour absorption system using ammonia water solution so work is further done with the recovery of waste heat of system using vapour absorption system with lithium bromide in double effect operating mode using ees software with the following pictorial representation.

In figure 7 analysis made using double effect lithium bromide system is shown, this figure shows that waste heat of intercooling in compression process is going in high pressure generator of double effect VAR system, it helped in analyzing the problem and solving the problem using software, in the software programming was done starting with evaporator and various input parameters used was waste heat gas temperature, evaporator pressure, evaporator working temperature & temperature of condenser.

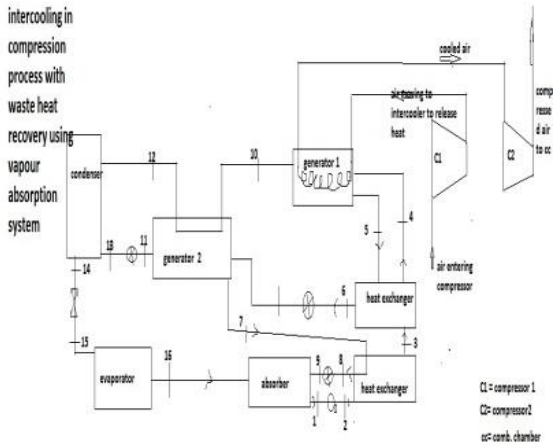


Figure 7: Combined cycle with intercooling using liBr-H2O VARs [22]

4. Result and Discussion

4.1 Variation of COP with generator temperature

Figure 8, shows that COP of the double effect vapour absorption system firstly increases with generator temperature and then become constant and at higher temperature it decreases.

Where t_g= generator temperature (K)

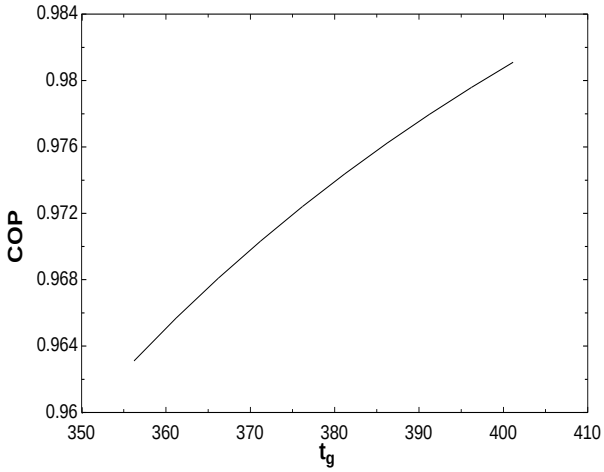


Figure 8: showing variation of COP with generator temperature

4.2 Variation of COP with temperature of condenser

Figure 9 showing variation of COP with the condenser temperature it shows that as the temperature at which heat is rejected into atmosphere increases from the present work data of 40^0 C to higher values COP of the system starts decreasing.
Where t_c= condenser temperature (K)

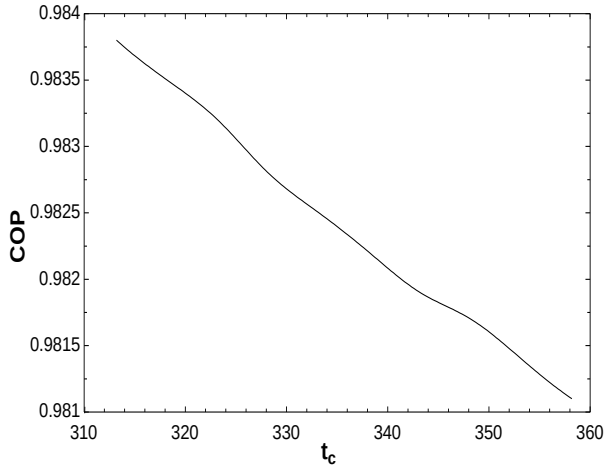


Figure 9: Variation of COP with condenser temperature

4.3 Variation of COP with evaporator temperature

Figure 10, shows that with increase in temperature of the evaporator i.e. the temperature at which heat is absorbed by the system increases there is simultaneous increase in the COP of the system.
Where t_e= evaporator temperature (K)

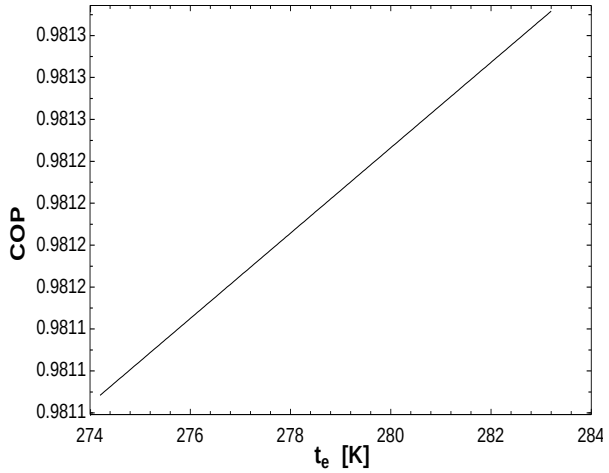


Figure 10: Variation of COP with evaporator temperature

4.4 Effect of temperature of generator on first and second law efficiency of the system

Figure 11, shows that COP increases with generator temperature to a particular point then become stagnant and after that decreases whereas second law efficiency of the system is more at lower temperature of generator.
Where t_g= temperature of generator (K)

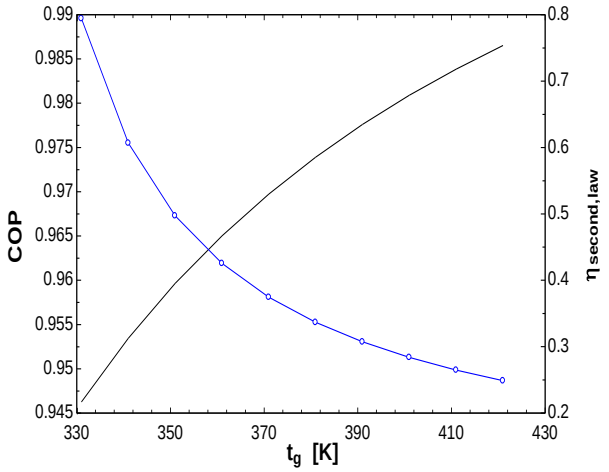


Figure 1: Variation of first law efficiency (COP) and second law efficiency (η_{second}) with the temperature of generator

4.5 Effect of temperature of condenser on first and second law efficiency of the system

Figure 12, shows the variation of condenser temperature on COP and second law efficiency of the double effect system, showing that as the temperature at which heat is rejected to atmosphere increases it would lead to decrease in COP and second law efficiency.
Where t_c= temperature of condenser (K)

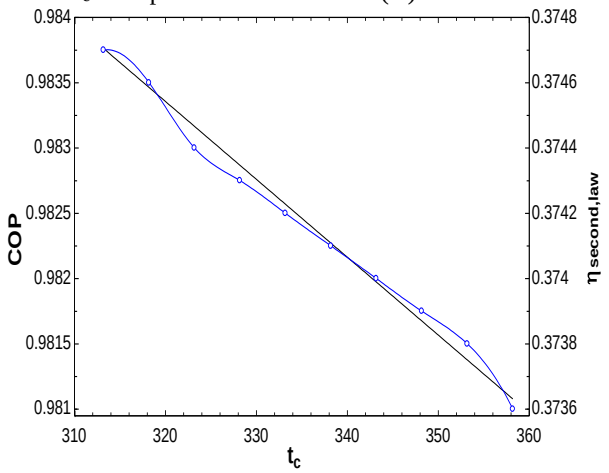


Figure 12: Variation of first law efficiency and second law efficiency with temperature of condenser

4.6 Effect of temperature of evaporator on first and second law efficiency of the system

Figure 13. shows effect of variation of evaporator temperature on first law efficiency(COP) and second law efficiency, showing that both first law and second efficiency increases with increase in evaporator temperature i.e. more the refrigerating effect with given heat input more would be efficiency of the machine

according to first and second law.
Where t_e= evaporator temperature (K)

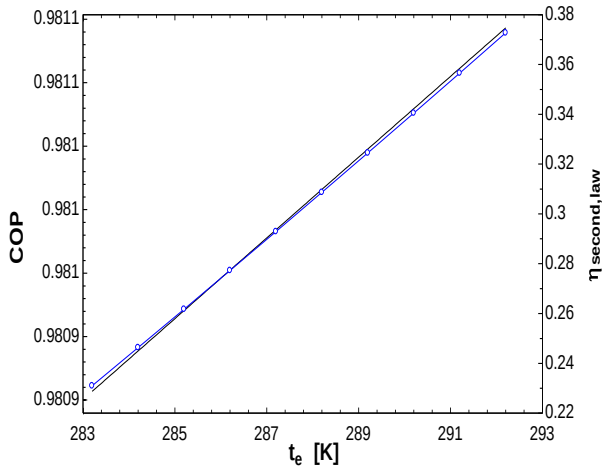


Figure 13: Variation of first law and second law efficiency with evaporator temperature

Table-3 shows that with decrease in temperature of generator first law efficiency of the system decreases whereas second law efficiency increases when refrigeration load is kept same because at lower temperature exergy destruction reduces as shown in the table above.

Table-3 Showing variation of VAR parameters With generator temperature (tg)

T_g (K)	COP	COP_{carnot}	EDR	$\eta_{second\ law}$
421	0.9865	3.963	3.017	0.2489
411	0.9839	3.715	2.776	0.2648
401	0.9809	3.455	2.522	0.2839
391	0.9776	3.181	2.254	0.3073
381	0.9739	2.893	1.97	0.3367
371	0.9697	2.589	1.67	0.3745
361	0.965	2.269	1.351	0.4254
351	0.9596	1.93	1.011	0.4972
341	0.9535	1.571	0.6482	0.6067
331	0.9462	1.191	0.2589	0.7944

Table-4 Showing variation of VAR parameters with generator temperature (tg)

T_g (K)	COP	Q_a (kJ/kg)	Q_g kJ/kg	R kJ/kg
421	0.9865	83.06	1719	2351
411	0.9839	83.06	1632	2351
401	0.9809	83.06	1545	2351
391	0.9776	83.06	1459	2351
381	0.9739	83.06	1373	2351
371	0.9697	83.06	1287	2351
361	0.965	83.06	1203	2351
351	0.9596	83.06	1119	2351
341	0.9535	83.06	1035	2351
331	0.9462	83.06	952.8	2351

5. Conclusion and Recommendations

The following conclusions can be drawn from above result

(i) Temperature of generator and heat supplied to generator greatly affect the cop of performance of the system in this double effect liber water vapour absorption system accompanying two heat exchangers shows that COP increases with temperature of generator and heat supplied till a particular value of COP then decreases.
(ii) The exergy destruction ratio is less at lower temperature of generator.
(iii) Second law efficiency of system decreases with increase in temperature of generator.
(iv) The COP is decreasing its value from 0.981 as the temperature of condenser increase so it shows that with increase in temperature at which heat is rejected to atmosphere it will decrease system COP.
(v) The COP of single effect system was less than double effect.
(vi) Temperature increase of condenser lead to decrease in second law efficiency.

References

[1] Y. Hwang, J. F. Judge, K. Kolos, A. Singh and R. Radermacher,(1996)Performance assessment of multistage absorption cycles, Journal of refrigeration, Vol-19, No. 7, pp.473-481, Published by Elsevier Science Ltd.
[2] J.M Gordon and Kim Choonng(1995)A general thermodynamic model for absorption chillers: theory and experiment, Journal of heat recovery system and CHP, Vol-15,No.1, pp.73-83, Published by Elsevier Science Ltd, Printed in great britain.
[3] Guangming and EijiHihara (1999) A new absorption refrigeration cycle using solar energy, Journal of solar energy,Vol-66,No.6,pp.479-482, Published by Elsevier Science Ltd.
[4] I Horuz (1998) A comparison between ammonia water and lithium bromide solutions in vapour absorption refrigeration system, Journal of heat mass transfer, Vol-25,No.5,pp.711-721, Published by Elsevier Science Ltd , Printed in USA.
[5] M.Talbi , B.Agnew (2002) Energy recovery from diesel engine exhaust gases for performance enhancement and air conditioning, Journal of applied thermal engineering, Vol-22,pp.693-702, Published by Elsevier Science Ltd.
[6] Paul kalinowski, Yunho Hwanga, Reinhard Radermachera (2009), Application of waste heat powered absorption refrigeration system to the LNG recovery process, International journal of refrigeration, Vol-32,pp.687-694, Published by Elsevier Science Ltd. & IIR, Available at science direct.
[7] M.Engler, G.Grossman(1997) Comparative simulation and investigation of ammonia water absorption cycle for heat pump applications, International journal of refrigeration,Vol-20,No-7,pp.504-516, Published by Elsevier Science Ltd. & IIR.
[8] DA-WEN SUN (1998) Comparison of the performance of ammonia-water, NH3-LiNO3 and NH3-NaSCN absorption

refrigeration system, Journal of energy conversion management, Vol-39, No-5/6,pp.357-368, Published by Elsevier Science Ltd.

[9] Andre AlexoManzela, Sergio MoraisHanrroit, LubenCabezas (2010) Using engine exhaust gas as energy source for an absorption refrigeration system, Journal of applied energy, Vol-87,pp.1141-1148.

[10] Shenyiwu, Ian W. Eames (2000)Innovations in vapour absorption cycle, Journal of applied energy,Vol-66,pp.251-266 Published by Elsevier Science Ltd.

[11] R.fathi, C.Guemimi, S.Ouaskit (2004)An irreversible thermodynamic model for solar absorption refrigerator , Journal of renewable energy, Vol-29, pp.1349-1365 Published by Elsevier Science Ltd.

[12] Jose (2006) Ammonia water absorption refrigeration systems with flooded evaporators, Journal of applied thermal engineering, Vol-26,pp.2236-2246, Published by Elsevier Science Ltd.

[13] M.Mostafavi and B.Agnewt (1997) Thermodynamic analysis of combined diesel engine and absorption refrigeration unit naturally aspirated diesel engine, Journal of applied thermal engineering, Vol-17, No-5,pp.471-478, Published by Elsevier Science Ltd.

[14] Jose.(1998) Heat recovery system to power an on board NH3-H2O absorption refrigeration plant in trawler chiller fishing vessels, Journal of applied thermal engineering,Vol-18, pp.1189-1205, Published by Elsevier Science Ltd.

[15] Ahmed Ouadha (2013) integration of an ammonia water absorption system with marine diesel engine, Journal of procedia computer science,Vol-19,pp.754-761, Published by Elsevier.

[16] S.S.Mathapati (2014) a study on automobile air conditioning using vapour absorption system, International journal of engineering research and journal science,Vol-2, Issue-4, ISSN.2091-2730.

[17] K.Balaji (2012) study of vapour absorption system using waste heat, IOSR Journal of engineering,Vol-2,Issue-8,ISSN.2250-3021,pp.34-39.

[18] V.K Bajpai (2012) design of solar powered vapour absorption system, Presented at proceeding of world congress on engineering ,Vol-3

[19] Ketan Bhore (2015) waste heat recovery of IC engine Using Vapour Absorption System, Journal of IERJ, ISSN 2395-1621,pp.223-229.

[20] Cengel and Boles (2011) Thermodynamics an engineering approach, 7th edition,ISBN-9780071072540,pp.305-513,publisher Mcgraw Hill Education.

[21] R.K Rajput (2015) Thermal engineering,9thedition, ISBN-9788131808047 ,pp.1202-1230, publisher Laxmi publications.

[22] C.P Arora (2003) Refrigeration and Air conditioning, 2nd edition,ISBN-0074630105, pp.135-227,427-465,publisher Mcgraw Hill Education.

Ann Oper Res
DOI 10.1007/s10479-017-2591-3

MULTIPLE OBJECTIVE OPTIMIZATION

Third party logistics (3PL) selection for cold chain management: a fuzzy AHP and fuzzy TOPSIS approach

Rajesh Kr. Singh[1] · **Angappa Gunasekaran**[2] · **Pravin Kumar**[3]

© Springer Science+Business Media, LLC 2017

Abstract Managing value chain of perishable food items or pharmaceutical drugs is known as cold chain management. In India, approximately 30% fruits and vegetables get wasted due to lack of effective cold chain management. Logistic providers play a crucial role in making cold chains more effective. Based on literature review, ten criteria are selected for the third party logistics (3PL) selection process. Some of these criteria are transportation and warehousing cost, logistic infrastructure and warehousing facilities, customer service and reliability, network management, etc. This study illustrates a hybrid approach for selection of 3 PL for cold chain management under fuzzy environment. A hybrid model of Fuzzy AHP and Fuzzy TOPSIS is proposed in this paper for the selection of an appropriate 3PL in order to outsource logistics activities of perishable products. Fuzzy AHP is used to rank different criteria for 3PL selection, then Fuzzy TOPSIS is used to select the best 3 PL based on performance. The results imply that logistic providers should focus on practices such as automation of processes and innovation in cold chain processes to become more competitive.

Keywords 3PL · Cold chains · Supply chain management · Sustainable performance · MCDM

1 Introduction

Managing value chain of products like food items, medicines, fruits, chemical products is a big challenge for organizations in the present volatile market. Most of such value chains are not able to sustain their performance due to huge losses and extra cost occurring at different stages (Manoj et al. 2008; Brandenburg and Rebs 2015). Singh et al. (2016) have

✉ Rajesh Kr. Singh
rksdce@yahoo.com

1 Management Development Institute, Gurgaon, India

2 School of Business and Public Administration, California State University, Bakersfield, USA

3 Delhi Technological University, Delhi, India

Published online: 28 July 2017

observed that geographical dispersion of customers and their unpredictable demands as well as the varying shelf life of products has increased complexity in cold chain management. In developing countries such as India, approximately 30% fruits and vegetables get wasted due to lack of cold chain infrastructure available. Managing such kind of perishable products is known as Cold chain management (CCM). CCM can be defined as the process of planning, implementing and controlling the flow and storage of perishable goods, related services and information in order to enhance customer value and to ensure low costs (Bogataj et al. 2005; Fearne et al. 2006). Limited shelf life of perishable products asserts the need of special equipment and facilities for storage, sales, and distribution of these products under varying temperatures and humidity in order to preserve their usage and quality for a longer period of time (Shabani et al. 2012). A cold chain protects a wide variety of food, pharmaceutical, and chemical products from degradation, improper exposure to temperature, humidity, light or particular contaminants to keep them frozen, chilled and fresh. According to Bogataj et al. (2005), any deviation in time-distance or temperature in the chain, could hamper the net present value of the products. Cold chain management plays a significant part in modern global food commodities business (Jol et al. 2007). The primary objective of Cold chain management is the achievement of desired levels of service and quality at minimum cost through necessary planning and coordination of all involved activities (Christopher 2011).

According to James and James (2010); Akdemir (2008) and Kuo and Chen (2010), cold chain logistics can be broadly divided into three processes: cold processing (primary chilling and secondary cooling), cold storage (storage of perishable products under controlled temperatures) and cold transportation and distribution (sorting, distribution and transportation of perishable products in restricted timeframe). According to Gao Xuling et al. (2006), three main features of a CCL system are: (i) a large amount of investment for construction of complex systems. (ii) Timeliness required for higher co-operation of various organization sectors. (iii) Sufficient control of operation costs. Since, it has become increasingly difficult for organizations to perform these intricate logistics operations effectively with their core competencies of manufacturing; they tend to outsource their logistics operations to 3PL (Large et al. 2011).

A 3PL is an independent firm which provides logistics services under a contract to a primary manufacturer, vendor, or user of a product or services (Aguezzoul 2008). According to Göl and Çatay (2007), 3PL service providers contribute to achieving greater flexibility, operational efficiency, improved customer service levels, and a better focus on their core business. Five major 3PL functions are transportation, warehousing, inventory management, order processing & information system and packaging (Delfmann et al. 2002). Many 3PL companies are present in the market, which has resulted in a cut-throat competition. As a result, selection of appropriate 3PL from the available lot is of strategic importance for any organization as it enhances their competitive advantage and at the same time, it ensures the long-term relationship between the two firms (Perçin 2009; Bhatnagar et al. 1999; Troyer and Cooper 1995). 3PL selection is of primary importance in the cold supply chain due to the specific needs of customer preferences.

The cold chain industry in India is mainly unorganized sector. This sector lacks in terms of modern supply chain practices as well as it is not well researched in Indian scenario. This study has tried to address issues related to slection of 3 PL by using Fuzzy Analytical Hierarchy Process (FAHP) and Fuzzy Technique for Order Preference by Similarity to Ideal Solution (FTOPSIS). Paper has been organized as follows: Sect. 2 deals with literature review, Sect. 3 lays out the proposed selection methodology of Fuzzy AHP and Fuzzy TOPSIS, Sect. 4 deals with the case illustration of the proposed methodology and Sect. 5 presents the results and conclusion of the research work.

2 Literature review: cold chain management

Cold chain management can be defined as a process of planning, implementing and coordination of efficient and effective flow and storage of perishable goods and related services in order to satisfy customer's requirements (Vorst and Van der 2000). All these activities should be properly scheduled for on time delivery of services (Manoj et al. 2008), Cold chain processes, particularly include sorting, distributing and transporting cold chilled frozen and fresh products (Kuo and Chen 2010). All food products have a temperature range under which they have to be kept for maintaining the food quality and food safety (Ovca and Jevšnik 2008). An increase in temperature may cause food poisoning or have a significant influence on Salmonellosis, Campylobacteriosis, Vibriosis, which are associated with diarrheal disease (Tirado et al. 2010). According to Coulomb (2008), the cold chain is necessary for health, avoiding diseases and deaths. Globalization has led to an increasing number of companies exporting food products. The increase in exports of food products due to globalization has put pressure for an effective logistics management system.

Due to the globalization of markets and competitive pressures, organizations are facing increasing demands to deliver customer-adapted products all over the world quickly and on time (Sohail and Al-Abdali 2005). Singh and Sharma (2015) have observed that supply chains doing better in terms of cost and responsiveness can sustain their performance. Involvement of logistics providers in a supply chain can reduce cost and delivery time (UNCTAD 2006). Cold chain logistics (CCL) may be considered as a logistics system involving refrigeration and temperature controlled compartments. Refrigeration is considerable in maintaining safety and quality of perishable products (James and James 2010). CCL involves transportation and storage of products like vegetables, fruits, meat, pharmaceuticals, etc. at various temperatures and under the strict timelines in order to ensure their satisfactory performance and quality (Guo et al. 2007). According to Shabani et al. (2012), cold chain logistic has emerged because of the limited shelf life of some products, which requires special equipment and facilities for sales, storage and distribution.

According to Christopher (2011), effective logistics management ensures that the requirement from customers is satisfied from the whole systems' point of view, by employing methods like good material flow coordination, information flows and expanding of the marketplace. Logistics operations involve planning, implementation and controlling the flow of goods, services, and related information. Appropriate cold chain logistic operations can yield various benefits such as keeping the products at an appropriate temperature, improving the efficiency of the whole supply chain and saving cost when implementing cold chain work. According to Montanari's (2008), data tracking and temperature monitoring are two significant components of the cold chain management system and further added that the implementation of monitoring in real time is of prime importance.

On the other hand, various challenges in the cold chain logistics system have been mentioned in the literature, particularly in the fields of innovative technologies, packaging, sustainability and customer satisfaction. As mentioned by Manzini and Accorsi (2012), innovative technologies mean specific techniques for inspecting the quality of food products, especially in raw materials. This is particularly done through RFID technology. It sufficiently reduces the number of recalls, which in turn saves cost for the company (Li and Chandra 2007). The unreliability in RFID implementation is a big challenge, especially in reading range and reading accuracy (Kumar et al. 2009). An innovative and good packaging would provide complete information for products, making it easier and simpler to register the goods, making it suitable for logistics operations like material handling, warehousing stor-

age systems and shipments. Thus, it will save time and enhance the efficiency of logistics. Hamprecht et al. (2005) have observed two major challenges in supply sustainability. First, the manufacturing process should be refined and extended regularly in order to ensure a sustainable quality of the product. Secondly, the environment and society performance should be controlled and should be integrated into the work. Christopher (2011) has observed that increasing customers' expectation has become a significant challenge for an organization because of increasing service-sensitive markets.

According to Perego et al. (2011), improvements in logistics are key factors in providing good customer service in terms of delivery, punctuality, timeliness, accuracy, and maintaining a sustainable performance. Because a company's sustainable performance comes from the delivery process as from the product itself, logistics has been upgraded from its traditional backroom function to a strategic boardroom function. A typical cold chain infrastructure generally consists of pre-cooling facilities, cold storages, refrigerated carriers, packaging, warehouse, traceability, retailer, and consumers, under the aegis of information management systems (Montanari 2008).

In developing countries, apart from high wastage of perishable items such as fruits and vegetables, logistic cost is also very high. For example, in context to India, logistic cost is around 14% of GDP as compared to 8% in developed countries. The major causes behind this is an unorganized cold chain sector and poor infrastructure. Therefore present study will try to suggest an approach for selection of 3 PL on the basis of the comprehensive performance framework.

2.1 Selection of 3PL

Nowadays, organizations are trying to give more focus on their core competencies. According to Diabat et al. (2013), third-party logistics (3PL) is a single professional service provider, who will manage the logistics functions of a company, including inventory management, warehouse operations, physical distribution of goods, shipment consolidation, information systems, product returns, etc. A 3PL provider is an external company hired to perform some or all of the logistics activities that have traditionally been performed within an organization (Perçin 2009). A 3PL provider is usually associated with the offering of multiple, bundled services, rather than just isolated transport or warehousing functions (Leahy et al. 1995). Cho et al. (2008) have observed that the use of 3PL will increase a firm's logistics capability and enhance its performance by leveraging the third-party's expertise.

3PL selection is a complex multi-criteria decision-making problem as it involves various criteria depending upon the requirements and specifications of the outsourcing firm (Aguezzoul 2008). Partners' culture, past experience, size, partners' technical know-how, financial assets, managerial experience and access to markets are also important criteria for a compatible partner selection. Holistic logistics operations include activities such as purchasing and supply, materials handling, materials management, production planning and control, transport, storage, distribution, project management, installation and servicing, re-use and recycling and strategic management. Evaluating 3PLs based on their abilities to conduct the above mentioned logistic activities effectively and efficiently helps companies to increase the value of their goods which strengthens the customers' satisfaction. According to Bowersox and Closs (1996), the logistic activities must be measured in terms of availability, operational performance, and flexibility. Miller et al. (2013) have also developed a decision-support-system (DSS) to improve the firm's ability to effectively utilize its storage capacity and meet customer shipping requirements across a widely dispersed network.

The study conducted by McGinnis et al. (1995) and Menon et al. (1998) in the USA concluded that both the firm's competitiveness strategy and external environmental affect the selection criteria for 3PL. They also listed eight important criteria for 3PL selection which are on-time shipment and deliveries, superior error rates, financial stability, creative management, ability to deliver as promised, the availability of top management, responsiveness to unforeseen occurrences and meet performance and quality requirements before price discussions occur. These findings were further bolstered by Sangam (2004), who concluded that the 3PL selection criteria should include general information about product lines, price, shipping volumes, financial stability, growth forecast, IT systems used, quality standards, the value added services, and the capacity and compliance. Rijswijk and Frewer (2008) have observed that that traceability is very important not only for food safety but also for food quality. To counter the traceability problem, Montanari (2008) has found the need for reliable IT infrastructure of the cold chain. The web platform, even allows a company to overcome traditional logistics problems (Gunasekaran and Ngai 2003).

Spencer et al. (1994) used on-time service delivery, service quality, communication, reliability, service speed and flexibility criteria for 3PL Selection. McGinnis et al. (1995) and Menon et al. (1998) employed on-time shipment and deliveries, superior error rates, financial stability, creative management, the ability to deliver as promised, the availability of top management, responsiveness to unforeseen occurrences and meeting of performance and quality requirements as criteria for evaluating 3PL firms. Dapiran et al. (1996) and Bhatnagar et al. (1999) have found service quality, workforce capability, and cost as the most important criteria for a 3PL selection. Efendigil et al. (2008) used 12 performance indicators for 3PL selection which are: on time delivery rate, confirmed fill rate, service quality level, unit operation cost, capacity usage ratio, total order cycle time, system flexibility index, integration level index, increment in market share, research and development ratio, environmental expenditures and customer satisfaction index. Moberg and Speh (2004) found four most important criteria for 3PL selection i.e. responsiveness to service requirements, quality of management, the track record of ethical importance and ability to provide value-added services. Wolf and Seuring (2010) while studying the environmental impacts as criteria for 3PL selection reported that, although a 3PL shows an increasing interest in environmental issues, outsourcing decisions are essentially made on traditional performance indicators such as price, quality, and on-time delivery.

The share of organized retailing in the USA is around 80%, Europe—70%, Brazil—40% and China—20% (PWC 2007). In developing countries, the status of organized retailing is not very good. One of the reasons for this may be unorganized logistic providers. It is observed that around 35–40% of the total production of fresh fruits and vegetables is wasted in India, which is about the total production of the Great Britain. The primary reason for this waste may be a lack of adequate storage, transportation, cold chain facilities and other infrastructure supports. Therefore, organizations need to manage their logistics in a systematic manner. Consideration of criteria and their importance totally depend on the needs and prevailing economic conditions of the buyer firm. Therefore, clear and realistic objectives and expectations of a 3PL arrangement will allow a company to establish its selection criteria and select the 3PL, which will meet and provide the best service to the buyer firm (Sangam 2004). Based on literature review, the criteria selected for a 3PL selection process in this study are transportation and warehousing cost, logistic infrastructure and warehousing facilities, customer service and reliability, network management, material handling capabilities, quality control and inspection, automation of processes, innovation and effectiveness of cold chain processes, IT applications for tracking and tracing and flexibility of processes. These are summarized in Table 1.

Table 1 Criteria shortlisted for 3PL selection

Codes	Criteria	References
C1	Transportation and warehousing cost	Vaidyanathan (2005), Kumar et al. (2006), Jharkharia and Shankar (2007), Manoj et al. (2008), Choy et al. (2008), Efindigil et al. (2008), Singh and Sharma (2015), Singh et al. (2016)
C2	Logistic Infrastructure and warehousing facilities	Zhou et al. (2008), Zang (2009), Soh (2010), Fu and Yin (2012), Kumar and Singh (2012), Agrawal et al. (2016)
C3	Customer service and reliability	Chow et al. (2005), Choy et al. (2008), Yan (2009), Zang (2009), Gupta et al. (2010), Kumar and Singh (2012), Miller et al. (2013), Singh et al. (2016)
C4	Network management	Thakkar et al. (2005), Vaidyanathan (2005), Ying and Dayong (2005), Singh et al. (2012), Zokaee et al. (2014), Agrawal et al. (2016)
C5	Material handling capabilities	Bolumole (2001), Gunasekaran and Ngai (2004), Vaidyanathan (2005), Agrawal et al. (2016)
C6	Quality control and inspection	Chan and Chan (2004), Singh (2011), Singh and Sharma (2015)
C7	Automation of processes	Choy et al. (2007), Gupta et al. (2010), Ho et al. (2012),
C8	Innovation and effectiveness of cold chain processes	Flint et al. (2005), Min et al. (2005), Porter and Kramer (2006), Melnyk et al. (2010)
C9	IT applications for tracking and tracing	Vaidyanathan (2005); Işiklar et al. (2007), Singh et al. (2008), Yan (2009), Gupta et al. (2010), Fu and Yin (2012), Kumar and Singh (2012)
C10	Flexibility of processes	Thakkar et al. (2005), Efindigil et al. (2008), Zang (2009) Gupta et al. (2010), Qureshi et al. (2008), Singh and Sharma (2014), Agrawal et al. (2016)

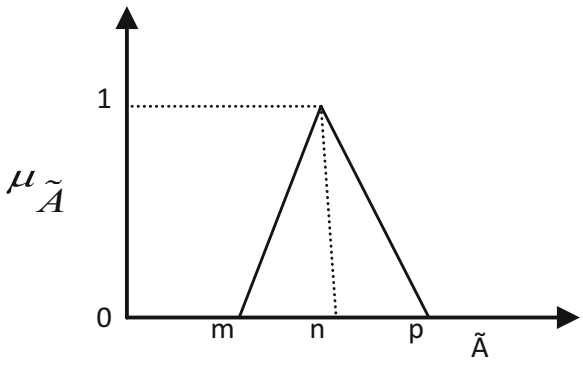
3 Methodological background

Hybrid approach consisting of Fuzzy AHP and Fuzzy TOPSIS is applied for 3PL selection in cold chain management in the present study. Fuzzy AHP is employed to determine the relative weights of the criteria while Fuzzy TOPSIS is used to ascertain the final rankings of 3PL alternatives. Theory and mathematics of this model are based on studies done by Sun (2010) and Torfi et al. (2010). Govindan and Murugesan (2011) used Fuzzy Extent analysis for 3PL selection. Kumar and Singh (2012) have also used Fuzzy AHP and TOPSIS approach for 3PL selection in global supply chains. Singh and Sharma (2015) have used fuzzy AHP and extent analysis for evaluating most competitive supply chains. In this research paper, a hybrid approach of FAHP and FTOPSIS is employed for 3PL selection for cold chain management. FAHP is used to find the relative weights of the shortlisted criteria and FTOPSIS is employed to determine final rankings of the alternatives. Işıklar and Büyüközkan (2006) used AHP-TOPSIS hybrid to evaluate mobile phone alternatives. Gumus (2009) used this approach to evaluate hazardous waste transportation firms. Dağdeviren et al. (2009) employed AHP-TOPSIS under fuzzy decision-making environment for the purpose of weapon selection. Therefore Fuzzy AHP and Fuzzy TOPSIS approach had been very useful and realistic under fuzzy and uncertain conditions.

AHP is a Multi-Criteria Decision-Making tool, which is used extensively for modeling the unstructured problems in different areas such as politics, economics, social and management sciences (Buyukozkan et al. 2007). Pure AHP has some shortcomings. AHP is used in crisp-information, decision applications where the pairwise comparison is made by using a ratio scale. The unreliability associated with the mapping of one's perception or judgments to a number are not taken into account (Büyüközkan et al. 2004). AHP works only with exact and ordinary data, whereas humans, because of their good ability for qualitative data processing make decisions in fuzzy environments (Torfi et al. 2009). Many studies used AHP integrated with fuzzy logic to solve different problems. Cakir and Canbolat (2008) used fuzzy AHP for an inventory classification system. Büyüközkan et al. (2004) used it to select the most appropriate software development strategy whereas Tolga et al. (2005) used it in the operating system selection problem. Pan (2008) used the application of fuzzy AHP for selection of suitable bridge construction method. Multiplicative priority rating methods for the AHP have been used by Stam and Duarte (2003). The level of faulty behavior risk has been evaluated by Dagdeviren and Yuksel (2008), based on the AHP methodology. Chen et al. (2008) used it to determine the weighting of subjective/perceptive judgment for criterion which was used to derive the fuzzy synthetic utility values of alternatives.

TOPSIS is a multi-criteria technique, which has been widely accepted because of its sound logic, the simultaneous condition of the ideal and anti-ideal solutions and easily programmable computation procedure (Kim et al. 1997). In TOPSIS, the rank of alternatives is calculated by finding its distance from the positive ideal solution and negative ideal solution, the alternative which has the shortest distance from the positive ideal solution and the longest distance from the negative ideal solution is the best. In TOPSIS the decision maker faces the difficulty of assigning precise performance rating to alternatives for the attributes under consideration. The crisp data used in TOPSIS are inadequate in the real life world, so linguistics assessment must be used instead of crisp values (Chu 2002). In the past 20 years, various methods have developed which integrates TOPSIS with fuzzy logic, which can be used for solving group decision-making problems. Chen (2000) has shown the usage of extensions of TOPSIS for group decision making in fuzzy environment. Feng and Wang (2000) used TOPSIS for evaluating the performance of different airlines. Chen et al. (2008) used interval-valued fuzzy TOPSIS method for experimental analysis.

Fig. 1 Triangular fuzzy number



3.1 Fuzzy set theory

Let U be the universe of discourse, U = $\{\mu_1, \mu_2, \mu_3 \ldots \mu_n\}$. According to Zadeh (1965), a fuzzy set Ã of U is a set of ordered pairs $\left\{\left(\mu_1, f_{\tilde{A}}(\mu_1)\right), \left(\mu_2, f_{\tilde{A}}(\mu_2)\right), \ldots \left(\mu_n, f_{\tilde{A}}(\mu_n)\right)\right\}$, where $f_{\tilde{A}}$, $f_{\tilde{A}} : U \rightarrow [0, 1]$, is the membership function of Ã and $f_{\tilde{A}}(\mu_i)$ indicates the grade of membership of μ_i in Ã. Among various membership functions, the triangular fuzzy number is the most prominently applied in engineering applications. According to Dubois and Prade (1980), this fuzzy number is characterized by triangular distribution functions with the linear and symmetric sides, which is parameterized by a triple (m, n, p). In this methodology, t (m, n, p) is denoted as triangular fuzzy number Ã, with $m \leq n \leq p$, where m and p stand for the lower and upper values for the support of Ã respectively and n stands for moderated value. Its membership function can be defined as:

$$f_{\tilde{A}}(\mu) = \left\{ \begin{array}{l} 0, \mu < m, \\ \frac{\mu - m}{m - n}, m \leq \mu \leq n, \\ \frac{p - \mu}{p - n}, n \leq \mu \leq p, \\ 0, \mu > p. \end{array} \right\} \tag{1}$$

The graph of the membership function of the triangular fuzzy number is shown in Fig. 1.

The algebraic operations on triangular numbers (Dubois and Prade 1980; Kaufmann and Gupta 1991) say $\tilde{A}$ and $\tilde{B}$ parameterized by triplet (m_1, n_1, p_1) and (m_2, n_2, p_2) respectively are stated below:

$$\begin{aligned} \tilde{A} + \tilde{B} &\approx (m_1 + m_2, n_1 + n_2, p_1 + p_2) \\ \tilde{A} - \tilde{B} &\approx (m_1 - p_2, n_1 - n_2, p_1 - m_2) \\ \tilde{A}.\tilde{B} &\approx (m_1.m_2, n_1.n_2, p_1.p_2) \\ \tilde{A}/\tilde{B} &\approx (m_1/p_2, n_1/n_2, p_1/m_2) \\ 1/\tilde{A} &\approx (1/p_1, 1/n_1, 1/m_1) \\ \ln(\tilde{A}) &\approx (\ln(m_1), \ln(n_1), \ln(p_1)) \\ \exp(\tilde{A}) &\approx (\exp(m_1), \exp(n_1), \exp(p_1)) \end{aligned} \tag{2}$$

The distance between $\tilde{A}$ and $\tilde{B}$ can be calculated using the vertex method as in the following equation:

$$d(\tilde{\mathrm{A}}, \tilde{\mathrm{B}}) = \sqrt{\frac{1}{3}\left[(m_1 - m_2)^2 + (n_1 - n_2)^2 + (p_1 - p_2)^2\right]} \tag{3}$$

Table 2 Membership function of linguistic scale

Fuzzy number	Linguistic	Scale of fuzzy number
9	Perfect	(8, 9, 10)
8	Absolute	(7, 8, 9)
7	Very good	(6, 7, 8)
6	Fairly good	(5, 6, 7)
5	Good	(4, 5, 6)
4	Preferable	(3, 4, 5)
3	Not bad	(2, 3, 4)
2	Weak advantage	(1, 2, 3)
1	Equal	(1, 1, 1)

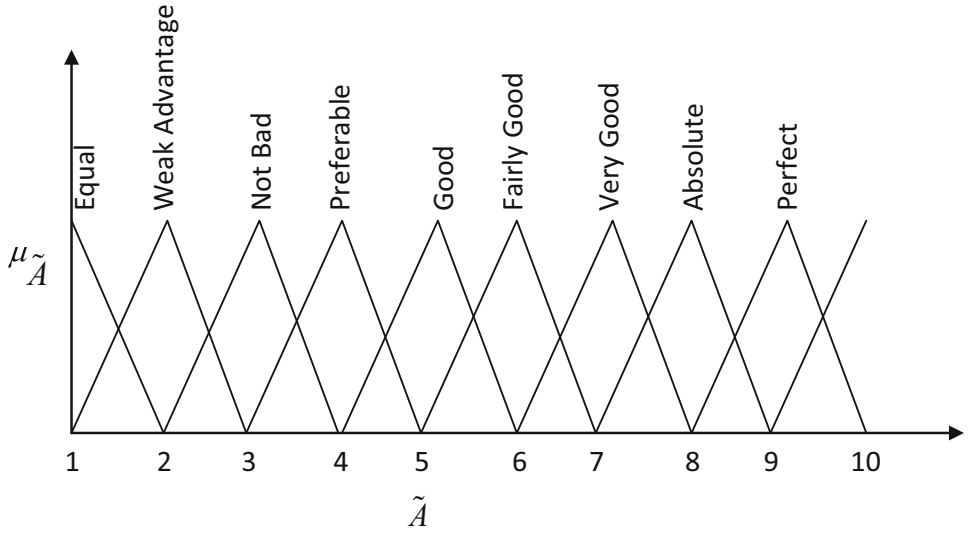


Fig. 2 The fuzzy scale used for pairwise comparison in AHP

3.2 Determination of linguistic variables

Linguistic Variables take values defined in the set of subjective linguistic terms. Linguistic terms are words or sentences in common language with the scale of fuzzy numbers associated with them to quantify their value. In this paper, fuzzy numbers defined by Gumus (2009) are employed along with their respective linguistic variables as shown in Table 2 and graphically represented in Fig. 2.

3.3 Fuzzy AHP

Analytical Hierarchy Process (AHP) is a multi-criteria decision-making tool in which a complex problem is broken down into multiple hierarchy levels representing multiple sub-problems. Each level consists of various attributes and criteria relative to each sub-problem. In this hybrid model, AHP is employed in a fuzzy environment to determine the relative weights of relevant criteria shortlisted for 3PL selection in the cold supply chain.

The process of carrying out Fuzzy AHP process is explained in the following steps.

Step 1 Construct a n × n pairwise comparison matrix of criteria in terms linguistic variables and then substitute the linguistic variables with their corresponding fuzzy scales, as shown in the following matrix Ã.

$$\tilde{A} = \begin{pmatrix} 1 & \tilde{a}_{12} & \cdots & \tilde{a}_{1n} \\ \tilde{a}_{21} & 1 & \cdots & \tilde{a}_{2n} \\ \vdots & \cdots & \ddots & \vdots \\ \tilde{a}_{n1} & \tilde{a}_{n2} & \cdots & 1 \end{pmatrix} = \begin{pmatrix} 1 & \tilde{a}_{12} & \cdots & \tilde{a}_{1n} \\ 1/\tilde{a}_{12} & 1 & \cdots & \tilde{a}_{2n} \\ \vdots & \cdots & \ddots & \vdots \\ 1/\tilde{a}_{1n} & 1/\tilde{a}_{2n} & \cdots & 1 \end{pmatrix} \tag{4}$$

where

$$\tilde{a}_{ij} = \begin{cases} \left(\frac{1}{p_i}, \frac{1}{n_i}, \frac{1}{m_i}\right); & \text{for} \quad \forall i < j \\ (1, 1, 1); & \text{for} \quad \forall i = j \\ (m_i, n_i, p_i); & \text{for} \quad \forall i > j \end{cases}$$

The pairwise comparison is based on the Saaty's research work on AHP (Saaty 1990).

Step 2 Geometric mean of each row of $\tilde{A}$ now using the geometric mean technique and then fuzzy relative weight matrix is deduced by Hsieh et al. (2004).

$$\tilde{r}_i = \left(\tilde{a}_{i1} \otimes \cdots \otimes \tilde{a}_{ij} \otimes \cdots \otimes \tilde{a}_{in}\right)^{1/n} \quad \forall i = 1, 2, 3 \ldots n \tag{5}$$

$$\tilde{w}_i = \tilde{r}_i \otimes (\tilde{r}_1 \oplus \cdots \oplus \tilde{r}_i \oplus \cdots \oplus \tilde{r}_n)^{-1} \quad \forall i = 1, 2, 3 \ldots n \tag{6}$$

where $\tilde{a}_{in}$ is a fuzzy comparison value of the criterion i to criterion n, thus, $\tilde{r}_i$ is geometric mean of fuzzy comparison value of the criterion i to each criterion, $\tilde{w}_i$ is the fuzzy weight of the ith criterion, can be indicated by TFN.

Thus, we get a n x 1 relative weight matrix w. Each element of this matrix consists of a triangular fuzzy number, $\tilde{w}_i = (mw_i, nw_i, pw_i)$.

3.4 Fuzzy TOPSIS

TOPSIS evaluates alternatives about each criterion on the basis of their distance from the positive ideal solution (most favorable value about that criteria) and negative ideal solution (least favorable value about that criteria). An index is defined called similarity to the positive ideal solution and remoteness to the negative ideal solution about a criterion. The shorter the distance to the positive ideal solution about a criterion and longer the distance to the negative ideal solution about that criterion, more strong is the alternative about that criterion. Considering the difficulty of the decision maker to assign precise performance rating for an alternative about a particular criterion, fuzzy numbers are used instead of precise numbers to extend TOPSIS to fuzzy decision-making environment. Fuzzy TOPSIS is further extended to group decision making by amalgamating the evaluations of multiple decision makers (Kumar and Singh 2012). The process of carrying out fuzzy TOPSIS is explained in the following steps.

Step 1 Devise a fuzzy performance matrix $\tilde{D}$ consisting of the evaluations of each alternative about each criterion under consideration. Appropriate linguistic variables must be chosen for this purpose. The linguistic variables are converted into the quantitative scales as shown in Table 3 and graphically represented by Fig. 3.

$$\tilde{D} = \begin{array}{c} \begin{matrix} C_1 & C_2 & C_j & \ldots & C_m \end{matrix} \\ \begin{bmatrix} \tilde{x}_{11} & \ldots & \tilde{x}_{1j} & \ldots & \tilde{x}_{1m} \\ \ldots & \ldots & \ldots & \ldots & \ldots \\ \tilde{x}_{i1} & \ldots & \tilde{x}_{ij} & \ldots & \tilde{x}_{jm} \\ \ldots & \ldots & \ldots & \ldots & \ldots \\ \tilde{x}_{n1} & \ldots & \tilde{x}_{nj} & \ldots & \tilde{x}_{nm} \end{bmatrix} \end{array} \tag{7}$$

Table 3 Linguistic scales for rating of each company

Linguistic variable	Corresponding triangle fuzzy number
Very poor ($\tilde{1}$)	(0, 1, 3)
Poor ($\tilde{2}$)	(1, 3, 5)
Fair ($\tilde{3}$)	(3, 5, 7)
Good ($\tilde{4}$)	(5, 7, 9)
Very good ($\tilde{5}$)	(7, 9, 10)

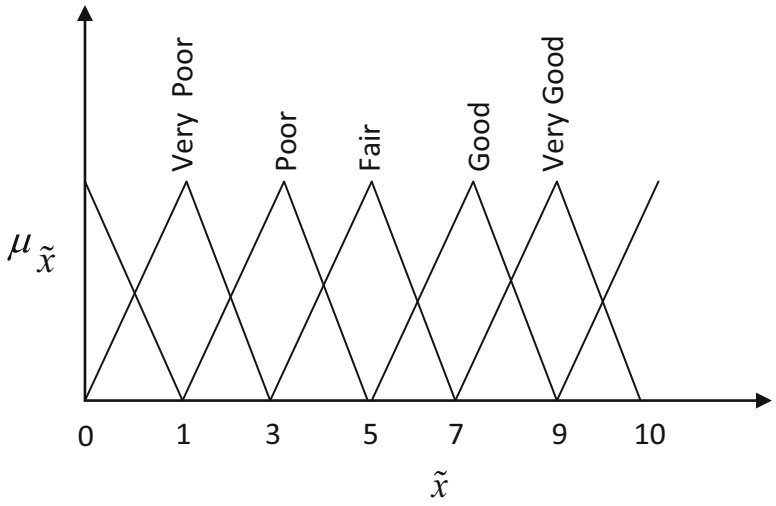


Fig. 3 The fuzzy scale used for rating the 3PLs with respect to the criteria

$$\tilde{x}_{ij} = \frac{1}{K}\left(\tilde{x}_{ij}^{1} \oplus \ldots \oplus \tilde{x}_{ij}^{k} \oplus \ldots \oplus \tilde{x}_{ij}^{K}\right) \tag{8}$$

where $i = 1, 2, \ldots, m$; $j = 1, 2, \ldots, n$ and $\tilde{x}_{ij}$ is the performance rating of alternative A_i with respect to criterion C_j evaluated by kth expert. $\tilde{x}_{ij}$ is a triangular fuzzy number of the form $(m_{ij}^{k}, n_{ij}^{k}, p_{ij}^{k})$.

Step 2 Normalize the fuzzy decision matrix to get matrix $\tilde{R}$ where

$$\tilde{R} = [\tilde{r}_{ij}]_{m\times n} \quad i = 1, 2, \ldots, m; \quad j = 1, 2, \ldots n \tag{9}$$

$$\text{where } \tilde{r}_{ij} = \begin{cases} \text{for benefit criteria} \\ \left(\frac{m_{ij}}{p_j^+}, \frac{n_{ij}}{p_j^+}, \frac{p_{ij}}{p_j^+}\right) \text{ where } p_j^+ = \max\limits_i p_{ij} \\ \text{for cost criteria} \\ \left(\frac{m_j^-}{p_{ij}}, \frac{m_j^-}{n_{ij}}, \frac{m_j^-}{m_{ij}}\right) \text{where} m_j^- = \min\limits_i m_{ij} \end{cases} \tag{10}$$

Step 3 Weighted fuzzy normalized decision matrix $\tilde{V}$ is calculated as shown:

$$\tilde{V} = [\tilde{v}_{ij}]_{m\times n} i = 1, 2, \ldots, m; \quad j = 1, 2, \ldots, n \tag{11}$$

$$\tilde{v}_{ij} = \tilde{r}_{ij} \otimes \tilde{w}_j \tag{12}$$

Step 4 Determine the fuzzy positive ideal solution (FPIS) and fuzzy negative ideal solution (FNIS): We know that elements in the weighted fuzzy normalized matrix $\tilde{V}$ are triangular

fuzzy numbers and their ranges belong to the interval [0, 1]. Then, we can define the FPIS as $\tilde{v}_j^* = (1, 1, 1)$ and FNIS as $\tilde{v}_j^- = (0, 0, 0)$; $j = 1, 2, \ldots, n$.

Step 5 Calculate the distance of each alternative from positive ideal solution (FPIS) and from negative ideal solution (FNIS) about each criterion using Eq. (3). Subsequently, we get two $m \times n$ matrices. Now, employing the area compensation method in each matrix we get two $m \times 1$ matrix.

$$d_i^+ = \sum_{j=1}^{n} d(\tilde{v}_{ij}, \tilde{v}_j^*), i = 1, 2, \ldots, m; \quad j = 1, 2, \ldots, n \tag{13}$$

$$d_i^- = \sum_{j=1}^{n} d(\tilde{v}_{ij}, \tilde{v}_j^-), i = 1, 2, \ldots, m; \quad j = 1, 2, \ldots n \tag{14}$$

Step 6 Calculate closeness coefficient (CC_i) which is defined as closeness to the ideal solution by the following formula.

$$CC_i = \frac{d_i^-}{d_i^+ + d_i^-}, \quad i = 1, 2, \ldots m \tag{15}$$

Thus, we will eventually get a $m \times 1$ matrix with final performance scores of each alternative about all the criteria considered. Greater the score of the alternative, better the alternative.

4 Case illustration

To illustrate Fuzzy AHP-Fuzzy TOPSIS hybrid approach suggested in this paper, a case study from food sector has been taken.

4.1 Profile of case company

Firm XYZ Ltd (Name Changed) is a health food manufacturing company situated on the outskirts of National Capital Region (NCR) of New Delhi, India. The company runs three product lines-two for health food powders (used as nutritional additives to milk) and one for ghee (Milk Fat). These products are packaged in various pack sizes of polythene bags, corrugated paper boxes, cartons and tin containers. The company has a total capital outlay of approximately INR 50 million and commands around 10–12% of the health food market in India.

Milk is the major raw material for products manufactured by the company. Milk suppliers include 8 contractors, 200 progressive dairy farmers, 12 distant direct suppliers and various village collection centers (VCCs), collecting milk from around 25,000 milk producers. All of these are spread across various small towns and villages within 50 km distance from the Plant. Milk is a perishable food product with a limited shelf life. Its collection, inspection, and transportation is a cumbersome process involving a complex delivery network. The company is also particular about the quality of ingredients goings into its final products and banks on the reliability and consistency in raw material quality and delivery. Moreover, the raw material transportation cost is borne by the company. Hence, in order to ensure timely and efficient procurement, inspection and transportation of milk and to effectively manage this complex procurement network, Company XYZ Ltd has decided to outsource its milk procurement activities to a Third Party Logistics (3PL) Service provider.

Table 4 Pairwise comparison of criteria

	C1	C2	C3	C4	C5	C6	C7	C8	C9	C10
C1	(1, 1, 1)	(1/6, 1/5, 1/4)	(1/3, 1/2, 1)	(1, 2, 3)	(4, 5, 6)	(1/5, 1/4, 1/3)	(3, 4, 5)	(1/4, 1/3, 1/2)	(2, 3, 4)	(3, 4, 5)
C2	(4, 5, 6)	(1, 1, 1)	(2, 3, 4)	(4, 5, 6)	(7, 8, 9)	(1, 2, 3)	(5, 6, 7)	(1, 2, 3)	(6, 7, 8)	(7, 8, 9)
C3	(1, 2, 3)	(1/4, 1/3, 1/2)	(1, 1, 1)	(2, 3, 4)	(5, 6, 7)	(1/3, 1/2, 1)	(3, 4, 5)	(1/5, 1/4, 1/3)	(4, 5, 6)	(5, 6, 7)
C4	(1/3, 1/2, 1)	(1/6, 1/5, 1/4)	(1/4, 1/3, 1/2)	(1, 1, 1)	(4, 5, 6)	(1/5, 1/4, 1/3)	(1, 2, 3)	(1/7, 1/6, 1/5)	(2, 3, 4)	(3, 4, 5)
C5	(1/6, 1/5, 1/4)	(1/9, 1/8, 1/7)	(1/7, 1/6, 1/5)	(1/6, 1/5, 1/4)	(1, 1, 1)	(1/9, 1/8, 1/7)	(1/5, 1/4, 1/3)	(1/9, 1/8, 1/7)	(1/3, 1/2, 1)	(1/3, 1/2, 1)
C6	(3, 4, 5)	(1/3, 1/2, 1)	(1, 2, 3)	(3, 4, 5)	(7, 8, 9)	(1, 1, 1)	(4, 5, 6)	(1/3, 1/2, 1)	(5, 6, 7)	(6, 7, 8)
C7	(1/5, 1/4, 1/3)	(1/7, 1/6, 1/5)	(1/5, 1/4, 1/3)	(1/3, 1/2, 1)	(3, 4, 5)	(1/6, 1/5, 1/4)	(1, 1, 1)	(1/6, 1/5, 1/4)	(1, 2, 3)	(2, 3, 4)
C8	(2, 3, 4)	(1/3, 1/2, 1)	(3, 4, 5)	(5, 6, 7)	(7, 8, 9)	(1, 2, 3)	(4, 5, 6)	(1, 1, 1)	(5, 6, 7)	(6, 7, 8)
C9	(1/4, 1/3, 1/2)	(1/8, 1/7, 1/6)	(1/6, 1/5, 1/4)	(1/4, 1/3, 1/2)	(1, 2, 3)	(1/7, 1/6, 1/5)	(1/3, 1/2, 1)	(5, 6, 7)	(1, 1, 1)	(1, 2, 3)
C10	(1/5, 1/4, 1/3)	(1/9, 1/8, 1/7)	(1/7, 1/6, 1/5)	(1/5, 1/4, 1/3)	(1, 2, 3)	(1/8, 1/7, 1/6)	(1/4, 1/3, 1/2)	(1/8, 1/7, 1/6)	(1/3, 1/2, 1)	(1, 1, 1)

Table 5 Rating of 3PLs with respect to the criteria by four decision-makers

		C1	C2	C3	C4	C5	C6	C7	C8	C9	C10
A1	DM1	(5, 7, 9)	(3, 5, 7)	(3, 5, 7)	(5, 7, 9)	(1, 3, 5)	(5, 7, 9)	(5, 7, 9)	(3, 5, 7)	(1,3,5)	(1,3,5)
	DM2	(1, 3, 5)	(5, 7, 9)	(1, 3, 5)	(3, 5, 7)	(5, 7, 9)	(3, 5, 7)	(5, 7, 9)	(3, 5, 7)	(3, 5, 7)	(5, 7, 9)
	DM3	(7, 9, 10)	(3, 5, 7)	(3, 5, 7)	(1, 3, 5)	(7, 9, 10)	(5, 7, 9)	(1, 3, 5)	(5, 7, 9)	(3, 5, 7)	(3, 5, 7)
	DM4	(1, 3, 5)	(3, 5, 7)	(5, 7, 9)	(3, 5, 7)	(7, 9, 10)	(3, 5, 7)	(1, 3, 5)	(3, 5, 7)	(5, 7, 9)	(3, 5, 7)
A2	DM1	(3, 5, 7)	(5, 7, 9)	(1, 3, 5)	(3, 5, 7)	(5, 7, 9)	(3, 5, 7)	(3, 5, 7)	(5, 7, 9)	(3, 5, 7)	(5, 7, 9)
	DM2	(3, 5, 7)	(3, 5, 7)	(1, 3, 5)	(1, 3, 5)	(1, 3, 5)	(5, 7, 9)	(5, 7, 9)	(3, 5, 7)	(3, 5, 7)	(3, 5, 7)
	DM3	(5, 7, 9)	(5, 7, 9)	(7, 9, 10)	(3, 5, 7)	(3, 5, 7)	(3, 5, 7)	(3, 5, 7)	(7, 9, 10)	(1, 3, 5)	(5, 7, 9)
	DM4	(3, 5, 7)	(1, 3, 5)	(7, 9, 10)	(5, 7, 9)	(5, 7, 9)	(3, 5, 7)	(5, 7, 9)	(1, 3, 5)	(3, 5, 7)	(5, 7, 9)
A3	DM1	(3, 5, 7)	(3, 5, 7)	(1, 3, 5)	(5, 7, 9)	(3, 5, 7)	(1, 3, 5)	(3, 5, 7)	(5, 7, 9)	(5, 7, 9)	(3, 5, 7)
	DM2	(5, 7, 9)	(1, 3, 5)	(5, 7, 9)	(3, 5, 7)	(1, 3, 5)	(5, 7, 9)	(3, 5, 7)	(5, 7, 9)	(1, 3, 5)	(5, 7, 9)
	DM3	(3, 5, 7)	(1, 3, 5)	(5, 7, 9)	(3, 5, 7)	(5, 7, 9)	(3, 5, 7)	(5, 7, 9)	(7, 9, 10)	(3, 5, 7)	(7, 9, 10)
	DM4	(5, 7, 9)	(5, 7, 9)	(3, 5, 7)	(1, 3, 5)	(3, 5, 7)	(5, 7, 9)	(1, 3, 5)	(5, 7, 9)	(7, 9, 10)	(3, 5, 7)

Table 6 Fuzzy decision matrix

	C1	C2	C3	C4	C5	C6	C7	C8	C9	C10
A1	(3.5, 5.5, 7.25)	(3.5, 5.5, 7.5)	(3, 5, 7)	(3, 5, 7)	(5, 7, 8.5)	(4, 6, 8)	(3, 5, 7)	(3.5, 6, 7.5)	(3, 5, 7)	(3, 5, 7)
A2	(3.5, 5.5, 7.5)	(3.5, 5.5, 7.5)	(4, 6, 7.5)	(3, 5, 7)	(3.5, 5.5, 7.5)	(3.5, 5.5, 7.5)	(3.5, 6, 8)	(4, 6, 8)	(2.5, 4.5, 6.5)	(4.5, 6.5, 8.5)
A3	(4, 6, 8)	(2.5, 4.5, 6.5)	(3.5, 4.5, 7.5)	(3, 5, 7)	(4, 5, 7)	(3.5, 4.5, 7.5)	(4, 5, 7)	(4.5, 7.5, 9.25)	(4, 6, 7.75)	(4.5, 6.5, 8.25)

Table 7 Fuzzy normalized matrix

	C1	C2	C3	C4	C5
A1	(0.437, 0.687, 0.906)	(0.466, 0.733, 1)	(0.4, 0.666, 0.9333)	(0.428, 0.714, 1)	(0.588, 0.823, 1)
A2	(0.437, 0.687, 0.937)	(0.466, 0.733, 1)	(0.533, 0.8, 1)	(0.428, 0.714, 1)	(0.411, 0.647, 0.882)
A3	(0.5, 0.75, 1)	(0.333, 0.6, 0.866)	(0.466, 0.6, 1)	(0.428, 0.714, 1)	(0.47, 0.588, 0.823)
	C6	C7	C8	C9	C10
A1	(0.5, 0.75, 1)	(0.375, 0.625, 0.875)	(0.378, 0.648, 0.81)	(0.387, 0.645, 0.903)	(0.352, 0.588, 0.823)
A2	(0.437, 0.687, 0.937)	(0.437, 0.75, 1)	(0.432, 0.648, 0.864)	(0.322, 0.58, 0.838)	(0.529, 0.765, 1)
A3	(0.437, 0.562, 0.937)	(0.5, 0.625, 0.875)	(0.486, 0.81, 1)	(0.516, 0.774, 1)	(0.545, 0.787, 0.97)

Table 8 Weighted fuzzy normalized matrix

	C1	C2	C3	C4	C5
A1	(0.019, 0.053, 0.125)	(0.07, 0.189, 0.418)	(0.026, 0.074, 0.182)	(0.014, 0.04, 0.101)	(0.006, 0.013, 0.03)
A2	(0.019, 0.053, 0.13)	(0.07, 0.189, 0.418)	(0.034, 0.089, 0.196)	(0.014, 0.04, 0.101)	(0.004, 0.01, 0.026)
A3	(0.022, 0.058, 0.139)	(0.05, 0.155, 0.361)	(0.466, 0.0672, 0.196)	(0.014, 0.04, 0.101)	(0.005, 0.009, 0.024)
	C6	C7	C8	C9	C10
A1	(0.05, 0.129, 0.302)	(0.009, 0.025, 0.063)	(0.048, 0.138, 0.29)	(0.006, 0.018, 0.046)	(0.004, 0.012, 0.031)
A2	(0.044, 0.118, 0.282)	(0.01, 0.03, 0.073)	(0.054, 0.138, 0.31)	(0.005, 0.448, 0.043)	(0.006, 0.016, 0.038)
A3	(0.044, 0.096, 0.282)	(0.012, 0.025, 0.063)	(0.061, 0.173, 0.359)	(0.008, 0.022, 0.052)	(0.007, 0.016, 0.036)

4.2 Data collection and analysis of results

The management of the company has set-up a team of four members to select a compatible and reliable 3PL company with whom the company can enjoy a long-term business partnership. These experts were working in the area of cold chains in the food industry for past 10 years. Based on the literature, database available and the experience of a team of experts, ten criteria are shortlisted for the selection of a compatible 3PL (Table 1). The team of experts then determined the relative importance of the shortlisted criteria using concepts of linguistic variables and Fuzzy AHP as discussed in Sects. 3.1 and 3.2. These 3PLs (A1, A2, A3) were rated using linguistic variables as depicted in Table 3. The pairwise comparison matrix for all selected criteria as devised by the four experts based on Eq. 4 is as given in Table 4.

By using Fuzzy AHP Eqs. (5) and (6), fuzzy relative weight matrix for all criteria are obtained as shown below:

$$\tilde{w} = \begin{pmatrix} (0.045, 0.078, 0.139) \\ (0.151, 0.259, 0.418) \\ (0.065, 0.112, 0.196) \\ (0.033, 0.057, 0.101) \\ (0.011, 0.017, 0.030) \\ (0.101, 0.172, 0.302) \\ (0.024, 0.041, 0.073) \\ (0.127, 0.214, 0.359) \\ (0.016, 0.029, 0.052) \\ (0.013, 0.021, 0.030) \end{pmatrix}$$

After opening the tenders for logistics companies, it was found that three 3PL companies, specializing in cold chain logistics have applied before the deadline. These three companies were named as A_1, $A_{2,}$ and A_3. Then each individual member of the team evaluated each of the 3PL companies on the basis of the ten shortlisted criteria. Four experts were selected to evaluate 3PL firms based on their expertise. All experts were having more than ten years experience in the area of cold supply chains. Criteria were selected based on literature review and as per the requirements of company XYZ Ltd in order to select a compatible 3PL and to ensure a long-term healthy relationship between the two firms.

Using Eqs. (7) and (8) in Sect. 3, we get a fuzzy performance matrix as shown in Table 5 for all the Decision Makers (DMs) j = 1, 2, 3, 4.

An average rating of all the 3PLs are computed giving equal importance to all the decion makers fuzzy decision matrix is prepared which is shown in Table 6.

The elements of fuzzy decision matrix are normalized to bring them on the same quantitative scale from 0 to 1 using the Eqs. (9) and (10) and a fuzzy normalized matrix is prepared as shown in Table 7.

In the Table 7, the normalized elements are multiplied by the corresponding weights of criteria and a weighted matrix is prepared using Eqs. (11) and (12). The weighted fuzzy normalized matrix is shown in Table 8.

Using Eqs. (13) and (14) respectively, the distances of the alternatives, i.e. 3PLs from the positive ideal solution (1, 1, 1) and negative ideal solution (0, 0, 0) are calculated as given below:

$$d_i^+ = \begin{pmatrix} 9.18648 \\ 9.17026 \\ 9.16884 \end{pmatrix}$$

$$d_i^- = \begin{pmatrix} 1.01128 \\ 1.02559 \\ 1.02902 \end{pmatrix}$$

Now, closeness coefficient based on closeness to ideal solution is calculated using Eq. (15) of Sect. 3 as shown below:

$$CC_i = \begin{pmatrix} 0.099166 \\ 0.100589 \\ 0.100906 \end{pmatrix}$$

In TOPSIS analysis, CC_i is defined as the closeness of the alternative to the positive ideal solution. Thus, greater the value of CC_i for an alternative better is its rank. In the present case, based on the above analysis, A_3 has got the highest CC of 0.100906 and it outperforms the other two alternatives in terms of selected criteria. As a result, A_3 is the major candidate to win the contract for milk procurement and logistics operations of company XYZ Ltd. A_3 is followed by A_2 and A_1. Reason behind top ranking of A3 may be, its strength on automation of processes, innovation in cold chain processes, IT applications for tracking and tracing, flexibility of processes. As market requirements are changing very fast in terms of lead time reduction, transparency, Govt. policies such as GST implementation, demonetisation, digital India and make in India, logistic providers need to be proactive in terms of these changes.

Conspicuous from the CC_i values of all the three 3PL firms in contention, the respective scores are very close to each other indicating the sensitive nature of cold chain logistics providers. It also reflects that 3PL market is highly competitive, therefore each company operates with very close tolerances in their services. This is primarily done in order to provide high-quality services to the clients at the lowest possible cost, thus giving a competitive edge over its competitors. Therefore, under such a highly competitive environment, Fuzzy AHP-Fuzzy TOPSIS proves to be a credible and reliable methodology to find the best 3PL.

5 Conclusion

Selection of 3PL is based on multiple criteria. In this study ten criteria, i.e. transportation and warehousing cost, logistic infrastructure and warehousing facilities, customer service and reliability, network management, material handling capabilities, quality control and inspection, automation of processes, innovation and effectiveness of cold chain processes, IT applications for tracking and tracing and flexibility of processes are considered for selection of third-party logistics service providers (3PL) for a cold chain. In cold chain, 3PLs have to work under highly uncertain and fuzzy condition. Therefore a hybrid approach of Fuzzy AHP and Fuzzy TOPSIS has been illustrated with the help of a case study of the Indian food industry. Fuzzy AHP is used to determine the relative weights of the different criteria shortlisted for 3PL selection in the cold chain. After determining the weights of the selected criteria, fuzzy TOPSIS is used to rank the available alternatives for selecting the best 3PL under fuzzy decision-making environment. This methodology incorporates the fuzziness associated with real life decisions, thus increasing the reliability and credibility of the process.

Managerial implications, limitations and future scope In this study, logistic provider A_3 is found most suitable 3 PL. On the basis of analysis done in the study, it is observed that the major reasons behind the top ranking of A_3 is its emphasis on automation of processes, innovation in cold chain processes, IT applications for tracking and tracing and flexibility of processes. Therefore, the findings imply that 3PL should focus on continuous process

improvement in cold chain by application of advanced technologies and other innovative means to meet dynamic and complex market requirements. As criteria and their relative ranking may vary from sector to sector, findings may not be generalized. For generalizing the findings, empirical study may be carried out as a future scope. Although the end results may differ, but the same methodology can be also applied in other sectors such as FMCG, automotive, service sectors such as banking and hotel industry for 3PL selection. In future, criteria may be selected related to sustainability measures such as use of renewable energy sources, use of recyclable and reusable packaging material and changing service quality measures. To further validate the robustness of the framework proposed, sensitivity analysis may be also carried out.

Acknowledgements Authors would like to express their sincere thanks to the Chief Editor of the journal and unanimous reviewers for valuable comments and suggestions to enhance quality and content of the paper. Authors also acknowledge the support of Mr. Ankit Bansal and Mr. Sidhant Issar, UG students in doing this research work.

References

Agrawal, S., Singh, R. K., & Murtaza, Q. (2016). Outsourcing decisions in reverse logistics: Sustainable balanced scorecard and graph theoretic approach. *Resources, Conservation and Recycling*, *108*, 41–53.

Aguezzoul, A. (2008). A preliminary analysis on third-party logistics selection. In *7th International Meeting for Research in Logistics AVIGNON* (pp. 24–26).

Akdemir, S. (2008). Designing of cold stores and choosing of cooling system elements. *Journal of Applied Science*, *8*(5), 788–794.

Bhatnagar, R., Sohal, A. S., & Millen, R. (1999). Third party logistics services: A Singapore perspective. *International Journal of Physical Distribution and Logistics Management*, *29*(9), 569–587.

Bogataj, M., Bogataj, L., & Vodopivec, R. (2005). Stability of perishable goods in cold logistics chains. *International Journal of Production Economics*, *93–94*(8), 345–35.

Bolumole, Y. (2001). The supply chain role of third-party logistics providers. *International Journal of Logistics Management*, *12*(2), 87–102.

Bowersox, D. J., & Closs, D. J. (1996). *Logistical management: The integrated supply chain process*. New York: McGraw-Hill Companies.

Brandenburg, M., & Rebs, T. (2015). Sustainable supply chain management: A modeling perspective. *Annals of Operations Research*, *229*(1), 213–252.

Büyüközkan, G., Kahraman, & Ruan, D. (2004). A fuzzy multi-criteria decision approach for software development strategy selection. *International Journal of General Systems*, *33*(2–3), 259–280.

Buyukozkan, G., Ruan, D., & Feyzioglu, O. (2007). Evaluating e-Learning web site quality in a fuzzy environment. *International Journal of Intelligent Systems*, *22*(5), 567–586.

Cakir, O., & Canbolat, M. S. (2008). A web-based decision support system for multi-criteria inventory classification using fuzzy AHP methodology. *Expert Systems with Applications*, *35*(3), 1367–1378.

Chan, F. T. S., & Chan, H. K. (2004). Development of the supplier selection model—a case study in the advanced technology industry. *Journal of Engineering Manufacture*, *218*, 1807–1823.

Chen, C.-T. (2000). Extensions of the TOPSIS for group decision-making under fuzzy environment. *Fuzzy Sets & Systems*, *114*(1), 1–9.

Chen, M.-F., Tzeng, G.-H., & Ding, C.-G. (2008). Combining fuzzy AHP with MDS in identifying the preference similarity of alternatives. *Applied Soft Computing*, *8*(1), 110–117.

Cho, J. J.-K., Ozment, J., & Sink, H. (2008). Logistics capability, logistics outsourcing and firm performance in an E-commerce market. *International Journal of Physical Distribution & Logistics Management*, *38*(5), 336–359.

Chow, H. K. H., Choy, K. L., Lee, W. B., & Chan, F. T. S. (2005). Design of a knowledge based logistics strategy system. *Expert Systems with Applications*, *29*(2), 272–290.

Choy, K. L., Chow, H. K. H., Tan, K. H., Chan, C. K., Mok, E. C. M., & Wang, Q. (2008). Leveraging the supply chain flexibility of third party logistics-hybrid knowledge based system approach. *Expert Systems with Applications*, *35*(4), 1998–2016.

Choy, K. L., Lee, C. L., So, S. C. K., Lau, H., Kwonk, S. K., & Leung, D. (2007). Managing uncertainty in logistics service supply chain. *International Journal of Risk Assessment and Management*, *7*(1), 19–43.

Christopher, M. (2011). *Logistic & supply chain management* (4th ed.). Cambridge: Pearson Education Limited.
Chu, T. C. (2002). Facility location selection using fuzzy TOPSIS under group decisions. *International Journal of Uncertainty, Fuzziness & Knowledge-Based Systems*, *10*(6), 687–701.
Coulomb, D. (2008). Refrigeration and cold chain serving the global food industry and creating a better future: Two key IIR challenges for improved health and environment. *Trend in Food Science & Technology*, *19*(8), 413–417.
Dagdeviren, M., & Yuksel, I. (2008). Developing a fuzzy analytic hierarchy process (AHP) model for behavior-based safety management. *Information Sciences*, *178*(6), 1717–1733.
Dapiran, P., Lieb, R., Millen, R., & Sohal, A. (1996). Third party logistics services usage by large Australian firms. *International Journal of Physical Distribution and Logistics Management*, *26*(10), 36–45.
Delfmann, W., Albers, S., & Gehring, M. (2002). The impact of electronic commerce on logistics service providers. *International Journal of Physical Distribution & Logistics Management*, *32*(3), 203–222.
Diabat, A., Khreishah, A., Kannan, A., Panikar, V., & Gunasekaran, A. (2013). Benchmarking the interactions among barriers in third-party logistics implementation. *Benchmarking: An International Journal*, *20*(6), 805–824.
Dubois, D., & Prade, H. (1980). *Fuzzy sets and systems: Theory and applications*. New York: Academic Press.
Efendigil, T., Önüt, S., & Kongar, E. (2008). A holistic approach for selecting a third-party reverse logistics provider in the presence of vagueness. *Computers & Industrial Engineering*, *54*(2), 269–287.
Feng, C. M., & Wang, R. T. (2000). Performance evaluation for airlines including the consideration of financial ratios. *Journal of Air Transport Management*, *6*, 133–142.
Flint, D. J., Larsson, E., Gammelgaard, B., & Mentzer, J. T. (2005). Logistics innovation: A customer value-oriented social process. *Journal of Business Logistics*, *26*(1), 113–147.
Fu, P., & Yin, H. (2012). Logistics enterprise evaluation model based on fuzzy clustering analysis. *Physics Procedia*, *24*(C), 1583–1587.
Göl, H., & Çatay, B. (2007). Third party logistics provider selection: Insights from Turkish automobile company. *Supply Chain Management: An International Journal*, *12*(6), 379–384.
Govindan, K., & Murugesan, P. (2011). Selection of third-party reverse logistics provider using fuzzy extent analysis. *Benchmarking: An International Journal*, *18*(1), 149–167.
Gumus, A.-T. (2009). Evaluation of hazardous waste transportation firms by using a two step fuzzy-AHP and TOPSIS methodology. *Expert Systems with Applications*, *36*(2), 4067–4074.
Gunasekaran, A., & Ngai, E. W. T. (2003). The successful management of a small logistics company. *International Journal of Physical Distribution & Logistics Management*, *33*(9), 825–842.
Gunasekaran, A., & Ngai, E. W. T. (2004). Information systems in supply chain integration and management. *European Journal of Operational Research*, *159*(2), 269–295.
Guo, L., Ma, Y., Sun, D., & Wang, P. (2007). Effects of controlled freezing-point storage at 0°C on quality of green bean as compared with cold and room-temperature storages. *Journal of Food Engineering*, *86*(1), 25–29.
Gupta, R., Sachdeva, A., & Bhardwaj, A., (2010). Selection of 3PL service provider using integrated fuzzy delphi and fuzzy TOPSIS. In *Proceedings World Congress on Engineering and Computer Science*, 20–22 October, San Francisco.
Hamprecht, F., Corsten, D., Noll, M., & Meier, E. (2005). Controlling the sustainability of food supply chains. *Supply Chain Management: An International Journal*, *10*(1), 7–10.
Ho, W., He, T., Lee, C. K. M., & Emrouznejad, A. (2012). Strategic logistic outsourcing: An integrated QFD and fuzzy AHP approach. *Expert Systems with Applications*, *39*(12), 10841–10850.
Hsieh, T.-Y., Lu, S.-T., & Tzeng, G.-H. (2004). Fuzzy MCDM approach for planning and design tenders selection in public office buildings. *International Journal of Project Management*, *22*(7), 573–584.
Işiklar, G., Alptekin, E., & Büyüközkan, G. (2007). Application of a hybrid intelligent decision support model in logistic outsourcing. *Computer and Operations Research*, *34*(12), 3701–3714.
James, S. J., & James, C. (2010). The food cold-chain and climate change. *Food Research International*, *43*(7), 1944–1956.
Jharkharia, S., & Shankar, R. (2007). Selection of logistics service provider: An analytic network process (ANP) approach. *Omega*, *35*(3), 2744–2789.
Jol, S., Kassianenko, A., Wszol, K., & Oggel, J. (2007). The cold chain, one link in Canada's food safety initiatives. *Food Control*, *18*(6), 713–715.
Kaufmann, A., & Gupta, M. M. (1991). *Introduction to fuzzy arithmetic: Theory and applications*. Van Nostrand Reinhold Co.
Kim, G., Park, C. S., & Yoon, K. P. (1997). Identifying investment opportunities for advanced manufacturing systems with comparative-integrated performance measurement. *International Journal of Production Economics*, *50*(1), 23–33.

Kumar, M., Vrat, P., & Shankar, R. (2006). A multi objective 3PL allocation problem for fish distribution. *International Journal of Physical Distribution and Logistics Management*, *36*(9), 702–715.
Kumar, P., & Singh, R. K. (2012). A fuzzy AHP and TOPSIS methodology to evaluate global 3PL. *Journal of Modelling in Management*, *7*(3), 287–303.
Kumar, R., Reintz, H. W., Simunovic, J., Sandeep, K. P., & Franzon, P. D. (2009). Overview of RFID technology and its applications in the food industry. *Journal of Food Science*, *74*(8), 101–106.
Kuo, J. C., & Chen, M. C. (2010). Developing an advanced multi-temperature joint distribution system for the food cold chain. *Food Control*, *21*(4), 559–566.
Large, R. O., Kramer, N., & Hartmann, R. K. (2011). Customer-specific adaptation by providers and their perception of 3PL-relationship success. *International Journal of Physical Distribution & Logistics Management*, *41*(9), 822–838.
Leahy, S. E., Murphy, P. R., & Poist, R. F. (1995). Determinants of successful logistical relationships: A third party provider perspective. *Transportation Journal*, *35*(2), 5–13.
Li, X., & Chandra, C. (2007). Efficient knowledge integration to support a complex supply network management. *International Journal of Manufacture Technology Management*, *10*(1), 1–18.
Manoj, U. V., Gupta, J. N. D., Gupta, S. K., & Sriskandarajah, C. (2008). Supply chain scheduling: Just-in-time environment. *Annals of Operations Research*, *161*(1), 53–86.
Manzini, R., & Accorsi, R. (2012). The new conceptual framework for food supply chain assessment. *Journal of Food Engineering*, *115*, 251–263.
McGinnis, M., Kochunny, C., & Ackerman, K. (1995). Third party logistics choice. *International Journal of Logistics Management*, *6*(2), 93–102.
Melnyk, A. S., Davis, E. W., Spekman, R. E., & Sandor, J. (2010). Outcome-driven supply chains. *MIT Sloan Management Review*, *51*(2), 33–38.
Menon, M., McGinnis, M., & Ackerman, K. (1998). Selection criteria for providers of third-party logistics services: An exploratory study. *Journal of Business Logistics*, *19*(1), 121–137.
Miller, T., Peters, E., Gupta, V., & Bode, O. (2013). A logistics deployment decision support system at Pfizer. *Annals of Operations Research*, *203*(1), 81–99.
Min, S., Roath, A. S., Daugherty, P. J., Genchev, S. E., Haozhe, C., Arndt, A. D., et al. (2005). Supply chain collaboration: What's happening? *The International Journal of Logistics Management*, *16*(2), 237–256.
Moberg, C. R., & Speh, T. W. (2004). Third-party warehousing selection: A comparison of national and regional firms. *American Journal of Business*, *19*(2), 71–76.
Montanari, R. (2008). Cold chain tracking: A managerial perspective. *Trends in Food Science & Technology*, *19*, 425–431.
Ovca, A., & Jevšnik, M. (2008). Maintaining a cold chain from purchase to the home and at home: Consumer opinions. *Food Control*, *20*(2), 167–172.
Pan, N.-F. (2008). Fuzzy AHP approach for selecting the suitable bridge construction method. *Automation in Construction*, *17*(8), 958–965.
Perçin, S. (2009). Evaluation of third-party logistics (3PL) providers by using a two-phase AHP and TOPSIS methodology. *Benchmarking: An International Journal*, *16*(5), 588–604.
Perego, A., Perotti, S., & Mangiaracina, R. (2011). ICT for logistics and freight transportation: A literature review and research agenda. *International Journal of Physical Distribution & Logistics Management*, *41*(5), 457–483.
Porter, E. M., & Kramer, R. M. (2006). Strategy and society: The link between competitive advantage and corporate social responsibility. *Harvard Business Review*, *84*(12), 78–92.
PWC. (2007). Farm to retail—overview of India's retail sector. In *Indo-US Economic Summit* (pp. 12–26). www.pwc.com/extweb/pwcpublications.nsf/docid/50e7c984c1feebe5ca25739f0023b7e7/$file/buidingstongpartnership.pdf.
Qureshi, M. N., Kumar, D., & Kumar, P. (2008). An integrated model to identify and classify the key criteria and their role in the assessment of 3PL service providers. *Asia Pacific Journal of Marketing and Logistics*, *20*(2), 227–249.
Rijswijk, W. V., & Frewer, L. J. (2008). Consumer perceptions of food quality and safety and their relation to traceability. *British Food Journal*, *110*(10), 1034–46.
Sangam, V. K. (2004). *Global logistics outsourcing trends: Challenges in managing 3PL relationship*. Palmerston: Massey University.
Singh, A. K., Subramanian, N., Pawar, K. S., & Bai, R. (2016). Cold chain configuration design: Location-allocation decision-making using coordination, value deterioration, and big data approximation. *Annals of Operations Research*. doi:10.1007/s10479-016-2332-z.
Saaty, T. L. (1990). How to make a decision: The analytic hierarchy process. *European Journal of Operational Research*, *48*(1), 9–26.

Shabani, A., Saen, R. F., & Torabipour, S. M. R. (2012). A new benchmarking approach in cold chain. *Applied Mathematical Modelling*, *36*(1), 212–224.
Singh, R. K., & Sharma, M. K. (2015). Selecting competitive supply chain using fuzzy AHP and extent analysis. *Journal of Industrial and Production Engineering*. doi:10.1080/21681015.2014.999723 (In press).
Singh, R. K., & Sharma, M. K. (2014). Prioritizing the alternatives for flexibility in supply chains. *Production Planning and Control*, *25*(2), 176–192.
Singh, R. K. (2011). Analyzing the interaction of factors for success of total quality management in SMEs. *Asian Journal on Quality*, *12*(1), 6–19.
Singh, R. K., Garg, S. K., & Deshmukh, S. G. (2008). Implementation of information technology: Evidences from Indian SMEs. *International Journal of Enterprise Network Management*, *2*(3), 248–267.
Singh, R. K., Kumar, R., & Shankar, R. (2012). Supply chain management in SMEs: A case study. *International Journal of Manufacturing Research*, *7*(2), 165–180.
Soh, H. (2010). A decision model for evaluating third party logistics provider using fuzzy analytic hierarchy process. *African Journal of Business Management*, *4*(3), 339–349.
Sohail, M. S., & Al-Abdali, O. S. (2005). The usage of third party logistics in Saudi Arabia: Current position and future prospects. *International Journal of Physical Distribution & Logistics Management*, *35*(9), 637–653.
Spencer, M. S., Rogers, D. S., & Daugherty, P. J. (1994). JIT systems and external logistics suppliers. *International Journal of Operations and Production Management*, *14*(6), 60–74.
Stam, A., & Duarte, A. P. S. (2003). On multiplicative priority ratings method for the AHP. *European Journal of Operational Research*, *145*, 92–108.
Sun, C. C. (2010). Performance evaluation model by integrating fuzzy AHP and fuzzy TOPSIS methods. *Expert Systems with Applications*, *37*, 7745–7754.
Thakkar, J., Deshmukh, S. G., Gupta, A. D., & Shankar, R. (2005). Selection of third party logistics (3PL): A hybrid approach using interpretive structural modeling (ISM) and analytic network process (ANP). *Supply Chain Forum: An International Journal*, *6*(1), 32–46.
Tirado, M. C., Clarke, R., Jaykus, L. A., McQuatters-Gollop, A., & Frank, J. M. (2010). Climate change and food safety: A review. *Food Research International*, *43*(7), 1745–1765.
Tolga, E., Demircan, M. L., & Kahraman, C. (2005). Operating system selection using fuzzy replacement analysis and analytic hierarchy process. *International Journal of Production Economics*, *97*(1), 89–117.
Torfi, F. A., Farahani, R. Z., & Rezapour, S. (2009). Fuzzy AHP to determine the relative weights of evaluation criteria and Fuzzy TOPSIS to rank the alternatives. *Applied Soft Computing*, *10*(2), 520–528.
Torfi, F., Farahani, R. Z., & Rezapour, S. (2010). Fuzzy AHP to determine the relative weights of evaluation criteria and Fuzzy TOPSIS to rank the alternatives. *Applied Soft Computing, 10*(2), 520–528.
Troyer, C., & Cooper, R. (1995). Smart moves in supply chain integration. *Transportation and Distribution*, *36*(9), 55–62.
UNCTAD. (2006). *Report of the Expert Meeting on ICT Solutions to Facilitate Trade at Border Crossings and Ports, United Nations Conference on Trade and Development*, Geneva.
Vaidyanathan, G. (2005). A framework for evaluating third party logistics. *Communications of ACM*, *48*(1), 89–94.
Vorst, J. G., & Van der, A. G. (2000). *Effective food supply chains generating, modeling and evaluating supply chain scenarios*. Dutch: Wageningen University.
Wolf, C., & Seuring, S. (2010). Environmental impacts as buying criteria for third party logistical services. *International Journal of Physical Distribution & Logistics Management*, *40*(1/2), 84–102.
Yan, G. E. (2009). Evaluation on competitiveness of TPL enterprises based on AHP and genetic algorithm. In *Proceedings of the 2nd IEEE International Conference on Computer Science and Information Technology*.
Ying, W., & Dayong, S. (2005). Multi-agent framework for third party logistics in E-commerce. *Expert Systems with Applications*, *29*, 431–436.
Zadeh, L. A. (1965). Fuzzy sets. *Information and Control*, *8*(3), 338–356.
Zang, J. (2009). The research of 3PLs provider selection based on rough set and PSO. In *Proceeding of the IITA International Conference on Services Science, Management and Engineering*.
Zhou, G., Min, H., Xu, C., & Cao, Z. (2008). Evaluating the comparative efficiency of Chinese third party logistics provider using data envelopment analysis. *International Journal of Physical Distribution and Logistics Management*, *34*(4), 262–279.
Zokaee, S., Jabbarzadeh, A, Fahimnia, B, Sadjadi, S. J. (2014). Robust supply chain network design: an optimization model with real world application. In *Annals of Operations Research*, November (pp. 1–30).

Threshold power of amplitude modulated laser beam in complex plasma

R. Sharma[1] and S. C. Sharma[1]

[1]*Department of Applied Physics, Delhi Technological University (DTU),*

Shahbad Daulatpur, Bawana Road, Delhi-110042, India.

Abstract

A theoretical investigation describing the effect of dust on the threshold power of the amplitude modulated laser beam propagating in complex plasma has been done. In this analysis, momentum and energy balance equations have been solved simultaneously to govern the relation between the beam width parameter and normalizes length of progression of amplitude modified beam advancing in complex plasma. The dependence of beam width parameter on the progression length have been evaluated for different values of dust grain size and dust charge state. Moreover, the dependence of critical power of self-focusing on dust grain size and dust charge state have also been investigated. It is found that the critical power augments with the increase in dust grain size as well as with the increase of the dust charge state.

Introduction

Numerous articles have been come out with the self-trapping of an electromagnetic wave in complex plasma (consist of electrons, ions and positively or negatively charged dust grains) being supported by several reviews.[1,2] Sometime, these small charged dust grains are responsible for reducing the attainment of industrial devices.[3,4] whereas some mechanization preferred their presence.[5] In addition, the presence of dust grains strongly influence the discharge properties of plasma.[6-8] Dust grains become charged on account of accumulation of electrons on its surface, secondary electron emission, photoemission etc. and cause the variation in electron temperature and electron density. Generally, electron concentration decreases with increase in size of dust grain which leads to variation in critical power of self-focusing. For regulating the complex plasma properties, understanding of networking between complex plasma domains and dust grain parameters is essential. In this paper, we describe the non-linear self-focusing of beam in dusty plasma due to interaction between electrons and the dust grains by considering the non-linear heating of electrons.

In general, curves have drawn to show the dependence of beam width parameter on the normalized length of progression for the distinct parameters of amplitude modified beam

advancing in complex plasma and to analyse the change in critical power of self-focusing with the formation and charging of the dust grain.

Dynamics of complex plasma

Let n_{0i}, n_{0e}, and n_{0d} are the density of complex plasma constituents i.e., ions, electrons and negatively charged dust grains, respectively. In equilibrium, $Z_{0d}en_{0d} + en_{0e} = Z_{0i}en_{0i}$, where –e is charge on electron, $-Z_{0d}e$ is the charge on dust and $Z_{0i}e$ is the charge on ion. Let us assume a high power amplitude modified electromagnetic beam travelling along z-direction in a complex plasma with the electric vector given by

$$\vec{E}=A_0(r,z)(1+\mu_0\cos\omega t)\exp[-i(\omega_0 t-kz)], \qquad (1)$$

where

$$A_0^2=A_{00}^2(1+\mu_0\cos\omega t)^2 e^{-r^2/r_0^2}, \qquad (2)$$

k is the propagation constant, ω is modulation frequency,μ_0 is modulation index, A_{00} is amplitude of electric vector, r_0 is the initial width of the beam .

For z >0,

$$A_0^2=\frac{A_{00}^2}{f^2}(1+\mu_0\cos\omega t)^2 e^{-r^2/r_0^2 f^2}, \qquad (3)$$

where f represents the beam width parameter, r_0 is the beam spot size. The momentum and energy balance of the equation is given by

$$m_e\frac{d\vec{v_e}}{dt}+m_e\nu\vec{v_e}=-e\vec{E}, \qquad (4)$$

and

$$\frac{3}{2}K_b\frac{dT_e}{dt}+\frac{3}{2}K_b\delta_{dusty}\nu(T_e-T_0)=-\frac{1}{2}e\vec{E}.\vec{v}, \qquad (5)$$

where m_e ,T_e ,and v_e are the mass, temperature and velocity of electrons, respectively. K_b is the Boltzmann's constant. δ_{dusty} is a part of energy transfer via charging collision of electrons with dust, elastic collisions of electron with dust and ions, represented as $\delta_{dusty}(=\nu_{chg}/\nu_{chg}+\nu_{ei}+\nu_{ed})$ and $\nu(=\nu_{chg}+\nu_{ei}+\nu_{ed})$ is the effective collision frequency, where $\nu_{chg}, \nu_{ei}, \nu_{ed}$ are the charging, electrons-ions and electrons-dust grains collision frequencies respectively. The Eqs. (1) - (5) solved simultaneously to obtain dielectric constant in the existence of dust particles which is substituted in wave equation for electric field vector

of propagating electromagnetic beam to obtain an equation to see the change in beam width parameter with the normalized length of progression, expressed as

$$\frac{d^2f}{d\xi^2} = -\frac{1}{R_n^2}\frac{1}{f^3}(1+\mu_0\cos\omega t)^2 + \frac{1}{R_d^2 f^3}, \qquad (6)$$

where $R_d = \frac{\omega_0}{c}\varepsilon_0^{1/2} r_0^2$, $R_n^2 \left(= r_0^2 \varepsilon_0 / \varepsilon_2 A_{00}^2\right)$, R_n is the typical length of self-focusing and $\varepsilon_2 = \left(\omega_p^2/\omega_0^2\right)\left(e^2/6m_e\delta_{dusty}T_0\omega_0^2\right)$ is an effective dielectric constant in complex plasma. In the right –hand side, the first part of Eq. (6) represent the nonlinear self-focusing term while the second diffraction divergence of the beam.

Threshold power of self-focusing

From Eq. (6), the critical power of self-focusing (for which $d^2f/d\xi^2 = 0$, $f = 1$, for every values of ξ) can be written as $P_{cr} = \varepsilon_0^{1/2} c^3 / 8\omega_0^2 \varepsilon_2$.

Results and discussion

Fig.1 (a) and Fig.1 (b) represent the deviation of beam width parameter with the normalized length of progression, $\xi = (z/R_d)$ for different parameters of dust grain size and dust charge number and Fig.2(a) and Fig.2(b) represent the rate of change of critical power of self-focusing with the dust grain size and dust charge number in the following domain: $\omega_p / \omega_0 = 31.167$, $\delta_{dusty} = 2.03 \times 10^{-4}$, $T_0 = 6.4$ eV, Z_d (dust charge state) = $- 2 \times 10^4$ and a_d (dust grain size) = 10^{-4}cm, $A_{00} = 10^5$ stat volt cm^{-1}, $\varepsilon_0 = 0.97$, $\varepsilon_2 = 0.8\times10^{-10}$,e $=4.8\times10^{-10}$esu.With these parameters ,critical power comes out to be 0.947×10^{18}ergs/s. Fig.1(a) and Fig.1(b) show that the self-focusing of the amplitude modulated beam increases with the increases in dust grain size because of dominating self-focusing term whereas decreases with the enhanced dust charge number due to strengthening in diffraction divergence term. Fig.3 and Fig.4 show that the critical power of self-focusing augmented with the increase in dust grain size as well as with the increase of the dust charge state. This is because with the increase of dust grain size and dust charge state, more and more accumulation of electrons take place on its surface which results in decrease of electron density and increase of critical power of self-focusing.

References

[1]A. Gahlot, RituWalia, Suresh C. Sharma, and R. P. Sharma, J. Plasma Physics **78**, 33(2012).

[2]M.S. Sodha, S. K. Mishra, and Shikha Misra, Phys. Plasmas **16**,123701 (2009).

[3]F. Verheest and P. Meuris, Phys. Lett. A **210**, 198 (1996).

[4]G. S. Selwyn, Jpn. J. Appl. Phys., Part 1 **32**, 3068 (1993).

[5]E.Stoffels, W.W.Stoffels, D. vender, G.M.W.Kroesen, and F.J de Hoog, IEEE transaction on Plasma Science 22, 2(1994).

[6]I. Denysenko, J. Berndt, E. Kovacevic, I.Stefanovic,V.Selenin, and J.Winter, Phys. Plasmas**13**, 074507(2006).

[7]I.Stefanovic, E. Kovacevic, J.Berndt, and J.Winter, New J. Phys. 5, 39.1(2003).

[8]G. Sambandan, V. K. Tripathi, J. Parashar, and R. Bharuthram, Phys. Plasmas **6**, 762(1999).

Figure Caption

Fig.1(a): Dependence of f on ξ, for different values of dust grain size labelled as a1, a2, a3 and a4 corresponds to dust radius, r_d = 1µm, 5µm, 10µm and15µm, respectively.

Fig.1(a): Dependence of f on ξ, for different values of dust charge number labelled as z1, z2, z3 and z4 corresponds $Z_d = -8\times10^3$, -6×10^3, -4×10^3, -2×10^3, respectively.

Fig.2(a): Variation of critical power P_{cr} (in ergs/s) with dust grain radius r_d.

Fig.2(b): Variation of critical power P_{cr} (in ergs/s) with dust charge state Z_d.

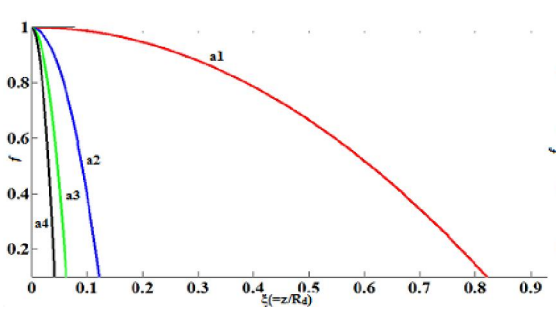


Fig1(a)

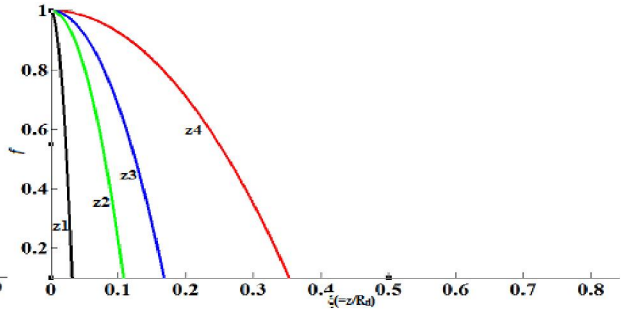


Fig1(b)

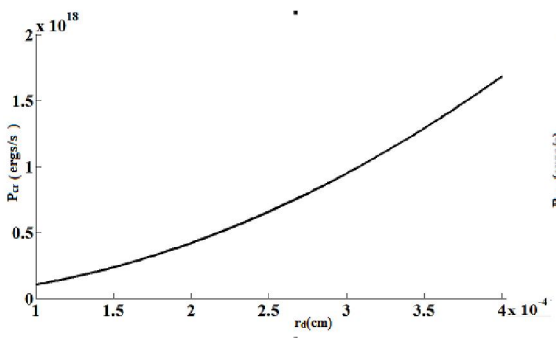


Fig2(a)

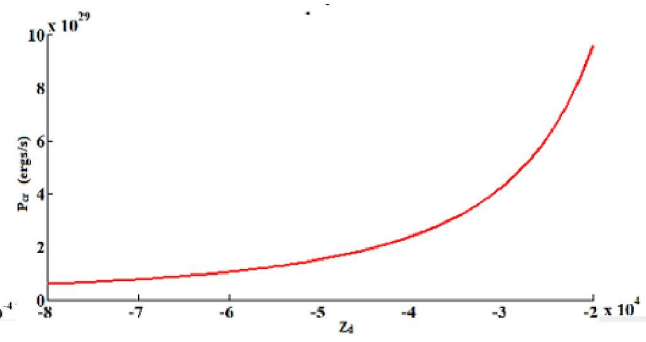


Fig2(b)

International Journal of Research in Engineering and Innovation (IJREI)
journal home page: http://www.ijrei.com
ISSN (Online): 2456-6934



Vapour compression refrigeration systems using nano materials mixed with R718 in secondary circuit of evaporator for enhancing thermodynamic performances

Radhey Shyam Mishra

Department of Mechanical, Industrial, Production and Automobiles Engineering
In-charge: Advanced Centre for Studies and Research in Energy Technologies,
Heat & Mass Transfer Labs, Delhi Technological University Delhi -110042
E-mail: rsmishra1651956@yahoo.co.in, professor_ rsmishra@yahoo.co.in, rsmishra@dtu.ac.in

Abstract

Now a day's refrigeration based equipment are most important for industrial and domestic applications. These systems utilized more energy as compared with other appliances. For reducing energy consumption, nanoparticle based refrigerant has better properties in terms of increased the heat transfer performance of base refrigerant in the vapour compression refrigeration system. Several types of solid and oxide materials could be used as the nanoparticles to be suspended in the conventional refrigeration systems. In this paper, the effect of the suspended copper oxide (CuO), Titanium Oxide (TiO_2), Aluminum Oxide (Al_2O_3), into eco friendly refrigerants (i.e. R134a, R407c and R404a) is investigated.

The use of nano refrigerant as a primary fluid in vapour compression refrigeration systems was studied in detailed and simulation program was develop to solve nonlinear equations of the system model using NTU approach and the effect of changes in performance parameters to the second law performance in terms of exergetic efficiency of VCR system carried out. The effect of the thermal conductivity, dynamic viscosity, and heat transfer rate of the nano-refrigerant/refrigerant of VCRS on system performance have been presented. © 2017 ijrei.com. All rights reserved

Keywords: VCR, Energy-Exergy Analysis, Energy-Exergy Analysis, Nano refrigerants

1. Introduction

Now a day's refrigeration based equipment are most important for industrial and domestic applications. Those systems utilize more energy compare to other appliances. The refrigeration systems have been severely investigated to reduce the energy consumption in many research articles. Hence, nanoparticle based refrigerant has been introduced a superior properties refrigerant that increased the heat transfer performance of base refrigerant of the refrigeration system. Many types of solid and oxide materials could be used as the nanoparticles to be suspended into the conventional refrigerants. In this project work, the effect of the suspended copper oxide (CuO), Titanium Oxide (TiO_2), Aluminum Oxide (Al_2O_3), into the R134a, R407c and R404 eco-friendly refrigerant will be investigated by using mathematical modeling.

The use of nano refrigerant a primary fluid in vapour compression refrigeration systems was studied and computational simulation program for the same is supposed to develop to solve the nonlinear equations of the system model. Also in this research work it is supposed to analyze the effect of these changes to the second law performance of the system. The investigation includes the thermal conductivity, dynamic viscosity, and heat transfer rate of the nano-refrigerant/refrigerant with complete system geometry of VCRS. It is also expected that after implementation of these systems in our existing systems how much cost can be reduce by this research work.

Corresponding R.S. Mishra
Email Id: rsmishradtu@gmail.com

2. Vapour compression Refrigeration systems

Vapour compression is used to transfer heat from low temperature zone higher temperature zone. It has four thermodynamics process as below. Isobaric Evaporation, Isentropic Compression, Isobaric Condensation, Throttling (Expansion), Vapour compression cycle can be used in temperature range 50 to -40°C easily. Nowadays, there is a high energy consumption associated with refrigeration and air conditioning systems. Most of these facilities are based on the vapour compression cycle. In order to reduce their consumption, it is necessary both to have efficient systems and to operate them properly. To achieve these objectives, it is convenient to use complete models, which take under consideration a large amount of factors and facilitate the design of efficient systems. The heat transfer from the refrigerant at the compressor discharge line to the condenser inlet has been modeled, due to the considerable length of the line in the experimental chiller facility, using expression. The condenser behavior is modeled by dividing the heat exchanger into two zones: the superheated vapor zone and the condensing zone, assuming no sub-cooling at the condenser outlet, as it has been stated in the assumptions. The overall heat exchanger is then For the computation of the convection heat transfer coefficient associated to the refrigerant one can distinguish between the convection heat transfer coefficient in the superheated vapor zone modeled with two energy balances, one using the secondary fluid heat flow rate.

3. Literature Review

A few studies have been illustrated as a part of literature review related to theoretical study and experimental investigation of refrigeration systems based on first law and second law analysis with different pairs of refrigerants, nanoparticle behaviour and application of nano fluid in vapour compression refrigeration system.

Jwo et al. [4] investigated the replacement of polyester lubricant and R-134a refrigerant with mineral lubricant and hydrocarbon refrigerant. The mineral lubricant contains Al_2O_3 nanoparticles to improve the lubrication and performance of heat-transfer. Their studies show that the R-134a at 60% and Al_2O_3 0.1 wt % nanoparticles were optimum .Under these conditions, the consumption of power was reduced by 2.4%, and the C.O.P. was increased by 4.4%. Peng et al. [5] investigated with an experiment that nucleates boiling heat transfer property of refrigerant/oil mixture containing diamond nano particles. The refrigerant used was R113 and the oil was VG68. They found out that the nucleate pool boiling heat transfer coefficient of R113/oil mixture with diamond nanoparticles is larger than the R113/oil mixture. They also proposed a general correlation for calculating nucleate boiling coefficient heat transfer of mixed refrigerant/oil with nanoparticles, which fully satisfies their experimental results. Henderson et al. [6] conducted an experimental analysis on the flow boiling heat transfer coefficient of R134a (refrigerant) based nano fluids in a horizontal tube. They found excellent dispersion of CuO nanoparticle with R134a and POE oil and the heat transfer coefficient increases more than 100% over baseline R134a/POE oil results. Bobbo et al. [7] conducted a study on the influence of dispersion of single wall carbon Nano horns (SWCNH) and Ti2O3 on the tribological properties of POE oil together with the effects on the solubility of R134a at different temperatures. They showed that the tribological behavior of the base lubricant can be either improved or worsen by adding nanoparticles. On the other hand the nanoparticle dispersion did not affect significantly the solubility. Bi et al. ([8] conducted an experimental study on the performance of a domestic refrigerator using Ti2O3 -R600a nano refrigerant as working fluid. They showed that the Ti2O3-R600a system worked normally and efficiently in the refrigerator and an energy saving of 9.6%. They too cited that the freezing velocity of nano refrigerating system was more than that with pure R600a system. The purpose of this article is to report the results obtained from the experimental studies on a vapour compression system. Lee et al. [9] investigated the friction coefficient of the mineral oil mixed with 0.1 vol.% fullerene nanoparticles, and the results indicated that the friction coefficient decreased by 90% in comparison with raw lubricant, which lead us to the conclusion that nanoparticles can improve the efficiency and reliability of the compressor. Wang and Xie [10] found that Ti2O3 nanoparticles could be used as additives to enhance the solubility between mineral oil and hydrofluorocarbon (HFC) refrigerant. The refrigeration systems using the mixture of R134a and mineral oil appended with nanoparticles Ti2O3, posses to give best performance by returning more vol of lubricant oil return to the compressor, and had the similar performance compared to the systems using polyol-ester (POE) and R134a. In the present study the refrigerant selected is R600a and the nanoparticle is alumina. Isobutane (R600a) is more widely adopted in domestic refrigerator because of its better environmental and energy performances. In this paper, a new refrigerator test system was built up according to the National Standard of India. A domestic R600a refrigerator was selected. Al_2O_3-R600a nano-refrigerant was prepared and used as working fluid. The energy consumption test and freeze capacity test were conducted to compare the performance of the refrigerator with nano-refrigerant and pure refrigerant so as to provide the basic data for the application of the nanoparticles in the refrigeration system. Heris et al.[11] in their experiment they have examined the convective heat transfer coefficient through a circular tube maintaining temperature of tube wall for boundary condition for nano fluids consisting containing Al_2O_3 and CuO oxide nanoparticles in water considering water as a base fluid. In the experiment they have chosen a tube having 6 mm diameter and length 1meter copper tube. Thickness of copper tube is taken 0.5 mm and another outer stainless steel tube having 32 mm diameter. In their experiment nano fluid flow inside the copper tube and

saturated stean in the annuli section of the steel tube makes constant wall temp. The fluid after then goes to a heat exchanger where water was used for cooling the test chamber. The experimental result concluded that homogeneous model (single phase correlation of nanofluid) was not able to calculate enhancement of coefficient of heat transfer of nanofluid. The experimental result shows that the heat transfer coefficient predicted for CuO/water and Al_2O_3 /water of homogeneous model were very close to each other but when they increase the vol. % concentration of nanoparticle much higher coefficient of heat transfer observed for Al_2O_3 /water. They have concluded that the coefficient of heat transfer of nanofluid depend upon many factor such as nanoparticle diameter and thermal conductivity of nanoparticle, movement of nanoparticle suspension process of nano particle etc. Y. He et al. [12] conducted an experiment to find out the behavior of nanofluid under laminar and turbulent flow. Their experiment consist a heating and cooling unit, a flow loop and a measurement unit. The test section consist a straight vertically oriented copper tube having 1834 mm length and 6.35 outer 3.97 mm inner diameter. In the experiment they heated the tube with help of 2 silicon rubber flexible heater. For the constant heat flux condition in the test section they provided a thermally insulated layer. For measurement the pressure drop 2 pressure transducer ware used. They have experimented the effect of Reynolds number nanoparticle size, concentration of nanopraticle in the base fluid. They concluded that suspension of nanoparticle into the host fluid the enhancement of thermal conductivity of base fluid may achieved and as well we go for decreasing particle size and increasing concentration the enhancement increases. Thus the nanoparticle concentration and particle size paly major role in enhancement of thermal conductivity of base fluid in both turbulent and laminator flow. They have also concluded that the pressure drop by using nanofluid were close to the base fluid. Kulkarni et al., [13] investigated the heat transfer performance also fluid dynamics performance of nanofluids using SiO2 nanoparticle suspended in the ration of 60:40 weight % in to the EG/water mixture. A test section they have taken for this experiment having copper tube 3.14 mm inside and 4.76 mm outer diameter and 1m length. To measure the wall temperature they fitted 6 no. of thermocouple on surface of the copper tube along the length, the outlet and inlet temperature measurement they used 2 thermocouple at the outlet and inlet section respectively. To isolate the thermal heat transfer two plastic fitting ware provided at the inlet and outlet section respectively. To obtain the constant heat flux four strip heater were used. The whole test section was insulated with 10 cm fiber glass to reduce the heat loss from the test section to the ambient. To maintain the constant inlet temperature of fluid four shell and tube type heat exchanger with counter flow were used. In their experiment they have investigated the effect of enhancement of convective heat transfer of nanofluid with diameter of nanoparticle 20nm, 50nm and 100nm in the turbulent region by increasing volume concentration of nanoparticle and pressure drop recorded when they increase the concentration of nanoparticle in the nanofluid. Hwang et al., [14] investigated the convective heat transfer coefficient of Al_2O_3 /water based nanofluid. In their experiment nanofluid considered flowing through circular tube having 1.812 mm inside diameter and maintaining constant heat flux for fully developed laminar regime. Al_2O_3 /water based nanofluids with various volume % concentration 0.01% to 0.3% are manufactured with two-step method. They have also obtained the thermo physical property of nanofluid such as density, viscosity, heat capacity and thermal conductivity. They have concluded that the convective heat transfer coefficient enhancement occurs with 0.01 and 0.3 vol % concentration of nanoparticle in fully developed laminar regime and heat transfer enhancement about 8 % obtained under the same Reynolds number of base fluid. They also concluded that enhancement in heat transfer coefficient were much higher that the thermal conductivity enhancement at the same vol % concentration of nanoparticle. Sharma et al.,[15] investigated to evaluate friction factor and heat transfer coefficient with a inserted twisted tape in the flow region of tube with Al_2O_3 nanpfluid they have consider a test section of L/D ration 160 and 1.5m length. For uniform heating test section were wrapped with 1 Kw .The aluminum strip having 0.018mm width and 1mm thick are used. Test section is subjected to 180° twist br holding both end of test section in lathe machine obtaining 5, 10 and 15 twist ratio. Ther result show enhancement in heat transfer coefficient with Al_2O_3 nanoparticle into the base fluid compare to the base water. The heat transfer coefficient was 23.7 % higher that the water at Reynolds number 9000. Yu et al., [16] investigated the heat transfer coefficient of silicon carbide nanoparticle having diameter 170nm and 3.7 vol % suspended into the pure water and found that an increment in heat transfer coefficient about 50-60 % compared to host fluid.their test section was stainless steel tube with 4.76 mm outside diameter and 2.27 inside diameter. Their test rig have heat exchanger flow meter horizontal tube, pre heater as a closed loop system. They concluded that enhancement is 14-32 % higher that the predicted value for single phase turbulent correlation of heat transfer. Also they found that the pressure loss is little lower than the Al_2O_3 water nanofluid. Torii and Yang [17] investigated the heat transfer coefficient of suspended diamond nanoparticle into the host fluid by maintaining constant heat flux. Their test section contain a flow loop, a digital flow meter, a pump, a reservoir and a tank. The test is prepared stainless steel tube having 4.3 mm outer diameter 4.0 mm inner diameter and 1000 mm length. The whole is heated with a dc electrode heater considering joule heating. They reported that (i) the heat transfer performance of nanofluid increases with the suspension of diamond nano particle into the water compared to pure water. (ii) Reynols number variation influence the enhancement occurs in heat transfer coefficient. Rea et al., [18] investigated the heat transfer

coefficient and viscous pressure loss for Al_2O_3 /water and zirconia-water nanoparticle based nanofluid flowing loop. The stainless steel vertical heated test section considered having outer diameter of 6.4 mm, an inner diameter of 4.5 mm and 1.01 m length. The test section 8 T type thermocouples sheathed and insulated electrically and soldered onto the outside wall of the tube along axial direction 5, 16, 30,44, 58, 89 and 100 cm from heated inlet section of the test facility. To measure the fluid temperatures Two same T-type thermocouples were inserted into the flowing passage of the channel after and before of the test section. They observed that the heat transfer coefficients increased 17% and 27%, in fully developed region compare to base water. The heat transfer of zirconia–water nanofluid increases by approx 2% at 1.32 vol. % in the inlet region and 3% at 1.32 vol % in the fully developed region. The observed pressure loss for nanofluids was higher than the base water having good agreement with predicted model for laminar flow. Murshed et al [19] carried out experiments with spherical and rod-shaped TiO_2 nanoparticles. The spherical particles were 15 nm in diameter and the rod-shaped particles were 10 nm in diameter and 40 nm in length. The base fluid was deionized water. The measurement method was transient hot wire. It should be mentioned here that they used oleic acid and cetyltrimethyl ammonium bromide (CTAB) surfactants (0.01 to 0.02 vol %). They maintained a nearly neutral (pH 6.2 to 6.8) suspension. For the first time, a nonlinear correlation between the volume fraction and conductivity enhancement was observed here at lower concentrations. This is interesting with respect to the temperature effect and pure metallic particles. They found that the conductivity enhancement was higher for rod-shaped particles than for spherical particles. Enhancement up to 29.7% was found with 5% spherical particles and up to 32.8% with rod-shaped particles. They attributed this to the higher shape factor (n =6) of the rods than of the spheres (n =3) in the Hamilton–Crosser [20] model. Xuan and Li [21] were first to show a significant increase in the turbulent heat transfer coefficient. They found that at fixed velocities, the heat transfer coefficient of nano fluids containing Cu nanoparticles at 2.0 vol% was improved by as high as 40% compared to the host water. The Dittus Boelter correlation failed to obtain the improved experimented heat transfer behavior of nanofluids. Recent unpublished work shows that the effect of particle size and shape and dispersion becomes predominant in enhancing heat transfer in nano fluids. Even greater heat transfer effects are expected for nano fluids produced by the one-step process. Therefore, there is great potential to "engineer" ultra-energy-efficient heat transfer fluids by choosing the nanoparticle material as well as by controlling particle size, shape, and dispersion. Mahbubul and Saadah [22] investigated the thermal performance of Al_2O_3/R134a nano refrigerant C.O.P. of nano refrigerant increased about 15% and thermal conductivity about 28.8 %, dynamic viscosity about 13.68 % and density of nano refrigerant about 11 % compare to the pure refrigerant in their study they have considered uniformly mass flux of nano refrigerant in a horizontal smooth tube. Faulkner et al. [23] conducted fully developed laminar convection heat transfer tests and made the startling discovery that water-based nanofluids containing CNTs provide significant enhancements to the overall heat transfer. First, the heat transfer coefficient of the nanofluids increase with Reynolds number. The heat transfer coefficient of the nanofluid were roughly twice those of plain water at the upper end of the Reynolds number range tested, and it appears that this enhancement will continue to increase with larger Reynolds numbers. Second, nanofluids outperform water, but nanofluids with low particle concentrations (1.1 vol %) perform better than those with higher concentrations (2.2 and 4.4 vol%). This is an unexpected and, indeed, counterintuitive result. This negative concentration dependence of the heat transfer enhancement could be due partially to the interaction between particles. Faulkner et al. proposed that the pseudo turbulence induced by rolling and tumbling CNT agglomerates in a microchannel results in micro scale mixing, which enhances the laminar heat transfer coefficient. Since heat transfer applications operate over a wide range of Reynolds numbers and heat fluxes, additional work is needed to develop nano fluids that can provide the most significant benefit to specific heat transfer applications. Wen and Ding [24] were first to study the laminar entry flow of nano fluids and showed a substantial increase in the heat transfer coefficient of water-based nano fluids containing γ-Al_2O_3 nanoparticles in the entry region and a longer entrance length for the nano fluids than water. Also in 2006 they have studied the laminar entry flow of water-based nano fluids containing multi walled carbon nanotubes (CNT nano fluids). For nano fluids containing only 0.5 wt% Carbon nano tubes, the maximum convective heat transfer coefficient enhancement reaches above 350% at Re equal to 800. Such a higher enhancement could not be considered purely for thermal conductivity enhancement. They proposed possible mechanisms such as thickness of thermal boundary layer, particle rearrangement, due to the presence of carbon nanotubes, and very high aspect ratio of Carbon nano tubes. Lee et al. [25]. They measured thermal conductivities of nano fluid at temperatures between 21 and 55°C, and the results were nothing less than miraculous. Over this small 34° C rise in temperature, the thermal conductivity enhancement was more than three times higher. With Al_2O_3, the enhancement increased from 2% to 10.8% at a 1% particle volume fraction and it went from 9.4% to 24.3% at a 4% particle-volume fraction. The same increase for CuO–water nano fluids was 6.5% to 29% for a 1% particle-volume fraction and 14% to 36% for a 4% particle fraction. This puts the entire phenomenological concept regarding nano fluids completely in perspective. In fact, all the theories proclaimed before this work was published crumpled at this observation because none of them could predict such a strong temperature effect. The other important observation from the preceding result is

that at elevated temperatures, neither Al_2O3 nor CuO-based nano fluids comply with the Hamilton–Crosser model. This is because the model is completely insensitive to temperature variations between 21 and 55°C. This clearly indicates that agreement of the Al_2O3 nano fluids with the Hamilton–Crosser model. Joaquin Navarro et al [26] in his investigation performance analysis of vapour compression refrigeration cycle (system) using R1234yf as a replacement of R134a. In their work, they the performance of vapour compression refrigeration system using both the refrigerant R1234yf and R134a with presence of internal heat exchanger also without internal heat exchanger under a large range of operating condition. Experimental result is obtained with varying evaporator temperature and condenser temperature and use of internal heat exchanger. From their result C.O.P and cooling capacity decreased 13 and 6 % respectively when R134a is replaced by R1234yf. However the presence of internal heat exchanger can help to control the reduction about 6 and 2 % respectively. The experimental result agreed with the mathematical analysis of the system considering pressure drop negligible.

4. Result and Discussion

A computational program has been developed to solve non linear equation of vapour compression refrigeration cycle for case (iii) mentioned in abstract. Considering same geometric parameter of the VCRS model theoretical analysis has been done using EES software for nano refrigerant flowing in primary circuit and R718 (water) flowing in secondary circuit of VCRS and results are given below.

4.1 Thermo physical property of nano refrigerant

In this section variation of thermo physical property of base refrigerant using nanoparticle suspended into base refrigerant at 5 Vol % are shown below.

4.1.1 Thermal conductivity of nano refrigerant using different nanoparticle and base refrigerant

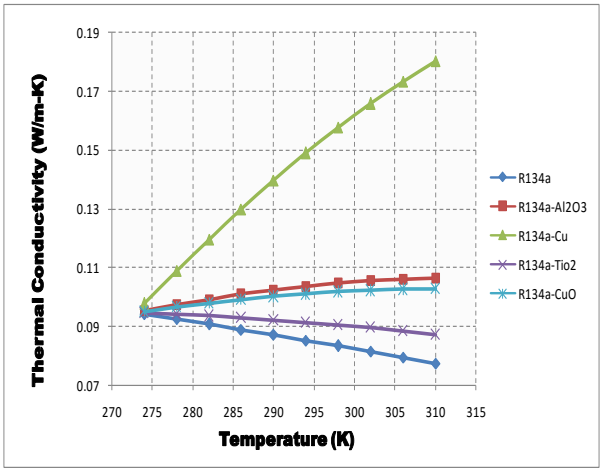


Fig.1: Variation of Thermal conductivity with Temperature of R134a using different nanoparticles

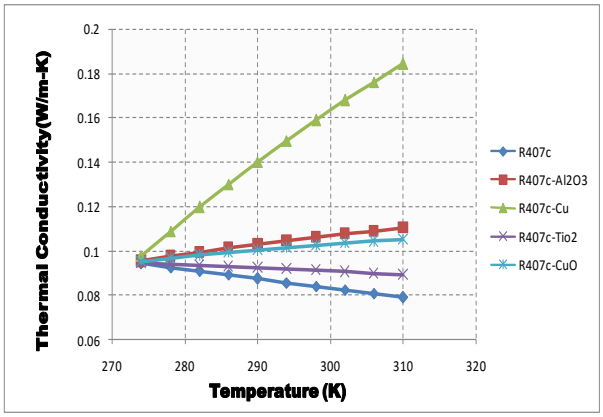


Fig.2; Variation of Thermal conductivity with Temperature of R407c using different nanoparticles

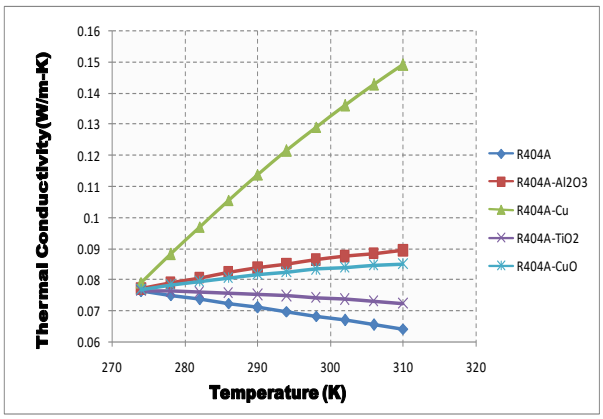


Fig.3. Variation of Thermal conductivity with Temperature of R404A using different nanoparticles

Fig. 1-3 show the enhancement in thermal conductivity of nano refrigerant when different kind of nanoparticle is suspended into the host refrigerant. The enhancement factor varies from 0.06 to 2 for different nanoparticle. From the Fig 3, the cu nanoparticle have more EF at higher temperature which value is approx 2.

4.1.2 Density of nano refrigerant with different nanoparticle and base refrigerant

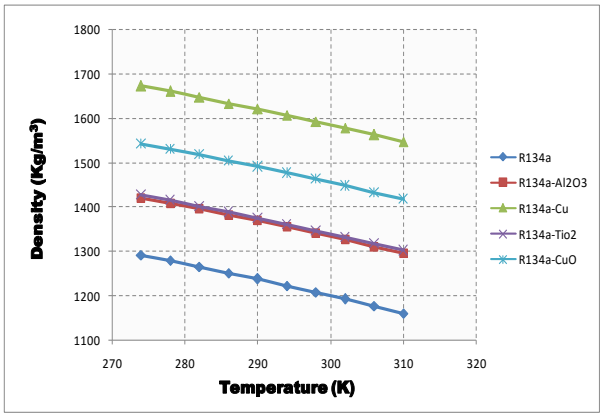


Fig.4 Variation of Density with Temperature of R134a using different nanoparticles

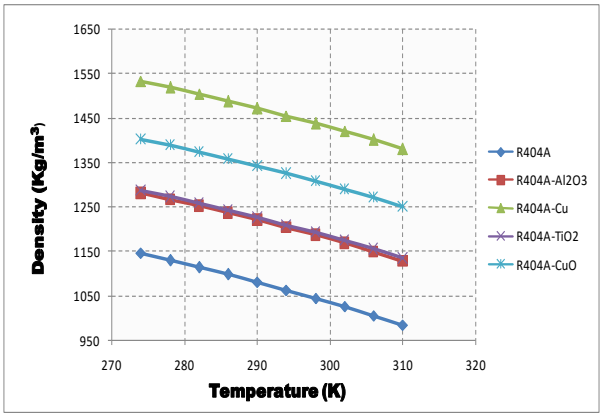


Fig.5 Variation of Density with Temperature of R404A with temperature using different nanoparticles

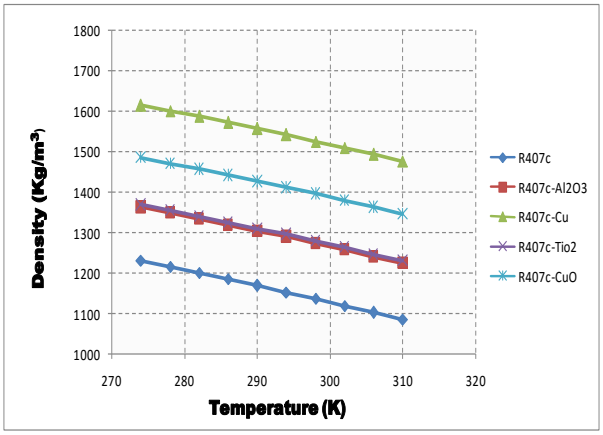


Fig.6 Variation of Density with Temperature of R407c using different nanoparticles

Fig.4-6 shows variation in density of nano refrigerant subject to temperature variation. Fig-4, shows that density variation of nano refrigerant is similar to pure refrigerant as higher temperature low density and lower temperature high.

4.1.3 Dynamic viscosity of nano refrigerant using different nanoparticle and base refrigerant

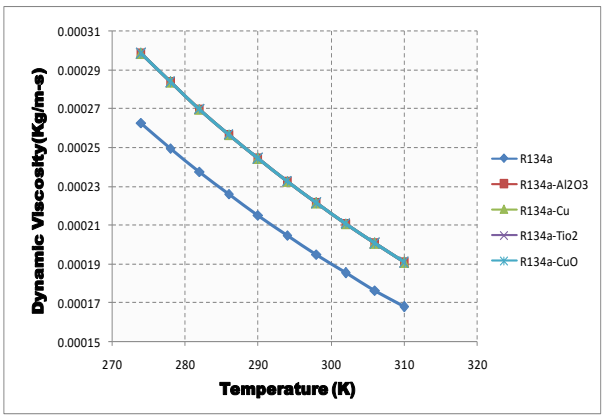


Fig.7 Variation of Dynamic viscosity with Temperature of R134a using different nanoparticles

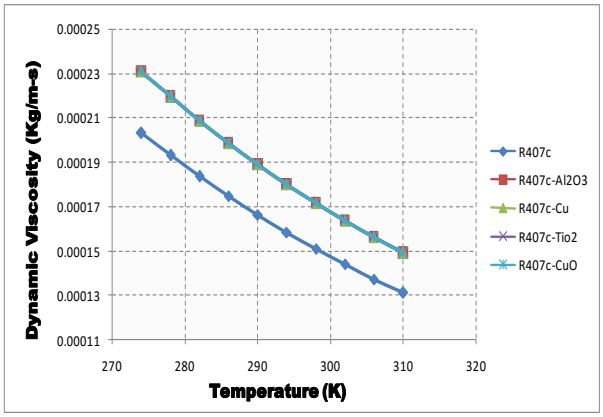


Fig.8 Variation of Dynamic viscosity with Temperature of R407c using different nanoparticles

Fig.6-9 shows variation in Dynamic viscosity of nano refrigerant subject to temperature variation.

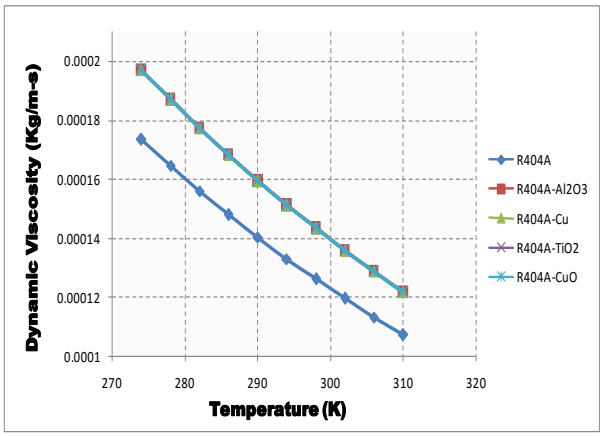


Fig.9: Variation of Dynamic viscosity with Temperature of R404A using different nanoparticles

Fig-9 shows that Dynamic viscosity variation of nano refrigerant is similar to pure refrigerant as higher temperature low viscosity and lower temperature high.

4.1.4 Specific heat of nano refrigerant using different nanoparticle and base refrigerant

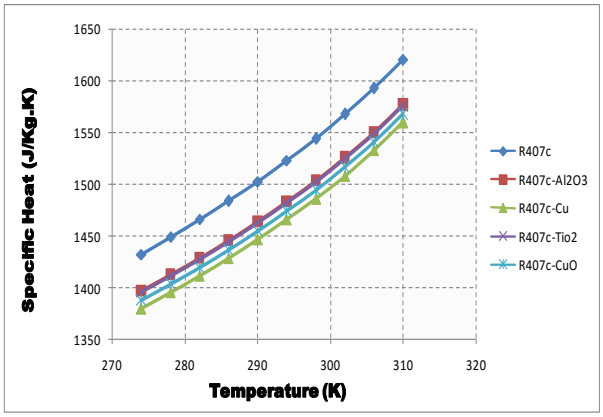


Fig.10 Variation of Specific heat with Temperature of R407c using different nanoparticles

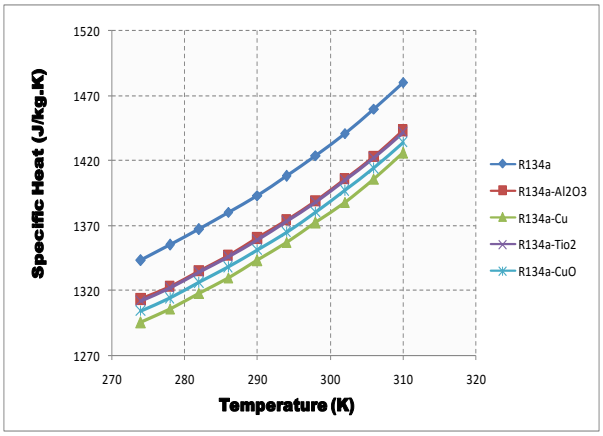


Fig.11 Variation of Specific heat with Temperature of R134a using different nanoparticles

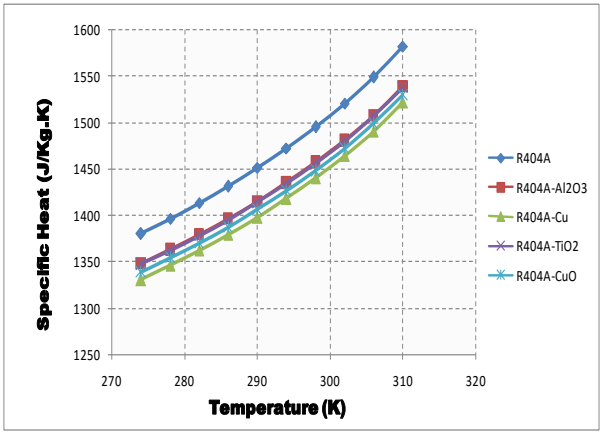


Fig.12 Variation of Specific heat with Temperature of R404A using different nanoparticles

Fig. 10-12 shows variation in specific heat of nano refrigerant subject to temperature variation. Fig shows that Specific heat variation of nano refrigerant is similar to pure refrigerant as higher temperature High Specific heat and lower temperature low. But when we go for higher vol % concentration of nanoparticle Specific heat will reduce.

4.2 Effect of volume fraction on Thermo physical property of nano refrigerant with different nanoparticle and base refrigerant (at 280K temperature

Density ratio shown Fig 13 is defined as the ratio of density of nano refrigerant (nanoparticle mixed with pure refrigerant) to the density of pure refrigerant. Thermal conductivity shown in Fig 14 is defined as the ratio of thermal conductivity of nano refrigerant (pure refrigerant mixed with nanoparticle) to the thermal conductivity of pure refrigerant.

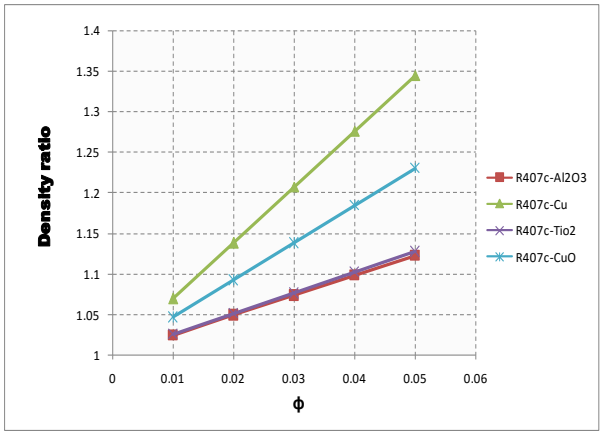


Fig.13 Variation of Density Ratio with volume fraction (ϕ) of R407c using different nanoparticles

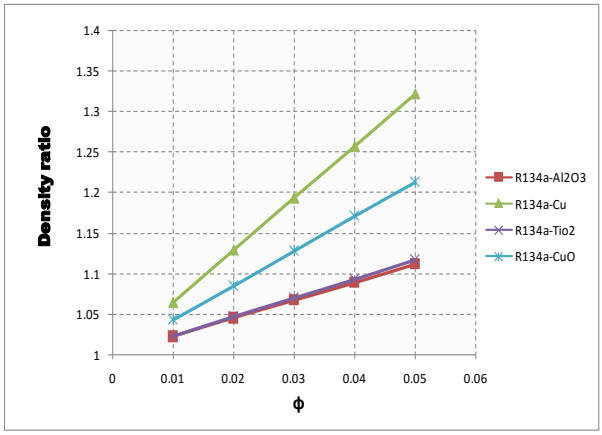


Fig.14 Variation of Density Ratio with volume fraction (ϕ) of R134a using different nanoparticles

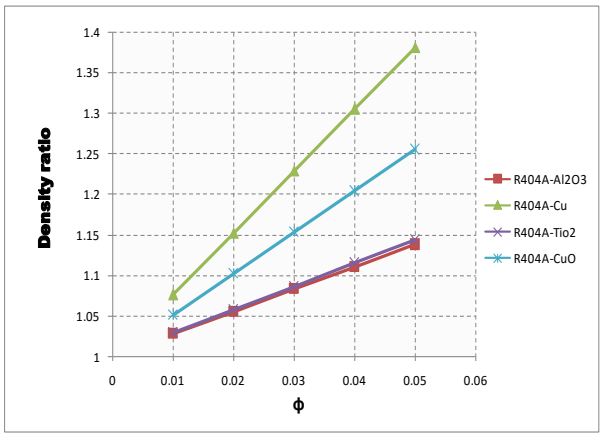


Fig.15. Variation of Density Ratio with volume fraction (ϕ) of R404A using different nanoparticles

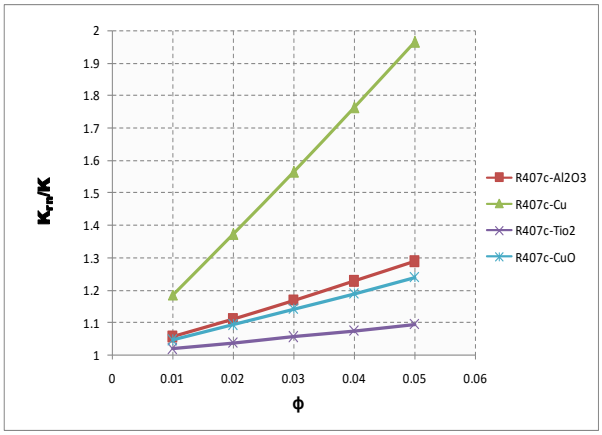


Fig.16 Variation of Thermal conductivity Ratio with volume fraction (ϕ) of R407c using different nanoparticles

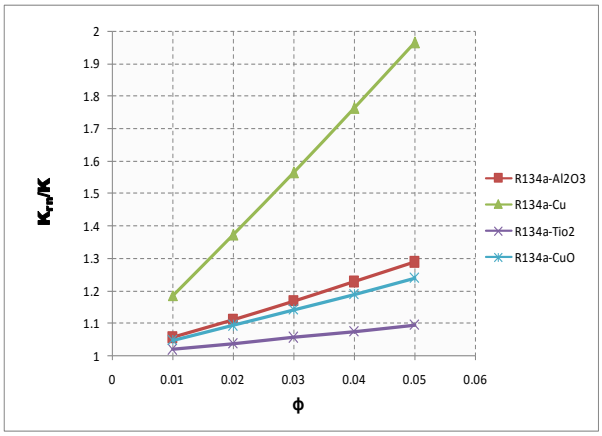


Fig.17 Variation of Thermal conductivity Ratio with volume fraction (ϕ) of R134a using different nanoparticles

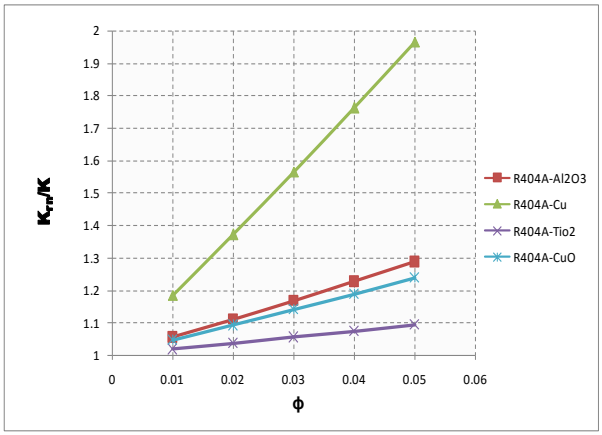


Fig.18 Variation of Thermal conductivity Ratio with volume fraction (ϕ) of R404A using different nanoparticles

Fig 15-18 shows that conductivity ratio of pure refrigerant to nano refrigerant increases with increasing concentration of nanoparticle into the host refrigerant. We can see that Cu nanoparticle based nano refrigerant have higher cond. Ratio than other nanoparticle and have approx two times higher than base refrigerant at 5 vol % concentration.

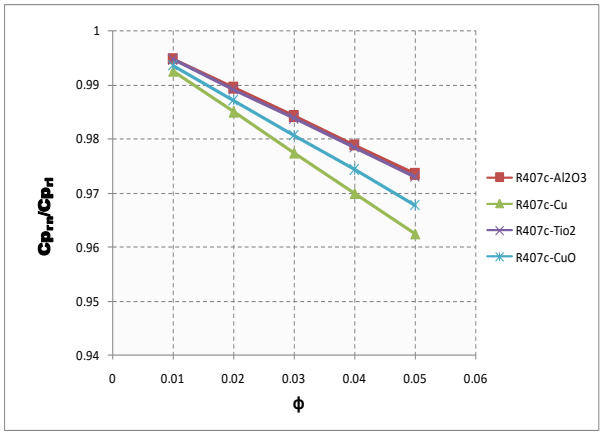


Fig.19 Variation of Specific heat ratio with volume fraction (ϕ) of R407c using different nanoparticles

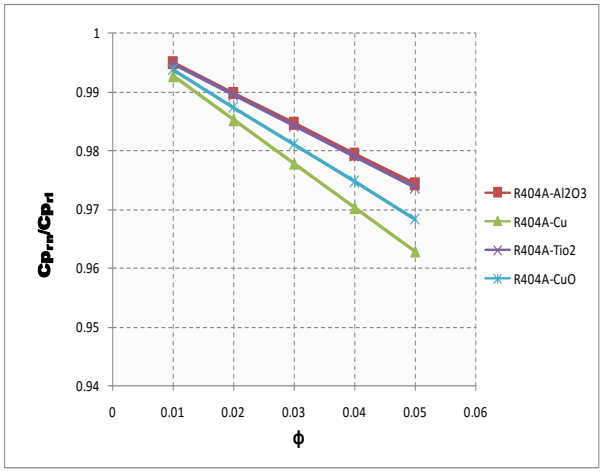


Fig.20: Variation of Specific heat ratio with volume fraction (ϕ) of R404A using different nanoparticles

Specific heat ratio shown in Fig 17-20 is defined as the ratio of specific heat of nano refrigerant (nanoparticle mixed with pure refrigerant) to the specific heat of pure refrigerant.

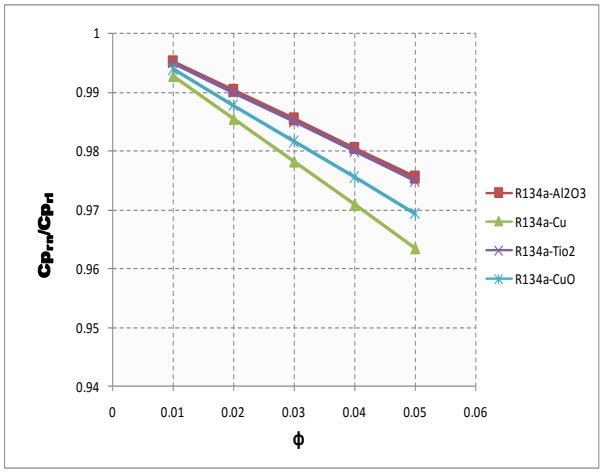


Fig.21 Variation of Specific heat ratio with volume fraction (ϕ) of R134a using different nanoparticles

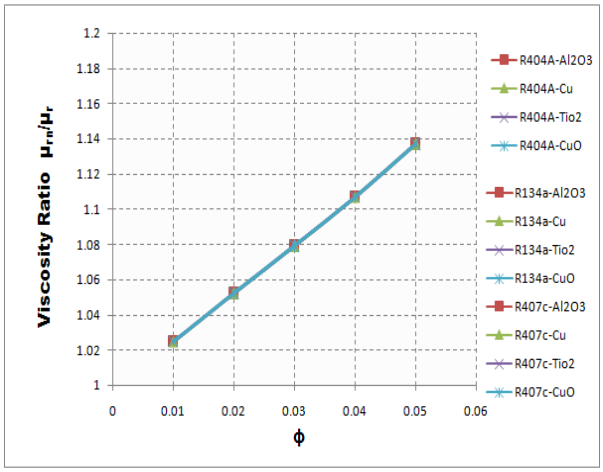


Fig.22 Variation of Viscosity ratio with volume fraction (ϕ) of all Nano refrigerant

Viscosity ratio shown in Fig 22 is defined as the ratio of Viscosity of nano refrigerant (nanoparticle mixed with pure refrigerant) to the Viscosity of pure refrigerant.

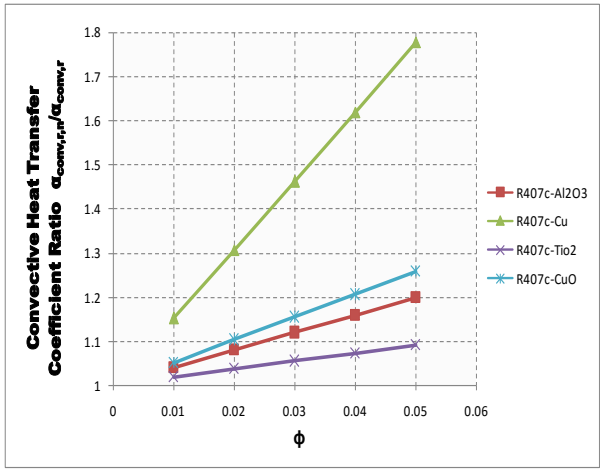


Fig.23. Variation of Convective heat transfer coefficient ratio with volume fraction (ϕ) of R407c using different nanoparticles

Convective heat transfer coefficient ratio shown in Fig 23-25 respectively is defined as the ratio of convective heat transfer coefficient of nano refrigerant (nanoparticle mixed with pure refrigerant) to the Convective heat transfer coefficient of pure refrigerant. Heat transfer Enhancement Factor shown in Fig.23-25 is defined as the ratio of heat transfer coefficient of nano refrigerant (nanoparticle mixed with pure refrigerant) to the heat transfer coefficient of pure refrigerant.

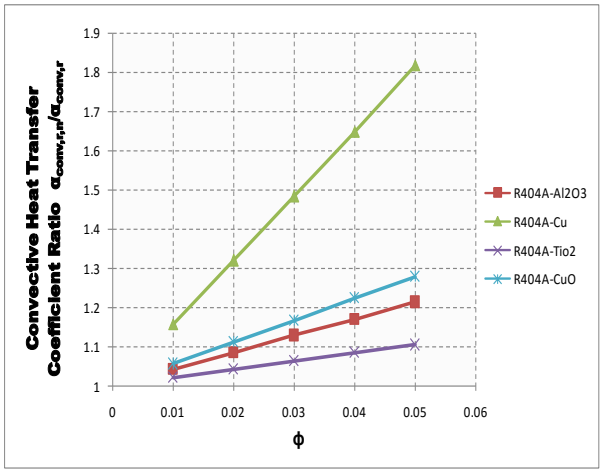


Fig.24 Variation of Convective heat transfer coefficient ratio with volume fraction (ϕ) of R404A using different nanoparticles

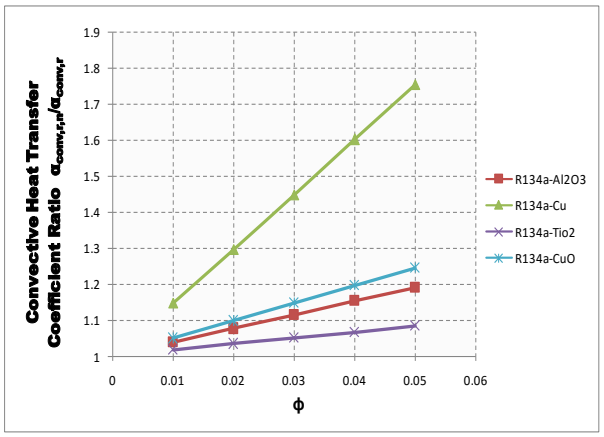


Fig.25. Variation of Convective heat transfer coefficient ratio with volume fraction (ϕ) of R134a using different nanoparticles

Fig 23-24 shows the convective heat transfer coefficient Ratio increases by increasing the concentration of nanoparticle. And copper nanoparticle based nanorefrigerant have highest convective heat transfer coefficient ratio than other particle its value ranges from 1 to 1.7.

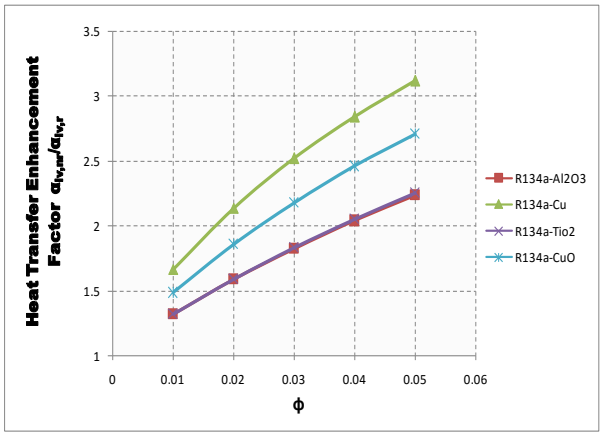


Fig.26. Variation of Heat transfer Enhancement Factor with volume fraction (ϕ) of R134a using different nanoparticles

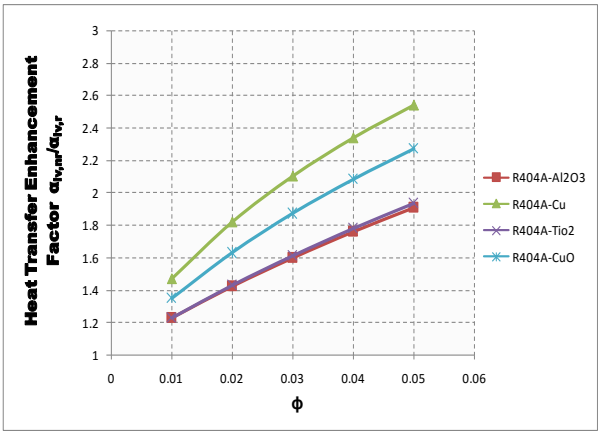


Fig.27 Variation of Heat transfer Enhancement Factor with volume fraction (ϕ) of R404A using different nanoparticles

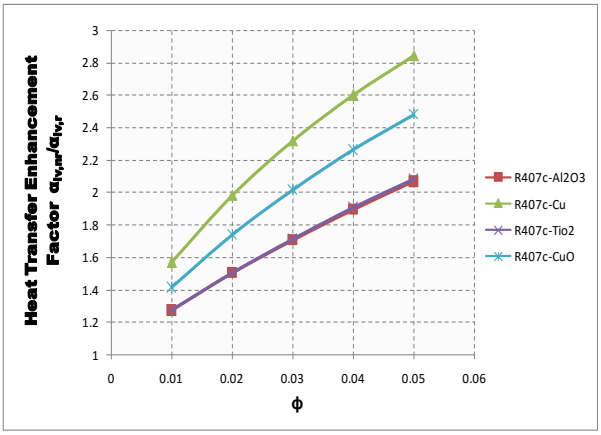


Fig.28 Variation of Heat transfer Enhancement Factor with volume fraction (ϕ) of R407c using different nanoparticles

Fig 25-28 show the heat transfer enhancement factor of nano refrigerant with different nanoparticle its value ranges from 1.2 to 3.2. As it can be seen that R134a with cu nanoparticle have highest EF approx 3.2 at 5 vol %. EF increases with increasing vol %.

4.3 Effect of nanoparticle volume fraction (ϕ) on the first law of thermodynamics (C.O.P.) of VCRS

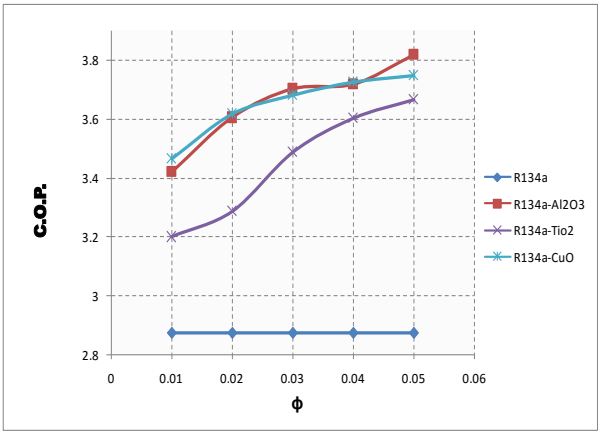


Fig.29 Variation of C.O.P with volume fraction (ϕ) of VCRS with R134a using different nanoparticles

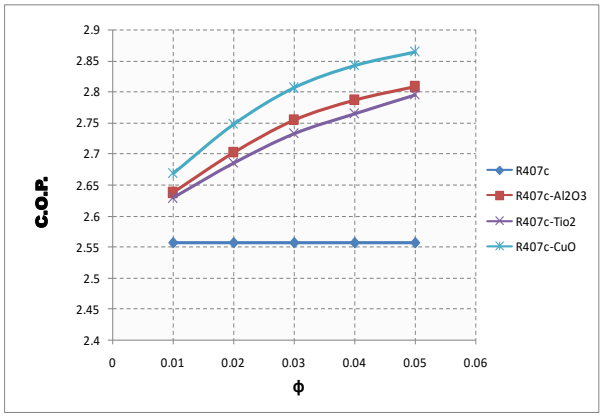


Fig.30 Variation of C.O.P with volume fraction (ϕ) of VCRS with R407c using different nanoparticles

Fig 28-31 shows that 1st law of thermodynamics enhancement of VCRS can be achieved by using nano refrigerant as a working fluid in VCRS. Fig.30 show that the maximum enhancement theoretically achieved about 35 % with combination of R134a with Al_2O_3 nanoparticle at 5 vol % based nano refrigerant. C.O.P. enhancements of VCRS with different combination of nano refrigerant.

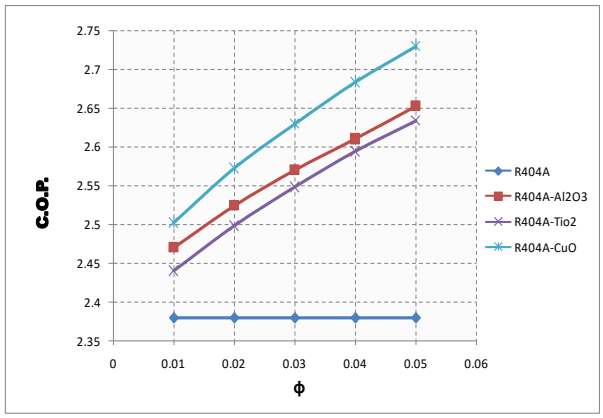


Fig.31: Variation of C.O.P with volume fraction (ϕ) of VCRS with R404A using different nanoparticles

4.4 Effect of nanoparticle volume fraction (ϕ) on the Exergy destruction ratio of VCRS

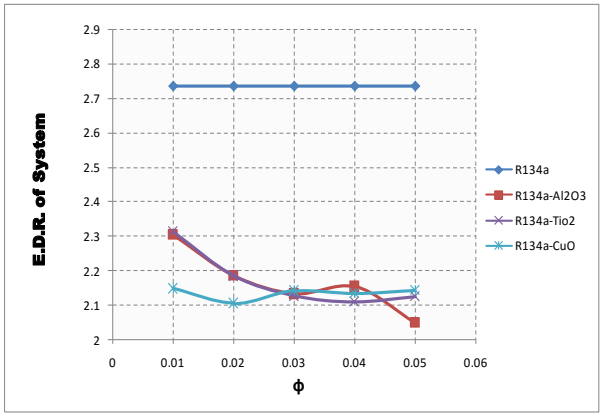


Fig.32 Variation of Exergy destruction ratio with volume fraction (ϕ) of VCRS with R134a using different nanoparticles

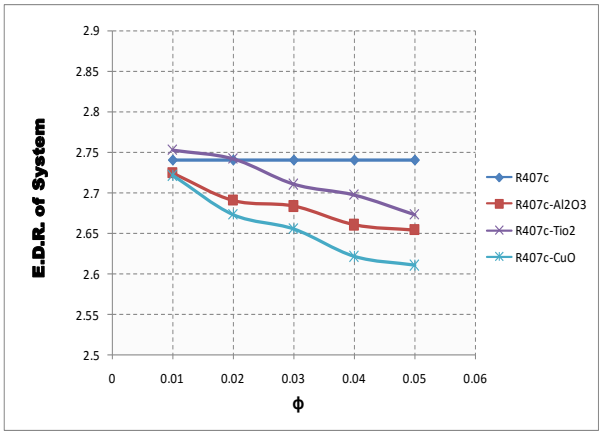


Fig.33 Variation of Exergy Destruction ratio with volume fraction (ϕ) of VCRS with R407c using different nanoparticles

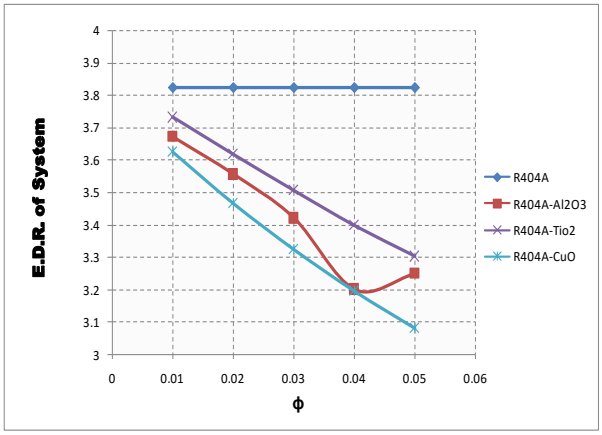


Fig.34 Variation of Exergy destruction ratio with volume fraction (ϕ) of VCRS with R404A using different nanoparticles

Fig 31-34 shows that the E.D Ratio of VCRS will reduce by using nanoparticle based nano refrigerants.

4.5 Effect of nanoparticle volume fraction (ϕ) on the second law efficiency of VCRS

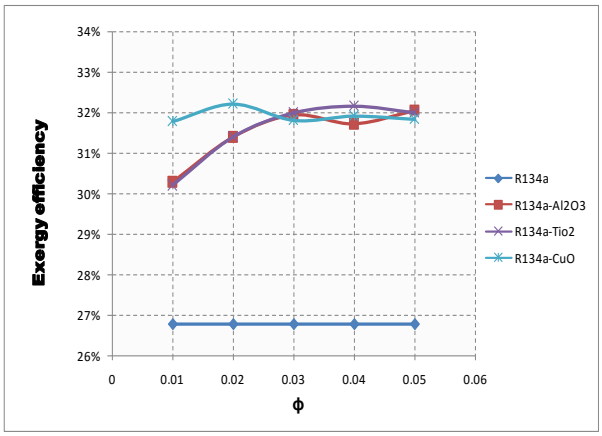


Fig.35 Variation of Exergy Efficiency with volume fraction (ϕ) of VCRS with R134a using different nanoparticles

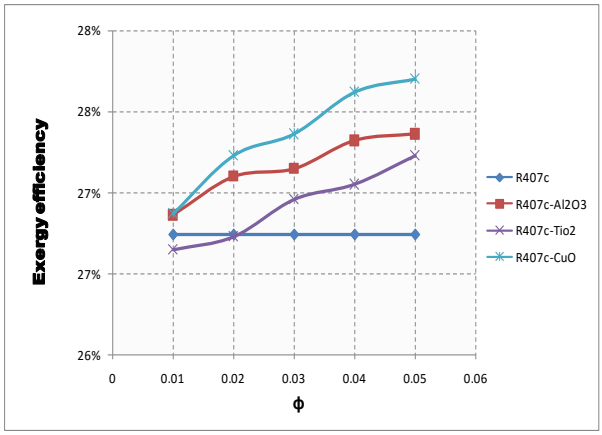


Fig.36. Variation of Exergy Efficiency with volume fraction (ϕ) of VCRS with R407c using different nanoparticles

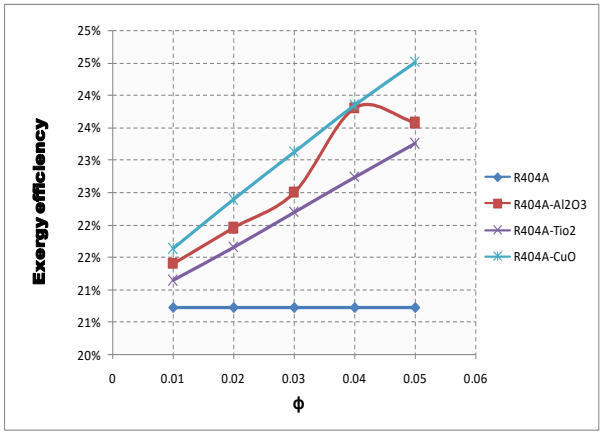


Fig.37 Variation of Exergy Efficiency with volume fraction (ϕ) of VCRS with R404A using different nanoparticles

Fig 33-37 shows that second law efficiency of vapour compression refrigeration system will increase by using nano-refrigerant. It can seen that the 2nd law efficiency of vapour compression refrigeration system using nano-refrigerant R134a/CuO is much higher than the other nano-refrigerant having value approx 30%.

A computational program has been developed to solve non linear equation of vapour compression refrigeration cycle for case (ii) mentioned in abstract. Considering same geometric parameter of the VCRS model theoretical analysis has been done using EES software for nano fluid (nano particle mixed with R718) flowing in secondary circuit and eco friendly refrigerant in primary circuit of VCRS and performance results are given in table-1.

Table 1: Enhancement in C.O.P using Al_2O_3 at 5 vol % nano fluid in secondary circuit as compared without nano refrigerants

For Al_2O_3 at 5 vol %		
Refrigerant	C.O.P.	Improvement C.O.P.
R134a	3.406	18%
R404A	3.0635	16.0%

R407c	3.110488	17.0%
R-152a	3.4102	18.0%
R-600	3.3402	17.1%
R-600a	3.466	20%
R-125	3.033016	15.0%
R-290	3.54312	20%

5. Conclusions

The research work presented in this thesis work following conclusion have been drawn.

- Use of nano particles enhances thermal performance of vapour compression refrigeration system from 8 to 35 % using nano refrigerant in primary circuit
- Use of nanoparticles enhances the thermal performance of vapour compression refrigeration system from 7 to 19 % using nano fluid in secondary circuit.
- Maximum enhancement in performance was observed using R134a/Al_2O_3 nano refrigerant in primary circuit and water in secondary circuit of VCRS.
- Lowest enhancement in performance was observed using R404Aa/TiO_2 nano refrigerant in primary circuit and water in secondary circuit of VCRS.

References

[1] Choi, S. U. S. (1995). Enhancing thermal conductivity of fluids with nanoparticles, in Developments and Applications of Non-Newtonian Flows D. A. Singer and H. P Wang, Eds., American Society of Mechanical Engineers, New York, FED–31/MD-66:99–105.

[2] Maxwell, J. C. (1873). Treatise on Electricity and Magnetism. Clarendon Press, Oxford.

[3] Kimoto, K., Y. Kamilaya, M. Nonoyama, and R. Uyeda (1963). An electron microscope study on fine metal particles prepared by evaporation in argon gas at low pressure, Jpn. J. Appl. Phys., 2: 702.

[4] Jwo et.al, 2009. Effect of nano lubricant on the performance of Hydrocarbon refrigerant system. J. Vac. Sci. Techno. B, Vol.27, No. 3, pp. 1473-1477.

[5] Hao Peng et.al., 2010. Nucleate pool boiling heat transfer characteristics of refrigerant/oil mixture with diamond nano parti cles. International Journal of Refrigeration, Vol.33, pp. 347-358.

[6] Henderson et al. (2010) Experimental analysis on the flow boiling heat transfer of R134a based nanofluids in a horizontal tube. IJHMT , Vol. 53, pp. 944-951.

[7] Bobbo S. et.al, 2010. Influence of nanoparticles dispersion in POE oils on lubricity and R134a solubility. International Journal of Refrigeration, Vol.33, pp. 1180-1186.

[8] Shengshan Bi, Performance of a Domestic Refrigerator using TiO_2-R600a nano-refrigerant as working fluid, Int J of Energy Conservation and Management, Vol. 52, 2011, 733-737.

[9] Lee K, Hwang YJ, Cheong S, Kwon L, Kim S, Lee J. Performance evaluation of nano-lubricants of fullerene nanoparticles in refrigeration mineral oil. Curr Appl Phys 2009;9:128–131.

[10] Wang RX, Xie HB. A refrigerating system using HFC134a and mineral lubricant appended with N-TiO_2(R) as working Fluids. In: Proceedings of the 4th international symposium on HAVC, Tsinghua University; 2003.

[11] S.Z. Heris, S.G. Etemad, M.N. Esfahany, Experimental investigation of oxide nanofluids laminar flow convective heat transfer, Int. Commun. Heat Mass Transf. 33 (2006) 529-535.

[12] Y. He, Y. Jin, H. Chen, Y. Ding, D. Cang, H. Lu, Heat transfer and flow behavior of aqueous suspensions of TiO_2 nanoparticles (nanofluids) flowing upward through a vertical pipe, Int. J. Heat Mass Transf. 50 (2007) 2272-2281.

[13] D.P. Kulkarni, P.K. Namburu, H.E. Bargar, D.K. Das, Convective heat transfer and fluid dynamic characteristics of SiO2-ethylene glycol/water nanofluid, Heat Transf. Eng. 29 (12) (2008) 1027-1035.

[14] K.S. Hwang, S.P. Jang, S. U. S. Choi, Flow and convective heat transfer characteristics of water-based Al_2O_3 nanofluids in fully developed laminar flow regime, Int. J. Heat Mass Transf. 52 (2009) 193-199.

[15] A. Sharma, S. Chakraborty, Semi-analytical solution of the extended Graetz problem for combined electro osmotically and pressure-driven microchannel flows with stepchange in wall temperature, Int. J. Heat Mass Transf. 51 (2008) 4875-4885.

[16] W. Yu, D.M. France, D.S. Smith, D. Singh, E.V. Timofeeva, J.L. Routbort, Heat transfer to a silicon carbide/water nanofluid, Int. J. Heat Mass Transf 52 (2009) 3606-3612.

[17] S.Torii, W.J. Yang, Heat transfer augmentation of aqueous suspensions of nanodiamonds in turbulent pipe flow, J. Heat Transf. 131 (2009) 043203-1 - 043203-5.

[18] U. Rea, T. McKrell, L.W. Hu, J. Buongiorno, Laminar convective heat transfer and viscous pressure loss of alumina-water and zirconia-water nanofluids, Int. J. Heat Mass Transf. 52 (2009) 2042-2048.

[19] Murshed S. M. S., K. C. Leong, and C. Yang (2005). Enhanced thermal conductivity of TiO_2-water based nanofluids, Int. J. Therm. Sci., 44: 367–373.

[20] Hamilton, R. L., and O. K. Crosser (1962). Thermal conductivity of heterogeneous two component systems, I & EC Fundam., 1(3): 187–191.

[21] Xuan, Y., and Q. Li (2003). Investigation on convective heat transfer and flow features of nanofluids, J. Heat Transfer, 125: 151–155.

[22] I.M. Mahbubul , A.Saadah Thermal performance analysis of Al_2O_3 R134a nanorefrigerant , international journal of heat and mass transfer 85 (2015) 1034-1040.

[23] Faulkner, D. J., D. R. Rector, J. J. Davidson, and R. Shekarriz (2004). Enhanced heat transfer through the use of nanofluids in forced convection, Paper IMECE2004-62147, presented at the 2004 ASME International Mechanical Engineering Congress and RD&D Expo, Anaheim, CA, Nov. 13–19.

[24] Wen, D., and Y. Ding (2004). Experimental investigation into convective heat transfer of nanofluids at the entrance region under laminar flow conditions, Int. J. Heat Mass Transfer, 47: 5181–5188.

[25] Lee K, Hwang YJ, Cheong S, Kwon L, Kim S, Lee J. Performance evaluation of nano-lubricants of fullerene nanoparticles in refrigeration mineral oil. Curr Appl Phys 2009;9:128–131.

[26] Joaquin Navarro, Francisco, Angel, 2013. Experimental analysis of internal heat exchanger influence on vapour compression system performance working with R1234yf as drop in replacement of R134a. Applied thermal Engineering, 59, 153-161.